GSI

GSI Report 2011-1
May 2011

SCIENTIFIC REPORT 2010

GSI Helmholtzzentrum für Schwerionenforschung GmbH
Member of the Helmholtz Association

GSI Scientific Report 2010

GSI Report 2011-1
<http://www.gsi.de/library/GSI-Report-2011-1/>

ISSN: 0174-0814
and GSI Report 2010-1

Publisher: GSI Helmholtzzentrum für Schwerionenforschung GmbH,
Planckstr. 1, 64291 Darmstadt, Germany, <http://www.gsi.de>
GSI is a member of the Helmholtz association of national research centres <http://www.helmholtz.de>.
E-only-edition: <http://www.gsi.de/library/GSI-Report-2011-1/>

Editor: Katrin Große,
Contact: gsilibrary@gsi.de, phone: +496159 712610, fax: +496159 713049.
Cover photograph: Gabi Otto.
Publication Date: May 2011
Technical Team at GSI: T. Badura, I. Giese, K. Große, V. Schaa and K. Schiebel.

For the production of this report templates and scripts of the JACoW collaboration (Joint Accelerator Conferences on Web <http://www.jacow.org>) were used.

Foreword

2010 was a year which like no other simultaneously reflected the glorious past, the successful presence and the exciting future of GSI. In July GSI officially celebrated its 40th anniversary, a little bit late, but nobody minded the fact that the date was shifted from december to a pleasant summer day. Most fittingly, the celebration was started by the official naming ceremony of element 112. Following the proposal of Sigurd Hofmann and his discovery team the International Union of Pure and Applied Chemistry decided to name the new element 'Copernicium' after the great astronomer Nicolaus Copernicus. The Hessian Prime Minister Roland Koch accepted the role of godfather of the sofar heaviest element in the periodic table. The anniversary celebration in the afternoon gave ample possibilities to look back at many of the discoveries and highlights GSI scientists and engineers made during the last four decades, but also to meet old and young friends and simply to enjoy the wonderful sunshine of the day.

The long-term future of GSI is FAIR. On October 4, nine countries (Finland, France, Germany, India, Poland, Rumania, Russia, Sweden and Slowenia) signed the international treaty to construct the Facility of Antiproton and Ion Research at the GSI site in Darmstadt. With this exciting and scientifically unique future at the horizon, GSI has already focussed its research and operational structure towards the challenges and opportunities ahead. The FAIR division has left GSI to become the backbone of the newly founded FAIR company. The research at GSI has been structured in 5 scientific columns, matching the four experimental pillars of FAIR (APPA, CBM, NuSTAR, and PANDA) and information technology and high-performance computing. These efforts are supported by the international Helmholtz Alliance EMMI and newly founded Helmholtz Institutes, focussing on hadron physics, the chemistry and physics of superheavies and accelerator research at the HI Mainz and on plasma, laser and atomic physics at the HI Jena. Together with the GSI accelerator division, now under the new leadership of Oliver Kester, the colleagues of the scientific and administrative infrastructures, the partners from the Helmholtzgemeinschaft and from other national and international institutions, the GSI researchers are getting 'fit for FAIR'.

Between history and future, the year 2010 also witnessed a variety of scientific 'firsts'. As planned, mid-size projects like the gas-filled separator TASCA and the SHIPTRAP device have been completed and already successfully used to take data towards pinning down the chemistry of element

114 or to trap nobelium atoms and to determine their mass, respectively. The latter was actually a double-first: Never has an artificially made element heavier than uranium been trapped nor has the mass of a superheavy been measured directly! The m-branch has become an attractive and fastly overbooked workhorse for material research with heavy ions. At the PHELIX laser, in user operation since 2009, the frequency has been doubled and a new 100-TW-beamline was installed at the experimental site Z6, which allowed, for example, to generate plasma-accelerated protons for injection into conventional accelerator structures. Finally, HITRAP and the HADES upgrade are on track and near operation. The former, a trap for highly charged ions, will allow for novel precision experiments in atomic physics and to test fundamental theories like QED. After having unambiguously identified radiation from the dense phase of the reaction zone in medium-ion collisions, HADES will exploit its enhanced capabilities, made possibility by an upgrade of the DAQ and time-of-flight system, by continuing its program with Au+Au collisions in the second half of 2011.

Of course, also the old GSI workhorses like UNILAC and SIS-18 accelerators, the ESR and the SHIP velocity filter have been exploited, as often before, to reach scientific milestones. Making use of the world-record uranium beam intensities at the SIS, achieved by Peter Spiller and his team, more than 60 new isotopes in the neighborhood of the magic neutron number N=126 have been discovered at the FRS Fragment Separator. Bombarding ^{248}Cm with the high-intensity GSI ^{48}Ca beam, isotopes of element 116 with mass numbers 292 and 293 have been produced and detected. The measured production cross sections and decay properties of the two isotopes agree well with results found previously at Dubna. At the ESR, $^{7}Li^{+}$ ions, produced in a Penning ion source, have been used for a precision test of special relativity, improving previous tests of time dilatation by a factor of 4.

GSI collaborates with more than 100 institutions on all continents. One new partner is the European Space Agency (ESA) which has selected GSI as the ground-based facility for investigations in space radiation protection in Europe. A first campaign has been concluded this year, with exciting results on biological effects of cosmic rays obtained by several European groups.

GSI has played a leading role in the design and construction of the ALICE detector at the CERN Large Hadron Collider. After successful runs with 7 TeV proton-on-proton collisions, ALICE took first lead-lead collisions at 2.76 TeV per nucleon pair on november 18 and published first papers on elliptic flow and suppression of charged particle production as well as on charged-

particle multiplicity densities in the remaining weeks of the year.

On november 22, the new supercomputer at the Center for Scientific Computing at the Goethe University Frankfurt has been inaugurated. This machine is not only one of the fastest computers in the world, it also convinces with its low energy consumption using about a quarter of the energy as other machines with the same computing power. The 'green' computer has been developed by Volker Lindenstruth, the head of the IT/high-performance computing research column at GSI. One of its tasks, within the Helmholtz International Center for FAIR, are simulations, data evaluation and high-performance computing towards construction of the FAIR accelerators and experiments.

The present Scientific Report gives again prove of the widespread and high-quality research activities performed at GSI. I wish you much pleasure at reading about achieved scientific milestones, but also about the plans and progress which brings us closer to our ultimate goal - to construct FAIR and to exploit its unprecedented research opportunities.

Karlheinz Langanke
GSI Director of Research

Contents

Status of the FAIR Project *

I. Augustin[1]
[1]on behalf of the FAIR Joint Core Team

General Status

The most part of 2010 was spent on the consolidation of the funding and the preparation of documents and procedures for the creation of the FAIR GmbH. This culminated in the signing of the convention on 4 October 2010 in Wiesbaden. At this event 9 countries (Germany, Finland, France, India, Poland, Romania, Russia, Slovenia and Sweden) signed the convention (see cover of the report). At the same day the FAIR GmbH (FAIR Company) was founded. In the meantime institutions representing six of these countries are shareholders of the company. Several others will join after the completion of the parliamentary process required by these countries.

A Business Management Contract has been signed by FAIR and GSI which distributes tasks and responsibilities between the two companies. The necessary policies and procedures to operate the FAIR GmbH has been set up. The FAIR Council, the Administrative and Finance Committee (AFC), the In-Kind Review Board (IKRB), and the Machine Advisory Committee (MAC) have started to operate. The Science Council of FAIR is being set up.

After the staff of the FAIR Joint Core Team is either assigned to FAIR or other units the FJCT will cease to exist.

Figure 1: Signing of the Business Management Contract by the managing directors of GSI and FAIR

FAIR Technical Division

FAIR and GSI are working closely together in the joint Project House, the All Accelerator Board (AAB). The central document, the Distribution of Work and Responsibilities has been agreed. The In-Kind Contract for the technical supervision, the Rules of Procedure for the AAB and the Accelerator Construction Agreement have been intensively discussed.

The work on In-Kind Contracts which comprises the work package descriptions (Technical Specifications) is proceeding. Altogether a set of about 800 documents covers the components of the accelerators of the Modularized Start Version. While the General Specification is available, work concentrates on the Technical Guidelines and Common Specifications of those subsystems which are known to be contributed via In-Kind Contracts.

Non-in-kind components with long lead times have been identified i.e. the superconducting multipole magnets for Super-FRS and SIS100; associated technical specifications have been requested from the GSI accelerator department to prepare international tendering processes.

FAIR Site and Buildings

After the financial evaluation of the construction project, architects and engineering companies started for the 2nd planning phase, aiming for the building permit by the Darmstadt civil construction authority (Bauaufsicht) by October/November 2011. In parallel, the application for obtaining the construction permit (Errichtungsgenehmigung gem Atomrecht) to the radiation safety authority (HMULEV) is in preparation.

FAIR Research Division

The Research Division is being built up. The staff has been mostly selected and respective personnel transfers are imminent. During the last year several experiments submitted Technical Design Reports which were all favorably evaluated by external experts. In one case the procedure led to the acquisition of detector components by the FAIR GmbH.

Acknowledgements

The entire FAIR Joint Core wishes to thank all colleagues who have supported us over the years. Without you FAIR could not have become a reality.

* Work supported by EU, FP7-211382

The ExtreMe Matter Institute EMMI

P. Braun-Munzinger[1,2,3] *and C. Ewerz*[1,4]

[1]ExtreMe Matter Institute EMMI, GSI, Darmstadt, Germany; [2]Research Division, GSI, Darmstadt, Germany; [3]TU Darmstadt, Germany; [4]University of Heidelberg, Germany

Since 2008 the Helmholtz Alliance 'Cosmic Matter in the Laboratory' is funded in the framework of the Alliance program of the Helmholtz Association. The aim of the Alliance program is to strategically enhance the profiles of the participating Helmholtz Centres and to transfer successful developments into one of the Helmholtz Association's research programs. The research performed within the Helmholtz Alliances is collaborative and brings together universities, Helmholtz Centres and other non-university research institutions. In the case of the alliance 'Cosmic Matter in the Laboratory' the funding contribution from the Helmholtz Association amounts to 18.745 Mio. Euro for six years.

A key step in the strategic positioning of the Helmholtz Alliance 'Cosmic matter in the Laboratory' was to establish a new, world-leading institute for research on matter at the extremes of density and temperature: the ExtreMe Matter Institute EMMI hosted by GSI. It was founded simultaneously with the start of the Alliance in April 2008.

The scientific aim of the ExtreMe Matter Institute is to perform forefront research in the area of matter under extreme conditions. This comprises in particular four key areas of the research field 'Structure of Matter' of the Helmholtz Association:

- quark-gluon plasma and the phase structure of strongly interacting matter
- neutron matter
- electromagnetic plasmas of high energy density
- cold quantum gases and extreme states in atomic physics.

The relevant science themes range from the quark-gluon plasma as it existed shortly after the Big Bang to ultracold quantum gases created in laboratory experiments, to the quantum dynamics of extreme fields, and from hot and highly compressed classical bulk plasmas and to the astrophysically relevant dense medium of nucleons and neutrons that governs the properties of the evolution of supernovae and neutron stars. It hence comprises the study of the coldest, of the hottest, and of the densest known forms of matter in the Universe. The key idea is to conduct this research in an interdisciplinary framework, based upon common underlying concepts for the theoretical and phenomenological understanding of the physical phenomena in the four areas.

Under the lead management of the GSI Helmholtz Centre for Heavy Ion Research the Alliance links 13 German and international research centers and universities as partner institutions:

- GSI Helmholtzzentrum für Schwerionenforschung, Darmstadt, Germany
- Forschungszentrum Jülich, Germany
- Ruprecht-Karls-Universität Heidelberg, Germany
- Johann Wolfgang Goethe Universität Frankfurt, Germany
- FIAS Frankfurt Institute for Advanced Studies, Germany
- Technische Universität Darmstadt, Germany
- Universität Münster, Germany
- Université VI, Paris, France
- Max-Planck-Institut für Kernphysik, Heidelberg, Germany
- Lawrence Berkeley National Laboratory, Berkeley, USA
- Joint Institute for Nuclear Astrophysics (JINA), USA
- RIKEN, Saitama, Japan
- University of Tokyo, Japan.

In addition, the Alliance benefits from the expertise of internationally renowned scientist who are closely linked to it as Associated Partners. Currently, the Alliance has 30 Associated Partners, among them two Nobel laureates.

The partner institutions have committed themselves to creating 18 senior positions, including full professorships and equivalent tenure-track and tenured positions, in the framework of the Alliance. During 2010 the recruiting process for several of these positions has been finalized. By now, 14 of the 18 positions are filled.

Among these positions are four EMMI Fellow positions in experimental physics at GSI, one for each of the main research areas of EMMI. Two of these tenure-track positions had already been filled in 2009 with Dr. Alexandre Gumberidze (atomic physics) and Dr. Paul Neumayer (plasma physics). In 2010, they have been joined by Dr. Ilya Selyuzhenkov (quark-gluon plasma physics) and Dr. Deniz Savran (neutron matter physics). The EMMI Fellows are currently building up their groups and have already started joint activities.

In May 2010, EMMI has signed a *Memorandum of Understanding* with the Polish Academy of Arts and Sciences in Krakow in which both institutions express their interest to establish long term scientific exchanges and collaborations. It is planned to organize a joint yearly workshop (Copernicus Days). In June 2010, a *Memorandum of Understanding* has also been signed with the Helmholtz Institute Jena in order to strengthen the cooperation of EMMI and HI-Jena in the areas of plasma physics and atomic physics. It is planned to organize joint annual lecture series and meetings, the location of which will alternate between Jena and GSI. Furthermore, an agreement has been made with the European Center for Theoretical Studies in Nuclear Physics and Related Areas (ECT*) in Trento to or-

ganize two joint ECT*-EMMI workshops per year. The first two workshops of this kind took place in 2010 at the ECT*.

An important activity of the ExtreMe Matter Institute EMMI is to organize and to host workshops and research programs on topical and interdisciplinary subjects in the area of matter under extreme conditions. 12 EMMI Workshops with strong international participation took place in 2010. In November 2010, the EMMI Physics Days were organized at GSI in which 180 EMMI members participated.

EMMI is about to move to the new office building at GSI. The building offers a lecture hall and four seminar rooms and will hence provide a unique infrastructure for the activities of EMMI, in particular for workshops and programs.

Several renowned experts have visited EMMI partner institutions for extended periods in 2010 as EMMI Visiting Professor, and have made progress in their collaborations with EMMI members.

EMMI is strongly committed to fostering the education and training of young researchers through a postdoctoral research program and training of graduate students. Structured PhD education for students within the Alliance is offered in close collaboration with the various Graduate Schools at the partner institutions, for example with the Helmholtz Graduate School for Hadron and Ion Research (HGS-HIRe), the Heidelberg Graduate School of Fundamental Physics (HGSFP) and the Helmholtz Research School Quark Matter Studies (H-QM). Many of the students in the Alliance have participated in various events (lecture weeks of HGS-HIRe, H-QM and HGSFP, graduate days of the HGSFP etc.) of these Graduate Schools in 2010.

In 2010 the research within EMMI resulted in more than 300 publications in refereed journals. Among the highlights are the following:

- The research program at the CERN Large Hadron Collider (LHC) has seen proton-proton collisions at 7 TeV for the first time. Furthermore, in November 2010 the first lead-lead (Pb-Pb) collisions took place. EMMI scientists of several EMMI partner institutions are members of the ALICE Collaboration and have been strongly involved in prioviding full functionality of detector components, in calibration and in data analysis. Among the most important results is the determination of important properties of the quark-gluon plasma created in the Pb-Pb collisions.
- The EMMI group in Paris has, in the framework of the CREMA collaboration, worked on a new measurement of the proton charge radius. Using laser spectroscopy of muonic hydrogen this experiment provided a measurement 10 times more accurate than the best previous determination. The result turned out to be 4% lower than previous measurements, resulting in a discrepancy of 5 standard deviations. This result has sparked considerable activity both on the theoretical and on the experimental side.
- EMMI members in Heidelberg have made considerable progress in experiments with cold atomic gases. In particular, they studied few-body physics in a three-component Fermi gas. For the first time, Efimov trimers – weakly bound universal three-body bound states – have been observed directly using spectroscopic techniques.
- At the radioactive-beam facility RIBF at RIKEN, 45 new neutron-rich isotopes have been created. They include a few classical waiting point nuclei for the r-process, such as ^{128}Pd. This constitutes a major progress towards the understanding of the r-process taking place in extremely neutron-rich astrophysical environments. It is likely to be responsible for the creation of a large fraction of the heavy elements in the Universe.
- Considerable progress has also been made in the theoretical understanding of various aspects of strongly coupled many-body systems which form the matter under consideration in all EMMI research areas. The findings concern, for example, thermo- and hydrodynamics, thermalization and turbulence that occur in strongly coupled systems. A variety of methods has been used, among them renormalization group methods, the string theory / gauge theory (AdS/CFT) correspondence, as well as large-scale computer simulations.

The first year of physics with the ALICE experiment at the LHC

The ALICE Collaboration[*]

The year 2010 was entirely focussed on first experiments with the CERN LHC accelerator. After the successful start in November and December 2009, with first results on multiplicity distributions in pp collisions at $\sqrt{s} = 900$ GeV [1], the research program started in March 2010 with pp collisions at $\sqrt{s} = 7$ TeV. For the whole 2010 running period the GSI/EMMI ALICE group was instrumental in providing a fully functional and well calibrated TPC as well as in developing calibration and analysis procedures for the TRD. The ALICE group focussed on a number of important physics analyses. Particular emphasis was placed on the following physics topics:

1. determination of charged particle transverse momentum spectra and their dependence on associated multiplicity, see publication [2].
2. analysis of Hanbury Brown–Twiss correlations and the determination of the radii of the emitting source in pp collisions, see publication [3].
3. analysis of transverse momentum spectra for identified charged particles in pp collisions at $\sqrt{s} = 7$ TeV, manuscript submitted for publication.
4. analysis of spectra and yields of strange particles produced in pp collisions at $\sqrt{s} = 7$ TeV, manuscript submitted for publication.
5. analysis of π^0- and η-meson production in pp collisions at $\sqrt{s} = 7$ TeV via conversion electron measurements.
6. determination of open charm production in pp collisions at $\sqrt{s} = 7$ TeV via the measurement of hadronic decays.
7. determination of open charm and open beauty production in pp collisions at $\sqrt{s} = 7$ TeV via the measurement of semi-leptonic decays.
8. measurement of J/ψ production in pp collisions at $\sqrt{s} = 7$ TeV.
9. measurement of the low mass electron-positron continuum and of low mass vector mesons in pp collisions at $\sqrt{s} = 7$ TeV.

For analyses five to eight, manuscripts are in final stages of preparation. The difficult low mass continuum analysis has just produced first, interesting results.

In addition to all these physics efforts for pp collisions, the ALICE group was instrumentally involved in preparation, running, and first analysis of the Pb–Pb collision data which were taken in November/December 2010 at $\sqrt{s_{NN}} = 2.76$ TeV. The main topics worked on by the GSI/EMMI group are:

1. determination of centrality in Pb–Pb collisions.
2. measurement of the nuclear modification factor in Pb–Pb collisions, see publication [4].
3. analysis of Hanbury Brown–Twiss correlations and the determination of the radii of the emitting source in Pb–Pb collisions, see publication [5].

In addition to all these tasks the group is responsible, together with GSI-IT, of operating the ALICE tier2 center at GSI as well as providing analysis platforms for all German ALICE members.

In total, the first year of physics at the LHC yielded many exciting new results and ten publications in refereed journals.

References

[1] K. Aamodt *et al.* (ALICE Collaboration), Eur. Phys. Jour. C 65 (2010) 111.

[2] K. Aamodt *et al.* (ALICE Collaboration), Phys. Lett. B 693 (2010) 53.

[3] K. Aamodt *et al.* (ALICE Collaboration), Phys. Rev. D 82 (2010) 052001.

[4] K. Aamodt *et al.* (ALICE Collaboration), Phys. Lett. B 696 (2010) 30.

[5] K. Aamodt *et al.* (ALICE Collaboration), Phys. Lett. B 696 (2010) 328.

[*] The list of members and institutions is available at `http://aliweb.cern.ch/General/Members/List_Institutes.html`

A p_T reference spectrum for pp collisions at $\sqrt{s} = 2.76$ TeV at ALICE

A. Arend, H. Appelshäuser, H. Büsching, P. Lüttig*
for the ALICE collaboration, Institut für Kernphysik, Goethe - Universität Frankfurt am Main, Germany

The first heavy ion run period with an energy of $\sqrt{s_{NN}} = 2.76$ TeV has successfully finished at CERN LHC. The suppression of charged particle production at large transverse momenta in central Pb–Pb Collisions [1] at this energy measured with the ALICE [2] experiment is one of the first exciting results using data taken during that run. This measurement is based on the nuclear modification factor (R_{AA}) and, furthermore, requires a p_T reference spectrum for pp collisions at the same energy which is not available as recorded data. In this report a pure data driven interpolation technique to obtain this reference spectrum is described. This method is exclusively based on p_T-spectra measured with the ALICE experiment in the pp runs at 0.9 and 7 TeV.

Construction of the reference spectrum

The described data driven interpolation method is founded on minimal physical assumptions. Based on the yields of the measured p_T-spectra at the energies of 0.9 and 7 TeV, the yield for 2.76 TeV has been interpolated for every p_T-bin only by assuming that the functional dependency is a power law. This bin-by-bin procedure is exemplary shown for the bin $p_T = 3.7$ GeV in Figure 1.

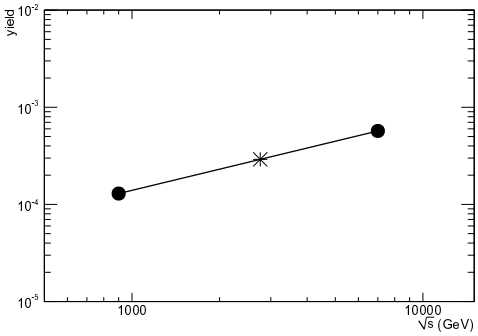

Figure 1: Demonstration of the applied interpolation method: the yield of the input spectra for every p_T-bin is plotted and the yield of the according target energy is interpolated assuming a power law. This figure is exemplary for $p_T = 3.7$ GeV.

The statistical errors of the resulting spectra are derived by applying Gaussian error propagation using the given statistical errors of the two input spectra. The systematic errors have been determined by comparing the resulting spectrum with spectra calculated with alternative approaches as described subsequently.

Resulting spectra and comparison to alternative approaches

The resulting spectrum is shown in Figure 2. Two alternative approaches to obtain the spectrum are plotted: the first one is a Pythia 8 based Monte Carlo calculation; the second one is to scale the measured spectra at 0.9 TeV using ratios originating from NLO calculations. The p_T spectrum measured by the CDF experiment at an energy of 1.96 TeV is displayed for comparison. The NLO scaled spectrum and the spectrum measured by CDF are used to evaluate the systematic errors of the interpolation method.

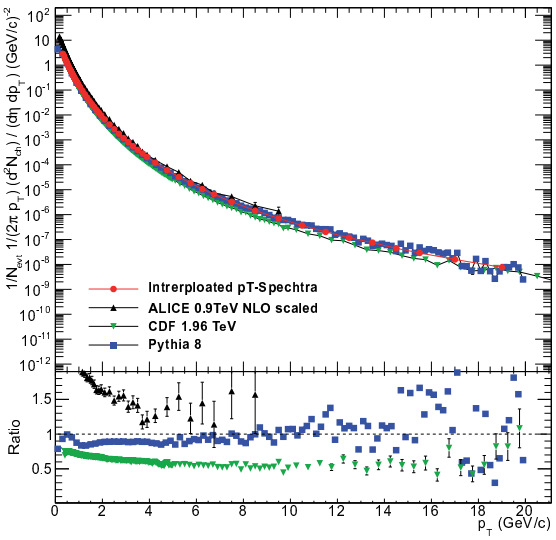

Figure 2: Upper pad: Resulting spectra using the interpolation method in comparison with Pythia 8, NLO-scaled 0.9 TeV data and the spectra measured by CDF. Lower pad: ratio of the displayed spectra to the spectra derived from the interpolation method.

References

[1] Suppression of Charged Particle Production at Large Transverse Momentum in Central Pb–Pb Collisions at $\sqrt{s_{NN}} = 2.76$ TeV, Phys. Lett. B **696** (2011) 30

[2] The ALICE experiment at the CERN LHC, 2008 JINST **3** S08002, 2010

* arend@ikf.uni-frankfurt.de

Two- and Three-Particle Correlations With an Intermediate or High-p_T Trigger Particle*

J.G. Ulery† *and H. Appelshäuser* [1]

[1]Institut für Kernphysik Goethe Universität, Frankfurt, Germany

Introduction

Currently at the Large Hadron Collider (LHC) protons have been collided at energies of up to 7 TeV and lead ions at energies up to 2.76 TeV per nucleon pair. These collisions produce an explosion of many particles and there are many ways to study them. One method is to look at jets. We, in particular, are looking at correlations of particles with an intermediate or high-p_T trigger particle. These intermediate or high-p_T particles are likely to come from jets. In *pp* collisions, these correlations can provide information on the fragmentation of the jet. In central heavy-ion collisions, these correlations can be used to study how the jet and medium produced in these collisions interact.

Two-Particle Correlations

Our 2-particle correlations are performed by looking at the angular correlations of a higher p_T, used to preferentially select on jets, and lower p_T particles in the event. Not all of the other particles in the event are correlated with the trigger particle so a background must be subtracted to extract our signal. The background is constructed by event mixing. All shapes that show up in the mixed event are from the detector acceptance effects on the correlation; therefore, we can use the mixed events to correct for this effect. Since we trigger on intermediate and high-p_T particles, we not only preferentially select jets we also bias towards events with higher multiplicity. This leaves the true level of the backgrounds uncertain. We make the assumption that the true signal goes to zero at the minimum and use this to determine the normalization for the background. Figure 1 shows the two-particle correlation in both azimuth and pseudorapidity from *pp* collisions measured in the ALICE detector at the LHC.

Three-Particle Correlations

Three-particle correlations have also been studied. These have been studied as the correlation between an intermediate or high-p_T trigger particle and pairs of lower p_T particles from the same event. These correlations can reveal more detail about the structures that might be seen in heavy-ion events. For instance they can tell whether structures are from conical emission and whether different structures that maybe been seen in the correlations are correlated with each other. These correlations have backgrounds from two-particle correlations in addition to the uncorrelated backgrounds. All of the backgrounds can be obtained from a combination of event mixing, two-particle correlations and flow measurements.

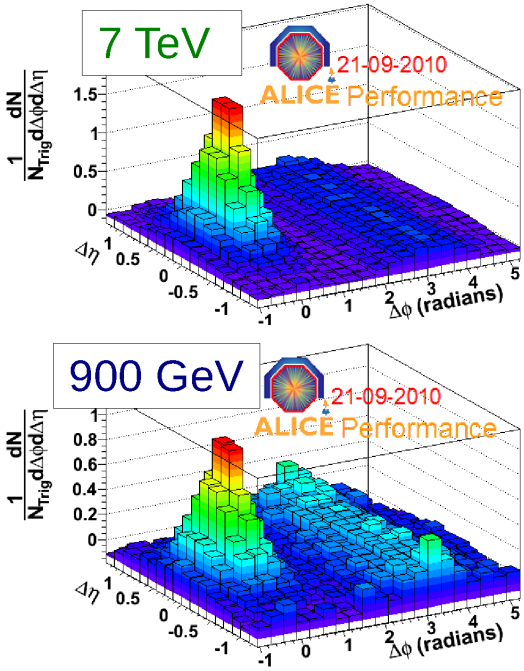

Figure 1: Two-particle correlations in azimuth and pseudorapidity in *pp* collisions measured in ALICE. Top $\sqrt{s} = 7$ TeV. Bottom: $\sqrt{s} = 900$ GeV.

Conclusions

Analysis of 2- and 3-particle jet-like correlations have been performed on Pythia and Hijing events. The analysis is currently underway on 0.9 and 7 TeV *pp* collisions and 2.76 TeV per nucleon pair Pb+Pb collisions taken in the ALICE experiment at the LHC. The analysis will provide information on fragmentation in *pp* collisions and medium modification in heavy-ion collisions. Preliminary results for *pp* collisions have been publicly presented [1].

References

[1] 5th International workshop on High-Pt Physics at LHC, Mexico City, Mexico, Sept 2010. http://indico.nucleares.unam.mx/materialDisplay.py?contribId=35&materialId=slides&confId=205

* Work supported by ExtreMe Matter Institute, GSI, and BMBF

† ulery@ikf.uni-frankfurt.de

Performance of an algorithm to discriminate quark and gluon jets with ALICE at the LHC

H. León Vargas[1], *C. Blume*[1], *and C. Klein-Bösing*[2]
[1]IKF, University of Frankfurt, Germany; [2]Institut für Kernphysik Münster, Germany

Introduction

In this report we study the feasibility of a method that allows to obtain jet samples, from proton-proton collisions, enhanced in quark or gluon content. We compare the performance of the method on pure Pythia Monte Carlo events and after the full reconstruction of the events through the simulation of the ALICE experiment. It is shown that the performance of the method is not deteriorated by experimental effects such as resolution and inefficiency. A more detailed explanation of the study is presented in [1].

The track multiplicity method

This method is based on a modified version of that proposed in [2] for segmented calorimeters, in this case for jets reconstructed using only charged particles. The track multiplicity algorithm is implemented in the following way: the tracks that compose a given jet are ordered in decreasing magnitude of transverse momentum. Then the transverse momenta of the ordered tracks are added until a certain fraction of E_T^{Jet} is recovered, in this case 90%. This minimum number of tracks is defined as the variable $NT90$.

Figure 1 shows the distributions of the mean values of $NT90$ for quark, gluon and all jets. One can observe that the mean values of this variable are larger for gluon jets compared to quark jets of the same E_T^{Jet}. This way it is possible to select quark or gluon jets based on the multiplicity needed to recover 90% of the E_T^{Jet}.

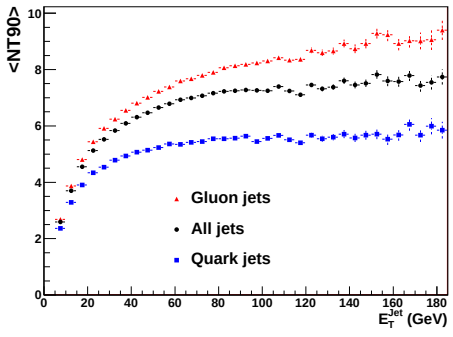

Figure 1: Mean values of $NT90$ as a function of E_T^{Jet} for Pythia jets.

Performance of the $NT90$ method

In order to evaluate the enhancement power of the variable $NT90$, the efficiency (Eq. (1)) and purity (Eq. (2)) for selecting quark/gluon jets was studied as a function of the cuts on $NT90$. This study was done for a fixed value of the E_T^{Jet} = 20 $\pm$ 5 GeV.

$$\varepsilon_{q/g} = \frac{\Sigma_i Jet^i_{q/g}|_{cut}}{\Sigma_i Jet^i_{q/g}} \quad (1) \qquad P_{q/g} = \frac{\Sigma_i Jet^i_{q/g}|_{cut}}{\Sigma_i Jet^i_{q+g}|_{cut}} \quad (2)$$

Figure 2 shows the results from the pure MC events and for the same events after the full detector simulation, for the selection of gluon jets from the minimum bias sample. The cuts are defined as the minimum value on the number of tracks necessary to recover 90% of E_T^{Jet}. As one can see, the inclusion of the detector response does not affect the performance of the method.

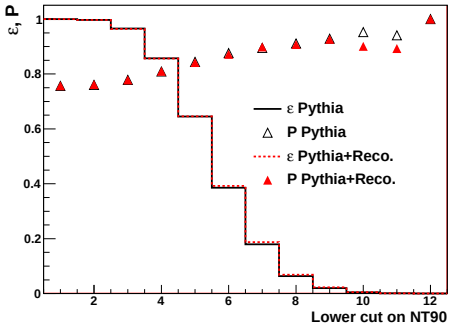

Figure 2: ε and P to select gluon jets from the as a function of the cut on $NT90$. The results from pure Pythia are shown with a solid line and open triangles and the results after the ALICE simulation with a dashed line and full triangles.

Conclusions

The feasibility of a method to obtain samples enriched on quark or gluon content has been studied. It was shown using a full simulation of ALICE that it is possible to use a tagging variable based on charged track multiplicity to obtain jet samples enhanced in quark or gluon content in proton-proton collisions.

It is clear that the $NT90$ tagging method biases the jet samples towards having a certain structure, i.e. soft gluon jets and hard quark jets. However $NT90$ can also be used as a jet structure observable that can be studied to compare jets from proton-proton collisions with those produced in heavy-ion collisions.

References

[1] H. León Vargas, *arXiv:1010.5899v1* (2010).
[2] J. Pumplin, *Phys. Rev. D* **44** (1991) 2025-2032.

Performance Studies for the Measurement of $\psi(2S)$ via the Decay Channel $\psi(2S) \rightarrow J/\psi\,\pi^+\pi^- \rightarrow e^+e^-\pi^+\pi^-$ with the ALICE Detector

M. Pohl[1], *C. Blume*[1], *F. Kramer*[1], *and the ALICE Collaboration*

[1]Goethe University, Frankfurt am Main, Germany

The measurement of quarkonia production in heavy-ion collisions plays a special role in investigations of the Quark-Gluon Plasma, as studied by the ALICE experiment at the LHC [1]. An important baseline for such studies are corresponding measurements in pp collisions. The ψ' is of particular interest because it allows to estimate the contribution of secondary J/ψ to the total measured yield which results from the decay of excited charmonium states. With a branching ratio of 2% the decay channel

$$\psi' \rightarrow J/\psi\,\pi^+\pi^- \rightarrow e^+e^-\pi^+\pi^- \qquad (1)$$

is about three times more likely than the dilepton decay [2]. For the study of geometrical acceptance and reconstruction efficiency of the central barrel detectors - Inner Tracking System (ITS), Time Projection Chamber (TPC) and Transition Radiation Detector (TRD) - a pure ψ' Monte Carlo data set is used, which is based on distributions measured by the CDF collaboration [3]. Every reconstructed track has to pass quality cuts and is afterwards identified by using MC information. Detector response and PID were parameterized and included in the identification process. After this procedure these particles are defined as the reconstructed particles. The first step is the J/ψ reconstruction via the $e^{\pm}$ daughter tracks. The second is the reconstruction of ψ' with these combinations and the $\pi^{\pm}$ tracks. The MC information allows to calculate the geometrical acceptance and the reconstruction efficiency. The geometrical acceptance

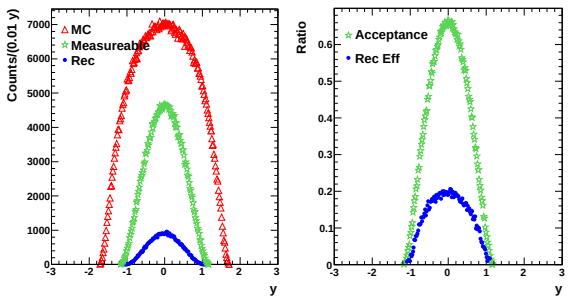

Figure 1: ψ' acceptance and reconstruction efficiency versus rapidity (y). The left plot shows the rapidity spectra of simulated (triangles), measurable (stars) and reconstructed (squares) ψ'. The right plot shows the acceptance, defined as the ratio of measurable and simulated spectra (stars) and the reconstruction efficiency, defined as the ratio of reconstructed and measurable spectra (squares).

is defined as the ratio between all measurable and all produced particles. Measurable particles are all particles, that fall into the acceptance of the central barrel detectors. Particles with charged daughter particles in the pseudorapidity interval $|\eta|_{\mathrm{daugther}} < 1.2$ are potentially measurable. In Fig. 1 the acceptance as a function of the rapidity is shown. The integral of the ratio spectrum corresponds to an overall geometrical acceptance of 35.7%. The ratio between all reconstructed and all measurable particles is termed reconstruction efficiency. It contains the efficiency of the reconstruction process, the particle identification and dead areas of the detectors. The integral of the ratio spectrum corresponds to a reconstruction efficiency of 16.4%. The differential geometrical acceptance and reconstruction efficiency as a function of the transverse momentum (p_{T}) are shown in Fig. 2.

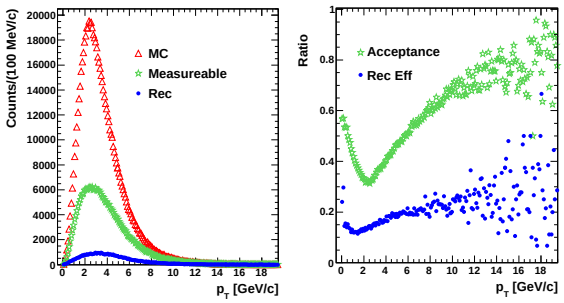

Figure 2: ψ' acceptance and reconstruction efficiency versus the transverse momentum (p_{T}). The left plot shows the p_{T} spectra of simulated (triangles), measurable (stars) and reconstructed (squares) ψ'. The right plot shows the acceptance defined as the ratio of simulated and measurable spectra (stars) and the reconstruction efficiency defined as the ratio of measurable and reconstructed spectra (squares).

A study of the signal-to-background ratio (S/B) of specific energies and in pp or Pb-Pb collisions is possible with a corresponding MC data set. This method of reconstruction produces a non negligible amount of background. Thus an improvement of the S/B ratio is an important issue. A promising way is a cut study for the transverse momentum (p_{T}) of the ψ' daughters. Since the rest masses of J/ψ and the pions add to 3.377 GeV and the rest mass of the ψ' is 3.686 GeV [2], there is a small amount of kinetic energy from the decay itself, so most of the daughters should have a low p_{T}. First steps for this study are in progress.

References

[1] The ALICE Collaboration, 2008 JINST 3 S08002, 2010.

[2] Particle Data Group, "Particle Physics Booklet", Institute of Physics Publishing, July 2010.

[3] D. Acosta et al., arXiv:hep-ex/0412071v1, 2004.

Event-by-event fluctuation studies of mean transverse momentum in *pp* collisions at $\sqrt{s}$ = 900 GeV and 7 TeV for the ALICE experiment

S. Heckel[1], *H. Appelshäuser*[1], *H. Büsching*[1], *and the ALICE collaboration*
[1]Institut für Kernphysik, Goethe-Universität, Frankfurt/Main, Germany

Event-by-event fluctuations of the average transverse momentum $\overline{p_T}$ of particles produced in heavy ion collisions have been proposed as a probe of phase instabilities near the QCD phase transition. Fluctuation measurements could also provide information about the onset of thermalisation in the system. The corresponding measurement of event-by-event fluctuations in *pp* collisions provides valuable information as a reference measurement for heavy ion collisions. The ALICE experiment at the CERN LHC has measured charged particle production in *pp* collisions at $\sqrt{s}$ = 900 GeV and 7 TeV. In preparation of the data analysis Monte Carlo simulations have been performed using the Pythia6 Perugia-0 event generator and are presented in the following.

In this analysis only events have been considered with a primary vertex along the beam axis not more than 10 cm from the nominal interaction point. On the single track level standard ALICE (2010) quality cuts for the TPC (Time Projection Chamber) and ITS (Inner Tracking System) analyses have been used. Furthermore, only tracks in the pseudorapidity range of $|\eta| < 0.8$ and in the transverse momentum range of $0.15 < p_T < 2$ GeV/c have been considered. Studies of the systematic uncertainties are ongoing. After all cuts, 3.9 M events from the $\sqrt{s}$ = 900 GeV Monte Carlo sample and 90 M events from the $\sqrt{s}$ = 7 TeV sample have been analysed.

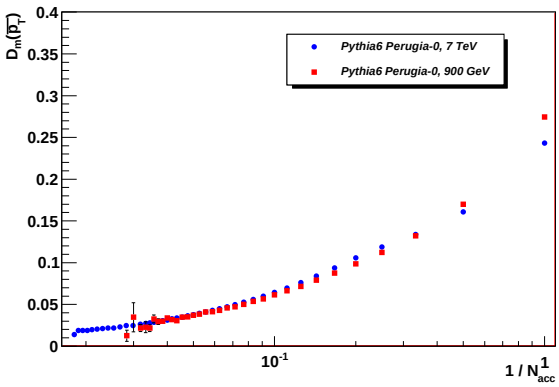

Figure 1: Dispersion $D_m(\overline{p_T})$ of the average event transverse momentum as a function of the inverse event multiplicity $1/m$. Errors are statistical only.

The event-by-event fluctuations of mean transverse momentum have been analysed in two different ways. As a first approach the dispersion $D_m(\overline{p_T})$ of the mean event transverse momentum $\overline{p_T}$ has been studied as described in [1]:

$$D_m(\overline{p_T}) = \frac{\langle \overline{p_T}^2 \rangle_m - \langle \overline{p_T} \rangle_m^2}{\langle \overline{p_T} \rangle_{sample}^2}$$

Angular brackets $\langle\rangle$ indicate an average over all events (for the whole $sample$ or for a multiplicity m), while $\overline{p_T}$ is the mean transverse momentum of a single event. Figure 1 shows $D_m(\overline{p_T})$ as a function of the inverse event multiplicity as obtained with the Monte Carlo simulations.

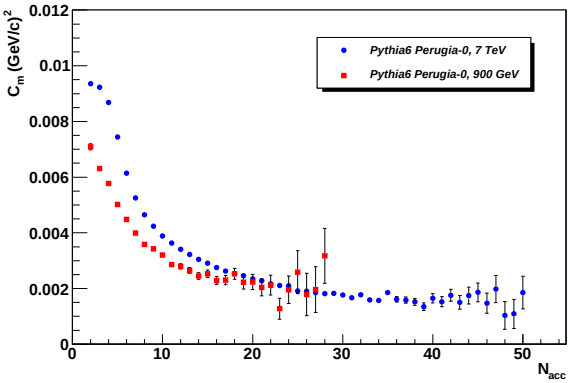

Figure 2: Two-particle p_T correlator C as a function of the event multiplicity m. Errors are statistical only.

In addition, the two-particle p_T correlator C has been analysed as described in [2]:

$$C = \frac{1}{\sum_{k=1}^{n_{ev}} N_k^{ps}} \cdot \sum_{k=1}^{n_{ev}} \sum_{i=1}^{N_k} \sum_{j=i+1}^{N_k} (p_{T,i} - \langle p_T \rangle)(p_{T,j} - \langle p_T \rangle)$$

This has been done for the whole data set, where n_{ev} is the total number of events, and as a function of the event multiplicity, where n_{ev} is the number of events with this multiplicity. N_k is the number of particles in event k and $N_k^{ps} = 0.5 \cdot N_k(N_k - 1)$ is the number of pairs in event k. The results averaged over the whole Monte Carlo samples are $C = 0.0054$ for $\sqrt{s}$ = 900 GeV and $C = 0.0066$ for $\sqrt{s}$ = 7 TeV. The multiplicity dependent results are shown in figure 2.

References

[1] D. Acosta et al., CDF Collaboration, Phys.Rev.D **65** 072005

[2] D. Adamova et al., CERES Collaboration, Nucl.Phys. A811:179-196, 2008

Online Drift Velocity Calibration with the Laser System of the ALICE-TPC

M. Arslandok[1], H. Appelshäuser[1], M. Ivanov[2], H.R. Schmidt[3], J. Wiechula[3], and the ALICE Collaboration

[1]Institut für Kernphysik (IKF), Goethe-Universität, Frankfurt; [2]GSI, Darmstadt; [3]Eberhard Karls Universität,Tübingen

The ALICE Time Projection Chamber (TPC) [1] is the main tracking detector of ALICE. For a precise reconstruction of particle tracks in the TPC, the calibration of the drift velocity, which in conjunction with the drift time provides the z position of the traversing particles, is essential. To reach the design goals, the required drift velocity resolution is of the order of 10^{-4}.

Online Drift Velocity Calibration Method

The online drift velocity calibration method provides calibration parameters required at the very beginning of the offline reconstruction process in order to determine the z position of the particle tracks with a sufficient accuracy before the combined track finding [2]. It uses the TPC Laser System which generates 336 straight laser tracks, similar to ionizing particle tracks, at known positions in the drift volume of the TPC. A subset of these tracks, showing sufficiently small distortion effects, is used in the analysis. The resulting time dependent drift velocity correction parameters are stored in a database and provide start values for the offline reconstruction process of the ALICE TPC.

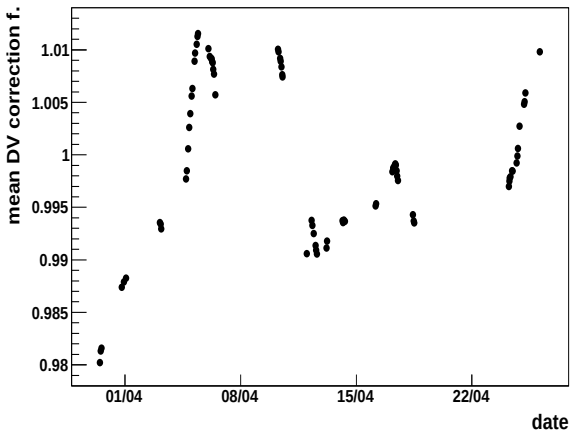

Figure 1: *Time dependence of the mean drift velocity correction factor distribution.*

The analysis was carried out on 45 physics runs, taken in April 2010. The raw data is filtered to remove noise and regions with large distortions and afterwards stored in a multidimensional histogram. The processing of the histogrammed data is done in several steps.

By looping over all the bins in the histogram, clusters of adjacent signals in space and time are reconstructed. These measured clusters are then associated to the ideal laser tracks by selecting the ones which have the minimum distance to the ideal cluster points.

After a further cleanup of the associated clusters, they are fitted with respect to the ideal clusters. The drift velocity correction factors, as well as the χ^2 values, were obtained as fit parameters. Fig.1 shows the mean drift velocity correction factors obtained for the analysed data taking period. As can be seen, the drift velocity is rather unstable in time, resulting mostly from pressure variations, but also slow changes in the gas composition. To test the performance of the method, the χ^2 and a comparison to a reference method were used as benchmarks.

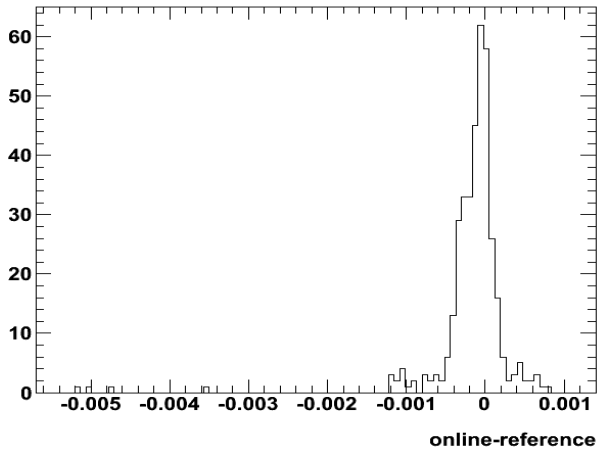

Figure 2: *Drift velocity correction factor difference between online and reference laser calibration method.*

Fig.2 shows the drift velocity correction factor difference between online and the reference laser calibration method. Having achieved a reasonable agreement between the online laser calibration method and the reference method on the level of about 2×10^{-4}, the study was finalized and the whole functionality of the code was implemented into a calibration class within the ALICE offline framework. The online drift velocity calibration method is currently being used in the first reconstruction pass in ALICE.

References

[1] ALICE TPC Collaboration, "The ALICE TPC, a large 3-dimensional tracking device with fast readout for ultra-high multiplicity events", Nucl. Instr. Meth. A622, 316-367, (2010).

[2] ALICE Collaboration, "ALICE Technical Design Report of the Computing", CERNLHCC-2005, 2005.

Calibration of the ALICE Transition Radiation Detector

R. Bailhache[1], J. Book[1], W. Yu[1], A. Andronic[2], M.Al Helwi[3], R. Grajcarek[3], K. Schweda[3], C. Blume[1], H. Appelshäuser[1], J. Stachel[3], and the ALICE TRD collaboration

[1]IKF, Frankfurt, Germany; [2]GSI, Darmstadt Germany; [3]University of Heidelberg, Heidelberg Germany

The Transition Radiation Detector (TRD) [1] is used to track charged particles and identify electrons at momenta above 1 GeV/c in the central barrel ($|\eta|<0.9$) of the ALICE experiment at the LHC. It is composed of 540 large area drift chambers filled with a gas mixture of $CO_2(15\,\%)/Xe$. The tracking and PID algorithms of the detector rely on the knowledge of drift velocity of the electrons in the gas and the amplification factor depending on the temperature and pressure, the gas composition and the chamber geometry.
In 2010, 7 out of the 18 TRD supermodules were installed in the ALICE setup. Approximately 10^9 proton-proton and 8×10^6 lead-lead minimum-bias collision events were collected at respectively $\sqrt{s}$=7 TeV and $\sqrt{s_{NN}}$=2.76 TeV. The calibration constants were corrected chamber by chamber for variations of the temperature, pressure and gas composition during physics data-taking. About 9 % of the 210 detectors had smaller anode or drift voltage. The static gain profiles of each chamber were moreover determined with dedicated data-taking periods, where radioactive Krypton was injected in the gas mixture [2].

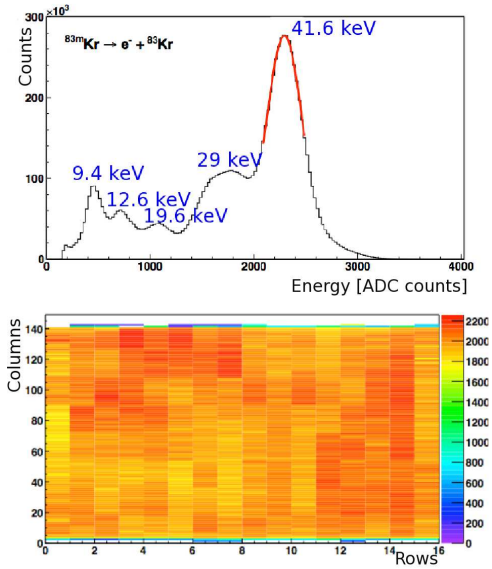

Figure 1: Top: Experimental Krypton spectrum of a single TRD chamber. Bottom: mean value of the Gaussian fit as function of the pad position in the chamber

The top panel of Fig.1 shows the energy spectrum of the Krypton decay as detected in one chamber. The five main decay channels are clearly visible. The gas gain is determined from the mean value of the Gaussian fit plotted in red. The gain profile of the chamber is presented in the bottom panel as function of the pad position.
Calibration procedures running on the High Level Trigger [3] during pp data taking provided a first estimation of the calibration constants chamber by chamber. A dedicated reconstruction pass performed offline at CERN allowed to improve the calibration accuracy. The amplification factor is extracted from the most probable value of the deposited energy distribution of the charged particles produced in the collisions. After removing the chambers with low anode voltage, the spread of the gain over the chambers is of the order of 10 %. At least 1000 tracklets per chamber are required to achieve an accuracy of about 2 %.
The drift velocity is extracted from the correlation between the azimuthal angles of the local tracklet in one chamber and the global refitted track using also information from the Time Projection Chamber. The dispersion of the drift velocity over the chambers is remarkable small (of the order of 3 %). Change of gas purifiers can be identified in time. The effect on the drift velocity is nevertheless small (of the order of 6 %). Fig.2 shows the drift velocity of each chamber as function of their electric drift field for a Pb-Pb run, compared to Magboltz simulations done for the corresponding gas mixture (Xe,CO_2(15 %)) at 1000 mbar.

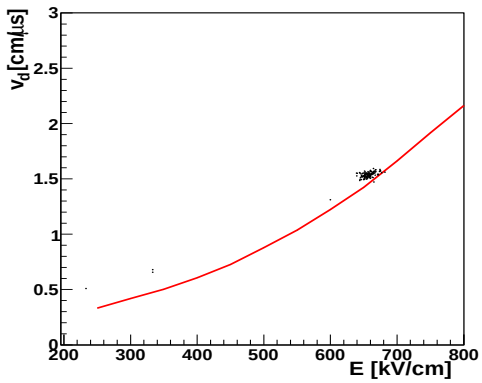

Figure 2: Drift velocity v_d as function of the drift field E in the chambers compared to Magboltz simulations

The calibration of the TRD is in constant development to improve the relative good quality already reached in 2010.

References

[1] ALICE Transition Radiation Detector Technical Design Report, ALICE TDR 9, CERN/LHCC 2001-021

[2] Gain calibration of the ALICE TRD with Krypton (^{m83}Kr), M.Al Helwi et al, GSI report 2009

[3] Implementation of the ALICE TRD into the High-Level-Trigger, T.Rascanu et al, GSI report 2009

Status of the CBM Experiment at FAIR*

P. Senger[1] and the CBM Collaboration
[1]GSI, Darmstadt, Germany

Observables

The Compressed Baryonic Matter (CBM) experiment is designed to explore the QCD phase diagram in the region of high net-baryon densities using rare diagnostic probes.. The layout of the CBM detectors is driven by the corresponding experimental requirements concerning reaction rates, radiation tolerance, particle densities, and selectivity. The experimental challenges are illustrated in figure 1 which depicts the yield of various particle species produced in central Au+Au collisions at 25 A GeV. The yield is defined as the product of particle multiplicity times branching ratio for the decay products under consideration, i.e the dileptonic decay of vector mesons (ρ, ω, φ, J/ψ) and the hadronic decay of open charm (D mesons). Note, that the particle yield per collision spans 13 orders of magnitude with leptons and hadrons in the exit channel, embedded in about 800 charged particles. Multi-strange hyperons, vector mesons and charmed particles will be measured for first time at FAIR energies with CBM which, therefore, has a substantial discovery potential.

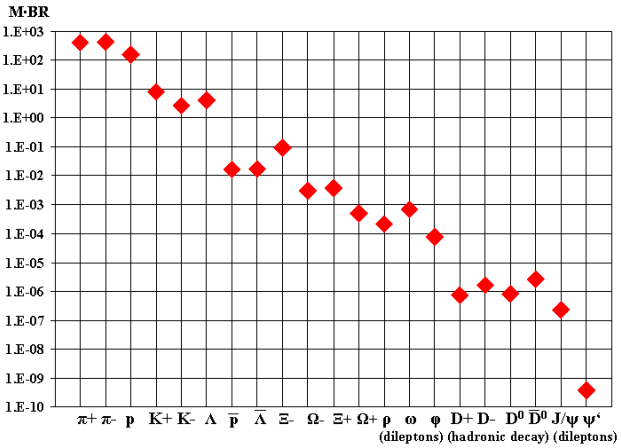

Fig.1: Particle multiplicities times branching ratio for central Au+Au collisions at 25 A GeV as calculated with the HSD transport code and the statistical model. For the vector mesons (ρ, ω, φ, J/ψ) the decay into lepton pairs was assumed, for D mesons the hadronic decay into kaons and pions.

*Supported by the Hessian LOEWE initiative through the Helmholtz International Center for FAIR (HIC for FAIR), and by EU/FP7 Hadronphysics2

Selected R&D activities for CBM

The superconducting dipole magnet
The CBM SC dipole magnet has a large aperture (gap height 130 cm, gap width 160 cm) in order to host the Silicon Tracking System (STS). The last STS station exhibits a height of about 120 cm including its Front-End boards and the thermal enclosure. In beam direction, the magnet yoke is very compact (length 100 cm) in order to achieve a polar angle acceptance of ±25°. The engineering design of the magnet is in progress.

The Micro-Vertex Detector
The precise determination of the secondary decay vertices of charmed particles requires a highly-granulated, fast, radiation-hard, and low-mass detector system. The CBM Micro-Vertex Detector (MVD) consists of silicon pixel stations which are based on ultra-thin "Monolithic Active Pixel Sensors" (MAPS). In 2010 sensors could be produced with a high resistivity CMOS process, resulting in a high signal-to-noise value even after irradiation with an integrated neutron dose of 10^{13} n_{eq}/cm^2. Further improvements are expected with smaller feature size. A prototype read-out-system and a mechanical detector design have been developed.

The silicon tracking and vertexing system
The CBM Silicon Tracking System (STS) is based on double-sided micro-strip sensors. Large-area prototype detectors with outer dimensions of 6.2 cm by 6.2 cm and 1024 AC-coupled strips per side have been produced. The front and back side strips are inclined by a stereo angle of 15°. Short strips in the sensor corners are interconnected to a strip in the opposite corner via a second metallization layer. The sensors will be used to build a demonstrator ladder. Further double-sided micro-strip test sensors with new radiation tolerant structures have been designed.
The sensors are read out via low-mass cables of up to 50 cm length in order to keep the active area of the detector free of electronics. The cables consist of micro-line-structured aluminium layers on polyimide carrier foils.
Two prototype Silicon tracking stations consisting of double-sided silicon micro-strip sensors, ultrathin readout cables, and self-triggering readout electronics have been successfully tested at COSY with a 3 GeV proton beam. Detailed simulations have been performed in order to understand the expected radiation damage in the sensors. The layout of the detector stations, i.e. the number and size of the sensors mounted on the vertical ladder-structures, has been optimized to reduce the number of spare parts while preserving the tracking performance.

The Ring Imaging Cherenkov (RICH) detector
The RICH photo-detector exhibits an active area of 2.4 m^2 which is covered by multi-anode photomultipliers (MAPMTs). Beam tests at GSI and CERN, and measurements with LEDs in the laboratory demonstrated that the Hamamatsu H8500 with 64 pixels is very well suited for the detection of single Cherenkov photons. Properties like the quantum efficiency (with and without wavelength shifting films), crosstalk and the performance of MAPMTs in the presence of magnetic fields have been successfully studied. The MAPMT signals were read-out by the self-triggered electronics with nXYTER chip. The results were very promising, also in view of the possible use of a future CBM ASIC for the RICH photo detector.. The RICH gas system has been designed and is presently being built. The reflectivity of different mirrors has been investigated.

The Transition Radiation Detector
The CBM Transition Radiation detector (TRD) has to provide electron identification and pion suppression by a factor of the order of 100 for momenta above 1 GeV/c at hit rates of 100 kHz/cm^2. Such a high pion suppression factor (corresponding to a pion efficiency of 1 %) together with an electron efficiency of better that 90%, can only be achieved with 9 -12 layers of TRD chambers, resulting in an overall detector area of almost 1000 m^2. Several prototype detectors have been developed to fulfil the requirements. One approach is to use fast multi-wire chambers with a thin amplification region with and without drift section. These detectors were read out by a newly developed self-triggered SPADIC chip which both amplifies and digitizes the pulses from the CBM TRD. Another option is a two-dimension position sensitive prototype TRD with diagonally split rectangular (i.e. triangular) read-out pads which allow for a position determination in both coordinates: across and along the pads, respectively. This detector is read out by a new Fast Analogue signal Processor (FASP). The various prototype TRDs were successfully tested at CERN using a mixed beam of electrons and pions with momenta of 1 – 5 GeV/c.

The Muon Detection System
In order to identify the soft muons from vector meson decays in a large combinatorial background the CBM muon detector is designed as an instrumented hadron absorber. The detection system comprises 6 iron slabs of different thickness (20 cm -100 cm) with detector triplets behind each iron absorber (18 detector layers in total). The development of the muon tracking detectors concentrates on the construction and test of prototype gaseous detectors based on different technologies: the detector layers behind the first and second hadron absorber (particle density up to 500 kHz/cm^2) will be based on GEM technology, or hybrid detectors combining different technologies. Various prototype detectors have been built and tested with radioactive sources and particle beams: double and triple thin GEMs, double thick GEMs, and thin and thick GEMs with Micromegas. We investigate the use of single mask GEM foils which can be produced in large size at moderate costs. In the third and forth absorber gap (particle density up to 5 kHz/cm^2) we may either use hybrid detectors, or Micromegas with a resistive strip layer suppressing the sparks. The latter technology allows to build large area detectors. For the last detector layers where the occupancy is low we foresee multiple-layer straw tubes. Prototype triple GEM detectors read out by a free streaming FEE and DAQ system have been successfully tested at COSY with a 3 GeV proton beam. The hybrid detectors have been successfully tested with 5 GeV proton and pion beams at CERN.
A start version of the muon detection system has been developed with 3 absorber layers and 3 detector triplets only. This system would allow to identify J/ψ mesons in Au+Au collisions at SIS100, i.e. at beam energies below the production threshold of J/ψ mesons in nucleon-nucleon collisions which is 11.3 GeV.

Timing multigap RPCs
Time-of-light measurements in CBM require a large-area, highly-granulated and fast detector which will be based on Multigap Resistive Plate Chambers (MRPC). Hit rates up to 20 kHz/cm^2 are expected to occur in the inner part of the CBM-TOF wall. Prototype MRPCs have been built with electrodes made of special glass with a resistivity of the order of 10^{10} Ωcm. With a 10 gap MRPC a time resolution of about 70 ps was achieved at a rate 20 kHz/cm^2. In order to cope with the high particle density per event at small emission angles, a high-granularity MRPC has been developed. This prototype exhibits a symmetric structure with 2x8 glass electrodes, and a read-out electrode with short strips (46 mm long). The resulting time resolution is 57 ps. A MRPC with electrodes made of low resistivity ceramics has been built and tested at rates up to 200 kHz/cm^2. At large polar emission angles, i.e. in most of the active area of the CBM ToF detector, the hit rate is of the order of 1 kHz/cm^2. At these low rates, a conventional MRPC in multi-strip configuration with thin standard float glass can be used. For this application, a fully differential prototype MRPC has been built and tested successfully at COSY with a proton beam, together with a high granularity prototype MRPC with low-resistivity glass electrodes. In the test experiment both detectors were read-out with self-triggered front-end electronics.

Event reconstruction based on time stamps
The free-streaming CBM data read-out system sends the hit information of each detector together with time stamps into the data acquisition chain. The hits have to be associated to physical events by the reconstruction algorithms. A software package has been developed which allows the generation of Monte-Carlo data consisting of hits with individual time stamps, and removing the correlation of detector hits with events. The next step is to develop "4 -dim" event reconstruction algorithms which take the time information into account for track reconstruction and pattern recognition.

Annealing studies on X-ray and neutron irradiated CMOS MAPS*

D. Doering[1], *M. Deveaux*[1], *C. Dritsa*[1], *M. Domachowski*[1], *I. Froehlich*[1], *M. Koziel*[1], *C. Muentz*[1], *and J. Stroth*[1]

[1]Goethe University Frankfurt/M, Max-von-Laue-Str. 1, 60438 Frankfurt/M, Germany

Monolithic Active Pixel Sensors (MAPS) have been proposed as sensor technology for the vertex detector of the CBM experiment [3]. The development of MAPS toward the radiation hardness required by CBM is the matter of a joint research program of the IPHC/Strasbourg, the University of Frankfurt and the GSI/Darmstadt.

It is a known fact that the lifetime of silicon-based sensors might be extended by recovering radiation damage by means of annealing [4]. A prominent example of this annealing is the recovery of surface and bulk defects. The past studies on MAPS have shown that a thermal treatment may reduce the leakage current of X-ray irradiated diodes [2]. We therefore considered annealing as an interesting method to recover the performances of irradiated sensors. However, it had to be studied if the benefits of annealing would eventually be canceled by a potential reverse annealing of bulk damage, when defects create a complex defect cluster. To do so, we performed a systematic study on the annealing of MAPS.

The annealing studies were carried out with the MIMOSA-19 prototype sensors received from IPHC Strasbourg. The chips were irradiated with 10^{13} $\mathrm{n_{eq}/cm^2}$ unmoderated fission neutrons [1]. Consecutive to the neutron irradiation, the chips were bonded, characterized and stored for one year at room temperature. Another characterization was performed to identify potential long term room temperature annealing, which was not observed. Once those studies were completed, several of the neutron irradiated samples and some not irradiated ones were exposed to $200\ \mathrm{kRad}$ of $10\ \mathrm{keV}$ X-rays at room temperature and their characterization started three hours later. The measurements were regularly repeated in order to study room temperature annealing. As shown later, this effect went mostly into saturation after $\sim 280\ \mathrm{h}$ and the sensors were heated up to $+80\ ^\circ\mathrm{C}$ in order to search for the consequences of annealing at this temperature. This thermal treatment was regularly interrupted in order to perform further measurements. To magnify the radiation induced leakage current, which was the point of interest, the sensors were kept at $+20^\circ\mathrm{C}$ during the measurements.

The results of our measurements are shown in Figure 1, which displays the leakage current of the differently irradiated sensors as function of the annealing time. The left part of the plot represents the annealing time at room temperature, while the right part the annealing time at $T = +80\ ^\circ\mathrm{C}$. Note that in the second part, the time needed for measurements and time of room temperature storage are neglected. This explains the step at $t = 290\ \mathrm{h}$, which was

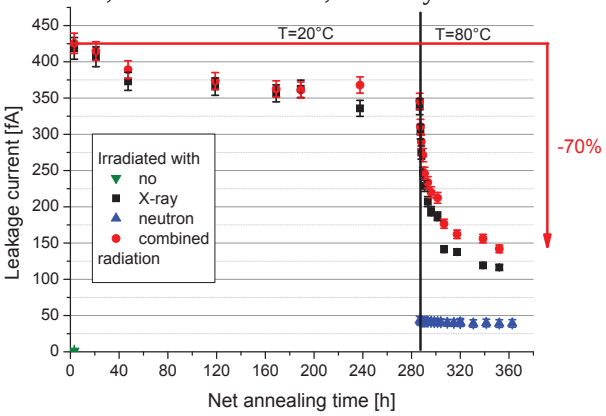

Figure 1: Results of the annealing study.

caused by few days of room temperature annealing. After X-ray irradiation, an exponential room temperature annealing occured, which reduces the leakage current by $\sim 20\%$. At $T = +80\ ^\circ\mathrm{C}$, we observed a more pronounced effect. After keeping the sensor in hot atmosphere for $75\ \mathrm{h}$, the leakage current of the pixels was observed to decrease to 30% of the pre annealing value. For pure neutron irradiated sensors the leakage current decreased by $\sim 10\%$. This may be attributed to an annealing of the ionizing damage caused by the γ-background of the neutron beam. The annealing behavior of the sensors irradiated with both, X-ray and neutron radiation, is mostly determined by the annealing of the ionizing damage. The observed decrease of the leakage current after annealing is likely specific for chosen sensor prototype. However, the trend which was found should be representative for the general case and therefore it can be concluded that annealing might be a helpful tool to reduce the effects of ionizing radiation damage in CMOS Monolithic Active Pixel Sensors.

References

[1] Harald Breitkreutz et al. Spectral fluence rates of the fast reactor neutron beam MedApp at FRM II. *Nucl. Instr. and Meth. A*, 593(3):466 – 471, 2008.

[2] G Deptuch. *A New Generation of Monolithic Active Pixel Sensors for Charged Particle Detection*. Dissertation, IPHC Strasbourg, 2002.

[3] M. Deveaux et al. Design considerations for the Micro Vertex Detector of the Compressed Baryonic Matter experiment. *POS(VERTEX2008)028*.

[4] G. Lindstroem et al. Radiation hard silicon detectors–developments by the RD48 (ROSE) collaboration. *Nucl. Instr. and Meth. A*, 466(2):308 – 326, 2001.

*This work has been supported by the BMBF (06FY9099I), HIC for FAIR and GSI.

Development of high precision pixel sensors for the CBM vertex detector*

M. Winter, for the IPHC team[1]
[1]IPHC, Strasbourg, France

The physics program of the CBM experiment translates into stringent constraints on its Micro-Vertex Detector (MVD). CMOS sensors, which are granular and thin enough, are developed since several years to adapt them to the high hit rate expected. An important step was achieved in 2010 with a high resistivity CMOS process, which was investigated with two sensors.

Study of a high-resistivity process

The first full scale sensor featuring fast read-out with integrated zero-suppression, called MIMOSA-26 [1], was manufactured in 2008/2009 in a 0.35 μm CMOS technology based on a standard, low resistivity, epitaxial layer. More recently, high resistivity epitaxial layers became available, reducing the thermal diffusion of the signal charges, for the benefit of the SNR and thus the radiation tolerance. MIMOSA-26 was re-fabricated with a 400 $\Omega \cdot cm$ resistivity, 10, 15 or 20 μm thick, epitaxial layer. Laboratory measurements were performed by illuminating these sensors with ^{55}Fe and ^{106}Ru sources[2]. The SNR obtained with the high-resistivity epitaxial layer ($\sim$ 35-40) was about twice higher than with the standard layer ($\sim$ 20).

Sensors were tested with a $\sim$ 100 GeV particle beam at the CERN-SPS. The results are summarised in figure 1. The latter shows that the detection efficiency remains close to 100 % for high discriminator threshold values, indicating that even after a potential increase of the noise, consecutive e.g. to irradiation, a threshold value should still be found with a detection efficiency well above 99% and an affordable fake hit rate.

The sensitivity to non-ionising radiation was investigated for a fluence of 10^{13}n$_{eq}$/cm^2. The sensor performances were measured at the CERN-SPS for a temperature of 0°C (see figure 1). A threshold of 5-6 mV allows keeping the fake hit rate below 10^{-4} with a detection efficiency of nearly 100 %.

Optimisation of the sensor performances

In order to optimise the detection performances of the sensor in this new, high-resistivity, process, a dedicated prototype was manufactured in Spring 2010. By subdividing the sensitive area in sub-arrays, each equipped with different pixels, alternative amplification schemes were investigated as well as a larger pitch (20.7 μm instead of 18.4) and enclosed transistor designs. The sensor detection performances were assessed in the laboratory and with a test beam as already mentioned for MIMOSA-26.

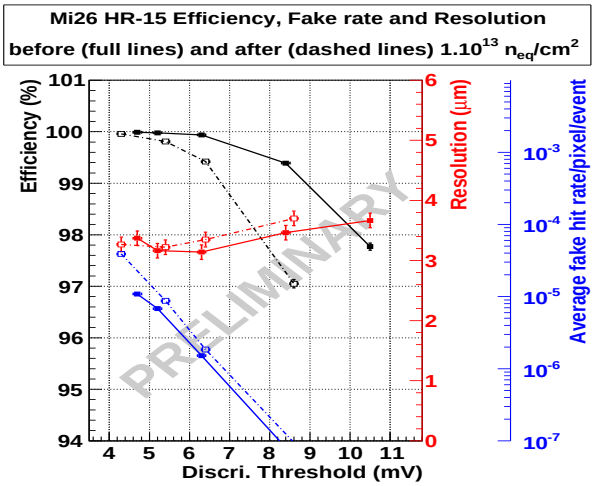

Figure 1: *MIMOSA-26 beam test results for a 15 μm thick high-resistivity epitaxy. The detection efficiency (in black), fake hit rate (in blue) and spatial resolution (in red) are shown as function of the discriminator threshold. They are displayed at 20°C before irradiation (full lines) and after an equivalent dose of $10^{13}n_{eq}/cm^2$ at 0°C (dashed lines).*

Beam tests were in particular performed at a temperature of +30°C with pixels featuring a 20.7 μm pitch read out in 125 μs, irradiated with 1 MeV neutrons (fluence of $3{\cdot}10^{12}$n$_{eq}$/cm^2) and 10 keV X-Rays (150 kRad). A detection efficiency of 99.8 % was still observed for a 5 mV threshold, with a fake hit rate well below 10^{-4}. One may derive from these results that for typical CBM-MVD running conditions (20-40 μs integration time and negative operating temperature), a substantially larger irradiation level would still be affordable. This study is under way.

Outlook

The next step of the development will consist in moving from the coarse 0.35 μm technology used up to now, to a substantially smaller feature size, i.e. 0.18 μm. This translation is expected to benefit to several aspects of the sensor, in particular to the ionising radiation tolerance. A first prototype (MIMOSA-27) was fabricated in such a technology in 2010. Its tests at the CERN-SPS are foreseen in Spring 2011.

References

[1] M. Winter et al., GSI Scientific Report 2010.

[2] M. Deveaux et al., "Radiation tolerance of a column parallel CMOS sensor with high resistivity epitaxial layer", accepted for publication by JINST

* Work supported by EU within the projects EUDET (FP-6), Hadron Physics 2 (FP-7), HIC for FAIR, and BMBF (06FY9099I).

Expected data rates of the CBM-MVD at SIS100 based on realistic beam intensity fluctuations*

S. Seddiki[1,2], M. Deveaux[1], C. Dritsa[1,2], C. Müntz[1], and J. Stroth[1,3]
[1]IKF, Frankfurt, Germany; [2]IPHC, Strasbourg, France; [3]GSI, Darmstadt, Germany

The Micro-Vertex Detector (MVD) of the CBM experiment will be located close to the collision point and exposed to very high track densities from heavy ion collisions produced at high interaction rates. The design of the MVD requires a detailed knowledge of the detector occupancies and the corresponding data rates, which were simulated in this work.

The first step of the study was to determine typical beam intensities for standard systems forseen at SIS-100 i.e. p-Au collisions at 30 GeV and Au-Au collisions at 10 A GeV bombarding energy. Two main constrains on the beam intensity were considered: the hit densities and the radiation dose in the 1^{st} MVD station placed 5 cm downstream the target. First, studies demonstrated that a maximal hit density of ~ 17.5 mm^{-2} can be reached in the MVD per read-out cycle [1]. Secondly, simulations of the radiation dose received by the MVD indicated it could endure $\sim 5 \times 10^{13}$ p-Au and $\sim 5 \times 10^{12}$ Au-Au collisions [2], assuming a non-ionizing radiation hardnesss of 10^{14} n_{eq} cm^{-2}. This last value might be in reach for the future sensor at SIS-100, according to measurements performed with MIMOSA-25 featuring a high resistive epitaxial layer [3].

Simulations of the occupancies in the MVD stations located at 5-10-15 cm from the target were peformed using UrQMD + GEANT3.21, as discussed in [4]. These simulations included the production of δ-electrons by the passage of Au ions in the Au target (this is neglected in case of the p-Au collisions). The geometry of the MVD sensors and stations located at 5 and 10 cm from the target were taken according to [6]. The third station was considered by scaling the number of sensors required to satisfy the CBM acceptance. These simulations suggest that in the case of p-Au collisions, the beam intensity is limited by the radiation hardness of the MVD to a mean value of $\sim 10^9$ protons/s. As for the Au-Au collisions, the beam intensity is limited by the high hit densities originating from the δ-electrons to a maximal value of $\sim 2 \times 10^7$ ions/s.

The second step is to estimate the amount of data provided by the MVD sensors in each 30 μs long read-out cycle. To account for the beam fluctuations of SIS-100, we assumed a factor of three for the ratio between the maximum and the average beam intensity. This number was motivated by observations made with the HADES beam diagnostics at SIS-18 [5]. 10^3 collections of hits created in the sensors in each read-out cycle were simulated assuming a mean fluence of 3×10^4 protons and ~ 200 Au ions passing through the target per read-out cycle. The number of nuclear collisions was computed using a Poisson distribution considering a 1% interaction target. These collisions were then chosen randomly in a sample of 10^3 central p-Au and 500 Au-Au minimum bias collisions.

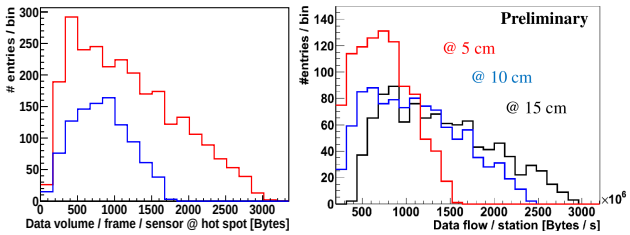

Figure 1: *Left panel: Data volume per read-out cycle in the sensor exposed to the highest track densities, in case of the p-Au (blue curve) and Au-Au collisions (red curve). Right panel: Data flow per station for p-Au collisions.*

To compute the data volume, the data format of MIMOSA-26 [7] was assumed, since this chip has a binary read-out and integrates a sparsification circuit to reduce the amount of data. The left panel of Fig.1 shows the data volume per read-out cycle in the sensor exposed to the highest track densities. A huge amount of data is generated by δ-electrons in Au-Au collisions (red curve), up to ~ 3 KB. As a result, the memory in the current MIMOSA-26 on-chip circuitry (up to $\sim$ 1KB) may have to be increased by a factor of ~ 3, and its output clock frequency (up to 120 MHz) by a factor of ~ 7. The right panel presents the data flow per station for p-Au collisions. Due to the proton beam intensity, two orders of magnitude higher than in the case of a Au ion beam, the overall data flow (3 MVD stations) may reach 7 GB/s.

References

[1] C. Dritsa, 'Feasibility studies of open charm reconstruction with pile-up', CBM coll. meeting, Darmstadt, April 2010

[2] D. Bertini, 'Radiation dose simulations', CBM coll. meeting, Darmstadt, March 2009

[3] W. Dulinski, VIPS-2010, Workshop, Pavia, April 2010

[4] S. Seddiki, 'Occupancy study of the Micro-Vertex Detector for the CBM experiment', CBM Annual Report, 2009

[5] P. Forck et al., 'Beam Diagnostics Developments for Current Operation of SIS18 and HEBT', GSI Scientific Report 2005

[6] T. Tischler, 'Status of the mechanical design of the CBM Micro-Vertex Detector', in this report

[7] A. Himmi, 'Mimosa 26 User Manual', V.1.0, December 2008

* In collaboration with IPHC. Work supported by BMBF (06FY173I), GSI Darmstadt (F&E)

Status of the CBM-MVD prototype readout*

C. Schrader, N. Bialas, S. Amar-Youcef, M. Deveaux, I. Fröhlich, M. Koziel, J. Michel, C. Müntz, B. Neumann, S. Schreiber, T. Tischler, and J. Stroth for the CBM-MVD Collaboration

Institut für Kernphysik, Goethe-Universität, Frankfurt am Main

The readout system of the prototype of the CBM-MVD is intended to form a flexible software and hardware solution, which provides the bandwidth and scalability needed for a use in the final MVD. It will be developed based on the state of the art prototype sensor MIMOSA-26 [1]. Despite the readout speed of this sensor is not yet optimised for the final MVD, MIMOSA-26 provides already today the full architecture foreseen for the final MVD and may therefore serve as a useful model of the final sensor.

The MIMOSA-26 sensor handles 570 hits per frame and provides digital output data-stream of 160Mbit/s send via two digital output lines. The data stream holds addresses of the pixels containing hits and frame numbers. A firmware update of our MAPS-readout-board [2] allowed us to readout the MIMOSA-26 sensors. Furthermore, we were able to reduce the data-stream to 80Mbit/s by removing redundant information.

The future sensors equipping the first generation CBM-MVD will presumably handle a several times higher occupancy than MIMOSA-26. Therefore, the data stream of this sensor will likely range up to 800 Mbit/s [3].

The concept of the readout system of the MVD-prototype is designed accordingly. Figure 1 shows a sketch envisaged architecture of the prototype readout chain. Two sensors will be bonded on a flex-print cable which transfers the data via a fine pitch connector to a front-end board. The future radiation environment requires the use of radiation tolerant, passive, board. This board serves as an interface between the flex-print cables and conventional copper wires. Moreover, it distributes the sensor clock and the slow control signals. The data of the two digital output channels of each sensor are transferred via LVDS cables to a converter board. Currently we consider two functionalities for this board. By embedding it into a vacuum flange, we aim to use this board to pass the cables out of the vacuum of the combined MVD and target chamber. The second task is the data conversion from LVDS to 8 bit/10 bit encoded, 1 Gbit/s, optical signals (see figure 2 for details). A readout controller board receives the optical signals. It hosts an FPGA which controls the data acquisition and allows using on-line data reduction and filtering algorithms. Slow control will be done by JTAG boundary scan which allows accessing to the internal register of the individual sensors. The slow control ensures also latch-up handling, on-line temperature and current monitoring.

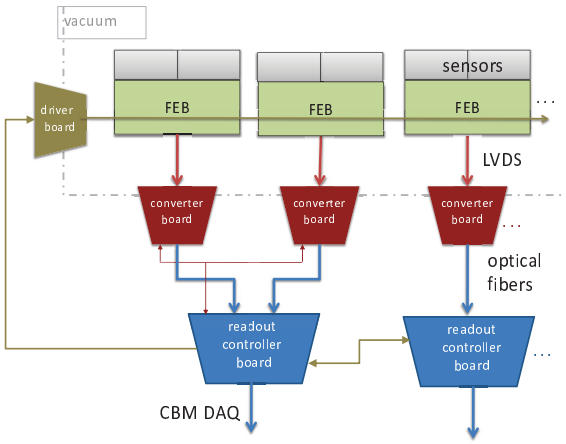

Figure 1: The prototype read-out chain.

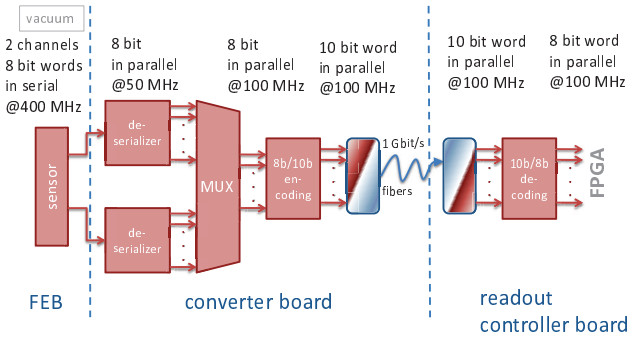

Figure 2: The data flow with the different conversion steps.

The boards are submitted for production and will be assembled and tested in the next months. In parallel to the hardware developments, the related FPGA firmware are being developed.

References

[1] C. Hu-Guo, Nim A 623,1 P480-482

[2] C. Schrader, A Readout System for the Micro-Vertex-Detector Demonstrator for the CBM experiment at FAIR, PhD thesis

[3] S. Seddiki, Data rates of the CBM-MVD expected at SIS-100, CBM coll. meeting Roumania, Oct. 2010

Work supported by GSI, BMBF (06FY9099I), EU (FP7-WP26), HIC for FAIR.

Status of the mechanical design of the CBM MVD*

T. Tischler, S. Amar-Youcef, M. Deveaux, I. Fröhlich, M. Koziel, C. Müntz, C. Schrader, and J. Stroth for the CBM-MVD Collaboration

Institut für Kernphysik, Goethe-Universität, Frankfurt am Main

For the design of the Micro Vertex Detector (MVD) for the CBM experiment we are following two approaches. The first approach uses advanced technologies regarding sensor integration and interconnections. The second one is a more conventional approach with well definded building blocks (sensor, carrier, cooling, read-out cables, FEE), which however incooperates advanced materials and concepts under the aspects of minimising the material budget as well as vacuum operation. The latter will be discussed here.

Sensor, support and cooling

The sensor technology we will use in the MVD is based on Monolithic Active Pixel Sensors (MAPS). The sensor for the final MVD will be MIMOSIS-1, which will be thinned down to a thickness of 50 µm. Due to the fact that this sensor is still to be developed, we are currently working with a precursor named MIMOSA-26 [1]. The form factor of this precursor does not fit the one of the final sensor which will be adapted during the development phase.

The support material in the active area of the MVD will be the CVD diamond with a thickness of 300 µm to add only a small amount to the material budget. An effective cooling is mandatory due to operation in vacuum. The CVD diamond covers this part by providing an outstanding heat conductivity of about 2000 $\frac{W}{mK}$ at low temperatures.

Outside of the active area of the MVD, copper plates are currently discussed to be used for cooling of the CVD diamond (and sensors) and read-out electronics. The cooling approach is the following: via cooling the copper we are cooling the diamond on which the MIMOSIS-1 sensors are mounted. The interconnections ensuring an optimal heat transfer between CVD diamond and copper heat sinks as well as between cooling fluid and copper heat sinks are key points which are still subject of detailed studies.

Design

The design of the MVD, worked out with Autodesk [2], is constrained by the CBM Experiment. For the first station a disk featuring an inner radius of 5.5 mm and an outer radius of 25 mm has to be covered with sensors, for the second station the inner radius is 5.5 mm and the outer radius is 50 mm. Based on the form factors of the sensors which are still under consideration and are not necessarily the same for both stations this acceptance translates to 40 double-sided arranged sensors for the first and 76 double-sided arranged sensors for the second station, compare with figure 1 for the first station. In figure 2 the preliminary concept of the vacuum vessel housing both MVD stations is sketched, comprising the support structures, heat sinks for the read-out electronics, read-out electronics, FPCs, read-out cables and cooling tubes (both not in appropriate numbers). The dimensions of this vacuum vessel are: $800 \cdot 600 \cdot 200$ mm^3.

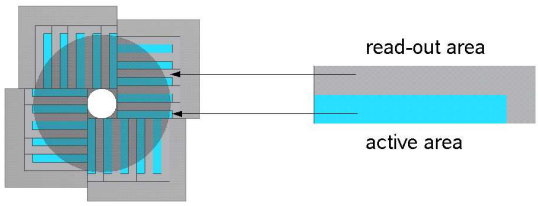

Figure 1: Double-sided sensor arrangement of the first MVD station, acceptance of the first station (grey disk) and MIMOSIS-1 sensor with subdivision in active and passive parts are shown.

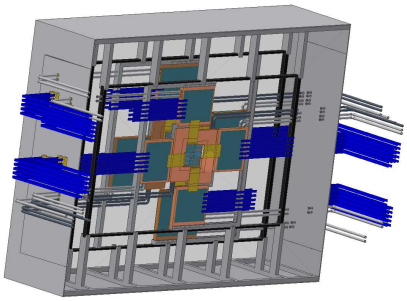

Figure 2: Complete vacuum vessel housing the MVD.

Transfer to Simulation

For the ongoing physics simulations a simplifed model of the first MVD station containing the support material, the sensors (which explicitly were divided in active and passive areas), the heat sink for the sensors and for the electronics has been sucessfully transformed from CAD to ROOT-geometry with a Converter provided by the Panda Collaboration [3].

References

[1] MIMOSA-26, IPHC, Strasbourg, France, http://www.iphc.cnrs.fr.

[2] Autodesk Inventor 2010, http://www.autodesk.de.

[3] Panda CAD-Converter, http://panda-wiki.gsi.de.

*Work supported by GSI, BMBF (06FY9099I), EU (FP7-WP26), HIC for FAIR, H-QM Helmholtz Research School.

Development of low-mass readout cables for the CBM Silicon Tracking System *

J.M. Heuser[1], *V. Borshchov*[2], *S. Chatterji*[1], *M. Singla*[3], *and W. Müller*[1]

[1]GSI, Darmstadt, Germany; [1]State Enterprise Scientific Research Technological Institute of Instrumental Engineering (SE SRTIIE), Kharkov, Ukraine; [3]Goethe University, Frankfurt, Germany

Low-mass readout cables are of critical importance in the Silicon Tracking System (STS) under development for the CBM experiment. The aperture of the tracking stations is planned to be kept free of readout electronics that is arranged at the perimeter of the fiducial area instead. The signals from the double-sided silicon microstrip detectors are routed through multi-line fine-pitch cables to those readout boards, bridging distances of up to around 50 cm. Prototype cables are being developed in cooperation with SE SRTIIE of the State Space Agency of Ukraine [1].

The cable is based on microline-structured aluminum layers on polyimide carrier foils. Line pitches down to a few tens of micrometers are feasible depending on the length of the cable to be realized. The electrical connection of the lines to both the detectors and the readout electronics are laid out as tab bonds through openings in the polyimide foil.

Demonstrators of a fine-structured single-layer cable tab-bonded to prototype microstrip detectors CBM02 were realized in the year 2008. The aluminum signal lines are 14 μm thick, 20 μm wide and have 50 μm pitch at the detector. The objects have been used in the recent STS beam test [2]. Further optimized specimen, shown in Fig. 1, have been produced in 2010 to complete a reference tracking system for forthcoming in-beam tests of STS components.

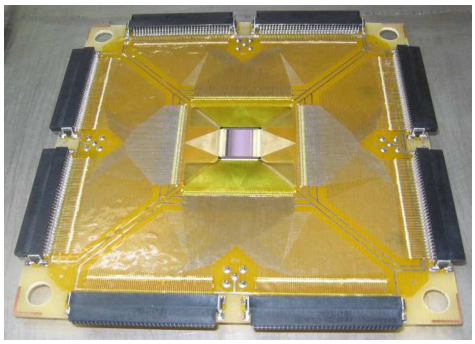

Figure 1: Demonstrator board 2b-4 with a CBM02 detector.

High line densities up to 50 μm pitch can only be produced in short cables. From about 7 cm lenth on the signal paths must be arranged staggered across two signal layers at e.g. double line pitch. Demonstrators of such multilayer cables have been produced already last year [3]. In the first approach they yielded non-symmetric capacitive load to the readout electronics. This is shown in Fig. 2, obtained with the simulation package RAPHAEL of Synopsis TCAD. A improved cable design is shown in Fig. 3. It is being used in the demonstrator module shown in Fig. 4 with three daisy-chained microstrip detectors and a multilayer readout cable of 1024 signal lines. Measurements of the line capacitances yield close values for the upper and lower layer, about 0.3 pF per cm. The material budget of the cable is between 0.1% and 0.17% radiation length.

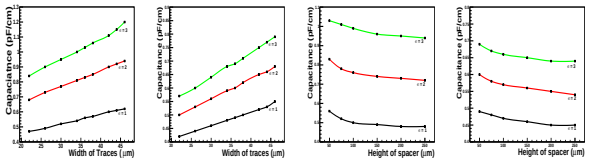

Figure 2: Line capacitance in the upper and lower signal layers as a function of the width of the traces (left two plots) and the thickness of the spacer (right two plots).

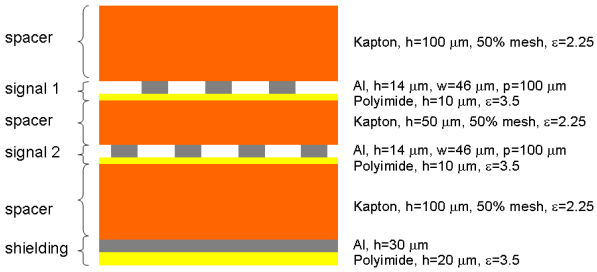

Figure 3: Cross section of the readout cable.

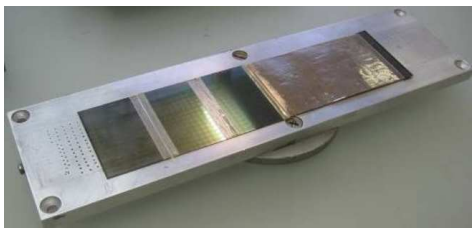

Figure 4: Demonstrator 2a with ISTC03/CBM03 detectors.

Further electrical parameters, e.g. the line resistivity as a source of noise, are being addressed together with the designers of the front-end electronics. Also the radiation hardness of the polyimide material is being studied [4].

References

[1] http://www.nkau.gov.ua/nsau/nkau.nsf/indexE
[2] J.M Heuser et al., GSI Scientific Report 2010
[3] GSI Scientific Report 2009 63
[4] D. Severin et al., GSI Scientific Report 2010

* Work supported by EU-FP7 HadronPhysics2 and Helmholtz International Center for FAIR.

Development of microstrip detectors for the CBM Silicon Tracking System *

J.M. Heuser[1], *L. Long*[2], *H.G. Ortlepp*[2], *S. Chatterji*[1], *A. Lymanets*[3,4], *I. Sorokin*[3,4], *M. Singla*[3], *C.J. Schmidt*[1], *V. Kleipa*[1], *C. Simons*[1], *W. Niebur*[1], *L. Xu*[5], *and A. Hastir*[6]

[1]GSI, Darmstadt, Germany; [2]CiS Forschungsinstitut für Mikrosensorik und Photovoltaik GmbH, Erfurt, Germany; [3]Goethe University, Frankfurt, Germany; [4]Kiev Institute for Nuclear Research, Kiev, Ukraine; [5]University of Science and Technology of China, Hefei, China; [6]Guru Nanak Dev University, Amritsar, India

The second prototype of a full-size microstrip detector for the CBM Silicon Tracking Detector System has been developed in cooperation with CiS [1]. It will be used for the construction of a demonstrator ladder, the building block of the silicon tracking stations. A batch of 24 wafers was produced in July 2010 and first detectors have been characterized at GSI. A further achievement in the cooperation with CiS was the design and fabrication of double-sided test detectors with novel radiation tolerant structures.

Full-size prototype detector CBM03

The design CBM03 [2] has been realized on 4" masks and was produced on high-resistivity n-type float-zone wafers of 300 μm thickness. It includes one large double-sided microstrip detector, several small double-sided detectors and other test structures. The large-area detector has outer dimensions of 6.2×6.2 cm^2 and comprises 1024 AC-coupled strips per side forming a stereo angle of 15° between the front and back side strips. Short strips in the detector corners are interconnected to a strip in the opposite corner via a second metallization layer. The strips are biased with both poly-silicon resistors and punch-through structures. Both detector sides have the same segmentation and contact pattern which limits the complexity of the microcables for their connection to the readout electronics.

For the characterization of the detectors new infrastructure has been developed and set up at GSI. This includes a program-controlled voltage-scan test station and a wafer prober Süss-PA300. The bulk current-voltage (I-V) and capacitance-voltage (C-V) behaviour can serve as primary acceptance criteria. For this test every detector is installed in a simple fixture, shown in Fig. 1-left. The sandwich of two identical printed circuit boards has a square opening with a thin balcony structure milled in that accepts the detector. Bias is provided to the detector through two wire bonds. The scan is then run with a program-controlled precision source-measure unit and a LCR meter. Results of the characterization are shown in Fig. 2. Individual strips are characterized on the probe station. Fine needles can be brought into contact with the readout or bias pads as shown in Fig. 1-right. One important inspection concerns the insulation between the implanted strip and the metal electrode. It is formed by an about 0.2 μm thin SiO_2 layer. This layer is prone to defects that short the capacitor. A strip-by-strip investigation has shown that the current CBM03 detectors exhibit such defects. The reason for the shorts is being investigated. Further characterization of the sensor will involve measurement of interstrip parameters, e.g. resistance and capacitance and their alteration after exposure to radiation.

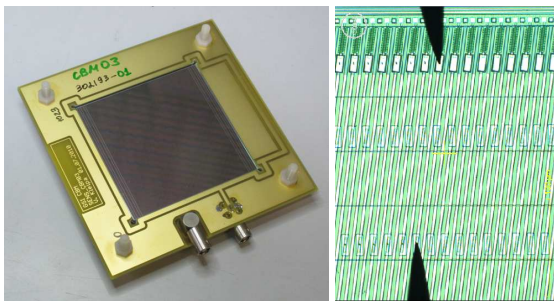

Figure 1: A CBM03 microstrip detector mounted on a test board for characterization under bias voltage (left). Microscope photograph of a CBM03 detector on a probe station for testing individual strips (right).

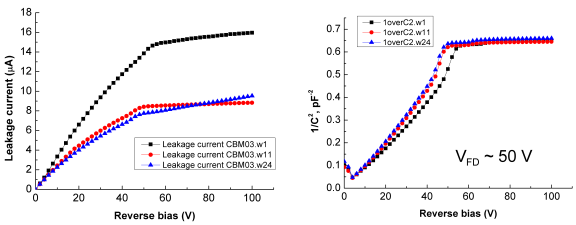

Figure 2: Characterization of CBM03 detectors. Plots of I vs. V (left) and $1/C^2$ vs. V (right) allow extracting the full depletion point, here around 50 V.

Radiation tolerant test detectors FSD-CBM04

Prototypes of double-sided microstrip detectors with new radiation tolerant structures have been designed and manufactured by CiS. The test detectors comprise Shottky barriers between the strips to increase their charge collection after irradiation. GSI is research partner for the evaluation of the detectors before and after irradiation, to be performed in 2011.

References

[1] http://www.cismst.de

[2] CBM Progress Report 2009 10

*Work supported by EU-FP7 HadronPhysics2, Helmholtz International Center for FAIR, Bundesministerium für Wirtschaft und Technologie INNO-KOM-Ost, and GSI Summer Student Programme.

Performance simulations with a realistic model of the CBM Silicon Tracking System *

A. Kotynia[1] *and J.M. Heuser*[2]
[1]Goethe University, Frankfurt, Germany; [2]GSI, Darmstadt, Germany

Efficient charged particle tracking and high momentum resolution are central performance requirements of the CBM Silicon Tracking System (STS). The aim of the ongoing layout studies is to design a highly granular and low-mass detector system which can track up to 1000 charged particles that are typically generated in one central Au+Au collision at 25 GeV/nucleon projectile energy.

Detector Layout

The STS comprises eight tracking stations located at 30, 35, 40, 50, 60, 75, 95 and 100 cm downstream of the target (Fig. 1). The stations have a modular structure and are constructed from 300 μm thick double-sided silicon microstrip sensors. Groups of sensors (sectors) are individually read out with electronics located at the perimeter of the stations. The number, position and segmentation of the layers are optimized for efficient track reconstruction and high momentum resolution. On the other hand, from the point of view of mass production and logistic, it is highly desirable to limit the number of different sensors and ladders to the minimum possible.

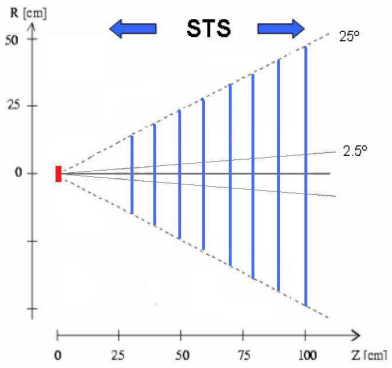

Figure 1: Schematical side-view of the STS system.

Material budget

The silicon detector is designed minimizing the total amount of material: the silicon sensors have the minimum thickness capable to provide a good signal-to-noise ratio, namely 300 μm. The simulated amount of material for the STS corresponds to 0.3% X_0 for the silicon sensors; a comparable effective thickness is added by the cables, where the simulated amount of material equals 70 μm silicon equivalent, giving 0.08% X_0 for every cable layer. A maximum value of approximately 1% X_0 is reached in the outer parts of every station, where 8 layers of cables overlap. Applying cables into simulation framework worsens the momentum resolution from 1.1% to 1.5%.

Silicon sensors

The full STS will use only four types of silicon sensors. In the innermost parts of the first three stations, where particle occupancy is expected to reach 5%, 2 cm long strips have been chosen: high granularity allows minimizing ghost hits. However, to reduce material budget in the regions where occupancy is lower than 5%, it is possible to use up to three 6 cm sensors chained together, creating effective strip lengh up tp about 18 cm.

The expected strip occupancies and required spatial resolution suggest a strip pitch of 60 μm. A value of 58 μm was chosen here, because it allows to divide the sensitive width of the sensor into 1024 strips, corresponding to 8 read-out chips of 128 input channels each. On either side of the double-sided sensor the strips are tilted by $+7.5°$ or $-7.5°$ with respect to the vertical edge, creating $15°$ stereo angle between the opposite sides. This allows reconstructing multiple hits from the same sensor at the expense of a poorer spatial resolution in the vertical direction, keeping high resolution in horizontal direction for better reconstruction of the particle momenta in the 1 T dipole field.

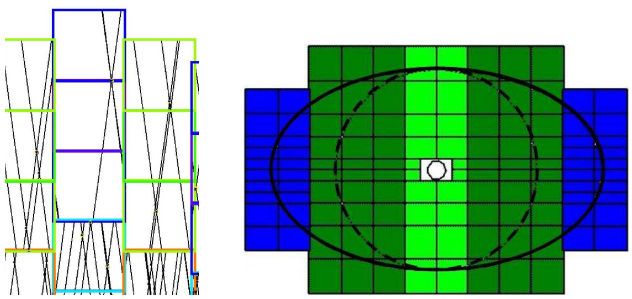

Figure 2: Left: Event display showing active strips in one of the STS stations; the stereo angle between front and back strips is $15°$. Right: Second STS stations, placed at 40 cm downstream from the target; different colors represents different ladder types, each ladder build from 10 sensors

* Work supported by EU-FP7 HadronPhysics2 and Helmholtz International Center for FAIR.

Station layout

For all stations the full height of the sensitive area can be covered by ladders of 10 sectors (see Fig. 2). Neighboring ladders overlap by 5 mm, in order to avoid dead space caused by the guard ring structures of the sensors. The number of ladders was chosen to cover 25° acceptance. To reduce the possibility that the actually covered area is larger than the nominal one, outer parts of stations 2-8 are equipped with ladders from previous stations. The presented layout allows constructing the full STS with only eight types of ladders. The total number of sensors, ladders and read-out channels are summarized in the table.

Table 1: Summary of STS components

Station	Ladders	Sectors	Sensors	R/O chips	Channels
1	8	80	80	1280	164k
2	12	120	120	1920	247k
3	12	120	120	1920	247k
4	14	136	172	2176	279k
5	14	136	156	2176	279k
6	14	136	192	2176	279k
7	16	156	220	2496	319k
8	16	156	232	2496	319k
Total	106	1040	1292	16640	2133k

For comparison, a purely geometric estimate of the minimum number of read-out channels that would be required to cover the geometrical acceptance of $2.5^\circ - 25^\circ$ at maximum 5% sensor occupancy, yields 12k read-out chips. The difference between this estimate and the number of r/o chips quoted for the proposed layout is mainly due to the neccesity to limit the number of different sensors and ladders to the minimum possible.

Performance studies

Such layout has been used to implement the STS in the CBM simulation packages. Simulations which have been developed include the complete chain of physical processes caused by a charged particle traversing the detector: from charge creation in the silicon to the digitize output signals. he first step of STS hit reconstruction is performed by an algorithm called cluster finder. A cluster is a group of signals originated by a particle traversing a portion of the detector. A signal has to pass a threshold to be taken into account, otherwise it is rejected. In the STS case, the threshold is constant for every channel and equals 4000 e^-. The accepted signals coming from adjacent strips of a sensor side are grouped together in a cluster. The total charge of a cluster is defined as the sum of the single strip signals. The multiplicity of fake clusters composed of two or more strips was found to be higher than expected. Therefore, clusters with total charge below 7000 e^- are rejected from further analysis. The position is given by the center-of-gravity [1] equation:

$$X_{COG} = \frac{\sum_{cluster} S_i x_i}{\sum_{cluster} S_i} \quad (1)$$

where x_i is the position of the ith strip included in the cluster and S_i the signal on the strip; the sums are over all the strips included in the cluster.

In next step the association of two clusters lying on the opposite sides of the double-sided sensor is performed. The last step defines the hits and their properties.

Applying realistic detector response functions [2] such as:

- ▷ signal sharing between strips
- ▷ charge collection inefficiency
- ▷ Lorentz shift due to presence of the magnetic field
- ▷ channel dead time
- ▷ random noise added to the charge signal

together with a Cellular Automaton for track finding and a Kalman Filter for track fitting, results in track finding efficiency of 97% for fast primary tracks and 75% for secondary track, with a momentum resolution 1.1%. Such results were obtain with a noise width of 0.5k electrons and a charge threshold level of 4k electrons.

Since the granularity of the detector changed in comparison to the one presented in [3], the time for track reconstruction of central Au+Au collisions decreased from 3.6 to 2.3 seconds/event on a single core CPU. The STS granularity has also a strong impact on number of combinatorial hits. It was possible to reduce the number of ghost hits by 10%.

Conclusions

The simulations described in this report take into account the properties of the STS detector. The results obtained with our algorithm indicate a preference for a detector geometry with high granularity. As far as the predictions of realistic cable thickness are correct, the results obtained show clearly that the solution with a minimum number of different ladders is the preferred one, from performance and maintenance points of view. However, the external constrains that define the size of STS stations are not yet finally defined. Consequently, details of the layout may be subject to change.

References

[1] Nucl. Instr. Meth. A497 (2003) 389-396,

[2] A.Kotynia, *Simulation of realistic detector response in the CBM Silicon Tracking System*. CBM Progress Report 2009-07,

[3] A.Kotynia, *Progress with performance simulations of the CBM Silicon Tracking System*. CBM Progress Report 2009-07.

Simulation study of n-XYTER front-end electronics in overflow situations for early prototyping of detectors in the CBM experiment *

T. Balog[1,2], *C.J. Schmidt*[1], *W. Müller*[1], *and J.M. Heuser*[1]
[1]GSI, Darmstadt, Germany; [2]Comenius University, Bratislava, Slovakia

In high interaction rate experiments a situation can occur when the data rate temporarily exceeds the available bandwidth. In a conventional triggered system these overload situations are handled with common dead time mechanisms which discard the affected fraction of the events. With self-triggering front end electronics such overload situations would lead, without further measures, to uncontrolled data losses and potentially large number of incomplete events. Thus mechanisms are needed to control data losses and to ensure that complete events are recorded at least part of the time in case of overload.

Simulations with SystemC

The self-triggering n-XYTER chip has been developed for neutron physics experiments and is used also for early prototyping of CBM detectors [1]. This study investigates possible modifications of the n-XYTER chip architecture to control data losses. The simulations are being performed using the hardware description language SystemC which is built on C++ standard extended with class libraries and a runtime system [2]. SystemC addresses the need for a system design and verification language that spans multiple hardware and software platforms.

We have simulated the behavior of systems with one, ten, hundred and thousand chips. Each chip has 128 channels comprising a fast shaper, a pile-up rejector and a FIFO. The selection of the FIFO in which the data has to be written is made according to the Uniform distribution. The period of data reading by the Token Ring is 32 ns for every n-XYTER chip. The Token Ring is able to read data only from one FIFO in one period. We have investigated the behavior of the chip with data incoming at average frequencies of 64 MHz, 52 MHz, 40 MHz, 32 MHz, 16 MHz, 8 MHz and 2 MHz. The dead time for each channel has been assumed to 30ns which is the recovery time needed by the fast shaper to see the next incoming hit. Furthermore pile-ups can occur. The time window for pile-up after incoming data is assumed to be 300 ns which is the shaping time of the slow shaper. For all the modules after the Token Ring we assumed that no data loss occurred. To introduce controlled data losses a counting module has been added. Every channel has its own counter which increments by one with incoming data in the FIFO. In case of reaching the number of counts which agrees with the depth of the FIFO the particular FIFO is closed. All FIFOs are opened again and counters are set to zero after the epoch period has elapsed. An epoch period is defined as the time needed for reading all cells from all FIFOs in one chip by the Token Ring.

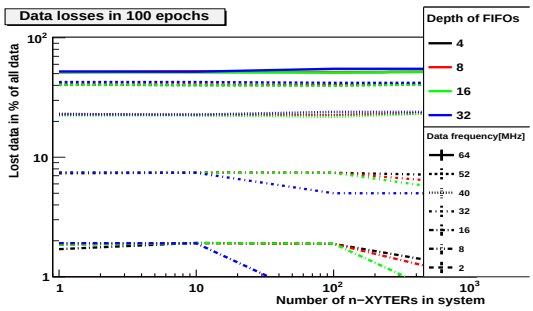

Figure 1: Data losses of the simulated system with respect to system size and average frequency of incoming data.

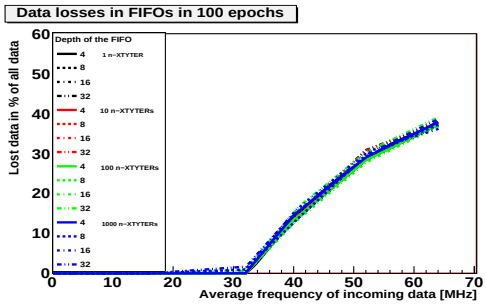

Figure 2: Data losses at the FIFO of the simulated system with respect to the average frequency of incoming data.

Results

We can see in Fig. 1 that the data losses do not significantly change with size of the system. With increasing frequency there are also no significant looses until the average frequency of incoming data is same as the frequency of the Token Ring, as shown in Fig. 2. The biggest losses occur at the FIFOs. This is due to the reading period of the Token Ring which is approximately 4 μs per channel while the average period of incoming data is also 4 μs (2 μs for 64 MHz) but with statistical fluctuations.

Another investigation has been made to find out how data losses depend on the depth of the used FIFOs – 4, 8, 16 and 32 cells. The result shows no significant changes within the investigated frequency range.

References

[1] GSI Scientific Report 2009 63
[2] http://www.systemc.org

* Work supported by EU-FP7 HadronPhysics2, Helmholtz International Center for FAIR and EU-FP7 MC-PAD.

Simulation study on the radiation tolerance of microstrip detectors for the CBM Silicon Tracking System*

S. Chatterji[1], *M. Singla*[2], *and J.M. Heuser*[1]
[1]GSI, Darmstadt, Germany; [2]FIAS, University of Frankfurt, Germany

We are using the three-dimensional TCAD simulation package from Synopsys [1] to simulate double sided silicon strip detectors (DSSDs) for the CBM Silicon Tracking System (STS). The STS will consist of eight stations of DSSDs at a distance of 30-100 cm from the target. The expected neutron fluence will vary from 1×10^{13} $n_{eq}cm^{-2}$ to 1×10^{15} $n_{eq}cm^{-2}$ depending on the location of the sensors. Hence we have done detailed simulations to understand the expected radiation damage in DSSDs and to foresee if these DSSDs will be able to survive the full lifetime of the expected CBM run. We have simulated two types of DSSDs, one having orthogonal strips and other having a stereo angle of ±7.5 °. Fig. 1 shows a zoom on the n-side of the simulated detector.

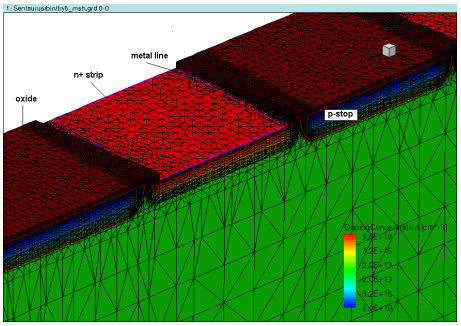

Figure 1: Zoomed frontal view of the simulated DSSD.

Modelling of the Radiation Damage

We have simulated the impact of irradiation by varying the effective doping concentration (N_{eff}) and minority carrier lifetime (τ) with fluence (ϕ) using the Hamburg model [3]. The effect of surface damage has also been studied by varying the oxide charge density (Q_F) at the Si-SiO_2 interface. The values of integrated fluence and corresponding values of N_{eff} and τ are listed in Table 1. The University of Perugia trap model [2] was applied. The time line assumes CBM operating at highest interaction rates.

Results and Validation

Fig. 2 shows the simulated versus measured Current-Voltage (I-V) and backplance Capacitance-Voltage (C-V) behaviour before irradiation for a DSSD with orthogonal strips of size 1.5×1.5 cm^2. One can observe that the simulation is comparable with the measurements. Fig. 3 shows the plot of leakage current density versus fluence for DSSDs with a stereo angle of $\pm7.5°$. The simulated value of damage constant (α) for DSSDs with orthogonal strips and with stereo angle of ±7.5 ° are 3.6×10^{-17} A/cm and 4.0×10^{-17} A/cm respectively while the experimental value is $\alpha = (3.99\pm0.03)\times10^{-17}$ A/cm [4]. We will compare the simulated α with our detectors after irradiations in 2011.

Table 1: Fluence profile of neutrons expected for CBM

Year	Int. Fluence $*10^{14}$(n/cm^{-2})	$N_{eff}*10^{11}$ (cm^{-3})	$\tau_{electron}$ (μsec.)	τ_{hole} (μsec.)
0	0	9	1000	300
0.05	0.05	7.41	4.98	4.92
0.3	0.3	-1.72	0.833	0.831
1	1.0	-34.3	0.250	0.250
2	2.0	-89.9	0.125	0.125
3	3.0	-150	0.083	0.083
4	4.0	-214	0.062	0.062
5	5.0	-278	0.05	0.05
6	6.0	-343	0.041	0.041

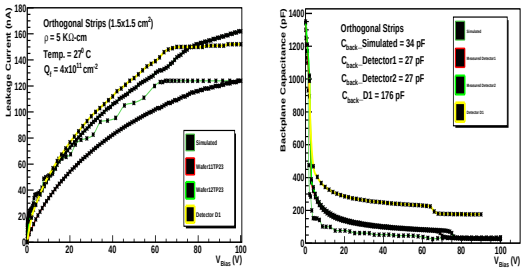

Figure 2: Simulated I-V and C-V curves compared with measurements of several CBM01/02 prototype detectors.

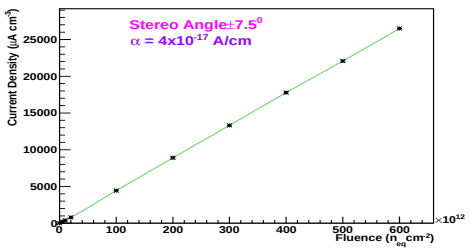

Figure 3: Variation of leakage current density with neutron fluence for the silicon microstrip detector with stereo angle.

References

[1] http://www.synopsys.com/home.aspx
[2] IEEE Trans. Nucl. Sci. NS-53 (5) (2006) 2971.
[3] Nucl. Instrum. Methods. A 439 (2000) 282.
[4] M.Moll, Radiation damage in silicon particle detectors-microscopic defects and macroscopic properties, Thesis/Dissertation, Hamburg, 1999.

* Supported by EU-FP7 HadronPhysics2 and Helmholtz International Center for FAIR

Test of prototype modules of the CBM Silicon Tracking System in a proton beam at COSY *

J.M. Heuser[1], W. Niebur[1], W. Müller[1], S. Linev[1], J. Adamczewski-Musch[1], V. Friese[1], B.W. Kolb[1], S. Chatterji[1], T. Balog[1,3], A. Lymanets[2,4], I. Sorokin[2,4], and M. Singla[2]

[1]GSI, Darmstadt, Germany; [2]Goethe University, Frankfurt, Germany; [3]Comenius University, Bratislava, Slovakia; [4]Kiev Institute for Nuclear Research, Kiev, Ukraine

In December 2010, prototypes of CBM's silicon tracking detector system, the muon detection system, and readout electronics were tested in a 3 GeV/c proton beam at COSY, Forschungszentrum Jülich, Germany [1]. The experimental area "Jessica" was equipped with newly prepared infrastructure from GSI, shown in Fig. 1, foreseeing forthcoming CBM in-beam tests there on a regular basis.

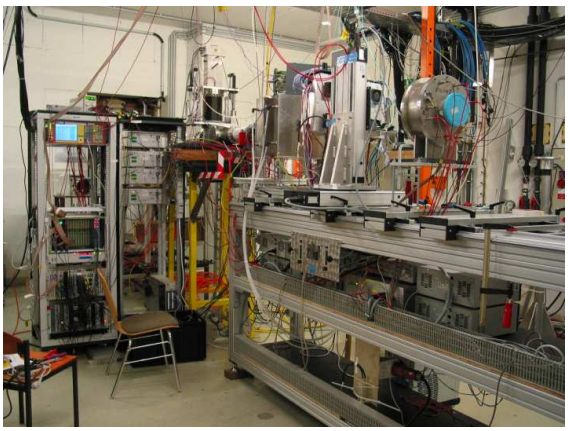

Figure 1: Test beam stand in the Jessica cave at COSY.

Silicon Tracking Stations

The prototype Silicon Tracking System comprised two stations based on double-sided silicon microstrip, ultra-thin readout cables, and self-triggering readout electronics (Fig. 2-left). The detectors SPID-CBM02 originate from a cooperation with CiS, Erfurt, and have 256 orthogonal strips per side with 50 μm strip pitch. The detectors were assembled into boards at SE SRTIIE, Kharkov, Ukraine. The readout boards developed at GSI are based on the self-triggering n-XYTER chip. Numerous improvements as compared to the in-beam test of 2009 [2] were introduced on hardware and software levels.

By implementing proper shielding and grounding techniques the electronic noise was reduced to about 600 e^-, which is now dominated by the preamplifier noise. The n-XYTER temperature was stabilized with water cooling, which abated the problem of the baseline drift significantly. In addition, an automatic baseline calibration was implemented in the data acquisition software and run between the beam spills. A detector control application based on the EPCIS [3] framework has been developed and ran on a dedicated PC. All the auxiliary hardware, including power supplies, stepping motors for the GEM and the beam monitoring detectors, water cooling units and temperature sensors were operated and monitored remotely. Some of the measured process variables (STS bias voltages, GEM detector position, temperatures) were periodically inserted into the data stream to study the detector response as a function of those values and to allow for temperature and high voltage corrections in on-line and off-line data analyses.

Measurements

The amplitude response of the silicon detector system has been measured as a function of the bias voltage and of the beam incidence angle. Landau-like spectra were clearly seen on the p-side at all bias voltages (50 V – 90 V) and on the n-side starting from 60 V. A cluster analysis of the charge collected in adjacent strips shows peaks at around 140 ADC units corresponding to the most probable signal from the minimum ionizing particles (Fig. 2-right). The signal-to-noise ratio was about 20 in this point. According to a previous calibration of the n-XYTER gain [4] only 60% of the expected charge seems to have been collected on either side of the detector. The reason for the apparently low collection efficiency is to be investigated.

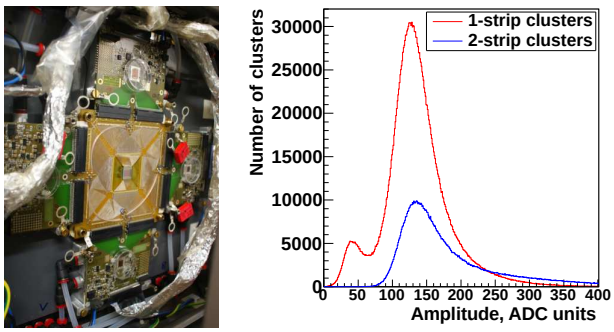

Figure 2: Opened STS station with the silicon detector board surrounded by readout electronics (left). Typical amplitude response spectra, here from the detector n-side, at 70 V bias and normal beam incidence (right).

References

[1] http://www.fz-juelich.de/ikp/cosy/en/
[2] GSI Scientific Report 2009 67
[3] http://www.aps.anl.gov/epics
[4] GSI Scientific Report 2009 84

* Work supported by EU-FP7 HadronPhysics2, Helmholtz International Center for FAIR and EU-FP7 MC-PAD.

Design studies for a CBM RICH prototype

D. Kresan and C. Höhne
Justus Liebig Universität Gießen, Germany

A RICH Prototype which will be scalable to the full CBM-RICH is planned and driven by the following considerations: verification of the concept of the CBM-RICH detector; validation of the CBM-RICH simulations with the CbmRoot framework by testing the ring finding and fitting algorithms; getting experience building and running the RICH detector including an evaluation of the concept of read-out plane and mirror adjustment and alignment; requirement to write a Technical Design Report.
In order to have approximately the same amount of Cherenkov photons per electron/pion track the length of the radiator and the gas type was kept as in the layout of the CBM-RICH [1], i.e. at 1.9 m. The positioning and alignment of the mirror and the Photo Multiplier (PMT) plane was adjusted to achieve the focusing of the light cone from Cherenkov radiation of electrons passing the detector.
The schematic ROOT drawing of the detector layout is shown in figure 1.

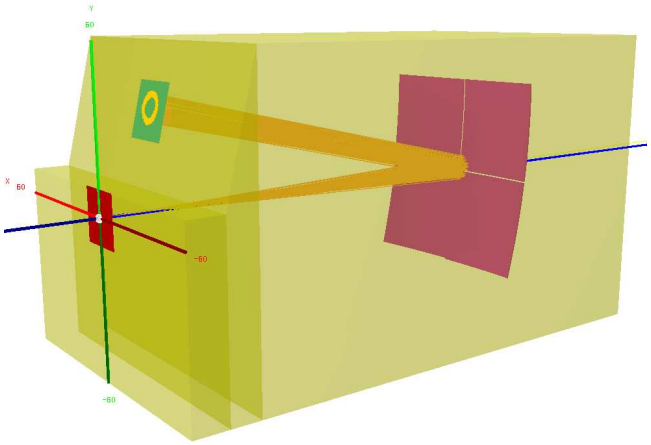

Figure 1: Schematic drawing of the prototype geometry.

Picture includes the radiator (transparent yellow), beam entrance window (red), MAPMT plane (green) and 4 rectangular mirrors (pink). Z-axis is the beam axis. The X-Y dimensions of the gas radiator is 1.2×1.2 m^2, the total length is 2.1 m.
The beam line T9 at CERN PS delivers secondary beam of hadrons and electrons. The beam focal point in the simulation was placed 1 m in front of the detector. The smearing was done for position of a particle at the focal plane and for polar angle according to the beam characteristics at T9 [2]. Momentum of a particle has uniform distribution from 1-10 GeV/c. Azimutal angle is also uniformly distributed from -180° to 180°. The beam in the simulation consists of 50% electrons and 50% negative pions.
The photodetector at the reconstruction stage is implemented as an array of 4×4 MAPMTs each 64 channels (1024 channels in total). Hits are created from projected photons by applying tabulated quantum efficiency of the PMTs. In addition 50 (5%) channels are fired in each event, simulating in this way a more pessimistic noise level. Both the signal and noise hits were taken as input for the ring finding algorithm [3]. The ring finding algorithm is based on standard implementation of Hough transform finder in CbmRoot. As a fitter, the standard Ellipse Fitter is used. The performance of the Hough transform ring finding algorithm is electron efficiency 99.1% and pion misidentification 3.3%.
Particles were identified by the cut on the main axis of the reconstructed ellipse. Ellipses with a $>$ 4.4 cm were considered to be originated from electrons, a $<$ 4.4 cm - from pions. Figure 2 shows the distribution of the ellipse main axis versus momentum of the particle (left picture) and pion misidentification as a function of momentum (right picture).

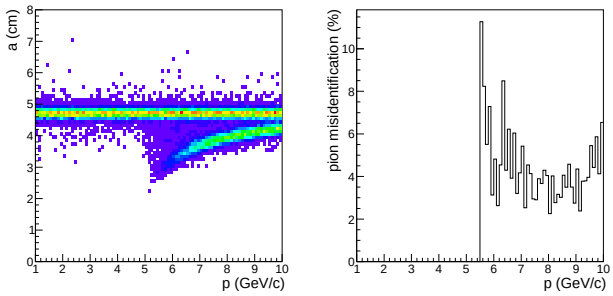

Figure 2: Left picture - distribution of the ellipse main axis versus momentum, right picture - pion misidentification as a function of momentum.

The Full RICH Prototype was successfully implemented and tested in the CbmRoot framework. Results of the reconstruction show ability of the Hough transform ring finding algorithm to cope with very high noise level and in a sufficient way to distinquish between electrons and pions.
Supported by HIC for FAIR.

References

[1] S. Lebedev *et al*, CBM Progress Report 2008, p. 20

[2] http://ps-div.web.cern.ch/ps-div/Reports/PA9321/Tables/Table9.html

[3] S. Lebedev *et al* J. Phys. Conf. Ser. 219, **032015** (2010)

Investigation of cross talk in Multi Anode Photomultipliers for the CBM RICH photodetector

J. Eschke[1] *and F. Meyer*[2]
[1]GSI, Darmstadt, Germany; [2]University of Bielefeld, Germany

A key item of the CBM physics program is the precise measurement of low-mass vector mesons and charmonium in their leptonic decay channel. In CBM, electrons will be identified using a gaseous RICH detector combined with several TRD detectors positioned behind a system of silicon tracking stations [1]. The concept of the RICH detector foresees an array of multi-anode photomultipliers (MAPMTs) for the (2.4 m^2) photodetector.

Beam tests at GSI (2009) and CERN (2010) and measurements with LEDs in the laboratory could demonstrate that the Hamamatsu H8500 with 64 pixels with a pixelsize of 58×58 mm^2 is very well suited for the detection of single Cherenkov photons and therefore very likely will be used for the CBM RICH photodetector [2] [3].

In all these tests the signals of the MAPMT were attenuated by a factor of 50 in order to be compatible with the self-triggered readout electronics based on the n-XYTER ADC chip.

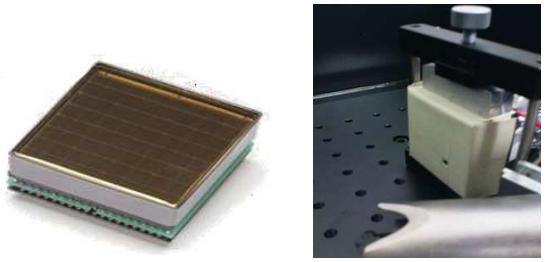

Figure 1: Single photon illumination of 1 pixel of the MAPMT with a LED

An important feature of H8500 MAPMT to be investigated is the crosstalk between neighboring pixels. For determination of the crosstalk a light emitting diode (LED) with a wavelength of 350 nm was pulsed with ∼10 ns pulses with signal amplitudes of ≈ 4.5 Volts. A distance between the LED and the MAPMT of ≈ 20 cm in combination with the voltage at the operating threshold of this particular LED assured that not more than 1 photon per Pulser trigger signal reached one MAPMT pixel.

Figure 1 shows the Hamamatsu H8500, which has been covered by an aperture with a 3×3 mm^2 hole. Only the center part of 1 pixel has been illuminated at once.

A clear separation of uncorrelated, low-amplitude noise events from signals of single photons with higher amplitude was achieved by a cut on the time difference between the Pulser trigger signal and the hits in the MAPMT.

Figure 2 shows the event-integrated yield of MAPMT hits in linear and loarithmic scale. The uncovered pixel shows the largest number of hits. However the direct 8 neighbor pixels, but also the 16 second neighbor pixels exhibit an non neglidgible signal yield, even though they could not be directly excited by photons.

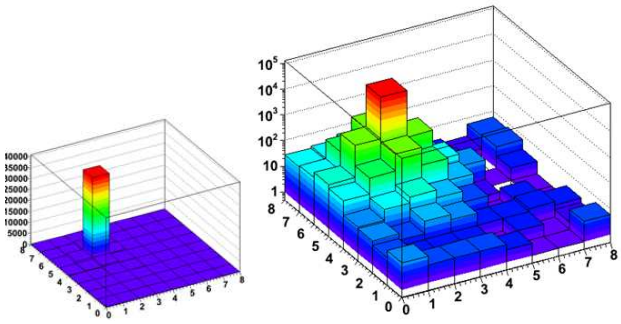

Figure 2: Yield of fired MAPMT cells from single photon illumination of 1 pixel

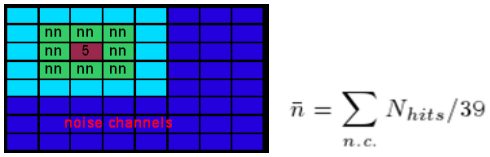

$$\bar{n} = \sum_{n.c.} N_{hits}/39$$

Figure 3: Calculation of average noise ($\overline{n}$)

For quantitative determination of this cross talk the average noise level in the 39 non neighboring MAPMT pixel has been calculated (see Figure 3) and subtracted.

$$x = \frac{\sum\limits_{nn} N_{hits} - 8\bar{n}}{N_{central} - \bar{n}}$$

The fraction of cross talk in the direct 8 neighbor pixels (x) compared to the central, illuminated pixel has been determined by measurents illuminating four different pixels of this MAPMT to be 7.7% on average. The measurement will be repeated by single photon illumination with a template of the same size as the MAPMT pixels. It is expected that these measurement will give a cross talk of more than 10%.

References

[1] C. Höhne, *CBM-RICH layout optimization*, CBM Progress Report 2007, Darmstadt 2008

[2] J. Eschke *et al.*, GSI sientific report 2009 and 2010

[3] J. Kopfer *et al.*, GSI sientific report 2010

Quantum efficiency and gain homogeneity measurements of H8500 MAPMTs for the development of a CBM RICH prototype camera*

J. Kopfer[1], *K.-H. Becker*[1], *K.-H. Kampert*[1], *C. Pauly*[1], *J. Pouryamout*[1], *and J. Rautenberg*[1]
[1]Bergische Universität Wuppertal, Germany

The camera of the RICH detector in the CBM experiment is forseen to consist of approximately 860 Hamamatsu H8500 multianode photomultiplier tubes (MAPMTs). A RICH prototype is currently being built. Knowing the MAPMT characteristics is crucial for understanding the expected detector performance. Gain homogeneity and spectral response in terms of quantum efficiency (QE), i.e. the number of generated electrons per incident photon, have been measured at Bergische Universität Wuppertal.

Quantum efficiency

The QE of a PMT is mainly determined by photocathode and window material. MAPMTs with bialkali (BA) and superbialkali (SBA) photocathodes as well as borosilicate and UV glass windows have been tested.

The QE is measured by operating the PMT as a photocell, i.e. shortening all dynodes and applying a voltage of ≈ -100 V between the photocathode and the dynode system. The photocathode is illuminated with monochromatic light from a deuterium and tungsten-halogen lamp in the wavelength range between 200 nm and 800 nm using a double grating monochromator. For spatially resolved measurements the light is coupled to a light fibre which is connected to a xy-stage. The photocurrent is measured by a picoamperemeter and the QE is determined using a calibrated photodiode as a reference.

Figure 1 (top) shows the wavelength dependent QE for MAPMTs with different types of photocathode and window material. SBA cathodes have a maximum QE of ≈ 35 % and BA cathodes ≈ 25 %. UV glass windows let pass light down to the deep UV resulting in a QE of ≈ 5-10 % at 200 nm whereas borosilicate blocks the light at around 300 nm. Folding these QE curves with the $1/\lambda^2$-spectrum of Cherenkov light leads to 89.6 % of detected Cherenkov photons for BA + UV glass and 83.2 % for SBA + borosilicate when compared to SBA + UV glass which exhibits the maximum yield. As the difference of QE between SBA and BA cathode vanishes towards UV and due to the $1/\lambda^2$ dependence of the Cherenkov spectrum the benefit of using SBA instead of BA is just 10 %.

Spatially resolved QE measurements reveal relative inhomogeneities of ≈ 25 % over the photocathode surface. A gradient from down right to top left as well as a circular structure are visible (figure 1 bottom).

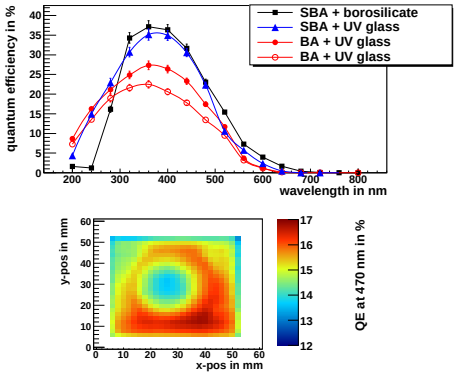

Figure 1: QE as function of wavelength for H8500 MAPMTs (top) and spatially resolved at 470 nm for a MAPMT with BA cathode and UV window (bottom).

Gain homogeneity

The Gain has been measured using a pulsed LED emitting at 470 nm. A voltage of -1000 V was applied between cathode and anode. The charges of the pulses were sampled by VME based 100 MHz flash ADCs [1]. Using the xy-stage MAPMTs were scanned with a resolution < 1 mm. The average values of each MAPMT pixel normalized to the maximum are shown in figure 2 for a SBA (left) and BA cathode (right).

The ratio between minimum and maximum charge is 1:1.4 for SBA and 1:1.3 for BA which is slightly better than stated by the manufacturer.

The results demonstrate that MAPMTs are suitable for the construction of the CBM RICH detector and will be implemented in prototype simulations [2].

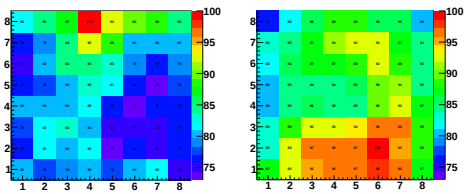

Figure 2: Normalized gain distribution of a MAPMT with SBA (left) and BA cathode (right).

References

[1] K.-H. Becker et al., CBM Progress Report 2009, p.24

[2] C. Höhne, D. Kresan, this report

* supported in part by GSI project WKAMPE1012 and by BMBF grant 06WU9195I

Single Cherenkov photon measurements with Multi-Anode-Photomultipliers for performance studies of the CBM RICH photodetector *

J. Eschke[1], *C. Höhne*[2], *K.-H. Kampert*[3], *J. Kopfer*[3], *D. Kresan*[2], *and C. Pauly*[3]
[1]GSI, Darmstadt, Germany; [2]Giessen University, Germany; [3]Wuppertal University, Germany

In November 2010 the CBM-RICH group together with other CBM groups took part in a test beamtime at CERN PS target area T10. We report on first results from the analysis of the obtained data.

Overview and goals

Our goal for this beamtime was to further study the Cherenkov photon detection with Hamamatsu H8500 Multianode PMTs using a proximity focusing test setup. This test provided valuable experience for the preparation of a fullscale gas Cherenkov prototype setup [1] to be tested at CERN in autumn 2011.

Setup and data analysis

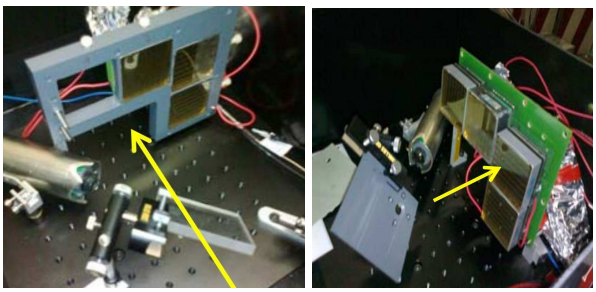

Figure 1: Proximity focusing setup with Plexiglas radiator (left) and quartz radiator with pin hole mask (right).

The experiment was setup inside a light-tight box, similar to earlier tests at GSI [2]. This time, 4 MAPMT were mounted in a L-shaped arangement in front of a Cherenkov radiator, covering roughly 25% of the generated Cherenkov cone. Two alternative kinds of radiator were used: an 8mm thick Plexiglas sheet, and a 4mm thick quartz radiator. Both were oriented such that the plane normal was pointing towards the PMTs in order to minimize ring distortion due to refraction at the radiator surface. Two different kinds of PMT mountings were tested (see fig. 1): During first runs the PMTs were hold by a plastic frame and connected directly via ribbon cables to the readout electronics. Later, the PMTs were plugged on a special PCB board, allowing for a better positioning and good shielding of the PMTs. Such a solution is foreseen to be used for the full detector and was tested here for the first time. Each pair of two PMTs was connected via attenuator boards to individual nXYter Frontend boards (FEB) each providing 128 readout channels.

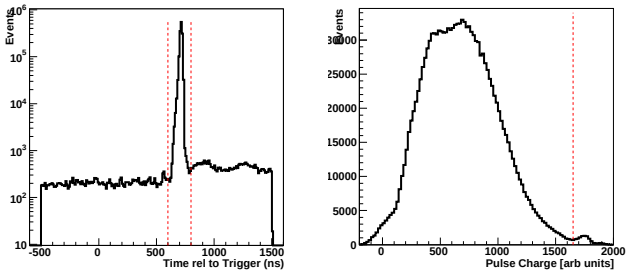

Figure 2: Time and amplitude distibution for individual hits. The dotted lines visualize cuts applied in the further data analysis.

A secondary beam of mixed pions and electrons in a momentum range between 1 and 6 GeV/c was used for the experiment, entering the box through a light tight entrance window. After crossing the radiator it passed the PMT plane with the beam center a few cm away from the PMT cathodes. The Cherenkov cone at these momenta has a nearly fixed opening angle of 46.6 degree for both radiators. The projected ring image, however, is smeared out due to the large beam spot of several cm. A pinhole mask of 1cm diameter on top of the radiator was used in some of the runs to limit the origin area of photons in order to obtain nevertheless a sharp ring image.

A coincidence condition of several scintillating finger detectors before- and behind the setup provided a trigger signal used for normalization of the data. All obtained data, together with the trigger signal and data from the silicon tracking station (STS) in front of our setup were synchronized and stored in ROOT trees for later analysis.

Results

First results from the data analysis are shown in fig. 2 and fig. 3. The time distribution of MAPMT hits in relation to the trigger (fig.2 left) shows a clear coincidence peak with background below the peak on the permille level. A cut on these coincident hits is applied for all later analysis. The amplitude sum spectrum (fig.2 right) is dominated by the peak corresponding to single photon response, a small peak around ADC values of 1700 is induced by signal overflow. These high amplitudes are mainly caused by direct hits of charged beam particles. Integrated hit distributions are shown in fig. 3 for three different setups, together with their corresponding hit multiplicity distribu-

* supported in part by GSI project WKAMPE1012 and by BMBF grant 06WU91951

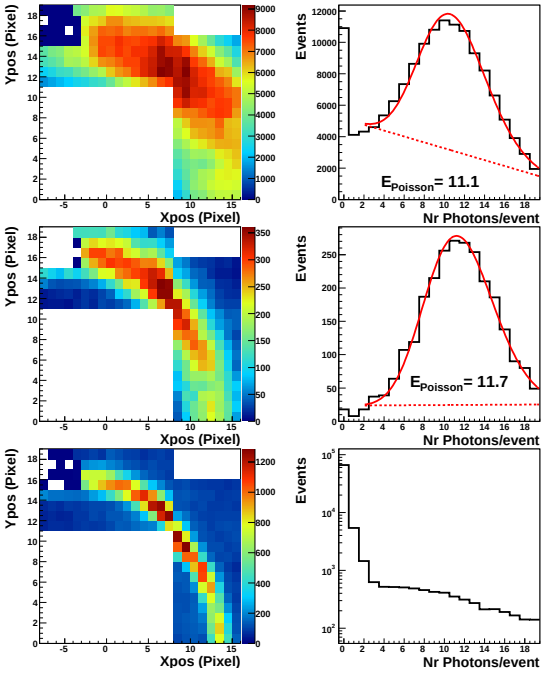

Figure 3: upper line: Integrated image of Cherenkov ring and hit multiplicity for data with Plexiglas radiator without pin hole. middle line: Same data including additional cut on $\geq$1 hit in STS. lower line: Data obtained with quartz radiator using 1cm pin hole. fitted line: Poisson fit plus linear background.

tions. Data obtained with the Plexiglas radiator without pinhole mask show a broad structure due to the large size of the beam. Applying a coincidence condition on ≥ 1 hit in the STS limits the acceptance range significantly and leads to a less smeared ring image. Missing hits in the upper left corner are caused by a broken cable. In both cases the hit multiplicity nicely reflects a Poisson shaped distribution on some linear background. A χ^2-fit yields an average multiplicity of 11-12 Cherenkov photons per event. In case of the quartz radiator with pinhole mask the observed ring image is well focused. However, the acceptance area is now much smaller then the trigger corridor causing many events without Cherenkov photons. The multiplicity distribution in this case is dominated by background and does not show any poisson shaped peak structure, probably due to partial shadowing by the pinhole mask. An average photon number can not be extracted for this configuration so far, a full Monte Carlo simulation is being prepared to understand this distribution quantitatively.

Expected photon yield

The total number N of produced Cherenkov photons per incident charged particle is

$$N = \int_{\lambda_1}^{\lambda_2} \frac{1}{\lambda^2}\, d\lambda \cdot L \cdot 2\pi\alpha \cdot z^2 sin^2\theta_C \qquad (1)$$

with the low wavelength end of radiator transmission λ_1, high wavelength end of photocathode quantum efficiency λ_2, radiator length L, fine-structure constant α, incident's particle charge z in units of the electron charge, and Cherenkov angle θ_C. The number of expected Cherenkov photons in the photodetector is lower than the number of produced photons. Limiting factors are the finite transmittance of the radiators (80 % above 390 nm for Plexiglas, 85 % above 200 nm for quartz), the geometric coverage of the MAPMTs (89 % for the H8500 series), the wavelength dependent quantum efficiency of the MAPMTs, and the geometrical acceptance of the photodetector. Considering refraction of photons at the radiator-air interface and dead MAPMT pixels due to the broken cable leads to a geometrical acceptance of 21.5 % for the Plexiglas radiator and 20 % for the quartz according to a simple geometry simulation shown in fig. 4. For the above analyzed runs MAPMTs with bialkali photocathode and UV glass window were used. The number of photons detected by the photodetector is then expected to be 8.0 for the Plexiglas radiator and 15.5 for the quartz.

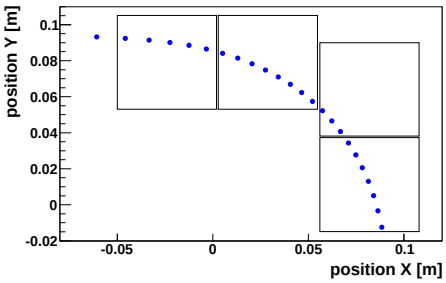

Figure 4: Geometrical acceptance of the photodetector. The dots display the position of expected Cherenkov photons on the photodetector plane. The ring is distorted due to refraction.

Summary and conclusion

For data taken with the Plexiglas radiator the measured number of Cherenkov photons per event succeeds the theoretical expectation of 8 photons/event significantly. This might be partly dedicated to crosstalk between neighboring pixels (see [3]), which would increase the observed hit multiplicities. Another possible contribution could be an underestimation of the transmittance of Plexiglas for UV photons. Anyway, the high photon yield shows the good single photon detection capabilities of H8500 PMTs. A full Monte Carlo simulation of the setup is being prepared to further improve the quantitative understanding of the data.

References

[1] D. Kresan et al, this report
[2] J. Eschke et al, CBM progress report 2009
[3] J. Eschke et al, this report

CBM TRD Readout with the SPADIC Amplifier / Digitizer Chip

T. Armbruster[*]*, P. Fischer*[†]*, and I. Perić*
University of Heidelberg, Germany

Abstract

The SPADIC chip is being developed for the readout of the CBM Transition Radiation Detectors (TRD). Each channel of the latest prototype contains an input protection, a charge amplifier / shaper with a noise of 800 e^- at 30 pF input capacitance, a 9 Bit, 25 MHz ADC and a memory to store a train of signal samples. An interface PCB to connect the SPADIC to prototype TRD chambers as well as a suited fast USB 2.0 based data acquisition board have been designed. Suited software to control the system and to read out the chip in the general framework of the CBM DAQ has been provided. First real detector data has been acquired during a test beam campaign at CERN.

The SPADIC Chip

The basic readout concept is to perform both the amplification and the digitization of the (charge) pulses from the CBM TRD in a single front-end ASIC. It is intended to continuously digitize the whole shaper pulses which allows for a flexible subsequent feature extraction (amplitude, time, ...) either directly on the chip or in some FPGA (both options are currently subject of discussion). The group in Heidelberg has started the development of the SPADIC (Self triggered Pulse Amplification and Digitization asIC) chip 2008. The latest prototype SPADIC 0.3 contains 26 channels with different amplifier versions out of which 8 are equipped with pipelined 9 Bit ADCs running at 25 MHz. The system noise including the ADC has been measured to $\approx 800\,e^-$ at a peaking time of 80 ns and a capacitive input load of 30 pF while consuming 3.6 mW for the front-end and 4.5 mW for the ADC per channel. Using static input signals the resolution of the ADC is close to 8 Bit (INL slightly larger than 0.5 LSB). The prototype chip also contains an on-chip digital memory which can record snapshots of up to 42 ADC data samples that can be read out later at slower speed. The architecture is self-triggered so that an amplitude above a programmable threshold triggers data storage on a per channel basis.

The final chip will also include a digital IIR filter to eliminate long ion tails as well as a fast serial interface compatible to the CBM DAQ data format. With the help of measured detector pulses the optimal filter structure (filter order, topology, word widths, ...) is presently being evaluated. A first iteraton of the filter will already be realized in the next ASIC prototype. A web page about the SPADIC chip has been created at `http://spadic.uni-hd.de`.

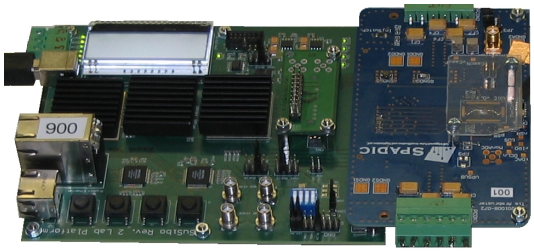

Figure 1: SUSIBO Readout Board (left) and Interface Board with SPADIC chip (right).

Chip Readout System

In order to read out several SPADIC chips when mounted on the test chambers, a versatile fast data acquisition board and a suited SPADIC interface board (see Fig. 1) have been developed and tested. The SUSIBO ('SuS Interface BOard') contains a USB 2.0 interface, a large Xilinx FPGA, memory, Ethernet IO and a differential interface to the trigger logic. It is controlled by custom software running under Linux. The interface board houses a SPADIC chip (wire bonded to the PCB), interface and biasing circuitry and a ZIF connector to connect TRD chamber prototypes to the amplifier inputs. Eight units have been assembled for use mainly in the 2010 TRD beam test. A 2^{nd} generation interface board with improved interfacing and better signal routing is presently being prepared.

Test Beam with TRD Chambers

The readout system has been used successfully in the 2010 CBM test beam campaign at CERN to read out TRD prototype detectors from Frankfurt and Münster. A screen shot of the online event display with two detector pulses is shown in Fig. 2. The data is presently being analyzed.

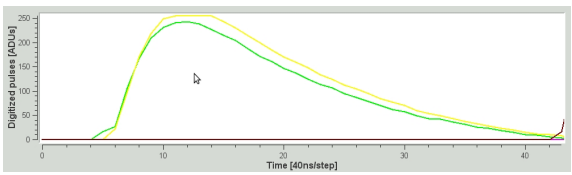

Figure 2: Online display of detector pulses digitized with SPADIC.

[*] tim.armbruster@ziti.uni-heidelberg.de
[†] peter.fischer@ziti.uni-heidelberg.de

First beam test of the Frankfurt prototype for the CBM TRD

W. Yu[1], *H. Appelshäuser*[1], *A. Arend*[1], *M. Hartig*[1], *P. Dillenseger*[1], *P. Reichelt*[1], *and the CBM Collaboration*

[1]Institut für Kernphysik, Goethe-Universität, Frankfurt am Main, Germany

As one of the key components in the CBM experiment, the Transition Radiation Detector (TRD) will play a significant role in the particle identification. A fast detector with double sided readout chambers[1] and a ALICE type of detector with both drift and amplification regions have been designed for the circumstance of high particle rates. We propose to build a fast detector with an amplification region only. Simulation studies combining dE/dx and transition radiation show that such a simple detector can fullfil the requirement of particle identification[2]. If such design can be realized and verified by more sophiscated studies and beam tests, it will noticeably reduce the cost and simplify the construction.

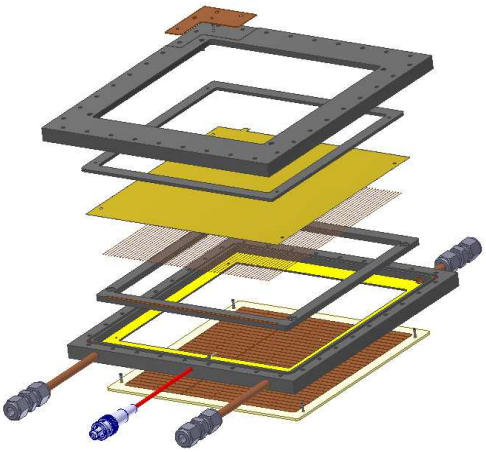

Figure 1: Sketch of the readout chamber.

The IKF group in Frankfurt participated in the beam test in Novermber 2010 at CERN and tested its two prototype detectors. Both detectors are equipped with a readout chamber, which has an amplication region of 1 cm. The sketch of the readout chamber can be seen in Figure 1. The chamber size is 15×15 cm^2 and it is enclosed by an aluminized kapton foil and a simple PCB for the charge sensitive readout. Inside the readout chamber a plane of anode wires is located in the center for gas amplification. The pitch between anode wires is 5 mm for one chamber and 2.5 mm for the other. Anode wires are made of Au plated W, 20 μm in diameter. Rectangular pads with a conservative size of 5×50 mm^2 are chosen to read out particle induced signals. In the beam test 8 neighbouring pads in the middle column grouped together from each chamber are read out by 8-channel SPADIC chip, developed to be a self-triggered pulse amplification and digitization ASIC[3]. The radiator is a sandwich construction of Rohacell HF71 foam and polypropylene fibres. Figure 2 shows one of the prototype detectors during the beam test.

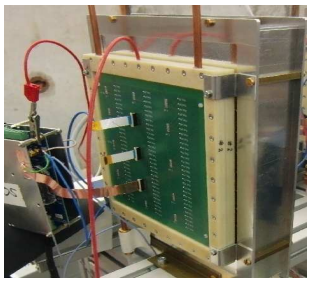

Figure 2: Prototype detector in the beam test.

The setup of the Frankfurt prototypes can be found in the overview of this CERN beam test[4]. Both detectors were tested at beam momenta of 2, 3, 4 and 5 GeV/c respectively. Two gas mixtures were used in the test: Xe-Co2, and Ar-Co2, with the ratio of 80:20 in both cases. Figure 3 shows a very preliminary result of the integrated ADC spectra from pions (blue line) and electrons (red line) separately. Here the data was collected by the chamber of 2.5 mm wire pitch at the beam momentum of 5 GeV/c and with the gas mixture of Xe-Co2.

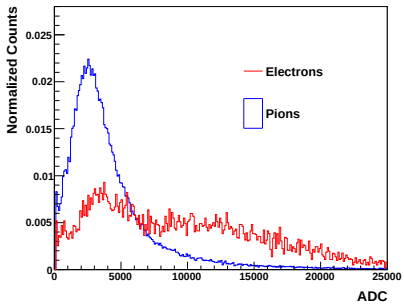

Figure 3: Integrated ADC spectra from pions (blue line) and electrons (red line).

References

[1] M. Klein-Bösing *et al*, Nucl. Instr. Meth. Phys. Res. A 585 (2008) 83-87.

[2] P. Reichelt *et al.*, "Study on electron/pion discrimination with the CBM Transition Radiation Detector", this report.

[3] T. Armbruster *et al*, "CBM TRD Readout with the SPADIC Amplifier / Digitizer Chip", this report.

[4] D. Emschermann and C. Bergmann, "First common beam test of the CBM STS, RICH and TRD subsystems at the CERN Proton Synchrotron", this report.

First common beam test of the CBM STS, RICH and TRD subsystems at the CERN Proton Synchrotron*

D. Emschermann[1] *and C. Bergmann*[1] *for the CBM collaboration*
[1]IKP Münster, Germany

A first common beam test of the CBM **T**ransition **R**adiation **D**etector (TRD), **R**ing **I**maging **Ch**erenkov (RICH) and **S**ilicon **T**racking **S**ystem (STS) subsystems was performed for one week at the CERN Proton Synchrotron in November 2010 [1]. The measurements were carried out at the T10 beamline in an electron/pion beam with momenta of 2 to 5 GeV/c. The beamline setup is presented in Figure 1.

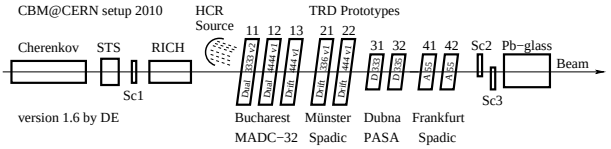

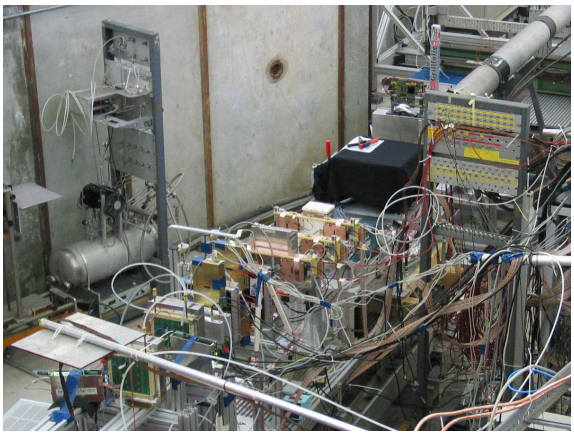

Figure 1: Setup of the prototypes along the T10 beamline.

Upstream we began with a STS station, followed by a RICH prototype, then came 9 TRD prototypes from the 4 laboratories in Bucharest [2], Münster, Dubna and Frankfurt [3]. Besides the above mentioned prototypes, the setup was comprising a Cherenkov detector and a Pb-glass calorimeter for e/pi identification (see Figure 2), as well as three beam trigger scintillators.

The STS station was commissioned in beam at CERN to prepare for the following December beamtime at COSY. The RICH was based on a proximity focussing setup with a solid (plexiglass) radiator and four Hamamatsu MAPMTs allowing to reconstruct Cherenkov ring segments [4]. The readout of the STS and RICH subsystems was based on the nXYTER frontend, readout by the CBM readout controller (ROC).

For the TRD, various MWPC geometries were under test and two complementary approaches for the signal processing were investigated: The TRDs from Münster and Frankfurt were readout with the custom SPADIC [5], a self-triggered sampling ADC, while the detectors from Bucharest and Dubna used a VME based peak sensing ADC. Part of the test program were high voltage scans, $ArCO_2$ and $XeCO_2$ gas mixtures, variation of the incident beam angle and momentum and different versions of radiators.

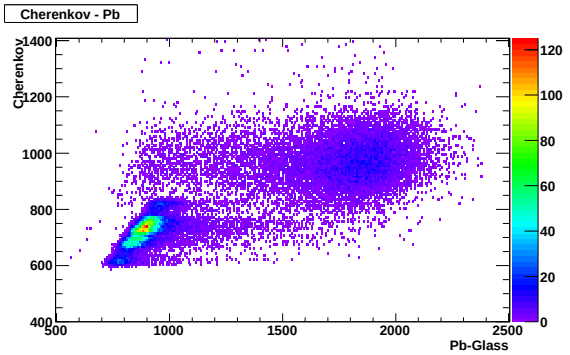

Figure 2: e/pi separation for a run at 2 GeV/c.

A hybrid DABC/MBS setup was prepared allowing to read the beam monitoring detectors and all (self-)triggered prototypes and in a common data aquisition system [6]. The analysis of the beamtime data, e.g. pion efficiency and position resolution for the TRDs, is still ongoing.

In autumn 2011 the tests will be iterated with another common CBM beamtime at the CERN PS/T9 beamline, allowing for higher momenta.

References

[1] David Emschermann, CBM Testbeam 2010 Website, http://cbm.uni-hd.de/testbeam2010

[2] M. Petris et al, Two-dimension position sensitive Transition Radiation Detector in beam- tests using new Fast Analog Signal Processor (FASP), GSI Scientific Report 2010

[3] W. Yu et al, First beam test of the Frankfurt prototype for the CBM TRD, GSI Scientific Report 2010

[4] J. Eschke et al, Single Cherenkov Photon measurements with Multi-Anode Photomultipliers for the CBM RICH, GSI Scientific Report 2010

[5] Tim Armbruster, The SPADIC Project Website, http://spadic.uni-hd.de

[6] S. Linev et al, DABC as data aquisition framework for CBM, GSI Scientific Report 2010

* Work supported by BMBF and the HadronPhysics2 project financed by EU-FP7.

Front End Electronics for High Counting Rate TRD *

A. Caragheorgheopol[1], *D. Bartoş*[1], *V. Catanescu*[1], *V. Văleanu*[2], *and V. Vasiliu*[2]
[1]NIPNE, Bucharest, Romania; [2]ISS, Bucharest, Romania

Fast Analog Signal Processor FASP-0.1 [1, 2] is a prototype ASIC designed at NIPNE for HCR-TRD having in mind the CBM experiment at FAIR. In this contribution we report on relevant measured parameters of ASIC analog channels and a FEE based on FASP, designed and built for in-beam tests of our HCR-TRD prototypes [3].

ASIC measured parameters [4, 5]

- Quiescent supply current (V_D = 3.3V): 30mA $\pm$1mA.
- Output baseline shift :
  - with power supply (V_D = 3.0- 3.6V): $< 0.07\%$;
  - with detector leakage current (I_L=$\pm$ 50nA): $<9\mu$V/nA.
- Conversion gain G vs. C_{det} (for FAST outputs):
- Integral nonliniarity (INL)(0-1V linear range):

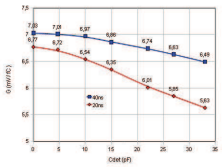

Gain slope:
0.50% for τ = 20 ns
0.23% for τ = 40 ns

Figure 1:

INL = 1.0% for τ =20ns, FLAT output;
INL = 0.2% for τ =40ns, FAST output.

- Overload recovery (for FAST outputs, τ = 40 ns): first pulse: x10 overload ; second pulse: after 400ns (corresponding average pulse rate $>$ 300kcps).

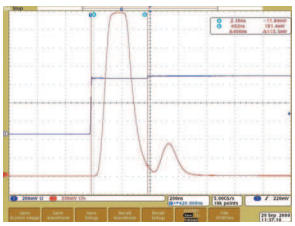

Figure 2:

- Electronic noise charge ENC vs. C_{det} for FAST outputs:

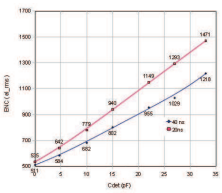

Noise slope vs. shaping time:

30.0 e/pF for τ = 20 ns
23.3 e/pF for τ = 40 ns

Figure 3:

* Work supported by EU-FP7/HP2-WP18 Grant No 227431 and Romanian NASR/CAPACITATI-Modul III contract nr. 42. and NASR/NUCLEU Project

Front End Electronics

FEE was designed to cope with the requirements for in-beam test of 3 different HCR-TRD prototypes:

- acceptable immunity to the "pick-up" noise;
- long transmission line of detector signals to ADC;
- NIM logic standard for request/grant protocol;
- 16 analog signal channels for each detector (48 total).

FEE is splitted in two units (Fig.4). The first one, motherboard, houses one FASP ASIC for wich it provides power supply, all DC references voltages (THRESHOLD, BASELINE,etc.), 8 analog buffers with differential outputs (each buffer can be switched to handle FAST or FLAT TOP signal), and NIM logic standard interface (EVT, REQ, RDY, RST signals). Motherboard is a three layers PCB of 100x120mm^2 size. The second one, adapter board, has two identic sections. Each section has 8 differential input channels providing single-ended outputs. DC output levels can be adjusted to match ADC inputs. Adapter board is three layers PCB of 78x74mm^2 size.

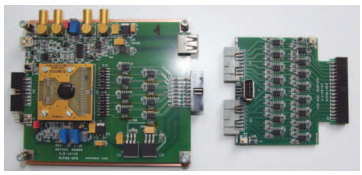

Figure 4: ASIC MB (Left) and Adapter(Right).

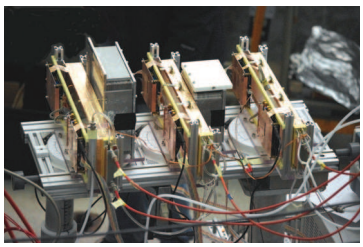

Figure 5: Experimental set-up used in the in-beam test.

HCR-TRD prototypes, the described FEE (48 channels) and geometry control mechanism (Fig.5) were succesfully tested at T10 beam line of the CERN PS accelerator, last November .

References

[1] V.Catanescu, CBM 10th Colaboration Meeting, Sept. 25-28,2007, Dresden
[2] V.Catanescu, et al., DPG,Bochum, March 18,2009
[3] M.Petris et al., contribution to this Sci.Rep.
[4] A. Caragheorgheopol et al., 14th CBM Colaboration Meeting, Split,Oct.6-9,2009.
[5] A. Caragheorgheopol et al., CBM FEE/DAQ Workshop, Feb. 22-23,2010,GSI

Performance studies on the CBM TRD using J/ψ

W.Yu[1], *H.Appelshäuser*[1], *M.Hartig*[1], *and the CBM Collaboration*
[1]Institut für Kernphysik, Goethe-Universität, Frankfurt am Main, Germany

The Transition Radiation Detector (TRD) will be one of the key components of the CBM experiment. It will be used for particle tracking and for the identification of electrons and positrons[1]. J/ψ production in the dielectron channel is a unique physics process to study the performance of the TRD. In the framework of CBMRoot mixed samples of J/ψ and background events are simulated in the detector setup. Then J/ψ particles are reconstructed with the TRD and other tracking detectors in the same framework. The limit of the TRD hit resolution is studied using the ratio of reconstructed J/ψ signal to background, which provides useful information to determine the size of readout pads.

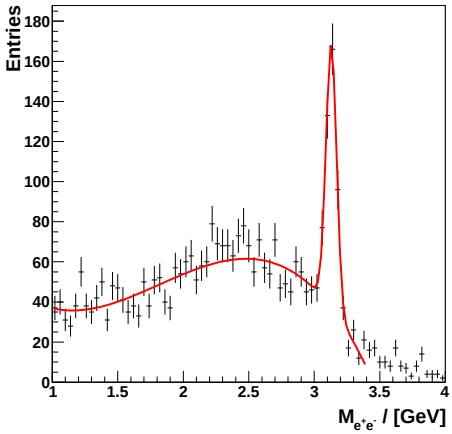

Figure 1: Invariant mass spectrum of J/ψ.

In the current CBMRoot the TRD is composed of 3 stations downstream from the target at 450 cm, 675 cm and 900 cm respectively. In this geometry configuration each station has 4 layers. Each layer has a 29 mm thick radiator in the front followed by a 6 mm thick gas detector. J/ψ signals are produced by HSD via the central Au+Au collision and forced to decay to electron-positron pairs. Background events are generated using UrQMD under the same condition. Electron-positron pairs decaying from J/ψ and background events are subsequently mixed together with the same proportion. This mixed sample is then used as input for the detector simulation. A global tracking method which uses spatial hits from TRD and the forward silicon tracking system (STS) is applied on the track reconstruction. To focus on the TRD performance only idealized clusterization is used for STS. Monte-Carlo generated hits from TRD are smeared with different values in order to check the limit of the detector resolution. p_t of electrons-positrons is required to be larger than 1 GeV/c. Figure 1 shows the invariant mass spectrum reconstructed by the electron-positron pairs from this simulation.

The ratio of signal to background from the spectrum of J/ψ invariant mass provides a useful way to check the detector performance. However, this ratio can not be directly extracted so far from Figure 1. The proportion of J/ψ signals to background events with the same ratio in this simulation is far from the reality. Experimentally J/ψ is a very rare physics process. Due to this mixture the combinatorial background formed by one of the decay electrons or positrons and one electron or positron from the background events is significantly enhanced compared to the reality. This distorts the background in the J/ψ invariant mass spectrum dramatically. A reliable ratio of signal to background can be obtained by removing this distorted combinatorial background source in the simulation. Figure 2 shows the ratio of signal to background extracted from the J/ψ invariant mass spectrum by varying the smearing of TRD hits. Here, the above mentioned combinatorial background has been removed. It can be clearly seen that the ratio stays constant when the hit resolution is less than 1 mm.

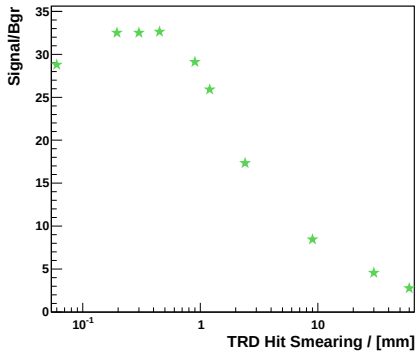

Figure 2: Ratio of signal to background from the J/ψ invariant mass spectrum by varying the smearing of TRD hits.

Studies on a mixed sample of J/ψ and UrQMD events provide the limit on TRD resolutions. Signal to background ratio is found to drop significantly when the hit resolution is worse than 1mm. Further studies need to be carried out on the MC data with more realistic detector digitisation and clusterisation. Feasibility study on the TRD online trigger for J/ψ can also be performed using a stand alone TRD tracking method developed by M.Krauze, A.Bubak and W.Zipper.

References

[1] B. Friman *et al.*, "The CBM Physics Book", Lecture Notes in Physics, Vol.**814**

Study on electron/pion discrimination with the CBM Transition Radiation Detector*

P. Reichelt† [1], *H. Appelshäuser*[1], *M. Hartig*[1], *and the CBM Collaboration*
[1]Institut für Kernphysik, Goethe-Universtität, Frankfurt am Main, Germany

In the CBM experiment at FAIR, a Transition Radiation Detector (TRD) is foreseen for tracking and electron/pion discrimination. Up to twelve detector layers are considered, each with a thin gas volume in order to have sufficiently fast readout for the intended high collision rates. In this report, we present a combined simulation study of the electron/pion discrimination dependence on the detector thickness and on two methods of combining the signals of the individual layers. The influence of the radiator performance is discussed.

Single TRD performance

For discriminating electrons from pions in the momentum region of a few GeV/c, a TRD profits from their different energy loss through ionization, but mostly from the additional transition radiation produced by electrons. A complete TRD setup should suppress the number of misidentified pions by a factor of 100 (i.e. a pion efficiency of 1%) while keeping 90% electrons in the sample (electron efficiency of 90%), whereas - because of the statistical nature of both signal contributions - a single detector cannot achieve this unless it has a very thick active volume. For a moderate electron efficiency however, even a detector of around 1 cm thickness rejects more than 90% of the pions, see figure 1. The simulation is a stand-alone Monte Carlo, with TR-production matched to ALICE-TRD sandwich radiator measurements and dE/dx based on Geant 3.21 [1].

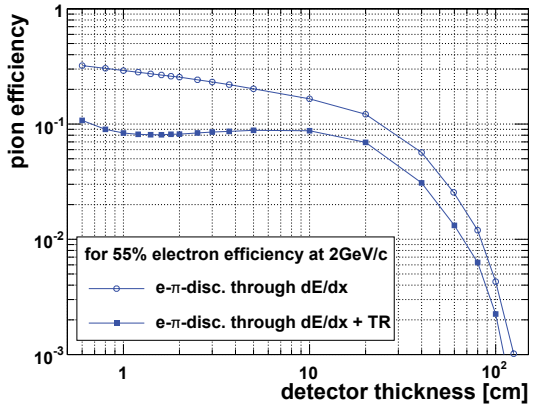

Figure 1: Pion efficiency as function of detector thickness for 55% electron efficiency.

Multiple TRD layers

The performance of multiple detectors depends on the method of combining their signals. For a setup of 12 layers of 1 cm and demanding 90% electron efficiency for the full system, a pion efficiency of 3.4% can be reached by just analyzing the sum of all signals. It is more powerful however to decide for each layer between electron and pion and accept electrons with at least k out of n electron-like signals. Figure 2 shows that the lowest pion efficiency can be reached with a single layer electron efficiency of $p = 64\%$ and demanding at least 6 electron-like signals. The resulting pion efficiency is 0.2%.

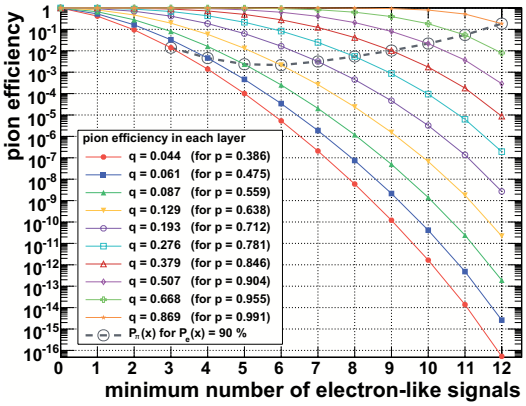

Figure 2: Pion efficiency from 12 detectors of 1 cm. The dashed line shows values for 90% electron efficiency.

Radiator Performance

The yield of TR and its spectrum depends on the radiator type and composition. An increase in the photon yield by 20% with respect to the ALICE radiator would e.g. reduce the pion efficiency by a factor of 4 to only 0.05%. Also the energy range of the TR-photons is not ideal for absorption in a thin detector. The largest amount of deposited TR-energy is reached with an almost 50% softer TR-spectrum (w. resp. to ALICE), having a mean of 7 keV and also leading to 0.05% pion efficiency. On the other hand, one finds that a substantial increase of the detector thickness from 1 to 1.6 cm gives a pion efficiency of 0.09%, suggesting that the radiator offers a bigger potential for improvements.

References

[1] P. Reichelt, Master Thesis, Goethe-Universität Frankfurt (to be submitted Feb. 2011).

* Work supported by BMBF and GSI
† preichelt@ikf.uni-frankfurt.de

Two-dimension position sensitive Transition Radiation Detector in beam- tests using new Fast Analog Signal Processor (FASP) *

M. Petriş[1], *M. Petrovici*[1], *V. Simion*[1], *D. Bartoş*[1], *G. Caragheorgheopol*[1], *V. Cătănescu*[1], *F.Constantin*[1], *C. Bergmann*[2], *D. Emschermann*[2], *S. Linev*[3], *W. Mueller*[3], *and J. P. Wessels*[2]

[1]NIPNE, Bucharest, Romania; [2]University of Münster, Germany; [3]GSI, Darmstadt, Germany

The new two-dimension position sensitive TRD prototype architecture for CBM experiment developed by us is based on diagonally split rectangular pads of the read-out electrode [1]. The choice of triangular-pad geometry allows for position determination in both coordinates: across and along the pads, respectively. The TRD prototype used in the present tests has a readout electrode of 25 μm thickness kapton foil having on both sides evaporated Al/Cr layers with the mentioned pad structure.

The first version of the prototype was built with an anode-cathode distance of 3 mm (DSTRD-V1) and a read-out electrode with a double sided pad structure [2] - [3] similar with small size double sided TRD prototype which showed that such a geometry preserves the performance up to 2x10^5 part.$\cdot$cm$^{-2}\cdot$s^{-1} counting rate. In order to improve the charge sharing between the pads for position reconstruction, the second version was built with a 4 mm anode-catode distance (DSTRD-V2).

Both detectors were tested with the 5.9 keV X-ray ^{55}Fe source using both the anode and pad signal, respectively. 80% Ar + 20% CO_2 gas mixture was flushed trough the counter. For pad signal processing we used the new FEE - Fast Analog signal Processor (FASP) [4] developed in our group. It has 8 input/output channels and can provide two type of outputs: a fast output with a semi-Gaussian shape (Fig. 1-blue line) and a flat top output (Fig. 1-red line) [5].

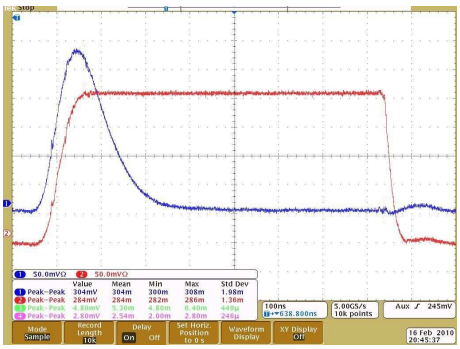

Figure 1:

The obtained pulse height spectrum (10% energy resolution in sigma) for the pad signal of DSTRD-V2, processed by the FASP fast output is presented in Fig. 2 - left side. The applied anode voltage was 1750 V. Fig. 2 - right side shows the obtained pulse height spectrum (10.4% energy resolution in sigma) for flat top output and 1800 V anode voltage. Both FASP outputs were digitized with an AD811 converter, the fast output via a main amplifier with 300 ns shaping time, the flat top output directly.

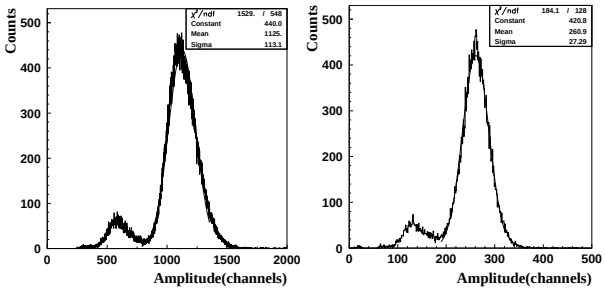

Figure 2:

The detectors were tested with electron and pion beam of 1 - 5 GeV/c momenta at T10 beam line of the CERN PS accelerator in a joint measurement campaign of the CBM Collaboration. The signals delivered by 16 triangular pads were processed by the FASP using the flat top output. They were digitized by a 32 channels peak sensing Mesytec ADC (MADC-32).

Figure 3 shows the pulse height distributions of electrons and pions for 2 GeV/c momentum, a gas mixture of 80% Xe + 20% CO_2 and operating the DSTRD-V1 counter with 1700 V anode voltage.

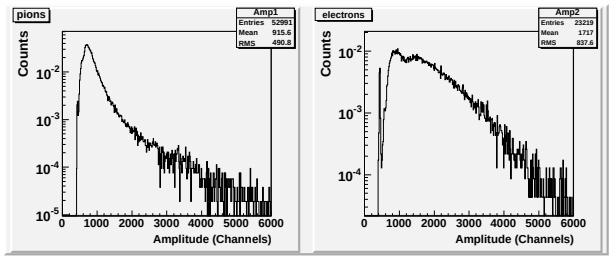

Figure 3:

The detailed analysis is in progress.

References

[1] D. Bartoş et al. CBM Progress Report 2009, (2010), p. 31,

[2] M. Petrovici et al, NIM. A 579, (2007), 961

[3] M. Klein-Bösing et al., NIM A 585(2008), 83

[4] V. Cătănescu et al. CBM Progress Report 2009, (2010), p. 47

[5] A. Caragheorgheopol et al., this Scientific Report

* Work supported by EU-FP7/HP2-WP18 Grant No 227431 and Romanian NASR/CAPACITATI-Modul III contract nr. 42. and NASR/NUCLEU Project

Development of ceramics RPC for high rate capability timing detector application *

R. Eißmann[1], *B. Kämpfer*[1], *R. Kotte*[1], *A. Laso Garcia*[1], *L. Naumann*[1], *R. Peschke*[1], *D. Stach*[1], *C. Wendisch*[1], *and J. Wüstenfeld*[1]

[1]Helmholtz-Zentrum Dresden-Rossendorf, Germany

The installation of timing Resistive Plate Chambers (RPC) is under consideration for the very forward, high rate environment of the Compressed Baryonic Matter (CBM) experiment [1]. For that purpose prototype timing RPC have been developed at Helmholtz-Zentrum Dresden-Rossendorf (HZDR). Electrodes with a volume resistivity of about $10^9\,\Omega$cm [2, 3] are considered for detectors with high rate capability $\leq 2{\cdot}10^4\,\mathrm{s}^{-1}\mathrm{cm}^{-2}$. Special ceramics composites have been developed and processed. In 2010 two prototypes with dimensions of the ceramics electrodes of $10\times10\,\mathrm{cm}^2$ and one prototype with $20\times20\,\mathrm{cm}^2$ have been exposed at the electron accelerator ELBE at HZDR with 32 MeV single-electron beam pulses. The flux of the primary beam is tunable from few electrons/s to 10^7 electrons/s. The exposed region amounts to about $10\,\mathrm{cm}^2$. Position dependent efficiency (Fig. 1) and time resolution (Fig. 2) distributions have been measured over the full detector area by moving the RPC perpendicular to the beam axis. The behaviour of both small RPCs is very similar, even though the surface roughness differs by one order of magnitude (40 nm resp. 400 nm). A four times larger RPC has been assembled as a more realistic demonstrator for the innermost CBM-TOF segment. The construction differs in few details only. No additional inner support structure has been provided, though both linear dimensions increased by a factor of two. A two-dimensional efficiency plot is shown in Fig. 3 for a beam flux of $4.2{\cdot}10^4\,\mathrm{s}^{-1}\mathrm{cm}^{-2}$. For all RPCs the highest applied field amounts to 105 kV/cm in the four gas gaps of 300 μm width.

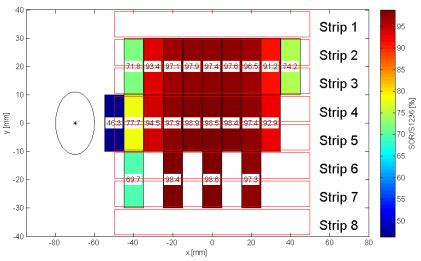

Figure 1: Efficiency of the $10\times10\,\mathrm{cm}^2$ RPC as a function of the beam position for an electron flux of $2{\cdot}10^5\,\mathrm{s}^{-1}\mathrm{cm}^{-2}$. The ellipse shows the shape of the beam.

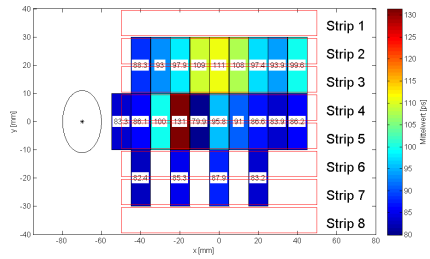

Figure 2: Same as Fig. 1, but for the time resolution (σ).

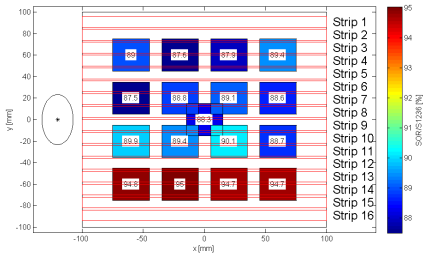

Figure 3: Efficiency of the $20\times20\,\mathrm{cm}^2$ RPC as a function of the beam position for an electron flux of $4.3{\cdot}10^4\,\mathrm{s}^{-1}\mathrm{cm}^{-2}$.

References

[1] I. Deppner et al., doi:10.1016/j.nima.2010.09.165

[2] L. Naumann et al., NIM A 628 (2011) 138

[3] L. Naumann et al., doi:10.1016/j.nima.2010.09.121

* Work supported by BMBF 06DR9059D.

High granularity, symmetric differential readout - timing multigap RPC *

M. Petriş[1], *M. Petrovici*[1], *V. Simion*[1], *D. Bartoş*[1], *G. Caragheorgheopol*[1], *F. Constantin*[1], *I.Deppner*[2], *N. Herrmann*[2], *P. Loizeau*[2], *K. Doroud*[3], *and M.C.S. Williams*[4]

[1]NIPNE, Bucharest, Romania; [2]Physikalisches Institut der Universitaet Heidelberg, Germany; [3]CERN, Geneva, Switzerland; [4]INFN, Bologna, Italy

In this contribution we report the results of R&D activity concentrated on the development of a multigap RPC prototype with strip readout for high counting rate and high multiplicity environment as it is required by the low polar-angle region of CBM-TOF detector. In order to cope with the strong counting rate requirements of the inner part of the CBM-TOF wall ($\sim$ 2x10^4 part.$\cdot$cm$^{-2}\cdot$s^{-1}), we built few prototypes using as resistive electrodes a special low resistivity glass with a resistivity of the order of 10^{10} Ωcm [1, 2]. The obtained results showed that very good time resolution MRPC for high counting rate environment, up to 16,000 part.$\cdot$cm$^{-2}\cdot$s^{-1} are feasible. Nevertheless, the low polar-angle region requires not only a high counting rate performance, but also a high granularity detector to meet the multiplicity challenge (up to 1000 tracks/event at 25$\cdot$A GeV Au+Au collisions).

For this particular region of the TOF wall we designed and built a RPC prototype with a readout electrode with short 46 mm length strips.

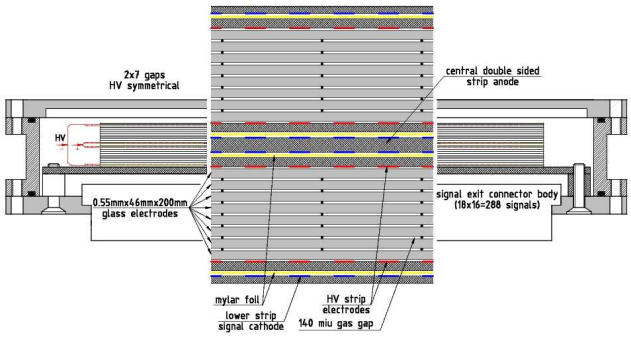

Figure 1: Sketch of the RPC configuration.

A cross section through this configuration is shown in Fig. 1. It is a completely symmetric two stack structure, with high voltage electrodes for both positive and negative polarities. Each high voltage electrode has an identical strip structure as the readout electrodes. Each stack has seven gaps of 140 μm each, defined by eight resistive electrodes made from a normal high resistivity float glass ($\sim$ 10^{12} Ωcm). The strips of the high voltage electrodes were in contact with a resistive layer painted on the last glass electrode. The readout electrodes (the cathodes and central double-sided anode) have a strip structure of 2.54 mm pitch and 1.1 mm strip width. The anode and cathode signals are connected by twisted pair cables and sent to the differential FEE based on NINO chip [3].

The detector was tested in beam at T10 beam line of the CERN PS accelerator with a 6 GeV/c momentum negative pions. 90%$C_2F_4H_2$ + 5%SF_6 + 5% iso-C_4H_{10} gas mixture was used.

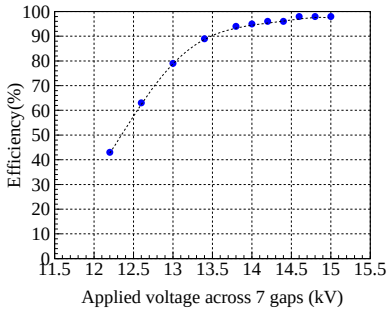

Figure 2: The efficiency versus applied voltage.

The efficiency was estimated over 95% for an applied HV larger than 2kV/gap, reaching a maximum of 98% (Fig.2). The efficiency was estimate as the number of hits in RPC with valid time and time over threshold information divided by the number of triggers.

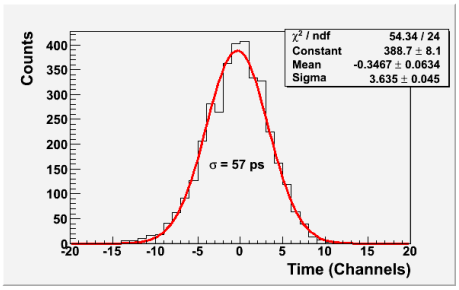

Figure 3: Time of flight spectrum.

The time of flight distribution was obtained as the mean of the time information recorded at the both end of a measured strip relativ to the reference signal delivered by a plastic scintillator. We performed for each measured strip a time walk correction and subtracted quadratically the contribution of the scintillator reference counter (61 ps) and the electronics jitter (33 ps). The obtained time resolution was 57 ps (Fig.3) for 2.09 kV/gap.

References

[1] D. Bartoş et al. 2008 NSS/MIC, Vols. 1-9 Book Series: IEEE Nuclear Science Symposium - Conf. Rec. Pg: 1933-1935.

[2] M.Petriş et al. , Rom. Journ. Phys. 2010, in press.

[3] F. Anghinolfi et al., Nucl. Instr. And Meth. A 533(2004), 183

*Work supported by EU-FP7/HP2-WP18 Grant No 227431 and Romanian NASR/CAPACITATI-Modul III contract nr. 42. and NASR/NUCLEU Project

Performance of a differential CBM-TOF demonstrator*

I. Deppner†[1], *N. Herrmann*[1], *P.-A. Loizeau*[1], *K. Wisniewski*[1], *C. Xiang*[1], *Y. Zhang*[1], *M. Ciobanu*[2], *and J. Frühauf*[2]

[1]Physikalische Institut Uni. Heidelberg, Heidelberg, Germany; [2]GSI, Darmstadt, Germany

Currently Multigap Resistive Plate Chambers (MRPC) are the optimal choice to fulfill the CBM-TOF requirements [1]. For the low rate region (< 1 kHz/cm^2) a MRPC in multi-strip configuration with thin standard float glass can be considered. Here we report on results obtained during a test experiment at COSY/Jülich with an fully differential MRPC prototype developed at Physikalische Institut in Heidelberg (more details regarding this prototype see [2]). In addition a high granularity MRPC prototype from Bucharest with electrodes made of low resistive glass delivered from China [3] was tested.

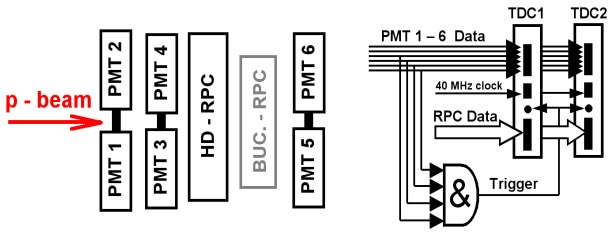

Figure 1: Experimental setup - left: detector arrangement, right: trigger and data processing.

Figure 1 shows the experimental setup as used in the test experiment. The trigger was formed by coincidence between two plastic scintillators read out by two photomultipier tubes (PMT) each (PMT 3 - 6 see fig.1 right). An additional pair of PMTs (PMT 1,2) was used for time resolution measurement. All PMTs and the HD-MRPC were connected to customized designed preamplifier cards called PADI [4]. In order to extract the time over threshold information the LVDS signals from PADI output were split and fed into two different TDCs (Caen V1290A). One of them measured the rising edge and the other the falling edge of the signal. Both TDCs were synchronized by a external 40 MHz clock. The time over threshold information of each contributing channel was used to correct the pulse height dependencies (walk) of the mesasured time difference between the average of the PMT and the RPC times. Additional corrections on the nonlinearities of the TDC were done in order to minimize the electronic time resolution. Figure 2 show the time resolution of one strip of the RPC (only two strips were covered by the trigger scintillator) as a function of the applied high voltage (HV) for two thresholds settings at $thr. = 30mV$ and $50mV$ including the electronics resolution estimated to be about 30 ps. At the nominal operation voltage (HV = 11.7 kV), the time resolution is in the order of 50 ps, whereat for the higher thresholds small signals are not detected, and therfore a better time resolution is obtained as compared to a lower threshold. The efficiency which is about 93 % for $thr. = 30mV$ at nominal operation voltage is diminished by 3 % for $thr. = 50mV$.

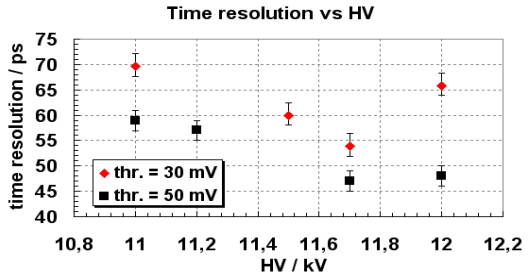

Figure 2: Time resolution as a function of high voltage for different preamplifier thresholds.

In Fig. 3 the average cluster size ,i.e., the number of neighboring strips that fire simultaneously is depicted as a function of the high voltage. The average cluster size depends on the threshold, for both thresholds the dependence on the HV is nearly linear and with simular slope of about 0.46 kV^{-1}. At HV = 11.7 kV, the cluster size reaches values between 1.4 and 1.6.

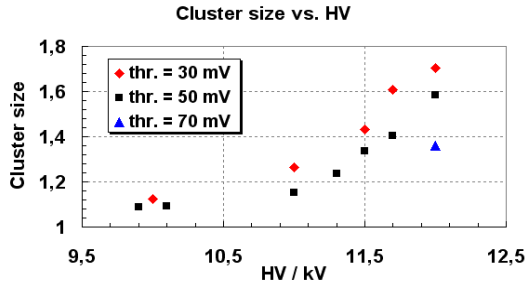

Figure 3: Cluster size as a function of high voltage for different preamplifier thresholds.

References

[1] I. Deppner et al, Nucl. Instrum. and Methods A, 2010 (in press), doi:10.1016/j.nima.2010.09.165

[2] I. Deppner et al, CBM Progress Report 2009

[3] Y. Wang et al, this Report

[4] M. Ciobanu et al., IEEE NSS, Dresden, (2008), 2018-2024

*Work supported by BMBF 06HD9121I and EU/FP7 I3 Hadron Physiks 2

†deppner@physi.uni-heidelberg.de

Status of the analysis chain for CBM-TOF demonstrator data*

P.-A. Loizeau[1], N. Herrmann[1], I. Deppner[1], K. Wisniewski[1], C. Xiang[1, 4], M. Ciobanu[2], H. Deppe[2], H. Flemming[2], J. Frühauf[2], K. Koch[2] and S. Manz[3]

[1]Physikalisches Institut, Universität Heidelberg, Germany; [2]GSI, Darmstadt, Germany; [3]Kirchhoff-Institut für Physik, Heidelberg, Germany; [4] Institute of Particle Physics, Huazhong Normal University, China

The CBM experiment will apply for the first time a data driven data acquisition concept for all subsystems. We develop the TOF part of this system and present here the analysis chain of the CBM-TOF demonstrator. Testing is done using self-triggered data acquired last November at COSY, Jülich.

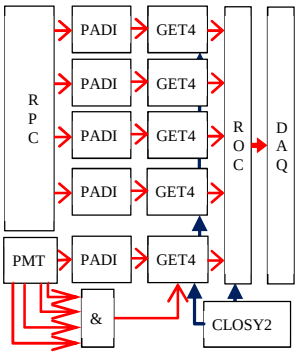

Figure 1: Setup used at COSY in Nov. 2010. RPC = Resistive Plate Chamber PADI = pre-amplifier GET4 = time digitizer ROC = readout controller CLOSY2 = Clock generation PMT = 4 plastic scintillators read out by 2 photomultipliers each.

The setup used to take the test data is sketched in Fig.1 and consists of a fully differential 16 strips MMRPC [1], the full CBM-TOF readout chain [2] and the DABC DAQ. In total 40 channels were connected: 32 for the double-ended detector strips and 8 for the PMTs used as reference system. Additionally, a logic signal of the coincidence of the four main PMTs was fed in the external synchronization input (ExtSync) of one TDC, giving a reference point in the data stream. Three runs were recorded, amounting for 40GB of data and around 1.5M "events" (ExtSync).

The analysis procedure on data produced by this setup is organized in three steps: hit building, event building and calibration.

The first step is realized inside a GO4 unpacker and consists itself of three operations described in Fig.2: data are cleaned, reordered and used to build hits. Cleaning the data is required because the ROC transfers all data to the DABC DAQ system. This means that unsynchronized data are still present, which are useless in a multi-chip environment. Those data messages are also not time ordered because there is a token ring readout system in the digitizer chip. Finally the rising and falling edges provided by the TDC have to be matched to produce full hits with time and Time over Threshold (ToT) information.

The cleaning is done by rejecting chip by chip invalid epochs blocks, i.e. groups of 26.2144µs periods called epochs. An epoch block is invalid when the TDC loses its synchronization with the common clock system, which can be checked every 25 epochs.

* Work supported by BMBF 06HD9121I & EU/FP7 I3 HadronPhysics2

The data messages must be time ordered inside each valid 25 epochs block for each chip, before being able to associate rising and falling edges in hits. As those hits are saved when the falling edge is found but must be ordered by their rising edges for event building, a buffer of two blocks and a second time ordering are necessary. The data are finally saved in a ROOT tree used by the next steps.

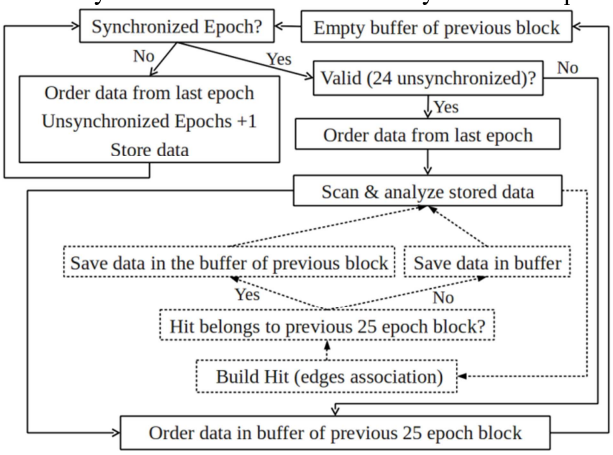

Figure 2: Cleaning and hit building procedure.

The second step is done in a ROOT macro. Two options are available to build events:

a) A narrow time window is searched for the occurrence of signal coincidences. When one is found, all signals in a wider time window are associated.
b) The ExtSync is used as reference. The data around a time window around it are put together as event. This speeds up the data analysis.

The same macro can be used for both as ExtSync is saved in data as an additional "fake" channel.

The third step is also done by a ROOT macro. The calibration consist of the walk correction on the 4 main PMTs and the 2 RPC channels corresponding to one strip. Fig. 3 shows an example obtained with beam test data.

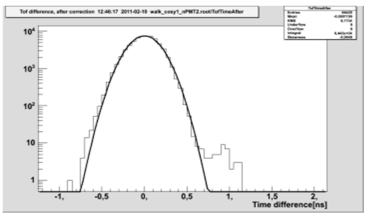

Figure 3: Time difference between reference system and one RPC strip, after partial calibration, with a Gaussian fit.

References

[1] I. Deppner et al., "Performances of a differential CBM-TOF demonstrator", also in this report
[2] J. Frühauf et al., "Status of the CBM-TOF Readout-Chain", also in this report

Status of the CBM-TOF-Readout-Chain

J. Frühauf[1], N. Herrmann[2], I. Deppner[2], P.-A. Loizeau[2], C. Xiang[2,4], K. Wisniewski[2], M. Ciobanu[1], H. Flemming[1], H. Deppe[1], K. Koch[1] and S. Manz[3]

[1]GSI, Darmstadt, Germany, [2]Physikalisches Institut Uni. Heidelberg, Germany, [3]Kirchhoff Institut für Physik, Heidelberg, Germany, [4] Institute of Particle Physics, Huazhong Normal University, China

The current CBM-TOF-Readout-Chain consists out of six different modules. A board with two preamplifier and discriminator ASICs [1] (FEET-PADI) with four channels each and a digitiser board with two event-driven TDC ASICs [2] (FEET-GET4) are used as front-end electronic. These ASICs are specially developed for the CBM-ToF detector. An adapter board (R2F-Board) is used as an interface between the readout controller and the front-end cards, and an FPGA based readout controller (ROC) transfers then the data to the data acquisition (DAQ) hosted on a computer. A very precise clock-generator [3] (CLOSY2) provides the two used system frequencies. There is a 250MHz frequency for the ROC and in addition a phase coupled 156.25MHz frequency, which is needed by the TDC. A third signal is send out by the CLOSY2 for synchronization of the two provided clocks and to create epoch markers. A clock distribution (CLOCKDISTRIBUTION2) is needed to spread out these three signals in a tree. This is realized by a 1:10 splitter for each CLOSY2 signal.

The test-setup in the laboratory is shown in the Fig. 1.

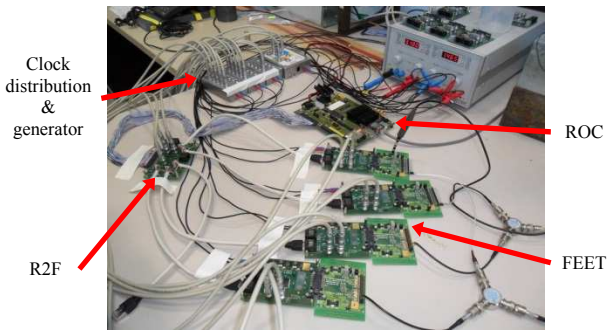

Figure 1: Readout Chain

There are four FEET-PADI directly connected to the FEET-GET4. The same input pulse is used for all 32 channels. The signal is split into four and injected into the parallel input of the FEET-PADI board. There they are getting amplified and discriminated and are afterwards led into the FEET-GET4 to mark each rising and falling edge with a timestamp. With this setup it is possible to measure the time resolution of the complete readout chain. In order to characterize the system, the combined resolution of two channels is measured when they belong: a) to the same chip (chip-level) b) to 2 chips on the same pcb (pcb-level) and c) to 2 different pcbs (pcb-pcb-level). In Fig. 2 the resolution plot for chip-level is shown.

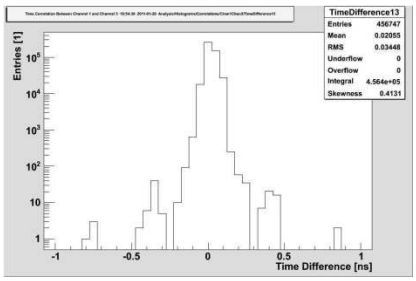

Figure 2: Resolution chip-level

The results of the different time resolutions after a gaussian fit are listed in Tab. 1.

	σ / ps
chip-level	36,94
pcb-level	38,94
pcb-pcb-level	40,22

Table 1: Resolution Readout Chain

This setup was used in a beamtime to readout an RPC [4] with 16 strips (32 channels) and a reference system which consists out of 8 photomultipliers. Preliminary results of the achieved data as well as the ongoing work on the analysing tool for this system are presented in "Status of the analysis chain for CBM-TOF demonstrator data" in the same report [5].

References

[1] M. Ciobanu, N. Herrmann, K.D. Hildenbrand, M. Kis, A.Schüttauf, “PADI, a fast Preamplifier - Discriminator for Time-of-Flight measurements”, IEEE NSS, Dresden, (2008), 2018-2024

[2] H.Flemming, H.Deppe: "The GSI event-driven TDC with 4 channels GET4", IEEE NSS, Orlando, FL, (2009), 1082-3654

[3] K.Koch: CLOSY: A very Precise Clock Generator for Timing Measurements and Synchronisation of the CBM ToF Wall, GSI Scientific Report 2009, p82 (http://www.gsi.de/informationen/wti/library/scientificreport2009/PAPERS/FAIR-EXPERIMENTS-80.pdf)

[4] I. Deppner et al., “Performance of a differential CBM-TOF-Demonstrator”, same report

[5] P.-A. Loizeau et al., “Status of the analysis chain for CBM-TOF demonstrator data”, same report

DABC as data acquisition framework for CBM

S. Linev[1], J. Adamczewski-Musch[1] and J. Fruehauf[1]

[1]GSI, Darmstadt, Germany

Optical transport for ROC

For development of the different software components for the CBM readout controller (ROC) [1], the Data Acquisition Backbone Core (DABC) [2] was used. The ROC board was primarily developed to read out data from nXYTER-based frontends. With a new FPGA firmware the readout of GET4/FEET frontends is also possible [3]. In addition to the existing Ethernet based data transport, an optical fibre data transport via a special PCIe board (AVNET) was implemented to the ROC software and tested. The optical protocol [4] was designed to transport data, control and clock information over the same media. Data rates up to 200 MB/s can be achieved here. Additionally, the optical connections allow clock synchronisation between many ROCs. Usage of the optic transport in ROClib is absolutely transparent and does not require any changes in user software compared to the Ethernet case.

Synchronisation with MBS

The ROC produces a time-stamped data flow and does not require external triggers for signal measurements. On the other hand, there is a lot of existing hardware, useful for different detector tests, which is read with trigger-based MBS DAQ. To synchronise the data taken by MBS with the data taken by ROC, a special SYNC-sender module was developed based on the VULOM board. This module sends a SYNC message to all ROCs every time the MBS trigger is produced. A DABC software module was implemented to search for such SYNC messages in the ROC data, and to associate subsequent data messages with the corresponding MBS trigger. The data combined together by such software can be analyzed in a Go4 analysis.

SPADIC readout

The SPADIC is a prototype chip for TRD readout, developed in Uni Heidelberg [5]. It allows to read out detector signal shapes with external trigger. Trigger signal input is compatible with ROC SYNC message, therefore MBS with a SYNC-sender module can be used as a trigger producer for SPADIC.

Based on a library for USB readout of SPADIC [5], a DABC plugin was developed to acquire SPADIC data with DABC; this plugin was integrated into ROClib. Data from SPADIC are represented as MBS events. These can be combined together with ROC and MBS data, synchronized by the SYNC message number.

TRD/RICH/STS beamtime in CERN

In this beamtime in November 2010, 4 different TRD prototypes were read out: two with MBS, another two with DABC with 6 SPADICs. In addition, one STS station and a RICH setup were read out with 3 ROCs. A DABC application was implemented to combine data from all these inputs together.

STS/GEM beamtime in COSY

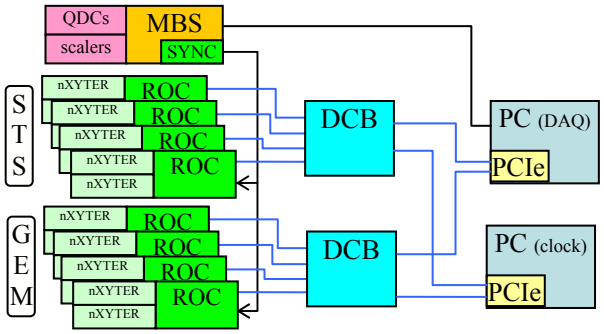

Figure 1: COSY beamtime setup.

Figure 1 shows the DAQ setup of the COSY beamtime in December 2010: all 8 ROCs were optically connected via special Data Combiner Boards (DCB) to the AVNET PCIe board, read out by the DABC application. An additional connection for each DCB provides a clock distribution – thus all ROC clocks were running synchronously. An MBS system was used to read out beam monitor scintillators; synchronisation with ROC data was done via a SYNC sender module.

Status and outlook

Current software shows good stability and robustness in all beam tests performed up to now. Further developments are planned for closer integration of the DAQ with experiment control system EPICS.

References

[1] J. Adamczewski-Musch, H.G. Essel, S. Linev, Usage of DABC in software development for CBM DAQ, GSI scientific report 2009, p. 334

[2] J. Adamczewski, H.G. Essel, N. Kurz, S. Linev, Data Acquisition Backbone Core DABC, IEEE Trans.on Nucl. Science, Vol.55, No.1, pp. 251-255, Feb. 2008.

[3] S. Manz, U. Kebschull, Design and Implementation of the Read Out Controller for the GET4 TDC of the CBM ToF Wall Prototype, GSI scientific report 2009, p. 333

[4] F. Lemke, S. Schenk, U. Bruening, Prototype Results of an Optical Communication Network for the CBM DAQ-System, GSI scientific report 2009, p. 87

[5] Tim Armbruster, http://www.spadic.uni-hd.de

DABC data acquisition input for slow control variables

J. Adamczewski-Musch[1], B.W. Kolb[1] , and S. Linev[1]

[1]GSI, Darmstadt, Germany

Introduction

The Data Acquisition Backbone Core (DABC) is a software framework to run DAQ with distributed event building on high performance Linux clusters [1]. There are several use cases, especially in test beam times where the setup during data taking is intentionally changed very often, and the interpretation of the acquired detector data depends on the experimental set-up. Usually, the set-up is managed by a slow control system like EPICS [2], which has powerful tools to archive the set-up values. For online analysis, however, a direct access to such values in the DAQ data stream can be very useful, e.g. for a conditional analysis depending on certain settings. Moreover, it is possible to perform a fast scan of detector properties with the control system and record simultaneously the measured data in the same file. Because of this an EPICS data input for DABC was developed.

DABC data input for EPICS

The DABC framework has plug in interfaces to attach any kind of data sources to the DAQ [3]. Such *DataInput* interface was implemented as *EpicsInput* plug-in for reading a set of slow control process variables from an EPICS IOC server. This implementation is based on the existing Easy Channel Access (ezca) extension library [4], featuring basic C functions to request named variables from any EPICS IOC.

This DABC ezca-plugin can be configured by XML file which contains the names of the process variables to be fetched. Currently an expandable set of integer or double values can be treated, other EPICS records may be implemented in future versions. One special EPICS record defines a "flag" variable which is polled by DABC with a configurable repetition time, e.g. 100ms. Only if this flag variable shows a specific value, e.g. 0, the complete set of the defined records is acquired from the IOC. Thus by setting this variable, the IOC can decide the refresh rate of the data recorded to the DAQ stream. This can be done by an EPICS timer, or when a change of the set-up is significant for the DAQ.

The *ezca::DataInput* instance puts each acquired set of EPICS process variables into an MBS event/subevent structure. The order of the EPICS records in the subevent data field is currently defined by the order of records in the DABC configuration file. Additionally, the MBS event identifiers can be specified in the DABC set up.

The processing DABC module, connected to the *ezca::DataInput* transport, may combine this EPICS subevent with MBS subevents of the DAQ data stream from other data sources, e.g. an external MBS system, or the CBM readout controller (ROC). Since the EPICS data rate is much lower than the usual DAQ data rate, synchronization between EPICS records and the other event data can be done in the subsequent analysis software by means of the system time stamp which is recorded in the ezca subevent payload, and should be also available in the subevents of other data sources.

Application for CBM test beam at COSY

A CBM test beamtime was performed at COSY in December 2010 [5]. The set up of detector voltages and motor positions was controlled by one EPICS IOC. The DABC DAQ was configured with the ezca plug-in such that all variables of the IOC were recorded with the full data stream every 10 s. Thus it was possible in the attached Go4 online monitoring analysis [6] to visualize these EPICS variables together with the detector display: for instance, the motor controlled positions of the GEM detectors were shown; also the settings of a beam enclosing "ROLU" scintillator frame.

During the voltage scan of the STS detectors, the recorded EPICS data allow to directly correlate the detector signals with the settings in the final analysis.

Besides the EPICS data, the DABC data stream also contained a "spill-on/spill off" message from a signal directly fed into the ROCs by a beam trigger sensor. This allowed an automatic baseline calibration of the ROCs in the Go4 online analysis whenever the synchrotron beam was paused. Although the mechanism of getting the set-up state was different here, the principle of a conditional analysis steered by slow control variables within the DAQ data stream would be the same for the EPICS records.

References

[1] J. Adamczewski-Musch, H. G. Essel, N. Kurz and S. Linev, "Data Flow Engine in DAQ Backbone DABC", *IEEE TNS* Vol.57, No.2, April 2010, pp 614-617.

[2] EPICS http://www.aps.anl.gov/epics/

[3] J. Adamczewski-Musch, H. G. Essel, and S. Linev, „The DABC Framework Interface to Readout Hardware", Proceedings of the 17th IEEE Real-Time Conference, Lisboa 2010, to be published in *IEEE TNS*

[4] EZCA, http://www.aps.anl.gov/epics/extensions/ezca

[5] J.M. Heuser et.al, "Test of prototype modules of the CBM Silicon Tracking System in a proton beam at COSY", this report

[6] http://go4.gsi.de

Demonstrator Beam Time Results for the Clock Distribution and Synchronization of the CBM DAQ-System*

F. Lemke, S.Schenk, and U. Bruening[1]
[1]University of Heidelberg, Mannheim, Germany

Introduction

Due to new requirements for the DAQ system the previously planned hierarchical CBM network structure using Read-Out Controllers (ROC) for detector read-out, Data Combiner Boards (DCB) for data combining and Active Buffer Boards (ABB) for data buffering and First Level Event Selection (FLES) attachment was extended. The usage of a unified link for three different data types such as Data Transport Messages (DTM), Detector Control Messages (DCM), and Deterministic Latency Messages (DLM) and the communication principles and packet structures will not be changed, because it has proven its reliability [1] [2]. But new detector read-out chips and high level data flow handling concepts generated new feature requests. Therefore, a new CBMnet V2.0 has been designed and will be implemented supporting lane handling for unbalanced communication, large messages, an adapted data loss strategy in cases of overloads, easy meta data detection, and a fully reliable communication for data streams. The new planned CBM network structure using the CBMnet V2.0 is shown in figure 1. An alternative for the ROC is now connected to the CBM network via a HUB ASIC, for data aggregation and rate conversion of data from detector read-out chips or FEBs, combined with a opto converter board providing an electrical to optical conversion for the communication links. Within the inner network part the DCB was replaced by a Data Processing Board (DPB) and an Experiment Control System (ECS). The back-end part using ABBs attached to FLES within computing clusters will stay the same. For the HUB ASIC chip and the opto converter the analysis and conception has already started, its implementations will be major parts within future work packages.

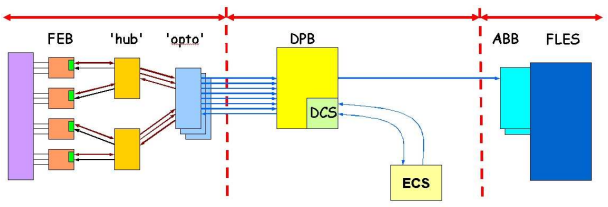

Figure 1: Planned CBM Network Structure

Demonstrator Setup and Tests

For the proof of concept and to enable the read-out over optics for the detectors used during beam time, a read-out chain consisting of the previously developed prototypes was created. The demonstrator build-up used during the beam time tests in december 2010 is presented in figure 2. It shows the two DCBs used as DPB prototypes. They were connected to an ABB that served as emulation for the ECS providing the clock and a system synchronization with DLMs via the CBM protocol V1. Both DCBs have four bidirectional connections to the front-end for attachment of 4 ROCs using the unified CBM protocol for synchronization and data acquisition. The received data is combined to a single datastream within the DCBs and sent to an ABB plugged into a workstation running the current version of the DABC software for data collection. During the complete COSY test beam time from 13th to 19th december the optical read-out demonstrator has been used. The data acquisition ran problem-free. The ECS emulation providing the control system and the clock distribution was reliable. The network synchronization worked without errors and delivered the targeted bitclock synchronization, so that a synchronization with less than 400ps was guaranteed. The concept of using the unified link providing DLMs for synchronization has now shown its valuable improvement for future detector system solutions.

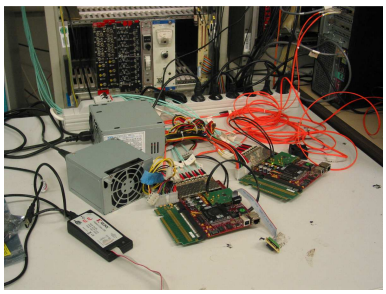

Figure 2: DCBs used in Demonstrator Build-up

References

[1] Frank Lemke, Sebastian Manz, Wenxue Goa, ”Time synchronization and measurements of a hierarchical DAQ network”, Deutsche Physikalische Gesellschaft EV (DPG10), Fruehjahrstagung, Bonn, Germany, March 15-19, 2010.

[2] Frank Lemke, David Slogsnat, Niels Burkhardt, Ulrich Bruening, ”A Unified DAQ Interconnection Network with Precise Time Synchronization”, Journal Paper, IEEE Transaction on Nuclear Science (TNS), VOL. 57, No. 2, April 2010.

* Work supported by GSI, BMBF FAIR-CBM 06HD9117l

Design and Implementation of an Object-Oriented Framework for Dynamic Partial Reconfiguration

N. Abel, A. Beyer, F. Grüll, N. Meier, and U. Kebschull
Kirchhoff Institute of Physics, Heidelberg University, Heidelberg, Germany

Nowadays, two innovative future trends regarding embedded hardware development and hardware description can be found. The first trend concerns the hardware itself. Modern FPGAs (Field Programmable Gate Arrays) provide the possibility that parts of the configuration can be exchanged while the rest of the circuit is running untouched — which is called dynamic partial reconfiguration (DPR).

The second trend concerns the way hardware is described. Currently, the most important hardware description languages (HDLs) are VHDL and Verilog. Although they allow to describe hardware on a very high level, the developer still has to handle registers, clocks and clock domains. Using an HDL operating on the algorithmic level, this is not necessary any longer — the corresponding synthesis process is called high level synthesis (HLS).

Although both, DPR and HLS are very important future trends regarding hardware design, they develop rather independently. Most of today's software-to-hardware compilers focus on conventional hardware and therefore have to remove dynamic aspects, such as the instantiation of calculating modules at runtime. On the other hand, DPR tools work on the lowest possible layer regarding FPGAs: the bitfile level. Thus, currently the use of DPR leads to a struggle with architectural details of the FPGAs and the corresponding synthesis and implementation tools.

Our workgroup focuses on a combination of DPR and HLS, since DPR can change the programming paradigm in future HDLs with regard to dynamic instantiations. Dynamic aspects would not be a problem any longer, but could be realized on the target FPGA using DPR. Beyond that, a high level language support of DPR could help it to become a commonly used method. The aim of our work is to find a solution how HDLs on algorithmic level and DPR can be combined, solely using language constructs which are already well-known to software-developers.

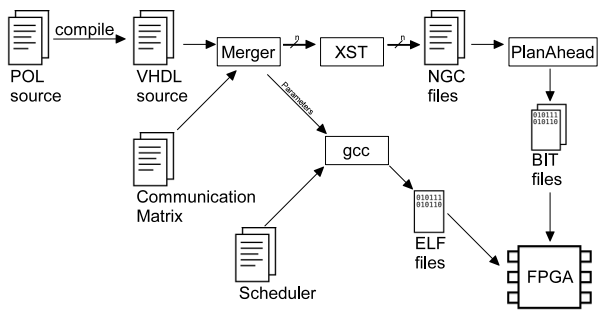

Figure 1: The implementation toolflow of the framework

As a first step, the typical structure and behavior of reconfigurable hardware has been analyzed. Thereby it turned out that the best way to describe such hardware is to make use of the object-oriented paradigm combined with multi-threading. In consequence, an enriched subset of Java, forcing the programmer to make use of multiple objects running in parallel, has been defined: POL (Parallel Object Language).

The specification of POL comes with a set of requirements. The most challenging part is the high degree of flexibility regarding object instantiation and inter-object communication. POL allows the user to instantiate and to destroy objects as well as to establish and to dissolve their connection at *any* position in the code. Beyond that, POL allows an overmapping of the FPGA.

In order to enable the evaluation of the possibilities and limitations of POL, a development framework has been implemented. This framework includes an emulator which allows the execution of POL in software [1], a compiler which is responsible for the translation from POL to VHDL [2], a so called Communication Matrix which serves as fast and flexible communication structure on the FPGA [3], and a scheduler (running on an embedded processor) that decides which hardware module is loaded when (figure 1).

For performance analysis, an audio filter has been implemented. It shows that overmapping can be used in environments with a data rate of $\sim$100 000 samples/s, while scenario-based scheduling algorithms can be used in streaming applications with data rates of $\sim$100 000 000 samples/s. These maximum data rates are solely possible due to the usage of object-orientation in POL and the corresponding optimizations of the reconfiguration times [4].

References

[1] A. Beyer, "Development of an Emulator for the execution of POL-Code inside a Java-Environment", bachelor thesis, Heidelberg, Germany, 2008

[2] F. Grüll, "The Parallel Object Language", diploma thesis, Heidelberg, Germany, 2009

[3] N. Meier, "Development of a Framework for Dynamic Partial Reconfiguration serving the Object Oriented Hardware Programming Language POL", diploma thesis, Heidelberg, Germany, 2008

[4] N. Abel, "Design and Implementation of an Object-Oriented Framework for Dynamic Partial Reconfiguration", PhD thesis, Heidelberg, Germany

Memory Kernel Development of the Active Buffer

A. Wurz[1], W. Gao[1], A. Kugel[1], R. Männer[1]*

[1]Informatik V, ZITI, University of Heidelberg, Germany

The Active Buffer for the CBM experiment needs larger size for its kernel. Originally the Active Buffer board (ABB) used the built-in FIFO of the Xilinx FPGA, 128 KB. And in 2010 we completed the large-size DDR2 SDRAM FIFO project on the AVNET Virtex5 board by cleaning hidden bugs. [1] Additional data count module is added and verified. Final logic bugs are fixed. This buffer is used in last beam tests and works well.

Block diagram

We use a 64-bit DDR2 SDRAM module of 256 MB as the kernel memory. Figure 1 shows the block diagram of the large-size FIFO.

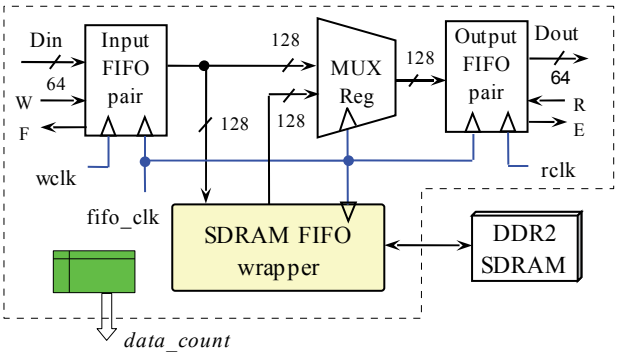

Figure 1: Large-size FIFO block diagram

The DDR2 SDRAM module is outside the FPGA. Inside the FPGA we use two smaller built-in FIFOs, 4KB each, as the interface module, which qualifies the entire FIFO to behave as a standard FIFO.

Development notes

1) data into and out of the SDRAM module are aligned to the row boundary, to have a better and simplified management over the SDRAM module. Only when the data amount in the small input FIFO block reaches a row size of the DDR2 SDRAM, is the data transfer into the FIFO wrapper executed. And on the other side, only after the output FIFO is able to accommodate a row-size data, is the data directed from the SDRAM to the output FIFO. The advantage lies in minimized row-open and row-close operation for the SDRAM module.

2) internal data run in double-width data bus, i.e. 128-bit bus, which suffices the possibly full data rate, even if the SDRAM overhead, such as auto refresh and row recharge, have to be taken into account.

3) PAD delays are variable and calibratable, so that the design has a general application scope to variety of boards. On the Xilinx Virtex5 LX110T FPGA board, IODELAY is used with variable delay value adjustment.

4) The clock frequency for the SDRAM module is some percent higher than the external FIFO clock frequency, to compensate the SDRAM operation overhead such as refresh, recharge. In the ABB2 system, we use 166 MHz as the the kernel clock rate and accordingly, the PCIe DMA fabric logic clock rate is 125 MHz.

5) data count must be additionally built. Data count is for DMA read logic to determine when to issue the request and for software to know how many data are ready in the Active Buffer.

Test and verification

Timing performance can go easily to over 125 MHz for Virtex5 FPGA with speed grade -1. The numbers of flip-flops and (4-input) look-up-tables used for this FIFO wrapper are both under 1000 and the number of 18Kb RAM blocks is 4. For the adjusting of data bus arrival of the SDRAM module, 4 `IDELAYCTRL`s are used.

Simulation and real test work very well. Additionally we make a stand-alone test design intensely targeting the FIFO behaviour. In a long and sustained test with manual button presses, the FIFO behaves very well in terms of performance and stability. The peak bandwidth goes to

$$125\text{MHz} \times 2 \times 32\text{bit} = 8\ \text{Gbps}$$

in the system. Figure 2 is an example snapshot from ChipScope Analyzer.

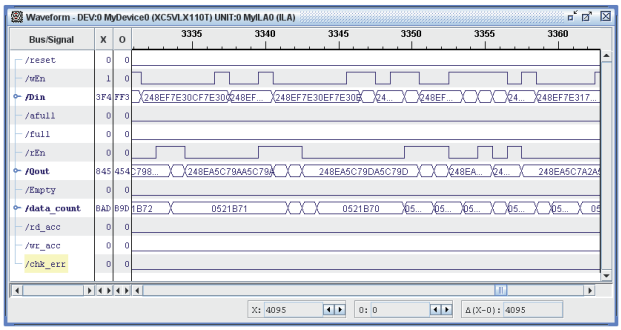

Figure 2: DDR2 SDRAM FIFO behaviour

The newer version logic of PCIe DMA integrated with this large-size FIFO works well in system and is verified in the COSY beam test at FZ Jülich in December 2010.

References

[1] W. Gao, et al. "Improved Active buffer Board of CBM", CBM Progress Report 2008. *p*.58.

* wenxue.gao@ziti.uni-heidelberg.de

Radiation Tolerance of the Universal Read Out Controller

N. Abel, H. Engel, J. Gebelein, D. Gottschalk, S. Manz, A. Oancea, and U. Kebschull
Kirchhoff Institute of Physics, Heidelberg University, Heidelberg, Germany

The Universal ROC

Since 2007 our contribution focused the Silicon Tracker's FEE (Front End Electronic), consisting of the nXYTER, an ADC (Analog Digital Converter) and a ROC (Read Out Controller). Since 2009 we are also designing and implementing readout logic for the GET4 chip [1] and the TRD FEE. To keep the re-usability as high as possible, we split the ROC into two fully independent modules: the readout logic and the transport logic. This modularization of the Read Out Controller and the consequential separation of the control software into different layers, enabled us to provide a Universal ROC, which offers quick access to a long-run tested transport logic and allows us to easily add a new readout logic for further FEE setups. [2]

Radiation Tolerance

The heart of the Universal ROC is an SRAM based FPGA, since FPGAs provide the best combination of performance and long-term flexibility. However, there is a crucial problem regarding FPGAs: the radiation which is inevitable in high energy physics experiments can cause the FPGA's doped silicon to change its electrical properties, depending on its Linear Energy Transfer (LET). This physical separation of electron-hole pairs results in spontaneous Single Event Effects (SEE) as well as long-term Total Ionizing Dose (TID) cumulation within the material. SEEs, especially Single Event Upsets (SEU) and Single Event Transients (SET), show up as permanent, but non-destructive binary bit flips within logic memory or as short glitches on the routing network. This becomes extremely critical for latches or flip-flops at clock signal setup/hold times. TID effects are not that critical for short-term applications, but preponderantly problematic for long-term considerations. They increase the number of stuck charges resulting of the electron-hole pair separation, leading to modification of the chips doped semiconductor properties. Overall, hardware failures may occur in nonrelevant circuits or may lead to spontaneous unexpected system behavior, but most critical they can lead to a total system halt, known as Single Event Functional Interrupt (SEFI). [3]

According to this problem, very specialized shielded radiation hard materials have been and currently are developed for military and space grade FPGAs, realized within the Xilinx Virtex QPro II, 4 and 5 series, complemented by a configuration refresh feature called "scrubbing". As some of these chips are not available for commercial applications due to military export restrictions, common devices are provided with special TID mitigation techniques and SEE failsafe combinations of logic blocks. Basically, such ambitions in securing the logical hardware design layer can be realized by three different approaches: spatial redundancy, temporal redundancy and various combinations of both. Spatial redundancy features synchronous data sampling of combinational logic at multiple routes to mitigate SEUs. The addition of adjacent voters is required to analyze processed data values. Well known candidates using this principle are Dual and Triple Modular Redundancy (DMR/TMR), mostly accompanied by Error Detection and Correction Codes (EDAC). Temporal redundancy enables a single combinational logic circuit to be sampled at multiple times. Additional voter circuitry compares all of the results and decides whether an error occurred or not. The combination of both spatial and temporal redundancy leads to SEU and SET immunity.

Conclusions

The usability of FPGAs in radiation environments highly depends on the usage of mitigation technologies such as scrubbing, spatial or temporal redundancy. This has a strong influence on the board design as well as on the FPGA design: the Universal ROC is implemented on a board (namely the SysCore Board) which provides an external FLASH memory and an additional radiation hard flash-based FPGA which are required to realize the scrubbing technology[4]. Furthermore the modules (transport logic as well as readout logic) are using a combination of spatial and temporal redundancy. The implemented architecture layers and methods have been practically tested under experimental conditions within different particle accelerator beams. The Universal ROC had been directly placed into the center of the particle beam line to get comprehensible results at a maximum ionization impact. These tests will be continued in 2011 and will be used to develop a radiation tolerant Universal ROC.

References

[1] S. Manz, "GET4 readout chain", CBM Collaboration Meeting, 2009, Split, Croatia

[2] N. Abel et. al, "Design and Implementation of an Universal Read Out Controller", GSI Progress Report 2009, Darmstadt, Germany

[3] J. Gebelein et. al, "FPGA Fault Tolerance in Particle Physics Experiments" it - Information Technology 52 (2010) Heft 4 Schwerpunktthema, Oldenbourg Wissenschaftsverlag

[4] D. Gottschalk, "Concept and Status of the SysCore 3 Board" CBM FEE/DAQ Workshop 2010, Frankfurt, Germany

A SIMD Implementation of the Deterministic Annealing Filter for the CBM Experiment*

R. Frühwirth[1], H. Gjersdal[2], I. Kisel[3], A. Strandlie[2,4], and M. Zyzak[5,6]

[1]HEPHY, Austria; [2]Uni-Oslo, Norway; [3]GSI, Darmstadt, Germany; [4]Gjøvik University College, Norway; [5]Uni-Frankfurt, Germany; [6]Uni-Kyiv, Ukraine

The main challenge of the CBM experiment is an extremely high track density. This leads to overlapping of the hits and the distortion of their position. In order to reduce an influence of the attached distorted or noise hits on the reconstructed track parameters the Deterministic Annealing Filter (DAF) [1] is under development within the Kalman filter (KF) package.

The idea of DAF is to introduce "temperature" depending weight to each hit and perform several filtration iterations gradually "cooling" the system. With "cooling" weights for noise hits are gradually decreasing to zero, while for true hits they are remaining high. After the first pass of the Kalman filter based smoother with equal weights the track position is predicted at every layer of the detector. Based on these predictions the probability, that a hit belongs to the track, and the weight of a hit are calculated. Decreasing the temperature the influence of noise hits is suppressed with each next iteration. On each iteration weights are recalculated using smoothed track parameters from the previous iteration.

Most modern CPUs has SIMD units, which currently can give speedup of factor 4 for single-precision floating-point calculations. In the nearest future speedups of 8 and 16 will be available. Therefore in order to utilize the whole potential of CPU the implementation of DAF should be based on the SIMD instruction set.

Currently the DAF implementation is based on the SIMD KF track fitter [2]. The Kalman filter mathematics has been modified in order to include weights of hits. Since DAF needs smoothed track parameters, the KF based smoother has been added to the KF package. The smoother is implemented as two Kalman filters processing in opposite directions: forward and backward. Parameters and covariance matrices of the track, that are calculated by these filters, are merged at the hit position. During the iteration in DAF the same hit weights are used both for the forward and backward filters. Weights are calculated by:

$$p = \frac{1}{1 + \exp\left((\chi^2 - \chi^2_{\text{cut}})/(2T)\right)},$$

where p is a weight of the hit on the station; T — "temperature" of the current iteration, the values of $T = 9$, 4, 1 and 0.1 are used in the algorithm; χ^2 is a squared distance between the hit and a smoothed track position normalized on the hit and track parameters errors; χ^2_{cut} is a threshold, which determines the region, where the hit is accepted (the value of $\chi_{\text{cut}} = 4$ has been used, that provides the probability of 99,995% to attach a correct hit for the normal distribution).

Tests for time and fit quality of the algorithm have been performed on the lxir039 computer with 2 Xeon X5550 processors at 2.7 GHz and 8 MB L3 cache, one core has been used. A setup of 2 stations of the Micro-Vertex Detector (MVD) and 8 stations of the Silicon Tracking System (STS) has been used. For tests 20000 long reference primary tracks, reconstructed with the CA track finder, have been used. The tracks could have on average up to 0.5% incorrectly attached hits.

To test the algorithm the hit on the 4^{th} STS station has been displaced by a certain amount of the hit error (σ_{hit} = 17 μm) along the X direction from the Monte-Carlo position. The percentage of rejected hits has been calculated on all stations of the detectors. The obtained results are given in Table 1. As one can see, the current implementation gives good noise hits rejection for distant hits. The execution time of DAF is 14 μs per track.

Hit displacement		unshifted	5 σ_{hit}	10 σ_{hit}	20 σ_{hit}
MVD	1	0.4	0.4	0.4	0.4
	2	0.7	0.7	0.7	0.7
STS	1	0.3	0.3	0.3	0.3
	2	0.4	0.4	0.4	0.4
	3	0.4	0.7	0.8	0.5
	4	0.5	43.9	85.0	98.7
	5	0.5	1.6	1.6	0.8
	6	0.6	0.6	0.6	0.6
	7	0.6	0.6	0.6	0.6
	8	0.1	0.1	0.1	0.1

Table 1: Percentage of rejected hits depending on the distance from the shifted hit on the 4^{th} STS station to its Monte-Carlo position.

The DAF algorithm will be further investigated within the CA track finder.

References

[1] R. Frühwirth and A. Strandlie, Track fitting with ambiguities and noise: a study of elastic tracking and nonlinear filters. Comp. Phys. Comm. 120 (1999) 197-214.

[2] S. Gorbunov, U. Kebschull, I. Kisel, V. Lindenstruth and W.F.J. Müller, Fast SIMDized Kalman filter based track fit, Comp. Phys. Comm. 178 (2008) 374-383.

*This work was supported by the Hessian LOEWE initiative through the Helmholtz International Center for FAIR (HIC for FAIR)

CA Based Track Finder with STS Detector Inefficiency*

I. Kisel[1], *I. Kulakov*[2,3], *I. Rostovtseva*[4], *and M. Zyzak*[2,3]
[1]GSI, Darmstadt, Germany; [2]Uni-Frankfurt, Germany; [3]Uni-Kyiv, Ukraine; [4]ITEP, Moscow, Russia

The CBM experiment at FAIR is being designed to study heavy-ion collisions at extremely high track densities up to 1000 tracks per central collision in the Silicon Tracking System (STS). Double-sided strip detector modules will be used in STS, that leads to up to 85% additional combinatorial space points. The Cellular Automaton (CA) based algorithm [1] is used for track reconstruction in the STS detector of the CBM experiment. The algorithm creates short track segments (triplets) in each three neighboring stations, then links them into track-candidates and selects them according to the maximum length and minimum χ^2 criteria.

The experimental conditions become more complicated if one takes into account the detector inefficiency. Therefore the stability of the track reconstruction algorithm with respect to the detector inefficiency is important. The track reconstruction algorithm has been investigated in order to improve its stability. New features have been added in the algorithm: triplets can skip one station with a missing hit; gathering individual hits by track-candidates; merging separate parts of the same track.

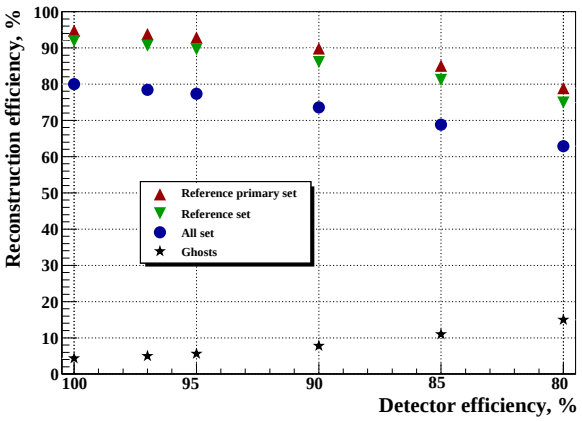

Figure 1: Reconstruction efficiencies and ghost rate versus the detector strip efficiency.

For tests 100 central Au+Au UrQMD events at 25 AGeV have been simulated. The track reconstruction with the detector strip efficiencies of 100, 97, 95, 90, 85 and 80 per cent has been investigated. The track reconstruction efficiency and track fitting quality were monitored.

Track reconstruction efficiency is defined as the number of reconstructed tracks assigned to generated particles divided by the number of all reconstructable tracks. Reconstructable tracks are those, which have momentum greater than 0.1 GeV/c and intersect the sensitive regions of at least four consecutive stations. A reconstructed track is assigned to a particle, if at least 70% of its hits have been caused by this particle. A reference track should have a momentum greater than 1 GeV/c in addition. The reference set of tracks can also include tracks of particular physics interest: secondary tracks from interesting decays or primary tracks coming from the target region. If a reconstructed track is not assigned to any particle it is called ghost.

The dependence of the track reconstruction efficiency on the detector strip efficiency is shown in Figure 1. The efficiencies for all reconstructable tracks, reference tracks and primary reference tracks and ghost rate are presented. As one can see, the algorithm is robust and shows a slight reconstruction efficiency degradation with respect to the detector inefficiency. In particular, decreasing of the detector efficiency from 100% to 95% leads to decreasing of the track reconstruction efficiency only by 3%.

Detector strip efficiency, %	100	97	95	90	85	80
x, μm	12	13	13	14	14	15
y, μm	57	60	61	65	69	73
t_x, mrad	0.35	0.36	0.37	0.38	0.40	0.42
t_y, mrad	0.60	0.61	0.61	0.63	0.64	0.66
p, %	1.22	1.25	1.28	1.34	1.41	1.48

Table 1: Residuals of track parameters versus the detector strip efficiency.

Track fit quality at the first track point has been investigated with respect to the detector inefficiency as well. Resolutions become slightly worse due to the smaller number of hits in a track (see Table 1). Resolutions and pulls (resolutions normalized on estimated errors) of all track parameters are unbiased.

Summarizing, the algorithm of track reconstruction has been improved and shows stability with respect to the STS detector inefficiency.

References

[1] I. Kisel, Event reconstruction in the CBM experiment, Nucl. Instr. and Meth. A566 (2006) 85-88.

*This work was supported by the Hessian LOEWE initiative through the Helmholtz International Center for FAIR (HIC for FAIR)

First steps towards a time-based simulation and reconstruction for the CBM experiment

V. Friese[1] *and E. Kryshen*[2]
[1]GSI, Darmstadt, Germany; [2]PNPI, Gatchina, Russia

Simulation, reconstruction and analysis for the CBM experiment are performed using the FAIRROOT software framework. The feasibility studies performed so far include the transport of events through the CBM geometry, the simulation of the detector response according to the present knowledge on detector and read-out electronics properties, and full hit, track and vertex reconstruction. With these tools, the feasibility of the measurement of all major observables of the CBM physics programme was demonstrated.

However, the framework, and consequently all simulation results, are based on event-by-event processing, i.e. the association of hits in the detector to physical events is given *a priori*. This corresponds to a conventional experiment where events are defined by a hardware trigger before readout. The data acquisition concept of CBM, in contrast, will not employ a latency-limited trigger, but foresees autonomous, self-triggered read-out electronics which will send time-stamped hit information into the DAQ chain whenever the corresponding detector channel is activated. The association of the hit information to physical events must thus be performed in software.

In order to demonstrate the feasibility of such a read-out concept, in particular for event rates as high as envisaged for CBM, the following tasks arise:

- The detector response simulation shall consider the Monte-Carlo time information and, in turn, provide a time tag for the produced detector hit, taking into account the anticipated behaviour of the detector and, in particular, of the front-end electronics. This means for instance that a double hit in a detector channel is not defined by two tracks in this channel within one event, but within a given time interval (detector dead time).

- Based on this time-based hit information, an algorithm for "event building", i.e. the association of hits to physical events must be developed. In the simplest case (low interaction rates), when the average time between two subsequent events is large compared to the variation of hit times within one event, this can be done using the time information alone. The already developed event-based reconstruction can then proceed as before.

- For high interaction rates, events will overlap in time. The association of hits to events is thus no longer trivial. Then, space-time correlations must be employed, such that track and event reconstruction will operate in four dimensions instead of the common three ones.

As a first step towards these developments, the software framework was extended to facilitate the treatment of data based on time and not on events. A dedicated task class (`CbmMCStreamer`) regroups the Monte-Carlo hits delivered by the event-by-event transport according to their hit time into time slices (*epochs*), thus destroying the correlation of the MC hits to the input events from the generator. The format for this new data level is still a ROOT TTree, but now with one entry per epoch instead of one entry per event. The size of the epoch is adjustable to the user's convenience. It should be noted that the epoch on the MC level need not conicide with any time scale defined by the read-out and DAQ system, but is in first place just a mean to discretise a continuous data stream. Parameters for the MC-Streamer are the average interaction rate and a model of the time profile of the beam.

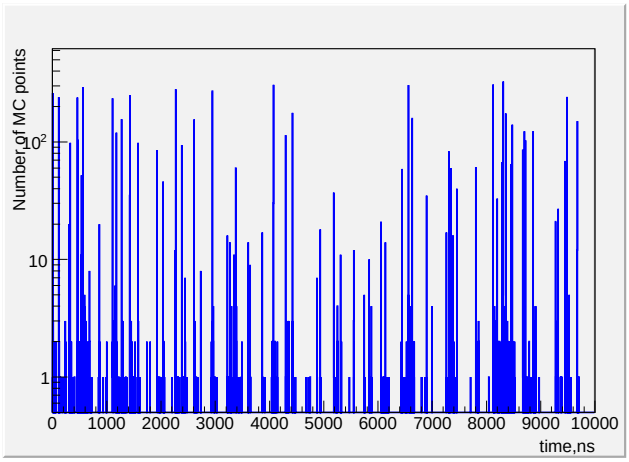

Figure 1: Time sequence of MC hits in the CBM silicon tracking system, assuming an average interaction rate of 10 MHz and a white beam, for Au+Au collisions at 25A GeV

As a simple application of the new data format, Fig. 1 shows the time sequence of MC hits in the CBM-STS detector system, assuming an average interaction rate of 10 MHz with a white beam. With the new data format as input, the development of advanced, time-based digitisers for the different detector systems will be the next steps towards the full simulation and reconstruction of the data flow in CBM.

L1 CA Track Finder with Realistic STS Clusterization

I. Rostovtseva[1], *D. Golubkov*[1], *I. Kisel*[*2], *and Yu. Zaitsev*[1]
[1]ITEP, Institute for Theoretical and Experimental Physics, Russia; [2]GSI, Darmstadt, Germany

In realistic process of strip clusterization some loss of information inevitably occurs due to merging of clusters. A merged cluster is a group of strips, fired by more than one MC point. For Au+Au collisions at 25 AGeV simulated with `cbmroot` version Jun10, about 12% of hits are created from merged clusters (at least in one projection) and more than $\sim 50\%$ of tracks contain hits from merged clusters. This may affect the tracking performance and the present work considers this influence on L1 Cellular Automaton Track Finder (CA) [1].

The "removal procedure" of the CA, which removes from further consideration hits attached to found track candidates, does not allow tracks to have hits in common and thus by default does not take into account possible merging of the clusters. Therefore it is able to remove true hits together with fakes if the corresponding cluster (at least in one projection) has been included in some other track.

This particular source of loss in the track finding efficiency was considered in our talk [2]. To recover the efficiency without significantly increasing the clone and ghost rates we tried to optimize the removal procedure (in order to remove maximum of non-merged and minimum of merged clusters), using the information about: the total cluster charge, the mean charge of the clusters on the track, and the size of the cluster. The charge distributions significantly differ for single- and many-strip clusters, so we considered them separately. Figure 1 shows the dependence of the efficiency, the ghost and clone rates after the first step of the algorithm on the cut on the minimal cluster charge.

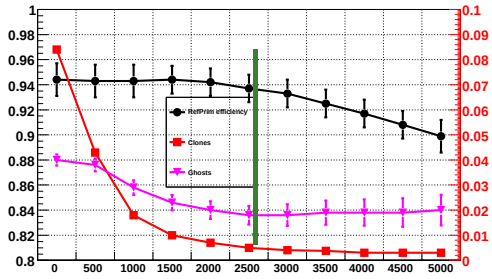

Figure 1: `RefPrim` efficiency (circles), Clones (squares), Ghosts (triangles) versus cut on the total cluster charge.

We chose to cut on the minimal total cluster charge for many-strip clusters below 2500 to remove clusters with low charge which are more likely to be non-merged. The effect of the difference in charge distribution between merged and non-merged single-strip clusters is less pronounced.

Because the cluster charge depends on the type of the particle, its momentum and the angles, one can expect to achieve some improvement by cutting on "normalized charge" obtained by dividing the charge of the cluster by mean$(\{c_i\})$, the mean value of cluster charges on the track. We have also studied different truncated mean definitions: mean$(\{c_i\} \setminus c_{\max})$, and mean$(\{c_i\} \setminus \{c_{\max}, c_{\min}\})$ to increase robustness. No significant difference could be found between the results obtained using the cut on total cluster charge or cutting on any of the studied normalized cluster charges.

Table 1: Comparison of CA performance with default and modified removal procedure.

Track category	**Jun10** %	**charge $<$ 2500** %
RefSet (> 1 GeV$/c$)	89.0	94.1
RefPrim	90.4	95.1
RefSec	80.2	87.8
All set	82.5	87.6
Extra set (< 1 GeV$/c$)	66.2	71.2
Clone	0.6	1.0
Ghost	3.4	3.3

As displayed in Table 1 (taken from [2]), using the optimal cut on the total charge of many-strip clusters at the first step of the CA algorithm, it was possible to recover the tracking efficiency for the reference set of tracks to $\sim 94\%$ while keeping low clone and ghost rates.

It is necessary to underline that the amount of merged clusters significantly depends both on the properties of the detector, on the digitization algorithm and local track occupancy, so it will be subject to change along with the development of the detector design and changes in the operational conditions. Due to these strong dependencies we have decided not to include the described modifications in the official release of the L1 CA. Nevertheless, the presented study may be used at a later phase of adjusting the tracking algorithm to the performance of the real detector.

References

[1] I. Kisel, "Event reconstruction in the CBM experiment," Nucl. Instrum. Meth. A **566** (2006) 85.

[2] I. Rostovtseva, D. Golubkov, I. Kisel, Yu. Zaitsev, "Status of L1 Track Finder," 16th CBM collaboration meeting, Mamaia, Romania, 28 September 2010.

* I.Kisel@gsi.de

Scalability of the CA Based Track Finder in the CBM Experiment*

I. Kisel[1] *and I. Kulakov*[2,3]

[1]GSI, Darmstadt, Germany; [2]Uni-Frankfurt, Germany; [3]Uni-Kyiv, Ukraine

The main challenge of the CBM experiment is a high interaction rate up to 10^7 collisions per second. The average track density is about 1000 particles per central Au+Au collision. The tracking system of CBM is positioned within a dipole magnet and is build of double-sided silicon strip detectors. In addition to such high input rate and complicated event topology, the full event reconstruction and selection will be done at the First Level Event Selection (FLES) stage. This requires utilization of the full potential of modern many-core CPU/GPU architectures. Since developments of modern processors tend to increase a number of cores rather than a CPU frequency, a good scalability of the event reconstruction is essential.

The core of track reconstruction in the CBM experiment is the Cellular Automaton (CA) based reconstruction [1] in the Silicon Tracking System (STS). It is the most sophisticated and time consuming part of the event reconstruction, therefore it should have a good scalability with respect to number of cores.

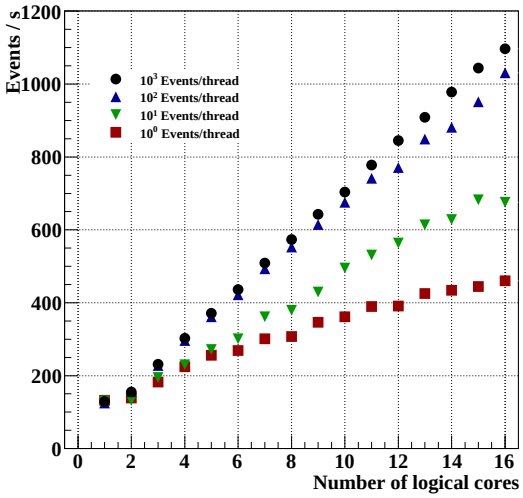

Figure 1: Scalability of the CA track finder for minimum bias events.

A standalone package [2] was used for the investigation of the CA track reconstruction scalability. Tests were performed on the lxir039 computer with two Xeon X5550 processors having 8 cores in total at 2.7 GHz and with 8 MB L3 cache. Each physical core has two logical cores due to the hyper-threading technology. In order to investigate the scalability, track finding has been run on various numbers of cores. The Intel Threading Building Blocks (TBB) software package [3] has been used for parallel execution between cores.

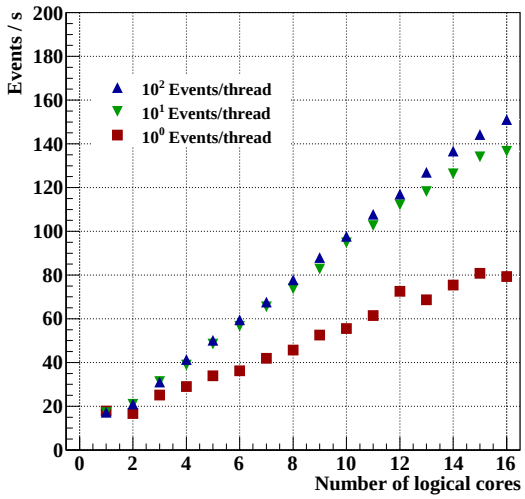

Figure 2: Scalability of the CA track finder for central events.

In Figure 1 the scalability on the logical cores is shown for minimum bias events. Here the track reconstruction has been parallelized by execution of one thread per one logical core. Reconstruction of 1, 10, 100 and 1000 events has been executed per each thread. In the same way the track reconstruction has been executed for 1, 10 and 100 central events (see Figure 2). The figures show a good linear scalability for large groups of events, while for small groups of events an overhead is observed.

In conclusion, running on a computer with 8 cores the CA based track finder demonstrates the maximum throughput of 150 central or 1100 minimum bias events per second using the Intel Threading Building Blocks. The strong many-core scalability of the CA track finder makes possible to keep the reconstruction at the event-level parallelism.

References

[1] I. Kisel, Event reconstruction in the CBM experiment, Nucl. Instr. and Meth. A566 (2006) 85-88.

[2] I. Kisel at al., A standalone package for on-line event selection in the CBM experiment, CBM Progress Report 2008, p. 79.

[3] Intel Threading Building Blocks, http://www.threadingbuildingblocks.org

*This work was supported by the Hessian LOEWE initiative through the Helmholtz International Center for FAIR (HIC for FAIR)

Status of the electron identification algorithms for the RICH and TRD detectors in the CBM experiment

S. Lebedev[1,2]*, C. Höhne*[3]*, and G. Ososkov*[2]

[1]GSI, Darmstadt, Germany; [2]JINR, Dubna, Russia; [3]University Giessen, Germany

RICH detector

In the ring reconstruction algorithm [1] a further speedup optimization was studied and event level parallelism was investigated. In order to test the ring reconstruction algorithm, central UrQMD Au+Au collisions at 25 $AGeV$ beam energy with 10 embedded primary e^+ and e^- were simulated. The test computer has two Intel Core i7 CPUs with 4 cores each at 2.67 GHz (16 logical cores in total).

The ring reconstruction efficiency is the same for the scalar and parallel version and equals to 93% integrated over momentum, the number of fake rings is 2.7 per event, the number of clone rings is 0.9 per event which has to be compared to a total number of 80 rings per event. A speed up factor of 74 is achieved by the optimization of the algorithm. Using SIMDization and multithreading the speed of the algorithm was increased further by a factor of 2. In total a speed up factor of 143 was achieved (from 357 ms/event to 2.5 ms/event) for the optimized parallel version in comparison to the initial algorithm.

Event level parallelism was also studied. Events are accumulated in a buffer and then groups of events are reconstructed in parallel in different threads (different CPU cores). A thread scheduler was developed in order to control the creation and life cycle of the threads. It allows to run threads on a certain CPU core. The scalability of the event level parallelism was investigated: N events were read from the event buffer, an individual thread was created for this group of events and the reconstruction was executed. The first thread executes on the first logical core of the first CPU, the second thread executes on the second logical core of the first CPU. The next two threads execute on the second core and so on. Our tests show that the performance increased linearly in dependence on the number of running threads. Using the computer CPUs at a maximum (16 running threads) algorithm reconstructs more than 1800 central events per second (500 μs/event) and roughly 8000 mbias events per second (125 μs/event).

Table 1: Pion suppression in the RICH detector for two different algorithms.

	ANN	Cuts
π suppression ($p < 6GeV/c$)	500	200
π suppression ($p > 6GeV/c$)	260	130

Two algorithms for electron identification in the RICH detector were implemented: 1) standard ring radius cut method, 2) method based on the ANN [2]. The comparison of the pion suppression results assuming 93% electron identification efficiency is presented in Table 1.

TRD detector

In addition to previous studies [3] further investigations of the electron identification algorithm in the TRD were performed. To calculate the pion suppression factor 10^6 electrons and 10^6 pions were simulated with the following parameters $\theta = (2.5°, 25°)$, $\phi = (0°, 360°)$ and a momentum of 1.5 GeV/c. A set of radiator parameters was used which was tuned to describe the experimental results (3rd set in [3]). The BDT method was applied for this study [4].

Due to the high track multiplicity and density, the track reconstruction algorithm sometimes assigns wrong hits to a track. For example, from 12 hits of an electron track 11 hits were found correctly and one hit was wrongly substituted by a pion hit. The effect of this was studied in two ways (see Table 2): 1) assign wrong pion hits to an electron track, 2) assign wrong electron hits to a pion track.

Table 2: Pion suppression in the TRD detector in dependence on the number of wrong hits per track.

Number of wrong hits	0	1	2	3	4	5
π supp., variant 1	660	225	89	37	17	9
π supp., variant 2	660	215	74	30	13	7

The BDT method was adopted to identify electrons which have 6 to 12 hits in the TRD. This is necessary because 1) different geometries with different number of layers have to be investigated; 2) detector inefficiency; 3) tracks which do not pass through all layers should also be identified; 4) the track reconstruction algorithm might find only a part of a track. The dependence of the pion suppression on the number of hits per track is presented in Table 3. The gain of the pion suppression due to the additional hit is also presented. The gains here are calculated as pion suppression for track with N hits divided by the pion suppression for track with (N-1) hits.

Table 3: Pion suppression in the TRD detector in dependence on the number of hits per track.

# of hits	12	11	10	9	8	7	6
π supp.	660	500	334	215	132	85	54
Gain	1.33	1.55	1.50	1.63	1.55	1.6	—

References

[1] S. Lebedev et al. CBM Progress report 2009, p. 79

[2] S. Lebedev et al. CBM Progress report 2008, p. 84

[3] S. Lebedev et al. CBM Progress report 2009, p. 81

[4] G. Ososkov et al. "e^-/π separation with TRD", https://www.gsi.de/documents/DOC-2009-Oct-232-1.pdf

Status of tracking in the TRD and MUCH detectors of the CBM experiment

A. Lebedev[1,2], *C. Höhne*[3], *I. Kisel*[1], *and G. Ososkov*[2]

[1]GSI, Darmstadt, Germany; [2]LIT JINR, Dubna, Russia; [3]University Giessen, Germany

In this report the status of the track reconstruction in the Transition Radiation Detector (TRD) and muon system (MUCH) of the CBM experiment is presented. Global track reconstruction in the electron and muon setup of the CBM detector, i.e. with either TRD or MUCH system, is based on track following using reconstructed tracks in the STS as seeds. In the STS track reconstruction is based on the cellular automaton method and provides initial track parameters as starting point for the following track prolongation. This track following is based on the standard Kalman filter technique and is used for the trajectory recognition and estimation of track parameters in TRD and MUCH. Tracks are prolongated subsequently from one detector station to the next adding hits in the detector stations.

The detailed layout of the detectors is still under investigation. In the high track density region of the TRD and MUCH stations, a pad layout is foreseen based on MWPC or GEM technology. For the downstream detector stations in MUCH, where track densities are low, straw tube chambers are under discussion. The first TRD station can be used as tracking station after the last MUCH absorber.

In the performed studies the algorithms were tested using central Au+Au collisons at 25 AGeV beam energy from UrQMD. In addition, for the reconstruction in TRD, 5 primary e^+ and 5 primary e^- with momenta 1 GeV/c $\leq$ p $\leq$ 10 GeV/c were embedded in each event. The performance in the muon system was evaluated by embedding 5 primary μ^+ and 5 primary μ^- per event with momenta 2.5 GeV/c $\leq$ p $\leq$ 25 GeV/c.

A study has been done in order to compare the tracking efficiencies for five different MUCH layouts: 1) `MUCH1` is the standard MUCH with 6×3 detectors with pad readout, 2) `MUCH2` has 13 detectors with pad readout, 3) `MUCH3` has 3×3 detectors with pad readout and straw tube detectors in the last 3×3 stations, 4) `MUCH4` is the same as `MUCH2` but with TRD after the last absorber, 5) `MUCH5` is the same as `MUCH3` but with the TRD after the last absorber, i.e. `MUCH5` is the version which will most likely be realized concerning current plans. Table 1 shows track finding efficiencies for these MUCH geometries for two algorithms: nearest neighbour and branching. The reconstruction efficiencies are only slightly different for the different MUCH layout options.

Concerning the TRD layout, the influence of the TRD detector position resolution on the tracking efficiency was studied. The position resolution for the x coordinate was fixed to 300 μm. In the y direction it has been varied from 100 μm to 30 cm. Nearest neighbour tracking was used in this study. The track finding efficiency is presented in figure 1. The efficiency stays acceptable up to a position resolution of several centimeters. For larger polar angles where track densities are lower the detector resolution can be up to 6–7 cm.

	MUCH geometry				
	`MUCH1`	`MUCH2`	`MUCH3`	`MUCH4`	`MUCH5`
NN	93.8	94.4	93.8	92.8	92.8
Branch	94.0	94.7	94.1	94.9	94.9

Table 1: Track finding efficiency for muon tracks for five different MUCH geometries in %. NN – nearest neighbour algorithm; branch – branching algorithm.

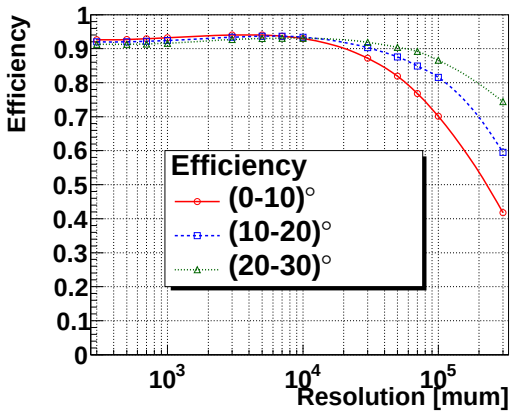

Figure 1: Track finding efficiency for TRD in dependence on position resolution for different polar angles.

The speed of the tracking software is extremly important for data analysis in CBM. A fast parallel track reconstruction algorithm which uses available features of modern processors was further investigated. The algorithm uses two features of modern CPUs: a SIMD instruction set and multithreading. The results of the algorithm speedup for the MUCH system are presented in table 2.

	Track fitting		Track finding	
	Time	Speedup	Time	Speedup
Initial	1200	-	730	-
Optimization	13	92	7.2	101
Vectorization	4.4	3	4.9	1.5
Multithreading	0.5	8.8	1.5	3.3
Final	0.5	2400	1.5	487

Table 2: Speedup of the track fitting (time is shown per track in μs) and track finding algorithm (time is shown per event in ms) for track reconstruction in MUCH.

Towards Parallel Track Reconstruction with Intel ArBB*

I. Kisel[1], *I. Kulakov*[2,3], *H. Pabst*[4], *and M. Zyzak*[2,3]

[1]GSI, Darmstadt, Germany; [2]Uni-Frankfurt, Germany; [3]Uni-Kyiv, Ukraine; [4]Intel, Germany

The Intel Array Building Blocks (ArBB) software [1] is a data-parallel programming environment designed to effectively utilize the power of existing and upcoming throughput-oriented features on modern processor architectures, including Intel's multi-core and many-core platforms. Intel Array Building Blocks provides a generalized vector parallel programming solution that frees application developers from dependencies on particular low-level parallelism mechanisms or hardware architectures. It is comprised of a combination of standard C++ library interface and powerful runtime. It produces scalable, portable, and deterministic parallel implementations from a single high-level source description. It allows to parallelize on both data and task levels in an easy way.

The track reconstruction is a task, which needs a lot of computational power. At the same time all modern high energy physics experiments operate with huge data rates and require fast reconstruction procedures. In order to operate effectively in such difficult conditions the full utilization of CPU is required. Parallel programing is considered now as the only way to utilize the full power of CPU, since all modern CPUs have more than one core and contain SIMD unit. All the charateristics of ArBB make it perfectly suitable for fast track reconstruction and fitting tasks.

The SIMDized Kalman filter track fitter [2] has been modified using ArBB. Results obtained with the ArBB version have been compared with results of the SIMD version [3]. Tests for time and track fit quality of the algorithm have been performed on the 8-cores computer lxir039 with two Xeon X5550 processors at 2.7 GHz and 8 MB L3 cache. The computer has 16 logical cores due to the hyper-threading technology.

For time tests two types of calculations have been performed: using 1 logical core only and using all 16 logical cores. Tests on a single logical core has been done in order to compare the level of the code vectorization using SIMD instructions, on all cores — in order to compare parallelization level between cores and utilization of the full potential of the CPU as well. The ArBB version shows practically the same time results, as the SIMD one (see Table 1).

	SIMD		ArBB	
Cores	1	16	1	16
Time, μs	0.42	0.05	0.43	0.06

Table 1: Fitting time per track of the SIMD and ArBB versions executed on one core and all cores

*This work was supported by the Hessian LOEWE initiative through the Helmholtz International Center for FAIR (HIC for FAIR)

Residuals and pulls (residuals normalized on the estimated errors) of the estimated track parameters have been calculated at the production vertex in order to test the track fit quality. In Figure 1 residuals and pulls for the track postition x, the track slope in the XZ plane t_x and the inverse particle momentum, signed according to charge, q/p are shown. Obtained results are the same as in the SIMD version.

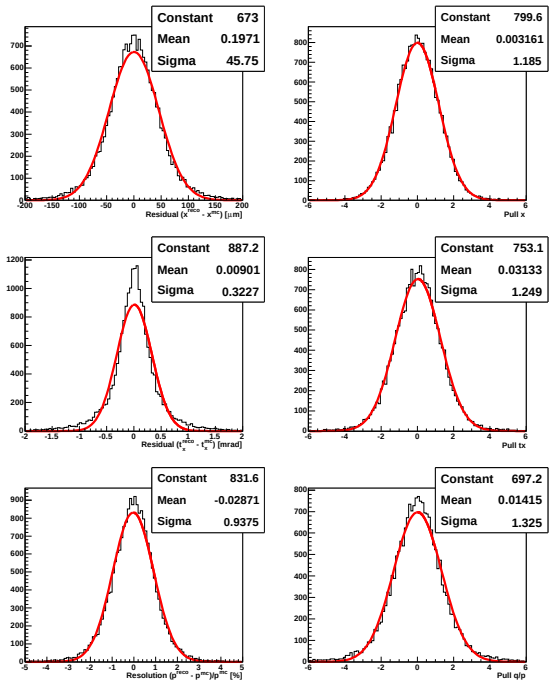

Figure 1: Residuals and pulls of the estimated track parameters calculated with the ArBB version of the Kalman filter track fitter.

As the next task we consider modification of the Cellular Automaton (CA) based track reconstruction algorithm using ArBB.

References

[1] Intel Array Building Blocks, http://software.intel.com/en-us/articles/intel-array-building-blocks.

[2] S. Gorbunov, U. Kebschull, I. Kisel, V. Lindenstruth and W.F.J. Müller, Fast SIMDized Kalman filter based track fit, Comp. Phys. Comm. 178 (2008) 374-383.

[3] I. Kisel, M. Kretz, and I. Kulakov, Scalability of the SIMD Kalman Filter Track Fit Based on the Vector Classes, GSI Scientific Report 2009, p. 56.

Track Reconstruction in the STAR TPC with a CA Based Approach*

Y. Fisyak[1], *I. Kisel*[2], *I. Kulakov*[3,4], *J. Lauret*[1], *and M. Zyzak*[3,4]

[1]BNL, Brookhaven, USA; [2]GSI, Darmstadt, Germany; [3]Uni-Frankfurt, Germany; [4]Uni-Kyiv, Ukraine

STAR [1] is an active collider heavy-ion experiment at RHIC/BNL (Upton, USA). The main tracking detector of the experiment is the Time Projection Chamber (TPC). Due to the collision rate increasing (up to 40 KHz for Au+Au 200 GeV/n and up to 1 MHz for pp 500 GeV) and recording rate (up to 10 KHz) the STAR experiment requires a fast track reconstruction procedure which can deal with high track densities (up to 5000 tracks).

A track reconstruction algorithm based on the Cellular Automaton (CA) was proposed for the STAR TPC reconstruction. The CA algorithm is based on local reconstruction and therefore is robust, fast and easily parallelizable, that makes it perfectly suitable for high track densities and collision rates. The algorithm has been already implemented in the ALICE HLT TPC CA track finder package [2]. The CA reconstruction is performed in two stages: the local reconstruction of tracks in each TPC sector (sector reconstruction) and the tracks merging between sectors (merger). It is parallelized at both data (using the SIMD instruction set) and task (using the Intel Threading Building Blocks technology) levels. The memory usage in the algorithm is optimized.

The CA algorithm has been adapted for the STAR TPC geometry, which is similar to the ALICE TPC geometry. The sector reconstruction part has been divided in two iterations: reconstruction of high and low momentum tracks. More accurate criteria for merging of tracks have been implemented. Detailed optimization of the code of the algorithm has been done in order to make it more efficient, robust and flexible.

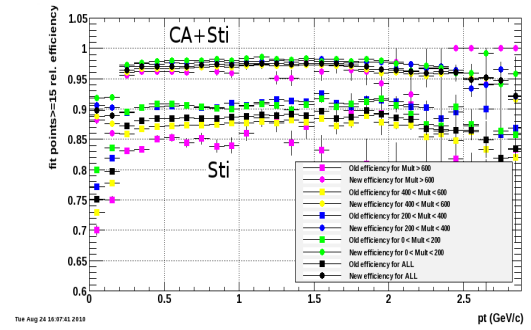

Figure 1: Reconstruction efficiencies versus p_t for different event track multiplicities. Here squares denote the standard Sti track finder, circles — the CA+Sti version.

The adapted CA track finder has been implemented in the STAR ROOT framework and has been moved to the official repository. The comprehensive tests with simulated and real data have been performed. In the current implementation the TPC CA track finder works within the STAR reconstruction framework as seed finder. The standard Sti reconstruction procedure is run after the CA track finder. It performs refit of the found tracks and search for additional tracks. The comparison of efficiencies for real Au+Au collisions at 200 GeV/n with the CA track finder (CA+Sti) and without (Sti) shows that the reconstruction efficiency of CA+Sti is higher by 3% for primary tracks and 9% for all set of tracks (see Figure 1). The efficiency with the CA algorithm is stable with respect to higher track multiplicities. Reconstructed track parameters are practically the same. The tracks reconstructed with CA+Sti contain slightly more hits than ones reconstructed with Sti alone. CA+Sti is a factor of 1.5 faster than Sti alone (see Figure 2). For very high occupancy events CA+Sti speeds up the reconstruction by a factor of 10. The TPC CA track finder takes only 10% of the total event reconstruction time.

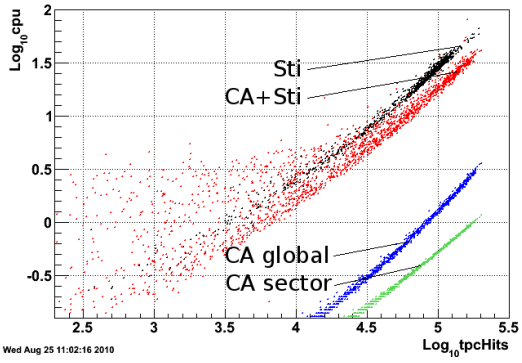

Figure 2: CPU consumptions versus number of hits in TPC. Here "CA global" denotes full time of the CA algorithm, "CA sector" — time for the sector reconstruction stage of the CA algorithm.

In conclusion, the fast and efficient track reconstruction procedure has been developed for the STAR TPC detector based on the ALICE HLT CA track finder.

References

[1] STAR Collaboration, Conceptual Design Report for the Solenoid Tracker at RHIC, LBL PUB-5347, June 15, 1992.

[2] M. Kretz, Efficient Use of Multi- and Many-Core Systems with Vectorization and Multithreading, University of Heidelberg, Diplomarbeit, 2009.

*This work was supported by the Hessian LOEWE initiative through the Helmholtz International Center for FAIR (HIC for FAIR)

$D^{\pm}$ decay reconstruction in p+C collisions at SIS100 energies with CBM

I. Vassiliev[1,2], *I. Kisel*[2], *and the CBM Collaboration*
[1]IKF, Goethe University, Frankfurt, Germany; [2]GSI, Darmstadt, Germany

The investigation of p+A collisions up to 30 GeV and A+A collisions from 4A to 11A GeV beam energies is considered as part of the CBM research program and will be performed in the first phase of FAIR with a start version of the CBM detector at the SIS100 accelerator. This start version consists of two detector systems: the Silicon Tracking System (STS) placed in a magnetic field for the measurement of momenta and vertices and a Time-Of-Flight (TOF) wall placed 10 m downstream of the target for hadron identification.

To study the feasibility of $D^{\pm}$ decay measurement in the CBM experiment, a set of 10^5 central (b=0 fm) p+C events at 30 GeV were simulated. $D^{\pm}$ decay to $K^{\mp}, \pi^{\pm}, \pi^{\pm}$ hadrons has been used in order to simulate a signal. Realistic STS geometry with 2 MAPS at 5 cm (thickness 300 μm) and 10 cm (thickness 500 μm) and 8 double-sided segmented strip detectors (thickness 400 μm) was tested. δ-electrons produced by 15k protons and 50 minimum bias interaction (assuming up to 5MHz interaction rate) simulated additional background hits in the MAPS detectors. The primary vertex was reconstructed with high accuracy (60 μm in z direction, 10.0 μm in x and y) from about 4.5 tracks (on average) fitted in the STS with a non-homogeneous magnetic field by the SIMDized Kalman filter procedure described in [1].

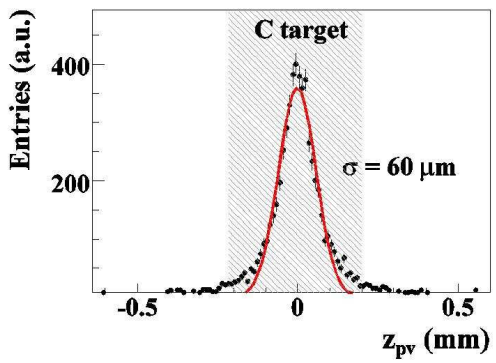

Figure 1: Z-distribution of the reconstructed primary vertex. Dashed region corresponds to carbon target. The 3-prong vertex was considered as a D^+ decay candidate if it was found more then 450 μm (7.5σ) downstream the target.

A fast track finder was used to reconstruct the $D^{\pm}$ decay. The $D^{\pm}$ particle is reconstructed from its three daughter particles assuming the geometrical target center as the production point. The resulting $D^{\pm}$ z-vertex resolution is 51 μm. The 3-prong vertex was considered as a $D^{\pm}$ decay candidate if it was found more then 450 μm downstream the target. Primary vertex was constructed from all non $D^{\pm}$ tracks and $D^{\pm}$-particle. The combinatorial background is suppressed mainly by the vertex cut χ^2_{geo} and χ^2_{topo} for good quality detached vertices.

The shape of the background in the signal invariant mass region was estimated using the event mixing technique. The resulting background plus D^+ and D^- signal spectra calculated using Hadrons String Dynamics (HSD) model are shown. Predicted multiplicities are $2.7 \cdot 10^{-8}$ for D^+ and $5.7 \cdot 10^{-8}$ for D^- correspondently. Branching ratio is 9.5%. Two sets of cuts have been studied. Relatively soft ($\chi^2_{primary} > 3\sigma$) single track cuts allowed to keep the total reconstruction efficiency about 13.2% Assuming moderate interaction rate of 1.5 MHz one can expect about 335 D^+ and 712 D^- per 10^{12} p+C central collisions (one week of data taking) would be collected by the CBM detector with the signal to background ratio about 0.6 and 1.2 correspondently Hard ($\chi^2_{primary} > 4\sigma$) single track cuts decrease the total reconstruction efficiency to 11.6% Under the same conditions one can expect about 290 D^+ and 617 D^- per 10^{12} p+C central collisions. The signal to background ratio will increase up to 1.4 and 3.0 correspondently

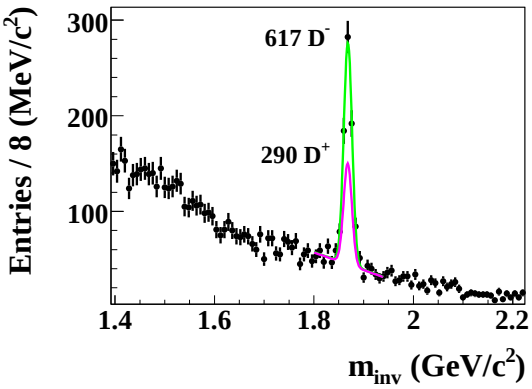

Figure 2: Reconstructed D^- and D^+-mesons in 10^{12} central p+C collision at 30 GeV using hard cuts. Green line is D^- signal plus exponential background, magenta is estimated D^+ signal.

References

[1] I. Kisel, et al., Comp. Phys. Comm. 178 (2008) 374-383.

D^0, D^+ and Λ_c decay feasibility study in the CBM experiment

I. Vassiliev[1,2], *I. Kisel*[2], *and the CBM Collaboration*
[1]IKF, Goethe University, Frankfurt, Germany; [2]GSI, Darmstadt, Germany

One of the major experimental challenges of the CBM experiment is to trigger on the displaced vertex of the D-meson or Λ_c decay via hadronic modes in the environment of a heavy-ion collision. This task requires fast and efficient track reconstruction algorithms and high resolution secondary vertex determination. Particular difficulties in recognizing the displaced vertex of the rare Open Charm decays are caused by weak K^0_S, and hyperon decays which produce displaced vertices downstream the target, very low multiplicity of the Open Charm production, low branching ratios, multiple scattering in the beam pipe and detectors.

To study the feasibility of D^0, D^+ and Λ_c decays reconstruction in the CBM experiment a set of 10^4 central Au+Au UrQMD events at 25 AGeV was simulated. D^0, D^+ or Λ_c decay to hadrons was forced and added to each event in order to simulate a signal in the environment of background hadrons. Realistic STS geometry with 2 MAPS at 5 cm (thickness 300 μm) and 10 cm (thickness 500 μm) and 8 double-sided (thickness 400 μm, different z-position of the stations) segmented strip detectors was used. Assuming 0.1 MHz interaction rate and 30 mksec reading time for the MAPS detectors, δ-electrons produced by 300 gold ions and 3 minimum bias interactions were added to each central event in order to simulated additional background hits in the MAPS detectors. Cluster finding method described in [2] was used for the STS. The primary vertex was reconstructed with high accuracy (6 μm in z direction, 1 μm in x and y) from about 450 tracks reconstructed in the STS in a non-homogeneous magnetic field by the SIMDized Kalman filter procedure described in [1].

A fast track finder was used to reconstruct D^0, D^+ or Λ_c decays. The algorithm first finds the primary vertex using all reconstructed tracks, and then the Open Charm particle is reconstructed from its two or three daughter particles using the primary vertex as the production point. D^0, D^+ or Λ_c z-vertex resolutions are: 52 μm, 56 μm and 69 μm correspondently. Because of originating from a displaced decay vertex, D^0, D^+ or Λ_c daughter tracks have a non-vanishing impact parameter at the target plane. Since the majority of the primary tracks have very small impact parameter, large part (99%) of the background tracks was rejected using a cut on their χ^2 distance to the primary vertex. The combinatorial background is suppressed mainly by the geometrical and topological vertex cuts. Numbers for multiplicity, cut efficiencies, acceptance, z-vertex resolution, mass resolution, signal to background ratios and yields per 10^{12} minimum bias interactions calculated using Hadrons String Dynamics (HSD) and Statistical Model (SM) are presented in Table 1.

The shape of the background in the signal IM region has been estimated using the event mixing technique. The resulting background plus $\bar{D}^0$ and D^0 signal spectra calculated using HSD model are shown.

	$D^0 + \bar{D}^0$	$D^+ + D^-$	Λ_c^+
decay channel	$K^{\mp}\pi^{\pm}$	$K^{\mp}\pi^{\pm}\pi^{\pm}$	p $K^-\pi^+$
HSD multiplicity	$1.5 \cdot 10^{-4}$	$4.2 \cdot 10^{-5}$	-
SM multiplicity	$8.2 \cdot 10^{-4}$	$8.4 \cdot 10^{-5}$	$4.9 \cdot 10^{-4}$
branching ratio	3.8%	9.5%	5.0%
acceptance	29.2%	40.1%	71.0%
z-resolution (μm)	52	56	69
total efficiency	3.95%	4.75%	0.05%
$\sigma_{im}[MeV/c^2]$	11.0	11.0	11.0
SM $S/B_{2\sigma}$ ratio	2.1 (6.4)	1.1 (2.4)	0.6
HSD $S/B_{2\sigma}$ ratio	0.16 (0.5)	0.55 (1.2)	-
SM yield/10^{12}mb	225k +78k	95k+179k	3.2k
HSD yield/10^{12}mb	41k +14k	47k+89k	-

Table 1: Acceptance and efficiencies, mass resolution, and signal-to-background ratio (S/B) in a $2\sigma_m$ region around the peak for D^0, D^+ or Λ_c decays reconstruction in central Au+Au collisions at 25 AGeV beam energy. The total efficiency is calculated from the product of geometrical acceptance, reconstruction and cut efficiencies.

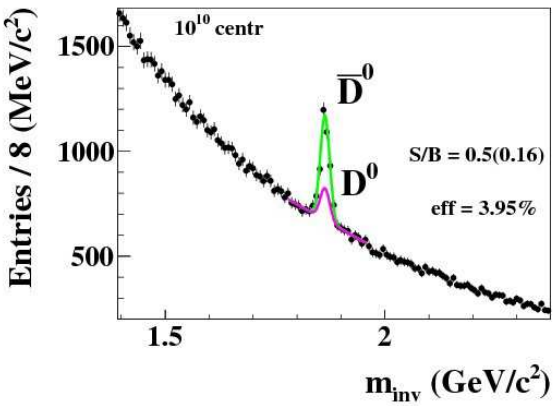

Figure 1: Reconstructed $\bar{D}^0$-mesons in 10^{10} central Au+Au collision at 25 AGeV. Green line is $\bar{D}^0$ signal, magenta is D^0.

References

[1] I. Kisel et al., Comp. Phys. Comm. 178 (2008) 374-383.

[2] A.Kotynia et al., CBM Progress Report (2009) p7.

Ξ^-, Λ and K^0_s on-line reconstruction at Au+Au at 10AGeV in the CBM experiment

I. Vassiliev[1,2], V. Akishina[3], and the CBM Collaboration

[1]Goethe-Universität, Institut für Kernphysik, Frankfurt am Main, Germany; [2]GSI, Darmstadt, Germany; [3]Moscow State University, Moscow, Russia

The main goal of the CBM experiment is to study the behaviour of nuclear matter in the conditions of high baryonic density in which the transition to a deconfined quark gluon plasma phase is expected. One of the signatures of this new state is the enhanced production of strange particles; therefore hyperon reconstruction is essential for the understanding of the heavy ion collision dynamics. Hyperons will be measured in CBM by their decay into charged hadrons, which are detected in the Silicon Tracking System (STS).

To study the feasibility of Ξ^-, Λ and K^0_s on-line reconstruction in the CBM experiment, a set of 5k central Au+Au UrQMD events at 10 AGeV were simulated. At 10 AGeV central Au+Au UrQMD event contains on average 12 K^0_s, 20 Λ and 0.18 Ξ^-. The Ξ^- decays to $\Lambda + \pi^-$ with branching ratio 99.9% and $c\tau$ = 4.91 cm. The STS geometry with 8 double-sided segmented strip detectors were used for tracking. No kaon, pion or proton identification is applied. In order to reconstruct the $\Lambda \rightarrow p\pi^-$ decay the proton mass was assumed for all positively charged tracks and pion mass for all negatively charged ones. K^0_s is reconstructed assuming pion mass for both tracks. The combination of single track cut ($\chi^2_{prim} > 3\sigma$) and geometrical vertex ($\chi^2_{geo} < 3\sigma$) cut allows to see clear signal (see Fig. 1 and Fig. 2) of K^0_s and Λ.

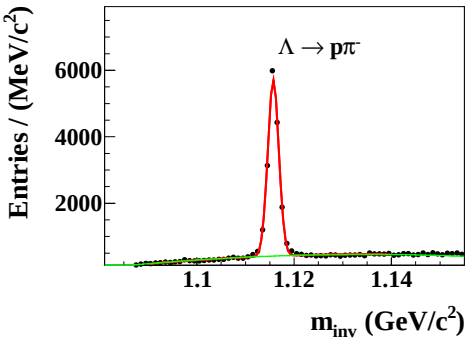

Figure 2: The proton π^- invariant mass spectrum. About 2.8 Λs per event were reconstructed. Red line is signal Gaussian fit, green line is polynomial background.

Λ mass value; only pairs inside 1.116 $\pm 6\sigma = 10 MeV$ were accepted; primary Λ rejection, where only Λ with $\chi^2_{prim} > 5\sigma$ and z-vertex greater than 4 cm are chosen. Selected Λs were combined with the secondary π^- ($\chi^2_{prim} > 3\sigma$) tracks and Ξ^--KFParticle were created. The Ξ^--KFParticle were accepted to a Ξ^- candidate if it has good quality geometrical and topological vertex reconstructed greater than 3 cm downstream the target plane.

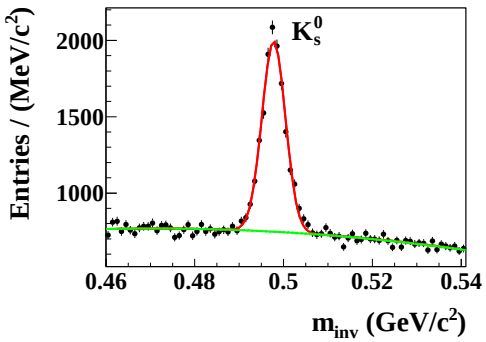

Figure 1: The $\pi^+\pi^-$ invariant mass spectrum. About 1.6 K^0_s per event were reconstructed. Red line is signal Gaussian fit, green line is polynomial background.

The Ξ^- reconstruction includes several steps: tracks with $\chi^2_{prim} > 3\sigma$ are selected for a Λ search, where oppositely charged tracks were paired to form a Λ-candidate; good quality geometrical vertex ($\chi^2_{geo} < 3\sigma$) was required to suppress combinatorial background. The invariant mass of the reconstructed pair is compared with the

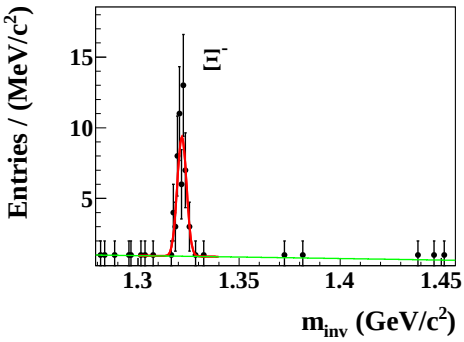

Figure 3: Reconstructed invariant mass spectrum of $\Lambda\pi^-$ candidates. 51 Ξ^- were reconstructed, S/B ratio is about 17, reconstructed mass value is 1.321 GeV/c^2

The resulting invariant mass spectrum is shown in Fig. 3. The signal reconstruction efficiency is about 5.5%. The reconstructed mass value $1.321 \pm 0.003\, GeV/c^2$ is in a good agreement with the simulated one. Invariant mass resolution value is 2.3 MeV/c^2.

Ω^- decay feasibility study in the CBM experiment at SIS300 energies

I. Vassiliev[1,2], I. Kisel[2], V. Akishina[3], and the CBM Collaboration

[1]Goethe-Universität, Institut für Kernphysik, Frankfurt am Main, Germany; [2]GSI, Darmstadt, Germany; [3]Moscow State University, Moscow, Russia

One of the signatures of a phase transition from nuclear matter to a deconfined quark gluon plasma is the enhanced production of strange particles. Also the yield of particles carrying strange quarks is expected to be sensitive to the fireball evolution. Ω^- hyperon consisting of 3 strange quarks, is one of the most interesting objects. Like all other hyperons Ω^- will be measured in the CBM-detector by its decay into charged hadrons, which are detected in the Silicon Tracking System (STS) and in the Time-of-Flight detector (TOF).

To study the feasibility of Ω^- decay reconstruction in the CBM experiment, a set of 10k central Au+Au UrQMD events at 25 AGeV were simulated. At 25 AGeV central Au+Au UrQMD event contains in average only 0.022 Ω^-. In order to calculate Ω^- reconstruction efficiency Ω^- decay to $\Lambda + K^-$ has been forced and embedded to the UrQMD events. The Ω^- decays to $\Lambda + K^-$ with branching ratio 67.8% and $c\tau$ = 2.46 cm. Λ decays most often happen in the STS detector. The STS geometry with 8 double-sided segmented strip detectors were used for tracking. Proton identification with TOF is applied. In order to reconstruct the $\Lambda \rightarrow p\pi^-$ decay each identified proton track has been combined with every negatively charged tracks for which the pion mass assumed.

The Ω^- event reconstruction includes usual steps: fast tracks finding and fitting [1, 2], where all tracks are found and secondary Λs search described in [4].

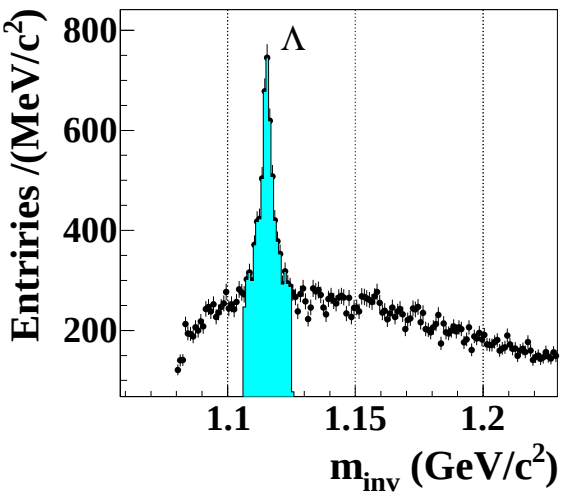

Figure 1: Secondary Λ ($\chi^2_{prim} > 5\sigma$) candidates inside a $1.116 \pm 6\sigma$ window was used for the Ω^- reconstruction

Selected secondary Λ candidates were combined with the secondary negatively charged tracks assuming Kaon mass, K^- ($\chi^2_{prim} > 7\sigma$) and Ω^--KFParticle were created. The Ω^--KFParticle was accepted if it has good quality geometrical and topological detached vertex: ($\chi^2_{geo} < 3\sigma$, $\chi^2_{topo} < 3\sigma$) and z-vetrex greater than 3 cm downstream the target plane.

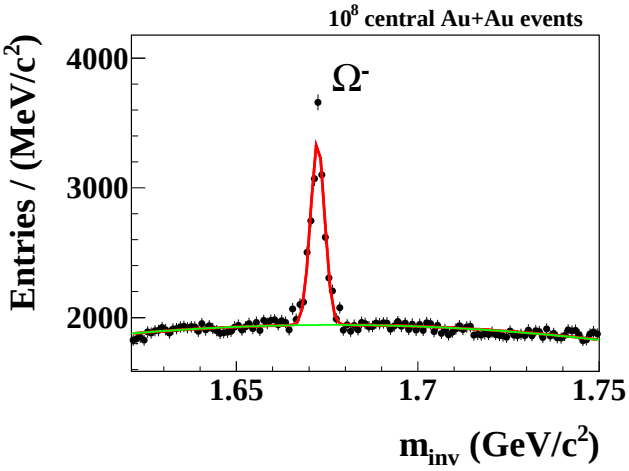

Figure 2: Reconstructed invariant mass distribution of Λ K^- pairs. Ω^- reconstruction efficiency is 0.55% at a S/B ratio of 0.4. The reconstructed mass value is 1.672 GeV/c^2. Red line is signal Gaussian fit, green line is polynomial background.

The invariant mass spectrum is shown in Fig. 2. The signal reconstruction efficiency is about 0.55%. The reconstructed mass value 1.672 ± 0.003 GeV/c^2 is in a good agreement with the simulated PDG's data. Invariant mass resolution value is 2.3 (MeV/c^2).

References

[1] I. Kisel, Nucl. Instr. and Meth. A566 (2006) 85-88.

[2] S. Gorbunov et al., Comp. Phys. Comm. 178 (2008) 374-383.

[3] M.Zyzak, I.Kisel, Vertexing status, 14. CBM Collaboration Meeting, October 6-9, 2009, Split, Croatia

[4] I. Kisel, I.Vassiliev et al., CBM Progress Report 2009, p.59.

Subthreshold J/ψ production in Au+Au collisions at SIS100 studied with a start version of the CBM muon detector *

A. Kiseleva[†1], *C. Höhne*[2], *E. Kryshen*[3], *A. Lebedev*[4,5], *M. Ryzhinskiy*[3], *and P. Senger*[5]
[1]Univ. Frankfurt; [2]Univ. Giessen; [3]PNPI, Gatchina; [4]JINR-LIT, Dubna; [5]GSI Darmstadt

The CBM experiment at FAIR will measure the leptonic decay of vector mesons both in the di-electron and the di-muon channel. A particular challenge is the identification of the soft muons from ρ, ω, and ϕ mesons produced in nucleus-nucleus collisions at beam energies between 15 and 45 AGeV. To perform these measurements an instrumented hadron absorber system has been designed which comprises 6 iron plates of variable thickness (see first column in table 1) and 18 gaseous tracking chambers located in triplets behind each iron slab [1]. The detector layers are segmented into read-out pads with a minimum size of 0.28×0.28 cm^2, and a maximum size of 4.48×4.48 cm^2, corresponding to a total of 560000 channels.

The identification of energetic muons from charmonium decays is less demanding. We developed a start version of the CBM muon detection system which can be used for the measurement of J/ψ mesons already at SIS100 beam energies. As a first step, we have simulated the reconstruction of J/ψ mesons in 25 GeV $p + Au$ collisions at using the LIT global tracking package for full track reconstruction [2]. It turned out that a setup consisting of 2 iron absorber layers (thickness 20 cm and 205 cm) and 2 detector stations with 3 detector layers each would be sufficient to identify J/ψ mesons with an efficiency of 13% and a signal-to-background ratio of above 100 [3].

In a second step we have investigated the possibility to identify J/ψ mesons in nucleus-nucleus collisions at SIS100 energies. We have used the UrQMD event generator to calculate the background for Au+Au collisions at 10 A GeV, and calculated the corresponding J/ψ multiplicity with the HSD code. Please note, that the threshold energy to produce J/ψ mesons in p+p collisions is 11.3 GeV. The muon detector start version which was optimized for proton-nucleus collisions turned out to be insufficient because of many track mismatches resulting in a large combinatorial background (see last column in Table 1). In order to improve the track reconstruction we have inserted one more detector triplet after an iron absorber of 70 cm thickness while keeping the overall absorber thickness constant (225 cm). The result is very promising: J/ψ mesons can be identified with an efficiency of 3.3 % and a signal-to-background ratio of 0.6 (see second column in table 1).

These simulations demonstrate that a start version of the muon detection system for charmonium measurements can be built with 3 detector stations as illustrated in figure 1: a highly granulated detector triplet consisting of Gas-Elektron-Multipliers (GEM) behind the first hadron absorber (20 cm iron), a second detector triplet optionally based on Micromegas technology behind the second absorber (70 cm iron), and a large-area low-granularity detector triplet behind the last absorber (135 cm iron). The last triplet consists either of straw-tube detectors, or the first TRD station will be used. The different detector options are under investigation.

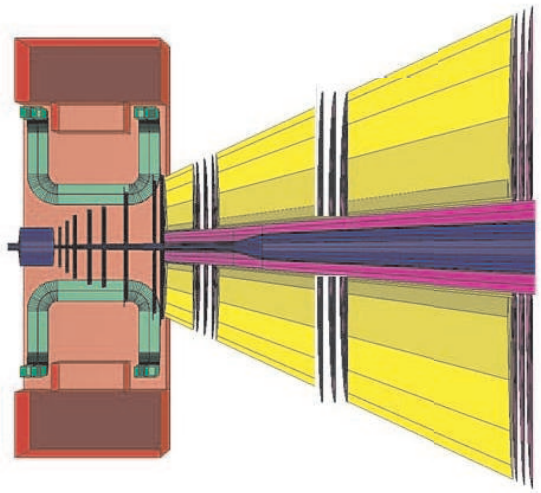

Figure 1: Start version of the CBM muon detection system for J/ψ meson measurements in nucleus-nucleus collisions at $SIS100$ beam energies.

detectors	18	9	6
Fe (cm)	3x20+30+35+100	20+70+135	20+205
$\varepsilon(J/\psi)$	7%	3.3%	1.3%
S/B	0.5	0.6	0.08

Table 1: Efficiency and signal-to-background (S/B) ratio for J/ψ mesons from central Au+Au collisions at 10A GeV for three different absorber/detector combinations.

References

[1] A. Kiseleva, et al., Optimization of the CBM muon detection system, GSI Scientific Report 2008.

[2] A. Lebedev et al., Status of the global track reconstruction algorithms for the CBM experiment at FAIR, GSI Scientific Report 2009.

[3] A. Kiseleva, et al., Possible start version of the CBM muon detector system at SIS100, GSI Scientific Report 2009

*Work supported by the Hessian LOEWE initiative through the Helmholtz International Center for FAIR (HIC for FAIR), and by EU/FP6 Hadronphysics2

† a.kiseleva@gsi.de

Directed flow measurements of charged kaons in ^{58}Ni+^{58}Ni at 1.91 AGeV *

T. I. Kang[†1,2], *V. Zinyuk*[3], *N. Herrmann*[3], *R. Averbeck*[2], *K. D. Hildenbrand*[2], *B. Hong*[1], *M. Kiš*[2], *Y. Leifels*[2], *J.L. Liu*[3,4], *K. Piasecki*[3], *W. Reisdorf*[2], *A. Schüttauf*[2], *and the FOPI Collaboration*[2]

[1]Korea University, Seoul, Korea; [2]GSI, Darmstadt, Germany; [3]Physikalisches Institut, Universität Heidelberg, Germany; [4]Harbin Institute of Technology, Harbin, China

As a consequence of chiral symmetry restoration, charged kaons are believed to undergo a modification of their effective mass with growing baryon density. This modification is described by a kaon-nucleon potential and manifests itself in their collective motion in a dense environment, as created, e.g., in a heavy-ion collision. The collective motion is evaluated by the measurement of asymmetries in the azimuthal distribution of kaons in the final state, with respect to the reaction plane.

The FOPI experiment recorded 16×10^6 ^{58}Ni+^{58}Ni collisions in S325 experiment in 2007 and 53×10^6 collisions in S325e experiment in 2008, corresponding to the most central 60% of the reaction cross section ($0 < b < 7$ fm in the sharp cutoff approximation). Totally, 232,200 K^+ with a ratio of signal to background (S/B) better than 9 and 5,500 K^- with S/B better than 4 are identified. With the newly installed MMRPC [1] we are able to identify K^+ up to a momentum of p_{lab} =1.0 GeV/c and K^- can be separated from the background up to 0.9 GeV/c.

Fig. 1 shows the Fourier expansion coefficient v_1 for K^+ (panel a) and K^- (panel b) compared to the HSD [2] and IQMD [3] model predictions as a function of normalized rapidity $y_0 = y_{lab} / y_{cm} - 1$. The kaon data are obtained in the following acceptance:

polar angle	K^+ (GeV/c)	K^- (GeV/c)
$30° \leq \theta \leq 52°$	$0.13 \leq p_{lab} \leq 0.9$	$0.13 \leq p_{lab} \leq 0.7$
$52° \leq \theta \leq 110°$	$0.13 \leq p_{lab} \leq 0.55$	$0.13 \leq p_{lab} \leq 0.45$

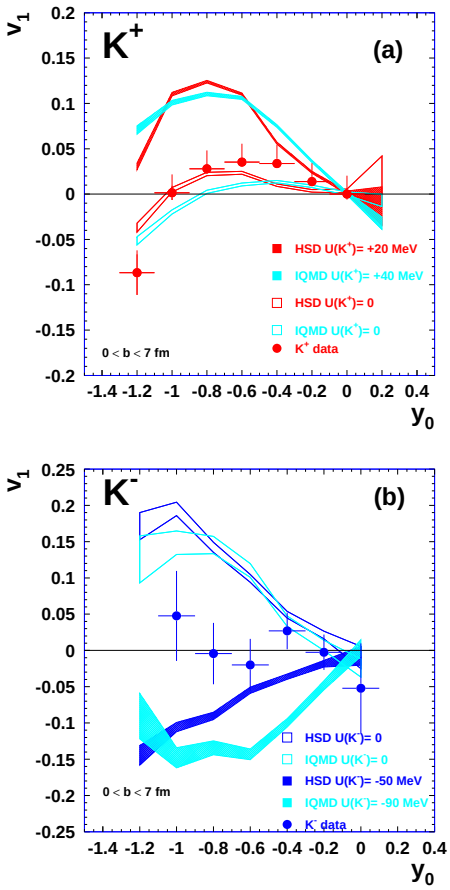

Figure 1: Directed flow of K^+ (a) and K^- (b) (points) in comparison to HSD and IQMD model predictions. The filled bands denote the calculations with in-medium potential and the unfilled band the ones without.

The K^+ flow data is shifted to zero at mid rapidity, which is reflected in systematic errors. As it is seen in Fig. 1 (a) and Fig. 1 (b), K^+ shows anti-flow and K^--flow, within errors, is consistent with zero. The data are not described by the currently available version of the models, neither with nor without the assumption of a KN-potential.

Especially the failure of the models for the K^+-distribution is surprising, since with the HSD calculations the differential flow of K^+ in central collisions [4] and the K^0_s spectra in π-induced reactions [5] could be successfully described by implementing a potential $U_K(\rho = \rho_0, p = 0) = 20 \pm 5$ MeV with a linear baryon density dependence. While also the new data, that are consisted with the ones in [4], point to the presence of a potential for the most central collisions, the integrated distributions are not compatible with the calculations.

In the case of K^- the data tends to a smaller value of a K^-N-potential, than the ones presented in Fig. 1 (b) for both models, HSD and IQMD.

More detailed model calculations are necessary to interpret the data.

References

[1] A. Schüttauf *et al.*, Nucl. Phys. B Pro. Supp. **158** (2006) 52

[2] W. Cassing, U. Mosel, Prog. Part. Nucl. Phys. **25** (1990) 235

[3] C. Hartnack and J. Aichelin, J. Phys. G **28** (2002) 1649-1656

[4] P. Crochet *et al.*, Phys. Lett. B **486** (2000) 6-12

[5] M. L. Benabderrahmane *et al.*, Phys. Rev. Lett. 102, (2009) 182501.

* Work supported by DFG 446 KOR 113/216/0-1, BMBF 06HD9121I and EU/FP7 I3 HadronPhysics2.

† t.i.kang@gsi.de

Status on ϕ mesons from Ni+Ni collisions at 1.91A GeV*

K. Piasecki†[1,2], *N. Herrmann*[1], *and FOPI collaboration*[1]

[1]Physikalisches Institut, Universität Heidelberg; [2]Faculty of Physics, University of Warsaw, Poland

It has been suggested that a considerable part of negatively charged kaons produced in the Heavy Ion collisions stems from the decays of ϕ mesons [1,2]. As the ϕ meson lifetime is about cτ = 50 fm, the contribution of this source to K^- yield is mostly not affected by the in-medium interactions. The ϕ/K^- yield ratio also plays a role in estimating the correlation length R_C within the canonical approach of the Statistical Model. Therefore it is important to extend the experimental knowledge on this ratio.

Details of the S325 experiment were described in [3]. The present paper reports the analysis status from all the acquired data on Ni+Ni collisions at 1.91A GeV. $7.8{\cdot}10^8$ events were registered after the trigger selection of about 50% most central collisions corresponding to $\sigma = 1.35$ b. Two Time-of-Flight detection systems were installed: Multi-strip Multi-gap Resistive Plate Chamber (MMRPC) and Plastic Barrel (PLB) covering polar angles $30° < \vartheta_{lab} < 100°$ with respect to the target shifted 40 cm upstream from its nominal position. Charged kaons were identified in MMRPC up to momenta 1.15 GeV/c (K^+) and 0.8 GeV/c (K^-) and in Plastic Barrel up to 0.6 GeV/c (K^+) and 0.5 GeV/c (K^-). Positively charged kaons were found on an average signal to background level of 4.4. The efficiency was determined in a full GEANT simulation where kaons were sampled from a homogeneous p_t-y distribution. For a series of narrow slices of rapidity the p_t distributions were fitted with Boltzmann functions and extrapolated outside the region of detector acceptance. The rapidity distribution obtained by integrating the p_t spectra for each slice is shown in Fig. 1. An integration of this distribution delivers the K^+ yield of 0.041 per central collision.

ϕ mesons were investigated in the K^+K^- decay channel (BR = 49.1%). The maximum momenta for kaon products identified in the MMRPC were slightly lower: 0.9 (0.7) GeV/c for K^+ (K^-). The invariant mass spectrum of the ϕ meson candidates was compared to the background distribution determined using the event mixing technique and normalized in the range $1.05 < m_{inv} < 1.18$ GeV/c^2. After background subtraction about 125 ϕ mesons were found within 2σ integration range. The efficiency was determined in the GEANT simulation, where ϕ mesons were sampled from an isotropic thermal source using the Siemens-Rasmussen formula assuming three options: T = 90 MeV, β_{flow} = 0, T = 90 MeV, β_{flow} = 0.17 and T = 100 MeV, β_{flow} = 0.25. The efficiency was found to be within 0.68% and 0.97%. The ϕ meson yield was found to be $(5.5{\pm}0.5{\pm}1.5){\cdot}10^{-4}$ per central collision.

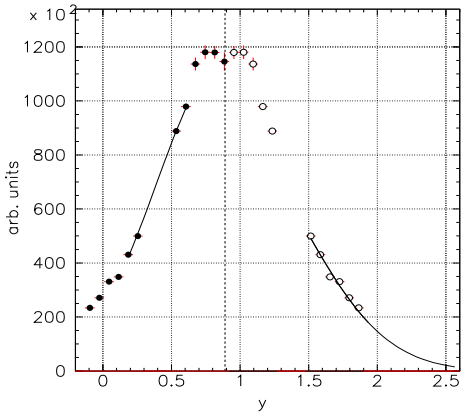

Figure 1: Rapidity distribution of K^+. Experimental data (full dots) were mirrored (empty dots) with respect to the rapidity of the center of mass (dotted line). Solid curves indicate the inter- and extrapolations necessary to obtain the total yield.

Benefitting from the measured yield ratio $K^-/K^+ = 0.031{\pm}0.005$ [4], one obtains $\phi/K^- = 0.44$. A careful investigation of all the systematic errors is ongoing.

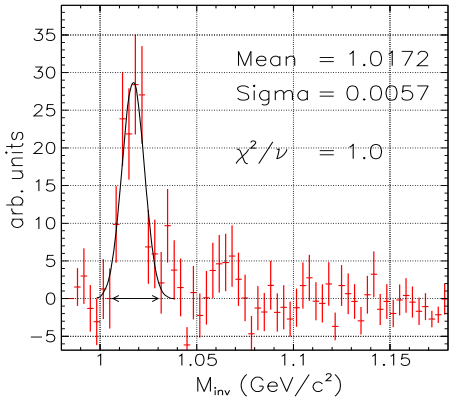

Figure 2: ϕ meson signal on the invariant mass plot of K^+K^- pairs after subtraction of combinatorial background. Arrow indicates the integration range.

References

[1] A. Mangiarotti et al., Nucl. Phys. A 714, 89 (2003)

[2] G. Agakishiev et al., Phys. Rev. C 80, 025209 (2009)

[3] K. Piasecki, N. Herrmann, P. Gasik and Z. Tymiński, GSI Scientific Report 2008, p. 190

[4] M. Menzel et al., Physics Letters B 495 (2000) 26

*Work supported in part by BMBF 06HD9121I and EU/FP7 I3 HadronPhysics2

† kpiaseck@physi.uni-heidelberg.de

Search for hyper-triton in Ni+Ni collisions at 1.91A GeV *

Y.P.Zhang† [1], *N.Herrmann*[1], *K.Wisniewski*[1], *K.Piasecki*[1,2], *and FOPI collaboration*[1]

[1]Physikalisches Institut, Universität Heidelberg, Germany; [2]Faculty of Physics, University of Warsaw, Poland

Production of hypernuclei in heavy-ion collisions is a unique way to study the interaction between strange baryons and the surrounding nuclear matter [1]. At ultrarelativistic energies, the production of (anti-)hyper-tritons has been already measured by the STAR experiment at RHIC [2]. In this contribution, we report on the first measurement of the production of hyper-triton in Ni+Ni collisions at 1.91A GeV, carried out with the FOPI spectrometer at SIS18 in GSI/Darmstadt. The FOPI spectrometer was described in more detail in [3].

Hyper-triton is the lightest hypernuclei. It decays weekly, but its half-life is not known precisely, and can be in the order of 100 - 300 ps [2]. In the FOPI experiment, hyper-tritons can be identified by reconstructing the invariant mass of their charged decay-products. In this contribution, we show the identification in the two-body decay channel: ${}_{\Lambda}t \rightarrow \pi^- + {}^3He$. π^- were registered in the Central Drift Chamber (CDC) and were identified by correlating their momenta with specific energy loss. Proper identification of ${}^3He$ required in addition information about the velocity of the particle, measured by the Time-of-Flight Barrel, which surrounds the CDC, is made of Multi-strip Multi-gap Resistive Plate Chamber (MMRPC) and has an excellent intrinsic TOF resolution of about 60 ps. In order to extend the geometrical acceptance of the CDC and the RPC system towards mid-rapidity, the target used for this experiment was shifted along the beam axis by 40 cm, upstream from its normal position in the center of the CDC. The huge combinatorial background was suppressed by imposing stringent selection criteria on the quality and topology of reconstructed trajectories of π^- and ${}^3He$ pairs. This involved, among others, detailed analysis of the decay kinematics and its influence on the correlations between the selected decay-products of hyper-tritons, e.g., distances of closest approach of the reconstructed trajectories to the primary interaction point, position of the decay-vertex, emission angles and momenta of the involved particles.

The solid, red histogram in figure 1(a) depicts the reconstructed invariant mass of $(\pi^-, {}^3He)$ pairs, selected in 56 million semi-central collisions. The dashed, blue line in figure 1(a) corresponds to the combinatorial background, which was reconstructed by the mixed-event method and normalized to the signal spectrum in the region depicted by the horizontal line (3.03-3.6 GeV/c^2). The red histogram in figure 1(b) shows the distribution obtained after subtracting the normalized background from the signal spectrum. The error bars correspond to the statistical fluctuations only. As depicted by the black line in figure 1(b), the distribution was fitted by a Gaussian in the vicinity of the visible excess around 3 GeV/c^2, which is interpreted as the signal due to decays of hyper-tritons. The reconstructed mass and the decay-width of hyper-tritons can be obtained from fit parameters , which are also used to calculate the significance of the signal, the signal-to-background ratio and the production probability of hyper-tritons. The resulting values, shown in the insert of the figure 1(b), depend strongly on the strategy employed to select the reconstructed trajectories of $(\pi^-, {}^3He)$ pairs. The ongoing analysis concentrates on estimating the systematic errors due to the implemented selection criteria and on evaluating the detection efficiency of hyper-tritons, by means of MC simulations of the detector response and its geometrical acceptance. The hyper-triton signal will be also searched for in the second decay channel: ${}_{\Lambda}t \rightarrow \pi^- + p + d$.

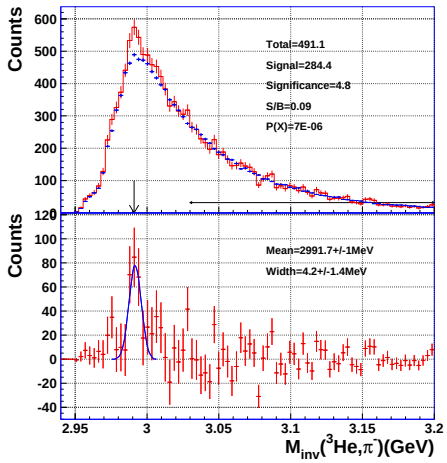

Figure 1: (a) Invariant mass distribution of $\pi^- - He^3$ pairs (solid line) and mixed-event background (dotted line). The horizontal arrow depicts the normalization range. (b) Invariant mass distribution after subtracting the normalized background distribution.

References

[1] A. K. Kermann, M. S.Weiss, Phys. Rev. C 8, 408 (1973); .V. Evlanov, A.M. Sokolov, V.K. Tartakovsky et al, Nuclear Physics A 632 (1998) 624.

[2] The STAR Collaboration, Science, 328, 58 (2010) and reference therein.

[3] T. I. Kang, N. Herrmann, R. Averbeck et al. GSI Scientific Report 2009, P231.

* This work was supported by BMBF 06HD9121I

† ypzhang@physi.uni-heidelberg.de

Symmetry Energy from Elliptic Flow in ^{197}Au + ^{197}Au *

P. Russotto[1], *P.Z. Wu*[2], *M. Zoric*[3,4], *M. Chartier*[2], *Y. Leifels*[3], *R.C. Lemmon*[5], *Q. Li*[6], *J. Łukasik*[3,7], *A. Pagano*[8], *P. Pawłowski*[7], *and W. Trautmann*[3]

[1]INFN-LNS and Università, I-95123 Catania, Italy; [2]University of Liverpool, Liverpool L69 7ZE, United Kingdom; [3]GSI Helmholtzzentrum für Schwerionenforschung GmbH, D-64291 Darmstadt, Germany; [4]Ruder Bošković Institute. HR-10002 Zagreb, Croatia; [5]STFC Daresbury Laboratory, Warrington WA4 4AD, United Kingdom; [6]School of Science, Huzhou Teachers College, Huzhou 313000, China; [7]IFJ-PAN, Pl-31342 Kraków, Poland; [8]INFN-Sezione di Catania, I-95123 Catania, Italy

Two years ago, the elliptic-flow ratio of neutrons with respect to protons or light complex particles in reactions of neutron-rich systems at relativistic energies has been proposed as an observable sensitive to the strength of the symmetry term in the equation of state (EoS) at supra-normal densities [1]. This was derived from the analysis of the existing FOPI/LAND data for ^{197}Au + ^{197}Au collisions at 400 MeV/nucleon in comparison with predictions of the UrQMD transport model [2]. This work has been continued, resulting in a value of $\gamma = 0.9 \pm 0.4$ for the exponent describing the density dependence of the potential term proportional to $(\rho/\rho_0)^\gamma$ [3]. Together with the kinetic term proportional to $(\rho/\rho_0)^{2/3}$, the squeeze-out data thus indicate a moderately soft behavior of the symmetry energy, in contrast to results obtained from the analysis of pion ratios [4, 5].

The enhanced sensitivity of the squeeze-out ratios to the isovector parts of the EoS is illustrated in Fig. 1. The calculations were performed with two parameterizations of the momentum dependence of the in-medium cross sections, labelled FP1 and FP2 [6], which differ by about 30% in their predictions for the elliptic flow of $Z = 1$ particles [3]. The squeeze-out ratios are approximately the same on the absolute scale and lead to very similar results $\gamma \approx 1.0$ for the density dependence of the symmetry term (Fig. 1, lower panels). A lower value $\gamma = 0.52 + -0.23$ is obtained when the impact-parameter range is restricted to the mid-peripheral interval $5.5 \leq b < 7.5$ fm, associated with stronger elliptic flows but probably also smaller compression in the central reaction zone. Considering this systematic uncertainty leads to $\gamma = 0.9 \pm 0.4$ as the overall result obtained with the present data.

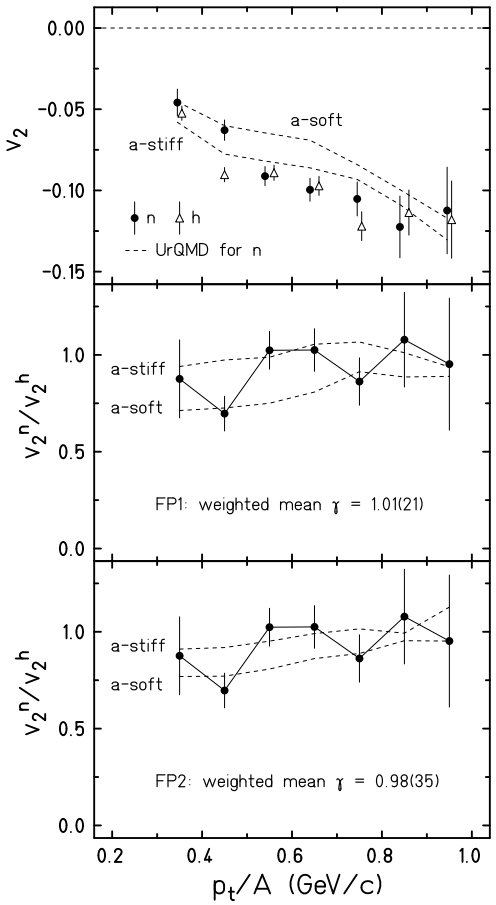

Figure 1: Differential elliptic flow parameters v_2 for neutrons (dots) and hydrogen isotopes (open triangles, top panel) and their ratio (lower panels) for moderately central ($b < 7.5$ fm) collisions of ^{197}Au + ^{197}Au at 400 MeV/nucleon, integrated within the rapidity interval $0.25 \leq y/y_p \leq 0.75$, as a function of the transverse momentum per nucleon p_t/A. The symbols represent the experimental data. The UrQMD predictions for $\gamma = 1.5$ (a-stiff) and $\gamma = 0.5$ (a-soft) obtained with the FP1 parameterization for neutrons (top panel) and for the ratio (middle panel), and with the FP2 parameterization for the ratio (bottom panel) are given by the dashed lines.

References

[1] W. Trautmann et al., GSI Scientific Report 2008, p. 179.
[2] Q. Li et al., J. Phys. G 31 (2005) 1359; J. Phys. G 32 (2006) 151; J. Phys. G 32 (2006) 407.
[3] P. Russotto et al., preprint 2011 [arXiv:1101.2361].
[4] Zhigang Xiao et al., Phys. Rev. Lett. 102 (2009) 062502.
[5] Z-Q. Feng and G-M. Jin, Phys. Lett. B 683 (2010) 140.
[6] Qingfeng Li, Caiwan Shen, and M. Di Toro, Mod. Phys. Lett. A 9 (2010) 669.

* Work supported by EU under contract No. FP7-227431 (Hadron-Physics2).

Test of the triple telescope prototype for the ASY-EOS experiment*

J. Łukasik†[1], *J. Brzychczyk*[2], *A. Budzanowski*[1], *B. Czech*[1], *S. Kupny*[2], *P. Lasko*[2], *P. Pawłowski*[1], *I. Skwirczyńska*[1], *Z. Sosin*[2], *A. Wieloch*[2], *M. Kiš*[3], *Y. Leifels*[3], *and W. Trautmann*[3]

[1]IFJ-PAN, Kraków, Poland; [2]IFUJ, Kraków, Poland; [3]GSI, Darmstadt, Germany

Prototypes of the triple telescope modules have been tested at GSI using the ^{197}Au beam at 400 AMeV and the 3% Pb target. The modules are planned to become building blocks of the charged particle detector that is being built for the ASY-EOS experiment [1]. The final detector will consist of 36 modules covering about 160 msr and is expected to provide complementary to LAND information on isotopic composition of light reaction products. The prototype modules consisted of two CsI(1500 ppm of Tl) crystals [2] readout by 500 μm thick, 28x28 mm^2 photodiodes [3] and of additional photodiode in front of the module serving as a first ΔE layer for direct detection only (see Fig. 1).

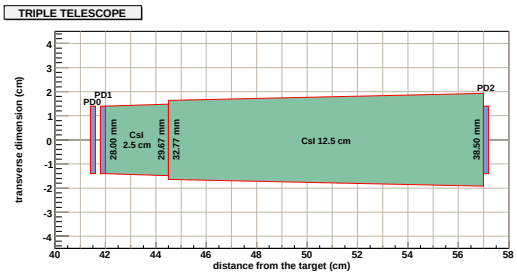

Figure 1: Schematic view of the triple telescope module.

The signals from photodiodes were integrated by the custom-made low-noise charge preamplifiers and digitized with 100 MHz, 14 bits Flash ADCs [4].

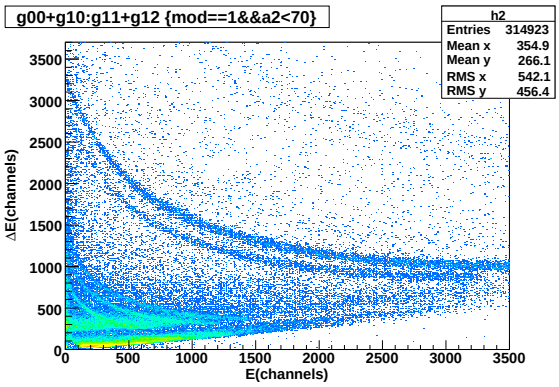

Figure 2: $\Delta E - E$ spectrum for the first two layers of the triple telescope. The strong lines correspond to p, d, t, ^{3}He and α. Punch through signals have been vetoed with the signals from the 12.5 cm long scintillator.

* Work supported by Polish Ministry of Science and Higher Education under grant No. DPN/N108/GSI/2009. We acknowledge financial support by MPD programme of Foundation for Polish Science through structural funds of the European Union.

† jerzy.lukasik@ifj.edu.pl

The photodiode reading out the 2.5 cm long crystal (PD1 in Fig. 1) worked in a "Single Chip Telescope" [5] configuration and provided signals composed of three components: the direct (ionization) signal and the fast and slow light components from the scintillator. These three components differed by their decay times and their individual strengths were extracted off-line from the stored waveforms. The method of deconvolving the signals consisted in using the parametrized shapes of the three components, finding the baseline and the starting time of the signal, and using the least square algorithm to determine the amplitudes. Fig. 2 shows the $\Delta E - E$ spectrum for the first two layers of the triple telescope, where the ordinate represents a sum of the direct ionization signals from the first two photodiodes. This ΔE signal corresponds effectively to the energy loss in 1 mm of Si. The background comes from the reactions in the scintillator and is substantial at these beam energies.

Even better mass resolution (up to Z=5) has been obtained for the $\Delta E - E$ map for the scintillator pair (not shown here). Instead, we present an identification map of an amplitude from the long scintillator vs arctangent of the slow over fast components [6] of the light signals. It shows a clean identification for the light isotopes (Fig. 3).

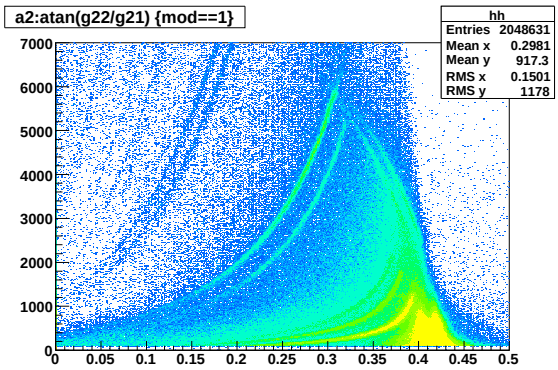

Figure 3: Identification lines using amplitude from the long scintillator vs arctangent of the slow over fast components. The strong lines correspond to p, d, t, ^{3}He and α.

The obtained results are very satisfactory, verify the design of the detector and allow to anticipate its good performance.

References

[1] www.irb.hr/users/mkis, www.ct.infn.it/asyeos2010
[2] IMP-CAS, Lanzhou, China.
[3] HAMAMATSU Si Photodiode for Direct Detection (S5377).
[4] CAEN V1724 digitizer.
[5] G. Pasquali et al., NIM A 301(1991) 101.
[6] Method devised by CHIMERA Collaboration, private comm.

Dielectron measurement in p+p interactions at 3.5 GeV with HADES *

A. Rustamov[1] *and the HADES Collaboration*
[1]GSI, Darmstadt, Germany

We report on the inclusive dielectron (e^+e^- pair) production in p+p collisions at 3.5 GeV kinetic beam energy. For the first time at this beam energy preliminary values of inclusive production cross section of π^o, η, ρ and ω mesons are extracted [1]. Moreover, sensitivity of the data to the electromagnetic N-Δ transition vertex is probed in the time-like range.

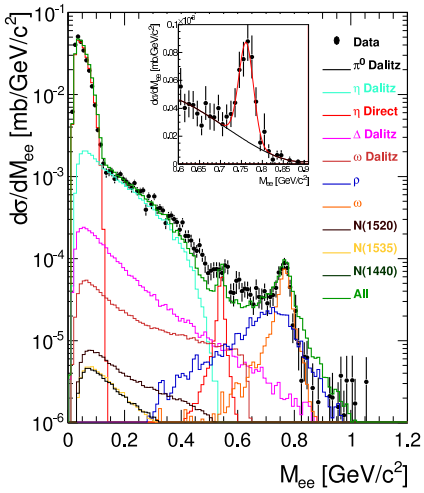

Figure 1: Measured invariant mass distribution of electron pairs emitted into the acceptance of HADES in p+p interactions at 3.5 GeV compared to simulations. The data are corrected for detector and reconstruction efficiencies and normalized to the simultaneously measured elastic data. The inset shows ω peak on a linear scale, fitted with a Gaussian plus a polynomial for the background.

Fig. 1 shows the comparison of the measured dielectron spectra to simulations performed with the PLUTO event generator [2] inside the geometrical acceptance of HADES. The low-mass region of the spectra is dominated by Dalitz decays of π^o, η, ω as well as by the Dalitz decay of the $\Delta(1232)$ resonance. The evident peak around the pole mass of the ω meson, with width of 17 $\pm$ 2 MeV, corresponds to its direct decay into e^+e^- pairs. In the simulation pions are produced through nucleon resonances, as described in [3], while for all other particles, except Δ, constant matrix elements, i.e. phase-space production, are used. The Δ isobar production is parametrized according to [4] while its production cross section of 17mb is taken from the PYTHIA event generator. For the differential Daltitz decay rate of the baryon resonances the calculations of [5, 6] are adopted, with a constant value of the transition form factor fixed at the photon point. It should be emphasized that, in order to be compatible with the data, the upper limit for the $\eta \rightarrow e^+e^-$ branching ratio of [7] has to be scaled down by a factor of 3. As it is seen from Fig. 1, the employed cocktail results in a rather crude description of the data in the mass range around 0.6 GeV/c^2. This is not surprising as it is not so obvious that the assumption of constant magnetic form factor for the N-Δ transition vertex is still valid at this energy. A much better description of the data is accomplished with a particular model for the N-Δ transition form factor based on dominance of the vector mesons (only ρ for Δ) (see Fig. 2). In this case the $\eta \rightarrow e^+e^-$ branching ratio needs to be scaled down even more, by a factor of 13.

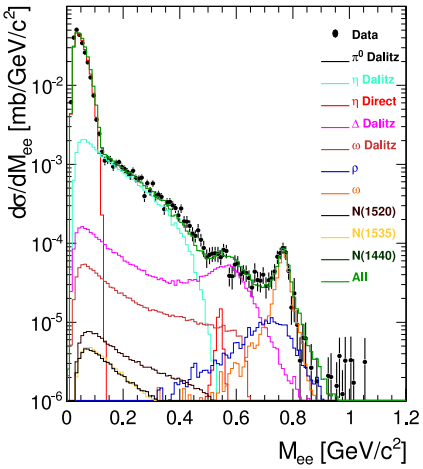

Figure 2: Same as Fig 1, but a model for the N-Δ electromagnetic transition form factor is used (see text).

References

[1] A. Rustamov *et al.*, (HADES Collab.), AIP Conf. Proc. 1257, 736 (2010).

[2] Froehlich *et al.*, arXiv:0909.5373 [nucl-ex].

[3] K. Schmidt *et al.*, Phys. Rev. C 79 064908 (2009).

[4] V. Dmitriev *et al.*, Nucl. Phys. A 459, 503 (1986).

[5] M. I. Krivoruchenko and Amand Faessler Phys. Rev D, 65, 017502 (2001).

[6] Gy. Wolf *et al.*, Acta Phys. Hung. A22/3-4 239-244 (2005).

[7] Particle Data Group, J. Phys. G, 37, 7A (2010).

[8] F. Iachello and Q. Wan, Int. J. Mod. Phys. A 20 1846 (2005).

* Work supported by BMBF.

Inclusive dielectron spectroscopy in p+Nb collisions at E_{kin} = 3.5 GeV*

M. Weber[1], *M. Lorenz*[2], *and the HADES collaboration*

[1]Technische Universität München, Garching, Germany; [2]Goethe-Universität, Frankfurt am Main, Germany

The conditions necessary for a study of hadron properties in surrounding nuclear matter at ground state density and vanishing temperature can be approximately fulfilled in proton-induced reactions with heavy nuclei. In a first attempt, the HADES collaboration has measured e^+e^- pair production in p+Nb collisions at $E_{kin} = 3.5$ GeV. Altogether $9 \cdot 10^9$ collisions have been inspected with respect to the lepton signal content.

All possible combinations of identified e^+/e^- tracks have been formed event by event and corrected for detector and reconstruction efficiencies. Invariant mass spectra of the unlike-sign pairs were constructed from well identified single e^+/e^- tracks and have been corrected for the combinatorial background (CB) from like-sign pair combinations within the same event. The CB was significantly reduced by cutting on the track fitting quality and the pair opening angle $\alpha_{ee} > 9°$ to suppress external γ conversion.

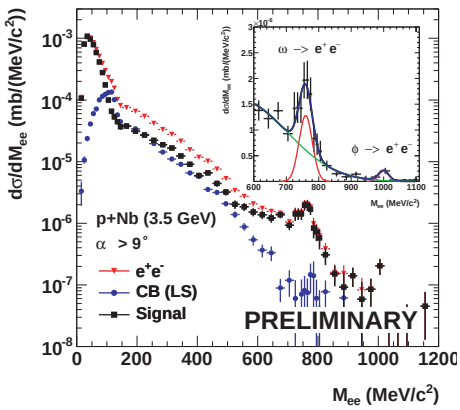

Figure 1: Invariant mass spectrum of e^+e^- pairs inside the HADES acceptance before (black dots) and after (red triangles) combinatorial background (blue dots) subtraction for p+Nb collisions at $E_{kin} = 3.5$ GeV. The inset shows a zoom into the ω and ϕ meson region with signal and background fits (curves) on a linear scale.

We have measured a total of 64827 ± 294 signal pairs with an invariant mass distribution as shown in Fig. 1. The low-mass part of the spectrum ($M_{ee} < 150$ MeV/c^2, 55038 pairs) is dominated by π^0 Dalitz decays, while the intermediate part ($150 < M_{ee} < 550$ MeV/c^2, 9012 pairs) can be attributed predominantly to $\Delta(1232)$ and η Dalitz decays [2]. In the vector meson mass region (777 pairs) the peaks around 780 MeV/c^2 and 1000 MeV/c^2 signal the direct decays of $\omega \rightarrow e^+e^-$ and $\phi \rightarrow e^+e^-$, respectively.

Inclusive e^+e^- production cross sections inside the HADES acceptance ($\approx$ 40 % for the vector mesons) were calculated by analyzing the simultaneously measured charged pions and by normalizing the obtained π^- yields to an independent data set [1]. From a pure Gaussian fit (see inset in Fig. 1) we obtain for the direct vector meson decays $\sigma_{\omega,acc} = (65.8 \pm 4.6$ (stat) ± 18.4 (sys)) nb and $\sigma_{\phi,acc} = (7.8 \pm 1.7$ (stat) ± 2.2 (sys)) nb. The underlying signal continuum in this mass region may be attributed to ρ decays. In this mass region 35 % of all pairs have small pair lab momenta of $p_{ee} < 800$ MeV/c.

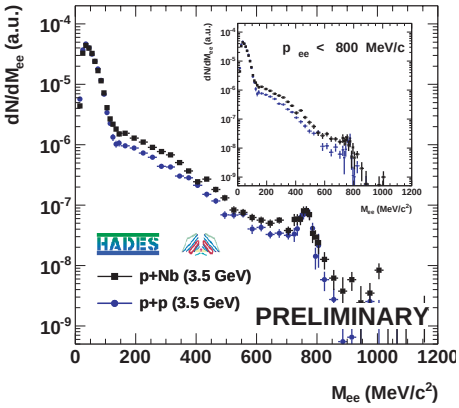

Figure 2: Signal spectra for p+p (blue dots) and p+Nb (black dots) collisions. The p+Nb spectrum is scaled down by a factor of $R_{pA} = 33.7$ to fit the yield in the π^0 mass region (50 MeV/$c^2 < M_{ee} < 120$ MeV/c^2). The inset shows the signal distributions for pair lab momenta $p_{ee} < 800$ MeV/c.

In Fig. 2 the invariant mass distribution of the signal is compared to a reference spectrum measured in a previous p+p run at the same beam energy [2]. The two spectra are normalized to $R_{pA} = A^\alpha$ with $\alpha = 0.69$ such as to obtain the same π^0 yield per participating nucleon. In the ω/ρ region the corresponding yields are comparable for both reaction systems, also when restricting the comparison to low pair momenta (see inset in Fig. 2). The yield in the intermediate mass region (200 MeV/c$^2 < M_{ee} < 600$ MeV/c^2) is significantly enhanced by about 50% and even increases at small lab momenta to about 60%. In the high mass region the yield of slow ρ mesons ($p_{ee} < 800$ MeV/c) overwhelms the signal from direct ω decays. This points either to additional sources or to different production and/or absorption mechanisms of the contributing hadrons. A refined analysis and the comparison to model calculations is still ongoing.

References

[1] A. Bolshakova et al. (HARP-CDP Kollaboration), *EPJ* **C64**, 181 (2009)

[2] A. Rustamov et al. (HADES Collaboration), *AIP Conf. Proc.* **1257**, 736 (2010)

* Work supported by BMBF grants 06MT9156 TP5 and 06FY9100I

Production of charged pions in reaction p+Nb at 3.5 GeV

P. Tlusty[1], *M. Weber*[2], *P. Salabura*[3], *and the HADES Collaboration*

[1]Nuclear Physics Institute, Academy of Sciences of Czech Republic, 25068 Rez, Czech Republic; [2]Technische Universität München, 85748 München, Germany; [3]Jagiellonian University of Cracow, 30-059 Kraków, Poland

The High Acceptance DiElectron Spectrometer HADES [1] is devoted mainly to study production of dielectron pairs from proton, pion and nucleus induced reactions at 1-2 AGeV. At the same time, the spectrometer provides detection and high quality identification of charged particles in a large solid angle.

In this contribution we focus on the analysis of charged pion production in p + ^{93}Nb collisions at 3.5 GeV. The results contribute to the data from systematic studies of pion production in proton-nucleus collisions (see e.g. [2]), and serve as a reliable tool for normalization of the dielectron data obtained in the same experiment.

In the experiment a beam of protons with kinetic energy 3.5 GeV and intensity 2×10^7 per 10 second spill was incident on a segmented Nb target (12 rings, each 0.45 mm thick) with 2.9% total nuclear interaction length. The presented data were collected under the LVL1 trigger condition which was based on a fast determination of the charged-particle multiplicity (M_{ch}) in the time-of-flight detectors. Events with $M_{ch} \geq 3$ were selected.

For the particle identification, the energy loss of particles detected in the time-of-flight detectors was used.

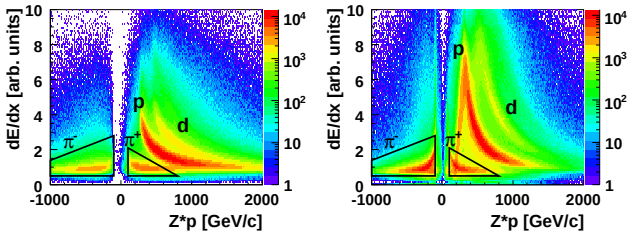

Figure 1: Distribution of the energy loss versus charge*momentum of particles detected in inner TOFINO (left) and outer TOF (right) detectors

Fig. 1 shows the distribution of the energy loss versus charge $\times$ momentum, together with cuts selecting regions with positive and negative pions. π^- mesons can be identified with high purity in a large interval of momenta $p \geq 150 MeV/c$, while the range for π^+ is limited to the region $150 \leq p \leq 600 MeV/c$ due to an overlap with protons at higher momenta.

After the particle identification was done for all tracks, the resulting yields were corrected for efficiency and purity of the PID method, as well as for the detector and tracking efficiencies. The detection/tracking efficiency has been obtained from Monte Carlo simulations.

The resulting pion multiplicities are compared to existing data from a systematic study of pion production from p+A reactions measured by the HARP-CDP Collaboration [2], and in this way provide a natural normalization of the measured dielectron data (usually normalized to a number of neutral pions).

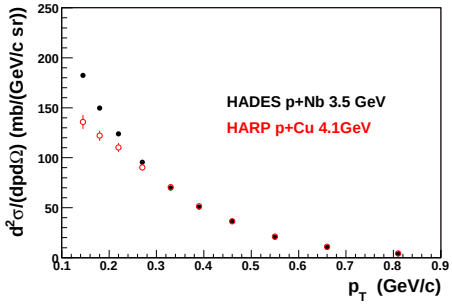

Figure 2: Inclusive cross section for π^- production in p + ^{93}Nb collisions at 3.5 GeV in the polar angle range $20° \leq \theta \leq 75°$.

Results for π^- are shown in Fig. 2. The cross section was obtained from the pion multiplicity in the following way: first we corrected it for enhancement by a factor of 1.42 caused by the LVL1 trigger (deduced from simulations), and then scaled it to the HARP-CDP data for p+Cu at 4.15 GeV. From the systematic [2] the estimated difference of the π^- cross section between these two systems is only 4%. The scaling factor $\sigma_R = \sigma_{\pi^-}(HARP)/M_{\pi^-}(HADES)$ is in fact the total reaction cross section for p + ^{93}Nb at 3.5 GeV. As seen in Fig. 2, the cross section shapes at low momenta differ. The origin of this dicsrepancy needs to be investigated. Neverthelles, the difference between two systems and energies is most probably not the reason, as seen in [2]. Therefore, only a region of $p_T > 300 MeV/c$ was used for the normalization. The resulting total reaction cross section is 886 mb. Statistical errors are negligible, while the systematic error is estimated as 15%, with uncertainty of the trigger enhancement factor as a main source. The result differs only by 10% from the value 982 mb calculated by a parametrization of the total absorption cross section [3].

References

[1] G. Agakishiev *et al.* (HADES Collaboration) Eur. Phys. J. **A41** (2009) 243.

[2] A. Bolshakova *et al.* (HARP Collaboration), Eur. Phys. J. **C64** (2009) 181.

[3] R. K. Tripathi, F. A. Cucinotta, J. W. Wilson, Nucl. Instr. and Meth. **B117** (1996) 347

Measurement of the $\Sigma^+(1385)$ in elementary collisions *

E. Epple[1], *L. Fabbietti*[1], *J. Siebenson*[1], *and the HADES Collaboration*
[1]Excellence Cluster Universe Technische Universität München, Germany

The study of rare resonances with strange content produced in p+p and p+Nb collisions at 3.5 GeV kinetic energy has recently been addressed by the HADES collaboration at GSI. Here we present the results obtained for the $\Sigma^+(1385)$ resonance produced in p+p collisions at 3.5 GeV. The spectral function and the differential cross-section of the resonance could be evaluated. With a nominal mass of 1385 MeV/c^2 and a width of about 40 MeV/c^2, this rather broad resonance is lying close to the $\Lambda(1405)$ in the mass spectrum. The study of the $\Lambda(1405)$ is of great importance to understand quantitatively the the Kaon-Nucleon interaction [1], and the detailed knowledge of the $\Sigma(1385)$ line shape is a prerequisite to extract a clean signature of the $\Lambda(1405)$. Furthermore, the $\Sigma^+(1385)$ resonance can be utilized to approach the topic of in-medium properties of baryonic resonances. The knowledge of the resonance properties in a low-density and finite-temperature environment is a prerequisite to interpret the experimental results obtained for proton-nucleus and heavy-ion collisions.
A total statistics of $1.2{\cdot}10^9$ p+p collisions with a kinetic energy of 3.5 GeV have been collected with the HADES spectrometer at GSI. The following semi-exclusive reaction, which includes a non detectable neutron, has been selected from the available statistics:

$$p + p \rightarrow \Sigma^+(1385) + K^+ + n \rightarrow \Lambda + \pi^+ + K^+ + n \quad (1)$$

Exploiting the further decay $\Lambda \rightarrow$ p + π^-, a total of 4 charged particles (1 K$^+$, 1 p, 1 π^+ and 1 π^-) have been reconstructed for each event making use of the tracking and time of flight detectors of HADES. The event type shown in (1) is selected requiring a Λ candidate out of the $p - \pi^-$ invariant mass and making the hypothesis that the missing particle is a neutron. Under this constraint a kinematic fit of the selected candidates was applied to improve the momentum resolution. One of the challenging parts of this analysis consists in evaluation of the contribution of misidentified kaons to the total background. Indeed, due to the lack of a start detector during this particular experimental campaign, the purity of the kaon selection via the standard velocity measurement was rather limited. A dedicated analysis based on the explicit sideband selection of the wrong identified kaon candidate has been developed to evaluate quantitatively the background contribution. The details of this analysis are described in [2]. Posterior to the event selection, the line shape of the $\Sigma^+(1385)$ has been studied by means of the $\Lambda - \pi^-$ invariant mass. Additional contributions to this spectrum stem from decays like $p+p \rightarrow \Sigma^0 + K^+ + n + \pi^+$ and $p+p \rightarrow \Lambda + K^+ + n + \pi^+$. The contributions of these channels has been estimated using a full scale simulation. The simulation allows to understand the shape of the resulting invariant mass while the total yield has been estimated via a simultaneous fit of the experimental data employing the sum of all the background and signal sources. The final $\Lambda - \pi^-$ invariant mass after the background subtraction is shown in Fig. 1. The points show the experimental data together with the statistical (vertical bars) and systematic (shaded boxes) errors. After the acceptance and efficiency correction a fit to the experimental data by means of a relativistic p-wave Breit-Wigner function, including the Blatt- Weisskopf corrections, delivers a mass and width of 1383 and 38.9 MeV/c^2 respectively for the $\Sigma^+(1385)$ resonance. These values are in good agreement with the ones of the PDG. A total production cross-section of 9.3 μb has been extracted, normalizing the efficiency corrected yield to the rate of p+p elastic collisions. The systematic errors are currently under study. Additionally, the differential cross-section of the

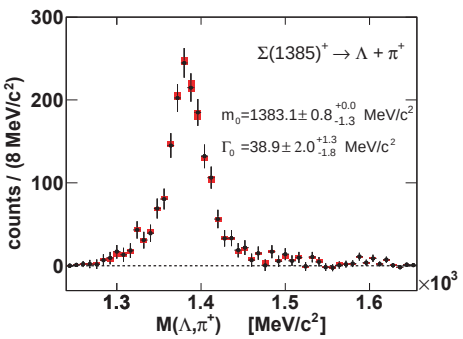

Figure 1: Invariant mass distribution of the selected $\Lambda - \pi^+$ pairs after the background subtraction. The symbols correspond to the experimental data, the vertical bars the statistical errors and the shaded boxes the systematic errors.

$\Sigma^+(1385)$ was extracted. The non isotropic distribution of the $\Sigma^+(1385)$ obtained in the p+p center-of-mass reference system is mainly induced by the spin of the resonance (3/2). Nevertheless, since the reaction takes place well above the threshold, the contribution of higher order waves in the exit channels is rather probable. The angular distribution of the K$^+$ and neutron are currently under investigation to evaluate this issue more quantitatively.

References

[1] L. Fabbietti et al. (HADES), Nucl. Phys. A 835:333-336, 2010.

[2] J. Siebenson et al. (HADES), PoS BORMIO2010:052,2010, arXiv:1009.0946.

* Work supported by BmBf, Vor.: 06M79156

The HADES Upgrade: first Results*

The HADES Collaboration

During the year 2010 the HADES Upgrade project has been finalized and the spectrometer has been commissioned in three test beam times at the end of the year.

The HADES upgrade program had the following main goals: (1) The installation of a new Resistive Plate Chamber (RPC) detector to increase the time resolution and granularity of the time-of-flight system at the lower polar angles ($\theta < 45^o$). (2) The increase of the DAQ capability to cope with the high rates and high multiplicity environment of Au+Au collisions (3) the replacement of the innermost plane of multiwire drift chambers (MDCI) to increase the tracking efficiency and stability of the systems. (4) instalation of the Forward Wall Hodoscope and finally, (5) the installation of the new Start-Veto system for accurate start time measurement and beam quality monitoring.

RPC Detector The complete RPC [1] detector system consisting of a total of 1116 cells with dedicated front-end (with a very fast discriminator and charge to width conversion) and digital electronics has been operating stably since January 2010 and participated in the commissioning beamtimes described below. The selected detector granularity results in a double hit probability of less than 10% for Au+Au collisions. The time resolution measured in Au+Au collisions amounts to 77 ps on average and the position resolution along the cells is close to $\sigma = 10$ mm. The matching efficiency between the RPC and the tracking system has been determined to be above 94%.

MDC plane I All six chambers of MDC-I have been installed and tested by means of beams and radioactive sources. The new optical readout reduces the noise level in the data substantially which resulted in a lower threshold setting and therefore higher sensitivity. The main gain is that we could reduce the HV of the chambers and therefore increase the stability of the detector. Even though the required efficiency could be reached during commissioning beam times, the performance of the detectors is not yet satisfactory due to a O_2 contamination in the detector counting gas. This problem will be solved by improving the gas tightness of the chambers and this work is still in progress. All other 18 chambers have been successfully commissioned for the upcoming Au+Au run.

Start-Veto System The newly built HADES Start-Veto detection system [8] based on diamond material has been installed into the HADES spectrometer and successfully commissioned. It consists of two diamond detectors: the Start detector with a size of 4.7 mm x 4.7 mm made of monocrystalline diamond and the Veto detector with a size of 10 mm x 10 mm made of polycrystalline diamond material. The readout of the system is based on an amplifier/discriminator board equipped with NINO [9] ASICs followed by the standard HADES TRB for time measurement. As the Start detector does not merely provide a Time-of-Flight (ToF) measurement but is also a part of the beam monitoring system, a dedicated segmentation of the metal surface has been used to allow an easy beam focusing procedure. With this device a very good Au-beam focus was obtained with the diameter of the beam spot at the target region of about 3 mm (99.9% of all beam ions are inside this area). The measured time resolution of the detectors was below 50 ps.

Data Acquisition System To reach the performance allowing for efficient use of the available beam time the data-rate capability has been increased by a factor of about 20. The system runs at event rates of 20 kHz for heavy ion systems (100 kHz for light systems) and at a total data rate of 250 MByte/s sustained (400 MByte/s during the beam spill).

This goal has been achieved by a complete replacement of the read-out system and for some detectors (RICH, TOF, FWall) additionally the replacement of the front-end electronics. All detectors have been equipped with custom designed, FPGA-based boards that control the read-out of the front-end electronics and transport data using optical links.

The newly built FEE of the RICH detector is now equipped with boards based on the APV ASIC [2] which aims at a higher sensitivity as compared to the old system.

The FEE of TOF and the Forward Wall Hodoscope consist of analogue boards based on the NINO ASIC [9] for concurrent Time-of-Flight (ToF) measurement and Time-over-Threshold (ToT) measurement for energy loss extraction. The read-out is based on the Trigger and Readout Board (TRB) [3] featuring 128 TDC channels with 100 ps binning and a time resolution of 30 ps, using the HPTDC ASIC developed at CERN. The PreShower detector is read out by an Add-On board attached to the TRB equipped with 96 channel, 40 MSPS ADCs.

Furthermore, for the MDC system digital data transmission from the FEE to the data concentrators has been exchanged to optical links. This change significantly reduced the amount of noise introduced in the detector. Hence, thresholds applied on the analogue signals could be decreased, leading to a better separation between noise and

* Work supported by EU grant 515876, BMBF and the Helmholtz International Center for FAIR (HIC for FAIR).

signals [4].

In total, about 550 FPGAs have been installed distributed over the whole detector. The communication between boards is accomplished by glass fiber connections (2 GBit/s) and plastic optical fiber (FOT/POF) connections (250 MBit/s). All transmissions are performed based on a custom designed network protocol, TrbNet [5], combining high priority trigger information, data transfer and slow control on a single network connection.

The trigger and read-out sequence is controlled by the Central Trigger System (CTS) [6], a FPGA-based board receiving trigger signals from analogue detector signals and making the Level 1 trigger decisions.

The link to mass-storage is formed by four servers ("Eventbuilders") [7] that receive data from the front-ends by standard Gigabit Ethernet connections, assemble the data slices to events and forward the data to disk and tape storage.

Commissioning In summer and autumn several commissioning beam times with Ni, U and Au ions and segmented Au targets have been performed. In November 2010 the commissioning beam time utilizing a ^{197}Au beam at 1.25 AGeV took place. During 30 hours of beam a total of more than 500 million events and 5 TB of data were taken.

The HADES data acquisition system was triggered by coincidence between a hit in the start detector and the combined multiplicity signal from TOF and RPC detectors. Two different threshold settings were available during the experiment: (1) M_3 which required a hit multiplicity in META detector larger than or equal three and (2) M_{30} based on the condition that the META multiplicity should be grater than 30. In figure 1 the offline reconstructed hit multiplicity from Au+Au reactions in the META detector is plotted for the trigger M_3. The hit multiplicity reaches values up to 200 particles per event and increases below 50 particles per event. This strong increase indicates that some reactions took place outside the target which can be seen when checking the signal from the veto detector, as depicted in in figure 1. These events can be easily reduced by requesting the Start and M_3 trigger in anticoincidence to the veto signal.

During the experiment, high multiplicity events were taken at event rates of 12 kHz and at data rates of about 200 MByte/s. These results were limited by the intensity of the Au beam available during this beam time. For low-multiplicity minimum-bias events, an event rate of 50 kHz was reached, corresponding to a data rate of about 350 MByte/s.

Based on the measured performance of the system we are confident that the goal of 20 kHz for the most central Au+Au collisions can be reached. During the whole experiment data was collected and written to disk without any data loss. It should be mentioned, that pulser tests reached values of 63 kHz event rate for small sized events and a peak data rate of 700 MByte/s for big events.

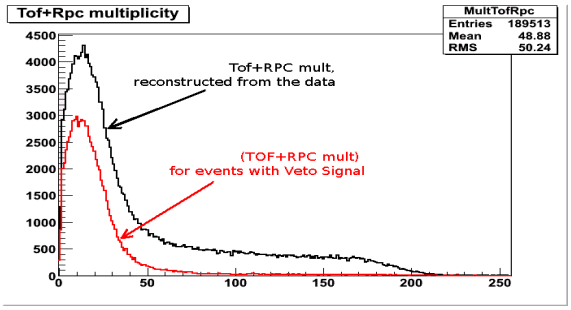

Figure 1: Hit Multiplicity measured in the Tof and the RPC detectors for trigger set to Start detector and multiplicity in the META detector larger than 2. Requiring the signal in the veto detector the reactions originating from places outside the target can be selected.

Based on on-line data analysis several detector correlations were studied and and gave a preliminary estimation of reconstruction efficiencies and resolutions. In figure 2 the correlation between PreShower hits and RPC hits inside one sector is shown. Due to the high hit multiplicity per event a significant background in the histogram is visible. The correlated pairs of hits create a clear peak around 0 cm with a width of $\sim$5 cm (FWHM) corresponding to the PreShower pad size (4 cm). The online correlation of tracking hits and PreShower hits shown in figure 3 is centered around 2.5 cm which indicates that the preliminary alignment of the META detector has to be improved. Also the width of the distribution, which is about 1 cm broader than the pad size of the PreShower detector, indicates that the very preliminary alignment of the MDC system used for this data analysis needs further improvements. Since during the upgrade process almost all detection systems were partially or completely disassembled, the whole Spectrometer elements have to be aligned again. This time consuming procedure has been started after the November beam time and not all activities are finished yet.

All spectrometer elements, except MDC-I, showed stable in-beam performance at nominal interaction rates. We are looking forward to take production beam Au + Au in 2011.

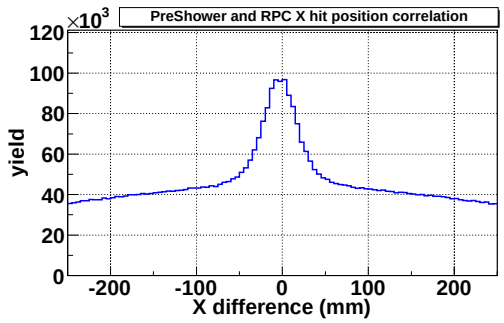

Figure 2: Difference between hit positions measured in RPC and in PreShower detectors. The background visible in the pictures indicates the high hit multiplicity in the system. The width of about 5 cm corresponds to the size of the PreShower pad.

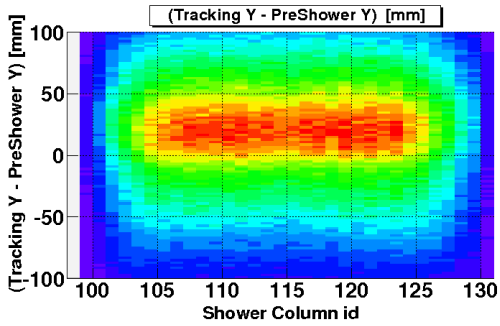

Figure 3: Difference between tracking Y position and PreShower Y position as a function of PreShower column. The width of the distribution (about 5 cm) corresponds to the size of the PreShower pads.

References

[1] The HADES RPC inner TOF Wall, D.Belver et al., Nucl. Instrum. and Meth. in Phys. Res. A. 602 (2009) 687-690 [10.1016/j.nima.2008.12.090]

[2] M. Raymond *et al*, CERN/LHCC/2000-041, 130-134

[3] I. Fröhlich et al, "A General Purpose Trigger and Readout Board for HADES and FAIR-Experiments.", IEEE Trans.Nucl.Sci. 55 (2008) 59-66

[4] K. Göbel, "Vorbereitung der HADES-Driftkammern auf hohe Spurmultiplizitäten mittels Optimierung des Signal-zu-Untergrund-Verhältnisses", Master Thesis, Univ. Frankfurt, t.b.p.

[5] J. Michel, "Development of a Realtime Network Protocol for HADES and FAIR Experiments", diploma thesis, Univ. Frankfurt 2008. [GSI-Doc: DOC-2008-Oct-34-1.pdf]

[6] M. Palka *et al*, HADES Central Trigger System, this volume

[7] S. Yurevich *et al*, HADES Eventbuilding System, this volume

[8] J. Pietraszko *et al*, The diamond Start-Veto system for HADES heavy ion experiment, this volume

[9] F. Anghinol *et al*, NINO: an ultra-fast and low-power front-end amplifier/discriminator ASIC, NIMA 533 (2004) 183-187

A diamond Start-Veto system for the HADES heavy ion experiment.*

J.Pietraszko[1], *W.Koenig*[2], *M.Weber*[3], *and the HADES collaboration.*

[1]Institut für Kernphysik, Goethe-Universität Frankfurt, Germany; [2]GSI Helmholtz Centre for Heavy Ion Research GmbH, Darmstadt, Germany; [3]Physik Department E12, Technische Universität München, Garching, Germany

Diamond detectors have been extensively used and play a key role in the HADES experiment. They are well known mainly for their radiation hardness and high drift velocity of both electrons and holes which make them ideal as detectors for ToF measurements and as beam monitoring devices. For the upcoming HADES heavy ion experiments a monocrystalline diamond detector has been proposed as a start and beam monitoring detector. The main advantage of the monocrystalline material over the polycrystalline is its excellent charge collection efficiency which results in very good energy resolution. At present diamond producers can deliver monocrystalline diamond material with size of about 5 mm x 5 mm and even bigger. During the HADES test run in November 2010 a set of two newly produced beam detectors was used. A start detector with size of 4.7 mm x 4.7 mm located 2 cm in front of an Au segmented target, was made of monocrystalline diamond material. The thickness of the detector was chosen to be 50 μm in order to reduce as much as possible the interaction probability of the beam ions in the detector material, which for 50 μm diamond equals 0.26 $\%$. The Veto detector with thickness of 100 μm, located 70 cm downstream of the target, was made of polycrystalline material. Both detectors and the Au segmented target were aligned with the beam line axis to provide an easy beam focusing procedure. The detectors were operated at 1 V/μm voltage. The metallization of the Start detector consisted of a 50 nm Cr layer deposited on the diamond and followed by a 150 nm Au layer. For the Veto detector an Al metallization was used. The detector segmentation is shown in figure 1. Each detector consists of 8 readout segments glued to the PCB which serves as a holder and provides electrical connections to an amplifier/discriminator board. The board is equipped with a NINO chip [1], which offers 8 input channels, and delivers 8 fast LVDS signals for trigger purposes and 8 fast LVDS signals sent to the HADES TRB [2] board for ToF measurement. The TRB board is equipped with four HPTDCs [3] which were configured to operate in very high resolution mode (25 ps/bin). The measured intrinsic time resolution of the TRB board was 18 ps, shown in the right panel of figure 2.

During the experiment an ^{197}Au beam with kinetic energy of 1.25A GeV and intensity of about 10^6/s - 10^7/s was delivered from the SIS accelerator. Using the segmented start detector the beam was focused onto the inner four segments. The diameter of the beam spot achieved after focusing at the target point was below 3 mm. Using both the start and the veto detectors it was possible to measure the time resolution of the system. The obtained result was better than 50 ps. A histogram for a single channel is shown in figure 2. Another very crucial aspect for HADES is the long-term stability of the detector as the upcoming HI run is expected to last 5 weeks. Based on 30 hours of stable operation at 1 V/μm we expect also smooth operation during the HI production run in 2011.

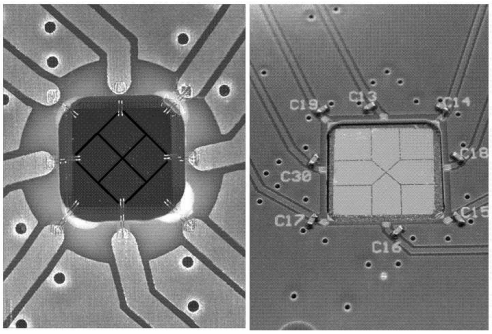

Figure 1: Enlarged pictures of the segmentation of the metal surface of the Start detector with size 4.7 mm x 4.7 mm (left) and Veto detector with size 10 mm x 10 mm (right).

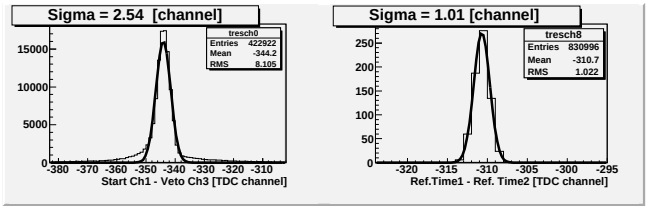

Figure 2: Left: Time resolution of the diamond detector for an ^{197}Au beam. The obtained single channel time resolution was $2.54 * 25ps/sqrt(2) = 45ps$. Right: intrinsic time resolution of the TRB board measured by subtracting reference times measured in two channels. The obtained single channel time resolution was 18 ps.

Acknowledgements: For the preparation of the detectors, metallization and bonding of the diamonds we highly appreciate the support of the GSI Detector Laboratory and the GSI Target Laboratory.

References

[1] F. Anghinol*et al* NIMA 533 (2004) 183-187

[2] M. Traxler, 128 channel high resolution TDC with integrated DAQ-system, GSI Scientific Report (2005) 281

[3] HPTDC, J. Christiansen, Digital Microelec. Group, CERN

* supported by: Helmholtz Gruppe(VN-NG-330), BMBF (06FY9100I)

The Central Trigger System (CTS) for the HADES Experiment*

M. Palka[1,2] for the HADES Collaboration

[1]Jagiellonian University, Cracow, Poland; [2]Johann Wolfgang Goethe University, Frankfurt, Germany;

During the last year, the HADES detector setup has been improved in order to achieve several goals, in particular to enhance the capability of the readout electronics [1] [2] (up to 10^5 events/s). This is required to enable HADES to cope with heavy ion beams at SIS18 and later at the SIS-100 at FAIR. Here, one of the major changes of the DAQ upgrade was the replacement of the copper-based cables by high speed optical transmission based media.

In this context, the new CTS (Fig. 1) board has been developed. The basic requirement for the CTS hardware is that it has to take the signals coming from several detectors, the TOF (6 inputs), RPC (6) and signals from START (8), VETO (8) detectors and other physical triggers PT (8) to combine them into one trigger signal based on adjustable algorithms like multiplicities and vetos.

To enable the above-mentioned features the CTS was equipped with two FPGAs. The first one (Lattice SCM40) is used for the trigger logic, the second one (Lattice ECP2M100) for the standard HADES DAQ operations. The latter FPGA is required for a new dedicated network protocol (TRBNet [4]). The connectivity is provided by four $2\,Gbit/s$ optical connections, four 34 pin connectors for detector signals, three 34 pin connectors to send reference time, one 34 pin connector for general purpose and a high data-rate connector to the TRBv2 [3] (on the back of the board). The TRBv2 is needed also for the power supply.

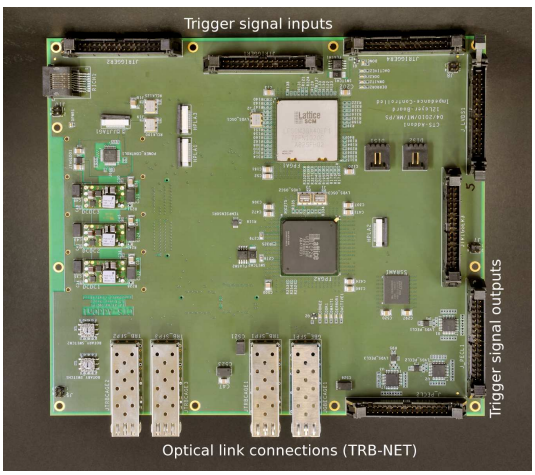

Figure 1: New CTS board.

The CTS functionality is focused on finding coincidences to generate the final trigger signal for selecting interesting physical events. Therefore, the internal FPGA logic (Lattice SCM40) consists of several components. The first input element is used to create pulses, which correspond to the rising edges of the signals. The accuracy of the edge detection of 1.25 ns is achieved by using the DDR architectural components available in this FPGA. By this means, the signals are sampled with 800 MHz, although the digital clock of the logic has only 200 MHz. Consequently, each signal is encoded in a vector and the value represents the sub-clock precision.

This ensures that the signals can be modified with 1.25 ns precision. After the first phase of input signal manipulation the next steps are involved respectively with delaying (in range $0-1.3\,\mu$s), downscaling ($0-2^{15}$) and setting the width (0-80 ns). The logic is able to make sector-wise coincidences (as HADES is divided into six sectors) and also to perform coincidences of START or VETO detector with all other trigger signals.

To be constantly able to monitor the behavior of the CTS a few additional features were implemented, e.g. every second 32-bit scaler values are sent by the CTS and added to the data stream. We monitor the scaler values after the delay and downscaling, at the points where individual signals are offered as a final trigger with coincidence with the start or veto and finally accepted amount of the individual triggers. In addition, all CTS internal register settings and values are inserted into the data stream.

To properly set all parameters, like delays and widths, almost all signals (in total 110 signals) inside the FPGA must be monitored with a oscilloscope. This is realized by using two multiplexers, which forward two selected signals to the 34 pin connector (after using the output DDR component) wired to the oscilloscope. To make a proper judgment of the beam settings quality the CTS counts signals from START, VETO, RPC or TOF and creates four histograms each having 500 samples. Each sample corresponds to the number of hits in a given adjustable time.

The second FPGA (Lattice ECP2M100) is used to interface with the SCM FPGA and with TRBNet. This enables the access to all registers of the SCM FPGA with one optical connection. A second link is used to transmit the CTS data (as described above) to the event builders [5].

The new CTS hardware was successfully used during the HADES tests and commission beam times in late 2010.

References

[1] M. Palka *et al*, Proceedings of IEEE NSS, October 2008, Dresden, Conference Record N06-6

[2] The HADES collaboration, this volume

[3] I. Fröhlich *et al*, IEEE Trans.Nucl.Sci. 55 (2008) 59-66

[4] J. Michel *et al*, GSI report 2009

[5] S. Yurevich *et al*, this volume

* Work supported by EU grant 515876 and by HIC for FAIR

The HADES Event Building System*

S. Yurevich[1], *M. Böhmer*[2], *G. Korcyl*[4], *J. Michel*[3], *J. Stroth*[3,1], *and M. Traxler*[1]

[1]GSI Helmholtzzentrum für Schwerionenforschung GmbH, 64291 Darmstadt, Germany; [2]Technische Universität, 80333 München, Germany; [3]Institut für Kernphysik Goethe-Universität, 60438 Frankfurt, Germany; [4]Jagiellonian University, 30-059 Krakow, Poland

The HADES experiment relies on an efficient data acquisition system to reach trigger rates from 20 kHz for heavy ion reactions up to 100 kHz for light collision systems. The main components of the HADES data acquisition system [1, 2] are designed to be capable of a total sustained throughput of 250 MB/s and a peak throughput of 400 MB/s. The HADES DAQ is illustrated in Fig. 1 with the emphasis on the data flow. TRB-Net [3] combines via optical 2 Gb/s links the Front-End Electronics (FEE) with HUB2-AddOn boards where the data is packed in a special HADES data format and sent to the Event Builders (EB) over Gigabit Ethernet (GbE). The EBs merge the event fragments to the complete events and write the output data to the mass storage systems.

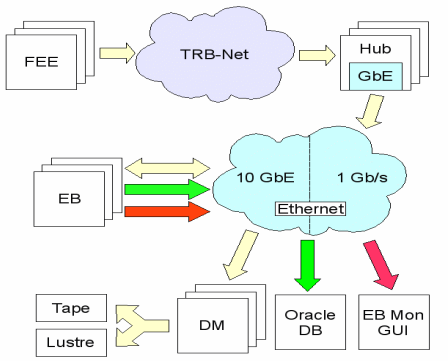

Figure 1: The event building system.

The large input data rate to the EB system demands parallel data processing. The EB system consists of four rack servers, each equipped with two six-core AMD Opteron processors, 44 TB hard disk space, 64 GB memory and dual port 10 Gbps PCI Express NIC each. The servers are connected to a Brocade TurboIron 10 Gb switch. The EB system can be logically viewed as a coupled set of event building processes, each consisting of receiving and building parts interconnected by double buffers. In the current setup sixteen event building processes run on four EB servers. The extensive tests as well as the experience gained in the recent test beam-times have shown that a single EB process is capable of accepting the data rates exceeding 100 MB/s. The total accumulated data rate reached 700 MB/s (in peak). The fill-up levels of the EB buffers remained low in spite of the varying subevent sizes by a factor of 10. The receive performance of the EBs is lossless for the large events (large network packet sizes) generated in heavy ion collisions. However, smaller events (smaller packet sizes) generated by light colliding systems overloaded the Ethernet controller at high trigger rates and packet loss was detected. Processing of small incoming network packets requires more CPU interrupts and causes an increase in overall system utilization. To gain better performance the subevents are aggregated in the HADES-Hubs by the FPGA-based implementation of GbE and are then packed in a transport queue format and sent to the EB in one UDP packet.

The data is further sent directly by the EB process via the RFIO mechanism to the mass storage system over the 10 Gb/s link. Recent tests have shown a stable data transfer to the five Data Movers (DM) via sixteen TCP/IP network connections. Then the data is migrated to tapes [4]. The total local data disk space of 160 TB is sufficient for about 5 days data taking without connection to the mass storage system. Any fraction of data can be in parallel written to the Lustre file system [5]. Further stress tests are on-going.

In addition to writing the main data stream, the EB also records the analysis related information for each experimental RUN and data file (which is passed to the Oracle data base by a dedicated application) as well as performance data and other monitoring data.

The HADES DAQ system as well as the startup process are fully configurable. Most of the parameters of the system (i.e., TRB-Net addresses, TDC settings, MAC and IP addresses of EBs, buffer sizes etc.) are stored in the ASCII configuration files and can be easily changed/tuned. The startup procedure of a complete DAQ takes half a minute. All the FPGAs can also be reprogrammed at the startup if necessary.

In summary, the EB system has demonstrated stable and efficient operation during recent test beam-times.

References

[1] M. Palka et al, Proceedings of IEEE NSS, October 2008, Dresden, Conference Record N06-6

[2] The Hades Collaboration, “The HADES Upgrade: Results”, this volume

[3] J. Michel, diploma thesis, Univ. Frankfurt 2008.

[4] H. Göringer et al, this volume

[5] W. Schön et al, this volume

* Work supported by EU grant 515876 and by HIC for FAIR

CERBEROS: a beam tracker system for HADES *

L. Fabbietti[1], *W. Koenig*[2], *R. Lalik*[1], *R. Münzer*[1], *J. Pietraszko*[3], *and the HADES Collaboration*

[1]Excellence Cluster Universe Technische Universität München, Germany; [2]GSI, Helmholtz Gesellschaftt für Schwerionenforschung, Darmstadt, Germany; [3]Institut für Kernphysik, Goethe-Universität Frankfurt, Germany

Cerberos[1] is a new development for pion-beam trackers to be employed in future experiments with HADES at GSI. This system is composed of three large area silicon detectors distributed along the pion beam chicane and a diamond-based start detector [1] close to the HADES spectrometer. The position sensitive silicon detectors have been provided by Micron Semiconductor Ltd. They are 2x128 strips, 10 cm width (760 μm strip width) and 300 μm thick double-sided silicon detectors with high radiation hardness. The mono-crystallin diamond device provides a time resolution of about 100 psec. Due to the large momentum spread (around 8%) of the secondary pion beam, it is necessary to measure exactly the positions along the chicane and time of flight of each incoming pion to determine the momentum precisely. The first two silicons of Cerberos are located about 5 m behind the pion production target, The third silicon is placed in the HADES spectrometer just in front of the start detector. Currently we are developing the readout of the silicon detectors. Each device is connected to a front-end electronics (FEE) composed of two parts. First DC and AC (AC decoupling due to high voltage potential on the detector) preamplifiers with 32-channels, respectively for the ohmic and junction detector sides, are present on the board. The preamplifier architecture is a combination of a charge sensitive amplifier (CSA) and current amplifier and can work with both signal polarities. Due to low energy consumption and power dissipation the preamplifier can be used in vacuum, a key-feature for our application. The second part of front-end electronics

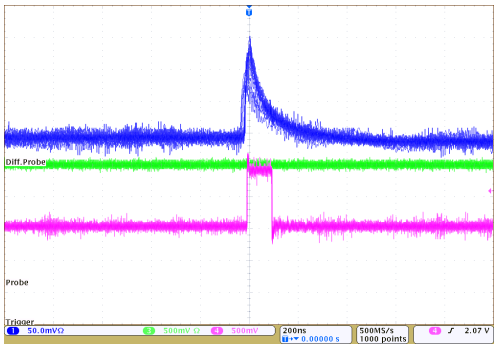

Figure 1: Screenshot of 5.5 MeV α particle hit registered on detector ohmic side. The blue curve shows the pulse obtained after the booster stage on input of discriminator, the pink signal shows LVDS output of the discriminator. This signal is then sent to a TDC on TRB.

consists of a 32-channels booster serving for shaping and time-over-threshold (TOT) processing. The discriminator used for the TOT determination is sensitive only to positive input pulses, thus two different booster boards, with two inverting and only one transistor stages respectively, are used to process the positive and negative input pulses. Due to high power dissipation the booster can not work in the vacuum and must be actively cooled. Figure 1 shows an example of the signal delivered by the booster board. The blue curve shows the output of the booster stage with the signal by an α source as input. The pink signal corresponds to the LVDS (Low Voltage Differential Signal) output of the discriminator. We are currently working on the optimization of the system to minimize the electronic noise and tune the discriminator threshold in the MIP regime. The Cerberos DAQ is based on the standard HADES TRB (TDC Readout Board) boards equipped with four TDC[2] devices for data readout and with additional HUB (data transfer) and CTS[3] addons as well as HADES software for system control. Fig. 2 shows a scheme of the acquisition chain. Cerberos can work inside HADES system or separately after providing a valid trigger for its own CTS. The Cerberos offline software is also fully compatible with HADES thus they can be later easily integrated with the rest of the system. In the future our efforts will concentrate on improving the booster shaping stage which should give a better TOT signal, reducing discriminator output latching to have the opportunity to measure signals induced by MIPs and to reduce noise level to decrease discriminator output jitter. In the future we will also test the possibility to use a n-XYTER ASIC as a front-end integrated readout.

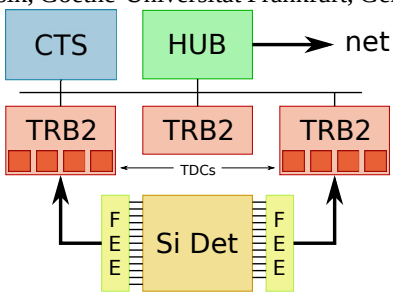

Figure 2: DAQ scheme

References

[1] J. Pietraszko et al. (HADES), Nucl. Instr. Meth, A 618 121 (2010)

[2] Jahrebericht Hades Upgrade

* Work supported by F&E Project:TMFABI1012

[1]Cerberos stands for *CEntRal BEam tRacker for piOnS*

[2]Time-to-Digital Converter

[3]Central Trigger System

The HADES lead glass calorimeter.*

J.Pietraszko[1], L. Fabbietti[2], F. Guber[3], A. Ivashkin[3], A. Kugler[4], K. Lapidus[2], E. Lisowski[6], A. Reshetin[3], P. Salabura[5], Yu.G. Sobolev[4], P. Tlusty[4], and the HADES collaboration.

[1]Institut für Kernphysik, Goethe-Universität Frankfurt, Germany; [2]Excellence Cluster Origin and Structure of the Universe, 85748 München, Germany; [3]Institute for Nuclear Research, Russian Academy of Science, 117312 Moscow, Russia; [4]Nuclear Physics Institute, Academy of Sciences of Czech Republic, 25068 Rez, Czech Republic; [5]Smoluchowski Institute of Physics, Jagiellonian University of Cracow, 30-059 Kraków, Poland; [6]Cracow University of Technology, Kraków,Poland

The HADES collaboration has finished recently the upgrade project [1] which focused on improving the experimental apparatus for measuring heavy systems at SIS18 and at SIS100.

One of the main physics objectives of HADES at SIS100 at the future FAIR facility will be to provide high-quality dielectron data at baryon densities and temperatures not accessible by other detectors, neither in the past nor in the foreseeable future. For the SIS18 energy range, production of neutral mesons has been studied extensively by the TAPS collaboration via photon calorimetry. However, for the 2-40A GeV range no data at all do presently exist, with the consequence that any interpretation of future dielectron data would have to depend solely on theoretical models, e.g. transport calculations or appropriate hydrodynamical models. In order to remedy this situation the HADES collaboration proposes to measure the respective π^0 and η meson yields together with the dielectron data. This can be achieved by replacing the HADES PreShower detector, located at forward angles ($18^\circ < \theta < 45^\circ$), with an electromagnetic calorimeter of a total area of about 8 m^2.

The calorimeter should serve the following two main functions in HADES: (1) detection of photons emitted from HI and p,π induced reactions allowing π^0 and η reconstruction from the measurement of their decays into 2 γ and (2) improved electron identification and pion rejection.

For this detector we plan to recuperate a lead-glass calorimeter from the former OPAL experiment at LEP and adapt it to HADES. The existing OPAL modules are 9.4x9.4 cm^2 and their use would hence result in smaller granularity (about 840 modules in total) than presently available from the PreShower detector. The energy resolution of this solution is comparable to the one of shashlik modules and amounts to about 6 $\%$ at 1 GeV. Mainly due to the cost, time constraints and good performance expected for lead glass we follow the latter option.

The available lead glass modules were tested at the MAMI accelerator in Mainz with photon beams in order to measure the detailed energy resolution for the whole energy range relevant for the reactions at FAIR. The measured energy resolution is below 6$\%$ at 1 GeV, as shown in figure 1, and is consistent with our detector requirements.

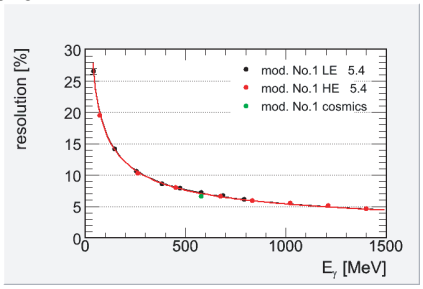

Figure 1: Energy resolution of lead glass measured with photon beams as a function of photon energy.

The second important function of the planned calorimeter for HADES, e/pi separation, has been measured at CERN with secondary pion/electron beams. The experimental results are perfectly reproduced in the simulation prepared for the lead glass calorimeter. Based on these results we obtain the purity of dielectrons for the momentum range from 0.25 GeV/c up to 1.0 GeV. For the momenta below 450 MeV/c very good π/e separation can be obtained based only on the ToF measurement in RPC (100 ps time resolution). For higher momenta the ToF method is not sufficient and the calorimenter has to be employed to obtain a purity close to 95 $\%$ for e^- and 90$\%$ for e^+.

As the total weight of the lead glass modules for the electromagnetic calorimeter, together with its mechanical installation, will exceed 20 tons, special attention has been paid to the integration of the detector into the HADES spectrometer. The proposed solution is shown in figure 2 and is based on completely separated mechanical infrastructure for the calorimeter.

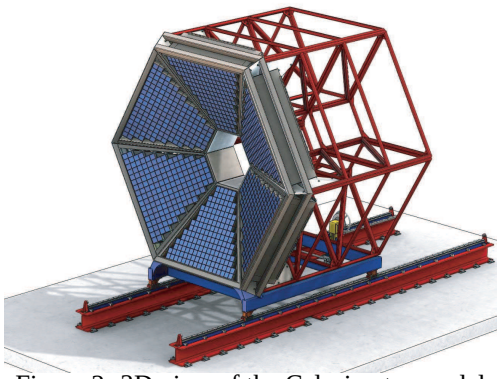

Figure 2: 3D view of the Calorimeter model.

References

[1] The HADES collaboration *et al*, The HADES Upgrade: Results, this volume

*Work supported by: Helmholtz Gruppe(VN-NG-330), grants MSMT LC07050, LA316 and GA ASCR IAA100480803 (Czech Rep.) and the Helmholtz International Center for FAIR (HIC for FAIR).

Extending the Linear Sigma Model with (Axial-)Vector Degrees of Freedom to $N_f = 3$*

D. Parganlija†[1], *F. Giacosa*[1], *D. H. Rischke*[1,2], *P. Kovács*[3], *and Gy. Wolf*[3]

[1]Goethe University, Frankfurt/Main, Germany; [2]FIAS, Frankfurt/Main, Germany; [3]RMKI, Budapest, Hungary

In the 2009 edition of the GSI Scientific Report, we reported on vacuum properties of low-lying non-strange mesons (the energies of which are up to approximately 1.5 GeV) within a linear sigma model with (axial-)vector degrees of freedom and global chiral invariance [1].

However, there are abundant and precise experimental data in the strange-meson sector as well [2]. These mesons are in general well-established resonances in the energy region that we would like to describe within our model. Their structure - at least in the scalar sector - is ambiguous, as in the case of the non-strange scalar mesons [3]. Additionally, these particles are expected to play an important role not only in meson vacuum phenomenology but also at non-zero temperatures, most notably in the restoration of the chiral symmetry. For these reasons, we present here our results regarding an extension of the $N_f = 2$ Linear Sigma Model with (axial-)vector degrees of freedom to $N_f = 3$ (extended Linear Sigma Model - eLSM) [4].

The extension of the model from to three flavours proceeds by defining three-dimensional matrices containing scalar (σ_N, σ_S, $\vec{a}_0$, K_S), pseudoscalar (η_N, η_S, $\vec{\pi}$, K), vector (ω_N^μ, ω_S^μ, $\vec{\rho}^\mu$, $K^{\star\mu}$) and axial-vector (f_{1N}^μ, f_{1S}^μ, $\vec{a}_1^\mu$, K_1^μ) degrees of freedom. As in Ref. [3], in the non-strange sector, we assign the fields $\vec{\pi}$ and η_N to the pion and the $SU(2)$ counterpart of the η meson, $\eta_N \equiv (\overline{u}u + \overline{d}d)/\sqrt{2}$. The fields ω_N^μ and $\vec{\rho}^\mu$ represent the $\omega(782)$ and $\rho(770)$ vector mesons, respectively, and the fields f_{1N}^μ and $\vec{a}_1^\mu$ represent the $f_1(1285)$ and $a_1(1260)$ mesons, respectively. In the strange sector, we assign the K fields to the kaons; the η_S field is the strange contribution to the physical η and η' fields; the ω_S, f_{1S}, $K^\star$ and K_1 fields correspond to the $\phi(1020)$, $f_1(1420)$, $K^\star(892)$, and $K_1(1270)$ mesons, respectively. In accordance with Ref. [3], where the scalar $\bar{q}q$ states were found in the energy region above 1 GeV, we assign the scalar kaon K_S to the physical $K_0^\star(1430)$ state. Preliminary results from our extended model seem to point to the predominantly strange and non-strange sigma states to be above 1 GeV as well [4] (these states arise from the mixing of the pure quarkonium state σ_N and the pure glueball state σ_S).

We have so far given particular attention to the masses of the axial- vector resonances and some strange-meson decays. All the meson fields in our model are $\bar{q}q$ states; we therefore assign our tree-level masses of the $\vec{\rho}$, ω_S and $K^\star$ resonances to their PDG values [2] as these resonances are expected to be predominantly $\bar{q}q$ states. For the axial-vector resonances $\vec{a}_1$, f_{1S} and K_1, where it is not clear whether they are predominantly $\bar{q}q$ states we look for suitable values in the vicinity of the PDG mass values under the condition that the overall fit for all the model parameters (that is also influenced by m_{a_1}, $m_{f_{1S}}$ and m_{K_1}) has a minimal χ^2 value. We are then able to calculate the values of 1142 MeV $\leq m_{a_1} \leq$ 1191 MeV, 1276 MeV $\leq m_{K_1} \leq$ 1292 MeV and 1406 MeV $\leq m_{f_{1S}} \leq$ 1423 MeV [4]. The stated values are fairly close to the experimentally measured ones (within 20 MeV, except for mass of the broad a_1 resonance for which only an estimated value of $m_{a_1} \simeq 1230$ MeV is available [2]) appearing to confirm the hypothesis that the axial-vector resonances $\vec{a}_1$, f_{1S} and K_1 are predominantly $\bar{q}q$ states. Given that we started with the assertion that the vector states $\vec{\rho}$, ω_S and $K^\star$ are also predominantly $\bar{q}q$ states, we can therefore build respective model-consistent pairs of chiral partners ($\vec{\rho}$ - $\vec{a}_1$, ω_S - f_{1S} and $K^\star$ - K_1). These chiral partners are expected to become mass-degenerate after the restoration of the chiral invariance and therefore in this way an order parameter for the chiral transition is determined. Note that the stated pairing of chiral partners would not be possible if the axial-vector resonances were not predominantly $\bar{q}q$ states because then their structure would differ to those of the mentioned vector states.

We also briefly report that a calculation of some strange-meson decay widths. We have calculated the $K^\star \rightarrow K\pi$ decay width with the experimental value [2] $\Gamma^{\rm exp.}_{K^\star \rightarrow K\pi} = (48.7 \pm 0.8)$ MeV and our value $\Gamma^{\rm th.}_{K^\star \rightarrow K\pi} = (51.1 - 52.8)$ MeV. We have also considered the $\omega_S \equiv \phi(1020) \rightarrow K^+K^-$ decay width that has been found to be strongly phase-space dependent because it is close to the KK threshold. However, a suitable value of $m_{\omega_S} \simeq 1015$ MeV (close to the experimental value of 1019.5 MeV) allows us to obtain the experimental decay width value of $\Gamma^{\rm exp.}_{\phi(1020) \rightarrow K^+K^-} = (2.08 \pm 0.04)$ MeV.

As an outlook, we plan a study of meson properties and interactions in vacuum (especially in the scalar sector) and at non-zero temperatures and of the chiral transition.

References

[1] D. Parganlija, F. Giacosa and D. H. Rischke, GSI Scientific Report 2009, p. 255

[2] K. Nakamura *et al.* (Particle Data Group), J. Phys. G **37**, 075021 (2010).

[3] D. Parganlija, F. Giacosa and D. H. Rischke, Phys. Rev. D **82**, 054024 (2010) [arXiv:1003.4934 [hep-ph]].

[4] D. Parganlija, F. Giacosa, D. H. Rischke, P. Kovacs and G. Wolf, arXiv:1009.2250 [hep-ph]; D. Parganlija, F. Giacosa, P. Kovacs and G. Wolf, arXiv:1011.6104 [hep-ph].

* Work supported by the GSI F&E Project.

† parganlija@th.physik.uni-frankfurt.de

Exotic light and heavy hadrons for PANDA *

Amand Faessler, Thomas Gutsche, and Valery E. Lyubovitskij

Institut für Theoretische Physik, Universität Tübingen, Kepler Center for Astro and Particle Physics,
Auf der Morgenstelle 14, D-72076 Tübingen, Germany

One of the key targets of current and future experimental programs is the study of hadron spectroscopy which is e.g. the part of the PANDA experiment at FAIR (GSI). In particular, the activity of our group is closely related to the scientific program of the PANDA Collaboration: gluonic excitations, charmonium, D meson and baryon spectroscopy.

The complexity of the hadronic mass spectra allows for the possibility that existing and newly observed hadrons can be interpreted as molecular states (or hadronic molecules) [1]. Such an interpretation is possible, when the mass of the hadronic molecule m_H lies slightly below the threshold of the corresponding hadronic pair. In the light meson sector, possible candidates for hadronic molecules are the scalar mesons $a_0(980)$ and $f_0(980)$ treated as $K\bar{K}$ bound states. Including the heavy flavor meson sector other possible molecular states can arise. For example, the charm $D^*_{s0}(2317)$ and $D_{s1}(2460)$ mesons can be treated as DK and D^*K bound states, respectively. Other candidates for a hadronic molecule interpretation are the sets of the so-called X, Y and Z mesons, which are now under intensive experimental and theoretical study. In the baryonic sector, the canonical example for a molecule is the deuteron and the most popular candidate for a hadronic molecule is the negative–parity $1/2^-$ resonance $\Lambda(1405)$ considered as a $N\bar{K}$ bound state. Also, there are candidates in the heavy baryon sector, e.g. the charmed baryon $\Lambda_c(2940)$ recently discovered by the BABAR Collaboration which can be treated as a $D^{*0}p$ bound state.

In a series of papers we developed the formalism for the treatment of hadronic (mesonic and baryonic) molecules based on the compositeness condition [2], which was originally applied to the study of the deuteron as a bound state of proton and neutron [2]. In particular, we presented a detailed analysis of strong, electromagnetic and weak decay properties of mesons and baryons containing light and heavy quarks using the molecular picture [3]. The summary of our results for the strong, radiative and weak decay properties of heavy meson molecules is shown in Table 1.

Also we recently developed a soft-wall holographic approach [4], using the correspondence of string theory in Anti-de Sitter (AdS) space and conformal field theory (CFT) in physical space-time [5]. Our approach is based on light-front holography (LFH) suggested by Brodsky and Teramond [6]. The LFH is a covariant and analytic model for hadron structure with confinement at large and conformal behavior at short distances. It is analogous to the Schrödinger theory for atomic physics. It provides a precise mapping of the string modes in the AdS fifth dimension z to the hadron light-front wave functions in physical space-time in terms of the light-front impact variable ξ, which measures the separation of the quark and gluonic constituents inside a hadron. Therefore, different values of the holographic variable z correspond to different scales at which the hadron is examined. The mapping was obtained by matching certain matrix elements in the two approaches - string theory in AdS and light-front theory in Minkowski space-time. Our soft-wall model has been successfully applied to the description of the mass spectrum of meson and baryons (reproducing the Regge trajectories), meson decay constants and nucleon generalized parton distributions [4]. In future we plan to apply this approach to the study of exotic meson and baryon resonances.

Table 1. Properties of hadronic molecules.

Quantity	Our results
$\Gamma(D^*_{s0}(2317) \to D_s\pi)$, keV	61 ± 14
$\Gamma(D_{s1}(2460) \to D^*_s\pi)$, keV	65 ± 15
$\Gamma(D^*_{s0}(2317) \to D^*_s\gamma)$, keV	0.55 ± 0.08
$\Gamma(D_{s1}(2460) \to D_s\gamma)$, keV	3.05 ± 0.68
$\Gamma(Y(3940) \to J/\psi\omega)$, MeV	5.47 ± 0.34
$\Gamma(Y(4140) \to J/\psi\phi)$, MeV	3.26 ± 0.21
$\Gamma(Y(3940) \to \gamma\gamma)$, keV	0.33 ± 0.01
$\Gamma(Y(4140) \to \gamma\gamma)$, keV	0.63 ± 0.01
$\Gamma(\Lambda_c(2940)^+ \to pD^0)$, MeV	0.14 ± 0.04
$\Gamma(\Lambda_c(2940)^+ \to \Sigma^0_c\pi^+)$, MeV	0.95 ± 0.35
$\Gamma(\Lambda_c(2940)^+ \to \Lambda^+_c\gamma)$, keV	113 ± 29

References

[1] M. B. Voloshin and L. B. Okun, JETP Lett. 23 (1976) 333; A. De Rujula, H. Georgi and S. L. Glashow, Phys. Rev. Lett. 38 (1977) 317.

[2] S. Weinberg, Phys. Rev. 130 (1963) 776; A. Salam, Nuovo Cim. 25 (1962) 224.

[3] A. Faessler, T. Gutsche, V. E. Lyubovitskij and Y. L. Ma, Phys. Rev. D 76 (2007) 014003; 77 (2008) 014013; Y. B. Dong, A. Faessler, T. Gutsche, and V. E. Lyubovitskij, Phys. Rev. D 77 (2008) 094013; 81 (2010) 074011; T. Branz, T. Gutsche and V. E. Lyubovitskij, Phys. Rev. D 80 (2009) 054019; D 79 (2009) 014035; 82 (2010) 054025.

[4] T. Branz, T. Gutsche, V. E. Lyubovitskij, I. Schmidt and A. Vega, Phys. Rev. D 82 (2010) 074022; A. Vega, I. Schmidt, T. Branz, T. Gutsche and V. E. Lyubovitskij, Phys. Rev. D 80 (2009) 055014; A. Vega, I. Schmidt, T. Gutsche and V. E. Lyubovitskij, arXiv:1010.2815 [hep-ph].

[5] J. M. Maldacena, Adv. Theor. Math. Phys. (1998) 231 [Int. J. Theor. Phys. 38 (1999) 1113].

[6] S. J. Brodsky and G. F. de Teramond, Phys. Lett. B 582 (2004) 211; Phys. Rev. Lett. 102 (2009) 081601.

* Work supported DFG Contract No. FA67/31-2 and No. GRK683; EU HadronPhysics2, Grant Agreement No. 227431.

The role of the tetraquark at finite baryon density*

S. Gallas†[1], *F. Giacosa*[1], *and D. H. Rischke*[1,2]

[1]Goethe University, Frankfurt/Main, Germany; [2]FIAS, Frankfurt/Main, Germany

The origin of mass of the nucleon m_N is an important topic in field of nuclear physics. In the linear sigma model the mass of the nucleon is generated by a chiral condensate ϕ which appears if chiral symmetry is spontaeneously broken. The nucleon mass vanishes in the phase of restored symmetry where $\phi \to 0$. In an extended linear sigma model the chiral partner of the nucleon N^* can be introduced in the so-called mirror assignment, disussed and studied in [1, 2]. The mirror assignment allows to write down a nucleonic mass term parametrized by m_0 in a chirally invariant way. Thus the mass of the nucleon is not longer generated only by the quark condensate but also by m_0. The vacuum phenomenology of this mass parameter was extensively analysed in [2]. The value of m0 has been calculated through a fit procedure to known experimental quantities, obtaining: $m_0 = 460 \pm 130$ MeV. Going from the vacuum to the range of finite baryon density, the parameter m_0 not longer has to be a constant, but can be identified with other condensates. In the framework of dilatation invariant interactions, the mass term originates from the condensation of two scalar-isoscalar states: the dilaton or glueball field G and the tetraquark field χ: $m_0 = a\chi + bG$, where the subscript 0 denotes the condensates of the fields. In a first approximation the effect of the glueball can be neglected since, due to its relatively high mass of about 1.5 GeV its exchange between the nucleons is almost insignificant, that is $b = 0$. If the value of the mass is fixed to $m_0 = 500$ MeV the following results are obtained.

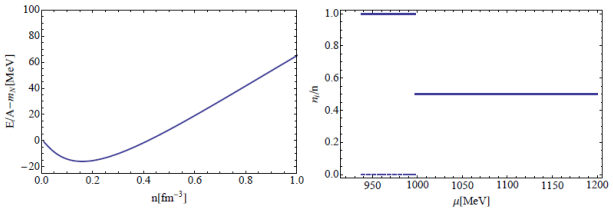

Figure 1: Left panel: Energy per baryon as a function of the density for the case $m_0 = 500$ MeV. The model can describe the saturation of nuclear matter. Right panel: Density fractions of the nucleons (solid line) and their chiral partners (dashed line). The chiral phase transition leads to the sudden appearance of the chiral partners at high densities.

The left panel of Fig. 1 shows the energy per baryon E/A as a function of the baryon density n. The typical constrains of nuclear matter, meaning the manifestation of the saturation of nuclear matter at the minimum of the energy per nucleon with $E/A_{min} = 16$ MeV and $n = 0.16$ fm$^-3$, can be reproduced in the framework of the model. The chiral phase transition occurs at a chemical potential $\mu \sim 1$ GeV and is accompained by the appereance of the chiral partner of the nucleon, see right panel of Fig. 1, in which the ratio between the density of the individual baryons and the total baryonic density is shown. The value of the compressibility turns out to be 194 MeV, a value which is very close to the standard range of $K = 200 - 300$ Mev [3]. Thus, by associating the mass parameter with the tetraquark condensate χ_0 we get a viable model to study the properties of nuclear matter at finite baryon density.

References

[1] B. W. Lee, Chiral Dynamics (Gordon and Breach, New York, 1972). C. E. Detar and T. Kunihiro, Phys. Rev. D39, 2805 (1989). D. Jido, M. Oka, and A. Hosaka, Prog.Theor.Phys. 106, 873 (2001), hep-ph/0110005. D. Jido, Y. Nemoto, M. Oka, and A. Hosaka, Nucl.Phys. A671, 471 (2000), hep-ph/9805306.

[2] S. Gallas, F. Giacosa, and D. H. Rischke, Phys.Rev. D82, 014004 (2010), 0907.5084.

[3] D. H. Youngblood et al., Phys. Rev. C69, 034315 (2004). C. Hartnack, J. Aichelin, and H. Oeschler, Int. J. Mod. Phys. D16, 153 (2007).

* Work supported by the GSI F&E Project.

† gallas@th.physik.uni-frankfurt.de

Heavy quark-antiquark potential and its mass dependence*

A. Laschka, N. Kaiser, and W. Weise
Physik Department, Technische Universität München, D-85747 Garching, Germany

The potential between two heavy quarks has been an object of fundamental interest for many decades. Nowadays this potential is properly defined in non-relativistic effective field theory. While the long distance part can be studied in lattice QCD simulations, a perturbative expansion in the strong coupling is expected to work at short distances.

The perturbative static potential between infinitely heavy quarks at two-loop order has the following form in momentum space:

$$\tilde{V}^{(0)}(q) = -\frac{16\pi\alpha_s(q)}{3q^2}\left\{1+\frac{\alpha_s(q)}{4\pi}\,a_1+\left(\frac{\alpha_s(q)}{4\pi}\right)^2 a_2\right\}, \quad (1)$$

where q is the three-momentum transfer. Expressing $\alpha_s(q)$ in a power series about α_s at a fixed scale μ leads via a Fourier transform to the standard static potential in r-space. However, this r-space potential suffers from renormalon ambiguities [1] and shows a badly convergent behavior.

We work in the potential subtracted (PS) scheme proposed by Beneke [1] and use the following definition of the static r-space potential:

$$V^{(0)}(r,\mu_f) = \int\limits_{|\vec{q}|>\mu_f} \frac{d^3q}{(2\pi)^3}\, e^{i\vec{q}\cdot\vec{r}}\,\tilde{V}^{(0)}(q)\,, \quad (2)$$

where $\tilde{V}^{(0)}$ is now understood without resorting to any power series expansion. The momentum space cutoff μ_f is introduced in order to exclude the uncontrolled low momentum region of $\tilde{V}^{(0)}(q)$. At short distances, this potential depends only marginally on μ_f. The perturbative potential, valid at small distances, can be matched at intermediate distances to results from lattice QCD (see Fig. 1).

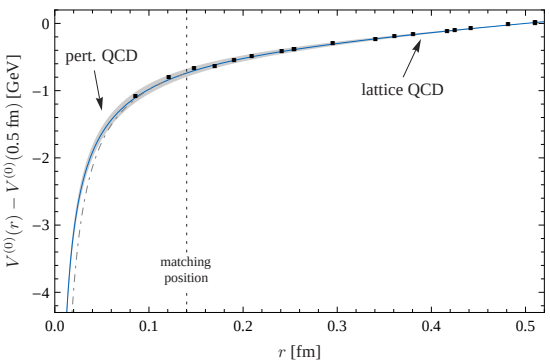

Figure 1: The static quark potential, matched at $r = 0.14$ fm to results from lattice QCD.

The overall constant of the static potential can be fixed by solving the Schrödinger equation and comparing with the experimental quarkonium masses. This leads to heavy quark masses in the potential subtracted (PS) scheme that can be converted to the $\overline{\rm MS}$ mass scheme. In the $\overline{\rm MS}$ scheme we find the values $\overline{m}_b = 4.20$ GeV (bottomonium case) and $\overline{m}_c = 1.23$ GeV (charmonium case).

The heavy quark-antiquark potential has a power series expansion in the inverse quark mass m:

$$V(r) = V^{(0)}(r) + \frac{V^{(1)}(r)}{m/2} + \frac{V^{(2)}(r)}{(m/2)^2} + \dots\,. \quad (3)$$

Here $V^{(1)}$ is still spin independent and the first mass dependent correction to the static potential. It reads in momentum space:

$$\tilde{V}^{(1)}(q) = -\frac{2\pi^2\alpha_s^2(q)}{q}\big\{1+\mathcal{O}(\alpha_s)\big\}\,, \quad (4)$$

and can be transformed to position space analogously as in Eq. (2). The long distances part of $V^{(1)}(r)$ has been determined in lattice QCD [2]. As shown in Fig. 2, a matching with the perturbative potential at intermediate distances works equally well at order $1/m$.

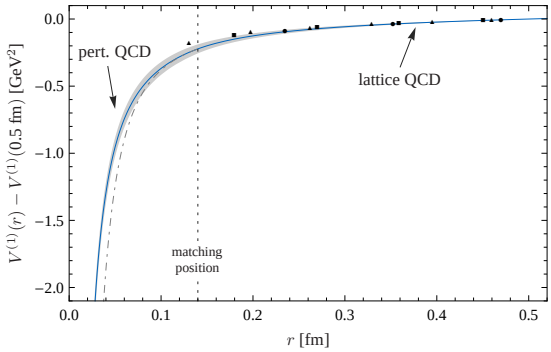

Figure 2: The order $1/m$ potential, matched in coordinate space to a potential from lattice QCD.

To obtain values for the quark masses at this order a readjustment of the PS mass is needed. This leads to the $1/m$-improved $\overline{\rm MS}$-values $\overline{m}_b = 4.18$ GeV for the bottom quark and $\overline{m}_c = 1.28$ GeV for the charm quark. A more detailed presentation can be found in [3].

References

[1] M. Beneke, Phys. Lett. B434, 115 (1998); A. H. Hoang, et al., Phys. Rev. D59, 114014 (1999).

[2] Y. Koma, M. Koma, and H. Wittig, Phys. Rev. Lett. 97, 122003 (2006); M. Koma, Y. Koma, and H. Wittig, PoS Confinement8, 105 (2008).

[3] A. Laschka, N. Kaiser, and W. Weise, preprint (2011).

* Work supported in part by GSI, BMBF and the DFG Excellence Cluster "Origin and Structure of the Universe".

Mapping the phase diagram of strongly interacting matter *

V. Skokov [1], *K. Morita* [1], *and B. Friman* [1]
[1]GSI, Darmstadt, Germany

The properties of strongly interacting matter at finite temperature, $T \neq 0$, and baryon density, $n_B \neq 0$, has been studied extensively in recent years. The Phase Diagram (PD) is being explored experimentally in heavy-ion collisions and examined theoretically in models as well as in first-principle calculations of QCD. In the non-perturbative regime of QCD, Lattice Gauge Theory (LGT) provides a powerful tool for computing the thermodynamic properties of strongly interacting matter. The so-called sign problem, however, has impeded progress in lattice calculations at finite baryon density.

The extrapolation from the $\mu = 0$ ensemble can be performed, e.g. by means of a Taylor expansion in μ/T. This method is applicable only within the radius of convergence of the series, R^{μ}. The radius of convergence of the Taylor series is limited by the distance to the closest singularity in the complex μ plane. Conversely, the convergence properties of a power series yields information on the singularities of the original function. Of particular interest are those singularities corresponding to the critical point of a second-order phase transition, to a crossover transition or to a spinodal line.

The convergence properties of the Taylor series in μ has been studied in model calculations [1]. It was found that on the order of 20 terms are needed to obtain reliable information on the structure of the PD. This is well beyond what is presently available in LGT calculations. Thus, the prospects for extracting useful information on the phase structure of QCD directly from the Taylor expansion in μ seem rather bleak at present.

In [2] we present a method for unravelling a singularity in the complex μ plane, connected with a second-order phase transition, given a finite number of terms in a series expansion of thermodynamic functions. The method, which utilizes a conformal mapping of the Taylor expansion in μ, yields reliable results already at fairly low orders of the series.

As an illustration we consider the mean-field approximation to the chiral quark model (QM) in the chiral limit. The approach can be extended to more general models.

The thermodynamic functions are analytic in the cut complex μ plane. The cuts are associated with the singularities mentioned in the introduction. It is convenient to apply the mapping $\lambda = e^{\mu/T}$, which takes both the thermal cuts (associated with zeros of the inverse Fermi-Dirac function) and the copies of the critical branch point onto the real axis.

We then define the map

$$w_{\rm g}(\lambda;\lambda_{\rm g}) = \frac{\sqrt{\lambda\lambda_{\rm g}-1}-\sqrt{\lambda_{\rm g}-\lambda}}{\sqrt{\lambda\lambda_{\rm g}-1}+\sqrt{\lambda_{\rm g}-\lambda}}\,. \qquad (1)$$

The analytical structure of the thermodynamic function in the $w_{\rm g}$ plane now depends on the value of $\lambda_{\rm g}$ relative to $\lambda_{\rm c}$ ($\lambda_{\rm c} = e^{\mu_c/T}$, where μ_c corrsponds to the second-order critical point for a given T).

For $\lambda_{\rm g} > \lambda_{\rm c}$, $\lambda_{\rm c}$ and $1/\lambda_{\rm c}$, are mapped onto points inside the unit circle at $w = \pm w_{\rm c} = \pm w_{\rm g}(\lambda_{\rm c};\lambda_{\rm g})$. Since $w = \pm w_{\rm c}$ are the singularities that are closest to the origin, the radius of convergence of the Taylor expansion in w is given by $R^w = w_{\rm c}$. If, on the other hand, $\lambda_{\rm g} < \lambda_{\rm c}$, the critical point is mapped onto the circumference of the unit circle and consequently the radius of convergence equals unity, $R^w = 1$. Thus, given R^w as a function of $\lambda_{\rm g}$, the location of the critical point, $\lambda_{\rm c}$, can be obtained e.g. by applying the inverse mapping to $w = R^w$. Hence, the dependence of the radius of convergence on $\lambda_{\rm g}$ can be used to determine the location of a second-order critical point.

In reality the radius of convergence is known only approximately, because not all terms of the Taylor expansion are known. The radius of convergence can be defined as a function of the parameter $\lambda_{\rm g}$ as $R^w_n = |c^w_n|^{(-1/n)}$. By analysing the dependence of R^w_n on $\lambda_{\rm g}$, we obtain an approximative phase diagram for the QM model, which in Fig.1 is confronted with the mean-field result.

References

[1] B. J. Schaefer *et al.*, PoS C **POD2009**, 017 (2009).

[2] V. Skokov, K. Morita and B. Friman, arXiv:1008.4549 .

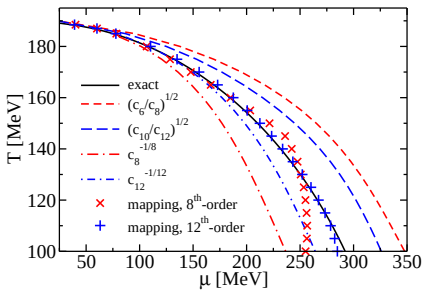

Figure 1: The PD of the QM model in the chiral limit. The solid line represents the critical line of the second-order phase transition.The symbols were obtained using the mapping technique discussed the text, while the dashed and dash-dotted lines are obtained using estimates of the radius of convergence based on the power series in μ.

* Work supported in part by FIAS.

Probing deconfinement with the PNJL model at imaginary chemical potential *

K. Morita [1], *V. Skokov* [1], *B. Friman* [1], *and K. Redlich* [2]

[1]GSI, Darmstadt, Germany; [2]Institute of Theoretical Physics, University of Wroclaw, Poland

QCD at imaginary chemical potential (μ) provides a useful perspective on the phase diagram of strongly interacting matter; at finite densities (real chemical potential) lattice QCD suffers from the sign problem. Based on the analytic structure at imaginary μ, information on the thermodynamics for real μ can be obtained by means of an analytic continuation. The reliability of this procedure can be assessed by studying effective models that have the symmetries of QCD. In this work [1], we explore the phase structure of the two-flavor Polyakov loop extended Nambu-Jona-Lasinio model at imaginary μ in the mean-field approximation. In particular, we focus on the confinement-deconfinement transition.

In the model, the dynamics of the Polyakov loop is implemented by introducing the effective potential $\mathcal{U}[\Phi, \Phi^*; T]$ with the $Z(3)$ symmetry of a pure gluonic theory. We compare results obtained with the two widely-used potentials, the "logarithmic" and the "polynomial" ones. While the two potentials exhibit a first-order transition in the pure $Z(3)$ case, in agreement with lattice simulations, the thermodynamics of a system with quarks can be qualitatively different. Nevertheless, we find a characteristic behavior of the chiral order parameter and the thermodynamic potential independent of the choice of $\mathcal{U}$. This can be illustrated by exploring the $\theta = \mu_I/T$ dependence of these quantities. On the one hand, for $\Phi \ll 1$, we find that they show a modulation proportional to $\sim \cos 3\theta$ on top of θ independent contribution. The period $2\pi/3$ is, as pointed out by Roberge and Weiss [2], a consequence of the $Z(3)$ symmetry in the pure gauge sector. On the other hand, for $\Phi \sim 1$ we find a $\cos\theta$-modulation with cusps at $\theta = \pi/3 + 2\pi k/3$, where k is an integer. The cusps appear as a result of the transition from one $Z(3)$ sector to another, corresponding to the Roberge-Weiss (RW) transition. A typical phase diagram obtained with the logarithmic potential is shown in Fig. 1. We find a critical endpoint (CEP) of the deconfinement transition at finite θ as well as a first-order RW endpoint at $\theta = \pi/3$. This is, however, not independent upon the choice of $\mathcal{U}$. The polynomial potential exhibits the second-order RW endpoint at $\theta = \pi/3(+2\pi k/3)$ and a crossover deconfinement transition elsewhere.

The effect of quarks is nicely illustrated by varying the four-fermion coupling G_s in the NJL sector away from the physical value $G_s = 5.5$ GeV^{-2}. The chiral condensate in vacuum is reduced as the coupling decreases. Hence the dynamical quark mass also decreases and the thermal contribution from quarks is enhanced. This implies that the first-order deconfinement transition is weakened and

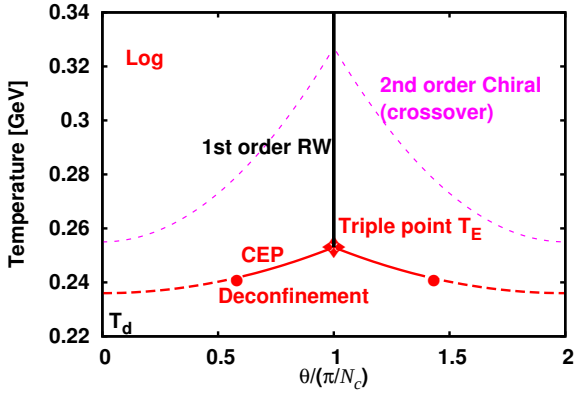

Figure 1: Phase diagram on $T - \theta$ plane with the logarithmic potential in the chiral limit.

that the corresponding CEP moves towards $\theta = \pi/3$. For stronger coupling, we find the opposite behavior. Since the dynamical quark becomes heavier, effects due to quarks are reduced. This drives the CEP to smaller θ and eventually the deconfinement transition at zero and real chemical potentials is of first order. Figure 2 displays the location of the CEP (T_d, μ_c^2) as a function of G_s; for $G_s \geq 6.5$ GeV^{-2} $\mu_c^2 \geq 0$. For the polynomial $\mathcal{U}$, a much heavier quark mass is needed to make the transition first order. This is connected with the smaller latent heat of the pure $Z(3)$ system for the polynomial $\mathcal{U}$.

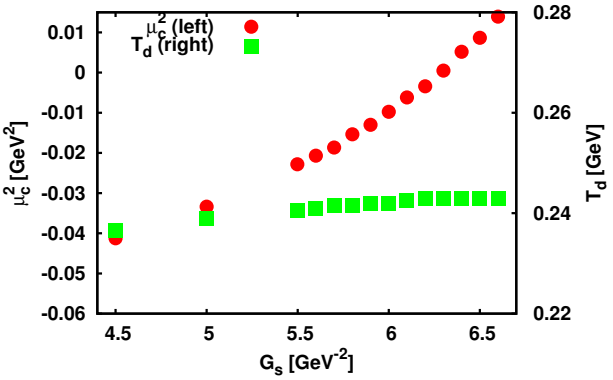

Figure 2: Location of the CEP as a function of the four fermion coupling G_s.

References

[1] K. Morita *et al.* (to be published)

[2] A. Roberge, N. Weiss, Nucl. Phys. B275 (1986) 734.

* Work supported in part by FIAS.

Meson fluctuations and kurtosis of the Polyakov loop extended quark-meson model *

V. Skokov [1], *B. Stokic* [1], *B. Friman* [1], *and K. Redlich* [2]

[1] GSI, Darmstadt, Germany ; [2] Institute of Theoretical Physics, University of Wroclaw, Poland

The Polyakov loop extended Nambu–Jona–Lasinio (PNJL) or quark meson (PQM) models reproduce the essential characteristics of QCD thermodynamics, as obtained in the lattice calculations, already in the mean-field approximation. However, to correctly account for the critical behavior and scaling properties near the chiral phase transitions one needs to go beyond the mean-field approximation and include fluctuations and non-perturbative dynamics. These can be accounted for by using the functional renormalization group (FRG). So far this method was applied in the NJL and quark–meson models, where the FRG equations were formulated for quarks coupled to mesonic fields.

In ref. [1], a truncation of the PQM mode, suitable for a functional renormalization group analysis, was put forward. In the PQM model, a coupling of the quarks to a gluonic background, the Polyakov loop, was introduced. In this way the Polyakov loop dynamics is represented by a corresponding background temporal gauge field. We use the functional renormalization group approach to include fluctuations of the meson fields, while the Polyakov loop is treated on a mean-field level. The coupling of the quarks to the effective gluon fields has an important effect on the thermodynamics. In ref. [1], this is illustrated by examining the PQM and QM models in the FRG approach as well as in the mean-field approximation. Here we only show results for the kurtosis, which is experimentally accessible in heavy-ion collisions.

* Work supported in part by the FIAS.

In Figs. 1 and 2, we show the kurtosis $R_{4,2}$

$$R_{4,2} = \frac{c_4}{c_2}, \quad c_n(T) = \frac{\partial^n [p\,(T,\mu)/T^4]}{\partial(\mu/T)^n}\bigg|_{\mu=0}. \quad (1)$$

as a function of temperature and different chemical potential. Both in the FRG approach and in the mean-field approximation for the PQM model, the kurtosis drops from $R_{4,2} \simeq 9$ to $R_{4,2} < 1$ in the transition region, as expected due to the change in quark content of the baryon carrying effective degrees of freedom. At low temperatures the effective three quark states dominate, while at high temperatures single quarks prevail. In the mean-field approximation, the kurtosis exhibits a well defined peak at the transition temperature. The height of the peak depends on the explicit breaking of chiral symmetry, i.e. on the value of the pion mass in vacuum (see Ref. [1]). The inclusion of mesonic fluctuations weakens this dependence. For a physical value of m_π, the kurtosis at vanishing net baryon density decreases monotonously with temperature in the FRG approach. However, at non-zero baryon density (see Figs. 1 and 2) the kurtosis exhibits a characteristic structure near the chiral crossover transition also when meson fluctuations are included [2].

References

[1] V. Skokov, B. Stokic, B. Friman and K. Redlich, Phys. Rev. C **82**, 015206 (2010) [arXiv:1004.2665 [hep-ph]].

[2] V. Skokov, B. Friman and K. Redlich, arXiv:1008.4570 [hep-ph].

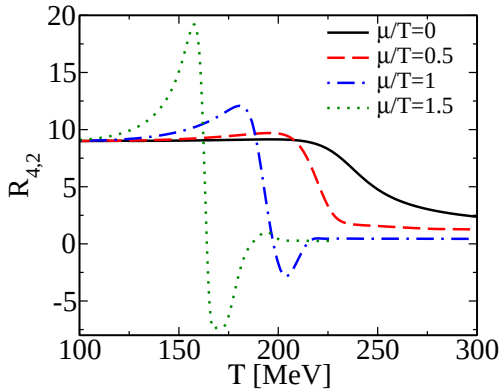

Figure 1: The kurtosis $R_{4,2}$ as a function of temperature for the PQM model in the FRG approach.

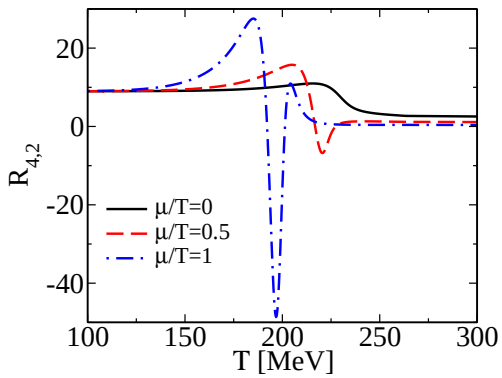

Figure 2: The same as in Fig. 1 but in the mean-field approximation.

Mass of charmonium in hot and dense hadronic matter *

Kenji Morita [1] *and Su Houng Lee*[2]

[1]GSI, Darmstadt, Germany; [2]IPAP, Yonsei University, Seoul, Korea

Charmonium in hot and dense matter provides a probe of the confinement property in QCD. It should be noted that a mass shift of a charmonium state in hot hadronic environment could be a precursor phenomenon, as demonstrated by a consequence of the decreasing string tension in the context of interquark potential [1]. As a complimentary framework, we have elaborated an approach which relates the temperature dependence of local operators to the mass shift and width broadening. In this report, we present results based on the second order Stark effect of QCD [2].

The perturbative QCD formalism for calculating the interaction between heavy quarkonium and partons was first developed by Peskin [3] in the non-relativistic limit. The formula for the mass shift reduces to the second-order Stark effect in QCD. The information needed from the medium is the electric field square. For the ground state charmonium with momentum space wave function normalized as $\int \frac{d^3p}{(2\pi)^3}|\psi(\boldsymbol{p})|^2 = 1$, the mass shift is given as

$$\Delta m = -\frac{1}{18}\int_0^\infty \frac{dk^2\, k}{k^2/m_c + \epsilon}\left|\frac{\partial\psi(k)}{\partial k}\right|^2 \left\langle \frac{\alpha_s}{\pi}\Delta \boldsymbol{E}^2 \right\rangle_T \quad (1)$$

where $k = |\boldsymbol{k}|$ and $\langle \frac{\alpha_s}{\pi}\Delta \boldsymbol{E}^2\rangle_T$ denotes the value of change of the electric condensate from its vacuum value. Here, ϵ is the binding energy and m_c the charm quark mass. These parameters are fit to the size of the wave function obtained in the Cornell potential model, and to the mass of J/ψ assuming it to be a Coulombic bound state in the heavy quark limit. The fit gives $m_c = 1704$ MeV, $a = 0.271$ fm and $\alpha_s = 0.57$.

For the temperature dependent electric condensate, we construct a resonance gas model of the gluon condensate in hot and dense hadronic matter. We can express the gluonic part of the trace anomaly and the twist-2 gluon condensate on the analogy of those in the nuclear matter as $M_0^{\rm had} = \sum_i \rho_i m_i^0$ and $M_2^{\rm had} = \sum_i \rho_i m_i A_G^i$ with m_i being the mass of hadron i and m_i^0 being its chiral limit. Then the particle number density ρ_i is calculated by a resonance gas model with the excluded volume correction in which the volume parameter v_0 is adjusted to fit the lattice data. The second moment of the gluon distribution funnction A_G is set to 0.9. The electric condensate can be obtained with

$$\left\langle \frac{\alpha_s}{\pi}\Delta \boldsymbol{E}^2 \right\rangle_T = \frac{2}{9}M_0(T) + \frac{3}{4}\frac{\alpha_s}{\pi}M_2(T). \quad (2)$$

We plot the temperature dependence of the electric condensate for four cases in Fig. 1. $v_0 = 1.19\text{fm}^3$ and $v_0 = 0$ correspond to the current uncertainty in the equation of state from the lattice data.

* Work supported in part by FIAS and Korean Ministry of Education

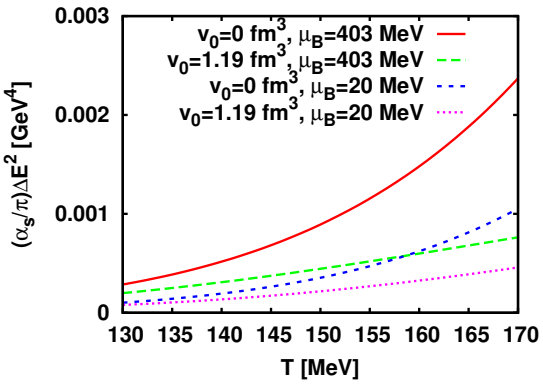

Figure 1: Temperature dependent part of the electric condensate $\langle \frac{\alpha_s}{\pi}\Delta \boldsymbol{E}^2\rangle$. Each line stands for the case of different chemical potential and the excluded volume.

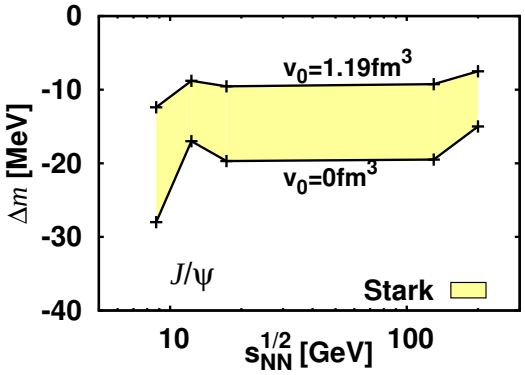

Figure 2: Mass shift of J/ψ from the second order Stark effect. The horizontal axis denotes the collision energy for the system. The band indicates the range of the possible mass shift value corresponding to uncertainty in the electric condensate.

One sees the electric condensate changes larger when the chemical potential becomes so. We compute the resultant mass shift for temperatures and chemical potentials deduced from the statistical model. As shown in Fig. 2, we expect 10–30 MeV mass shift of J/ψ at hadronization temperature and chemical potential for a wide range of the collision energy from SPS to RHIC.

References

[1] T. Hashimoto, O. Miyamura, K. Hirose, T. Kanki, Phys. Rev. Lett. 57 (1986) 2123.

[2] K. Morita, S. H. Lee. arXiv:1012.3110.

[3] M. E. Peskin, Nucl. Phys. B 156 (1979) 365.

The renormalization group and quark number fluctuations in the Polyakov loop extended quark-meson model at finite baryon density *

V. Skokov [1], *B. Friman* [1], *and K. Redlich* [2]

[1] GSI, Darmstadt, Germany ; [2] Institute of Theoretical Physics, University of Wroclaw, Poland

In this report, we highlight the main results of ref. [1], where the functional renormalization group (FRG) approach was used to account for fluctuations of the meson fields, in the Polyakov loop extended quark–meson (PQM) model. The Polyakov loop is still treated as a background field on the mean-field level. Here we extend our previous work [2] to finite baryon chemical potential. The phase diagram and the position of the critical end point (CEP) in the model are determined by exploring the dependence of the chiral order parameter and the quark number susceptibility on thermodynamic variables. We compute the moments (cumulants) of the net-quark number density (c_n) at finite temperature and chemical potential in the presence of mesonic fluctuations, and discuss the influence of non-perturbative effects on properties of the first four moments near the chiral crossover transition. We find that the cumulants exhibit characteristic structures near the crossover transition; for sufficiently large values of the chemical potential the higher cumulants even turn negative. The role of the ratios c_3/c_1 and c_4/c_2 as probes of the deconfinement and chiral phase transitions are discussed. Such ratios may in fact provide an experimentally accessible signal for the QCD phase transition. We also discuss the properties of various susceptibilities near the chiral phase transition at finite net-quark density within the Landau (mean-field) and scaling theories.

In the chiral limit, the second order phase boundary is identified by a diverging chiral susceptibility. At finite quark mass, the chiral transition is of the crossover type. In this case the pseudocritical temperature and chemical potential are determined by a maximum of the chiral susceptibility or alternatively of the temperature derivative of the chiral order parameter. Furthermore, the position of the CEP is according to $Z(2)$ universality indicated by a divergence of the net-quark-number susceptibility c_2.

In Figs. 1 and 2 we show the phase diagrams of the PQM model as obtained within the FRG approach and in the mean-field approximation. For a physical pion mass and moderate values of the chemical potential the PQM model exhibits a smooth crossover chiral transition. The transition region is shown as bands where the temperature derivative of the order parameter exhibits a 5%-deviation from its maximal value. At larger chemical potentials the crossover line terminates at the CEP, where the transition is of second order and belongs to the universality class of the three dimensional Ising model. We find a clear shift of the position of the chiral phase boundary to higher temperatures owing to mesonic fluctuations.

* Work supported in part by the FIAS.

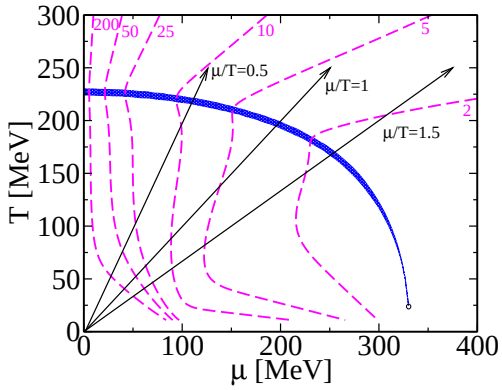

Figure 1: The phase diagrams for the PQM model in the mean-field approximation. The shaded regions are defined by 5%-deviations of the temperature derivative of the chiral order parameterfrom its maximal value. The arrows show the lines corresponding to different values of μ/T. The dashed curves indicate isentropes for $s/n_q = 2$, 5, 10, 25, 50, 200.

References

[1] V. Skokov, B. Friman and K. Redlich, arXiv:1008.4570 [hep-ph].

[2] V. Skokov, B. Stokic, B. Friman and K. Redlich, Phys. Rev. C **82**, 015206 (2010) [arXiv:1004.2665 [hep-ph]].

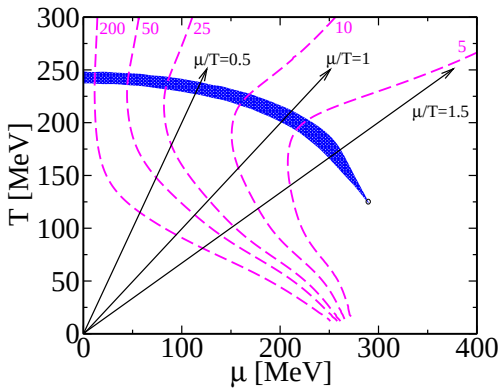

Figure 2: The same as in Fig. 1, but for the FRG approach.

Dileptons from the strongly interacting quark-gluon plasma (sQGP)*

O. Linnyk† [1], *E. L. Bratkovskaya*[1,2], *V. Ozvenchuk*[2], *and W. Cassing*[3]

[1]Institut für Theoretische Physik, Goethe Universität Frankfurt am Main, Germany; [2]Frankfurt Institute for Advanced Studies, Germany; [2]Institut für Theoretische Physik, Justus Liebig Universität Gießen, Germany

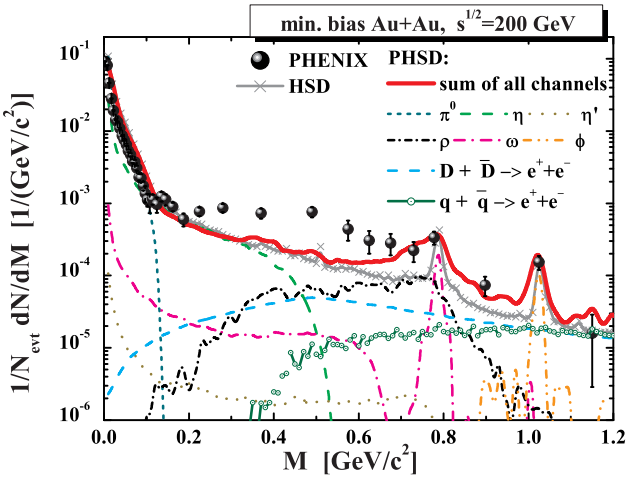

Figure 1: The PHSD results for the mass differential dilepton spectra in case of inclusive $Au+Au$ collisions at $\sqrt{s}$ = 200 GeV in comparison to the data from PHENIX [3, 4] in the low mass region ($M=0-1.2$ GeV).

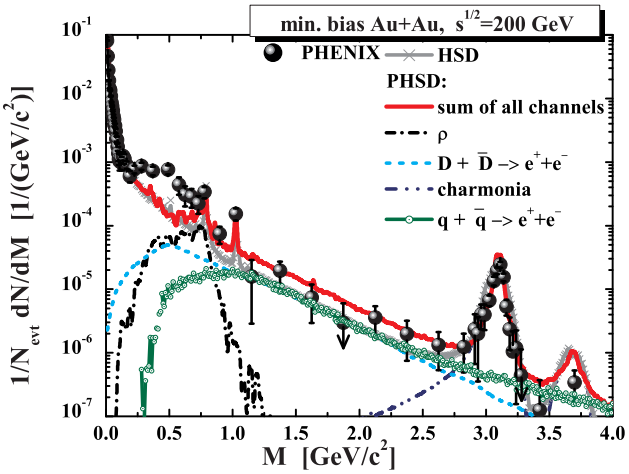

Figure 2: The PHSD results for the mass differential dilepton spectra in case of inclusive $Au+Au$ collisions at $\sqrt{s}$ = 200 GeV in comparison to the data from PHENIX [3, 4] for $M=0-4$ GeV.

To address the dilepton production in a hot and dense medium – as created in heavy-ion collisions – we employ an up-to-date relativistic transport model, i.e. the Parton Hadron String Dynamics [1] (PHSD) that incorporates the explicit partonic phase in the early reaction region. The approach consistently describes the full evolution of a relativistic heavy-ion collision from the initial hard scatterings and string formation through the dynamical deconfinement phase transition to the quark-gluon plasma (QGP) as well as hadronization and to the subsequent interactions in the hadronic phase.

Dilepton radiation by the quasiparticles proceeds dominantly via the following elementary processes: $q+\bar{q}\rightarrow\gamma^*$, $q(\bar{q})+g\rightarrow\gamma^*+q(\bar{q})$, and $q+\bar{q}\rightarrow g+\gamma^*$. Note that in our calculations the running coupling α_S (which depends on the local energy density according to a parametrization of lQCD data) is of the order $O(1)$ and thus the contribution of the higher order diagrams is not subleading! Also, we take into account the non-perturbative spectral functions and self-energies of quarks and gluons thus going beyond the leading twist [2].

By implementing the off-shell partonic processes into the PHSD transport approach, we calculate the dilepton spectra in $Au+Au$ at $\sqrt{s}$=200 GeV and compare to the PHENIX data [5, 3, 4] in Figs. 1 and 2. In Fig. 1 we show the our results for low masses ($M=0-1.2$ GeV); in this region, the yield in PHSD is dominated by hadronic sources and essentially coincides with the HSD result. There is a discrepancy between the PHSD calculations and the data in the region of masses from 0.2 to 0.6 GeV. The discrepancy is not amended by accounting for the radiation from the QGP, since the latter is 'over-shone' by the radiation from hadrons integrated over the evolution of the collision. In contrast, the partonic radiation is visible in the mass region $M=1-4$ GeV as seen in Fig. 2. The dileptons generated by the quark-antiquark annihilation in the sQGP constitute about half of the observed yield in the mass range between the masses of the ϕ and the J/Ψ mesons. Thus, accounting for partonic radiation in PHSD fills up the gap between the hadronic model results [6, 7] and the data at $M>1$ GeV.

References

[1] W. Cassing and E. L. Bratkovskaya, *Phys. Rev.* C **78** (2008) 034919, *Nucl. Phys.* A **831** (2009) 215.

[2] O. Linnyk, J. Phys. G **38** (2011) 025105.

[3] A. Toia *et al.*, PHENIX Collaboration, *Nucl. Phys.* A **774** (2006) 743; *Eur. Phys.* J **49** (2007) 243; S. Afanasiev *et al.*, PHENIX Collaboration, arXiv:0706.3034 [nucl-ex]

[4] A. Adare *et al.*, PHENIX Collaboration, Phys. Rev. C **81** (2010) 034911.

[5] A. Adare *et al.*, PHENIX Collaboration, *Phys. Lett.* B **670** (2009) 313

[6] E. L. Bratkovskaya, W. Cassing and O. Linnyk, *Phys. Lett.* B **670** (2009) 428.

[7] J. Manninen, E. L. Bratkovskaya, W. Cassing and O. Linnyk, arXiv:1005.0500 [nucl-th].

*Work supported by the "HIC for FAIR" program and by the "Helmholz-Quark Matter" graduate school .

† linnyk@fias.uni-frankfurt.de

Thermal conductivity effects in dynamics of first-order phase transitions *

V. Skokov [1] *and D. N. Voskresensky* [1,2]
[1] GSI, Darmstadt, Germany ; [2] MEPhI, Moscow, Russia

The dynamics of first-order phase transitions in various system, e.g. in the Early Universe, in neutron stars and heavy ion collisions, has recently been a subject of growing interest. At low collision energies the nuclear gas-liquid first-order phase transition is probable whereas at high collision energies the hadron – quark gluon plasma first-order transition may occur. Within a hydrodynamical approach dynamical aspects of first-order phase transitions were recently studied in Refs. [1, 2].

It is well known, that, at least in the mean-field approximation, the isothermal spinodal (ITS) line and adiabatic spinodal (AS) line are different. From the exact thermodynamic relation one obtains

$$u_{\tilde{s}}^2 = u_T^2 + \frac{T}{nmc_V}\left[\left(\frac{\partial P}{\partial T}\right)_n\right]^2 .$$

Here T is the temperature, P is the pressure, n is the density of the conserving charge (here baryon number), m is the particle mass, $\tilde{s} \equiv s/n$ is the entropy per baryon, c_V is the specific heat density at a fixed volume, $u_{\tilde{s}}^2 = m^{-1}(\partial P/\partial n)_{\tilde{s}}$ and $u_T^2 = m^{-1}(\partial P/\partial n)_T$. The variable $u_{\tilde{s}}$ has the meaning of the adiabatic sound velocity (at $\tilde{s}$ =const) and u_T, of the isothermal sound velocity (at T =const). The former quantity characterizes propagation of sound waves in ideal hydrodynamics. In non-ideal hydrodynamics at finite values of the thermal conductivity, κ, the propagation of sound waves is defined by the interplay between u_T and $u_{\tilde{s}}$. The conditions $u_T = 0$ and $u_{\tilde{s}} = 0$ define $T(n)$-curves: the isothermal spinodal (ITS) line and adiabatic spinodal (AS) line, respectively. The maximum temperature points on these lines are the critical temperature T_{cr} (on the ITS line) and the adiabatic maximum temperature $T_{P,max}$ (on the AS line). In the mean-field approximation, c_V has finite non-negative values. Therefore, $u_T^2 \leq 0$ on the AS line ($u_{\tilde{s}} = 0$). Note, that even in the region near the critical point, where thermodynamic fluctuations are strong (fluctuation region), a mean-field treatment can be applied to describe a dynamic evolution, if the system spends in this region a shorter time than that needed for a development of the critical fluctuations.

Calculations performed in mean-field models show that T_{cr} is significantly higher than $T_{P,max}$, e.g. within the NJL model, one obtains $T_{P,max} \sim T_{cr}/2 \simeq 45$ MeV for the chiral transition. At such small temperatures, manifestations of the chiral and deconfinement transitions in heavy-ion collisions are unlikely. Note, that in *ideal* hydrodynamics instabilities arise at the AS boundary. Therefore, in the literature, there has been some controversy about whether the onset of spinodal instabilities happens at the ITS or AS lines.

To find onset of instabilities we let dynamic variables $a = (n, s, T)$ to be modulated as $\delta a = \delta a_0 \exp[\gamma t + i\mathbf{pr}]$. For simplicity, we assume that $p \ll p_T$, where p_T is the mean thermal momentum. This assumption allows to reduce the relativistic hydrodynamic equations to non-relativistic ones. From the linearized equations of non-ideal hydrodynamics we find the growth rate, $\gamma(p)$,

$$\gamma^2 = -p^2\left[u_T^2 + \frac{(\frac{4}{3}\eta + \zeta)\gamma}{mn} + cp^2 + \frac{u_{\tilde{s}}^2 - u_T^2}{1 + \frac{\kappa p^2}{(c_V\gamma)}}\right],$$

where η and ζ are the shear and bulk viscosities and the coefficient $c > 0$ is due to the surface tension between regions with different densities. The solutions are two density modes (existing even in the limit $\kappa = 0$) and one thermal mode (non-existent for $\kappa = 0$).

For the sake of simplicity, let us consider the case of zero shear and bulk viscosities and non-zero, but small thermal conductivity. For $-u_T^2 \ll 1$, i.e. slightly below the ITS line, we get for the most rapidly growing mode $\gamma = \gamma_m$, $p = p_m \ll p_T$: $\gamma_m \simeq \frac{\kappa u_T^4}{4cc_V u_{\tilde{s}}^2}$, $p_m^2 \simeq -u_T^2/(2c)$. For any small but finite value κ, the solution γ_m results in instability already for $u_T^2 < 0$ (i.e. below the ITS line). Contrary, in case $\kappa = \eta = \zeta = 0$, i.e. within ideal hydrodynamics, the instability appears, when the system trajectory crosses the AS line rather than the ITS line. Since in reality $\kappa \neq 0$ *always*, we conclude that the instability condition $u_{\tilde{s}}^2 < 0$ should be replaced in favor of $u_T^2 < 0$. For large values of κ, the density mode proves to be the most rapidly growing one, but the condition for the onset of instability, $u_T^2 = 0$, is not changed.

According to our findings, signatures of QCD spinodal instabilities may be observed in experiments with heavy ions in some collision energy interval that corresponds to the first-order phase transition region of the QCD phase diagram. One of the possible signatures is a manifestation of fluctuations with a typical size $r \sim 1/p_m$ in the rapidity spectra, see details in Ref. [2]. In Refs. [1, 2], the problem of the nucleation in metastable regions of the first-order phase transitions was also discussed with an emphasis on effects of the finite viscosity and thermal conductivity.

* Work supported in part by FIAS and DFG.

References

[1] V. V. Skokov and D. N. Voskresensky, arXiv:0811.3868 [nucl-th]; Nucl. Phys. A **828**, 401 (2009).

[2] V. V. Skokov and D. N. Voskresensky, Nucl. Phys. A **847**, 253 (2010).

Vacuum fluctuations and the thermodynamics of chiral models *

V. Skokov [1], *B. Friman* [1], *E. Nakano* [1], *K. Redlich* [2], *and B.-J. Schaefer* [3]

[1] GSI, Darmstadt, Germany ; [2] ITP, University of Wroclaw, Poland ; [3]Institut für Physik, Universität Graz, Austria

In [1], the consistency of mean-field calculations of many-body systems within chiral effective models like the Nambu-Jona-Lasinio (NJL) and the Quark-Meson (QM) models as well as their Polyakov loop extended versions PNJL/PQM is addressed. In particular, the role of the lowest order fermion vacuum contribution was discussed. In the NJL/PNJL model, this term is responsible for the dynamical breaking of the chiral symmetry in vacuum and is therefore necessarily taken into account. In the QM/PQM model, the spontaneous breaking of the chiral symmetry is due to the meson potential. Hence, for qualitative considerations, the fermion vacuum loop is frequently omitted.

We show that a mean-field approximation, where the fermion vacuum term is neglected, commonly referred to as the no-sea approximation, leads to a distortion of the critical behavior at the chiral transition. In particular, in this approximation the order of the transition in the chiral limit is *always* first order. In contrast, when this term is included, the transition is of first or second order, depending on the choice of coupling constants and on the baryon density.

The commonly omitted vacuum contribution of fermions with mass m_q to the thermodynamic potential of QM/PQM model reads

$$\Omega_{q\bar{q}}^{\rm vac} = -2N_f N_c \int \frac{d^3p}{(2\pi)^3}\sqrt{m_q^2+\vec{p}^{\,2}}\,\theta(\vec{p}^{\,2}-\Lambda^2), \quad (1)$$

where the divergence is regularized by the ultraviolet cutoff Λ. N_c (N_f) is the number of colors (flavours), which defines the fermion degeneracy factor.

In the high temperature expansion of the thermodynamic potential we show analytically how the vacuum term (1) determines the order of the chiral phase transition in the chiral limit. A correct account of the vacuum term results in a second-order phase transition at $\mu = 0$, as expected.

For non-zero pion mass, the vacuum term has an important effect on observables, e.g. on the fluctuations of the net quark number density. These are characterized by the generalized susceptibilities,

$$c_n(T) = \left.\frac{\partial^n[p\,(T,\mu)/T^4]}{\partial(\mu/T)^n}\right|_{\mu=0}. \quad (2)$$

A particular role is attributed to the so-called kurtosis of the net quark number fluctuations $R_{4,2} = c_4/c_2$. The dependence of the ratio $R_{4,2}$ on the cutoff Λ in the PQM model including the vacuum contribution (1) is shown in Fig. 1 for a physical value of m_π. For small Λ, the kurtosis develops a peak near T_C, which is maximal for $\Lambda \to 0$. Such a strong dependence on Λ is unphysical and must be removed by a suitable renormalization of the vacuum term.

The renormalized fermion vacuum contribution is given by $\Omega_{q\bar{q}}^{\rm reg} = -\frac{N_c N_f}{8\pi^2} m_q^4 \ln(m_q/M)$, where M is an arbitrary renormalization scale parameter. The properly renormalized thermodynamic potential is free of any dependence on the unphysical ultraviolet cutoff, and independent of the renormalization scale M.

The renormalized kurtosis shows an intersting dependence on the pion mass (see Fig. 2), which however is weaker than without vacuum fluctuations. Thus, an appropriate renormalization of the fermionic vacuum term is essential for a consistent formulation of the thermodynamics of the QM/PQM model.

References

[1] V. Skokov, B. Friman, E. Nakano, K. Redlich and B. J. Schaefer, Phys. Rev. D **82**, 034029 (2010) [arXiv:1005.3166].

* Work supported in part by the FIAS.

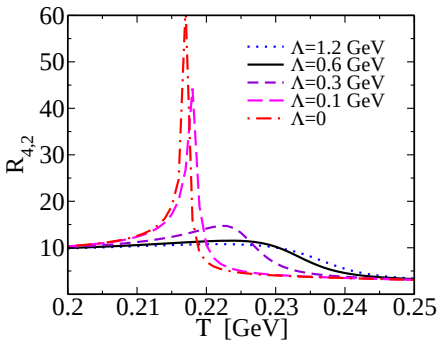

Figure 1: The kurtosis in the PQM model as a function of temperature for several values of cutoff parameters Λ.

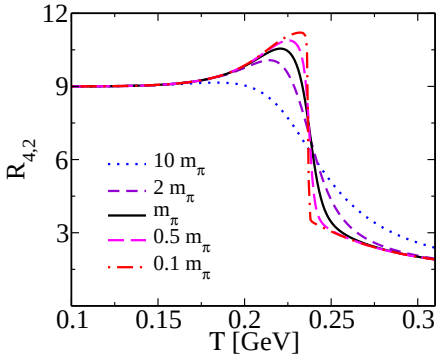

Figure 2: The kurtosis $R_{4,2}$ as a function of temperature for several values of the pion mass in the PQM model, including the renormalized fermion vacuum term.

Di-jet correlations in heavy-ion collisions within the HSD transport approach

V.P. Konchakovski[1,2], *E.L. Bratkovskaya*[3,4], *W. Cassing*[1], *and M.I. Gorenstein*[2,3]

[1]ITP, Giessen, Germany; [2]BITP, Kiev, Ukraine; [3]FIAS, Frankfurt, Germany; [4]ITP, Frankfurt, Germany

A systematic study of correlations in pseudorapidity and azimuthal angle for high-p_T charged hadrons in heavy-ion collisions at the top RHIC energy has been performed within the Hadron String Dynamics (HSD) transport approach [1]. The study shows that a significant part of the high p_T hadron attenuation seen experimentally can be attributed to inelastic interactions of 'leading' pre-hadrons with the dense hadronic environment. It turns out that the 'far-side' correlations are suppressed by up to 60% in central collisions due to the pre-hadronic interactions in line with earlier studies. Since a much larger suppression is observed experimentally in central reactions there should be strong additional partonic interactions in the dense QGP medium created in Au+Au collisions at RHIC [2, 3]. Furthermore, our calculations do not show a 'ridge' in $\Delta\eta$ on the near-side which also indicates additional non-hadronic correlations.

The di-jet correlations are measured as a function of azimuthal angle $\Delta\phi$ and pseudorapidity $\Delta\eta$ between the trigger and associated particles:

$$C(\Delta\eta, \Delta\phi) = \frac{1}{N_{trig}} \frac{d^2 N_{assoc}}{d\Delta\eta \, d\Delta\phi} \,, \qquad (1)$$

where N_{trig} is the number of trigger particles. To obtain the di-jet correlations one has to subtract a background distribution. In our calculations we use the mixed events method which allows to properly subtract the background by taking associated particles for each trigger particle from another randomly chosen event.

In Fig. 1 we present the HSD results for p+p and Au+Au collisions for the associated differential particle $(\Delta\eta,\ \Delta\phi)$ distribution (1). We use the same cuts as the STAR Collaboration, $4 < p_T^{trig} < 6$ GeV/c and $2 < p_T^{assoc} < 4$ GeV/c [2]. In the HSD transport calculations we obtain on average 0.5 trigger particle in an event for this set of cuts. The away side structure is suppressed in Au+Au collisions in comparison to p+p, however, HSD doesn't provide enough high p_T suppression to reproduce the Au+Au data. The additional suppression should be attributed to a QGP produced at relativistic heavy-ion collisions. The di-jet correlations obtained in the HSD transport simulations of Au+Au collisions (Fig. 1, *bottom*), furthermore, do not show a ridge structure in the pseudorapidity for the near-side jet as in the data [2, 3].

We conclude that the HSD hadron-string medium does not show enough suppression for the away-side jet-associated particles. For the first time the medium response on the interactions has been taken into account in the present non-perturbative HSD calculations. The non-perturbative calculations, however, do not reproduce the long-range rapidity correlations for the near-side jet while supporting the results from perturbative investigations. It is interesting to check in future whether the recently proposed Parton Hadron String Dynamics model (PHSD) [4] – incorporating explicit partonic degrees of freedom and dynamical hadronization – will be able to reproduce the observed structures.

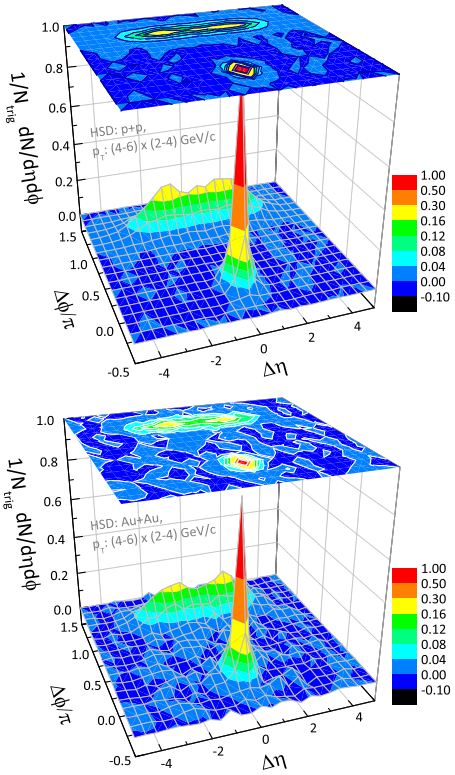

Figure 1: The associated particle $(\Delta\eta,\ \Delta\phi)$ distribution (1) for p+p (*top*) and central Au+Au (*bottom*) collisions at $\sqrt{s} = 200$ GeV within the HSD transport approach.

References

[1] V. P. Konchakovski, E. L. Bratkovskaya, W. Cassing and M. I. Gorenstein, Phys. Rev. C **82**, 037902 (2010).

[2] B. I. Abelev *et al.* [STAR collaboration], Phys. Rev. C **80**, 064912 (2009); M. van Leeuwen [STAR collaboration], Eur. Phys. J. C **61**, 569 (2009).

[3] B. Alver *et al.* [PHOBOS Collaboration], Phys. Rev. Lett. **104**, 062301 (2010).

[4] W. Cassing and E. L. Bratkovskaya, Phys. Rev. C **78**, 034919 (2008); Nucl. Phys. A **831**, 215 (2009).

Sine-Gordon model in functional renormalization

V. Pangon[1,2]
[1]GSI, Darmstadt, Germany; [2]FIAS, Frankfurt, Germany

Motivation

$SU(N)$ Yang-Mills theories, which are expected to describe the strong interaction in the case $N = 3$, are one of the most studied models in theoretical physics. While their asymptotic UV behavior is well under control thanks to asymptotic freedom, the need of non-perturbative techniques to describe the IR behavior has rapidly appeared to be mandatory. The reasons of this non-perturbativity of the IR are actually two-fold:

- The gauge coupling, due to its negative β-function, is growing when the renormalization scale is lowered so that at some point, we expect the perturbative small coupling expansion to breakdown.
- The Haar measure, ensuring the gauge invariance in the path-integral formulation, makes at the non-perturbative level Yang-Mills theories to be compact in the field variables. This compactness gives rise in particular to the possibility of tunnelling between equivalent tree-level vacua.

The first source of non-perturbativity is rather obvious from the UV flow study, while the second one is more subtle. The latter implies that already performing a perturbative computation -a saddle point approximation around the tree-level vacuum- decompactifies the original theory we want to solve into a polynomial one. As the fluctuations are integrated out, we feel more and more the large field effects which are not properly given by the perturbative expansion.

Functional renormalization

Functional renormalization is one of the most-powerful non-perturbative techniques currently available. Since we are solving directly functionals, one has access to global information, not only small deviations around the tree-level vacuum from a weak-coupling expansion. In particular, one can preserve non-perturbatively the compactness quite easily. The only approximation made is non-perturbative in essence and comes from the truncation of the functional space we make to solve the flow equation.

Simplest case : sine-Gordon model

The sine-Gordon model in $d = 2$ is the simplest compact field theory and amounts in euclidean spacetime in :

$$S[\phi] = \int d^2x \Big[\frac{1}{2}(\partial_\mu \phi)^2 + u\, cos(\beta\phi)\Big]$$

When u is small enough, the one-loop considerations already tells us at Local Potential Approximation that this model exhibits two phases separated by the Coleman fixed point $\beta_c^2 = 8\pi$. For $\beta > \beta_c$, the Fourier component of the potential shrinks as the cut-off is lowered, signaling us that the effective potential, being non-interacting, accepts only a trivial minimum. On the other hand, for $\beta < \beta_c$, the effective potential will exhibit a serie of vacua i.e. the periodicity symmetry is spontaneously broken. This is demonstrated by studying the β-function for the coupling u, which in this case exhibits asymptotic freedom. As a result, we expect the broken phase of the sine-Gordon model to give us some insights into the IR behavior of Yang-Mills theories.

Broken phase of the sine-Gordon model

In [1], we demonstrated at the Local Potential Approximation within Wegner-Houghton RG that the broken phase was non-perturbative and reaching a set of attractive IR fixed points. This set of fixed points can not be reached by a Fourier expansion of the potential, which corresponds to an expansion on UV eigendirections of an RG transformation, telling us that we found a change of classification of relevance between the IR and the UV, which is also expected in Yang-Mills theories.

The Wegner-Houghton RG scheme suffers a severe limitation due to the sharp cut-off procedure : no order beyond LPA makes sense in this approach within gradient expansion of the blocked action. As a result, it is impossible to study properly the Kosterlitz-Thouless cross over that is driven by the anomalous dimension. We thus investigate in [2] the use of the Effective Average Action RG -the most widely spread scheme- where the wave function renormalization can be cleanly defined. The price to pay is the addition of a regulator that explicitly breaks the periodicity symmetry. After demonstrating that this breaking is actually soft, we then show that all regulators reproduce the Coleman frequency.

The IR study of the flow tells us that also within this scheme, for various regulators, the broken phase exhibits a continuum of IR attractive fixed points. In addition, universality of the IR β-functions against the bare value of u has been established, even for strongly coupled bare theories. Finally, we demonstrate that the effective potential is actually exactly independent of u, even in the non-perturbative sector, emphasizing a new kind of universality.

References

[1] V. Pangon, S. Nagy, J. Polonyi & K. Sailer, *Phys. Lett.* **B694** 89 (2010)
[2] V. Pangon, submitted *Phys. Rev. D*, *hep-th/1008.0281*

The phase boundary for the QCD transition at small chemical potentials*

F. Karsch[1,2,3], *O. Kaczmarek*[1], *C. Miao*[2], *S. Mukherjee*[2], *P. Petreczky*[2], *C. Schmidt*[†3,4], *W. Söldner*[3,4], *and W. Unger*[1]

[1]Universität Bielefeld, D-33615 Bielefeld, Germany; [2]BNL, Upton, NY 11973, USA; [3]GSI, D-64291 Darmstadt, Germany; [4]FIAS, D-60438 Frankfurt, Germany

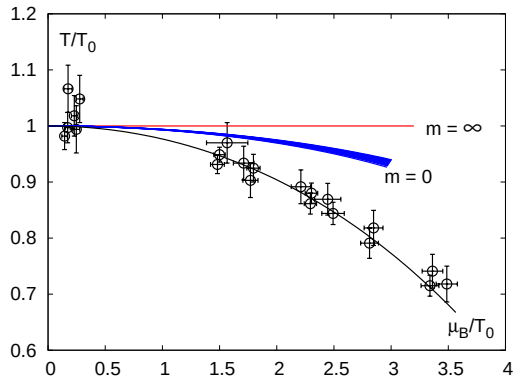

Figure 1: Curvature of the critical line in the crial limit ($m = 0$) and heavy quark limit ($m = \infty$), compared to freeze-out data and parametrization from [2].

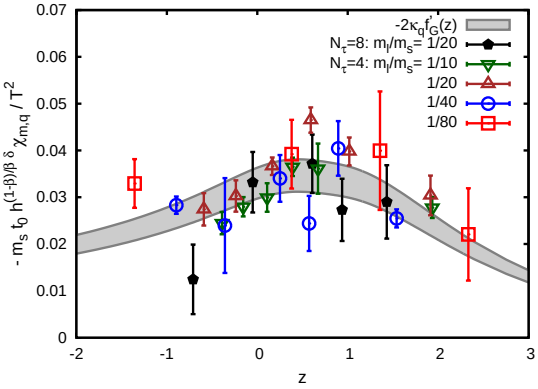

Figure 2: The scaled mixed susceptibility as function of the scaling variable $z = t/h^{1/\beta\delta}$. The data are compared to the O(2) scaling curve. The band shows a 10this curve which arises from statistical errors on the calculated observables as well as from the errors on the scaling parameters t_0,z_0.

In a recent work [1] we have shown that the curvature of the phase transition line in the chiral limit can be obtained from an analysis of the universal scaling properties of a certain mixed susceptibility ($\chi_{m,q}$) which is defined by the leading order Taylor expansion coefficient of the chiral condensate with respect to the light quark chemical potential. Numerical calculations have been performed for (2+1)-flavor QCD keeping the heavier strange quark mass close to its physical value and decreasing the two degenerate light quark masses towards the massless limit. We will make use of a recent scaling analysis [1, 2] of the chiral order parameter performed with an improved staggered fermion action. This study showed that the chiral order parameter is well described by a universal scaling function characteristic for a three dimensional, $O(N)$ universality class. As a result for the critical line in the chiral limit we find

$$T(\mu_B)/T(0) = 1 - 0.0066(7)(\mu_B/T)^2 + \mathcal{O}((\mu_B/T)^4) \; .$$

This curvature is about a factor two larger than the reweighting results obtained in (2+1)-flavor QCD [3]. It is however consistent with results obtained in calculations with imaginary chemical potentials. In fact it lies in between the 2-flavor [4] and 3-flavor [5] simulations performed with the standard staggered fermion formulation and also is consistent with results reported from (2+1)-flavor simulations with imaginary chemical potential performed with the action used also in this study (p4-action)[6]. The result is most relevant for comparison with the experimentally determined freeze-out curve as shown in Fig. 1. The parameterization found in [7] has a curvature that is about a factor 3-4 larger which suggests that (for sufficiently large values of the chemical potential) the freeze-out line does not follow the critical line. The mixed suscebtibility $\chi_{m,q}$ from which we have determined the curvature is shown in Fig. 2, together with the corresponding O(2) scaling function.

*This work has been supported in parts by contracts DE-AC02-98CH10886 with the U.S. Department of Energy, the BMBF under grant 06BI401, the Gesellschaft für Schwerionenforschung under grant BILAER, the Extreme Matter Institute under grant HA216/EMMI and the Deutsche Forschungsgemeinschaft under grant GRK 881. CS has been partially supported through the Helmholtz International Center for FAIR which is part of the Hessian LOEWE initiative.

† chr.schmidt@gsi.de

References

[1] O.Kaczmarek *et al.*, arXiv:1011.3130 [hep-lat].

[2] S. Ejiri *et al.*, Phys. Rev. D **80**, 094505 (2009).

[3] Z. Fodor and S. D. Katz, JHEP **0203**, 014 (2002); Z. Fodor and S.D. Katz, JHEP **0404**, 050 (2004).

[4] P. de Forcrand, O. Philipsen, Nucl. Phys. B **642**, 290 (2002).

[5] P. de Forcrand and O. Philipsen, JHEP **0701**, 077 (2007).

[6] R. Falcone, PoS Lattice 2010, 183 (2010).

[7] J. Cleymans, H. Oeschler, K. Redlich and S. Wheaton, Phys. Rev. C **73**, 034905 (2006).

Net-baryon number fluctuations in (2+1)-flavor QCD*

C. Schmidt† [1,2]

[1]GSI, D-64291 Darmstadt, Germany; [2]FIAS, D-60438 Frankfurt, Germany

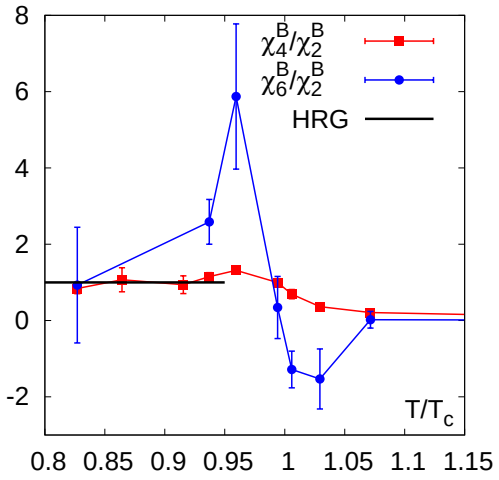

Figure 1: Shown are $4^{\rm th}$ and $6^{\rm th}$ order net-baryon number fluctuations, normalized by the quadratic fluctuations at $\mu_B = 0$, as a function of temperature.

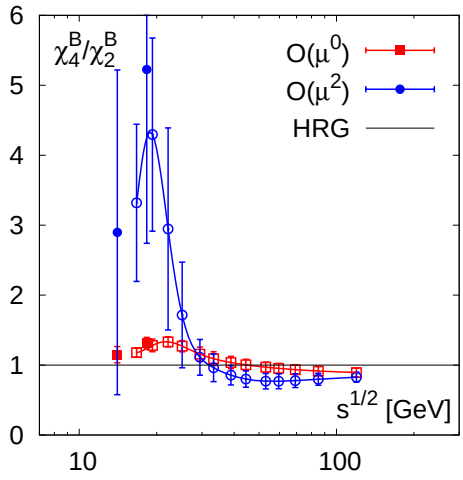

Figure 2: Shown is the ratio of $4^{\rm th}$ to the $2^{\rm nd}$ moment of the net-baryon number fluctuations along the freeze-out curve, as a function of the center of mass energy $\sqrt{s}$.

Fluctuations of conserved charges, as baryon number and strangeness are generally considered to be sensitive indicators for the structure of the thermal medium that is produced in heavy ion collisions. In fact, if at non-vanishing baryon number a critical point exists in the QCD phase diagram, this will be signaled by divergent fluctuations of all quantities that can be connected to the fluctuations of the chiral order parameter as, e.g., the baryon number density.

We present here results from lattice calculations of net-baryon number fluctuations in QCD with dynamical light and strange quark degrees of freedom. The results are based on calculations with an improved staggered fermion action (p4-action) that strongly reduces lattice cutoff effects at high temperature and are performed as joined work of the RBC-Bielefeld Collaboration.[1] The values of the quark masses used in this calculation are almost physical; the strange quark mass, m_s, is fixed to its physical value while the light up and down quark masses are taken to be degenerate and equal to $m_s/10$. This corresponds to a pion mass of $m_\pi \approx 220$ MeV.

We calculate Derivatives of the partition function with respect to the baryon chemical potential μ_B which are also know as moments of net-baryon number fluctuations. The second derivative defines the quadratic fluctuation χ_2^B, while higher derivatives give higher moments $(\chi_4^B, \chi_6^B, \ldots)$. In Fig. 1 we show χ_4^B and χ_B^6, normalized by the quadratic fluctuations χ_2^B. For temperatures $T \lesssim 0.9 T_c$ the fluctuations seem to agree with the predicted HRG result which is unity for both quantities. For temperatures $T \gtrsim 0.9 T_c$ the fluctuations start to deviate from the HRG model. As expected χ_6^B increase more rapidly close to T_c, since this quantity diverges in the chiral limit, where as χ_4^B will develop a kink. In Fig. 2 we plot the ratio χ_B^4/χ_B^2 as function of the center of mass energy $\sqrt{s}$ along the chemical freeze-out curve by using a suitable parameterization.[2] These results can be directly compared to the net-proton number fluctuation that are measured in heavy ion experiments [3]. Note that the ratios have been expanded to obtain their leading order μ_B-dependence. We expect that for center of mass energies of $\sqrt{s} \lesssim 20$ GeV, *i.e.* $\mu_B/T \gtrsim 1.5$, higher orders become significant. It is thus important for the understanding of future heavy ion experiments to obtain χ_8^B to good accuracy from first principal lattice calculations.

References

[1] RBC-Bielefeld Collaboration in preparation.

[2] J. Cleymans, H. Oeschler, K. Redlich and S. Wheaton, Phys. Rev. **C**73 (2006) 034905.

[3] M. M. Aggarwal *et al.* (STAR Collaboration), Phys. Rev. Lett. **105** (2010) 22302.

* Results presented here are based on joint work of the RBC-Bielefeld collaboration. Numerical calculations have been performed on the QCDOC installations at Brookhaven National Laboratory. This work is partly supported by contract DE-AC02-98CH10886 with the U.S. Department of Energy and by the Hessian initiative LOEWE through the Helmholtz International Center for FAIR.

† chr.schmidt@gsi.de

Dilepton production in p+p collisions at $\sqrt{s}$ = 200 GeV*

J. Manninen†[1], *E. L. Bratkovskaya*[2], *W. Cassing*[1], *and O. Linnyk*[2]

[1]Institut für Theoretische Physik, Universität Giessen, 35392 Giessen, Germany; [2]Institut für Theoretische Physik, Universität Frankfurt, 60054 Frankfurt, Germany

We study production of electron-positron pairs within an extended statistical hadronization model [1] and compare the results with the invariant mass spectrum [2] of the e^+e^- -pairs in proton-proton collisions at $\sqrt{s}$=200 GeV measured by the PHENIX collaboration.

In $p+p$ collisions in the low mass region[1] (LMR), majority of correlated electron-positron pairs arise in the direct and Dalitz decays of low mass mesons. We have evaluated the yields of all mesons within the statistical hadronization model in order to estimate the amount of di-electrons coming from their decays. It is find out that once the emission from all relevant sources are considered and the geometrical and kinematical acceptance of the experiment is taken into account, one can describe the measured invariant mass spectrum very well within the simple model in the LMR.

In the intermediate mass region[2] (IMR), the di-electron radiation is dominated by the decays of open charm mesons. We have estimated the di-electron emission from the open charm hadrons within a simple PQCD inspired model (described in [1]) and further studied the angular correlations among the emitted D-meson within the HSD transport approach [3, 4]. Our results both in LMR and IMR are shown in the Figure 1b. We have studied the effect of the angular correlations among the D -mesons in two limiting cases: the emitted D -mesons are always emitted in 180 degree angle (solid line) as well as the case in which the D -mesons are totally un-correlated with each other (dashed line). It turns out that the correlated picture is strongly favored over the un-correlated one in the proton-proton collisions.

In summary, we have studied the di-electron production in $p+p$ collisions at $\sqrt{s}$ = 200 GeV and found out that the measured invariant mass spectrum can be understood well up to the J/ψ mass within the simple models we have studied in this work.

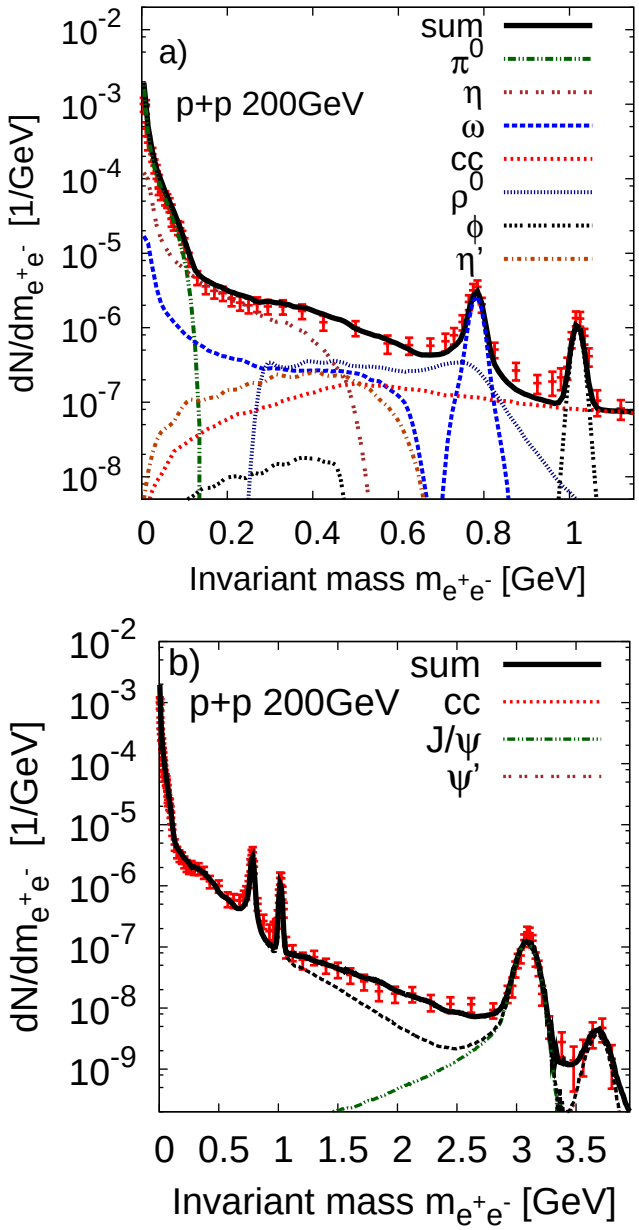

Figure 1: Invariant mass spectrum of pairs of electrons and positrons in proton-proton collisions at $\sqrt{s}$ = 200 GeV. The data are from the PHENIX collaboration [2] while the contribution from different dilepton emitting sources are calculated as explained in the text. The full thick line denotes the sum from all relevant sources. The LMR is shown in the upper panel while the whole invariant mass range is shown in the bottom panel.

References

[1] J. Manninen, E. L. Bratkovskaya, W. Cassing and O. Linnyk, arXiv:1005.0500 [nucl-th].

[2] A. Adare *et al.* [PHENIX Collaboration], Phys. Lett. B **670** (2009) 313.

[3] W. Ehehalt and W. Cassing, Nucl. Phys. A **602** (1996) 449.

[4] W. Cassing and E. L. Bratkovskaya, Phys. Rept. **308** (1999) 65.

*This work was supported by DFG and LOEWE programs

†Mannisenjaakko@gmail.com

[1] $m_{e^+e^-} < 1$ GeV

[2] $1 < m_{e^+e^-} < 3$ GeV

Fragmentation and strangeness at PANDA*

T. Gaitanos[1], *A.B. Larionov*[1,2], *H. Lenske*[1], *and U. Mosel*[1]

[1]Inst. für Theor. Physik, Universität Giessen, Germany; [2]Russian Research Center Kurchatov Institute, Moscow, Russia

Hypernuclear physics offers the unique possibility to study the behaviour of the hyperon-nucleon (YN) and the hyperon-hyperon (YY) interaction inside excited hadronic matter [1] at terrestrial laboratories, such as the FAIR facility at GSI, Darmstadt. Such investigations are important for a better understanding of the strangeness sector of the equation of state, a topic of current research, and also relevant for nuclear astrophysics, e.g., the properties of neutron stars [2]. So far the empirical situation has been rather scarce. However, with the high-intensity heavy-ion beams at GSI the hypernuclear ($S = -1$) production rate is considerably enhanced (HypHI project, [3]), while high luminosity antiproton beams at the future FAIR facility are expected to abundantly produce double-strangeness ($S = -2$) hypernuclei (part of the PANDA project, [4]).

The theoretical study of reactions involved in the HypHI project has been already investigated [5] by using fully covariant kinetic theory in the spirit of the Giessen-BUU approach [6] for the non-equilibrium reaction dynamics. Fragment formation occurs at the final stage of such reactions and it is modelled by a statistical decay of excited (residual) nuclei (Statistical Multifragmentation Model, SMM, provided by A. Botvina [7]), while the formation of hypernuclei is simulated by a coalescence method. Recently, we have extended the theoretical framework by including all necessary channels of double-strangeness hyperon production, in particular, those involving the direct production of the cascade particle Ξ ($S = -2$) from $p\bar{p}$ collisions, and those involving secondary processes with associated production/absorption of double-strangeness Ξ-hyperons.

We have applied the GiBUU+SMM model in collisions induced by antiprotons at relativistic energies just above the Ξ-production threshold ($E_{lab} = 3 - 10$ GeV). Fig. 1 shows an example of our theoretical studies in terms of rapidity spectra of different light fragments and hyperons. Light fragments are produced near the mid-rapidity region with the help of the statistical model [7], and they fit well experimental fragmentation data in such reactions (not shown here). On the other hand, the rapidity spectrum of Λ-hyperons is very broad due to secondary effects, thus the production of single-strangeness (and even double-strangeness) hypernuclei may be expected. On the other hand, cascade particles mostly leave the residual excited source, and the overlap rapidity region between them and the fragments is almost negligible. The situation may be different at lower beam energies ($E_{lab} \sim 3$ GeV) by producing slower cascade hyperons, as experimentally desired, however, the statistics of the present theoretical and still running GiBUU calculations is still too low.

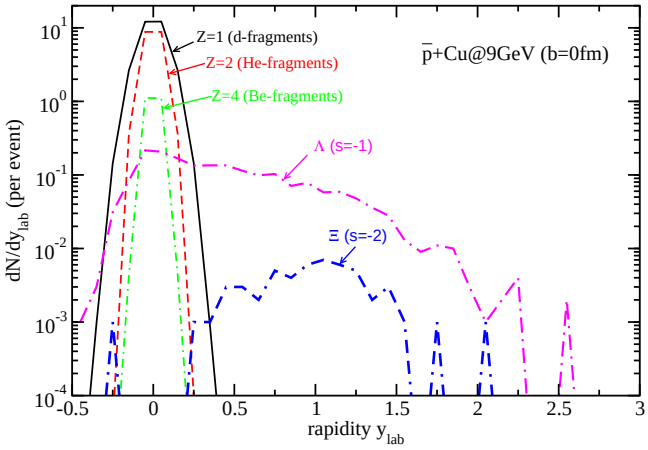

Figure 1: Rapidity distributions of different particles (fragments and hyperons, as indicated) for $\bar{p} + Cu@9$ GeV collisions at b=0fm centrality.

We have studied the production of fragments and particles with strangeness degree of freedom in antiproton-induced reactions related to the future PANDA program at GSI in the framework of a hybrid BUU+SMM approach, which accounts properly for the pre-equilibrium dynamics and the statistical decay of excited residual nuclei. We predict an overlap in velocity between light fragments and hyperons, which is very pronounced for Λ particles, but moderate for double-strangeness Ξ hyperons. Predictions of single and maybe double strangeness hypernuclei directly on the primary target are under study and might be helpful for the upcoming PANDA experiment, in which one intents to measure the properties of double-strangeness hypernuclei.

References

[1] A.D. Wroblewski, Acta Physica Polonica, B35 (2004) 901.

[2] J. Schaffner, I. Mishustin, Phys. Rev. C53 (1996) 1416.

[3] C. Rappold et al. (HypHI collaboration), Nucl. Phys. A622 (2010) 231.

[4] J. Pochodzalla, Nucl. Phys. A754, 430c (2005).

[5] T. Gaitanos, H. Lenske, U. Mosel, Phys. Lett. B675 (2009) 297.

[6] $http://gibuu.physik.uni-giessen.de/GiBUU/wiki$.

[7] J.P. Bondorf et al., Phys. Rep. 257 (1995) 133.

* Work supported by BMBF

In-Medium Properties of Vector Mesons in a Transport Approach*

J. Weil†[1] *and U. Mosel*[1]

[1]Institut für Theoretische Physik, JLU Giessen, Germany

While the vacuum properties of most hadrons are known to reasonable accuracy today, it is a much-debated question how these properties change in nuclear matter. In particular for the light vector mesons there have been various theoretical predictions regarding their in-medium properties.

One of the expected in-medium effects is the so-called 'collisional broadening' of the meson spectral function, due to inelastic collisions with the hadronic medium. A second class of predictions claim that the vector meson masses will be shifted in the medium. These changes of the peak mass are connected to the partial restoration of chiral symmetry in the medium and have been studied via QCD sum rules. This effect has been claimed to be seen in experiments, but is still being discussed controversially. For a recent review on in-medium effects see [1].

For studying in-medium effects, the more prominent hadronic decay modes of the vector mesons suffer from the drawback that they are affected by strong final-state interaction with the hadronic medium – in contrast to the rare dilepton decay modes, which only feel the electromagnetic force. Therefore the latter are ideally suited to carry the in-medium information outside to the detector, undisturbed by the hadronic medium.

Experimentally, dilepton spectra from elementary nuclear reactions are being studied e.g. with the CLAS detector at JLAB, where photons with energies of a few GeV are shot on nuclei [2], or by the E325 experiment at KEK, where 12 GeV protons are used as projectile [3]. Also the HADES detector at GSI has an ambitious program for measuring dilepton spectra from pp, pA and AA reactions [4]. On the side of the hadronic decays, most notably $\omega \to \pi^0\gamma$ is being investigated by the CB/TAPS group in photon-induced reactions at ELSA accelerator [5].

For the numerical simulation of these processes we use the GiBUU transport model, which provides a unified framework for various types of elementary reactions on nuclei as well as heavy-ion collisions [6, 7, 8]. This model takes care of the correct transport-theoretical description of the hadronic degrees of freedom in nuclear reactions and all the subtleties this may involve, including the propagation, collisions and decays of particles in a nuclear environment. For the investigation of in-medium properties of vector mesons, the most crucial parts of the transport model are: 1) The production mechanisms of vector mesons on nuclei, e.g. $\gamma N \to VX$ or $NN \to VX$. 2) The description of the VN interaction, which is responsible for absorption and collisional broadening. 3) A proper off-shell treatment in the propagation of vector mesons and the handling of density-dependent spectral functions. 4) A correct description of the background processes (Dalitz decays, Bremsstrahlung, etc).

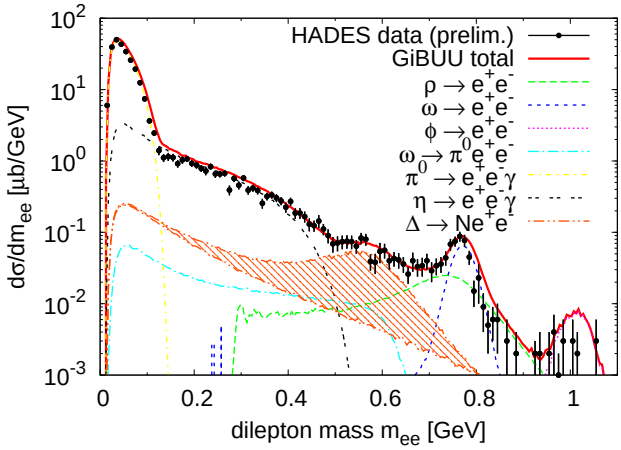

Figure 1: Dilepton spectrum for p+p@3.5GeV: GiBUU transport simulation compared to preliminary data [9].

Fig. 1 shows a comparison plot of a GiBUU simulation to preliminary HADES data for p+p collisions at 3.5 GeV. The simulation results have been corrected for the HADES acceptance and reasonably reproduce the shape of the data over most of the spectrum. In the intermediate mass region it seems like the inclusion of a proper transition form factor for the Delta Dalitz decay (dashed area) might be crucial in describing the data [10]. Without such a form factor, the simulation will underestimate the data in this region. We also achieve a reasonable agreement with the data in transverse momentum and rapidity spectra. With this level of agreement in the elementary p+p collisions, we have a good base line for studying in-medium effects in reactions like p+Nb and Ar+KCl.

References

[1] S. Leupold, V. Metag, U. Mosel, Int. J. Mod. Phys. E 19 (2010) 147-224.

[2] M.H. Wood et al., Phys. Rev. C 78 (2008) 015201.

[3] M. Naruki et al., Phys. Rev. Lett. 96 (2006) 092301.

[4] I. Fröhlich et al., Int. J. Mod. Phys. A 24 (2009) 317-326.

[5] M. Nanova, J. Weil et al., arXiv:1008:4520.

[6] http://gibuu.physik.uni-giessen.de

[7] M. Effenberger et al., Phys. Rev. C 60 (1999) 044614.

[8] P. Mühlich, U. Mosel, Nucl. Phys. A 773 (2006) 156-172.

[9] A. Rustamov et al., AIP Conf. Proc. 1257 (2010) 736.

[10] Q. Wan, F. Iachello, Int. J. Mod. Phys. A 20 (2005) 1846.

* Work supported by HGS-HIRe.

† janus.weil@theo.physik.uni-giessen.de

Ξ hyperon production in antiproton-nucleus collisions*

A.B. Larionov[†1,2], *T. Gaitanos*[1], *H. Lenske*[1], *and U. Mosel*[1]

[1]Institut für Theoretische Physik, Universität Giessen, D-35392 Giessen, Germany; [2]RRC "I.V. Kurchatov Institute", 123182 Moscow, Russia

Strangeness production in $\bar{p}$-induced reactions on nuclei has been a challenge to the theoretical and experimental studies since about 20 years, when Rafelski [1] suggested that an enhanced Λ hyperon production in $\bar{p}$+Ta collisions at 4 GeV/c is the signature of the formation of the super cooled quark-gluon plasma. Later on, however, Cugnon et al [2] performed the intranuclear cascade model analysis of the extended data set on Λ and K_S production in $\bar{p}$-nucleus collisions, which seems to disfavour the unusual production mechanisms. The production of the $S = -2$ hyperons, not measured so far in $\bar{p}$-nucleus collisions, might be, moreover, sensitive to the exotic mechanisms, since it requires simultaneous creation of the two $s\bar{s}$ quark pairs.

To understand the mechanisms of the Ξ hyperon production in $\bar{p}$-nucleus interactions within a conventional binary-collision and resonance decays picture, we have performed the GiBUU model [3] calculations. The Ξ hyperon production is included in the model via the following most important reaction channels: $\bar{K}N \to \Xi K$, $\bar{K}N \to \Xi K\pi$ and $\bar{N}N \to \bar{\Xi}\Xi$. For the first two channels, the cross sections at $\sqrt{s} < 2.2$ GeV have been obtained by parameterizing available experimental data. At higher invariant energies, the meson-baryon collisions are simulated via the PYTHIA package. For the latter channel, the constant cross section of 4 μb is assumed according to Ref. [4] above the threshold $\sqrt{s_{\rm thr}} = 2.63$ GeV ($p_{\rm lab,thr} = 2.58$ GeV/c). We have also included the processes $\bar{\Delta}N \to \bar{\Xi}\Xi$ and $\Delta\bar{N} \to \bar{\Xi}\Xi$; the corresponding cross sections were obtained from the cross section of the $\bar{N}N \to \bar{\Xi}\Xi$ channel by simple isospin relations. Also other channels of the Ξ production in antibaryon-baryon collisions at $\sqrt{s} > 2.4$ GeV, e.g. $\bar{N}N \to \bar{\Xi}\Xi^*$ ($\sqrt{s_{\rm thr}} = 2.85$ GeV, $p_{\rm lab,thr} = 3.24$ GeV/c), are included via the FRITIOF package. The produced Ξ hyperon is allowed to rescatter on nucleons or to be absorbed into a YY pair. The simulation has been performed in the relativistic mean field mode with the Ξ-meson coupling constants taken as 1/3 of the nucleon-meson coupling constants, as follows from a schematic light quark counting picture.

Fig. 1 shows the inclusive momentum distribution of the Ξ hyperons produced in $\bar{p}^{197}$Au collisions at 3 GeV/c with partial contributions from various production channels. The two largest contributions are provided by (anti)kaon-baryon collisions, $\sim 32\%$, dominated by the $\bar{K}N \to \Xi K$ channel, and by the decays $\Xi^* \to \Xi\pi$, $\sim 28\%$. The latter are largely populating the soft part of the Ξ-momentum spectrum. It is surprising, that we also observe a rather large, $\sim 16\%$, effect from the (anti)kaon-hyperon collisions, generated entirely by PYTHIA. However, the direct channel, $\bar{N}N \to \bar{\Xi}\Xi$ contributes less than 5%. This channel seems to produce the spectrum strongly dropping towards low momenta, in qualitative agreement with the results of Ref. [4]. In view of still low numerical statistics ($\sim 10^6$ $\bar{p}$-nucleus collision events), we are presently not able to reliably calculate the $\bar{\Xi}^+$-triggered momentum spectrum of Ξ^-'s, which is of interest for the double Λ production experiment by PANDA at FAIR [4, 5]. We will attempt this in the ongoing extended study of strangeness production within the GiBUU model.

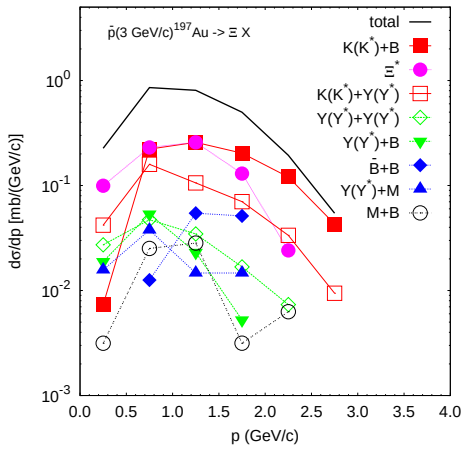

Figure 1: Momentum spectrum of the produced Ξ hyperons (i.e. Ξ^-'s and Ξ^0's) from $\bar{p}^{197}$Au collisions at 3 GeV/c. Thick solid line — total inclusive spectrum. Other lines show partial contributions sorted according to the parent particles of a Ξ. "B" denotes any nonstrange baryon, i.e. nucleon, Δ or higher baryonic resonance. "M" denotes any nonstrange meson, i.e. $\pi, \eta, \rho, \sigma, \omega, \eta'$. Since both K^0 and $\bar{K}^0$ are treated as K_L in PYTHIA, the total contribution of the $K(K^*)$ and $\bar{K}(\bar{K}^*)$ is denoted as "K" ("K^*").

References

[1] J. Rafelski, Phys. Lett. B **207**, 371 (1988).

[2] J. Cugnon, P. Deneye, and J. Vandermeulen, Phys. Rev. C **41**, 1701 (1990).

[3] http://gibuu.physik.uni-giessen.de/GiBUU.

[4] F. Ferro, M. Agnello, F. Iazzi, K. Szymańska, Nucl. Phys. A **789**, 209 (2007).

[5] J. Pochodzalla, Nucl. Phys. A **754**, 430 (2005).

* Work supported by BMBF.

† Alexei.Larionov@theo.physik.uni-giessen.de

Observed radiation damage of the rectangular LAAPDs of the PANDA-EMC*

A. Wilms[1] *and J. Albert*[2]
[1]GSI, Darmstadt, Germany; [2]IKF, University Frankfurt, Germany

Introduction

For the readout of the PANDA electromagnetic calorimeter (EMC) rectangular large area Avalanche Photodiodes (APDs) with an active area of $(7 \times 14)\,mm^2$ are under investigation. First irradiations of APD samples with two different kinds of resin have been done at KVI Groningen, Netherlands, using a $90\,MeV$ proton beam. The irradiation cycle was stopped after reaching an integrated fluence of $10^{13}\,p/cm^2$ corresponding to 10 years of PANDA operation. In this report the results of the leakage current measurements during device irradiation will be presented and discussed.

Leakage current measurement

The first samples of rectangular APDs with two different kinds of resin were irradiated end of 2009 with $90\,MeV$ protons at KVI Groningen, Netherlands. The leakage current of the devices were monitored during the complete irradiation cycle which includes two different beam current values. One example of this monitoring is shown in fig. 1 where the large step in the current originating from the increase of the beam current by a factor of ten can be clearly seen. During those two beam current phases the beam current value has to be stabilized to ensure the visibility of eventually occuring changes of the APD leakage current which is detected as a non-linearity of the leakage current increase during irradiation (e.g. a spontenous change in slope of the measured APD current or in the worst case: complete APD breakdown). As shown in fig. 1 this APD shows two different leakage current curves corresponding to the two different beam current values without showing untypical behaviour in contrast to the measured APD current shown in fig. 2, where a clearly visible breakdown of the APD took place after increasing the beam current by a factor of ten.

Irradiation results, Discussion & Outlook

As a results of the APD sample irradiation in each resin case half of the devices died during this beam time, which indicates an independence of the observed radiation damage from the used resin type. To get an idea concerning the origin of the observed device performance under irradiation the damaged devices were sent back to the manufacturer and for each a hot electron emission measurement was done and a typical picture taken there is shown on the left side of fig. 3.

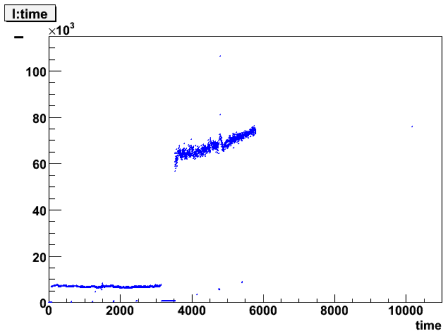

Figure 1: Leakage current measurement during irradiation without visible damage.

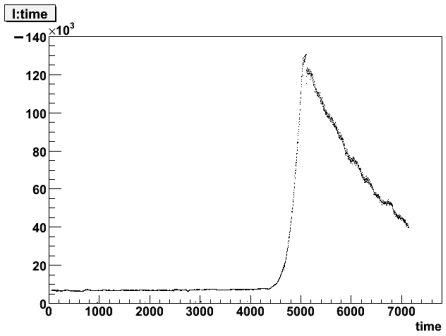

Figure 2: Leakage current measurement during irradiation with visible untypical behaviour.

The 'hot' region around one edge of the active area of the APD, in which the bonding wire is located, can be clearly seen.

New samples without bonding wire will be irradiated soon to get a closer look on the influence of the soldering or the material of the wire on the APD performance regarding their radiation hardness properties.

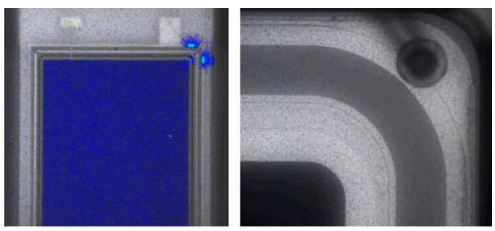

Figure 3: Hot electron emission measured after proton irradiation (left), microscopic view of the 'hot' region (right).

* Work supported by FP7, HadronPhysics II, contract No. 227431.

Developments and Preparations for the PANDA-EMC

R. W. Novotny, D. Bremer, W. Döring, V. Dormenev, P. Drexler, T. Eissner, T. Kuske, M. Moritz, R. Schubert, and for the PANDA collaboration
2nd Physics Institute, Justus-Liebig-Universität, Giessen, Germany

Several major steps have been performed to prepare the final design of the electromagnetic calorimeter (EMC) of the target spectrometer of PANDA [1]. The main activities have focused on the quality control of the delivered PWO crystals, detailed studies on the recovery of radiation damage and the analysis of measurements of the response to high-energy photons using prototype detectors.

The quality control as well as the detailed analysis of all 7355 PWO-II crystals, delivered by the manufacturer BTCP in Russia, was completed. Only 458 crystals had to be rejected corresponding to a fraction of 6.2% and confirms the excellent performance. The very selective limit on radiation hardness was the primary reason for rejection (85%).

The final operation of the calorimeter at the low temperature of T=-25°C requires extremely high radiation resistivity of the crystals since thermo-activated recovery processes are drastically slowed down. Therefore, the maximum loss of light output due to the deterioration of the optical transparency is primarily determined by the concentration of intrinsic defects created during the growing process.

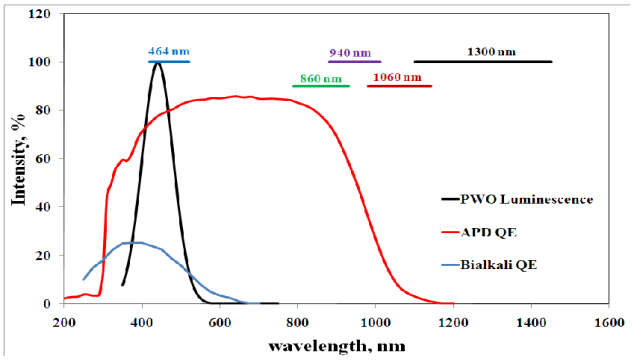

Figure 1: Spectral ranges of the applied LED light sources for successfully stimulated recovery in comparison to the distributions of the luminescence of PWO and the quantum efficiencies of a bialkali photo cathode or an avalanche photo diode, respectively,

One can overcome or at least significantly compensate the damage by the recently discovered new effect of *stimulated recovery* [2]. It turned out that exposing the crystal to external light up to the infrared region of 1300nm could recover the optical transparency within a short period. The mechanism has been confirmed as well at low temperatures but leading to longer recovery times. In addition, some of the contributing defect centres show sensitivity on the selected wavelength as observed in first EPR measurements. Detailed ongoing studies focus on the understanding of the underlying mechanisms and the optimisation of wavelengths and photon fluxes for a realistic future EMC operation. As illustrated in Fig. 1 the mechanism can be applied even on-line if the chosen photo sensor is blind for the external light source.

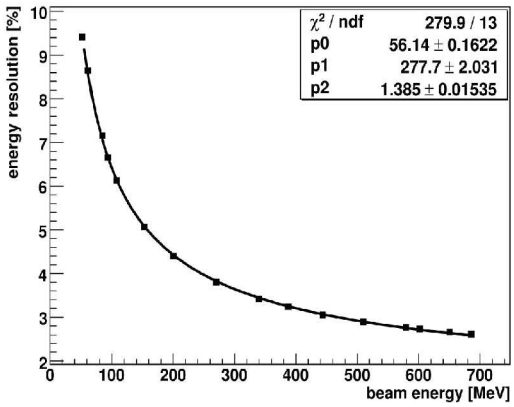

Figure 2: The energy resolution of the PROTO60 using energy marked photons measured at the tagged photon facility at MAMI Mainz.

In close collaboration with the groups at KVI (Groningen) and Orsay, respectively, response measurements of the barrel prototype PROTO60 have been continued and analysed. As a further improvement, the mechanical support structure of the PROTO60 allows to flip the array into vertical position in order to select cosmic muons passing the crystal along the full length of 200mm providing an additional absolute calibration point at approximately 210MeV deposited energy.

The energy resolution (see Fig. 2) has been achieved using a peak-sensing ADC. An alternative digitization with a sampling ADC leads to an even further improved energy and time resolution according to the analysis performed by the group at KVI. Additional tests simulating the impact of the Barrel DIRC and dead material on the energy resolution have been performed and indicate significant deterioration at energies below 200MeV. Additional investigations are in preparation.

In addition, the assembly of a new significantly improved detector matrix comprising 6x6 crystals and implementing for the first time the read-out of each crystal with two rectangular LAAPDs via the pre-amplifier ASIC APFEL has been started.

References

[1] "Technical Design Report for: PANDA Electromagnetic Calorimeter (EMC)", arXiv:0810.1216v1, October 2008.
[2] V. Dormenev et al., Nucl. Instr. and Meth. in Phys. Res. A 623 (2010) 1082-1085.

Optical Quality of PANDA Barrel DIRC Prototype Radiators*

R. Hohler[1,2], *G. Kalicy*[1,2], *D. Lehmann*[1], *M. Patsyuk*[1,2], *K. Peters*[1,2], *G. Schepers*[1], *C. Schwarz*[1], *and J. Schwiening*[1]

[1]GSI, Darmstadt, Germany; [2]Goethe Universität Frankfurt, Germany

The PANDA experiment at the facility for anti-proton and ion research (FAIR) will study the strong interaction by precision spectroscopy. A detector system with excellent particle identification (PID) is therefore required. Charged hadron identification in the barrel region will be performed by ka compact ring imaging Cherenkov detector based on the DIRC (Detection of Internally Reflected Cherenkov light) principle. The design of the PANDA Barrel DIRC [1] is based on the BABAR DIRC [2] with several important improvements, such as focusing optics and fast photon timing. The radiators are long, rectangular bars made from synthetic fused silica. The efficiency of the photon transport inside the radiator bar depends on the quality of the bar surface polish, in particular on the surface roughness.

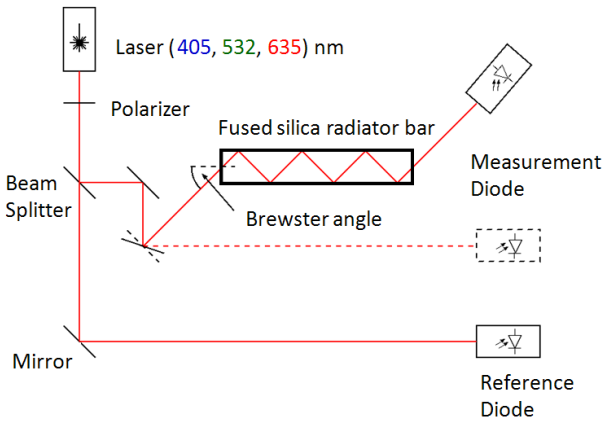

Figure 1: Schematic of the optical setup.

A motion-controlled setup, shown in Fig. 1, was built to measure the reflection coefficient and surface roughness of prototype radiator bars using three laser wavelength. The beam enters the bar at Brewster angle (to prevent reflection of the polarized laser light at the bar ends) and propagates to the end of the bar with typically 15 to 35 total internal reflections, depending on the length and orientation of the bar. The transport efficiency is determined from the ratio of the laser intensity before and after the bar using the measurement diode. A reference diode corrects temperature effects and laser intensity fluctuations. The relation between the total internal reflection loss and the surface roughness is given by the scalar scattering theory [3] and can be written as:

$$\mathcal{R} = 1 - \left(\frac{4\pi \cdot \sigma \cdot \cos\alpha \cdot n}{\lambda} \right)^2 . \qquad (1)$$

The reflection coefficient $\mathcal{R}$ is the probability of a single reflection in the radiator, σ the surface roughness, n the refractive index, λ the wavelength, and α the reflection angle inside the radiator bar. To extract the reflection coefficient from the measured transport efficiency one has to consider the bulk attenuation of the particular test bar, which is determined in a separate measurement using the same setup.

The bulk transmission and surface roughness were measured for synthetic fused silica bars produced by several manufacturers using different production processes. Figure 2 shows the data of a set of measurements for a prototype bar produced by Schott-Lithotec with a cross-section of 17 mm $\times$ 35 mm and a length of 800 mm. The laser beam is reflected from the wide sides of bar with 31 internal reflections. Scalar scattering theory describes the data well with a surface roughness value determined from the fit as $\sigma = (9.5 \pm 0.7)$ Å, consistent with the manufacturer's specifications.

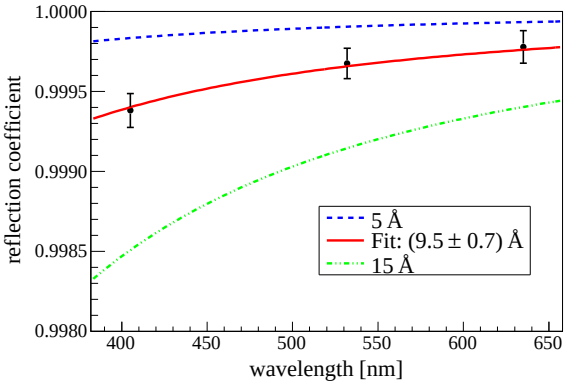

Figure 2: Reflection coefficient as a function of the wavelength for a bar produced by Schott-Lithotec. The solid line shows a fit to the data and the dashed lines are the expected result for 5 and 15 Å, respectively.

References

[1] C. Schwarz et al., "The barrel DIRC of the PANDA Experiment," Nucl. Instr. Methods A 595 (2008) 112.

[2] I. Adam et al., "The DIRC Particle Identification System for the BABAR Experiment," Nucl. Instr. Methods A 538 (2005) 281.

[3] P. Beckmann and A. Spizzichino, "The Scattering of Electromagnetic Waves from Rough Surfaces," Pergamon (1963) 1. Edition.

*This work was supported by HIC for FAIR, EU FP6 grant, contract number 515873, DIRACsecondary-Beams, and EU FP7 grant, contract number 227431, HadronPhysics2.

Rate Capability and Lifetime of Microchannel Plate PMTs*

A. Lehmann[†1], *A. Britting*[1], *W. Eyrich*[1], *S. Reinicke*[1], *F. Uhlig*[1], *and PANDA Cherenkov group*

[1]Physikalisches Institut IV, Universität Erlangen-Nürnberg, Erwin-Rommel-Str. 1, D-91058 Erlangen

Because of their excellent time resolution and their immunity to magnetic fields of up to 2 Tesla microchannel plate (MCP) PMTs are the favoured photon sensors for the DIRC Cherenkov detectors of the PANDA experiment. Despite these superior features the MCP-PMTs available until recently showed two major drawbacks compared to standard dynode PMTs: gain instabilities at high photon rates and a limited lifetime.

The expected average antiproton-proton annihilation rate of 20 MHz in PANDA will produce a single photon rate of up to several MHz/cm^2 at the sensor's surface. Assuming a gain of 10^6/photon this flux will add up to an integrated anode charge of several C/cm^2/year, dependent on the DIRC type and on the position of the DIRC focal planes.

In the latest models of MCP-PMTs measures are taken to significantly improve the rate capability and the lifetime. The stability of the gain at high rates is improved by using lower resistive materials to ensure a faster discharging of the MCPs. Two approaches are pursued to increase the lifetime: a) BINP and Hamamatsu shield the photo cathode against feed-back ions with a very thin layer of aluminium-oxide either at the first or the second MCP; b) Photonis improves the MCP surfaces by electron scrubbing and increases the vacuum inside the tube to reduce the rest gas.

Among other setups to measure the performance parameters (like e.g., the rate capability) of MCP-PMTs our group has built a test bench that allows a long-term illumination of MCPs with pulsed LED light. The signal of the MCP-PMT is continuously monitored and recorded with a CAMAC DAQ system. In time intervals of 1 to 4 days the quantum efficiency (QE) of the MCP's photo cathode is determined with an in-house setup. More information about this and other setups and results can be found in [1, 2].

Our group has performed lifetime measurements for 3 MCP-PMTs: a single anode tube (#82) with 6 μm pores from BINP in Novosibirsk, Russia; this device is equipped with a 10 nm aluminium-oxide layer at the entrance of the first MCP stage to stop feed-back ions. Further two new 8x8 pixel multi-anode MCP-PMTs from Photonis (XP85012 with 25 μm pores and XP85112 with 10 μm pores) with an improved vacuum were investigated.

The results of the lifetime measurements are shown in Fig. 1. From the plot it is obvious that the QE is decreasing with the accumulated anode charge: at 400 nm and 80 mC/cm^2 the QE is reduced by ≈50% for the BINP tube. The longest lifetime shows the XP85112 with an extrapolated loss of 50% QE at ≈200 mC/cm^2. This is still not enough for both versions of the PANDA DIRCs, but further improvements are currently pursued with Photonis. The next lifetime measurement is planned with a new Hamamatsu R10754-00-L4 MCP-PMT with 10 μm pores and a protection layer between the two MCPs.

Fig. 2 shows the relative gain versus the anode current. Assuming a gain of 10^6 the anode current can be translated into a rate of single photons given at the upper axis. The expected photon rate (after QE) at the barrel and the endcap DIRC are indicated in the figure. Clearly, the latest MCP-PMT models of Hamamatsu (R10754-00-L4) and Photonis (XP85012, XP85112) are much more stable at high rates than those of BINP and the original Photonis (XP85011). Both tubes are suitable for the barrel DIRC and presumably also for the endcap DIRC.

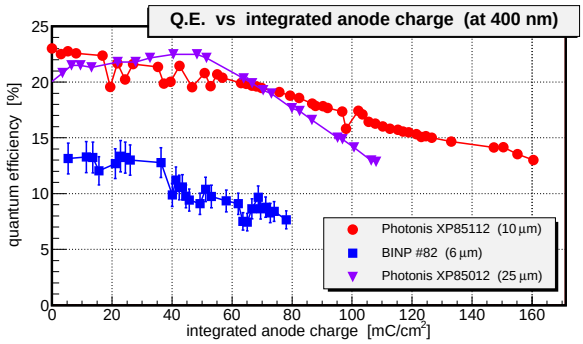

Figure 1: Quantum efficiency of the measured MCP-PMTs at 400 nm as a function of the integrated anode charge.

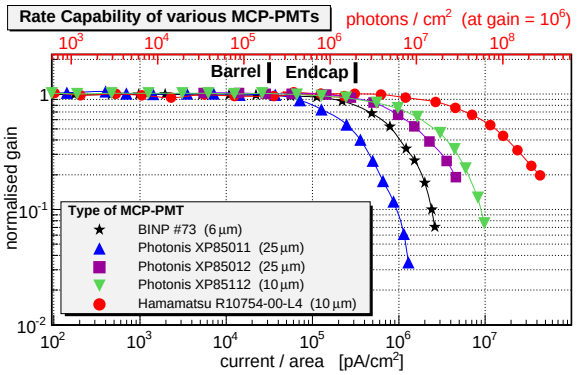

Figure 2: Rate capability of various models of MCP-PMTs.

References

[1] A. Lehmann et al., GSI Scientific Report 2009, p. 7.

[2] A. Lehmann et al., Nucl. Instr. and Meth. A (2010), doi:10.1016/j.nima.2010.09.071.

* Work supported by BMBF and GSI

† lehmann@physik.uni-erlangen.de

Simulation and Reconstruction of the PANDA Barrel DIRC*

M. Patsyuk[1,2], D. Dutta[1,3], R. Hohler[1,2], K. Goetzen[1,2], G. Kalicy[1,2], K. Peters[1,2], C. Schwarz[1], and J. Schwiening[1]

[1]GSI, Darmstadt, Germany; [2]Goethe Universität Frankfurt, Germany;
[3]Nuclear Physics Division, Bhabha Atomic Research Centre, Mumbai, India.

The PANDA experiment at the facility for anti-proton and ion research (FAIR) will study the strong interaction by precision spectroscopy. A detector system with excellent particle identification (PID) is therefore required. Charged hadron identification in the barrel region will be performed by a compact ring imaging Cherenkov detector based on the DIRC (Detection of Internally Reflected Cherenkov light) principle.

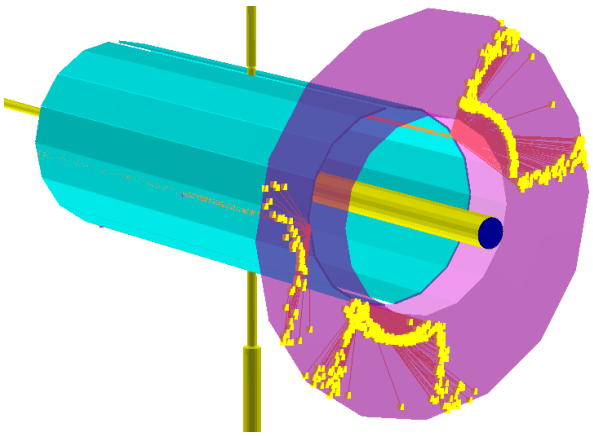

Figure 1: Display of a simulated event with three tracks in the barrel DIRC detector. The bar boxes are shown in cyan, the locations of Cherenkov photons on the detector plane are shown in yellow.

The design of the PANDA barrel DIRC [1], shown in Fig. 1, is based on the BABAR DIRC [2] with several important improvements, such as focusing optics and fast photon timing. The radiators are long, rectangular bars made from synthetic fused silica, each bar is 2500 mm long with a cross-section of 17 mm × 33 mm. Six bars comprise one bar box and 16 bar boxes surround the beam line at a radial distance of 50 cm. Cherenkov photons, emitted by a particle traversing the radiator bar, propagate along the length of a bar. A mirror, attached to the forward end of the bar, reflects them back to the readout end where they are focused via a doublet lens and an expansion volume on a flat detector plane. An array of multi-anode MCP-PMTs is used to detect the photons and measure the arrival time with a precision of approximately 100ps.

Several key design elements still need to be optimized. Among those is the shape of the radiator, where a 20 cm wide fused silica plate could be used in each bar box instead of six narrow bars, reducing the cost of radiator production. Furthermore, the lens doublet could be replaced with a mirror to focus the photons or a prism could be placed at the readout end of the bar in order to compress the phase space of the Cherenkov ring image and thus reduce the number of detector channels. Decisions about DIRC design choices will be based on the expected detector performance, in particular the single photon Cherenkov angle resolution and the photon yield per particle, which can be simulated using PandaRoot and Geant.

A new reconstruction method was developed, based on a proven BABAR-DIRC algorithm [2], which exploits the unique DIRC feature that the Cherenkov angle can be determined from a photon direction vector, defined by the exit point of the radiator bar and the location of the detector pixel, and the particle momentum vector, measured by the tracking system. This photon direction vector is determined using simulation and stored for fast reconstruction in lookup tables. As proof of principle we studied a simplified DIRC geometry without a focusing system, where the fused silica bars were directly attached to the expansion volume. A lookup table was created in simulation for a given bar, using a "Photon Gun" technique in which Cherenkov photons were produced at the end of a bar with directions covering the whole detector plane. For each pixel the initial photon direction was stored in the lookup table. The reconstruction was then applied to a sample of simulated events with single charged pions. The reconstructed single photon Cherenkov angle resolution is 17 mrad, in good agreement with the expected value, defined by the size of the bar, detector pixel, and expansion region, and the number of detector photons is between 20 and 60, depending on the polar angle of the track.

Following the successful test of the reconstruction algorithm we will next study the performance of different focusing options (thick lens, thin lens, focusing mirror) and radiator shapes (thickness, width, single plate instead of 6 bars) to provide the information required for the selection of the most effective barrel DIRC detector design.

* This work was supported by HIC for FAIR, EU FP6 grant, contract number 515873, DIRACsecondary-Beams, and EU FP7 grant, contract number 227431, HadronPhysics2.

References

[1] C. Schwarz et al., *"The barrel DIRC of the PANDA Experiment,"* Nucl. Instr. Methods **A** 595 (2008) 112.

[2] I. Adam et al., *"The DIRC Particle Identification System for the BA-BAR Experiment,"* Nucl. Instr. Methods **A** 538 (2005) 281.

Studies for the PANDA Disc DIRC*

M. Düren† [1], *I. Brodski*[1], *K. Föhl*[1], *A. Hayrapetyan*[1], *P. Koch*[1], *K. Kreutzfeldt*[1], *B. Kröck*[1], *O. Merle*[1], *A. Rink*[1], *M. Sporleder* [1], *H. Stenzel*[1], *N. Stöckmann*[1], *and M. Zühlsdorf*[1]

[1]II. Phys. Inst., Justus-Liebig-Universität, Heinrich-Buff-Ring 16, 35392 Giessen, Germany

3D Disc DIRC Design for PANDA

Excellent particle identification (PID) capabilities in the whole detector acceptance of the PANDA antiproton experiment at FAIR are needed for the scientific programme of hadron spectroscopy in the charmonium region. A PID detector based on the DIRC principle [1] is proposed for the forward endcap region of the PANDA central detector as it allows a very compact design.

In the proposed DIRC with disc-shaped radiator the generated Cherenkov light propagates by total internal reflection to the photon sensors at the disc rim. There are two concepts of accessing the Cherenkov angle information. Based on angle-to-position projection, the focussing light guide design [2] images the photons onto a pixelised photon detector. Based on angle-to-time conversion, the time-of-propagation (TOP) design [3] reconstructs the Cherenkov angle from the photon arrival time differences.

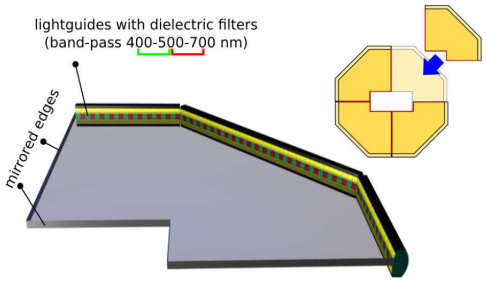

Figure 1: In the 3D disc DIRC design, each radiator quadrant is equipped with small light guides at the rim.

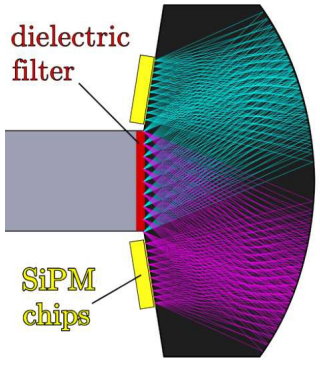

Figure 2: The light guides focus the Cherenkov light onto SiPMs on both sides of the disc.

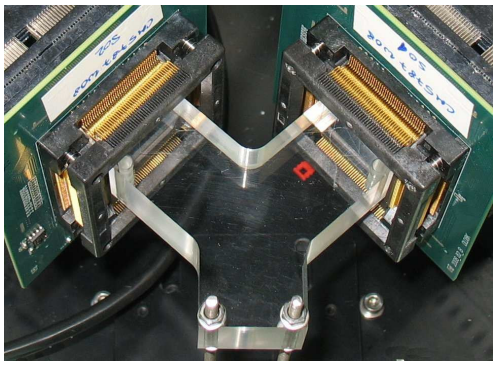

Figure 3: Y-shaped acrylic glass Cherenkov radiator attaching to two Philips digital SiPMs.

In the last year a 3D-Design has been developed that combines the two concepts (see Fig. 1). Small light guides at the rim of the disc simultaneously allow accurate TOP and angle measurements for each photon. The octagonal disc is made from four identical quadrants that can be manufactured in one piece and are mechanically and optically decoupled. The T-shaped light guides focus light on both side of the disc to minimize time shifts (see Fig. 2). Simulation and pattern reconstruction code for this design has been written.

Testing digital silicon photomultipliers

The 3D-Design assumes using Philips digital silicon photomultipliers that are currently being developed. They contain the readout electronics including the TDC on one chip. Each photodiode cell can be individually deactivated to allow for removing the noisiest cells.

In 2010, we have started to evaluate prototype SiPM detectors in test beam experiments using various Cherenkov set ups (see Fig. 3).

References

[1] The BaBar-DIRC Collaboration, I. Adam *et al.*, The DIRC Particle Identification System for the BABAR Experiment, Nucl. Instr. and Meth. A **538** (2005) 281

[2] K. Föhl *et al.*, The focussing light guide disc DIRC design, 2009 JINST 4 P11026

[3] M. Düren *et al.*, The Panda time-of-propagation Disc DIRC, 2009 JINST 4 P12013

* Work supported by GSI, BMBF and HIC for FAIR

† Michael.Dueren@uni-giessen.de

Readout System for $\overline{\text{P}}$ANDA Silicon Strip Prototyp Studies*

R. Schnell† [1], *K.-Th. Brinkmann*[1], *and H.-G. Zaunick*[1]

[1]Helmholtz-Institut für Strahlen- und Kernphysik, Universität Bonn, Nussallee 14-16, 53115 Bonn, Germany

The $\overline{\text{P}}$ANDA MVD

The PANDA Experiment at FAIR will include a Micro-Vertex-Detector (MVD) for tracking and vertexing. The MVD will be composed of silicon pixel detectors and double-sided silicon strip detectors. The strip part will contain approximately 200,000 channels that need to be read out with highly integrated front-ends.

A specific feature of the PANDA detector is the data acquisition concept [1]. Contrary to contemporary particle physics experiments there will be no central trigger. Each sub-detector should be able to recognize detector hits individually. Therefore the deployed front-end electronic shall be qualified to distinguish physical events from noise and send this hit information along with a precise time stamp to the event builder.

Current developments

All current research was done with the APV25 front-end chip [2]. In contrary to future requirements, this front-end needs an external trigger. The APV25 front-end chips were used to built sensor modules based on double-sided sensors with a strip pitch of 50 µm and a total size of 2x2 cm^2. These modules were included in a tracking station (Figure 1) to perform tracking and scattering studies. The data acquisition was performed with an FPGA powered readout system based on modular VME boards and Sampling-ADC-Mezzanine cards [3]. This readout system features a real-time data reduction with baseline and pedestal correction as well as determination of the noise for each channel. A hit finder searches for detector hits and forwards them to storage for offline analysis. Data transmission and the control of many parameters concerning the readout system is handled via the VMEbus.

The tracking station was deployed in several beam times. Measurements were performed with a proton beam at COSY (Jülich), with an electron beam at DESY (Hamburg) and a photon beam at ELSA (Bonn).

Outlook

As already mentioned, the MVD needs a free running front-end being able to identify valid detector hits without the need of an external trigger.

An example for this kind of front-ends is the n-XYTER [4]. Its architecture enables hit detection and timing, but still provides analog pulse height information. Currently there are efforts to develop this front-end towards a FAIR-XYTER for different kinds of detectors to be used at various experiments. It should include enhancements like a on chip digitalization, a reduced power consumption and fast digital links.

Figure 1: The tracking station at COSY-Jülich. The four aluminum boxes contain the silicon strip detectors. A pair of scintillation detectors for triggering is placed at each end of the setup.

Another option could be a modified version of the pixel front-end ToPix3 [5]. It utilizes the Time-over-Threshold technique to measure the deposited energy. This solution would provide comparable readout structures between pixel and strip part.

Future tests of hardware, such as silicon strip sensors as well as front-end chips will be done with our modular FPGA-based readout system. Its modular concept in both hardware and software offers large flexibility due to the reconfigurability of the FPGA.

References

[1] PANDA Collaboration: Technical Progress Report, http://www-panda.gsi.de, (2005)

[2] L. Jones: APV25-S1 User Guide Version 2.2., (2001)

[3] M. Becker, K.-Th. Brinkmann, K. Koop, R. Schnell, Th. Würschig and H.-G. Zaunick: FPGA-based Readout for Double-Sided Silicon Strip Detectors, Proceedings of the Topical Workshop on Electronics for Particle Physics TWEPP10, Aachen, Germany, JINST 6 (2011)C01008, doi:10.1088/1748-0221/6/01/C01008

[4] A.S. Brogna et al., Nucl. Instr. Meth. A 568 (2006) 301

[5] D. Calvo et al., Nucl. Instr. Meth. A 617 (2010) 560

* Work supported by BMBF [06BN9005I] and GSI [BNBRIN1012].

† schnell@hiskp.uni-bonn.de

High density cluster jet target for PANDA*

A. Täschner[†1], *D. Bonaventura*[1], *A.-K. Hergemöller*[1], *A. Khoukaz*[1], *E. Köhler*[1], *and H.-W. Ortjohann*[1]

[1]Institut für Kernphysik, Westfälische Wilhelms-Universität, Münster, Germany

Cluster jet targets have been used successfully as internal targets at storage rings in many hadron physics experiments. As an example, the Münster type cluster jet targets are used in the currently running ANKE experiment and the former COSY-11 experiment, both situated at the COSY accelerator in the Forschungszentrum Jülich.

Future experiments like the PANDA experiment at FAIR will be 4π-detectors where the distance between the target source and the interaction region will be increased by a factor of three compared to former setups. At this larger distance the target thickness is decreased by a factor of ten compared to the one at the distance used in traditional experiments. Thus new studies on higher target beam densities are necessary in order to compensate for this effect.

For this purpose a target test station was build up at Münster with the same geometry as the PANDA experiment. At this test station a new improved cluster source was developed which is able to provide the same target thickness as the traditional targets, but at the increased distance. This prototype of a cluster jet target for the PANDA experiment allows for a target thickness in the order of 10^{15} atoms/cm^2 at a distance of two meters behind the cluster source.

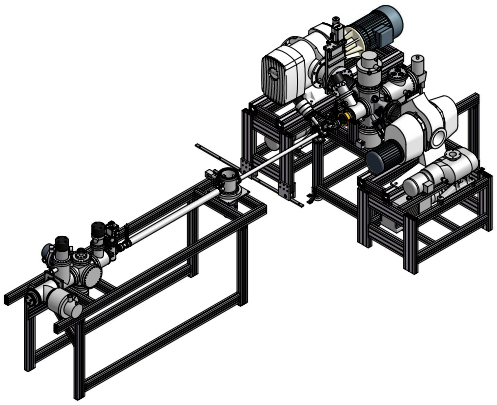

Figure 1: Cluster jet target station in Münster.

Based on the successful demonstration of the capabilities of this prototype the PANDA collaboration decided that two target stations will be used: one Münster type cluster jet target and one pellet target. The cluster jet target station will be used for the experiments in the so called high resolution mode. It will be installed as first target for the commissioning and the following physics runs.

The current developments at the prototype have several aims: With the current configuration the increase of the vacuum pressure in the interaction region due to the cluster source is acceptable but a decrease of this gas background would improve the beam lifetime and the signal to background ratio of the experiment. Therefore an improvement of this vacuum pressure is of high interest. Another topic is the further increase of the target thickness of the target by using improved Laval nozzles for the cluster production. These nozzles are developed at GSI and promising candidates will be tested at the target station in Münster in order to measure the target thickness in a setup comparable to the final system at the PANDA experiment.

In order to decrease the vacuum pressure in the interaction region the most promising method is to use a slit shaped collimator for the cluster beam preparation in place of one with a round opening. This type of collimator has been used before at the COSY-11 experiment [1] where it was installed in order to improve the momentum resolution so the width of the η'-meson could be measured [2]. In parallel the vacuum conditions at the COSY-11 experiment were improved by a factor of ten leading to a significant increase of the lifetime of the proton beam allowing for a flat top length of the beam of one hour.

The slit shaped collimator shown in figure 2 consist of two parts. The bottom part is designed to adapt the top part to the mounting thread of the normal collimators. The top part with the slit can be rotated so that the alignment of the slit is freely adjustable. Both parts were manufactured in the workshop in Münster. The slit itself was cut by a laser beam into the stainless steel holder at the Laserzentrum of the FH Steinfurt. In order to investigate the dependence of the cluster beam properties on the slit dimensions several different versions of the top part were created and are studied using the target station in Münster.

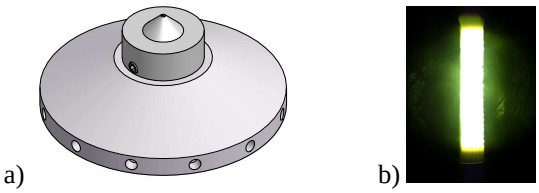

a) b)

Figure 2: a) Technical drawing of the assembly of the new two-part collimator with slit shaped hole. b) Photo taken with a microscope of one of the new slits illuminated from below. The slit has a length of 0.86 mm and a width of 0.128 mm.

References

[1] A. Täschner *et al.*, Annual Report, IKP, FZ Jülich, 2006.

[2] E. Czerwinski *et al.*, Phys. Rev. Lett. **105**, 122001 (2010)

* Work supported by EU (FP6 and FP7), BMBF and GSI.

† taschna@uni-muenster.de

First Test of a Prototype GEM-TPC for PANDA*

Heinz Angerer[1], Felix Böhmer[1], Sverre Dørheim[1], Christian Höppner[1], Bernhard Ketzer[1], Igor Konorov[1], Sebastian Neubert[1], Stephan Paul[1], Sebastian Uhl[1], Maxence Vandenbroucke[1], Martin Berger[2], Jia-Chii Chen[2], Francesco Cusanno[2], Laura Fabbietti[2], Robert Münzer[2], Rahul Arora[3], Jochen Frühauf[3], Jörg Hehner[3], Mladen Kiš[3,7], Volker Kleipa[3], Jochen Kunkel[3], Nikolaus Kurz[3], Yvonne Leifels[3], Holger Risch[3], Christian J. Schmidt[3], Sandra Schwab[3], Daniel Soyk[3], Bernd Voss[3], Jan Voss[3], Joachim Weinert[3], Reinhard Beck[4], David Kaiser[4], Michael Lang[4], Roman Schmitz[4], Dieter Walther[4], Alexander Winnebeck[4], Philipp Müllner[5], Ken Suzuki[5], Johann Zmeskal[5], and Norbert Herrmann[6]

[1]Technische Universität München, Physik Department, 85748 Garching, Germany; [2]Technische Universität München, Exzellenzcluster Universe, 85748 Garching, Germany; [3]GSI Helmholtzzentrum für Schwerionenforschung mbH, 64291 Darmstadt, Germany; [4]Helmholtz-Institut für Strahlen- und Kernphysik, 53115 Bonn, Germany; [5]Stefan-Meyer-Institut für subatomare Physik, 1090 Vienna, Austria; [6]Universität Heidelberg, Physikalisches Institut, 69120 Heidelberg, Germany; [7]RBI, 10000 Zagreb, Croatia

Introduction

High-precision spectroscopy of hadrons in the strange and charm sector, as envisaged in the PANDA experiment [1–3], requires an excellent charged particle tracking system with a very low material budget in order not to spoil the energy and mass resolution of the apparatus. Therefore, a cylindrical Time Projection Chamber (TPC) was proposed as the central tracking detector for PANDA. In addition to its excellent tracking properties, a TPC would strongly improve particle identificatio (PID) in the sub-GeV region, which is very important for most of the interesting physics channels and for rejection of low-momentum pions from $\overline{p}p$ annihilation. Owing to the beam properties at the High Energy Storage Ring (HESR), the TPC has to operate at high particle rates and in a continuous mode, i.e. without gating. The use of GEM foils as amplificatio stage instead of conventional MWPCs allows us to bypass the necessity of a gating structure, as the back drift of ions into the drift volume has been shown to be intrinsically suppressed due to the asymmetric internal fiel configuratio in a GEM-based gas amplificatio system [4].

In parallel to measurements with a small test chamber [5], a large prototype detector has been designed and built [6]. The prototype has been commissioned with cosmic rays before it was installed in the FOPI experiment [7] at GSI at the end of 2010. The application of the prototype in a running physics experiment constitutes a very useful test and provides valuable data on the tracking performance of an ungated GEM-TPC in PANDA. For FOPI, in turn, the TPC will provide a significan improvement for the detection of Λ-vertices. Here we report on the design of the prototype, the front-end and readout electronics employed, and present firs results obtained during the beam test in FOPI.

*Supported by the German BMBF, the EU 7th framework program, the DFG Cluster of Excellence 'Universe', the Maier-Leibnitz Labor der LMU und TU München, and GSI.

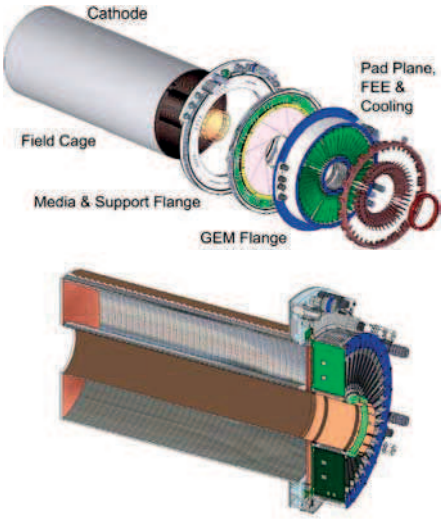

Figure 1: CAD exploded view (top) and cross section (bottom) of the GEM-TPC prototype.

Design of the GEM-TPC Prototype

The overall size of the large GEM-TPC prototype is Ø450 mm × 880 mm. Fig. 1 shows two 3-D CAD views of the prototype. It consists of two concentric cylinders forming the inner and outer fiel cage, respectively, the media and support flange the GEM flange the pad plane, the front-end electronics and the cooling system. The active volume is contained between the inner diameter of 105 mm and the outer diameter of 300 mm, and has a drift length of 729.4 mm (for comparison: the fina PANDA TPC will be 1500 mm long and have an outer diameter of 840 mm). In order to minimize the material budget of the detector structure, extremely light-weight materials are used in the barrel and forward regions. The cylindrical fiel cage vessel consists of a self-supporting sandwich structure made of a Rohacell core and Kapton® insulation layers with a

total thickness of 4.69 mm. The downstream end cap is made up of the same sandwich structure but the thickness is 6.76 mm to withstand the operational voltage of up to 30 kV.

The electric fiel in the drift volume is define by the HV plane made of a copper-clad aluminum foil on the inside of the downstream end cap, and precision staggered cylindrical fiel cage rings along the barrel part, stepwise degrading the HV to the potential at the top GEM foil. For improved homogeneity, the cylindrical fiel cage consists of two sets of copper strips on both sides of an insulating Kapton foil, where the outer strips cover the gaps between the inner strips. The potential on each ring is define by a precision resistor chain of 486 MΩ total resistance located outside the gas volume. The outer surface of the fiel cage is covered by aluminized Kapton foil and acts as shielding against external electromagnetic pickup. Two Teflo ® tubes are glued through the outer surface of the chamber for the exhaust of the gas supply near the cathode end.

On the upstream end a rigid support flang (media flange is glued to the fiel cage vessel, which provides mechanical stability and serves as the mounting structure for the GEM-TPC to the external support. In addition, the flang provides interfaces for all external supplies like gas, high- and low voltage and sensors for temperature, gas fl w and pressure.

The gas amplificatio stage of the prototype consists of a stack of three standard GEM foils (Cu/Kapton® 5/50 μm of thickness with double-conical hole pattern 50/70/140 μm $\emptyset_{Cu}/\emptyset_K$/pitch). The GEM foils are segmented on one side into eight iris-shaped sectors, each powered separately through a 10 MΩ resistor, thus minimizing the probability of discharges. The size of the foils is comparable to the ones already used in the COMPASS experiment [8]. Each GEM foil is stabilized with a rigid outer support ring and a thin inner support ring. The gaps between the GEM foils are 2 mm, while the distance between the last GEM and the pad plane is 3.92 mm. The GEM foils are individually supplied with high voltage in order to allow for an optimization of the ion backfl w into the drift volume. The fina GEM stack as well as the anode pad plane are mounted to the upstream side of the support flange All necessary connections from the support flang to the fiel cage as well as to the GEM stack are made internally, facilitating the access to these components without the need to disconnect supply lines.

The anode pad plane encloses the gas volume on the upstream side of the TPC. Due to symmetry considerations a hexagonal pad shape was chosen for the prototype. Fig. 2 shows a magnifie section of the layout of the pad plane used in the prototype. The active area on the readout plane of the GEM-TPC prototype has an inner (outer) radius of 105 mm (300 mm) and is covered by 10254 hexagonal pickup electrodes (*"pads"*). The outer diameter of the pads is 3 mm.

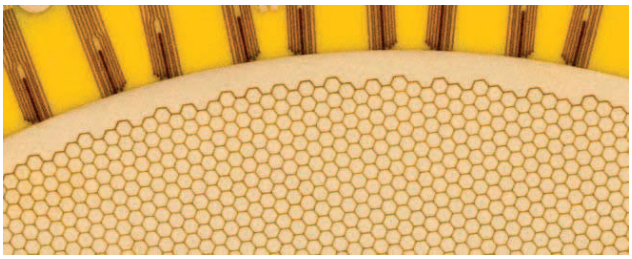

Figure 2: Enlarged view of a part of the pad layout.

Front-End and Readout Electronics

The signal induced on the pads is read out using front-end cards equipped with four AFTER ASICs [9] each, a dedicated chip for TPCs with micro-pattern gas detector readout, originally developed for the T2K experiment. Each card reads out 256 channels, thus 42 cards are needed to cover the entire pad plane.

The AFTER ASIC itself has 72 input channels, 64 of which are connected to pads on the readout plane. Each channel is equipped with a charge-sensitive preamplifie and shaper with programmable time constants and charge sensitivity. The input signals are sampled with an adjustable frequency between 10 and 50 MHz, the analog samples being stored on a 511-cell deep switched capacitor array. In addition to the 72 input channels, the array features 4 internal channels which can be used for correction of common mode and fi ed pattern noise (FPN).

Figure 4 shows a typical noise spectrum of one such front-end chip (the 4 unconnected FPN channels are clearly visible). One ADC channel in Fig. 4 corresponds to $\sim 400\,e^-$. In general, after installation in the fina GEM-TPC prototype setup in FOPI, the chips showed an excellent noise performance of $\sim 700\,e^-$ at 10 pF input capacitance with very good uniformity (c.f. Fig. 5).

Upon reception of an external trigger all memory cells

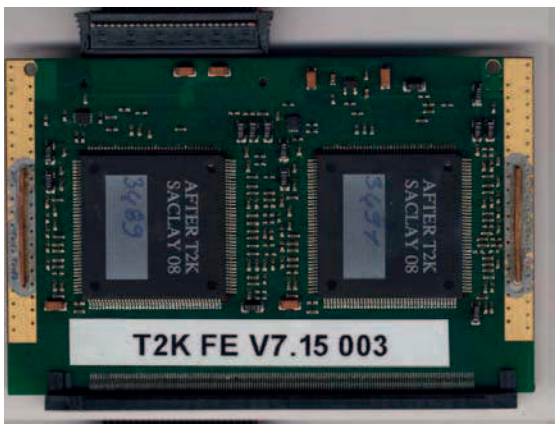

Figure 3: The TPC front-end card. The card is connected to the pad plane with the connector at the bottom, and sends its data to the ADC via a fla cable (connector at the top left). Each card is equipped with 4 AFTER ASIC chips.

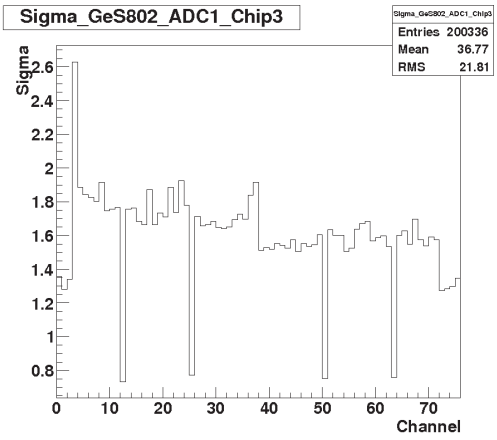

Figure 4: Noise of one AFTER chip connected to the GEM-TPC prototype. 1 ADC channel corresponds to $\sim 400\,\mathrm{e}^-$.

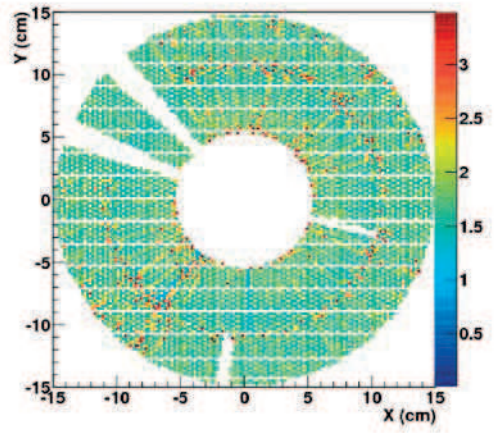

Figure 5: Noise uniformity of the full readout electronic setup.

for the 76 channels are multiplexed to a single differential signal line at 20 MHz. During this time, the input to the chip is blocked, causing considerable dead time. In the future it is planned to increase the multiplexing frequency to 40 MHz, thus halving the dead time. At this point it should also be noted that the AFTER T2K chips rely on external trigger information and are thus not suitable for the fina PANDA TPC, where a self-triggering system will be required.

The analog data from the chip is digitized by a custom-made, pipelined ADC. Each ADC board serves up to 4 front-end cards. Using FPGA logic, FPN correction and zero suppression is applied online. To read out the 42 front-end cards, 11 such ADC boards are used. Using fibe optic cables the ADCs are connected to three GeSiCA VME-modules [8] which distribute triggers, and multiplex the data from the ADCs to a second fibe optic line going to a PCI-interface card in a PC. From the data the computer builds events and sends them to the FOPI DAQ. The in-spill data rate was of the order of $20 - 30\,\mathrm{MB/s}$.

An important aspect of the front-end electronics is power consumption and cooling. Every chip is dissipating $\sim 625\,\mathrm{mW}$ of heat, amounting to a total of $2.5\,\mathrm{W}$ for one front-end card. Cooling away this excess heat is crucial for controlling the temperature gradient inside the active drift volume of the TPC (as the front-end cards are mounted directly on the pad plane). During the test at FOPI, cooling of the front-end electronics was realized with a water cooling system. Each front-end card was equipped with copper cooling plates, transporting the dissipated energy away from the chips to a heat exchanger connected to a ring-shaped distribution system. A Huber Unichiller® UC080t-H with a maximum cooling power of 2000 W is installed for the water cooling of the cards with Glysantin G48/BASF (Glycol & Ethandiol) as an additive to avoid freezing. Polyurethane (PU) pipes are employed to supply the coolant to each card.

Experimental Setup

For the beam test the prototype was installed inside the Central Drift Chamber (CDC) of FOPI (as shown in Fig. 6). For the test a krypton beam with an energy of $1.2\,\mathrm{AGeV}$

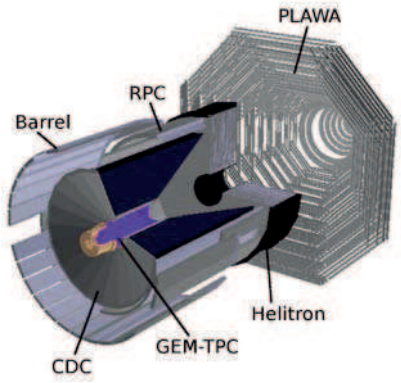

Figure 6: Schematic view of the experimental setup. CDC: Central Drift Chamber, Barrel: Scintillator barrel, RPC: RPC barrel, Helitron: Forward drift chamber, PLAWA: Plastic scintillator wall.

and an intensity of $40 \cdot 10^4$ particles per spill ($\sim 10\,\mathrm{s}$), and a gold beam with $1.0\,\mathrm{AGeV}$ and an intensity of $40 \cdot 10^3$ particles per spill were used. An aluminum target with a nuclear interaction probability of ∼2% was used for both beams. During the krypton run and part of the gold run the target was located close to the drift cathode of the GEM-TPC in order to keep the track density inside the TPC volume at a low level. For the second part of the gold run the target was moved $34\,\mathrm{cm}$ further upstream into the center of the chamber. The drift fiel strength was slowly increased towards the nominal $350\,\mathrm{V/cm}$. The drift gas used during the whole test was $\mathrm{Ar/CO_2}$ with a mixing ratio of

Figure 7: Photo of the installed prototype GEM-TPC inside FOPI.

90/10, supplied by a gas exchange system with the fl w set to 90 l/h. The oxygen content of the drift gas mixture was constantly monitored by an Orbisphere 3600 analyzer and found to be $\sim 62 - 68$ ppm throughout the test.

The triple GEM stack was operated at a voltage across the foil of 348 V for the GEM foil facing the drift volume, 317 V for the second foil and 278 V for the last foil. With this setting one achieves a gas amplificatio of ∼4000. In Fig. 7 one can see the full setup inside the FOPI detector. Inside FOPI a magnetic fiel of 0.3 T was applied.

First Results from Beam Test

During the beam-time $\sim 650 \cdot 10^3$ Kr+Al events with a track in the TPC and in the CDC for external tracking were recorded. In this firs test more than 95% of the more than 10000 channels were read out and the chamber was stable. Figure 8 shows a typical event inside the chamber, not originating from the target. One can clearly see low energy particles bent in the magnetic fiel and straight tracks generated from particles with higher energy. On average, there are 8 tracks per event inside the chamber. Figure 9 shows an event caused by an interaction in the target.

Furthermore, to determine distortions in the drift fiel and the spatial resolution performance of the detector, tracks from cosmic particles were measured with the TPC using the plastic scintillator barrel of FOPI as trigger. In total $\mathcal{O}(10^5)$ such tracks were recorded and are currently being analyzed making use of pattern recognition and tracking software developed over the last years for PANDA TPC simulations. Figure 10 shows the cluster occupancy in the projection along the drift and projected onto the pad plane for clusters found by the pattern recognition for the cosmic tracks.

Conclusions

A large-size prototype of a GEM-TPC without gating grid has been built and was successfully commissioned using cosmic tracks. It was installed in the FOPI experiment at GSI for a beam test, during which firs events from Kr-Al and Au-Al interactions have been recorded in a 0.3 T field

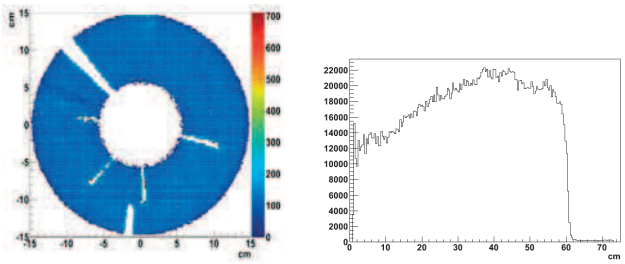

Figure 10: Occupancy of the detection plane (left) and along the drift (right).

The analysis of the data is currently in progress. Further beam tests are planned for spring 2011, and will include systematic studies of the momentum resolution, the particle identificatio capabilities, and the effect of high interaction rates of this novel detector.

References

[1] PANDA, M. Kotulla, et al., Technical progress report for PANDA: Strong interaction studies with antiprotons, FAIR-ESAC/Pbar/Technical Progress Report (February 2005).

[2] B. Ketzer, Int. J. Mod. Phys. A 21 (2006) 5675.

[3] PANDA, W. Erni, et al., Physics Performance Report for PANDA: Strong Interaction Studies with Antiprotons (2009).

[4] S.B.S.Lotze, et al., Charge transfer of GEM structures in high magnetic fields in: 9th Topical Seminar on Innovative Particle and Radiation Detectors, Siena, Italy, 2004.

[5] Q. Weitzel, et al., Development of a high-rate GEM-based TPC for PANDA, in: 2007 IEEE Nuclear Science Symposium Conference Record, IEEE, Piscataway, NJ, 2007.

[6] L. Fabbietti, et al., Nucl. Instr. Meth. A 628 (2011) 204.

[7] J. Ritman, et al., Nucl.Phys.Proc.Suppl. 44 (1995) 708.

[8] COMPASS Collaboration, P. Abbon, et al., Nucl. Instr. Meth. A 577 (2007) 455.

[9] P. Baron, et al., IEEE Trans. Nucl. Sci. 55 (2008) 1744.

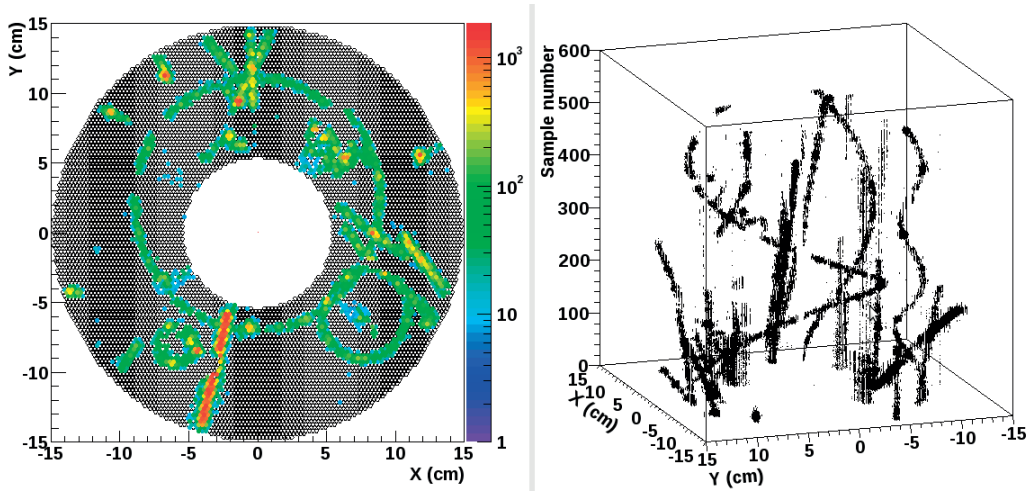

Figure 8: A typical off-target event inside the GEM-TPC from an interaction upstream of the target. The right side shows the raw samples plotted in three dimensions. The left side shows the projection onto the readout plane.

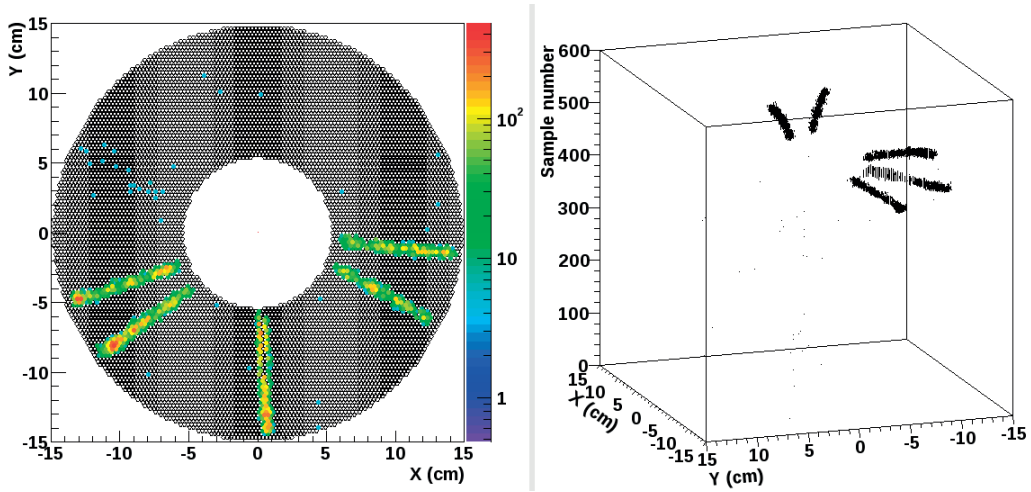

Figure 9: A typical target event inside the GEM-TPC. The right side shows the raw samples plotted in three dimensions. The left side shows the projection on the readout plane.

The Slow Controls System of $\bar{P}$ANDA

D. Protopopescu[1], H. Brand[2], F. Feldbauer[3], C. Motzko[3], P. Mullen[1], and P. Zumbruch[2]

[1]School of Physics and Astronomy, University of Glasgow, G12 8QQ, UK; [2]Gesellschaft für Schwerionenforschung, D-64291 Darmstadt, Germany; [3]Institut für Experimentalphysik, Ruhr-Universität Bochum, D-44780, Germany

Abstract

The Slow Controls framework of the $\bar{P}$ANDA experiment is discussed, with an accent on recent progress, available documentation and tools, and development trends foreseen for the near future.

Experiment Control System

We envisage the Slow Controls System of the $\bar{P}$ANDA experiment [1] rather as an Experiment Control System (ECS) [2], since it must control vital processes as machine state, run start/stop, must handle critical conditions and at the same time must supervise data acquisition parameters and ensure the quality of the physics data. Despite its complexity, we aim to deliver a complete monitoring and control system, tested and fine tuned well ahead of the first HESR beam at FAIR.

Framework and Components

The basis of the $\bar{P}$ANDA ECS is EPICS [3]. EPICS is a set of Open Source software tools, libraries and applications developed collaboratively and used worldwide to create distributed real-time control systems for scientific instruments and industrial applications. EPICS expertise already exists within the GSI community and the framework will be used by other FAIR experiments such as NuSTAR and CBM [4]. EPICS can also interface with LabVIEW [5], which is used for the $\bar{P}$ANDA Target controls.

On top of EPICS, we will have an integration layer build with AFECS [6]. AFECS is a pure Java based software framework developed at Jefferson Lab, VA. AFECS is designed to work with EPICS and, due to its agent-based architecture, is able to interface with any type of hardware or software component. In addition, MonALISA [7] components and services will be used for DAQ and physics data monitoring and control, since the $\bar{P}$ANDA software framework is based on ROOT [8], which has built-in MonALISA communication capabilities. User interfaces will be built in CSS [9], which is the industry standard nowadays and is fully supported by the EPICS community.

Tools and Documentation

The prototyping and implementation of the $\bar{P}$ANDA ECS started in 2008 with the collection of the requirements from the various $\bar{P}$ANDA subdetector groups [10]. This allowed for the organisation and standardisation of the Process Variable names, hardware for control and monitoring, and provides a means for continual updates during the prototyping and design stage. It also supplies a mechanism to automatically create EPICS channel database files for the early prototyping of local control components and GUIs (thus ensuring naming conventions are observed etc.).

An electronic logbook (eLog) for $\bar{P}$ANDA is up and running on a dedicated GSI server since early 2010. The software of this eLog was custom written within the $\bar{P}$ANDA ECS group [11], to make sure it contains the best features of existing electronic logbooks, but has been adopted in the meantime by other experimental groups, such as A2@MAMI and WASA@FZJ.

The main source of information however remains the group's wiki [2] set up in 2007, where organisational information, links to subdetector groups our forum and mailing list, databases and tools, howtos and manuals, and a talk archive are provided. As things progress towards component prototyping, dedicated howtos are being added.

Near Future

Since the majority of $\bar{P}$ANDA subdetector groups are presently at the stage of prototyping and in-beam testing, various control system components are already required. Using EPICS and CSS from the start presents obvious advantages, so early adoption by the subdetector groups is supported by providing them with customised, step-by-step 'recipes' on how to set up a test EPICS environment and how to write one's GUIs from scratch (see [2]). During 2011, the main task of the ECS group will be to support, supervise and integrate components developed within those subgroups, while collaborating closer with the accelerator group and other experiments from within FAIR.

References

[1] $\bar{P}$ANDA website: http://www-panda.gsi.de
[2] DCS wiki: http://panda-wiki.gsi.de/cgi-bin/view/DCS
[3] EPICS home page: http://www.aps.anl.gov/epics/
[4] CBM: http://www.gsi.de/forschung/fair_experiments/CBM
[5] LabVIEW at NI: http://www.ni.com/labview/
[6] AFECS home page: http://www.jlab.org/ gurjyan/afecs.htm
[7] MonALISA website: http://monalisa.cern.ch
[8] The ROOT framework, http://root.cern.ch
[9] Control System Studio, http://css.desy.de/
[10] see options on http://panda-controls.gsi.de/DB
[11] $\bar{P}$ANDA eLog http://panda-controls.gsi.de/DB
[12] http://nuclear.gla.ac.uk/twiki/bin/view.pl/Main/CSSGUIs

Global Track Finder for PANDA experiment

R. Karabowicz
GSI, Darmstadt, Germany

Detector description

The setup of the PANDA experiment [1, 2] will contain several tracking detectors: the innermost silicon Micro-Vertex Detector, the barrel-shape Central Tracker (STT or TPC), the barrel endcap-type GEM Tracker, and the forward detector build of straw tubes. The first three detectors are placed in almost constant 2 Tesla field of the solenoid magnet, while the last one uses a dipole magnet for bending of the particle trajectories.

There are several tracking projects under development in the PANDA experiment. Most of the local track finders that look for tracks in separate detectors are already well performing. The merging of the locally found trajectories into global tracks is advanced. Another approach bases on the conformal mapping and aims at reconstructing particle trajectories globally in all the barrel detectors simultanously. In this paper an alternative global tracking algorithm will be presented.

Global track finder

The track finder uses fact of the approximate field homogeneity inside the solenoid PANDA magnet. In this case the particle trajectories may be approximated by helices with helix axis parallel to the beam axis (Z axis). The projection of the helix on the X-Y plane perpendicular to the beam axis forms a circle. The algorithm focuses on the primary trajectories, that is the ones emerging from or around the interaction point.

The algorithm operates essentially on two, initially empty, arrays: one containing possible trajectories, the other storing unused detector hits. The algorithm loops over all the hits created in different detectors and matches them first to already existing tracks and subsequently to unused hits. In the case when the hit is close enough to any trajectory it is attached to it. The hits that were not connected with any track are matched to the unused hits. Here only combinations of hits that are no farther than 45° in X-Y plane are considered, and in the case that another track is created, the corresponding hit is removed from the unused hits array. The hit that was not matched in this step is stored in the unused hit array. After the loop over the detector hits the short tracks are removed, the hits from the unused hits array are again matched to found tracks, and similar tracks are merged.

Results

The tracking efficiency was studied by simulating 2 positive and 2 negative muons in the full range of azimuthal angles (ϕ) and polar angle (θ) range from 2° to 100°. The momentum magnitude varied from 300 MeV/c to 10 GeV/c. The final tracking efficiency exceeds 90% for the primary tracks in the wide range of particle momenta, as well as ϕ and θ emission angles, see top three panels of Figure 1. The tracking efficiency drops for tracks with momentum lower than 1 GeV/c mainly due to increasing multiple scattering. The gaps in the ϕ dependence around $\pm 90^\circ$ originate from the vertical holes in detectors' acceptances for the target pipe. The momentum resolution shows very little dependence on momentum magnitude or ϕ angle. However it worsens for θ angles below 20° (bottom panel in Figure 1) where the track curvature is not large enough to reconstruct momentum.

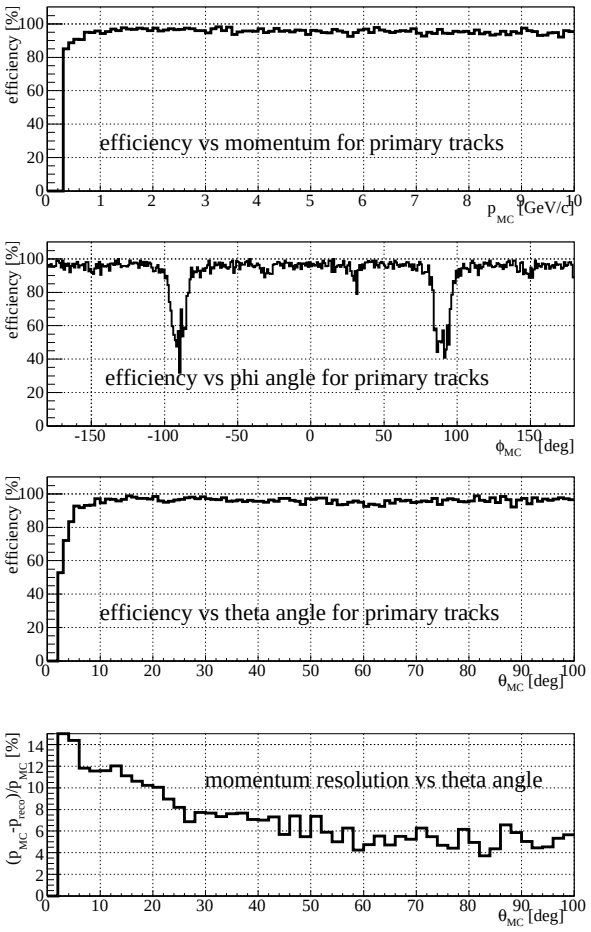

Figure 1: Track efficiency versus: momentum magnitude (top), ϕ angle (second from top), θ angle (third from top). Bottom figure shows momentum resolution as a function of θ angle.

References

[1] Physics Performance Report, PANDA Collaboration, W. Erni *et al.*; arXiv:0903.3905v1v1.

[2] Technical Progress Report, PANDA Collaboration.

Hardware and Software Developments for $\bar{P}$ANDA

J. Becker, F. Feldbauer, M. Fink, P. Friedel, F.H. Heinsius, T. Held, C. Motzko, B. Kopf, M. Leyhe, B. Roth, T. Schröder, J. Schulze, M. Steinke, U. Wiedner

Inst. f. Experimentalphysik I, Ruhr-University Bochum

The $\bar{P}$ANDA electromagnetic calorimeter

The hardware developments of the Bochum group concentrated in 2010 mainly on components for the forward part of the electromagnetic calorimeter. Those are supposed to be tested in a prototype of 216 PWO crystals. We concentrated our efforts mainly on four topics:

- photo detectors
- cooling of the calorimeter
- slow control devices
- preparation of the prototype mechanics

The high-counting rate and the high-dose radiation environment in the innermost part of the forward end cap require the use of vacuum photo triodes (VPTs) or vacuum photo tetrodes (VPTTs) as *photo detectors*. Since one supplier has disappeared from the world market we tested new types of the two remaining producers. For the different VPTs and VPPTs the amplification factors were measured, the dark current was determined and a surface scan of the photosensitive surface was performed. The latter was done in an especially for this purpose constructed device, which delivers light pulses only to very limited, well-defined points of the surface. The result of such a scan performed with different photo sensors can be seen in figure 1.

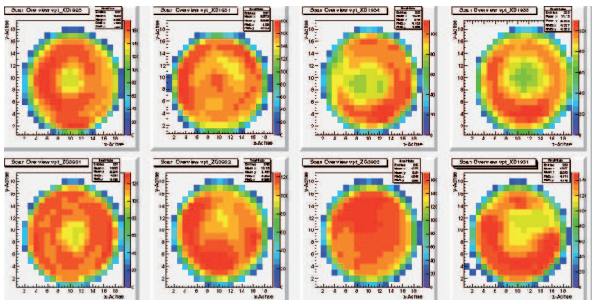

Figure 1: Response to surface light exposure for different VPTs

Since the VPTs or VPPTs will be used in the magnetic field of the $\bar{P}$ANDA solenoid, the performance of the tubes in a magnetic field up to 1.2 T has to be checked. The angle of the mounted tubes relative to the field lines is up to 17° in $\bar{P}$ANDA. In our laboratory apparatus we tested angles up to 20° and a typical result is shown in figure 2. In a fixed position, but a varying magnetic field between 0 and 1.2 T the amplification varies between +7% and −7% for VPTs and +25% and −20% for VPTTs. Putting the VPTs or VPTTs at an relative angle reduces the amplification by maximal 10% (figure 2) for VPTs, while for VPTTs an increase of up to 25% and a decrease of up to 20% is observed.

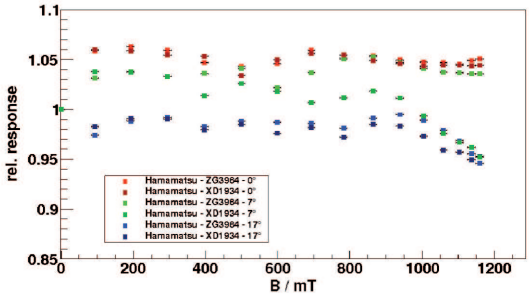

Figure 2: Amplification of VPTs dependent on the angle relative to a magnetic field

The *cooling concept*, which is necessary to increase the sensitivity of the PWO crystals, has been developed and simulated with a special software package. The necessary temperature of −25° with a maximal gradient of 2° along the crystal can be achieved by directly cooling the mounting back plate of the crystals by special cooling channels and an additional front-plate cooling through radiation hard polyurethane pipes. The whole calorimeter is packed into a 30 mm thick polystyrol insulation on the side and backside. The front side has a special low-mass vacuum shield with incorporated insulation foils. All concepts have been tested in laboratory for verification.

The low-temperature operation of the EMC requires a constant *slow-control monitoring* of the temperature and humidity inside the EMC. Therefore we developed low-mass temperature sensors consisting of Pt-wire and a THMP electronic control unit. These boards can also be used to monitor the atmospheric pressure.

The transparency of the crystals themselves and subsequent electronic chain is planned to be monitored by a lightpulser system. In order to minimize its size and the use of mechanical moving parts, we designed a special system utilizing high-power LEDs combined with LCD absorbers (fig. 3). This lightpulser system reproduces light pulses equivalent to γ radiation between 10 MeV and 15 GeV.

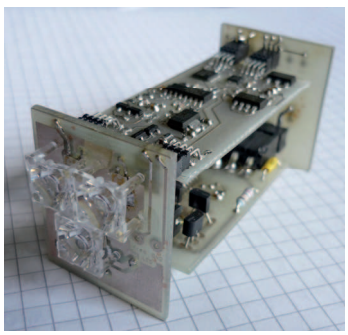

Figure 3: Lightpulser unit for the EMC

Software developments for $\bar{P}$ANDA

During the operation of $\bar{P}$ANDA a regular calibration is necessary to ensure the high-resolution of the EMC. We developed for this purpose a software package that continuously determines calibration constants for the individual crystals utilizing the two photons from the decay of neutral pions. The underlying algorithm is an iterative process to best approximate the values of the π°. Figure 4 proves that the resolution and the actual mass value for neutral pions can be improved significantly using this method in MC simulations.

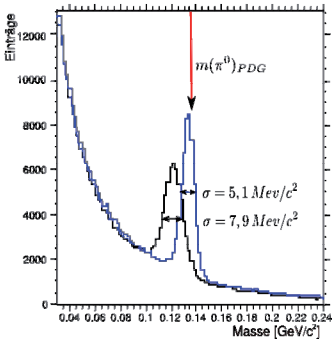

Figure 5: Reconstructed π° invariant mass before (black) and after the energy calibration.

The Bochum group is in the process together with the University Mainz and GSI to develop a partial-wave analysis package (PWA) for $\bar{P}$ANDA. The idea of this package is that it could be used also for other hadron physics experiments with:

- utilizing a user-friendly interface
- being so flexible that it incorporates all physics programs of $\bar{P}$ANDA and other hadron physics experiments
- automatically generating the amplitudes
- calculating amplitudes independent of the formalism (e.g. covariant tensor formalism, canonical formalism or helicity formalism, or …)
- creating an automated documentation about the different fits and their respective results
- having an abstract interface so that different minimizing algorithms could be used.

The basic framework of this software was already realized in 2010. Both, the covariant tensor formalism and the helicity formalism are implemented and the fit minimization is done with either the software package MINUIT2 or GENEVA. A likelihood-based minimization works in multi-thread mode.

The software package was tested among other data on antiproton annihilation data that were recorded within the Crystal Barrel experiment at LEAR at CERN in the 1990s. The purpose of analysing this data is to get a better understanding of the antiproton annihilation mechanism and thereby to optimize the PWA strategies for $\bar{P}$ANDA.

In particular the annihilation channel $\bar{p}p \rightarrow \omega\pi^0$ is well suited to study the annihilation mechanism since no intermediate resonances are present. We wanted to determine the maximum angular momentum that is present in the initial antiproton-proton annihilation process. Also the helicity distribution of the ω meson was determined in dependence of the antiproton momentum. The data consisted of three different antiproton momenta: 600 MeV/c, 1200 MeV/c and 1940 MeV/c. The maximum-contributing angular momenta were determined to be J_{max}=3 for 600 MeV/c and J_{max}=5 for 1940 MeV/c confirming the generally used assumption that the angular momentum behaves like $J_{max}= p_{cms}/200$ MeV/c. The quality of the PWA fits in describing the data can be seen in figure 6 where the fit to the data of the ω production angle is shown.

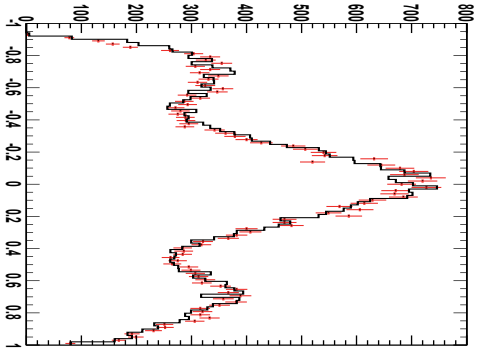

Figure 6: Distribution of the ω angular production angle. Data are in red while the PWA fit results are shown a black curve.

In order to determine the polarization of the ω we determined the spin density matrix element ρ° in the helicity system of the ω. This can be done by either by using the results of the PWA or by extracting it out of the measured ω-decay-angle distribution. Both results agree reasonably well as shown in figure 7.

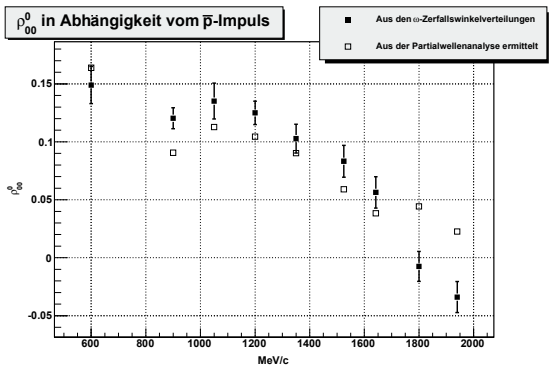

Figure 7: spin density matrix element for different antiproton momenta. The results for the PWA fits (black points) agree reasonably well with the determination from the ω-decay-angle distribution.

Monte-Carlo Simulation of a X(3872) Resonance Scan at $\overline{\mathrm{P}}$ANDA*

J. S. Lange, M. Galuska, T. Geßler, W. Kühn, S. Künze,
Y. Liang, D. Münchow, B. Spruck, M. Ullrich, and M. Werner
Justus-Liebig-Universität Gießen, II. Physikalisches Institut

The X(3872) is a charmonium(-like) state which was first observed in its decay X(3872)→J/$\psi\pi^+\pi^-$ in B decays [2] [3] and inclusive production in $p\overline{p}$ collisions [4] [5]. In particular, the observation of its radiative decay into $J/\psi\gamma$ allows the assignment of positive charge parity C=+1. The observation of isospin violation in the decay X(3872)→$J/\psi\rho(\rightarrow\pi^+\pi^-)$ raised the question, if it might be a charmonium state at all. As its mass is within Δm<1 MeV of the $D^0\overline{D}^{0*}$ threshold, it might be interpreted as an S-wave molecular state [1]. The width is unknown and probably can only be determined at $\overline{\mathrm{P}}$ANDA. The current upper limit is $\Gamma\leq$2.3 MeV [2], whereas $\overline{\mathrm{P}}$ANDA might be able to set an upper limit in the order of a few hundred keV using the cooled antiproton beam. A detailed simulation of a resonance scan of the X(3872) in the reaction $p\overline{p}$→X(3872)→$J/\psi\pi^+\pi^-$ using the PandaRoot framework was carried out. Recent improvements in the software since the $\overline{\mathrm{P}}$ANDA Physics Report [6] are in particular: *(a)* usage of detailed field maps (grid sizes 1-4 cm) of a B_z=2 T in the central region and dipole field of 2 Tm in the forward region (with flux effects in the iron of the muon subdetector and interference of the fields taken into account), *(b)* usage of a realistic track finder and track fitter (here for TPC and MVD), based upon conformal map and Kalman filter techniques, and *(c)* simulation of final state radiation [7]. In about ≃30% of all $J/\psi\rightarrow e^+e^-$ decays an additional photon is radiated. The particle identification uses the ratio E/p as a variable for discrimination of charged pions and leptons. E is the deposited shower energy in the EMC, p is the reconstructed track momentum by the track finder. For resonant X(3872) formation, the required beam momentum is p_{beam}=6.99100 GeV/c. Our baseline assumption is a peak cross section of $\sigma_{X(3872)}$=50 nb. The ratio of branching fractions of the X(3872) decays into the final states $D^0\overline{D}^{0*}$:$J/\psi\pi^+\pi^-$:$J/\psi\gamma$ is assumed to be 9:1:0. The reconstruction efficiency of ≃50% is dominated by the track reconstruction efficiency for the low momentum charged pions. All these factors lead to a reconstructable cross section of 250 pb. For resonance scans, the HESR will be operated in the high resolution mode with Δp/p=10^{-5}, which corresponds to a luminosity of $\mathcal{L}$=2×10^{31} cm^{-2}s^{-1}. Assuming an accelerator duty factor of 50%, this leads to an integrated luminosity of $\mathcal{L}_{int}$=0.86 pb^{-1}/day. The main background is meson production in processes such as $p\overline{p}\rightarrow\pi^+\pi^-\pi^+\pi^-$ with two misidentified charged pions (as leptons) in the EMC. The cross section for this process is 50 μb [8], i.e. a factor ≃10^3 larger than the signal. It is important to investigate the shape of the background e.g. in the 2-particle mass spectrum. For this purpose, a DPM (dual parton model) event generator [9] was used. In fact, a varying background shape in the region of the J/ψ was found and fitted with a first order Chebyshev polynomial. The background fit was performed for the sideband, and the fitted background was subtracted in the signal and sideband region. Fig. 1 shows the background fit subtracted signals of the tagged J/ψ from the X(3872) decay. As a preliminary result, the width of the resulting resonance curve was found to be ≃20% larger than the input width of the X(3872). Details of the analysis are described elsewhere [10].

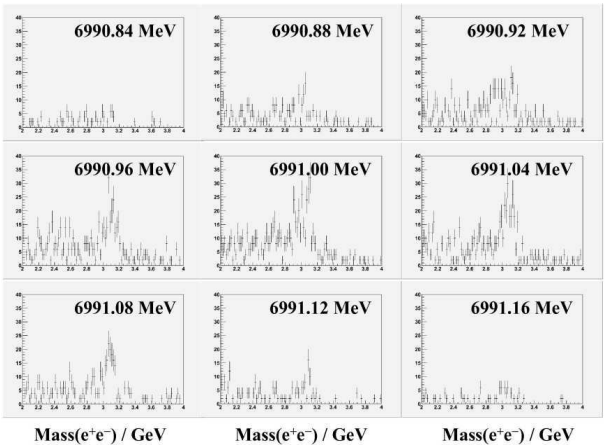

Figure 1: MC simulation of a resonance scan of the X(3872) at $\overline{\mathrm{P}}$ANDA, with 9 scan points of different antiproton beam momenta and data taking of 2 days for each point. The plots show the background subtracted, tagged $J/\psi\rightarrow e^+e^-$ signal from the X(3872)→$J/\psi\pi^+\pi^-$ decay. Only statistical errors are shown.

References

[1] N. A. Tornqvist, Phys. Lett. B590(2004)209, Phys. Rev. Lett. 67(1991)556
[2] Belle Collaboration, Phys. Rev. Lett. 91(2003)262001
[3] BaBar Collaboration, Phys. Rev. D71(2005)071103
[4] CDF-II Collaboration, Phys. Rev. Lett. 93(2004)072001
[5] D0 Collaboration, Phys. Rev. Lett. 93(2004)162002
[6] $\overline{\mathrm{P}}$ANDA Collaboration, arXiv:0903.3905
[7] E. Barberio, B. v. Eijk, Z. Was, Comp. Phys. Comm. 66(1991)115
[8] V. Flaminio et al., CERN-HERA-79-03
[9] V. Uzhinsky, A. Galoyan, hep-ph/0212369, and references therein
[10] J. S. Lange et al., arXiv:1010.2350

* Work supported by BMBF (06GI9107I) and HICforFAIR

Description of fully differential Drell-Yan pair production *

F. Eichstädt†[1], *S. Leupold*[2], *and U. Mosel*[1]

[1]Institut für Theoretische Physik, Universität Giessen; [2]Department of Physics and Astronomy, Uppsala University, Sweden

The research project covers the effects of intrinsic quark distributions of transverse momentum and mass on the unpolarised production of Drell-Yan (DY) pairs. A lot of experimental effort is being devoted to measurements of the DY process: In antiproton-proton collisions at $\overline{\text{P}}$ANDA (FAIR) [1] and PAX [2], in proton-proton collisions at RHIC [3], J-PARC [4], IHEP [5] and JINR [6] and in pion-nucleon collisions at COMPASS [7]. At $\overline{\text{P}}$ANDA, for example, unpolarised cross sections will be among the first to be measured, since single and especially double polarised experiments will be possible only later in the project.

The standard collinear perturbative QCD leading-order description already shows some shortcomings at high center-of-mass (c.m.) energies [8]: A K-factor is needed to account for the absolute size of the cross section and the transverse momentum (p_T) spectrum of the DY pair is inaccessible. A next-to-leading-order calculation can improve on the K-factor part, but shows divergent behavior in the p_T spectrum for $p_T \to 0$. At $\overline{\text{P}}$ANDA the limits of the standard collinear perturbative QCD description will be revealed even further, since measurements will be taken at comparatively low hadron c.m. energies of $\sqrt{s} \approx 5.5$ GeV and in an invariant mass range of 1.5 GeV $< M < 2.5$ GeV. At such low energies and thus large ratios of $\tau = M^2/s$ non-perturbative (higher-twist) effects are expected to play an important role. This highlights the need to model these effects in a phenomenological picture, at which this project is aiming at.

To account for the shortcomings of the standard description and for the above mentioned higher-twist effects at $\overline{\text{P}}$ANDA energies we study a QCD inspired phenomenological parton model that incorporates full transverse momentum dependent quark kinematics and which in addition allows for mass distributions of quarks. We have revised a previous model of this type [9, 10, 11] and found that in these works important physical constraints were not considered. We have rectified [12] and extended this approach: A calculation including all hard subprocesses to order α_s was performed. As mentioned above two of these processes, namely gluon Bremsstrahlung and gluon Compton scattering, show divergent p_T spectra for $p_T \to 0$, which stem from u-channel exchange quarks. The earlier introduced mass distributions for these exchange quarks effectively provide a cut off for the divergencies and thus in our model the p_T spectra are integrable. We find that in our full model we can describe DY transverse momentum and invariant mass spectra at different energies without the need for a K-factor, for an example see Fig. 1. Finally fixing our phenomenological distributions at available data one aim is to make predictions for DY pair production at $\overline{\text{P}}$ANDA.

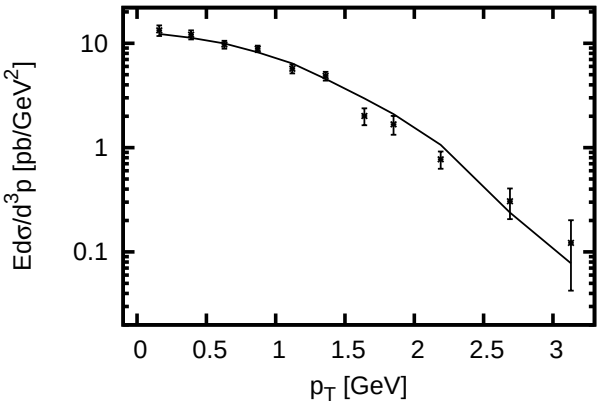

Figure 1: p_T-spectrum obtained in our full model. Data are from E866 [13] for invariant masses $4.2 <$ M [GeV] < 5.2, around midrapidity. Only statistical errors are shown.

References

[1] M. F. M. Lutz, B. Pire, O. Scholten and R. Timmermans [The PANDA Collaboration], arXiv:0903.3905 [hep-ex].

[2] V. Barone *et al.* [PAX Collaboration], arXiv:hep-ex/0505054.

[3] G. Bunce, N. Saito, J. Soffer and W. Vogelsang, Ann. Rev. Nucl. Part. Sci. **50**, 525 (2000).

[4] S. Kumano, AIP Conf. Proc. **1056**, 444 (2008).

[5] V. V. Abramov *et al.*, arXiv:hep-ex/0511046.

[6] A. Sissakian, O. Shevchenko, A. Nagaytsev and O. Ivanov, Eur. Phys. J. C **59**, 659 (2009).

[7] F. Bradamante [COMPASS Collaboration], Nucl. Phys. A **622**, 50C (1997).

[8] S. Gavin, R. Kauffman, S. Gupta, P. V. Ruuskanen, D. K. Srivastava and R. L. Thews, Int. J. Mod. Phys. A **10**, 2961 (1995).

[9] O. Linnyk, S. Leupold and U. Mosel, Phys. Rev. D **71**, 034009 (2005) [Erratum-ibid. D **75**, 059901 (2007)].

[10] O. Linnyk, K. Gallmeister, S. Leupold and U. Mosel, Phys. Rev. D **73**, 037502 (2006).

[11] O. Linnyk, S. Leupold and U. Mosel, Phys. Rev. D **75**, 014016 (2007).

[12] F. Eichstaedt, S. Leupold and U. Mosel, Phys. Rev. D **81**, 034002 (2010).

[13] J. C. Webb *et al.* [NuSea Collaboration], arXiv:hep-ex/0302019.

* Work supported by HIC for FAIR.

† fabian.eichstaedt@theo.physik.uni-giessen.de

Status of the HypHI project

T.R. Saito[*1,2], *S. Bianchin*[1], *O. Borodina*[1,2], *V. Bozkurt*[1,3], *B. Guekuezuem*[1,3], *D. Khaneft*[1], *E. Kim*[1,4], *Y. Ma*[1], *F. Maas*[1,5], *S. Minami*[1], *D. Nakajima*[1,6], *B. Oezel-Tashenov*[1], *C. Rappold*[1,7], *and the HypHI collaboration*

[1]GSI, Darmstadt, Germany; [2]KPH, Mainz Univ., Germany; [3]Nigde Univ., Turkey; [4]Seoul Nat. Univ., South Korea; [5]Helmholtz Institute Mainz, Germany; [6]Tokyo Univ., Japan; [7]Strasbourg Univ., France

The HypHI project aims to perform precise hypernuclear spectroscopy with induced reactions of stable heavy ion beams and RI-beams on fixed stable target materials [1]. In heavy ion induced reactions, hypernuclei are produced as projectile fragments with coalescence of a hyperon which is produced in the participant region of the collision. It has been discussed that it is only the way to study hypernuclei at extreme isospin and their magnetic moments as well as hypernuclei with three or more strange quarks. Because of experimental difficulties, precise hypernuclear spectroscopy with heavy ion beams impinged in a fixed target has never been performed.

We have already performed two experiments, Phase 0 and 0.5. The Phase 0 experiment was performed in 2009 with ^{6}Li projectiles at 2 A GeV on a carbon target with a thickness of 8 g/cm^2. The experiment concentrates to produce and identify light hypernuclei such as $^{3}_{\Lambda}$H, $^{4}_{\Lambda}$H, $^{4}_{\Lambda}$He and $^{5}_{\Lambda}$He. In the setup, there were three layers of scintillating fiber detectors [2], two drift chambers, a start counter for Time-of-Flight (TOF) measurements and three TOF walls to measure stop time of TOF. The Phase 0.5 experiment was performed in 2010. A projectile of ^{20}Ne at 2 A GeV was impinged in a carbon target in order to produce and identify heavier hypernuclei. The experimental setup of Phase 0.5 was similar to Phase 0, however, some modifications on the detector arrangement and the trigger to the data acquisition system were made in order to accept heavier fragments and large particle multiplicities. Physics subjects of the both experiments are;

- production mechanisms of hypernuclei with heavy ion induced reactions,
- hyperon-nucleon fundamental interactions,
- weak-decay of hypernuclei,
- dibaryons with strangeness,
- Σ-hypernuclei,
- hypernuclear radii.

Analyses of the data of the Phase 0 experiment on $^{3}_{\Lambda}$H and $^{4}_{\Lambda}$H have been completed by reconstructing two-body mesonic decay modes. In the analysis, track candidates are found by pre-tracking with a simple geometrical methods. It provides rough estimates on the track coordinate and momentum as well as particle identifications. These information are used as a seed in the track fitting procedure with the Kalman filter. Details on the track fitting algorithm are discussed in ref. [3]. After the track fitting procedure, topological methods are applied to find hypernuclear candidates. So far, peaks of $^{3}_{\Lambda}$H and $^{4}_{\Lambda}$H in the invariant mass distribution have been clearly observed on a background distribution without any subtractions. The width and significance of the peak are preliminary 4.1 MeV and 5.6 σ for $^{3}_{\Lambda}$H and 4.3 MeV and 11.9 σ for $^{4}_{\Lambda}$H. Lifetime of these hypernuclei has also been preliminary deduced at 146 +46 -29 ps and 139 +56 -31 ps, respectively. These clear observations have already revels that the heavy ion induced reaction is a powerful tool for the precise hypernuclear spectroscopy. Further data analyses on the hypernuclei with three-body modes, dibaryons with strangeness, Σ-hypernuclei and hypernuclear radii as well as the analyses on the Phase 0.5 experiments are in progress.

The HypHI project is supported by the Helmholtz Association as the Helmholtz-University Young Investigators group VH-NG-239 and by German Research foundation with a contract number SA 1696/1-1.

References

[1] T.R. Saito et al., Nuclear Physics A835 (2010) 110-116

[2] D. Nakajima et al., Nuclear Instruments and Methods in Physics Research A 608 (2009) 287-290

[3] C.Rappold et al., Nuclear Instruments and Methods in Physics Research A662 (2010) 231-235

* t.saito@gsi.de

Clustering algorithm for data analysis of the Fiber detectors of HypHI project

C.Rappold[*1], *O. Borodina*[1,3], *V. Bozkurt*[1], *E. Kim*[1], *F. Maas*[1,3], *S. Minami*[1], *D. Nakajima*[1,5,6], *T.R. Saito*[1,3], *and W. Trautmann*[1]

[1]GSI, Darmstadt, Germany; [2]Mainz University, Mainz, Germany; [3]KVI, Groningen, The Netherlands; [4]KEK, Tsukuba, Japan; [5]Tokyo University, Tokyo, Japan

The HypHI project aims to study hypernuclei by means of collisions of stable heavy ion and RI beams on stable target materials. As the first step (Phase 0), the feasibility of hypernuclear spectroscopy with heavy ion beams was investigated with a ^{6}Li beam at 2 A GeV impinged on a ^{12}C target by identifying $^{3}_{\Lambda}$H, $^{4}_{\Lambda}$H and $^{5}_{\Lambda}$He hypernuclei [1]. The Phase 0 experiment was performed in August and October 2009. In addition a new experiment has been performed in March 2010, in which a ^{20}Ne beam was impinged on a ^{12}C target at an energy of 2 A GeV.

A dedicated algorithm for hit clustering has been considered to replace the current algorithm which is not flexible enough to handle the experimental behavior of the fiber detectors. The new algorithm should be able to handle channel gaps within a hit cluster which corresponds to the cross talk behavior of the PMT of the fiber detectors. As well outliners, corresponding to noisy channels, should not affect the clustering procedure and could be detected for possible rejection. The algorithm should also provide good clustering whatever is the detector occupancy, which is the fraction of fired channels over the total number of channels of considered fiber layer. The most important feature of the algorithm is that it should not require the number of clusters as an input since event by event the hit pattern on detectors are different, so that prior assumption is impossible.

The proposed algorithm is based on *Hierarchical* clustering algorithm which consists in agglomerate fired channels using the distance matrix as clustering criteria. The definition of the distance gives different behavior on the clustering procedure. The complete-link method is used, in which the distance corresponds to the maximum euclidian distance between pairwise channels, producing compact clusters [2]. The use of a goodness criterion allows to assess the quality of each cluster and of the full hit partition. By using this kind of criteria, produced hit clusters can be merged in order to improve the global goodness of the clustering context. The number of clusters is then obtained when the criterion is optimal. The algorithm uses the *silhouette factor*, $s(i)$, proposed in [3]. For each channel i:

$$s(i) = \frac{b(i) - a(i)}{\mathrm{Max}(a(i), b(i))}$$

where $a(i)$ is the average distance to other channels in the considered hit cluster and $b(i)$ is the average distance to channels of the nearest hit cluster. All hit clusters which can be improved are considered to be merged with their closest hit cluster. The optimal partition is obtained when the merge procedure gives no more improvement of the context.

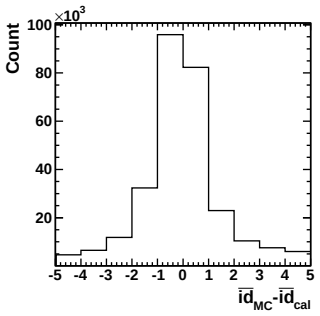

Figure 1: Difference of the id of cluster center from MC and from the found cluster.

Monte Carlo simulation has been used to evaluated the performance of the new algorithm. It simulates hit pattern on the detector layer, with a random number of hit clusters with a random cluster size. Outliners (noisy channels) and missing channels are also included. It shows that the clustering algorithm properly found all MC hit clusters when the detector layer is up to 25% of occupancy. The algorithm misses up to a maximum 4 hit clusters when the detector occupancy reaches 50%. In this case, the channels of the missing hit clusters are shared amount the found hit cluster. Then found hit clusters are not exactly the MC hit clusters, and the channel id of the center of the hit cluster is changed compared to the one of the MC hit cluster. Fig. 1 shows the difference of the mean value of channel id of the MC clusters and of the found clusters. Arround 70% of the found clusters have a difference of one channel or less with the corresponding MC cluster. It shows a good estimation of the hit cluster pattern even with high detector occupancy.

References

[1] Proposal of the HypHI Phase 0 experiment, the HypHI collaboration.

[2] , W. B. Frakes and R. Baeza-Yates, Data Structures and Algorithms, Eds. Prentice-Hall, Upper Saddle River, NJ, 1327 (1992)

[3] Kaufman, L. and Rousseeuw, P. Finding Groups in Data: an Introduction to Cluster Analysis. New York: Wiley (1990)

[*] c.rappold@gsi.de

Chiral thermodynamics of nuclear matter*

S. Fiorilla, N. Kaiser, and W. Weise
Physik-Department, Technische Universität München, D-85747, Garching, Germany

The thermodynamical properties of nuclear matter are studied using the framework of in-medium chiral perturbation theory [1]. Our approach relies on the separation of long- and short-distance dynamics and an ordering scheme in powers of small momenta including the nuclear Fermi momentum. The calculation is performed up to three-loop order. Contributions to the free energy density originate from chiral 1π- and 2π-exchange, with inclusion of virtual Δ-isobar excitations as well as the associated 2π-exchange three-nucleon forces. Fig. 1 shows the equation of state of isospin-symmetric nuclear matter for temperatures $T \leq 25\,\mathrm{MeV}$. These pressure isotherms display a first-order liquid-gas phase transition, with a critical temperature of $T_c = 15.1\,\mathrm{MeV}$. Above T_c isospin-symmetric nuclear matter exists only in the gas phase.

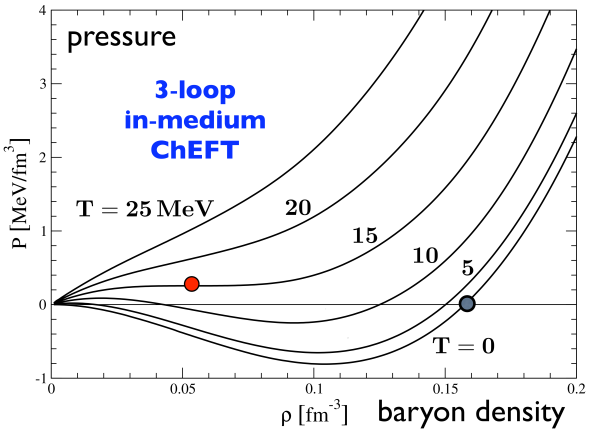

Figure 1: Equation of state of symmetric nuclear matter at different temperatures.

With increasing isospin-asymmetry the free energy density and pressure at a fixed nucleon density grow and nuclear matter becomes less bound. At the same time the coexistence region of liquid and gas phase shrinks. This behaviour is summarized in Fig. 2, which shows the reduction of the coexistence region in the $T\rho$ plane with increasing isospin-asymmetry. At a proton fraction of $\simeq 0.05$ the liquid component has disappeared completely.

As a further application of our approach, which treats the pion exchange dynamics explicitly as a function of the pion (or quark) mass, we investigate the dependence of the quark condensate $\langle\bar{q}q\rangle$ on the baryon density and the temperature [2]. The contributions beyond the linear density approximation are given by the derivative of the interaction part of the free energy density with respect to the pion mass. One can see from Fig. 3 that at low temperatures

* Work supported in part by BMBF, GSI and the DFG Cluster of Excellence "Origin and Structure of the Universe".

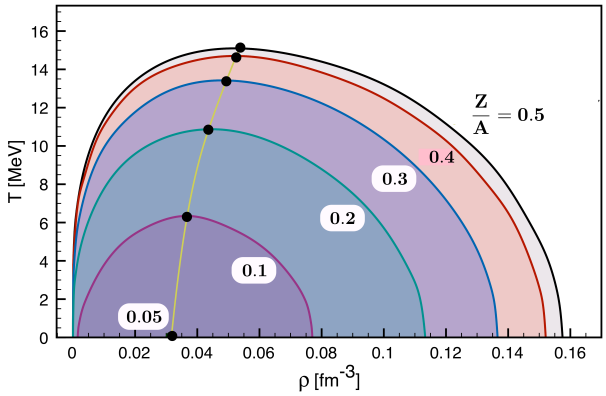

Figure 2: Phase diagram and coexistence region of liquid and gas phase of nuclear matter for different proton fractions.

the correlation effects due to 2π-exchange tend to stabilize the in-medium chiral condensate. At higher temperatures, $T \approx 100\,\mathrm{MeV}$, the linear density dependence of the dropping condensate is restored. Altogether we conclude from this analysis that there is no indication of a chiral phase transition at least up to twice normal nuclear matter saturation density $2\,\rho_0 \simeq 0.3\,\mathrm{fm}^{-3}$, and at temperatures $T \lesssim 100\,\mathrm{MeV}$.

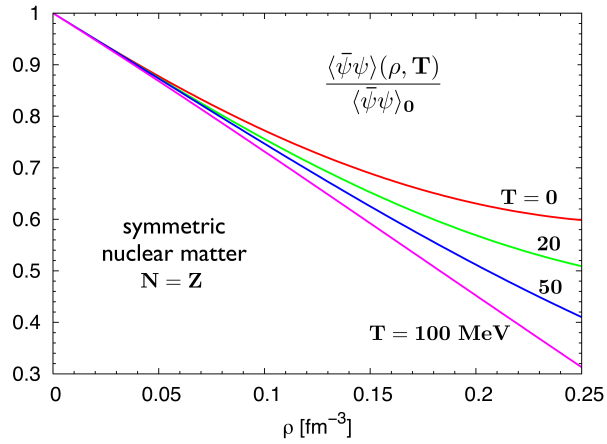

Figure 3: Ratio of the in-medium chiral condensate in symmetric nuclear matter to its vacuum value versus baryon density for different temperatures.

References

[1] S. Fritsch, N. Kaiser, W. Weise, Nucl. Phys. A **750** (2005) 259.

[2] N. Kaiser, P. de Homont, W. Weise, Phys. Rev. C **77** (2008) 025204.

[3] S. Fiorilla, N. Kaiser, W. Weise, in preparation.

Electromagnetic transition form factors of light vector mesons

C. Terschlüsen[*1] *and S. Leupold*[2]

[1]Institut für Theoretische Physik, Universität Gießen, Germany; [2]Institutionen för fysik och astronomi, Uppsala Universitet, Sweden

Electromagnetic form factors are used to study the intrinsic structure of hadrons. While form factors for transitions of pseudoscalar mesons can be calculated using chiral perturbation theory, the form factors for the hadronic resonances ρ-, ω-, and ϕ-meson were so far described with phenomenological models as standard vector meson dominance (VMD). The success of standard VMD is ambiguous: On the one hand, there are form factors as, e.g., the one for the transition $\eta \to \gamma$ which are well described. On the other hand, there are form factors where standard VMD fails to describe the available experimental data. One of these form factors, which could not been described so far, is the $\omega \to \pi^0$ transition form factor. As it can be seen in Fig. 1, the form factor calculated with standard VMD (dot-dashed line) does not describe the data taken by the NA60 collaboration for the decay $\omega \to \pi^0 \mu^+ \mu^-$ [1]. Thereby, the form factor is plotted as a function of the invariant mass $m_{l^+l^-}$ of the dilepton l.

In [2], a counting scheme for both the light vector mesons (A) and pseudoscalar mesons (B) was proposed. There, all meson masses where treated as soft, i.e.

$$m_A \sim Q,\, m_B \sim Q \tag{1}$$

for a typical momentum Q. Thus, a derivative will scale as

$$\partial_\mu \sim Q \tag{2}$$

if decays are considered. The counting scheme was used in [3] to calculate in leading order the form factors for the transitions of the light vector mesons ω and ϕ into pseudoscalar mesons. One of the considered transitions was the $\omega \to \pi^0$ transition. The corresponding form factor is also plotted in Fig. 1 (solid line). Obviously, the experimental data are well described by this form factor whereas the standard VMD form factor fails to do so. Our calculation only misses the last three data points.

Additionally, the partial decay widths,

$$\Gamma_{\omega\to\pi^0\mu^+\mu^-} = (9.85 \pm 0.58) \cdot 10^{-7}\,\mathrm{GeV}, \tag{3}$$
$$\Gamma_{\omega\to\pi^0 e^+e^-} = (6.93 \pm 0.09) \cdot 10^{-6}\,\mathrm{GeV}, \tag{4}$$

agree very well with the experimental values [4],

$$\Gamma^{\mathrm{exp}}_{\omega\to\pi^0\mu^+\mu^-} = (8.15 \pm 2.13) \cdot 10^{-7}\,\mathrm{GeV}, \tag{5}$$
$$\Gamma^{\mathrm{exp}}_{\omega\to\pi^0 e^+e^-} = (6.54 \pm 0.54) \cdot 10^{-6}\,\mathrm{GeV}, \tag{6}$$

for both the decay of an ω-meson into a neutral pion and a dimuon and the decay into a dielectron.
Furthermore, the decays of an ω-meson into an η-meson and a dilepton and of a ϕ-meson into an η-meson and a dilepton were considered in [3]. Again, the available experimental data are described well.

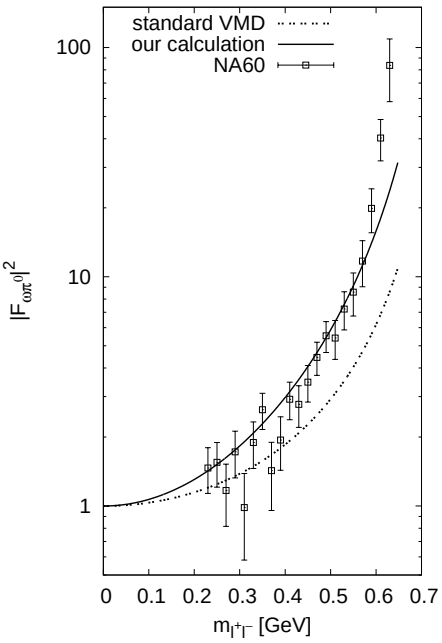

Figure 1: Form factor of the $\omega \to \pi^0$ transition calculated with the standard VMD model (dot-dashed line) and our calculation (solid line) in comparison to data taken by the NA60 collaboration for the decay into dimuons.

The presented work is intimately connected to the physics at FAIR: The understanding of vector meson dominance is a key ingredient to explore the in-medium changes of hadrons which could be deduced by HADES and CBM from the dilepton emission of a nucleus-nucleus collision. Concerning (vacuum) hadron physics the developed power counting scheme will form the input (scattering kernel) for coupled-channel calculations which use pseudoscalar and vector mesons as active degrees of freedom. This will be important to unravel the nature of hadronic resonances which will be produced and studied with high accuracy by $\bar{\mathrm{P}}$ANDA.

References

[1] R. Arnaldi et al., Phys. Lett. B 677 (2009), 260.

[2] M.F.M. Lutz, S. Leupold, Nucl. Phys. A 813 (2008), 96.

[3] C. Terschlüsen, S. Leupold, Phys. Lett. B 691 (2010), 191.

[4] K. Nakamura et al., J. Phys. G 37 (2010), 1.

* carla.terschluesen@theo.physik.uni-giessen.de

Large-N_c operator analysis of 2-body meson-baryon counterterms in the chiral Lagrangian

M.F.M. Lutz[1] *and A. Semke*[1]
[1]GSI, Darmstadt, Germany

The chiral $SU(3)$ Lagrangian with the baryon octet and decuplet fields has been widely used in the literature. So far the sector of the chiral Lagrangian involving the decuplet fields is much less explored as compared to the sector involving the baryon octet fields. A new type of application was suggested in Ref. [1] where the leading order term involving the decuplet fields was used as the driving term in a coupled-channel computation. It was shown that the s-wave interaction of the Goldstone bosons with the decuplet states leads to the formation of a resonance spectrum with $J^P = \frac{3}{2}^-$ quantum numbers reasonably close to the empirical one. In order to improve such an approach it is important to consider chiral correction terms. The purpose of the present work is to study the Q^2 counter terms involving the baryon decuplet fields systematically [2]. Corresponding terms for the baryon octet fields are known (see e.g. [3, 4]). A complete and minimal list of the terms involving the decuplet fields is presented in this work for the first time [2].

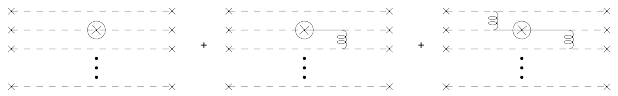

Figure 1: Expansion in terms of quark-gluon vertices.

In order to reduce the number of unknown parameters, the expansion in the inverse number of colors, N_c, is performed also in [2]. We apply the technology developed in Refs. [5, 6]. We consider matrix elements of the product of two axial-vector quark currents in baryonic states. The leading terms in the low-energy expansion of them are governed by the Q^2 chiral Lagrangian. The $1/N_c$ expansion of these matrix elements is most economically carried out in terms of effective spin-flavor quark operators, which parameterize an infinite number of quark-gluon diagrams. The diagrammatic representation of matrix elements of an one-body quark operator in terms of quark-gluon vertices and in terms of effective n-body operators is shown in Figs. (1) and (2), respectively. The infinite tower of quark-gluon diagrams parameterized by a single effective two-body operator is indicated in Fig. (3).

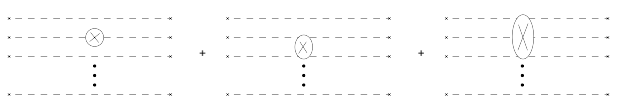

Figure 2: Expansion in terms of effective vertices.

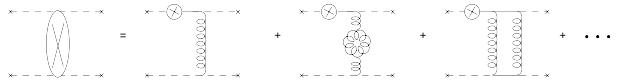

Figure 3: Diagrammatic representation of a two-body operator.

The N_c scaling behaviour of the matrix elements arise via the N_c-dependence of the quark-gluon vertices and, consequently, via the scaling behavior of the effective operators. At the given order in the $1/N_c$ expansion, the relevant operators are determined applying the operator reduction rules of Ref. [6].

A rigorous correlation of the chiral Q^2 parameters is achieved upon the evaluation of matrix elements of current-current correlation functions. Matching the results obtained in both, the low-energy and the $1/N_c$ expansions, leads to several constraints for the chiral parameters. All together we find 25 chiral symmetry preserving terms relevant at order Q^2. At leading order in the $1/N_c$ expansion we derive 18 sum rules, which reduce the number of free parameters to 7.

At present such sum rules can not be confronted directly with empirical information. They are useful constraints in establishing a systematic coupled-channel effective field theory for meson-baryon scattering beyond the threshold region. A further possible application is the chiral extrapolation of the baryon octet and decuplet masses where the considered Q^2 counter terms turn relevant at subleading orders.

References

[1] E.E. Kolomeitsev and M.F.M. Lutz, Phys. Lett. **B 585** (2004) 243.

[2] M.F.M. Lutz and A. Semke, Phys. Rev D. (in print).

[3] Ch.-H. Lee, G.E. Brown, D.-P. Min and M. Rho, Nucl. Phys. **A 585** (1995) 401.

[4] M.F.M. Lutz and E. E. Kolomeitsev, Nucl. Phys. **A 700** (2002) 193.

[5] M.A. Luty and J. March-Russel, Nucl. Phys. **B 426** (1994) 71.

[6] R. Dashen, E. Jenkins and A.V. Manohar, Phys. Rev. **D 49** (1994) 4713.

On causality, unitarity and perturbative expansions

I.V. Danilkin[1,2], *A. M. Gasparyan*[1,2], *and M.F.M. Lutz*[1]
[1]GSI, Darmstadt, Germany; [2]ITEP, Moscow, Russia

Recently a novel scheme for studying hadronic interactions beyond the threshold region was introduced by two of the authors [1]. The main objective of that work is a controlled realization of the causality and unitarity condition in a perturbative application of the chiral Lagrangian. The starting point are partial-wave dispersion relations. A generalized potential is constructed from the chiral Lagrangian in the subthreshold region and analytically extrapolated to higher energies. The partial-wave scattering amplitudes are obtained as solutions of non-linear integral equations.

For quantum field theoretic systems, where it is already difficult to compute the interaction, our method proves very efficient. The purpose of the present study is an illustration of the method for a schematic system where the exact solution is known [2].

We consider the quantum mechanics of two particles defined by a superposition of a long-range and a short-range Yukawa potentials. Typically the long-range forces are rather weak and perturbative but the short-range forces are strong and nonperturbative. For example in nucleon-nucleon scattering the central part of the pion-exchange potential has a coupling constant that is three times smaller than its critical value. We renormalize the short-range force as to arrive at a closer correspondence to effective field theories.

The analytic properties of the scattering amplitude generated by a Yukawa potential is well understood. A key observation is the known analytic structure of the generalized potential $U(q^2)$.

$$U = T - \int_0^\infty \frac{dq'^2}{\pi} \frac{q^2+\mu_M^2}{q'^2+\mu_M^2} \frac{\rho(q'^2)}{q'^2-q^2-i\epsilon} |T(q'^2)|^2 \,.$$

If the Taylor expansion of $U(q^2)$ around $q^2 = 0$ is known (analogously to the effective field theories), we can use the method of conformal mapping to analytically extrapolate the generalized potential onto the whole positive real axis with $q^2 \in (0, \infty)$. This method consists in expansion of the generalized potential in terms of a new variable ξ. We studied various combinations of attractive and repulsive potentials and observed a rapid convergence of the expansion in ξ in all cases. The example of attractive short-range potential is illustrated by Fig. 1, where one can see the dependence of the scattering phase shift on the reduced energy q^2/μ^2.

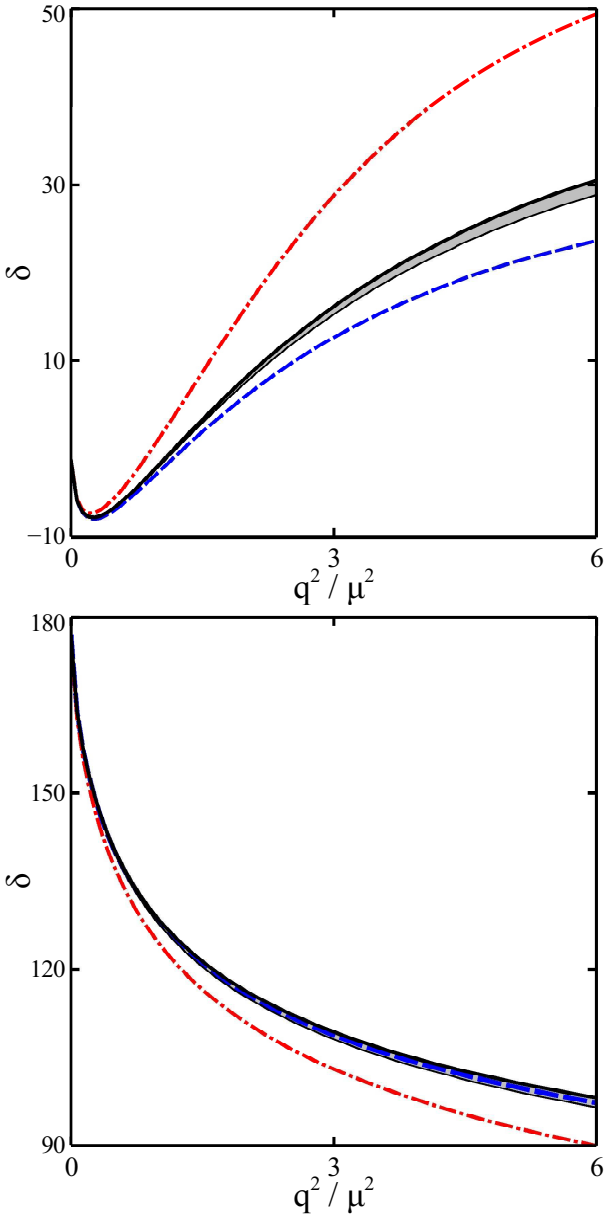

Figure 1: Case study with attractive short-range force. The upper and lower figures follow with repulsive and attractive long-range potential. The first second and third orders in ξ-expansion are denoted by dashed, dash-dotted lines and thin solid lines respectively. The exact phase shifts is denoted by the thick solid line.

References

[1] A. Gasparyan and M. F. M. Lutz, Nucl. Phys. A **848**, 126 (2010) [arXiv:1003.3426 [hep-ph]].

[2] I. V. Danilkin, A. M. Gasparyan, M. F. M. Lutz, [arXiv:1009.5928 [hep-ph]].

Photon- and pion-nucleon interactions in a unitary and causal effective theory

A. M. Gasparyan[1,2] *and M.F.M. Lutz*[1]
[1]GSI, Darmstadt, Germany; [2]ITEP, Moscow, Russia

In recent years photon- and pion-nucleon interactions have been successfully used as a quantitative challenge of chiral perturbation theory (χPT), which is a systematic tool to learn about low-energy QCD dynamics [1]. The application of χPT is however limited to the near threshold region. A method to extrapolate χPT results beyond the threshold region using analyticity and unitarity constraints was proposed recently in [2].

Our approach is based on the chiral Lagrangian involving pion, nucleon and photon fields including terms relevant at the order Q^3. The relevant counter terms of the Lagrangian are adjusted to the empirical data available for photon and pion scattering off the nucleon. We focus on the s- and p-wave partial-wave amplitudes and do not consider inelastic channels with two or more pions. We recover the empirical s- and p-wave pion-nucleon phase shifts (cf. Fig. 1) and pion photoproduction multipoles up to about 1300 MeV quantitatively.

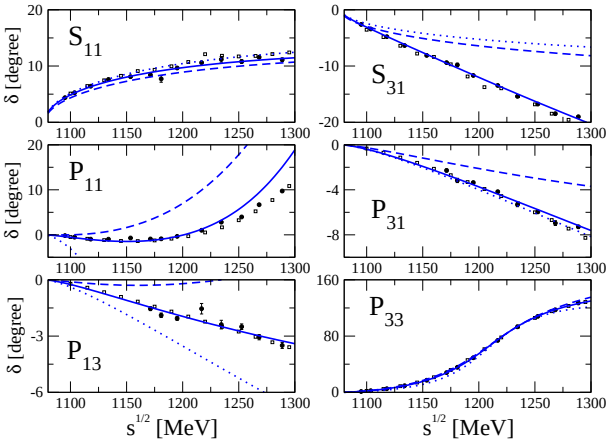

Figure 1: Results of the fit for πN S and P-wave phase shifts. The solid curves correspond to the full Q^3 results, the dashed curves to Q^2 results, and the dotted curves to Q^1 calculation.

Our result for the photon asymmetry close to the pion production threshold is in a disagreement with an old measurement at MAMI which obtained a significantly larger value. We observe a sign change for this observable near threshold (see Fig. 2). New results from MAMI which are currently being analyzed should shed more light on this issue. A possible inconsistency of the old results with some preliminary new results is currently being discussed.

Most predictive in our scheme is proton Compton scattering, which involves no additional free parameter. Our results for the differential cross section and beam asymmetry agree well with empirical data. The photon threshold region, the pion-production threshold region, and the isobar region are equally well reproduced. This is nicely illustrated by Fig. 3, which shows the energy dependence of the cross section at fixed scattering angle $\theta \simeq 90^\circ$.

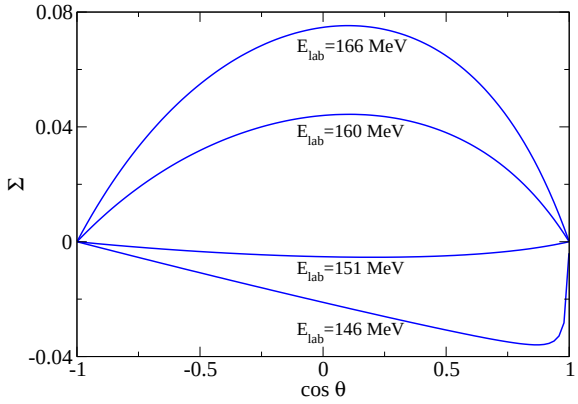

Figure 2: Energy dependence of the photon asymmetry in neutral pion photoproduction from the coupled-channel theory. The solid lines correspond to our calculation with only s- and p-wave multipoles included. The effect of higher partial waves is shown by the dashed lines.

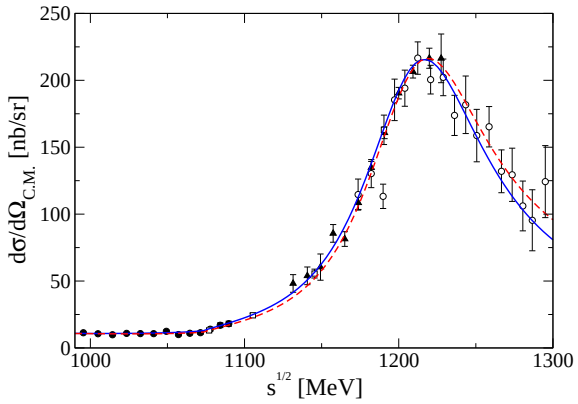

Figure 3: Compton scattering off the proton as a function of energy at scattering angle $\theta = 90^\circ$. The solid lines follow from the our partial-wave amplitudes with $J \leq 3/2$. The dashed lines show the effect of partial-wave contributions with $J > 3/2$.

References

[1] V. Bernard, Prog. Part. Nucl. Phys. **60**, 82 (2008) [arXiv:0706.0312 [hep-ph]].

[2] A. Gasparyan and M. F. M. Lutz, Nucl. Phys. A **848**, 126 (2010) [arXiv:1003.3426 [hep-ph]].

Universality of short-range nucleon-nucleon correlations

W. Horiuchi[1], *H. Feldmeier*[1], *T. Neff*[1], *and Y. Suzuki*[2,3]

[1]GSI, Darmstadt, Germany; [2]Niigata University, Niigata 950-2181, Japan; [3]RIKEN, Wako 351-0198, Japan

In nuclei, the nuclear interaction induces strong short-range correlations among the nucleons. Realistic nucleon-nucleon interactions, which reproduce the nucleon-nucleon scattering phase-shifts and deuteron properties, contain short-range repulsive and tensor components. Due to the short-range repulsion, nucleon pairs will not be found at distances below 0.5 fm. This is reflected by a high momentum component in the momentum distribution. The tensor correlations induce further momenta above the Fermi momentum. Though these correlations can only be measured indirectly, some physical observables may reflect the high momentum component. These days short-range correlations attract increasing interest. Early measurements which try to extract information on the short-range correlations have been carried out at JLab [1]. These correlations also provide important information on the saturation property in nuclear matter.

We investigate the structure of short-range correlations in many-body states. The highly correlated many-body states are represented with an explicitly correlated basis which enables us to get a precise solution of a many-body Schrödinger equation for a realistic interaction [2, 3]. The variational parameters in the basis are determined by a stochastic variational method [2, 4] and the basis dimension is increased until good convergence is reached. We investigate the wave functions of ^{3}H, ^{3}He and ^{4}He using the Argonne V8′ interaction.

The antisymmetrized many-body state Φ_{JM} contains all information about the nuclear system. Its A-body density is a function of A position or momentum vectors and $4 * A$ spin-isospin possibilities and hence can not be visualized easily. Therefore we integrate and sum over $A-2$ single-particle degrees of freedom and are left with the two-body density. This represents an average over all particle pairs in the many-body state. In addition we integrate over the center of mass position of the pair and obtain the two-body densities for the four spin-isospin channels which are possible for a nucleon pair. The relative two-body density is given by

$$\rho^{\rm rel}_{SM_S,TM_T}(\boldsymbol{r}) = \frac{1}{2J+1}\sum_M \times \langle \Phi_{JM}| \sum_{i<j}^{A} \hat{P}^{SM_S}_{ij}\hat{P}^{TM_T}_{ij}\delta^3(\hat{\boldsymbol{r}}_i - \hat{\boldsymbol{r}}_j - \boldsymbol{r})\,|\Phi_{JM}\rangle\,. \quad (1)$$

This is the probability density to find a nucleon pair at the relative position $\boldsymbol{r} = \boldsymbol{r}_1 - \boldsymbol{r}_2$ in the spin S, M_S and isospin T, M_T channel. The operators $\hat{P}^{SM_S}_{ij}$ and $\hat{P}^{TM_T}_{ij}$ project on spin and isospin of the pair, respectively.

Fig. 1 shows cuts of the normalized two-body density $\rho^{\rm rel}_{11,00}(\boldsymbol{r})/\rho^{\rm rel}_{11,00}(\boldsymbol{r}_n)$ along the z-direction and the x-direction. We normalize the quantities at $\boldsymbol{r}_n = (0, 0, 1{\rm fm})$, where the densities are close to their maximum value. It is surprising to see in Fig. 1 that for small distances all five densities practically coincide along the z-axis. The same holds true when going along the x-axis, although the normalization was done on the z-axis. This means that not only the central correlations but also the angular dependence of the tensor correlations are almost identical at short distances. The short-range central and tensor correlations exhibit universal behavior at short distances below about 1 fm. They do not depend on the nuclear many-body states for which they have been calculated.

This universality confirms the basic assumption of the unitary correlation operator method (UCOM) [5]. In the UCOM, short-range correlations are described explicitly with central and tensor correlation operators. In Fig. 1, we also display the two-body density of ^{4}He calculated with the UCOM and find very good agreement with the accurate calculation.

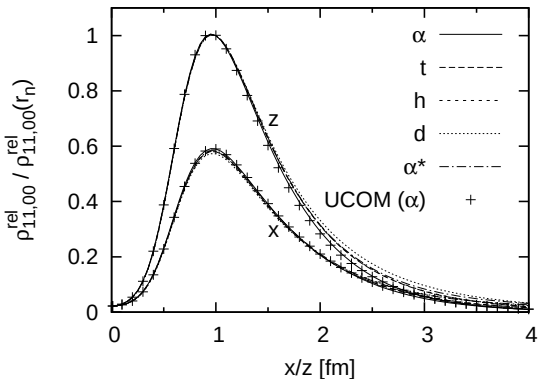

Figure 1: Cuts of $\rho^{\rm rel}_{11,00}(\boldsymbol{r})/\rho^{\rm rel}_{11,00}(\boldsymbol{r}_n)$ at $\boldsymbol{r}_n$=(0,0,1fm) for deuteron (d), triton (t), ^{3}He (h), ^{4}He (α) and the first excited state of ^{4}He (α^*). The result with the unitary correlation operator method (UCOM) for ^{4}He is also displayed.

References

[1] R. Subedi *et al.*, Science 320, (2008) 1476.

[2] K. Varga and Y. Suzuki, Phys. Rev. C 52, (1995) 2885.

[3] Y. Suzuki, W. Horiuchi, M. Orabi, and K. Arai, Few Body Syst. 42, (2008) 33.

[4] Y. Suzuki and K. Varga, "Stochastic Variational Approach to Quantum-Mechanical Few-Body Problems", Lecture Notes in Physics, Vol. 54, Springer, Berlin Heidelberg.

[5] R. Roth, T. Neff, and H. Feldmeier, Prog. Part. Nucl. Phys. **65**, (2010) 50.

Status of the NuSTAR@FAIR projects

T. Nilsson[1] and C. Scheidenberger[2] for the NuSTAR collaboration

[1]Chalmers University of Technology, Sweden, [2]GSI Darmstadt and Justus-Liebig-University Gießen, Germany

The NuSTAR facility at FAIR will open up completely new possibilities to investigate a multitude of aspects within the domain of **Nu**clear **ST**ructure, nuclear **A**strophysics and **R**eactions. Through the availability of unique beams of unstable nuclei, the possibilities to vary the isospin parameter will be unprecedented. Being accompanied by a number of complementary state-of-the-art experimental set-ups, the NUSTAR programme will be able to address contemporary questions within fundamental physics such as:

- What are the limits of existence of nuclei?
- What is the isospin dependence of the effective nucleon-nucleon interaction and of the equation of state of nuclear matter?
- How is the shell structure modified in exotic nuclei and how do new collective modes manifest themselves far away from stability?
- How are the heavy elements produced in the universe?

The crucial infrastructure for these investigations is the forthcoming fragment separator Super-FRS, that will be able to operate at the dramatically increased primary beam intensities delivered by SIS-100, reaching up to 10^{12} primary ions per second. This will happen through a three-stage separation scheme, where superconducting magnets will be utilised to a large extent. This design will permit increasing the acceptance substantially compared to the existing FRS at GSI, and for the "hot" fission products having large transversal momenta, the overall intensity increase will be in the range of 10^3 - 10^4. The Super-FRS layout includes three branches that are designed for specific characteristics of the secondary beams, connected to three experimental areas; the high-energy, the low-energy and the storage ring branch. The Super-FRS is by itself a highly sophisticated device and an intense R&D effort is underway to be able to handle the intense beams foreseen. This includes radiation-hard super-conducting magnets, high-power targets, beam dumps and surrounding shielding as well as tracking detectors for particle identification at high rates, see contribution by M. Winkler et al. in this report. As such, the Super-FRS will constitute an integral part of any NuSTAR experiment, and is being constructed within an international collaboration. The Super-FRS is schematically shown in Figure 1. After having settled the modularized start version (MSV) in 2009, the present efforts concentrate on its realization. Following the founding of FAIR GmbH during 2010, the collaboration implied in the conception of the Super-FRS was reinforced in order to involve outside scientists even further. Immediately after the foundation, in early October 2010, the NuSTAR sub-collaborations met in a common NuSTAR week, for the first time outside GSI, held at Lund University, Sweden. The meeting replaced the specific collaboration meetings. During part of the meeting, emphasis was put on the synergies between the NuSTAR (and other FAIR) projects through six topical common working groups convening. Furthermore, an adjacent symposium on storage-ring physics at the NESR was held, together with the SPARC and FLAIR collaborations within the APPA scientific pillar. Here, first steps towards a roadmap for storage-ring physics at GSI/FAIR were taken, including a reinforced programme at the existing ESR, since the NESR appears only in module 4 of the MSV. Thus, the experimental projects within NuSTAR are progressing on their respective R&D- and construction programmes, to be coherent with the corresponding time-scales implied by the modularization of the FAIR facility.

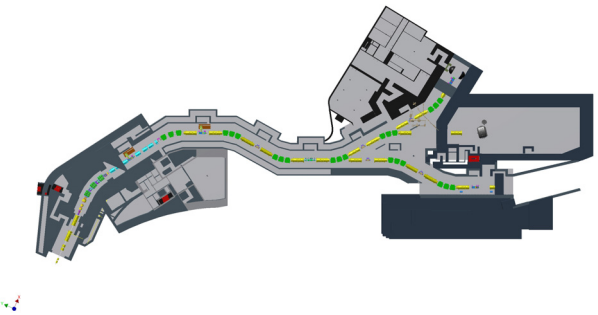

Figure 1: The Super-FRS from the production target up to its final achromatic focal planes.

The R^3B setup will be situated at the high-energy branch of the Super-FRS, envisaging a broad programme of physics investigations by reactions at relativistic energies using unstable beams. The goal is to characterise these reactions fully by complete kinematics studies for all outgoing fragments, protons, neutrons and gamma rays, and from this information draw conclusions concerning structure and dynamics of exotic nuclear systems. For example, studies on open quantum systems at and beyond the drip-lines, single-particle strength evolution with isospin and reaction rates that are crucial for nuclear astrophysics are to be performed. The current ALADIN-LAND setup in the existing Cave C is in the process of transforming to the early phases of the R^3B, with upgrades in detector systems and read-out electronics. Simultaneously, the running programme as well serves as pilot experiments for the future programme. Gradually, all existing systems will be replaced by state-of-the-art detectors, such as diamond detectors for heavy-ion tracking, a

micro-vertex tracker for recoil particles, the CALIFA calorimeter for gamma rays and light ions and the NeuLAND neutron detector. Also the large-aperture dipole magnet GLAD will be taken into operation in Cave C before being moved to the HEB cave at FAIR.

The low-energy branch will host the needed elements for precision measurements with slowed-down and stopped ions, obtained through employing the energy buncher, as well to be functioning as a spectrometer. Stopping the ions in a subsequent cryogenic gas cell will permit extracting low-energy, low-emittance beams suitable for laser spectroscopy and trap experiments, while preserving the chemical insensitivity, which is intrinsic to the in-flight production and separation method. The envisaged availability of low-energy antiprotons as well as low-energy radioactive ion beams (RIB) opens up prospects for antiprotonic exotic atoms as a powerful tool for nuclear structure studies, as proposed in the exo+pbar experiment.

HISPEC will be doing in-beam spectroscopy with exotic beams, employing the AGATA advanced tracking gamma-ray spectrometer in order to obtain maximum efficiency and resolution for a large range of reaction types at intermediate energies. Here, a rich physics programme will open up and AGATA will be complemented by further systems for reaction product identification and spectroscopy, like the LYCCA device. Following approval of the LYCCA TDR, the first phase, LYCCA-0, has been commissioned at GSI during 2010. The device will be operating within the PRESPEC campaigns in the coming years, also in conjunction with the AGATA demonstrator, which will run for physics experiments at GSI from mid 2012 on.

The DESPEC project aims at complete, high-resolution decay spectroscopy on stopped beams as a tool to study the structure of exotic nuclei. The project comprises a multitude of methods and detection systems for particles and gamma rays. The AIDA implantation detector for beta-, proton- and alpha-particle spectroscopy is already in the construction phase. Additional systems for low- and intermediate neutron detection like BELEN and MONSTER are currently entering into the demonstrator phase, with first results emerging.

The MATS and LaSPEC projects have a scientific focus on investigations of ground-state properties such as masses, spins, and electromagnetic moments of short-lived nuclei. This will be made possible by using Penning trap and laser spectroscopy, also with highly charged ions. MATS and LaSPEC have during 2010 received approval for their TDR, published in [0], and prototype setups are being constructed and utilised at the Mainz TRIGA reactor before the implementation at FAIR.

In the MSV, the ring branch of the Super-FRS will only comprise the CR, but already large parts of the ILIMA project accommodated here will be extremely competitive in exploring the mass surface far from stability through isochronous mass spectrometry. Many nuclei lying within the r-process path will become attainable for direct mass measurements for the very first time. These measurements, together with half-life studies and the measurement of beta-delayed neutron emission probabilities, will yield urgently needed data for a detailed understanding of r-process nucleosynthesis. Time-of-flight detectors and a novel concept for the use multiple Schottky probes is currently ongoing.

The class of experiments crucially in need of the NESR will, when the further modules of the FAIR project have been realised, constitute a new domain within RIB science, where FAIR will increase its uniqueness on the global perspective. This encompasses the EXL project, aimed at low momentum-transfer reactions with the internal target in the NESR that are complementary to what is attainable with R^3B, the ELISe electron-ion scattering project that will permit e.g. investigations of charge distributions using elastic electron scattering on unstable species, and eventually the AIC antiproton-ion collider that will share the electron ring ER with ELISe to permit matter radii studies of exotic nuclei through antiproton annihilation reactions. Albeit having a longer time perspective for completion, there are major progresses also among the NESR-based projects (see further contributions to this report), e.g. pilot reaction experiments in the ESR in view of EXL and the recent completion of a document defining the physics performance of ELISe [0].

In conclusion, 2010 has been a year of both evolution and adaptation to the MSV for the NuSTAR projects, with concrete progress of many subsystems in terms of TDRs, pilot experiments, demonstrators and the final-stage first systems being realised. This all points towards an extremely exciting future for science, using radioactive beams at FAIR.

[1] D. Rodríguez et al., Eur. Phys. J. Special Topics 183, 1 (2010).
[2] A. Antonov et al., accepted for publication in Nucl. Instr. Meth. A.

Super-FRS Design Status Report

M. Winkler[1], K.-H. Behr[1], A. Breidert[1], A. Brünle[1], H. Geissel[1,2], M. Gleim[1], C. Karagiannis[1], A. Kelic[1], B. Kindler[1], E. Kozlova[1], A. Kratz[1], M. Krause[1], H. Leibrock[1], Yu.A. Litvinov[3,1], B. Lommel[1], C. Mühle[1], G. Münzenberg[1], I. Mukha[1], C. Nociforo[1], W.R. Plaß[2], A. Prochazka[1], C. Scheidenberger[1,2], C. Schlör[1], H. Simon[1], M. Tomut[1,4], H. Weick[1], C. Will[1], J.S. Winfield[1], and M. Yavor[5]

[1]GSI, Darmstadt, Germany; [2] JLU Giessen, Germany; [3] MPI Heidelberg, Germany; [4]NIMP, Bucharest, Romania; [5]IAI RAS, St. Petersburg, Russia.

System and building design

Figure 1 shows the layout of the Super-FRS which was adapted to the Modularized Start Version (MSV) of FAIR. The preliminary planning of the NUSTAR buildings was finished and for the buildings within the MSV the approval planning was started which covers in particular the shielding design including access labyrinths and media ducts [1].

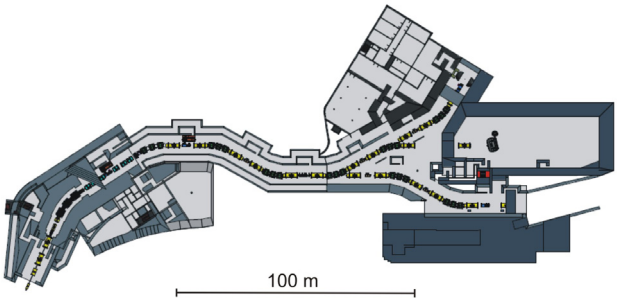

Figure 1: Layout of the Super-FRS facility including the NUSTAR buildings (Modularized Start Version).

Radiation damage

The latest results on radiation damage studies in graphite for target and beam catchers show that ion-induced structural transformation follows different paths for the energy range dominated by electronic loss and elastic collisions, respectively [2]. The material evolves toward glassy carbon in the first case or towards nanocrystalline and latter amorphous carbon in the other case. Strong stresses develop at the interface between irradiated and non-irradiated material. Cracks appear when the highly stressed interface between beam spot and non-irradiated material is situated in the vicinity of another stress concentrator. However, high temperature irradiation experiments at the GSI M-branch with online monitoring of radiation damage show that this effect is reduced at temperature of about 900 ^{0}C and especially at 1500 ^{0}C where the vacancies are highly mobile [3].

Remote handling and hot cell complex

Due to the high radiation and activation in the target area and the Pre-Separator of the Super-FRS remote handling will be applied for maintenance purpose. The concept is based on a vertical plug system which involves a combination of beam-line inserts (e.g. target, beam-catchers, etc.) with a local mobile shielding that can be removed individually from their vacuum chamber as one unit ('plug'). The plugs can be transported to a close-by hot cell using a shielded flask. The plugs will be inserted from the top into the cell. Inside the cell the inserts can be exchanged using standard handling tools (power manipulator, master-slave manipulator, etc.). Consumables and other activated waste can be packed into standard 200 l barrels which can be stored temporarily in the storage cell. Figure 2 shows the layout of the hot cell complex.

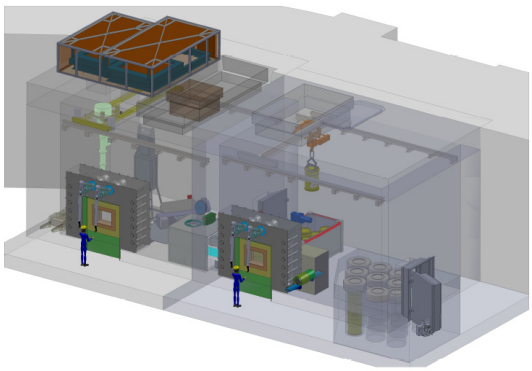

Figure 2: The hot cell complex consists of a maintenance cell (left side) and the storage cell (right side).

Magnets

The prototype of a radiation resistant dipole underwent a complete testing program for the factory acceptance test at BINP Novosibirsk. The required gap field of 1.6 T could be reached with the nominal current of 640 A. A complete magnetic field map was measured. After re-machining of the detachable pole end plates the magnet is within the specified integral homogeneity of $\pm 3 \times 10^{-4}$. Long term stability tests, ramping tests and thermal stability tests were performed without any problems.

Final quench tests as well as further cold tests of the superconducting dipole magnet developped together with the FAIR China Group have been performed successfully by IMP in Lanzhou. The obtained data will be required for the development of the series production of the SC dipoles magnets for Super-FRS.

References

[1] A. Plotnikov *et al*., this report.
[2] M. Krause *et al*., this report.
[3] M.Avilov *et al.*, this report

#m.winkler@gsi.de

Commissioning of the LYCCA-ToF-ΔE-E detector array*

A. Wendt[1], J. Taprogge[1] M.A. Bentley[4], P. Boutachkov[2], J. Cederkall[3], D. DiJulio[3], J.Gerl[2], P. Golubev[3], R. Hoischen[2,3], N. Kurz[2], E. Merchan[2], S. Pietri[2], P. Reiter[1], D. Rudolph[3] and L. Scruton[4]

[1]Institut für Kernphysik, University of Cologne, Germany; [2]GSI, Darmstadt, Germany; [3]Department of Physics, Lund University, Sweden; [4]University of York, United Kingdom

The Lund-York-Cologne-CAlorimerter LYCCA is a new Time-of-Flight, ΔE-E telescope detector array for NUSTAR´s future High-resolution In-flight SPECtroscopy (HISPEC) campaign. It will be employed for tracking and particle identification after nuclear reactions with secondary radioactive beams at the FRS final focal plane [1]. In 2010 the PRESPEC campaign started as precursor of HISPEC with commissioning of newly developed HISPEC detectors and first in-beam γ-ray-spectroscopy measurements with the former Euroball cluster germanium detectors.

LYCCA combines several detectors at different positions around the secondary target as illustrated in Fig. 1. At the target position a fast plastic scintillator timing detector [2] and a position sensitive double-sided segmented silicon strip detector (DSSD) are located. After a flight path of 3.5 m the LYCCA chamber is housing a second timing detector and the ΔE-E-modules.

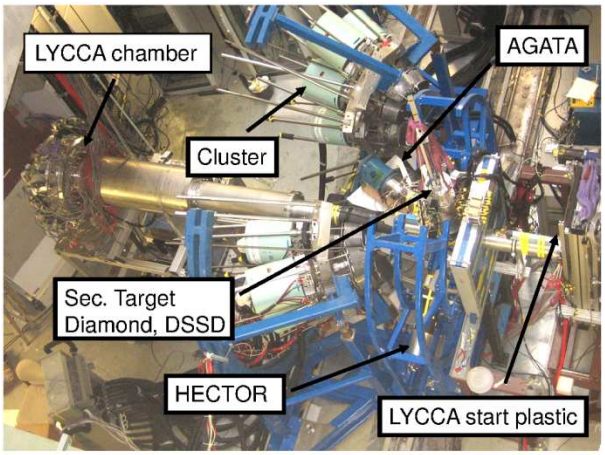

Figure 1: LYCCA detectors in the FRS-S4 area.

The charge and total kinetic energy (TKE) of the incoming ions is determined via a ΔE-E measurement. A first implementation of LYCCA comprises 12 ΔE-E telescope modules, with a DSSD and 9 CsI scintillators per module. Both DSSD sides are 32 times segmented providing an active area of 58x58 mm^2. The single CsI scintillator covers a front face of 19x19 mm^2. Crystals with an active length of 13 or 33 mm are available.

The mass of the reaction product is measured by combining the ToF information with the ion´s TKE. The short flight path of requires highest ToF resolution. To distinguish between neighbouring isotopic masses in the region of A=100 a combined (start and stop detector) ToF-resolution better than 100 ps is needed, which calls for either new approaches in scintillator-based timing measurements [2] or new materials such as diamond detectors.

First commissioning experiments were performed at the FRS S4 position with primary beams of ^{64}Ni at 550 AMeV and its fragmentation product ^{63}Co. More than 600 energy and timing channels were successfully put into operation and were included in the FRS detector assembly. Measured energy resolution values for DSSD and CsI detectors compare very well with results of simulations [3,4]. The very good timing resolution of the plastic scintillators is obtained by combining 32 photo multiplier signals per event and detector [2]. Table 1 summarizes typical resolution values of the detectors and expected ones from LISE simulations.

Detector	^{64}Ni exp.	^{64}Ni sim.
DSSD ΔE @ 348 MeV	3,1%	4,5%
CsI E @ 5,27 GeV	1,1%	1,3%
Stop-Plastic	29 ps	

Table 1: Resolution values (FWHM) of LYCCA detectors

The measured energy resolution values are slightly better than the simulated ones. These results were confirmed by later experiments with ^{86}Kr and ^{124}Sn beams. We suspect that energy straggling in materials is overestimated by the calculations. Fig. 2 shows the ΔE-E spectra of neutron deficient Sn and In isotopes, which allows Z identification. Fig. 3 shows the TOF-E spectra gated on In isotopes. Data shown here are taken from a Coulomb excitation measurement of a neutron deficient Sn isotope.

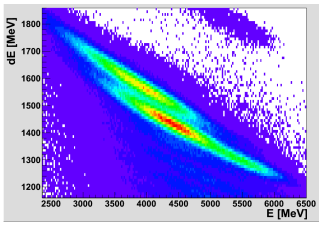

Figure 2: ΔE vs E

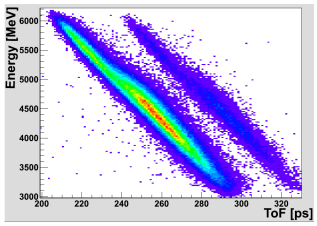

Figure 3: ToF vs E

In summary LYCCA was brought into operation fulfilling the requested specifications. Especially the mass separation up to A=100 can be achieved.

References

[1] D. Rudolph et al. "LYCCA Technical design report" http://wwwnsg.nuclear.lu.se/lycca.

[2] R. Hoischen et al., submitted to Nucl. Instr. Meth. A.

[3] M.J. Taylor et al., Nucl. Instr. Meth. A606, 589 (2009).

[4] D. Bazin et al., "The program LISE: a simulation of fragment separators" NIM-A 482, 1-2, 307-327 (2002).

* Supported by the German BMBF (06KY9136 TP7), the F&E project KJOLIE1012, the HGS-HIRe and the Swedish Research Council

Development of slowed down beams at GSI/FAIR.

F. Naqvi[1,2], P. Boutachkov[2], M. Górska[2], J. Gerl[2], F. Farinon[2], K. Hadynska[4], R. Janik[5], I. Kojouharov[2], N. A. Kondratyev[6], A. Marcos A.G.[7], I. Mukha[2], P. Napiorkowski[4], C. Nociforo[2], D. Pietak[4], W. Prokopowicz[2], S. Pietri[2], A. Prochazka[2], H. Schaffner[2], P. Strmen[2], and H. Weick[2]

[1]Institut für Kernphysik, Universität zu Köln, 50937 Köln, Germany; [2]Helmholtzzentrum für Schwerionenforschung, D-64291 Darmstadt, Germany; [4]Faculty of Physics, University of Warsaw, PL-00681 Warsaw, Poland; [5]Comenius University, 818 06 Bratislava, Slovakia; [6]Flerov Laboratory of Nuclear Reactions, JINP, 141980 Dubna, Russia; [7]Centro Nacional de Aceleradores CNA, 41092 Seville, Spain

The GSI/FAIR [1] facility will provide high-intensity relativistic beams of radioactive ions. To perform multi-step Coulomb excitation the relativistic beams will be slowed down to Coulomb barrier energies using a thick degrader. In contrast to the ISOL facilities, in the experiments with such slowed down beams, short lived fragments can be accessed with high survival probability after the deceleration. Feasibility studies of the slowed down beam setup involving deceleration of a ^{64}Ni beam upto the Coulomb barrier energy in a thick Al degrader was performed at the FRagment Separator (FRS) at GSI. The characteristics of a primary ^{64}Ni beam after deceleration were investigated with a detector system optimized for an event-by-event identification. A comparison of experimental data with the simulations is presented in this report.

Slowing down the beam in a thick degrader produces significant energy and angular straggling. The simulated energy spread for a primary ^{64}Ni beam at 250 MeV/u, slowed down to 13 MeV/u in a homogeneous Al degrader of 3.95 g/cm^2 corresponds to 9 MeV/u (FWHM) [3]. During the deceleration nuclear reactions also occur, which leads to the production of unwanted isotopes. The simulated integrated background contribution amounts to $\sim 0.1\%$ of the slowed down ^{64}Ni ions in an energy window of $\pm$0.5 MeV/u at 10 MeV/u [4]. This energy window corresponds to the time resolution of the TOF detectors used in the present experiment.

The experimental setup included a plastic scintillator and an Al degrader positioned at the final focal plane of FRS followed by two position sensitive micro-channel plate (MCP) detectors [3]. The beam velocity after the degrader was obtained from the time-of-flight (TOF) measurement between the fast scintillator and the MCP detectors. The extracted energy distribution (from TOF measurement) of the dominant ^{64}Ni ions after the degrader is shown in Fig. 1. The width of the energy distribution was 8 MeV/u (FWHM). In order to estimate the background underneath the ^{64}Ni energy peak, the simulated background distribution was scaled to the observed distribution in the range of 20 - 60 MeV/u. This resulted in a peak-to-background ratio of 2% in an energy range of 13 $\pm$ 0.5 MeV/u. The difference of an order of magnitude between the simulated and the experimental values is due the technical specifics of the experimental setup.

Summarzing, the experimental results are qualitatively in agreement with the performed simulations and hence, support the suitability of the slowed down beams for selected secondary reactions.

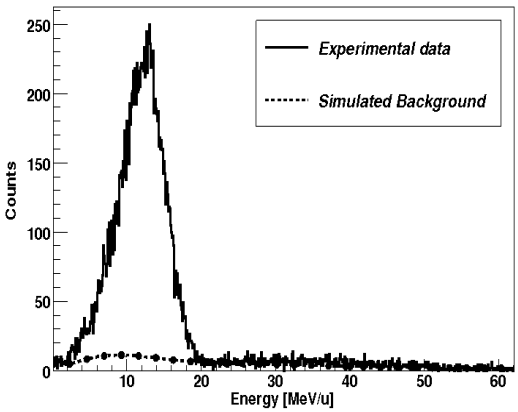

Figure 1: Energy distribution of ^{64}Ni ions after slowing down in Al degrader. An average energy of 13 MeV/u was obtained with a width of 8 MeV/u. The dashed curve represents the simulated background.

References

[1] www.fair-center.org.

[2] N. Iwasa *et al.*, Nucl. Instrum. Methods Phys. Res. B **126**, 284 (1997).

[3] F. Naqvi *et al.*, Acta Phys. Polonica B, (to be published).

[4] P. Boutachkov *et al.*, GSI scientific report (2007).

Tagging of alpha particles with a large scale, high timing resolution beam profile monitor

*M. Pfeiffer**, *G. Pascovici, S. Thiel, N. Warr, and J. Jolie*
Institut für Kernphysik, Universität zu Köln, Germany

A prototype of a new beam profile monitor with tracking and TOF capabilities for degraded beams at HISPEC/DESPEC at FAIR has been built at the Institute of Nuclear Physics at the University of Cologne [1]. The device constists of two detectors in series, each with an active area of 80x100mm^2. The working principle is based on secondary electrons being created by the ions passing through a thin sheet of material $\left(140-180\mu\mathrm{g/cm}^2\right)$. Afterwards the electrons are accelerated and deflected out of the projected ion beam path by an electrostatic top-assembly [2]. The final sub-assembled electron-detector consists of a chevron MCP-stack giving a fast timing signal and a position-sensitive dual delay line [3] (see figure 1).

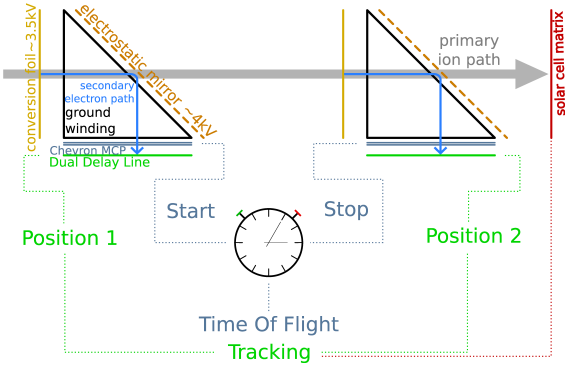

Figure 1: Schematic working principle.

Using the spectrometric information from a 32 solar cells matrix (16 x 2 OR-wired), we performed several experiments with different configurations of various alpha sources and masks (i.e. the institute's logo, different holes, etc.). By gating on individual solar cell pixels, it was possible to select a given trajectory between the source and that pixel, thereby demonstrating a proof of concept of the tracking capabilities.

The timing resolution for TOF could be decreased to a value of $210(59)\mathrm{ps}$ with a fully divergent alpha beam from a triple alpha source covering the whole active area. Simulations showed, that the intrinsic resolution should be in the order of $< 150\mathrm{ps}$. A major impact on the timing resolution in this domain are the energy-straggling of the alphas by the coating of the source and the thickness of the emitter material itself. We plan to further increase the resolution by the use of a collimated, monoenergetic ion beam.

Since the timing resolution of our detector depends the coating of the source, we can use the detector to qualitative probe the structure of different sources. We investigated the build-up of a triple alpha source by tagging single alpha particles emitted by the source. Using the TOF resolution, it is even possible to determine that the different emitters are mounted in a layered structure instead of being mounted all together in one single layer. Additionally, the energy information was used to identify the emitting isotope. We could determine the order of the different layers from the degradation of the time resolution from one layer to the next, as seen in figure 2.

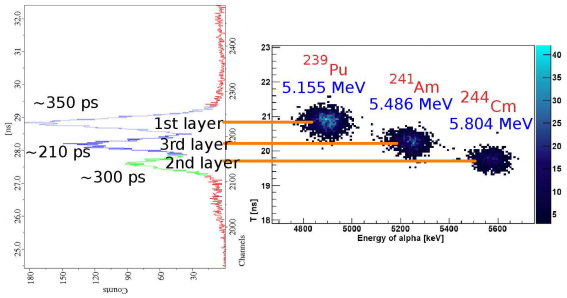

Figure 2: TOF vs. Energy and projection of the Y axis, showing the timing resolution of the different emitters and thus their order inside the source.

Concerning the spatial resolution,the detector shows a large difference between the X and Y axis (where Y goes from bottom to top whilst X goes from left to right, as seen in the direction of the beam). While the Y-resolution is rather constant over the whole area, the X-resolution gets worse with increasing position in Y. One reason seems to be the heliocentrical ground winding, as simulations show [4]. Another reason seems to be the influence of corner effects, which are stronger in the top of the electrostatic top assembly than in the bottom (concerning the Y-axis), but this is still under investigation.

Work supported by F & E project KJOLIE and KJOLIE1012.

References

[1] M. Pfeiffer et al, GSI SciRep 2009 (2010), No. 1, p. 30

[2] E.M. Kozulin et al, Instr. and Exp. Tech. (2008), Vol. 56, No. 1, p. 44

[3] W. Starzecki et al, Nucl. Instr. Meth. (1982), Vol. 193, p. 499

[4] K. Kosev et al, NIM in Phys. Res. A (2008), Vol. 594, No. 2, p. 178

* pfeiffer@ikp.uni-koeln.de

FRS Ion Catcher: Setup, Status and Perspectives*

W.R. Plaß[1,2], S. Ayet[1,2], U. Czok[1], P. Dendooven[3], T. Dickel[1,2], J. Ebert[1], H. Geissel[1,2], E. Haettner[1,2], C. Jesch[1], W. Kinsel[1,2], M. Ranjan[3], M. Petrick[1], M.P. Reiter[1], S. Purushothaman[2], D. Schäfer[1], T. Schäfer[1], C. Scheidenberger[1,2], J. Van de Walle[3], H. Weick[2], and M.I. Yavor[4]

[1]Justus-Liebig-Universität Gießen, Germany; [2]GSI, Darmstadt, Germany; [3]KVI, University of Groningen, The Netherlands; [4]Institute for Analytical Instrumentation, Russian Academy of Sciences, St. Petersburg, Russia

At the FRS Ion Catcher at GSI, exotic nuclei, which have been produced by projectile fragmentation or fission and separated and range-bunched in the FRS, will be slowed-down, thermalized in a cryogenic stopping cell, extracted and made available to precision experiments with ions almost at rest. A novel multiple-reflection time-of-flight mass spectrometer (MR-TOF-MS) [1][2] will be used to perform mass measurements of very short-lived and rare nuclei (half-lives down to ms, ∼10 detected nuclei) with accuracies on the level of 10^{-7}. It will also provide isobarically clean beams for mass-resolved decay spectroscopy experiments. In addition, the FRS Ion Catcher will serve as test bench for the cryogenic stopping cell [3] of the Low-Energy Branch (LEB) of the Super-FRS at FAIR.

The beam line of the FRS Ion Catcher (Fig. 1) is designed according to a novel concept [4]: It is based on a versatile system of RF quadrupoles (RFQs), which despite its compactness (length ∼2 m) allows for differential pumping in the vicinity of the stopping cell and for ion beam cooling, transport, bunching, beam monitoring and mass separation. It is thus ideally suited to the space-restricted area at the final focus of the FRS. Vacuum separation between stopping cell and beam line is realized using a gate valve and a retractable RFQ segment. An electrically switchable RFQ switchyard enables introduction of reference ions from alkali and laser ablation ion sources as well as distribution of ions to different experimental stations. A triple-RFQ system that implements a subset of these capabilities has recently been developed for the SHIPTRAP facility and has been shown to provide ion beam cooling, bunching and mass separation with a suppression of neighboring isotopes by at least 4 orders of magnitude, while achieving a transmission efficiency of almost unity [5].

The beam line of the FRS Ion Catcher is currently under construction and will be installed at GSI together with the stopping cell and the MR-TOF-MS during the first half of 2011. A first on-line experiment is planned to be performed shortly afterwards. Besides on-line commissioning of the cryogenic stopping cell of the LEB, the experimental program will address mass measurements and decay spectroscopy of both, very neutron-rich nuclides, e.g. at the N=82 shell closure, and very proton rich nuclides, such as heavy N=Z nuclei.

References

[1] W.R. Plaß et al., Nucl. Instrum. Methods B 266 (2008) 4560.

[2] T. Dickel, PhD Thesis, Gießen University (2010).

[3] S. Purushothaman et al., GSI Sci. Rep. 2009 (2010), p. 27.

[4] W.R. Plaß et al., Eur. Phys. J. Special Topics 150 (2007) 367.

[5] E. Haettner et al., this volume.

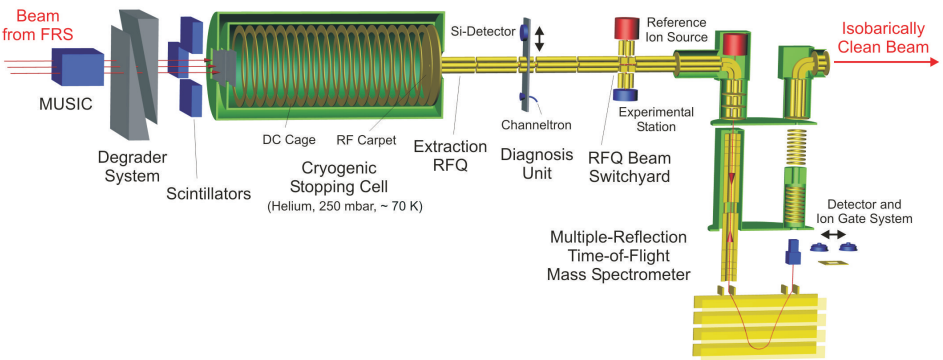

Figure 1: Schematic figure of the FRS Ion Catcher setup. Exotic nuclei produced, separated and range-bunched in the FRS are injected into the cryogenic stopping cell. They are thermalized and extracted using DC and RF electric fields and separated from the buffer gas in an extraction RFQ. Various detectors can be moved into the RFQ beam line. Introduction of reference ions and ion beam distribution is achieved using an RFQ beam switchyard. A multiple-refelcetion time-of-flight mass spectrometers serves for high-resolution mass mass measurements and as isobar separator.

* Work supported by the BMBF under contract No. 06GI9114I.

Offline test of a Cryogenic Stopping Cell for the Low-Energy Branch of the Super-FRS at FAIR

S. Purushothaman[1], *P. Dendooven*[2], *T. Dickel*[3], *H. Geissel*[1,3], *W. R. Plaß*[1,3], *M. Ranjan*[2], *D. Schäfer*[3], *C. Scheidenberger*[1,3], *and J. Van de Walle*[2]

[1]GSI, Darmstadt; [2]KVI, University of Groningen, Netherlands; [3]Justus-Liebig-Universität Gießen

Here we report the first successful offline test of the cryogenic gas stoping cell developed for the low-energy branch of the Super Fragment Separator (Super-FRS) at FAIR in Darmstadt, Germany. This gas cell has a stopping volume of length 1 m and diameter 0.25 m. A DC field throughout the length of the cell and a RF carpet with DC field superimposed at the exit side to guide the ions towards the exit-hole without hitting the wall are opted to ensure the fast and efficient extraction of the ions stopped throughout the volume of the cell (Figure 1). Once the ions reach the exit hole, the gas flow will drag them out of the stopping volume. Extensive simulations were performed to guide the design of the DC and RF ion guides of the stopping cell [1].

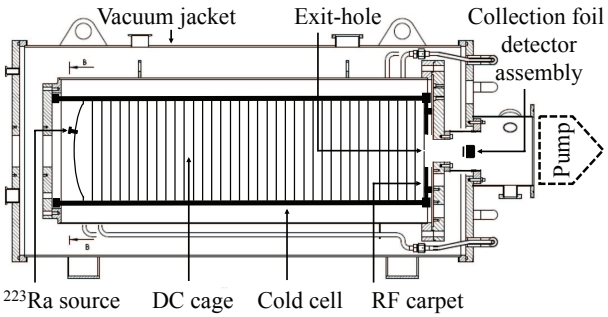

Figure 1: Experimental setup

Alpha-decay recoil ions from a 3 kBq ^{223}Ra source served as energetic probes for this offline test. Gas cell is cooled down to 87 K and the helium gas flow to the gas cell is regulated to maintain a pressure of 50 mbar (equivalent to 170 mbar at room temperature). The 100 keV recoil ^{219}Rn ions are thermalized in the helium gas. Here the high purity of the helium gas is ensured by operation at low temperature. The choice for cryogenic operation is based on earlier work on ion survival and transport in a closed cell [2, 3].

In this experiment an average DC electric field of 10 V cm^{-1} applied across the DC cage to transport the ions towards the RF carpet. A DC field of 5 V cm^{-1} is applied across the radius of the carpet which operates at a frequency of 5 MHz. A peak-to-peak RF voltage of up to 120 V was used during these measurements. Extracted ions are collected onto a aluminum foil kept at -1 kV at a distance 12.5 cm away from the exit hole. A silicon detector is placed behind the aluminum foil to measure the alpha decays of the ^{219}Rn collected on the foil. Extraction of ^{219}Rn ions is measured as a function of peak-to-peak RF voltage (Figure 2).

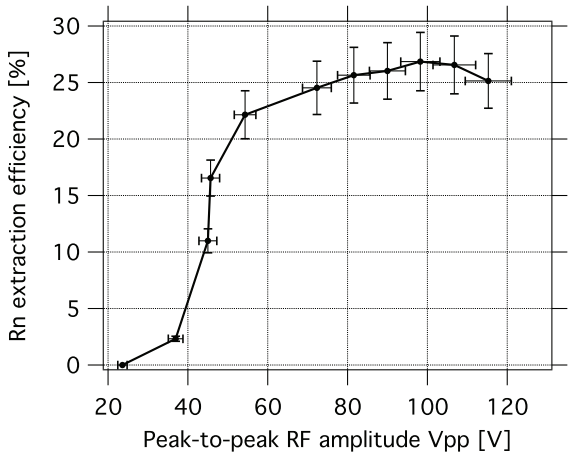

Figure 2: Overall extraction efficiency of ^{219}Rn ions as a function of peak-to-peak RF voltage.

The observed behavior of the extraction efficiency as a function of peak-to-peak RF voltage is in line with results from our simulation work [1]. If the stoping helium gas is ultra-pure and the applied electric field is high enough to transport ions out of the ionization region before neutralization, a maximum of about 30% of the ^{219}Rn recoils will survive as ions during thermalization [2, 4]. The maximum extraction efficiency of ^{219}Rn ions in this experiment is measured to be 27(3)% , indicating ∼100% transport and extraction efficiency of the thermalized ions from the gas cell. Further offline tests are underway and will be compared with systematic simulations. Online commissioning of the cryogenic gas stopping cell at GSI is planned for the third quarter of 2011.

References

[1] Daniel Schäfer, Diploma thesis, Justus-Liebig-Universität Gießen, 2010.

[2] P. Dendooven et al., Nucl. Instrum. Meth. A, 558 (2006) 580.

[3] S. Purushothaman et al., Nucl. Instrum. Meth. B, 266 (2008) 4488.

[4] S. A. Eliseev et al., Nucl. Instrum. Meth. B, 258 (2007) 479.

Further Advances in the Development of a Multiple-Reflection Time-of-Flight Mass Spectrometer for Isobar Separation and Mass Measurements at the LEB*

T. Dickel[1,2], *C. Jesch*[1], *W. R. Plaß*[1,2], *S. Ayet*[1,2], *U. Czok*[1], *H. Geissel*[1,2], *F. Lautenschläger*[1], *M. Petrick*[1], *C. Scheidenberger*[1,2], *B. Sun*[1,2], *and M. I. Yavor*[3]

[1]Justus-Liebig-Universität, Gießen, Germany; [2]GSI, Darmstadt, Germany; [3]Institute for Analytical Instrumentation of the Russian Academy of Sciences, St. Petersburg, Russia

A multiple-reflection time-of-flight mass spectrometer (MR-TOF-MS) is a compact, high-performance, multi-purpose, non scanning mass spectrometer[1]. A MR-TOF-MS has been built and characterized[2]. It features high mass resolution ($\geq 10^5$), high mass accuracy ($\approx 10^{-7}$), fast operation ($\approx$ ms), high transmission efficiency (up to 70 %) and single ion sensitivity. It is intended for use at low energy radioactive ion beam (RIB) facilities as an isobar separator, for direct mass measurements of very short-lived nuclei and as a diagnostic device. In particular, the MR-TOF-MS is part of the Low-Energy Branch of the Super-FRS at FAIR [3].

Current Status and Further Developments

Based on the settings found previously [4], further optimization gained improved insight in the instrument. The mass resolving power has been improved by a factor of two to 600,000. This resolving power is independent on the number of ions over a large range of ions per cycle (Fig. 1).

Developments for further advances in the instrument's performance are underway. Currently, the achievable mass resolving power is limited by the stability of the voltages supplying the analyzer. The electronic circuits stabilizing these voltages have been re-engineered, improving the stability from currently 2.5 ppm to 1 ppm. In the current setup, only the potential on four of the analyzer electrodes was stabilized. For further improvements, all eight electrodes will be provided with stabilizing electronics. Additionally, high precision power supplies have been acquired.

The current temperature dependence of the TOF is 20 ppm/K. The integration of the re-engineered electronics and a temperature stabilization of the system will gain an improvement of an order of magnitude. The extremeley low dark count rate of the detector in the interval of a mass line (≈ 1 per year) allow mass measurements of extremely rare nuclides.

Further improvements that will be implemented are the removal of mechanical deficiencies, an improved ion-optical layout and the increase of the kinetic energy of the ions from 750 eV to 1.3 keV.

It is assumed that by implementing these improvements, the mass resolving power of the MR-TOF-MS will be increased by a factor 2, bringing the resolution of many isomeric states within reach.

* Work supported by th BMBF under contract No 06GI9114I and by GSI under contract GIMET2

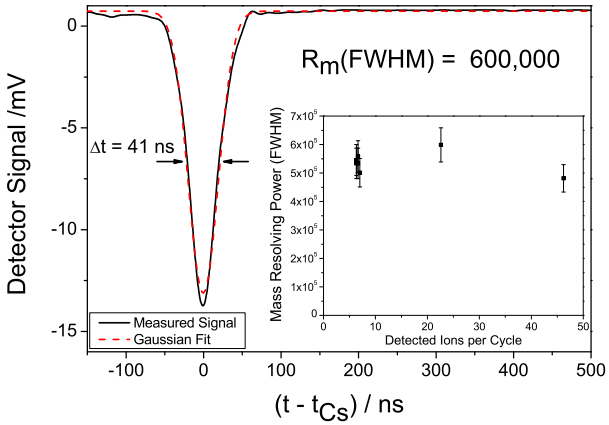

Figure 1: Mass spectrum of ^{133}Cs with a mass resolving power of 600,000 FWHM. Note the Gaussian peak shape. Inset: Dependence of the resolving power on number of ions per cycle.

For the use of the MR-TOF-MS as isobar separator, the efficient recapture of the ions after mass separation and subsequent transport to the connected experiments is paramount. An energy buncher[1], utilizing pulsed and static retarding fields, has been designed. Simulations show that the buncher will enable efficient injection into a recapture RFQ by reducing the energy distribution by a factor ≈ 20.

Outlook

A second MR-TOF-MS intended and customized for isobar separation at TITAN of TRIUMF (Canada) is in design state, featuring a novel type of RFQ-type switch yard. It will be used as a prototype for MR-TOF-MS at other facilities.

First mass measurements of exotic nuclei with the present MR-TOF-MS will be performed at the FRS Ion Catcher in 2011.

References

[1] W. R. Plaß et al., Nucl. Instrum. Methods B, 266 (2008) 4560.

[2] T. Dickel, Doktorarbeit, Justus-Liebig-Universität, 2010.

[3] D. Rodriguez et al., EPJST, 183 (2010).

[4] T. Dickel et al., GSI Scientific Report 2009, p. 28.

Cooling, mass separation and bunching of fusion-evaporation ions with radiofrequency quadrupoles*

E. Haettner[1,2], *W. R. Plaß*[1,2], *S. Ayet*[1], *U. Czok*[1,2], *T. Dickel*[1,2], *H. Geissel*[1,2], *W. Kinsel*[1,2], *T. Schäfer*[1], *and C. Scheidenberger*[1,2]

[1]Justus-Liebig-Universität Gießen, Germany; [2]GSI, Darmstadt, Germany

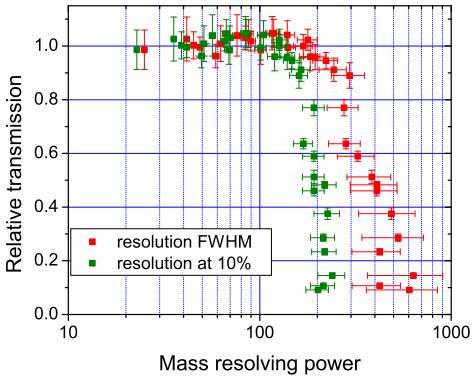

Figure 1: Relative transmission of the cooler – mass filter – combination as a function of the mass resolving power measured for Cs ions. The mass resolving power were determined at FWHM and 10% level.

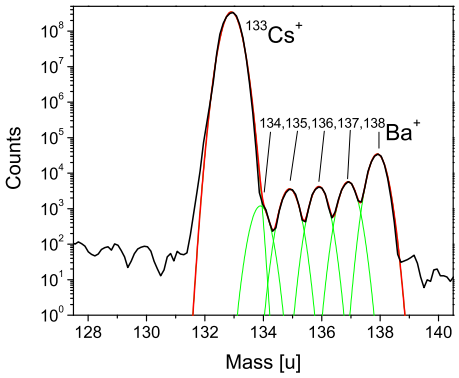

Figure 2: Separation of ^{133}Cs and the five most abundant $^{134-138}$Ba isotopes in the mass filter at 90% relative transmission. The FWHM resolving power is 240. Note that abundances use a logarithmic scale and that neighboring isotopes can be suppressed by more that 4 orders of magnitude.

An RFQ cooler, mass filter and buncher for the SHIPTRAP experiment have been designed and built [1]. This RFQ system will allow for better separation of nuclei of interest from contaminants at SHIPTRAP and thus for improved selectivity and sensitivity of the experiment.

Mass filter. A stabilization of the RF amplitude was implemented and thus the achievable mass resolving power of the mass filter for a given transmission improved considerably compared to the values reported previously [1]. A relative transmission of 90% up to a mass reolving power of 240 (FWHM) or 160 (10% peak height) has now been demonstrated for ^{133}Cs ions (Fig. 1). Similarly, for ^{39}K ions one has a relative transmission of 90% up to a mass reolving power of 80 (FWHM) or 70 (10% peak height).

Figure 2 shows the separation of neighboring masses using an earth-alkaline (Ca, Sr, Ba) ion source. The five most abundant $^{134-138}$Ba isotopes are separated. An additional line is found at mass 133 and is identified as ^{133}Cs, which is also present as contamination in the ion source. Figure 2 demonstrates a supression of neighboring mass lines by at least a factor of 10^4.

Buncher. The role of the RFQ buncher is to capture and trap the filtered ion beam delivered by the mass filter. The ions are then extracted in ion bunches and delivered to the Penning trap. Important properties such as energy spread, peak width, storage time, ion temperature and transmission and bunching efficiency were determined. It was found that a peak width (FWHM) of the ejected ions of 40 ns can be reached without exceeding the energy width acceptance of the Penning trap. This will allow for a fast broadband time-of-flight mass spectrometry at the diagnosis MCP in front of the Penning trap. For a typical time-of-flight of 30 μs between the buncher and the MCP, the peak width corresponds to a mass resolving power of 375.

Since the Penning traps are operated with a typical cycle time of about 1 s it is important to be able to store the ions sufficiently long in the RFQ buncher. A storage time with a time constant of about 20 seconds was measured for Cs^+ and O_2^+ ions.

Absolute transmission. Of particular importance for a successful use at SHIPTRAP is to obtain the highest possible transmission of nuclei of interest. Thus the absolute transmission of the complete system was measured with a stable Cs ion beam and a calibrated beam deflection unit. A transmission close to 100 % was found.

Conclusion. An RFQ system consisting of an RFQ cooler, RFQ mass filter and RFQ buncher has been built for the SHIPTRAP experiment. The system shows excellent performance and will enable mass measurements and mass-selected decay spectroscopy, e.g. of very proton-rich nuclides around ^{80}Zr and ^{94}Ag.

References

[1] E. Haettner *et al.*, GSI Scientific Report 2009 (2010) 296.

*Work supported by the Helmholtz Association and GSI (VH-NG-033), BMBF (06GI185I).

Online Study of the Rate Acceptance of a Time-of-Flight Detector and a New Anode Design with Improved Signal Quality for IMS at FRS-ESR*

N. Kuzminchuk[1, 2], S. Ayet[1, 2], M. Diwisch[1], B. Fabian[1], H. Geissel[1, 2], R. Knöbel[2], W. R. Plaß[1, 2], C.Scheidenberger[1, 2], B. Sun[1, 2], H. Weick[2] and the FRS-ESR-Collaboration

[1]Justus-Liebig Universität, Gießen, [2]GSI, Darmstadt, Germany.

For Isochronous Mass Spectrometry at the FRS-ESR facility a time-of-flight detector is used for measurements of the revolution times of stored ions. In the detector, ions passing a thin carbon foil release secondary electrons (SE), which are transported to microchannel plates (MCPs) by electric and magnetic fields. Because of the high revolution frequencies in the ESR, a high rate acceptance is required as well as good timing characteristics.

Rate acceptance

Offline studies show that MCPs with 5µm pore size can accept a higher count rate than MCPs with the same active diameter but with a commonly used pore size of 10 µm[1]. To show the advantages of a 5µm pore size MCP, the saturation effects were investigated online with Ne and Ni primary beams in the ESR using carbon [10µg/cm^2] and CsI [17µg/cm^2] foils in the time-of-flight detector. Figure 1 shows the average number of ions found per turn for both experimental data and from model predictions.

To compare the experimental data with simulations a Monte Carlo code is used to calculate the ion survival probability for a specific number of ions in the ring. The simulations include the ion optics, apertures in the ESR and the energy loss in the foil.

The dashed blue (10µm pore size MCPs) / solid red (5µm pore size MCP) lines represent the calculations, which combine these Monte Carlo simulations with a model for the dead time effect. It is known that because of the finite recharging time of an MCP channel one can observe a saturation effect. This model describes a loss of detection efficiency at high rates, which also depends on the energy loss in the foil and on the number of emitted secondary electrons. The number of SE does not change with turn number, but the detection efficiency of the MCP drops from 60% to about 10% when increasing the rate from 10 MHz to 100 MHz [2].

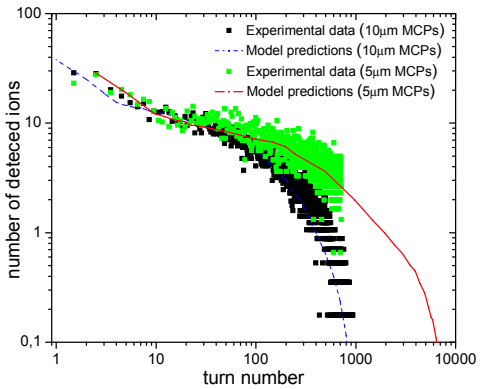

Figure 1: Development of the average ion number found per turn. Green squares present the experimental data with 5µm MCPs, black squares show the data with 10µm MCPs. Red triangles and squares show the corresponding calculations. All the data are scaled with a charge number Z^2/A and normalized to 14 ions at turn number 10.

The analysis of both experimental data confirms that the calculated function with an exponential decrease of detection efficiency describes the data within a reasonable agreement. Achieved results as it was expected from off-line measurements and calculations, less amount of energy loss in thinner carbon foil and about 4 times higher rate resistant 5µm pore size MCPs are significantly improved an ion survival in the ring.

Optimisation of the MCP signal quality

A new design of an anode was made to optimise the MCP signal quality. First tests show that by decreasing the capacitance between the anode and the MCPs the peak width can be reduced by a factor of up to two and the rise time improved by about of 20% (Figure 2).

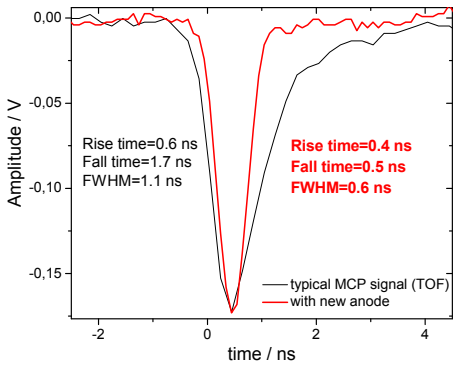

Figure 2: MCP signal shape from a present (black curve) and new anode design (red curve).

The rising slope influences the precision of the timing determination and the resolution, while with smaller value of the falling slope better separation between the weak and strong close signals can be performed during the data analysis.

References

[1] N. Kuzminchuk et al., GSI Annual Report 2009 (2010), p.35.

[2] B. Fabian, PhD thesis, Universität Gießen, 2008.

* Work supported by the BMBF under contract No. 06GI9115I

Particle Rate Calculations for the Super-FRS

J.S. Winfield[1#]

[1]GSI, Darmstadt, Germany.

The program LISE++ [1] has been used to calculate the expected total intensity of all nuclear fragments at the several focal planes along the Super-FRS for some "typical" future experiments. The purpose is to provide data for the calculation of radiation shielding beyond the target region of the Super-FRS [2]. The heat load into the degraders is also an important issue. All three branches of the Super-FRS, each with its own characteristic final energy, were explored: the High-Energy branch (HEB), the Low-Energy branch (LEB), and the Ring branch (RB). The transfer matrices used in LISE++ were taken from 1st-order GICOSY [3] ion-optics and the angular acceptances from 3rd-order MOCADI [4] simulations.

Case Studies

Eight case studies were made, either using abrasion-fission (AF) or projectile fragmentation (frag.), as follows:

1. 1.5 GeV/u ^{238}U beam, AF → **^{132}Sn**, final energy 1 GeV/u (HEB),
2. 1 GeV/u ^{40}Ar beam, frag. → **n-rich C, N & O** isotopes, final energy ~800 MeV/u (HEB),
3. 1.5 GeV/u ^{238}U beam, AF → **^{132}Sn**, final energy 740 MeV/u (RB),
4. 1.3 GeV/u ^{124}Xe beam, frag. → **^{104}Sn**, final energy 740 MeV/u (RB),
5. 1 GeV/u ^{238}U beam. frag. → **^{210}Hg**, final energy 150 MeV/u (LEB),
6. 400 MeV/u ^{124}Xe beam, frag. → **^{100}Sn**, final energy 10 MeV/u (LEB),
7. 800 MeV/u ^{238}U beam, AF → **^{78}Ni**, final energy 300 MeV/u (LEB),
8. 1.5 GeV/u ^{98}Mo beam, frag. → **^{90}Sr**, final energy 806 MeV/u (HEB).

For all cases, the primary beam intensity was assumed to be 10^{12} pps. This may be somewhat more than the anticipated initial SIS100 intensities [5], but the philosophy was to accommodate probable increases throughout the lifetime of the facility. The selected fragment for the last case, ^{90}Sr, was chosen close to stability, with the aim of transmitting ~10^6 pps to the R^{3}B cave. Such conditions might be realised for the Super-FRS either to measure nuclear reactions with very small cross-sections or for calibrations.

Aluminium is a good choice of degrader material, giving high transmission for all nuclei, and this was used for cases 4-6 and 8. However, up to 60 mm thickness of aluminium would be needed for the other cases, and copper was used for cases 1-3, 7.

#j.winfield@gsi.de

Results

The calculated rates in particles per second incident on the wedge degraders in the Pre-Separator (degr. 1) and the Main-Separator (degr. 2) are given in Table 1. Also given in the third column is the power deposited in the first degrader in Joules per second (W). The power deposited in the second degrader is negligible and is not shown.

Table 1. Total rates of all fragments at the degraders and after the final focus (in pps) for the eight cases discussed. The power deposited in the 1st degrader is given in column 3 if it is more than 0.1 W. "At final focus" means the total rate transmitted through the final selection slits at the end of the respective branch of the Super-FRS.

Case	Incident on degr. 1	Power into degr.	Incident on degr. 2	At final focus
1	1.9×10^{10}	84.8 W	1.8×10^{8}	4.6×10^{6}
2	3.1×10^{7}	-	4.0×10^{4}	3.7×10^{3}
3	1.5×10^{10}	81.5 W	9.7×10^{7}	3.2×10^{6}
4	1.9×10^{9}	2.9 W	9.3×10^{5}	3.9×10^{4}
5	1.8×10^{10}	236.0 W	7.9×10^{4}	9.7×10^{2}
6	1.2×10^{8}	-	2.5×10^{4}	2.8×10^{-1}
7	3.9×10^{8}	1.4 W	5.5×10^{5}	2.2×10^{2}
8	3.4×10^{9}	19.4 W	1.1×10^{7}	1.9×10^{6}

Discussion

The total rate of particles incident on the degraders and at the final focus is worst for case #5 where part of the 90+ charge state of the ^{238}U beam reaches the degrader in the Pre-Separator. However, the total count rates for the cases of ^{132}Sn as the chosen nucleus (#1 and #3) are comparable to case #5. The $^{238}U^{90+}$ at roughly 700 MeV/u passing through the first degrader in case #5 loses ~240 J/s energy – which is not an excessive heat load: it leads to a temperature rise of less than 3 K if the beam spot size at the degrader has a diameter of 4 cm^2.

References

[1] O.B. Tarasov and D. Bazin, Nucl. Instr. Meth. B **266** (2008) 4657.
[2] E. Kozlova et al., GSI Scientific Report 2007, GSI Report 2008-1 (2008) p. 247.
[3] http://www-linux.gsi.de/~weick/gicosy/.
[4] N. Iwasa et al., Nucl. Instr. Meth. B **126** (1997) 284.
[5] P. Spiller et al., GSI Scientific Report 2007, GSI Report 2008-1 (2008) p. 50.

Ion charge identification with silicon pixel detectors and scintillators

P.S. Marrocchesi[1], C. Angelini[2], M.G. Bagliesi[1], A.Basti[2], G. Bigongiari[1], S. Bonechi[1], M.Y. Kim[1], T.Lomtadze[2], P. Maestro[1], F. Morsani[2],

O. Adriani[3], L. Bonechi[3], M. Bongi[3], G. Castellini[3], P. Spillantini[3],

C. Nociforo[4], K.-H. Behr[4], A. Brünle[4], H. Geissel[4,5], C. Karagiannis[4], A. Kratz[4], J. Kurcewicz[4], C.Scheidenberger[4,5], C. Schlör[4], J.S. Winfield[4], and M. Winkler[4]

[1]Univ. of Siena and INFN; [2]Univ. of Pisa and INFN; [3]Univ. of Firenze, IFAC-CNR and INFN; [4]GSI, Darmstadt, Germany; [5]Justus-Liebig University, Gießen, Germany

The main goal of the S387 experiment was to test the performance of charge-sensitive detectors that were designed to separate - via multiple dE/dx measurements - ultra-relativistic ions of cosmic origin in the experiment CALET. The latter is a space instrument to be launched by JAXA at the end of 2013 to the International Space Station (ISS) where it will take data for 5 years [1].

The GSI projectile Fragment Separator (FRS) [2] has proved to be a versatile tool for production of relativistic exotic isotopes. During the test performed in October 2010, a $^{56}Ni^{26+}$primary beam was accelerated at E_{SIS}=1000-1300 MeV/u with an intensity of about 10^7ions/spill. A Be target (1.036 g/cm^2) was used to produce different charged ions by fragmentation reactions. Along the separator, no matter was present in order to accept the largest number of different species according to the acceptance of the optical device, which was set in achromatic mode. Fragment settings having A/q~2 were used. At the last focal point, up-stream of the telescope, the FRS standard equipment for particle identification was placed. Plastic scintillators provided the external trigger by the coincidence of the signals coming from two counters positioned up(down)-stream the telescope. The produced fragments were clearly identified in charge starting from Ni down to Z=9 by the MUSIC detector [3], for the same FRS setting. The count rate on the detectors was kept below 1 kHz.

Two different prototypes were tested: a telescope of 4 layers of pixelated silicon arrays with 64 pixels/sensor and 1 cm^2 pixel size [4,5]; a 10 mm thick fast scintillation counter coupled with a light-guide to a photomultiplier (R9880U). The prototypes were embedded into a high resolution tracker composed of a total of 8 silicon strip layers and scintillating fibers readout by SiPM photosensors and Multi-Anode PhotoMultipliers (MAPMT).

As shown in Fig. 1, where the scintillator signal is plotted vs. the (averaged) signal from the pixelated arrays, individual nuclei from Be to Fe were clearly separated. The partial saturation of the light fom the EJ204 scintillator was fitted and found to be consistent with the halo model of [6].

The separation of B from C is of particular importance to CALET as one of the science goals is the measurement of the ratio B/C of the relative abundances of the two elements as a function of energy up to a few TeV/n. As shown in Fig. 2, the measured charge resolution with the scintillator (in units of the elementary charge) was found to be close to 0.14 for Boron, while a better charge resolution of 0.1 was achieved with the Silicon Array.

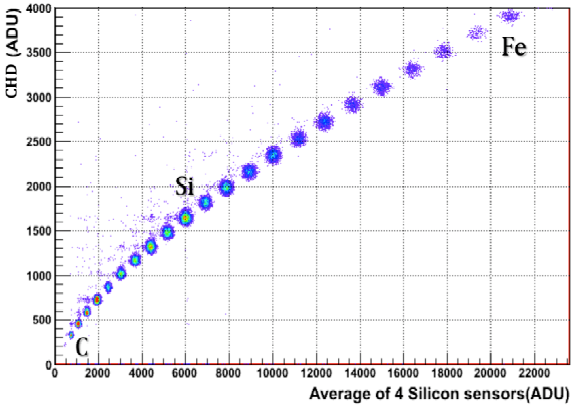

Fig. 1: Scintillator vs. Silicon Array charge measurements.

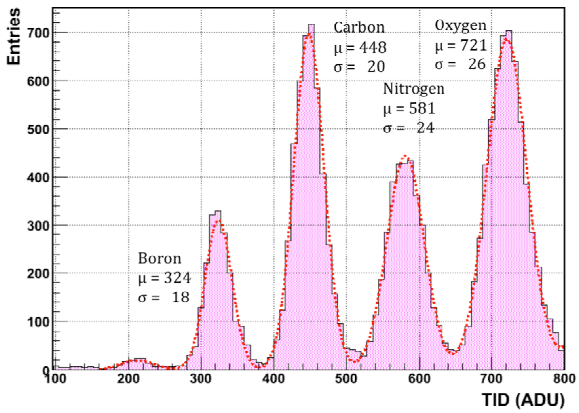

Fig. 2 Charge resolution in the BCNO region with the scintillator.

References

[1] S. Torii et al., Nuclear Physics B (Proc. Suppl.), Vol.150 (2006) 390-393

[2] H. Geissel et al. NIM B 70, (1992) 286.

[3] A. Stolz et al., GSI Report 1998, p. 174.

[4] P. S. Marrocchesi et al., Nucl. Inst. & Methods A572 (2007) 316-318

[5] P. S. Marrocchesi et al.,J.Phys.Soc.Jpn. vol.78 (2009) 181-183

[6] R. Dwyer et al., Nucl. Inst. & Methods A242 (1985) 171-176

Search for heavy neutron-rich isotopes in the element range Yb-U

J. Kurcewicz[1], S. Pietri[1], F. Farinon[1,2], H. Geissel[1,2], C. Nociforo[1], A. Prochazka[1,2], H. Weick[1], P. Allegro[3], A. Bail[16], G. Bélier[16], J. Benlliure[4], G. Benzoni[5], M. Bunce[6], M. Bowry[6], P. Boutachkov[1], R. Caballero-Folch[17], E. Casarejos[19], I.Dillmann[1,2], A. Estradé[1,18], A. Evdokimov[1,2], J.Gerl[1], M. Górska[1], A. Gottardo[7], N. Gregor[1], R. Janik[8], R. Knöbel[1], I. Kojouharov[1], T. Kubo[9], Yu. A. Litvinov[1,10], E. Merchan[1], I. Mukha[1], F. Naqvi[1,11], B. Pfeiffer[1], M. Pfützner[12], W. Plaß[2], M. Pomorski[12], Zs. Podolyak[6], P. Regan[6], B. Riese[1], M.V. Ricciardi[1], H. Schaffner[1], C. Scheidenberger[1,2], B. Sitar[8], P. Spiller[1], J. Stadlmann[1], P. Strmen[8], B. Sun[2,13], I. Szarka[8], J. Taïeb[16], H. Takeda[9], I. Tanihata[14], S. Terashima[9], J.J. Valiente-Dobón[7], J.S. Winfield[1], M. Winkler[1], H.-J. Wollersheim[1], Ph. Woods[15]

[1]GSI, Darmstadt, Germany; [2]JLU Giessen, Germany; [3]USP, Sao Paulo, Brazil; [4]USC, Santiago de Compostela, Spain; [5]INFN-Universita di Milano, Italy; [6]University of Surrey, Guildford, UK; [7]LNL-INFN Legnaro, Italy; [8]Comenius University, Bratislava, Slovakia; [9]RIKEN Nishina Center, Wako, Japan; [10]MPI-K, Heidelberg, Germany; [11]IKP, Köln, Germany; [12]IEP, Warsaw, Poland; [13]Beijing University, China; [14]Osaka University, Japan; [15]University of Edinburgh, UK; [16]CEA DAM DiF, Arpajon, France; [17]UPC, Barcelona, Spain; [18]SMU, Halifax, Canada; [19]Universidade de Vigo, Spain

As a continuation of the programme of neutron-rich isotopes studies, an experiment investigating heavy isotopes in Os and At regions was recently performed at the projectile fragment separator (FRS) [1] of GSI Darmstadt. The ^{238}U beam delivered by the SIS synchrotron in spills lasting about 2 s with a repetition period of 4 s impinged on a 1.6 g/cm^2 thick beryllium target placed at the entrance to the FRS. The primary beam intensity measured by the secondary electron monitor (SEETRAM) was of the order of $2*10^9$ ions/spill. The reaction products were separated by the FRS operated in an achromatic mode.

The FRS, combining two stages of magnetic selection and an energy loss in two degraders located at the first (S1) and second (S2) focal plane, allows a full identification of reaction products with respect to their nuclear charge Z and mass A. After the first magnetic selection and passing through the 2 g/cm^2 S1 degrader, reaction products are slowed down in a 731 mg/cm^2 aluminium degrader located at the intermediate focal plane. A second magnetic selection is applied to the ions leaving the S2 degrader. To decrease the proportion of not-fully stripped ions, a niobium and iron foil strippers were placed behind the target and the degraders, respectively.

The experimental setup preserved a high compatibility with a previous experiment performed in October 2009. The time-of-flight measurement was performed between two pairs of plastic scintillator detectors, one located in the intermediate focal plane and the other one at the final focus. The typical flight time was around 160 ns and the obtained ToF resolution was on the order of σ=40 ps.

Four TPC detectors, two placed at the intermediate and two located at the final focal plane provided tracking information (position and angle of ions).

At the exit of the spectrometer, two ionization chambers (MUSIC) were mounted with a 89 mg/cm^2 copper stripper placed in front of the second one. The MUSIC detectors delivered the energy loss signal of fragments, thus providing the information about their atomic number.

The final focal point of the separator was surrounded by the RISING germanium detector setup [2]. Isomer tagging technique was applied in order to facilitate the identification of the reaction products. The γ-radiation accompanying the decay of isomeric states in ^{204}Pb, ^{205}Pb and ^{210}Po was observed.

In this experiment several $B\rho$ settings of the FRS were used, which were chosen to yield optimum secondary beam intensities for the neutron-rich Os and At isotopes. A preliminary identification spectrum, which is a sum of events registered at the final focal plane of the FRS in aforementioned settings, is shown in Figure 1. From the online spectra we could positively identify new isotopes in the Os region. A more detailed analysis is in progress.

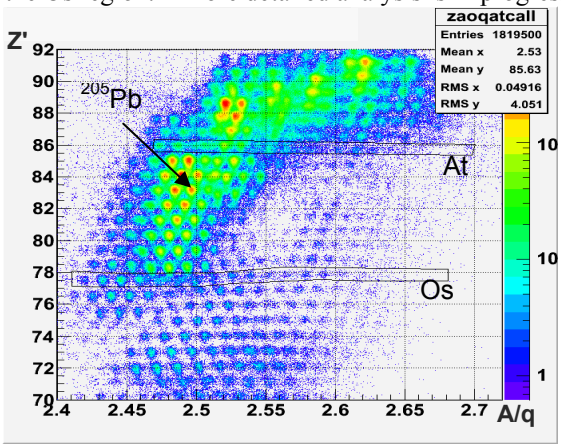

Figure 1: Preliminary identification spectrum of ions registered at the last focal plane (S4) of the fragment separator. The figure is a superposition of data from several FRS $B\rho$ settings optimised for neutron-rich At and Os isotopes.

This experiment is part of a campaign with the first goal to measure the production cross sections and to map the outskirts of the chart of nuclides up to uranium. The next steps will be half-life measurements and studies of secondary reactions and momentum distributions.

References

[1] H. Geissel et al. NIM B 70, (1992) 286
[2] S. Pietri et al. NIM B 261, (2007) 1079

Momentum distributions analysed after 1n knockout reaction at the FRS

A. Prochazka[1,2], C. Nociforo[1], R. Kanungo[3], T. Aumann[1], D. Boutin[2], A. Brünle[1], B. Davids[4], M. Diakaki[6], F. Farinon[1,2], H. Geissel[2], R. Gernhäuser[5], R. Janik[7], B. Jonson[8], B. Kindler[1], R. Knöbel[1,2], R. Krücken[5], N. Kurz[1], M. Lantz[8], H. Lenske[2], Yu.A. Litvinov[1,11], B. Lommel[1], K. Mahata[1], P. Maierbeck[5], A. Musumarra[9], T. Nilsson[8], C. Perro[3], C. Scheidenberger[1], B. Sitar[7], P. Strmen[7], B. Sun[2], I. Szarka[7], I. Tanihata[10], H. Weick[1], and M. Winckler[1]

[1]GSI, Darmstadt, Germany; [2]Justus-Liebig University, Giessen, Germany; [3]Saint Mary's University, Halifax, Canada; [4]TRIUMF, Vancouver, Canada; [5]TU München, Germany; [6]National Technical University, Athens, Greece; [7]Comenius University, Bratislava, Slovakia; [8]Chalmers University of Technology, Göteborg, Sweden; [9]INFN-LNS and University of Catania, Catania, Italy; [10]Research Center for Nuclear Physics, Osaka, Japan; [11]MPIK, Heidelberg, Germany

The one-nucleon knockout reaction is a well established tool for the investigation of the structure of exotic nuclei. The shape of the longitudinal momentum distribution of the residual fragments after the reaction is sensitive to the orbital angular momentum of the removed neutron. The absolute value of the measured removal cross section contains spectroscopic information. At the FRS, we have investigated the structure of several neutron-rich sd shell nuclei, e.g. around N=16 where a new shell gap for the oxygen isotopes was observed [1] and around the Island of Inversion where N=20 is not a good magic number anymore [2]. Details on the performed experiment are given in [1].

Here we want to describe an alternative type of the momentum analysis methods. We have chosen the ^{26}F nucleus as an example. The position distribution of the ^{25}F ions at the final focal plane of the FRS (set in a dispersion-matched mode) after one-neutron removal has several contributions in addition. One contribution is due to the atomic interaction with additional matter present at the mid-focal plane like detectors, windows, air, etc.. Another important contribution comes from the position (momentum) resolution of the FRS itself. This additional broadening of the width of the distribution is about 3% for ^{26}F. We have used two methods to take these contributions into account:

- the theoretical momentum distribution curves are convoluted with the spectrometer function (in momentum) and compared with the measured momentum distribution.
- the measured position distribution and spectrometer function (in position) are deconvoluted and the resulting position distribution is transformed to the momentum distribution and then directly compared with the theoretical curves.

The convolution method is easier to perform, but the momentum distribution can contain contributions from higher order ion optics, mainly in the tails. These are taken into account in the deconvolution method. The theoretical momentum distributions have been extracted from a Glauber model calculation. The curves calculated for one-neutron knockout from ^{26}F assuming a neutron knocked out from $d-$ and $s-$orbitals are shown in the Fig. 1. Both are plotted for a spectroscopic factor equal to one. In case of the second method, the deconvolution of the data has been done by using the iterative deconvolution algorithm, Golden deconvolution, described in Ref. [3]. The data points representing the deconvoluted momentum distribution of the ^{25}F are plotted in Fig. 1. The momentum distribution has been fitted (χ^2 minimization) with the the two possible configurations with their spectroscopic strengths as free parameters.

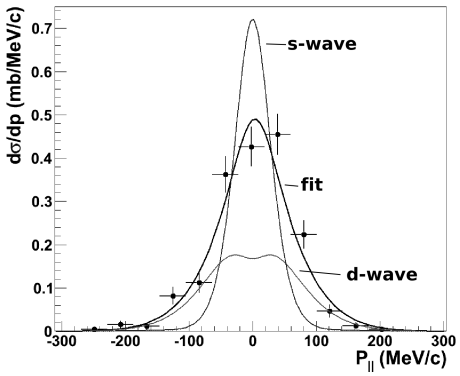

Figure 1: The deconvoluted longitudinal momentum distribution of the fragments after the one-neutron removal reaction from ^{26}F. The theoretical curves corresponding to the neutron knocked out from d- and s- orbitals are obtained from Glauber model calculations.

The preliminary results for the ^{26}F momentum distribution of the deconvolution method are 0.45 ± 0.2 and 1.2 ± 0.3 for s and d contribution, respectively. Using the convolution method the corresponding results are 0.54 ± 0.2 and 1.2 ± 0.3. The fitted values obtained with the two methods are in excellent agreement for ^{26}F and the other nuclei studied [1], demonstrating that the higher order optical contributions are in this cases not so important.

References

[1] A. Prochazka, PhD Thesis 2011.

[2] R. Kanungo et al., Phys Lett. B685 (2010) 253.

[3] M. Morhac et al.,Nucl. Instr. and Meth. B86 (1994)119.

One-neutron removal measurements from neutron-rich fluorine isotopes

A. Prochazka[1,2], C. Nociforo[1], R. Kanungo[3], T. Aumann[1], D. Boutin[2], A. Brünle[1], B. Davids[4], M. Diakaki[6], F. Farinon[1,2], H. Geissel[2], R. Gernhäuser[5], R. Janik[7], B. Jonson[8], R. Knöbel[1,2], R. Krücken[5], N. Kurz[1], M. Lantz[8], H. Lenske[2], Yu.A. Litvinov[1,11], B. Lommel[1], K. Mahata[1], P. Maierbeck[5], A. Musumarra[9], T. Nilsson[8], C. Perro[3], C. Scheidenberger[1], B. Sitar[7], P. Strmen[7], B. Sun[2], I. Szarka[7], I. Tanihata[10], H. Weick[1], and M. Winckler[1]

[1]GSI, Darmstadt, Germany; [2]Justus-Liebig University, Giessen, Germany; [3]Saint Mary's University, Halifax, Canada; [4]TRIUMF, Vancouver, Canada; [5]TU München, Germany; [6]National Technical University, Athens, Greece; [7]Comenius University, Bratislava, Slovakia; [8]Chalmers University of Technology, Göteborg, Sweden; [9]INFN-LNS and University of Catania, Catania, Italy; [10]Research Center for Nuclear Physics, Osaka, Japan; [11]MPIK, Heidelberg, Germany

The dripline of fluorine isotopes is located at larger neutron numbers (N) compared to oxygen isotopes, where the dripline is reached at N=16. One additional proton is able to bind at least six additional neutrons. According to a Monte Carlo shell model calculation the disappearing of the N = 20 shell in the light neutron-rich nuclei can cause a configuration mixing and the intruder states can have a significant contribution in fluorine isotopes around N = 20 [2]. The intruder configurations can explain the extended dripline for fluorine isotopes.

At the fragment separator (FRS) at GSI we studied the structure of $^{25-27}F$ isotopes by measuring the inclusive longitudinal momentum distributions of the residual fragments after the one-neutron removal reaction. The FRS was operated in a dispersion-matched mode. The position distribution at the final focal plane was measured using TPC detectors. Details on the performed analysis are given in [1].

The measured one-neutron removal cross sections and widths (FWHM) of the corresponding longitudinal momentum distributions for the fluorine nuclei are plotted in Fig. 1 as full circles. A simple shell model description of these isotopes suggests a valence neutron orbital $2s_{1/2}$ for ^{25}F and $1d_{3/2}$ for ^{26}F and ^{27}F. The ^{25}F nucleus has the $2s_{1/2}$ neutron orbital fully occupied, as shown by the narrower momentum distribution width. Starting from A=26 the neutrons occupy the $1d_{3/2}$ orbital. Thus, one expects a broadening of the momentum distribution. This broadening was measured and is shown in the bottom panel of Fig. 1.

The measured momentum distributions were compared with the theoretical ones extracted from a Glauber model calculation [4]. The momentum distributions were described with two configurations having the neutron knocked out from d- or $s-$orbital. From fitting the theoretical curves to the data, one estimates the relative weights of the two assumed configurations. The obtained relative admixtures of the $l = 0$ and $l = 2$ components are in agreement with the simple shell model picture. The preliminary relative weight of the $l = 2$ component increases from 23 $\pm$ 10% up to 88% $\pm$ 12% going from A=25 to A=27.

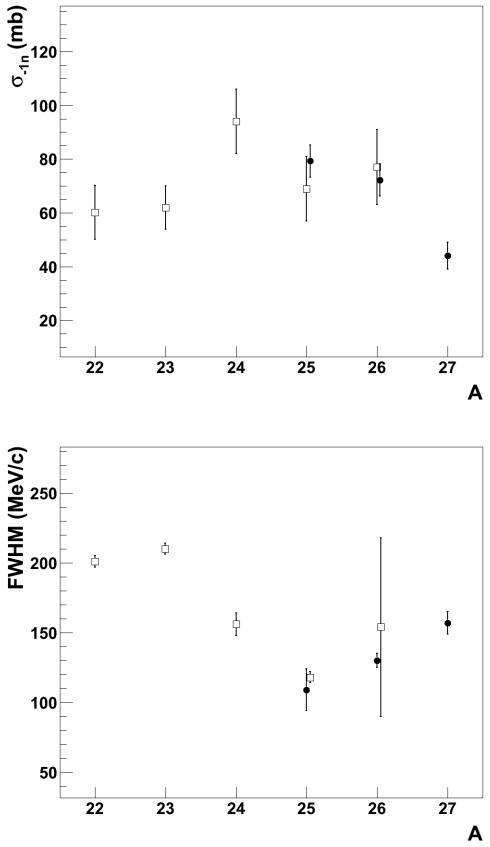

Figure 1: The measured one-neutron removal cross sections and widths (FWHM) of the corresponding momentum distributions for fluorine isotopes. The full circles are our preliminary data, the empty boxes are experimental data taken from Ref. [3].

References

[1] A. Prochazka, et al., GSI Annual Report 2010

[2] Y. Utsuno,et al. Phys. Rev. C64 (2001), 011301

[3] C. Rodriguez-Tajes, Phys. Rev. C82 (2010)024305

[4] C.A. Bertulani, Com. Phys. Com. 175 (2006) 175

Relativistic one-nucleon knockout reactions from light carbon isotopes*

V. Volkov[1,#], T. Aumann[1,2], D. Cortina-Gil[3], J. Enders[1], F. Farinon[2], H. Geissel[2], M. Holl[1], N. Iwasa[4], R. Janik[5], R. Krücken[6], P. Maierbeck[6], C. Nociforo[2], A. Prochazka[2], C. Rodriguez-Tajes[3], H. Simon[2], E. C. Simpson[7], B. Sitar[5], P. Strmen[5], K. Sümmerer[2], J. A. Tostevin[7], H. Weick[2], J. S. Winfield[2]

[1]TU Darmstadt, Germany; [2]GSI, Darmstadt, Germany; [3]Universidad de Santiago de Compostela, Spain; [4]Tohoku University, Japan; [5]Univerzita Komenskeho, Bratislava, Slovakia; [6]TU München, Germany; [7]University of Surrey, UK.

Knockout of single nucleons from fast beams allows one to investigate the single-particle structure of nuclei, in particular for rare isotopes, see Refs. [1,2]. It has been argued [3] that nucleon knockout reactions provide access to spectroscopic factors even on an absolute scale. Measured spectroscopic factors C^2_{exp} are smaller than those predicted within a shell-model calculation, C^2_{th}. The quenching factor $R_s = \sigma_{exp}/\sigma_{th} = C^2_{exp}/C^2_{th}$ from relativistic knockout appears to approach unity for small binding energies of the knocked out nucleon, whereas for deeply bound nucleons significant quenching $R_s << 1$ is observed, see, e.g., [4,5].

Experiment S341 studied, among others, the inclusive knockout reactions ^{9}Be(^{12}C,^{11}C)X, ^{9}Be(^{11}C,^{10}C)X, ^{9}Be(^{10}C,^{9}C)X, and ^{9}Be(^{9}C,^{8}B)X, thereby covering a broad range of binding energy difference values. The reactions with residues ^{9}C and ^{8}B benefit from the fact that the ground state is the only bound state in these nuclei. The reactions ^{9}Be(^{12}C,^{11}C)X and ^{9}Be(^{9}C,^{8}B)X have been carried out before and may serve for benchmarking the experiment.

The experiment used an incident ^{12}C beam from the SIS at 1670 MeV/nucl. impinging on a 4 g/cm^2 beryllium sheet at the FRS target position. At the intermediate F2 focus of the FRS, a 4.9 g/cm^2 Be target served as secondary breakup target after charge identification in a preceding scintillator. The outgoing residues were tracked using time-projection chambers (TPC). To maximize transmission, the reaction residues were detected at the third FRS focus F3 using TPC tracking and scintillation detectors for charge identification and time-of-flight measurement.

The ongoing data analysis resulted in preliminary cross-sections between 21(2) mb [for (^{10}C,^{9}C)] and 51(4) mb [for (^{12}C,^{11}C)]. Using the Glauber model for describing the reaction [6] and predictions for the spectroscopic factors from typical shell-model interactions for the p-shell, we extract the following preliminary quenching factors: 0.53(5) for (^{12}C,^{11}C), 0.47(7) for (^{11}C,^{10}C), 0.51(5) for (^{10}C,^{9}C), and 0.72(6) for (^{9}C, ^{8}B). In fact, the current values obtained from our analysis suggest for the three neutron-knockout reactions comparable values of the quenching factors within the experimental uncertainties. Including the knockout of one weakly bound proton from 9C, we still find evidence for a reduction of spectroscopic strength, but – at least in light nuclei – a possible scaling with the binding-energy difference may be weaker than suggested previously [4,5].

We point out that part of the discrepancy between the theoretical and experimental spectroscopic factors might originate from the choice of the wave functions. Using a Greens-function Monte Carlo (GFMC) overlap function for the (^{10}C,^{9}C) reaction [6], the value of R_s increases from 0.51(5) to 0.66(6) due to the decrease of the theoretical spectroscopic factor from 1.60 (WBT shell-model interaction) to 1.04 (GFMC).

Figure 1 displays a summary of the preliminary results.

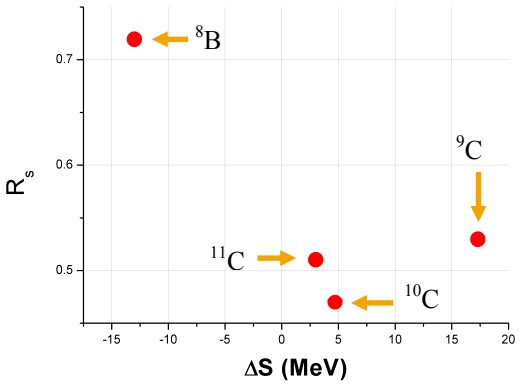

Figure 1: Reduction factors Rs as a function of the binding-energy difference ($\Delta S = S_n$-S_p for neutron knockout, $\Delta S = S_p$-S_n for proton knockout) for the for one-nucleon knockout reactions investigated in the S341 experimental campaign. The quenching factor is based on an eikonal approach for the description of the reaction process and shell-model spectroscopic factors using the WBT interaction for the reactions (^{12}C,^{11}C), (^{11}C,^{10}C), and (^{10}C,^{9}C) and the PJT interaction for (^{9}C,^{8}C).

References

[1] P. G. Hansen, J. A. Tostevin, Annu. Rev. Nucl. Part. Sci. 53, 219 (2003)
[2] T. Aumann, Eur. Phys. J A 26, 441 (2005)
[3] B. A. Brown et al., Phys. Rev. C 65, 061601(R) (2002)
[4] A. Gade et al., Phys. Rev. Lett. 93, 042501 (2004)
[5] A. Gade et al., Phys. Rev. C 77, 044306 (2008)
[6] R. B. Wiringa, private communication

* Work supported through the GSI – TU Darmstadt cooperation contract and through and BMBF, contract 06DA9040I.
#v.volkov@gsi.de

Elastic Proton Scattering of Ni isotopes

S. Terashima[*1], *I. Tanihata*[†2], *R. Kanungo*[†3], *H. Sakaguchi*[2], *A. Estradé*[3,1], *Y. Matsuda*[4], *B. Riese*[1], *H. Weick*[1], *T. Adachi*[9], *K. Boretzky*[1], *P. Boutachkov*[1], *P. Egelhof*[1], *F. Farinon*[1,8], *H. Geissel*[1,8], *C. Goergen*[11], *P. Golubev*[10], *M.N. Harakeh*[1,9], *R. Hoischen*[10], *K. Hirota*[2], *S. Ilieva*[1], *R. Janik*[7], *N. Kalantar-Nayestanaki*[9], *R. Knöbel*[1], *J. Kurcewicz*[1], *Yu.A. Litvinov*[1], *Y. Maeda*[5], *I. Mukha*[1], *A. Najafi*[9], *C. Nociforo*[1], *H. J. Ong*[2], *H. Otsu*[6], *G. Pascovici*[11], *S. Pietri*[1], *A. Prochazka*[1,8], *P. Reiter*[11], *C. Rigollet*[9], *D. Rudolph*[10], *C. Scheidenberger*[1,8], *S. Shende*[10], *H. Simon*[1], *B. Sitar*[7], *P. Strmen*[7], *J. Taprogge*[11], *M. Uchida*[3], *J.Van de Walle*[9], *A. Wendt*[11], *J.S. Winfield*[1], *M. Winkler*[1], *and J. Zenihiro*[2]

[1]GSI, Darmstadt, Germany; [2]RCNP, Osaka, Japan; [3]Saint Mary's University, Canada; [4]Tohoku University, Japan; [5]Miyazaki University, Japan; [6]RIKEN Nishina Center, Japan; [7]CUB Bratislava, Slovakia; [8]JLU, Giessen, Germany; [9]KVI, Groningen, The Netherland; [10]Lund University, Sweden; [11]University of Cologne, Germany

The density distribution of the nucleus is one of its most fundamental properties, and is directly connected with its size and shape. Proton elastic scattering in the intermediate-energy region has been used to study the density profile [1, 2]. In the case of unstable nuclei, it is possible to measure elastic proton scattering by a missing-mass technique , detecting recoil light ions to identify a reaction channel such as elastic, inelastic, breakup, etc.

The experiment was performed at the GSI FRagment Separator (FRS). ^{58}Ni beam from the SIS18 was used for calibration and ^{86}Kr as primary beam to produce neutron rich ^{66,70}Ni. Projectile fragments were clearly identified by $B\rho$-ΔE-$B\rho$ technique. Three ionization chambers (MUSIC) and six time-projection chambers (TPC) were used to measure the energy-loss ΔE and position of the ions at the focal planes to properly derive the magnetic rigidity $B\rho$. The isomer tagging technique was applied to estimate the isomer ratio in the fragment beams by the ITAG system [3].

The hydrogen targets and the recoil protons detectors were located at the final focal plane F4, which is schematically shown in Fig. 1. The ^{58,66,70}Ni beams bombarded two different hydrogen targets to account for different sensitivities in the momentum transfer regions. A solid hydrogen target (SHT) of 8.6 mg/cm^2 was used to cover, in particular, the high momentum transfer region. This target was a further extension to the thicker windowless SHT [4]. The other target was a conventional thin polyethylene foil (CH_2) of 1.0 mg/cm^2. Recoil protons from the SHT and the CH_2 tilted to 45° were identified using the *E*-ΔE and *E*-*TOF* methods by NaI(Tl) and plastic scintillators and by CsI(Tl) and Si strip detectors, respectively.

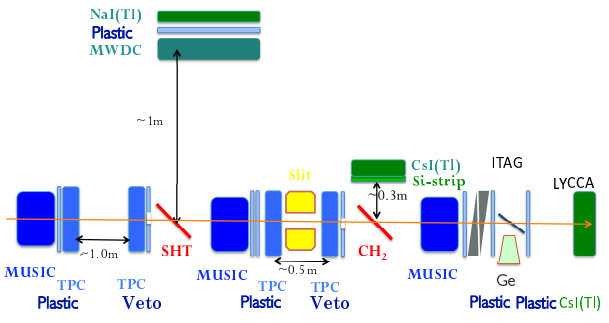

Figure 1: Schematic view of the detector setup at the F4.

Figure 2 shows a kinematic correlation for ^{58}Ni on the SHT covering the momentum transfer from 0.6 to 2.0 fm^{-1}. Elastic-scattering events can be clearly identified as the most intense locus and almost no background is observed in the positive Q-value region. A background run was also measured by the same settings with an empty target by removing hydrogen. In the other CH_2 target, the Si detectors could be covered the lower momentum transfer region. A clear elastic-scattering locus can be observed as shown in the inset of Fig. 2 even with the low statistics due to a thin target and worse beam focusing. Detailed analysis is in progress to extract the angular distribution of the differential cross section.

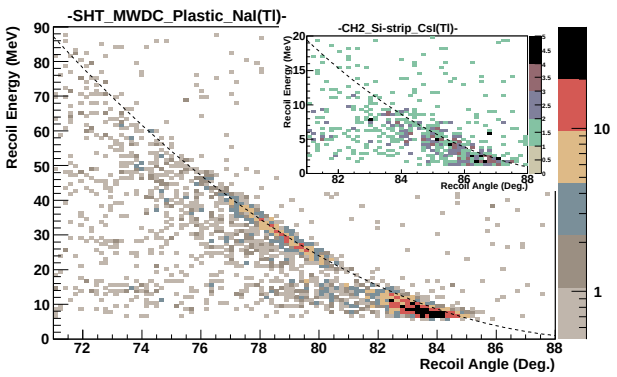

Figure 2: Kinematic correlation between recoil energy and recoil angle of protons from the SHT and the CH_2 (inset) for ^{58}Ni. Dashed lines show expected elastic channel.

References

[1] S. Terashima *et al.*, Phys. Rev. C 77, 024317 (2008).

[2] P. Egelhof *et al.*, Eur. Phys. J. A15, 27-32 (2002).

[3] F. Famion *et al.*, GSI Scientific Report 2009, p. 308.

[4] S. Ishimoto *et al.*, Nucl. Instr. Meth A 480 304 (2002).

* sa.terashima@gsi.de

† spokesperson

Matter radii of neutron-rich Mg and O isotopes

R. Kanungo[1], A. Prochazka[2,3], W. Horiuchi[2], C. Nociforo[2], T. Aumann[2], D. Boutin[3], D. Cortina-Gil[4], B. Davids[5], M. Diakaki[6], F. Farinon[2,3], H. Geissel[2], R. Gernhäuser[7], J. Gerl[2], R. Janik[8], B. Jonson[9], B. Kindler[2], R. Knöbel[2,3], R. Krücken[7], M. Lantz[9], H. Lenske[3], Y. Litvinov[2], B. Lommel[2], K. Mahata[2], P. Maierbeck[7], A. Musummara[10], T. Nilsson[9], C. Perro[1], C. Scheidenberger[2], B. Sitar[7], P. Strmen[7], B. Sun[2], Y. Suzuki[11,12], I. Szarka[7], I. Tanihata[13], Y. Utsuno[14], H. Weick[2], M. Winkler[2]

[1]Saint Mary's University, Halifax, Canada; [2]GSI, Darmstadt, Germany; [3]University of Giessen, Giessen, Germany, [4]Universidad de Santiago de Compostela , Santiago de Compostella, Spain, [5]TRIUMF, Vancouver, Canada, [6]National Technical University, Athens, Greece, [7]TU München, Munich, Germany, [8]Comenius University, Bratislava, Slovakia, [9]Chalmers University of Technology, Göteborg, Sweden, [10]Catania University and LNS-INFN, Catania, Italy, [11]CNS, Tokyo, Japan, [11]Niigata University, Niigata, Japan, [12]RIKEN, Saimata, Japan [13]RCNP, Osaka University, Osaka, Japan, [14]Japan Atomic Energy Agency, Tokai, Japan

The measurement of interaction cross sections of $^{32-35}$Mg and $^{22-23}$O is reported.

The matter density is one of the fundamental properties of a nucleus, which particularly for neutron-rich nuclei, exhibits formation of exotic structures like nuclear skin and halo. The matter radii provide constraints on the wave functions and help in understanding of deformation and shell effects.

The short-lived nature of neutron-rich nuclei and their weak yields make the task of determining the matter radii and density quite challenging. The traditional method of elastic scattering using simple hadronic probes is feasible in inverse kinematics for beams of moderate intensity. The measurement of total interaction cross section [1] at relativistic energies on the other hand has been found to be an efficient method to extract the matter radii which can be extended to very neutron-rich isotopes with extremely small yield.

We report the first measurements of root mean square matter radii of $^{33-35}$Mg from interaction cross section at 900*A* MeV. The radii of these neutron-rich Mg isotopes across the N=20 broken shell [2,3] provide interesting ground to study development of neutron skin and associated deformation. While the conventional N=20 shell closure disappears a new shell gap emerges at N=16. Of special interest is the isotopic chain of oxygen with ^{24}O appearing as a doubly magic nucleus at the drip-line [4,5]. We have measured the interaction cross section of ^{22,23}O to examine an existing anomaly [6] in understanding the large enhancement previously found for ^{23}O.

The experiments were carried out at the fragment separator FRS at GSI [7]. Secondary beams of the Mg and O isotopes were produced via projectile fragmentation of a ^{48}Ca primary beam on a Be target. The FRS was used in two stages with the reaction target being placed at the dispersive mid-plane. The first half of the FRS was used to separate and identify the incident beam. This was accomplished using energy-loss information from a multi-sampling ionization chamber, time-of-flight between two plastic scintillators and magnetic rigidity measured using position sensitive TPC detectors.

After interaction of the beam with a carbon or polyethylene target the unreacted secondary beam was transported to the final focus using the second half of FRS where it was identified using the same technique described above. This allows us to measure the interaction cross section based on the principle of transmission.

Figure 1 shows the measured interaction cross sections of the Mg isotopes. The open squares show existing measurements reported in Ref.[8]. The curve in Fig.1 shows the expected trend of cross sections if the radii followed the well known $r_0A^{1/3}$ rule. A clear deviation from this trend is observed as one moves to neutron-rich isotopes. This signals the formation of neutron skins.

The data analysis of the neutron-rich O isotopes interacting with a carbon target is in progress.

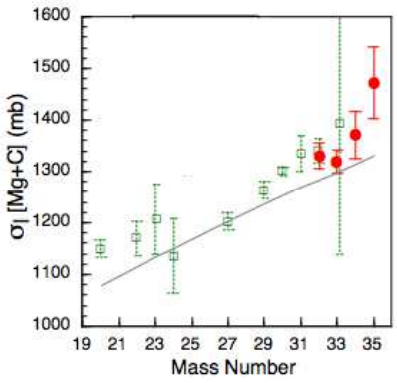

Figure 1: Interaction cross section of ^{A}Mg+C. The filled circles are new measurements reported in this work.

References

[1] I. Tanihata et al., Phys. Rev. Lett. 55 (1985) 2676.
[2] D. Guillemaud-Mueller et al. Nucl. Phys.A 426 (1984) 37.
[3] T. Motobayashi et al. Phys. Lett. B 346 (1992) 9.
[4] R. Kanungo et al., Phys. Rev. Lett.102 (2009) 152501.
[5] C.R. Hoffmann et al., Phys. Lett. B 672 (2009) 17.
[6] A. Ozawa et al., Phys. Rev. Lett. 84 (2000) 5493.
[7] H. Geissel et al., Nucl. Instrm. Meth. Res. B 70 (1992) 286.
[8] T. Suzuki et al., Nucl. Phys. A 630 (1998) 661.

Nuclear structure investigations of Al isotopes around N=20 shell closure

C. Nociforo[1,#], A. Prochazka[1,2], R. Kanungo[3], T. Aumann[1], D. Boutin[2], D. Cortina-Gil[4], B. Davids[5], M. Diakaki[6], F. Farinon[1,2], H. Geissel[1], R. Gernhäuser[7], R. Janik[8], B. Jonson[9], B. Kindler[1], R.Knöbel[1,2], R. Krücken[7], N. Kurz[1], M. Lantz[9], H. Lenske[2], Yu.A. Litvinov[1,], B. Lommel[1], K.Mahata[1], P. Maierbeck[7], A. Musumarra[10,11], T. Nilsson[9], C. Perro[3], C. Scheidenberger[1,2], B. Sitar[8], P. Strmen[8], B. Sun[2], I. Szarka[8], I. Tanihata[12], H. Weick[1], and M. Winkler[1]

[1]GSI, Darmstadt, Germany; [2]Justus-Liebig University, Gießen, Germany; [3]Saint Mary's University, Halifax, Canada; [4]Universidad de Santiago de Compostela, Santiago de Compostela, Spain; [5]TRIUMF, Vancouver, Canada; [6]National Technical University, Athens, Greece; [7]TU München, Garching, Germany; [8]Comenius University, Bratislava, Slovakia; [9]Chalmers University of Technology, Göteborg, Sweden; [10]Università di Catania, Catania, Italy; [11]INFN-Laboratori Nazionali del Sud, Catania, Italy; [12]Research Center for Nuclear Physics, Osaka, Japan.

The evolution of the configuration mixing in the ground state of the pf shell Al isotopes as a function of the neutron number has been studied through the longitudinal momentum distribution analysis of the residues in one-neutron removal reactions at relativistic energies. The experiment [1] was performed by using radioactive ion beams produced in-flight at the Fragment Separator (FRS) of GSI in order to investigate a wide region of the nuclear chart overlapping with the so called Island of Inversion.

The nuclear structure of nuclei in the Island of Inversion is interesting because of the observed breakdown of the N=20 shell closure in the Mg isotopes. The neutron-rich Al isotopes are located in a *transition* region between the normal shell structure nuclei (Z=14) and the Island of Inversion. Concerning the odd-mass Al isotopes (N=20,22), dominated by the unpaired $d_{5/2}$ proton, an influence of core polarization effects as a function of the neutron number is expected. For the even mass Al isotopes (N=21,23), information on the occupied orbital of the unpaired neutron can be extracted on the basis of shell model predictions. In this context, the longitudinal momentum distributions of the Al^{33-36} isotopes after one-neutron removal have been measured at the last focal plane of the FRS. The investigated isotopes were produced by projectile fragmentation of a ^{48}Ca SIS18 beam at 1 GeV/u with a Be (6 g/cm^2) target placed at the entrance of the FRS. They were separated and identified in flight up to the mid-focal plane of the separator, where the reaction target (C or CH_2) was located. Due to the high-resolution achromatic mode of the FRS a precise momentum measurement ($\Delta p/p \sim 1.5 \cdot 10^{-4}$) of the produced fragments Al^{32-34} was performed independently of the large momentum spread due to the reactions in the target. The ion separation and identification was obtained by using tracking detectors (Time Projection Chamber (TPC)[2]) together with the standard FRS detectors set in front and behind the reaction target, as well as at the final focus (see Fig. 1). A rate of ~100 ions/s was obtained for the most exotic Al system studied, i.e. ^{36}Al, with a primary beam intensity of about 10^9 ions/spill. Since the experiment intended to provide information concerning with the orbital angular momentum of the knocked out neutron, and thus the single-particle orbitals of the ground state of the studied nuclei, the inclusive momentum data have been analyzed within an eikonal model, with the condition that the final states reached are below the one-neutron separation energy in the final nucleus.

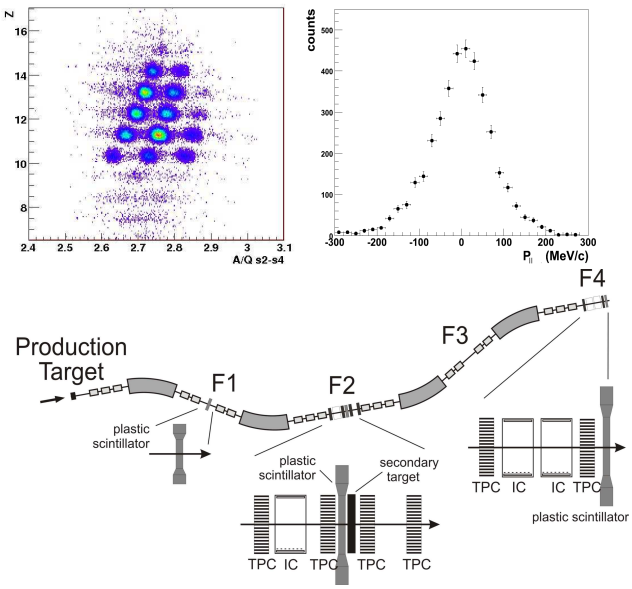

Figure 1: FRS experimental setup. Insets: Particle identification plot of fragments transported up to the mid-focal plane F2 and ^{32}Al mometum distribution at F4.

In case of the ^{33}Al nucleus, the data have been compared with the results of theoretical calculations in the sd-shell space [3]. The ^{32}Al momentum distribution shows a non-negligible presence of intruder configurations for the ^{33}Al (N=20). Further data analysis is still in progress.

References

[1] R. Kanungo et al., Phys, Lett. B685 (2010) 253.
[2] R. Janik et al., Nucl. Instr. and Meth. A598 (2009) 681.
[3] B. A. Brown, private communication.

#c.nociforo@gsi.de

Decay of drip-line nuclei near ^{100}Sn *

K.Straub[1], N.Al-Dahan[2], N.Alkhomashi[2], A.Atac[3], A.Blazhev[4], M.Böhmer[1], P.Boutachkov[5], N.Braun[4], L.Caceres[5], I.Čeliković[6], T.Davinson[7], G.deFrance[8], I.Dillmann[1], C.Domingo-Pardo[5], P.Doornenbal[9], T.Faestermann[1#], G.Farell[2], F.Farinon[5], H.Geissel[5], J.Gerl[5], R.Gernhäuser[1], N.Goel[5], M.Górska[5], A.Gottardo[7], H.Grawe[5], J.Gręboszˊ[10], T.Habermann[5], C.Hinke[1], R.Hoischen[5], R.Janik[11], M.Karny[12], A.Kaskas[3], I.Kojouharov[5], Th.Kröll[1], R.Krücken[1], N.Kurz[5], M.Lewitowicz[8], Y.Litvinov[5], Z.Liu[7], L.Maier[1], S.Myalski[10], F. Nebel[1], S.Nishimura[9], C.Nociforo[5], J.Nyberg[13], A.Parikh[1], S.Pietri [2,5], Zs.Podolyák[2], A.Procházka[5], P.H.Regan[2], C.Rigollet[14], H.Schaffner[5], C.Scheidenberger[5], S.Schwertel[1], P.-A.Söderström[13], S.Steer[2], K.Steiger[1], A.Stolz[15], P.Strmeň[11], H.Weick[5], H.J.Wollersheim[5], P.J.Woods[7], and the RISING collaboration

[1] TU München, [2]U of Surrey, [3]U of Ankara, [4]U of Köln, [5]GSI , [6]Inst. Vinca Belgrade, [7]U of Edinburgh, [8]GANIL, [9]RIKEN, [10]IFJ PAN Krakow, [11]U of Bratislava, [12]U of Warsaw, [13]U of Uppsala, [14]KVI - U of Groningen, [15]MSU

The analysis of the data obtained in 2008 [1] (Experiment S330) for neutron deficient nuclei produced by fragmentation of a ^{124}Xe beam is nearly completed. Here we concentrate on the decay properties of extremely neutron deficient nuclei neighbouring ^{100}Sn. The obtained half-lives, still preliminary, are listed in the table and are considerably more precise than the literature values from GANIL [2], GSI [3], and MSU [4], if available. For the N=Z-1 nuclei even the candidate for prompt proton emission ^{97}In decays with a half-life compatible with the expectation for a pure Fermi- plus Gamow-Teller β-decay between mirror nuclei.

T_z=(N-Z)/2	Nuclide	$T_{1/2}$	literature
-1/2	^{93}Ag	>200*ns*	>1500*ns* [2]
-1/2	^{95}Cd	73^{+53}_{-28} *ms*	-
-1/2	^{97}In	26^{+47}_{-10} *ms*	-
-1/2	^{99}Sn	>200*ns*	-
0	^{96}Cd	0.99(13)*s*	$1.03^{+0.24}_{-0.21}$ *s* [4]
0	^{98}In	32(6)*ms*	32^{+32}_{-11} *ms* [3] 47(13)*ms* [4]
0	^{98}In^{m}	0.86(21)*s*	$1.2^{+1.2}_{-0.4}$ *s* [3] 0.66(40)*s* [4]
1/2	^{101}Sn	2.10(10)*s*	1.7(3)*s* [5]
1/2	^{103}Sb	<200*ns*	>1500*ns* [2]

^{96}Cd is perhaps the heaviest waiting point nucleus in the rp-process before it reaches the ending Sn-Sb-Te cycle. Its half-life has just recently been determined for the first time [4]. Our value agrees but is more precise.

For ^{101}Sn we could, in addition to the half-life, also measure the spectrum of β-delayed protons with good statistics as shown in Fig. 1. Here the energy deposited in a single 1x1x0.7mm^3 pixel of the Si array is plotted. The events below 1.5MeV are due to β^+ particles. The branching ratio for this decay process is 20(1)%. In 11(3)% of the decays the first excited 2^+ state in ^{100}Cd is populated. From the fraction of 73(6)% of protons that follow β^+ emission, detected via coincident 511keV annihilation radiation, we can deduce the energy available for β-delayed proton emission Q_{EC}-S_p=6.6(3)MeV.

For ^{103}Sb we observe at least 10 times less events than predicted by cross section and transmission estimates. The only explanation is a half-life considerably shorter than the flight time through the FRS of 200ns. This is in line with the expectation that ^{103}Sb is a ground state proton emitter but contradicts the earlier positive identification of this nuclide after a fragmentation reaction [2].

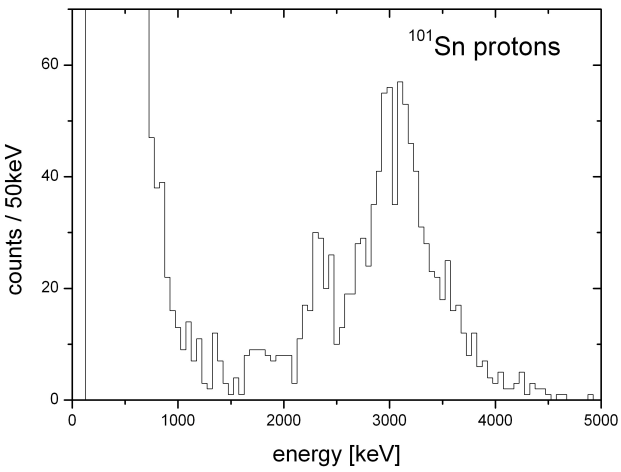

Fig.1: Spectrum of β-delayed protons from ^{101}Sn. The low energy distribution <1.5MeV is due to β-particles.

References

[1] K. Eppinger et al., GSI Scientific Report 2008, p.147
[2] K. Rykaczewski et al., Phys. Rev. C 52 (1995) R2310
[3] A. Stolz et al., AIP Conf. Proc. 610 (2002) 728 and T. Faestermann et al., EPJA15 (2002) 185
[4] D. Bazin et al., PRL 101 (2008) 252501
[5] average in ENSDF

* work supported by MLL, BMBF, DFG Excellence Cluster 153, GSI, EPSRC, STFC(UK), and EURONS
# thomas.faestermann@ph.tum.de

Measurement of α-decay half-life of bare and H-like ^{213}Fr ions

F. Farinon[1,2], C. Nociforo[1], A. Musumarra[3], K-H. Behr[1], F. Bosch[1], K. Blaum[4], C. Brandau[1], A. Brünle[1], R. B. Cakirli[4], C. Dimopoulou[1], A. Estrade[1], H. Geissel[1,2], P. Huelsmann[1], V. Ivanova[1], C. Karagiannis[1], R. Knöbel[1,2], C. Kozhuharov[1], J. Kurcewicz[1], N. Kuzminchuk[2], S. Litvinov[1], Y. A. Litvinov[1,4], I. Mukha[1], F. Nolden[2], P. Petri[1], S. Pietri[1], W. Plaß[1,2], A. Prochazka[1,2], M.W. Reed[5], B. Riese[1], M. S. Sanjari[1,6], C. Scheidenberger[1,2], D. Shubina[4], M. Steck[1], B. Sun[2], S. Terashima[1], P.M. Walker[5], H. Weick[1], J. S. Winfield[1], N. Winckler[1,4], and M. Winkler[1]

[1]GSI, Darmstadt, Germany; [2]Justus-Liebig Universität, Giessen, Germany; [3]INFN-LNS and University of Catania, Catania, Italy; [4]MPI-K, Heidelberg, Germany; [5]University of Surrey, Guildford, United Kingdom; [6]Johann Wolfgang Goethe-Universität, Frankfurt am Main, Germany.

The influence of the bound electron cloud on the α-decay constant λ has been discussed theoretically since the late 50s. Changes in the order of few per mil in Q-values and α-decay half-lives of fully stripped ions are expected and can provide information on the electron screening energy, thereby deducing reliable reaction rates in stellar environments [1]. The measurements of α-decay half-lives are feasible also for highly-charged radioactive nuclides. Using a ^{238}U beam at relativistic energies at the present FRS-ESR facility at GSI it is possible to produce, efficiently separate and store highly charged α-emitters.

We report on a pilot experiment of a measurement of the α-decay half-life of fully ionized and hydrogen-like (H-like) ^{213}Fr ions. The lifetime measurement of the corresponding neutral atoms was performed at the FRS by implanting the ions into an active Silicon stopper [2].

Radioactive ^{213}Fr ions have been produced via projectile fragmentation of $\sim 10^9$ ^{238}U^{73+} ions/spill, accelerated by the SIS-18 to 455 MeV/u. A 1.03 g/cm^2 thick Beryllium target has been used. The fully-ionized and H-like ^{213}Fr ions were separated in-flight by means of the Bρ-ΔE-Bρ method at the FRS and subsequently injected into the ESR. Stochastic and electron cooling were applied in both cases reducing the initial velocity spread to $\delta v/v \approx 5 \times 10^{-7}$ within 6-10 seconds. The identification of the cooled ions has been achieved exploiting the time-resolved Schottky Mass Spectrometry technique [3]. To perform half-life measurements it was necessary to scrape out the contaminant ^{213}Ra^{86+} which feeds ^{213}Fr^{86+} via EC with $T_{1/2} \simeq$ 163.8 (3) s [4]. An example of the measured Schottky frequency spectra of ^{213}Fr^{86+} with and without ^{213}Ra^{86+} contamination is shown in Fig. 1.

Several decay measurements of ^{213}Fr^{87+} and ^{213}Fr^{86+} have been performed. Decay curves of the parent ion have been fitted with an exponential function:
$N_{Fr}(t) = N_{Fr}(t_0) \times e^{-\lambda t}$, where $N_{Fr}(t)$ and $N_{Fr}(t_0)$ are the number of parent ions at the time t after the injection and t_0 the time of injection and λ is the decay constant in the laboratory frame.

The measured half-life value for α decay of bare and H-like ^{213}Fr (see Fig. 2) obtained from a preliminary analysis of these runs are in agreement with the value measured for neutral atoms ($T_{1/2} \simeq$ 34.82 (14) s [5]). Due to the poor statistics the uncertainties of the measurement was about 8%. Nevertheless, we proved the feasibility of the experiment and we gained valuable information for the main run. Since the growth of the number of daughter ions from the α decay can provide a cross-check for the measurement of half-life, in the future we will try to estimate how many ^{209}At daughters remain in the ring.

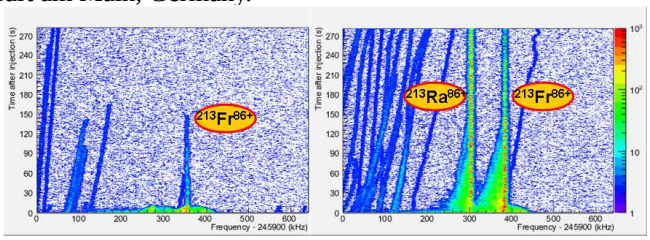

Figure 1: Schottky frequency spectra as a function of time after injection into the ESR. Left panel: ^{213}Fr^{86+} without ^{213}Ra^{86+} contamination. Right panel: the injected and cooled ^{213}Fr^{86+} and ^{213}Ra^{86+} ions.

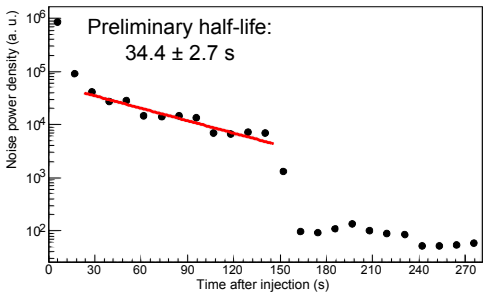

Figure 2: Decay curve of stored H-like ^{213}Fr^{86+} as a function of time after the injection into the ESR. The data points are referred to the laboratory frame and can be converted to the rest frame of the ions using the Lorentz factor γ = 1.39.

References

[1] Z. Patyk et al., Phys. Rev. C 78, 2008.

[2] A. Musumarra et al., GSI Sci. Rep. 2008, p. 150.

[3] F. Nolden et al., GSI Sci. Rep. 2010.

[4] M.J. Martin, Nuclear Data Sheets 63, p. 723 (1991).

[5] M. S. Basunia, Nuclear Data Sheets 108, p. 658 (2007).

Investigation of neutron-rich ^{197}Au projectile fragments with Schottky mass spectrometry at the ESR

D. Shubina[*1,2], *M.W. Reed*[3], *I.J. Cullen*[3], *P.M. Walker*[3], *K. Blaum*[1], *F. Bosch*[4], *C. Brandau*[4], *J.J. Carroll*[5], *D.M. Cullen*[6], *A.Y. Deo*[3], *B. Detwiler*[5], *C. Dimopoulou*[4], *F. Farinon*[4], *H. Geissel*[4,7], *E. Haettner*[7], *M. Heil*[4], *R.S. Kempley*[3], *R. Knöbel*[4], *C. Kozhuharov*[4], *J. Kurcewicz*[4], *N. Kuzminchuk*[4], *S.A. Litvinov*[4], *Yu.A. Litvinov*[1,4], *Z. Liu*[8], *R. Mao*[9], *C. Nociforo*[4], *F. Nolden*[4], *Z. Patyk*[10], *W.R. Plass*[7], *A. Prochazka*[4], *M.S. Sanjari*[4], *C. Scheidenberger*[4,7], *M. Steck*[4], *Th. Stöhlker*[2,4], *B. Sun*[4], *T.P.D. Swan*[3], *G. Trees*[5], *H. Weick*[4], *N. Winckler*[1], *M. Winkler*[4], *P.J. Woods*[8], *and T. Yamaguchi*[11]

[1]MPIK, Heidelberg; [2]Uni. Heidelberg; [3]Uni. Surrey; [4]GSI, Darmstadt; [5]YSU, Youngstown; [6]Uni. Manchester; [7]Uni. Gießen; [8]Uni. Edinburgh; [9]IMP, Lanzhou; [10]SINS, Warsaw; [11]Saitama University

Neutron-rich nuclides produced in fragmentation of ^{197}Au beams were studied in the storage ring ESR. The nuclides of interest were separated in flight with the fragment separator FRS and injected at relativistic energies of 400 MeV/u into the ESR. In the ESR the velocity spread of the ions was reduced by the stochastic and then electron cooling. The cooled ions were investigated with time-resolved Schottky mass spectrometry (SMS) [1], which allowed simultaneous determination of their masses and lifetimes.

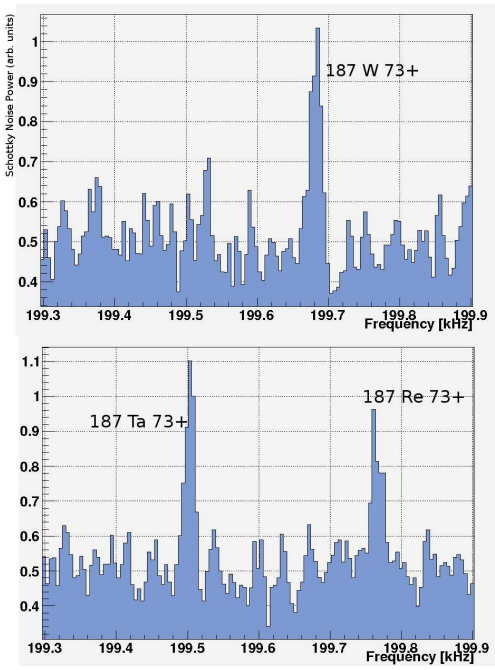

Figure 1: Examples of 30th harmonic Schottky frequency spectra for A=187 isobars from two injections into the ESR. Each spectrum was accumulated for 20 s. Each peak corresponds to a single stored ion.

Owing to the ultimate sensitivity to single stored ions, the time-resolved SMS allows us to identify the most rare nuclei species. For example, Schottky frequency spectra of single stored ^{187}Ta^{73+}, ^{187}W^{73+}, and ^{187}Re^{73+} ions, present in their ground states, are illustrated in Fig. 1.

* D.Shubina@gsi.de

The experiment has been conducted in two modes. In the first one, we searched for long-lived isomeric states with a narrow-band frequency analysis centered at the nuclei of interest. Long-lived isomeric states have been discovered in ^{183,184,186}Hf and Ta nuclides [2]. Excitation energies and lifetimes of these isomers have been determined. We note that an experiment is planned [3] to search for the predicted [4] isomer in ^{188}Hf.

In the second mode, the broad-band frequency spectra have been recorded in order to cover a large area on the chart of nuclides. The data analysis of these data is being finalized. A new ROOT-based analysis software has been developed, which contains the following parts:

- Creation of frequency spectra from raw data by means of Fast-Fourier Transformation (FFT);
- Automatic peak detection with adjustable thresholds and various projection algorithms for noise reduction.

Assignment of the corresponding particle identification to each peak in the frequency spectra has been completed. In total 54 neutron-rich nuclides ($69 \leq Z \leq 79$) have been identified. We found five nuclides with previously unknown masses, namely ^{185}Hf, ^{187,188}Ta and ^{192,193}Re. The final mass evaluation is in progress, for which a new software, based on the correlation matrix approach [1, 5], is being developed. The new program will allow consistent analysis of the data from individual storage-ring experiments as well as combined data from several experiments. As a longer-term project within the AAME initiative [6], it is planned to combine isochronous- and Schottky mass-spectrometry data obtained at the ESR and also at the CSRe, Lanzhou.

References

[1] Yu.A. Litvinov et al., Nucl. Phys. A756 (2005) 3.

[2] M.W. Reed et al., Phys. Rev. Lett. 105 (2010) 172501.

[3] P.M. Walker et al., GSI Experiment E109.

[4] P.M. Walker & G.D. Dracoulis, Hyp. Int. 135 (2001) 83.

[5] T. Radon et al., Nucl. Phys. A677 (2000) 75.

[6] B. Pfeiffer et al., GSI Scientific Report 2009 (2010) 219.

Longitudinal momentum distribution of monoenergetic electron neutrinos from orbital electron capture decay.

N. Winckler[1,2], F. Nolden[2], D. R. Atanasov[3], P. Buehler[4], V. Ivanova[2], M. S. Sanjari[2,5], D. Shubina[1], T. Yamaguchi[6] for the Two-Body Weak Decay Collaboration (TBWD@GSI)

[1]MPI-K, Heidelberg; [2]GSI, Darmstadt; [3]St. K. Ohridski University, Sofia; [4]SMI, Vienna; [5]J. W. Goethe Universitaet, Frankfurt; [6]Saitama University, Saitama

Schottky Mass Spectrometry (SMS) is frequently used for mass and lifetime measurements at the Experimental Storage Ring (ESR). This method is non-destructive and can be sensitive to single stored ions with a charge $q > 30$. This has offered the possibility to perform Single Ion Decay Spectroscopy (SIDS) where, for example, the orbital electron capture (EC) decay branch of hydrogen-like (H-like) ^{122}I, ^{140}Pr and ^{142}Pm has been investigated [1, 2]. Such a method requires a good sensitivity, i.e. a proper time resolution with an acceptable signal-to-noise ratio. Therefore a new dedicated resonant Schottky pick-up with higher sensitivity – by a factor of about 100 – has been developed and installed in spring 2010 at the ESR[3, 4]. The combination of this new detection system with a proper spectral analysis based on the multitaper method [5] has led to very successful results for SIDS experiments. Figure 1 illustrates the achievement of the method as the example of an EC-decay of a single H-like ^{142}Pm ion.

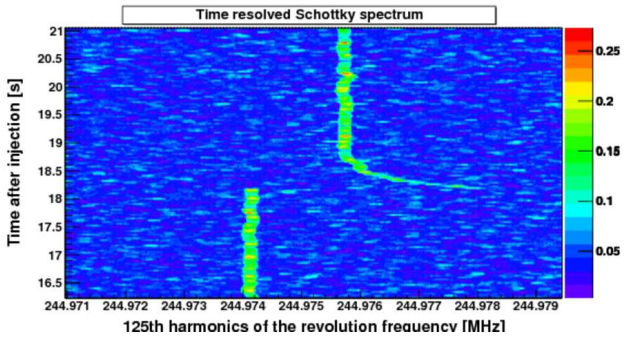

Figure 1: Example of a time-resolved Schottky spectrum obtained by a 1024 points (corresponding to time series of 32 ms) multitaper analysis. The selected part of the spectrum shows an EC-decay with a recoiling daughter ion emitted in forward direction with respect to the beam. This can clearly be seen from the disappearance of the parent trace and the appearance of the daughter trace at higher revolution frequency. The curved trace results from the electron cooling process.

One can see in Fig. 1 a waterfall diagram which shows very clearly the revolution frequency of a single ion in time steps of 32 ms. The time resolution is even sufficient to observe in detail the evolution of the ion revolution frequency right after the EC-decay, i.e. during the cooling of the EC-daughter recoil (curved trace). The relative difference between the revolution frequency at which the daughter ion appears, f_{DR}, and that one of the cooled daughter ion, f_{DC}, is proportional to the relative change of the longitudinal momentum $\delta p/p$ and to the phase-slip factor η. Because of the two-body kinematics of the EC-decay, the daughter ^{142}Nd ion and the emitted electron neutrino ν_e have same momenta but opposite directions. Therefore, by measuring the frequency differences $\delta f = f_{DR} - f_{DC}$ one obtains the longitudinal momentum distribution of the electron neutrino. One can show that $\delta f(\theta) \approx 3.91\text{kHz}\cos\theta$, where θ denotes the polar angle of neutrino (recoil) emission in the ion rest frame. For unpolarized beams, one expects in the center of mass an isotropic distribution, that is, a number of generated daughter ions $dN(\theta) = C\ 2\pi\ d(\cos\theta)$, where C is a constant. Accordingly, it follows that $dN/d(\delta f)$ is constant which is in a very good agreement with our measurement, as shown in Fig. 2.

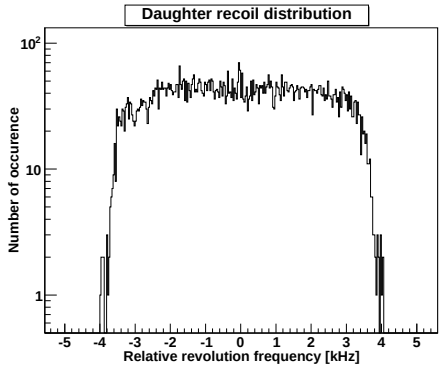

Figure 2: Daughter recoil distribution (Log scale) as a function of the revolution frequency difference, δf, with respect to the revolution frequency of the cooled daughter ions, f_{DC}.

It should be stressed that any (longitudinal) beam polarization would lead to a left-right asymmetry in Fig. 2. Vice versa, at a given and controlled beam polarization, this distribution provides the helicity of the electron neutrino.

References

[1] Yu. A. Litvinov et al., Phys. Lett. B664 (2008) 162-168.

[2] N. Winckler et al., GSI Scientific Report 2008, 2009-1 (2009).

[3] F. Nolden et al., to be published

[4] F. Nolden et al., GSI Scientific Report 2010, this issue.

[5] F. Nolden, Proc. of COOL 2009, Lanzhou, China (2009)

Isochronous mass measurements of short-lived $A = 2Z - 1$ nuclides

X.L. Tu[1,2], H.S. Xu[1], M. Wang[1], Y.H. Zhang[1], Yu.A. Litvinov*[3,4], Y. Sun[5], H. Schatz[6,7], X.H. Zhou[1], Y.J. Yuan[1], J.W. Xia[1], G. Audi[8], K. Blaum[3], C.M. Du[1,2], P. Geng[1,2], Z.G. Hu[1], W.X. Huang[1], S.L. Jin[1,2], L.X. Liu[1,2], Y. Liu[1], X. Ma[1], R.S. Mao[1], B. Mei[1], P. Shuai[9], Z.Y. Sun[1], H. Suzuki[10], S.W. Tang[1,2], J.S. Wang[1], S.T. Wang[1,2], G.Q. Xiao[1], X. Xu[1,2], T. Yamaguchi[11], Y. Yamaguchi[12], X.L. Yan[1,2], J.C. Yang[1], R.P. Ye[1,2], Y.D. Zang[1,2], H.W. Zhao[1], T.C. Zhao[1], X.Y. Zhang[1], and W.L. Zhan[1]

[1]IMP, Lanzhou; [2]Grad. Uni. CAS, Beijing; [3]MPIK, Heidelberg; [4]GSI, Darmstadt; [5]Shanghai Uni.; [6]JINA; [7]MSU, East Lansing; [8]CSNSM-IN2P3-CNRS, Orsay; [9]Uni. Hefei; [10]Uni. Tsukuba; [11]Uni. Saitama; [12]RIKEN, Wako

Isochronous mass spectrometry (IMS) [1] was applied to short-lived $A = 2Z - 1$ nuclei stored in the cooler-storage ring CSRe at the HIRFL-CSR facility in Lanzhou. Masses of three nuclei ^{63}Ge, ^{65}As, and ^{67}Se have been measured with high accuracy for the first time. The obtained results are essential for the rp-process nucleosynthesis in X-ray bursts.

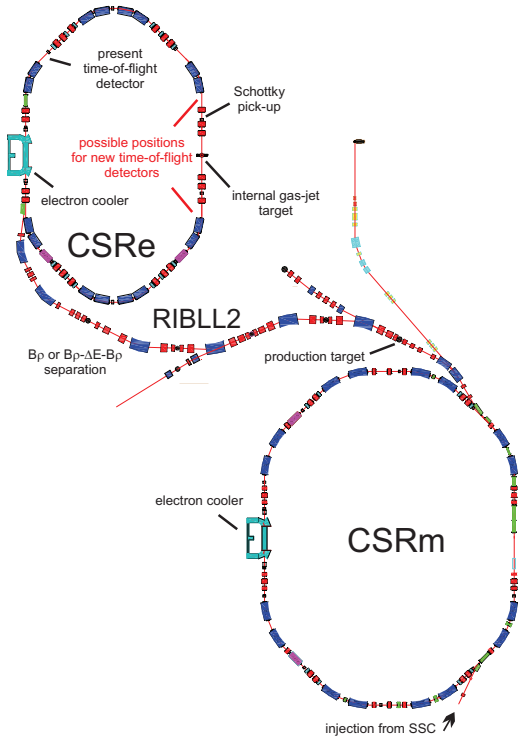

Figure 1: The HIRFL-CSR facility at IMP in Lanzhou.

The high-energy part of the HIRFL-CSR facility is illustrated in Figure 1 [2]. Exotic nuclei were produced by fragmenting ^{78}Kr primary beam, accelerated by CSRm, in a Be production target. The $A = 2Z - 1$ nuclides of interest were separated in flight with RIBLL2, injected and stored in CSRe. CSRe was tuned into an isochronous ion-optical mode requiring that the fragments are injected at $\gamma = \gamma_t = 1.395$. In this mode the revolution times of the ions are in first order independent of their velocity spread and are the measure of their mass-over-charge ratios [1].

* y.litvinov@gsi.de

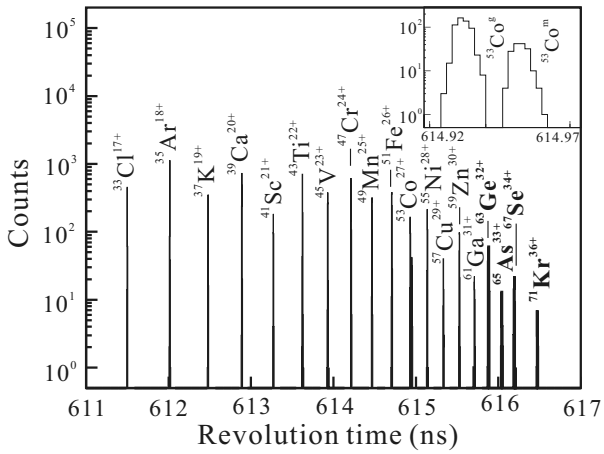

Figure 2: A part of the revolution time spectrum of $A = 2Z - 1$ nuclides. The insert shows resolved ground and isomeric ($T_{1/2} = 247$ ms, E^*=3.197 MeV) states of ^{53}Co.

The revolution times of the stored ions were measured using a dedicated timing detector [3].

All $A = 2Z - 1$ nuclides from ^{19}Ne through ^{71}Kr and all $A = 2Z - 2$ nuclides from ^{40}Sc through ^{56}Cu were observed. Fig. 2 illustrates the histogram of the extracted revolution times for a part of the $A = 2Z - 1$ nuclei [4]. Bold symbols indicate the nuclides whose masses were determined in this work. The resolving power of about 170'000 has been achieved (see, e.g., the insert of Fig. 2 where the ground and isomeric states of ^{53}Co are well-resolved).

Masses of ^{63}Ge, ^{65}As, and ^{67}Se nuclides were determined with a relative mass accuracy of about $1.5 \cdot 10^{-6}$. Using the mass excess of ^{64}Ge from [5], we obtained for the first time the proton separation energy in ^{65}As [4]. We experimentally confirmed that ^{65}As is slightly unbound with respect to proton emission, which yields that ^{64}Ge is not a significant waiting point of the rp-process in X-ray bursts for most of the relevant temperature-density conditions.

References

[1] M. Hausmann *et al.*, Hyperfine Int. **132** (2001) 291.

[2] H.S. Xu *et al.*, Chin. Sci. Bull. **54** (2009) 4749.

[3] B. Mei *et al.*, Nucl. Instr. Meth. **A624** (2010) 109.

[4] X.L. Tu *et al.*, Phys. Rev. Lett. (2011) in press.

[5] P. Schury *et al.*, Phys. Rev. **C75** (2007) 055801(R).

Changes of the ashes of an X-ray burst due to better known nuclear masses*

E. Haettner[1,2], D. Ackermann[2], G. Audi[3], K. Blaum[4], M. Block[2], S. Eliseev[4], T. Fleckenstein[1], F. Herfurth[2], F. P. Heßberger[2], S. Hofmann[2], J. Ketelaer[4], J. Ketter[4], H.-J. Kluge[2], G. Marx[6], M. Mazzocco[7], Yu. N. Novikov[2,8], W. R. Plaß[1,2], S. Rahaman[9], T. Rauscher[10], D. Rodríguez[11], H. Schatz[12], C. Scheidenberger[1,2], L. Schweikhard[6], B. Sun[1,13], P. G. Thirolf[14], G. K. Vorobjev[2,8], M. Wang[15], and C. Weber[9]

[1]Universität Gießen; [2]GSI, Darmstadt; [3]CSNSM-IN2P3-CNRS, Orsay, France; [4]MPI-K, Heidelberg; [5]Universität Mainz; [6]Universität Greifswald; [7]University of Padova, Italy; [8]PNPI, Gatchina, Russia; [9]University of Jyväskylä, Finland; [10]University of Basel, Switzerland; [11]University of Grananda, Spain; [12]NSCL and JINA, MSU, East Lansing, USA; [13]Beihang University, Beijing, PR China; [14]LMU, München; [15]Institute of Modern Physics, Lanzhou, PR China

The masses of ten proton-rich nuclides, among them the N=Z+1 nuclides ^{85}Mo and ^{87}Tc, relevant for nucleosynthesis modelling were measured with the Penning trap mass spectrometer SHIPTRAP [2]. Significant deviations in the mass values and separation energies compared to the values of the Atomic Mass Evaluation 2003 [1] (AME03) were found. The new experimental mass data were implemented in the Atomic Mass Evaluation and adjusted mass values were obtained following the procedure employed in [3]. Moreover, a new local ($80 \leq A \leq 95$) mass extrapolation based on the adjusted mass values was made using the methods and programs of [3]. Together with the new set of evaluated experimental data and the previously reported AME03 extrapolated mass values for A<80 and A>95 these data form a complete updated mass data set (AMEup).

To explore the impact of the new masses on the rp process in X-ray bursts reaction network calculations using the model of [4] were carried out. The baseline calculation uses the nuclear masses of the AME03 and calculated Coulomb mass shifts [5] for nuclides beyond N=Z. The results are compared to network calculations based on AMEup, combined with the same Coulomb mass shifts. The resulting final abundances show large differences between AME03 and AMEup in the region of A=86-96. The largest change is found for A=86 where the abundance increases by a factor of 20 (Fig. 1) due to an unexpectedly large decrease in S_{p} of ^{87}Tc. This change by a factor of 20 is by far the largest observed for abundances produced in rp process network calculations since the AME 2003 evaluation. It demonstrates that nuclear physics uncertainties can be larger than estimated and can introduce large uncertainties in nucleosynthesis model calculations.

The new results also open up the possibility for the formation of a ZrNb cycle induced by large ^{84}Mo(γ,α) or ^{83}Nb(p,α) reaction rates. For a given S_α value of ^{84}Mo the cycle will form at a sufficiently high temperature, effectively providing an upper temperature limit for any rp process along the proton drip line to produce nuclei beyond

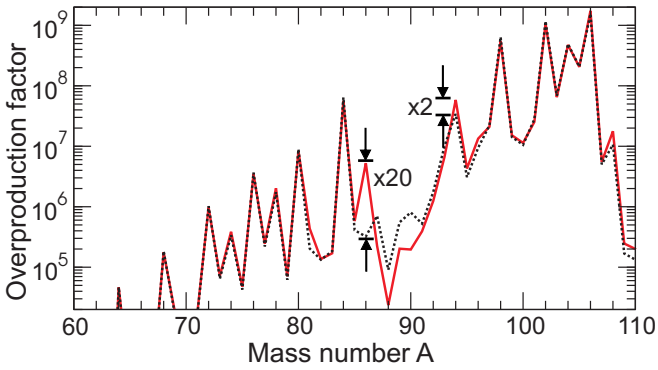

Figure 1: Calculated overproduction factors (produced abundance divided by solar system abundance) after an X-ray burst for the AME03 (dotted line) and the AMEup (solid line) mass sets.

A=84, including the light p-nuclei in the A=92-98 mass region. In order to explore this temperature limit, reaction network calculations were performed using a small test network with an initial ^{82}Zr abundance. For a S_α of ^{84}Mo lowered by one standard deviation a significant cycling was found beginning at 1.5 GK. However, calculations with the full X-ray burst model, which reaches peak temperatures of 2 GK, show that a cycle does not occur, because at the required high temperatures the reaction sequence already stops at ^{56}Ni. Nucleosynthesis proceeds beyond ^{56}Ni during burst cooling only when the temperature is lower than required to form a ZrNb cycle. The formation is nevertheless a possibility in an environment where the temperature is rising slowly enough to enable the rp process to proceed past ^{56}Ni before reaching high temperatures. Another possibility would be an rp process with seed nuclei beyond ^{56}Ni.

References

[1] G. Audi *et al.*, Nucl. Phys. A **729**, 337 (2003).

[2] E. Haettner *et al.*, GSI Scientific Report 2008 (2009) 134.

[3] A.H. Wapstra *et al.*, Nucl. Phys. A **729**, 129 (2003).

[4] H. Schatz *et al.*, Phys. Rev. Lett. **86**, 3471 (2001).

[5] B.A. Brown *et al.*, Phys. Rev. C **65**, 045802 (2002).

*Work supported by the Helmholtz Association and GSI (VH-NG-033), BMBF (06GI185I, 06ML236I, 06GF9103I), Max-Planck Society, Swiss NSF 200020-122287 and NSF grants PHY0822648 (Joint Institute for Nuclear Astrophysics) and PHY0606007.

(p, γ) reactions for astrophysics

G. Rastrepina[1,2], M. Weigand[1,2], S. Walter[3], F. Käppeler[3], R. Plag[1,2], R. Reifarth[1,2], Q. Zhong[1], and E062 collaboration[1]

[1]GSI, Darmstadt, Germany; [2]Goethe-Universität Frankfurt, Germany; [3]KIT, Karlsruhe, Germany

One of the important questions in nuclear astrophysics is how the observed abundances of elements came to be. For this reason, it is important to know the rates of all relevant reactions under the different conditions found in the universe.

Most of the elements heavier than iron have been and still are synthesized in neutron-induced reactions in stars of different stages. Nearly all of the observed abundances are either formed by the s- or the r-process in almost equal shares. However, some isotopes are primarily formed in the so-called p-process because they are shielded from the much more effective neutron-induced reactions. These p-process reactions require high temperatures (2-3 T_9) to overcome the Coulomb barrier and high proton densities. Type II Supernovae, catalysmic variables and accretion disks around black holes are places with the necessary conditions.

The qualitative description of the p-process requires large reaction networks. The most important components here are the proton- and γ-induced reactions and the associated β^+-decays. Most of the existing data in the Gamow window of the p-process have been obtained in activation measuremnets. This method is straightforward and can be pursued even with limited resources. But it is restricted to some reactions on stable isotopes and it requires radioactive product nuclei within a certain range of suitable half-lives and with well known decay properties.

In beam reaction measurements using proton beams are more universal, but still mostly applicable to stable or long-lived isotopes, since it is necessary to produce the respective sample. As an example for this technique, a new measurment of the ^{103}Rh(p,γ) reaction is descriped in the next pararaph. Essentially no limits on half life and properties of the reaction product exist, if the experiment is performed in inverse kinematics in a storage ring, since the reaction products can be identified by their mass-over-charge ratios, regardless whether they are stable or radioactive. Therfore, the technique can be applied to pactically all radioactive isotopes in the entire reaction network of the p-process. The only important condition is the required beam intensity in the ring, which can presently be met only for stable nuclei. A pioneering experiment on ^{96}Ru using this technique will be described in the last section.

The Karlsruhe 4πBaF$_2$-detector: ^{103}Rh(p, γ)

At the Karlsruhe Institute of Technology (KIT) ^{103}Rh(p,γ) capture events have been observed with the Karlsruhe 4πBaF$_2$-detector, which consists of up to 42 spherically arranged, hexagonal or pentagonal shaped BaF$_2$-crystals. The inner radius of the sphere is 10 cm. It is a high efficiency detector for γ-cascades able to run in a calorimetric mode.

The Gamow window for ^{103}Rh(p,γ) lies between 1.6 and 4.2 MeV. In order to reach the energy region of interest, the protons were accelerated with a pulsed 3.7 MV Van de Graaff accelerator to an energy of 2 and 3 MeV and fired on a metallic Rhodium target. The proton pulse width is about 2 ns with a repetition rate of 250 kHz. 42 channels of 8 bit Flash ADCs (Acqiris) were used for data acquisition.

Preliminary energy sum spectra of the 4π calorimeter show peaks in the expected region at 10.8 MeV and 11.5 MeV, respectively [1]. This corresponds to the Q-value of 8657 keV plus proton beam energy. In order to determine the correct count rates and the cross section for this reaction, it is necessary to improve the data processing to discriminate background signals. Furthermore the efficiency correction for the detector will be investigated with the GEANT simulation program [2].

Measurements in the ESR at GSI: ^{96}Ru(p, γ)

A major advantage of (p,γ) - reaction cross section measurements in the ESR is the universality of the technique. Stored and cooled bare ions may pick-up a proton or α-particle when they cross the H_2 or He gas jet. The products of the (p,γ) and (α,γ) reactions can be detected with an efficiency close to 100% with a position-sensitive particle detector downstream of the target. In a proof-of-principle experiment, two Double Sided Silicon Strip Detectors (DSSSD) have been used to detect the reaction products of the ^{96}Ru(p,γ) reaction at 9-11 AMeV [3]. Each detector had 16 strips in X- and Y- position. In this experiment detector was mounted in a pocket on the inner side of the beam at the ESR. The usage of a pocket resulted in a lower limit of the beam energy, since the ions had to penetrate the pocket in order to reach the detector. In order to finally reach the Gamow window of the p-process we plan to detect the reaction products with a the detector in vacuum during the next experiment.

References

[1] M. Weigand, S. Walter, F. Käppeler, R. Plag, R. Reifarth. Cross section measurements of ^{103}Rh(p, γ) with the Karlsruhe 4πBaF$_2$ detector. PoS(NIC XI)248

[2] J. Apostolakis. CERN program library long writeup, W5013. Tech. rep., CERN, GEANT library (1993)

[3] Q.Zhong, T. Aumann, S.Bishop, K. Blaum, K. Boretzky, et al. conference Series 202 (2010) 012011. Journal of Physics .

New Features of the Monte-Carlo Code MOCADI

N. Iwasa[1], *H. Weick*[2], *and H. Geissel*[2,3]

[1]Tohoku University, Sendai, Japan; [2]GSI, Darmstadt, Germany; [3]Justus-Liebig-Universität Giessen, Germany

MOCADI, the Monte-Carlo code for tracking of ions in ion-optical systems with non-Liouvillian elements, has been extended. New event generators for targets were added besides projectile fragmentation. General two-body kinematics with possible excitation energy of target and projectile nucleus and nuclear fission with different parametrizations of the total kinetic energy distribution of the fragments were included. Both cases lead to a complicated distribution with correlation of the fragments in the secondary beam. With MOCADI the acceptance in a beamline of complicated geometry can be taken into account as higher order optics given by transfer matrices is combined with the real apertures in the beamline. Also spontaneous nuclear decay along the flight path is now possible with a realistic distribution in time. The possibility to handle also electrostatic beamline elements correctly, makes MOCADI also applicable for velocity filters like SHIP and for fusion or heavy ion transfer reactions.

The option of atomic-charge state fluctuation in matter based on tables of atomic charge-exchange cross sections [2] is now implemented in the standard version. In this case the matter is divided into many layers based on the mean free path length of ions in a specific atomic charge state. The result will be the realistic charge-state distribution also in non-equlibrium and it allows to predict the additional broadening of momentum distributions due to the enhanced energy-loss straggling in matter. Also the resolution of ionisation chambers with charge-state fluctuation of the projectiles inside the chamber could be treated and shows the same pattern as the experimental results of the MUSIC chambers at the FRS.

A main field of application comes with the loop command which helps to evaluate trajectories in the ESR storage ring. For example the number of achievable turns for ions in the ESR penetrating at each revolution a thin carbon foil of a time-of-flight detector can be predicted and the result can explain the experimentally observed distribution [3]. Another example arethe trajectories and the survival probability of decay products in the ESR after the decay of the stored mother nuclei. The path and probabilty of storage does not only depend on the direction of the recoil but also very much on the position inside the ESR where the decay happens. For the example of alpha decay Fig.1 shows that on average more than half of the ^{209}At daughter nuclei can survive in the ring. But the survival probability in the dispersive arc of the ESR is lower due to the resulting dispersion mismatch.

In addition a graphical user interface (GMOCADI) for easier operating and control of the program was created.

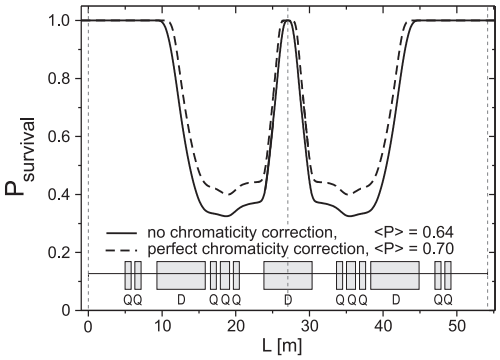

Figure 1: Survival probability of daughter nuclei from alpha decay of ^{213}Fr as function of position of decay over one half of the ESR. The ^{213}Fr ions circulated at a specific energy of 400 MeV/u and daughter ions which survived 200 turns in the MOCADI simulation were considered as within the acceptance. The two curves correspond to the extreme cases with and without any correction of chromaticity.

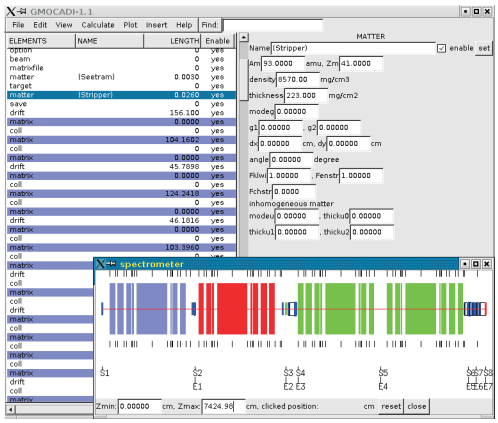

Figure 2: Snapshot of GMOCADI for a FRS simulation. On the left is the list of elements with one opened for editing. The lower window shows the FRS scheme with magnets marked as solid, high boxes. Degraders and detectors were used at the first, second and fourth focal plane, shown as smaller boxes. Due to the change in magnetic rigidity at these planes the magnets in between are grouped to one section shown each in different color.

References

[1] N. Iwasa, H. Geissel, G. Münzenberg, C. Scheidenberger, Th. Schwab and H. Wollnik, Nucl. Instr. and Meth. **B 126** (1997) 284.

[2] H. Weick et al., Nucl. Instr. and Meth. **B164/165** (2000) 168.

[3] N. Kuzminchuk et al., this GSI Annual Report.

Progress of Atomic Mass Evaluation Projects at GSI

B. Pfeiffer[*1], *U. Czok*[2], *Z. Patyk*[3], *C. Scheidenberger*[1,2], *and K. Venkataramaniah*[4]

[1]GSI, Darmstadt, Germany; [2]II. Phys. Inst., Gießen, Germany; [3]Soltan Institute for Nuclear Studies, Warsaw, Poland; [4]Sri Sathya Sai University, Prasanthinilayam, India

In order to counteract the general decline of data collection and evaluation in Europe [1], the GSI participates since 2007 in the activities of the *International Network of Nuclear Structure and Decay Data Evaluators*.

Advanced Atomic Mass Evaluation

In 2010, the screening of the literature for all nuclear data relevant for future compilations / evaluations of masses and decay properties has been continued (see Ref. [2]). The data up till mid-2010 are now structured for a compilation of mass measurements performed after the completion of the last mass evaluation in 2003 [3].

Atomic Mass Data Center

The last Atomic Mass Evaluation AME03 [3] had been prepared mainly by the *Atomic Mass Data Center* at Orsay. In the last decade, the number of mass related publications has grown considerably, as well as for established techniques (as α-spectroscopy) as for new high-precision techniques (as traps or time-of-flight installations). This caused a backlog of data to be treated for the evaluation. The *Future Mass Evaluation* (foreseen for 2013) therefore is prepared with the participation of nuclear structure specialists from Lhanzou, Argonne, GSI. In the last 2 years, most of the new α-decay data and results from Penning traps and time-of-flight measurements have been implemented.
Fig. 1 shows the relative mass uncertainties for about 2300 experimental masses (derived from around 10000 data points) for the AME03 compared to the actual status. The overall number has not increased much. The striking result is a replacement of less well determined mass values by higher precision ones (see, e.g., the increase in the green surfaces corresponding to $10^{-8} < \delta\mathrm{m/m} < 10^{-7}$).

Recent measurements by several groups (with important contributions from GSI) with advanced techniques at the ridge of the valley of stability indicate that the mass surface lies much higher (higher masses, less binding energy) than derived from the older data underlying the actual AME. This behaviour is largely due to an underestimate of earlier Q_β decay (and sometimes Q_α) energy measurements based on insufficient nuclear structure information, specially when going further away from stability. These changed mass surfaces will influence future mass models and thereby astrophysical calculations as, e.g., for the rp- and r-process of nucleosynthesis (see, e.g., [4, 5]).
From the measurements at GSI information on nuclear structure is obtained allowing to derive Q_α values. SHIPTRAP determines masses of spontaneously fissioning isotopes (endpoints of chains of α-emitters) allowing to fix the masses of superheavy isotopes.

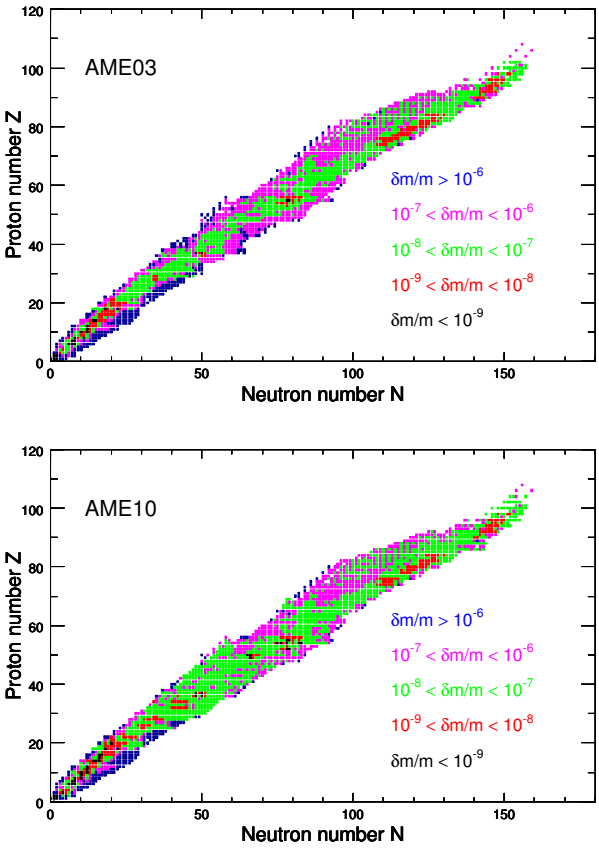

Figure 1: Nuclear charts with the relative mass uncertainties shown in a colour code for AME03 [3] (top) and the present status (bottom).

References

[1] A.L. Nichols, Nuclear Physics News 19(1), 3 (2009).

[2] B. Pfeiffer et al., GSI Scientific Report 2008, NUSTAR-EXPERIMENTS 16

[3] G. Audi et al., Nucl. Phys. A 729 (2003) 3; A.H. Wapstra et al., Nucl. Phys. A 729 (2003) 129; G. Audia et al., Nucl. Phys. A 729 (2003) 337.

[4] G. Audi et al., Int. Conf. on Nucl. Data for Science and Technology 2010, April 2010, Korea

[5] M. Wang et al., Int. Nucl. Phys. Conf. - INPC10, July 2010, Vancouver

* Present address: II. Phys. Inst., Gießen, Germany

Study of charge sharing effects in planar HPGe detectors

D. Karagyozov[1,2], R.Topchiyska[1,2], I.Kojouharov[1#] and H.Schaffner[1]

[1]GSI, Darmstadt, Germany; [2]University of Sofia, Bulgaria.

The recent development of HPGe detectors clearly indicates a trend toward segmented structures which are suitable for gamma-ray tracking and gamma-imaging techniques to be applied. Therefore, the effects related to these structures – cross-talk and charge sharing are of paramount importance for the detector spectroscopic properties. The charge-sharing effect has been studied mainly in the silicon detectors where it dominates sometimes over the other charge collection processes and only few studies report on HPGe detectors although this is an excellent case due to low impurity concentration, homogeneous electric field and the large sizes of the structures [1], [2].

The charge sharing effect competes with the induced charge effect and Compton scattering in segmented germanium detectors. The interplay of these effects may lead to wrong position determination of the interaction.

In order to estimate the scale of the phenomenon an experimental study of the charge sharing effect on HPGe planar single-side-strip detector is carried out. The detector has a square crystal with sizes of 32x32 mm and thickness of 12.5 mm. The front (segmented) side is contacted by Boron implantation and the non-segmented rear side is contacted by Li-diffusion. Accounting the 3.5 mm guard ring and the diffusion thickness, the effective size of the crystal becomes 25x25x12 mm. The front side is segmented onto 7 strips with a width of 3.57 mm. This side is scanned by a collimated ^{241}Am source along the axis transversal to the length of the strips and parallel to the front face with a step of 0.5 mm. The acquiring of the signals from all segments and the rear contact is triggered by the rear contact signal. On Fig 1 are displayed the spectra of segments 4 and 5 which we assumed to be in the middle of the crystal. The spectra are obtained under condition that the multiplicity of the events is always 2; only segments 4 and 5 are fired and gate is set on the

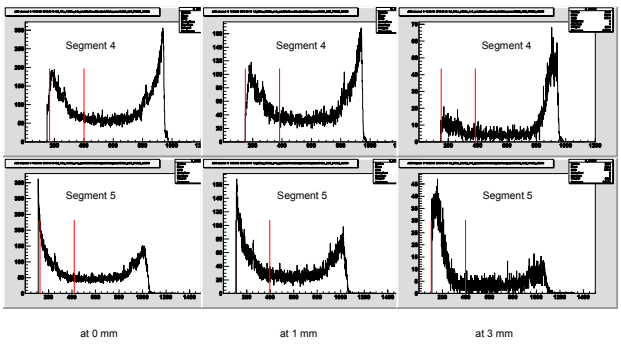

Figure 1: ^{241}Am spectra of segments 4 and 5 at positions shifted from the detector axis 0, 1 and 3 mm

60 keV line of the rear contact spectrum. Thus, only events which are possibly due to charge sharing between the strips during the charge collection are analyzed. One can see that the distribution at the right side of the spectrum, which corresponds of 60 keV, gradually increases and the part between the markers, corresponding to the charge sharing events, vanishes. The photon absorption at this energy is dominated by the photoeffect and therefore only negligible part of the events may be attributed to Compton scattering eventually leading to interactions in two neighbour segments. The spectra at 3 mm, which in fact demonstrate these rare events, reasonably have very low statistics (all spectra are acquired for equal time).

The small line on the left slope of the distribution at the right part of spectra and on the right slope of the distribution at the left side of the spectra corresponds to the 11.1 keV K_α – line of germanium. However, the propagation of these photons does not act as charge sharing which can be seen on Fig.2.

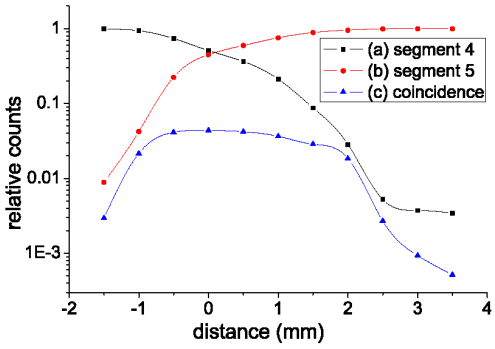

Figure 2: Charge sharing contribution to the count rate (normalized to the total count rate of both segments).

The contribution of the charge sharing remains almost constant over 1.5 mm depth of the segment which would be too much for propagation of the X-rays with energy of 11 keV. Nevertheless, the extent of the effect (~ few % at 60 keV) marks reasonable questions about the optimal segmentation width of the planar detectors.

References

[1] R.A.Kroeger, N.Gehrels, W.N.Johnson, J.D.Kurfess, B.P.Phlips, J.Tueller. Charge spreading and position sensitivity in a segmented planar germanium detector. Nucl. Instr. and Meth., A 422 (1999), 206

[2] J.Hayward, D.Wehe. Observation of charge sharing in an HPGe double sided strip detector, Nucl. Instr. and Meth, A579 (2007), 99

Characterisation of a planar germanium detector using a gamma scanner

N.Goel[a,b], *C.Domingo-Pardo*[a], *T.Engert*[a], *J.Gerl*[a], *I.Kojouharov*[a], *N. Pietralla*[b], *and H.Schaffner*[a]

[a]GSI, Darmstadt, Germany; [b]Technische Universitat Darmstadt, Institut fuer Kernphysik, D- 64289, Germany

Introduction

A novel scanning system [1],[2] for the position characterisation of HPGe detectors is implemented. The system is based on the pulse shape comparison scan (PSCS) method and is applied to acquire the position response of an n type planar germanium detector.

Experimental setup and results

A 300kBq ^{22}Na source is placed between the front surface of planar detector and the position sensitive detector (PSD) as shown in figure 1(a). This source emits pairs of 511 keV positron annihilation photons in opposite directions. The germanium detector is placed in the focal plane of the system at a distance of 15 cm from the source whereas the PSD is at 5 cm from it in order to cover the full surface area of the PSD. Both PSD and ^{22}Na are mounted on a common aluminium frame which can be rotated around the HPGe detector via a double disk ensemble. The disk can be rotated by any desired angle around the central rotating axis of the whole system. The acquistion is triggered by the 511 keV coincident events in the PSD and the germanium detector. A flash ADC(FADC) manufactured by SIS GmbH (mod. SIS3301) is used to digitise the preamplified charge pulses from the germanium detector. The Multi Branch System (MBS) of GSI, is used to read out the FADC and the readout electronics of the PSD. As described in [1], [2] pulse shape comparison (PSC) technique is employed to investigate the spatial response of the germanium detector at specified positions inside its volume. After the installation of both the HPGe and position sensitive detector, the pulses for all the trajectories which are inside the coincident cone of two detectors are recorded. The (x,y) position coordinates of these trajectories are provided by the PSD. The source and PSD are then moved by 90° via the rotating ensemble to shine the planar detector from sideways as shown in panel (b) of figure 1. The pulse shapes are again recorded for this configuration of the system. These two datasets are used to obtain the position coordinates of a specific interaction point inside the germanium detector volume. The comparison of pulses along two chosen trajectories in orthogonal view gives the pulse for the intersection point. This is done on the basis of a Δ^2 test [2]. The distribution of Δ^2 values for the comparison of all the pair of pulses in two selected trajectories is shown in figure 2(a). The higher values of Δ^2 refer to the pair of pulses which are farther from the crossing point of the selected γ-beam directions. By finding a reasonable compromise between the statistics of full energy events and the confinement of the intersection point, the upper Δ^2 value is selected. The average pulse is calculated from the ones which are below the threshold. Figure 2(b) shows the average pulse shapes obtained for 7 different positions namely at 1, 4, 7, 10, 13, 16, 19 mm from the p^+ contact of the detector. They agree well with the pulses obtained for the same detector using a conventional scanning system at IPHC Strassbourg [1] and also with the theoretical predictions [3] of the pulse shapes in a fully depleted planar germanium detector.

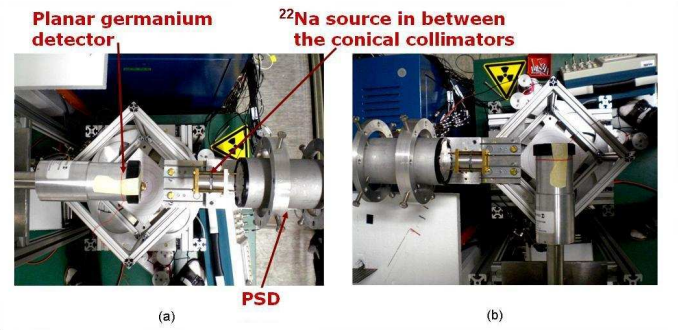

Figure 1: (a) The charge pulses are recorded when the PSD and ^{22}Na source are placed facing the front surface of planar germanium detector. (b) The measurement is repeated for orthogonal position of the PSD and ^{22}Na source, shining the germanium detector sideways.

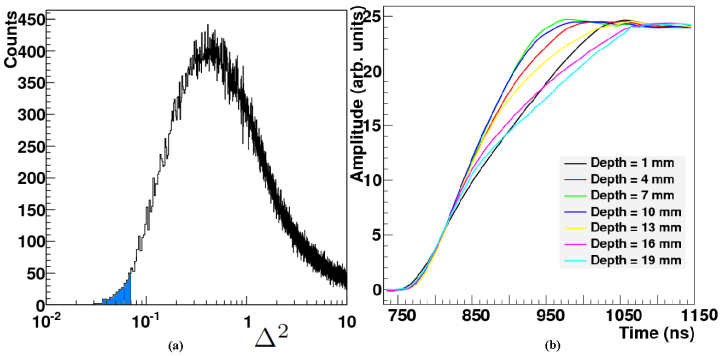

Figure 2: (a)The distribution of Δ^2 values for the comparison of pulses in the selected graphical cuts of side and front view, (b) Experimentally determined signal shapes inside a planar germanium detector at seven different interaction positions.

References

[1] C. Domingo-Pardo et al. " A novel method for the pulse-shape depiction of position sensitive semiconductor γ-ray detectors Part I: Characterization tests with a non-segmented planar detector", submitted to NIM A, November 2010.

[2] N. Goel et al. "Study of planar germanium detector response using the γ-ray imaging techniques, submitted NIM A, December 2010.

[3] G.F. Knoll, " Radiation detection and measurement", Third edition 1999.

Exploring the excitation spectrum of ^{13}Li and ^{14}Be using 3-body correlations*

H.T. Johansson[1], Yu. Aksyutina[1,2], T. Aumann[2], K. Boretzky[2], M.J.G. Borge[3], A. Chatillon[2], L.V. Chulkov[2,4], D. Cortina-Gil[5], U. Datta Pramanik[6], H. Emling[2], C. Forssén[1], H.O.U. Fynbo[7], H. Geissel[2], G. Ickert[2], B. Jonson[1], R. Kulessa[8], C. Langer[2,9], M. Lantz[1], T. Le Bleis[2,9], K. Mahata[2], G. Münzenberg[2], T. Nilsson[1], G. Nyman[1], S. Paschalis[10], W. Prokopowicz[2], R. Reifarth[2,9], A. Richter[11], K. Riisager[7], G. Schrieder[11], H. Simon[2], K. Sümmerer[2], O. Tengblad[3], H. Weick[2], and M. Zhukov[1]

[1]Chalmers University of Technology, Sweden; [2]GSI, Germany; [3]CSIC Madrid, Spain; [4]RRC Kurchatov Institute Moscow, Russia; [5]University of Santiago de Compostela, Spain; [6]SINP Kolkata, India; [7]Aarhus University, Denmark; [8]Jagellonian University Krakow, Poland; [9]University of Frankfurt, Germany; [10]University of Liverpool, United Kingdom; [11]Technische Universität, Darmstadt, Germany

The results of an experiment with a relativistic 305 MeV/u ^{14}Be beam impinging on a liquid hydrogen target are discussed. Proton knockout from ^{14}Be leads to the formation of unbound ^{13}Li system, while inelastic scattering results in unbound states of ^{14}Be. The experimental setup, consisting of the neutron detector LAND, the dipole spectrometer ALADIN and different types of tracking detectors, allows to reconstruct the momentum vectors of all decay products measured in coincidence.

A description of the three-body system is made in terms of Jacobi-coordinate basis: the relative momentum between two particles, $\mathbf{q}_{12}$, and the relative momentum between center of mass of a binary system and the third particle, $\mathbf{q}_{3-12}$. The correlations can be described by three variables: the total relative energy E_{cnn} in the three-body system, the angle θ between Jacobi momenta $\mathbf{q}_{12}$ and $\mathbf{q}_{3-12}$, and the fractional energy $\varepsilon_{12} = \mathbf{q}_{12}^2/E_{cnn}$. The coordinate system is labeled as T-system when 1,2 stand for neutrons and as Y-system when the core is labeled as 1.

The fractional energy ε and the angle θ are extracted from the experimental data, both in the T and Y systems. The obtained experimental distributions are then analyzed in terms of correlation functions, $W(\cos(\theta))$ and $W(\epsilon)$, representing the probability density for the whole system as a function of $\cos(\theta)$ and ϵ. This normalized functions are analyzed using an expansion of decay amplitudes in a restricted set of hyperspherical harmonics.

The obtained distributions for ^{11}Li+n+n, corresponding to the relative-energy interval 0 – 3 MeV are shown in Fig. 1, Ref.[1]. The analysis shows that ^{11}Li+n+n relative-energy spectrum can be interpreted as the $I^\pi = 3/2^-$ ground state together with excited states having a structure similar to the 2+ state in a spin-zero core plus 2n, but giving several states with $I^\pi = (7/2^-, 5/2^-, 3/2^-, 1/2^-)$ from the coupling to the $I^\pi = 3/2^-$ ^{11}Li core. For the excited states, the di-neutron component, $S = 0$ and $l_{nn} = 0$, is about 50%. The weight of the configuration where the two neutrons occupy the p-shell amounts to only 5%. The correlations in the ^{11}Li+n+n system related to the high-energy part of the relative-energy spectrum indicates the importance of configurations where the two neutrons occupy the d shell.

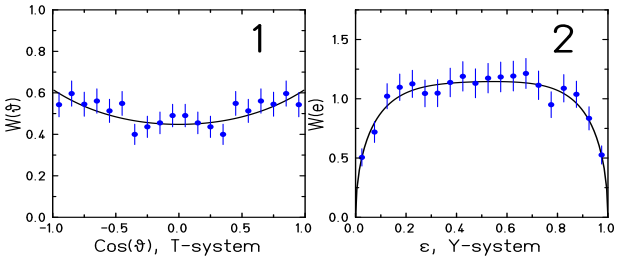

Figure 1: Angular (1) and energy (2) correlations between $^{11}\mathrm{Li} + \mathrm{n} + \mathrm{n}$ in the region of its ground state $0 \leq E_{cnn} \leq 3$ MeV. The solid lines correspond to a fit using an expansion of the decay amplitude in a restricted series of hyperspherical harmonics assuming $\mathrm{I}^\pi = 3/2^-$ and hypermomentum $K \leq 4$.

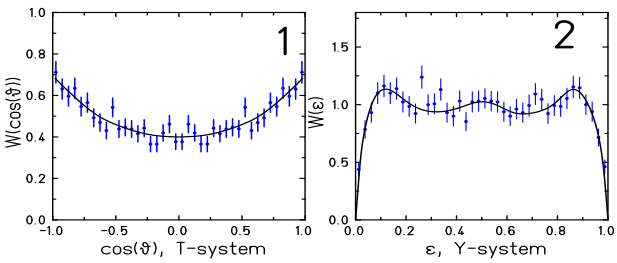

Figure 2: Angular (1) and energy (2) correlations between $^{12}\mathrm{Be} + \mathrm{n} + \mathrm{n}$ in $0.5 \leq E_{cnn} \leq 3.5$ MeV. The solid line is drawn to guide the eye.

Angular and energy correlations for ^{12}Be+n+n, corresponding to the relative-energy interval 0.5 – 3.5 MeV, are shown in Fig. 2. Complete interpretation of the data is still in progress.

References

[1] H.T. Johansson et al., Nucl. Phys. **A847**(2010)66.

*This work was supported by the Alliance Program of the Helmholtz Association (HA216/EMMI)

s-wave contribution in the n+^{12}Be relative-energy spectrum*

Yu. Aksyutina[1,2], *T. Aumann*[1], *K. Boretzky*[1], *M.J.G. Borge*[3], *A. Chatillon*[1], *L.V. Chulkov*[1,4], *D. Cortina-Gil*[5], *U. Datta Pramanik*[6], *H. Emling*[1], *C. Forssén*[2], *H.O.U. Fynbo*[7], *H. Geissel*[1], *G. Ickert*[1], *H.T. Johansson*[2], *B. Jonson*[2], *R. Kulessa*[8], *C. Langer*[1,9], *M. Lantz*[2], *T. Le Bleis*[1,9], *K. Mahata*[1], *G. Münzenberg*[1], *T. Nilsson*[2], *G. Nyman*[2], *S. Paschalis*[10], *W. Prokopowicz*[1], *R. Reifarth*[1,9], *A. Richter*[11], *K. Riisager*[7], *G. Schrieder*[11], *H. Simon*[1], *K. Sümmerer*[1], *O. Tengblad*[3], *H. Weick*[1], *and M. Zhukov*[2]

[1]GSI, Germany; [2]Chalmers University of Technology, Sweden; [3]CSIC Madrid, Spain; [4]RRC Kurchatov Institute Moscow, Russia; [5]University of Santiago de Compostela, Spain; [6]SINP Kolkata, India; [7]Aarhus University, Denmark; [8]Jagellonian University Krakow, Poland; [9]University of Frankfurt, Germany; [10]University of Liverpool, United Kingdom; [11]Technische Universität, Darmstadt, Germany

The exotic features of halo nuclei originates in low angular momenta of the valence nucleons and a large s-component is therefore often part of their structure. It is generally accepted that the strength of s-wave interaction can be characterized as a neutron-nucleus scattering length, a. However, this description may result into several puzzling examples: e.g., experiments point to that the relatively well-bound nucleus ^{14}Be contains a large $(1s)^2$ component, while the absolute value of a is small for n+^{12}Be. The appearance of an s-wave component in the experimental spectra is, however, a very gentle phenomenon and its interpretation meets difficulties due to the strong dependence on reaction mechanisms and the structure of the involved nuclei.

The ^{14}Be and ^{13}Be nuclei have both been studied in complete kinematics experiments at GSI with 305 MeV/u ^{14}Be beam impinging on a liquid hydrogen target. The results of this experiment have been analyzed together with earlier experiments [1, 2, 3] in order to decrease the ambiguity of the interpretation. The analysis of s-wave contribution in the n+^{12}Be relative-energy spectrum has been done and very preliminary results are given in this report.

The s- wave component was described in an R-matrix parameterization: $\delta_0 = \arctan(\gamma^2 P_0(\rho)/(E_r - E)) - \arctan(F_0/G_0)$ taking into account an additional phase shift originating in the structure of the initial nucleus.

The fit results in $E_r = 0.8$ MeV and $\gamma^2 = 0.9$ MeV. The reduced width is smaller than the Wigner limit, thus the s-wave appears in the relative-energy spectrum as a resonance (S-matrix pole position $E_S = 0.4 - \mathrm{i}0.8$). The phase-shift dependence on relative energy is shown in the upper panel in Fig. 1. First it should be mentioned that the derived scattering length is small, $a = -1.5$ fm. and that effective-range approximation can only be applied in a small energy region close to zero.

Further, the n+^{12}Be interaction potential, $U_0(r)$, was reconstructed from the phase shift. An inverse potential-scattering analysis is not clear-cut and its solution depends on the choice of the $U_0(r)$ parameterization. Calculations

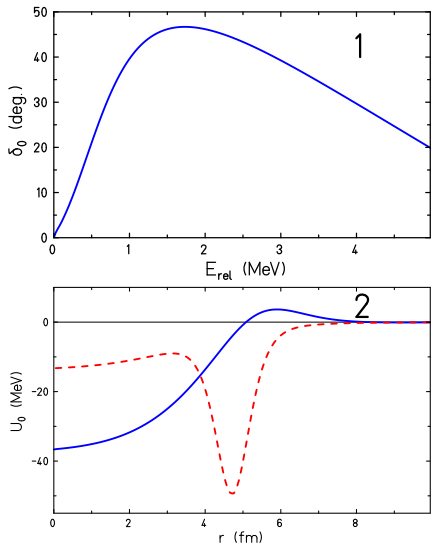

Figure 1: (1) s-wave phase shift for n+^{12}Be scattering obtained from analyses of experimental data. (2) Phase-equivalent potentials.

have shown that the Woods-Saxon potential alone cannot give the observed phase-shift dependence. Two solutions for the phase-equivalent potentials are shown in the lower panel in Fig. 1, (i) a potential with a surface repulsion (the full-drawn curve), and (ii) a potential with a surface attraction (the hatched curve). Both could explain the resonance character of the spectrum and, at the same time, indicate that the two-body description of ^{13}Be is a crude approximation for the system, which, in fact, has a few-body character.

Thus from the analysis of the experimental data the conclusion can be made that few-body dynamics plays a crucial rôle in an adequate description of neutron-halo properties and, in particular, in the structure of the ^{13}Be $1/2^+$ ground state.

References

[1] Y. Kondo et al., Phys. Lett. B 690 (2010) 245.

[2] H. Simon et al., Nucl. Phys. A 791 (2007) 267.

[3] J.L. Lecouey, Few-Body Systems, 34 (2004) 21.

*This work was supported by the Alliance Program of the Helmholtz Association (HA216/EMMI)

Nuclear matter density distributions of the neutron-rich nuclei ^{12,14}Be from intermediate energy proton elastic scattering in inverse kinematics

S. Ilieva[1], F. Aksouh[1], G. D. Alkhazov[2], K.-H. Behr[1], A. Bleile[1,4], A. Brünle[1], L. Chulkov[3], A. V. Dobrovolsky[2], P. Egelhof[1,4], H. Geissel[1], M. Gorska[1], G. Ickert[1], A. Inglessi[1], R. Kanungo[1], A. V. Khanzadeev[2], O. Kiselev[1,4], G. A. Korolev[2], X. C. Le[1], Y. Litvinov[1], W. Niebur[1], C. Nociforo[1], D. M. Seliverstov[2], L. O. Sergeev[2], H. Simon[1], V. A. Volkov[3], A. A. Vorobyov[2], H. Weick[1], V. I. Yatsoura[2], and A. A. Zhdanov[2]

[1]GSI, Darmstadt, Germany; [2]PNPI, Gatchina, Russia; [3]Kurchatov Institute, Moscow, Russia; [4]Institut für Physik and Institut für Kernchemie, Johannes Gutenberg Universität Mainz, Mainz, Germany

The proton-nucleus elastic scattering at intermediate energies is a well-established method for the investigation of the nuclear matter distribution in stable nuclei. When used in inverse kinematics it can be also applied for nuclei far from stability. An interesting phenomenon which appears in some light exotic nuclei is the halo structure, characterized with a long low-density tail in the matter distribution. The nuclei ^{12}Be and ^{14}Be, studied in the current experiment, are examples for such halo nuclei and their densities are of importance for the understanding of the nuclear structure.

The differential cross sections for proton elastic scattering on the isotopes ^{12}Be and ^{14}Be were measured at GSI. The isotopes were produced by fragmentation of an ^{18}O beam in the FRS. The central part of the experimental setup was the active hydrogen target IKAR in which the scattered protons were detected [1]. Additionally, multi-wire proportional chambers were used to track the scattered projectiles, and scintillators for particle identification.

The obtained differential cross sections (Fig. 1) were analyzed within the Glauber multiple-scattering theory using different parametrizations for the nuclear density distribution [2]. The results from the fits with different density

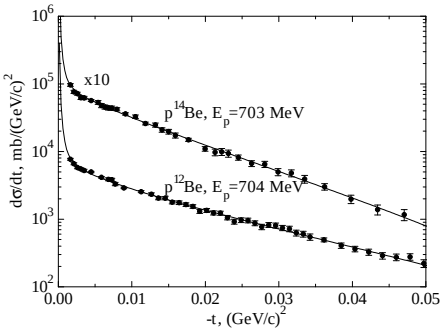

Figure 1: Experimental cross sections for p^{12}Be and p^{14}Be elastic scattering. The lines are fits to the cross section with a gauss-oscillator density parametrization within the Glauber multiple-scattering theory.

parametrizations agree with each other. The average densities obtained for the two isotopes are shown in Fig. 2. The error-bands include the total error from the fits with different densities.

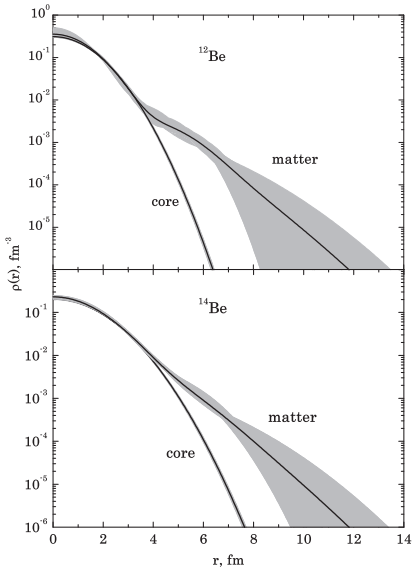

Figure 2: Matter and core density distributions deduced for ^{12}Be (top) and ^{14}Be (bottom) isotopes.

The average *rms* matter radii deduced from the present analysis are $R_m = 2.82 \pm 0.12$ fm for the ^{12}Be isotope and $R_m = 3.11 \pm 0.14$ fm for ^{14}Be, respectively. Extended nuclear-matter density distributions were observed in both nuclei. The halo structure of ^{14}Be was confirmed (possible 2 or 4 neutron halo configuration). Comparison with few-body calculations [3] supports inverse order of the d and s orbitals and relatively large s shell occupancy. The extended distribution observed in ^{12}Be supports the breaking of the shell structure and the disappearance of the $N = 8$ neutron magic number in this nucleus. The provided experimental data can be used as an input to theoretical calculations to further investigate the nuclear structure far off stability.

References

[1] S. R. Neumaier *et al.*, Nucl. Phys. A 712 (2002) 247

[2] G. D. Alkhazov *et al.*, Nucl. Phys. A 712 (2002) 269

[3] I. Thompson *et al.*, Phys. Rev. C 53 (1996) 708

Direct reactions of light exotic beams measured in complete kinematics at R^{3}B

T. Adachi[1], *Y. Aksyutina*[2,15], *J. Alcantara*[3], *S. Altstadt*[4], *H. Alvarez-Pol*[3], *N. Ashwood*[5], *T. Aumann*[6,2], *M. Barr*[5], *S. Beceiro*[3], *D. Bemmerer*[7], *J. Benlliure*[3], *K. Boretzky*[2], *G. Burgunder*[8], *M. Caamano*[3], *C. Caesar*[6], *E. Casarejos*[3], *W. Catford*[9], *S. Chakraborty*[10], *M. Chartier*[11], *L. Chulkov*[15,21], *D. Cortina-Gil*[3], *U. Datta Pramanik*[10], *P. Diaz*[3], *I. Dillmann*[2], *J. Enders*[6], *O. Ershova*[4], *A. Estrade*[2], *F. Farinon*[2], *L.M. Fraile*[12], *M. Freer*[5], *M. Freudenberger*[6], *D. Galaviz Redondo*[13], *H. Geissel*[2], *D. Gonzalez Diaz*[6], *J. Hagdahl*[8], *T. Heftrich*[4], *M. Heil*[2], *M. Heine*[6], *A. Henriques*[13], *M. Holl*[6], *A. Ignatov*[6], *H. Johansson*[8], *B. Jonson*[8], *N. Kalantar*[1], *R. Knöbel*[2], *T. Kroell*[6], *R. Krücken*[14], *J. Kurcewicz*[2], *M. Labiche*[7], *C. Langer*[4], *T. Le Bleis*[14], *R. Lemmon*[7], *J. Machado*[13], *J. Marganiec*[15], *A. Movsesyan*[6], *A. Najafi*[1], *T. Nilsson*[8], *C. Nociforo*[2], *V. Panin*[6], *S. Pietri*[2], *R. Plag*[4], *A. Prochazka*[2], *A. Rahaman*[10], *G. Rastrepina*[2], *R. Reifarth*[4], *G. Ribeiro*[9], *M.V. Ricciardi*[2], *C. Rigollet*[1], *K. Riisager*[22], *M. Röder*[16], *D. Rossi*[2], *J. Sanchez del Rio*[12], *D. Savran*[15,17], *H. Scheit*[18], *H. Simon*[2], *O. Sorlin*[8], *B. Streicher*[1], *J. Taylor*[11], *O. Tengblad*[12], *S. Terashima*[2], *R. Thies*[8], *T. Yasuhiro*[18], *E. Uberseder*[19], *J. Van de Walle*[1], *P. Velho*[13], *V. Volkov*[6], *A. Wagner*[7], *F. Wamers*[6], *H. Weick*[2], *M. Weigand*[4], *C. Wheldon*[5], *G. Wilson*[9], *C. Wimmer*[4], *J. Winfield*[2], *P. Woods*[20], *D. Yakorev*[7], *M. Zoric*[2], *and K. Zuber*[16]

[1]KVI Groningen, Netherlands; [2]GSI Darmstadt, Germany; [3]University of Santiago de Compostela, Spain; [4] University of Frankfurt, Germany; [5]Birmingham University, UK; [6] TU Darmstadt, Germany; [7] HZDR Dresden-Rossendorf, Germany; [8]GANIL, Caen, France; [9] University of Surrey, UK; [10] SINP Kolkata, India; [11] University of Liverpool, UK; [12] Universidad Complutense of Madrid, Spain; [13]University of Lisbon, Portugal; [14] TU Munich, Germany; [15]ExtreMe Matter Institute EMMI and Research Division, GSI Darmstadt, Germany; [16]TU Dresden, Germany; [17]Frankfurt Institut for Advanced Studies FIAS, Frankfurt, Germany; [18] RIKEN, Japan; [19]University of Notre Dame, US; [20]University of Edinburgh, UK; [21] RRC Kurchatov Institute Moscow, Russia; [22]Aarhus University, Denmark

An experiment has been performed by the R^{3}B collaboration aiming at the investigation of light neutron-rich nuclei utilizing kinematically complete measurements of reactions at relativistic energies with the R^{3}B-LAND reaction setup at Cave C. The physics topics to be studied comprise the measurement of astrophysical reaction rates relevant for r-process nucleosynthesis using heavy-ion induced electromagnetic excitation and quasi-free knockout reactions to study the evolution of shell and cluster structures close to and beyond the dripline. Concerning the latter topic, the evolution of neutron and proton shells is studied in (p, pn) and $(p, 2p)$ reactions, respectively. The evolution of alpha clustering in the ground states of beryllium isotopes as a function of increasing neutron number is investigated in $(p, p\alpha)$ reactions. Unbound (ground and excited) states will be populated and identified in $(p, 2p)$ reactions. Finally, the quenching of single-particle strength in neutron-proton asymmetric nuclei will be addressed by knocking out deeply bound protons and neutrons for nuclei with varying neutron-proton asymmetry.

The experiment has been carried out successfully in August 2010. A large A/Z range from 1.9 to 3 has been covered in 6 settings of the Fragment Separator and the beamline to Cave C. For the oxygen isotopic chain, data have been taken for all bound isotopes from the proton-dripline nucleus ^{15}O to the neutron-dripline nucleus ^{24}O. A primary beam of ^{40}Ar and a thin degrader has been used to ensure transport of radioactive ions from helium

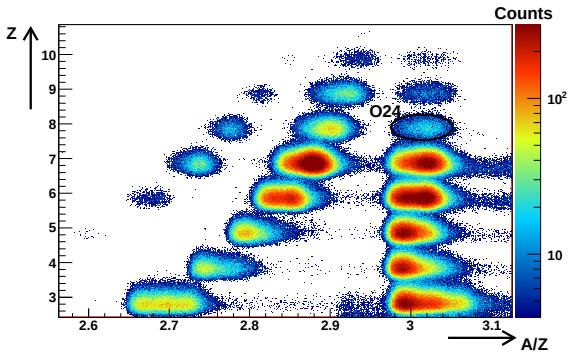

Figure 1: Mixed secondary beam incident on the R^{3}B target at Cave C produced by fragmentation of ^{40}Ar for a setting optimized for transport of ^{24}O.

to fluorine. Figure 1 shows the beam composition for the most neutron-rich setting optimized for transport of isotopes with $A/Z = 3$. Runs have been taken with carbon, CH_2, and lead targets for the study of different reactions. For this setting, for instance, the ^{17}C(n, γ) reaction rate, which is important for the r-process, will be extracted from Coulomb dissociation of ^{18}C. The same data set comprises the α knockout reaction on ^{12}Be, as well as the proton knockout from ^{26}F populating unbound states in ^{25}O. Finally, the neutron valence shell structure of ^{23,24}O will be investigated in (p, pn) reactions, and the deeply bound proton states in ^{24}O in $(p, 2p)$ reactions. Here the role of nucleon-nucleon correlations for neutron-proton asymmetric nuclei is of interest.

Quasi-free scattering off ^{12}C in inverse kinematics at the R^{3}B/LAND-setup

V. Panin[1,2], T. Aumann[1,2], J. Taylor[3], and the R^{3}B collaboration

[1]Kernreaktionen und Nukleare Astrophysik, GSI Darmstadt, Germany; [2]Institut für Kernphysik, TU Darmstadt, Germany; [3]Department of Physics, University of Liverpool, UK

An important part of the physics programme at the future R^{3}B (Reactions with Relativistic Radioactive Beams) experiment at FAIR will be based on the study of proton-induced reactions in kinematically complete measurements at relativistic energies. These are in particular the Quasi-Free Scattering (QFS) processes of the type (p,2p), (p,pn), etc. which will be used to investigate the single-particle and cluster structure of neutron-proton asymmetric nuclei. In order to establish the experimental technique of the measurements in inverse kinematics the benchmark experiment was performed in 2007 at R^{3}B/LAND-setup in Cave C. A ^{12}C beam at an energy of 400MeV/u has been chosen for this purpose since its structure is well studied and high-quality data from proton- as well as electron-induced knock-out reactions are available [1].

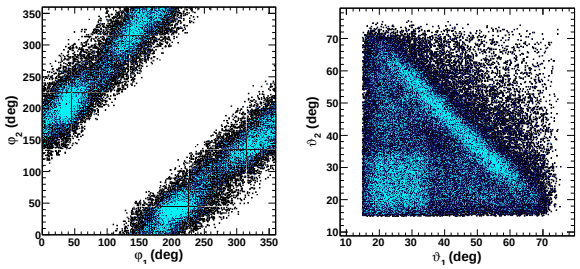

Figure 1: Angular correlations of two protons from ^{12}C(p,2p)X. Left - correlation of azimuthal angles (back-to-back kinematics); right - correlation of polar angles; the contribution of the reactions with Carbon is seen as uncorrelated events at small theta values.

A prototype setup was equipped with an array of 162 thick NaI scintilators (Crystal Ball) covering the full solid angle around the CH_2 target for the detection and energy measurement of high-energy protons and gammas emerging in proton knock-out reactions. Additionally six Si micro-strip detectors covered the forward hemisphere for accurate tracking of the protons in coincidence with residual heavy fragments. A typical angular correlation pattern for proton pairs is shown at Figure 1. Such distributions are seen as an indication for (p,2p) reactions induced by the Hydrogen component of the CH_2 target. Heavy fragments from the reactions were tracked after the ALADIN magnet using a ToF-Bρ technique. Figure 2 illustrates the charge and mass identification of the heavy residues after the magnet. The dominating part of the observed fragments are ^{11}B which have been produced via knock-out of valence protons occupying the outer p-shell. All other fragments stem from proton removal from the inner s-shell. This process results in a higher excitation energy of the residual ^{11}B which in turn decays via particle emission.

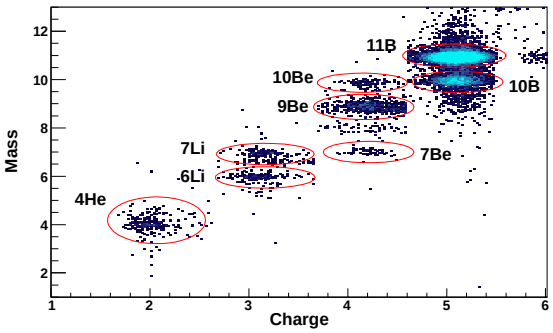

Figure 2: Fragments produced in ^{12}C(p,2p)X reactions.

Figure 3 shows the Doppler-corrected spectrum of γ-rays accompanying the residual ^{11}B and two forward-emmited protons fulfilling QFS kinematical conditions. The first excited states of ^{11}B can be recognized, and they serve as an evidence for the de-excitation of low-energy p-hole states.

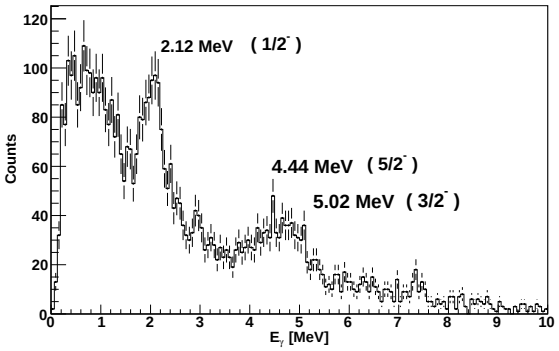

Figure 3: Doppler-corrected gamma spectrum in coincidence with ^{12}C(p,2p)^{11}B reaction.

The main objective for the future analysis will be to reconstruct the excitation energy of the s-hole state using the invariant mass method for all the break-up channels.

References

[1] G. Jacob and Th. A. J. Maris, Rev.Mod.Phys. 38 (1966) 121.

Exclusive Measurements of One-Proton-Removal Reactions with the Proton-Dripline Nucleus ^{17}Ne at Relativistic Energies

F. Wamers[1,2], T. Aumann[1,2], M. Heil[2], J. Marganiec[3], R. Plag[2,4], and the R^{3}B Collaboration

[1]Institut für Kernphysik, TU Darmstadt, Germany; [2]Kernreaktionen und Nukleare Astrophysik, GSI Darmstadt, Germany; [3]ExtreMe Matter Institute EMMI, GSI Darmstadt, Germany; [4]Goethe Universität, Frankfurt a.M., Germany

^{17}Ne is a proton-dripline nucleus that has raised special interest in nuclear-structure physics in recent years. As a Borromean 3-body system (^{15}O+2p), it is often considered to be a 2-proton-halo nucleus, yet lacking conclusive experimental and theoretical evidence about its structure.
In 2007, we have studied breakup reactions of ^{17}Ne secondary beams at 500 AMeV in inverse kinematics using the R^{3}B-LAND setup at GSI. One focus was set on the quasi-free one-proton knockout in a proton-rich polyethylene (CH_2) target, *i.e.*, ^{17}Ne(p,2p)^{16}F $\rightarrow$ ^{15}O+X. Recoil protons have been detected with Si-Strip detectors and with the surrounding 4π NaI *Crystal Ball* spectrometer, thus providing a clean signature for quasi-free (p,2p) events [1]. In this report we present results from the *carbon*-induced one-proton knockout reactions leading to excited states in the unbound ^{16}F (^{15}O+p). The experimental goal is the determination of the s^2/d^2 configuration mixture of the two valence protons in the ^{17}Ne ground state. Calculations based on a three-body cluster model show this mixture as being a decisive measure for the ^{17}Ne structure [2], and they calculated an s^2 weight of 48 %, *i.e.*, predicted a good indication for a two-proton halo in ^{17}Ne. In contrast, a more recent theoretical study [3] calculated an s^2 weight of only about 15 %. Disagreements like that highlight strongly the necessity of our investigations.

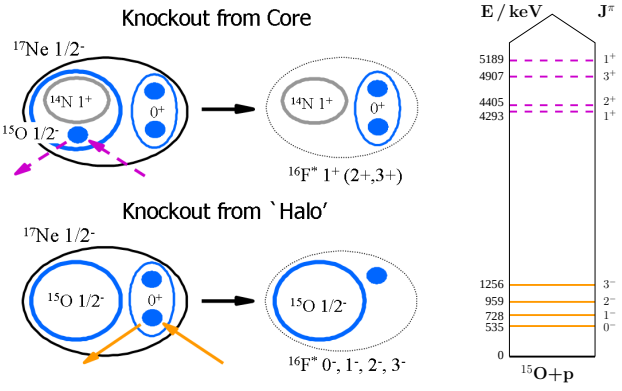

(a) Proton removal from core and 'halo' of ^{17}Ne. (b) ^{16}F=^{15}O+p.

Fig. 1: (a) Scheme of one-proton knockout from 'halo' (solid, orange) and core-states (dashed, purple) in ^{17}Ne, leading to a lower or higher excitation of the unbound ^{16}F, respectively [2]. (b) Corresponding ^{16}F level scheme.

In direct carbon-induced knockout reactions (see Fig. 1), protons can be removed from the ^{17}Ne 'halo' — being either in a $(2s_{1/2})^2$ or a $(1d_{5/2})^2$ configuration — as well as from $1p$-shell states in its ^{15}O core. Both processes populate the lower and the higher resonances in ^{16}F, respectively [2], as shown in Fig. 1. Using time-of-flight measurements and tracking techniques, we have deduced the energies and momenta of the final-state projectile-like ^{15}O core and of the remaining proton in coincidence. By using the invariant mass formalism, we have reconstructed the ^{16}F excitation energy from the ^{15}O+p relative energy, shown in Fig. 2. In contrast to earlier *inclusive* measure-

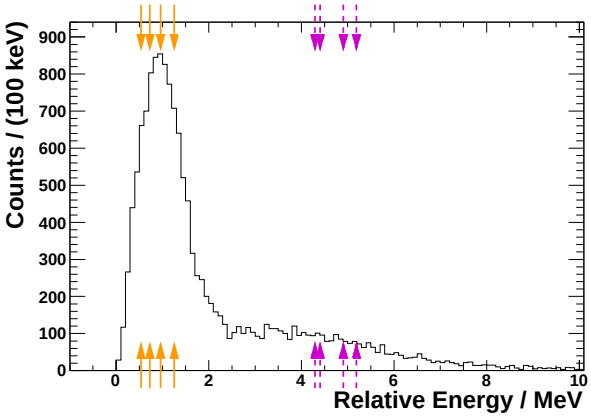

Fig. 2: Excitation energy of ^{16}F (^{15}O+p), seen in carbon-induced one-proton knockout from ^{17}Ne. The arrows indicate the position of the narrow ($\leq$100 keV) resonance states of ^{16}F, compare to Fig. 1. Low-lying strength (solid, orange arrows) indicates knockout from ^{17}Ne 'halo' states, whereas higher excitation (dashed, purple arrows) is attributed to knockout from ^{17}Ne core-states.

ments of proton-removal reactions from ^{17}Ne [4], we have *exclusively* observed the proton-knockout from 'halo' or from core states in ^{17}Ne, and we are able to select either one *via* a cut on the corresponding ^{16}F excitation energy in Fig. 2. In consequence, we will be able to extract observables which are closely linked to the s^2/d^2 ratio in the ^{17}Ne 'halo' — such as the ^{17}Ne two-proton-removal cross section, or the ^{15}O (core) momentum distributions — cleanly and unambiguously.

References

[1] Felix Wamers, GSI Scientific Report 2008.
[2] L. V. Grigorenko et al., Phys. Rev. C **71** (2005) 051604.
[3] T. Oishi et al., Phys. Rev. C **82** (2010) 024315.
[4] R. Kanungo et al., Eur. Phys. Jour. A **25** (2005) 327.

Investigation of the CNO-break-up reaction: $^{15}O(2p,\gamma)^{17}Ne$, by the Coulomb Dissociation of ^{17}Ne

J. Marganiec[1], *T. Aumann*[2,3], *M. Heil*[2], *R.Plag*[2,4], *F. Wamers*[2,3] *and the LAND-R*^{3}*B collaboration*
[1]ExtreMe Matter Institute EMMI, GSI Darmstadt, Germany; [2]Kernreaktionen und Nukleare Astrophysik, GSI Darmstadt, Germany; [3]Institut für Kernphysik, TU Darmstadt, Germany; [4]Goethe-Universität, Frankfurt am Main, Germany

I. INTRODUCTION AND MOTIVATION

The *rp* process takes place most notably in cataclysmic binary system, such as X-ray bursts [1]. At high temperature and density conditions, the CNO cycle and the *rp* process are linked by the α capture reaction on ^{15}O, which allows to process the initial CNO material towards heavier nuclei. However, the main obstacle for a continuous reaction flow between the CNO cycle and the FeNi-mass region are the waiting point nuclei. One of these waiting points is ^{15}O. The $^{15}O(2p,\gamma)^{17}Ne$ reaction could serve as a bypass of this point.

The three-body radiative capture can proceed sequentially [1] or directly from the three-body continuum [2]. It has been suggested that the reaction rate can be enhanced by a few orders of magnitude by taking the three-body continuum into account [2]. In order to verify these calculations, the $^{15}O(2p,\gamma)^{17}Ne$ cross section has to be investigated by studying the time-reversed process, the Coulomb dissociation of ^{17}Ne.

The proton dripline nucleus ^{17}Ne has a comparatively small $2p$ separation energy (S_{2p} = 970 keV) and represents a promising candidate for a two-proton halo [3]. The main uncertainty of the ^{17}Ne ground state is connected to the yet unknown mixture of the d^2 and s^2 configurations of the two protons outside the ^{15}O core. In the case of large s^2 weights of proton configurations the nucleus ^{17}Ne has a halo structure, while in the case of large d^2 weights the halo is strongly suppressed.

II. EXPERIMENT AND RESULTS

The cross sections for radiative capture not always can be determined from direct experiments. Especially, problems appear in cases of very small cross sections, unstable nuclei and three particles in entrance channel. For these situations the Coulomb Dissociation method is useful.

In this technique a nuclear Coulomb field is used as a source of the photodisintegration process, and instead of studying directly a radiative capture process [5] $b + c \rightarrow a + \gamma$ the time reversed process can be considered $a + \gamma \rightarrow b + c$.

The secondary ^{17}Ne ion beam, with energy E = 500 MeV/nucleon, has been produced by fragmentation of a ^{20}Ne primary beam. The incoming ^{17}Ne beam has been identified by means of energy-loss and position measurements with position-sensitive pin diodes, and time-of-flight measurements. It has been focused on a secondary target (Pb - 200 mg/cm^2 or C - 370 mg/cm^2). The reaction products have been identified using two Si-strip detectors before they have been deflected by a large-gap dipole magnet. After the magnet the heavy fragments have been detected with two scintillating fibre arrays and a two-layer Time-of-Flight (ToF) wall. For proton identification two drift chambers and a big two-layer ToF wall have been used [6]. By means of energy-loss and time-of-flight measurements particles have been identified.The measurements have been performed not only for a Pb target, but also for C and without any target to subtract the non-specific reactions, taking place outside of the target and reactions in the target due to nuclear interactions.

The outgoing oxygen fragments and protons have been tracked, and their mass and momenta have been determined. The excitation energy spectrum has been reconstructed. Preliminary integral Coulomb excitation cross section has been calculated - 242 mb.

The analysis is in progress. As a next step, differential Coulomb excitation cross section will be calculated. From this, photoabsorption and radiative capture will be obtained, which are not only relevant in the *rp* process but also are of interest with regard to the proton-halo structure of ^{17}Ne.

This project was supperted by the German Federal Minister for Education and Research (BMBF), EU(EURONS), ExtreMe Matter Institute EMMI, GSI Darmstadt and FIAS Frankfurt Institute for Advanced Studies.

[1] J. Görres *et al.*, *Phys. Rev. C* 51, 392, 1995
[2] L.V Grigorenko, M.V. Zhukov, *Phys. Rev. C* 72, 015803, 2005
[3] R. Kanungo *et al.*, *Phys. Lett. B* 571, 21, 2003
[4] L.V Grigorenko *et al.*, *Phys. Lett. B* 641, 254, 2006
[5] G. Baur and C.A. Bertulani, *Nuc. Phys.* A458, 188, 1986
[6] http://www-linux.gsi.de/∼rplag/land02/

Coulomb dissociation reactions on proton-rich Ar isotopes

C. Langer[*1,2], *O. Lepyoshkina*[3], *T. Aumann*[1], *K. Boretzky*[1], *R. Gernhäuser*[3], *R. Krücken*[3], *R. Plag*[1,2], *R. Reifarth*[1,2], *and the R*^{3}*B collaboration*

[1]GSI, Darmstadt, Germany; [2]Univ. of Frankfurt, Germany; [3]TU München, Germany

Introduction

The dipole strength response of neutron-deficient Argon isotopes was investigated in a Coulomb dissociation experiment using the LAND setup at GSI. Especially the study of low-lying strength components is interesting in several respects. Recent RQRPA calculations predict the appearance of low-lying E1 strength at excitation energies of $E_x \approx 9$ MeV for nuclei at the proton dripline in this mass region [1, 2]. In a macroscopic picture, this is discussed in the context of an out-of-phase oscillation of a thin proton skin against the isospin-saturated core. For nuclear astrophysics the measured (γ, p) reactions are interesting for the calculation of reaction cross-sections and radiative proton capture rates for the rp-process. In this hydrogen burning process a lot of nuclear structure information is still missing, for instance for the bottleneck nuclei ^{30}S and ^{34}Ar [3].

Experiment and Analysis

The experiment was performed at a beam energy of $E_b = 650$ AMeV. At this energy we profit from the huge flux of virtual photons, generated by the highly lorentz-contracted electromagnetic field of a heavy-Z ^{208}Pb target. The beam was produced by fragmentation of a ^{36}Ar primary beam on a 6.347 g/cm^2 Be-target, situated at the entrance of the FRS. Several ions with similar A/Z-ratio are identified at the entrance of Cave C, see Fig.1. After

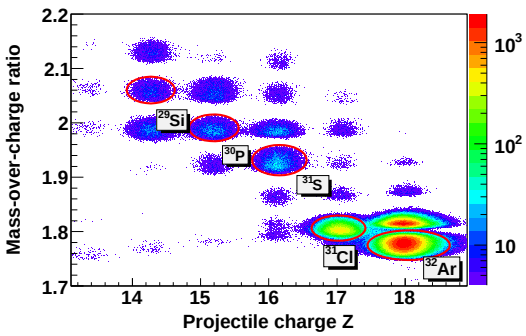

Figure 1: Incoming beam ID for the ^{32}Ar setting.

event-by-event identification (ID) of the incoming ions the reaction channel has to be chosen. As shown in Fig. 2 different fragment charges are measured behind the ALADIN magnet. One can see a lack of Chlorine ($Z = 17$) isotopes. Instead, we dominantly find Sulfur isotopes ($Z = 16$) and products from other decay channels. This can be explained by the low proton separation threshold in ^{31}Cl, produced in the ^{32}Ar$(\gamma, p)^{31}$Cl reaction. The mass is derived from fragment tracking through the magnetic field of ALADIN. This is done using the magnetic rigidity, time-of-flight and the charge Z in the outgoing channel. As a proof-of-principle case the unreacted ^{32}Ar beam is tracked and the resulting mass distribution is shown in Fig.3.

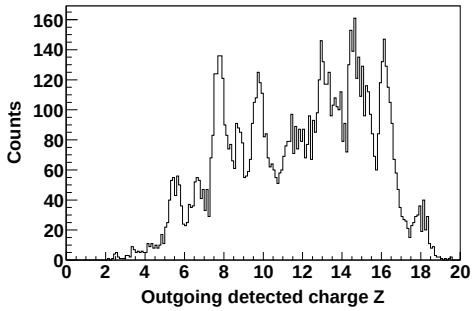

Figure 2: Outgoing charge ID with a cut on incoming ^{32}Ar.

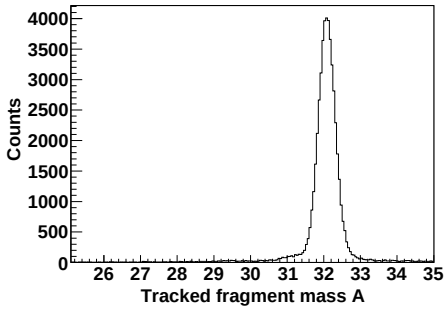

Figure 3: Mass distribution for the unreacted ^{32}Ar beam.

Outlook

The analysis of the mass for the reaction products is in progress and will be followed by the reconstruction of the integral coulomb break-up cross-section and the energy-differential cross-section $d\sigma_C/dE$ of different isotopes.

References

[1] N. Paar et al., Phys.Rev.Letters 94, 182501 (2005)

[2] C. Barbieri et al., Phys.Rev.C. 77, 024304 (2008)

[3] J. L. Fisker et al., ApJS. 608, L61 (2004)

*This project is supported by the HGF Young Investigators Project VH-NG-327.

Coulomb dissociation reactions on Mo isotopes for astrophysics applications

O. Ershova[1,2], *T. Aumann*[1], *H. T. Johansson*[1,3], *T. Le Bleis*[1,4], *A. Movsesyan*[1,5], *S. Paschalis*[6], *R. Plag*[1,2], *R. Reifarth*[1,2], *D. Rossi*[1,7], *and the S295 collaboration*[1]

[1]GSI, Darmstadt, Germany; [2]Univ. Frankfurt, Germany; [3]Chalmers Univ. of Technology, Sweden; [4]Univ. Strasbourg, France; [5]TU Darmstadt, Germany; [6]Univ. Liverpool, UK; [7]Univ. Mainz, Germany

Introduction

Photo-dissociation reactions play an important role in p-process nucleosynthesis, which takes place in supernova explosions. Theoretical calculations of isotopic abundances of the p-nuclei require a vast reaction network linking thousands of isotopes, where most of the reaction rates must be derived from the Hauser-Feshbach statistical model. However, as many rates as possible need to be determined experimentally, in order to provide a reliable reference for the calculations.

Measuring reaction rates on Mo isotopes is important to explain the problem of the significant underproduction of ^{92}Mo and ^{96}Ru in all existing models of p-process nucleosynthesis. Another aspect of the project is to verify the accuracy of the Coulomb dissociation method by comparing our data with experiments performed with real photons at S-DALINAC (TU Darmstadt) and ELBE (FZD) [1].

Experiment and preliminary results

At the FRS/LAND setup at GSI, Coulomb dissociation experiments on the stable ^{92,94,100}Mo and unstable ^{93}Mo isotopes were performed in order to extract (γ,n) and (γ,2n) reaction cross sections. The used method is ideal to investigate unstable isotopes, since the reaction is studied in inverse kinematics: a beam containing nuclei of interest impinges on a high-Z target (Pb). Under certain conditions, such as a sufficiently high energy and a large impact parameter, a reaction takes place between the projectile and a virtual photon originating from the Coulomb field of the target nucleus.

In order to extract the electromagnetic excitation cross sections from the measurement with the Pb target, background reactions must be taken into account. A measurement with a carbon target was performed to estimate the contribution of nuclear reactions at the target, whereas a measurement without any target was done to determine the background from all kinds of reactions outside the target.

Our setup provides the possibility to detect all reaction products, thus delivering kinematically complete data. The incoming and outgoing nuclei are identified with respect to A and Z on an event-by-event basis. Evaporated neutrons with all their characteristics are measured by the LAND detector [2]. Combining this information allows a clean selection of the reaction channel.

Preliminary integral Coulomb-excitation cross sections for three reaction channels are presented in Table 1. Statistical uncertainties of the data are less than 3%, but a non-negligible systematic uncertainty is present and is estimated at around 10%.

Although the setup should provide the possibility to reconstruct the excitation energy spectrum *via* the invariant mass method, difficulties were encountered on the way to understand the efficiency of the CsI γ-detector, which appeared to be unexpectedly low. The overall response of the setup is very complex and does not allow a deconvolution. We are investigating these issues.

Integrated Coulomb-excitation cross sections for ^{100}Mo were compared to the measurement by Beil *et al.* [3] after convoluting the latter with the E1 component of the virtual photon spectrum (see Table 1). Beil *et al.* used a monoenergetic photon beam produced by positron annihilation to measure the following total photoabsorption cross sections: $\sigma_\gamma(\gamma,n) = \sigma[(\gamma,n) + (\gamma,pn)]$ and $\sigma_\gamma(\gamma,2n) = \sigma[(\gamma,2n)+(\gamma,pnn)]$. In our data, the proton removal channels are clearly separated and are not analyzed. However, in the case of ^{100}Mo, the proton removal threshold is high enough to neglect the contribution of this channel. In the case of ^{92}Mo(γ,n), a direct comparison was not possible due to the low (γ,np) reaction threshold.

It should be noted that the photoabsorption data [3] might need to be scaled additionally by a factor 0.85, as suggested by Berman *et al.* [4]. The authors assume that the discrepancy might come from a wrong estimation of the photon flux and/or neutron detection efficiency by Beil *et al.* [3].

The data analysis is in progress. As a next step, the Coulomb-excitation cross section for ^{93}Mo will be calculated. It is of particular interest, since this isotope is unstable and its cross section has never been measured before.

Reaction	σ_{CE}(prelim.), mb	σ_{CE}([3]), mb
^{100}Mo(γ,n)^{99}Mo	812	876 ± 30
^{100}Mo(γ,2n)^{98}Mo	285	293 ± 20
^{92}Mo(γ,n)^{91}Mo	437	

Table 1: Integrated Coulomb excitation cross sections for three reaction channels

References

[1] M. Erhard et al., Phys. Rev. C 81(3) (2010) 034319.

[2] T. Blaich et al., NIM A 314(1) (1992) 136.

[3] H. Beil et al., Nucl. Phys. A 227(3) (1974) 427.

[4] B. L. Berman et al., Phys. Rev. C 36(4) (1987) 1286.

^{59}Fe(n,γ)^{60}Fe measured by Coulomb Dissociation at R^{3}B/LAND setup

T. Heftrich[*1], *E. Uberseder*[2], *T. Aumann*[4], *K. Boretzky*[3], *S. Haik*[3], *M. Heil*[3], *A. Kelic*[3], *R. Plag*[3], *R. Reifarth*[1], *V. Ricciardi*[3], *K. Sonnabend*[1], *H. Weick*[3], *M. Wiescher*[2], *and the s389 collaboration*

[1]University of Frankfurt, Germany; [2]University of Notre Dame, USA; [3]GSI Darmstadt, Germany; [4]TU Darmstadt, Germany

One of the fundamental signatures for active nucleosynthesis in our Universe is the observation of long-lived radioactive elements in our galaxy. Using high-resolution γ-ray observatories, such as COMPTEL, RHESSI, and INTEGRAL, the reaction rates of long-lived radioactive isotopes, for instance ^{18}F, ^{22}Na, ^{26}Al, ^{44}Ti and ^{60}Fe, can be determined [1]. A detailed analysis of the two long-lived radioactive isotopes ^{26}Al and ^{60}Fe will give important information about stellar nucleosynthesis. The production of ^{26}Al and ^{60}Fe is thought to be associated with the nucleosynthesis in hot carbon or oxygen shell burning in massive pre supernova stars and in the subsequent shock-front driven explosive nucleosynthesis of type II supernovae [2,3]. While the reactions associated with ^{26}Al have been studied extensively in the past, very little is known about the reactions associated with the production of ^{60}Fe. RHESSI and INTEGRAL [4,5] observed the characteristic smooth ^{60}Fe distribution of γ-radioactivity along the galactic plane [6]. Model predictions shows that the ^{60}Fe is produced in the supernova shock front as well as in a hot s-process environment during carbon shell burning in the massive supernova progenitor star. Based on simulations of hot carbon shell burning the radioactive isotope ^{60}Fe with a half-live of $t_{1/2}$=2.6 My is associated with the neutron capture process of stable iron istotopes for instance ^{58}Fe(n,γ)^{59}Fe(n,γ)^{60}Fe. Because of its short half-live ($t_{1/2}$=44.5 d), neutron capture on ^{59}Fe is very difficult to measure directly. Therfore, the coulomb dissociation cross section of the inverse reaction ^{60}Fe(γ, n)^{59}Fe provides important information via the principle via detailed balance. In order to prove this method, ^{59}Fe(γ, n)^{58}Fe was studied additionally to determine the already directly measured ^{58}Fe(n,γ)^{59}Fe cross section [7].

Coulomb dissociation measurements of ^{59}Fe and ^{60}Fe were performed at the R^{3}B/LAND Setup at GSI. The unstable iron isotopes were produced by fragmentation of a 660 AMeV primary beam of ^{64}Ni on a 4 g/cm^2 Be target at FRS. The beam energy at the lead target was 535 AMeV. With intensities of 2-5·10^7 particles/s, the ^{60}Fe beam on a 500 mg/cm^2 lead target produce a virtual photons with an energy of astrophysical intrest. Figure 1 shows the incoming particle identification from the experimental setup. It is possible to identify all reaction products with R^{3}B/LAND setup. The fast neutrons were detected with the LAND detector. The heavy fragments were detected with scintillator walls and fiber detectors.

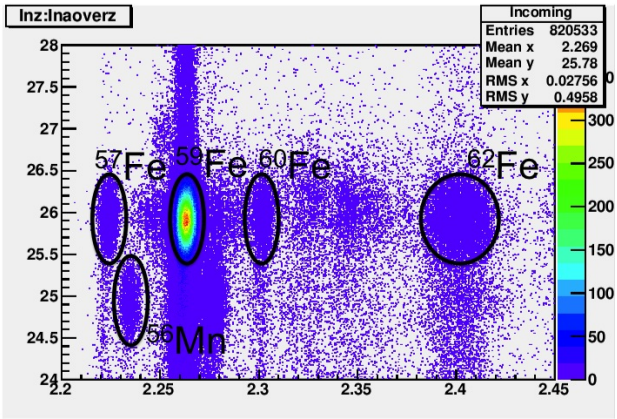

Figure 1: The incoming particle ientification from the experiment.

Conclusions and outlook

The experiment was successfully performed at the R^{3}B/LAND Setup and is currently under analysis. The next steps of the analysis are the identification of the outgoing particles, tracking of all reaction products and eventually energy-dependent information about the dissociation cross section ^{60}Fe(γ, n)^{59}Fe. Once the ^{59}Fe(n,γ)^{60}Fe is determined, nucleosynthesis simulations will be performed, leading to a better understanding of the late stages of massive stars.

References

[1] S. Woosley and T. Weaver, Astrophys. J. Suppl. 101 (1995) 181

[2] F. Timmes, S. Woosley, D. Hartmann, et al. Astrophys. J. 449 (1995) 204

[3] M. Limongi and A. Chieffi, Astrophys. J. 647 (2006) 483

[4] D. Smith, New Astr. Rev. 48 (2004) 87

[5] M. Harris, J. Knödlseder, P. Jean, et al. Astron. Astrophys. 433 (2005) L49

[6] W. Wang, M. J. Harris, R. Diehl, et al. Astron. Astrophys. 469 (2007) 1005

[7] M. Heil, F. Käppeler, E. Uberseder, et al. Phys. Rev. C 77 (2008) 015808

*supported by the HGF Young Investigator Project VH-NG-327 and ExtreMe Matter Institute EMMI.

Neutron-Induced Astrophysical Reaction Rates for Translead Nuclei

I. V. Panov[1,2,3], I. Yu. Korneev[3], T. Rauscher[1], G. Martínez-Pinedo[4], A. Kelić-Heil[4], N. T. Zinner[5,6], and F.-K. Thielemann[1]

[1]University of Basel Basel, Switzerland; [2] Institute for Theoretical and Experimental Physics, Moscow, Russia; [3] Kurchatov Institute, Moscow, Russia; [4] GSI, Darmstadt, Germany; [5] Harvard University, Cambridge, U.S.A.; [6] University of Aarhus, Denmark

Investigations of nucleosynthesis processes make use of reaction networks including thousands of nuclei and tens of thousands of reactions. Most of these reactions occur far from stability and thus cannot still be studied experimentally. Moreover, most of the nuclear properties are not known either. Therefore, predictions based on theoretical models are necessary. While close to stability partial experimental information is available, relying fully on theoretical information leads to relatively large variations in computed cross sections far from stability. This is especially true for the region of fissionable nuclei, which was the focus of the present investigation (see also [1]).

In previous astrophysical calculations fission, especially neutron-induced fission has often been neglected. However, it was shown recently that this channel plays important role in r-process nucleosynthesis [2,3]. Here we present extended calculations of neutron-induced fission rates for different model predictions of masses and fission barriers. The calculations have been done for large range of astrophysical temperatures ($10^8 \leq T(\mathrm{K}) \leq 10^{10}$). The present work also completes existing nuclear neutron-capture rate sets by extending the works of [4,5] to the region $84 \leq Z \leq 118$ in order to provide the necessary input for nucleosynthesis studies under high neutron densities. As in [5], the statistical model approach of Wolfenstein-Hauser-Feshbach was used employing more recent data and predictions for masses, spins, and fission barriers.

For a realistic and exhaustive exploration of synthesis conditions, simulations do not only have to vary astrophysical parameters, but also have to include a variation range of involved reaction rates given by different mass and fission barrier models. By comparing rates obtained with different choices of mass and fission barrier predictions we attempt to give a measure of the involved variations. The following mass- and fission-barrier-models have been used: FRDM [6], ETFSI [7,8], TF [9,10]. Details on the model calculations can be found in [1].

In Fig. 1, as an example, are given fission cross sections calculated for ^{261}U by combining different sets of masses and fission barriers. The difference at low energies is due to the different mass predictions used (comparing calculations with TF fission barriers but different neutron separation energies S_n). The small decrease in S_n, when predictions for masses and fission barriers (based on the two sets of input data) are changed from TF+TF to FRDM+TF, results in a decrease of the neutron-induced fission cross sections. The same influence is illustrated by the cases where sets of consistent determinations for S_n and B_f are replaced by sets from different mass predictions.

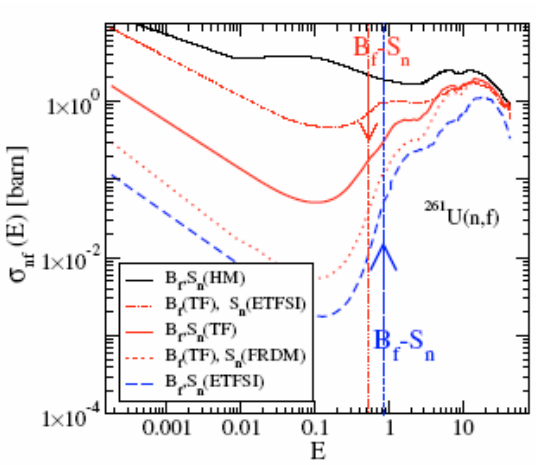

Figure 1: Dependence of neutron-induced fission cross sections $\sigma_{n,f}(E)$ on mass- and fission barrier predictions for ^{261}U. The sources for fission barriers B_f and neutron separation energies S_n are indicated in the panel. Arrows show the difference between fission barrier and neutron separation energy $B_f - S_n$ for ETFSI (dashed line) and TF (full line) predictions.

The (n,*f*)- and (n,γ)-rates calculated here were fitted as in previous work [4] in the common REACLIB seven parameter form, and these parameter are also tabulated. The complete tables are available at [11]. They provide the basis for r-process nucleosynthesis calculations where the abundance predictions for the highest mass numbers as well as the effect of fission cycling are strongly dependent on the interplay between neutron capture and fission

References

[1] I.V. Panov et al., Astron. & Astroph. 513 (2010) A61
[2] I.V. Panov, et al., 2004, Astron. Lett., 30, 647
[3] G. Martínez-Pinedo et al. 2007, Prog. Part. Nucl. Phys., 59, 199
[4] T. Rauscher et al, 2000, At. Dat Nucl. Dat Tab., 75, 1
[5 I.V. Panov et al. 2005, Nucl. Phys., A747, 633
[6] P. Möller et al, 1995, At. Dat Nucl. Dat Tab., 59, 185
[7] Y.Aboussir et al 1995, At. Dat Nucl. Dat Tab, 61, 127
[8] A. Mamdouh et al 2001, Nucl. Phys., A679, 337
[9] W.D. Myers et al., 1996, Nucl. Phys., A601, 141
[10] W.D. Myers et al, 1999, Phys. Rev. C, 60, 014606
[11] http://cdsweb.u-strasbg.fr/cgi-bin/qcat?J/A+A/513/A61

The Odd-Even Z Isospin Anomaly In The Yields From High-Energy Reactions

M. V. Ricciardi[1], *K.-H. Schmidt*[1], *D. Henzlova*[1], *A. Kelić-Heil*[1]

[1]GSI, Darmstadt, Germany

The expression "odd-even Z isospin anomaly" – introduced by L. B. Yang et al. [1] in 1999 – indicates the experimental evidence that the elemental even-odd effect decreases with increasing neutron-richness of the system. Since 1999, the analysis of experimental production cross-sections of final products of several nuclear reactions at very different energies confirmed the existence of this effect. An example of this effect is depicted in ***Figure 1*** (left panel), where the elemental yields produced in the reactions ^{136}Xe+Pb and ^{124}Xe+Pb at 1 *A* GeV are compared. The experiment was performed at the GSI, Darmstadt [2]. The projectile fragments from ^{124}Xe+Pb (N/Z = 1.30 for ^{124}Xe) show a stronger even-odd staggering than the products from the neutron-richer ^{136}Xe+Pb system (N/Z = 1.52 for ^{136}Xe). The difference in the strength of the even-odd staggering is shown in ***Figure 1*** (right panel).

We worked out that odd-even Z isospin anomaly is a direct consequence of the de-excitation process by particle evaporation occurring in the hot remnants of the nuclear reaction. In particular, the characteristics of the odd-even Z isospin anomaly can be reproduced providing that two effects are properly considered: 1) the *memory effect*, which express the fact final fragments hold some reminiscences of the primary impinging nuclei, and 2) the effect of pairing, which is responsible for the even-odd staggering in the yields.

The memory effect is reflected in the experimental observation that for each *Z* the mean values of the isotopic distributions of the final fragments produced in the two reactions do not coincide: if the original system was neutron rich the distribution is more shifted to the neutron rich side (see figures 9 and 11 of Ref. [2]).

The even-odd staggering in the yields correlates strongly with the lowest particle separation energy of the final experimentally observed nuclei, but it does not correlate with their binding energy, contrary to what at first one is tempted to think [3]. The lowest particle separation energy staggers among the isotopes of a given *Z*; the strength of the staggering is stronger along even-Z chains (see figure 5 of Ref. [3]). This is why in the experimental yields we observe a stronger even-odd staggering in the isotopic distributions of even elements.

Once the two effects discussed above are considered, the odd-even Z isospin anomaly is just a consequence of a mathematical game: take two Gaussians (isotopic distributions), shift them by a certain amount (memory effect), modulate them with a given staggering (pairing), make the integrals (elemental yields) and finally make the ratio of the integrals. The strength of the staggering has to be stronger if the two Gaussians represent the isotopic distributions of an even element. In this way, one can reproduce a pattern like that of Figure 1 (right panel). The memory effect is important, because if the were not a shift among the Gaussian, the integral would be always constant, independently of the staggering. The stronger staggering in the lowest particle separation energy of even-Z nuclei is important because it modifies the value of the integral (thus the value of the elemental yield) more for even-Z than for odd-Z.

With a statistical model without structural effects (pure liquid-drop-model) we calculated the isotopic distribution of the products of ^{136}Xe+Pb and ^{124}Xe+Pb at 1 *A* GeV. The model is correct enough for the present purpose because the distributions show a memory effect. We applied the very simple idea of lowest separation energy to get the even-odd staggering in the cross sections. We made the ratio of the elemental yields, and the result is presented in Figure 2. The result of out crude calculation shows that the calculated staggering qualitatively agrees with the experimental one, proving the validity of our simple idea.

To conclude, our study shows that it is precisely the memory effect combined with the characteristics of the lowest particle separation energy which determine the "isospin anomaly".

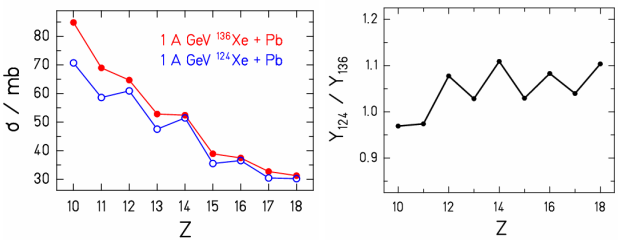

Figure 1: Left panel: Experimental elemental production cross-sections for the reactions 1 *A* GeV ^{136}Xe+Pb (dots) and ^{124}Xe+Pb (circles) [2]. Right panel: Ratio of cross sections for each element produced in the two reactions.

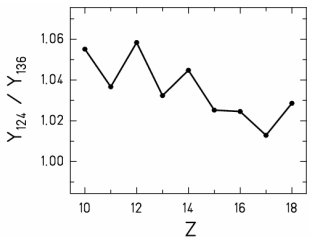

Figure 2: Calculated ratio of elemental cross sections for 1 A GeV ^{124}Xe+Pb and ^{136}Xe+Pb.

References

[1] L. B. Yang et al., Phys. Rev. C 60 (1999) 041602
[2] D. Henzlova et al., Phys. Rev. C 78 (2008) 044616
[3] M. V. Ricciardi et al., submitted to Phys. Rev. C (2010), arXiv:1007.0386

Fragmentation of Spherical Radioactive Nuclei as a Novel Probe of Transient Effects in Fission

C. Schmitt[1,2], K.-H. Schmidt[1], A. Kelić-Heil[1], A. Heinz[3], B. Jurado[4] and P.N. Nadtochy[5]

[1]GSI, Darmstadt, Germany; [2]GANIL, Caen, France; [3]Yale University, New Haven, U.S.A.; [4]CENBG, Bordeaux, France; [5]Omsk State University, Omsk, Russia.

The escape from a metastable state is a problem that appears in many various fields such as fluid mechanics, chemistry or nuclear physics. Systems that are initially out of equilibrium display a transient behaviour during which relaxation in all degrees of freedom takes place. The proper understanding of transient effects occurring before a quasi-equilibrium is reached is important due to their direct connection with the viscosity of the studied medium. Fission is an excellent probe to study such relaxation effects on the subatomic scale. Due to the transient effects, before the quasi-equilibrium is achieved fission is purely or partly inhibited. This delay of fission is commonly called the transient time τ_{trans}. In the present work (see [1]), very specific conditions for studying nuclear transient effects were achieved for the first time, using advanced technical installations at GSI, highly sensitive signatures, and elaborate model calculations.

The ideal initial conditions to study the transient effects are met with initially highly excited and fissile spherical nuclei [2]. Such an ideal scenario could be met for the first time at GSI. A two-step mechanism [3] based on fragmentation-induced fission was used to produce highly excited nearly spherical nuclei near N=126. Details on the experimental set-up and data analysis can be found in [1]. The experimental observable which is used to study the transient effects was the width σ_Z of the fission-fragment Z distribution. It has been shown [1,2,4] that, due to its strong correlation with the temperature at the saddle point, this observable is especially sensitive to the pre-saddle dynamics.

To isolate the influence of transient effects, the data are confronted with two types of calculations: A calculation based on Kramers' *time-independent* fission decay width [5] and a transient-type calculation using the realistic *time-dependent* formula for the *fission decay width* derived in [6]. Both options are implemented [7] in ABRABLA [8]. The difference between such two calculations is to be ascribed to the transient delay. For a sample of spherical projectiles, the measured σ_Z as a function of Z_1+Z_2 is compared in Figure 1 to Kramers- and transient-type predictions. In both calculations, the dissipation strength was fixed at $\beta = 4.5\times10^{21}$ s^{-1}. It can be seen that the slope of σ_Z with decreasing nuclear-charge sum depends strongly on the inclusion of transient effects in the calculation. This observation is valid independent of the value used for β (see ^{223}Ac case in Figure 1). Namely, it is *not* possible to reproduce the trend in σ_Z as a function of Z_1+Z_2 with the *time-independent* fission decay width and an artificial increase of β with decreasing Z_1+ Z_2 (for more details, see [1]). Thus, Figure 1 shows clear manifestation of transient effects in fission. For this set of nuclei an average τ_{trans} of (3.3±0.7)x10^{-21} s has been extracted. Our data indicate that this value is independent of excitation energy and fissility. These results are in favour of an overdamped motion of one-body nature at small deformation and high excitation energy. The extracted dissipation strength and transient time are, nonetheless, reduced compared to the predictions of the early one-body theory for compact shapes

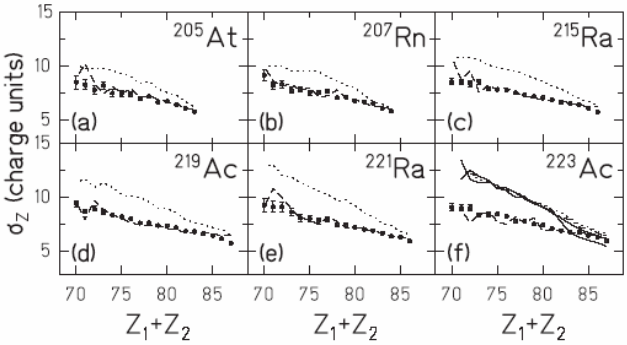

Figure 1. σ_z plotted as a function of Z_1+Z_2 for a set of radioactive beams. The data (dots) are compared to Kramers- (dotted line) and transient- (dashed line) type calculations, assuming β = 4.5×10^{21} s^{-1}. For the ^{223}Ac, additional Kramers-type calculations are shown with β = 7× 10^{21} s^{-1} (dash-dotted line), 10×10^{21} s^{-1} (solid thin line), and 20×10^{21} s^{-1} (solid thick line).

To conclude, for the first time the deexcitation of highly excited and highly fissile spherical nuclei was used to establish unambiguously the build-up of quasi-equilibrium in nuclear matter. The present work demonstrates that peripheral heavy-ion collisions at relativistic energies are a powerful tool to study fission dynamics. To deepen our understanding of the temperature and fissility dependences of viscosity, exclusive measurements are required for an accurate characterization of the decaying system. Such studies will strongly profit from the R3B set-up to be used at the FAIR facility.

References

[1] C. Schmitt et al., Phys. Rev. C 81 (2010) 064602
[2] C. Schmitt et al., Phys. Rev. Lett. 99 (2007) 042701
[3] K.-H. Schmidt et al., Nucl. Phys. A 665 (2000) 221
[4] B. Jurado et al., Phys. Rev. Lett. 93 (2003) 072501
[5] H.A. Kramers, Physica 7 (1940) 284
[6] B. Jurado et al., Nucl. Phys. A 747 (2005) 14
[7] B. Jurado et al., Nucl. Phys. A 757 (2005) 329
[8] A. Kelić et al., arXiv:09096.4193v1 [nucl-th]

Symmetry energy of fragments produced in multifragmentation

D Henzlova[1,4], A S Botvina[2], K-H Schmidt[1], V Henzl[1,5], P Napolitani[3] and M V Ricciardi[1]

[1] GSI Darmstadt, Germany; [2] Institute for Nuclear Research, Moscow, Russia; [3] IPN Orsay, Orsay cedex, France; [4] Los Alamos National Laboratory, Los Alamos, U.S.A; [5] MIT, Massachusetts, U.S.A.

In recent years, interest in the isospin degree of freedom of reaction products has considerably increased, motivated by the possibility of extracting information on the symmetry energy of hot nuclei and nuclear matter during the liquid–gas phase transition. It has been shown that the yield ratio of a given isotope produced in two reactions with different isospin asymmetries exhibits an exponential dependence on Z and N, an observation known as isoscaling [1]. Based on the statistical interpretation of isoscaling, the coefficient of the symmetry term in the nuclear mass can be extracted [2].

In this work (see [3]) we present the analysis of fragments in the charge range Z=10–13, which may be associated with multifragmentation at high excitation energy and subnuclear density, produced in the reactions of ^{136}Xe+Pb and ^{124}Xe+Pb at 1 A GeV. We combine the isoscaling analysis with the experimentally determined N/Z [4] of the final residues to investigate the symmetry energy of hot primary fragments. As a basis for our study we take the SMM model [5].

The isoscaling analysis is based on the production ratios R_{21} of fragments with a given N and Z in reactions with different isospin asymmetries:

$$R_{21} \propto \exp(\alpha \cdot N + \beta \cdot Z), \qquad (1)$$

where α and β are parameters.

Within the statistical approach, the isoscaling parameter α is shown to depend only on the coefficient γ of the symmetry term, on the temperature and on the isotopic composition of the sources:

$$\alpha \approx 4 \cdot \frac{\gamma}{T} \cdot \left(\frac{Z_1^2}{A_1^2} - \frac{Z_2^2}{A_2^2}\right) \qquad (2)$$

With the use of relation (2), the symmetry term may be extracted from α, provided T and the N/Z of the sources are known. Using above equations, from the experimental data presented in [4] we have obtained [3] an 'apparent' $\gamma_{ap} \approx 14 \pm 3$ MeV, that is essentially lower than the value of γ = 25 MeV. In the statistical approach, the formula (2) was obtained for the freeze-out conditions. In order to establish the connection between γ of the hot fragments and γ_{ap} obtained from observed cold fragments we made corrections for the secondary de-excitation (see [3]). Fig. 2 shows the calculated γ dependence on α extracted from the hot primary fragments in the freeze-out volume, and for the cold fragments after the secondary de-excitation. We show the two kinds of evaporation calculations: one is performed without considering evolution of symmetry energy during evaporation and the other one (new model), which includes this evolution. The new model predicts the final values of α much closer to the initial ones at smaller γ. The experimentally determined value of α can be reproduced only by lower values of the γ coefficient, e.g. $\gamma \approx$ 5–8 MeV and 11–12 MeV with the old and new evaporation calculation, respectively.

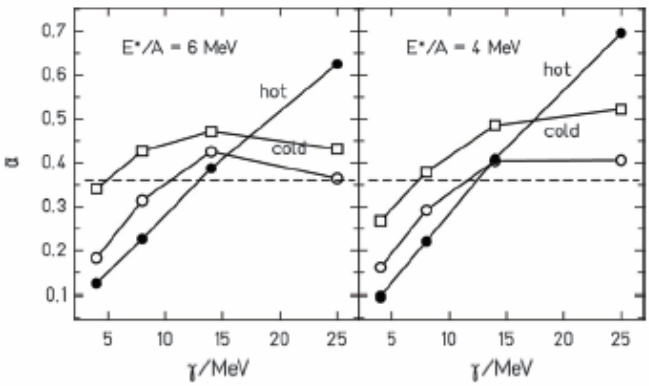

Figure 2: The isoscaling parameter α versus γ obtained in SMM calculations for ^{136}Xe and ^{124}Xe sources, and with the excitation energies 6 A MeV (left panel) and 4 A MeV (right panel). The solid symbols represent primary hot fragments, empty symbols show final cold fragments; the new evaporation model (open circles), the old evaporation model (open squares). The dashed line represents α extracted from the experimental data. For more details, see [3].

We have also used the N/Z ratio to investigate γ and obtained consistent results, see [3]. The coincidence of both methods makes us more confident about the decrease of the symmetry energy of hot light fragments. Our result shows that the properties of light nuclei can change during the nuclear liquid–gas phase transition. With the multifragmentation reaction one can investigate hot nuclei produced at the temperatures around T=3–8 MeV and at the densities of the matter around $\rho = (0.1–0.3)\ \rho_0$. As was demonstrated in [6], the decrease of the symmetry energy in hot fragments may have important consequences for supernova processes, where densities and temperatures close to the nuclear multifragmentation case can be reached.

References

[1] M.B. Tsang *et al.,* 2001 *Phys. Rev. Lett.* 86 5023
[2] A.S. Botvina *et al.,* 2002 *Phys. Rev.* C 65 044610
[3] D. Henzlova *et al.*, J. Phys. G: Nucl. Part. Phys. 37 (2010) 085010
[4] D. Henzlova *et al.*, Phys. Rev. C 78 (2008) 044616
[5] J.P. Bondorf *et al.,* 1995 *Phys. Rep.* 257 133
[6] A.S. Botvina et *al.,* 2004 *Phys. Lett.* B 584 233

The Symmetry Term from Multifragmentation and the Role of the Surface *

W. Trautmann[1], *S. Bianchin*[1], *A.S. Botvina*[2], *N. Buyukcizmeci*[3], *A. Le Fèvre*[1], *J. Łukasik*[1,4], *I.N. Mishustin*[2], *R. Ogul*[3], *C. Sfienti*[1,5], *and the ALADIN Collaboration*[†1]

[1]GSI Helmholtzzentrum, Darmstadt, Germany; [2]FIAS, Goethe University, Frankfurt, Germany; [3]Selçuk University, Konya, Turkey; [4]IFJ-PAN, Kraków, Poland; [5]Gutenberg University, Mainz, Germany

The ALADIN experiment S254, conducted in 2003 at SIS, was designed to study isotopic effects in projectile fragmentation at relativistic energies [1]. For the analysis of the experimental data, the Statistical Multifragmentation Model (SMM, Ref. [2]) has been used. By selecting a realistic ensemble of excited residual nuclei emerging after the fast dynamical stage of the reaction, it has been possible to describe important characteristics of the fragment charge distributions and correlations such as cross-section and multiplicity distributions and fragment-fragment correlations within events [3, 4].

The analysis of isotope distributions and of the neutron contents of produced fragments as well as the isoscaling analysis have shown that the properties of fragments at the breakup stage are different from those of cold isolated nuclei as assumed in the standard version of the SMM. In particular, the symmetry energy of fragments has to be considerably lowered in order to describe the observed neutron richness of the produced fragments. This is illustrated in Fig. 1 where the symmetry-term coefficient γ resulting from the isoscaling analysis is shown as a function of the sorting variable $Z_{\rm bound}$ [3, 4].

For comparison, four predictions are shown in Fig. 1, obtained with rather different approaches but all containing the effect of the surface-symmetry term whose importance increases for the lower-mass fragments. The coefficients of the mass formula of Myers and Swiatecki are adapted to ground-state masses [5], and values close to them have been used in other studies [6]. From the energies of isobaric analog states, a relation between the volume and surface capacitances of nuclei for absorbing asymmetry N-Z was derived by Danielewicz and Lee [7], while Kolomietz and Sanzhur have used a variational approach using Skyrme forces to derive equilibrium values for the volume-symmetry term with surface and curvature corrections for nuclei along the β-stability line [8]. Theoretical surface and volume terms were also obtained by Ono *et al.* [9] from fitting the ground-state binding energies calculated with the Antisymmetrized Molecular Dynamics (AMD) model.

With these parameterizations, an effective symmetry energy averaged over the set of partitions was calculated for the five bins in $Z_{\rm bound}$ after the experimental Z distributions had been converted to mass distributions using the projectile N/Z. The obtained results show similar trends. The smaller fragments produced at higher excitations cause the effective mean symmetry term to decrease with decreasing $Z_{\rm bound}$ in all four cases but at a slower rate than that resulting from the isoscaling analysis of the experimental yield ratios. Increased surface effects are expected if deformations and exotic shapes are present among the smaller fragments at the chemical freeze-out.

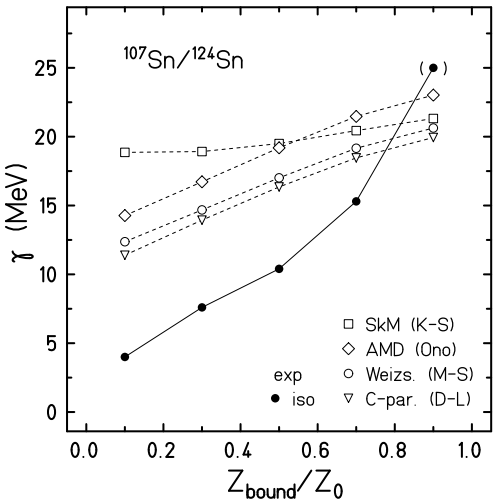

Figure 1: Effective symmetry term coefficient γ as expected from the changing fragment-mass distributions using surface and volume symmetry-term coefficients from Refs. [5, 7, 8, 9] (open diamonds, circles, triangles, and squares, respectively) in comparison with the coefficient γ for hot fragments obtained with the SMM from the isoscaling analysis for the ^{107,124}Sn pair of reactions (dots).

References

[1] C. Sfienti et al., Phys. Rev. Lett. 102 (2009) 152701.
[2] J.P. Bondorf et al., Phys. Rep. 257 (1995) 133.
[3] S. Bianchin et al., GSI Scientific Report 2009, p. 229.
[4] R. Ogul et al., preprint arXiv:1006.3723.
[5] W. D. Myers and W. J. Swiatecki, Nucl. Phys. **81**, 1 (1966).
[6] Ad. R. Raduta and F. Gulminelli, Phys. Rev. C **75**, 024605 (2007).
[7] P. Danielewicz and J. Lee, Int. J. Mod. Phys. E 18, 892 (2009).
[8] V. M. Kolomietz and A. I. Sanzhur, Eur. Phys. J. A 38, 345 (2008).
[9] A. Ono, P. Danielewicz, W. A. Friedman, W. G. Lynch, and M. B. Tsang, Phys. Rev. C **70**, 041604(R) (2004).

* Work supported by EU under contract No. HPRI-CT-1999-00001.
† w.trautmann@gsi.de

Production of New Neutron-Rich Isotopes of Heavy Elements in Fragmentation Reactions of ^{238}U Projectiles at 1*A* GeV

H. Alvarez-Pol[1], J. Benlliure[1], E. Casarejos[1], L. Audouin[2], D. Cortina-Gil[1], T. Enqvist[3], B. Fernandez-Domınguez[1], A. R. Junghans[4], B. Jurado[5], P. Napolitani[2,3], J. Pereira[1], F. Rejmund[6], K.-H. Schmidt[3], O. Yordanov[3]

[1] Universidade de Santiago de Compostela, Spain; [2] IPN, Orsay, France; [3] GSI Darmstadt, Germany; [4] Forschungszentrum Dresden-Rossendorf, Germany; [5] CENBG, Bordeaux, France; [6] GANIL Caen, France

The possibility to extend the present limits of the chart of the nuclides provides unique opportunities for investigating the nuclear many-body system with extreme values of isospin and most of the stellar nucleosynthesis processes leading to the production of the heaviest elements in our universe. This is the reason why presently, several new-generation in-flight radioactive-beam facilities are being commissioned, built, or designed.

The access to heavy neutron-rich nuclei—in the "northeast" region of the chart of nuclides—is a real challenge. Indeed, the heaviest known isotopes in this region are still located relatively close to the β stability line. A few years ago, it was proposed to use fragmentation reactions of heavy stable projectiles such as ^{238}U or ^{208}Pb at relativistic energies to populate that region of the chart of nuclides [1,2]. The extreme case for these reactions involves the proton-removal channels where the projectiles lose only protons, and the excitation energy gained is below the particle-evaporation threshold.

To test this idea, we performed an experiment at GSI Darmstadt using ^{238}U beam at 1*A* GeV. The fragmentation residues were analyzed with FRS. For details, see [3].

In Fig. 1 we represent the isotopic distributions of the cross sections measured in this work. The error bars are shown when larger than the data points. Those points in the figure surrounded by a square correspond to the *40 new* isotopes discovered in this experiment. In a few days' measurements we were able to reach cross sections as low as 100 pb. As expected, the production cross sections decrease drastically with the neutron number. On average, an additional neutron decreases the production cross section by about a factor 4. In the same figure we also compare the measured cross sections with predictions obtained with the codes EPAX [4] and COFRA [1,5]. The EPAX code describes rather well the production of residual nuclei relatively close in mass number to the projectile; however, it over-predicts the production cross sections of neutron-rich residual nuclei produced in mid-peripheral collisions where the projectile loses a larger number of nucleons. COFRA provides an overall good description of the cross sections of neutron-rich nuclei produced in fragmentation reactions induced by ^{238}U projectiles. A more detailed analysis indicates a slight overestimation of the cross sections of nuclei close to the projectile (e.g., Fr isotopes) and far from the projectile (e.g., Au and Pt isotopes).

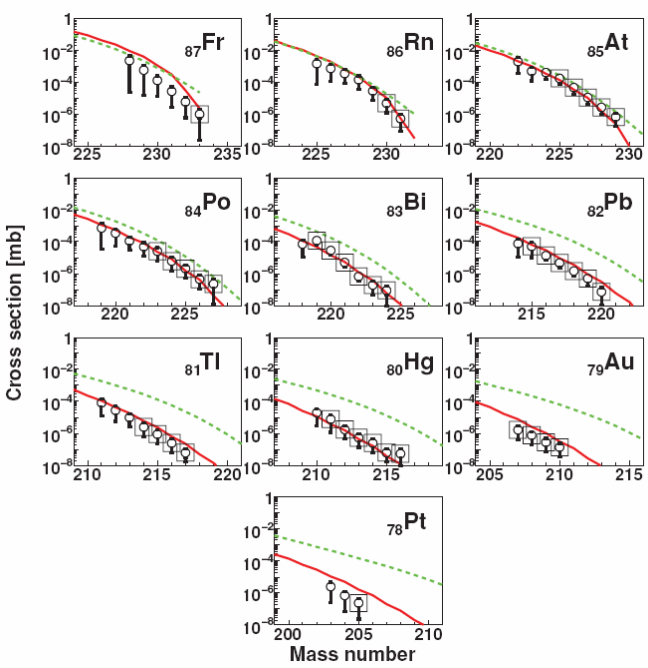

Figure 1: Isotopic distributions of the production cross sections of heavy neutron-rich nuclei determined in this work. Nuclei observed for the first time are surrounded by a square symbol. The experimental measurements are compared with the predictions obtained with the code COFRA (solid line) and EPAX (dashed line).

The large fluctuations in the number of abraded protons and neutrons in this type of reaction make it possible to populate cold-fragmentation reaction channels leading to the production of the most neutron-rich nuclei. These results pave the way for a considerable extension of the northeast limit of the chart of nuclides expected with the new generation of radioactive-beam facilities.

References

[1] J. Benlliure et al, Nucl. Phys. A 660, 87 (1999).
[2] J. Benlliure and K.-H. Schmidt, Nucl. Phys. A 746, 281 (2004).
[3] H. Alvarez et al, Phys. Rev. C 82, 041602R (2010)
[4] K. Suemmerer and B. Blank, Phys. Rev. C 61, 034607 (2000).
[5] www.usc.es/genp/cofra

Production of residual nuclides in the reactions ^{112,124}Sn+^{112,124}Sn at 1 A GeV

V. Föhr[1], A. Bacquias[1], E. Casarejos[2], T. Enqvist[3], A. Junghans[5], A. Kelic[1], T. Kurtukian[2], S. Lukic[1], D. Pérez[2], R. Pleskac[1], M. V. Ricciardi[1], K-H. Schmidt[1], J. Taíeb[4]

[1]GSI, Darmstadt, Germany, [2]Universidad de Santiago de Compostela, Spain, [3]CUPP Project, Pyhäsalmi, Finland, [4]CEA/DAM Bruyéres-le-Châtel, France, [5]FZD Dresden, Germany

It is currently a great interest of the scientific community to enlarge the experimental investigations towards rarely produced isotopes with extreme *N/Z* in order to investigate their structure-properties or to study the dependence of the nuclear equation of state on the isotopic composition of the system. In the meantime, the effects of the different isospin could be studied using stable nuclei with as much as possible different neutron-to-proton ratio.

In this report, we present two experiments performed at the Fragment Separator at GSI, where the isotopically resolved residues over the broad range of the nuclear charge were measured in the fragmentation of two symmetric systems: ^{112,124}Sn+^{112,124}Sn at 1 *A* GeV.

The experiments were performed in inverse kinematics, shooting the ^{112}Sn and ^{124}Sn beams into ^{112}Sn and ^{124}Sn targets, respectively. The fully stripped reaction products were identified at the FRS by detecting their nuclear charge, *Z*, with an ionization chamber and their mass, *A*, from the *A/Z* ratio deduced from the magnetic rigidity and from the time-of-flight between the mid plane and the exit of the spectrometer. Once the nuclides were identified, so *A* and *Z* were integer numbers, their velocity was precisely evaluated by the magnetic rigidity. The ratio of transmitted reaction residues can be calculated. By the known beam intensities, target properties and transmission ratios the production cross sections were calculated on the basis of the measured yields. The velocity spectra could be measured with a great precision, based on the magnetic rigidity. This knowledge gives a better insight into the reaction mechanism in which the residues were formed. More details on the analysis technique can be found in previous publications for experiments performed with the same experimental set-up [1, 2, 3, 4, 5, 6, 7, 8, 9,10, 11, 12, 13, 14, 15, 16, 17].

In Fig. 1 and in Fig. 2 we present the experimental production cross-sections on the chart of the nuclides for the reaction ^{112}Sn+^{112}Sn and ^{124}Sn+^{124}Sn, respectively. Due to technical problems encountered during the experiment, the production cross-section for some specific nuclides could not be measured. Nonetheless, the figures seem to indicate a "memory effect" that leads to the production of fragments which are on average more neutron rich for the ^{124}Sn+^{124}Sn system. This effect was also found in the projectile fragmentation of other systems, like ^{129}Xe+Al [18], ^{238}U+Ti [19], ^{124}Xe+Pb [16] and +^{136}Xe+Pb [16].

A more detailed analysis and the subsequent physic conclusion concerning the reactions ^{112}Sn+^{112}Sn at 1 *A* GeV and ^{124}Sn+^{124}Sn at 1 *A* GeV will follow in the future.

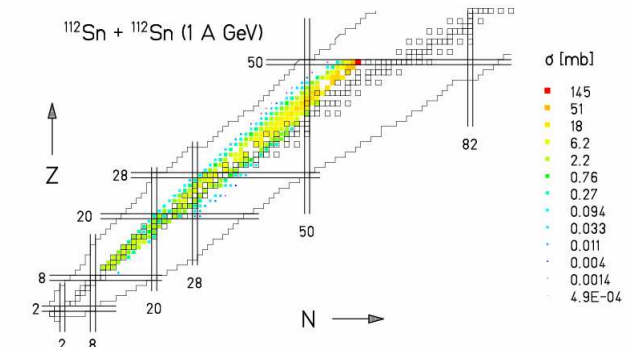

Figure 1: Experimental cross sections for ^{112}Sn+^{112}Sn at 1 *A* GeV

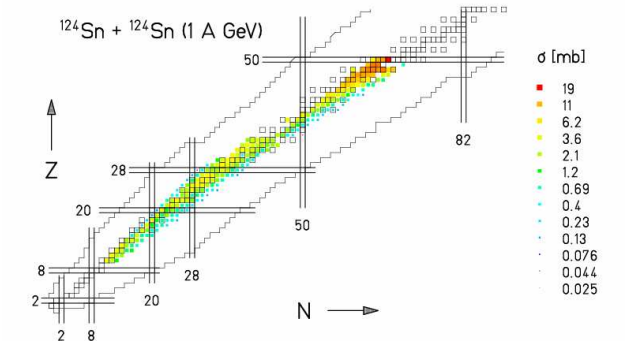

Figure 2: Experimental cross sections for ^{124}Sn+^{124}Sn at 1 *A* GeV

[1] T. Enqvist et al., Nucl. Phys. A 658 (1999) 47-66
[2] F. Rejmund at al., Nucl. Phys. A683 (2001) 540-565
[3] J. Benlliure et al., Nucl. Phys. A 683 (2001) 513-539
[4] B. Fernandez et al., Nucl. Phys. A 747 (2005) 227-267
[5] T. Enqvist et al., Nucl. Phys. A 686 (2001) 481-524
[6] T. Enqvist et al., Nucl. Phys. A 703 (2002) 435-465
[7] J. Taieb et al., Nucl. Phys. A 724 (2003) 413-430
[8] M. Bernas et al., Nucl. Phys. A 725 (2003) 213-253
[9] L. Audouin et al., Nucl. Phys. A 768 (2006) 1-21
[10] M. V. Ricciardi et al., Phys. Rev C 73 (2006) 014607
[11] M. Bernas et al., Nucl. Phys. A 765 (2006) 197-210
[12] E. Casarejos et al., Phys. Rev. C 74 (2006) 044612
[13] J. Pereira et al., Phys. Rev. C 75 (2007) 014602
[14] C. Villagrasa et al., Phys. Rev. C 75 (2007) 044603
[15] P. Napolitani et al., Phys. Rev. C 76 (2007) 064609
[16] D. Henzlova et al., Phys. Rev. C 78 (2008) 044616
[17] J. Benlliure et al., Phys. Rev. C 78 (2008) 054605
[18] J. Reinhold et al., Phys. Rev. C 58 (1998) 247-255
[19] K.H.Schmidt et al., Nucl.Phys.A710 (2002) 157-179

NeuLAND - Concepts for the Detection of Fast Neutrons

T. Aumann[1,2], P. Basu[3], D. Bemmerer[4], D. Bertini[1], A. Blanco[5], K. Boretzky[1], C. Caesar[2], S. Chakraborty[3], S. Chatterjee[3], M. Cherciu[6], U. Datta Pramanik[3], Z. Elekes[4], P. Fonte[5], D. Galaviz[7], D. Gonzalez Diaz[1], M. Haiduc[6], J. Hehner[1], M. Heil[1], A. Ignatov[2], M. Kempe[4], Y. Leifels[1], J. Machado[7], V. Maroussov[8], J. Panja[3], M. Potlog[6], A. Rahaman[3], R. Reifarth[9], M. Röder[10], D. Rossi[1], H. Simon[1], M. Sobiella[4], D. Stach[4], E. Stan[6], P. Teubig[7], A. Wagner[4], D. Yakorev[4], A. Zilges[8], K. Zuber[10], and the R[3]B collaboration

[1]GSI, Darmstadt, Germany; [2]TU Darmstadt, Germany; [3]SINP Kolkata, India; [4]HZDR, Dresden-Rossendorf, Germany; [5]LIP, Coimbra, Portugal; [6]ISS, Bucharest, Romania; [7]Univ. Lisbon, Portugal; [8]Univ. Cologne, Germany; [9]Univ. Frankfurt, Germany; [10]TU Dresden, Germany

Design goals

The acronym NeuLAND (new Large Area Neutron Detector) stands for the high-efficiency time-of-flight spectrometer for high-energy neutrons (200 to 1000 MeV) within the R3B experiment being designed for FAIR [1]. A spatial resolution of approximately $\sigma \approx 1$ cm and a time resolution of approximately $\sigma \approx 100$ ps are envisaged together with an efficiency of more than 90 % for one-neutron events, as well as a high multi-neutron recognition capability. In order to cover the full forward opening angle defined by the gap of the dipole magnet GLAD, the front face of NeuLAND must cover 80 mrad, thus demanding a face side of at least 2×2 m^2 for the minimum distance to the target of approximately 12.5 m. The depth of the detector depends critically on the detection media and must be scaled to match the efficiency goals accordingly. During 2010, two different concepts were followed within the work on NeuLAND prototypes and NeuLAND detector simulations. Since the decision on one of the concepts cannot be drawn yet on the basis of the results obtained up to now, we present here both of the conceptional ideas.

Status of the MRPC Concept

In order to benefit from the excellent timing properties of MRPCs (Multigap Resistive Plate Chambers) and their relatively low costs, a design based on active RPC detectors including inactive materials for the conversion of the high-energy neutrons was developed. Following positive results for the detection of slow protons using RPCs [2], first small prototypes for NeuLAND were developed at GSI, HZDR (former FZD) and SINP [3], and successfully tested using electron and neutron beams [4]. During 2010, the first full-size prototype of 2 m length and 50 cm height was built at HZDR and tested with single electrons during the autumn with promising results [5]. The full NeuLAND detector foresees four such modules per plane, 50-60 planes to reach the needed detector depth and up to 10.000 read-out channels. Simulations for the full detector based on MRPCs are in process in order to optimize quantities such as glass and converter thickness and to describe the multi-neutron response of the detector. For the mechanical design the results of a recent simulation of all the aspects of signal formation, transmission and cross talk in multi-strip RPCs [6] are taken into account.

Status of the Scintillator Concept

Since the beginning of 2010, a complementary concept to the converter-based solution is investigated in parallel. It is based on a fully active detector structure consisting of organic scintillator (BC408). The proposed detector sub-modules are of sizes ranging from 3×3 to 5×5 cm^2 and lengths of 2 to 3 m. The light read-out is foreseen at the far ends of the modules. Some single prototypes of 2 m length were built and read out with different types of photomultipliers (PM) and with so-called Si-PMs. Very first results show a time resolution of below 100 ps for 2 m bars. Simulations for a complete NeuLAND detector are performed both within Geant3 *via* R3BRoot and within FLUKA in order to determine the required modularity, size and depth of the detector. Algorithms for multi-neutron recognition are being developed, making use of the calorimetric properties of the full active detector [7].

Outlook

During the first half of 2011 the simulations for both of the detection concepts will be finalized including the simulations of key-experiments for R3B. Together with the results of further tests with full-size prototypes this will set the basis for the critical decision for the final NeuLAND detector concept leading to the Technical Design Report.

References

[1] R3B Technical Proposal, 2005, http://www-linux.gsi.de/∼wwwnusta/tech_report/13-r3b.pdf

[2] D. Rossi *et al.*, GSI Scientific Report 2006, http://www.gsi.de/informationen/wti/library/scientificreport2006/PAPERS/FAIR-EXPERIMENTS-19.pdf

[3] U.D. Pramanik *et al.*, DOI:10.1016/j.nima.2010.10.055

[4] C. Caesar *et al.*, DOI: 10.1016/j.nima.2010.09.163

[5] D. Bemmerer *et al.*, GSI Scientific Report 2010

[6] D. Gonzalez-Diaz *et al.*, GSI Scientific Report 2010

[7] M. Heil *et al.*, GSI Scientific Report 2010

NeuLAND: Simulations for the Scintillator Concept

M. Heil[1], *V. Maroussov*[2], *T.Aumann*[1,3], *K. Boretzky*[1], *C. Caesar*[3], *A. Ignatov*[3], *H. Simon*[1], *A. Zilges*[3], *and the R*^{3}*B collaboration*

[1]GSI, Darmstadt, Germany; [2]Univ. Cologne, Germany; [3]TU, Darmstadt, Germany

Within the scope of the R3B experiment at FAIR, a highly efficient time-of-flight spectrometer for high-energy neutrons (200 to 1000 MeV) is developed, called NeuLAND (new Large Area Neutron Detector). The design goals and an overview of the project is given in the contribution of T. Aumann *et al.* [1]. Here we present the detector concept based on a fully active detector built with only organic scintillator (BC408).

The simulations started with a comparison of such a design with the functionality of the existing LAND detector [2], based on alternating layers of iron converter and scintillator. The efficiency for the full neutron energy range is shown in table 1 for a 2 x 2 x 2m^3 pure scintillator detector and for LAND. We observe for the fully active structure a significantly enhanced efficiency for the lower neutron energies. More detailed simulations carried out both in GEANT3/FairRoot and in FLUKA show in addition a substantial improvement of the detected positions and times with respect to the primary interaction, when comparing fully active structure to structures with passive layers.

neutron energy	efficiency [%]	
[MeV]	scintillator only	LAND
50	89	-
100	97	-
170	97	78
270	94	85
470	95	93
600	96	94
800	97	96
1050	97	97

Table 1: Efficiency for neutrons at various energies for a full active scintillator structure and for LAND.

In the following paragraph, we will focus on the aspect of multi-neutron recognition with the current design of the NeuLAND detector, which consists of stacked scintillator bars with a cross section of 5 x 5 cm^2 and a length of 2 m. Each plane contains 40 bars, forming a surface of 2 x 2 m^2. The bars of two sucsessive planes are arranged perpendicular to each other. The total depth of the detector is 3 m, which implies 60 planes and corresponds to a total of 2400 bars. Each bar will be readout by two 1.5 inch photomultipliers on both ends. Previous simulations and tests with prototype scintillator bars have shown that such a structure fulfills the required design criteria concerning position and time resolution. The determination of the neutron multiplicity and the unique detection of all momenta for multi-neutron events is one of the most challenging tasks. In this respect, the calorimetric properties of the scintillator concept could be advantageous. Detector simulations with up to six neutrons per event were performed. The beam energy of the simulated events was 600 AMeV and relative neutron energies from 1 to 10 MeV were used. The total energy (light equivalent) was studied as a function of simulated neutrons. The resulting energy deposition spectra were fitted by a gaussian function, resulting in a linear correlation between the number of neutrons and the total deposited energy (see Fig. 1). Using this relation, a very good determination of the neutron multiplicity was achieved (see Table 2). A comparison with the properties of the existing LAND detector shows an improvement of almost a factor 2 for three and more neutrons.

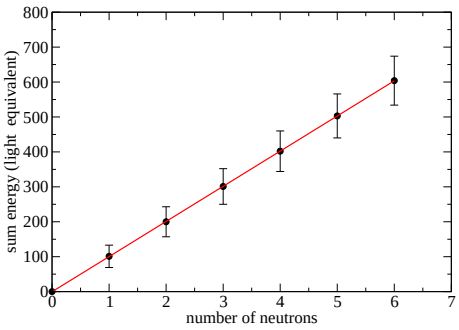

Figure 1: Correlation between the number of simulated neutrons and the total energy detected. The error bars represent 1 σ uncertainties.

		simulated					
	%	1n	2n	3n	4n	5n	6n
detected	1n	**0.94**	0.15	0.00	0.00	0.00	0.00
	2n	0.05	**0.75**	0.19	0.01	0.00	0.00
	3n	0.00	0.09	**0.67**	0.22	0.02	0.00
	4n	0.00	0.00	0.13	**0.60**	0.24	0.03
	5n	0.00	0.00	0.00	0.16	**0.57**	0.24
	6n	0.00	0.00	0.00	0.00	0.17	**0.52**
	7n	0.00	0.00	0.00	0.00	0.00	0.18
	8n	0.00	0.00	0.00	0.00	0.00	0.01

Table 2: Probabilities of multi-neutron hit recognition.

References

[1] T. Aumann *et al.*, GSI Scientific Report 2010 and references therein

[2] T. Blaich *et al.*, NIM **A314** (1992) 136

A 200 cm × 50 cm MRPC-based prototype for the NeuLAND detector at R^{3}B*

D. Bemmerer[1], T. Cowan[1,2], Z. Elekes[1], M. Kempe[1,2], M. Röder[2], M. Sobiella[1], D. Stach[1], A. Wagner[1], D. Yakorev[1,2], K. Zuber[2], and the R3B collaboration

[1]Helmholtz-Zentrum Dresden-Rossendorf (HZDR), formerly Forschungszentrum Dresden-Rossendorf (FZD);
[2]Technische Universität Dresden

A detector for high-resolution momentum measurements of neutrons in the energy range 0.2-1.0 GeV is being developed for the R^{3}B experiment at FAIR. Two solutions are currently being studied: A pure scintillator concept and an approach based on a sequence of converter material (iron) to produce secondary charged particles, and Multigap Resistive Plate Chambers (MRPC's) to detect these particles. Here, work on the latter solution is reported.

In recent years, a number of 40 cm × 20 cm MRPC-based NeuLAND prototypes been built at FZD, GSI, and SINP. Tests with the single-electron per bunch mode of the superconducting electron linac ELBE had shown that most of the prototypes fulfilled the design criterion of $\sigma_t <$ 100 ps time resolution and $\eta \geq 90\%$ efficiency, when using single-ended readout with FOPI front-end electronics and a 25 ps TDC. Recent experiments at ELBE have shown that the same is true also for differential readout, using the new PADI-3 front-end electronics. What was still missing, however, were simulations reproducing the test beam data and predicting the behavior for high-energy neutrons, and tests with a full-size prototype.

Now, in simulations within the R3BRoot framework [1], a digitizer has been developed following the avalanche caused by each 31 MeV electron. The electric-field-dependent drift velocity, Townsend and attachment coefficients [2] have been modeled. The induced charge on the readout electrode is then propagated to the front-end electronics at the end of the strip. The remaining free parameters are the growth cut parameter for the space charge effect and the correlation distance parameter for several avalanches. By adjusting them, the measured efficiency curve for the 40 cm × 20 cm prototypes was reproduced (fig. 1a).

These parameters were then adopted in the simulation to predict the behavior of a full MRPC-based NeuLAND detector. It shows nearly full efficiency for 400 MeV neutrons, as required. However, in the timing spectrum, in addition to a narrow peak near the "true" time-of-flight given by the first interaction of the neutron, there is an extended tail towards later times (fig. 1b). This is due to neutrons which scatter inside the inactive converter material but do not produce a detectable signal in the MRPC structure immediately behind it. As a result, approximately 40% of the incident neutrons are not detected within the required timing window. Further simulations are in progress to explore whether this feature can be improved.

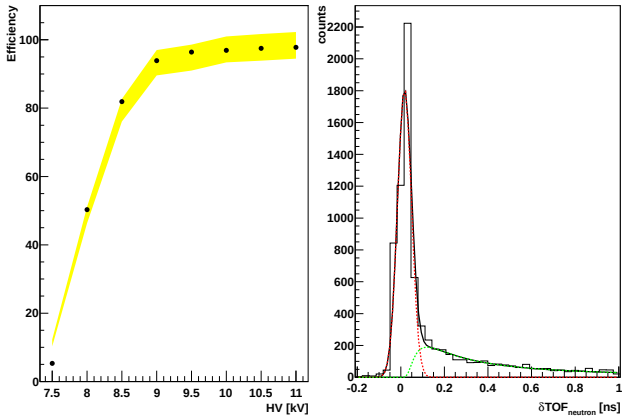

Figure 1: (a) Efficiency of a 40 cm × 20 cm MRPC prototype from experiment (points) and simulation (shaded area). (b) Simulated time-of-flight distribution for 400 MeV neutrons on a full MRPC-based NeuLAND.

Figure 2: Photo of the 200 cm × 50 cm prototype at the single-electron-beam test station of ELBE. 4 × 50 such units would be required for the full NeuLAND.

In parallel, the well-established 40 cm × 20 cm prototypes were scaled up to a 200 cm × 50 cm unit (fig. 2). Now, the first MRPC unit is available that has such a large size and includes a 4 mm thick central anode. Initial tests at the ELBE single-electron test beam station show very promising results for efficiency and time resolution. This work is pursued further in 2011. One or more such prototypes will be provided for a planned experiment at GSI using tagged neutrons from the breakup of the deuteron.

References

[1] D. Bertini, M. Al-Turany, I. Koenig, and F. Uhlig, J. Phys. Conf. Ser. **119**, 032011 (2008).

[2] W. Riegler, C. Lippmann, and R. Veenhof, Nucl. Inst. Meth. A **500**, 144 (2003).

*Supported by BMBF (06DR9058I) and GSI F&E (DR-GROS, DD-ZUBE1012).

Crosstalk free Multi-strip Resistive Plate Chambers?

D. Gonzalez-Diaz for the CBM and R3B collaborations[1]
[1]GSI, Darmstadt, Germany

Due to its highly-quenched operating mode, a gaseous detector of the Resistive Plate Chamber type (RPC) can work at constant fields in excess of 100kV/cm at ambient conditions. The very fast avalanche dynamics can thus result in exponential signal rise-times down to $t_{rise} = 100$ps, when not Space-Charge limited. The associated time resolution $\sigma_t = 50$-100ps is a consequence of this fact.

A most intriguing technological problem is the routing of such signals out of the RPC detector itself, usually made of densely packed multi-strip electrodes. Next generation RPCs (CBM, NeuLAND-R3B, iTOF-R3B) aim at doing it over up to 2m with little signal shaping and, as much as NeuLAND and CBM are concerned, with little or no crosstalk also. Present 'state of the art' 1m-long multi-strip RPCs (from the '4-pi' experiment at GSI) show, indeed, a fairly large cluster size of 4.5 strips/track.

The problem of signal transmission can be tackled through an N-conductor transmission line simulation. However, the structure of the solutions is complicated enough that no simple analytical estimates can be obtained in general. We have introduced in [1],[2] an analytical technique for obtaining the complete lossy solution, that is suited for RPC structures, and allows for simple solutions in several practical cases. As a result, some approximate RPC characteristics can be deduced (see [2] for details):

1. The low-frequency/short-distance crosstalk is proportional to the capacitive coupling C_{mutual}/C_{ground}.
2. The high-frequency/long-distance crosstalk is approximately proportional to the unbalance between the capacitive and the inductive coupling $C_{mutual}/C_{ground} - L_{mutual}/L_{self}$, the detector length, and the inverse of the signal rise-time.
3. Losses are dominated by the glass loss-tangent and the counter length D, largely independent from phenomena 1, 2. Typical glass-based counters have a cutoff frequency of $\sim$ 1GHz for 2 meters (Fig. 1-down).
4. In a high-frequency/long system the best transmission properties are obtained by accurate balance of the inductive and capacitive coupling,
5. Such a situation can be achieved through a compensation scheme (hereafter, 'electrostatic compensation') based on the fine adjustment of the system dielectrics.
6. As long as the coupling to the over-next neighbor is small, typical RPCs can be electrostatically compensated in general. We show in Fig. 1 the experimental verification of such a procedure for 2-strip RPCs in both the time and frequency domain.

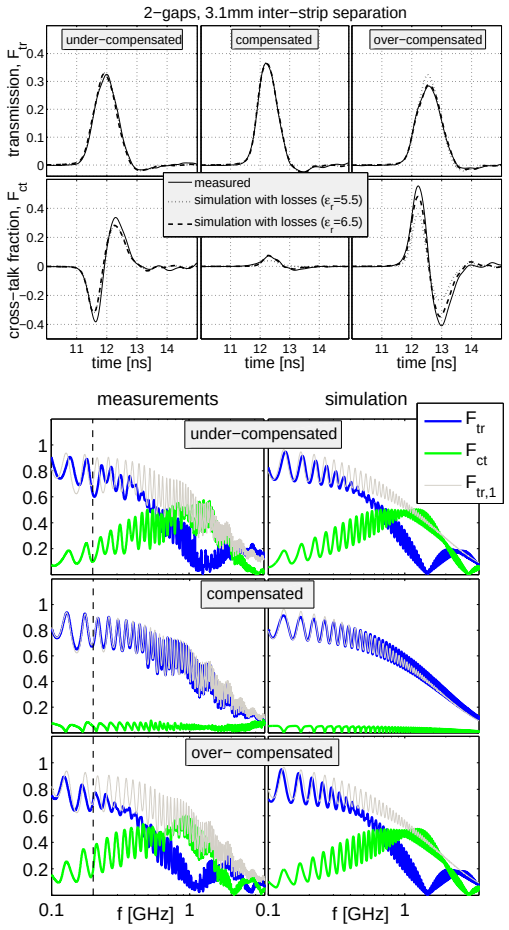

Figure 1: Up: Transmission characteristics for a 2m-long 2-strip RPC in time-domain. Shown is the measured transmission F_{tr} and crosstalk fraction F_{ct} $(-)$ for different degrees of compensation. Simulations overlaid as $\cdot\cdot$, $--$. Down: Transmission characteristics in frequency-domain (measurements: left-column, simulations: right-column). $F_{tr,1}$ is the transmission for a single strip, that approximately represents the theoretical limit of a compensated system. Details in [2].

This development opens the way to the construction of timing RPCs of virtually unlimited size, with performances similar to those achievable in small cells in terms of resolution, efficiency and crosstalk.

References

[1] D. Gonzalez-Diaz, doi:10.1016/j.nima.2010.09.067.

[2] D. Gonzalez-Diaz, H. Chen, Yi Wang, 'Signal coupling and signal integrity in multi-strip Resistive Plate Chambers used for timing applications', submitted to NIM.

Performances of RPCs prototypes for heavy ion identification at the R^{3}B experiment

Y. Ayyad[1], *J. Benlliure*[1], *E. Casarejos*[2], *I. Durán*[1], *C. Paradela*[1], *and the R^{3}B collaboration*

[1]University of Santiago de Compostela, Spain; [2]University of Vigo, Spain

The R^{3}B experiment at FAIR will be equipped with a time-of-flight wall for heavy ion identification (iToF) [1]. This detector should provide a time resolution of the order of 20 ps (sigma) in order to give us access to the mass identification of nuclei with mass numbers up to 200. This ToF wall should also cover a large area ≈2x1 m^2 but at the same time provide a sufficient granularity (few cm^2) for the identification of multi-hit events.

The technical solution proposed for this detector was the use of narrow-gap Resistive Plate Chambers (RPCs) [2]. RPCs are known to provide time resolutions below 100 ps with minimum ionizing particles, however, very little was known on their performances with relativistic heavy ions. Our R&D program focused then on the optimization of the design of this kind of detectors and associated electronics to the detection of heavy ions. First prototypes consisted in double 300 μm gas-gap RPCs made with 1 mm thickness soda-lime glass (15x6 cm^2), nylon fishing line as spacer and a single 150x20 mm^2 strip made of self-adhesive copper. HV was fed through a load resistor into the central plane where the signals were picked up through capacitors. The detectors were placed in a gas tight metallic box filled with $C_2H_2F_6$ mixed with SF_6 at 10%. A specific front-end card including protection against charge overloads, power supply filters, shaping amplification based on MAXIM-4223 amplifiers and signal adaptation for input and output ports was developed. Then the signals were digitized using the TACQUILA board.

The performances of these prototypes were investigated in specific detector tests with beams of electrons at 15 MeV provided by the ELSA facility at CEA/DAM and beams of relativistic heavy ions (^{12}C, ^{64}Ni, ^{179}Au and ^{238}U) delivered by the SIS18 synchrotron at GSI. The detection efficiency of the RPCs was investigates over a large range of ions surrounding the detectors with two plastic scintillators matching the active area of the RPCs. The results obtained are shown in the upper plot of figure 1. As can be seen, the detection efficiency is compatible with 100% for all measured ions with atomic numbers between 3 and 35. Alpha particles were detected with an efficiency around 97% while the detection efficiency of protons was around 75% [3,4].

The time resolution was determined from the relative time signals between two RPC detectors. The results obtained with bunches of electrons with a time spread of 5 ps are shown in the lower panel of figure 1 as a function of the intensity of electrons per bunch. The results shown a clear increase in the time resolution with the intensity of electrons, reaching for the highest intensities a time resolution around 25 ps very close to the intrinsic resolution of the TACQUILA board. In the same figure we also display a 35 ps resolution obtained with Z≈ 75 ions at 400 A MeV. The results obtained in this test clearly indicate that the present RPC prototypes for the iTOF detector almost fulfill the specifications required for the mass identification of heavy ions at the R^{3}B experiment. Further tests with large scale prototypes should confirm the present results.

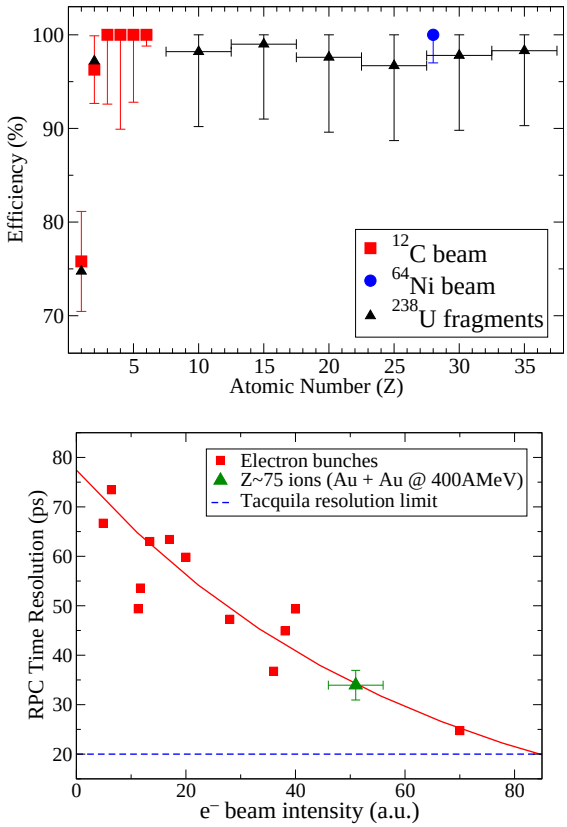

Figure 1: Upper panel: detection efficiency as a function of the atomic number of the measured ions. Lower panel: time-of-flight resolution (ps) as a function of the e- beam intensity (arb. units). The resolution obtained with Z≈ ions is also displayed (triangle). The dashed line is the limit imposed by the electronics (TACQUILA board).

[1] Technical Proposal for the design, construction, commisioning and operation of the R3B experiment.

[2] Nuc. Phys. B (Proc. Suppl.) 158 (2006) 186-189

[3] GSI Scientific Report 2008, pag. 54

[4] Nuc. Inst. Meth., doi:10.1016/j.nima.2010.08.079

Progress in the design of the CALIFA/R^{3}B detector*

H. Álvarez-Pol[1], V. Avdeichikov[2], M. Bendel[3], J. Benlliure[1], E. Casarejos[4], J. Cederkäll[2], D. Cortina-Gil[1], C. Cruz[5], P. Díaz[1], D. DiJulio[2], I. Durán[1], M. Gascón[1], R. Gernhäuser[3], P. Golubev[2], B. Jakobsson[2], H.T. Johansson[6], R. Krücken[3], T. Le Bleis[3], M. Mostazo[1], E. Nácher[5], T. Nilsson[6], C. Parrilla[4], A. Perea[5], J. Sánchez del Rio[5], O. Tengblad[5], R. Thies[6], J.A. Vilán[4], M. Winkel[3], P. Yáñez[4], and the R^{3}B collaboration

[1]Univ. Santiago de Compostela, Spain; [2]Univ. Lund, Sweden; [3]E-12, TUM, Garching, Germany; [4]Univ. Vigo, Spain; [5]IEM-CSIC, Madrid, Spain; [6]Chalmers, Gothenburg, Sweden

R^{3}B [1] (Reactions with Relativistic Radioactive Beams) is a versatile set-up that will provide high efficiency, acceptance and resolution, for kinematically complete measurements of reactions induced by high-energy radioactive beams. It will be located at the focal-plane of the high-energy branch of the Super-FRS and will be adapted to the highest beam-energies provided by this spectrometer, up to 1 A GeV, making possible a broad physics program with rare-isotopes.

CALIFA [1] (CALorimeter for In-Fligth emitted pArticles) will surround the target of the R^{3}B experiment and will act as total absorption γ calorimeter and spectrometer, as well as identifier of charged particles from target residues when operating in coincidence with the Target Recoil (tracking) Detector (TRD). This versatility is its most challenging requirement, demanding a huge dynamic range, from low energy γ-rays up to 300 MeV protons. This fact, along with the high-energy of the beams determine the conceptual design of the detector.

Typical reaction energy in the R^{3}B experiment, and thus the one used for CALIFA design, is 700 A MeV; β=0.82. The in-flight emission of protons and γ-rays is strongly affected by the Lorentz boost resulting in Doppler shift and broadening. This is particularly important at forward polar angle (for γ-rays see Figure 1), and imposes higher granularity and higher stopping capability of the forward detectors. The requirement to stop 300 MeV protons in the forward detectors creates, however, an efficiency problem due to the fact that more than 50% of these protons interact inelastically in a scintillator like CsI(Tl) (note that $\approx$ 20 cm of CsI(Tl) are needed to stop protons at this energy).
Based on these considerations, CALIFA is designed for the angular region $\approx 10^o$ - 130^o.

The detector is highly segmented ($\sim$ 3000 individual crystals) with different shape and angular aperture for different polar angle regions. The high granularity and total absorption efficiency determine the shape of the crystals. This design is intended to provide all the requirements stated in the Technical Proposal of the R^{3}B experiment and summarised in Table 1.

CALIFA has two major parts - the "Forward EndCap" covering 10^o-40^o and the "Barrel" covering 40^o - 130^o . To obtain high efficiency, an alveolar structure made of thin carbon fibre is devised. Groups of four crystals are inserted in the structure, minimizing the dead volume and the amount of material between detectors (see Figure 2). The alveoli are glued together, obtaining a honeycomb-like structure with strong mechanical properties. The structure is fixed by thicker carbon fibre tabs to the external mechanical support, formed by aluminium tiles that also hold the very front electronics modules. An additional support structure fixes the calorimeter in the measurement place, allowing the displacement of the Barrel and EndCap halves for service.

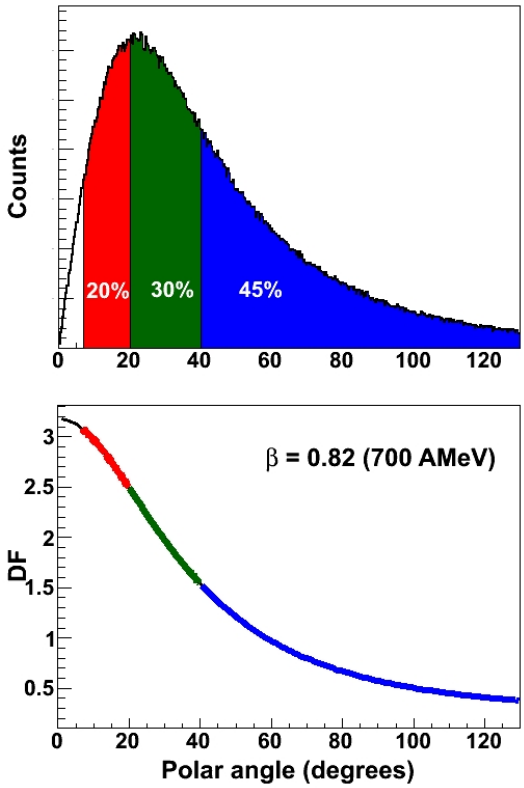

Figure 1: a) Angular distribution and b) Doppler shift of γ-rays emited in-flight by a relativistic projectile (700 A.MeV), DF stands for Doppler Factor and is the ratio between the energy in the laboratory to the source reference frame.

CsI(Tl) has been proposed as scintillating crystal for the Barrel part. It is well established, easy to machine and

* Work performed in the CALIFA/R3B Working group

Total absorption eff.	80%
γ sum energy	$(E_\gamma sum) / < (E_\gamma sum) > < 10\%$
γ multiplicity	$\sigma(N_\gamma) / < \sigma(N_\gamma) > < 10\%$
Calorimeter for LCP	Up to 300 MeV p
γ energy resolution	5% (FWHM at E_γ=1 MeV)
LCP energy resolution	2%

Table 1: Nominal specifications of the CALIFA/R^3B detector. LPC stands for Light Charged Particles

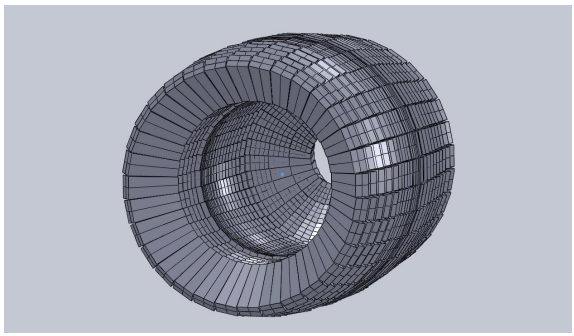

Figure 2: Drawing of the proposed crystal arrangement of a full model of CALIFA. Each box represents a carbon fiber alveolus holding four different crystals

fairly cheap. It has a good intrinsic resolution when coupled to PhotoDiodes (PD) for proton measurements and above all when coupled to Avalanche PhotoDiodes (APD) for γ measurements [3, 4].

The light output (LO) in a polished crystal of CALIFA type (Figure 3 left) depends mainly on focusing and light attenuation properties. Normally this gives a continuos exponential decrease in light response from the front area to the readout area (Figure 4). This position dependence in the collected light introduces a distortion in the measured proton and γ-ray energy especially when gain corrected summing of signals is introduced.
In order to improve the LO uniformity, shading or roughing (lapping) of the front part can be introduced. Both methods provide LO uniformity within $\pm$ 2% provided that the delivered crystals exhibit a smooth decrease ($\delta L < 5$ %) in LO from the front face. Lapping/roughing was applied to the rear half of the crystals using Al_2O_3 powder to achieve the results in Figure 4. The other option, is to specify these values of LO uniformity to the producers, increasing the final price of the crystal.

Encapsulation thickness is a critical parameter to guarantee high efficiency, particularly in the case of light charged particles. Our research, points to a solution where each individual CsI(Tl) crystal will be wrapped with a high quality reflector (ESR from 3M) avoiding light cross-talk between neighbouring crystals that are hold in the same carbon fiber alveolus.

The adaptation of APDs has also been addressed in collaboration with the producer (Hamamatsu). The main improvement comes from an enlargement of the light collection area. This has been achieved developing a new APD

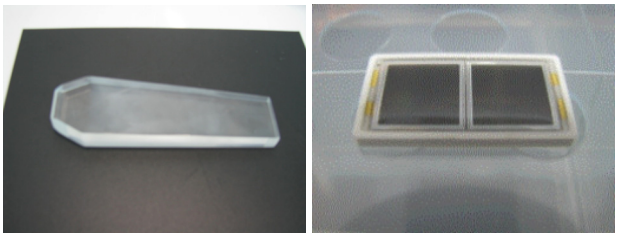

Figure 3: (Left) Typical CALIFA CsI(Tl) crystal, the dimension is $\approx$ 30x15 mm^2 for the entrance face. The crystal length is 130 mm. (Right) Double 10x10 mm^2 APD specifically developed for CALIFA

consisting on two 10x10 cm^2 units (S8664-10) mounted on a common ceramic frame (see Figure 3 right). The dark current of CALIFA APDs is selected by the producer and only those with lower values ($<$ 30 nA) are accepted, allowing a significant reduction of the associated threshold, of particular interest for low energy γ detection [3].

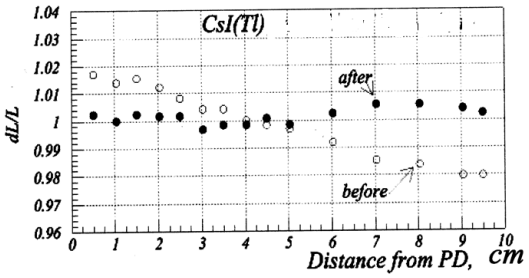

Figure 4: Example of Light Output uniformity for 130 mm long CsI(Tl) crystals before (empty symbols) and after (closed symbols) applying the lapping method

The energy resolution (ΔE/E) of those systems for light-charged particles required by CALIFA has been well achieved. For γ-rays the situation is more complex. Systematic measurements have only been carried out with CALIFA detectors read out by one single APD . Record resolutions of 4.5% at 662keV, have been achieved with small crystal samples (10x10x10 mm^3) and a single APD (10x10 mm^2 S8664-10) [3]. This resolution degrades when the crystal scale to real CALIFA sizes (130 mm long crystals). Although both cooling to 4^o and power stabilization was introduced it is barely possible to reach the resolution goal of e.g. 5 % at 1 MeV. However it appears from first measurements with matched double APDs that this can improve the light collection enough to meet the requirement [3] and Figure 5.

The CALIFA design and the response of individual crystals and prototypes have been simulated with different codes based on GEANT4 and ROOT, and lately inside the R3BRoot framework. The simulation code contains the geometrical description of the target and the different detectors along with a detailed geometry of different versions of the calorimeter.

The digitization of the crystal response includes the

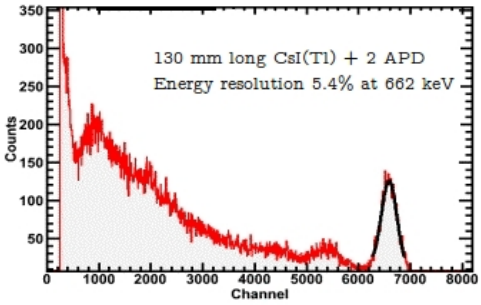

Figure 5: Example of the energy resolution obtained for 130 mm long CsI(Tl) crystal coupled to a double APD (Figure 3)

effects of LO uniformity and the experimental resolution, according to a scaling function of the energy, increasing the FWHM with the square root of the deposited energy in each crystal. The calorimeter hits are reconstructed using the signal in each crystal above a given threshold, including addback in neighbour crystals. The results are transformed to the projectile reference system in order to evaluate the Doppler broadening, using the polar angle information given by the crystals aperture. Additional studies on the light propagation on the proposed crystal shapes have been performed, in order to optimize the shape for the maximum light gathering at the APD position.

Small-scale prototypes consisting of up to 16 CsI(Tl) crystals with realistic sizes and read-out with APDs have been constructed [3, 4]. Since the energy deposition of energetic particles involves several crystals an adequate addback procedure to recover the information is needed. The efficiency of the method was tested with radioactive sources and then applied to the analysis of experiments with high energy particles.
Protons of 180 MeV delivered by The Swedberg laboratory in Uppsala were used to tests the performances of the prototypes. The energy resolution obtained for 180 MeV protons was around 1%, provided that the maximum wrapping thickness is 130 μm.
The response of this prototype to high-energy γ-rays has also been explored in the NEPTUN photon-tagger at Technical University of Darmstadt, in the Lund microbeam facility, and in the nuclear physics beam line in the CMAM in Madrid. At TUD, the prototype was irradiated with tagged-γ of 4, 7 and 10 MeV. The mean energy deposition and the multiplicity distribution obtained was cross-check with dedicated simulations.
The scintillation process in CsI(Tl) involves two different time constants whose ratio differs for different particles. It is therefore suitable for particle identification. For that, the digital Reconstructive Particle Identification (RPID) algorithm has been developed which seems superior to analog techniques with respect to separation and pileup effects. This algorithm, was tested off-line and the results are presented in reference [5].

An alternative solution to long CsI(Tl) for the end-cap is based on the use of a stack of two scintillation crystals, in a Phoswich configuration with a common read-out. The use of phoswhich has a strong advantage for identification of high-energy light-charged particles. The use of a double energy-loss method, instead of fully stopping the particle, would considerably reduce the losses due to nuclear reactions in the scintillation crystals.

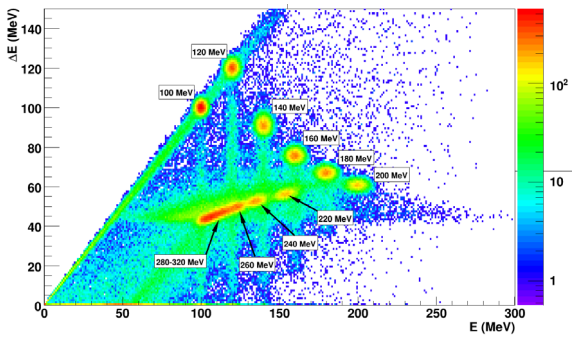

Figure 6: ΔE versus E plot obtained from Geant4 simulation of mono energetic protons in the range 20 360 MeV in steps of 20 MeV, interacting in CEPA. The different energies are clearly separated. Hadronic interaction and the Teflon wrapping have been included in the simulation.

The choice of $LaBr_3$(Ce) and $LaCl_3$(Ce), presently under study, was initially motivated by the very good intrinsic energy resolution (2.8 and 3.5 % (ΔE/E) respectively for 662 keV γ-ray) associated to these inorganic crystals. However, they are highly hygroscopic and required a thick encapsulation that could eventually reduced the efficiency required to CALIFA. Experimental results have been obtained with a prototype detector; a 20 mm diameter cylinder containing a 30 mm long $LaBr_3$(Ce) coupled with a 50 mm long $LaCl_3$(Ce) crystal and coupled to a Hamamatsu R530 8 stage photomultiplier. A test of the response of such system with high energy protons was performed at The Swedberg laboratory in Uppsala. Protons of 155 and 180 MeV were launched against the phoswich crystal and the resulting signals were detected using a flash ADC for pulse shape identification, see the GSI annual report of 2009 for details [6].

Towards the final definition of the Endcap design, an array of 3x3 truncated pyramid detectors has been proposed (CEPA, CALIFA Endcap Prototype Assembly), each crystal with a squared entrance face (side: 12 mm, opening angle 3). The individual detectors are comprised of a $LaBr_3$(Ce) crystal 40 mm long optically coupled to a $LaCl_3$(Ce) crystal 60 mm long and are wrapped in Teflon-equivalent of 0.5 mm. Due to the fact that the crystals are hygroscopic the assembly is encaged in 0.5 mm Al. In the case of high energy γ-rays (20 MeV) and with an array of 50x50x150 mm^3 is possible to recover up to 87% of the full γ-ray energy.

Pulse shape analysis has proved to be a successful technique to separate the energy deposited in each crystal of the phoswich detector for every particular event (see [6]). This allows us to use the former as a ΔE-Et telescope detector. In Figure 6 we can see a realistic Geant4 simulation showing how this technique can be applied to separate different proton energies ranging from 100 to 240 MeV with an energy resolution below 2%.
The possibility of exploring the phoswich solution with other scintillation crystals is foreseen.

Specific developments of FEE are ongoing. In a first step, the evolution of existing MPR-16-B Mesytec preamplifier module is considered. The RPID algorithm previously mentioned has been recently implemented on an FPGA for embedded real-time analysis and particle identification. This system was tested at GSI Darmstadt using a $^{197}Au^{65+}$ beam (E = 400 AMeV) and a Pb target with a CALIFA small-size CsI(Tl) prototype readout with APD. Two experimental setups were used. In both setups a Mesytec MPRB-16, 16-channel preamplifier, provided high voltage control and gain stabilization for the APD readout of the CsI(Tl) crystals. Amongst others, it features two switchable gains corresponding to 30 MeV and 300 MeV energy range. For offline analysis, data from two SIS3302 fast sampling ADC modules were utilized (8 input channels each, 16 bit resolution, 100 MHz sampling frequency).

For online data analysis a HADES RICH frontend board including two fast sampling ADCs (8 channels each, 12 bit resolution, 40 MHz sampling frequency) and a Lattice ECP2M 100 FPGA connected via TRB [7] to a PC was used. The current FPGA version features pileup correction based on the Moving Window Deconvolution algorithm (MWD) [8]. Later versions will include the RPID algorithm for real-time particle identification.

Figure 7 illustrates an obtained PID plot with a simple energy loss function fitted to it. Even using the preamplifier's 300 MeV range, the lines corresponding to distinct particle types are clearly separated. Beside the gamma line in the center and the proton line right beneath, a third line can be seen and even a fourth line becomes slightly apparent.

The large number of crystals and thus electronic channels of CALIFA prompts for a computerized solution for the slow control; setting voltages of each crystal, read-back and logging of temperature etc. A user-friendly interface has been developed and is ready to be implemented for control on the existing Crystal Ball.

In the near future, the detector concept is going to be tested by constructing and assembling a part of the forward region of the Barrel, called Demonstrator (see Figure 8). The Demonstrator comprises several modular portions or "petals", each one made of around 20 alveoli or 80 crystals, with an independent mechanical support which could fit to different experimental setups.

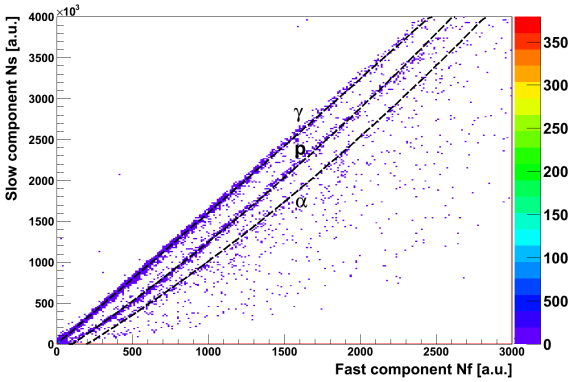

Figure 7: Particle identification achieved in a test recently performed at GSI using a FPGA (see text for details)

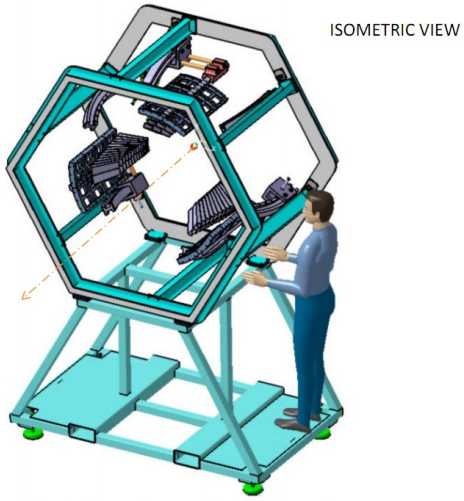

Figure 8: Schematic view of the CALIFA Demonstrator.

References

[1] R3B Technical Proposal.

[2] H. Alvarez et al., nucl. Ins.Meth B 266(2008) 4616

[3] Martin Gascón PhD, December 2010, USC. M. Gascón et al IEEE Trans. Nucl. Scie. 57, (2010) 1465, M. Gascón et al IEEE Trans. Nucl. Scie. 56 , (2009) 962

[4] D.D. DiJulio et al., Nucl. Instr. Meth A 612 (2009) 127, and Response of a CALIFA CsI(Tl) prototype to protons V. Avdeichikov et al, in this Annual report

[5] M. Bendel Diplomarbeit, November 2010, TUM. M Bendel et al in this GSI 2010 report

[6] http://www.gsi.de/informationen/wti/library/scientific report2009/PAPERS/FAIR-EXPERIMENTS-22.pdf .

[7] J. Michel et al. A Users Guide to the HADES DAQ Network, July 2010

[8] A. Georgiev and W. Gast, IEEE Trans. Nucl. Sci. 40 (1993)770

Particle-γ-Separation with CALIFA *

M. Bendel† [1], *R. Gernhäuser*[1], *R. Krücken*[1], *T. Le Bleis*[1], *M. Winkel*[1], *and the R3B Collaboration*

[1]Technische Universität München, Physik-Department E12

The basic properties of a good scintillator material for low and medium energy γ-ray detection are a high and linear light output with energy. In Thallium-doped Cesium Iodine (CsI(Tl)) both requirements are nicely fulfilled. The scintillation is based on two different scintillating states with two significantly different lifetimes of (0.6 and 3.25 μs). It is known, that the ratio of light output from the two main components is dependent on the ionization density of the absorbed particle ([SJW58]) and therefore dependent on the type of particle. This feature will be used in the CALIFA calorimeter for particle-γ-separation.

We have developed a new sensitive algorithm based on digital pulse shape analysis of the preamplifier signals from the photo sensors, called RPID (**R**econstructive **P**article **ID**entification) algorithm. Including the so called Moving Window Deconvolution (MWD) [GG93] this algorithm directly reconstructs the amplitudes of the two different time components in the light output.

For a test of this new method at the energies relevant for CALIFA we have performed an experiment at the Munich Tandem accelerator (Maier-Leibnitz laboratory, Garching). Using a $^{12}C(p,p')^{12}C$ reaction with a proton energy of $E_{kin} = 21MeV$. This allows to measure high energetic scattered protons as well as γ-rays from inelastic scattering with energies up to 15.1MeV at the same time. A $75\frac{mg}{cm^2}$ Carbon target and three 130 mm long crystals with APD readout at an angle of $\theta = 60$ with respect to the beam axis were used. We recorded digital signal shapes of $10\mu s$ length and a granularity of $10ns$, triggering on any energy deposit in the crystal.

Figure 1 shows the result of the RPID for the full unbiased set of the experimental data. The γ-rays and the protons are separated accurately also for low energies. The signal width for elastically and inelastically scattered protons is dominated by the target thickness and the energy loss of particles in the crystals wrapping. The black line is fitted to the proton line and based on this fit the red line is calculated as the function of elastic scattered protons that have not been stopped completely in one crystal. So it should even be possible to determine the full energy of particles that lost part of their energy in the non active material between the crystals. An energy spectrum of all events identified as γ-rays from the proton-carbon reaction is shown in figure 2. While the 4.4MeV photo peak and its single and double escape peak can be identified, the 15.1MeV peak only represents an edge like distribution. Simulations of the experiment show that positrons and electrons that are mainly generated in the first interaction emit bremsstrahlung photons with high energies escaping from the small detector setup and do not allow for a full energy absorption.

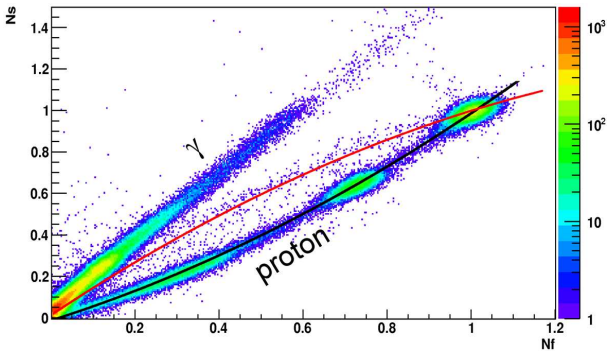

Figure 1: First result of the *Reconstructive Particle Identification Algorithm (RPID)*. Photons and protons are separated accurately also for low energies. The black line is fitted to the proton line and based on this fit the red line is calculated as the function of elastic scattered protons that have not been stopped completely in one crystal.

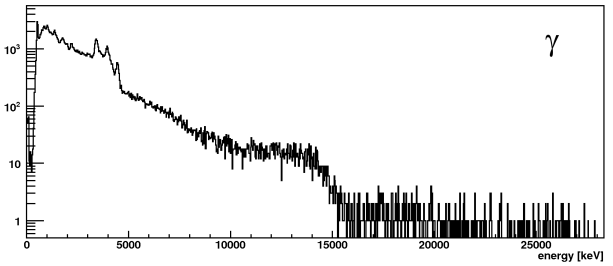

Figure 2: **γ-ray spectrum:** By means of the RPID algorithm the proton and γ-ray spectra can be separated. The 4.4MeV photopeak, single and double escape peak can be identified, while the 15.1MeV γ-rays are not fully absorbed.

After this successful test of the new RPID particle identification algorithm with γ-rays and protons the separation capabilities expected for protons, deuterons and alphas as well as a separation of neutron and γ interactions has to be tested.

References

[SJW58] R. S. Storey, W. Jack, and A. Ward, *Proceedings of the Physical Society*, 72(1), 1958.

[GG93] A. Georgiev and W. Gast, *IEEE Transactions on Nuclear Science*, IEEE Transactions on DOI - 10.1109/23.256659, 40(4):770 - 779, 1993.

* Work supported by MLL, GSI and BMBF (06mt9156)

† Michael.Bendel@ph.tum.de

Geiger-mode avalanche-photodiodes as readout for the CALIFA detector*

A. Ignatov[†1], *J. Enders*[1], *C. Henrich*[1], *T. Kröll*[1], *M. von Schmid*[1], *and the R^{3}B collaboration*
[1]TU Darmstadt, Darmstadt, Germany

The CALIFA spectrometer, which surrounds the R^{3}B target, will be used for detection of gamma-rays and high-energy protons. Of particular interest for this detector the energy resolution and its dependence on different configurations and components has to be studied. Cs(Tl) crystals with photomultiplier tubes (PMT) or avalanche-photodiodes (APD) readout as well as $LaBr_3$(Ce) so far with PMT readout only, show an energy resolution under 5% for 662 keV gamma-rays [1]. But PMTs are sensitive to magnetic fields and, therefore, cannot be used near the GLAD magnet. APDs show a strong dependence on temperature and bias voltage and require additional amplification. Therefore we consider SiPM [2] (Silicon Photomultiplier) to be another option for scintillator readout.

Essentially this device consists of a large number of APDs (pixels) connected in parallel with an applied bias voltage above the breakdown value, hence it is operated in Geiger-mode. Each pixel acts like a digital device. In case an incident photon creates an electron-hole pair in its sensitive volume, an avalanche is initiated. The output of the whole device, however, is the sum of the individual APDs signals, thus representing an analog response until the number of incident photons is smaller than the overall number of pixels. Preserving the insensitivity to magnetic fields of APDs, SiPMs have an internal amplification comparable to PMTs and are less sensitive to temperature and bias variations. Drawbacks are a small size of the sensitive area and a dynamic range limited by the number of pixels. Using an array of SiPMs can overcome these drawbacks. SiPMs provide also a better time resolution which can be important for some CALIFA applications.

Test setup

In our tests we used a small $LaBr_3$(Ce) sample crystal. This material provides very high light output (about 60 photons/keV) thus allowing to obtain excellent energy resolution [3]. The volume of the sample we used is about 2 cm^3 and it is encapsulated in an aluminium can as the material is hygroscopic. The readout is done through a 1 cm diameter quartz window with a Hamamatsu MPPC (Multi Pixel Photon Counter - Hamamatsu naming for SiPM). The properties of the scintillator and the readout device are listed in Table 1. The MPPC is coupled to the center of the quartz window with silicone grease. The assembly is wrapped with black tape to block external light.

A very first test was done without preamplifier. A ^{22}Na source provided 511 keV gamma-rays. The only partial coverage of the quartz window by the photosensor's active area together with the MPPC efficiency caused that only about 1-2% of photons had been detected. Thus, the output signal is too small to be processed by the subsequent electronics. Therefore, we used a preamplifier developed by CPTA [4] for their own SiPM devices to increase the signal. However, the obtained energy resolution was only about 20% FWHM at 511 keV.

Table 1: Scintillator and MPPC parameters.

$LaBr_3$(Ce) crystal	
Density [g/cm^3]	5.08
Wavelength of emission max. [nm]	380
Light yield [photons/keV]	63
MPPC S10931-025P	
Active area [mm^2]	3x3
Number of pixels	14400
Peak sensitivity wavelength [nm]	440
Gain	2.75*10^5

Discussion

The internal resolution of the scintillator and of the MPPC are much higher than the obtained result. The source of the rather poor energy resolution is considered to be a combination of the contributions due to statistics of the number of photons detected and the measurement conditions. The photon statistics in our case can be described by Poisson's law. Hence, the average number of MPPC pixels fired determines the achievable energy resolution. Estimation based on the described considerations predicts a two times better energy resolution for 511 keV gamma-rays.

To investigate this mismatch, a precise calibration in terms of pixels fired has to be done. Also, a preamplifier better suited for the shaping amplifier will improve the performance further. Bias voltage and temperature jitter and their contribution to energy resolution will be investigated.

References

[1] H. Alvarez-Pol et al., Technical status report for CALIFA (2008).

[2] D. Renkel, Nucl. Instr. and Meth. A 567 (2006) 48-56.

[3] J. Flamanc, C. Rocza "Compact $LaBr_3$(Ce) Gamma Ray Detector with Si-APD Readout", CAARI 2008 Proceedings.

[4] CPTA - Center of perspective technology and apparatus (www.cpta-apd.ru).

*Work supported by the state of Hesse through the LOEWE center HIC for FAIR, through the GSI-TU Darmstadt cooperation contract, and by the BMBF through contract 06DA9040I

† A.Ignatov@gsi.de

Progress in the design and construction of the R^{3}B-GLAD large acceptance superconducting spectrometer for GSI-FAIR*

B. Gastineau, C. Mayri, B. Baudouy, C. Berriaud, G. Disset, A. Donati, J-E. Ducret, D. Eppelle, P. Fazilleau, P. Graffin, J-L. Jannin, D. Loiseau, J-P. Lottin, M. Massinger, C. Pes, Y. Queinec, Z. Sun, P. Charon, P. Contrepois, H. Neyrial

IRFU, CEA-Saclay, 91191 GIF sur Yvette, France

The design and construction of the GLAD superconducting magnet for the R^{3}B collaboration has progressed on four trails in 2010:

1) The manufacture of the magnet cold mass in the premises of our industrial partner ASG *(SpA)* in Genoa *(Italy)*
2) The final design of the magnet's cryostat
3) The magnet safety system (MSS)
4) The preparation of the cold mass tests to be performed in Saclay in 2011.

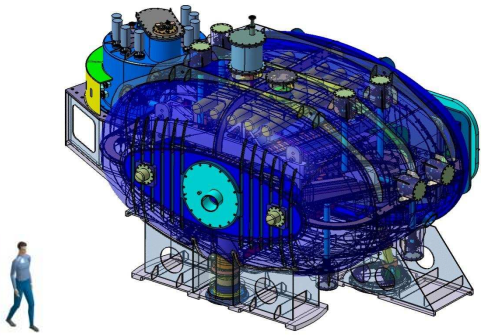

Fig. 1: the R^{3}B-GLAD magnet in its final cryostat.

The fabrication of the cold mass (CM) requires the winding of the coils using the superconducting cable, the fabrication of the casings from aluminium blocks & the integration of the coils in the casings. The manufacturing of the coil casings was completed & followed by the cold mass blank assembly in March 2010. The coil integration in the casings was performed afterwards. This delicate phase is rather difficult, as the boxes should be machined and the shims and wedge shapes adjusted to fit exactly to the real dimensions of the manufactured coils; this is in order to manage the variable gap studied to take into account the differential thermal shrinkage during the cooling down of the magnet. Thermal drains and temperature probes have also been mounted on the coils at the manufactory before the closure of the casings. The coils integrated in their casings have been delivered to Saclay at the end of 2010.

The final detailed design of the cryostat was performed in 2010. The final call for tenders was launched in September, with responses from the industry in November.

The magnet control system (MSS) is now completed. It has been tested on its software components & some hardware parts. It will be connected on the cold mass (CM) of the magnet for the CM tests in Saclay.

There will be two tests performed in Saclay next year. The first one will aim at testing components of the final cold busbar as well as the innovative concept used in the design of the R^{3}B – GLAD magnet for the blocking of the coils inside their casings. In this test, the reduced-scale model of the coils will be tested at liquid-helium temperature in the test-station SCHEMa in Saclay. The second test, performed at actual size, will be that of the cold mass itself, after its mechanical assembly and its instrumentation have been completed. The equipment & changes necessary for the test station to be used are underway: cooling lines, mechanics & cryogenic support for the 22 tons R^{3}B – GLAD cold mass inside the test-station vessel *(5 m diameter)*. The tests are planned for the first half of 2011 within the Saclay facility, which was used for the testing of the 70 coils of the magnetic-fusion stellerator W7X.

Fig. 2: *(Left)* A main coil in its casing, before & during installation of the cover. *(Right)* CM blank assembly.

References

- B. Gastineau *et al.*, IEEE Trans. Appl. Supercond., June 2010, vol. 20, issue 3, p. 328-331
- Z. Sun *et al.*, IEEE Trans. Appl. Supercond., June 2010, vol. 20, issue 3, p. 222-225
- C. Mayri et al., IEEE Trans. Appl. Supercond., June 2010, vol. 20, issue 3, p. 1985-1988
- P. Fazilleau *et al.*, IEEE Trans. Appl. Supercond., June 2010, vol. 20, issue 3, p. 2074-2077
- C. Pes *et al.*, IEEE Trans. Appl. Supercond., June 2010, vol. 20, issue 3, p. 1908-1911

Simulations of a new Si target recoil detector for R^{3}B*

N.I. Ashwood[1], R. Lemmon[2], M. Labiche[2] and the R^{3}B collaboration

[1]University of Birmingham, UK; [2]Daresbury Laboratory, UK.

Simulations for the new Si tracking detector have been performed in the R3BRoot framework. The initial design of the detector was based on previous simulation work done in the R3BSim framework [1]. In this case the detector consisted of two octagonal layers of double-sided Si wafers. The first layer was situated at a distance of 2.5 cm from the beam axis, with each wafer being 2 cm wide and 100 μm thick. The second layer was at 10 cm from the beam axis, with each wafer being 4 cm wide. The detector was 20 cm in length with a strip pitch of 100 μm in both layers. The intrinsic energy resolution was assumed to be 50 keV.

Elastic and quasi-free scattering physics generators were implemented into the R3BRoot framework. Simulations of the energy and angular resolutions for the p(^{12}C,p)^{12}C and ^{12}C(p,2p)^{12}C reactions were found to be in good agreement with those previously measured in R3BSim. The full energy of the protons were measured assuming that an array of CsI detectors, with 100% detection efficiency and 1.5% energy resolution, surrounded the Si array. Figure 1 shows the separation energy resolution (E(σ)) for (p,2p) events as a function of the strip pitch for various beam energies. The target used in this case was a cylindrical liquid hydrogen target measuring 1 cm in diameter and 5 cm in length.

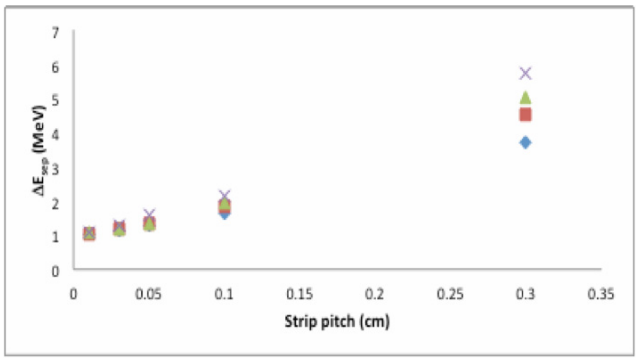

Figure 1 Separation energy resolution versus strip pitch for (p,2p) at various beam energies. The blue diamonds represent data taken at 0.5 GeV/A, red squares for 0.7 GeV/A, green triangles for 0.8 GeV/A and grey crosses for 1 GeV/A.

It is clear that between 0.01 cm and 0.05 cm that an E(σ) of below 1.5 MeV could be achieved with this geometry for all beam energies up to 1GeV/A. The angular resolution, taken as the residual of the simulated and actual opening angles of the two protons for (p,2p) events, ranges from 2 mrad to 12 mrad over the range of strip pitches.

The major contribution to the E(σ) was found to be the energy and angular straggling in the first layer of Si. This contributed ~70% of the resolution for strip pitches less than 0.05 cm. The new detector should therefore be designed with the first layer as thin as possible. Large effects to the resolution were also found from the intrinsic CsI detector resolution and straggling from the target. These parameters have yet to be fixed and thus will effect the overall resolution.

The efficiency for detecting both protons in (p,2p) events as a function of detector length, for various beam energies. Even for the lowest energy of 0.5 GeV/A the protons were emitted at forward angles, giving a detection efficiency of 20% for a 20 cm long detector, rising to 80% for a detector of 50 cm. As such the detector has to either be as long as possible or, more practically, include end-caps into the design. Another consideration in the overall design should be that strip redundancy has to be taken into account by including a third layer in the design. This will ensure that each proton will pass through at least 3 layers of Si, allowing the angle to be measured even if some strips do not fire. Wafer size is also an issue. The optimum wafer size for 100 μm Si with 300 μm strip pitch is 42.5 mm wide by 125 mm in length. To increase the length, or width, of each layer the wafers can be stitched together.

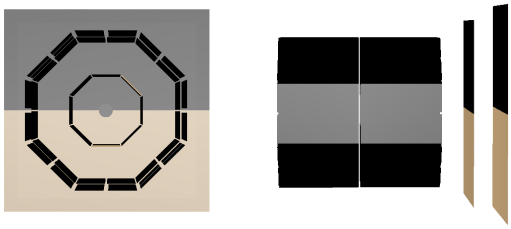

Figure 2 End on and side views of the current design for the Si tracking detector.

The current design on the Si tracking detector is shown in Figure 2. The detector barrel is 250 mm long, with the 1st layer is 58 mm, from the beam axis, the 2nd , 109 mm and the 3rd ,119 mm. End caps of 290 x 290 mm and 340 x 340 mm sit at 300 mm and 350 mm from the target position respectively. This geometry gives a (p,2p) E(σ) of 1.5 MeV for a ^{12}C beam at 0.5 GeV/A, assuming a CsI energy resolution of 3%. The strip pitch is 300 μm, meaning approximately 44k channels of electronics will be needed. Work on the final design and ASICS electrons is still on going.

References

[1] R3B Technical Proposal, http://www-land.gsi.de/r3b

* Work supported by EU, EURONS contract No. 506065.

Application of a DSSD detector as a differential pumping barrier for experiments at the ESR and the NESR at FAIR

B. Streicher[1,2], P. Egelhof[1], S. Ilieva[1], N. Kalantar-Nayestanaki[2], H. Kollmus[1], Th. Kröll[3], M. Mutterer[1], M. von Schmid[3], and M. Träger[1]

[1]GSI Darmstadt, Germany; [2]KVI Groningen, The Netherlands; [3]TU Darmstadt, Germany

The development of the silicon particle array for the EXL project has progressed in solving the vacuum issues connected with the use of telescope-like detector systems in the Ultra-High Vacuum (UHV) environment of the storage ring. In order to achieve UHV conditions it is necessary to bake all the components inside the storage ring up to 200 °C for a period of a couple of days which puts constraints on the choice of materials for the whole construction. To fulfill these requirements we developed a differential pumping concept, where the UHV is separated from the Auxiliary Vacuum (AV) using the innermost DSSD sphere as a vacuum barrier. In such a design, the subsequent layers of DSSDs and/or Si(Li) detectors, together with all unbakeable and thus outgassing components are placed in an AV where vacuum of at least three orders of magnitude worse will be sufficient. Since the vacuum barrier serves at the same time the purpose of an active window it also enables the detection of recoil particles varying from protons to alphas with low energy, down to about 100 keV, as a result of a low momentum transfer. The test was realized in a small vacuum chamber divided into two parts and separated by a custom machined CF150 flange with an opening of 4x4 cm^2 in the middle. The PCB was manufactured from aluminum nitride ceramic because of its low outgassing, good dielectric properties, high thermal conductivity and low thermal expansion coefficient close to that of silicon. The DSSD chip with an active area of 19×19 mm^2 and 64 strips on each side [1] was glued on a small step of the cut-out in the middle of the PCB. This PCB was installed over the opening in the CF150 flange using a ring made of aluminum wires of 1.5 mm diameter as a vacuum seal. Both sides of the DSSD were read-out on one side of the PCB (AV side) using 16 channels per side (four strips connected together) to monitor the detector's spectroscopic performance. After the bake-out, the vacuum on the UHV side reached the value of 1.2×10^{-10} mbar (see Fig. 1 and Ref. [2]) and the corresponding vacuum on the AV side was 2.2×10^{-7} mbar. Using the needle valve we introduced an artificial air leak on the AV side to observe its influence on the UHV side. While the pressure on the AV side increased due to the leak more than four orders of magnitude, the vacuum on the UHV side stayed well within the achieved 10^{-10} mbar range. Outgasing spectra were measured on the UHV side with a residual gas analyzer that show the features of a typical air leak and are free of organic compounds. The most pronounced increase was detected in molecular and atomic nitrogen, molecular oxygen as well as argon, which are the basic air constituents.

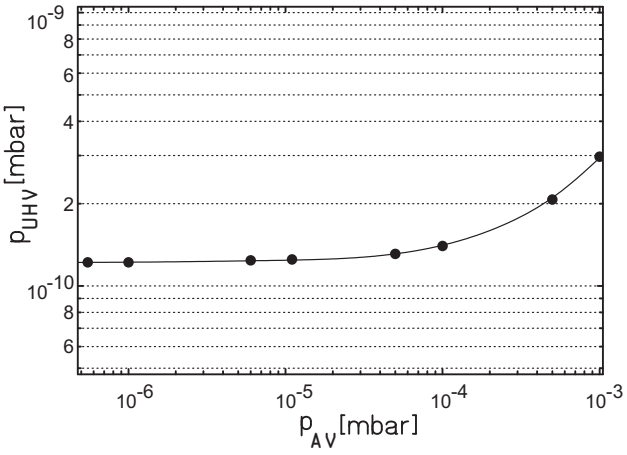

Figure 1: Dependence of the pressure on the UHV side on the AV side pressure influenced by an air leak artificially introduced through the needle valve installed on the AV side.

Our test results demonstrate the possibility of operating differential vacuum system in the storage ring environment using DSSDs as a vacuum barrier. It was shown that the PCB-DSSD system withstands the bake-out cycle and the mechanical sheer stresses connected with the thermal expansion with unhindered spectroscopy performance. Chosen materials facing the UHV environment proved to be clean of any UHV disturbing contaminants. The achieved vacuum difference ranged over more than six orders of magnitude with the vacuum on the UHV side staying well within the 10^{-10} mbar range, which is an acceptable vacuum for the interaction region with internal target at the storage ring. It shall be noted that the concept of this development can be potentially applied outside of the EXL project for experiments at storage rings like the ESR requiring the usage of DSSDs in the UHV. Due to the fact that the entrance detector serves the purpose of an active window, telescope-like detector configurations used in the UHV can measure low energy particles of about 100 keV as well as penetrating particles with energies of several hundreds of MeV stopped in subsequent detectors.

References

[1] B. Streicher *et al.*, GSI Scientific Report Vol. 2008-1 (2008) 55.

[2] B. Streicher *et al.*, submitted to Nucl. Instrum. Methods Phys. Res. A (2011).

An optimized design of the ELISe spectrometer for the electron/RI collider experiment at FAIR*

T. Adachi[1], G.P.A. Berg[2], N. Kalantar-Nayestanaki[1], H. Simon[3], M.N. Harakeh[1], H.J. Wörtche[1], I.A. Koop[4], M. Couder[2], and M. Fujiwara[5]

[1]KVI, University of Groningen, Groningen, The Netherlands; [2]JINA, Notre Dame, U.S.A.; [3]GSI, Darmstadt, Germany; [4]BINP, Novosibirsk, Russia; [5]RCNP, Osaka, Japan

For electron scattering off radioactive nuclei, the ELISe spectrometer will be constructed as a part of FAIR. The system consists of a Pre-Deflector (PD), a Quadrupole (Q), a Hexapole (H) and a vertically bending dipole Magnet (VM). In the conceptual design of the spectrometer, the proposed iron poles of PD are similar to a "clam-shell" gap to accept large azimuthal scattering angles [1]. However, this system is rather complicated to build and operate in order to keep and scale homogeneous magnetic fields. Besides, the ion-optics calculations show that the solid angle is too small, particularly at angles smaller than 15˚ due to the strong edge focusing at the front edge of PD [2].

In order to overcome these difficulties, we propose to change the design of PD to the constant gap [3]. Fig.1 shows the mid-plane of the constant gap PD. The main coils are wound around the iron-poles.

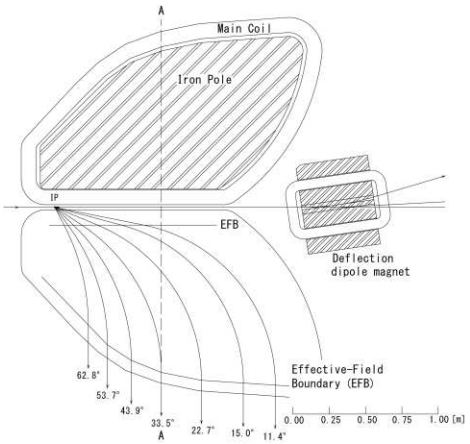

Figure 1: The mid-plane of the PD magnet.

Fig. 2 (a) shows the cross section of the upper part of the PD along the line A-A in Fig. 1. The half gap size is 65.0 mm. Fig. 2 (b) shows the magnetic field distribution calculated by using OPERA Vector Field for the total current per coil of 75.2 kA. The homogeneous magnetic field was reproduced without the ripples characteristic of the earlier design.

The ion-optical calculations were performed by using COSY Infinity. An example at 22.7˚ is shown in Fig. 3. The fringe field distributions at the entrance and the exit of the PD were reproduced by the Enge function derived from the magnetic field distribution of Fig. 2 (b). The angle acceptances in polar and azimuthal directions are ±30 mrad and ±60 mrad, respectively. From the angle acceptances determined by the ion-optical calculations, the solid angle of the spectrometer was calculated from 11.4˚ to 53.7˚.

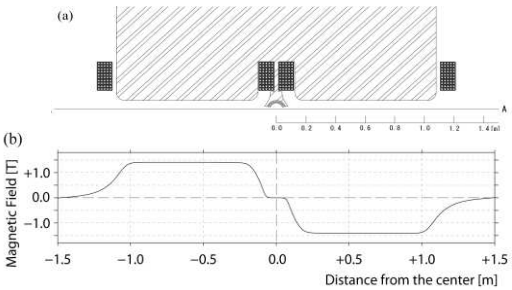

Figure 2: (a) The cross section of the upper part of the constant gap of the PD. (b) The magnetic field along the line A-A in Fig. 1.

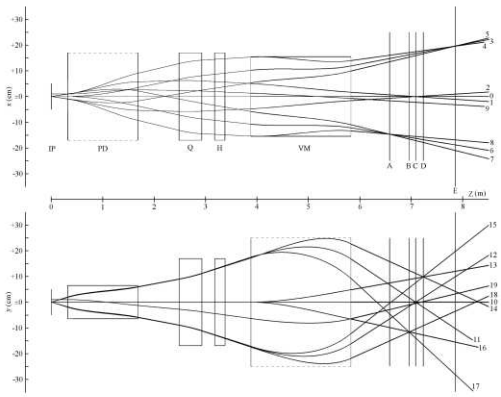

Figure 3: Ion-optical calculation for 22.7˚. The upper and lower panels show the calculations for the polar and azimuthal directions, respectively.

*This work was supported by the EC via the Intas programme contract number 05-1000008-8272.

References

[1] G.P.A. Berg et. al., Nucl. Instrum. Meth. A. in press.
[2] T. Adachi et. al., GSI scientific report (2010) p. 39.
[3] T. Adachi et. al., Nucl. Instrum Meth, A, in preparation.

High Resolution E-ToF Mass Identification for Heavy Ions with Calorimetric Low Temperature Detectors

A. Echler[1,2], A. Bleile[1,2], P. Egelhof[1,2], S. Ilieva[1], S. Kraft-Bermuth[3], J.P. Meier[1], and M. Mutterer[1]

[1]GSI, Darmstadt, Germany; [2]Johannes Gutenberg Universität, Mainz, Germany; [3]Justus-Liebig-Universität, Gießen, Germany

The direct in-flight mass determination of nuclides produced in heavy-ion induced reactions is an important task, requested in various fields of heavy-ion physics. It is in many cases mandatory for a unique identification of rare isotopes and an unambiguous interpretation of experimental data. The experimental technique often used for this purpose is a combined energy and time-of-flight (E-ToF) measurement. However, for low energetic heavy ions, ionization based energy detectors suffer from incomplete energy detection due to charge recombination, resulting in pulse-height defect and a relatively poor energy resolution. Therefore, for low energy heavy ions the mass resolution of an E-ToF spectrometer is usually limited by the performance of the energy detector.

This problem can be overcome by using calorimetric low temperature detectors (CLTD's) for the energy measurement. CLTD's provide, as compared to conventional ionisation detectors, due to their detection principle, substantial advantages in detector performance, such as energy resolution and energy linearity, etc. CLTD's have been frequently demonstrated to achieve an excellent relative energy resolution of ΔE/E = 1-2$\times 10^{-3}$, and a good energy linearity with a complete absence of pulse-heigt defect, in a wide range of ions and energies [1,2]. Thus a combination of CLTD's as high-resolution energy detectors with ToF detectors provides a detector system for high-resolution mass identification of low energetic heavy ions.

Recently a prototype of a E-ToF detector system was setup at GSI and tested with ^{238}U beams from the UNILAC. The ToF detector consists of two MCP-Chevron detectors, mounted in a relative distance of 1 m, and equipped with 10 and 4 μg/cm^2 carbon converter foils, respectively. The energy was measured by an array of 8 CLTD pixels (Fig. 1) with a total active area of 12$\times$6 mm^2, operated at 1.5 K.

The performance of the E-ToF system was tested with ^{238}U particles with a broad energy distribution of E = 0.1 - 1 MeV/u, produced by scattering the beam under small angles from a 20 mg/cm^2 thick Au-Target. With the present time resolution Δt (FWHM) $\approx$ 300 ps, which may be improved in future, a mass resolution of Δm (FWHM) = 1.53(5) amu was obtained (Fig. 2).

Possible future applications of such a E-ToF detector system are, after potential improvements in ToF-resolution and active solid angle, the mass identification of superheavy elements, heavy fission products, or reaction products in experiments with radioactive beams.

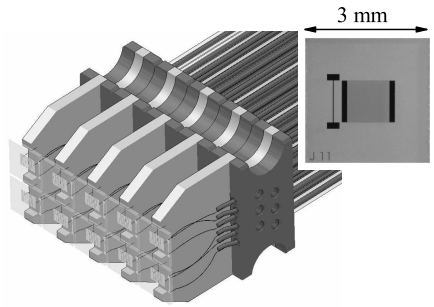

Figure 1: Design of a prototype array consisting of CLTD pixels. The single pixels consist of a thin-film superconducting aluminum transition edge temperature sensor, operated at $T_C \approx$ 1.5 K, which is evaporated onto a sapphire substrate serving as absorber with a thickness of 430 μm and an active area of approximately 3$\times$3 mm^2. Each column of two pixels is mounted individually. The inlay shows one single pixel, with the gold heater for temperature stabilization.

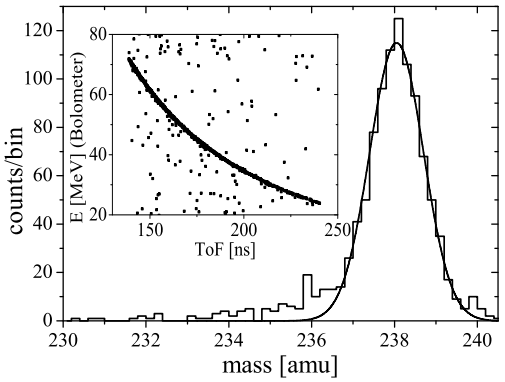

Figure 2: Mass spectrum of a CLTD pixel for ^{238}U in an energy range of 20 - 70 MeV and the corresponding 2-dimensional energy versus ToF graph. The mass resolution obtained is Δm (FWHM) = 1.53(5) amu.

References

[1] P. Egelhof and S. Kraft-Bermuth, "Cryogenic Particle Detection", Topics in Applied Physics Vol. 99, 2005 pp. 469-498.

[2] S. Kraft-Bermuth et al., Rev. Sci. Instrum. 80, 103304 (2009).

The Reaction ^{48}Ca + ^{248}Cm → ^{296}116* studied at the GSI SHIP

S. Hofmann[1,2], S. Heinz[1], R. Mann[1], J. Maurer[1,3], J. Khuyagbaatar[1], D. Ackermann[1], S. Antalic[4], W. Barth[1], M. Block[1], H.G. Burkhard[1], V.F. Comas[1], L. Dahl[1], K. Eberhardt[5], R.A. Henderson[6], J.A. Heredia[1], F.P. Heßberger[1,3], J.M. Kenneally[6], B. Kindler[1], I. Kojouharov[1], J.V. Kratz[5], R. Lang[1], M. Leino[7], B. Lommel[1], K.J. Moody[6], G. Münzenberg[1], S.L. Nelson[6], K. Nishio[8], A.G. Popeko[9], J. Runke[5], S. Saro[4], D.A. Shaughnessy[6], M.A. Stoyer[6], P. Thörle-Pospiech[5], K. Tinschert[1], N. Trautmann[5], J. Uusitalo[7], P.A. Wilk[6], and A.V. Yeremin[9]

[1]GSI, Darmstadt, Germany; [2]Goethe-Universität, Frankfurt, Germany; [3]HIM, Mainz, Germany; [4]Comenius University, Bratislava, Slovakia; [5]Johannes Gutenberg-Universität, Mainz, Germany; [6]LLNL, Livermore, USA; [7]University, Jyväskylä, Finland; [8]JAEA, Tokai, Japan; [9]JINR-FLNR, Dubna, Russia

Introduction

The favorite method proposed for producing superheavy nuclei in the laboratory was the fusion of heavy isotopes in the reaction ^{48}Ca + ^{248}Cm → ^{296}116* [1–3]. Using the gas-filled separator SASSY in Berkeley and the velocity filter SHIP in Darmstadt, this reaction was studied over a wide range of excitation energies in 1982–83 [4]. In these experiments, upper cross-section limits of 200 pb were determined for the production of element 116 isotopes at a range of lifetimes from 10 µs to 1d. In the range from 1d to 1 y upper limits of 20 pb were reached using chemical separation.

During the course of a systematic study of hot fusion reactions using a ^{48}Ca beam and various actinide targets, the reaction ^{48}Ca + ^{248}Cm was studied again at FLNR in Dubna in 2000–03. Six decay chains were assigned to the isotope ^{292}116 and five to ^{293}116 [5].

In a resumption of the experiments at SHIP using actinide targets we planned to repeat the irradiation of ^{248}Cm targets with ^{48}Ca ions, however, now at higher beam intensities and with larger area targets and improved detector system. Main aims of the new investigation were, firstly, testing the use and the safe handling of large area radioactive actinide targets at SHIP, secondly, to independently confirm synthesis and decay data of isotopes of element 116 published in [5], and, thirdly, to prepare future search experiments for new elements beyond the already known element 118 [5] using heavier beams and a ^{248}Cm target.

Experimental Techniques

Our study of the reaction ^{48}Ca + ^{248}Cm → ^{296}116* was performed from June 25 to July 26, 2010. During the first part ending on July 12, a beam energy of 265.4 MeV was chosen, in the second part ending on July 24 the beam energy was increased to 270.2 MeV.

The ^{48}Ca beam was delivered from the ECR ion source and the accelerator UNILAC at GSI. Metallic, isotopically enriched ^{48}Ca (89.5 %) and the ECR oven technique were used. Mean currents of 576 and 444 *p*nA (1 *particle* nA = 6.24×10^9 particles/s) on target were applied during irradiations at beam energies of 265.4 and 270.2 MeV, respectively.

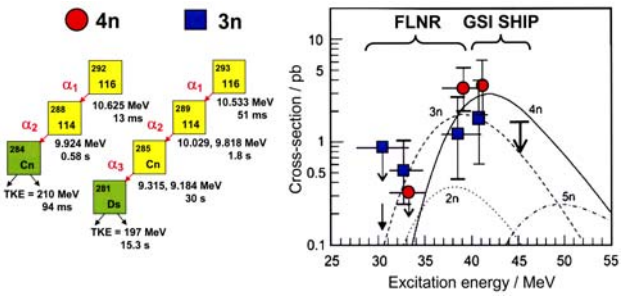

Figure 1: Cross-sections measured for the reaction ^{48}Ca + ^{248}Cm in [5] and in this work. The predictions of the excitation functions are from [11]. Data of the decay chains are α energies from this work, half-lives deduced from Fig. 3 and energies of spontaneous fission from [5].

The target material was provided by LLNL. An amount of 20 mg of ^{248}Cm was delivered to the Institute of Nuclear Chemistry of the Johannes Gutenberg-University in Mainz. There, eight targets were produced by molecular plating [6]. Thin titanium foils of 1.05 mg/cm^2 thickness served as backing material for the Cm_2O_3 layer of 0.460 mg/cm^2 thickness.

The eight targets were mounted on the circumference of the rotating wheel which we usually use in SHIP experiments. The rotation speed of the wheel was 375 rpm, so that all eight targets were irradiated within a period of 160 ms. The wheel rotated synchronously to the 50 Hz pulse structure of the beam. The length of the curium-oxide layer of 36 mm was determined so that it fitted to the duration of a beam pulse of 5.2 ms. The total amount of ^{248}Cm used in the experiment was 9.43 mg.

Properties and operation of SHIP are described in [7,8]. In most irradiations, an asymmetric setting of the first SHIP quadrupole triplet was used. Field gradients were calculated by a Monte Carlo method [9]. The setting resulted in an efficiency of 22 % for residues from 3n and 4n evaporation channels at the given target thickness.

In the focal plane of SHIP, event chains consisting of implanted evaporation residues and their subsequent α decay and/or spontaneous fission were identified by position-and-time correlations. Detection method and detector system are described in [8,10].

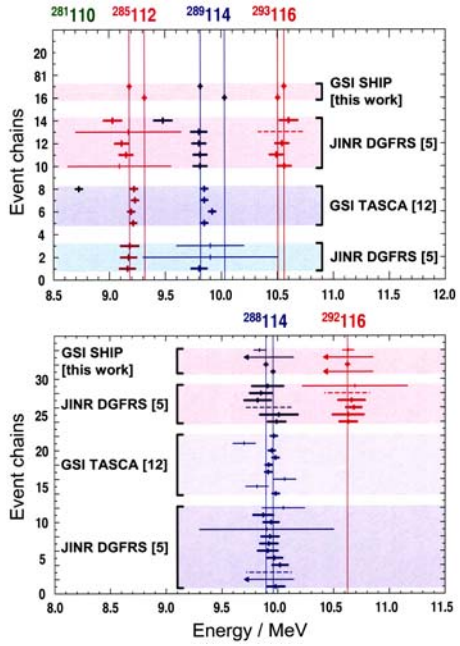

Figure 2: Comparison of α energies of event chains measured in this experiment with literature data for the decays of ^{293}116 and ^{292}116 produced in the reaction ^{48}Ca + ^{248}Cm [5] and of ^{289}114 and ^{288}114 produced in the reaction ^{48}Ca + ^{244}Pu [5,12]. The chains are terminated by spontaneous fission of ^{281}Ds (except one chain measured in [12]) and ^{284}Cn, respectively. Bold symbols with error bars mark energies of α's completely stopped in the stop detector, thin larger error bars mark energies obtained by summing of signals in stop and box detectors. Arrows mark escaped α's depositing only an energy loss in the stop detector from which, however, position and time can be deduced, and dashed lines mark missing α decays.

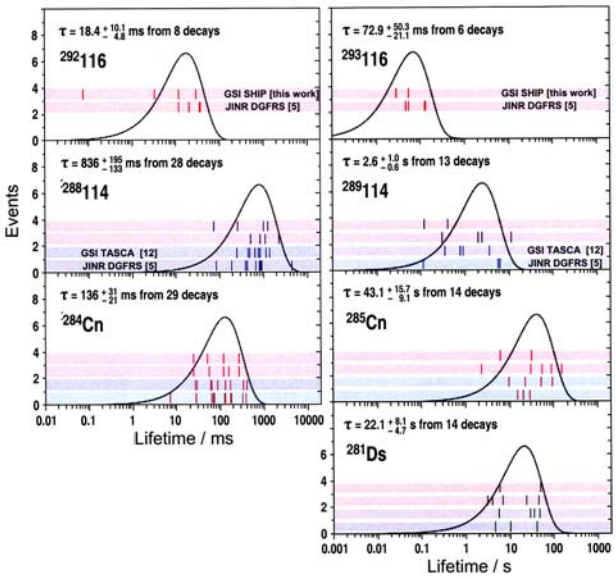

Figure 3: Lifetimes of decays studied in this work in comparison with results given in [5,12]. Note the different time scale in the left (ms) and in the right (s) column.

Results

The excitation energies of the compound nuclei for reactions at half of the target thickness were 41.0 and 45.2 MeV, respectively. These energies completed the excitation function which was studied at lower energies in [5], see Fig. 1. At 41.0 MeV we observed six decay chains, two were assigned to ^{293}116 (3n channel) and four to ^{292}116 (4n channel). No event was observed at E* = 45.2 MeV. The measured cross-sections or cross-section limits are shown in Fig. 1. They agree well with expectations based on the results given in [5] and also with theoretical predictions [11].

Alpha energies are compared with literature data in Fig. 2, measured lifetimes are shown in Fig. 3. We conclude that α energies as well as lifetimes agree well with literature data measured for the reactions ^{48}Ca + ^{248}Cm [5] and ^{48}Ca + ^{244}Pu [5,12] and thus represent another independent confirmation of results obtained in previous works. However, as a new result we observed α-decay fine structure in the decay chain of ^{293}116. The occurrence of fine structure or isomeric states was discussed in [13] for these odd-A nuclei where low spin and high spin quasi-particle states are predicted to be close in energy.

The agreement of the cross-sections measured at SHIP and at the gas-filled separator DGFRS rules out the previously discussed production by αxn channels. In this case, our cross-sections would have been at least a factor of five smaller due to the sensitive velocity dependence of the separation by SHIP. A convincing argument for ruling out pxn channels is given by the systematics of odd particle hindrance factors of partial fission half-lives of the nuclei studied in [5].

The positive results of our experiment and the safe handling of the radioactive target material demonstrated that SHIP is well prepared for further studies using actinide targets, in particular ^{248}Cm. The synthesis of isotopes of even elements confirmed now for elements 112, 114 and 116 represents a reliable base for assigning unambiguously new decay chains which are expected to occur from synthesis of element 120 in the reaction ^{54}Cr + ^{248}Cm.

References

[1] S.G. Nilsson et al., Nucl. Phys. A **115**, 545 (1968).
[2] S.G. Nilsson et al., Phys. Lett. B **28**, 458 (1969).
[3] R.K. Gupta et al., Z. Naturforsch. **32a**, 704 (1977).
[4] P. Armbruster et al., Phys. Rev. Lett. **54**, 406 (1985).
[5] Yu.Ts. Oganessian, J. Phys. G, **34**, R165 (2007).
[6] K. Eberhardt et al., NIM A **590**, 134 (2008).
[7] G. Münzenberg et al., NIM **161**, 65 (1979).
[8] S. Hofmann, G. Münzenberg, RMP **72**, 733 (2000).
[9] A.G. Popeko et al., NIM A **427**, 166 (1999).
[10] S. Hofmann et al., Z. Phys. A **291**, 53 (1979).
[11] V. Zagrebaev, Nucl. Phys. A **734**, 164 (2004).
[12] Ch.E. Düllmann et al. PRL **104**, 252701 (2010).
[13] S. Cwiok et al., Phys. Rev. Lett. **83**, 1108 (1999).

Mass Measurements of No and Lr isotopes with SHIPTRAP*

M. Block[1], *D. Ackermann*[1], *K. Blaum*[2,3], *C. Droese*[4], *Ch. E. Düllmann*[5,6,1], *M. Dworschak*[1], *M. Eibach*[3,5], *S. Eliseev*[2], *A. Gonschior*[5], *E. Haettner*[1,7], *F. Herfurth*[1], *F.P. Heßberger*[1,6], *S. Hofmann*[1], *J. Ketelaer*[2], *G. Marx*[4], *M. Mazzocco*[8], *E. Minaya Ramirez*[6], *D. Nesterenko*[9], *Yu. Novikov*[9], *W. R. Plaß*[1,7], *D. Rodríguez*[10], *C. Scheidenberger*[1,7], *L. Schweikhard*[4], *P. Thirolf*[11], *and C. Weber*[11]

[1]GSI, Darmstadt, Germany; [2]MPI-K Heidelberg, Germany; [3]Universität Heidelberg, Germany; [4]Universität Greifswald, Germany; [5]Universität Mainz, Germany; [6]Helmholtz Institut Mainz, Germany; [7]Universität Gießen, Germany; [8]Universita di Padova, Italy; [9]Petersburg Nuclear Physics Institute, Gatchina, Russia; [10]Universidad de Granada, Spain; [11]LMU München, Germany

High-precision mass measurements of radionuclides provide information about their binding energy and are thus a powerful method to study their nuclear structure and to benchmark nuclear models. The region of superheavy elements that owe their existence to nuclear shell effects is of particular interest. However, these nuclides can only be produced in fusion-evaporation reactions at rather low rates of a few particles per second or less. Therefore, information about their masses was so far exclusively available from the observation of their decay. Recently, the first direct measurements on transuranium nuclides, three nobelium (Z = 102) isotopes, have been performed with SHIPTRAP [1]. The obtained accurate mass values provide anchor points to fix α-decay chains as demonstrated for the nobelium isotopes $^{252-254}$No [2]. This is especially important for odd-odd and odd-A nuclides where the α decay typically populates excited states complicating an unambiguous mass determination.

SHIPTRAP receives radionuclides after separation from the primary beam in the velocity filter SHIP. It is presently the only Penning trap for high-precision mass measurements of elements above fermium. Recently, the masses of the nuclides ^{255}No and ^{255,256}Lr ($Z = 103$) produced in the reactions ^{208}Pb(^{48}Ca,n)^{255}No and ^{209}Bi(^{48}Ca,xn)$^{257-x}$Lr have been measured. A primary beam energy of 4.55 AMeV was chosen resulting in production cross sections of about 50–200 nb. The corresponding rate was as low as about one particle per minute entering the SHIPTRAP gas cell in the case of the nuclide ^{256}Lr, the lowest yield for which a Penning trap mass measurement was performed to date. The reaction products were decelerated in degrader foils and stopped in a gas cell in 50 mbar helium. The nuclides were extracted from the gas cell mainly as doubly charged ions. After cooling and accumulation in a radiofrequency quadrupole ion-beam cooler short bunches were injected into a double-Penning trap system inside a $B = 7$ T magnet. The mass was determined by measuring the cyclotron frequency $\nu_c = qB/(2\pi m)$ of the ions using a time-of-flight ion-cyclotron-resonance detection technique.

An example of a resonance for ^{255}No is shown in Fig. 1. An important development enabling these measurements was the implementation of active regulation systems controlling the pressure in the helium cryostat and the temperature in the bore of the superconducting solenoid [3]. In this way fluctuations of the magnetic field are reduced substantially and the time interval between successive calibration measurements can be increased. This is crucial for measurements of rare isotopes with low yield such as ^{256}Lr where a single resonance was recorded over a period of about 48 hours. Prior to our measurements the masses of both Lr isotopes listed in the Atomic-Mass Evaluation 2003 were only estimated from systematic trends. Now these isotopes have been established as new anchor points above uranium. In addition, the chain of neighboring nobelium isotopes whose masses have been measured directly has been extended across neutron number $N = 152$. This allows, for example, studying the neutron shell gap via the three-point difference of binding energies $\Delta^{(3)}(N) = (-1)^N/2[B(N+1) + B(N-1) - 2B(N)]$.

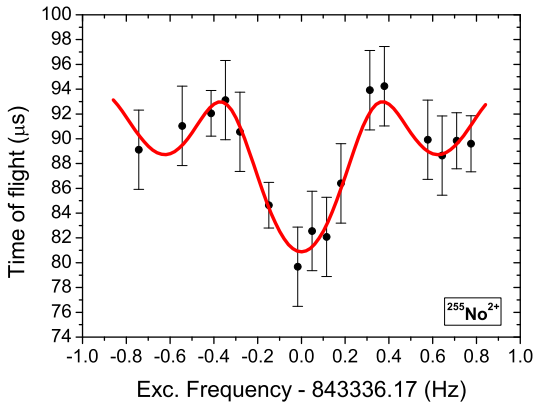

Figure 1: Cyclotron resonance of ^{255}No^{2+}. The solid line is a fit of the theoretical line shape to the data points.

The SHIPTRAP measurements on nobelium and lawrencium are important steps towards direct mass measurements of superheavy nuclides in the near future.

References

[1] M. Block et al., Nature **463** (2010) 785.

[2] M. Dworschak et al., Phys. Rev. C **81** (2010) 064312.

[3] C. Droese et al., Nucl. Instrum. Meth. A (2011) in Press.

* Work supported by the BMBF (06ML236I, 06ML9148, 06GF9103I, RUS-07/015), Rosminnauki(2.2.1), the Max-Planck Society, and the Research Center Elementary Forces and Mathematical Foundations

Investigation of ^{270}Ds and Its Decay Products

D. Ackermann[1], F.P. Heßberger[1], S. Antalic[2], M. Block[1], H.-G. Burkhard[1], V.F. Comas[1], P. Greenlees[3], S. Heinz[1], J.A. Heredia[1], S. Hofmann[1], S. Ketelhut[3], J. Khuyagbaatar[1], B. Kindler[1], I. Kojouharov[1], M. Mazzocco[4], M. Leino[3], B. Lommel[1], R. Mann[1], J. Maurer[1], A.G. Popeko[5], J. Sorri[3], J. Uusitalo[3] and A.V. Yeremin[5]

[1]GSI, Darmstadt, Germany; [2]Comenius University Bratislava, Bratislava, Slovakia; [3]JYFL, Jyväskylä, Finland; [4]University Padua, Padua, Italy, [5]FLNR, Dubna, Russia

In 2001 the results of a first measurement performed at SHIP for the reaction ^{64}Ni + ^{207}Pb to investigate ^{270}Ds and its decay products were reported [1]. In this attempt, a total of eight decay chains was observed. They consisted of evaporation residue(ER)-α-α-sf correlations which were all attributed to the production of ^{270}Ds followed by the sequential emission of two α-particles leading to the daughter nuclide ^{266}Hs and the granddaughter nuclide ^{262}Sg which eventually decayed by spontaneous fission. For ^{270}Ds in addition to the ground state α-decay, with a half-life of 100^{+140}_{-40} µs, an isomeric level which decays with a half-life of $6.0^{+8.2}_{-2.2}$ ms was observed. For the daughter ^{266}Hs only α-decay was reported, which was spread over a relatively wide range in decay time (almost two orders of magnitude) but was still consistent with a single α-decay half-life of $2.3^{+1.3}_{-0.6}$ ms. For the third member of the chain, ^{262}Sg, only spontaneous fission was detected with a half-life of $6.9^{+3.8}_{-1.8}$ ms.

In a new experiment in the period August – October 2010, we firstly established the maximum of the excitation function for the reaction ^{64}Ni + ^{207}Pb → ^{270}Ds + 1n at about 4.935 MeV/u, scanning an energy range from E_{beam} = 4.90 to 4.98 MeV/u. After that we continued the measurement at this energy. In total we accumulated 25 decay chains of ^{270}Ds, for which we measured in addition to the decay pattern observed in the first experiment, ER-α-α-sf (see above), also ER-α-sf and (ER)-α-α-α-sf correlations.

For eight of the collected decay chains we detected spontaneous fission of ^{266}Hs. With this we could detect the sf branch of ^{266}Hs, which was discussed in ref. [1]. The resulting branching ratio is 0.24 ± 0.09, including the eight events from the evaluation of the first run in 2001.

More importantly, however, also the searched for α-decay branch of ^{262}Sg was found. We detected a total of two α-decays, resulting in a ^{262}Sg α-decay branching ratio of 0.06 ± 0.04, again including the eight events from the first run. The observation of this α-decay establishes the missing link to ^{254}No for which a precise mass value employing the Penning trap system SHIPTRAP was measured recently [2]. Using the experimental $Q_α$-values we are now able to provide an experimental mass for the even-even nucleus ^{270}Ds. This is an important parameter for theoretical models which are used to predict masses and binding energies for the heaviest nuclei. The final results of this analysis will be published soon [3].

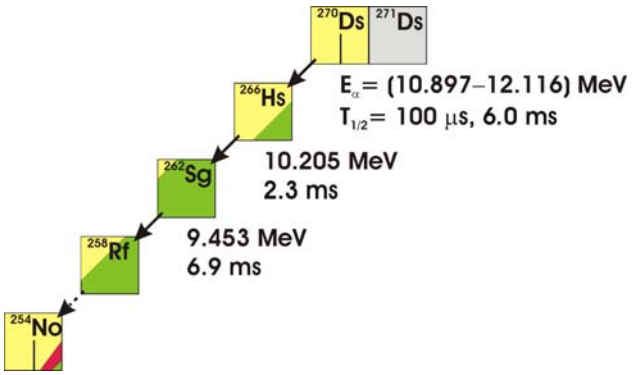

Figure 1: Decay properties of ^{270}Ds and its decay products. Alpha-energies are taken from the ongoing experiment and are still preliminary. Half-lives are from [1].

The α-decay of ^{258}Rf was not observed, but it is already known from a previous investigation [4] where an α-decay branching ratio of 0.31 ± 0.11 was reported. Fig. 1 shows the measured decay properties of ^{270}Ds and its decay products. The shown α-energies are from the ongoing experiment and are still preliminary values. The half-lives were taken from [1]. For ^{262}Sg the α-decay energy of the one event with full energy deposit in the stop Si-detector is shown. The average decay time for the two observed α-decays of 1.1 ms agrees well with the 6.9 ms half-live reported in [1]. The details of the decay properties for the isomeric and ground-state decays are presently under evaluation. In particular, the time structure for the ^{266}Hs in view of a possible isomeric state in this nucleus, and the detailed analysis of the α fine structure together with γ-rays observed in coincidence will be used to improve the understanding of the level scheme proposed already on the basis of the data obtained in the first measurement. For this purpose still improved statistics is necessary, which will be collected in a second part of the present experiment where we aim at accumulating a similar beam dose as in the first part.

References

[1] S. Hofmann et al., Eur. Phys. J. A **10**, (2001) 5.
[2] M. Block et al., Nature **463**, (2010) 785.
[3] D. Ackermann et al., to be published.
[4] J.M. Gates et al., Phys. Rev. C **77**, (2008) 034603.

Transfer Reaction Studies in ^{58,64}Ni + ^{207}Pb at SHIP

V. F. Comas [1,2], S. Heinz[1], S. Hofmann[1,2], D. Ackermann[1], J.A. Heredia[1,2], F. P. Heßberger[1], J. Khuyagbaatar[1], B. Kindler[1], B. Lommel[1] and R. Mann[1]

[1]GSI, Darmstadt, Germany; [2]Goethe-Universität, Frankfurt, Germany.

We studied multi-nucleon transfer reactions in a region of known α-emitters at Z>82 with the aim to investigate the possibility of using this process to produce new neutron-rich superheavy nuclei. We used projectiles with different neutron numbers covering beam energies from (0.9–1.2) times the Bass barrier in the reactions ^{58,64}Ni + ^{207}Pb. For these low beam energies the excitation energy of the transfer products is low which enhances their survival probability against fission, and also fewer neutrons are evaporated.

Theoretical calculations have been carried out using a combination of heavy beam plus heavy target, e.g. ^{238}U + ^{248}Cm [1] and a medium heavy beam plus heavy target e.g. ^{48}Ca + ^{248}Cm [2]. The predicted cross-sections for both combinations are on the same order of magnitude with values around 1 pb for ^{270}Sg (Z=106). They drop approximately one order of magnitude for each unit increase of Z. Experimental data exist for reactions ^{238}U + ^{248}Cm [3] and ^{40,44,48}Ca + ^{248}Cm [4] using radiochemical identification methods. Nuclei up to Z=101, N=157 and Z=100, N=156 were identified, respectively.

We used the velocity filter SHIP, which has an acceptance angle of (0±2) degrees in the laboratory system, to study reactions at energies close to the Bass barrier. SHIP has a strong identification power due to the detection method. The identification is done by measuring the radioactive decay properties of the target-like reaction products after being implanted in a position sensitive Si detector. The half-life detection limit is 20μs. Cross-sections down to 10 pb can be reached in one day of measurement at beam intensities of 1*p*μA.

We detected isotopes of elements with 84≤Z≤88 which were directly produced in the reaction, i.e they were not populated by decay of mother nuclei. Nuclei with Z≤83 could not be identified, mostly, because they are not α-emitters or have too long lifetimes. The data showed clear signatures of transfer products being produced in deep inelastic collisions, where considerable amount of energy is dissipated in the process. Fig 1 shows the isotopic distributions for Z=86, 87 and 88 using ^{58}Ni and ^{64}Ni beams. One can notice that with the ^{58}Ni beam more neutron deficient isotopes were produced, with a steep drop at N=127. In the case of ^{64}Ni beam the isotopic distribution is shifted to the more neutron-rich nuclei, reaching even N=132 and 133. The isotopic distributions are strongly influenced by the Q-values of the reactions. A sharp decrease in the Q-value for ^{58}Ni beams occurs for N≥127 while a more flat behaviour as a function of N towards the neutron-rich side can be seen for ^{64}Ni beams. For both beams the maxima of the isotopic distributions are shifted to lower neutron numbers with respect to the maxima of the Q-value distributions. For ^{64}Ni this difference, ΔN, is larger than for ^{58}Ni. With ^{64}Ni, ΔN increases with increasing proton number of the transfer products. For ^{58}Ni beams the difference, ΔN, is almost constant. Since we expect the primary distributions according to the Q-value distributions, on average, the excitation energy for the radium isotopes must be higher than for francium and radon isotopes. The excitation energies are lower for ^{58}Ni beams than for ^{64}Ni. We identified transfers up to 6 protons and ≥8 neutrons for the more neutron-rich beam ^{64}Ni. Isotopes with N=128–130 could not be detected due to short half-lives.

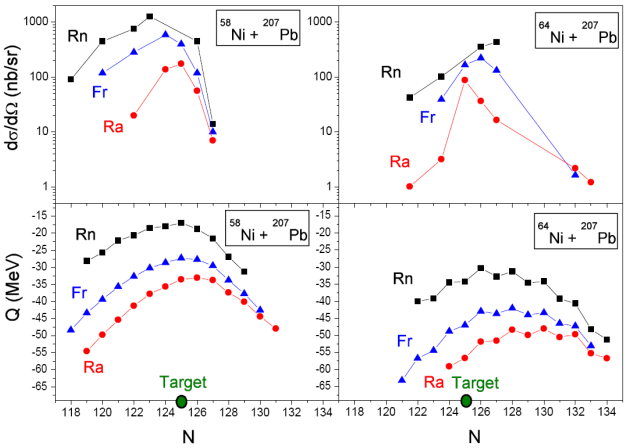

Figure 1: Rn, Fr, Ra isotopic distributions and reaction Q-values for ^{58}Ni and ^{64}Ni beams. The neutron number of the target nucleus ^{207}Pb is marked by the green dot. The error bars are not included in the figure.

We conclude that reaction products with lower excitation energies and higher cross-sections were found in ^{58}Ni beams. But much more neutron-rich transfer products were detected using ^{64}Ni beams, therefore, neutron-rich projectiles have to be used to reach new neutron rich superheavy nuclei.

In a recent follow-up experiment we studied the reaction ^{48}Ca + ^{248}Cm, to investigate transfer products in the region of Z=100. The analysis is still in progress. The Q-value distributions using this reaction promise the production of rather neutron-rich nuclei. For primary nobelium isotopes, e.g, we expect the maximum yield at ^{262}No.

References

[1] V.I. Zagrebaev, M.G. Itkis, Yu.Ts. Oganessian and W. Greiner, Phys. Rev. C **73**, 031602 (2006).

[2] G.G. Adamian and N.V. Antonenko, private communications.

[3] M. Schädel et al., Phys. Rev. Lett. **48,** 852 (1982).

[4] A. Türler et al., Phys. Rev. C **46,** 1364 (1992).

Cross-sections of ^{36}S and ^{34}S induced reactions with lead targets

J. Khuyagbaatar[1], D. Ackermann[1], H.G. Burkhard[1], V.S. Comas[1], W. Hartmann[1], S. Heinz[1], J.A. Heredia[1], F.P. Heßberger[1], A. Hübner[1], S. Hofmann[1], B. Kindler[1], B. Lommel[1], R. Mann[1], J. Maurer[1], K. Nishio[2], J. Steiner[1], A. Yakushev[1]
[1]GSI, Darmstadt, Germany; [2]JAEA, Tokai, Japan.

Fusion-evaporation reactions with ^{36}S projectiles and various Pb targets were used to produce neutron-deficient Cf isotopes [1] at SHIP. Measured cross-sections for the 2n and 3n evaporation channels from fusion reactions of ^{36}S+$^{206-208}$Pb were in the order of a few hundred nanobarns, which were unexpectedly high for the production of such neutron-deficient Cf isotopes [2,3] (see Fig. 1).

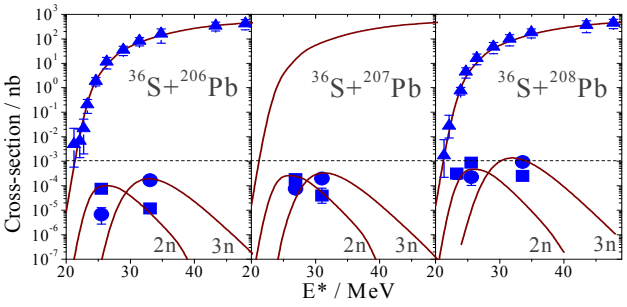

Figure 1: Experimental capture (triangles) and ER cross-sections of ^{36}S+$^{206-208}$Pb reactions (rectangles: 2n; circles: 3n) as a function of excitation energy of the compound nuclei $^{242-244}$Cf. The lines are representing HIVAP calculations. The dotted line marks the cross-section level of 1μbarn.

Cross-sections calculated using HIVAP [4] are also shown in Fig. 1. The HIVAP parameters were modified to reproduce the experimental capture and evaporation residue (ER) cross-sections of the reaction ^{36}S+^{206}Pb. Capture cross-sections measured at the tandem accelerator of Japan Atomic Energy Agency (JAEA) in Tokai, Japan, were taken from [5]. There the capture cross-sections have been measured by detecting fission fragments from fusion-fission and possible quasi-fission processes. In the HIVAP calculations (shown in Fig. 2) they represent fusion cross-sections based on the assumption that the quasi-fission (QF) channel is negligible. The calculated cross-sections of the 2n and 3n evaporation channels for the compound nuclei $^{242-244}$Cf agree well with the experimental ones (Fig. 1). The comparison of ER cross-sections for ^{34}S+^{208}Pb (also measured at SHIP [6]) and ^{36}S+^{206}Pb, which lead to the same compound nucleus ^{242}Cf (see Fig. 2) could be used to study entrance channel effects for the production of ^{239,240}Cf. These reactions have similar entrance channel asymmetries and the main difference is the reaction Q-values which was taken into account in the HIVAP calculations.

A significant enhancement of capture process due to the different nuclear structure of ^{34}S compared to ^{36}S has been observed at bombarding energies below the Coulomb barrier [5]. The results of HIVAP calculations with the same parameters as mentioned above well describe the experimental capture cross-sections for ^{34}S (see Fig. 2). The ER cross-sections of these reactions show significant differences in a wide range of excitation energies. About 25 and 10 times lower values for the 2n and 3n evaporation channels, respectively, were measured for ^{34}S+^{208}Pb than for ^{36}S+^{206}Pb close to the expected maxima of the excitation functions.

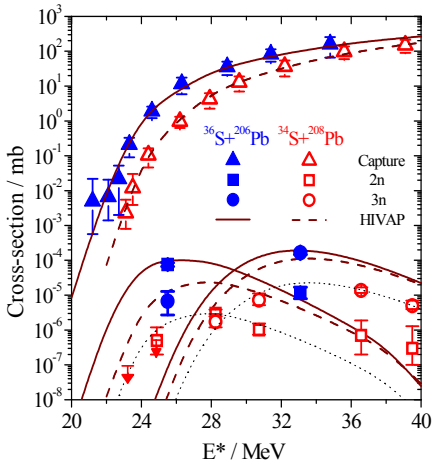

Figure 2: Experimental cross-sections are shown by open and full symbols (triangles: capture; rectangles: 2n; circles: 3n) for ^{34}S+^{208}Pb and ^{36}S+^{206}Pb respectively. Dashed and solid lines are the results from HIVAP calculations for ^{34}S and ^{36}S, respectively. Downward arrows mark upper limits for the cross-section. Dotted lines show the eye-guide for the ^{34}S ER data.

The experimental ER cross-sections have systematic uncertainties. They are expected to be reliable within a factor of two. However, the calculated ER cross-sections still overestimate the experimental ones in the case of ^{34}S. This discrepancy is not yet understood.
However, the ER cross-sections data for ^{36}S + ^{206}Pb are still very scarce. For a better understanding of this situation more detailed data on experimental excitation functions of ERs are required for both reactions.

Truly high ER cross-sections of ^{36}S induced reactions with lead and probably also with bismuth targets will allow to investigate neutron-deficient Cf and Es isotopes using different spectroscopic methods, for example in-beam spectroscopy and direct measurements of masses using a trap, which require high counting rates.

[1] J. Khuyagbaatar et al., EPJ A. **46**, (2010) 59.
[2] Yu. Lazarev et al., Nucl. Phys. A. **588** (1995) 501.
[3] Yu.Ts. Oganessian et al., PRC. **64** (2001) 054606.
[4] W. Reisdorf, Z. Phys. A **300**, (1981) 227.
[5] J. Khuyagbaatar et al., JAEA-Review 2009 (2010) 39.
[6] J. Khuyagbaatar et al., to be published.

Average charges of heavy ions in a gas mixture

J. Khuyagbaatar[1], D. Ackermann[1], L.-L. Andersson[2,3], J. Ballof[4], Ch.E. Düllmann[1,4,5], J. Even[4], A. Gorshkov[6], R. Graeger[6], F.-P. Heßberger[1], W. Hartmann[1], D. Hild[4], R. Hoischen[2], A. Hübner[1], E. Jäger[1], B. Kindler[1], J.V. Kratz[4], J. Krier[1], S. Lahiri[7], B. Lommel[1], M. Maiti[7], E. Merchan[8], D. Rudolph[2], M. Schädel[1], H. Schaffner[1], B. Schausten[1], J. Steiner[1], A. Türler[4], A. Yakushev[1]

[1]GSI, Darmstadt, Germany; [2]Lund University, Lund, Sweden; [3]University of Liverpool, Liverpool, UK, [4]University of Mainz, Mainz, Germany; [5]HIM, Mainz, Germany; [6]Technical University München, Garching, Germany; [7]Saha Institute of Nuclear Physics, Kolkata, India; [8]Universidad Nacional de Colombia, Bogota, Colombia.

At present, gas-filled separators are typically filled with either pure helium (He) or pure hydrogen (H_2). Hydrogen seems to provide better suppression of background related to target-like ions [1]. However, as the average charges are lower than in pure He, a stronger dipole magnet is needed to separate evaporation residues. Therefore, at the gas-filled separator TASCA, experiments were performed with a fill-gas mixture of these two gases to investigate whether this allows for a combination of the advantages of the two gases, i.e., which allows a good suppression of the background while still keeping rather high average charges of evaporation residues. However, no data exists how to predict the average charges of heavy ions in gas mixtures. Thus, we aimed to study systematically average charges of heavy ions.

Earlier studies at TASCA clearly showed that the average charge is a function of the gas pressure [1]. This so called "density effect" was investigated on ^{252,254}No ions and a corresponding semi-empirical expression for the determination of the average charges was given in [1]. These expressions were used for the prediction of pressure dependent average charges of No ions in pure He and H_2. The experimental setup and the nuclear reactions used in the studies reported here are the same as in [1]. Magnetic rigidities were deduced as described in [2].

Measured magnetic rigidities of ^{254}No ions in the mixtures at certain relative amounts of the gases ν (He/H_2), are shown in Fig. 1 as a function of the pressure. Clearly, the "density effect" is observed also in the mixtures.

Charge equilibration of heavy ions moving in the gas is determined by a system of coupled homogeneous linear equations for fractions of each charge state and cross-sections of "charge-exchange" collisions (see [3] for details).

Let us assume that the charge equilibration is also occurring in gas mixtures, and that heavy ions (with initial charge state fractions of F_i) after the "charge-exchange" collisions have fractions F_i^{mix} ($\sum F_i^{mix} = 1$) for each i-th charge state. Each heavy ion with an i-th charge state has a probability $P_{He}=\nu/(\nu+1)$ and $P_{H2}=1/(\nu+1)$ to collide with either a He or a H_2 atom, respectively, with $P_{He}+P_{H2}=1$. Then, the fraction of each i-th charge state in gas mixtures can be written as: $F_i^{mix} = F_i \cdot P_{He} + F_i \cdot P_{H_2}$.

Average equilibrated charges in the gas mixtures can be derived as:

$$\bar{q}^{mix} = \sum q_i \cdot F_i^{mix} = \frac{\bar{q}^{He} \cdot \nu + \bar{q}^{H_2}}{\nu + 1}$$

where, q^{He} and q^{H2} are average charges of ^{254}No ions in pure He and H_2 at the same pressure as the gas mixture, respectively. Corresponding magnetic rigidities can be put into the following expression:

$$(B\rho)^{mix} = \frac{(B\rho)^{He} \cdot (B\rho)^{H_2} \cdot (1+\nu)}{(B\rho)^{He} \cdot (\upsilon/\upsilon_0)_{H_2} + (B\rho)^{H_2} \cdot (\upsilon/\upsilon_0)_{He} \cdot \nu} \cdot (\upsilon/\upsilon_0)_{mix}$$

where (υ/υ_0) with different indices are the velocities of the ^{254}No ions in different gases (He and H_2 cases are given in [2]). In our experiments: $(\upsilon/\upsilon_0)_{mix}=2.39\pm0.03$. Predicted magnetic rigidities from the above expression with $(\upsilon/\upsilon_0)_{mix}=2.39$ are shown in Fig. 1 by open dots. Experimental magnetic rigidities are well reproduced for ν=1 and 2, except for some underestimations at 0.8 mbar. Slightly underestimated magnetic rigidities were also observed in the case of ν=3 and 4. Again, in these cases gas pressures were 0.8 mbar. This discrepancy could be due to the linear function which was used to fit the observed "density effect" within the region (1-2) mbar in the case of pure H_2 [2]. More detailed information will be given in [4].

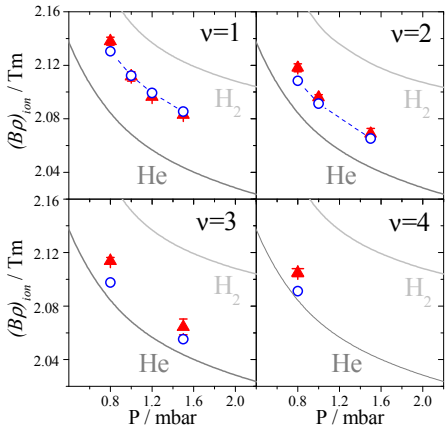

Figure 1: Magnetic rigidities of ^{254}No ions in gas mixtures ν depending on gas pressures P. Triangles and open circles are showing the measured and predicted magnetic rigidities, respectively. Lines are showing the fitted results for pure He and H_2 gases [1].

[1] J. Khuyagbaatar et al., GSI Sci. Rep. 2009 (2010) 171.
[2] J. Khuyagbaatar et al., this GSI Sci. Rep.
[3] H.-D. Betz, Rev. Mod. Phys. 44 (1972) 465.
[4] J. Khuyagbaatar et al., to be published

* These studies were financially supported the GSI F&E program and by the Research Center "Elementary Forces and Mathematical Foundations" (EMG).

Gas pressure influence on average charges of heavy recoils in TASCA

J. Khuyagbaatar[1], D. Ackermann[1], L.-L. Andersson[2,3], J. Ballof[4], W. Brüchle[1], Ch.E. Düllmann[1,4,5], J. Dvorak[5], K. Eberhardt[4], J. Even[4], A. Gorshkov[6], R. Graeger[6], W. Hartmann[1], F.-P. Heßberger[1], D. Hild[4], R. Hoischen[2], A. Hübner[1], E. Jäger[1], B. Kindler[1], J.V. Kratz[4], J. Krier[1], S. Lahiri[7], B. Lommel[1], M. Maiti[7], E. Merchan[8], D. Rudolph[2], M. Schädel[1], H. Schaffner[1], B. Schausten[1], E. Schimpf[1], A. Semchenkov[1,6], A. Serov[9], J. Steiner[1], A. Türler[4], A. Yakushev[1]

[1]GSI, Darmstadt, Germany; [2]Lund University, Lund, Sweden; [3]University of Liverpool, Liverpool, UK, [4]University of Mainz, Mainz, Germany; [5]HIM, Mainz, Germany; [6]Technical University München, Garching, Germany; [7]Saha Institute of Nuclear Physics, Kolkata, India; [8]Universidad Nacional de Colombia, Bogota, Colombia; [9]Paul Scherrer Intitute, Villigen, Switzerland

Several experimental works at gas-filled separators have been reported that lay the basis for a correct prediction of the average charges of heavy and superheavy ions [1-3]. These works resulted in differing semi-empirical parameterizations.

An interesting feature of heavy ion "charge-exchange" collisions is the so-called “density effect”, which has been observed at the Dubna gas-filled recoil separator DGFRS [2]. However, such an influence of the gas pressure has never been included in any of the above-mentioned semi-empirical expressions. The effect was also observed at the gas-filled separator TASCA [4]. Here we report results for ^{252,254}No ions which were produced in the fusion-evaporation reactions ^{48}Ca+^{206,208}Pb.

The experimental setup and the reactions were the same as in [4]. Average charges and magnetic rigidities of No ions were deduced using the experimental distribution of evaporation residues in a focal plane detector [4]. The analysis method was the same as in [3].

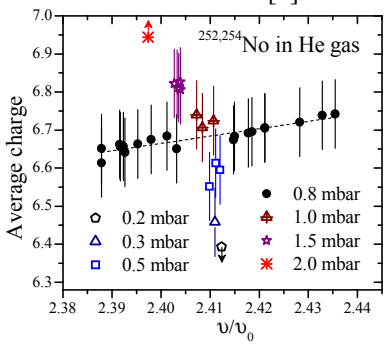

Figure 1: Measured average charges of the ^{252,254}No depending on their velocity (in units of the Bohr velocity). The line shows a linear fit. Arrows are marking limits for average charges.

Deduced average charges as a function of the velocity (expressed in units of the Bohr velocity, υ_0) are shown in Fig. 1. Average charges measured at 0.8 mbar gas pressure for both No ions (black solid dots) exhibit the linear dependence of the average charges on velocity. However, measured average charges at other pressures deviate significantly from this line. Deduced magnetic rigidities are shown in Fig. 2 for ^{252,254}No ions in helium (He) as well as for ^{254}No in hydrogen (H_2). These data show an increase of magnetic rigidities with decreasing pressure for both filling gases.

An expression to estimate the “density effect” has been given in [5] and we use it as a fit function for our experimental data. Average charges of heavy ions in a gas with pressure P can be presented as a sum of the equilibrated average charge and a correction term due to the "density effect", $q_{ion}=<q>+\Delta q$ [5]. Charge correction can be determined as $\Delta q=a/(b+y)$ with $y=[(\upsilon/\upsilon_0)P]^{-1}$ in according to [5]. The function $(B\rho)_{ion}=(c+dy)/(f+y)$ can be used to fit measured magnetic rigidities, with c,d and f being parameters.

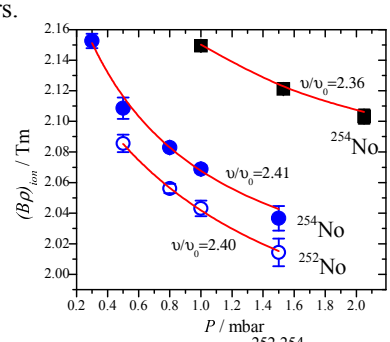

Figure 2: Magnetic rigidities of the ^{252,254}No ions as a function of the pressure. Circles and squares are denoting magnetic rigidities in He and H_2, respectively. Lines show fits to the data according to the relations given in the text.

Results of fits are shown in Fig. 2. The behavior of the fitted curves for both ^{252,254}No ions seems to be similar, as can be expected for ions with an identical atomic shell structure. The linear fit function $(B\rho)_{ion}= c+dy$ was used in the case of H_2 due to the limited number of experimental data points. These semi-empirical expressions which describe the “density effect” can be used as a correction for predicted average charges when using expressions from [1-3]. More detailed information will be provided in [6].

[1] A. Ghiorso., et al., NIM. A **269** (1988) 192.
[2] Yu. Oganessian et al., Phys. Rev. C **64** (2001) 064309.
[3] K.E. Gregorich et al., Phys. Rev. C **72** (2005) 014605.
[4] J. Khuyagbaatar et al., GSI Sci. Rep. 2009 (2010) 171.
[5] H.-D. Betz, Rev. Mod. Phys. **44** (1972) 465.
[6] J. Khuyagbaatar et al., to be published.

* These studies were financially supported the GSI F&E program and by the Research Center “Elementary Forces and Mathematical Foundations” (EMG).

Pulse Shape Analysis for the TASISpec Implantation Detector*

U. Forsberg[1], *P. Golubev*[1], *D. Rudolph*[1], *D. Ackermann*[2], *L.-L. Andersson*[3], *Ch.E. Düllmann*[2,4,5], *J. Even*[4], *J.M. Gates*[6], *J. Gellanki*[1], *F.P. Heßberger*[2,5], *R. Hoischen*[1,2], *E. Jäger*[2], *I. Kojouharov*[2], *J. Krier*[2], *N. Kurz*[2], *H. Schaffner*[2], *B. Schausten*[2], *M. Schädel*[2], *and A. Yakushev*[2]

[1]Lund University, Sweden; [2]GSI Helmholtzzentrum für Schwerionenforschung, Darmstadt, Germany; [3]University of Liverpool, UK; [4]Universität Mainz, Germany; [5]Helmholtz Institute Mainz, Germany; [6]Lawrence Berkely National Laboratory, USA

In TASISpec – TASCA in Small Image Mode Spectroscopy setup, which aims at decay spectroscopy of superheavy elements [1] – heavy ions are implanted into a double-sided silicon strip detector (DSSSD). Their subsequent decays are recorded in this, as well as in the surrounding silicon and germanium detectors. The use of sampling ADCs in the experimental setup open up for new possibilities, such as particle identification, as they allow for investigations of the actual pulse shapes from the detectors. Pulses from the DSSSD were integrated in charge-sensitive preamplifiers [2] and studied by splitting the signals between the standard electronics read-out chain and sampling ADCs (CAEN V1724) as shown in Fig. 1. The sampling ADCs digitise the pulses at a rate of 100 MHz. For each event, a time span of 2.56 μs around the arrival of the pulse was recorded and analysed offline. Triggers from the standard electronics were used. The accumulated data originates from a 3-line α source and an in-beam experiment in which the DSSSD was irradiated with heavy ions using the reaction ^{207}Pb(^{48}Ca,2n)^{253}No.

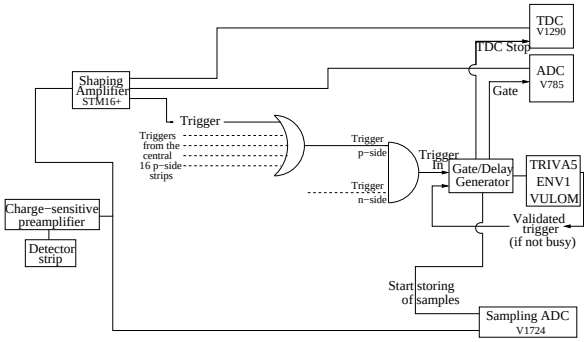

Figure 1: Electronics scheme for the DSSSD of TASISpec.

Any particle information present in the pulse shape resides within the rise of the pulse. The pulses were differentiated in order to emphasize this region of interest. Figure 2 shows the summed derivatives of pulses originating from the p-side (implantation side) of one pixel of the DSSSD; from α particles (red) and from implanted heavy ions (black). A difference between the pulse shapes appears in the "tail" of the derivative, which corresponds to the top of the original signal. This discrepancy was characterised by calculating the ratio of the integral over the particle-dependent area, and the integral of the main peak in the derivative. The regions used are marked in the figure.

* This work was supported by the Research Center "Elementary Forces and Mathematical Foundations".

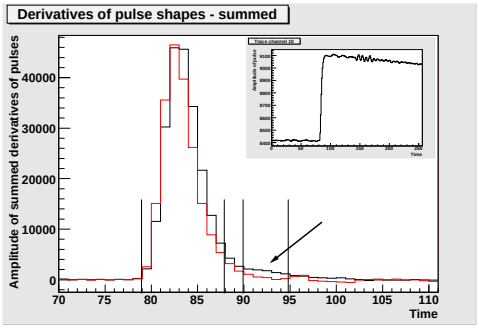

Figure 2: Summed derivatives of pulses from α particles (red) and implanted heavy ions (black). Insert: Typical pulse shape before software treatment.

The ratio between the two integrals was calculated for all pulses from the pixel, and the resulting distributions are shown in Fig. 3. The distribution from heavy ions is clearly shifted to the right compared to the one from α particles. Other pixels that were investigated show the same tendencies. This testifies that particle information is indeed present in the pulse shapes.

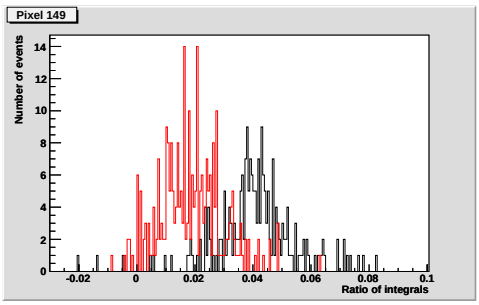

Figure 3: The ratio between the integrals for α particles (red) and implanted heavy ions (black).

In order to use the existing differences for a separation into α particles and implanted heavy ions, each strip, and possibly also every pixel, must be analysed individually in order to optimise the parameters used for the characterisation of the differences. This issue will be addressed in future analyses of pulse shapes from the TASISpec implantation detector.

References

[1] L.-L. Andersson *et al.*, Nucl. Instr. Meth. A **622**, 164 (2010)

[2] Ch. Görgen, G. Pascovici, Universität zu Köln

Ion-optical simulations for the Inelastic Reaction Isotope Separator IRiS

J. Dvorak[1] and Ch. E. Düllmann[1,2,3]

[1]HIM, Mainz, Germany; [2]GSI, Darmstadt, Germany; [3]Institute für Kernchemie, Universität, Mainz, Germany.

Introduction

An impressive advancement in investigation of superheavy elements (SHE) was achieved in the past 25 years. The heaviest currently reported superheavy element contains 118 protons and novel challenging experiments pursuing the synthesis of elements 119 and 120 are under preparation. Yet all of these heaviest currently claimed elements were synthesized in nuclear fusion reactions, which can yield only neutron deficient products. Neutron-rich isotopes of the heaviest elements, which are of special interest e.g. in the context of nuclear chemistry and nuclear astrophysics, cannot be produced this way. The only viable production mechanism for neutron-rich nuclides is through multi-nucleon transfer reactions (MNTR), the application of which will give access to tens of new neutron-rich isotopes of the heaviest elements. Currently available separators are optimized for fusion products emitted under 0° and are poorly suited for MNTR studies due to their limited angular acceptance.

A new Inelastic Reaction Isotope Separator (IRiS) [1], dedicated to the investigation of neutron-rich isotopes of the heaviest elements produced in MNTR, will be constructed and set-up at the GSI in a joint effort of an international collaboration, headed by the Johannes Guttenberg University Mainz, the Helmholtz Institute Mainz, and the GSI Helmholtzzentrum für Schwerionenforschung Darmstadt. The main design goal of the IRiS is the ability to separate the heavy products formed in MNTR and deliver them to a focal plane. Here ion implantation and decay is detected in focal plane detector. To perform (i) chemical studies, (ii) mass measurements, and (iii) nuclear and atomic spectroscopy of the heavy ions separated in the IRiS, the detector setup will be retracted and allow the separated products to enter a gas cell, where they will be stopped and extracted for further investigation. A conceptual design scheme is shown in Fig. 1.

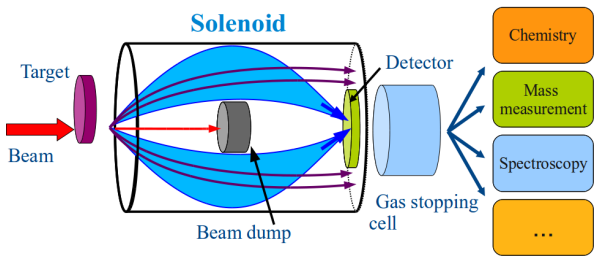

Figure 1: Schematic drawing of the IRiS design concept. Products are separated in a gas-filled solenoid magnet according to their magnetic rigidity. A beam dump stops the beam particles as well as 0° products.

Simulations

An essential part of the IRiS design process is the development of a computer simulation for the IRiS ion-optics. Due to the availability of theoretical predictions, the following two nuclear reactions were chosen as input for the simulation: ^{48}Ca+^{248}Cm at E_{CM}=209 MeV [2], and ^{238}U+^{248}Cm at E_{CM}=750 MeV [3]. The simulation code using the ROOT [4] framework is already highly advanced and includes: (i) Simulation of unreacted projectiles and products of elastic and inelastic scattering including MNTR; (ii) energy loss and straggling in the target; (iii) ion interaction with gas molecules and (iv) ion tracking in a realistic solenoidal magnetic field.

Simulation results

Simulations showed that relatively strong magnetic fields are necessary to achieve acceptable separation in a gas-filled solenoid. While several solenoid dimensions and magnetic field strengths were successfully tested, a stored energy of about 10 MJ was necessary in all cases. In symmetric ion-optical geometries, as shown in Fig. 2, efficiencies of typically about 20% for collecting the heaviest products ($Z \geq 102$) in the detector area were reached, while the detector count-rate due to background was estimated to about few kHz. Although not optimal for the identification of products in a focal plane detector, these conditions are well suited for use of a gas cell.

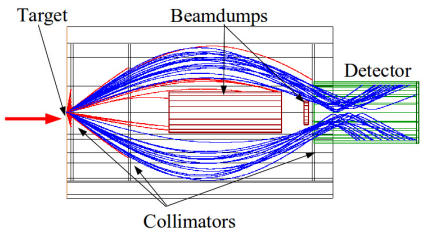

Figure 2: Trajectories of the heaviest products ($Z \geq 102$) produced in the reaction ^{48}Ca + ^{248}Cm.

Acknowledgements

C.E.D. acknowledges financial support from the Research Center "Elementary Forces and Mathematical Foundations" (EMG).

References

[1] J. Dvorak *et al.*, NIMA in press *http://dx.doi.org/10.1016/j.nima.2010.08.124*
[2] G.G. Adamian and N.V. Antonenko, private comm.
[3] V. Zagrebaev, private comm.
[4] ROOT- *http://root.cern.ch*

Prediction of Atomic Properties of Bi and Element 115

A. Borschevsky[1,2], V. Pershina[2], E. Eliav[3], and U. Kaldor[3]
[1]Massey University, Auckland, New Zealand; [2]GSI, Darmstadt, Germany; [3]Tel Aviv University, Israel

In this work, we perform fully relativistic benchmark calculations of polarizabilities (α), ionization potentials (IP), and electron affinities (EA) of element 115 and its lighter homologue, Bi. These properties are important for prediction of adsorption enthalpy (ΔH_{ads}) of the two elements on inert surfaces. Knowledge of ΔH_{ads} is required in order to guarantee the transport of the newly produced element from the target chamber to the chemistry set up. This is the first benchmark calculation of the polarizability of these elements.

Calculations of polarizabilities were performed using the DIRAC08 package [1], employing the finite field approach. In the Dirac-Coulomb (DC) *ab initio* method, the many-electron relativistic Dirac-Coulomb Hamiltonian

$$H_{DC} = \sum_i h_D + \sum_{i<j} 1/r_{ij} \quad (1)$$

is employed, where

$$h_D = c\vec{\alpha}\cdot\vec{p} + \beta c^2 + V_{nuc}\,. \quad (2)$$

The atomic orbitals (AO) are four-component spinors

$$\varphi_{nk} = \begin{pmatrix} P_{nk}(r) \\ Q_{nk}(r) \end{pmatrix}, \quad (3)$$

where $P_{nk}(r)$ and $Q_{nk}(r)$ are the large and small component, respectively. The uncontracted Faegri basis set [2] was used for both atoms and extended to convergence with respect to the calculated polarizabilities. Electron correlation was taken into account at the Fock space coupled cluster level, FSCCSD. The contribution of the triple excitations and the higher order relativistic effects was also estimated. The ground state of both atoms is $^2P_{3/2}$, which, in the presence of an electric field, splits into $^2P_{3/2,1/2}$ and $^2P_{3/2,3/2}$. The final polarizabilities of the two states, together with the average polarizability $\alpha(^2P_{3/2})$, are presented in Table I.

IPs and EAs were calculated using the Dirac-Coulomb-Breit (DCB) Hamiltonian. Correlation was taken into account by Fock space coupled cluster method, augmented by intermediate Hamiltonian approaches [3,4] to facilitate convergence. The van der Walls radii (R_{vdW}) were determined from a linear correlation with $R_{max}(np_{1/2})$-AOs of the group 15 elements.

Chemistry of element 115 will be defined by its valence $7p_{3/2}$ orbital, which is destabilized and expanded due to relativistic effects, compared to that of Bi. Trends in atomic properties follow the trend set by the valence orbital. Element 115 will have the lowest ionization potential in the group, lower than that of Bi by almost 2 eV. The electron affinity will also be lowest in the group, reflecting the relativistic destabilization of the $7p_{3/2}$ orbital.

R_{vdW} of 115 is the highest in the group. There is also a steep increase in the average polarizability of the $^2P_{3/2}$ state from Bi to element 115, and the difference in the polarizability of the $^2P_{3/2,1/2}$ and $^2P_{3/2,3/2}$ states is much more significant in the superheavy homologue. This is again due to the relativistic destabilization and expansion of the $7p_{3/2}$ orbital.

Table 1. Atomic properties of Bi and element 115: IP (in eV), EA (in eV), α (in a.u.), and van der Walls radii, R_{vdW} (in Å)

Property	Value	Method	Ref
		Bi	
IP	7.303	DC+FSCC	this
	7.289	exp.	[6]
EA	1.015	DCB+FSCC	this
	0.942	exp.	[7]
$\alpha(^2P_{3/2,1/2})$	53.51	DC+FSCC	this
$\alpha(^2P_{3/2,3/2})$	41.20	DC+FSCC	this
$\alpha(^2P_{3/2})$	47.63	DC+FSCC	this
$\alpha(^2P_{3/2})$	48.6	CASPT2+LDA	[8]
R_{vdW}	2.33	corr.	this
		Element 115	
IP	5.553	DCB+FSCC	this
	5.579	DCB+FSCC	[9]
EA	0.368	DCB+FSCC	this
	0.383	DCB+FSCC	[9]
$\alpha(^2P_{3/2,1/2})$	100.20	DC+FSCC	this
$\alpha(^2P_{3/2,3/2})$	46.46	DC+FSCC	this
$\alpha(^2P_{3/2})$	73.69	DC+FSCC	this
R_{vdW}	2.46	corr.	this

References

[1] DIRAC08, written by H. J. Ja. Jensen *et al*. (2008)
[2] K. Faegri, Theor. Chim. Acta **105**, 252 (2001)
[3] A. Landau *et al.,* J. Chem. Phys. **121**, 6634 (2004)
[4] E. Eliav *et al.*, J. Chem. Phy. **122**, 224113 (2005)
[5] V. Pershina *et al*. J. Chem. Phys. **122** (2005) 124301
[6] C.E. Moore, *Atomic Energy Levels* (U.S. Goverment Printing Office, Washington, DC, 1958 (1958)
[7] T. Andersen *et al*, J. Phys. Chem. Rev. Data **28**, 1511(1999)
[8] B.O. Roos *et al.*, J. Phys. Chem. A **108**, 2851 (2004)
[9] E. Eliav *et al*., Mol. Phys. **94**, 181 (1998)

Relativistic *ab initio* Study on CnAu in Comparison with HgAu

A. Borschevsky[1,2], V. Pershina[2], E. Eliav[3], and U. Kaldor[3]
[1] Massey University, Auckland, New Zealand; [2] GSI, Darmstadt, Germany; [3] Tel Aviv University, Israel

Predictions of the interaction of the heaviest elements with various surfaces are essential for their transportation and identification in the gas-phase chromatography experiments. In an earlier work [1], we predicted the adsorption enthalpy, ΔH_{ads}, of element 112 (Cn) and its homolog Hg on inert surfaces (PE and Teflon) on the basis of the fully relativistic Dirac-Coulomb (DC) Fock space coupled cluster (FSCC) calculations of atomic properties. We have shown that Cn and Hg could be easily delivered from the target chamber to the chemistry set up due to their rather low $-\Delta H_{ads}$. In another work [2], we performed the 4-component Density Functional Theory (4c-DFT) calculations for the MAu_n systems (M = Hg and Cn, n = 1 – 120), in order to predict ΔH_{ads} of these elements on gold, which is used as a surface material for the detectors of the chromatography column. Since the DFT theory (though being applicable to large systems) is known to be less accurate than the *ab initio* DC coupled cluster approach (still being used only for small systems), we have performed these additional benchmark calculations for the MAu (M = Hg and Cn) dimers to be prove conclusions made on the basis of the DFT results.

We have employed the 4*c*-DC Hamiltonian,

$$H_{DC} = \sum_i h_D + \sum_{i<j} 1/r_{ij}, \quad (1)$$

where

$$h_D = c\vec{\alpha}\cdot\vec{p} + \beta c^2 + V_{nuc}. \quad (2)$$

V_{nuc} is the nuclear attraction operator, and α and β are the four-dimensional Dirac matrices. For computational efficiency, the exact 2c-relativistic Hamiltonian (X2C) approximation was used [3]. This is one of the most economical and accurate approximations to the 4c-DC Hamiltonian. Electron correlation was taken into account using the FSCC method, which is considered to be one of the most powerful tools in quantum chemistry. The calculations were performed using the DIRAC08 computational package [4]. The Faegri basis set was used [5], consisting of the 24*s*20*p*15*d*10*f*2*g* orbitals for Au and Hg and the 27*s*23*p*18*d*13*f*3*g* orbitals for Cn.

MAu (M = Hg and Cn) are open shell systems; hence we started our calculation with the closed shell reference state, MAu^-. After solving the Dirac-Coulomb equations and correlating the closed shell reference state, one electron was removed to obtain the neutral system, which was, in turn, re-correlated. Results of the calculations are given in Table 1 in comparison with our previous 4c-DFT ones [2] and those performed within various other approximations: relativistic effective core potentials (RECP) with spin-orbit (SO) corrections [6], pseudo-potentials (PP) combined with single double (triple) excitation CC method (CCSD(T)) [7], and other DFT results [6,8,9].

Table 1. Equilibrium bond lengths, R_e (in Å), dissociation energies, D_e (in eV), and vibrational frequencies, ω_e (in cm^{-1}) of HgAu and CnAu

R_e	D_e	ω_e	Method	Ref.
	HgAu			
2.635	0.46	119	DC+FSCC	this
2.653	0.53	116	ARECP+CCSD(T)+SO	[6]
2.711	0.39	103	PP+CCSD(T)	[7]
2.713	0.51	104	DFT+SO (B98)	[6]
2.791	0.41	93	DFT (B3LYP)	[8]
2.67	0.67	99	4c-DFT (B88/P86)	[2]
2.68	0.56	-	2c-DFT (PBE0)	[9]
2.68	0.62	-	2c-DFT (BP)	[9]
	CnAu			
2.700	0.42	98	DC+FSCC	this
2.727	0.39	95	ARECP+CCSD(T)+SO	[6]
2.774	0.36	83	DFT+SO (B98)	[6]
2.73	0.51	74	4c-DFT (B88/P86)	[2]
2.74	0.39	-	2c-DFT (PBE0)	[9]
2.73	0.47	-	2c-DFT (BP)	[9]

There is excellent agreement between the present *ab initio* DC values on the one hand and 4c-/ 2c-DFT ones on the other hand for R_e(MAu), while the DFT D_e(MAu) are systematically overestimated. Nevertheless, all the calculations come to the conclusion that Cn is less bound to Au than Hg. This is due to the strongest relativistic effects on the 7*s*(Cn) AO in group 12, making it less accessible for bonding than the 6*s*(Hg) AO. Thus, our results are in agreement with the expected trend. The next exciting task would be *ab initio* DC calculations of the 114-Au bonding in comparison with the Cn-Au one: element 114 is expected to be also very inert due to the stabilized $7p_{1/2}^2$ electron pair.

References

[1] V. Pershina, A. Borschevsky, E. Eliav and U. Kaldor, J. Chem. Phys **128**, 024707 (2008).
[2] V. Pershina *et al.* J. Chem. Phys., **131**, 084713 (2009).
[3] M. Iliaš and T. Saue, J. Chem. Phys. **126**, 064102 (2007).
[4] DIRAC 08, written by H. J. Ja. Jensen *et al*. (2008).
[5] K. Faegri, Theor. Chim. Acta **105**, 252 (2001).
[6] A. Zaitsevskii, *et al*. Cent. Eur. J. Phys. **4**, 448 (2006).
[7] R. Wesendrup and P. Schwerdtfeger, Angew. Chem. Int. Ed. **39**, 909 (2000).
[8] Z. J. Wu, Chem. Phys. Lett. **406**, 24 (2005).
[9] A. Zaitsevskii *et al*. J. Chem. Phys. **132**, 081102 (2010).

Novel Studies on the Electronic Structures and Volatility of MBr_5 (M = Nb, Ta, and Db)

V. Pershina[1], J. Anton[2], and T. Jacob[2]
[1]GSI, Darmstadt, Germany; [2]Institut für Elektrochemie, Universität Ulm, Germany

Many experimental studies were devoted in the past to the investigations of volatility of group 4 and 5 elements halides and oxyhalies [1]. Relativistic electronic structure theory rendered at that time assistance to those investigations by predicting molecular properties and trends in volatility [2]. Even though there was good agreement between the theory and experiment in the case of oxyhalides, there was a disagreement in the case of pure halides. Thus, e.g., theoretical predictions based on the 4*c*-DFT calculations of the electronic density distribution in the MBr_5 systems indicated higher volatility of $DbBr_5$ (as a vapour pressure over the solid) than their lighter homologs in the chemical groups [3], while experimentally, the following trend was observed: Nb ≈ Ta > Db [4].

To resolve this contradiction, new studies were undertaken both experimentally and theoretically. Experimentally, volatility of MBr_5 (M = Nb, Ta, and Db) was to be studied with the use of the isothermal gas-phase chromatography with a quartz column [5]. HBr was used as a reactive gas and KBr aerosol particles as a transport material. Theoretically, attempts to predict the behaviour of the MBr_5 species in these experiments were undertaken by us in this study on the basis of the state of art fully relativistic 4*c*-DFT calculations of the MBr_5 properties: Due to the latest development in the relativistic electronic structure theory, very accurate calculations of molecular properties such as dissociation energies and optimized geometries (bond lengths) become possible [6], which was not the case 20 years ago.

For prediction of adsorption of MBr_5 on the quartz surface of the chromatography column, the following scenarios were considered: i) physisorption of MBr_5 on the (brominated) SiO_2 surface; ii) formation of the $KMBr_6$ salt on the surface; iii) formation and adsorption of $MOBr_3$; iv) the $(Si_sO)_2MBr_3$ formation on the surface. In this report, we present results of the calculations of properties of the MBr_5 molecules and their adsorption according to the first scenario, which turned out to be the most appropriate.

The total energy calculations have shown the MBr_5 formation to obey the following trend: $NbBr_5$ < $TaBr_5$ < $DbBr_5$. The calculated properties of MBr_5, needed for predictions of ΔH_{ads} via the physisorption model

$$E(x) = -\frac{3}{16}\left(\frac{\varepsilon-1}{\varepsilon+2}\right)\frac{\alpha_{at}}{\left(\frac{1}{IP_{slab}}+\frac{1}{IP_{at}}\right)x^3}, \qquad (1)$$

where IP is the ionization potential, α is the polarizability, x is the molecule-surface distance and ε is the dielectric constant of the adsorbent material, are given in Table I.

Table 1. Ionization potentials, IP (in eV), polarizabilities, α (in a.u.), equilibrium bond lengths, R_e (in Å), interaction distance, x (in Å), and adsorption enthalpies, $-\Delta H_{ads}$ (in kJ/mol), of MBr_5 (M = Nb, Ta, and Db)

Property	$NbBr_5$	$TaBr_5$	$DbBr_5$
IP	9.35	9.33	9.37
α_x	159.1	155.6	157.3
α_y	167.6	157.4	156.6
α_z	200.8	188.1	187.6
$<\alpha>$	175.8	167.0	167.1
R_e(ax/eq)	2.500/2.448	2.495/2.442	2.550/2.496
R_e(ax/eq)*	-	2.473/2.412	-
x	2.794	2.779	2.799

* Experimental values

Using the data of Table 1, $-\Delta H_{ads}$ of MBr_5 on the pure SiO_2 (ε = 2.81) and brominated with KBr (estimated ε = 5.1) quartz surfaces were predicted. The results are given in Table 2.

Table 2. Adsorption enthalpies, $-\Delta H_{ads}$ (in kJ/mol), of MBr_5 (M = Nb, Ta, and Db) on quartz surface

$-\Delta H_{ads}$	$NbBr_5$	$TaBr_5$	$DbBr_5$
on SiO_2, calc.	66	64	62
on SiO_2-KBr, calc.	77	75	73
experiment [5]	89 ± 5	101 ± 5	-

According to the present calculations, volatility of $DbBr_5$ should be higher than that of $NbBr_5$ and $TaBr_5$, though the differences in ΔH_{ads} between the species should be very small. This is in agreement with the earlier predictions [3]. The obtained trend is in reasonable agreement with the results on $NbBr_5$ and $TaBr_5$ [4,5] taking into account the experimental error bars. (The absolute values cannot be really compared due to the unknown value of ε). The predicted lower volatility of $DbBr_5$ in comparison with that of the homologs has been confirmed by results of the very recent gas-phase isothermal chromatography experiments [5].

References

[1] H. W. Gäggeler, A. Türler, In: The Chemistry of Superheavy Elements, Ed. M. Schädel, Kluwer, 2003, pp. 237-290.
[2] V. Pershina, Chem. Rev. **96** (1995) 1977.
[3] V. Pershina, *et al*. J. Chem. Phys. **98** (1992) 1116.
[4] H. W. Gäggeler, *et al*. Radiochim. Acta **57** (1992) 93.
[5] Qin Zhi, private communication.
[6] J. Anton, *et al*. Phys. Rev. A **69** (2004) 012505.

Towards fully-relativistic simulations of the adsorption of super-heavy elements on α-SiO_2 surfaces *

W. Gao[1], *Ch. E. Düllmann*[1,3,4], *J. Anton*[2], *T. Jacob*[2], *and V. Pershina*[3]

[1]Institut für Kernchemie, Universität Mainz, Germany; [2]Institut für Elektrochemie, Universität Ulm, Germany; [3]GSI Helmholtz-Zentrum für Schwerionenforschung, Darmstadt, Germany; [4]Helmholtz Institut Mainz, Germany

While in the last two decades super-heavy elements with $Z \leq 112$ have been studied, the focus of the present work is on the chemical properties of element 114. Our theoretical calculations have been motivated by two conflicting gas-chromatography experiments, which aimed on studying the interaction strength of element 114 with a gold surface. The experiment by Eichler *et al.* [1] reported adsorption in the chromatography column at only very low temperatures of approximately $-90\,^{\circ}\mathrm{C}$, from which they concluded a weak interaction between element 114 and the gold surface. In contrast, experiments performed at GSI [2] observed adsorption at room temperature, indicating a much stronger bond between element 114 and gold. To resolve this conflict further experiments will be performed at GSI within the next two years, where besides gold SiO_2 will be used as detector material.

Besides the previously mentioned experiments, extensive theoretical studies on the adsorption of element 114 on gold surfaces were performed using fully-relativistic DFT methods [3], while the adsorption on inert surfaces such as SiO_2 were estimated using semi-empirical methods in conjunction with computed properties of atoms, dimers, or small molecules [3, 4]. Unfortunately a fully-relativistic treatment of the entire adsorption process is beyond the capacities of nowadays computing ressources. However, this work can be divided into two steps: (i) extensive studies on SiO_2 bulk and surface properties (e.g. stable bulk-phases or possible surface structures and terminations) using a non-relativistic approach; (ii) fully-relativistic calculations on the adsorption process of element 114 on SiO_2, where the most stable and interesting surface structures obtained in the first step serve as basis.

So far we have focused on the first task, understanding the surface structure of SiO_2 under realistic experimental conditions. For these calculations, the CASTEP code [6] with Vanderbilt-type ultrasoft pseudopotentials [7] and the PBE exchange–correlation functional has been used. The obtained DFT-energies were then used in conjunction with the *ab initio* atomistic thermodynamics approach [5] to evaluate the surface phase diagrams, providing information of the surface stability as function of surrounding temperature and pressure. Starting with bulk systems, our calculations show that at experimental conditions ($p_{O_2} = 10^{-13}$ atm, $100\,\mathrm{K}<T<320\,\mathrm{K}$) the most stable bulk structure is the so called α-quartz. Using this crystal structure as basis, various surface orientations and morphologies were studied. We find that the thermodynamically preferred structure is the α-SiO_2(001) surface, which could assume three different morphologies: one Si-terminated and two different O-terminated structures.

Figure 1 shows the surface free energy, $\gamma(p,T)$, for the most stable surface structures as function of the oxygen chemical potential. Structure **a**, which is Si-terminated, is favored at $\Delta\mu_O < -6.24\,\mathrm{eV}$ ($T \gg 1000\,\mathrm{K}$ under UHV conditions). In the temperature range until $\sim$100 K the surface is O-terminated (structure **b**). The phase diagram shows the existence of a fourth, but less stable structure (structure **d**), which is terminated by a single O-layer.

After understanding the surface morphology of SiO_2 under experimental conditions, the next step will be to perform fully-relativistic DFT calculations on the actual adsorption process of elements 112 and 114 and their homologs on a α-SiO_2(001) surface (structure **b**).

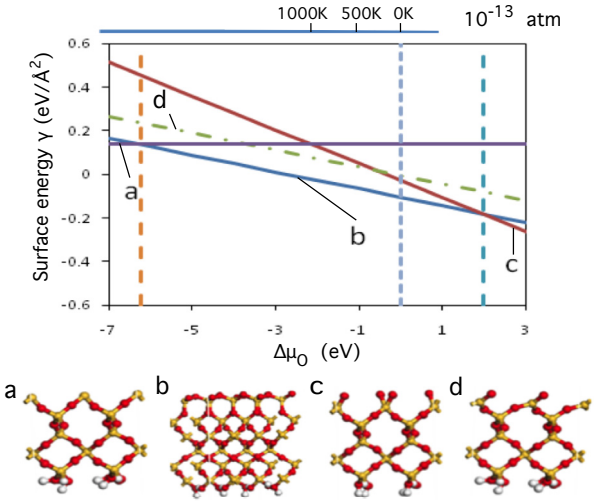

Figure 1: Surface free energy of the α-SiO_2(001) as function of $\Delta\mu_O$ or temperature at fixed pressure of 10^{-13} atm.

References

[1] R. Eichler *et al.*, Radiochim Acta **98** (2010) 133.

[2] A. Yakushev *et al.*, this Scientific Report.

[3] V. Pershina, J. Anton, and T. Jacob, J. Chem. Phys. **131** (2009) 084713.

[4] V. Pershina, T. Bastug, and B. Fricke, J. Chem. Phys. **122** (2005) 124301.

[5] K. Reuter and M. Scheffler, Phys. Rev. B **65** (2002) 035406.

[6] M. D. Segall *et al.*, J. Phys.: Condens. Matter **14** (2002) 2717.

[7] D. Vanderbilt, Phys. Rev. B **41** (1990) 7892.

* This work was supported by the Research Center "Elementary Forces and Mathematical Foundations" (EMG)

Microscopic calculation of the ^{3}He(α,γ)^{7}Be capture cross section

T. Neff, H. Feldmeier, and K. Langanke
GSI, Darmstadt, Germany

The ^{3}He(α,γ)^{7}Be reaction is one of the key reactions in the solar proton-proton chains and determines the production of ^{7}Be and ^{8}B neutrinos in the sun. In recent years the cross section has been remeasured in a great effort in several experiments at the Weizmann institute, by the LUNA Collaboration, by the Seattle group and by the ERNA Collaboration now providing high quality data. Nevertheless it is still necessary to extrapolate the measured cross sections down to the energies relevant in solar burning.

There have been many attempts to calculate the cross section, using an external capture picture, using potential models where the system is modeled by two pointlike clusters interacting via an effective nucleus-nucleus potential and using microscopic cluster models employing effective nucleon-nucleon interactions. None of this calculations is able to describe the experimental data.

In Ref. [1] we presented the first *ab initio* type calculation for this reaction. We use a realistic effective nucleon-nucleon interaction that is derived in the UCOM(SRG) approach [2]. Bound and scattering states are described microscopically in the Fermionic Molecular Dynamics (FMD) approach. FMD uses Gaussian wave packets as single particle states, the many-body basis states are Slater determinants projected on parity, angular momentum and total linear momentum. The FMD basis is very flexible and contains harmonic oscillator shell model and Brink-type cluster states as special limiting cases. At large distances we describe the system by antisymmetrized products of ^{4}He and ^{3}He clusters in their ground states. At short distances the clusters are polarized and we extend the model space with constrained FMD configurations obtained in variation after parity and angular momentum projection. The boundary conditions for bound and scattering states are imposed using the microscopic R-matrix approach developed by the Brussels group. Including the polarized configurations we obtain a good description of the bound state properties, like binding energies and charge radii and of the scattering phase shifts.

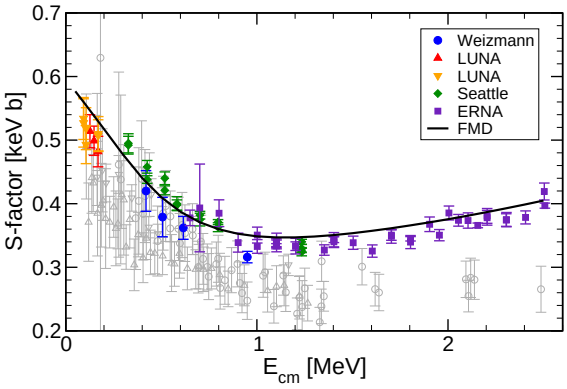

Figure 1: Astrophysical S factor for the ^{3}He(α,γ)^{7}Be reaction. Recent experimental data are given as colored symbols, older data as grey symbols. The FMD result is given by the black solid line.

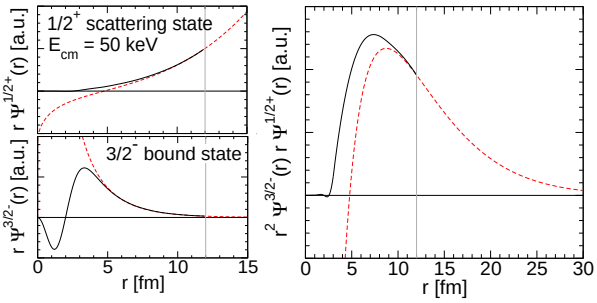

Figure 2: Left: Overlap functions (black solid lines) and Coulomb/Whittaker functions matched at the channel radius (red dashed lines) for the 50 keV $1/2^+$ scattering state and the $3/2^-$ bound state. Right: Dipole strength calculated with the overlap functions and Coulomb/Whittaker functions.

For the capture reaction we have to calculate the dipole transitions from the S- and D-wave scattering states into the $3/2^-$ and $1/2^-$ bound states. If we compare the calculated cross sections in form of the astrophysical S-factor as shown in Fig. 1 we find a good agreement with the recent experimental results regarding both energy dependence and absolute normalization.

To analyze the results we mapped the microscopic many-body wave functions onto overlap functions in the resonating group picture as shown in the left part of Fig. 2. The nodes in the wave functions reflect the existence of Pauli forbidden states. At large distances the motion of the clusters is governed by the Coulomb force and the relative motion is described by Coulomb and Whittaker functions. When we compare the dipole strength calculated with the overlap functions with the one calculated from the asymptotically matched Coulomb and Whittaker functions as shown in the right part of Fig. 2 we find noticable differences, indicating that the assumption of predominant external capture at low energies is not that well justified.

References

[1] T. Neff, arXiv:1011.2869 [nucl-th], *accepted for publication in Phys. Rev. Lett.*

[2] R. Roth, T. Neff, H. Feldmeier, Prog. Part. Nucl. Phys. **65**, 50 (2010).

Effective theory for deformed nuclei*

Thomas Papenbrock† [1,2,3,4]

[1]Department of Physics and Astronomy, University of Tennessee, Knoxville, TN 37996, USA; [2]Physics Division, Oak Ridge National Laboratory, Oak Ridge, TN 37831, USA; [3]GSI Helmholtzzentrum für Schwerionenforschung GmbH, 64291 Darmstadt, Germany; [4]Institut für Kernphysik, Technische Universität Darmstadt, 64289 Darmstadt, Germany

Introduction

The hallmark of nuclear deformation are rotational bands of the form

$$E(l) \approx A[I(I+1) - I_0(I_0+1)] \,. \qquad (1)$$

Here, $I \geq I_0$ denotes the angular momentum, A is a constant determined by fit to data, and I_0 is the spin of the band head under consideration. Rotational states are the lowest-lying excitations in nuclei far away from closed shells. Our understanding of nuclear rotations is based on the groundbreaking work by Bohr and Mottelson [1], its extension within the general collective model [2], and the interacting boson model [3]. These phenomenological models describe a large body of experimental data. However, as with all models, they are unable to provide us with theoretical error estimates or with systematic ways of improvement.

A model-independent description of low-energy phenomena can be based on an effective theory [4, 5]. For deformed nuclei, this program has been carried out in Ref. [6]. It consists of four steps, namely (i) the identification of the relevant low-energy degrees of freedom, (ii) the identification of relevant symmetries (and their breaking), (iii) the construction of a low-energy Lagrangian consistent with these symmetries, and (iv) the identification of a power counting. The rotational band of the $I_0 = 0$ ground state in even-even nuclei consists of states with even angular momentum $I = 0, 2, 4, \ldots$ and have positive parity. Thus, quadrupole phonons are the low-energetic degrees of freedom. The relevant symmetry is rotational invariance, but nuclear deformation corresponds to the spontaneous breaking of rotational symmetry. For axially deformed nuclei, the ground state is invariant under $SO(2)$ and the the Nambu-Goldstone modes thus parameterize the coset $SO(3)/SO(2)$ [5, 6]. For the construction of low-energy Lagrangians in the presence of spontaneous symmetry breaking one follows Ref. [7]. A key point in the construction is the nonlinear realization of the rotational symmetry. The power counting is based on the separation of scale between low-lying rotational states (the rotational band (1) are the quantized Nambu-Goldstone modes that result from the symmetry breaking in a finite system) and higher-energetic vibrations and single-particle excitations.

Results

The Nambu-Goldstone modes parameterize the coset $SO(3)/SO(2)$ which is isomorph to the two-sphere S^2. We can thus choose the polar angle β and the azimuthal angle α as the corresponding degrees of freedom. Building blocks of the low-energy Lagrangian are the functions $E_x \equiv \dot{\alpha}\sin\beta$ and $E_y \equiv -\dot{\beta}$ which transform as the x ad y components of a vector under rotations, respectively. Here, the dot denotes the time derivative ∂_t. Due to the nonlinear realization of the rotational symmetry, a Lagrangian that is formally invariant under $SO(2)$ is indeed invariant under $SO(3)$. Thus, $L = C_0(E_x^2 + E_y^2)/2$ is the simplest low-energy Lagrangian and of leading order. The low-energy constant C_0 has to be determined by fit to data. The Legendre transformation yields a low-energy Hamiltonian, and upon quantization one obtains the spectrum $E(I) = I(I+1)/(2C_0)$, which is essentially the band (1). Nuclei with a nonzero spin in their ground states are described by Lagrangians that break time-reversal symmetry. This leads to the addition of a Wess-Zumino term to the low-energy Lagrangian (with a new low-energy constant that fixes the ground-state spin), and yields the band (1). The covariant derivative $D_t = \partial_t + i\dot{\alpha}\cos\beta$ couples the Nambu-Goldstone modes to higher-energetic vibrations and single-particle degrees of freedom. Within the effective theory, the results of the general collective model [2] are reproduced in next-to-leading order. At next-to-next-to leading order, one finds terms that are not contained in the phenomenological models.

References

[1] A. Bohr and B. R. Mottelson, *Nuclear Structure*, Vol. II, World Scientific (Singapore, 1998).

[2] J. M. Eisenberg and W. Greiner, *Nuclear Theory*, Vol.1, *Collective and Particle Models*, North Holland, Amsterdam, (1985).

[3] F. Iachello and A. Arima, *The Interacting Boson Model*, Cambridge University Press (Cambridge, 1987).

[4] S. Weinberg, *The Quantum Theory of Fields*, Vol.II, Cambridge University Press (Cambridge, 1996).

[5] H. Leutwyler, Phys. Rev. D **49**, 3033 (1994).

[6] T. Papenbrock, arXiv:1011.5026; Nucl. Phys. A (2010), doi:10.1016/j.nuclphysa.2010.12.013.

[7] S. Coleman, J. Wess, and B. Zumino, Phys. Rev. **177**, 2239 (1969); C. G. Callan, S. Coleman, J. Wess, and B. Zumino, Phys. Rev. **177**, 2247 (1969).

* Work supported by the U.S. Department of Energy and the Alexander von Humboldt Stiftung.

† tpapenbr@utk.edu

Neutrinoless double beta decay of deformed nuclei within QRPA with realistic interaction*

Amand Faessler[1], *Dong-Liang Fang*[1], *Vadim Rodin*[1], *and Fedor Šimkovic*[2,3]

[1]Institut für Theoretische Physik der Universität Tübingen, D-72067 Tübingen, Germany; [2]Department of Nuclear Physics, Comenius University, SK-842 15 Bratislava, Slovakia; [3]BLTP, JINR, 141980 Dubna, Russia

Neutrinoless double beta decay ($0\nu\beta\beta$-decay) is a second order nuclear weak decay process with the emission of two electrons only [1]: $(A, Z) \rightarrow (A, Z + 2) + 2e^-$. This process is forbidden in the standard model (SM) of electroweak interaction since it violates the conservation of the total lepton number. The observation of $0\nu\beta\beta$ decay will immediately prove the neutrino to be massive and identical to its antiparticle (a Majorana particle). Thereby, $0\nu\beta\beta$ decay offers the only feasible way to test the charge-conjugation property of the neutrinos.

The fact that the neutrinos have non-vanishing masses has firmly been established by neutrino oscillation experiments. However, the oscillation experiments cannot in principle measure the absolute scale of the neutrino masses. One of the possible ways to probe the absolute neutrino masses at the level of tens of meV is to study $0\nu\beta\beta$ decay. Provided the corresponding $0\nu\beta\beta$-decay rates are accurately measured, reliable nuclear matrix elements (NME) $M^{0\nu}$ will be needed to deduce the effective Majorana neutrino mass from the experimental half-lives of the decay.

One of the best candidate for searching $0\nu\beta\beta$ decay is ^{150}Nd since it has the second highest endpoint, $Q_{\beta\beta}$ =3.37 MeV, and the largest phase space factor for the decay. The SNO+ experiment at the Sudbury Neutrino Observatory will use Nd loaded scintillator to search for neutrinoless double beta decay by looking for a distortion in the energy spectrum of decays at the endpoint [2]. It is expected to achieve the sensitivity of $T^{0\nu}_{1/2} \simeq 5 \cdot 10^{24}$ years after one year of running, with the best final value of about 3–4 times longer. With the NME of Ref. [3], obtained within the proton-neutron quasiparticle random phase approximation (QRPA) with neglect of deformation, already the initial phase of SNO+ will be able to probe $m_{\beta\beta} \approx 100$ meV, and will finally be able to achieve sensitivity of $m_{\beta\beta} \approx 50$ meV corresponding to the inverse hierarchy of the neutrino mass spectrum.

However, ^{150}Nd is well-known to be a rather strongly deformed nucleus. This strongly hinders a reliable theoretical evaluation of the corresponding $0\nu\beta\beta$-decay NME (for instance, it does not seem feasible in the near future to reliably treat this nucleus within the large-scale nuclear shell model). Recently, more phenomenological approaches have been employed to calculate $M^{0\nu}$ for strongly deformed heavy nuclei. The results of these models generally reveal a substantial suppression of $M^{0\nu}$ for ^{150}Nd as compared with the spherical QRPA result, but at the same time, the calculated NME are rather significantly spread.

The most microscopic state-of-the-art way approach to describe the effect of nuclear deformation on NME $M^{0\nu}$ and $M^{2\nu}$ (for two-neutrino $\beta\beta$-decay) is provided by the QRPA. In Refs. [4] a QRPA approach has been developed to calculate $M^{2\nu}$ with realistic residual interaction [the Brueckner G matrix derived from the charge-depending Bonn (Bonn-CD) nucleon-nucleon potential] in deformed nuclei. It was demonstrated in Refs. [4] that deformation introduces a mechanism of suppression of the $M^{2\nu}$ matrix element which gets stronger when deformations of the initial and final nuclei differ from each other.

The first QRPA calculations of $M^{0\nu}$ for ^{76}Ge, ^{150}Nd and ^{160}Gd with an account for nuclear deformation were performed in Refs. [5]. The effects of the short range correlations and the quenching of the axial vector coupling constant g_A were analyzed. The calculation showed a suppression of $M^{0\nu}$ for ^{150}Nd by about 40% as compared with our previous spherical QRPA result [3] that was obtained with neglect of deformation. With this new NME for ^{150}Nd one gets the corresponding half-life $T^{0\nu}_{1/2} = 4.1 \cdot 10^{25}$ y for the effective Majorana neutrino mass $\langle m_{\beta\beta} \rangle$ = 50 meV. The results show that neutrinoless double beta decay of ^{150}Nd, to be measured soon by the SNO+ collaboration, provides one of the best probes of the Majorana neutrino mass.

References

[1] F. Boehm and P. Vogel, *Physics of Massive Neutrinos*, 2nd ed. (Cambridge University Press, Cambridge, 1992); A. Faessler and F. Šimkovic, J. Phys. G **24**, 2139 (1998)

[2] C. Kraus and S. J. M. Peeters [SNO+ Collaboration], Prog. Part. Nucl. Phys. **64**, 273 (2010);
SNO+ project: `http://snoplus.phy.queensu.ca` .

[3] F. Šimkovic, A. Faessler, V.A. Rodin, P. Vogel, and J. Engel, Phys. Rev. C **77**, 045503 (2008).

[4] M. S. Yousef, V. Rodin, A. Faessler and F. Šimkovic, Phys. Rev. C **79**, 014314 (2009); D. Fang, A. Faessler, V. Rodin, M. S. Yousef and F. Šimkovic, Phys. Rev. C **81**, 037303 (2010).

[5] D. Fang, A. Faessler, V. Rodin, and F. Šimkovic, Phys. Rev. C **82**, 051301(R) (2010); and arXiv:1101.2149 [nucl-th], submitted to Phys. Rev. C.

* Work supported by the DFG under both SFB TR27 "Neutrinos and Beyond" and Graduiertenkolleg GRK683.

Neutrinoless double beta decay studied with energy density functional methods

Tomás R. Rodríguez[1,2] *and Gabriel Martínez-Pinedo*[1]
[1]GSI, Darmstadt, Germany; [2]UAM, Madrid, 28049, Spain

Neutrinoless double beta decay occurs whenever two neutrons inside the nucleus decay into two protons with the emission of two electrons (without neutrinos in the final state). This very rare decay, which has not been experimentally observed yet, is only possible if the single beta decay is energetically forbidden and the neutrinos are massive Majorana particles. The half-live of this process is directly related to the effective neutrino mass and the so-called nuclear matrix elements (NME), $M^{0\nu}$, according to the expression [1]:

$$\left[T^{0\nu\beta\beta}_{1/2}(0^+ \rightarrow 0^+)\right]^{-1} = G_{01}\left|M^{0\nu}\right|^2 \left(\frac{\langle m_{\beta\beta}\rangle}{m_e}\right)^2 \quad (1)$$

where $\langle m_{\beta\beta}\rangle$ is the effective Majorana neutrino mass, m_e is the electron mass, and G_{01} is a kinematical space factor. Therefore, the precise calculation of the NME's is very important to determine the effective neutrino mass once the half-life of the process is experimentally measured. In Ref. [2] we apply for the first time energy density functional (EDF) methods to evaluate the NME's for the most probable candidates. To compute both ground states and transition matrix elements we use an EDF based on Gogny D1S interaction [3] that includes beyond-mean-field correlations -particle number and angular momentum restoration and configuration mixing in the axial quadrupole degree of freedom. We consider the decay $A = 150$ as an illustrative example of the method. First, in Fig. 1(a) we represent the distribution of probability as a function of the quadrupole deformation β for ^{150}Nd and ^{150}Sm ground states. We observe that both nuclei are prolate deformed, being ^{150}Nd more deformed than ^{150}Sm. In Fig. 1(b) the intensity of the Gamow-Teller part of the NME depending on the deformation of the mother and granddaughter nuclei is shown. We see that the largest values correspond to having nearly the same deformation between the initial and final states. Furthermore, this structure can be related to the pairing energy of the nuclei involved in the process [2]. We find that the more paired are the nuclei the larger is the value of the NME, in agreement with Shell Model and QRPA calculations [4, 5]. Eventually, the value of the NME is obtained by convoluting the wave functions given in Fig. 1(a) with the intensity of the NME as a function of deformation. The area explored by the wave functions is represented with a shaded circle in Fig. 1(b). Finally, the values of the NME calculated for the most probable candidates to find neutrinoless double beta decay events are represented in Figure 2.

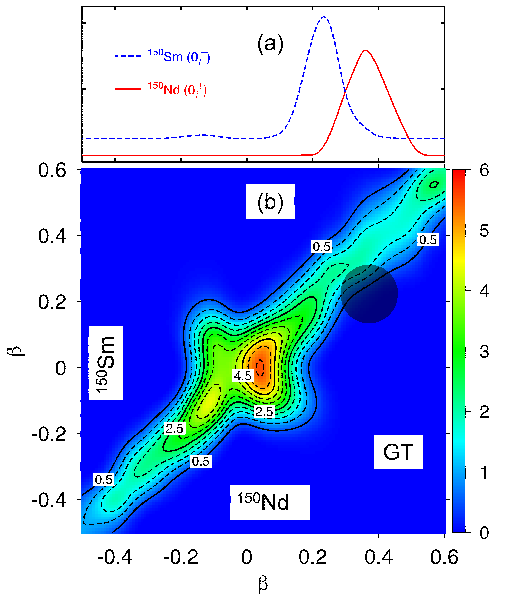

Figure 1: (a) Collective wave functions for ^{150}Nd (continuous) and ^{150}Sm (dashed) as a function of the quadrupole deformation. (b) Intensity of the NME as a function of the mother and granddaughter deformation for Gamow-Teller contributions. Shaded area corresponds to the region explored by the collective wave functions shown in (a).

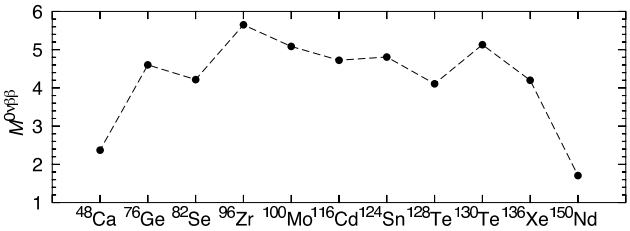

Figure 2: Neutrinoless double beta decay NME calculated with Gogny D1S-based EDF.

References

[1] F. T. Avignone, S. R. Elliott, J. Engel, Rev. Mod. Phys. **80**, 481 (2008).

[2] T. R. Rodríguez and G. Martinez-Pinedo, Phys. Rev. Lett. 105, 252503 (2010), arXiv: 1008.5260v2.

[3] J. F. Berger, M. Girod, and D. Gogny, Nucl. Phys. A **428**, 23 (1984).

[4] E. Caurier, J. Menéndez, F. Nowacki, and A. Poves, Phys. Rev. Lett. **100**, 052503 (2008).

[5] F. Simkovic, A. Faessler, V. Rodin, P. Vogel, and J. Engel Phys. Rev. **C** 77, 045503 (2008)

Impact of core vibrations on the single particle structure: from light to superheavy nuclei *

E.V. Litvinova[1,2] *and A.V. Afanasjev*[3]

[1]GSI Helmholtzzentrum für Schwerionenforschung, Germany; [2]Goethe-Universität, Frankfurt am Main, Germany;
[3]Mississippi State University, Mississippi 39762, USA

Self-consistent relativistic particle-vibration coupling (PVC) model [1] is applied to a systematic study of single-particle spectra of nuclei ranging from light to superheavy ones [2] and generalized to the case of superfluid systems [3].

An example of the obtained results compared to data is shown in Fig. 1. The column (sph) shows the single-particle spectra obtained in spherical relativistic mean-field (RMF) calculations with NL3* parametrization while column (sph+PVC) includes also particle-vibration coupling. Other columns display the results obtained with inclusion of deformation (def) [4], time-odd (TO) mean fields, and the results obtained by combining these effects with PVC ("def+TO+PVC"). One can see that the major impact comes from the PVC which causes general compression of the spectra leading to a better agreement with experiment and in some cases to changes of the level sequences.

The calculated spectroscopic factors of dominant single-particle levels in the vicinity of the Fermi surface vary between 0.5 and 0.9, see some examples in Table 1. Thus, these states retain basically their single-particle nature.

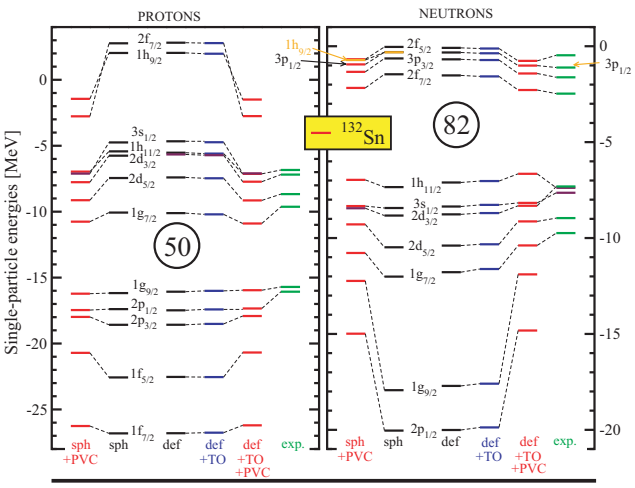

Figure 1: Single-particle scheme of ^{132}Sn.

The superheavy nucleus ^{292}120 has been predicted to have both proton and neutron spherical shell closures within the RMF theory [7, 8]. Our calculations show that the PVC decreases very little the sizes of neutron N = 172 and proton Z = 120 shell gaps, see Fig. 2.

* Work supported by HIC for FAIR and by the U.S. Department of Energy, grant DE-FG02- 07ER41459. V.

Table 1: Spectroscopic factors $S_k^{(d)}$ of the dominant single-particle levels in odd nuclei with cores ^{132}Sn and ^{56}Ni calculated within relativistic particle-vibration coupling model, compared to experimental data [5, 6].

Nucleus	State k	$S_k^{(d)th}$	$S_k^{(d)exp}$
^{133}Sn	2f7/2	0.89	0.86±0.16
	3p3/2	0.91	0.92±0.18
	1h9/2	0.88	
	3p1/2	0.91	1.1±0.3
	2f5/2	0.89	1.1±0.2
^{57}Ni	2p3/2	0.83	0.954±0.286
	1f5/2	0.79	1.400±0.420
	2p1/2	0.76	1.000±0.300
	1g9/2	0.79	

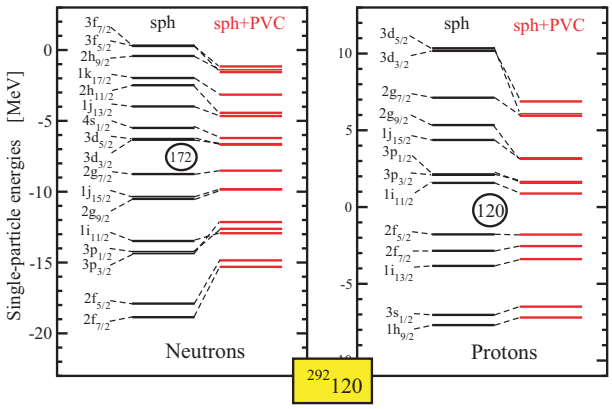

Figure 2: Single-particle scheme of a superheavy nucleus ^{292}120.

References

[1] E. Litvinova and P. Ring, Phys. Rev. C 73 (2006) 044328.

[2] E. Litvinova, A.V. Afanasjev, in preparation.

[3] E. Litvinova, in preparation.

[4] A.V. Afanasjev and H. Abusara, Phys. Rev. C 81 (2010) 014309.

[5] K.L. Jones et al., Nature 465 (2010) 454.

[6] Jenny Lee et al., Phys. Rev. C 79 (2009) 054611.

[7] M. Bender et al, Phys. Rev. C 60 (1999) 034304.

[8] A.V. Afanasjev et al. Phys. Rev. C 67 (2003) 024309.

The equation of state of nuclear matter below saturation in a generalized relativistic density functional approach.*

S.Typel[1,2,3] *and M. Voskresenskaya*[1]

[1]GSI, Darmstadt, Germany; [2]Excellence Cluster Universe, Garching, Germany; [3]TU München, Garching, Germany

Properties of nuclear matter are often calculated using mean-field concepts that only consider nucleons as basic constituents and assume a homogeneous matter distribution. In more advanced approaches auch as (Dirac) Brueckner Hartree-Fock models, two-body correlations are taken into account but the formation of deuterons is not correctly treated and non-uniform matter cannot be described.

However, at densities below saturation, the formation and dissolution of clusters, i.e. light and heavy nuclei inside the nuclear medium, and the appearance of so-called pasta phases affect the thermodynamical properties and change the composition of the matter substantially. These effects have to be taken into account for nuclear matter equations of state that can be used in astrophysical applications, e.g. the simulation of core-collapse supernovae.

At very low densities, nuclear matter is well described by nuclear statistical equilibrium (NSE) or virial approaches that explicitly treat nucleons and nuclei as degrees of freedom. These models fail already at densities much below saturation because a change of the cluster properties inside the medium is not considered, the interaction between the constituents is not fully included, and the dissolution of nuclei is modeled by a heuristic excluded-volume mechanism at most.

Recently, a relativistic mean-field (RMF) model with density-dependent meson-nucleon couplings was extended to include light clusters (^{2}H, ^{3}H, ^{3}He, ^{4}He) with medium-dependent properties [1]. Effectively, the cluster binding energies are shifted depending on density and temperature, mainly due to the Pauli blocking of states in the medium. Thus, it is possible to describe the Mott effect, i.e. the dissolution of clusters with increasing density, in a microscopic way. The generalized relativistic mean-field (gRMF) model interpolates successfully between the correct limits at very low densities, a mixture of nucleons and nuclei in chemical equilibrium, and saturation density where nuclear matter can be regarded as composed of neutrons and protons as quasi-particles.

The formation of clusters has a strong effect on the density dependence of the nuclear symmetry energy. As shown in Ref. [2], an agreement with experimental data from heavy-ion collisions is only obtained when clusters are considered in the model. Conventional mean-field models are not able to describe the observed enhancement of the symmetry energy at low densities.

The couplings of the original RMF model were fitted to properties of finite nuclei in a Hartree calculation. Since heavy nuclei in the rRMF model are described using a Thomas-Fermi approximation in spherical Wigner-Seitz cells, a modification of the couplings is required to obtain the correct low-density limit of the equation of state. In fact, it is sufficient to rescale the mass and absolute coupling of the σ meson, without changing the properties of uniform nuclear matter. Figure 1 shows a comparison of the gRMF predictions with a NSE calculation that uses experimental binding energies corrected for the Coulomb shift due to the surrounding electrons in neutral matter.

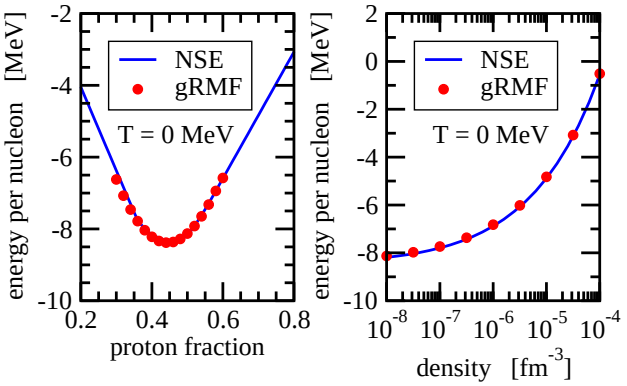

Figure 1: Left: energy per nucleon depending on the proton fraction at a density of 10^{-8} fm^{-3}. Right: energy per nucleon of symmetric nuclear matter depending on the density.

So far, only bound states of clusters were included in the gRMF model but scattering states become more relevant with increasing temperature. Hence, the model was further extended to a relativistic density functional that considers two-body correlations in the continuum. This can be achieved by considering them as effective resonances with temperature and density dependent resonance energies. Using an expansion in powers of fugacities, a comparison with the virial equation of state, which is correct at very low densities, leads to constraints for the continuum contributions that are currently explored.

References

[1] S. Typel, G. Röpke, T. Klähn, D. Blaschke and H. H. Wolter, Phys. Rev. C **81**, 015803 (2010).

[2] J. B. Natowitz, G. Röpke, S. Typel, D. Blaschke, A. Bonasera, K. Hagel, T. Klähn, S. Kowalski, L. Qin, S. Shlomo, R. Wada and H. H. Wolter, Phys. Rev. Lett. **104**, 202501 (2010).

* This research was supported by the DFG cluster of excellence "Origin and Structure of the Universe", CompStar, a Research Networking Programme of the European Science Foundation, and HGS-HIRe for FAIR.

The ^{76}Se Gamow-Teller strength distribution and its importance for stellar electron capture rates

Q. Zhi[1], *K. Langanke*[1,2,3], *G. Martínez-Pinedo*[1], *F. Nowacki*[4], *and K. Sieja*[4]

[1]GSI Helmholtzzentrum für Schwerionenforschung, Darmstadt, Germany; [2]Institut für Kernphysik, TU Darmstadt, Darmstadt, Germany; [3]Frankfurt Institute for Advanced Studies, Frankfurt, Germany; [4]IPHC, IN2P3-CNRS et Université de Strasbourg, Strasbourg, France

Electron captures on nuclei play an essential role for the dynamics of the collapsing core in a supernova [1]. Recent theoretical studies predicted that, due to nuclear correlations across the $N = 40$ shell gap, electron captures on nuclei with proton numbers $Z < 40$ and neutron numbers $N > 40$ would not be strongly suppressed due to Pauli blocking of Gamow-Teller (GT) transitions. This prediction has recently been confirmed by the experimental determination of the single-particle occupation numbers in ^{76}Se and by the measurement of the ^{76}Se GT$_+$ strength distribution [2]. This nucleus has 34 protons and 42 neutrons and hence its GT$_+$ strength would be completely Pauli-blocked in the independent particle model. However, the experiment reveals a summed strength of B(GT) = 0.7 ± 0.2 in the excitation energy interval E_x = 0–5 MeV mainly distributed over 6 individual states [2].

We have performed shell-model calculations based on three different model spaces and residual interactions. The first study is based on a ^{48}Ca core and considers the full pf shell for protons and the $(p_{3/2}, p_{1/2}, f_{5/2}, g_{9/2})$ orbits for neutrons (NS interaction). The other two calculations assume a ^{56}Ni core and consider the $(p, f_{5/2}, g_{9/2})$ orbits for both protons and neutrons (RG and JUN45 interactions). See ref. [3] for more details.

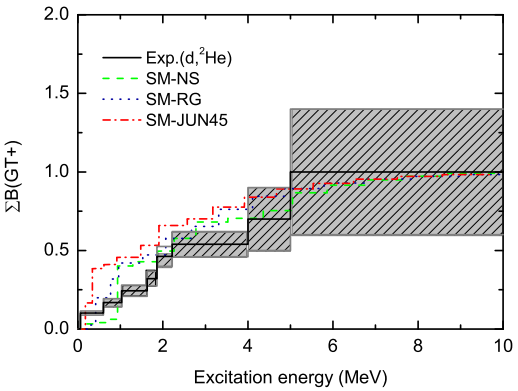

Figure 1: Running sum of GT$_+$ strength from experiment and shell model calculations with different interactions. The calculated total GT strengths are normalized to the experimental data.

Figure 1 shows the running sum of the (normalized) GT distributions. The computed electron capture rates for the various shell model GT distributions and for the experimental data are shown in figure 2. The rates obtained from the experimental GT$_+$ strength distribution are very close to those obtained from theoretical GT$_+$ strength, reflecting the quite similar energy dependencies of these distributions. However, we find that recovering the total GT$_+$ strength and achieving convergence in the GT$_+$ distribution is a rather slow process requiring the consideration of higher-order particle-hole configurations. Thus, models accounting only for 2p-2h configurations [5] are steps in the right direction to a consistent description of stellar capture rates for these later pre-trapping conditions, but they might not be sufficient to realistically describe the unblocking mechanism.

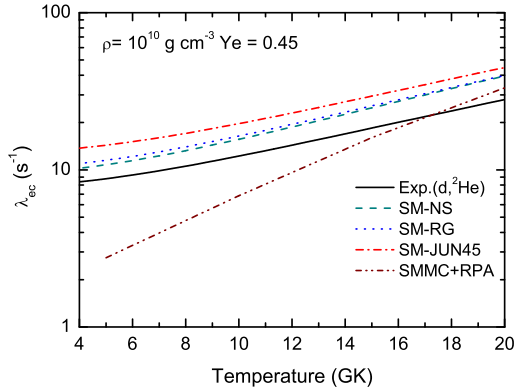

Figure 2: Various captures rates at $\rho = 10^{10}$ g/cm^3 as function of temperature. The electron-to-nucleon ratio in this plot has been set to $Y_e = 0.45$. SMMC+RPA refers to Shell Model Monte Carlo approach used in Ref. [4].

References

[1] H.-T. Janka, K. Langanke, A. Marek, G. Martínez-Pinedo, B. Müller, Phys. Repts. **442** (2007) 38.

[2] E.-W. Grewe, *et al.*, Phys. Rev. C **78** (2008) 044301.

[3] Q. Zhi, K. Langanke, G. Martínez-Pinedo, F. Nowacki, K. Sieja, Nucl. Phys. A (2011), in print

[4] A. Juodagalvis, K. Langanke, W. R. Hix, G. Martínez-Pinedo, J. M. Sampaio, Nucl. Phys. A **848** (2010) 454.

[5] A. A. Dzhioev, *et al.*, Phys. Rev. C **81** (2010) 015804.

Stellar enhancement factors in a parity dependent approach

L. Huther[1], *H.P. Loens*[1], *G. Martinez-Pinedo*[1] *and K. Langanke* [1,2,3]

[1] GSI Helmholtzzentrum für Schwerionenforschung, Planckstr. 1, 64291 Darmstadt, Germany
[2] Technische Univeristät Darmstadt, Darmstadt, Germany
[3] Frankfurt Institute for Advanced Studies, Ruth-Moufang-Str. 1, Frankfurt, Germany

Introduction

The s-process takes place in stellar environments with temperatures between 8 to 100 keV. In such a plasma the nuclei follow a Maxwell-Boltzmann distribution. Reactions between nucei are characterized by a reaction rate that depends on the temperature of the stellar environment. Reaction rates based on experimental cross sections $\langle\sigma v\rangle_{lab}^{exp}$ do not account for the thermal excitation of the nuclei. This effect can be included by the so-called stellar enhancement factors (SEF), defined as the theoretical ratio of the stellar reaction rate $\langle\sigma v\rangle^{*}$, that describes the reaction in a stellar plasma including contributions of excited states, and the laboratory reaction rate $\langle\sigma v\rangle_{lab}$, that describes the reaction with the nucleus being in its groundstate. In our work we calculated the SEF for (n,γ)-reactions of all s-process nuclei in a statistical model with parity dependent level densities.

Theory

In the statistical model the cross-section from the target state μ with spin J_i^μ and parity π_i^μ to a final state ν with spin J_m^ν and parity π_m^ν via a compound state with excitation energy E, spin J and parity π is given by

$$\sigma^{\mu\nu}(E_{i,j}) = \frac{\pi\hbar^2}{2M_{i,j}E_{i,j}} \frac{1}{(2J_i^\mu+1)(2J_j+1)} \sum_{J,\pi} \frac{T_j^\mu T_o^\nu}{T_{tot}} \quad (1)$$

where $E_{i,j}$, $M_{i,j}$ are the center-of-mass energy as well as the reduced mass of target and projectile. J_j is the spin of the projectile. The transmission coefficients are an abbreviated description $T_j^\mu = T(E,J,\pi,E_i^\mu,J_i^\mu,\pi_i^\mu)$, $T_o^\nu = T(E,J,\pi,E_m^\nu,J_m^\nu,\pi_m^\nu)$ and describe the transitions from the compound state to the initial and final state, respectively. T_{tot} describes the transitions to all energetically possible channels. The transmission coefficients are calculated by solving the Schördinger-equation with the use of a global optical potential. The dependence in parity is accounted following the procedure of ref [3].

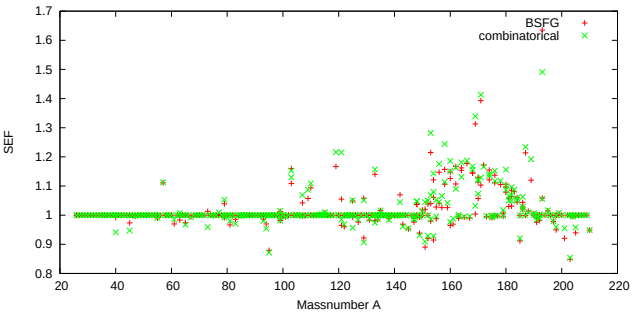

Figure 1: The SEF for all s-process nuclei at a temperature of 30 keV with the two level-density descriptions used in this work.

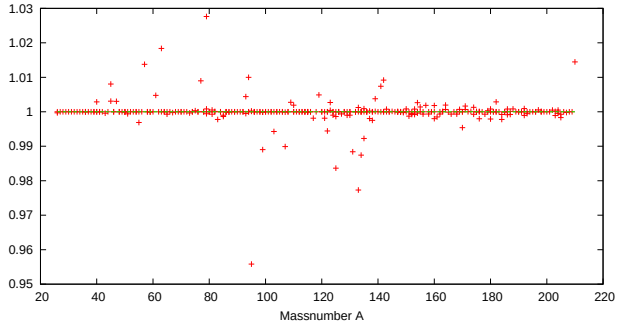

Figure 2: The ratio of SEF obatined with and without parity dependent level densities . Note that in this plot the temperature is 90 keV and the used level density is the back-shifted Fermi-gas model.

Results

In our calculations we used two different level-density descriptions, namely the combinatorial level-density of ref. [1] and the phenomenological back-shifted Fermi-gas model of ref. [2]. Figure 1 shows the sensitivity of the SEF for all s-process nuclei to the level density used. Figure 2. explores the impact of the parity dependent approach.

The inclusion of parity dependent level densities results in minor changes for the SEF, which are however not negligible for an accurate description of s-process abundances. Furthermore, we notice that larger differences arise from using different level densities. This calls for an improved description of level densities, hopefully based on microscopic calculations. See [4] for further details.

References

[1] S.Hilaire and S.Goriely, Nucl. Phys. A **779** (2006) 63-81

[2] T.Rauscher *et al.*, Phys. Rev. C **56** (1997) 1613-1625

[3] H. P.Loens *et al.*, Phys. Lett. B **666** (2008) 395-399

[4] L.Huther *et al.*, Eur. Phys. J. A **47** (2011) 1-7

Nucleosynthesis of heavy elements by the r-process

I. Petermann[1], *K. Langanke*[1,2,3], *and G. Martínez-Pinedo*[1]

[1]GSI Helmholtzzentrum für Schwerionenforschung, Darmstadt, Germany; [2]Institut für Kernphysik, TU Darmstadt, Darmstadt, Germany; [3]Frankfurt Institute for Advanced Studies, Frankfurt, Germany

About half of the elements heavier than mass number $A \sim 60$ are made within the r-process, a sequence of rapid neutron captures and β decays [1]. The r process occurs in environments with extremely high neutron densities. Then neutron captures are much faster than the competing decays. Hence the r-process path runs through such extremely neutron-rich nuclei that most of their properties (i.e mass, lifetime and neutron capture cross sections) are experimentally unknown and have to be modelled, based on experimental guidance if available [2].

Recently we have developed an r-process code which consistently couples an extended nuclear network with trajectories describing the dynamics of the astrophysical environment. Besides using state-of-the-art prediction for nuclear masses, halflives and neutron capture rates, the network explicitly accounts for all relevant reactions including the various fission processes (spontaneous, neutron-, beta- and neutrino-induced fission) and their yield distributions. First applications studied the r-process in a supernova environment with parametrized trajectories chosen to allow for sufficiently large neutron-to-seed ratios so that the r-process reaches the range of fissioning nuclei. The studies focussed on different topics.

Varying the nuclear input (masses, half-lives, neutron capture and fission rates) it was studied whether fission can indeed result in the robust r-process abundance patterns as observed in metalpoor stars [3]. Figure 1 shows the isotopic abundances obtained for different sets of nuclear masses and fission barriers and different values of the electron-to-nucleon ratio, Y_e. It is found that the relative abundances of r-process elements (for $Z > 40$) only slightly change when the Y_e value is varied.

Due to nuclear models the existence of long-lived superheavy elements with charge numbers around $Z \sim 120$ is conceivable. While the production of such elements is the goal of experimental attempts at different laboratories, Nature might have chosen the r-process to produce such nuclides. However, during the r-process only very neutron-rich nuclides with rather short life-times will be produced. If these after freeze-out should produce long-lived superheavies, the decay chain of the progenitor nuclei must not pass through a region of the nuclear chart in which fission dominates over beta decays. It is found that current nuclear models predict the nuclides to pass through regions of fission dominance. If true, the decay leads to two medium-heavy nuclei rather than producing superheavies.

The observation of the isotopes ^{232}Th and ^{238}U with halflives of a few billion years in the same old stars, allows for the age determination of these stars from the observed abundance ratio using the radioactive decay of the isotopes as clocks. This procedure presumes a good knowledge of the production ratio of the isotopes. The calculations show that both isotopes are partly or even predominantly produced via alpha-decay of other long-lived nuclides. In this way a larger part of the nuclear chart is involved in the production of the observed neighboring nuclides leading to a larger dependence on uncertain nuclear input.

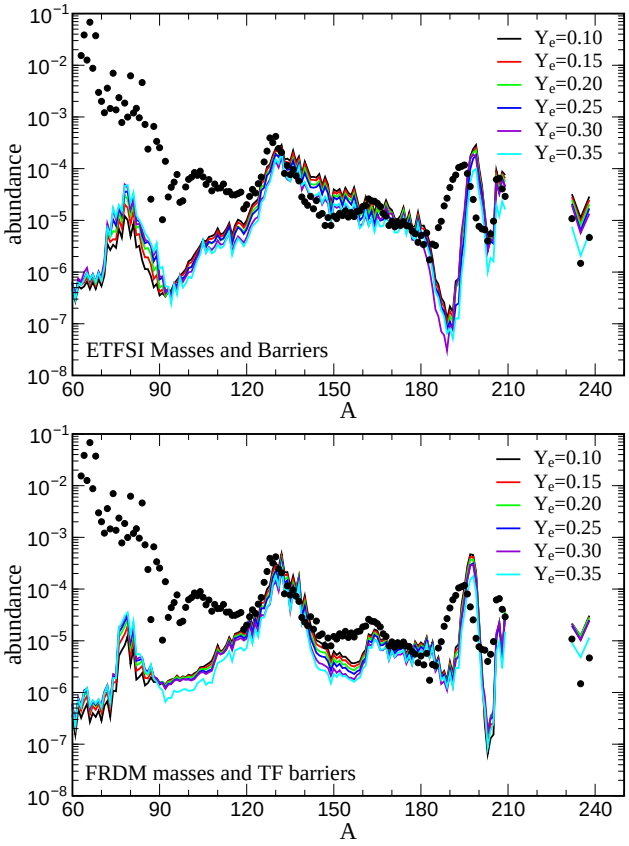

Figure 1: Final r-process abundances as a function of the Y_e value of the ejected material. Smaller Y_e values correspond to larger neutron-to-seed values.

References

[1] M. Arnould, S. Goriely, K. Takahashi, Phys. Repts. **450** (2007) 97.

[2] H. Grawe, K. Langanke, G. Martínez-Pinedo, Rep. Prog. Phys. **70** (2007) 1525.

[3] C. Sneden, J. J. Cowan, R. Gallino, Ann. Rev. Astron. Astrophys. **46** (2008) 241.

Collective neutrino oscillations and νp-process nucleosynthesis

B. Ziebarth[1], *G. Martínez-Pinedo*[1], *K. Langanke*[1,2,3], *T. Fischer*[1], *and T. Schösser*[1]

[1]GSI Helmholtzzentrum für Schwerionenforschung, Darmstadt, Germany; [2]Institut für Kernphysik, TU Darmstadt, Darmstadt, Germany; [3]Frankfurt Institute for Advanced Studies, Frankfurt, Germany

The νp-process occurs in matter ejected from a hot proto-neutron star formed after a supernova explosion that cools by emitting large amounts of neutrinos and antineutrions of all flavors. Roughly speaking the surface of the proto-neutron star is like a black body for neutrinos. Inside the proto-neutron star the neutrinos are trapped due to inelastic scattering, outside they propagate freely and therefore their energy spectrum does not change any more. The transition between these two regimes, which is different neutrino flavors, determines the shape of the final energy spectrum. Consequently, the average neutrino energy is flavor dependent. A new phenomenon known as collective neutrino oscillations [1] has been shown to occur in this environment with potential implications for νp-process nucleosynthesis.

The νp-process has been suggested to be a primary process for the production of neutron-deficient nuclei during explosive nucleosynthesis of core collapsing supernovae. The matter of the innermost ejecta of these supernovae is heated to temperatures above 10^{10} K. Due to these high temperatures the matter consists of fully dissociated protons and neutrons, which are subject to a large flux of neutrinos and antineutrinos emitted by the proto-neutron star. The ratio between protons and neutrons depends on weak interaction processes. The dominant processes are neutrino and anti-neutrino absorptions and their inverses,

$$\begin{aligned} \nu_e + n &\rightleftarrows p + e^-, \\ \bar{\nu}_e + p &\rightleftarrows n + e^+. \end{aligned} \qquad (1)$$

The neutrino and antineutrino spectra are such that proton rich composition is favoured. During the expansion the matter cools and once it reaches temperatures of about 2×10^9 K, the ejecta's composition has changed to protons, ^{4}He, and iron group nuclei with N≈Z, mainly ^{56}Ni. In this proton-rich environment the synthesis of heavier elements by proton captures is very inefficient due to 'bottleneck' nuclei, like ^{64}Ge, with long beta-decay half-lifes, small proton-capture rates, and large photo dissociation, (γ, p), rates. This problem can be overcome if we consider that the matter is subject to a large flux of neutrinos and antineutrinos which are emitted from the proto-neutron star.

As all the neutrons are bound inside nuclei neutrino absorption involves transitions to nuclear states with higher energies and thus is heavily suppressed. The situation is different for antineutrinos that can be absorbed by protons either free or bound in heavier nuclei. Antineutrino absorption on free protons is the dominating process due to their large abundance. The $\bar{\nu}_e$ capturing process produces neutrons that can be used to overcome the bottlenecks by (n, p)-reactions. The νp-process denotes this sequence of (p, γ)-reactions and following (n, p)-reactions or beta-decays [2].

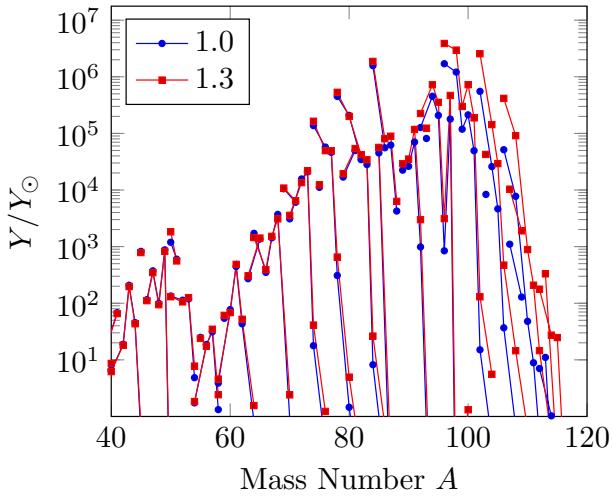

Figure 1: Impact of collective neutrino oscillations on νp-process abundances

Collective neutrino oscillations occur for the high neutrino densities present in the environment where νp-process nucleosynthesis takes place. A recent study [3] has shown that collective neutrino oscillations swap the spectra of $\bar{\nu}_e$ and $\bar{\nu}_{\mu,\tau}$ neutrinos in certain energy intervals bounded by sharp spectral splits. The net result is that for energies larger than some threshold energy, $\bar{\nu}_e$ neutrinos acquire the spectra of the hotter $\bar{\nu}_{\mu,\tau}$ neutrinos. We have estimated that this effect increases the rate for antineutrino absorption on protons by a factor that varies between 1.2 and 1.5 [4]. The increase is sensitive to the original difference in average energies between $\bar{\nu}_e$ and $\bar{\nu}_x$ but it is almost independent on the energy at which the split occurs. Figure 1 shows that the increase can have a strong impact on the production of the light p-process nuclei (^{92,94}Mo, ^{96,98}Ru, ^{102,104}Pd).

B. Ziebarth thanks the GSI summer student program for financial support.

References

[1] H. Duan, G. M. Fuller, Y. Qian, Ann. Rev. Nucl. Part. Sci. **60** (2010) 569.

[2] C. Fröhlich, *et al.*, Phys. Rev. Lett. **96** (2006) 142502.

[3] B. Dasgupta, A. Dighe, G. G. Raffelt, A. Y. Smirnov, Phys. Rev. Lett. **103** (2009) 051105.

[4] T. Schösser, Diploma Thesis, Techische Universität Darmstadt (2011).

Electromagnetic counterparts of compact object mergers powered by radioactive decay of r-process nuclei

B. D. Metzger[1], *G. Martínez-Pinedo*[2], *A. Arcones*[2,3], *S. Darbha*[4], *E. Quataert*[4], *D. Kasen*[4], *R. Thomas*[5], *P. Nuget*[5], *I. V. Panov*[6], *and N. T. Zinner*[7]

[1]Department of Astrophysical Sciences, Princeton University, USA; [2]GSI Helmholtzzentrum für Schwerionenforschung, Darmstadt, Germany; [3]Institut für Kernphysik, TU Darmstadt, Darmstadt, Germany; [4]Astronomy Department and Theoretical Astrophysics Center, University of California, Berkeley, USA; [5]Lawrence Berkeley National Laboratory, Berkeley, USA; [6]Department of Physics, University of Basel, Switzerland; [7]Department of Physics, Harvard University, Cambridge, USA

The most promising astrophysical sources of gravitational waves (GWs) for ground-based interferometers such as LIGO and Virgo are the inspiral and merger of binary neutron star (NS) and black hole systems. Maximizing the scientific benefits of a GW detection will require identifying a coincident electromagnetic counterpart. One of the most likely sources of isotropic emission from NS mergers is a supernova-like transient powered by the radioactive decay of r-process elements synthesized in the merger ejecta. We have performed the first calculations of the optical transients from NS mergers that self-consistently determine the radioactive heating from a nuclear reaction network and which determine the resulting light curve from a Monte Carlo radiation transfer calculation.

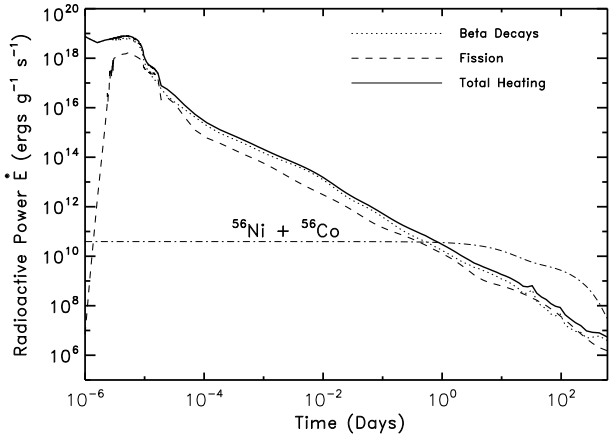

Figure 1: Radioactive heating rate per unit of mass $\dot{E}$ in neutron-star merger ejecta due to the decay of r-process material. Time starts when material is ejected.

We employ a dynamical r-process network that includes neutron captures, photodissociations, β-decays and fission reactions (see [1, 2] for more details). Ejecta trajectories are from the numerical NS-NS merger calculations of [3]. Our results for the total radioactive heating rate $\dot{E}$ as a function of time following the ejection are shown in Figure 1. The large heating rate at early times is due to the r-process, which ends when neutrons are exhausted at $t \sim 1$ s $\sim 10^{-5}$ days. Heating on longer timescales results from the synthesized unstable isotopes decaying to stability.

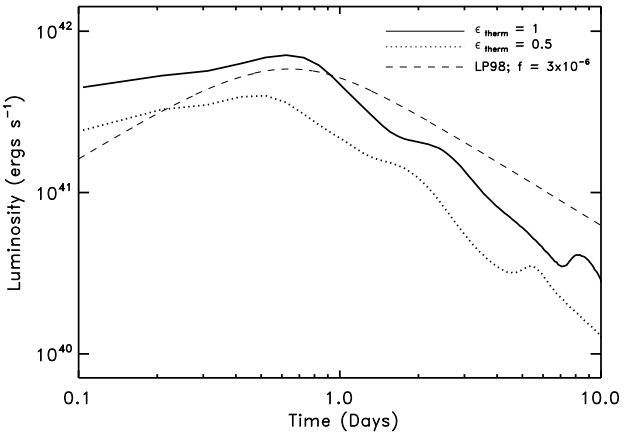

Figure 2: Bolometric light curve of the radioactively-powered transient from a NS-NS/NS-BH merger, assuming a total ejecta mass of 10^{-2} $M_\odot$. For comparison the model of reference [4] is also shown.

We have calculated the light curves of NS merger ejecta using the time-dependent radiative transfer code SEDONA [5], which is modified to include the radioactive heating $\dot{Q} = \varepsilon_{\rm therm}\dot{E}$ as shown in Figure 1. Figure 2 shows the obtained bolometric light curve. The predicted peak luminosity is $\sim 10^{41}$ erg s^{-1}. This type of transient may be detectable following a short duration Gamma-Ray Burst or blindly with present or upcoming optical transient surveys. As the emission due to NS merger ejecta is powered by the production of r-process elements, current optical transient surveys can directly constrain the unknown origin of the heaviest elements in the Universe.

References

[1] B. D. Metzger, A. Arcones, E. Quataert, G. Martínez-Pinedo, Mon. Not. Roy. Ast. Soc. **402** (2010) 2771.

[2] B. D. Metzger, *et al.*, Mon. Not. Roy. Ast. Soc. **406** (2010) 2650.

[3] C. Freiburghaus, S. Rosswog, F.-K. Thielemann, Astrophys. J. **525** (1999) L121.

[4] L. Li, B. Paczyński, Astrophys. J. **507** (1998) L59.

[5] D. Kasen, R. C. Thomas, P. Nugent, Astrophys. J. **651** (2006) 366.

Are neutrino-driven winds the r-process site?

Tobias Fischer[1,2] *and Gabriel Martínez-Pinedo*[1]

[1]GSI, Helmholtzzentrum für Schwerionenforschung GmbH, Darmstadt; [2]Technische Universität Darmstadt

Supernova (SN) explosions of massive stars have long been investigated as the favored production site of heavy elements in the Universe via the *r*-process [1].

The SN remnant at the center, a proto-neutron star, contracts continuously via deleptonization which is given by neutrino emission of all flavors. It results in an outflow of matter known as neutrino-driven wind. The important aspect with respect to possible nucleosynthesis processes is the composition of the wind that depends on the spectra of electron neutrinos and antineutrinos. Recent simulations [2, 3] show that the electron neutrino and antineutrino fluxes are very similar, resulting in ejecta with electron fraction $Y_e \geq 0.5$ (see Figure 1). The *r*-process cannot be expected in these ejecta. The proton-rich conditions and the large neutrino fluxes, however, may allow for the νp-process.

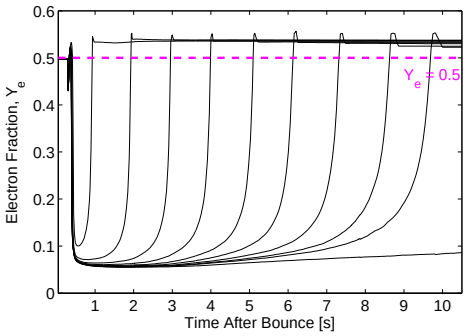

Figure 1: Y_e-evolution of the SN ejecta.

In order to understand why matter stays proton-rich, we consider the evolution of the neutrino fluxes and mean energies for the electron neutrinos and antineutrinos, which are responsible for composition changes via charged current reactions on nucleons. The large differences between the electron neutrino and antineutrino fluxes and mean energies obtained by the Livermore group [1], could not be confirmed. These flux differences even increase in the Livermore simulations with time, while we find the opposite. This aspect is related to the evolution of the neutrinospheres R_ν (i.e. the neutrino flavor and energy dependent spheres of last scattering). It could be shown that R_{ν_e} and $R_{\bar{\nu}_e}$ move closer together during the proto-neutron star deleptonization [2], i.e. the neutrino spectra for ν_e and $\bar{\nu}_e$ become increasingly similar with time after the onset of explosion. This in turn indicates the reducing dominance of the charged current reactions. We analyze the evolution of the inverse mean free paths for the individual reactions considered, based on fully consistent dynamical radiation transport simulations [4]. The results show that neutral

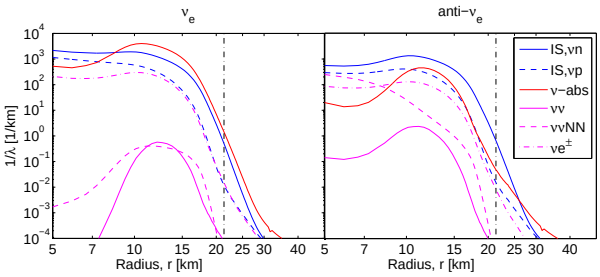

(a) 1 second after bounce

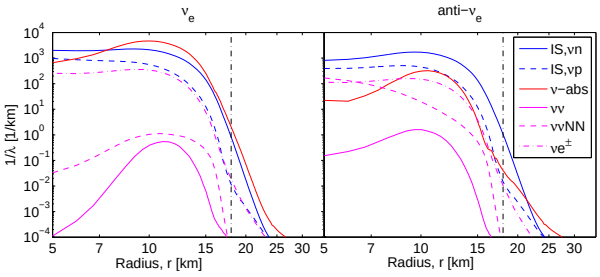

(b) 2 seconds post bounce

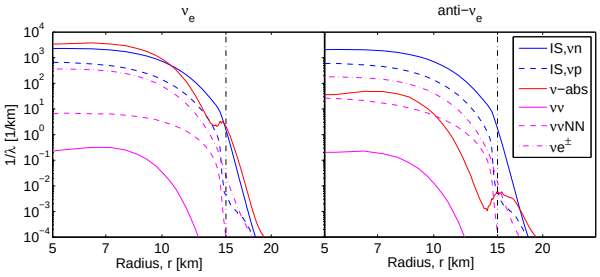

(c) 7 seconds after bounce

Figure 2: Radial profiles of the individual neutrino inverse mean free paths at selected post bounce times (vertical dash-dotted lines: R_ν).

current reactions, in particular neutrino–nucleon scattering, starts to dominate over (anti)neutrino absorption processes during the deleptonization (see Figure 2). The reaction rates for electron (anti)neutrino absorption on (protons) neutrons reduce significantly in comparison to the scattering rates, due to final state electron blocking and the increasing nucleon degeneracy at the neutrinospheres.

References

[1] S. E. Woosley, et. al., Astrophysical. J., **433**, 229 (1994).

[2] T. Fischer, et al., Astron. Astrophys., **517**, A80 (2010)

[3] L. Hüdepohl, et. al., Phys. Rev. Lett., **104**, 251101 (2010)

[4] T. Fischer and G. Martínez-Pinedo, (in preparation)

A low-mass multi-sampling ionization chamber for fission studies

B. Voss, C. Kaya, J. Kunkel for the SOFIA-collaboration

GSI, Darmstadt, Germany.

Performing the **S**tudies-**O**n-**FI**ssion-with-**A**ladin experiment (SOFIA) at CaveC at GSI following the ideas of former experiments [1] requires the precise measurement of the fission fragment produced after electromagnetic excitation of a projectile fragment. In order to achieve this, it is necessary to determine the nuclear charge, mass and kinetic energy of each fission fragment after prompt neutron emission in coincidence with the total neutron multiplicity prior to any β^- decay on an event-by-event basis.

A sketch of the experimental set-up is shown in Fig. 1. The experimental conditions are quite challenging: $5\text{x}10^9$ primary ^{238}U ions/s of 1 GeV/u impinge on a Beryllium target at the entrance of the FRS (not shown) producing (radioactive) secondary beams with energies of up to 600 MeV/u and intensities of 10^3 to 10^5 ions/s. These secondary beams are then impinging on an active lead-target of ≈1.5 g/cm^2 total thickness located at the entrance of CaveC where the exotic actinides undergo coulomb excitation and subsequent fission. The products of this process have intermediate nuclear charge and are identified in a dedicated detector setup measuring Bρ-TOF and energy loss. In order to keep the multiple scattering at an acceptable level, the flight-path sections after the active target will be filled with Helium at atmospheric pressure except for the places where the parts of the detector system will be installed. The determination of the nuclear charge of the fragments will be performed by a **MU**lti-**S**ampling **I**onization **C**hamber with two identical active volumes (TwinMUSIC) symmetric to the cathode plane. The detector features low mass in directions transversal to the beam in order to minimize secondary reactions produced by the primary beam particles also impinging on the central cathode of the detector. The design is shown in Fig. 2 and 3. The housing is made from standard industrial aluminium profiles and forms a faraday cage which may be evacuated. The frames of the outer skeleton serve for high-precision mounting of the various 'active' parts of the two sections which are formed by: anodes with ten active electrodes of (200 x 50) mm^2 each and two screening electrodes of (200 x 10) mm^2 surface each on PCB boards of 3.2 mm thickness. The adjustable distance to the adjacent Frisch-Grids has been chosen to 5 mm. These grids are equipped with W-Re wires of 20 µm diameter and 2 mm spacing in a diagonal arrangement. The wire layers are kept on ground potential with respect to the anodes at high voltage, generating a ≈500 V/cm electric field in order to reduce drift-time and -spread. For the 100 mm wide field cage with an uncoiled length of 1.8 m a self-made low-mass version of a Kapton® foil of 7 µm thickness as well as an industrial fall-back version on a 50 µm foil are produced. Both realize a staggered strip-line design of strips with 1 mm width and 0.5 mm gaps.

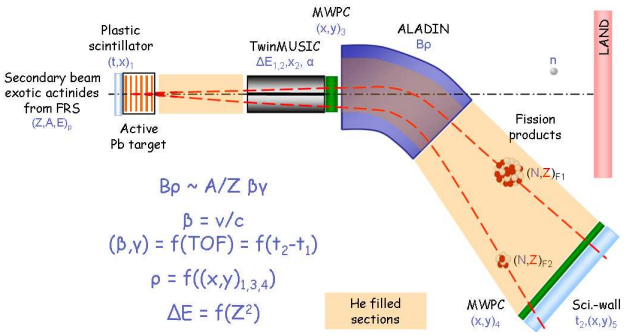

Figure 1: Sketch of the methods principle and the experimental setup to fully identify fission fragments.

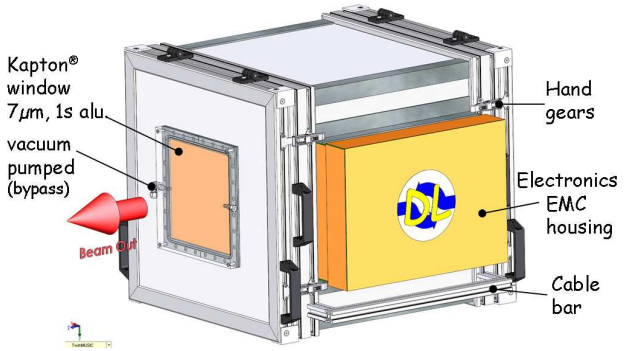

Figure 2: 3D model of the TwinMUSIC housing.

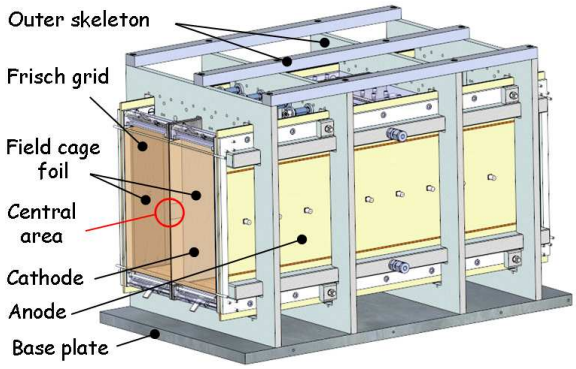

Figure 3: 3D model of the TwinMUSIC detector-unit installed inside the detector housing shown in Fig. 2.

The field-defining electrodes are made from Aluminium and Copper with thicknesses of <1 µm and 12 µm, respectively. The cathode kept on 5 kV potential consists of an aluminized 7 µm thick Kapton® foil. In order to minimize the material on the beam axis its central region of 20 mm height is stabilized with Nylon® fishing lines of 300 µm diameter only. The detector will be read out by customized electronics.

References

[1] K.-H. Schmidt et al, NPA 665 (2000) 221

Homogeneous Large Area CVD-Diamond Detectors for Tracking and ToF*

E. Berdermann[1#], M. Ciobanu[1], P. Moritz[1], M. S. Rahman[1], M. Träger[1], S. Gsell[2], M. Fischer[2], M. Schreck[2], and C. Stehl[2] for the CARAT Collaboration

[1]GSI, Darmstadt, Germany; [2]Universität Augsburg, Germany

In the last year, we continued with the development of large-area diamond sensors grown at the University of Augsburg by chemical vapour deposition (CVD) on wafer scale Ir/YSZ/Si(001) substrates. Early results of diamond-on-iridium (DoI) sensors [1] were indicating significant defect densities within the detector bulk, which led to reduced charge collection efficiencies CCE = Q_{Coll}/Q_{Gen}= 40% (with Q_{Gen} the particle induced charge and Q_{Coll} the charge measured by the sensor) and broad spectra of energy resolution $\delta E/E \approx 30\%$. These values were obtained with traversing ^{241}Am-α-particles for the favourable case of a sensor of thickness d = 12µm = α-range in diamond.

A remarkable improvement of the crystal-quality has been achieved in 2010 by using ultra-pure H_2/CH_4 gas mixtures and optimized growth techniques [2]. Two DoI samples D1 and D2 of thicknesses d_{D1} = 293 µm and d_{D2} = 320 µm, respectively, were investigated. Ti/Pt/Au quadrant electrodes with common mass potential were applied in order to prove the spatial homogeneity of the detector performance. Almost symmetrical IE_D characteristics with respect to the bias polarity were obtained for each sector, while the dark current at electric fields $E_D \geq \pm$ 2 V/µm were of the order of 10^{-13} A, well comparable to homoepitaxial single-crystal (SC) diamond sensors.

Charge Collection Properties

The most sensitive parameters revealing both the crystal quality and the sensor performance are the CCE and the energy resolution δE/E measured with line sources using spectroscopy electronics [3]. Charge losses are a measure for defects (dislocations, traps, recombination centres), whereas the measured line widths for the homogeneity of crystal structure and detector response. Figure 1 shows ^{241}Am-α-spectra obtained from sectors Q1, Q3, and Q4 of D2 compared to the spectrum measured with sector Q1 of a SC diamond sensor of identical area but smaller thickness d_{SC} = 50 µm.

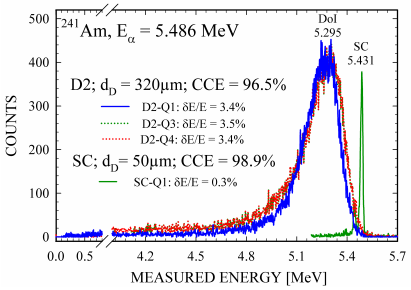

. **Figure 1:** ^{241}Am-α-spectra of sensor D2 (d_{D2} = 320µm) compared to the α-distribution obtained with a homoepitaxial sensor of same area but smaller thickness d =50µm.

* Work supported by the EU projects: HadronPhysics2 contract No. RII3-CT227431 and MC-PAD.

The similarity of the spectra obtained from all DoI sectors demonstrate the good spatial homogeneity of the detector response, and thus of the crystal structure. The peak values correspond to an excellent CCE_{D2} = 96.5%, which is slightly lower than the CCE_{SC} = 98.9% measured for the SC sample. The right hand parts of the DoI lines are Gaussians of a relative energy resolution $\delta E/E_{D2} \approx 3.5\%$ (compare $\delta E/E_{SC} \approx 3‰$), whereas the low-energy tail is a convolution of the unresolved ^{241}Am-α satellite lines and of α-signals affected by trapping.

Timing Properties

The intrinsic time resolution of D1 and D2 was measured with ^{40}Ar ions of E = 200 AMeV using DBA amplifiers. An excellent σ_{intr} = 18ps was obtained - as frequently confirmed also for polycrystalline and SC diamond sensors.

However, the broadband (BB) signal shapes (representing the internal electric field profile) cannot be understood. Triangular signals of ultra-fast rise time << 200 ps and FWHM ≈ 1.5 ns were recorded for sensor D1 at E_D = ± 2 V/µm (Fig. 2, blue signals), which indicate inhomogeneous internal fields and non-negligible charge trapping. This is in contradiction to the high CCE ≈ 93% measured with spectroscopy electronics also for this sample. We tested the effect of the measurement system's bandwidth (BW) to the signal shape with a thin (d = 12 µm) 'early' DoI sensor (Fig. 2, red/green signals). An improvement of the pulse area $A \propto Q_{Coll}$ by a factor 2 was obtained by modifying the DBA from BW = 2.3 to 3.4 GHz and by using, in addition, a 6 GHz DSO.

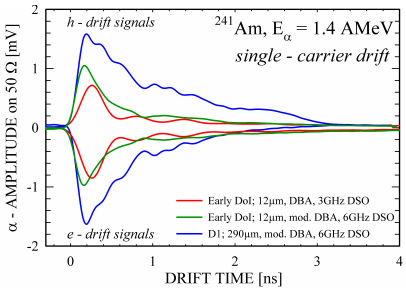

Figure 2: α-induced transient current signals in D1 (blue) and in an 'early' sample of d_D = 12µm. The red-green set of signals show the influence of the BW and the green-blue one the superior CCE of DoI sensors grown in 2010.

References

[1] E. Berdermann et al., GSI Annual Report 2009
[2] C. Stehl et al., "Growth of Heteropeitaxial CVD-Diamond Films on Ir/YSZ/Si(001) for Detector Applications", this Annual Report (2010).
[3] E. Berdermann et al., Diam Rel. Mat. 17 (2008) 1159

Growth of Heteroepitaxial CVD Diamond Films on Ir/YSZ/Si(001) for Detector Applications*

C. Stehl[1], S. Gsell[1], M. Fischer[1], M. Schreck[1,#], E. Berdermann[2], M. S. Rahman[2], and M. Träger[2]

[1]Universität Augsburg, Germany; [2]GSI, Darmstadt, Germany

In the framework of the CARAT collaboration, which executes work package 15 of the EU FP7 "HadronPhysics2" project, the diamond group at the University of Augsburg is responsible for the development and growth of heteroepitaxial diamond films, which shall be used in particular for tracking and ToF measurements of heavy ions and minimum ionising particles.

Motivation

For future particle accelerator experiments, e.g. at FAIR, we are developing novel, advanced diamond sensors grown by chemical vapour deposition (CVD), capable on one hand of replacing the commonly used silicon tracking devices and being on the other hand an advantageous alternative to polycrystalline or single-crystal diamond sensors used so far in beam diagnostics and timing applications. By using heteroepitaxial diamond films grown on Ir/YSZ/Si(001) we want to bridge the gap between polycrystalline (which exhibits inhomogeneous incomplete charge collection) and single-crystal CVD diamond (i.e. of small areas), enabling the fabrication of large-area diamond sensors of good homogeneity, high drift velocity of the charge carriers, and of almost complete collection of the particle induced charge.

Sample Preparation

The growth of heteroepitaxial diamond films on the Ir/YSZ/Si(001) multilayer system by microwave plasma enhanced CVD was established at the University of Augsburg in 2004 [1]. A layer of YSZ (yttria-stabilised zirconia) is deposited on a 4-inch Si wafer by pulsed laser deposition. In a second step a film of Ir is deposited on top of the YSZ layer by electron beam evaporation. Fig. 1 shows a schematic of the substrate's layer structure.

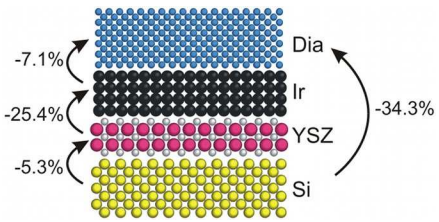

Figure 1: Structure of the Ir/YSZ/Si(001) substrate with diamond on top, numbers indicating relative lattice mismatches [1].

The diamond films are grown at present on substrates of 20×20 mm^2 lateral extension from a H_2/CH_4 plasma. This process yields material of very good crystalline quality with a FWHM of the x-ray diffraction (XRD) rocking curve of less than 0.2°, and inherits the potential of being scaled up in order to synthesise wafer-size diamond films in the future [2].

For detector applications the best material quality is needed. Therefore, thick films of diamond (ca. 1 mm) were grown in order to reduce the density of lattice defects (especially dislocations) in the final samples, which were prepared from the growth side of the film by laser cutting. Special care was also taken concerning the purity of the plasma and the reactor chamber to ensure low impurity concentrations (esp. of N, Si, and B) in the diamond films.

Results

Two samples with a thickness of ca. 300 µm were prepared for measurements of the detector performance at GSI. Photoluminescence and cathodoluminescence spectra indicated very low concentrations of N, Si, and B (see fig. 2). Raman spectra and XRD measurements showed a clear improvement over the hitherto state of the art.

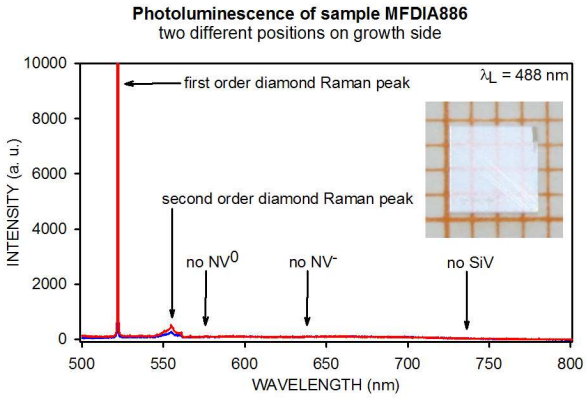

Figure 2: Raman/Photoluminescence spectrum of one sample, showing the complete absence of graphitic carbon contributions and of impurity peaks from NV and SiV centres. The inset shows a photo of the final sample.

The detailed results will be described in an extended scientific publication.

References

[1] S. Gsell, T. Bauer, J. Goldfuß, M. Schreck, and B. Stritzker, Applied Physics Letters 84 (2004) 4541.

[2] M. Fischer, S. Gsell, M. Schreck, R. Brescia, and B. Stritzker, Diamond & Related Materials 17 (2008) 1035.

* Work supported by the EU, FP7 Proj. RII3-CT-227431.

matthias.schreck@physik.uni-augsburg.de

Electrical and Photo Conductivities in Heteroepitaxial Quasi Single-Crystal CVD-Diamond Detectors*

M. S. Rahman[1#], E. Berdermann[1], M. Ciobanu[1], M. Traeger[1], E. Layevski[2], C. Nebel[2], M. Schreck[3], and C. Stehl[3]

[1]GSI, Darmstadt, Germany; [2]IAF, Fraunhofer, Freiburg Germany; [3]Universität Augsburg, Germany.

The properties of CVD Diamond (CVDD) detectors such as high mobility of charge carriers, radiation hardness, and low dark conductivity provide a detector material, which is suggested to be applied in high intensity heavy-ion beam environments where classical detector devices cannot be operated [1]. In the future FAIR experiments radiation-hard materials with large area will be required for a variety of detection applications. Heteroepitaxial 'quasi' single crystal CVD diamond grown on wafer-scale Ir/YSZ/Si(001) substrates was investigated as an alternative to small-area homoepitaxial single crystal CVDD (scCVDD). Recent samples D1 and D2 of thicknesses d_{D1} = 290µm and d_{D2} = 320µm, respectively, showed interesting results in terms of structural homogeneity, charge collection efficiency, and dark conductivity.

We investigated the conduction mechanisms (both dark and photo conductivities) of several DoI films by measuring the dark currents at various temperatures (room temperature to 673K) up to biasing voltages of ± 1000V. The photo conductivity was tested with contacts consisting of different metals (e.g. Ti/Pt/Au, Al) by irradiating the samples with UV-vis-light from a Xenon source.

Dark conductivities

The dark current vs the electric field E_D (I-E_D characteristics) was measured for various DoI samples of different thicknesses and for scCVDD films at room temperatures using Keithley 6517A electrometers and a metallically shielded dark box under nitrogen flow, as shown in Fig.1. The dark current of all DoI samples (Fig.1a) is by one order of magnitude lower than the current observed with the scCVDD film; similar results have been reported in [1, 2]

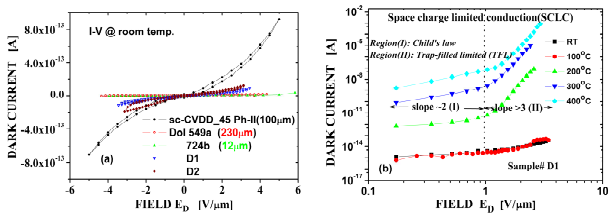

Figure 1: (a) The electric field dependence of the dark current (I-E_D characteristics) of various DoI films at room temperature compared to scCVDD (black). At ± 2V/µm, the dark current of the DoI samples is I_{DoI} < 0.05pA whereas $I_{sc} \approx 0.2$pA, (b) Same as in (a) for DoI sensor D2. A space charge limited conduction mechanism is indicated (see text).

After studying all possible conduction mechanisms, the appropriate electron transport mechanism for the DoI material was found to be the space charge limited conduction (SCLC), that is, a defect dominated conduction mechanism. The SCLC theory describes the dark currents as follows:

$$I_{Child} = 9/8\,\mu\kappa_D(V^2/d^3), \qquad I_{TFL} = 9/8\,\mu\kappa_D\theta(V^2/d^3),$$

where μ is the electron mobility, κ_D is the dielectric constant, V the applied bias, d is the detector thickness, and θ the ratio of the free to the trapped charge carriers. In Fig. 1(b), the curves I-E_D (473 to 673K) show two distinct regions: one where Child's law holds (slope ~ 2) and a second one with slope > 3, which indicates a trap-filled-limited (TFL) conduction. This suggests that a huge amount of traps are present in the bulk. Optical cross polarizer imaging of the tested samples also showed homogeneously distributed dislocations in the volume [1]. The activation energy of the traps in the new samples was determined to E^{ac}= (1.026 - 1.318) ± 0.074 eV, which is similar to the value E^{ac} = 1.4eV reported previously [2].

Photo conductivities

In order to investigate the photoconductivity of D1 and D2, the current induced by UV light injection was measured as a function of the photon energy and plotted in Fig. 2 in arbitrary units. According to the measured photocurrents D2 is less defective compared to sample D1. The E^{ac} is attributed to shallow traps. It is worth mentioning that we varied type of different metal contacts on DoI films but almost no difference in the behaviour of the dark current could be observed.

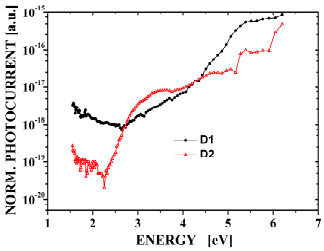

Figure 2: The photoelectric characteristics of D1 and D2.

References

[1] E. Berdermann *et al.*Diam.Rel. Mater.,19(2010), 358.

[2] A. Stolz, *et al.* Diam. Rel. Mater., 15 (2006), 807.

* Work supported by EU projects: MC-PAD contract No. 214560 & HadronPhysics2 contract No. RII3-CT227431.

Development of the n-XYTER front end board FEB-D for CBM

C.J. Schmidt[1], C. Simons[1], V. Kleipa[1], and R. Schönholz[2]
[1]GSI, Darmstadt, Germany; [2]Würth Elektronik GmbH & Co. KG, Niedernhall, Germany

Introduction

Employment of highly integrated ASIC front-end electronics in GSI and FAIR detector systems is crucial in view of current and future detector granularity, overall channel number and radiation length to be minimized. Yet, integration of such multi-channel readout chips into detectors brings a severe technological gap up to light, where channel pitch on silicon is found on the order of 50 μm, whereas standard PCB technology realistically allows to create structures at a pitch of 150 μm down to 100 μm in extreme cases. The n-XYTER 128 channel mixed signal chip [1, 2] is used as a prototype detector readout chip for FAIR detector prototyping. It allows to realize a purely data driven readout, which does not rely upon an external trigger. This chip was exemplarily integrated onto a front-end test board (FEB) for the CBM STS project in the past [2]. This work rapidly illuminated the challenges that go about with bridging the technological gap in feature size from silicon to current PCB production capabilities, if an intermediate pitch adapter is to be omitted. With version FEB D, this challenge could be resolved in a cooperative effort between the GSI detector laboratory and the German PCB manufacturer Würth Elektronik.

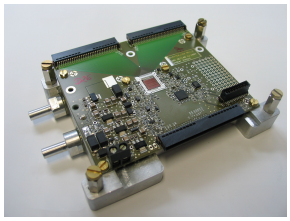

Silicon meets PCB manufacturing and bonding technology

In the earliest revisions of the CBM STS-FEB, a new approach was followed, which allowed to alleviate the the pitch requirements for the pcb-side by a factor of two. Namely, connecting bond pads on the pcb were allocated at twice the necessary pitch on two layers of the pcb, the top layer and a lower layer at a 100 μm depth within the pcb. The bond pads on the lower level needed to be left open through a milled-out window in the pcb in which the chip and half the input bond pads were allocated. This design, which avoids the use of routing-space intensive interconnects into buried layers and makes jumping the gap from 50 to 100 μm pitch feasible, was elaborated with an industrial pcb manufacturer in the past. However, it quickly turned out that with the bonding necessities, much higher surface quality specifications for the bond surfaces are necessary. They could not be fulfilled even though the 100 μm pitch turned out to be feasible in purely electrical terms. With FEB D, these problems could finally be overcome by equal distribution of the challenges to the pcb side and to bonding. Namely, using the two pcb-layer pitch reduction and increasing the overall pitch to 134 μm, pushing the fanned-out bonding angles to an extreme, together with a new scooping pcb technology that allows to excavate a buried conductor layer by means of a CO_2 pulsed laser, FEB D could be produced by the company Würth Elektronik. The bond pads on the pcb had to be realized with an asymmetric conductor width and spacing of 84 μm and 50 μm. The bond pads then were coated by immersion silver plating, which showed to be the only way to achieve a bondable surface quality without introducing shorts between neighboring pads, as experienced with standard gold platings previously on these structures.

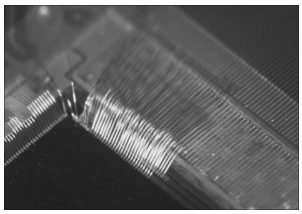

In the FEB D design, the n-XYTER chip is placed directly upon a copper cooling block, which itself is glued to the back of the PCB, covering the milled out through-hole for the chip from the back. The inner-layer bond pads are thus allocated on a balcony type gallery around the opening for the chip.

FEB D production and yield

All in all 44 FEB D boards were manufactured and populated with electronic parts. The n-XYTER was finally bonded on the detector laboratories Delvotek 64000 automatic bonding machine. For each chip 361 aluminum wire bonds were attached through wedge-wedge bonding. This small scale production proved to yield about 90% working FEBs, where previously untested chips were employed. Most of the boards have already found their application in various CBM beam times this fall and in diverse other applications.

References

[1] NIM A, 568 (2006) 301-308
[2] CBM-Progress Report 2006 p. 49

Facility for Testing the Ageing Properties of Construction Materials for High Rate Gas Detectors

A. AbuHoza[1], S. Biswas[1], U. Frankenfeld[1], J. Hehner[1], C.J. Schmidt[1] and H.R. Schmidt[2]
[1]GSI, Darmstadt, Germany; [2] University of Tübingen, Germany

Experiments like CBM at FAIR will make use of gas detectors at high interaction rates. The construction materials for serial production of the detectors have to be chosen carefully in order to ensure the operation of the detector over the projected lifetime of the experiment. Deterioration of the detectors´ performance ("ageing") is a serious threat for gas detectors in high rate experiments [1].
We have set up the infrastructure to carry out gas detector ageing tests on such materials at the GSI Detector Laboratory. This involves the appropriate irradiation sources (X-ray, radioactive sources), an ultra-clean gas system, read-out- and monitoring systems, material analysis etc.

A schematic sketch of the test stand is shown in Fig. 1. A standard wire chamber is continuously purged by counting gas at a given flow, which is routed through an out-gassing box. The box contains the construction material under investigation, e.g. glues. A second wire chamber is connected to the same gas line upstream the out-gassing box. This chamber serves as a reference to monitor non-ageing related changes due to environmental conditions (temperature, pressure, gas mixture, oxygen content).

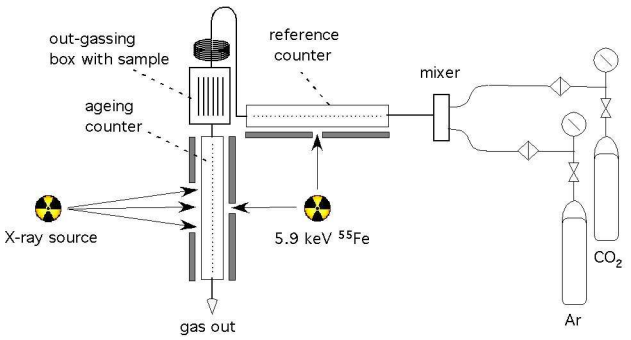

Figure 1 Schematic sketch of the setup used to investigate the ageing behaviour of gas counters

During an ageing run the chamber is irradiated during intervals of e.g. 10 minutes with an X-ray source. Between the irradiation intervals pulse height spectra employing a 5.9 keV ^{55}Fe X-ray source are recorded both for the ageing and the reference chamber. Comparing the mean position of the 5.9 keV peak for the two wire chambers will sensitively indicate the onset of ageing.
Fig. 2 show the ratio of the mean peak position in the ageing and the reference counter for the case where no material was inserted into to out-gassing box. As can be seen, this ratio is stable with respect to e.g. temperature and pressure induced variations of the mean. It proves to be constant within the error bars. In contrast, Fig. 3 shows the same ratio for the case of silicon glue RTV-3145, well know for its influence on the ageing of gas chambers, being under investigation in the out-gassing box: the ratio deteriorates to 60% with an accumulated charge of 2.5 mC/cm wire length, indicating severe ageing effects.

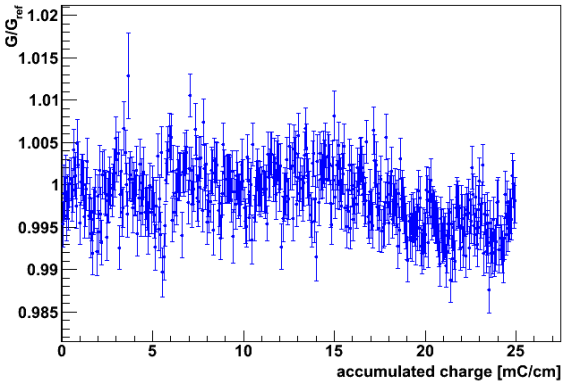

Figure 2 Ratio of the ^{55}Fe 5.9 keV X-ray mean peak position for ageing and references counter without material in the out-gassing box.

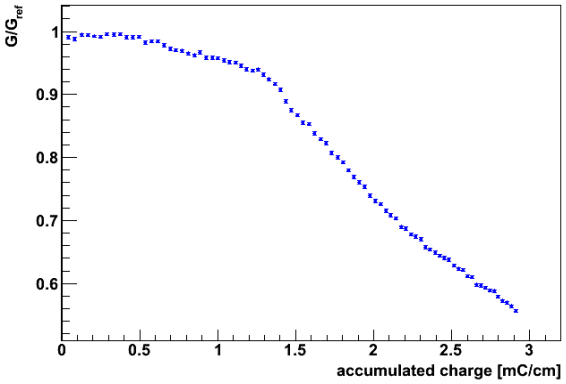

Figure 3 Same ratio as in Fig. 2, but now with RTV-3145 ageing sample in the out-gassing box.

The measurement and analysis procedures are fully automated, relieving the investigator of baby-sitting the test stand during the time-consuming measurement. The facility will in general be available to all experimental groups at FAIR, who want to characterize their construction materials which are in contact with gas detectors.

References

[1] M. Titiov, "Radiation Damage and Long-term Ageing in Gas Detectors", arXiv:physics/0403055 v1

PEXOR Linux device driver and DABC integration

J. Adamczewski-Musch[1], H.G. Essel[1], J. Hoffmann[1], N. Kurz[1], S. Linev[1], S. Minami[1], and W. Ott[1]

[1]Experiment-Electronics, GSI, Darmstadt, Germany

The PEXOR board

The *PciExpress Optical Receiver* board (PEXOR) was developed at GSI [1]. It features a Lattice FPGA and four 2 Gbit "small form-factor pluggable" optical transceivers (SFP). The optical protocol to read out a chain of GSI front-end boards has been implemented [2]. The hardware has previously been tested with drivers and software on LynxOS, developed for the GSI DAQ system MBS.

Linux device driver

A device driver has been developed to apply the PEXOR hardware for Linux OS. It is realized as a *char* driver kernel module, currently for kernel versions ≥ 2.6.27. The driver operations for *read()* and *write()* implement PIO to the PEXOR on-board memory. Operation *mmap()* allocates kernel buffers for DMA operations and maps these to user space addresses. The *pexor* kernel module manages these buffers with internal pools. Initiating a DMA transfer, retrieving and releasing DMA buffers is handled from user space by *ioctl()* operations.

The *gosip* protocol [2] for communication between PEXOR and frontend devices via the SFP connections was integrated to the kernel module. Thus a user program does not need to apply this protocol explicitly, as for the previous LynxOS driver, but calls higher level *ioctl()* operations to access the SFP slaves.

Besides, register i/o to the full address space of the board's PCIe memory is also available by *ioctl()*. Hence it is also possible to apply this driver for another FPGA configuration of the PEXOR, e.g. to utilize a different protocol.

The driver features a shared interrupt handler which is provided for data trigger interrupts from an attached TRIXOR trigger module. Handling of a "DMA is complete" interrupt which may be used with future versions of the PEXOR firmware is also prepared: the received DMA buffers are managed by a "bottom half" interrupt tasklet. This function is also used in the non-interrupt mode, although here it is invoked directly after polling for a bit of the DMA status register.

Finally, the kernel module exports some internal information, such as register contents and numbers of DMA buffers, to *sysfs* for user inspection.

C++ driver library

Together with the kernel module, a plain C++ library has been developed with higher level functionalities. It features thread safe classes representing different PEXOR board instances (i.e. hardware versions) with methods to work transparently with the driver from user space. It defines wrapper classes for the kernel DMA buffers and their memory pool, and some auxiliary classes for logging and performance benchmarks.

DABC integration

The Data Acquisition Backbone Core (DABC) is a software framework to run DAQ with distributed event building on high performance Linux clusters [3]. The PEXOR hardware was integrated to this framework by implementation of the DABC *Device* and *Transport* interface classes [4]. These encapsulate the C++ driver library as described above.

Performance measurements

For first performance tests, random data was once written to the memories of EXPLODER frontend boards connected to the PEXOR, and then collected in a non triggered read-out loop: via SFP from all front ends into the PEXOR on-board memory, and subsequently via polling-mode DMA into the buffers of the host PC. The maximum achieved DABC readout speed of 4 connected SFP chains (parallel SFP read out, asynchronous mode) was <250 Mbytes/s [4]. This is in agreement with the expected theoretical limit of 280 Mbyte/s, stemming from the overall serialization of the data transfers: SFP (800 Mbytes/s with 4 parallel readout chains), DMA (550 Mbytes/s), and memory copy between DMA kernel buffers and DABC user buffers (2 GBytes/s). It can be improved in the future by multiple data buffering on the PEXOR board, and further integration of the DMA kernel buffers to the DABC memory pool.

References

[1] J. Hoffmann, N. Kurz, S. Minami, W. Ott, S. Voltz, "PCI-express Optical Receiver", GSI scientific report 2008, p 258.

[2] S. Minami, J. Hoffmann, N. Kurz, W. Ott, "Design and Implementation of a Data Transfer Protocol via Optical Fibre", Proceedings of the 17th IEEE Real-Time Conference, Lisboa 2010.

[3] J. Adamczewski-Musch, H. G. Essel, N. Kurz and S. Linev, "Data Flow Engine in DAQ Backbone DABC", *IEEE TNS* Vol.57, No.2, April 2010, pp 614-617.

[4] J. Adamczewski-Musch, H. G. Essel, and S. Linev, „The DABC Framework Interface to Readout Hardware", Proceedings of the 17th IEEE Real-Time Conference, Lisboa 2010, to be published in *IEEE TNS*

Development of Front-End Electronics for Silicon-Strip Detectors at FAIR*

M. Holl[1], *J. Enders*[1], *and H. Simon*[2]

[1]Insitut für Kernphysik, Technische Universität Darmstadt; [2]GSI-Helmholtzzentrum für Schwerionenforschung, Darmstadt

At the planned Facility for Antiproton and Ion Research, silicon strip detectors are foreseen to be used in several experiments on nuclear-structure physics, including R^{3}B and EXL. Because of the many similarities between the detectors for the two experiments, in a first step a common silicon demonstrator will be realized. Front-end electronics for this demonstrator are currently under development and this report shows a first implementation. The goal is to obtain an efficient and fast readout while having a power consumption low enough to run the system in ultra-high vacuum and a large dynamic range from about 100 keV to a few MeV energy loss.

A block diagram of the readout system is depicted in fig.1. It consists of a front-end board housing a combination of readout- and triggering ASICs, an ADC sampling the data and an FPGA configured to control the acquisition (sequencer).

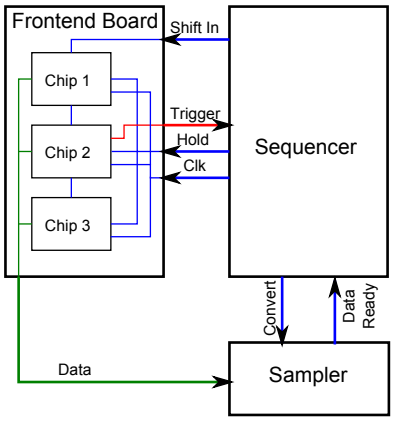

Figure 1: Readout system for the silicon demonstrator.

As readout chips, members of the VA asic family by Gamma Medica [1] have been chosen. These chips have a low power consumption suitable for the use in vacuum and a high dynamic range. They can also be combined with the TA trigger ASICs [2], giving the system internal trigger capabilities.

The ADC to be used is the module V550 by CAEN [3] and programmable FPGA-based VME modules have been developed at GSI [4]. Such a module receives the triggers generated by the TA chips and forwards them to the trigger bus for validation. Connected to this is the detection and flagging of pile-up. The module is also responsible to generate the signals to control the readout sequence for both the VA chips and the ADC and monitor their responses. It is further taking care of the slow control of the readout and triggering ASICs and of the integration of the front-end board into the data acquisition system via its VME connectors. Finally, test modes have been implemented that allow one to check whether both VA and TA chips work correctly. While the front-end board will now be built, the other components are already available, and a code for the configuration of the FPGA has been written in the hardware description language VHDL. The correct function of the code has been verified by simulations based on testbenches and a simple model of the front-end board also written in VHDL. The communication of the FPGA module with the ADC and the data acquisition system has also been evaluated using the test setup shown in fig. 2. The setup consisted of a VME crate containing the modules of the readout system (1), an oscilloscope used for monitoring (2), a pulse shaper used to generate the analog input for the ADC(not pictured), several converters (e.g. 3), and a FPGA configured with the frontend board model. The system was shown to work properly.

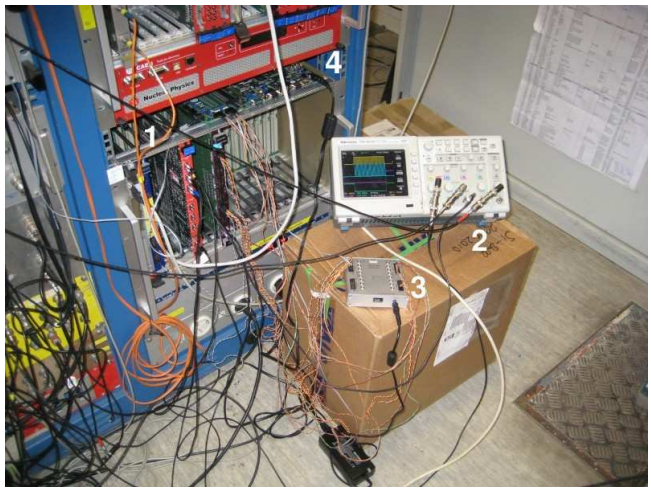

Figure 2: Overview of the test setup.

References

[1] "Va32HDR14.2 Documentation", Gamma Medica-Ideas, http://www.gm-ideas.com

[2] "TA32CG2 Description", Gamma Medica-Ideas, http://www.gm-ideas.com

[3] "Technical Information Manual MOD V550/V550 B", CAEN, http://www.caen.it

[4] J. Hoffmann,"VULOM3, VME Universal Logic Module", http://www.gsi.de/informationen/wti/ee

* Supported by the state of Hesse through the LOEWE center HIC for FAIR, and through the GSI-TU Darmstadt cooperation contract.

TRLO II – flexible FPGA trigger control

H.T. Johansson[1], A. Henriques[2], C. Langer[3], H. Simon[3], and the R^{3}B-collaboration
[1]Chalmers, Gothenburg, Sweden; [2]Universidade de Lisboa, Lisbon, Portugal; [3]GSI, Darmstadt, Germany

Based on the TRLO [1] firmware for the VULOM [2], an enhanced digital trigger and experiment control has been developed and tested at the LAND/R^{3}B setup. The complete new system debuted late summer last year in about six weeks of production experiments operating reliably.

Trigger functionality

The original TRLO firmware replaces the trigger chain of logic matrix, trigger box, priority encoder, pattern unit and scalers. The new development retains this functionality, but reorganized to operate the entire FPGA with one 10 ns clock period instead of 2.5 ns for the trigger decisions. This delays the timing-critical master start signal by about 20 ns, becoming just comparable to the NIM-based LAND trigger, at 55 ns from detector trigger input to delivered master start. Saving resources, the revision also allows more functionality in the trigger decision path, mainly adjustable delay and stretch for trigger alignment.

The state-machine for event control houses the priority encoder and trigger pattern recording (detector triggers surviving trigger box downscale). It is augmented with pending triggers. A pending trigger will either be handled directly, or in case of dead-time, directly after the current event. The pending triggers are used to guarantee delivery of spill-on/off events, as well as calibration triggers at fixed rates. Previously, the latter required dead-time-dependent downscale factor adjustments at the NIM trigger boxes.

The trigger state machine is also able to operate in multi-event mode with large buffers for trigger patterns and times, as well as respecting the busy signal from converter modules. It has been carefully constructed to not allow trailing parts of detector trigger coincidences to make mis-timed master starts. All setup is controlled with VME registers.

General logics, monitoring and recording

In addition to the pure trigger-related logics, many general logic functions are implemented. All functions can select any function output as input via VME-controlled multiplexers. Front-panel inputs and signals from the trigger system are function outputs and vice versa. The functions include: pulsers (programmable frequency), logic matrix, downscale, gate-and-delay, edge-to-gate conversion (e.g. for spill mimic), and coincidences. Any module input can also be multiplexed to any output without clocking.

Auxillary information can be collected in many ways:

- Scalers, for the trigger signals, with selectable inputs, and on every signal source for debugging. Latched 32-bit counters, in a hybrid flip-flop / block RAM implementation using only 25 flip-flops per channel.
- Timer latches (latch global timer on a signal edge).
- Multi-entry buffer (RAM FIFO) for the timer-latches.
- Self-triggering soft-scope. Internal recording into a circular buffer, FIFO for zero-suppressed multi-trace output via block RAM.
- Input pattern latch (all multiplexer sources).
- Dead-time recording: duration and last release latch.

Trigger alignment

Before the detector trigger signals can be used to build physics triggers by coincidences, they must be aligned in time to account for different detector latencies and cable lengths. This was previously achieved by measurement of coincidences with an oscilloscope and adjustment of variable NIM delays. The delays are now furnished in 10 ns steps in the TRLO II. Measurements are performed with the internal multi-trace soft-scope, self-triggering on rotating coincidences, driven by a small acquisition loop on the read-out processor. The accumulated traces can then be analysed for average timing differences and thus presented to the user, who can reconfigure the trigger input delays.

Outlook

A time-stamp functionality (20 ns resolution) is implemented by sending the local 64-bit clock count serially over any output to another TRLO II module with the corresponding receiver. A handful of signals can also be multiplexed over the serial line with 10 μs latency.

TDC slopes can be calibrated by start and stop signals with random but known intervals. The start is issued by an asynchronuous VME strobe and the stop is generated a requested number of clock cycles later. A delay-line measures the sub-cycle location of the start signal.

As the TRIDI1 (trigger distribution) modules have the same internals as a VULOM, they can also be loaded with a TRLO II firmware. The local DAQ system can then be either a subsystem, or a stand-alone system, without requiring any recabling.

References

[1] J. Frühauf et al, “Trigger Logic for FOPI Experiment”, GSI Scientific Report 2008.

[2] J. Hoffman; VULOM4, VME Universal Logic Module http://www.gsi.de/informationen/wti/ee/elekt_entwicklung/vulom4_e.html

Evolution of a prototype silicon strip detector readout ASIC for the STS*

K. Kasinski[1#], R. Szczygiel[1], and P. Grybos[1]

[1]AGH University of Science and Technology, Krakow, Poland.

TOT01 prototype readout ASIC for the CBM STS detector has been manufactured and tested in 2010. Its purpose was to test the usability of the Time-over-Threshold method in this application[1,2].

The tests revealed a significant potential of the TOT architecture. It is able to provide low-noise, low-power and simple solution for energy measurement [3]. Since is possible to smoothly adjust the chip's noise vs. speed characteristic to meet the application specific requirements its performance has been presented for two arbitrary, opposite settings called "fast" and "slow". The table below summarizes the TOT01 ASIC performance.

GBW	1.2 GHz	**Power**	1.2 mW/ch
Gain	1600 [V/V]	**ENC** $_{\text{fast, Cdet=28pF}}$	700 e-
Gain	~13 mV/fC	**ENC** $_{\text{slow, Cdet=4pF}}$	162 e-

TOT02, an upgraded version of this ASIC has been submitted, fabricated and preliminarily tested. The chip consists of 16 channels, improved ToT-based CSA and discriminator in radhard layout and a digital back-end.

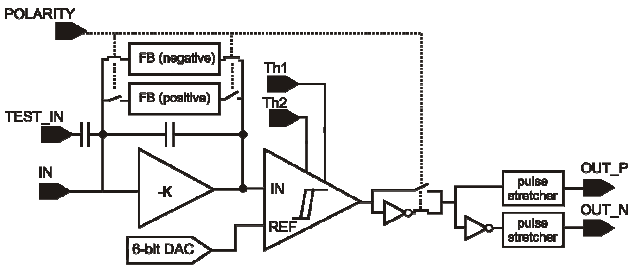

Figure 1: Analog part of the ASIC channel

Analog part contains enhanced charge sensitive amplifier (CSA) architecture (folded cascode with booster) and modified constant current, complementary discharge circuits. These changes were to minimize the pulse tail which for lower threshold caused energy resolution deterioration.

The CSA is followed by a discriminator supplied with a 6-bit DAC for the DC level spread correction. The pulse-stretchers added between the discriminator and the digital back-end prevent from short glitches which could corrupt the operation of the latches.

The digital back-end implements timestamp latches triggered by the discriminator output pulse edges, token ring and serializer. Each channel is supplied with two latches triggered by the consecutive edges of the discriminator. The timestamp value latched first is the event time while the difference between two latches represents the pulse length and should directly translate to the deposited energy.

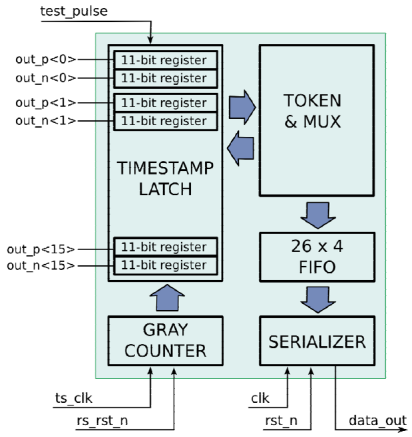

Figure 2: Digital back-end.

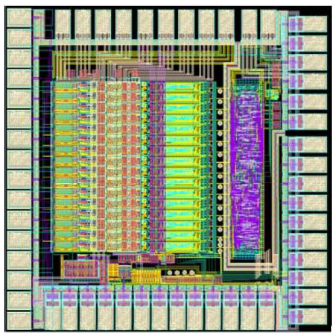

Figure 3: TOT02 ASIC layout.

The test setup of the TOT02 ASIC consists of the main test board incorporating independent power supply and biasing circuitry with many debugging features. The board supports both direct detector placement and remote detector connection through an ERNI connector (standard connector for STS detectors). The configuration and readout is performed by National Instruments DAQ card interfaced to the ASIC through fast level-translators for readout and shift registers for slow control.

The test are ongoing, we expect to receive the results soon.

References

[1] Kasinski K., Szczygiel R.: *Prototype readout ASIC for silicon strip detectors readout using Time-over-Threshold method.* CBM Progress Report 2009.

[2] Kasinski K., Szczygiel R., Grybos P.: *First test results of TOT01 ASIC prototype.* 15th CBM Collaboration Meeting, GSI, Darmstadt, 12-16 April 2010.

[3] Kasinski K., Szczygiel R., Grybos P.: *TOT01, a time-over-threshold based readout chip In 180nm CMOS technology for strip detectors.* 2011 *JINST* **6** C01026.

First High-Energy Collisions with the ALICE TRD Global Tracking Unit*

F. Rettig[†1,2], *S. Kirsch*[1,3], *D. Hutter*[2], *and V. Lindenstruth*[1]

[1]Frankfurt Institute for Advanced Studies, Goethe University Frankfurt, Germany; [2]Kirchhoff-Insitute for Physics, Heidelberg, Germany; [3]CERN, Geneva, Switzerland

The Transition Raditation Detector (TRD) of the ALICE experiment is designed to provide fast triggers based on the online reconstruction of charged particle tracks within approximately 6.5 μs after the collision. A total of 1.2 million analog channels for 540 readout drift chambers are processed by more than 65 500 multi-chip modules to find and parameterize short track segments. Via 1 080 optical detector links these track segments are transferred to the Global Tracking Unit (GTU, [1]), a system consisting of 109 FPGA-based dedicated processing nodes arranged in a three-layer hierarchy. In the lowest processing layer the GTU performs a full, three-dimensional online reconstruction of charged particle tracks with $p_t \geq 2$ GeV in less than 1.6 μs. Trigger algorithms for various signatures are then applied at the two higher layers. The GTU is also a central element in the TRD read-out chain, providing buffers for multiple events. In case an event successfully passed all trigger stages, the GTU forms the TRD readout data stream for subsequent transmission to the DAQ system.

Online Track Reconstruction and Trigger

During last years proton-proton and first pb-pb collision phases, the GTU provided highly reliable read-out operation for the TRD with seven supermodules installed at the experiment. A total of $1.2 \cdot 10^9$ events were recorded yielding more than 130 TBytes of data. During the shutdown phase at the end of the year, three new supermodules and their corresponding GTU segments were successfully put into operation.

Starting in mid-2010, the GTU provided online track reconstruction and track-based trigger algorithms for various signatures, like high-p_t e^-, e^-/e^+-pairs as well as jets (Fig. 1). With no application of TRD level-1 triggers planned in the past run period, all necessary data to comprehend trigger calculations and decisions were recorded in the raw data stream for subsequent offline analysis. Based on that, tuning of relevant front-end electronics parameters and a detailed trigger performance analysis is ongoing.

Multi-Event Buffering

Besides the developments related to fast triggering, one focus was to improve the highly reliable data transport and implement control logic capable of administering the buffering of multiple events (MEB)[2]. The approach chosen features a hardware/software co-design with decicated

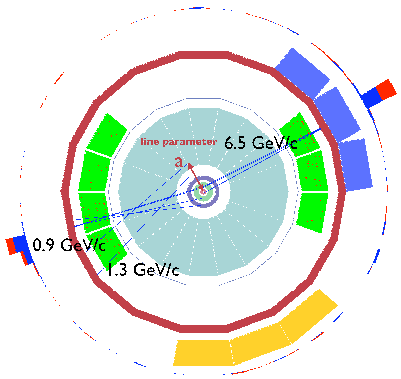

Figure 1: Jet event in a proton-proton collision triggered by the Global Tracking Unit. The line parameter a is used as a measure of transverse momentum with $\Delta p_t / p_t < 1\%$.

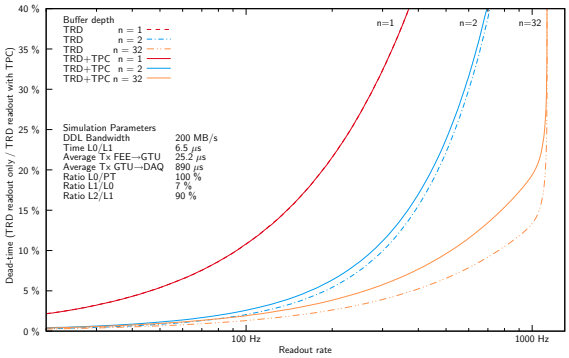

Figure 2: Detector dead-time reduction by MEB (pb-pb).

hardware entities to generate the required control signals. Simultanously, one of the embedded CPUs supervises the operation of GTU segment and can interact to resolve abnormal, erroneous situations. MEB simulations (Fig. 2) illustrate the benefit in dead-time reduction, especially in pb-pb collisions.

References

[1] S. Kirsch, et al., An FPGA-based high-speed, low-latency processing system for high-energy physics, IEEE Proc. Intl. Conf. on Field Programmable Logic and Applications (FPL), Milano, 08-2010, (2010)

[2] D. Hutter, Multi-Event Buffering und HDL-Simulationsframework für die Global Tracking Unit des ALICE-Übergangsstrahlungsdetektors, Diploma thesis, (2010)

[3] J. de Cuveland, A track reconstructing low latency trigger processor for high-energy physics, Dissertation, (2009)

* Work supported by BMBF FSP201

† {rettig,kirsch}@compeng.uni-frankfurt.de

Further Enhancements of the Front-End-Electronics Communication Software*

R. Keidel[1], *M. Bittorf*[1], *and E.S. Conner*[1]
[1]ZTT, University of Applied Sciences, Germany

The InterComLayer (ICL) of the Front-End-Electronics communication (FeeCom) chain has been refactored and enhanced to adapt to the requirements which have arisen during daily usage by the pertinent detectors in ALICE. A major focus has been set on the implementation of a dynamic watch dog time out system, bug fixing and full support of all log channels.

Software Architecture

The FeeCom chain consists of three layers: the Fed-Client as dedicated DIM module in the PVSS on the supervisory layer, the ICL located on the control layer and the FeeServers connected to the Front-End-Electronics (FEE) operating on the field devices.

The ICL acts as distributor and collector for the system. It distributes commands issued from the supervisory layer to the FeeServers running on the field layer and collects their data and answers before relaying them further to the PVSS. Preparation of command data inside the ICL is achieved via access to the Configuration Database and detector-specific CommandCoders (CoCo) of the respective detectors. Data exchange is performed over well defined APIs (Application Programmers Interface; FED-API (Front-End-Device-API), FEE-API, CoCo-API) [1] [2]. Data transport between the different layers employs Distributed Information Management (DIM) as the underlying protocol [3].

Refactorings and Implementations

The overall performance has been improved by the consequent usage of String handling frameworks in combination with the logging facility. The log level handling has been debugged and allows now to adjust the amount of log messages, which are offered on several DIM channels. All DIM messages are throttled by a frequency adjustable central barrier to avoid message flooding and prevent therefor effectively the breakdown of listening process visualisation systems.

The message routing of watch dog time out alerts has been changed. The upcoming concurrency issues could be solved by the implementation of a dedicated "actor pattern" architecture (see figure 1). A positive side effect is the performance upscaling feature with the number of available hardware cores of the hosting system (see figure 2).

* Work supported by GSI; Vorhaben: ALICE Softwareanwendung zur Modellierung von Prozesssteuerungsschnittstellen / EPICS; WOKEI.

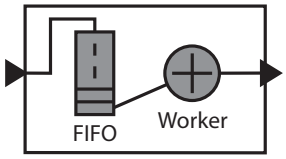

Figure 1: Actor Pattern: a thread safe FIFO buffer accepts incoming immutable messages. A worker thread takes a message from the buffer and sends the message via the DIM framework. The worker thread has no monitor acquired during this sending procedure. This prevents the occurrence of deadlocks.

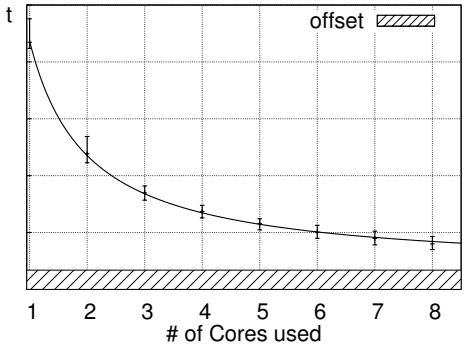

Figure 2: Performance scaling of the actor design with the number of available hardware cores. Besides the scheduling overhead for the threads of the actors is a reciprocal correlation between the number of cores and the performance test duration observed.

References

[1] R. Keidel, et al: Enhancements of the Front-End-Electronics Communication Software, GSI Scientific Report 2009 (Instruments-Methods-42), GSI Report 2010-1, June 2010, Editor: K. Große

[2] S. Bablok: Heterogeneous Distributed Calibration Framework for the High Level Trigger in ALICE, PhD Thesis, University of Bergen (Norway), printed by Allkopi, February 2009, ISBN: 978-82-308-0740-8

[3] C. Gaspar, M. Doenszelmann, Ph. Charpentier: DIM, a Portable, Light Weight Package for Information Publishing, Data Transfer and Interprocess Communication, Presented at: International Conference on Computing in High Energy and Nuclear Physics 2000, Padova (Italy), February 2000.

TRIPLEX, an Upgrade for the TACQUILA System

K. Koch, H. Simon, C. Caesar

GSI, Darmstadt, Germany

Introduction

Due to the fact that the LAND TOF wall electronics are not very reliable after many years and various components are out of maintenance, a new timing measurement setup is needed. For that reason a modified version of a current in-house development (TACQUILA [1]) for timing measurements comes into consideration for replacement.

For remote parameterization of this new LAND TOF wall timing measurement setup, new add-on electronics for the TACQUILA system has been developed (TRIPLEX)

A typical TACQUILA system consists of a timing digitizing card, a charge measurement piggy back and an amplification board. Additionally an intermediate card can be used for further purposes as double-hit timing or time over threshold measurements [2].

Requirements

The requirements for a remote control board are e.g. determination of the thresholds, preparing of an 'or' signal as well as an analogue sum and multiplicity output. Above all, a pulser should be integrated on board.

Further on, the boards should be cascadable for incoming and out coming signals and optional for the control path. An overview is shown in figure 1.

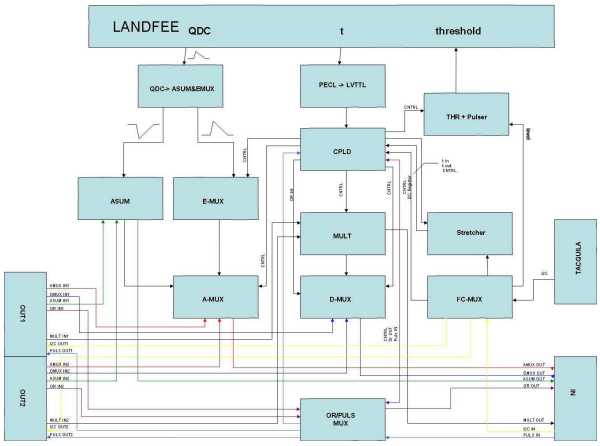

Figure 1: Block diagram of TRIPLEX.

Description

The interconnection between this cards are realised by differential signals to suppress cross talk between lines and noise pick up along the signal paths. On board all signals are processed in single ended mode to have a larger variety of needed electronic devices.

One of the main parts is a fast CPLD that operates as a routing device with logic functions. This offers the opportunity to a high integration level and flexibility.

An I^2C bus with multiplexer functionality enables among other things a single channel monitoring of the incoming signals at the end of the cascaded chain. A Photograph of TRIPLEX is shown in figure 2.

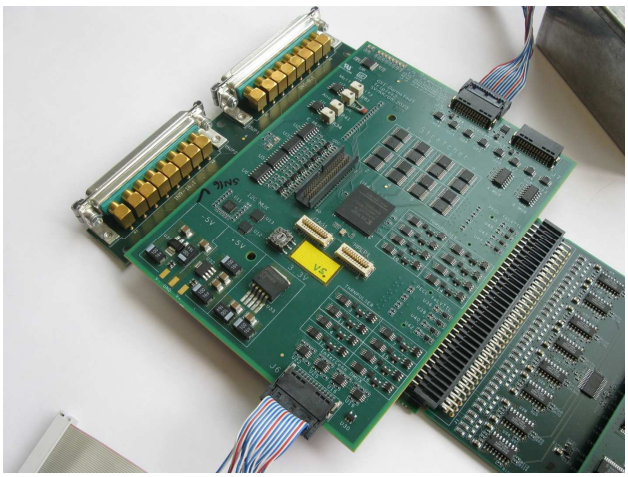

Figure 2: A TRIPLEX board mounted on top of an amplification board (LANDFEE) of the TACQUILA system.

First results and outlook

In a beam time at the end of 2010 five systems have been successfully deployed in the LAND environment. The analysis of the data shows good results and the handling of the system was reliable. To have an optimised system, only some minor changes in the TRIPLEX supporting amplification board (LANDFEE) are necessary.

References

[1] K.Koch, H.Hardel, R.Schulze, E.Badura and J.Hoffmann, “A New Multi Channel Front-End Board for TOF Experiments with Excellent Timing Resolution”, GSI Scientific Report, p. 231, 2003, http://www.gsi.de/informationen/wti/library/scientificreport2004/PAPERS/INSTMETH-12.pdf.

[2] K.Koch, “High Resolution Double-Hit Timing and Time Over Threshold Measurement Feasibility for the TACQUILA System”, GSI Scientific Report, p. 255, 2007, http://www.gsi.de/informationen/wti/library/scientificreport2007/PAPERS/INSTRUMENTS-METHODS-49.pdf.

The control system for the new 100 mm target wheel at TASCA

T. Torres[1], E. Jäger[1] and J.Krier[1]

[1]GSI Helmholtzzentrum für Schwerionenforschung GmbH, Darmstadt, Germany;

A new target wheel system for the gas-filled separator TASCA with a 100 - mm diameter target wheel was designed and built. For this, a new motor control system was developed, basically consisting of a stepper motor [1], a stepper motor terminal [2], a control PC [2] and I/O terminals [2] for the input and output signals for the control loop.

The stepper motor terminal [2] is responsible to drive the motor in a controlled way, using a ramp function, up to the required frequency of 2250 revolutions per minute (rpm). The macro pulse signal (50 Hz HEAG signal) is connected to an input terminal and is used to synchronize the motor frequency to the HEAG signal. The exact wheel position (or more precisely the target position during the beam irradiation) is controlled and regulated using the master pulse (beam signal) as an input and the feedback of the wheel position at this time. To determine the wheel position during the 5 - ms long macropulse signal, (corresponding to the beam pulse) an optical position detection system was implemented. The system uses optical fiber sensors composed of the fiber units and the amplifier units [3]. Holes in the target wheel allow the laser to shine through when the wheel is at an exactly defined position: one set of holes generates a signal every 90° and the other one every 360°. These signals are connected to input terminals and processed for the control loop.

The implemented software [2] control system is based on the design and experience won with a similar system employing a large target wheel containing eight target segments used earlier at TASCA. It was designed and developed using the function principle of the finite state machine model, i.e., with the process being divided into states where each state has its input and output conditions. According to this, the transition to the next state (or if necessary to a previous state) will be given. Each state performs one or more functions required from the system. There is a principal task where this state is running and the additional tasks or subprograms (subroutines) which are called on each state as far as necessary. Defined states are implemented where the user has the possibility to stop the wheel movement; in this case the system will return to the initial state. Control functions are included to detect if there is an error present or if a movement function reports an error. Similar to the stop state, the error state is programmed to stop the axis movement in a very slow way with a ramp function, in order to protect the targets.

The setups required for the wheel movement like motor velocity, acceleration, beam cycle time, offset position from the master signal are preset such that the user is not required to enter these values.

As the used motor frequency of 2250 rpm is outside of the range of conventional stepper motor applications, there is the possibility that the motor fails to follow the rotation field and ends in a standing situation. Therefore a mechanism to detect the motor rotation or standing condition using the signal of the optical sensor system was implemented.

A user interface, divided into two areas was developed; in one window, the “operation window”, the user is allowed to start or stop the movement and gets feedback information like the actual wheel movement status, the frequency of the wheel, if it is synchronous with the beam structure and error messages. The other one, the “service window”, allows the user to change parameters for the synchronization of the master pulse to the target and includes other additional functions for improvements on the system development and maintenance.

The system was successfully tested with 5.5 MeV/u ^{24}Mg beam, in November 2010. Figure 1 shows an irradiated target wheel containing four tape targets to visualize the beam position. The beam hit each of the four targets at the correct position.

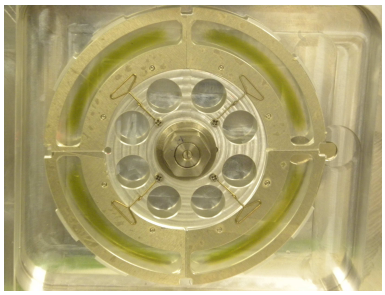

Figure 1: The new TASCA target wheel after a test irradiation with ^{24}Mg beam.

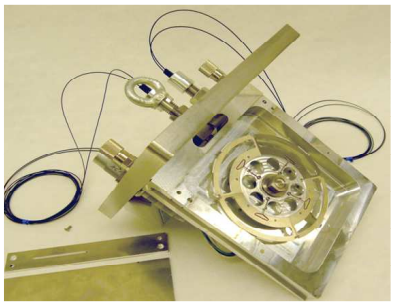

Figure 2: The complete assembly of the 100 mm target wheel in its cassette.

References

[1] High torque stepper motor ST5709X2508, Nanotec, www.nanotec.com

[2] Bus Terminals and TwinCAT software, Beckhoff, www.beckhoff.com

[3] Optical fiber sensors, OMRON, www.omron.com

A 32-Channel High Resolution Time-to-Digital Converter (TDC) in a Lattice ECP2M Field-Programmable-Gate-Array (FPGA)*†

C. Ugur‡[1], *E. Bayer*[2], *N. Kurz*[1], *and M. Traxler*[1]
[1]GSI, Darmstadt, Germany; [2]Goethe-Universität Frankfurt, Frankfurt, Germany

The development of the TDC on Xilinx Virtex-4 FPGA [1] has been continued. The dead-time could be decreased to 15 ns by pipelining. In order to test the design in experiments it was moved to the VULOM-4 boards and adapted to triggered systems. Since the differential timing signals were converted to single ended signals on the VULOM-4 board before being fed into the FPGA, a slight decrease in resolution (14 ps RMS) was observed in laboratory measurements between some channels. For this reason a new version of the VULOM-4 board is prepared with shorter single ended signal lines.

First detector measurement data were collected with the CBM setup by using 32 channels on two VULOM-4 boards. The analysis of the collected data is still ongoing. In order to explore the consequences of using a different FPGA architecture and thus increasing the knowledge of TDC designs in FPGAs the existing TDC design was adapted to the Lattice ECP2M FPGA.

A 32-channel TDC was implemented on a Lattice ECP2M. The fine time interval calculations were achieved by Tapped-Delay-Line method using dedicated carry-chain lines. A Multi-bit adder structure was used in order to form the delay line. Each channel has an individual fine counter, an encoder and a First-In-First-Out memory block (FIFO). A common coarse counter generates time flags for the time information of each conversion. The time-to-digital conversion and the data read-out were undertaken at 200 MHz and 100 MHz clock frequency respectively.

The time interval between the rising edge of a trigger signal and the rising edge of the next system clock was measured at the fine counter. The result generated by the fine counter in thermometer code [2] was converted to a binary code in the encoder and stored in the FIFO with a time stamp generated by the common coarse counter as well as a channel number. The data was calibrated offline by using the bin-by-bin calibration method [3].

In our measurements we used two channels in order to measure the time difference between two triggers. The triggers were generated by Tektronix Data Timing Generator DTG5078. Sets of measurements with different time differences were done in order to test the stability and the consistency of the TDC.

The time difference was increased logarithmically starting from zero up to one microsecond in order to observe the effects on the measured mean value and RMS. Figure 1 shows the change of the mean value with the increasing time difference in logarithmic scale. The RMS calculated for the time differences for up to two clock periods (10 ns) was 15 ps. As one transition was used in order to determine the time measurements, the time resolution was also 15 ps.

With rising time differences the resolution of the TDC decreased and reached 35 ps for 1 us time difference. This deviation is induced by the PLL used as time reference and it will be removed from the future design. Figure 2 shows the measurement results obtained within one system clock cycle with 100 ps increase.

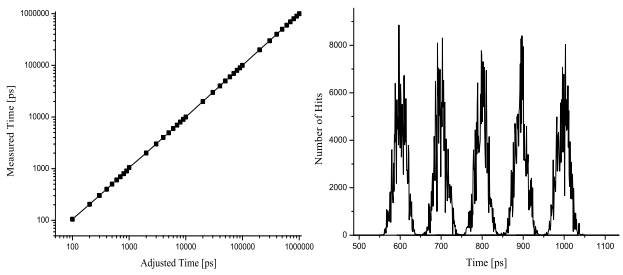

Figure 1: (a) The change of mean value over logarithmically increasing time difference (After channel offsets were cancelled), (b) Five time differences with 100 ps difference.

In order to observe the temperature dependency of the TDC, a series of measurements between 48°C and 80°C were done. The increasing temperature caused malformation of the calibration look-up-table. In parallel RMS value got worse. However, updating the calibration look-up-table overcame this problem.

Some of the important parameters of the designed TDC are as follows: Maximum bin width 48 ps, average bin width 20 ps, highest time resolution 15 ps, maximum conversion time 45 ns, dead time 30 ns, delay chain length 288.

The current results suggest that the designed TDC works very well in different FPGA architectures, e.g. Lattice ECP2M FPGA and Xilinx Virtex-4. Further tests will be done on the EXPLODER board [4].

References

[1] E. Bayer and M. Traxler, GSI Scientific Report 2009, p.325.

[2] C. Favi and E. Charbon, IEEE ISFPGA, February 2009.

[3] J. Wu and Z. Sh, IEEE Nuclear Science Symposium Conference, 19-25 Oct. 2008.

[4] http://www.gsi.de/informationen/wti/ee/elekt_entwicklung/exploder.html.

* Work supported by EU grant 515876.

† This work was supported by the Hessian LOEWE initiative through the Helmholtz International Center for FAIR (HIC for FAIR).

‡ c.ugur@gsi.de

Low Noise Preamplifier ASIC for the PANDA EMC

Peter Wieczorek[1] *and Holger Flemming*[1]
[1]GSI - Experiment Electronics, Darmstadt, Germany

Introduction

For the electromagnetic calorimeter of the PANDA - Experiment the ASIC - Design - Group of the GSI - Experiment - Electronics is developing an integrated charge sensitive preamplifier and shaper optimized for the readout of avalanche photo diodes with large detector capacitance and high event rates.

The described APFEL 1.3 - ASIC is the third iteration of the ongoing development. Based on the good analog performance of the previous ASIC which was presented in [1] only some few changes were required. The main focus of APFEL 1.3 was the revised configurability of the ASIC for the proper operation over a wide temperature range.

Conceptual Overview

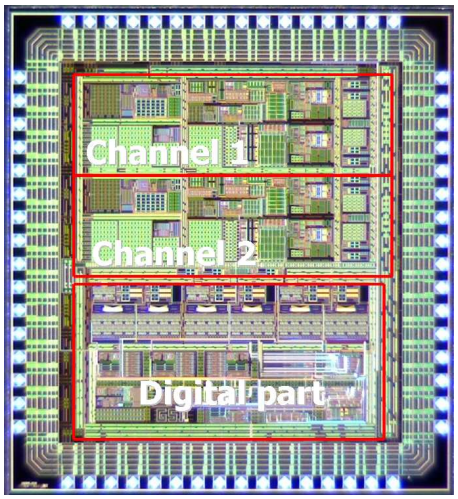

Figure 1: Die microphotograph of the APFEL 1.3 - ASIC.

The APFEL - ASIC shown in figure 1 has two equivalent analog channels each consisting of a charge sensitive amplifier, a shaper stage and differential output drivers. After the first integrator stage the signal path is splitted into two subpaths. One of these subpaths has an amplification of 32 in comparison to the other to get larger output signals in the low energy range which are less sensitive to interferences by pick up noise outside the ASIC.

A consequence of the high amplification in the analog chain is a high temperature dependency on the output DC voltages and a change of the operating points of the amplifiers. To solve this adjustable voltage references are implemented.

As references voltage DACs are used. To get the right DAC settings for a given temperature an autocalibration unit is implemented on chip. This autocalibration adjusts the DC voltages and make sure that the readout path can cover the whole dynamic range for the prevalent temperature.

For monitoring purposes of the electronics a testpulser is implemented which injects charge at the input of the preamplifier. The serial interface allows to write and read the DAC settings and to trigger the autocalibration process or the testpulser. A detailed description of the ASIC is given in [2].

Measured Results

The noise measurements for different temperatures and detector capacitances are plotted in figure 2.

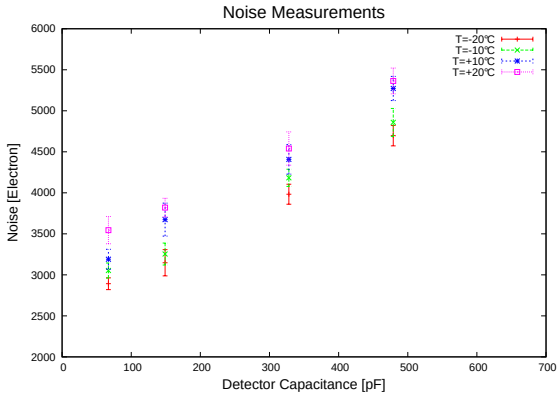

Figure 2: Results of the noise measurements.

The characterization of the third ASIC iteration at a temperature of $T = -20^\circ\,C$ and a detector capacitance of 300 pF results in an equivalent noise charge of $ENC = (3906 \pm 117)\,e^-$ (or 0.62 fC) and a maximum input charge of 6.3 pC. Therefore a dynamic range of over 10 000 follows. The peaking time of the shaped signal was measured to $\tau_p = (248 \pm 3)$ ns. The event rate independent power consumption of one channel is $P = (56.5 \pm 0.5)$ mW.

Conclusion

The measured results show that the noise performance of the ASIC fulfills the specification given by the PANDA collaboration. Especially the results for the equivalent noise charge are distinguished as well as the large dynamic range.

References

[1] P. Wieczorek and H. Flemming, “Low Noise Preamplifier ASIC for the PANDA EMC”, GSI Scientific Report 2006, June 2007 p. 4.

[2] P. Wieczorek and H. Flemming, “Low Noise Preamplifier ASIC for the PANDA EMC”, CR IEEE Nuclear Science Symposium, 2010

First System Tests of an Integrated Preamplifier for the PANDA EMC

Peter Wieczorek[1], *Jörn Adamczewski - Musch*[1], *Sergey Linev*[1], *and Sven Löchner*[1]
[1]GSI - Experiment Electronics, Darmstadt, Germany

Introduction

The first system tests of the APFEL - ASIC for the PANDA Experiment with tagged photons took place at MAMI, Mainz. Therefore the at GSI developed readout and data acquisition system was used. The visualization and data analysis was done with the GSI Objected Oriented On - line Off - line system (Go4) [1].

Setup

For the system tests a matrix of 16 lead tungstate crystals was build up as they will be used in the electromagnetic calorimeter of the PANDA Experiment. Each crystal was connected to one avalanche photo diode which was read out by one channel of the APFEL - ASIC. The used readout and data acquisition system is presented in [2]. All measurements were done at a temperature of T= $-20°$ C.

For the data taking at MAMI 14 available tagger energies between 20 MeV and 420 MeV were chosen and used as a global trigger for the readout system. In addition the tagger information was included in the data stream file with the transient information of the measured data.

Transient Analysis

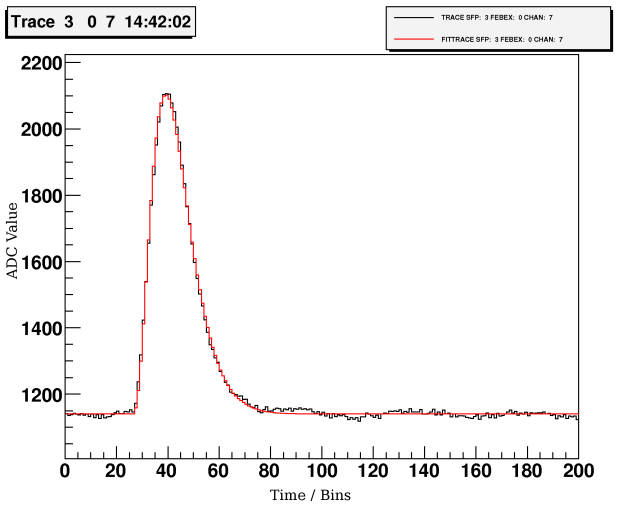

Figure 1: Transient plot for a detected photon.

In figure 1 a stored transient for a detected photon is shown. To extract energy and time information the well known transfer function of the APFEL - ASIC is fitted to the data points.

The energy and time information of the photon is calculated from the peak maximum of the pulse. The energy spectra was fitted afterwards with the Novosibirsk - function.

Results

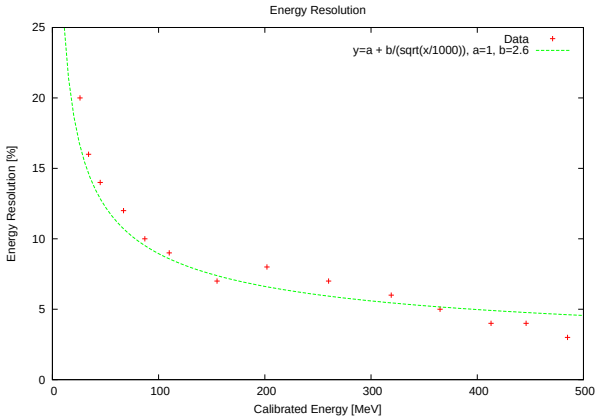

Figure 2: Results of the energy measurements at MAMI.

The analysis of the data is mainly focused on the energy resolution of the readout system. Figure 2 shows the results of the analyzed energy resolution. The used fit is described by the equation

$$\frac{\sigma}{E}[\%] = 1\% \oplus \frac{2.6\%}{\sqrt{E(GeV)}}. \qquad (1)$$

The calculated time resolution for the complete readout system is better than 12 ns.

Summary

The reached energy resolution is 30 % worse than the requirements of the PANDA Experiment. To improve the results the connection between APFEL - ASIC and FEBEX - ADCs as well as the shielding of the setup is under study. Also the use of two APDs for each crystal promises a significant improvement. In parallel new beam time measurements with the matrix at higher energies are planned.

References

[1] J. Adamczewski - Musch, S. Linev, GSI: http : //go4.gsi.de

[2] P. Wieczorek et. al, GSI “Readout and Data Acquisition System for Large Area Avalanche Photo Diodes”, GSI Scientific Report 2010

Readout and Data Acquisition System for Large Area Avalanche Photo Diodes

Peter Wieczorek[1], *Jörn Adamczewski - Musch*[1], *Jan Hoffmann*[1], *Nikolaus Kurz*[1], *Sergey Linev*[1], *Sven Löchner*[1], *Shizu Minami*[1], *and Wolfgang Ott*[1]

[1]GSI - Experiment Electronics, Darmstadt, Germany

Introduction

Motivated by pending tests of the APFEL - ASIC [1] for the electromagnetic calorimeter of the PANDA Experiment a readout and data acquisition system was developed by the GSI - Experiment - Electronic department which is also applicable for other detectors with large sensor capacitances. The readout chain consists of the charge sensitive preamplifier and shaper ASIC - APFEL, a digitiser board called FEBEX and a PC based data acquisition system (MBS) [3]. For the visualization and data analysis the GSI Objected Oriented On - line Off - line system (Go4) was used.

Preamplifier and Shaper ASIC APFEL

The APFEL - ASIC is optimized for the readout of large area avalanche photo diodes with high capacitances and event rates up to 350 kHz. On chip two equivalent analog channels are implemented. Each channel consists of a charge sensitive preamplifier, a shaper stage and two differential output drivers. For operating the ASIC in a wide temperature range programmable voltage references are implemented on chip. An overview of the ASIC is given in [1].

FEBEX - Board

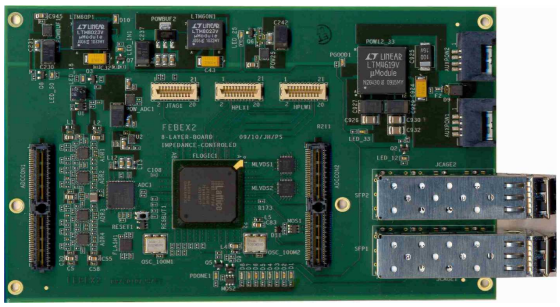

Figure 1: Picture of the FEBEX - board.

As digitizer the 8 channel FEBEX - board [2] shown in figure 1 is used. The input side contains 8 differential analog inputs which are connected via input buffers to ADCs. These buffers allows an ohmic adjustment. The used ADCs have an input range of $\pm$ 1 V with a resolution of 12 bit and a sampling rate of 65 MS/s each. The implemented FPGA manages the data transfer and it is forseen for pulse shape analysis and feature extraction. The output data transfer is realized with an optical link [2].

PC Based DAQ

As receiver for the data communication a PCI Express card named PEXOR was used which was developed to connect front end boards like FEBEX to standard PCs. The GSI Multi Branch System (MBS) was used as DAQ - Software.

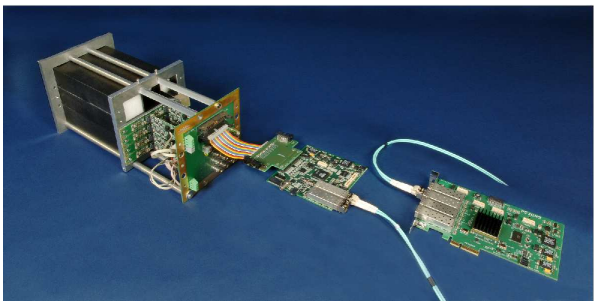

Figure 2: Picture of the matrix readout chain.

Figure 2 shows the complete setup. All presented readout electronics components were developed at the GSI - Experiment - Electronics department.

Data Analysis

The visualization and the data analysis were done with GSI Objected Oriented On - line Off - line system (Go4). The Object-Oriented system Go4 based on ROOT with extensions for the specific requirements of the low and medium energy nuclear and atomic physics experiments [4].

Summary

A full readout system for pre - amplification to On - and Offline analysis was presented which was successfully used in a system test for the PANDA - EMC [5].

References

[1] P. Wieczorek and H. Flemming, “Low Noise Preamplifier ASIC for the PANDA EMC”, GSI Scientific Report 2010

[2] J. Hoffmann, GSI: http : //www.gsi.de/ informationen/wti/ee/elekt_entwicklung/febex.html

[3] N. Kurz, GSI: http : //daq.gsi.de

[4] J. Adamczewski - Musch, S. Linev, GSI: http : //go4.gsi.de

[5] P. Wieczorek et. al., GSI “First System Tests of an Integrated Preamplifier for the PANDA EMC”, GSI Scientific Report 2010

Status of the FairRoot simulation and analysis framework

M. Al-Turany, D. Bertini, R. Karabowicz, and F. Uhlig
GSI, Darmstadt, Germany

The FairRoot framework [1], is the simulation, reconstruction and data analysis framework for the FAIR experiments. It is based on ROOT [2], and the Virtual Monte-Carlo (VMC) interface [3]. It includes core services for detector simulations and offline analysis. The framework, is designed to optimize the accessibility for beginners and developers, to be flexible (i.e. able to cope with future developments), and to enhance synergy between the different physics experiments within the FAIR project.

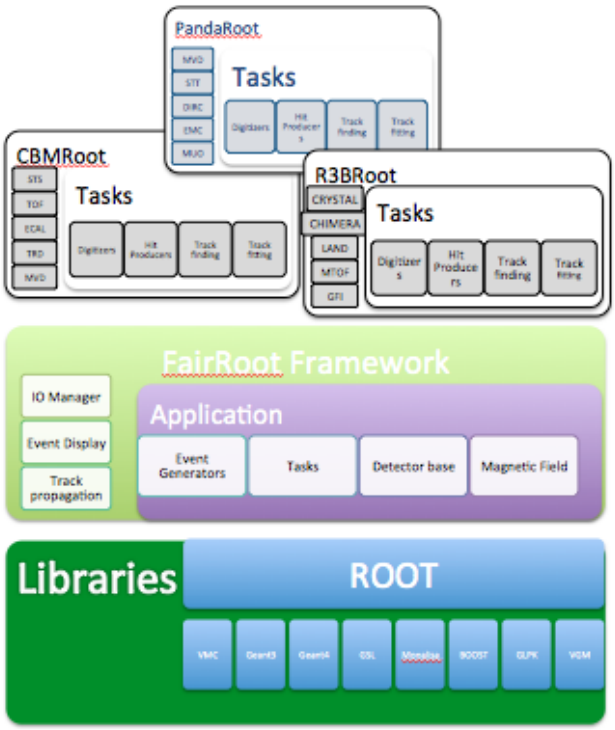

Figure 1: FairRoot at different experiments

FairRoot supports many systems and compilers. The nightly build system compiles and tests the status of the project on many different platforms. The accumulated results from each of these platforms are send to a web server. The results are displayed on dashboards where all developers can immediately see if there is any problem on any of the different systems. These tasks are achieved by using the open source tools CMake, CTest and CDash [4] with a set of macros that define certain tests.

The different implementations of FairRoot for the different experiments are shown in Figure 1. The base classes and general packages are kept in FairRoot to make them available for all experiments.

Since the last year, R3B experiment at FAIR [5] started using FairRoot. Examples of some of the implemented parts of R3B experiments are shown in Figure 2.

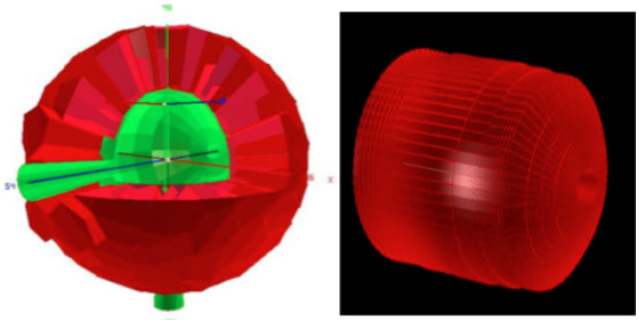

Figure 2: Geometry of crystal ball and califa detectors in R3BRoot

Among the new developments within the FairRoot framework are a global track finder for the PANDA experiment [6] and a new Database interface for detector parameters and their variation in time[7]. Usage of GPUs within FairRoot is also described in [8].

References

[1] FairRoot: http://fairroot.gsi.de.

[2] R. Brun and F. Rademakers. Root - an object oriented data analysis framework. *Nuclear Instruments and Methods in Physics Research A*, 389:81–86, Sep. 1997.

[3] R. Brun, F. Carminati, I. Hrivnacova, and A. Morsch. Virtual Monte-Carlo. In *Computing in High Energy and Nuclear Physics*, pages 24–28, La Jolla, California, 2003.

[4] I. Kitware. Cmake: http://www.cmake.org.

[5] R3B http://www.gsi.de/fair/experiments/NUSTAR/R3b.html

[6] R. Karabowicz, Global Track Finder for PANDA experiment, GSI report 2010.

[7] D. Bertini, Database support within R3BRoot, GSI report 2010

[8] M. Al-Turany, Runge-Kutta algorithm for track propagation on GPUs, GSI report 2010

Software Development Infrastructure for the FAIR Experiments

F. Uhlig[1]
[1]GSI, Darmstadt, Germany

Introduction

Beside the framework itself the FairRoot core team also provides some software development tools for the experimental groups using FairRoot as base for their own developments. This tools should help the developers to concentrate on his main topic, the development of the experiment specific simulation and analysis software, which includes also the independence of a specific code development tool. Each user can work with the tool he is used to. The tools used by the developers ranges from a simple editor like *vi* to IDE (Integrated Development Environments) like *XCode*. The CMake [1,2] based build system will created the native build files for each environment out of simple configuration files which are stored in a portable text format.

The main components of the software development infrastructure are the source code repository and the test and build system. The so called software testing server is used to store and view the information produced by instances of the test and build system. The project management software provides a web interface to the source code repository, a bug tracking, and a wiki system which are tightly integrated. This makes it for example possible to link bug tickets directly to the problem in the code, which allows the user to move with one click in the web browser from the description of a problem to the erroneous code block.

Some components will described in more detail below. A detailed description of most of the components can be found at [3].

Source Code Revision Control System

As revision control system we use Subversion (SVN) [4] which is the de facto standard for central revision control systems. The main SVN repository at GSI hosts beside the FairRoot framework also the source code of all supported experiments. This somewhat complicated repository structure has some advantages. First of all it is easily possible to couple the experiment specific code with the base framework without having the need to copy the code of the FairRoot framework. The base framework is included to the experiment specific code (CbmRoot, PandaRoot etc.) as external packages. This setup is completely transparent for the user so he will not see that some of the code comes from a different repository. Another benefit of this SVN setup for the experiments is that we can provide features like continuous integration and backup of the source code on every commit to the repository. This support is triggered by the repository itself.

Project Management

We use trac [5] as project management software which combines the advantages of a wiki and a bug tracking system with a powerful web front end to our subversion repository. Any of these tools alone is very useful and may be even needed to manage a larger software project but the tight connection of these tools under one hood even enhances the value of the single tools. All tools use a wiki markup language that allows to easily create hyperlinks. This simplifies the connection from a bug report to a line of code in a specific revision of the software or make it possible to create a hyperlink from the commit message to a closed feature request.

The source code browser allows to navigate in the source tree, check older revisions or commit messages. This includes also as diff-like comparison between different code revisions.

The issue tracking system is absolutely necessary to keep track of the development process. This includes also the ability to report software problems or request new features in a well defined and traceable way. I also makes sure that the request is assigned to the correct developer.

Trac also allows to define milestones which define states of the project like a stable version or the implementation of a feature. The tickets can be assigned to such a milestone and the roadmap shows this milestones together with the open and closed tickets and by this means shows the progress towards the milestone. The timeline shows all events like new commits to the repository or new tickets in the project ordered in time.

The wiki allows to create and organize a collection of linked information without much afford. Due to the easy creation of cross links the complete system becomes a valuable source of Information. If there are still features missing they can be added using a plugin mechanism. There are already many plugins like support for other version control systems or a spam filter available.

References

[1] K. Martin and B. Hoffmann. Mastering CMake, A Cross-Platform Build System, Kitware Inc., 2007

[2] CMake: http://www.cmake.org

[3] F. Uhlig and M. Al-Turany, “Monitoring the software quality in FairRoot”, in proceedings of ”13th International Workshop on Advanced Computing and Analysis Techniques in Physics Research”, PoS(ACAT2010)043

[4] TRAC: http://trac.edgewall.org/

[5] SVN: http://subversion.apache.org/

Runge-Kutta algorithm for track propagation on GPUs

M. Al-Turany
GSI, Darmstadt, Germany

In the last few years, the graphics processor units (GPUs) have moved from the traditional fixed-function 3D graphics pipeline toward a flexible general-purpose computational engine. With the NVIDIA Compute Unified Device Architecture (CUDA), one can get orders-of-magnitude performance increases over standard multi-core processors, while programming with a high-level language such as C and C++. Track parameter propagation has often been handled by the Runge-Kutta-Nystroem method [1], which is designed to solve second-order differential equations, such as the equation of motion of a particle in a magnetic field. The basic idea of this method is to divide the integration interval into steps and solve these independently. The Geant3 [2] algorithm based on Runge-Kutta method for solving the kinematic equations of charged particles in a magnetic field was ported to CUDA. The algorithm itself is hardly parallelizable, however, one can propagate all tracks in an event in parallel [4]. However, the major problem for parallelization of track propagation is the usage of the field map. Field maps are typically used as lockup tables with some interpolation algorithms for values between the measured (or calculated) points of the table.

Field map in Texture memory

Field maps are typically used as look up tables with some interpolation algorithm to give the field value between the points. The distance between the points is usually chosen so that a linear interpolation is accurate enough to give reasonable values for the field. In this work the dipole field from the PANDA [3] experiment was used. The field map (three dimensional array) was bound to the texture memory of the device, where the field values are accessible from all threads in the grid. Moreover, the linear interpolation of the field is done by a dedicated hardware [5].

In this work we tried to test different hardware with different numbers of cores in order to investigate also the scalability of the code in this situation. The specification of the hardware (GPU devices) used in this work are summarized in table 1.

To make the test, 1 GeV protons where generated and send with different starting angles through the field. Different events where generated by changing the number of protons per event. The tracks (protons) in each event where propagated at once through the dipole field (1.5 meter distance between starting and final plane). The gain in performance for different cards and events is summarized in table 2. The gain was calculated by dividing the CPU time over the GPU time.

Card	GeForce 8800 GT	Tesla C1060	Fermi GTX 480
CUDA Cores	112	240	480
Memory (MB)	512	4096	1536
Freq. (GHz)	1.5	1.3	1.4
Max. No. of threads	10752	30720	23040
Max Power Consumption (W)	105	200	250

Table 1: Hardware used

Track/Event	GeForce 8800 GT	Tesla C1060	Fermi GTX 480
10	3.5	6	13
50	11	28	52
100	12.3	47	84
500	18.5	80	138
1000	21	111	161
2000	21	137	171

Table 2: Gain in performance for different cards

Conclusion

CUDA permits working with familiar programming concepts while developing software that can run on a GPU. One has to choose carefully on which level the parallelization should take place and how to divide the data into small chunks for distribution among the thread processors (GPUs). Finally understanding the different memory regions of the GPU is also crucial for getting better performance and help in simplifying some problems.

References

[1] Handbook Nat. Bur. Of Standards, procedure 25.5.20

[2] CERN, Geneva, Switzerland. *GEANT – Detector Description and Simulation Tool*, march 1995 edition, 1993.

[3] J.G. Messchendorp, Strong interaction studies with PANDA. http://arxiv.org/abs/1001.0272v1

[4] M. Al-Turany and F. Uhlig Applying CUDA Computing Model To Event Reconstruction Software PoS(ACAT2010)014

[5] Nvidia. *NVIDIA CUDA Programming Guide*, 2.3.1 edition, 8 2009.

ALICE TPC Tracking on GPU for Pb-Pb Run in December 2010

D. Rohr[1]

[1]Frankfurt Institute for advanced Studies, Frankfurt, Germany

GPU Tracking

A fast online tracker based on a cellular automation principle and the Kalman filter was developed for the ALICE HLT [1]. The tracker was ported to run on NVIDIA GTX295 GPUs [2]. A dynamic scheduler ensured good utilization of the GPU. On top of that, the introduction of a pipeline allowed to process the tracking on the GPU, the initialization on the CPU, and the DMA transfer in parallel. In 2010 the new Fermi GPU generation was released. For expansion and compatibility reasons the tracker was adapted and optimized for the Fermi architecture.

Commisioning

34 compute nodes equipped with GTX480 GPUs were installed in fall 2010 at the ALICE HLT. The GPU tracker was commissioned and tested during the Pb-Pb run in December. Due to reduced luminosity it was not necessary to process the entire tracking on the GPU. Instead, the run was used to test the GPU tracker in the HLT framework. All tests were successful and the tracker ran stable. Fig. 1 shows an event reconstructed using the GPU tracker. To ensure that the GPU tracker output matches the CPU version, statistics of CPU and GPU runs were compared (See Fig. 2). No difference in CPU and GPU tracking efficiency was found.

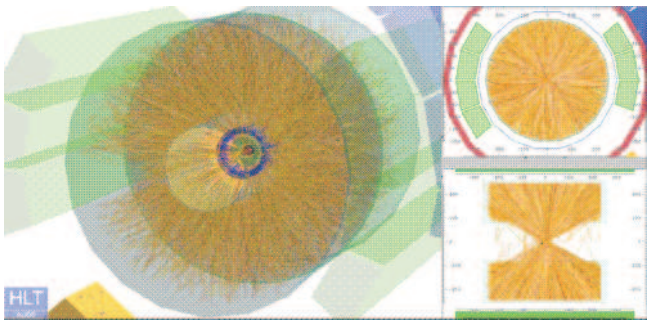

Figure 1: Snapshot of Online Event Display.

Further Optimizations

The original GPU tracker was developed on quad-core Nehalem nodes. However, the GPU compute nodes employ twelve-core Magny-Cours Processors. The overall performance of the Magny-Cours is clearly better. However, when it comes to single-core performance they are inferior to the quad-cores. The GPU tracker only used a single CPU core and was slowed down by the new CPUs. The problem became even more critical due to a change in the output format which is more compute intensive. The pipeline [2] did no longer work well since the GPU was waiting for the single CPU core most of the time.

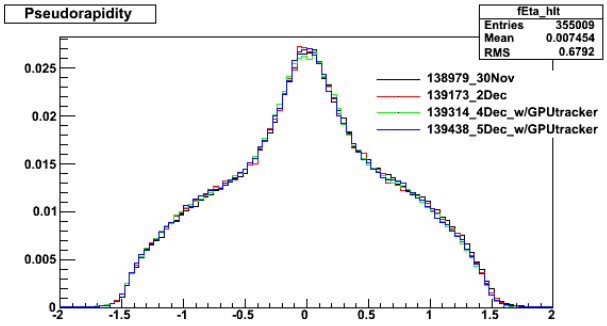

Figure 2: QA Statistiks for GPU Tracker.

This was solved by multithreading the CPU part of the GPU-tracker. Contrary to the pipelin, other optimizations originally made for the 295 could directly be used for the GTX580, e.g. the dynamic scheduler ensures a GPU utilization of close to 70%. In late 2010 the GTX580 was released. Fig. 3 shows a performance comparison.

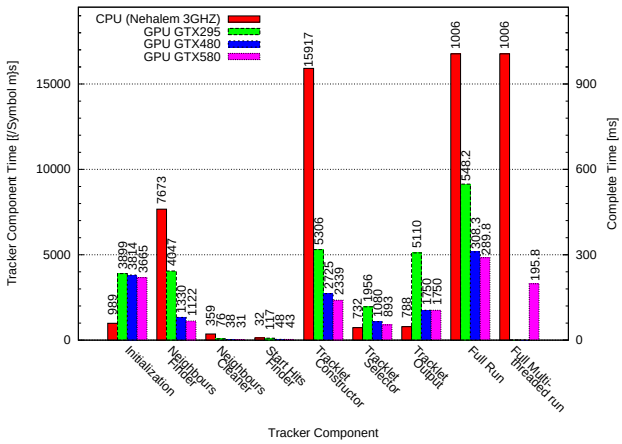

Figure 3: Tracker Performance on different architectures.

References

[1] S. Gorbunov, M. Kretz, D. Rohr, “Fast Cellular Automaton tracker for the ALICE High Level Trigger”, GSI Scientific Report 2009, http://www.gsi.de/scirep2009/

[2] D. Rohr, “ALICE TPC Online Tracking on GPGPU based on Kalman Filter“, University of Heidelberg, Diploma Thesis, http://www.kip.uni-heidelberg.de/Veroeffentlichungen/details.php?id=2035

Grid Activities at GSI*

K. Schwarz for the e-infrastructure group/Scientific Computing[1]
[1]GSI, Darmstadt, Germany

This article describes the work of the GSI Grid Group with the aim to enlarge and operate an ALICE tier2 centre within the global environment of the LHC Computing Grid and to prototype a possible FAIR grid environment.

ALICE tier2 centre

Due to the first heavy ion runs at LHC end of 2010 the ALICE tier2 centre received it's first real challenges. The main tasks of a tier2 centre are Monte Carlo simulations and individual data analysis. The Pb-Pb runs have been transferred to GSI continuously, and first corresponding papers have been published.

The available disk space is distributed among an xroot cluster (300 TB) and Lustre (1 PB). The xroot cluster is configured as a Grid Storage element and globally accessible, while Lustre is used for local data storage.

The number of CPUs has been increased up to 2700 cores. Throughout the year GSI participated in centrally managed ALICE Grid production and data analysis activities. The overall job share of GSI and Forschungszentrum Karlsruhe has been 15% of all ALICE jobs worldwide.

The entire infrastructure of the ALICE tier2 centre is monitored in detail by using MonaLisa.

Cluster Virtualisation

A project has been started to develop an Infrastructure as a Service (IaaS) prototype, as well as strategies and corresponding utilities to use these resources efficiently [1]. On 16 physical boxes a cluster of 100 virtual machines has been made available using OpenNebula for cloud building, libvirt as abstraction layer, and KVM as hypervisor. The cluster is being managed by using Chef, via predefined recepies a complete PBS-cluster including server and virtual worker nodes with fitting applications already on board can be created on the fly. One of the first applications was a virtual ALICE Grid site which was running in production mode and computed about 42000 jobs for the ALICE VO.

Based on the experiences gained at GSI the corresponding tools have been ported successfully to the environment of Frankfurt Cloud [2]. By using these virtual clusters on demand FLUKA simulations for the GSI Radiation Safety department and nuclear structure calculations have been produced.

* Work supported by BMBF - Förderkennzeichen PHL08/001 (Integration philippinischer und südostasiatischer Rechenzentren in das FAIR-Projekt)

D-Grid and PROOF on Demand

Although the D-Grid project officially came to an end the in this context developed "PROOF on Demand" (PoD) utilities enjoy a high popularity. PoD [3] is a set of software tools developed at GSI via which each user can dynamically create individual PROOF clusters.

The development is going on and and new releases are being published. Next to more supported plugins (currently PoD environments can be started via gLite, LSF, SGE, PBS, and ssh) also the user community is increasing. In the ALICE context PoD starts to be established as standard, and first ATLAS installations have been done in Munich.

The compute resources bought from D-Grid fundings are available in the D-Grid information system and can be used with D-Grid methods.

Preparation for FAIR tier0

PANDA-Grid[4] has been extended to 18 sites, among these 3 universities from the Philippines and 1 university from Thailand. The collaboration with these sites has been strenghtened by several working visits of Asian scientists.

CBMGrid is up and running. First small productions have been running successfully using the CBM Grid infrastructure. The largest CBM Grid site is Dubna, supported by the JINR-BMBF grant.

The collaboration between ALICE and the FAIR experiments intensified significantly. Synergy effects have been identified within the development of the experiment frameworks AliRoot and FAIRRoot [5] as well as in the context of Grid computing. Recent success stories are the fact that the cmake based build system has been taken over by the AliRoot/ROOT team, the development of the AliEn - Oracle interface [6] as well as the prototyping of an inter VO Grid interface. A joined FAIRGrid-AliEn developers week has been held at CERN.

References

[1] Cluster Virtualisation at GSI, GSI Annual Report 2010.

[2] Radiation Simulation and Nuclear Structure Calculations at Frankfurt Cloud, GSI Annual Report 2010.

[3] PROOF on Demand, GSI Annual Report 2010.

[4] The Software and Middleware at PANDA Grid, GSI Annual Report 2010.

[5] Status of the FairRoot Simulation and Analysis framework, GSI Annual Report 2010.

[6] Oracle backend for AliEn, GSI Annual Report 2010.

The Software and Middleware of PANDA Grid

D. Protopopescu[1], A. Amoroso[2], P. Bühler[3], M. Ciubancan[4], M. Dahlinger[5], R. Dosdall[6], C. Grigoraş[7], S. Lusso[2], J. Messchendorp[8], V. Mitsyn[9], A. Montiel Gonzales[5], D. Pantea[4], P. Saiz[7], K. Schwarz[5], M. Al-Turany[5], F. Uhlig[5], and J. van der Weele[8]

[1]University of Glasgow, UK; [2]University Department of Physics and INFN Torino, Italy; [3]SMI Vienna, Austria; [4]IFIN-HH Bucharest, Romania; [5]GSI Darmstadt, Germany; [6]Forschungszentrum Jülich, Germany; [7]CERN, Geneva, Switzerland; [8]KVI Groningen, The Netherlands; [9]JINR Dubna, Russia

Abstract

PANDA Grid is the computing tool of the $\bar{\text{P}}$ANDA experiment, and during the last years it has evolved beyond passive computing infrastructure, into a complete and transparent solution for physics simulation, reconstruction and analysis, an integrated toolset right at the fingertips of the physicist.

Grid Status

PANDA Grid [1] uses AliEn [2] middleware, developed by ALICE [3] and used outside CERN by several FAIR experiments, like $\bar{\text{P}}$ANDA [4] and CBM [5]. The data analysis software, distributed via the built-in package management mechanism of AliEn, is centered on PandaRoot [6], a framework developed partly within the $\bar{\text{P}}$ANDA collaboration, partly within the larger FAIR community. Grid monitoring and data supervision are done via MonALISA [7].

While practically being the first up-and-running $\bar{\text{P}}$ANDA experiment component, PANDA Grid is continually evolving. It has grown to encompass 17 sites from 13 institutes in 9 countries, including EGEE/EGI sites integrated via VOBox tools. Two new GSI associated sites were added during 2010 and Orsay is joining at the time of writing.

Software and Middleware Tools

PandaRoot is an extension of FairRoot [8], a framework jointly developed by CBM and $\bar{\text{P}}$ANDA. FairRoot is fully based on ROOT [9], and provides a common framework for both simulations and data analysis. In the $\bar{\text{P}}$ANDA computing model, the 'user' software consists mainly of ROOT macros using modular precompiled libraries from PandaRoot. The Grid infrastructure is used for software distribution via the package manager service (PackMan) provided by the middleware layer. PandaRoot and FairRoot are distributed separately, as interdependent source packages, compiled on sites. We possess now a completely integrated and automatic system for package installation, compilation and testing, supervised directly by PandaRoot developers. The user has only to customize a couple of scripts in order to pursue his/her own physics.

This is due to concerted efforts during the last few years to seamlessly integrate software and middleware, production and management tools, MySQL and ORACLE database support, and to the addition of a user-friendly browser-based supervision layer, that ensures minimal administrative overhead.

The middleware we employ is the perfect tool for the job, as AliEn already provides advanced data production tools: various mechanisms for job split and merging, catalogue tags and triggers, file collections, automatic data replication across multiple storage elements, etc. But besides these built-in mechanisms, the MonALISA layer enabled us to develop in 2010 a range of supervision tools and command mechanisms that make PANDA Grid both easy to administer and easy to use for large scale productions.

Close communication between the groups participating in software development and Grid deployment is maintained via periodical Data Challenges [10], numerous ad-hoc meetings within the FAIR community and CERN, and dedicated workshops [11], hosted in turn by various participant institutes. Four PANDA Grid workshops were held during 2009-2010, in the Philippines, Italy, UK and Switzerland, the last one being a joint ALICE-PANDA developer's meeting hosted at CERN.

Our Data Challenges (DC), during which large quantities of data are produced via a full chain of simulation, digitization and reconstruction are an excellent tool for stress-testing the middleware, software, site data storage and network capabilities. The jobs run during the DCs are either theoretical calculations or data simulations used for the design and prototyping of the $\bar{\text{P}}$ANDA detector.

References

[1] PANDA Grid documentation wiki at GSI: http://panda-wiki.gsi.de/cgi-bin/view/Computing/PandaGrid

[2] AliEn website: http://alien.cern.ch

[3] The ALICE experiment at the CERN LHC, The ALICE Collaboration *et al.*, 2008, JINST 3 S08002

[4] $\bar{\text{P}}$ANDA website: http://www-panda.gsi.de

[5] CBM: http://www.gsi.de/forschung/fair_experiments/CBM

[6] http://panda-wiki.gsi.de/cgi-bin/view/Computing/PandaRoot

[7] MonALISA website: http://monalisa.cern.ch

[8] M. Al-Turany *et. al*, Status of the FairRoot Simulation and Analysis framework, INSTR. METH. 59, GSI Scientific Report 2008

[9] The ROOT framework, http://root.cern.ch

[10] see 'Data Challenges' links in [1]

[11] see PWG site: http://nuclear.gla.ac.uk/grid-workshop/

PROOF on Demand*

A. Manafov, P. Malzacher

GSI, Darmstadt, Germany

PROOF [1] is an extension of ROOT [2] enabling interactive analysis of large sets of files in parallel on clusters of computers. Normally users get PROOF provided by administrators as a pre-installed shared cluster. To avoid certain disadvantages of "static" PROOF clusters PoD [3] has been developed.

PROOF on Demand is a tool-set, which dynamically sets up a PROOF cluster at user request, on any resource management system (RMS).

PoD is a user oriented product with an easy to use GUI and a command-line interface. It is fully automated, and no administrative privileges, special knowledge or preconfigured nodes are required to use it.

Features

- **Easy to use.** The process of installation is very simple and fully automated. PoD works out of the box. Its distribution contains preconfigured modules and everything users need to just immediately start to work with it right after the installation.
- **GUI & Command-line.** PoD provides a simple and intuitive graphics user interface in order to simplify access to its functionality. For user's convenience there is also a command line interface, it helps to manage a PoD cluster remotely or use it in a batch mode.
- **Native PROOF connections.** Whenever possible, PoD setups direct PROOF connections between nodes. It results in a full functional PROOF cluster. Users get native speed and the whole range of PROOF features. To use native connections an incoming traffic must be allowed on PoD workers for a defined port. Otherwise PoD uses packet-forwarding algorithms.
- **Packet-forwarding.** When worker nodes are behind a firewall then PoD uses its packet-forwarding algorithms to maintain the PROOF traffic. The algorithms are very efficient, there will be no speed penalty, but some PROOF functions are limited.
- **Multiuser/-core environment.** PoD implements automatic port mapping algorithms to properly handle cases when several users start PoD instances (servers/ workers) on the same machine. PoD also automatically manages situations when multiple PoD workers are started on the same node. Private PoD instances can't disturb each other.
- **Different job managers.** PoD supports different job managers via a plug-in system. It is a very easy to extend system. PoD is currently shipped with the following plug-ins: SSH, LSF (Load Sharing Facility), PBS Pro/OpenPBS/Torque (Portable Batch System), Grid Engine (Oracle/Sun Grid Engine), Condor, gLite.

Use case

The main use case of PoD is to set up a distributed PROOF cluster on the Grid and/or local RMS. The first thing, a user has to do, is to start the server side processes on a central machine; in terms of PoD it is a user interface machine. The next step is to submit PoD jobs to worker nodes. As soon as a job arrives at a remote worker node, it automatically configures the environment and starts all needed client services including an xproofd worker and a pod-agent in client mode. In case the pod-console is used as session management tool, each new connection is immediately reflected in the GUI. When the instantiated PROOF workers of all submitted PoD jobs are connected, or when the user is satisfied with the number of connected worker processes, the PROOF analysis can be processed as if on a native PROOF cluster. The user then starts a ROOT session, e.g. on the private laptop, and connects to the PROOF master, registers the data, and runs the analysis script. Since pod-agent can manage disconnects, the user can also disconnect from ROOT, restart the ROOT session, and reconnect to the same PROOF cluster without having to resubmit the PoD jobs.

Summary

As PoD matures as a product, it is used more and more as a standard for setting up dynamic PROOF clusters in many different institutions in HEP community. Additionally there are already several Cloud based installations, which use PoD as a PROOF cluster solution. With PoD there is no need to maintain a dedicated PROOF analysis facility. PoD users create themselves private dynamic PROOF clusters on general purpose batch farms, Grid or Cloud systems.

Upcoming versions of PoD are going to support an out-of-server user interface. Users will be able to select a remote computer acting as PoD server (PROOF master). In this case PoD UI will be just a lightweight control center and could run on different OS types. Also an AliEn plug-in is going to be developed in collaboration with the ALICE Offline team. This cooperation will help PoD to provide a fast interactive PROOF experience on the AliEn Grid.

References

[1] The Parallel ROOT Facility (PROOF) http://root.cern.ch/drupal/content/proof
[2] An Object Oriented Data Analysis Framework (ROOT) http://root.cern.ch
[3] PROOF on Demand (PoD) http://pod.gsi.de

Cluster-Virtualization at GSI

D. Klein, P. Malzacher, V. Penso, and M. Zynovyev
GSI, Darmstadt, Germany

In future many new groups of customers, like the FAIR experiments, will challenge GSIs shared computing facility. Difficulties are expected in supporting all these new scientific applications and their sometimes conflicting requirements. The Scientific Computing Department started a project to develop an Infrastructure as a Service (IaaS) prototype, as well as strategies and corresponding utilities to use such resource efficiently.

Motivation

Segmenting large clusters of physical compute resources into separated Virtual Clusters (VCs) is achieved by moving applications with their dependencies into Virtual Machines (VMs). User groups have the advantage of working inside their private, perfectly tailored environment altogether independent from other customers of the same compute facility. IaaS technology manages VMs across hardware pools and permits fast re-allocation of resources to maximise utilization. VM management - configuration, monitoring, and operation - of multiple VCs is a demanding task. We use the Infrastructure as Code (IaC) paradigm to describe configurations of VCs in program code, so called recipes. Administrators will then be able to install and maintain multiple VCs by manipulating sets of recipes.

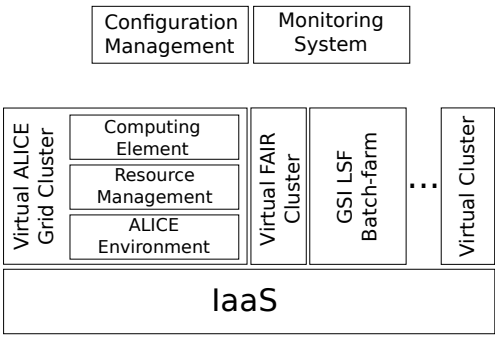

Figure 1: Virtual Clusters on Infrastructure as a Service

Figure 1 illustrates an IaaS facility hosting multiple VCs, among them a virtual ALICE Grid Site[1]. The Configuration Management (CM) controls all VCs according to recipes, and scales them depending on the load by adding and removing VMs automatically. Change requests from customers and operational incidents visible in the monitoring are resolved using the same CM.

Approach

After evaluating existing IaaS technologies we have selected OpenNebula[2] for our prototype, because of its excellent customization capabilities. In total this facility is capable of hosting more than hundred VMs. The CM software Chef[3] maintains and applies the recipes to install and operate VCs. Simplified, the work-flow looks as followed:

- The CM orders a pool of VMs from the IaaS facility and waits until the VMs register back to the CM.
- Once an empty VM is available the CM appoints the resource management and monitoring master, installs the software, and starts the services.
- All other VMs get the corresponding client software deployed including user specific application libraries, and they autonomously start to publish monitoring information.
- The list of available worker nodes gets automatically fed into the resource management and jobs are distributed as soon as resources are available.
- Once the virtual cluster is executing user jobs the CM tracks the monitoring to replace broken workers, and, depending on the load, scales the number of workers.

Results

During the last year the IaaS prototype at GSI executed thousands of VMs with varying purposes ranging from application software and IT service evaluation to on-the-fly deployed clusters for data analysis and simulation. Among these a virtual ALICE Grid Site connected to the production system has executed more than 40 thousands jobs so far. Most important, we have developed tools to automatically deploy VCs running the resource management system Torque[4] and the monitoring system Ganglia[5]. We have been able to use the same tools on resources of the Frankfurt Cloud[6] to compute radiation simulation for FAIR. Generally, we develop tools using standardized interfaces to assure seamless migration to commercial Cloud providers to cover peak resource demands. In 2011 we plan to implement better integration of CM and monitoring, and simultaneously make the tools generic to simplify adaption for other use-cases.

References

[1] ALICE Grid, http://alimonitor.cern.ch/map.jsp

[2] OpenNebula, http://www.opennebula.org

[3] Chef, http://opscode.com/chef

[4] Torque, http://www.clusterresources.com/

[5] Ganglia, http://ganglia.sourceforge.net/

[6] Frankfurt Cloud, http://www.frankfurt-cloud.com

Radiation Simulation and Nuclear Structure Calculations at Frankfurt Cloud

D. Klein, P. Malzacher, V. Penso, and M. Zynovyev
GSI, Darmstadt, Germany

Frankfurt Cloud[1] is a research project for Infrastructure as a Service (IaaS) technology at Goethe University Frankfurt. In late 2010 a prototype infrastructure became available and the GSIs Scientific Computing department has been invited to use this facility in order to run applications from the HEP community. This opportunity allows to gain more experience in off-loading compute jobs to external providers in order to cover excess demands. The strategy is to deploy application specific Virtual Clusters (VCs) including management and monitoring components into Frankfurt Cloud.

Virtual Clusters

Experience from running applications on GSIs local IaaS facility[2], and the tools developed in this context have been successfully transfered to the computing environment at Frankfurt Cloud. VCs feature a resource manager (Torque[3]) and a monitoring system (Ganglia[4]), deployed and integrated using the Configuration-Management-System (CMS) Chef[5]. Following the Infrastructure as Code (IaC)[6] paradigm the adjustment to Frankfurt Cloud finished in less than two weeks, although the facility is still under development and does not provide a programmatic interface (API) yet.

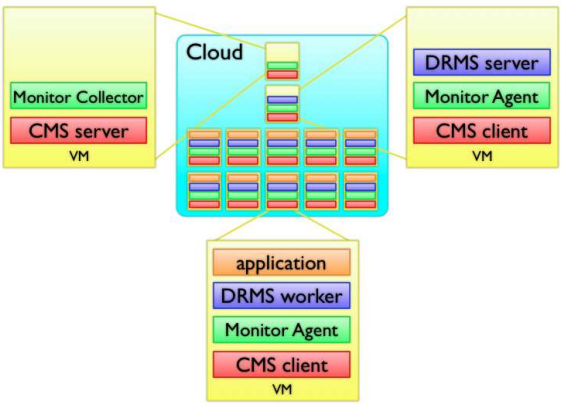

Figure 1: Virtual Cluster Architecture

Figure 1 illustrates the architecture of a VC. Dedicated Virtual Machines (VMs) are used to host the CMS and the monitoring system, as well as the Distributed-Resource-Management-Systems (DRMS). Job execution hosts can be added and removed dynamically according to the overall utilization. Each application is executed in its own VC instance to reduce interference between different software environments. All service and application specific software is deployed and configured by the CMS. Generally IaC and the CMS are capable of combining different VM operating systems, DRMSs, monitoring systems and software packages to build perfectly custom-made application environments.

Applications

Two applications producing much needed results have been operated at Frankfurt Cloud. The first was a Scientific Linux cluster running FLUKA[7] Monte-Carlo-Simulations. It produces a significant amount of results for the GSIs Radiation Safety department regarding the construction of FAIR accelerator buildings. The second VC was used for state-of-the-art nuclear structure calculations with energy density functional methods[8]. Nuclear ground states for several Calcium, Titanium and Chromium isotopes were evaluated to study the systematics of the double beta decay process. This decay is interesting not only for the Nuclear physics community but also for Astrophysics and Particle physics communities.

Outlook

In order to gain more experience with IaaS facilities we plan to host a virtual ALICE Grid site[9]. Furthermore non-trivially-parallel compute jobs will be tested, such as Message Passing Protocol (MPI) enabled applications. It is very important for us to use our tools with many different applications and different IaaS providers to make sure that this approach is adaptable to any kind of scientific application. Plans also include the refinement of the autonomous operation of VCs, for example the development of algorithms for auto-scaling the cluster size depending on the load.

References

[1] Frankfurt Cloud, http://www.frankfurt-cloud.com

[2] Cluster-Virtualization at GSI, GSI Annual Report 2010

[3] Torque, http://www.clusterresources.com/

[4] Ganglia, http://ganglia.sourceforge.net/

[5] Chef, http://opscode.com/chef

[6] Web Operations: Keeping the Data on Time, O'Reilly Media, 2010, p. 65.

[7] FLUKA, http://www.fluka.org

[8] T. R. Rodríguez, and G. Martínez-Pinedo, "Neutrinoless double beta decay studied with energy density functional methods", GSI Annual Report 2010.

[9] ALICE Grid, http://alimonitor.cern.ch/map.jsp

Central GSI Oracle Database Services

M.Dahlinger[1], *B.Karlson*[1], *I.Koenig*[1]

[1]GSI, Darmstadt, Germany

Overview

IT provides a central highly available database service including web-access for experiments, scientific-technical infrastructure and administration.

The service is based on an active-active two-node *Oracle 10g database* cluster (RAC) with SAN attached fast storage array, and a two-node web server (*Oracle Application server 10*) with hardware load balancer and single sign-on (SSO based on *Oracle Internet Directory*). We also provide a complete test environment for database and web development.

Database Management, Online Backups and monitoring is controlled using *Oracle Enterprise Manager Grid* control and *nagios*. An external service provider guarantees constant service on agreed service-level (all working days, 24x7 if needed for beam-times).

Upgrade to a two-node 16 core system *and Oracle 11gR2 database* is currently work in progress.

Users and Applications

Four databases are in use for production and development by the experiments HADES [1], Alice, CBM and PANDA. Main infrastructure applications based on Oracle database are:

- Identity Management IdM for users, accounts, roles, devices
- Accelerator control-room logbook
- Safety and radiation protection:: Online-instructions, access control systems
- Administrative: project-time recording, facility management

Current developments

HADES: Control, monitoring and configuration data of the new DAQ frontends, nodes and event builders was interfaced to Oracle allowing to merge it with offline parameters for final data analysis.

IdM: Application for the administration of users, accounts and resources for IT. Development of >100kloc of PL/SQL language based code including web-interface for users and administrators have been carried out. A common account (GSI Web login) for web based applications has been rolled out (>2000 users).

References

[1] I.Koenig, "The HADES Oracle database and its interfaces for experimentalists", CHEP2009, Prague, http://indico.cern.ch/contributionDisplay.py?sessionId=60&contribId=289&confId=35523

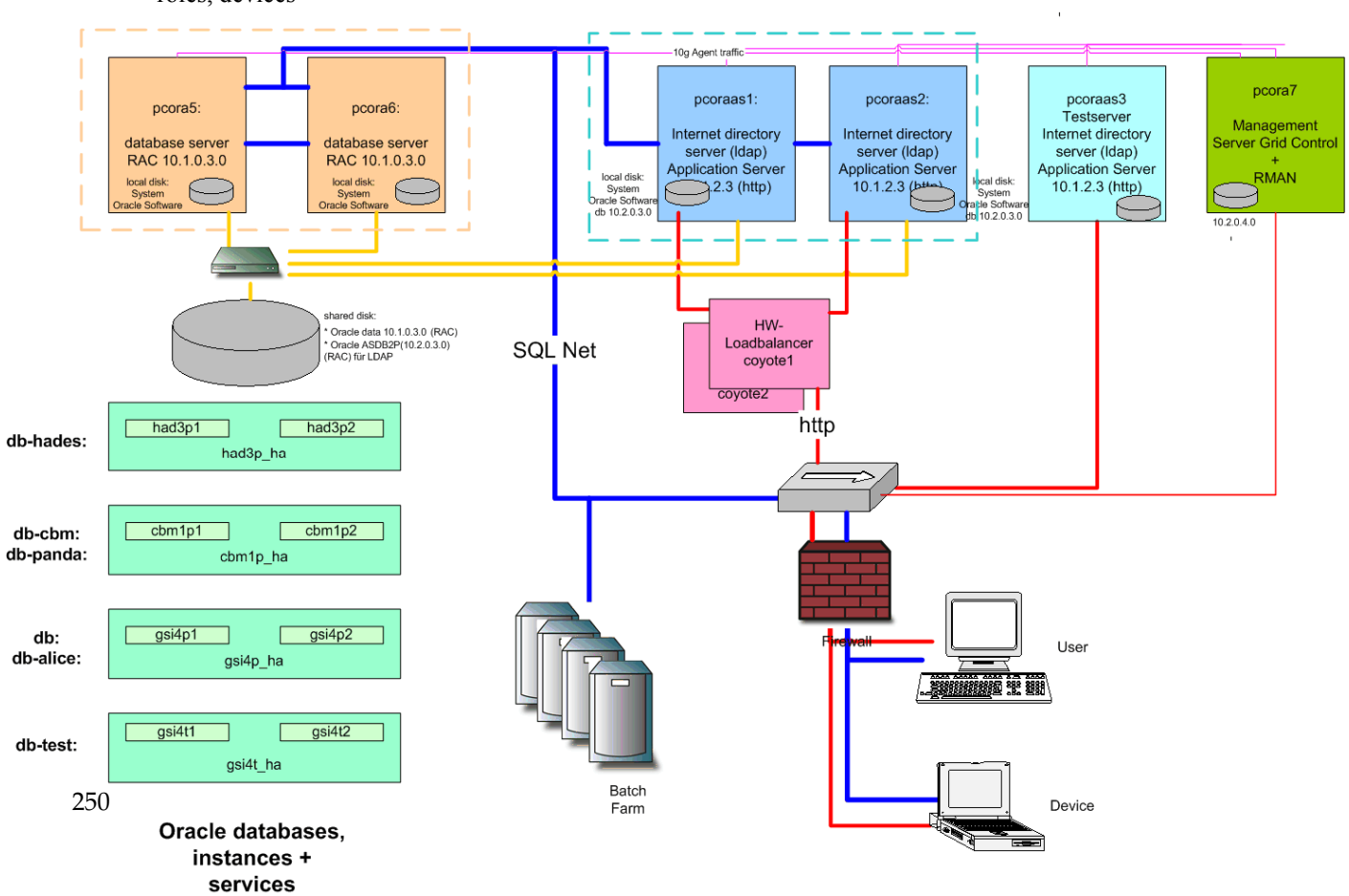

Oracle backend for AliEn

A. Montiel González [*1], *M. Dahlinger*[1], *P. Malzacher*[1], *P. Saiz*[2], *S. Schreiner*[2], *and K. Schwarz*[1]
[1]GSI, Darmstadt, Germany; [2]CERN, Geneve, Switzerland

AliEn [1] is a lightweight GRID framework based on Perl, started by the ALICE offline Project at CERN. It constitutes the production environment for simulation, reconstruction and analysis of physics data of the ALICE Experiment. This middleware has been deployed by the experiments PANDA and CBM. As part of the facility, they will run their central services at GSI-FAIR. AliEn was originally developed to run only on MySQL database. It is necessary to open this middleware to be able to run on any other database, specifically on Oracle, to be able to take advantage of the corresponding GSI services.

Design

AliEn uses the Database Interface (DBI)[2] module from Perl for creating the communication with the database. It sends any query to the corresponding Database Driver (DBD) module. The DBD is responsible for sending queries to the specific Relational Database Management System (RDBMS). The DBI makes porting an application from one database to another fairly easy as long as vendor specific SQL is not used. However using standard SQL not only constrains the performance, but also the functionality. Therefore, AliEn uses specific SQL statements and functions for MySQL. The backend for Oracle in AliEn has been implemented by designing a new interface to the database. In Figure 1 the interface *Database* is shown. This used to be the only entry point to the database. This module keeps the same functionality, but now it is implemented by submodules that correspond to each driver (in this case Oracle and MySQL). These modules will send the queries to the corresponding drivers on the selected database.

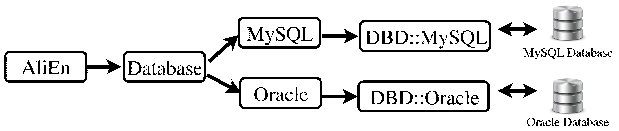

Figure 1: Integration of the new interface in AliEn

Implementation

Perl is a powerful language for report processing. An important part of the implementation exploits this feature, it takes the sql query and processes it, returning the corresponding one in Oracle. However, most of the implementation consists of writing compatible code for both databases in the module *Database*, leaving specific functions for the submodules. Furthermore, refactorization of the rest of the code has been considered. These have been the main changes while porting:

Data Definition

- Different syntax for each data type.
- Reimplementation of user defined functions.
- Specific functions of the driver, like *addtime, conv, insrt, now*.
- *Autoincrement* non existent in Oracle.

Data Manipulation

- Some of the reserved words for Oracle are used as name for the columns. These have been quoted. This quotation has to be considered when creating, inserting, updating and deleting.
- Empty strings are special cases. They are considered as null value for MySQL.

File space and storage

- Data storage is different from one system to another, affecting the way of connecting and its administration. Oracle introduces the concept of *schema*. This one needs to be indicated in the url that connects to the database. Each database in MySQL corresponds to a *schema* in Oracle.

Administration and Security

- Privileges and authentication methods differ.
- A user is a *schema* for Oracle. This makes a difference with the creation of users in the application. On MySQL every user is mapped in the database, in Oracle this is done by granting the connection through a single user on the database.

Conclusions

The considerations above have been implemented in the interface. Oracle backend is included in the new release AliEn v2.19. The new interface enables porting to a different database engine easily. The complete successful validation of the testbed is in progress. New performance test for Oracle will be included.

References

[1] Buncic, P. and Peters, A. J. and Saiz, P., and Grosse-Oetringhaus, J.F.,The architecture of the AliEn system, CHEP 2004, Interlaken, Switzerland (2004)

[2] http://search.cpan.org/ timb/DBI-1.616/DBI.pm

[*] Supported by MCIIN, ref. ES 2008-150, Gobierno de España

Database support within R3BRoot

Denis Bertini[1]
[1]Scientific Computing ,GSI, Darmstadt, Germany

Introduction

Since the setup of a typical nuclear experiment, such as the R3B experiment at FAIR[3], is varying depending on the physic case to study, the software for simulation and analysis should be able to handle a large amount of different parameters and their variation in time. For that purpose, the R3BRoot framework [2][4] implements a database interface which provides a simple, uniform concept regardless of the data being accessed. Furthermore the database interface can access data from more than one database instance using a dedicated database connectivity implementation.

Database Connectivity

The database connection is done via the ROOT TSQLServer class [1]. For accessing the data more than one database connection can be used according to the user-defined URLs list. At initialisation time, the list order reflects the access priority. The first database in the list is used for searching the data, if it fails the next database in the list is used until the complete set of data can be retrieved. This gives the user the flexibility to create its own database from a subset of the official one and to put it ahead in the list.

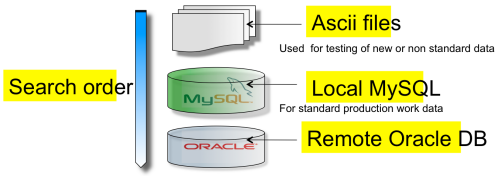

Figure 1: The ordered priority list of databases

Context sensitive version management

Ultimately, any of the data retrieved could depend on the run or the event being processed. Detector relevant parameters, such as calibration constants, will change with time and the interface has to retrieve the right ones for the current run or event.

For this reason, all requests for data through the interface must supply information about:

- The type of data: real or Monte Carlo
- The type of Detector.
- The date and time of the run or event (in UTC)

This information is called a Context. In the database all information is tagged by a Context i.e by a validation range which identifies the type of data and detector and the ranges of date times for which it is valid.

Validation Range Table

This table consists of rows of ValidationRange objects, each defined with a unique sequence number which is used as a key into the main data table

Main Data Table

Each rows of the Main Data Table has a sequence number corresponding to an entry in the Validation Range Table. The interface first find a match in the Validation Range Table for the corresponding context and then retrieves all rows in the Main Data Table that match its sequence number.

Minimizing the I/O

Another important point is to minimise IO. Some requests, particularly for detector relevant parameters, can pull in large amounts of data but users must not load it once at the start of the job and then use it repeatedly since it may not be valid for all the data they process. Also multiple users may want access to the same data and it would be inefficient for each to have their own copy. To deal with both of the above problems, the interface uses the concept of handle or proxy . When accessing a particular table, a table-specific pointer object is created. the corresponding object is usually very small is suitable to be stack based and passed by value, thus reducing considerably the risk of a memory leak. During construction of the pointer, a request for data is passed down through the interface and the results table, which could be large, is created on the heap. The interface places the table in its cache and the user's pointer is attached to the table, but the table is owned by the interface, not the user.

References

[1] R. Brun, F. Rademakers, P. Canal, I.Antcheva , D. Buskulic, O. Couet, A. and M. Gheata *ROOT User Guide* CERN, Geneva 2005.

[2] R. Brun, F. Carminati, I. Hrivnacova, A. Morsch *The Virtual Monte Carlo* Computing in High Energy and Nuclear Physics, 2003, 24-28 March 2003, La Jolla, California

[3] http://www.gsi.de/fair/experiments/NUSTAR/R3b.html

[4] The FAIR simulation and analysis framework 2008 J. Phys.: Conf. Ser. 119 032011

The GSI Archive Storage

H. Göringer, M. Feyerabend, S. Sedykh
GSI, Darmstadt, Germany

Overview

The GSI archive storage systems provide safe, reliable, and redundant long term storage of all user and experiment data. Fast and highly parallel data access is available for 24 hours a day and 7 days a week.

- **Backup/Archive** functionalities are available with the commercial Tivoli Storage Manager (**TSM)**.
- **Experiment data** archive and storage is provided with **gStore,** the GSI made client/server system.

gStore is based on automatic tape libraries (ATL) for long term archiving and on data movers (DM) with large read and write disk caches (overall ~125 TB currently) all connected via Storage Area Network (SAN). Hiding tape operations the data movers provide fast and parallel file access. Besides that they have high speed connections to the lustre file system. gStore is fully scalable in both, data capacity and I/O bandwidth. Design principles and functionality of gStore are described in more detail in several GSI reports, talks, and in a paper [1].

Storage Resources and Status

In November 2010, a new IBM 3584-L23 ATL has been installed in the computing centre replacing an IBM 3494 and two StorageTek L700 ATLs, which have been scraped. At the end of 2010, the new ATL was filled with nearly 0.5 PB of data. More details on used and available storage capacities can be found in table 1.

resource	used	max
3584-L23 RZ: gStore	390 TB	2.3 PB
backup	100 TB	
3584-L23 BG2: gStore copies	130 TB	1.3 PB
backup copies	15 TB	
overall data mover disk cache	< 90%	125 TB
lustre file system [2]	~80%	1.0 PB
overall gStore I/O bandwith:		
DM disk <-> clients (LAN)		1.8 GB/s
DM disk <-> tape (SAN)		2.0 GB/s

Table 1: Status GSI Storage December 2010

Copies of experiment (raw) and backup data are stored in a second ATL in the remote BG2 building. This concept prevents from loss of valuable data in case of media damage and enables disaster recovery.

gStore Enhancements

1. Recursive file operations are possible now with some gstore actions ('query', 'stage', 'unstage'), either using the new gstore command flag '-recursive' or appending the wildcard character '*' as trailer to the path name mask. Such operations are performed for all matching files in all matching directories and in all subdirectories below.

2. Large files > 2GB. Since December 2010 all gStore server processes run on 64 bit operating systems and support large file sizes. However, at GSI there is a mixture of 32 bit Linux systems (e.g. most desktops) and 64 bit systems (e.g. most batch farm nodes) in operation. Therefore there are two new gStore command clients offered:

1. **'gstore',** the **32 bit client**, has been upgraded and runs on all Linux systems. Obviously local files can only be handled if < 2GB. However, actions can also be done with larger files if they are only handled on the (64 bit) servers ('query', 'stage', 'unstage', 'delete').
2. **'gstore64',** a ne**w 64 bit client**, runs only on 64 bit systems but handles files with any size (as supported by the operating system) and with all subcommands.

Both commands, gstore and gstore64, are fully identical with respect to the subcommands and command options.

Online Migration of Experiment Data

Using gStore RFIO clients in event builders data from running experiments can be transferred directly to the gStore write cache and optionally to lustre, where they are immediately available for monitoring and online analysis. gStore RFIO clients are implemented in the Hades DAQ system and in MBS (version 5.0 and higher). Tests with the Hades DAQ have been performed with data rates of 250 MB/s for several hours. After a minor hardware increment planned for the first quarter of 2011 this rate can be increased to 500 MB/s to fulfill a recent Hades request.

Outlook

To enable reading from gStore with overall data rates of ~1 GB/s, heavy file staging actions from tape to disk will be parallelized with as many data movers as possible.

In order to use temporarily not needed write cache data movers for major stage or retrieve activities, new tools must be developed to manage switching of data movers between read and write cache. For that purpose write cache files on affected data movers must be migrated to tape, or vice versa stage files with assured life time must be moved to other data movers automatically.

In 2011, a first release of a FUSE-based Posix interface for gStore will be available.

References

[1] see http://www.gsi.de/informationen/wti/it/exp_daten/daten_speicherung_e.html as starting point for more info.
[2] see W. Schön et al: HPC Computing, this report

I/O Optimized Cluster for Data Analysis

W. Schoen, E. Duve, S. Haller, C. Huhn, B. Neuburger, T. Roth[1]
[1]GSI, Darmstadt, Germany

Abstract: The clustered parallel filesystem Lustre with an aggregate I/O capacity of about 0.5 Tb/s allows purely CPU bound analysis even for the data intensive analysis jobs of LHC and GSI experiments. The design, implementation and maintenance of this cluster is done by the HPC department of GSI. It is one of the largest Lustre installations worldwide and the only installation in the multi Petabyte area purely based on commodity hardware.

Introduction

Modern experiments with many thousand channels deliver huge amounts of data. Without high I/O capacity, the CPUs used in the data analysis would be idle most of the time, waiting for data. A cluster file system bundling thousands of disks can deliver a sufficiently large aggregate I/O capacity. The decisive point is the performance under massively parallel concurrent access to the file system. Because of its scalability, the fastest supercomputer centers are using Lustre as their cluster file system. Cluster file systems are very complex and not trivial to design or maintain.

Development

Lustre is Open Source and developed and maintained by research labs, supercomputing centers and computer companies. Recently two non-profit organizations were founded to coordinate the future Lustre development: openSFS [1] in the USA and EOFS [2] in Europe. GSI is one of the founders of the EOFS.

Design of Lustre

The key feature is a separation of the meta data from the object data. The meta data contains file names, ownership, timestamps and object locations. The object location is a reference to an address on one of the object storage targets (OST). For creation or reading of a file, a Lustre client will contact the meta data target (MDT) on the meta data server (MDS) to get a reference to the location. The object data is exchanged directly between client and OST avoiding a bottleneck due to meta data operations. However, without the meta data, the clients cannot access the object data. The MDT infomation is therefore mission critical. At GSI, the MDS are two nodes in a HA configuration synchronized via drbd. In addition, two generations of the meta data target (MDT) are stored, containing a MDT a few days older, to avoid a fatal loss of data in case the MDS-HA cluster is destroyed by complete hardware failure or other disasters. The production MDS are 48 core computers with 128 GB RAM each. The MDT is based on 11 parallelized RAID 1 pairs of fast disks. The object data are distributed over 150 OSS with an aggregate RAM of 1.6 TB.

Connectivity and capacity

The 150 OSS of Lustre have an aggregate I/O capacity of ca. 0.5 Tb/s. The cluster at GSI consists of about 3,500 disks with a multi Petabyte storage capacity. Most of the disks are 1 TB SATA drives. The OSS and the MDT are connected by 10 Gb Ethernet. The clients are connected by 1 Gb Ethernet. The total capacity of the system is 400 million files. The meta data of a subset of 65 million files can be kept in the MDS RAM.

Results

The production Lustre cluster is used by LHC experiments and GSI/FAIR experiments. Due to the high I/O capacities, the analysis jobs e.g. of ALICE or HADES are purely CPU bound, guaranteeing a highly efficient use of the HPC farm.

Outlook

The current Lustre is based on ethernet connections. The Lustre cluster will be extended by Infiniband based OSS and clients by fall 2011. This Infiniband part of Lustre will be the core cluster for the future to allow low latency applications e.g. lattice QCD in addition to the already running applications.

Figure 1: Blue lights indicates access to an OST. Red lights are automatic spare disks of the RAID 6 arrays.

References

[1] www.openfs.org

[2] www.eofs.org

Green IT and Efficient Computing at the LOEWE-CSC

M. Bach[1,2], M. Boroviak[3], J. de Cuveland[1,2], I. Geier[3], J. Gerhard[1,2], H.-C. Jankowiak[1,3], S. Kalcher[1,2], T. Kalkbrenner[3], M. Kretz[1,2], , G. Laubender[1,3], V. Lindenstruth[1,2,4], H. J. Lüdde[3,5], D. Rohr[1,2], T. M. Steinbeck[1,2]

[1]Frankfurt Institute for Advanced Studies, University Frankfurt, Germany; [2]Institute for Computer Science, University Frankfurt, Germany; [3]Center for Scientific Computing, University Frankfurt, Germany; [4]GSI, Darmstadt, Germany; [5]Institute for Theoretical Physics, University Frankfurt, Germany

In the autumn of 2010 the LOEWE-CSC Computer has been installed at the Center for Scientific Computing (CSC) of the University of Frankfurt. One of the primary applications for which this system will used will be computing for HIC for FAIR. This will be facilitated by the fact that it is planned to connect the system to the FAIR HPC link with a capacity of at least 10 Gbit/s, if possible even up to 40 Gbit/s.

Figure 1: The LOEWE-CSC

Hardware

The LOEWE-CSC is a hybrid computer usable for all kinds of high performance computing applications. It consists of 826 compute nodes in total, distributed over 30 racks. 786 of these nodes are equipped with 2 AMD CPUs with 2.1 GHz clock frequency and 12 cores each. These nodes are also equipped with an AMD Radeon 5870 GPU. The use of GPU computing allows a performance improvement of almost a factor of 5 compared to pure CPU usage for well adapted programs. For applications that are not easily adaptable to GPU usage 40 more nodes do not contain a GPU but are equipped with 4 of the AMD CPUs. All compute nodes are connected via a common InfiniBand high performance cluster interconnect and can access 420 PB of shared storage.

Performance & Software

Owing to the achievable absolute performance and the innovative cooling model of the LOEWE-CSC, it was possible to reach rank 22 on the November 2010 TOP 500 supercomputer list [1] and even rank 8 in the Green 500 list [2] of the most energy efficient supercomputers. One major contributing factor to this achievement is the high efficiency of utilizing the available computing power of the used LINPACK benchmark implementation. With its total achieved speed of 299 TFLOPS the cluster has reached 71 % of its absolute total theoretical capability, the highest efficiency of any GPU based cluster in the TOP 500. Efficiencies for the combined CPU and GPU usage on a single node and for a single GPU are even higher at 84 % and 91 % respectively. This high grade of utilization of the available processing resources was reached by a sophisticated distribution of the workload among the CPUs and GPU of a node. A key point that was observed for the distribution is to take care that all available computing resources are in use as much as possible and that no unit has to wait for results from another one, wasting compute power by leaving it unused.

Cooling

One further specialty of the LOEWE-CSC is its cooling model. The approach here is to transfer the heat to the cooling liquid as early as possible without using special, and therefore expensive, liquid cooled components. The fans which are already present in the compute nodes are used to draw in air at the front of the rack and push it out through a water-cooled heat exchanger at the back of the rack. Avoiding active cooling elements in this way, the ratio of the energy consumption for the whole system relative to the energy consumption just for the computers (Power Usage Efficiency, PUE) could be reduced to below 1.1. Typical values for comparable installations currently range between 1.6 and 2.0.

References

[1] TOP 500 Supercomputer November 2010 List, http://top500.org/lists/2010/11.

[2] Green 500 November 2010 List, http://www.green500.org/lists/2010/11/top/list.php.

Accelerator Operation Report

W. Bayer, U. Scheeler*, P. Schuett
GSI, Darmstadt, Germany

This report describes the operation statistics of the GSI accelerator facility in the year 2010. The presented information is based on the data of the GSI electronic operation logbook OLOG [1] which allows for a detailed evaluation of operation statistics especially for the time-sharing operation mode of the accelerators.

General Overview

From January till October 2010 four beam time blocks were scheduled. The first one was used exclusively for UNILAC experiments. In total, the SIS has been operated for 5616 hours and the UNILAC for 6350 hours, which split into 4574 hours for experimental beam time and 1776 hours for the commissioning of the accelerator after shutdown.

The first longer shutdown period (in parallel to the UNILAC operation) lasted from January till February 23rd. Within this shutdown the upgrade of the SIS vacuum system was finished and the RFQ section of the High Charge State Injector was upgraded. The second longer shutdown started on November 26th. It was used to maintain the post stripper section and to restore damaged drift tubes of the Alvarez cavities.

Table 1: Overall beam time of the accelerator facility

	2010	2009
Integral target time for all experiments	**10438h**	9201 h
Time for retuning	**76 h**	56 h
Time of interruption	**2704h**	2720 h
Total beam time	**13218 h**	11978 h

In Table 1 the total beam time of the whole facility is shown. In total, 10438 hours of beam-on-target-time were successfully delivered to the different physics experiments, about 1237 hours more than in 2009. The category 'retuning' includes the time necessary to improve the beam performance during the running experiment. The 'time of interruption' covers the categories ‘accelerator setup’ (1092 h), ‘ion source service’ (346 h) and ‘unscheduled down time’ (1266 h). These are all events which lead to a break of the running beam for the corresponding experiment. Altogether these times add up to the 'total beam time'. This amount is due to time sharing operation higher than the above mentioned operation hours. Compared to 2009 the ratio between target time and total beam time (availability of the facility) increased slightly 2% up to 79%. Restrictions in the duty cycle and beam energy due to technical problems at the High Current Injector and at the Alvarez section forced a change in the beam time schedule, which is not included in the statistics. This of course affected the experimental program.

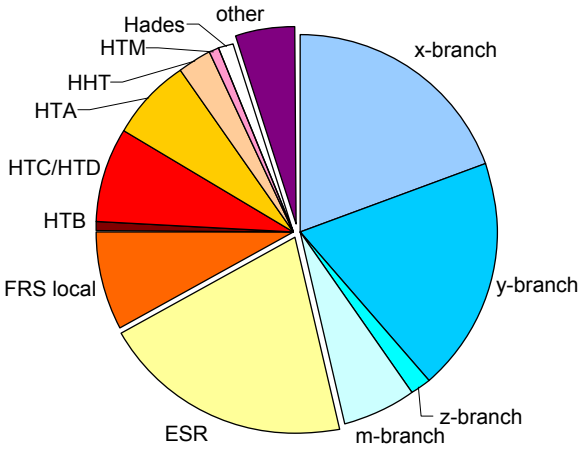

Figure 1: Distribution of target time to the different experimental areas

Figure 1 displays the distribution of target time for different experimental areas with the fraction of the 4 beam branches of the UNILAC on the right side, the ESR below and the different experimental caves behind the SIS on the left side. Details corresponding to the different experimental programs are given in [2].

UNILAC Experiments

Details of the beam time for UNILAC experiments are shown in Table 2. Over the year, 18 different experiments were performed at the UNILAC. In total, 4994 hours of target time for physics experiments have been achieved.

Beam was used for the SHIP Program (2204 hours) and for experiments of Material Science (1542 hours) and Nuclear Chemistry department (594 hours). The fraction of target time decreased 1% compared to last year. We observed an increase of time for ion source service and for accelerator setup and a decrease in unscheduled down time.

Table 2: Beam delivered to UNILAC experiments

	Time	Fraction
Target time for experiments	4994 h	78,9%
Time for retuning	35 h	0,6%
Accelerator setup	590 h	9,3%
Ion source service	203 h	3,2%
Unscheduled down time	510 h	8,0%
Total beam time	**6676 h**	**100%**

* u.scheeler@gsi.de

SIS Experiments

The heavy ion synchrotron delivered beams to 23 fixed target experiments and to 9 experiments at the ESR. In total 5445 hours of target time have been achieved. A more detailed overview is given in Table 3.

In 2010 the target time for the ESR (direct beam and beam via FRS) increased to 2206 hours, 308 hours for HITRAP commissioning is included in this amount. About 900 hours of beam time were delivered to HTC, which was thus the main user at the SIS. For about 925 hours beam was used at the FRS to produce exotic isotopes.

Table 3: Beam delivered to SIS/ESR experiments

	Time	Ratio
Target time for experiments	5445 h	79,1%
Time for retuning	40 h	0,6%
Accelerator setup	676 h	9,8%
Ion source service	143 h	2,1%
Unscheduled down time	582 h	8,5%
Total beam time	**6885 h**	**100%**

Accelerator operation

Figure 2 shows the total beam time for all accelerated isotopes during 2010. Over the year 18 different isotopes have been accelerated. The rare isotopes (^{24}Mg, ^{48}Ca, ^{64}Ni) were produced by the ECR ion source, which has been operated for 3798 h. Preferentially UNILAC experiments were provided with these beams. The Penning ion source was mainly operated with ^{40}Ar, ^{152}Sm and ^{197}Au (in total 3970 hours of operation). The high-current ion source was used for 3959 hours. Especially ^{40}Ar and ^{86}Kr beams were delivered from the MUCIS ion source, ^{238}U was accelerated from the MEVVA ion source for 2186 hours.

Table 4: Statistics of all unscheduled down time events

	Down time	No. of events
Power supplies	396 h	298
Vacuum and structures	253 h	52
Beam diagnostics	29 h	25
Operation	12 h	15
Safety-/ Interlock system	19 h	28
Ion Sources	251 h	88
RF system	272 h	408
Controls	48 h	35
Infrastructure	47 h	21
Others / ambiguous	109 h	54
Total of unscheduled down time	**1436 h**	**1024**

In Table 4 all unscheduled down time events are shown in more detail. Compared to 2009 about 80 hours more of down time events were recorded, which is in comparison to the increased operation time a relative decrease.

In April a technical problem at the ECR ion source caused a break of five days of ^{48}Ca operation. A thunderstorm in July cut the power connection and many subsystems of vacuum and power converters failed and broke down. It took two days to come back to full operation. As well as in 2009 during commissioning for the 4th block the breakdown of one drift tube cooling threatened a stop of the operation. The formerly established special mode of low duty cycle operation allowed standard beam conditions for SIS injection and the operation could be continued. For the UNILAC experiments with energies above 8.6 MeV/u the duty cycle needed to be severely restricted. Before the operation starts in 2011 the damaged drift tube will be replaced.

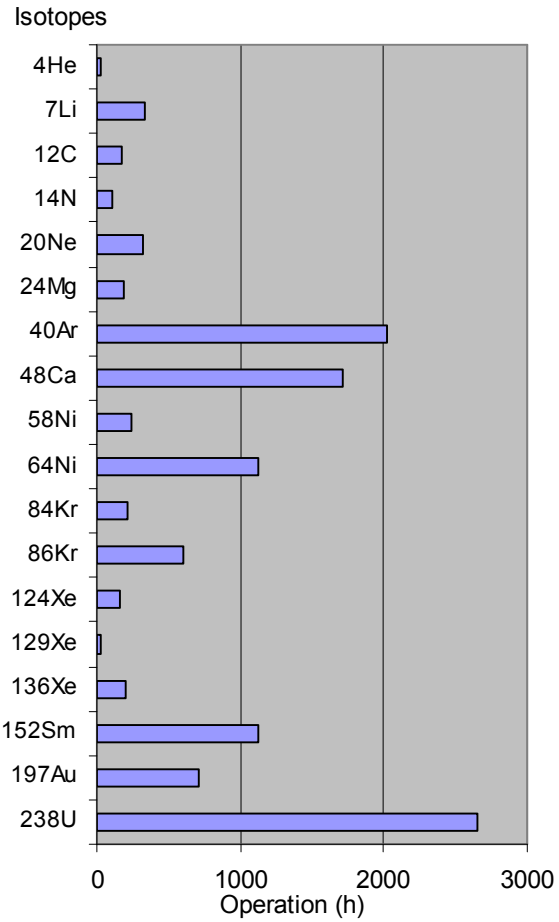

Figure 2: Total beam time for the different ion species

For accelerator experiments at the UNILAC 667 hours, at SIS 271 hours, and at ESR 161 hours beam were delivered, which is for UNILAC an increase by a factor of four compared to last year.

References

[1] P.Schuett, The GSI Operation Logbook OLog, WAO2010

[2] Report of beam time coordinator, this report

Space Charge Lens for Focusing Heavy Ion Beams*

K. Schulte[1], M. Droba[1], O. Meusel[1], and U. Ratzinger[1]

[1]Institute of Applied Physics (IAP), Goethe University, Frankfurt, Germany

Introduction

Space charge lenses (SCL) can be considered as an alternative concept for the focusing of low energy ion beams. Based on IAP experience a scaled up SCL was designed.

To investigate the performance of the SCL for dedicated applications a joint IAP/GSI-experiment is under preparation [1].

Space Charge Lens

A SCL has been designed for a possible application at the GSI High Current Injector. With a maximum potential of 50 kV and a maximum magnetic field of 160 mT, the lens is well suited for focusing an U^{4+} beam with an energy of 2.2 keV/u. The overall length of the prototype is 436 mm with an aperture of 150 mm (figure 1).

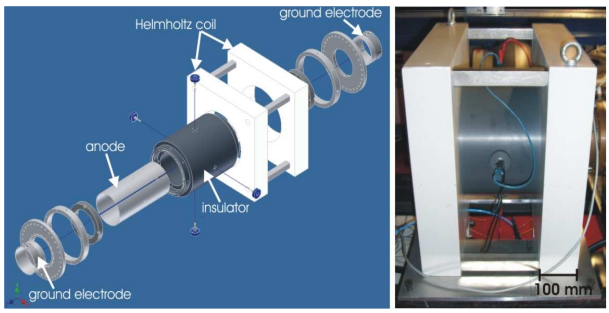

Figure 1: Exploded drawing (left) and photo of the constructed space charge lens (right).

Focusing free of aberration requires a homogeneously distributed electron cloud trapped within the lens volume.

Numerical simulations using Φ_A=30 kV electrode potential and a magnetic field of B_z=13 mT for the confinement of the non neutral plasma results in a nearly homogeneous electron density distribution of $n_{e,max}=2.7\cdot10^{14}$ m^{-3}. This yields in a linear selffield of E_r=117 kV/m at r=50 mm.

Due to the enlarged distance of the Helmholtz coil the produced magnetic field is non-uniform in the z direction. In comparison to a homogeneous magnetic field, this leads only to minor changes in the density distribution. Figure 2 shows the measured on-axis magnetic field at 5A current compared to the numerical simulation.

The SCL has already been tested for its vacuum capability and installed in the future test stand.

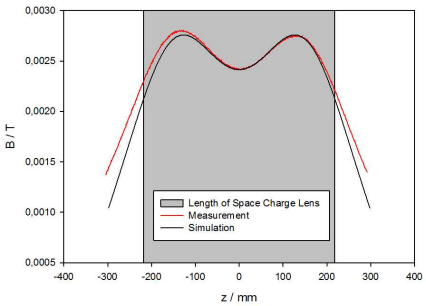

Figure 2: Measured (I=5A) and calculated on-axis magnetic field of the two coil array.

Diagnostics and Experiment

From previous work it is well known that the performance of the SCL depends on thermodynamic properties of the non neutral plasma. Therefore one important issue when using SCL is defining the plasma state to optimize the focusing capability.

A new experimental set-up (figure 3) will provide the opportunity to determine the plasma parameters and the time dependency of the plasma state at different confinement conditions [2].

Afterwards, beam experiments will be performed to establish working points of the SCL. Possible plasma-beam-interactions will be investigated in detail.

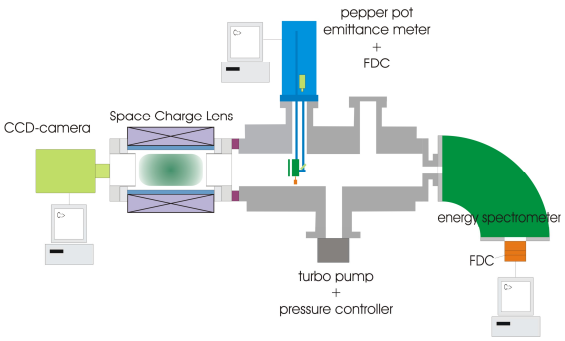

Figure 3: Scheme of the future test stand to study the electron cloud under varying confinement conditions.

References

[1] A. Adonin et al., “Measurements of Transverse Ion Beam Emittance Generated by High Current Ion Sources at the GSI Test Injector Facility HOSTI”, Rev. Sci. Instrum. 81, 02B707(2010).

[2] K. Schulte et al. , “Space Charge Lens for Focusing Heavy Ion Beams”, LINAC’10, Tsukuba, Japan, MOP102, (2010).

* Work supported by HIC for FAIR, BMBF No. 06FY90891.

#Schulte@iap.uni-frankfurt.de

UNILAC Status and Developments

W. Barth, G. Clemente, L. Dahl, P. Gerhard, L. Groening, M. Maier, S. Mickat, M.S. Kaiser, H. Vormann, S. Yaramishev, GSI, Darmstadt, Germany

Status of Operation

In the first three months the upgrade of the HLI -RFQ was completed. [1] For this reason regular operation with heavy ion beams from the Electron Cyclotron Resonance (ECR) ion source accelerated in the High Charge State injector (HLI) started in April. The UNILAC experiments used the HLI-beam with a duty factor of up to 30%. A ^{40}Ar-beam were delivered for about 3 weeks performing the commissioning of the RFQ and the re-commissioning of the entire HLI. Concerning the limited beam time the ECR source operation was focused on the production of four different isotopes (^{12}C, ^{24}Mg, ^{48}Ca, ^{64}Ni) only. During a six weeks block with nickel beam in a SHIP-experiment were supplied. Beside UNILAC-experiments dedicated to nuclear chemistry, plasma physics and material research used the nickel beam in a parasitic mode. ^{48}Ca was used for two long beam blocks of four weeks each. In the first block the beam was delivered to TASCA and SHIPTRAP. During the second block the reaction ^{48}Ca + ^{248}Cm → ^{296}116 [2] was successfully performed at the SHIP, confirming the synthesis and decay data of isotopes of element 116 studied at FLNR in Dubna. Additionally experiments in the X-branch (X2, X6 and X7) and in the plasma physics cave were performed with calcium beam also. Two short runs of one week each for further biology experiments with a carbon beam and for the TASCA-Separator (^{24}Mg) were accomplished between the long blocks. The ECR-beams were also injected into the SIS 18 for high energy fixed target experiments as well as for ESR-experiments.

The Penning (PIG) ion source provided ^{7}Li, ^{20}Ne, ^{40}Ar, ^{84}Kr, ^{136}Xe, ^{152}Sm, ^{197}Au and ^{238}U beams with medium intensity, especially for high duty factor experiments with heavy ions at UNILAC-beam energies. Mainly heavy ions were delivered for material research experiments at the M-branch and at X0, and other UNILAC-experiments in the X-branch (X2, X6, X7, X8). Light ions as well as heavy ions with short pulses from the PIG were accelerated in the UNILAC for the SIS 18.

The MUlti Cusp Ion Source (MUCIS), operating with noble gases, provided high current beams for the SIS 18 (^{40}Ar, ^{86}Kr, ^{124}Xe). The Metal Vapour Vacuum Arc (MEVVA) ion source delivered ^{58}Ni and ^{238}U beams also for SIS-injection. The UNILAC was in operation for more than nine weeks of regular uranium beam experiments.

The ECR-operation was disturbed for one week by a failure in the rf-supplying system (rf-tuner) and due to problems with contamination in an ECR-chamber. Furthermore the start of regular operation with the new RFQ was delayed. After several breakdowns due to thermal load problems, the operation of the RFQ was limited while operation became more complicated. But for all that the UNILAC operated with a sufficient reliability. [3]

UNILAC-Shutdown Activities

During eleven weeks of shutdown time different measures especially at the 40 years old ALVAREZ-tanks were accomplished repairing defects and preventatively aiming for a sufficient operation performance: Power supplies for the Alvarez 3 and 4 inner tank quadrupoles as well as for the A2 intertank quadrupoles were installed, enabling stronger beam focussing. The Alvarez tank revision program starting two years ago was finished for tank no. 1, while the activities at tank 2 were continued by checking the sealing at the pre-vacuum system. Furthermore the chemical rinsing program was completed by applying this procedure for the cooling system of the drift tubes and the tank mantle of ALVAREZ 3 and 4. Among other problems the damaged cooling resulted in an overheating of four ALVAREZ drift tubes and its quadrupoles. Accordingly after a long time of beam operation with limited duty factor and reduced focussing strength, new drift tubes were installed in the winter shutdown 2010/11.

UNILAC-Upgrade Measures

Different UNILAC-upgrade measures were planned and partly accomplished in essence:

- Advanced optimization of the HSI-RFQ-performance
- Preparation of the HSI-LEBT-Upgrade for FAIR
- Mounting of additional BIF-stations in the UNILAC and the transfer line to the SIS18 (FAIR-UNILAC-Upgrade)
- HLI-RFQ-Upgrade
- Preparation of the cw-LINAC-Demonstrator [4]

Machine Experiments

Five days of machine experiments were performed with an high current argon beam mainly for the investigation of resonance effects in the poststripper. Additionally eleven days with a high current uranium beam from the MEVVA- source were accomplished for further optimization of the HSI-beam and mainly for life time measurements with medium charge state uranium beams in the SIS. Foil stripping [5] at a low beam energy (1.4 MeV/u) was introduced, aiming in very high beam currents for injection into the SIS ($1\cdot10^{11}$ U^{39+}-particles/100µs) used for machine experiments in the synchrotron first time.

References

[1] P. Gerhard, et. al., Status of the HLI-RFQ-Upgrade (this rep.)
[2] S. Hofmann, Reaction $^{48}Ca + ^{248}Cm \rightarrow ^{296}116$ studied at SHIP, (this rep.)
[3] U. Scheeler et. al., Accelerator Operation Report, (this rep.)
[4] S. Mickat, et al., Status of the cw-LINAC demonstrator (this rep.)
[5] H. Vormann, et. al., Carbon foil tests, (this rep.)

Carbon foil stripper tests with a high current uranium beam at 1.4 MeV/u

W. Barth, G. Clemente, L. Dahl, P. Gehard, L. Groening, M. S. Kaiser, B. Lommel, M. Maier, S. Mickat, W. Vinzenz, H. Vormann

GSI, Darmstadt, Germany

U^{4+}-beams from the MeVVa and the Penning ion source were used for machine investigations of the GSI-UNILAC and synchrotron (SIS18). Carbon stripper foils (20, 40, 50 µg/cm^2), temporarily replacing the UNILAC gas stripper, were used at 1.4 MeV/u to provide for highly charged uranium ions (around 39+) to be delivered to the SIS18 for beam life time measurements (low current high duty factor). High current tests to check the durability of the carbon foils (with low duty factor) showed no measurable variation of the stripped beam in the poststripper DTL during the life time of the foils. With foil life times of more than 8 hours, the high current U^{39+} operation is a notable option for the future [1].

Beam measurements

All 19 foils (diameter 30 mm) were prepared and glued on target holders in the GSI target laboratory (Fig. 1).

A high current uranium beam from the MeVVa was used to accelerate 0.5 MW-beam pulses (1 Hz, 100 µs) up to 1.4 MeV/u. A maximum beam intensity of 9 emA U^{39+} was achieved behind charge separation. The maximum poststripper transmission was 95 % (Fig. 2). Up to 10^{11} uranium particles per 100 µs were obtained in the transfer line to SIS18 (according to 6 emA U^{39+}).

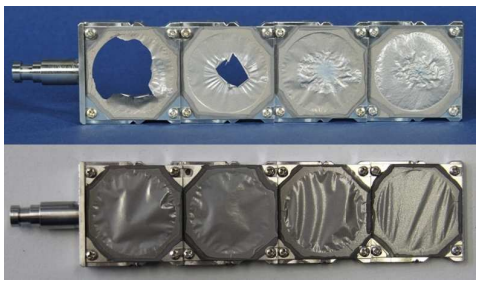

Fig. 1: Foil stripper before (bottom) and after (top) high current operation. For the second foil (top, from the right) an energy of 11 kJ was deposited.

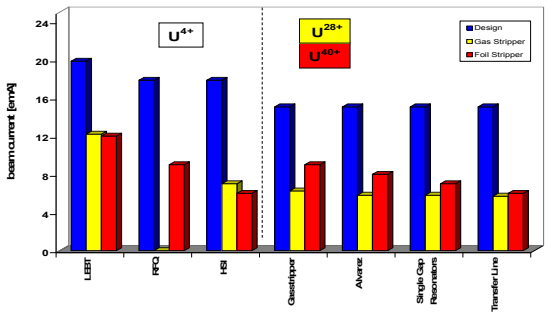

Fig. 2: Beam transmission along the UNILAC.

Carbon foils with different thicknesses were used during nine days of operation, conditioned by low intensity uranium or argon beams from the Penning source, to reduce sudden damage or thickness decrease. A maximum integral energy of 25 kJ was deposited by the high current heavy ion beam until the foil was destroyed. After operation, polycrystalline graphite in the target center was observed, a sign for very high temperatures. The life time of the 20 µg/cm^2-foils (high current uranium average operating time 11±4 h) was appr. three times higher compared to the thicker foils (Fig. 3). A second set of 20 µg/cm^2-foils with lower cleanness of the raw material had a slightly shorter life time.

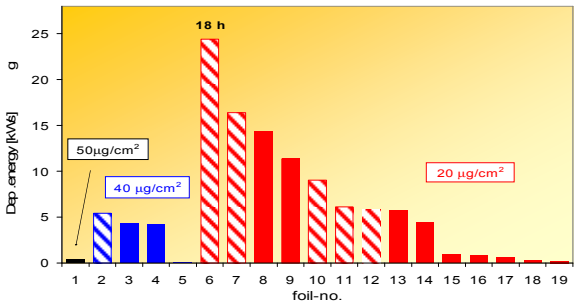

Fig. 3: Deposited beam energy for all 19 stripper foils; streaky marked foils were destroyed.

With the 20 µg/cm^2-foil the main charge state was 39+ (20 % yield). The energy loss (depending on the target thickness) for the favourable 20 µg/cm^2-foil was 17 keV/u (1.2 %), acceptable for the poststripper section (40 µg/cm^2: 26 keV/u). The measured longitudinal emittance for foils was 35 % higher compared to gas stripper operation (12 keV/u*ns). The transversal U^{39+} emittance in the poststripper section was 50 % higher compared to the U^{27+} beam from the gas stripper. Applying further foil stripping at 11.4MeV/u the beam emittance for U^{73+} exceeds significantly the emittance for U^{39+}(Fig. 4).

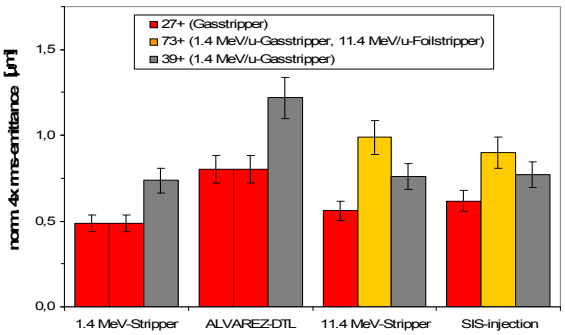

Fig. 4: Measured emittance for different stripper scenarios.

References

[1] W. Barth et. al., High Current U^{40+}-operation in the GSI-UNILAC, LINAC2010, Tsukuba, Japan (2010)

Commissioning and Operational Experience of the HLI-RFQ

P. Gerhard[*1], *W. Barth*[1], *L. Dahl*[1], *K. Tinschert*[1], *W. Vinzenz*[1], *and H. Vormann*[1]
[1]GSI, Darmstadt, Germany

Introduction

The high charge state injector (HLI) at the UNILAC provides beams mainly for the super heavy element research (SHIP, TASCA). It comprises an ECR ion source, a radio frequency quadrupole (RFQ), an IH structure and two bunchers [1]. High average beam intensities of rare isotopes are the domain of the HLI. An upgrade program, aimed at increased beam intensity, quality and duty cycle, was started in 2005 [2]. As one part of this, a new RFQ [3] was delivered to GSI in 2009. High power rf commissioning started in November, accompanied by beam emittance measurements of the beam from the ECRIS [4].

Commissioning

The first beam commissioning in Feb. 2010 was focussed on the RFQ. Additional beam diagnostics and magnets allowed for accurate measurements of the beam emittance directly behind and the transmission through the RFQ (fig. 1 and [5]). Beam energy was also measured, and a working point was defined.

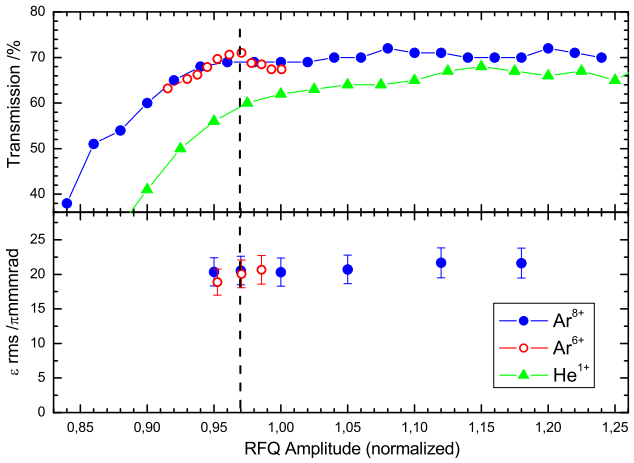

Figure 1: Measured transmission through the RFQ (top) and emittance behind the RFQ (bottom). The working point is indicated by the dashed line.

After the additional components were removed, the RFQ was finally set up for regular operation. The second beam time end of March was dedicated to the commissioning of the complete HLI. Investigations focussed on the interplay of the three rf cavities RFQ, rebuncher and IH, and the beam matching to these structures. Operating parameters for all components were achieved.

In both campaigns different charge states of Argon were used in order to explore different rf and magnet settings. Beam matching to the RFQ was optimized up to 80% transmission, good matching of the beam to the IH could be achieved.

One of the main features of the new RFQ is the cw operation capability. This leads to a high thermal load of up to 60 kW. During commissioning 35 kW could be reached, but three breakdowns occurred, all related to the contact springs connecting the tuning plates to the stems (fig. 2). In April, all contacts were replaced by a more robust type. After three months of operation again one contact had to be replaced. Therefore new tuning plates using a solid silver foil as contact were constructed [5], replacement started in November 2010.

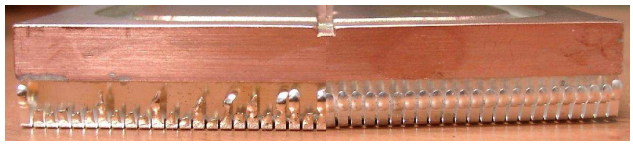

Figure 2: Contact springs burnt (left) and renewed (right).

Beam Operation

Several long beam times (about 480 shifts in total) were successfully completed [6]. High beam transmissions could be achieved, leading to sufficient particle intensities on the targets. Due to the thermal load problems, operation was limited to 15 kW after the last breakdown, severely impairing the performance, especially the duty cycle. As a side effect, operation became complicated and unstable.

Conclusion & Outlook

The commissioning as well as operational experience are promising that the new RFQ will enhance the performance of the HLI as planned. The rf problems have to be solved by the new tuning plates. Work is still in progress, beam recommissioning is planned for February 2011.

References

[1] N. Angert *et al.*, LINAC90, LA-12004-C, p. 749
[2] P. Gerhard *et al.*, EPAC'08, THPP021
[3] M. Vossberg *et al.*, PAC09, FR5EP064
[4] P. Gerhard, GSI Scientific Report 2009, p. 148
[5] P. Gerhard *et al.*, IPAC'10, MOPD028
[6] S. Hofmann *et al.*, (this report)

* p.gerhard@gsi.de

Scintillation Screen Studies at UNILAC Energies

E. Gütlich[1,2], W. Ensinger[2], P. Forck[1], K. Gütlich[1], R. Haseitl[1], A. Reiter[1], and B. Walasek-Höhne[1]
[1]GSI, Darmstadt, Germany; [2]Technical University Darmstadt, Darmstadt, Germany

Scintillating screens are commonly used for more than fifty years at accelerator facilities, for several types of measurements. Their imaging qualities are not well understood, especially for high current ion beam operations. Therefore, inorganic scintillators were investigated for ion energies between 4.8 and 11.4 MeV/u. The light yield, imaged beam width and higher statistical moments of the obtained profile show strong dependence on the scintillating materials deployed and their temperature [1].

A novel experimental setup for spectroscopic investigations has been developed, to determine the influence of the ion beam intensity on the spectra of the materials. The setup allows to investigate the spectrum of the material along one transversal axis (X-direction), and thus to distinguish the spectrum of the center of the ion beam from outer regions. The investigated strip of the beamspot has a typical height of 1 mm (in Y-direction), and depends on the slit setting of the spectrometer. The height of 1 mm is small compared to a typical gauss-like beam width σ=3 mm. Fig. 1 depicts the spectrum of one of the investigated materials (Al_2O_3). The spectrum shows a broad band between 300 and 500 nm, which consists of three color centers (oxygen vacancy with one or two electrons); F^+ (330 nm), F^0 (420 nm), F_2^+ (390 nm) [2]. Additionally, the Cr^{3+} line around 693 nm coincides with the second order of the color centers. Except for the intensity of the chromium line, the spectrum of the center of the ion beam is very similar to the one of the outer part. This shows that there is no significant dependence of the shape of the color-centers spectrum on the beam intensity. High current results presented here are quite similar to the low current results in the literature, for example [3].

To validate the imaging qualities of the screens, different profile measurement methods were compared. To obtain a better resolution compared to SEM-Grid (1.5 mm), a scraper scan method was established. In this method a totally-absorbing scraper is scanning through the ion beam. For each scraper position the remaining beam current behind the scraper is measured via a current transformer. The first derivative of the current signal gives the beam profile with very good resolution (e.g. 0.05 mm). In Fig. 2 (left) the three methods are compared for an Ca ion beam at 4.8 Mev/u and are in good agreement.

At similar beam flux rate $(ions/cm^2/s)$ as Fig. 2 (left) and 11.4 MeV/u, the obtained beam profile from the Al_2O_3 screen (resolution: 10Px/mm) disagrees with the two reference methods, see Fig. 2 (right). A $F^0 \rightarrow F^+$ conversion could be excluded by the spectroscopic investigations (F^0 emission is only detectable by UV-enhanced optics). The disagreement at higher beam energy has been attributed to the overlapping of ion tracks in space and time. A model is under development to explain the experimental findings for Al_2O_3 and evaluate its ability as an accurate scintillator for high current ion beams.

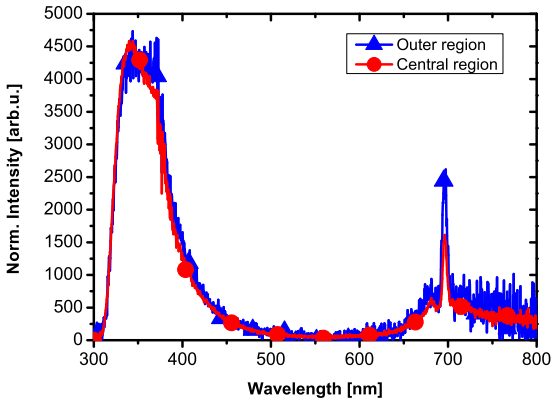

Figure 1: Scintillation light spectra of the outer and inner part of the beam spot on Al_2O_3. Parameters of Ca^{10+} beam: 3 ms macropulse length, 1 Hz repetition rate with $6 \cdot 10^{10}$ ppp at 4.8 MeV/u.

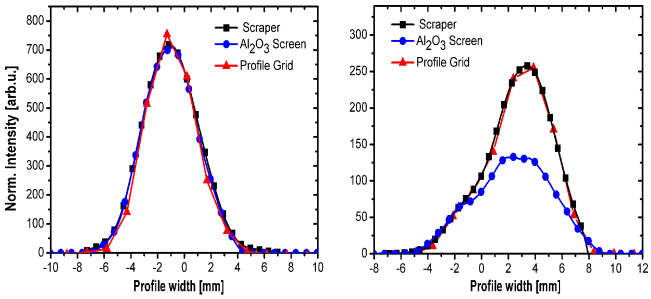

Figure 2: Comparison of the beam profiles obtained with SEM-Grid, Scraper and Al_2O_3 Screen. Parameters of Ca^{10+} beam, Left: 5 ms macropulse length, 1 Hz repetition rate with $4.3 \cdot 10^{10}$ ppp at 4.8 MeV/u. Right:1.2 ms macropulse length, 1 Hz repetition rate with $1.8 \cdot 10^{10}$ ppp at 11.4 MeV/u.

References

[1] E. Gütlich et al., "Scintillation screen investigations for high current ion beams", 2010, IEEE Transactions Nuclear Science, Vol. 57, No. 3., pp. 1414 (Correction in Vol. 57, No. 4 (August 2010)).

[2] B. D. Evans, "A review of the optical properties of anion lattice vacancies and electrical conduction in $\alpha - Al_2O_3$", 1995 Journal of Nuclear Materials, 219, pp. 202.

[3] V. A. Skuratov, "Luminescence of LiF and $\alpha - Al_2O_3$ crystals under high density excitation", 1998 Nuc. Inst. and Meth. B, 146, pp. 385.

UNILAC Beam Profile Measurements at High Currents using BIF

C. Andre, F. Becker, H. Bräuning, C. Dorn, R. Fischer, P. Forck, H. Graf, R. Haseitl, T. Hoffmann, K. Lang, R. Lonsing, R. Mahr, M. Schwickert, B. Walasek-Höhne

GSI, Darmstadt, Germany

Overview

To cope with the demands of FAIR for UNILAC high-current operation, non-intercepting beam diagnostics is mandatory. A new diagnostic for transverse beam profile measurements, the Beam Induced Fluorescence monitor (BIF) was developed. After the first BIF installation in 2008 (Unilac section US1), three new monitors were installed (Unilac section UA4 and transfer-line sections TK2 and TK6) and several upgrades were performed to make the monitors more reliable and easier to use for the upcomming handover to operation. For FAIR several BIF monitors are destined for p-Linac, HEBT and SFRS and it is foreseen to realize all slow controls by Siemens SPS and FESA-based software.

Principle and Installation

The BIF principle is based on the observation of fluorescent light, emitted by excited gas (e.g. nitrogen) molecules [1]. A custom designed image-intensified camera system (Proxitronic) performs single-photon counting to ensure single-shot measurements at low inserted gas pressure.

Each BIF monitor consists of two perpendicularly mounted cameras to measure transversal beam profiles in horizontal and vertical plane, see fig. 1. Further hardware details are described in [2]. A newly integrated Siemens SPS controlled by FESA serves all slow controls (gain settings, iris control, calibration LEDs) and controls all power supplies for the instruments in the tunnel [3]. Several protection procedures are implemented to prevent the image intensifiers from damage.

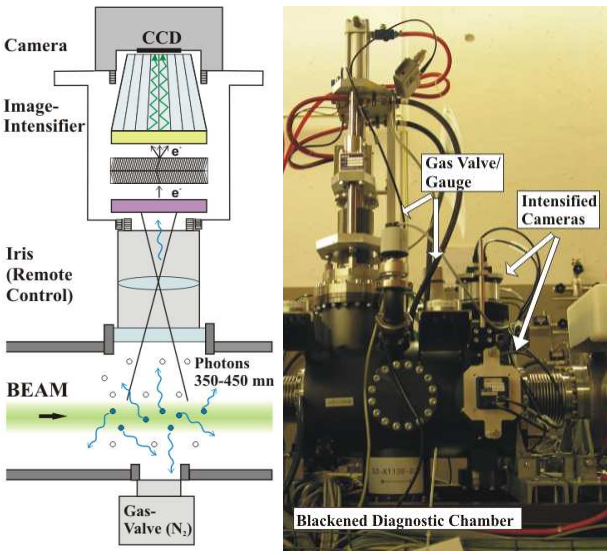

Figure 1: BIF principle and installation at US1

Software and Operation

The system is operated by the ProfileView software [4], either via X-terminals in the main control room or a Linux-PC. An easy-to-use GUI ('User Mode') is designed for the operating crew to run BIF as a standard beam profile monitor. Only the gas-pressure is a free parameter controlled by the user to adjust the ligth yield. All other parameters are automatically set to reasonable values. The GUI shows profiles of up to three monitors (horizontal and vertical plane) at the same time. An example is shown in fig. 2.

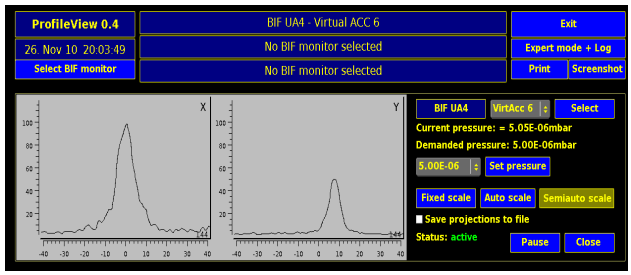

Figure 2: ProfileView in 'User Mode'

An additional 'Expert Mode' enables experienced users to set all other parameters, like e.g. gain for the multichannel plates and phosphor screens, aperture of the iris and the timing manually. In the Expert Mode original images can be displayed and saved. It is used for debugging or research experiments.

Outlook

After the proof of functionality and extensive testing, all installed BIF monitors will now be equipped with Siemens SPS devices and handed over to the operating team. The installation of two additional monitors (Unilac section US4 and UT1) is planned for 2011.

References

[1] F. Becker et al., "Beam Induced Fluorescence (BIF) Monitor for Transverse Profile Determination of 5 to 750 MeV/u Heavy Ion Beams ", DIPAC 2007, Venice, May 2007, p.33

[2] C. Andre et al., "Commissioning of Beam Induced Fluorescence Monitor at Unilac", GSI Scientific Report 2008, Darmstadt

[3] R. Haseitl et al., "Integration of Programmable Logic Controllers into the FAIR Control System using FESA", PCaPAC 2010, Saskatoon, Oct. 2010, p.44

[4] R. Haseitl et al., "ProfileView – A Data Acquisition System for Beam Induced Fluorescence Monitors", DIPAC'09, Basel, May 2009, p.134

Status of the UNILAC Makro-Puls-Selektor (MAPS)

H. Reeg, M. Hartung, H. Brand, M. Schwickert[1], M. Kümmerling[2]

[1]GSI, Darmstadt, Germany; [2] Fa. Hörmann-IMG GmbH, Nordhausen, Germany

Since 15 years the MAPS has been an indispensable tool for daily operation of the UNILAC, to visualize the actual beam current of the UNILAC macropulses at given locations being measured by 45 beam current transformers (BCTs). It also shows an overlay of the beam current signal with each related gate pulse, to allow for checks and adjustments of the integration timing. Additionally, synchronous information about the gated-average beam current as measured by the selected transformers along the beam path is displayed, thus an online display of 2 BCTs and the related ion transmission can be observed.

Layout of the MAPS System

The existing MAPS is based on a PC under MS-DOS. This aged instrument offers a maximum number of 32 BCT channels, of which only 2 can be selected by a custom-made MUX. The related C^{++} code is archaic, not supported anymore, and no LAN connection is foreseen.

For the new MAPS the PC was replaced by a PXI-crate (National Instruments PXI-8186) running a LabVIEW™ realtime server application [1,2]. In order to increase the maximum number of BCTs up to 128, a new MAPS data bus had to be implemented. To handle the heavy data load a new interface bus technique became necessary, in order to concentrate the data sets of presently 64 transformers.

The digital signals (gate pulses, triggers) of up to 64 BCTs are analyzed and processed in a FPGA board (NI PXI-7811R), while the analog signals are digitized by 8 ADC boards (NI PXI-6133). The data sets of the BCTs from each crate are serialized and transmitted by special interface cards. The data telegrams are then further processed by a SerDes unit and transferred into the PXI-7811R via a new PXI interface. All cards have been redevelopped, comprising Actel®FPGAs [3]. A schematic layout of the data transport subsystem is given in Fig. 1.

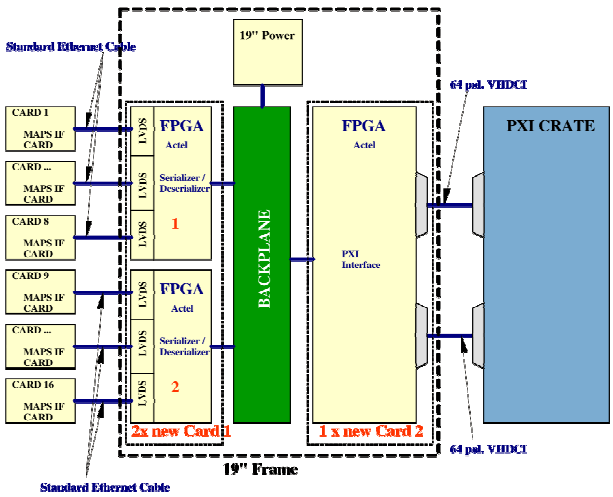

Fig. 1: Layout of the MAPS data transport subsystem

The hardware for the new MAPS system is now readily installed in local control area 4 and has undergone thorough commissioning and detailed performance tests. Initial communication problems between the MAPS interface cards and the National Instruments FPGA adapter have been resolved, as well as minor timing and network problems. At present only BCTs of the UM branch are connected to the new MAPS for testing purposes.

Besides a hardware upgrade, the goal of the new MAPS system was a software enhancement. The new server software supports multi-client connections, thus data storage e.g. of actual beam currents or transmission data will be available, in parallel to the macro pulse readout. The first version of the client GUI is shown in Fig. 2. It is designed very similar to the old MAPS, in order to serve as an exact replacement of the old display, well matched to the needs of the operators.

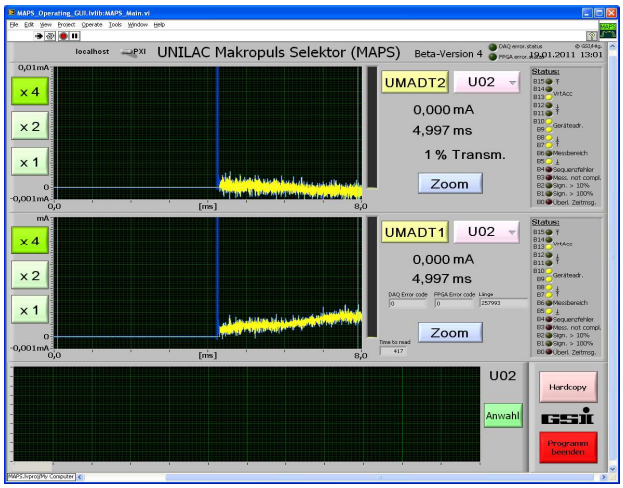

Fig. 2: New MAPS client application; Top and center box: beam currents in 2 BCTs, Bottom box: transmission data

Outlook

Final debugging of the client software is ongoing, and in a next step, the display will be extended for more BCTs. Trending diagrams and data logging will be implemented after a test installation of the MAPS client (see Fig. 2) in the GSI main control room, which is planned for summer 2011.

The GSI authors wish to thank the Hörmann-IMG staff for their excellent design and realization of the MAPS and LVDS/PXI adapters, and fruitful discussions.

References

[1] GSI Report 2005-1, p. 325
[2] www.ni.com
[3] www.hoermann-img.de

Novel High-Resolution Analysis for Linac Phase Probes

A. Reiter, W. Kaufmann, C. Kleffner

GSI, Darmstadt, Germany

Phase probes are a crucial diagnostic tool for pulsed particle beams of linear accelerators. In this contribution we present a new data analysis which has been established during commissioning at the HIT and CNAO medical centres, and which has delivered improved results, at GSI most recently at the HITRAP decelerator.

Hardware & Data Analysis

For the compact 7 MeV/u injectors of the HIT and CNAO [1] facilities (RFQ+IH-DTL, f_{rf}=216 MHz), a new phase probe acquisition and monitoring system was designed consisting of:

- improved phase probe design (f_{Max} < 3 GHz)
- high-quality amplifiers (20-60 dB, 1 GHz bandwidth)
- ADC acquisition system (4 GSa/s, 1 GHz BW)

Additional input signals for the time-of-flight (beam energy) and phase relations measurements were derived from tank probes which monitor the RF power in an accelerator or a buncher. All measurements compare data of two probes and, at first, determine the time offset between those signals.

In a twofold manner the new analysis exploits the periodic nature of phase probe signals and sampling process, and can be summarised in four steps:

1. In-pulse average: Raw data sampled within one macro-pulse are divided into blocks of length $N*\tau_{rf}$ (N = 49, τ_{rf} = RF period) where the integer N is chosen such that each block starts at a multiple of the 250 ps sampling period. These blocks are averaged to improve the signal-to-noise ratio.
2. Interleaving: The averaged data block is projected from N into one single RF period. This improves the timing resolution theoretically to ~5 ps.
3. Smoothing, if needed: FFT filter, moving average
4. Time offset calculation based on the position of the maximum in the cyclic cross correlation function defined by the two processed data vectors

This analysis can be adapted to typical combinations of sampling and radio frequency, and yields a robust estimate, since it takes into account all acquired data, it constructs a function with one local maximum, and it has no free parameters − N, probe distance, sampling and radio frequency are fixed. Compared to other approaches which were investigated, data of poorer quality could be analysed. The procedure overcomes ambiguity problems of methods that arbitrarily choose two "representative" signals to derive a single time offset but disregard the majority of the data. A particularly inefficient example is the commonly used zero-crossing method which only considers the signal part around the base line and, unlike the cross correlation, is susceptible to DC offsets and drifts.

Results & Conclusions

At HIT and CNAO, a ~10 ps timing resolution (1 keV/u or $\Delta E/E \sim 1.4 \cdot 10^{-4}$) was achieved which permits to monitor degradation of the 100 µg/cm^2 carbon stripping foils.

At GSI, a particularly challenging test environment is the HITRAP decelerator [2] due to a short ~3 µs beam pulse, low currents of a few µA and 0.1 Hz repetition rate. Fig. 1 shows phase probe signal DP4 of a 4 MeV/u ESR beam after the double drift buncher DDB (108 & 216 MHz) over three RF periods. Neither raw data (dots) nor in-pulse average (squares, offset for clarity), resulting from step 1 over 6 blocks of 380 ns or 1891 samples, clearly identify the bunched structure of the beam.

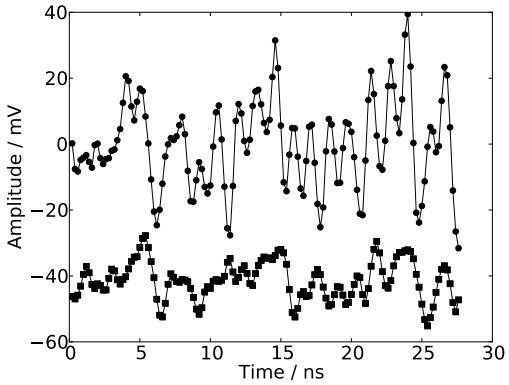

Figure 1: Raw data (dots) and in-pulse average (squares)

Interleaving and smoothing (steps 2 & 3) concentrate all 1891 samples in one RF period and unravel a weak double bunch structure as illustrated in Fig. 2. Behind the IH-DTL where a mixture of energies complicates the data, even more complex pulse shapes were observed. The validity of the analysis was then confirmed by the pulse shape sensitivity to small changes of machine parameters.

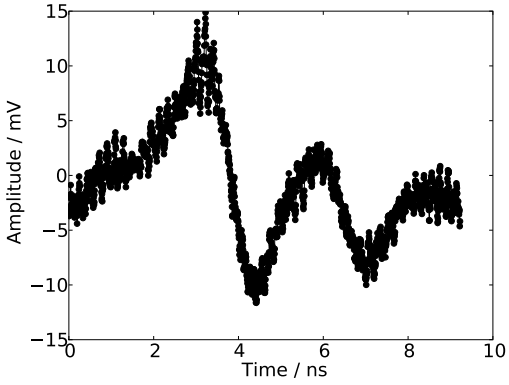

Figure 2: Pulse shape reconstructed from raw data

References

[1] B. Schlitt, WE205, LINAC08, Victoria, BC, Canada
[2] O. Kester, FR-02, HIAT09, Venice, Italy

The status of the cw-LINAC demonstrator

S. Mickat[1], W. Barth[1], M. Kaiser[1], F. Dziuba[2], H. Podlech[2], U. Ratzinger[2], K. Aulenbacher[3]
[1]GSI Helmholtzzentrum für Schwerionenforschung, Darmstadt, Germany
[2]IAP Institut für Angewandte Physik, Universität Frankfurt, Germany
[3]KPH Institut für Kernphysik, Universität Mainz, Germany

Introduction

The continous wave (cw) LINAC demonstrator is an important milestone towards the superconducting (sc) cw-LINAC dedicated to the SHE-program at GSI [1]. It is the first section of the proposed cw-LINAC comprising a sc Cross-bar H-Mode (CH) cavity and two sc solenoids (fig. 1). Full performance tests of the demonstrator are supposed to be in 2013 at the GSI High Charge Injector (HLI). The demonstrator is financed by the Helmholtz Institute Mainz (HIM).

cw-LINAC Demonstrator

A study has worked out which provided a concept to assemble the cryostat with the solenoids and the cavity as well as to adjust the components to the beam axis (fig. 1). Two caps at both sides allow to open the cryostat and to install an auxiliary construction. The construction is used to insert a base frame, which carries the aligned components into the cryostat without stressing the magnetic and the thermal shield. When the base frame is fixed by so-called Nuklotron-suspensions the auxiliary construction can be removed and the caps can be closed.

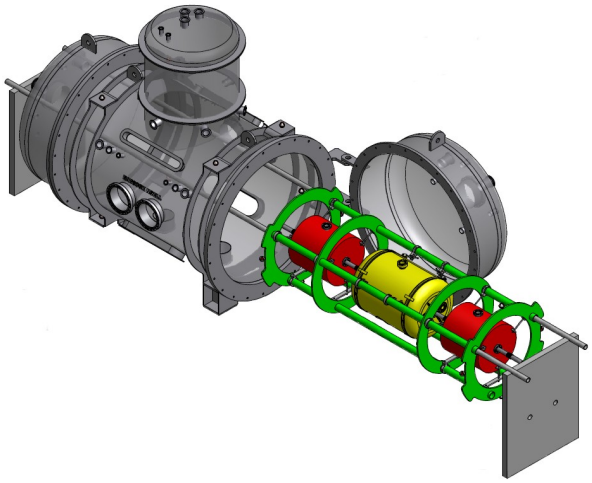

Figure 1: The actual layout of the demonstrator is shown. A base frame carries the cavity embedded by two solenoids. For assembling the cryostat an auxiliary construction is needed.

Setup at HLI

The favoured place to setup the Demonstrator is in straightforward direction of the HLI at GSI [1]. For the longitudinal matching the existing buncher UN6 BB14 can be used. In addition first beam dynamical investigations show that next to the existing transversal focusing elements only a further dublet is needed (fig. 2).

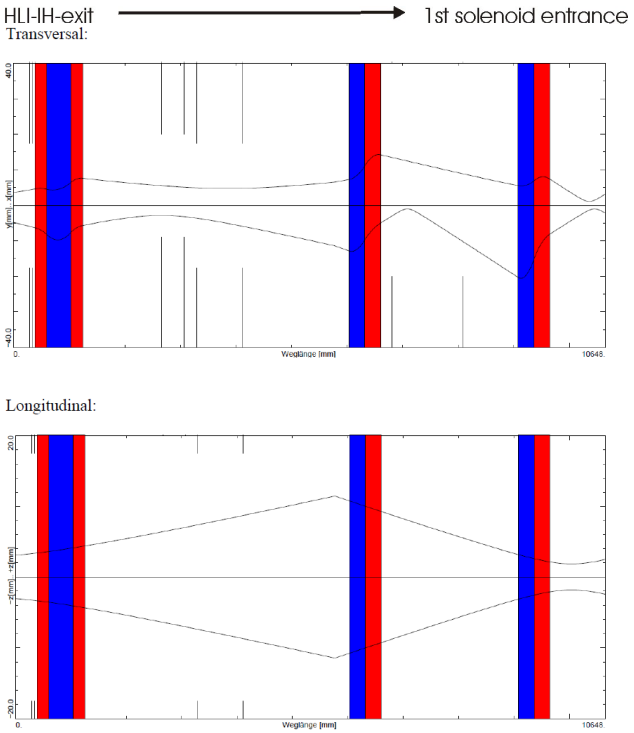

Figure 2: The beam transport behind the HLI-IH to the first solenoid of the demonstrator was calculated by using MIRKO. In addition to the existing triplet and duplet a further duplet is needed for transversal focusing. Longitudinally the existing buncher is used.

Projectstatus and -schedule

	cw-LINAC -Demonstrator
2010	Ordering of the the rf-amplifier and the LHe-supply
2011	Ordering of the cryostat & solenoids and the cavity
2011-2012	Delivery of the components 1st tests (warm + cold)
2013	Full performance test at GSI HLI
>2017	commissioning "sc cw-LINAC"

References

[1] S. Mickat et al.: "The status of the cw-LINAC-demonstrator", ACC-OTHERS-03, p.162, GSI SCIENTIFIC REPORT 2009

The Superconducting CH-Cavity for the cw Linac Demonstrator*

F. Dziuba†[1], *M. Amberg*[3], *M. Busch*[1], *H. Podlech*[1], *U. Ratzinger*[1], *S. Mickat*[2,3], *and W. Barth*[2,3]

[1]Institut für Angewandte Physik, Goethe Universität, Frankfurt, Germany; [2]GSI, Darmstadt, Germany; [3]HIM, Johannes Gutenberg Universität Mainz, Germany

Abstract

The GSI applied for a new superconducting (sc) cw linac in parallel to the existing UNILAC which fulfills the needs in the research field of Super Heavy Elements (SHE). Therefore the design effort for a cw linac demonstrator, which comprises a horizontal cryomodule and a sc CH-cavity embedded between two sc solenoids, has started.

The superconducting cw linac

The dedicated linac has to provide ion beams with A/q up to 6 and energies up to 7.3 AMeV. Above an energy of 3.5 AMeV the linac is fully energy variable. The front end is the existing high charge injector which is at present receiving an upgrade program towards the required duty factor. The main acceleration of approximately 35 MV will be provided by 9 sc CH-cavities operated at 217 MHz (see fig. 1)[1].

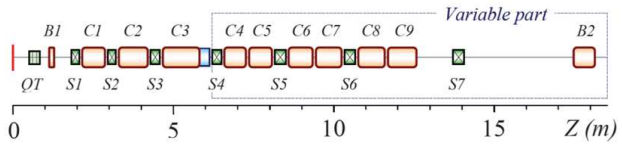

Figure 1: Schematic overview of the cw heavy ion linac. The demonstrator cavity corresponds to C1.

The 217 MHz CH-Cavity

The 217 MHz sc CH-cavity for the cw linac demonstrator (see fig. 2 top) will provide a gradient of 5.1 $\mathrm{MV/m}$ at a total length of 690 mm [2]. To match the design frequency during the fabrication process is the major challenge. Concerning this, the tuning of the cavity will be done by static and dynamic tuners placed on the girders between the stems: 9 static tuners with fixed height are foreseen to readjust the frequency of the cavity during the fabrication. Additionally, 3 bellow tuners, driven by stepping motors are supposed to control the frequency. One bellow tuner is added to a fast reacting piezo element. The slow tuners adjust the frequency after cooling down, while the fast tuner regulates small frequency shifts during operation. Table 1 shows the main parameters of the 217 MHz cavity. The rf design of the first cavity is finished. Further rf and mechanical simulations concerning the cavity tuning are in progress. The call for tender has been released.

* Work supported by HIM, GSI, BMBF Contr. No. 06FY9089 I

† dziuba@iap.uni-frankfurt.de

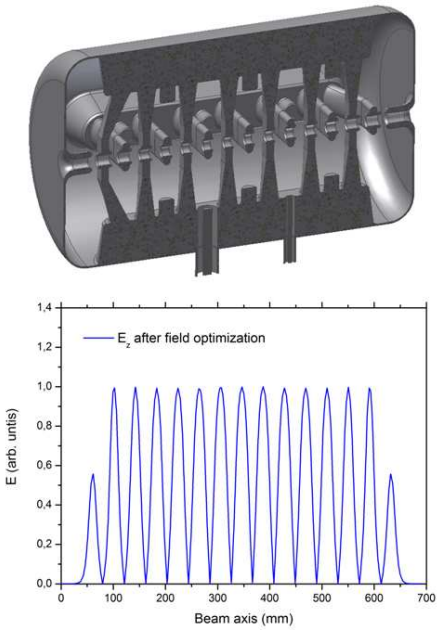

Figure 2: Sideview of the 217 MHz cavity (top) and E_z along the beam axis after field optimization (bottom).

Parameter	Unit	
Beta		0.059
Frequency	MHz	217
Gap number		15
Total length	mm	690
Cavity diameter	mm	420
Cell length	mm	40.82
Aperture	mm	20
Accelerating gradient	$\mathrm{MV/m}$	5.1
E_p/E_a		6.5
B_p/E_a	$\mathrm{mT/(MV/m)}$	5.9
R/Q	Ω	3540
Dynamic bellow tuner		3

Table 1: Main parameters of the 217 MHz CH-Demonstrator.

References

[1] S. Minaev et al., A Superconducting Energy Variable Heavy Ion Linac with Constant Beta, Multi-Cell Cavities of CH-Type, Phys. Rev. STAB 12, 120101.

[2] F. Dziuba et al., Development of superconducting crossbar-H-mode cavities for proton and ion accelerators, Phys. Rev. STAB 13, 041302 (2010).

Status of the 325 MHz, sc CH-Cavity for heavy Ion Linacs*

M. Busch†[1], *H. Podlech*[1], *U. Ratzinger*[1], *W. Barth*[2,3], *and M. Amberg*[3]

[1]Institut für Angewandte Physik, Goethe Universität, Frankfurt, Germany; [2]GSI, Darmstadt, Germany; [3]HIM, Johannes Gutenberg Universität, Mainz

Abstract

Currently the 325 MHz CH-Cavity, which is proposed for beam tests at GSI UNILAC, is under construction. First cryo-tests are determinded for mid-2011. One focus of the new cavity will be the new tuning system consisting of bellow tuners. The design of these bellow tuners is still in progress in order to avoid multipacting scenarios. The challenge of this project will be the exact achievement of the goal frequency after all the fabrication steps which have to be planned very thoroughly.

CH-Cavity Status

The geometry of a 325 MHz, 7 cell, $\beta = 0.15$ CH-cavity has been designed and optimized at the Institute for Applied Physics, Frankfurt University. It is currently under construction at Research Instruments [1]. Parts like stems (see fig. 1) and girders are already deep-drawn.

Figure 1: Fabricated stems of the CH-Cavity.

Compared to the first CH-Cavity the new cavity is equipped with inclined end stems, additional flanges at the tank caps for cleaning procedures , slow / fast bellow tuner inside the cavity and large power coupler due to changed stem geometry: Inclined end stems yield a more homogeneous field distribution along the beam axis compared to straight stems because the volume for the magnetic field in this area and hence the inductance is increased. The longitudinal dimensions of the cavity can be reduced by about 20%-25% since an extended end cell is not needed for field flattening. The flanges at the tank caps provide a convenient way to process the cavity surface chemically. The 7-cell, 325 MHz cavity shown in fig. 2 will be tested with a pulsed, intense, heavy ion beam from the UNILAC.

Bellow Tuners

For the tuning of the cavity three types of tuners are determinded: 4 static tuners with a diameter of 40 mm and a height of up to 60 mm to adjust the frequency after fabrication. They are positioned between the stems, the height will be fixed after adjustment.

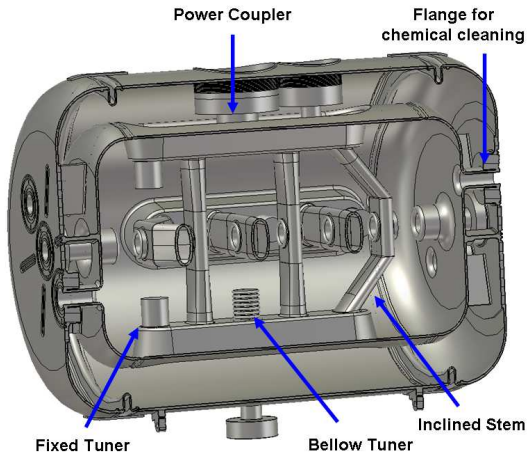

Figure 2: RF design of the 325 MHz sc CH-cavity.

Furthermore there will be two bellow tuners (a fast and a slow one) inside the cavity. They are attached on the girder between the stems and will be driven by a piezo and a step motor, repspectively. The slow tuner adjusts the frequency after cooling the cavity down, while the fast one regulates the frequency during operation. The desired frequency shift for each tuner is $100 - 130 Hz/\mu m$. Simulations have been performed to investigate appearance of multipacting levels. For this type of tuner the results yield that the probability of multipacting decreases from the left to the right picture (fig. 3).

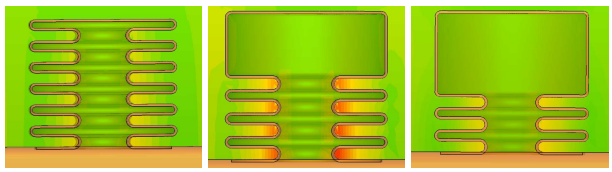

Figure 3: Investigation of multipacting for bellow tuners with different cell number.

References

[1] M. Busch, U. Ratzinger, H. Podlech, A. Bechtold, H. Liebermann, F. Dziuba, M. Amberg, "Recent Superconducting CH-Cavity Development", p. 4911-4913, PAC 2009, Vancouver, Canada.

[2] M. Busch, H. Podlech, M.Amberg, F. Dziuba, U.Ratzinger, "Superconducting CH-Cavity Development", p. 753-755, IPAC 2010, Kyoto, Japan.

* Work supported by BMBF 06FY9089 I

† busch@iap.uni-frankfurt.de

SIS18 Status Report

P. Spiller, W. Barth, L. Bozyk, O. Chornyi, Y. El-Hayek, H.G. Koenig, H. Klingbeil, H. Kollmus, M. Kirk, U. Laier, D. Ondreka, P. Puppel, H. Ramakers, H. Reich-Sprenger, J. Stadlmann, B. Zipfel

GSI, Darmstadt, Germany

High Charge State Operation - Intensity Status

For several ion species, the peak intensities reached in the previous years could be reproduced in 2010. Especially the intensity of U^{73+}-beams could be slightly increased up to $6x10^9$ ions per cycle. For several lighter ions (e.g. for Ar, N) SIS18 has been operated close to the space charge limit. Figure 1 shows the maximum intensity per cycle achieved for highly charged ions with a charge state produced by stripping in the transfer channel.

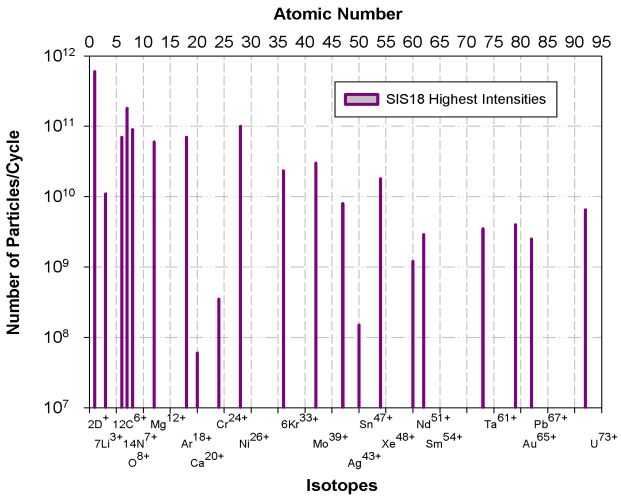

Figure 1: Peak intensities in SIS18 for various ion species. Shown are the intensities per cycle of the accelerated (before extraction) highly charged ions.

Intermediate Charge State Heavy Ion Operation

The machine development program towards highest intensities of beams with intermediate charge state heavy ions has been continued. Several runs have been performed with various (heavy) ion species and charge states. The major intensity step achieved in the year 2009, with more than 10^{10} ions per cycle could be repeated (figure 2). It has been shown that this intensity level represents the actual machine performance achieved by partially completing the technical measures summarized in the SIS18 upgrade [1, 2].

The latest progress in operation with intermediate charge state heavy ions has been achieved by a slight increase of the charge states (U^{39+} instead of U^{28+}). The new charge state could be produced by replacing the gas stripper in the UNILAC by a foil stripper [3]. Since the second stripper stage in the transfer channel (normally used to generate highly charged ions) has been bypassed, the intensity of the U^{39+} beam was comparable with the intensity of the U^{28+} beams. Thus, also for the U^{39+}-beam the number of accelerated ions exceeded the level of 10^{10} ions (see figure 2). However, the increased charge state enables acceleration to a higher final energy (350 MeV/u instead of 200 MeV/u) which is of particular interest for the running experimental program at GSI.

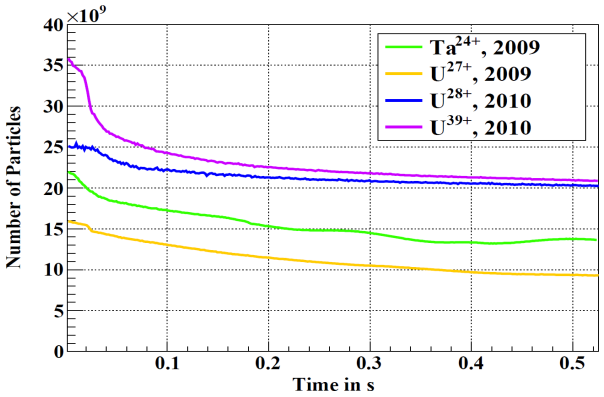

Figure 2: Intensity evolution within SIS18 cycles for various heavy ions with intermediate charge states.

Prediction made with the STRAHLSIM code [4] for the life time of the U^{39+} beam could surprisingly not been confirmed by the corresponding measurements. According to the applied capture and ionization cross sections it was expected, that the life time of U^{39+} beams is significantly longer than of the U^{28+} beams and the charge related beam loss and its consequences for the dynamic vacuum were supposed to be correspondingly lower. In order to confirm the measured life times, the measurement method itself and its dependence on various parameters (e.g. intensity, tune etc.) has been investigated in the frame of machine experiments [5]. By measurements and STRAHLSIM simulations, it could be shown, that the dynamics vacuum affects the results of the life time measurements down to intensities of the order of a few 10^8 ions (figure 3). The selection of the charge state plays an important role for an appropriate design concept of a future linac replacing the existing ALVAREZ section. Therefore, a measurement campaign has been conducted to determine the life time for several charge states of Uranium beams under comparable conditions (figure 4). The dependence of the life time from the charge state can be clearly noticed. Unfortunately, the transition to the life time of charge state 28+ could not yet been measured. However, it is known from previous measurements that the trend which can be seen in the plot, does not continue down to charge states around 28+.

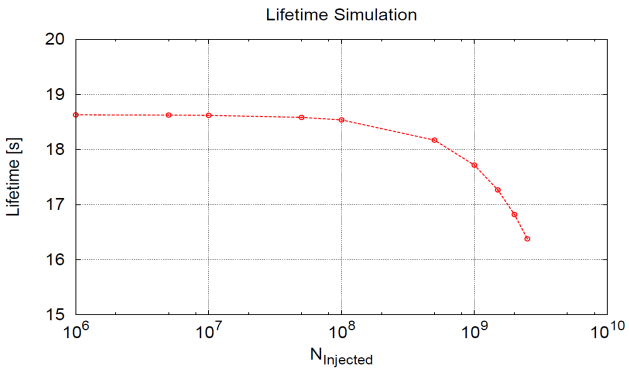

Figure 3: Calculate dependence of beam life time as a function of the beam intensity for U^{39+} ions.

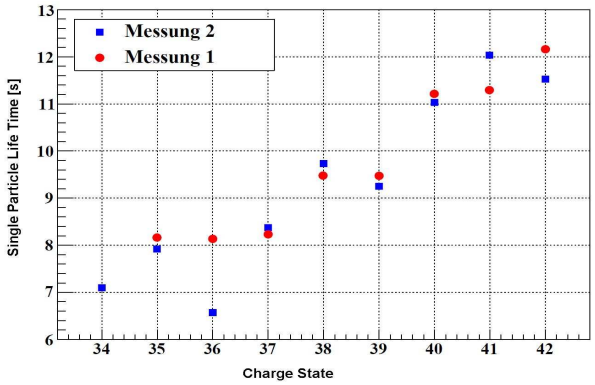

Figure 4: Life time of various Uranium beams with different charge states at 11.4 MeV/u in the SIS18.

Longitudinal Bunch Manipulations and Resonance Driven Beam Loss

Major progress has been achieved with the integration of the new multi harmonic, low level Rf system into the control system [6]. The new hardware, which will be applied for the Rf systems of the new FAIR synchrotrons SIS100/300, has been tested with beam for various use cases and allows complex longitudinal bunch manipulations such as bunch merging, splitting or batch compression. In the frame of machine experiments, bunch merging could be demonstrated with the existing cavities controlled by the new LLRF system. The new system will be used to generate well synchronised dual harmonic buckets in distributed Rf systems. E.g. the new MA loaded h=2 acceleration cavities presently under development for SIS18, will be synchronized and controlled by means of the new LLRF system with respect to the existing ferrite cavities. In order to investigate the potential benefit from a dual harmonic operation for resonance driven beam loss, a dual harmonic bucket has been generated with the presently available two existing cavities at harmonics 4 and 8 (figure 5) [7].

For these measurements, the injection plateau has been extended to one second. Although the measurements have been conducted at moderate intensities (in the order of $2x10^9$ U^{73+}-ions), in case of bunched beams major beam loss has developed.

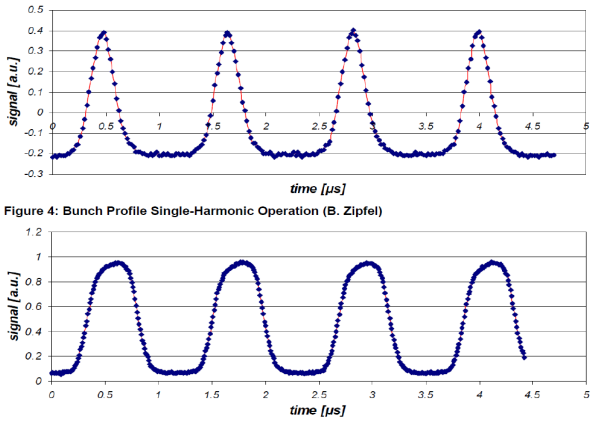

Figure 4: Bunch Profile Single-Harmonic Operation (B. Zipfel)

Figure 5: SIS18 bunches during single harmonic operation at h=4 (top) and dual harmonic operation (bottom) with h=4 and 8 generated with the two existing Rf system using the new low level Rf system.

At equal intensity, no beam loss was observed without bunching. Parallel to the beam loss process, the longitudinal distribution in the bunches performed a transition from flat-top bunches (dual harmonic) to "parabolic" bunches, similar to a single harmonic operation (figure 6). It could be shown that the transition depends on the working point. The underlying beam dynamics process will be a matter of intensive future investigations.

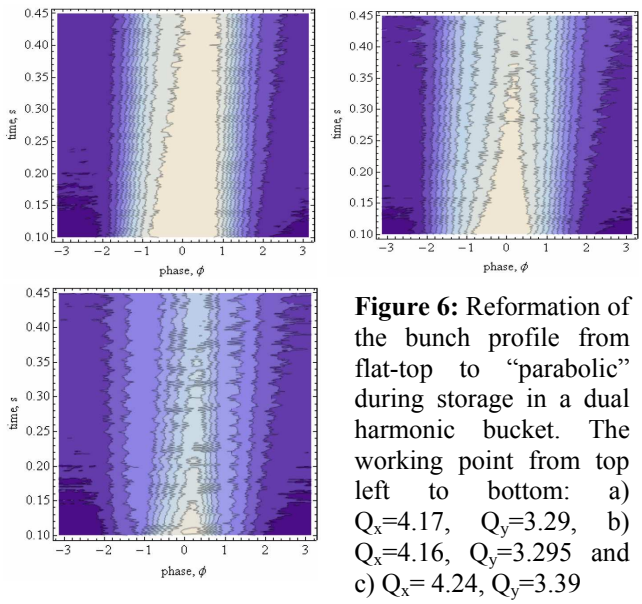

Figure 6: Reformation of the bunch profile from flat-top to "parabolic" during storage in a dual harmonic bucket. The working point from top left to bottom: a) Q_x=4.17, Q_y=3.29, b) Q_x=4.16, Q_y=3.295 and c) Q_x= 4.24, Q_y=3.39

References

[1] P. Spiller et al., Proceedings of IPAC10,(2011)
[2] P. Spiller et al., GSI Annual Report 2009,(2010)
[3] W. Barth, internal note "UNILAC Arbeitsnotiz" (2010)
[4] P. Puppel et al, Proceedings of IPAC10, (2011)
[5] L. Bozyk, internal note, (2010)
[6] H. Klingbeil et al., GSI Memo 26102010
[7] H. Klingbeil et al., GSI-Memo 13122010

Tune Measurements with High Intensity Beams at SIS-18*

R. Singh[1,2], *P. Forck*[1], *P. Kowina*[1], *P. Moritz*[1], *and T. Weiland*[2]
[1]GSI, Darmstadt, Germany; [2]Technische Universitt Darmstadt (TEMF), Germany

Introduction

To achieve a high current operation close to the space charge limit, a precise tune measurement during a full accelerating cycle is required [1, 2]. A tune measurement system was recently commissioned at GSI synchrotron SIS-18, which allows for online evaluation of the actual tune value using digitally recorded position data. Presented here are the first set of experiments conducted using this system. The results show the influence of beam current on the tune spectra. More experimental details and results can be found in [3]. The tune measurement system is based on beam excitation using Pseudo random noise generator followed by digital processing of BPM data so obtained as described in [3, 4].

Experiments and Results

Experiments were conducted with an U^{73+} beam at injection energy of 11.4 MeV/u for one second on the injection plateau. The measurement was repeated for a series of intensities of stored ions from $2.5*10^7$ to $2.5*10^9$. At each intensity level, regular measurements were done with different levels of noise excitation ranging from 0.25 mW/Hz to 6.25 mW/Hz in both transverse planes. The influence of noise levels on the tune spectrum, emittance growth and beam losses were investigated at each current level. The beam current was measured using a beam current transformer and the transverse beam profile was measured by an Ionization profile monitor [5].

With increase in beam current, a shift of the tune spectra was observed as shown in Fig .1. However, the tune spectrum itself was independent of various beam excitation levels, and only an increase in signal to noise ratio (SNR) was observed as shown in Fig .2. Further similar measurements are planned with higher currents suited for comparision with beam physics simulations.

Since the system allows for online tune determination during the full cycle, it can be used to improve in-situ adjustment of acceleration settings by the operators. Further work is ongoing to make the system robust under various operating conditons like bunch shapes, beam intensities and ion species. In its final stage, this system will be an effective tool for further beam physics investigations.

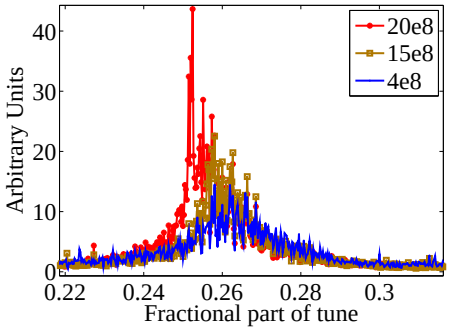

Figure 1: Change in vertical tune spectra at different beam currents. The spectrum for each current level is an FFT of 4096 position points and an average over 5 such FFTs.

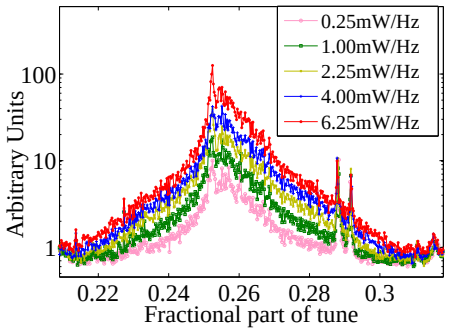

Figure 2: Vertical tune spectra at various beam excitation levels, we observe negligible change in the spectrum but significant improvement in SNR with increase in excitation. The spectrum is calculated by averaging over 10 FFTs of 4096 position points.

References

[1] A. Hofmann, "Tune shifts from self fields and images", CAS, University of Jyvaskyla, Finland(1992) ed. by S.Turner, CERN-94-01, p.329, 1994.

[2] R. Steinhagen, "Tune and chromaticity Diagnostics", CAS Beam Diagnostics, Dourdan(2008) ed. by D. Brandt, CERN-2009-005, p. 317, 2009.

[3] R. Singh et al.,"Observation of space charge effects on tune at SIS-18 with new digital base band tune measurement system", Proc. HB, Morschach, Switzerland, 2010.

[4] P. Kowina et al.,"Digital baseband tune determination", Proc. BIW'10, Santa Fe, U.S.A, p .341,2010.

[5] T. Giacomini, Proc. of BIW'04, "Development of Residual Gas Profile Monitors at GSI", Proc. BIW'04, Knoxville, USA,p. 286,2004.

*This work is supported by DITANET (novel DIagnostic Techniques for future particle Accelerators: A Marie Curie Initial Training NETwork),Project Number ITN-2008-215080

4:2:1 Bunch Merging in SIS18

B. Zipfel, H. Klingbeil, U. Laier, K.-P. Ningel and C. Thielmann

GSI, Darmstadt, Germany

Introduction

On Oct 19th, 2010 a bunch merging experiment was performed in order to test the new digital LLRF topology and to verify the control system integration. The 4:2:1 bunch merging use case was chosen because its complex control scheme includes many requirements for the realization of the SIS18 upgrade and FAIR.

LLRF Control Topology

The LLRF topology is the same that was previously used to realise dual harmonic operation at the SIS18 [1]. In the final configuration, no modifications will be required for dual harmonic operation, bunch splitting/merging or other multi-harmonic use-cases. For this purpose, distribution amplifiers will switch locally generated reference signals, and proper parameters will be set in the digital modules, all remotely controlled.

The interface between central control system and LLRF logic is provided by a FPGA interface board (FIB [3]) with special firmware and an optical token ring. For phase synchronisation of different harmonics, signal delays are compensated as good as possible. Two DSP systems [2] synchronise the phases of the cavity gap voltages to the appropriate local reference. The coherent local references for different harmonics *h* are generated with configurable DDS [3] boards receiving the revolution frequency ramp (equivalent to *h=1*) from the central control system. Feedback loops to stabilise bunches longitudinally were not used for the experiment.

Experimental Parameters and Results

The cavity S08BE2 generated the RF frequency at *h=2,* the cavity S02BE1 that at *h=4* and *h=1*. The transitions between harmonic numbers (50ms duration) were managed by simultaneous linear amplitude up and down ramping for the corresponding cavity.

Table 1: SIS18 parameters for flat-top bunch merging

Ion species		$^{238}U^{73+}$
Kinetic energy E	MeV/u	300
Revolution freq. f_0	kHz	904,9
Harmonic number h		$4 \rightarrow 2 \rightarrow 1$
RF frequency f_{rf}	kHz	$3620 \rightarrow 1810 \rightarrow 905$
Gap voltage U_{rf}	kV	$4 \rightarrow 2 \rightarrow 1$

For acceleration, the ramps provided by the central control system were used. On flat-top at constant frequency, de- and rebunching ramps as well as the timing during the merging process were generated manually.

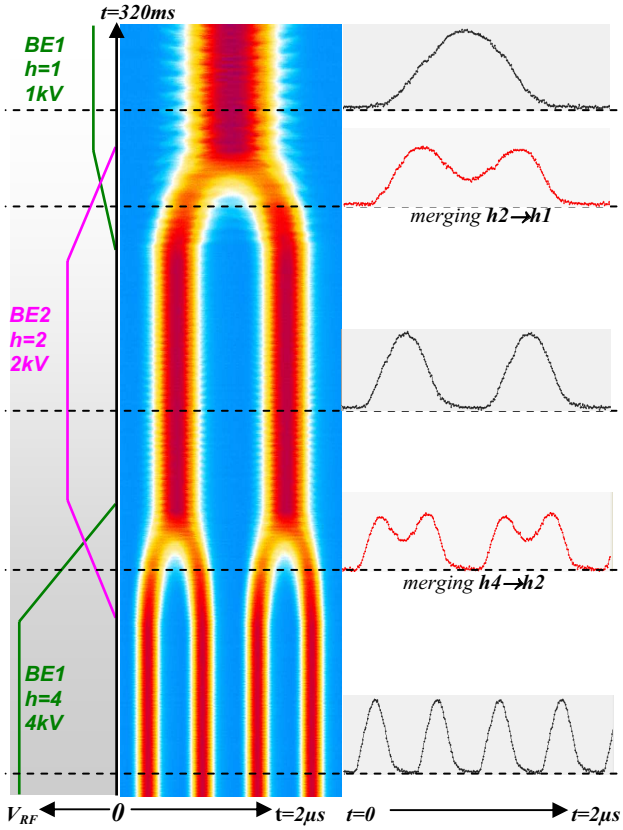

Figure 1: RF sequence, waterfall plot and bunch profiles.

Conclusion

The measurement results clearly show that the multi-harmonic LLRF system works properly and operates as a prototype for FAIR LLRF systems. Control system integration for further bunch gymnastics scenarios can be finalized. In order to improve the bunch shape and emittance, ramps for RF-amplitude and RF-phase will be optimised by automatic calibration procedures. Customization of the RF control system will benefit of the flexibility of the digital modules of the new LLRF system.

References

[1] K.-P. Ningel, H. Klingbeil, U. Laier, B. Zipfel, C. Thielmann, P. Hülsmann, “Dual Harmonic Operation at SIS18”, IPAC’10, Kyoto, May 2010, p. 1410.

[2] H. Klingbeil, "A fast DSP-Based Phase-Detector for Closed-Loop RF Control in Synchrotrons”, IEEE Trans. Inst. Meas., Vol. 54, No. 3, June 2005, p.1209-1213

[3] H. Klingbeil et al.: "A Cavity Synchronization System for Heavy Ion Synchrotrons Based on DSP, DDS and FPGA Technology", LLRF05, CERN, Oct. 2005

Time and Space Resolved Simulations of Dynamic Vacuum and Charge Exchange Beam Loss in SIS18

P. Puppel[1,2], *P. Spiller*[1], *and U. Ratzinger*[2]
[1]GSI, Darmstadt, Germany; [2]Goethe-Universität, Frankfurt a.M., Germany

Introduction

The FAIR project is aiming for highest heavy ion beam intensities of U^{28+} beams. Intermediate charge state ions are exposed to a high probability of charge exchange due to interactions with residual gas particles. Ions which underwent a charge exchange deviate strongly from the magnetic rigidity of the reference ion and hit the vacuum chamber after dispersive elements, where in turn an energy-dependent strong gas desorption takes place. The pressure rise in the accelerator, driven by the desorption processes is dependent on the intensity of the ion beam and is referred to as dynamic vacuum.

So far, StrahlSim used a model which assumes that the beam loss due to ionization depends only on the average pressure inside the machine. In the last year, the StrahlSim code was modified to account for the real distance of the desorbed gas from the pump, and thereby the real conductance and pumping speed. These parameters are especially interesting in systems which provide either very high localized pumping speeds (e.g. NEG coated vacuum chambers) or which show localized gas desorption. In order to simulate these local effects, a time and space resolved pressure profile must be accounted.

Modeling of Time and Space Resolved Pressure Evolution

The longitudinal pressure profile is modeled using the equation system given in [1]. The pressure change is given by the differential equation

$$V\frac{\partial P}{\partial t} = \frac{\partial}{\partial z}C\frac{\partial P}{\partial z} - SP + Q, \qquad (1)$$

where V is the volume, C the vacuum conductance, S the pumping speed, Q the outgassing and z the longitudinal coordinate along the ring [1].

The time evolution is carried out independently for each gas component. At present, StrahlSim supports hydrogen, nitrogen, oxygen, argon, water, carbon monoxide, carbon dioxide, and methane. The vacuum system is discretized in elements with a typical length of 0.1 m, while the sampling points do not have to be equidistant [2].

Simulations using Longitudinal Time Dependent Pressure Profiles

The amount of beam loss at a given position in the machine is determined by the energy-dependent charge exchange cross sections and the pressure. The locations of impact of the charge exchanged beam ions and therefore the locations of pressure bumps are determined by tracking calculations using linear ion optics.

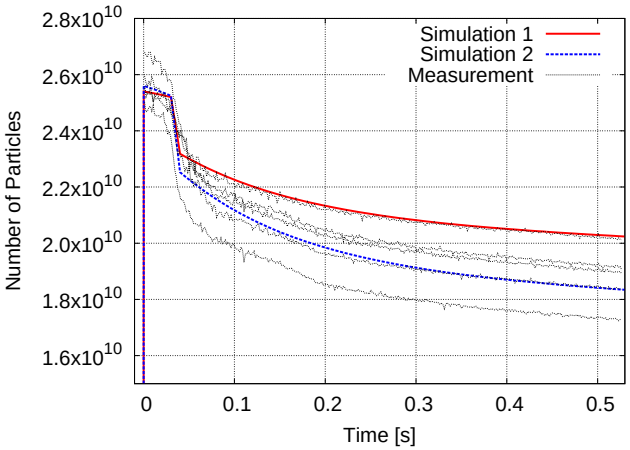

Figure 1: Simulated and measured beam loss of U^{28+} over a SIS18 cycle.

In order to benchmark the new StrahlSim code, the simulated beam loss during a SIS18 cycle was compared to measurements performed in March 2010 [2], see fig. 1. In simulation 1, 2.9×10^{10} U^{28+} particles are injected and 12.4 % injection and 7.5 % Rf-losses are assumed. In simulation 2, 3.2×10^{10} particles are injected with 20 % injection and 10 % Rf-losses. These parameters have been taken from the measurements. Without dynamic vacuum effects, both parameter sets would yield approximately 2.3×10^{10} extracted particles. The higher initial beam loss in simulation 2 causes a larger pressure rise and therefore more beam loss over the rest of the cycle.

Furthermore, the StrahlSim code was used to simulate the long term beam performance of SIS18. The saturation of the NEG-coated vacuum chambers by desorbed gases and the effect of decreased desorption yields due to beam scrubbing have been considered. For the operation of a NEG-coated synchrotron with very high intensities of intermediate charge state heavy ions, the beam scrubbing seems to be a stabilizing effect [3].

References

[1] V. Ziemann, Vacuum 81, 866–870 (2007).

[2] P. Puppel et al., Proceedings of IPAC10 (2010).

[3] P. Puppel et al., Proceedings of ICFA HB2010 (2010).

Dynamic Pressure Measurements after SIS18 Vacuum Upgrade

M.C. Bellachioma, L. Bozyk, J. Cavaco, H. Kollmus, A. Krämer, J. Kurdal, and H. Reich-Sprenger
GSI, Darmstadt, Germany

Introduction

In the last five years SIS18 has undergone a major upgrade program to improve the beam lifetime and beam intensities to reach the requirements for the operation as an injector for FAIR [1]. One part of this program was an upgrade of the vacuum system, which was completed by the end of 2009 [2]. First results of medium charge ion beam lifetimes and intensities with improved vacuum performance will be presented together with an example of the dynamic pressure evolution during high current U^{28+} operation.

The Vacuum Upgrade

To reach the required lifetime and intensities the static and dynamic vacuum pressure in the synchrotron had to be improved. To improve the static pressure and the provided pumping speed 24 dipole magnet chambers, 11 long quadrupole chambers, 5 short quadrupole chambers, and 5 straight vacuum chambers were replaced by NEG-coated UHV chambers [3] during the upgrade shutdowns from 2006 to 2009. To overcome the dynamic vacuum instability a collimation system equipped with thin film coated absorbers was designed and commissioned in addition. These ion catcher chambers were NEG coated too. In total now app. 65 % of the SIS18 circumference is equipped with NEG coated chambers.

Results

Fig. 1 shows the pressure evolution in the synchrotron sectors S12 (injection), S01, S02, S03 and in the first two ion catchers after injection during high current U^{28+}-ion operation. The three peaks correspond to continuous ion operation and in between beam settings were changed. Highest pressure increase is observed in S12 where the injection septum is located. The pressure increase is decreasing with downstream beam propagation and in S03 nearly completely gone. Also the pressure increase in the ion catcher S01 is higher compared to the ion catcher S02. This clearly demonstrate that the ion catcher system is able to prevent the pressure propagation from the injection through the whole ring vacuum caused by heavy ion induced desorption. Fig. 1 also shows that the pressure in the injection region goes up to the 10^{-9} mbar region, whereas the rest of the dynamic accelerator vacuum keeps in the 10^{-10} mbar region and below. This leads to highest charge exchange rates in the injection region. As a consequence a vacuum upgrade of the injection septum is foreseen for 2011 by installing additional NEG cartridges.

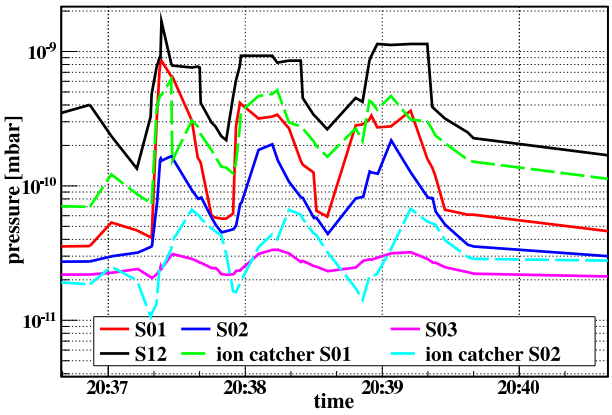

Figure 1: Pressure evolution at injection (S12) and in the first three sections of SIS18 during high current operation with U^{28+}-ions.

The commissioning of the upgraded UHV system was performed in 2010 with U^{28+} and U^{39+} operation. Results are shown in Fig. 2. These experiments showed a significant improvement in the achievable U^{28+} beam lifetime observed for high and low current operation caused by the overall upgrade program. The low current beam life time with static vacuum conditions could be increased from 3 to $\approx$ 10 s. Additionally the maximum intensity of extracted U^{28+}-ions could be increased by a factor of 100 to now $2 \cdot 10^{10}$.

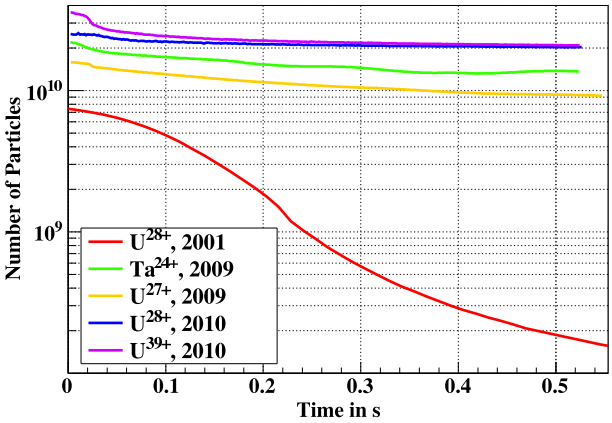

Figure 2: Beam lifetime and intensities for different runs during and after SIS18 upgrade compared to the 2001 measurement (red).

References

[1] P. Spiller et al., GSI Scientific Rep. 2009 (2010) 156
[2] M.C. Bellachioma et al., GSI Scientific Rep. 2009 (2010) 154
[3] M.C. Bellachioma et al., Vacuum 82 (2008) 435

TOPOS: A new Tool for Beam Position Measurements at SIS18

K. Lang[1], P. Forck[1], T. Hoffmann[1], G. Jansa[2], W. Kaufmann,[1] and P. Kowina[1]

[1]GSI, Darmstadt, Germany; [2]Cosylab d.d., Ljubljana, Slovenia

The new Tune, Orbit and Position Measurement System for the SIS18, called TOPOS, is a replacement for the present POSI BPM System. Currently TOPOS is installed in parallel and uses the same analogue amplification chain as POSI.

TOPOS consists of 12 Libera Hadron units [1] for front-end processing. The Libera stations sample the four analog plate signals of a BPM pick-up with four 14 Bit ADCs at 125 MHz. One of the main improvements of the TOPOS is the capability of Bunch-By-Bunch measurement and recording. To achieve a proper position calculation at bunch rates from 850 KHz up to 6 MHz, several processing steps like bunch detection [2] and baseline restitution [3] have to be performed online. Implementation of these algorithms is done inside Libera's FPGA which uses the sampled ADC values to perform the signal correction and calculation of the beam position values.

For validation of consistency of the measured positions and timing purposes, the Liberas receive in addition four digital signals. Two signals are used as Start- and Stop-Trigger. Three timestamps are calculated for time measurement and consistency checking. These timestamps are derived from the rf signal of the accelerating cavity. To minimize measurement divergences due to skew, jitter and clock inaccuracy, all Liberas are clocked synchronously with an 125 MHz timing signal. All these signals are generated externally and distributed by a low skew fan-out.

Because of the high signal dynamics over the different acceleration cycles, information about the signal in form of SNR and over- and under-load (including ADC-clipping) is retained. The complete set of measurement data and parameters are collected in a 96 Bit data package per bunch and produces a maximum data rate of about 580 MBit/s per BPM. The data stream of all 12 Libera stations is handled by a dedicated 10 GbE LAN and two so called Concentrator and Control Computers (CCCPs). TOPOS is also the pilot project for DAQ software integration in FESA at GSI, which was realized on the CCCPs [4, 5]. In the design and implementation phase of TOPOS great care was taken to realize a scalable and modularized data acquisition system for BPMs which serves also as a prototype for the future SIS100.

Conclusion and Test Results

After first tests with the new system in 2009, benchmarking and verification of the measurement method was conducted in 2010. A detailed comparison of TOPOS data with the POSI measurements under real beam conditions showed ambiguous results. For some BPMs the measured positions of both systems were in good agreement, while others showed a big deviation (Fig. 1). For further investigations of these results both systems were identically attached to a signal generator to simulate defined pickup signals and the data delivered by both acquisition systems was compared. This test revealed, that for those BPMs, which showed peculiar results in the comparison measurements with beam, POSI delivered positions, differing from the expected position value, whereas TOPOS showed good results. As a consequence the analog signal processing of POSI is being checked now in-depth and first observations hint on erroneous electronic components.

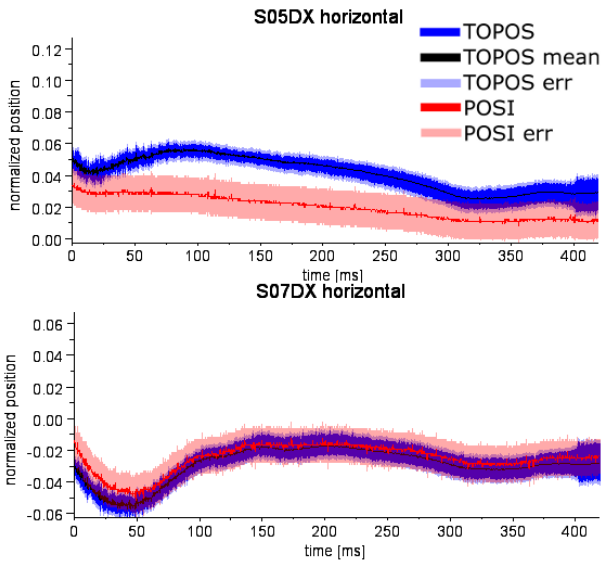

Figure 1: Comparison of TOPOS and POSI measurements in horizontal plane at BPMs no. 5 and 7. ($7.7 \cdot 10^{10}$ Ar^{11+}, accelerated from 11.4 to 490MeV/u, S/N ~30 dB).

Outlook

Beam tests with the new TOPOS system will be continued and hand-over to the operating team is planed for autumn 2011. Meanwhile the system is already used for tune measurements on a bunch-by-bunch manner [6].

References

[1] www.i-tech.si
[2] U. Rauch et al., Proc. of 5th CARE-HHH-ABI Workshop, Charmonix, Dec. 2007, p.58.
[3] A.Galatis et al., Proc. of EPAC 2006
[4] G. Jansa et al., Proc. of ICALEPCS, Kobe, Oct. 2009, p.759.
[5] T. Hoffmann et al., GSI Scientific Report 2008, p.123.
[6] R. Singh et al., contribution to this Annual Report.

Laminated Manganese-Zinc-Ferrites for Bunch Compressor Applications

M. Mehler[1], H. G. König[1]

[1]GSI, Darmstadt, Germany.

Abstract

A ferrite ring core has been investigated to find an alternative for magnetic alloys in bunch compressor applications. The characteristics of a manganese-zinc-ferrite ring core (MN8CX®) with a size of (660x290x25.4)mm applicable for frequencies f<800kHz are described. It has a 3dB-bandwidth of Δf=230kHz@2kV at an adjusted centre frequency f_R=400kHz, a shunt impedance R_P=(55±5)Ω@2kV and an inductance L_P=11µH@2kV.

Characteristics of the MN8CX® ring core

The shape of the ring core is octahedral, constructed from 8 laminated glued wedges. The 3 laminations decrease the eddy currents which are due to the low resistance ρ=12Ωm [1], therefore increasing the shunt impedance R_P>50Ω@2kV. The thickness T of the glue between the layers is larger than 100µm (Fig. 1) for optimization of efficiency. The sum thickness of the 8 cuts between the wedges must be ≤0.40mm for L_P≥11µH.

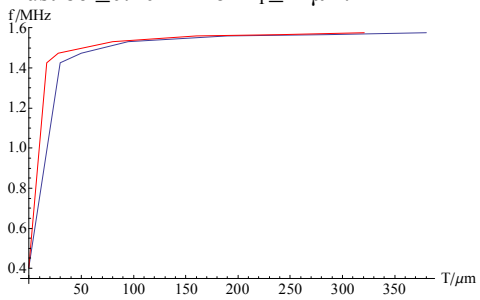

Figure 1: Measured intrinsic resonance frequency f of MN8CX® ring core (f_{Min}=404kHz@T=0µm) versus glue thickness T between the 3 layers.

The bandwidth (Fig. 2) of the ring core was measured near the centre frequency of the SIS100 Bunch Compressor frequency range of (310-560)kHz.

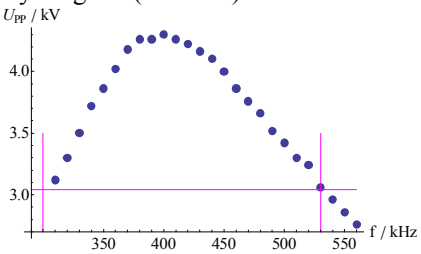

Figure 2: Measured voltage values. (pink: 3dB-bandwidth at a centre frequency f_R=400kHz; U_{PP}: peak-peak value)

The mean RF flux density for one ring core during operation will be B=(120-220)mT@(560-310)kHz. The resulting relative DC permeability for the upper and lower part of the hysteresis at these points are between μ_r=(3104-3459)@220mT and μ_r=(4351-4590)@120mT (by linear least square fit of 11th order in Fig. 3) for a ring shaped core. With 8 cuts the effective values decrease to μ_r=(1682-1781)@220mT and μ_r=(1993-2038)@120mT. Therefore the cuts should be as small as technically possible to preserve the low quality factor Q which is a feature of the material.

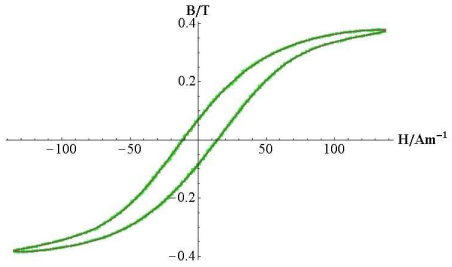

Figure 3: Measured hysteresis of MN8CX with a size of (100x50x50)mm.

The flux density B_A at the expected working point of the amplifier will be about B_A=105mT for an anode current I_A=60A. That gives a maximal flux density of about B_{Max}=B+B_A=325mT (saturation flux density according to datasheet: 450mT).

The measured shunt impedances R_P are, amongst others, voltage amplitude dependent. The values start from R_P~105Ω@200V down to R_P~55Ω@2kV. At low voltage amplitudes R_P decreases with the frequency. At high voltages the measured values stayed constant over the interesting frequency range.

Conclusion

The measurements show that laminated manganese-zinc ferrites are a good alternative to magnetic alloys (e.g. [2], [3]) with respect to realizing the SIS100 bunch compressor system. One cavity of that type would be loaded with about 20 ring cores in order to reach a gap voltage of 40kV in the required frequency range.

Acknowledgement

The authors wish to thank CMI for their good cooperation during the construction of the MN8CX® ring core and those colleagues in the GSI RF department who supported the measurements.

References

[1] Ceramic Magnetics Inc.: 'MN8CX datasheet', Rev. 7/07, http://www.cmi-ferrite.com/Products/Materials/data/MN8CX.pdf.

[2] Hitachi Metals, Ltd.: 'Nanocrystalline soft magnetic material FINEMET®', Hitachi Apr.05.

[3] VAC GmbH&Co.KG: 'Vitroperm 500F – Vitrovac 6030 F', Edition 2003.

ESR Operation and Development

C. Dimopoulou, A. Dolinskii, P. Forck, T. Giacomini, R. Hettrich, P. Hülsmann, U. Laier
S. Litvinov, F. Nolden, P. Petri, U. Popp, S. Sanjari, G. Schreiber, I. Schurig, M. Steck
GSI, Darmstadt, Germany

The ESR storage ring was successfully equipped with two new diagnostics devices. A resonator for narrow band detection of longitudinal Schottky noise was installed in the straight section in front of the internal gas target. It has an improved signal to noise ratio compared to the existing broad band Schottky pick-up. Thus it can either provide improved signal quality for low intensity beams or better time resolution in the detection of particles by Schottky diagnostics [1]. Immediately after commissioning, the new Schottky detection system was employed in the program investigating time modulations in the decay of radioactive nuclei. The second new diagnostics device is a profile monitor which uses the ionization of the residual gas by fast projectiles. The electrons produces by the ionization are amplified in a micro channel plate and afterwards are accelerated onto a phosphorus screen and observed by a CCD camera. This optical picture is transfered to the computer for further analysis. The beam profiles detected by the new monitor system were used in an experiment studying space charge limitations in low energy high brightness cooled beams [2].

Various beam dynamics studies at the ESR were continued. A new ion optical mode for isochronous storage of rare isotope beams was tested in beam experiments [3]. The first results demonstrate the possibility to increase the injection efficiency of rare isotope beams from the fragment separator by operating the ESR with superperiodicity 1. This allows independent adjustment of the dispersion in the straight sections and consequently flexible matching of the injection section to the previous transfer line and optimization of the dispersion value at the time of flight detector used for isochronous mass measurements.

In preparation of the FAIR project the accumulation method proposed for antiprotons in the HESR could be successfully demonstrated [4]. It uses accumulation in longitudinal phase space by a combination of barrier buckets and stochastic cooling. As in previous accumulation experiments the second ESR cavity was modified for broad band operation with a maximum peak voltage of 120 V limited by the available broad band amplifier. The ESR stochastic cooling system was applied in the usual way to the 400 MeV/u beam with special caution in the choice of the amplification due to the existence of coherent signals in the time modulated beam. Various waveforms (fixed barriers, moving barriers, sinusoidal rf at harmonic h=1) were generated with a stand alone signal generation system. The different waveforms were successfully employed for accumulation, further analysis and comparison of the results is needed to identify the optimum choice of the rf waveform for the accumulation in the HESR.

For HITRAP commissioning the ESR cycle has been optimized. The beam from SIS is injected at the usual intermediate energy of 30 MeV/u of the HITRAP cycle. At this injection energy the charge state that is accelerated in SIS is used. For commissioning it is not important to provide bare ions, however, injection at the lower energy allows a reduction of the ESR cycle time. The higher repetition rate is more favorable for commissioning. As the lower injection energy is identical with the usual intermediate energy for cooling, no significant modification of the ESR cycle is necessary, if highest charge states or radioactive beams will require injection at higher energies in the future.

In two HITRAP commissioning runs a krypton beam with the charge state 33+ as delivered from SIS was decelerated from 30 to 4 MeV/u. The cycle time was 20-30 seconds depending on the requirements of the parallel SIS users which determine the SIS super-cycle. The lifetime of the charge state produced before the injection into SIS at 11.4 MeV/u is closer to the equilibrium charge state for the energy of 4 MeV/u and consequently the lifetime in the residual gas of the ESR is longer than for the bare ion.

The bunching of the decelerated beam at 4 MeV/u into a single bunch was tested. By an additional capacitive load on the gap the frequency of a standard ESR cavity is reduced. This way all ions could be extracted in one bunch of a few hundred nanosecond length. It was observed that strong bunching results in rapid beam loss. An experimental investigation was launched aiming at identifying the reason for the beam instability. The low frequency rf system allows delivery of a single bunch to HITRAP.

Various experimental programs were continued with ESR beams. For the first time the detection of single ions for the experiment studying time modulations in the beta decay of radioactive nuclei was performed with the newly installed Schottky resonator resulting in an improvement of the signal to noise ratio by more than an order of magnitude and in an time resolution of 32 ms. For the $^{7}Li^{1+}$ beam at 58.9 MeV/u delivered to the time dilatation experiment up to 1×10^{9} particles could be stored due to improved intensity from the injector chain. In experiments with a slow extracted beam produced by electron capture of a stored 190 MeV/u $^{238}U^{90+}$ beam an extraction rate of more than 10^{5} s^{-1} $^{238}U^{89+}$ in a continuous beam was achieved.

References

[1] F. Nolden et al., this annual report.

[2] T. Giacomini et al., this annual report.

[3] S. Litvinov et al., this annual report.

[4] C. Dimopoulou et al., this annual report.

Experimental Investigation of an Improved Isochronous Mode for the ESR

S. Litvinov[1], *A. Dolinskii*[1], *C. Dimopoulou*[1], *H. Geissel*[1], *B. Franczak*[1], *R. Knöbel*[1], *Yu. Litvinov*[1,2], *F. Nolden*[1], *M. Steck*[1], *and H. Weick*[1]

[1]GSI, Darmstadt, Germany; [2]MPI-K, Heidelberg, Germany

The Isochronous Mass Spectrometry (IMS) is an experimental technique for direct mass measurements of short-lived exotic nuclei which has been developed at the storage ring ESR of GSI [1]. A bottleneck for the present IMS experiments is the low transmission from the fragment separator FRS to the ESR, which is mainly due to large negative dispersion in the straight sections of the ESR (see Fig. 1). In order to facilitate the transmission and to improve the isochronicity of the ring, the present isochronous optics of the ESR has been modified [2]. In comparison with the present isochronous optics the new improved optics was calculated using 10 quadrupole families, since the 20 ESR quadrupoles are connected to the power supplies in pairs (instead of 5 quadrupole families for the present mode). In the new isochronous optics the ESR is achromatic with respect to the cooler and has a smaller negative dispersion at the target position ($D\approx$-5 m) (see Fig. 1). The achromatism of the ESR increases the injection efficiency and the isochronicity of the ESR shall be improved [2]. This calculated setting has been tested in a dedicated machine experiment.

In the experiment we used a $^{238}U^{90+}$ beam with an energy of 390 MeV/u ($\gamma = 1.42$) in the ESR. The injection scheme of the new optics is completely different from the present one. In addition a new setting of horizontal correctors was required for the injection. Therefore, the desired isochronous optics ($\gamma_t = 1.42$) was reached iteratively, starting from the well known standard ESR operation mode ($\gamma_t \approx 2.4$) and stepwise changing of all quadrupole values by about 10%. After each step the beam was injected, stored and cooled and the γ_t was deduced from revolution frequency measurements. The final isochronous setting

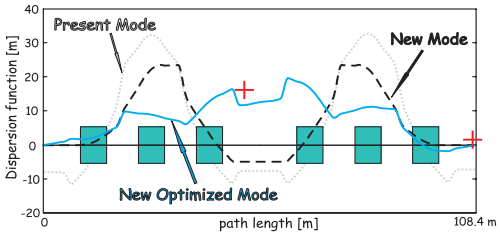

Figure 1: Calculated dispersion function of the present (grey dashed curve) and the new (black dashed curve) isochronous optics. The dispersion of the new optimized optics is described by the blue solid curve and the red crosses indicate their measured dispersion values. The path length axis starts at the middle of the cooler position. Cyan squares represent the dipoles.

was further optimized, making the dispersion function positive at the target (see Fig. 1). This has been performed in order to get more stable conditions for the stored beam. In order to check this optics the dispersion in the straight sections was measured. The measurements were performed using the standard instrumental technique [3]. The measured dispersion is 2.2 and 15.8 meters at the cooler and the target correspondingly, whereas the calculated values are 0.0 and 13.0 meters, which is a reasonable agreement (see Fig. 1). The discrepancy can be understood taking into account different features of the machine like, a recently observed error, that two of four quadrupoles of one quadrupole family, namely the E01QS3D and E02QS6D quadrupoles, were powered with a current which was about 6% higher than the nominal. In Fig. 2 two measured

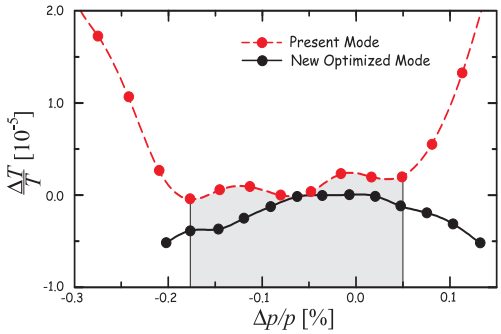

Figure 2: The measured isochronicity curve as a function of the momentum shift of the ESR for the present optics (dashed curve) and the new optics (solid curves). For both optics a sextupole correction was applied. The grey box indicates the "good" isochronicity region where the high-order effects are negligible.

isochronicity curves of the present and the new optimized isochronous optics are presented. It can be clearly seen that in the "good" isochronicity region ($\Delta p/p\sim0.23\%$) the new optics agrees well with the present one. Thus, the first experimental verification of the new improved isochronous optics was successfully performed. The ESR was operated with superperiodicity 1, which provides flexibility of the dispersion adjustment in the two straight sections separately. Moreover, having optics with both negative and positive dispersion at the target, it is promising to find an intermediate setting with zero dispersion, which will greatly improve the time-of-flight detector efficiency. For future experiments, it is proposed to calculate an additional horizontal bump in order to inject and store the fragment beam on the central orbit where the isochronicity properties are better and the influence of high-order imperfections is negligible. In addition, a complete ion-optical analysis of the new optics is planned to be performed.

References

[1] M. Hausmann, et al., Nucl. Instr. Meth. A 446, 569 (2000).

[2] S. Litvinov, et al., GSI Scientific Report 2009, p. 139 (2010).

[3] S. Litvinov, PhD thesis, Giessen University (2008).

A New Resonant Schottky Pickup for the ESR at GSI

F. Nolden[1], *P. Hülsmann*[1], *Yu. A. Litvinov*[1,2], *P. Moritz*[1], *C. Peschke*[1], *P. Petri*[1], *M. S. Sanjari*[*1,3], *M. Steck*[1], *H. Weick*[1], *J. X. Wu*[4], *Y. D. Zang*[4], *S. H. Zhang*[4], *and T. C. Zhao*[4]

[1]GSI, Darmstadt; [2]MPI-K, Heidelberg; [3]IAP, Goethe Universiät-Frankfurt am Main; [4]IMP, Lanzhou

A new resonant Schottky pickup was installed and commissioned in the ESR in early 2010. Spectra containing single ions could be observed and several other experiments have profited dramatically from the new device. The resonator has a much higher sensitivity than the existing parallel plate broad band Schottky pickup. Both pickups were operated simultaneously during experiments to have a high resolution narrow band (new resonator) and a low resolution broad band monitoring (old pickup) of the beam. In particular, the new device has proved to be beneficial for experiments with secondary rare isotope beams.

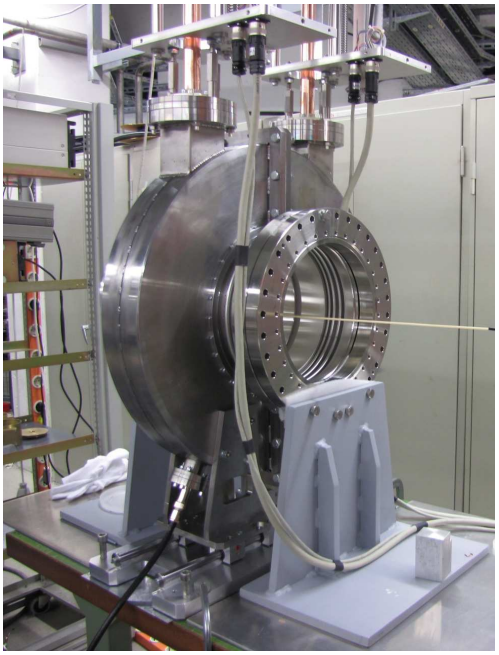

Figure 1: The resonant pickup on the test bench.

The pickup is a modified pillbox resonator mounted on a ceramic gap, which provides the rf connection between the vacuum pipe and the resonator. The resonator is made of cast steel and was copper plated on its inner side at the galvanic workshop of GSI. The resonant frequency of the resonator is 245 MHz. It can be changed by ± 2 MHz using motor-driven plungers in order to match a harmonic of the revolution frequency of the beam. The Schottky power is extracted from the resonator by a magnetic loop coupler, which reduces the unloaded quality factor by a factor of two. The loaded Q of the resonator is 565, and the R/Q is about 55 Ω. Figure 1 shows the resonator before installation. The ceramic rod in the center was used to measure the longitudinal shunt impedance of the device. The two halves of the resonator are mounted on sliding carriers, which allow to decouple them from the beam in order to prevent potential beam instabilities. A similar device was built for the CSRe storage ring at IMP, Lanzhou in China.

Figure 2 shows how the signals of the resonator are processed and which noise sources appear. On resonance, the noise spectrum is dominated by the unavoidable thermal 300 K noise from the resonator. The preamplifiers are special low-noise devices. The bandpass filters in the processing chain are needed to prevent overloading the broad band amplifiers A2 and A3.

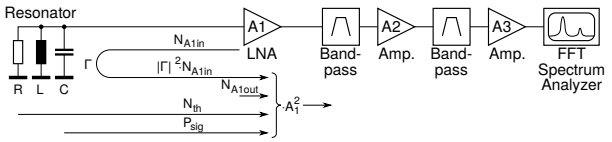

Figure 2: Signal processing chain

The spectra in figure 3 show how the velocity spread of individual $^{142}Pm^{59+}$ ions is reduced by electron cooling after switching off stochastic precooling. Six particles with different initial velocity are cooled towards a common velocity, defined by the cooling electrons. The Schottky power from single particles is well above the thermal noise floor. As the initial transverse emittances of the ions differ, the cooling times are different, as well. The cooling curves can be explained quantitatively. The spectra are obtained off-line by time resolved frequency analysis from complex time domain samples, each with 32ms length.

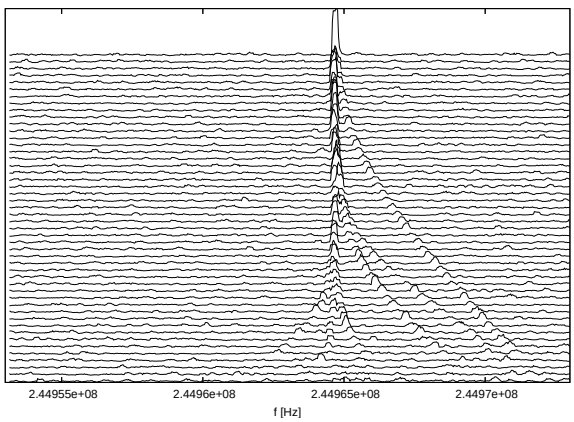

Figure 3: Waterfall diagram showing cooling traces of single particles.

*Work supported by HIC-for-FAIR within the framework of the LOEWE program, State of Hesse, Germany.

Commissioning of the Optical Ionization Profile Monitor in the ESR

T. Giacomini[1], J. Dietrich[2], P. Forck[1], P. Görgen[1], S. Kamerdzhiev[2], G. de Villiers[3]
[1]GSI, Darmstadt, Germany; [2]COSY, Jülich, Germany, [3]iThemba Labs, South Africa

A new Optical Ionization Profile Monitor OIPM was installed in the ESR in June 2010 and a similar device is being prepared for SIS18. The new OIPM provides fast and reliable non-destructive beam profile measurements at the existing SIS18 and ESR and serves as a precursor for the installations at FAIR [1]. The OIPM will provide two different readout techniques, a fast readout mode on a turn-by-turn basis with 1 mm resolution and, secondly, a high resolution mode of 100 profiles/s with 0.1 mm resolution. The ionisation products are guided by a transverse electric field to a position sensitive MCP-PS detector (Micro-Channel-Plate plus Phosphor Screen) [2]. Fast mode measurements will be performed using a multi-channel photomultiplier.

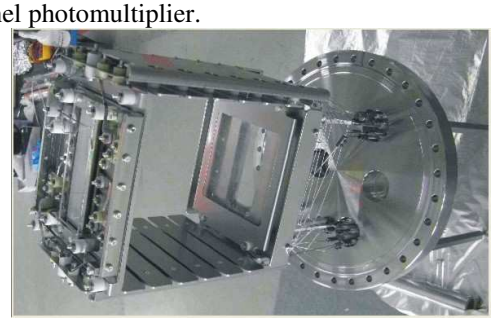

Figure 1: Photograph of the electrical field box with MCP-PS

Fig. 1 shows the electric field box of the ESR OIPM for one beam plane. The data acquisition system consists of a PXI front-end connected to 2 CCD cameras which are read out by a LabView server application. Both, the server and the PC client program for remote control via network were developed by a commercial partner. The data acquisition system was improved to work with very fast CCD cameras for profile rates up to 500 profiles per second on both planes.

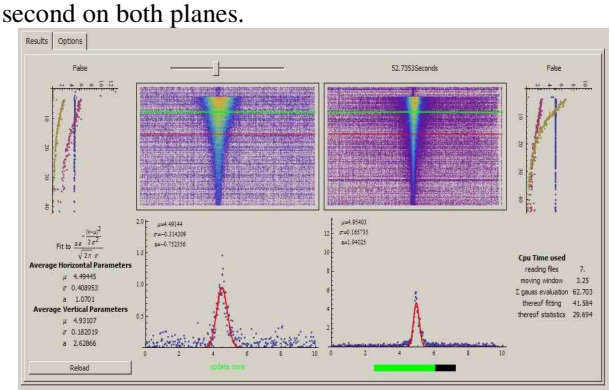

Figure 2: Evolution of the horizontal and vertical ion beam profile in the ESR from injection during storage. 4MeV/c, $5 \cdot 10^7$ Ar^{18+}-ions.

First measurements were performed in September 2010 with the ESR OIPM in high resolution mode. The data were analysed in a first approach with Mathematica,. Fig. 2 displays a beam profile post analysis for horizontal and vertical beam profiles. The two waterfall plots show the beam width evolution as a function of time, while the graphs on the outer right and left side show the parameters for each profile. The two graphs below the waterfall plots depict the horizontal and vertical beam profiles at a fixed time during the measurement. The upper horizontal line in the waterfall plots indicates the time respective the actual shown profile number. A Gaussian fit is added to the two beam profiles in the two lower graphs.

The SIS18 OIPM assembling process started in summer 2010. A defect at the inner machine-made supports enforced to disassemble it partly and, due to the complex cleaning and NEG coating process, led to a time delay for installation.

To overcome distortions of the measured profiles due to the space charge effect during residual gas electron detection, a guiding magnetic field in parallel to the electric field is necessary. The design and calculations of the SIS18 OIPM magnet were finished in 2010. The final design and calculation report meeting was held in June 2010 in IKP at FZ Jülich. The magnetic system was designed in collaboration with iThemba LABS, South Africa and IKP at FZ-Jülich. The magnet openings are as large as 540 mm because the magnetic field is applied outside of the vacuum tank.

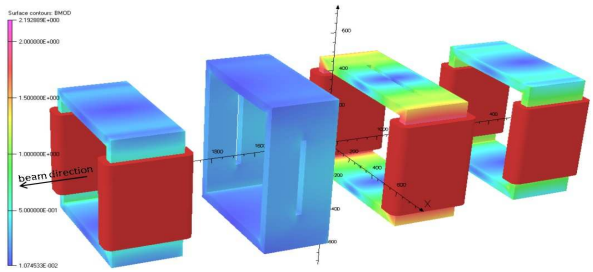

Figure 3: Magnet Design, 2 Main Dipoles, 2 Correctors

Outlook

It is planned to finish the assembling process for the SIS OIPM in spring 2011 and install it in the SIS18 in the next scheduled shutdown. The manufacturing of the magnetic system will be subject of a call for tender. As a next step a readout and control software for the new OIPMs will be implemented.

References

[1] M. Schwickert et al., "Beam Diagnostic developments for FAIR", Proc. DIPAC09, Basel (2009).
[2] T. Giacomini et al., "Development of a residual gas profile monitor with high resolution and fast readout", Proc. BIW04, Knoxville (2004).

Establishing of accelerator technical specifications for FAIR

P.Busch, U.Weinrich

[1]GSI, Darmstadt, Germany

Introduction

The task to coordinate the establishing of the technical specification documents for the FAIR accelerator was given to the GSI accelerator department in March 2010.

The aim of the process is to provide the necessary specifications in order to be able to launch the procurement of subsystems or components.

Specification progress

In FAIR project the procurement will take place either through in kind contributions or normal tendering processes. The total amount of accelerator components to be procured is in the range of 20000 in more than 500 different types of component classes.

The accelerator layout is rather complex and requires a large variety of components. On the other hand it is important for quality assurance and operation purpose to define technical and procedural overall standards wherever possible. Having this in mind as well as the different ways of worldwide procurement it was decided to establish the following different classes of specification documents:

1. General Specifications (GS)
2. Technical Guidelines (TG)
3. Common Specifications (CS)
4. Detailed Specifications (DS)

The GS are written in one document which defines standards and procedures to be followed by all suppliers of accelerator components. The document quality was brought to a level which should ensure both sufficient quality assurance and the possibility for accelerator institutes worldwide to contribute in kind.

The TG describe the basic technical standards which have to be followed by several technical systems. Out of the actually envisaged 144 documents 127 documents have been written. In total 106 have reached the quality requested for tendering processes and contracts.

The CS describe the technical standards which are valid for all components of a technical system – for example beam diagnostics. They reference the GS and TG documents. Out of the actually envisaged 45 documents 34 documents have been written. In total 17 have reached the quality requested for discussions with the potential in kind contributors.

The DS describe the detailed specifications for accelerator components. They reference the GS, TG and CS documents. Actually 215 documents have been named. Only 21 document have been written so far and the review will just start now. On the other hand quite a lot of lists of technically agreed parameters exist. Therefore technical discussions with potential in kind contributors can be started for different components.

Summary

At the end of 2010 the following situation was reached:

1. 183 documents have been written by 39 authors – nearly all of them of the GSI accelerator division.
2. The intense review process has lead to more than 120 documents which can be used for discussions with potential in kind contributors in order to prepare the in kind awarding and contracts.
3. There exist now some technical systems for which the technical specifications documents have reached the level to start the procurement.

The large effort spent to reach this achievement has been reached despite still ongoing technical layout of the accelerator and interfacing work with the site & buildings part of the project.

Outlook

The now well established procedures for the writing, reviewing and releasing will be continued. Remaining process definition for the Detailed Specification will be established. During the year 2011 a large fraction of the accelerator components will receive technical specifications enabling the procurement.

Project Status of the New Setting Generation System for GSI and FAIR

D. Ondreka, J. Fitzek, R. Hellmich, M. Kirk, H. Liebermann,
R. Müller, S. Reimann, B. R. Schlei, J. Struckmeier
GSI, Darmstadt, Germany

Since 2008, a project group at GSI is developing a new unified setting generation system for the accelerators of GSI and FAIR. The system is realized using the CERN LSA (LHC Software Architecture) framework [1]. This report summarizes the progress since the establishment of a working prototype system for SIS18 by the end of 2009.

At the beginning of 2010, the LSA system was prepared for a test with beam. On March 13, 2010 SIS18 was operated for the first time using set values provided by the LSA system. A beam of $^{238}U^{73+}$ was accelerated up to 300 MeV/u and fast extracted. This event constituted an important mile stone in the evaluation of the LSA framework, proving both the principal suitability of the framework for modelling accelerators of the type operated at GSI and FAIR as well as the validity of the implemented physics model for SIS18 [2].

After this successful test the focus of the project group was set onto two major topics: (i) the extension of the physics model to include synchrotron operation modes as planned for FAIR; (ii) the extension of the LSA framework to support modification of the length of cycles, a feature not supported by the present LSA system but indispensable for the realization of the flexible operation of circular accelerators in the GSI and FAIR facilities.

Concerning the physics model, a major step forward was taken by implementing the algorithms for acceleration with a dual harmonic RF system including the correction of longitudinal space charge effects. Dual harmonic acceleration in SIS18 is an essential ingredient to satisfying the demanding intensity requirements of the FAIR scientific program. The LSA system is now ready to calculate the appropriate set values for the RF system. A collection of set values for SIS18 and SIS100 in reference cycles for the various operation modes in the FAIR facility has been compiled. It will be the basis for the specification of devices yet to be constructed. On the other hand, since the present SIS18 RF system already supports dual harmonic acceleration, it will now be possible to perform machine studies with beam to verify the model, in particular with respect to the intensity dependent effects. A corresponding beam time request has been issued under the F-PAC budget.

The practical usability of the LSA system was still hampered by the limitation to fixed cycle lengths inherent in the present LSA framework. This limitation will in the long run be removed by an extension of the LSA framework. Meanwhile, a temporary solution was implemented which allows to control SIS18 using the LSA prototype system much like with the present system SISMODI. In combination with the extended physics model, this opens the possibility to use the LSA system during machine experiments in an efficient way.

The experience with the temporary solution was very helpful in devising the specifications for the mentioned extension of the LSA framework. An LSA collaboration meeting dedicated to this topic was held in June 2010 at CERN. A strategy and a time schedule for the implementation of the extension were fixed. As significant changes to the internal structures of LSA are required, the extension will be realized in several steps, each being implemented and tested first with the GSI prototype before incorporating the changes into the common code base of the LSA framework. The extension is expected to be completed in 2012.

In addition to these major topics, some consolidation work was done concerning the physics model. First, the software structure implementing the algorithms was reorganized to account for its significantly grown extent and complexity. Also, procedures were developed for setting up the data structures required for rebuilding the LSA database from scratch or adding additional accelerators automatically. These procedures will enhance the capabilities for generic modelling of circular accelerators with the LSA system and reduce the maintenance effort.

Another development activity was devoted to supporting the new quadratic interpolation function generator for ramped devices, where conceptual studies led to a choice of algorithm. The implementation is expected to be completed in 2011.

Apart from the work directly related to the LSA system, the platform independent version of the ion optical simulation program MIRKO was developed further: now, a Java based rich client version for offline use has been implemented. In a next step, online interaction with the control system will be incorporated. Recently, the possibility to export ion optical lattices in MAD input format has been added to MIRKO.

In 2011, the emphasis regarding the physics modelling will be on implementing and testing of multiple harmonics RF techniques relevant for FAIR, as well as on including the ESR as a storage ring prototype. Regarding the LSA framework, the main focus will be on the implementation and test of the flexible length extension within the LSA collaboration with CERN.

References

[1] Grzegorz Kruk et al, "LHC Software Architecture (LSA) - Evolution Toward LHC Beam Commissioning", ICALEPCS'07, WOPA03.

[2] Jutta Fitzek et al, "Settings Management within the FAIR Control System Based on the CERN LSA Framework", PCAPAC'10, WEPL008.

Status of the FAIR Proton Linac

L. Groening[1#], W. Barth[1], R. Brodhage[2], G. Clemente[1], N. Chauvin[3], O. Delferrière[3], M.S. Kaiser[1], B. Launé[4], C. Mühle[1], U. Ratzinger[2], G. Schreiber[1], C. Simon[3], W. Vinzenz[1], C. Will[1]
[1]GSI, Darmstadt, Germany; [2]IAP, University of Frankfurt a.M., Germany; [3]CEA/Saclay, Gif-sur-Yvette, France; [4]CNRS/Orsay, Orsay, France

Introduction

The FAIR proton linac [1] has to provide the primary proton beam for the production of antiprotons. It will deliver a 70 MeV beam to the SIS18 with a repetition rate of 4 Hz. The room temperature linac will be located north of the existing UNILAC complex. Its conceptual layout is shown in Fig. 1 and its main beam parameters are listed in Tab. 1.

Tab. 1: Main parameters of the proton linac for FAIR.

Final energy	70 MeV
Pulse current	70 mA
Protons per pulse	$7 \cdot 10^{12}$
Repetition rate	4 Hz
Trans. beam emittance	4.2 µm (tot. norm.)
Rf-frequency	325.224 MHz

DTL Design

The layout of the DTL has been revised. The use of rf-coupled CH-cavities (CCH) at energies beyond 35 MeV proofed to be not advantageous any more. The available power from the klystrons can be fully used also by a single CH cavity. Single cavities are easier w.r.t. the mechanical layout. CCH will be used just up to the extended diagnostic section.

External Magnets

CEA/Saclay took the charge of design, production, testing, and delivery of some p-linac magnets, i.e. CEA has finished the detailed specifications of the LEBT solenoids, the two dipoles, and the two quadrupoles in the inflection chicane. Production of the magnets has been started.

BPM / Phase Probes

The combined BPM / phase probe devices require R&D also within 2011. CEA completed estimates concerning the achievable resolutions w.r.t. transverse centre-of-bunch position and-rf-phase GSI proposed a preliminary layout of the geometry and it is currently refined. Its sensitivity to spurious primary rf-fields, sneeking to the BPMs from the cavity, is evaluated. The probes are to be installed within the end-tubes of the rf-cavities together with quadrupole triplets. Several options for the cabling are under investigation. The layout of the read-out electronics and data acquisition has started

Rf: Cavities, Power Sources

The production of a prototype cavity has been started (Fig. 2) at the NTG Company.

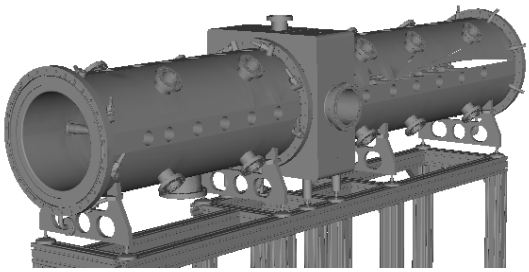

Figure 2: Prototype cavity (2.9 m) of the proton linac.

The tank mantle is completed. Production drawings of the full cavity, except the drift tubes and stems, are completed and are currently checked by the GSI construction office w.r.t. FAIR standards.

The klystron for the cavity test stand is already on-site, the power converter is specified, and a loan contract with the provider is to be signed soon. The other components comprising the test stand are to be tendered within 2011. For the total of seven high-power rf-sources the THALES company together with CNRS/Orsay currently prepares a conceptual layout together with a budgetary estimate. Both is expected to be completed at the beginning of 2011.

References

[1] *Technical Report "Proton Linac"*, https://edms.cern.ch/document/994418/1

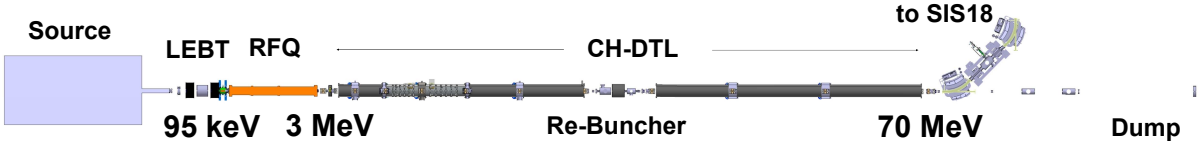

Figure 1: Conceptual layout of the FAIR proton linac.

#la.groening@gsi.de

Prototype construction of the second cavity for the FAIR proton linac.

R. Brodhage[1], U. Ratzinger[1], G. Clemente[2], L. Groening[2], H. Podlech[1], and R. Tiede[1]
[1]Institute of Applied Physics, Goethe University, Frankfurt, Germany; [2]GSI, Darmstadt, Germany

For the 70 MeV, 35 mA proton injector for FAIR a beam dynamics design based on a CH-DTL was developed successfully during the last years. This report will focus on the prototype construction of the second coupled cavity. The main changes will be presented as well as the most recent developments in tuning and manufacturing.

Introduction

The linac is mechanically grouped in two units, with a length of about 9 m and 12 m respectively. In between there will be a diagnostics section affording two lenses and one rebuncher to provide sufficient beam transport.

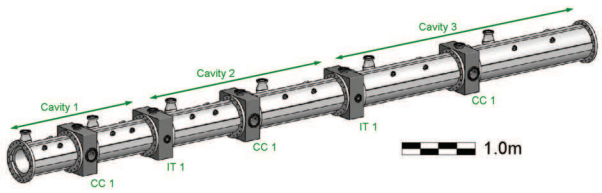

Figure 1: Scetch of the 35 MeV p-linac section.

The coupled prototype cavity

The low energy section comprises 13 gaps, followed by the coupling cell and the 14 gap high energy section. The whole cavity has an inner length of about 2.8 m.

Mechanical Design

The prototype cavity probes the second cavity of the low energy section. The concept of having two very long screwed vacuum units leads to tight tolerances with respect to the plane orientation of the end flanges as well as with respect to their transverse positioning against the beam axis. To avoid mechanical deformation the linac will be mounted on a rail system with flexible supports - as applied for the GSI Unilac. Alternatively, each tank could be mounted on a robust support and aligned via a 3-point adjusting device with respect to the beam axis.

The acceleration sections of the cavity contains no screwed connections. Therefore a Q-value within 5% of the theoretical value is expected. This was demonstrated successfully by a 8-cell test cavity.

Status of Cavity Construction

End of 2008 the Construction process of the prototype cavity started. At this time only minor production steps, like drilling longitudinal cooling channels into the outer tanks, have been made.
In 2009 and 2010 further optimisations and improvements have been made, so that the production became delayed by some months.
In early 2011 the holes for the drifttube structure will be drilled into the outer tanks and the flanges for vacuum and diagnostics will also be attached.

Optimisation of the intertank section

During the mechanical design period it occurred, that the intertank sections of the proton linac would cause long drifts from the last gap center of one cavity to the first gap center of the neighboured cavity. Therefore the actual tank lengths were shortened and an additional end plate, which forms the actual space available for RF at the cavity ends was introduced. This can be seen in Figure 2.

Due to the modified end geometry, the gap voltages decreases in the last gaps. To compensate this effect, the already inclined stems were slanted by another few degree. The impact of this adjustment on the voltage was very significant and showed, that the voltage distribution can be easily corrected.

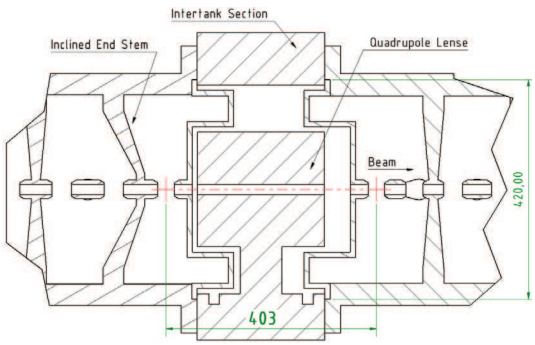

Figure 2: Cut through an intertank part of the proton linac.

References

[1] G. Clemente, H. Podlech, U. Ratzinger, R. Tiede, S. Minaev, "HIPPI-Relevant Activities at IAP-Frankfurt on the Development of the Room Temperature CH-DTL", CARE-Report-2008-014-HIPPI

[2] R. Brodhage, U. Ratzinger, S. Minaev, G. clemente, H. Podlech, R. Tiede, "Status of the Prototype Construction of the second cavity for the FAIR proton linac", IAP-ACCC-260609

Design of the BPM System for the FAIR Proton-LINAC

P. Forck[1], P. De Antoni[2], G. Clemente[1], P. Galdemard[2], L. Groening[1], M. Kaiser[1], W. Kaufmann[1], P. Kowina[1], O. Napoly[2], U. Ratzinger[3], F. Senée[2], and C. Simon[2]

[1]GSI, Darmstadt, Germany; [2]Centre CEA-Saclay/DSM/Irfu, Gif sur Yvette, France; [3]Universität Frankfurt, Germany

Demands for the BPM System

Beam Position Monitors (BPM) will serve as the main beam diagnostic tool for the FAIR Proton-LINAC [1]. These monitors will be installed at 14 locations along the LINAC. They will determine three beam quantities, namely the beam centre-of-mass with a spatial resolution of 0.1 mm, the mean beam energy and the relative beam current. The beam energy is recorded from the time-of-flight of bunches between two successive BPMs. It is challenging to achieve an accuracy for the time measurement of 10 ps corresponding to a phase difference of 1° with respect to the accelerating frequency of 325 MHz.

The entire BPM system is designed within a collaboration between GSI and CEA/Saclay with contributions from Universität Frankfurt and Company Instrumentation Technology [2].

Model for CST Simulations

To estimate the BPM properties, numerical simulations with CST Particle Studio [3] were performed earlier [4,5]. The results show the achievable spatial resolution for different beam energies and the signal shape as required for the mean energy determination. This type of calculations are now extended and improved.

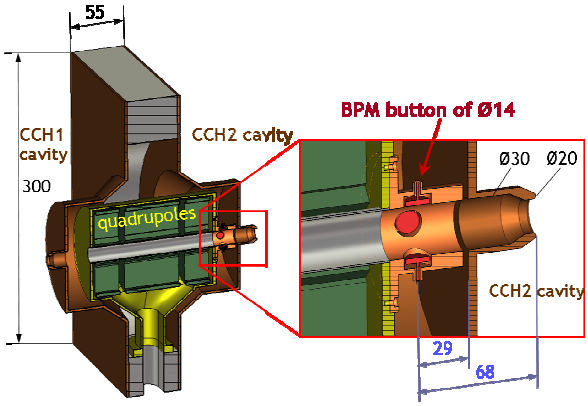

Figure 1: CST model for the inter-tank section behind CCH1 cavity housing the quadrupole triplett and the attached buttom BPMs.

At four locations the BPMs will be an integral part of the inter-tank section between the CCH cavities [1] and mounted within an evacuated housing, see Fig. 1. As the BPM centre is only 68 mm apart from the upstream drift tube boundary (see Fig. 1), the residual field distribution at the BPM location as generated by cavity excitation (so called rf-leakage) has to be evaluated and compared to the beam-induced signal on the BPM. To control the field propagation into the tube, the shape of the transition cone and the length of the slit between the cavity and the BPM tube have to be optimized. For this purpose a CST model of the inter-tank section coupled to the cavity field was created representing the details of the mechanical realization. Special numerical procedures were applied to cope with the orders of magnitude different values of the field inside CCH cavity and the resulting field at the BPM location. This CST model will be used to simulate the BPM signal generated by the non-relativistic beam as well.

Electronics Scheme

After pre-amplification of the signals in the vicinity of the BPMs, a state-of-the-art digital processing scheme is studied. This scheme is schematically depicted in Fig. 2. To suppress the rf-leakage contribution a band-pass filter matched to the 2nd harmonics of the acceleration frequency (650 MHz) leads to signal conditions well suited for the digitalization with a high resolution ADC. Here the technique of under-sampling will be applied with a sampling rate matched to a ratio of 4/11 with respect to the acceleration frequency. Using well established digital methods, the amplitude and phase of the individual signal can be evaluated in the FPGA digital electronics. From these data the beam position and mean energy can be extracted in a flexible manner with a selectable time resolution between 1 and 40 µs. A precursor device was realized and a first test proves the required stability of this hardware [2]. Further hardware tests and signal simulations will be performed within the collaboration.

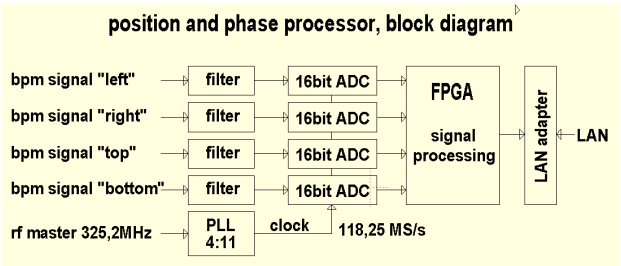

Figure 2: Digital signal processing scheme block diagram.

References

[1] L. Groening et al., "FAIR Technical Design Report for proton LINAC", March 2009, https://edms.cern.ch/document/994418/1.

[2] www.i-tech.si.

[3] www.cst.com.

[4] P. Kowina et al., "Simulation Studies for the p-Linac BPMs" GSI Annual Report 2008, p. 93.

[5] P. Kowina et al., "FEM-Simulations–a powerful Tool for BPM Design", DIPAC'09, Basel, 2009, p. 35.

FAIR SIS100 Design and Status Report

P. Spiller, O. Boine-Frankenheim, U. Blell, L. Bozyk, G. Franchetti, E. Fischer, E. Floch, M. Kauschke A. Krämer, H.G. Koenig, H. Klingbeil, M. Kirk, U. Laier, A. Miraeu, J. P. Meier, C. Mühle, H. Müller, P. Puppel, N. Pyka, H. Ramakers, H. Reich-Sprenger, P. Schnizer, J. Stadlmann

GSI, Darmstadt, Germany

Introduction

SIS100 is the main accelerator of the FAIR complex [1] and is optimized for the acceleration of partly stripped heavy ions. A carful comparison performed in 2010 has shown, that in terms of dynamic vacuum effects and the thereby driven charge exchange beam loss, SIS100 is the most demanding project world wide. Important for such a comparison is the knowledge of the integrated cross section for ionization and electron capture at collision with the residual gas atoms. For the integration and comparison, realistic cycles of the relevant machines and projects have been considered [2].

Even though the overall layout of SIS100 has been fixed already several years ago, major studies on the level of the system design had to be performed to complete the specifications for the machine components.

Pre-Series Dipole Magnet and Beam Loss

A major technical change will be realized with the production of the pre-series dipole magnet. In contrary to all prototype magnets built so far, the pre-series dipole will be equipped with a single layer coil operated at twice the electrical current. This measure has been initiated to enable the operation with pure triangular cycles (and to assure a reliable operation with the reference cycle 2c). For this purpose, the hydraulic resistance of the Nuclotron-type cable has to be reduced. A second major development concerns the thin wall vacuum chamber. Effective cooling is necessary to provide sufficient cryo-pumping for the generation of the desired XHV conditions in SIS100 with a partial pressure of heavy components of the order of 10^{-12} mbar. Two ways of active chamber cooling shall be tested in the frame of the realization of the pre-series magnet. A cooling realized by cooling pipes welded to the vacuum chamber or contact cooling realized by springs attached to the rips of the chambers. The specifications for the pre-series magnet were prepared until mid of 2010.

However, in order to clarify remaining questions in connection with the field quality requirements, the procurement of the pre-series dipole magnet has been delayed for half a year. The delay was needed to demonstrate that a situation with sufficiently low beam loss can be achieved on the rather long injection plateau. Here, the bunched beam has a space charge tune shift of about dQ=-0.25. Thus, beam dynamics simulations have indicated severe beam loss from the involvement of resonances near the proposed working point. It could be demonstrated, that the beam loss caused by trapping in a sextupolar resonance, which is excited by the field errors of the dipole magnet, can be minimized by means of the proposed sextupolar correction system. As a side product of these studies, the strength of the sextupole correction magnets, which has been estimated several years ago, has been confirmed.

Design of the Cryomagnetic System

Several design issues of the cryomagnetic system have been adressed. Especially the standard quadrupol module has been further detailed. Cryomechanical studies were performed to analyse the shrinking process and the relative movement of the different componentes in the module during the cool-down process.

The design of the bus bar system has been revised to minimize cross-talk and to move critical components, e.g. the dc circuit brakers to the ends of the module. A prototype of the cryo-collimator has been designed and is actually being set-up for beam tests at GSI (see L. Bozyk, this report). The advantages and disadvantages of a combined quadrupole module comprising two quadrupole magnets, and separated modules for each of them, have been compared. A final engineering study on the reliability of the welded hydraulic connections is presently being completed.

Rf Systems

In the frame of the realization of the new h=2 acceleration system for SIS18, major developments for the low level Rf system needed to control distributed Rf systems, operated at different harmonics, have been successfully completed. By means of the new multi harmonic LLRf system various bunch manipulations needed in SIS100 have been demonstrated in SIS18. The new LLRf system will be used for the control of the distributed Rf acceleration and compression systems of SIS100.

A new replacement for the MA-core material for the SIS100 bunch compressor cavities has been proposed. It turned out, that a ferrite material may have advantage over the so far considered amorphous MA-material at the extremely low operation frequencies (of about 0.5 MHz). Furthermore, the new proposed materail does not contain Cobalt, which is potentially activated during beam operation. However, a final decision on the choice of the material has not yet been taken.

Injection and Extraction Systems

In order to relax the technical requirements in terms of cooling and electrical power, the blade thicknesses of all magnetic septa has been evaluated and could be increased partly. In the frame of a dedicated design study, the last warm section in the extraction straight, where the magnetic extraction septa, the internal beam dump and a warm resonance sextupole are situated has been further detailed. In order to reach the desired UHV parameters, the magnetic septa have to be baked-out. The mechanical system needed for opening the septa yoke was part of the engineering studies. By combining the vacuum chambers of the first and second septum magnet, the distance from the last (third) septum to the following s.c. quadrupole cryostat could be slightly enlarged. Thereby, the internal beam dump (see report by N. Tahir et. al), could be places behind the septum. The distance between the septum and the following quadrupole module allows the installation of local shielding wall to prevent the s.c quadrupole magnets from quenching. Furthermore, the warm sextupole magnet for resonance extraction could be integrated in front of the septum.
A major design change has been taken with respect to the magnetic kicker systems. Tests performed by the GSI UHV department have shown that the ferrite material which considered to be used for the kicker yokes, provides sufficiently low outgassing yields to place them into the XHVenvironment. Therefore, it has been decided to combine the bunch of neighbouring kicker modules ain the injection- and extraction systems in a common vacuum tank. Thereby, the overall length of the kicker systems could be reduced in comparison with the former design concept using ceramic chambers. Still an issue is the integration of the kicker module situated in the missing dipole gap befor the transfer system to SIS300.

A part of the pulse power generator of the bipolar extraction kicker system is presently being set-up at GSI. The goal is to demonstrate the functionality of the proposed electrical circuit which makes use of the independent switching of two parallel Thyratrons. A pulse forming network (PFN) has been built for the setup and first switching tests could be successfully performed - the parallel Thyratron did not show any cross-talk.

Due to the high specific energy deposition of heavy ions and the very high beam intensity in SIS100, the wires of the electrostatic septa are exposed to high beam load. A dedicated tests with heavy ion beams form SIS18, at comparable beam densities has been performed succsesfully (see report by N. Pyka et. al). For this purpose, the wires were installed in the focus of the plasma physics final focusing system.

The specifications and technical parameters for the KO exciter have been revised. Tracking simulations for the slow extraction process with transverse noise excitation have been performed. The results for the required band width and voltage of the KO exciter have been benchmarked by machine experiments in SIS18. For the first time, slow extraction has been realized for a heavy ion beam with intermediate charge state (U^{28+}).

Cryogenic and Electrical Supply Systems

A major step has been achieved in planning the cryogenic supply system for SIS100 and its connection to the machine cryogenic system (bypass line). Since this system defines the position of the three large niches and their connections to the supply tunnel, their layout has been of special importance and was crucial for the civil construction planning. It has been decided that the cryogenic feed-in and electrical powering system are connected to the bypass-lines (rather than to a feed-in cryostat in the missing dipole gap) of the straight sections. Reference magnets, He distribution box and the lead boxes are situated in the first floor on top of the supply tunnel. The main niches of the synchrotron tunnel contain the feed-boxes and are used to access the accelerator tunnel. On the other side, the niches are connected to the first floor with a number of He-transfer lines and cold links which carry the electrical bus bar system (see figure 1).

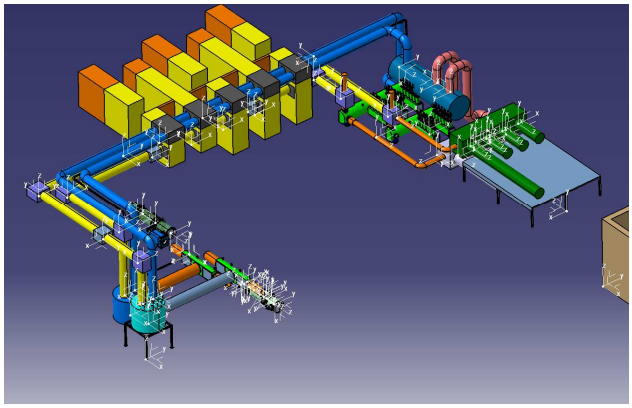

Figure 1: Cryogenic and electrical supply system distributed over the first floor on top of the supply building (right side) and the niches of the accelerator tunnel (left side).

References

[1] P. Spiller et al., Proc. of PAC05
[2] P. Spiller et al, Proc. of ICFA HB2010(2011)

R&D and Engineering Studies for the SIS100 Extraction System

N. Pyka, U. Blell, C. Mühle, H. Müller, M. Petryk, and P. Spiller
GSI, Darmstadt, Germany

Major components of the extraction system of SIS100 [1] are in the final design phase. Especially the magnetic septa which guide the beam into the high energy beam transport system have been studied in detail. The radiation hardness of the proposed wires for the electrostatic septa for high intensity operation has been verified with beam at the HHT cave at GSI.

Design and integration of the extraction septa

Due to the large magnetic rigidity of the SIS100 beam, the maximum achievable septum angle and the distance of the deflected beam to the edge of the circulating beam is rather small (3 mrad and 11mm). On the other hand, the extracted beam has to bypass the next quadrupole magnet with an angle of 3 1/3 deg. In fact, this large total deflection angle can be realized with three magnetic septa. Since the gap between two neighbouring s.c. quadrupole units is quite short, the integration of the resonance sextupole magnet, three magnetic septa and the internal beam dump in such a cell is challenging.

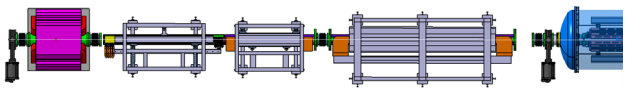

Figure 1: Cell number four of the extraction straight (top view). From left to right: resonance sextupole magnet, three magnetic septa, internal beam dump omitted (gap position), s.c. quadrupole cryostat.

The XHV conditions needed in SIS100 require bakeable vacuum chambers of the magnetic septa. Therefore, the septum has been designed with the option to remove the coil and the yoke for the installation of heater tapes, see figure 2. The insulation of the coil has to be kept below 80°C during baking-out at 300°C. For technical details of the septa see [2].

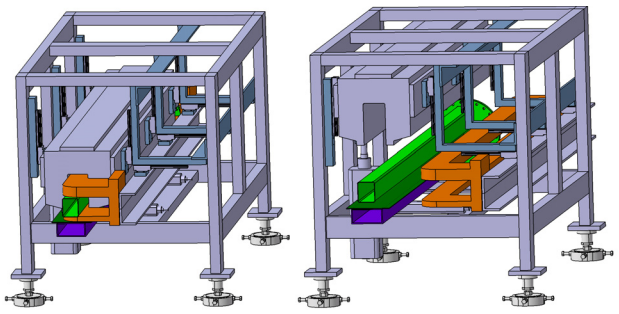

Figure 2: Left: Design of the third magnetic extraction septum. Vacuum chambers (purple: SIS100, green: extracted beam), vertical steerer (orange), horizontal steerer omitted, yoke (grey). Right: Same with yoke and coil displaced to access for the bake-out of the vacuum chambers.

Beam test of SIS100 electrostatic septum wires

Slow extraction from SIS100 is performed by means of a third order resonance and electrostatic septa. Due to the high intensity beams of heavy ions, the thermal load and the risk of destruction of septum wires is rather high. Simulations show that very thin tungsten wires (Ø25 µm) may reduce sufficiently the thermal impact. At the expected extraction conditions, the equilibrium between the thermal load and the energy loss via radiation leads to a temperature of about 1300 K. In addition, a large Re fraction (25%) increases the ductility and provides a larger safety margin for the applied mechanical strain to the septum wires. A defined strain is necessary to automatically remove a wire from the high voltage area in case of rupture.

A first test of such wires (3% Re only) has been performed at the HHT cave at GSI [3] where it is in fact possible to achieve SIS100 conditions in the focal plane of a special fine focusing system. A bunch of 50 wires was clamped in a test frame with defined tension (figure 3) and installed in the target manipulator of HHT. The target manipulator allows a precise positioning of the wires in the beam. The beam optics of the fine focusing system has been set for a focal spot of 0.4 x 1 mm. For the measurements, a U^{73+}-beam slowly extracted from SIS18 has been used. Under these conditions a temperature of about 1500 K could be achieved, which is well above normal operating conditions of SIS100. After the irradiation, the wires did not show any visible damage. A long term test of such wires and a breaking test are planned for 2011.

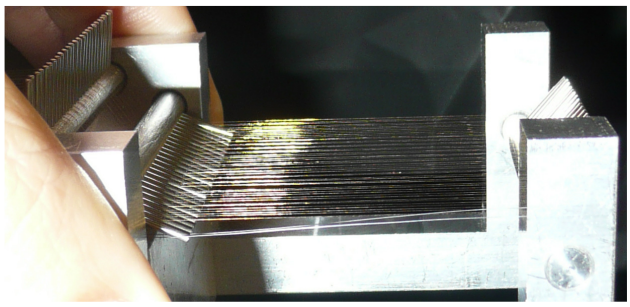

Figure 3: Test array of the 50 septum wires (Ø25 µm, W-Re3%).

References

[1] N. Pyka et al., Proceedings of PAC09, TU6RFP034
[2] N. Pyka et al., internal note (2010), and GSI-MT-Ptab-2010-04.0
[3] N. Pyka et al., internal note (2010)

Construction of a Cryocatcher Prototype for SIS100*

L. Bozyk[1,2], *D. H.H. Hoffmann*[1,2], *H. Kollmus*[1], *and P. Spiller*[1]
[1]GSI, Darmstadt, Germany; [2]TU Darmstadt, Germany

Introdution

SIS100, the main accelerator of the FAIR-facility will provide high intensity intermediate charge state heavy ion beams. In order to assure a reliable operation, a special ion catcher system is under development. In total, 60 cryocatcher will be installed to minimize the pressure rise in the cryogenic arcs. These ion catcher provide special low desorption yield surfaces. Thereby, the amount of ionization loss due to charge exchange in collisions with residual gas molecules is stabilized during operation.

The design of the cryocatcher has already been presented in [1]. Now the construction of a prototype (see figure 1), including test-cryostat is described.

Construction of the Cryocatcher Prototype

In order to achieve a uniform temperature distribution, the cryocatcher chamber will be coated with 1 mm copper. The coating is explosively plated onto stainless steel before the chamber is manufactured. Several tests have been performed to guarantee the cryo-suitability of this coating technique.

Since freezing-out of gas molecules on the surface of impact has to be avoided, the cryocatcher itself will be kept at a higher temperature than the chamber. To minimize the heat load onto the cooling system, the cryocatcher support has to act as a cold-warm-transition (cwt). The cwt contains a bellow which provides a high thermal resistance and closes the vacuum.

The actual support of the cryocatcher consists of a copper block inside the bellow. It provides a good thermal contact to the warmer side of the bellow, where the vacuum is closed by copper. In this way, a thermal contact to the ion catcher from outside can be established. The thermal contact is used for connecting the cryocatcher to the thermal shield.

The cryocatcher itself is a 25 cm long copper block. The front part is electrically insulated from the rear part, such that an electrical measurement of ions hitting the cryocatcher is possible. The copper catcher has a Nickel-Gold coating, which provides low desorption yields at room temperature [2].

The cryocatcher is surrounded by a secondary chamber. This secondary chamber prevents the desorbed gases from reaching the beam axis and provides additional cold surfaces for pumping. The position of the cryocatcher inside this secondary chamber minimizes the pressure rise on the beam axis.

* Work supported by EU (FP7 project COLMAT) and FIAS

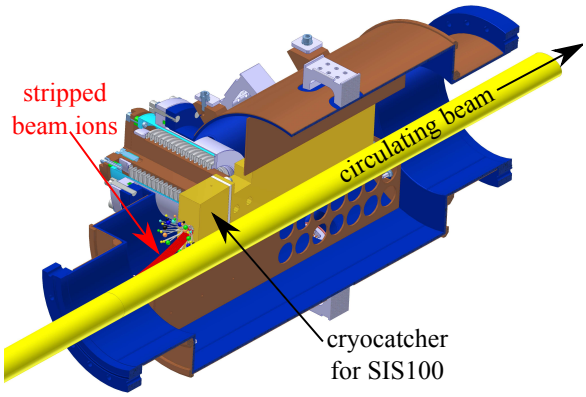

Figure 1: 3D-modell of the cryocatcher prototype with surrounding UHV-chamber (blue) and explosively plated copper surface (brown).

Test-Setup and Measurements

The prototype cryocatcher will be mounted inside a dedicated test-cryostat containing a LN2-cooled thermal shield and a cold-warm-transition for the connection to the warm beam line. Like the cryomagnetic units of SIS100, the cryostat will contain a LHe-filled supply line, to which the cold chamber is connected via flexible copper stripes. Several temperature sensors will be used to verify the thermal model of the prototype cryocatcher and to measure the cooling. The heat load of the prototype will be determined by the He evaporation rate. Since the pressure rise during ion bombardment is the central quantity to be investigated, a shielded hot extractor gauge is installed close to the cryocatcher at an optimized position. Since the thermal shield and consequently the cryocatchers in SIS100 will not have the same temperature along the ring, the temperature of the prototype cryocatcher will be varied during beam tests. The dependence of the pressure rise on the beam energy will also be measured. In front of the cold-warm-transition, a further extractor gauge, a residual gas spectrometer, and a dose valve are situated. The dose valve is needed to control the flow of test-gases into the cryocatcher chamber.

The construction and test of the cryocatcher prototype at GSI is a workpackage of the EU-FP7 project COLMAT. The manufacturing of the components is almost finished and the beam tests are expected for in the first half of 2011.

References

[1] L. Bozyk et al, GSI scientific report 2009

[2] M. Bender, Dissertation, Goethe-Uni Frankfurt (2008)

Development of FAIR superconducting magnets and cryogenic system*

[1]D. Acker, [1]A. Bleile, [1]E. Fischer, [1]E. Floch, [1]O. Gumenyuk, [1]G. Hess, [1]M. Kauschke, [1]F. Klos, [1]Th. Knapp, [1]H. Leibrock, [1]J. Macavei, [1]F. Marzouki, [1]A. Mierau, [1]J.P. Meier, [1] C. Muehle, [1] H. Mueller, [1]I. Pschorn, [1]P. Schnizer, [1]C. Schroeder, [1] S.Y. Shim, [1] A. Stafiniak, [1] K. Sugita, [1]F. Walter, [1] B. Weckenmann, [1]M. Weipert, [1]Y. Xiang

[1]GSI, Darmstadt, Germany

Introduction

This report shortly summarizes the R&D work done in 2010 for the different superconducting magnet systems for FAIR, as well as their cryogenic supplies and cryostats.

Superconducting Magnets

Rapidly cycling magnets for SIS100

A second full size straight dipole model built at JINR Dubna and a curved dipole (BINP Novosibirsk) were tested [1, 2]. The measured data confirm the previous R&D results summarised for the SIS100 dipoles and successfully evaluated at MAC3 [3, 4]. The new design of a curved dipole with a high current coil was confirmed and a detailed specification was made toward industrial manufacturing. Intensive beam dynamic calculations and additional field quality analysis had shown that this dipole should be urgently fabricated as a pre-series prototype [5, 6]. Intensive work was also made to optimise the design of the vacuum chamber requested to act as a cryo-pump [7, 8].

The theoretical work for adequate description of toroidal magnetic fields within the elliptical aperture of the curved magnets as well as the preparation work for the practical magnetic measurements were continued [9, 10].

The design work for the corrector magnets was continued within 3D static and dynamic field quality calculations [11].

Rapidly cycling magnets for SIS300

IHEP continued its work on the quadrupole and correction magnets of the SIS300. The first quadrupole prototype could be finished and will be tested in 2011. The designs of the corrector magnets and the complete cryomodule, as well as for the cryogenic system of SIS300 are well advanced. For further details see the contribution of A. Ageyev et al [12].

The R&D for the curved 4.5 T dipole at the Italian National Institute of Nuclear Physics INFN (DISCORAP-project) was successfully continued in the last year. The magnet is ready for the first tests in a vertical cryostat, the delivery to GSI is foreseen for the summer of 2011. Details on the progress of the project can be found in the presentation of P. Fabbricatore [13].

Magnets for the Super-FRS

The FAIR China Group, consisting of the Institute of Modern Physics (IMP Lanzhou), CAS, the Institute of Plasma Physics (ASIPP, Hefei), CAS, and the Institute of Electric Engineering (IEE, Beijing), CAS, developed in cooperation with GSI a prototype of superconducting dipole magnets for the Super-FRS. The qunech tests and last required cold tests of the magnet have now been successfully performed by IMP in Lanzhou [14]. The experimental data will be helpful for the development of the series production of dipoles for Super-FRS.

A MAC Review Committee discussed on the two different Super-FRS multipole magnet design studies from CEA, France (cosine theta design) and CIEMAT, Spain (superferric design) at CERN on 14th April 2010 0. The committee members unanimously agreed to recommend to the FAIR Management the superferric design as the basis for the Super-FRS Multiplets. A call for tenders for a Multiplet prototype is planned 2011.

Quench and Electrical Systems

Quench calculations were performed on Super-FRS quadrupoles which helped to select the superferric option. The superconducting electrical connections for HEBT 300 were updated. Bus bars arrangements with minimized mutual inductances were applied to the SIS100 dipoles and are currently applied to SIS100 quadrupoles. Common specifications related to quench protection were established for SIS100 HTS and copper current leads, for superconducting bypass lines, feed-in lines and superconducting links. Detailed functional specifications were issued for quench detection applied to SIS100 and Super-FRS.

Test Facility for Model and Prototype Magnets

The test facility was upgraded in order to operate the 2 test benches more independently and to prepare it for the use of new current leads for SIS100 magnets. After this upgrade the facility runs for about 4500 h mainly for testing the BINP-SIS100-prototype and tests for the SIS100 beam vacuum chamber for the GSI vacuum group.

Cryogenics

The optimization of the building layout towards the requirements of the modular version went further during the year and led also to a new scheme for the helium transfer lines. The design of the traces for the transfer lines and

* Work supported by EU, EURONS contract No. 506065.

the helium gas lines is started to find reasonable solution for the technical and radiation protection requirements within the foreseen budget. The interfaces of responsibility for the planning are fixed now.

Again the question of radiation protection at the feed in of the helium transfer lines into experimental areas was raised and is still under investigation.

The feed-in position for SIS 100 (and SIS 300) was optimized and now determined in the first piece of by-pass line in the straight section in beam direction. With this information also the position of the cryogenic niche could be fixed. In addition the technical design of the high current leads was started. The temperature distribution of the SIS100 beam pipe was examined by FEM [16]; the cooling scheme is still under discussion.

For the Super-FRS the cryogenic distribution system was revised and integrated in the building planning.

Cryostats

SIS100

To overcome the suspension loosening of the existing stainless steel based cold mass suspension system, the material of the suspensions was changed to Ti6Al4V. First calculations showed the structural stability of such a suspension system [17]. This could also be proven experimentally. A series of measurements were performed to investigate the cold mass stability during thermal cycling. The development of the SIS100 synchrotron assembly was continued and solutions for the cryogenic feed-in and for the cryogenic bypass line have been suggested.

A new solution for the integration of the SIS100 quadrupole magnets was proposed by JINR. A comparison with the existing solution one was performed and a study on the industrial production feasibility and product reliability of the integrated quadrupole doublet concept was initiated.

FEM – based calculations of the mechanical behaviour of quadrupole doublet components during cool-down process were performed by CUT [18]. For thermal characterisation of the SIS100 beam pipe cold-warm-transition (CWT) a dedicated test setup was developed and manufactured.

Super-FRS

Further optimisation is needed for of the coil cryostat of the first Super FRS dipole magnet, which is planned for 2011. A first analysis of the configuration of Super FRS magnet multiplets was showing the potential for the modularisation of the cryogenic integration concept.

References

[1] E. Fischer et al. „Design and test status of the fast ramped superconducting SIS100 dipole magnet for FAIR", IEEE T. Appl. Supercon, to be published.

[2] E. Fischer et al. "First test of a fast ramped superconducting curved dipole for FAIR", ICEC23, Wrozlaw, Poland, July 2010

[3] E. Fischer and P. Schnizer. Report to the MAC, GSI, February 2010 https://indico.gsi.de/materialDisplay.py?materialId=10&confId=841.

[4] L. Evans et al MAC3 – committee report, GSI,. February 2010

[5] P. Schnizer et al, "SIS100 dipole magnet design, evaluation of the field quality", report to MAC, GSI, December 2010

[6] L. Evans et al, MAC4 – committee report, GSI, January 2011

[7] I E. Fischer et al. IPAC'10, Kyoto, June 2010, pages 331 –333.

[8] E. Fischer et al. „Thermal conduction cooling of the SIS100 vacuum chamber and its field distortion", IGTE14, Graz, September 2010

[9] P. Schnizer et al. "Field measurements on curved superconducting magnets", IEEE T. Appl. Supercon, to be published.

[10] P. Schnizer, B. Schnizer, P. Akishin, and E. Fischer. "Toroidal circular and elliptic multipole expansions within the gap of curved accelerator magnets", IGTE14, Graz, September 2010

[11] K. Sugita et al, IPAC'10, Kyoto, June 2010, pages 337 –339

[12] A. Ageyev et al., "IHEP activity for SIS300 development in 2010", this annual report.

[13] P.Fabbricatore et al., "R&D activity in 2010 at INFN for fast cycled magnets with curved shape for FAIR", this annual report.

[14] "Super-FRS Superconducting Dipole Prototype for FAIR projects passed final test", http://english.imp.cas.cn/ns/icn/201007/t20100723_56903.html

[15] "MAC Review Committee on FAIR Super-FRS Multipole Magnet Design", https://indico.gsi.de/conferenceDisplay.py?confId=91

[16] S. Y. Shim et al, "UHV Beam Pipe Comparative Study for Fast Ramped Superconducting Accelerator Magnets MAC Review Committee on FAIR Super-FRS Multipole Magnet Design", Proceedings of the ICEC, Wraclaw, Polen, July 2011.

[17] J. P. Meier, "Calculation of the BINP Dipole Magnet Suspension System", Internal Note, GSI, Darmstadt, Germany, 2010

[18] M. Sitko, B. Skoczen, "Structural Analysis of Quadrupole Doublet", Report, Cracow University of Technology, Cracow, Poland, 2010

Influence of the beam pipe on the field quality of the SIS100 dipole magnet*

S. Koch§[1] *and T. Weiland*[1]

[1]Technische Universitaet Darmstadt, Institut fuer Theorie Elektromagnetischer Felder (TEMF), Schlossgartenstrasse 8, 64289 Darmstadt, Germany

Calculation of the Field Quality

The field quality in the aperture of the SIS100 dipole magnet during ramping is investigated by means of 3D Finite Element simulations. Fig. 1(a) shows the cross-section of the yoke including the coils and the beam pipe. The

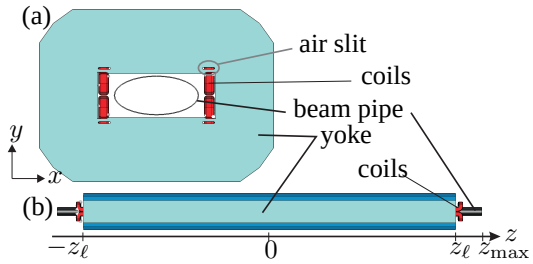

Figure 1: (a) Transversal cross-section of the full-size prototype dipole magnet including the elliptical beam pipe (half-axes 65 mm and 30 mm, thickness 0.3 mm); (b) longitudinal cross-section of the magnet (length $\ell = 2.8$ m).

magnetic flux density is sampled along numerous circles along the z-axis of the magnet. The circular multipole coefficients are evaluated at the reference radius $r_{\mathrm{ref}} = 28$ mm. In order to account for the 3D effects, e.g., local saturation near the end regions and the bended coil ends, the magnetic flux density is integrated in z-direction according to

$$\mathbf{B}^{\mathrm{int}}(x,y) = \int_{-z_{\max}}^{+z_{\max}} \mathbf{B}(x,y,z)\mathrm{d}z \; . \qquad (1)$$

The multipole coefficients are calculated based on two sets of data. Firstly, the center field at $z = 0$ in Fig. 1(b) is sampled and considered to be constant with respect to z. Secondly, the true 3D field is used for evaluating (1). For the static case, the coil current is chosen such that the maximum aperture field is 2.1 T. In order to investigate the transient behavior of the multipole coefficients, excitation cycle 2c reaching the same maximum field as for the static simulation at the flat-top is used [1].

Numerical Results

The relative integral sextupole coefficients during ramping are shown in Fig. 2 for the center field without beam pipe as well as for the 3D field in two configurations with and without the beam pipe respectively. A dynamic sextupole component appears in presence of the beam pipe. Due to eddy-current relaxation effects in the conductive

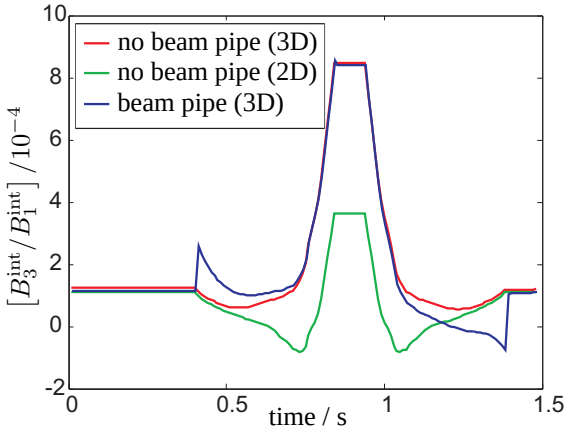

Figure 2: Comparison of the integral sextupole coefficients based on the 3D field solution with and without the beam pipe and on the central field at $z = 0$ without beam pipe.

Table 1: Comparison of the relative integral multipole coefficients based on the center field (quasi-2D) and on the 3D field solution (3D) for the static and the transient case.

$r_{\mathrm{ref}} = 28$ mm		static beam pipe no	static beam pipe yes	transient beam pipe no	transient beam pipe yes
$\frac{B_3^{\mathrm{int}}}{B_1^{\mathrm{int}}}/10^{-4}$	quasi-2D	3.62	3.56	3.62	3.70
	3D	8.53	8.46	8.49	8.54
$\frac{B_5^{\mathrm{int}}}{B_1^{\mathrm{int}}}/10^{-4}$	quasi-2D	0.33	0.32	0.33	0.32
	3D	0.78	0.79	0.78	0.79

model parts [2], the symmetry with respect to the flat-top is lost in this case. Furthermore, a significantly higher value for the sextupole coefficient is observed when considering the 3D field solution for the multipole analysis. Table 1 shows the maximum values of the multipole coefficients over the transient excitation cycle together with the respective values from a static simulation at maximum aperture field. It is obvious that, at least at the selected reference radius, the end regions provide the major contribution to the increased multipole coefficients.

References

[1] "FAIR Baseline Technical Report", March 2006, http://www.gsi.de.

[2] E. Fischer, R. Kurnyshov and P. Shcherbakov, "Analysis of the Eddy Current Relaxation Time Effects in the FAIR SIS 100 Main Magnets", IEEE Trans. Appl. Supercond., Vol. 17(2), p. 1173–1176, Jun. 2007.

*Work supported by GSI Helmholtzzentrum fuer Schwerionenforschung GmbH, Darmstadt, Germany.

§ koch@temf.tu-darmstadt.de

Magnet Field Evaluation for the SIS100 Main Magnets *

E. Fischer† [1], *P. Schnizer*[1], *A. Mierau*[1,2], *P. Akishin*[3], *F. Klos*[1], *and B. Schnizer*[4]

[1]GSI, Darmstadt, Germany; [2]TU, Darmstadt, Germany; [3]JINR, Dubna, Moscow Region, Russia; [4]TU, Graz, Austria

Introduction

SIS100, the first new machine to be build within the FAIR project, is the world's second fast ramped heavy ion synchrotron using superconducting magnets. These magnets have been actively developed over the last years with the first full size dipole magnets built and measured [1, 2, 3, 4]. The vacuum chamber, a thin piece of metall for minimal eddy currents, is also used as a cryopump, so its cooling had to be optimised [5, 6].

These already built magnets are not of the final design; modifications are required to reach an cycle repetition rate of 1 Hz. This final design in given with all its details in [7].

Out of all the R&D still going on the following topics were selected: 1.) a proper description of the field, 2.) measurement of the multipoles at the end, 3.) final field quality optimisation.

Toroidal multipoles

The dipole magnets are curved; typically these magnets are measured using search coils; a method not directly applicable as the pole shoe is not accessible [8]. Therefore a rotating coil probe system is used [9]. The straight coil probe is well adapted to straight magnets. For curved magnets circular local toroidal multipoles are the ones to use [10]. Proper treatment shows that mainly the measured quadrupole is affected.

The vacuum chamber is elliptic and the magnet is curved; thus elliptic toroidal multipoles are an adequate description. The potential equation is then given by

$$\begin{aligned}\bar{\Phi}_{cn}(\bar{\eta},\bar{\psi}) &= (\bar{h})^{-1/2} ce_n(\bar{\eta},\bar{\psi}) + O(\bar{\epsilon}^2), &(1)\\ &= \mathcal{S}(\bar{\eta},\bar{\psi})\cosh(n\bar{\eta})\cos(n\bar{\psi}) + O(\bar{\epsilon}^2), &(2)\\ \bar{\Phi}_{sn}(\bar{\eta},\bar{\psi}) &= (\bar{h})^{-1/2} se_n(\bar{\eta},\bar{\psi}) + O(\bar{\epsilon}^2), &(3)\\ &= \mathcal{S}(\bar{\eta},\bar{\psi})\sinh(n\bar{\eta})\sin(n\bar{\psi}) + O(\bar{\epsilon}^2) &(4)\end{aligned}$$

with

$$\mathcal{S}(\bar{\eta},\bar{\psi}) = \left(1 + \bar{\epsilon}\frac{1}{2}\cosh(n\bar{\eta})\cos(n\bar{\psi})\right). \qquad (5)$$

Benchmarking the field

SIS18, the heavy ion synchrotron, operated well over one decade, was used as a test bench for the high current modes of SIS100.

The end field of this magnet was mapped with a hall probe on a box. Then the field on a inner straight elliptic cylinder was calculated. The results, obtained for measuring a uniform toroidal field with a rotating coil probe allow concluding that the curvature mainly affects the quadrupole.

Table 1: The multipoles of the SIS18 dipole

I [kA]	B_1 [T]	b_3	b_4	b_5	b_6	b_7	b_8
2	1.0480	−5.72	0.01	−1.61	0.57	−1.25	−0.28
3.5	1.7236	−2.74	0.67	−1.72	1.13	−0.84	−0.42

The central field of the SIS18 magnet has a homogeneity of ± 200 ppm, so it was too small that harmonics could be deduced from the measured data. So total harmonics were calculated from the end harmonics, assuming that the middle field is without distortions. The coil aperture width of the CSLD dipole foreseen for SIS100 is $\approx 71.42\,mm$ and the aperture height $34\,mm$ [7, 1]. This gives a focal length f of ≈ 62.8 mm. These coil aperture dimensions and the defined good field region of $a = 57.5\,mm$ and $b = 30\,mm$ let to a reference radius $R_{Ref} = 40\,mm$. The coil aperture of the SIS18 magnet is $a \approx 116.5$ mm and $b = 45mm$. This gives a focal length $f^{SIS18} \approx 107.4$ mm. Using the ratio R_{Ref}/f one obtains

$$R_{Ref}^{SIS18} = \frac{R_{Ref}}{f} f^{SIS18} \approx 68.4 \approx 65mm \qquad (6)$$

Thus the multipoles for SIS18 are given for a reference radius of $R_{Ref}^{SIS18} = 65\,mm$.

The results are given in Fig. 1 and in Table 1. The multipoles represent nicely the field for a main field of 1 T, but fail for 1.72 T. The second one can be explained by the fact that the range of the measurement machine was only 1 m. Due to saturation effects the field was not zero in the end, and thus $\frac{\partial B(s)}{\partial s} \neq 0$; a prerequesite for calculating plane harmonics. The measurement shows that the ends of the SIS18 significantly deterioriates the integral field quality of the magnet (which is roughly $\pm 200\,ppm$. The integral multipoles, given in Table 1, are roughly three times smaller than the ones found for SIS100 [1].

Optimising the field quality

The end field is deterioriated by the end coil. Therefore it shall be optimised introducing harmonics of the opposite sign near by the end of the magnet yoke. As the iron non linearity is of importance an insert is foreseen (see Fig. 2), which can be remachined after the magnet was measured. The calculations, performed up to date, show that the sextupole can be reduced significantly at injection. But now the magnet has to be built and measured to assert the cal-

* Work supported by the BMBF

† e.fischer@gsi.de

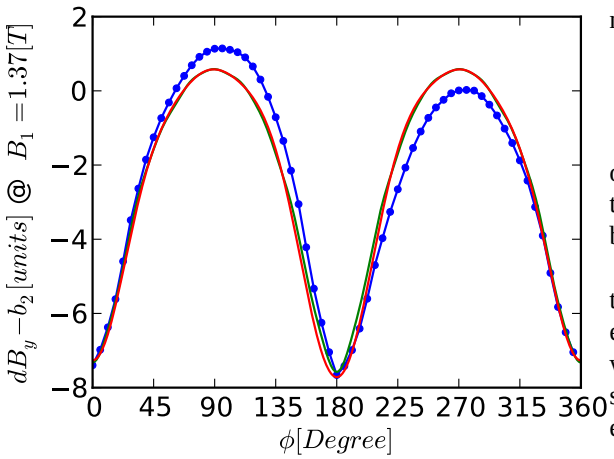

(a) $B_1 \approx 1.05$ T

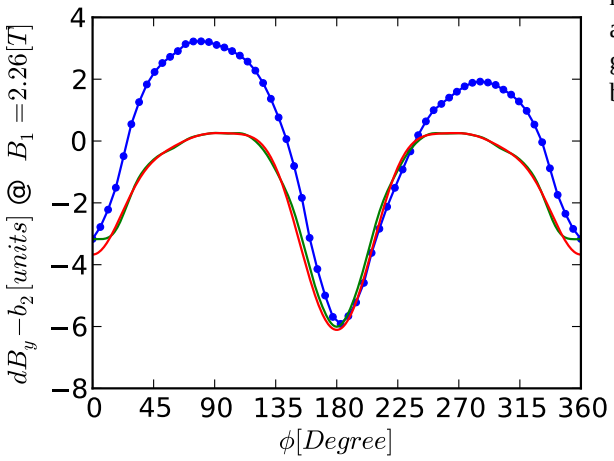

(b) $B_1 \approx 1.72$ T

Figure 1: The end field of the magnet: measured (blue curve), and interpolated using the elliptic (green) and circular (red) multipoles.

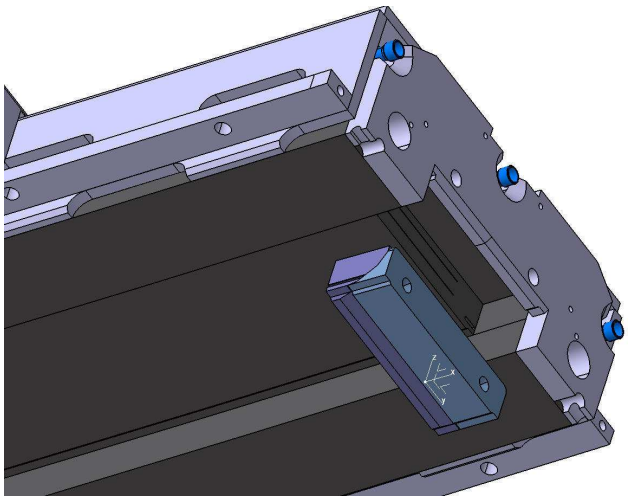

Figure 2: The insert for field optimisation

culations and to define the end profile of the series dipole magnets.

Conclusion

The magnet design is now finalised since the beginning of this year. The field description is now elaborate, so that the field in curved magnets with an elliptic vacuum chamber can be described in all its details.

The measurement of the SIS18 magnet, together with the field description, allows calculation of multipoles of the end field. The found multipoles should be cross checked with beam measurements beam. The results presented here support using the SIS18 as a test bench for the beam loss expected in SIS100.

The insert in the end follows the base idea, used to optimise the end field of $\cos\theta$ magnets: balance the unwanted harmonics, unavoidable due to the design, by introducing appropriate harmonics of the opposite sign, were the design gives more freedom. Here an insert, in the yoke end, will be used for optimising the total field quality of the magnet.

References

[1] E. Fischer et al. IEEE T. Appl. Supercon., 20(3):164–167, June 2010.

[2] L. Potanina et al. *IEEE T. Appl. Supercon.*, 20(3):1395–1398, June 2010.

[3] E. Fischer et al. First test of a fast ramped superconducting curved dipole for FAIR. ICEC23, Wrozlaw, Poland, July 2010.

[4] E. Fischer et al. Design and test status of the fast ramped superconducting SIS100 dipole magnet for FAIR. IEEE T. Appl. Supercon, to be published.

[5] E. Fischer et al. IPAC'10, Kyoto, June 2010, pages 331 – 333.

[6] E. Fischer et al. Thermal conduction cooling of the SIS100 vacuum chamber and its field distortion. IGTE14, Graz, September 2010

[7] E. Fischer and P. Schnizer. Report to the MAC, GSI, February 2010 `https://indico.gsi.de/materialDisplay.py?materialId=10&confId=841`.

[8] P. Schnizer et al. Field measurements on curved superconducting magnets. IEEE T. Appl. Supercon, to be published.

[9] P. Schnizer, E. Fischer, H. Kiesewetter, F. Klos, T. Knapp, T. Mack, A. Mierau, and B. Schnizer. IEEE T. Appl. Supercon., 20(3):164–167, June 2010.

[10] P. Schnizer, B. Schnizer, P. Akishin, and E. Fischer. Toroidal circular and elliptic multipole expansions within the gap of curved accelerator magnets. IGTE14, Graz, September 2010

Numerical calculation of ring coupling impedance for synchrotron accelerators SIS-18 and SIS-100*

L. Hänichen[1], *O. Boine-Frankenheim*[2], *W.F.O. Müller*[1], *and T. Weiland*[1]

[1]Technische Universität Darmstadt, Institut für Theorie Elektromagnetischer Felder (TEMF), Schlossgartenstrasse 8, 64289 Darmstadt, Germany; [2]GSI, Darmstadt, Germany

Introduction

Coupling impedances are the source of coherent instabilities and corresponding beam intensity limits for the operation of high current accelerators such as the SIS-100 synchrotron for the GSI FAIR project. The coupling impedances are defined as follows:

$$Z_{||}(\omega) = \frac{1}{q^2}\int d^3x E \cdot J_{beam}, \quad (1)$$

$$Z_{x,y}(\omega) = \frac{i}{q^2\Delta}\int d^3x \rho_{x,y} \cdot (E_{x,y} \mp v B_{y,x}), \quad (2)$$

where E is the longitudinal electric field and $E_{x,y}$ and $B_{y,x}$ are the transverse electric and magnetic fields excited by the beam. Coupling impedances can be determined through bench measurement [1], analytically [2] or numerically by solving a discretized form of Maxwell's equations [3]. This work focuses on finding suitable methods for the numerical calculation of coupling impedances for the relevant beamline components.

Impedance contribution of ferrite devices

Ferrite Kickers are commonly used for synchrotron injection and extraction. It has been demonstrated that the dominant impedance contributions as a continuous part which originates from the ferrite material and multiple spikes that originate from the adjacent pulse forming network.

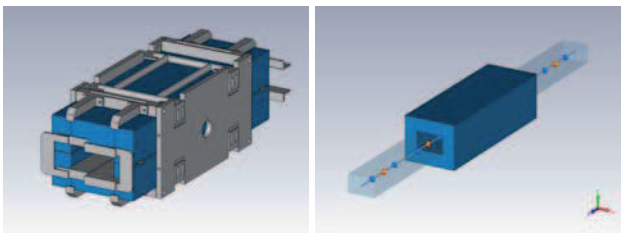

(a) Single SIS-100 kicker (b) Simplified model

Figure 1: The figures show the SIS-100 ferrite kicker of which five are located in one tank (a) and the simplified geometry used for investigating the impedance contribution of the ferrite block (b).

In frequency domain, the hysteretic magnetization process is commonly approximated using a complex permeability $\mu(f) = \mu'(f) - j\mu''(f)$ which maintains the linear property of the equation. Time domain wake field codes such as CST PARTICLE STUDIO ® use a dispersion model based on μ data. The results of the two approaches have been compared [4].

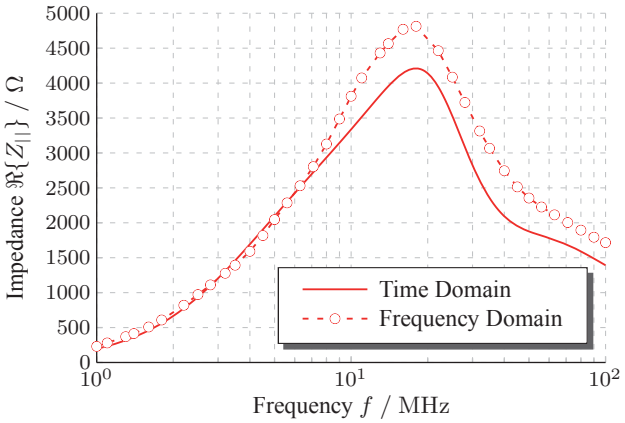

Figure 2: Real part of the longitudinal coupling impedance.

Summary and Outlook

Good agreement has been found between two simulation approaches. Uncertainties wrt/ material data are expected to have a strong influence on the coupling impedance which necessitates perturbation analysis. The increased complexity of the SIS-100 components requires higher computational effort and thus improvement of the simulation tools. Eventually the simulation results may be compared with measurement results. The energy deposit related to ferrite losses must be calculated to assure thermal integrity under high current operation. Measures to suppress beam driven energy deposit can be verfied.

References

[1] F. Caspers, "Bench methods for beam-coupling impedance measurement.", Lecture Notes in Physics, 1992, Geneva.

[2] A. M. Al-Khateeb, O. Boine-Frankenheim and R.W. Hasse "Comparison of the longitudinal impedance from different source terms.", Nucl. Instruments and Meth. in Physics Res. A, 2008.

[3] B. Doliwa, H. DeGersem and T. Weiland, "Numerical calculation of coupling impedances for kicker modules.", FAIR report, 2006, Darmstadt.

[4] L. Hänichen, O. Boine-Frankenheim, W.F.O. Müller and T. Weiland "Coupling impedance contribution of ferrite devices: theory and simulation.", Proceedings of the IPAC, 2010.

* Work supported by GSI and BMBF under contract 06DA9050

Slow Extraction from SIS-100 with Magnet Errors and Space Charge

Stefan Sorge, Beam Physics Department, GSI, Darmstadt, Germany

The heavy ion synchrotron SIS-100 will play a key role within the FAIR project. Although it is optimised for fast extraction, also slow extraction will be used [1]. A major requirement is to provide high-intensity beams, particularly, of the heavy reference ion U^{28+}. Uncontrolled beam loss within high-intensity operation can lead to irradiation of the device and degradation of the vacuum resulting in a reduced beam life time [2, 3]. During slow extraction, particles can become lost, particularly, due to collisions with the blade of the electro-static (ES) septum.

Slow extraction is based on the excitation of a 3rd order resonance resulting in the formation of a triangular stable area in the horizontal phase space. The extracted particles leave the stable phase space area along separatrices. The momentum spread generating a tune spread inherently creates a cross section of the ES septum blade for particle collisions. Hence, the tune spread is reduced by correcting the horizontal chromaticity ξ_x. The extraction process is influenced by magnet errors and space charge fields.

In the present study, systematic errors in bending and quadrupole magnets [4, 5] as well as the "frozen" space charge of the ion beam were included in a particle tracking model [6] based on the MAD-X code [7]. In the simulations, 5000 test particles were 15000 times tracked through the lattice, where the conditions presented in table 1 were assumed. To extract the test particles, they were excited by 26 kickers, each providing a horizontal sinusoidal momentum kick $\Delta x^{'}(t) = \Delta x^{'}_a \sin(2\pi f t)$. The frequencies f were equally spaced between the resonance tune and the horizontal tune modified by the space charge.

Table 1: Beam parameters used in the simulations.

Working point, ν_x, ν_y	$17.3, 17.8$
Time structure of the beam	Coasting beam
Reference ion	U^{28+}
Max. number of ions per pulse	$5 \cdot 10^{11}$
Slow extraction energy range	$(0.4 - 2.7)$ GeV/u
Transverse emittance (2σ):	
at $E = 0.4$ GeV/u	(24×10) mm mrad
at $E = 2.7$ GeV/u	(6.4×2.7) mm mrad
RMS momentum spread	$5 \cdot 10^{-4}$

Generally, the results of the simulations suggest that slow extraction will work if magnet errors and space charge are present. So, the horizontal triangular stable phase space area and the separatrices are only slightly modified, see figure 1. On the other hand, magnet errors as well as space charge increase the beam loss, see table 2. Here, the effects of magnet errors and space charge are similar at low energies, whereas at high energies the influence of magnet errors is larger than that of space charge. Nevertheless, the obtained beam loss remains below an acceptable level.

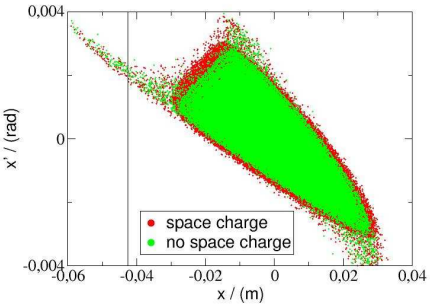

Figure 1: Phase space plot calculated with 100 test particles without magnet errors at $E = 0.4$ GeV/u. The space charge tune shift is $(\Delta\nu_{sc,x}, \Delta\nu_{sc,y}) = (-0.028, -0.043)$.

Table 2: Beam loss obtained from simulations.

$E = 0.4$ GeV/u

	without spc.	with spc.
without mgn. errors	(3.8 ± 0.3) %	(5.2 ± 0.5) %
with mgn. errors	(5.7 ± 0.3) %	(9.0 ± 0.7) %

$E = 2.7$ GeV/u

	without spc.	with spc.
without mgn. errors	(3.6 ± 0.7) %	(3.6 ± 0.5) %
with mgn. errors	(6.0 ± 0.8) %	(7.2 ± 0.7) %

References

[1] FAIR Technical Design Report - SIS100, GSI Darmstadt 2008.

[2] E. Mustafin, O. Boine-Frankenheim, I. Hofmann, H. Reich-Sprenger, and P. Spiller, NIM A 510 (2003) 199-205.

[3] C. Omet, P. Spiller, J. Stadlmann, and D. H. H. Hoffmann, New Journal of Physics **8** (2006) 284.

[4] P. Akishin, A. Mierau, P. Schnizer, and E. Fischer, "Calculated Multipoles for the SIS 100 Curved Single Layer Dipole CSLD", GSI Report, Darmstadt, June 2010.

[5] V. Kapin and G. Franchetti, GSI-Accelerator-Note-2010-004, GSI, Darmstadt, 2010.

[6] S. Sorge, "Slow Extraction from SIS-100 at high Beam Intensity", Proc. of HB-2010, Morschach, Switzerland, 2010.

[7] MAD-X code, see `http://mad.web.cern.ch/mad` .

Simulation Studies of Electron Cloud Effects for FAIR

F. Petrov[*1,2], *O. Boine-Frankenheim*[1,2], *and Th. Weiland*[2]
[1]GSI, Darmstadt, Germany; [2]TEMF, TU-Darmstadt, Germany

Introduction

Electron clouds (EC) can be the source of coherent instabilities and emittance growth in intense ion beams in synchrotrons. The electron are produced at the wall by secondary emission or by residual gas ionization. The cross sections for residual gas ionization by highly charged heavy ions are several orders of magnitude larger than for protons. Here we present simulation studies for the EC build-up in the drift sections and for the corresponding beam stability issues in SIS-18 and SIS-100.

Simulation Results and Discussion

The numerical model used for the simulations is an improved version of the one applied in [1]. The interaction between the beam and the EC is introduced according to the scheme proposed in [2]. In this model each bunch slice is represented by one macroparticle with an analytical space charge field. Because of the absence of the longitudinal motion of particles in this model Landau damping is included in a simple analytical way. The ionization cross sections are calculated for the measured decomposition of the gas in the beam pipe. The maximum secondary emission yield (SEY) for the stainless steel beam pipe is varyied from $\delta_s = 1.5$ to 2.2. The energy for the maximum SEY is set to 250 eV. The dependence of the reflection coefficient from the electron energy is taken from [3].

Depending on the bunch profile the main sources of electron production can differ significantly.

Numerical simulations for coasting beams in SIS-18 show that the electrons originate mainly from residual gas ionization. For coasting beams the electrons can accumulate in the field of the beam and potentially cause a two-stream instability. In Fig. 1 the evolution of the neutralization degree and of the beam's dipole oscillation amplitude are shown. The dipole oscillations shake-off the electrons from the beam leading to a much lower χ compared to the previous results shown in [1]. The oscillation amplitude remain roughly the same. The dominant lines in the coherent oscillation spectrum are the ones close to the electron trapping frequency.

For bunched beams the peak transverse fields are several times higher and electron leaving the bunches in the gaps hit the wall with about 100 eV causing a rapid exponential EC build-up. Simulations show that electron production due to the secondary emission is very sensitive to the longitudinal bunch profile, bunch length and surrounding geometry. Fig. 2 shows the maximum concentration of electrons in SIS-18 for 3 geometries corresponding to

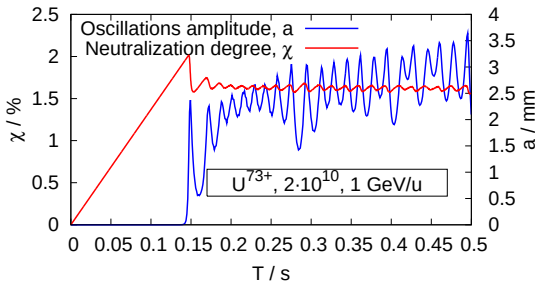

Figure 1: Neutralization degree and coherent oscillations in U^{73+} coasting beam.

drift section, dipole section and section with maximal radius. One can see that build-up of the cloud dramatically depends on the geometry and secondary emission. In these simulations the bunch oscillations are suppressed and further self-consistent simulations are necessary.

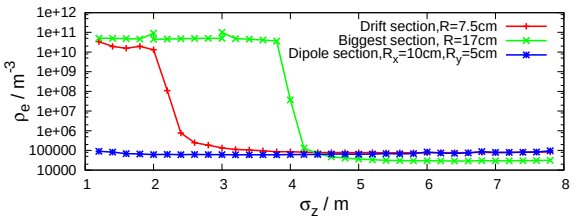

Figure 2: Maximum of electron density in SIS-18 as a function of bunch length for different geometries assuming 4 parabolic bunches. $U^{73+}, E = 1GeV/u, N_{tot} = 4 \cdot 10^{10}, \delta_s = 2.1$ for drift and 1.8 for dipole sections.

Outlook

Direct and beam based measurements of the EC presence in SIS-18 are planned using dedicated button pickups for the electrons as well the Schottky monitors for the coherent beam oscillations. The simulation studies will focus on the EC build-up in the SIS-18 and SIS-100 dipole and quadrupole sections. Possible cures, like wall coating or barrier rf gaps in the coasting beam, will be studied.

References

[1] F. Petrov, O. Boine-Frankenheim, Th. Weiland, GSI Scientific Report 2009

[2] Ohmi et al, Proc. of ECLOUD'04, p.351 (2004)

[3] Cimino, et al., Phys. Rev. Lett. 93, 014801 (2004)

* petrov@temf.tu-darmstadt.de

Halo Collimation of Protons and Heavy Ions in SIS100*

I. Strašík[1,2,#] and E. Mustafin[1]

[1]GSI, Darmstadt, Germany; [2]Frankfurt University, Germany

Introduction

Various processes related to the beam dynamics can cause the beam halo formation which is one of the reasons for uncontrolled beam losses. The beam losses interact with the accelerator structure and can cause various problems such as: vacuum degradation due to desorption process, superconducting magnets quenches, activation of the accelerator structure, background in experiments or radiation damage of the equipment and devices [1]. The purpose of the halo collimation is to reduce above mentioned problems and to provide a well defined storing location for beam losses.

Proton Collimation in SIS100

For the proton beam-operation we propose to use a two-stage collimation system [2]. The two-stage collimation system consists of: a) primary collimator (a thin foil) which acts as a scatterer of the halo particles and b) secondary collimators (bulky blocks) which are necessary to intercept the scattered particles (see Fig. 1).

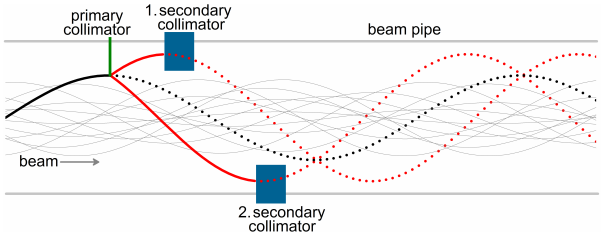

Figure 1: Scheme of the two-stage collimation system.

Efficiency of the collimation system can be affected by various parameters such as: phase advances between the collimators, position of the collimators in the lattice, retraction distance and number of the secondary collimators, scattering on the primary collimator or using a bent-crystal collimation method. Phase advances between the primary and the secondary collimators were calculated to be optimal for the retraction distance 0.1 [2]. Fig. 2 shows the transport of the scattered halo-particles in the horizontal phase-space. It can be seen the scattering on the primary and the interception with the secondary collimators. In this case the collimation efficiency is only 62 %.

The efficiency can be improved over 90 % with small retraction distance of the secondary collimators and strong scattering on the primary collimator. However, for the small retraction distance is there higher probability that the halo particles are being intercepted directly by the secondary collimators. Stronger scattering is reached with a thick foil what results in a shower of secondaries and consequently a hot spot generation.

* Work supported by program EuCard, WP 8, ColMat.

i.strasik@gsi.de

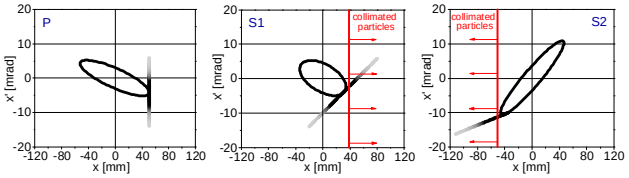

Figure 2: Phase space plots at the primary collimator (P) and 1st (S1) and 2nd (S2) secondary collimator.

The efficiency can be influenced also by number of the secondary collimators but this requires more space in the SIS100 lattice. The bent-crystal channelling technique could be used as a smart solution to improve the collimation efficiency [3]. Key issues of this technique are low channelling efficiency in the energy range of few GeV and low angular acceptance of the incident beam.

Heavy-Ion Collimation in SIS100

Collimation of U^{28+} ions is based on the charge exchange of the ions using a stripping foil. It was found out in previous studies that most of the uranium ions lost during the slow extraction are intercepted by two quadrupoles and the collimator between them. These two quadrupoles were originally designed as superconducting as all the other ones in the SIS100 lattice. But in order to avoid quenches they were changed for a warm version and are planned to be replaced regularly because of the activation. This fact could be utilized also in the halo collimation design. The stripping foil could be placed in front of the quadrupole doublet and stripped uranium ions are then intercepted by the warm quadrupoles and the collimator between them which play the role of the absorbers.

Conclusions

Calculations showed that to reach the collimation efficiency of proton beam using conventional two stage system over 90 % is possible only in case of the small retraction distance and strong scattering on the primary collimator. However this brings several problems described in the paper. The efficiency can be also improved using more secondary collimators than two or using a crystal as the primary collimator. For the heavy-ion collimation the stripping and interception of the U^{28+} was considered.

References

[1] K. Wittenburg, "Beam halo and bunch purity monitoring", Proceedings of the CERN Accelerator School, Dourdan, France, June 2008, p. 557.

[2] J.B. Jeanneret, Physical Review Special Topics - Accelerators and Beams 1 (1998) 081001.

[3] V.M. Biryukov, “Crystal channeling and its application at high-energy accelerators”, Springer, 1997.

Design of an Internal Beam Dump in SIS100 for Removal of Beam in Emergency Cases

N.A. Tahir[1], V. Sultanov[2], N. Pyka[1], and P. Spiller[1]
[1]GSI, Darmstadt, Germany; [2]IPCP, Chernogolovka, Russia

A beam abort system assures controlled beam dumping during all phases of acceleration in SIS100. This system makes use of a bipolar kicker system, which is able to deflect the beam upwards for extraction or downwards for the emergency dumping. The internal beam dump is a beam pipe which is partly filled with graphite and steel. The emergency dumping is supposed to be a seldom event in case of fail functions in the beam transport system towards the experiments or internal device errors in SIS100. Since SIS100 will accelerate high intensity heavy ions beam, the beam dump will be exposed to high energy deposition during the dumping process. Thus the carbon block has to absorb the beam energy and withstand the thermal and mechanical shock waves. The mechanical shock absorption is assured by the steel shell around the graphite block. The length of the graphite covers the range of the primary uranium ions at maximum beam energy. However, fragments of the original ions and a bunch of fast neutrons and gamma rays will leave the internal beam dump. Thus, to prevent the s.c. quadrupoles from quenching, further shielding must be installed between the beam dump and the following quadrupole.

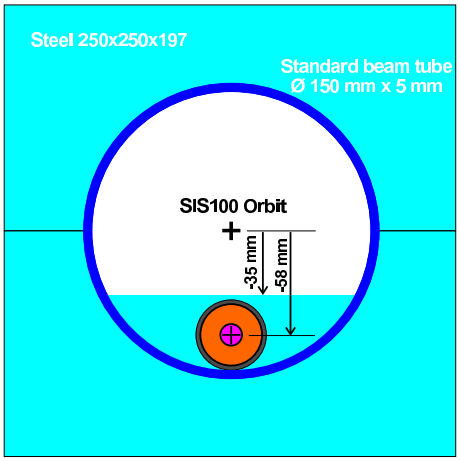

Figure 1: Front view of internal beam dump: C insert (grey), dumped beam at 100 Tm (purple), 12 Tm (beige)

Due to their high specific energy deposition, uranium ions have the highest potential for destruction in SIS100. In the following we present 3D numerical simulations of the interaction of 2.7 GeV/u uranium ions (maximum energy) with a solid graphite target. The beam intensity is, $N = 5x10^{11}$, the duration of the beam pulse is 3.5 μs, and σ of the transverse beam intensity distribution is 3.3 mm. The target length is considered to be 20 cm.

The range of 2.7 GeV/u uranium ions in solid carbon is about 16 cm. In Fig. 2 is presented the 3D temperature distribution in the target near the Bragg peak at the end of the pulse (3.4 μs). It is seen that the maximum temperature around the Bragg peak location (a few mm length) is of the order of 4700 K which is above the sublimation temperature of about 3800 K. However, the maximum temperature in the bulk of the target remains safely below the sublimation temperature. For example, at 10 cm into the target, the maximum temperature is about 1500 K. Therefore, the target may be damaged in a small region close to the Bragg peak while the rest of the target will remain intact. Fig. 3 presents the corresponding pressure distribution which shows a maximum pressure of 0.21 GPa. The special structure in the distribution is due to the cylindrical propagation of the compression wave. It is also important to investigate if this outgoing pressure wave will also cause some damage to the target. This will involve simulations of a compound target made of carbon followed by steel. These studies are intended for the year 2011.

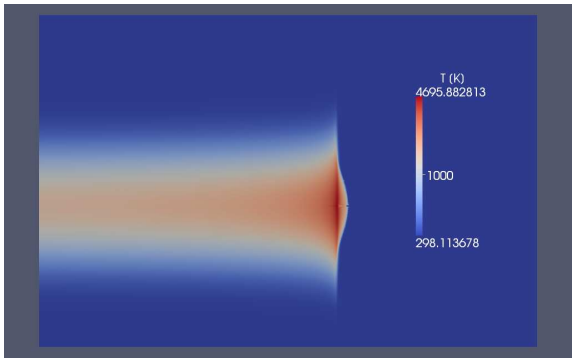

Figure 2: Temperature distribution near the Bragg peak at t = 3.4 μs.

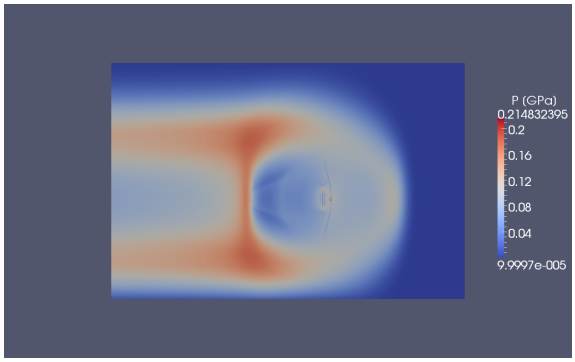

Figure 3: Pressure distribution near the Bragg peak at t = 3.4 μs.

Development of a Bipolar Kicker System for SIS100

K. Samuelsson[1,2], J. Florenkowski[1], J. Krieg[1], I. Petzenhauser[1], U. Blell[1], P. Spiller[1], V. Hinrichsen[2]

[1]GSI, Darmstadt, Germany; [2]TU Darmstadt, High Voltage Laboratories, Darmstadt, Germany

Introduction

A bipolar kicker system for extraction and emergency dumping is under development for the FAIR synchrotron SIS100. The bipolar kicker system provides the possibility to dump the beam at any time during the acceleration cycle and to change the direction of the kick within one revolution. Combining the functions of two unipolar kicker systems in one device is advantageous in terms of technical effort, system costs and space requirements in the supply building.

First measurements

First experimental investigations on possible problems with cross-talk between the Thyratrons in a bipolar kicker system [1] have been conducted. Due to cross talk it may be implied that both Thyratons become conductive although only on has been triggered.

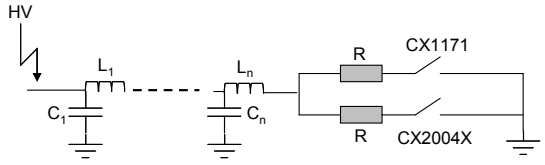

Figure 1: Electrical circuit of the experimental set-up.

As energy storage a Pulse Forming Network (PFN) has been set up (figure 2).

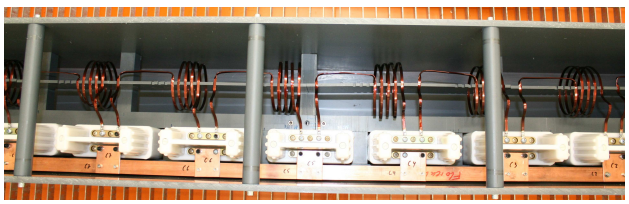

Figure 2: Pulse forming network.

Measurements of the frequency responses of the (PFN) have been performed. The cut-off frequency of a PFN is defined as

$$f_c = \frac{1}{2\pi\sqrt{L'C'}}\,\mathrm{Hz} \qquad (1)$$

Considering the given PFN parameters the theoretical cut-off frequency is 378 kHz. Thus, the measured cut-off frequency of 340 kHz is in good agreement with theory, see figure 3. The figure 4 shows the measured currents of the Thyratron CX2004X depending on the loading voltage of the PFN. The current through the parallel Thyratron CX1171 shows the same behaviour. Up to a voltage of 35 kV, no cross-talking has been observed so far.

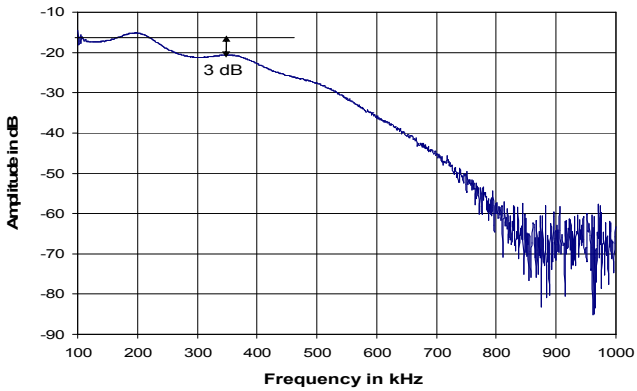

Figure 3: Measured frequency response of the PFN

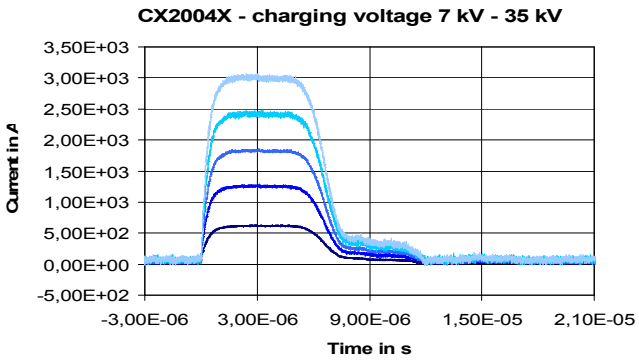

Figure 4: Discharge current of the Thyratron CX2004X.

Further investigations

As next step it is planned to increase the operation voltages up to 80 kV with the existing set-up. After this step a pulse transformer will be integrated in the circuit as described in [1]. Furthermore, a transmission line, similar to the final kicker system, will be included. Since the pulse transformer may distort the pulse created in the PFN and transmitted to the magnet, minor adjustments must be performed at the PFN. If one of the Thyratrons conducts a so called faulty shoot, its influences on the beam has to be minimized. Two approaches are taken into account: One option is to work with an active circuit to form a short on the secondary side and thereby eliminate the generation of a magnetic field in the magnet. The second option is to directly trigger the second Thyratron after the faulty shot, such that the two current pulses cancel each other and no field will be induced in the magnet.

References

[1] K. Samuelsson, Test Set-up of a Bipolar SIS100 Kickersystem, GSI Scientific Report 2009.

FAIR HEBT System – Design and Status Report

F. Hagenbuck, S. Ratschow and P. Spiller

GSI, Darmstadt, Germany

Modifications in the HEBT System Layout

As a consequence of the introduction of the modularized FAIR start version [1], modifications in the layout of the High Energy Beam Transport (HEBT) System [2] have been conducted.

The most important change was induced by a new APPA building. According to the modules 0-3, plasma physics and atomic physics share a common building which contains two beam lines. The eastern beam line is essentially a copy of the former HEAP beam line. The western beam line is available for plasma physics experiments. The proposed focusing system will have a length of 40 m. It combines the features of the former HIHEX and LAPLAS lines within one system. This beam line provides the option for a perpendicular beam from SIS18 onto the same target. The APPA building replaces the former PP and HEAP caves and occupies the space where these caves were originally planned.

Module 0-3 foresees operation of CR and HESR without RESR (module 5). Thus, the transfer line from CR to RESR had to be displaced to the western straight of CR and a new beam line (THE1) to HESR had to be laid out. After RESR is built, THE1 must be removed and replaced by a new transfer line from CR to RESR and a new beam line from RESR to HESR. All magnets from THE1 can be reused. However, since RESR is placed 1.2 m higher than CR, HESR and the beam line in between, additional magnets for the two vertical transitions will be needed. These lines are all situated on the same level as SIS18.

Furthermore CR and RESR have been increased in circumference. Therefore, minor modifications of the beam lines surrounding them were required. Furthermore, after the SIS100/300 layout was updated, adaptations had to be performed to the latest version.

The focusing system for the NC cave is proposed to be built in two stages: An initial version fitting for 100 Tm beams from SIS100 and a full version for the 300 Tm beam.

To fulfil the requirements for the beam halo at the CBM/HADES target, a halo collimation system has to be integrated in the beam lines from SIS100 and from SIS300 without changing their layout. Additional constraints are given in the superconducting beam line from SIS300 where collimators can only be placed in warm sections. Studies, still underway, are done at ITEP, Moscow [3]. For both beam lines, the current design is based on a collimation system using solely thick collimators (e.g. W, l=500mm) at appropriate positions rather than a two stage collimation system with an initial thin scraper foil.

The layout of the beam diagnostics- and correction system has been updated according to the new layout of the HEBT system.

Technical Systems Design

For beam diagnostics, standardised chamber types, also used for pumping were designed and assigned to the beam lines. The presently available chamber designs cover the needs of the major fraction of the beam lines. Thus, the positions of diagnostics elements could be integrated into the overall system layout.

Meanwhile, the CATIA design of the HEBT system contains all major elements of the beam lines, e.g. the magnets including steerers, diagnostics as well as proposed positions for collimators, beam plugs, dedicated pumping chambers and valves. Nomenclatures were assigned to all elements and marked in the layout files. These files still serve as the main basis for the building planning.

The 3D (CATIA) modelling of the beam lines was pushed further with the help of an external engineering company. While the model was updated to the current layout of the HEBT system, its data structure was harmonised with the structure of the HEBT system layout. Placeholders were exchanged for the diagnostics chambers as described above and connection boxes for quadrupoles and dipoles and also supports for quadrupoles were included. Furthermore, the model of the bypass line of the SIS300 beam lines was completely revised. Its position was shifted to the right hand side of the beam line. Dimensions were updated according to current size estimations.

Major effort was taken for the planning for the supply buildings. Positions and space requirements for the individual power supply units, the current lead box, supply units for beam diagnostics etc. were determined. Types and the amount of required cables for the beam line components have been estimated. Paths for cable trays and tubes, connecting the supply buildings to the beam line sections, as well as for the superconducting link from the current lead box to the bypass line of the SIS300 beam line were investigated. In order to provide the input needed for the building planning, the routes of transport along the beam line tunnels were further worked out. E.g. the ramp for the extraction line from SIS100 was modified and handed over to the FAIR S&B department.

References

[1] FAIR Green Paper - The Modularized Start Version, GSI, October 2009

[2] FAIR Technical Design Report (TDR) - High Energy Beam Transport, GSI, December 2008

[3] M. Kats, private communication.

Development of an Improved Cryogenic Current Comparator for FAIR *

F. Kurian[1], R. Geithner[2,3], P. Kowina[1], M. Schwickert[1], H. Reeg[1] and R. Neubert[2]

[1]GSI, Darmstadt, Germany; [2]Friedrich-Schiller-Universität Jena, Germany; [3]Helmholtz-Institut Jena, Germany

The high intensity and high energy of ion beams, along with the requirements for slowly extracted beams in various HEBT sections in the FAIR facility demand for a non-intercepting beam current measuring unit which can measure nA dc-currents with good accuracy. It is foreseen to install Cryogenic Current Comparators (CCC) in FAIR beam lines because of their excellent current resolution of less than 50 pA/√Hz. An enhanced version of this system is under development in collaboration between FSU/HI Jena, MPI-K Heidelberg and GSI.

CCC Working Principle and Resolution

In a CCC the magnetic field surrounding the passing ion beam is measured using a superconducting toroidal pickup coil with a ferromagnetic core. The shielding currents of the induced magnetic field are measured by a DC SQUID. Previous studies [1, 2] had shown that the CCC resolution is dominated by the noise contribution of the ferromagnetic core. Since the SNR improves for increasing permeability μ_r of the core material, a detailed study of high-permeability materials was carried out. As a result the nano-crystalline Nanoperm ($\mu_r \approx 4E4$) was selected and toroids (Ø 252 mm, height: 30 mm) were purchased at Magnetec [3]. To further increase the sensitivity stacks of 3 cores were combined for the CCC pickup.

Sensor Characterization

To ensure the performance of the novel toroids down to 4.2 K, the temperature and frequency dependence of the relative permeability were studied. A number of wire turns were applied to the Nanoperm cores to form toroidal coils. The serial inductance and the serial resistance of these coils were measured in a frequency range from 20 Hz to 2 MHz at 300 K, 77 K and 4.2 K with a high performance LCR-Meter Agilent E4980A.

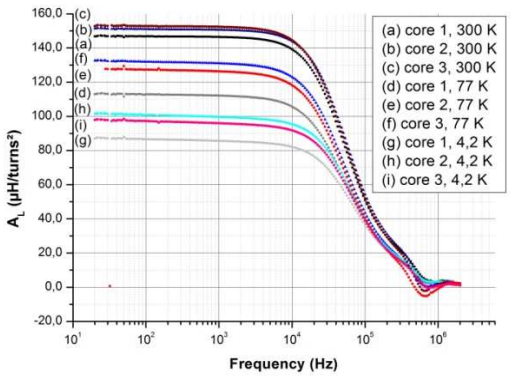

Figure 1: Frequency dependent inductance factor A_L of the Nanoperm cores at different temperatures.

The change of the inductance factor A_L, i.e. the coil inductance on the tested core divided by the square of the number of turns is very low in the frequency range between 20 Hz and 10 kHz, see Fig. 1. The value of A_L decreases to approximately 100 µH with decreasing temperature from 300 K to 4.2 K. The nano-crystalline Nanoperm cores therefore are well suited for the CCC.

Reconstruction of the CCC Prototype

At present the CCC system built at GSI in the 1990'ies is being re-commissioned. Initially the CCC unit had been installed in the HTP beam line and the measurements had shown a resolution of 250 pA/√Hz. The left side of Fig. 2 depicts the inner part of the cryostat containing the CCC sensor inside a thermal shielding. The pickup coil (right side) is covered with lead to provide a superconducting magnetic shielding. The sensor and SQUID cartridge are installed inside the liquid helium dewar (bottom part of the left picture) with two warm holes for the connection to the beam line.

Figure 2: Left: View inside cryostat with open lHe dewar, right: beam pipe with lead-shielded pickup coil

As a first step of the re-commissioning the cryostat is being prepared for cool down after resting in idle state for a long time. At present all vacuum components are cleaned and partly renewed to reach the necessary operating vacuum of <1E-7 mbar. Additionally, an in-depth maintenance of the GM refrigerator system and cold head is planned.

References

[1] R. Geithner et al., Rev. Sci. Instrum. 82, (2011), 013302.

[2] R. Geithner et al., Applied Supercond. Conf., (2010), Washington, USA, accepted.

[3] www.magnetec.de

* Work supported by EU, DITANET, Project No. ITN-2008-215080.

Status of the Design of the Antiproton Production Area

K. Knie[1], A. Dolinskii[1], V. Gostishchev[1], U. Kopf[1], P. Sievers[2] and M. Steck[1]
[1]GSI, Darmstadt, Germany; [2]CERN, Geneva, Switzerland.

Design of the proton beam dump

Every 10 s, the antiproton-production-target will be bombarded by a pulse of 2×10^{13} primary protons with an energy of 29 GeV (for an overview see [1]). This corresponds to a total beam power of about 10 kW. After passing of the first dipole primary protons and antiprotons are no longer in-line and the primaries have to be dumped. Behind the target a significant part of the beam power is carried by secondary particles, thus only about 4 kW will be deposited in the beam dump. The Monte-Carlo particle transport code FLUKA [2] was used to optimize the design of the beam dump (see fig. 1). It will consist of three materials:

i) Graphite for a smooth stopping of the beam. Its activation is very low.

ii) Iron: the high density allows an effective stopping of the particles, thus a relatively small size of the dump can be achieved. However, the activation is high due to the relatively high nuclear charge of iron.

iii) Concrete: its activation is low, it is needed to shield the remnant activity produced in iron and it is, compared to iron, very inexpensive.

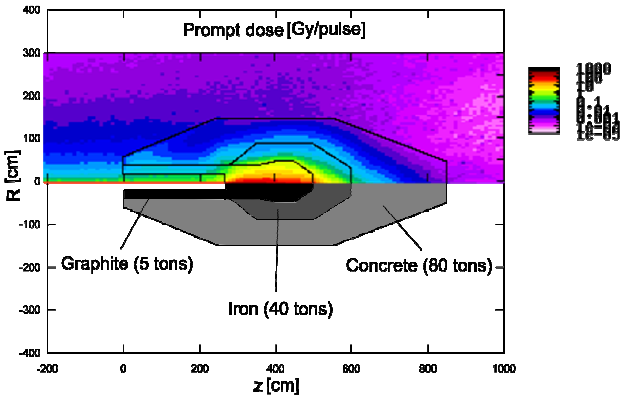

Figure 1: Upper panel: prompt dose in the beam dump as calculated with FLUKA. Lower panel: materials and their weights used in this simulation.

Pbar losses in atmosphere

It is planned to have five quadrupoles and three pairs of collimators between the target station and the first dipole [1], which separates the antiproton beam from the primary beam and the main part of the secondaries. These components will be highly activated. Even after one year of cooling, equivalent dose rates up to 0.1 Sv/h are expected in their direct vicinity. Therefore, their maintenance or replacement would be extremely complex. However, this can be considerably simplified, if one abstains from operating this part of the pbar separator (about 20 m behind the target) under vacuum but operates it in atmosphere and uses helium-bags, where possible. A simulation with a combination of the Monte Carlo codes FLUKA [2] and MARS [3] and an own particle tracking code was performed. The calculations predict a reduction of the overall pbar yield (i.e. pbars collected by the CR per primary proton) of 8 to 9 % due to scattering and annihilation.

Concept for the target handling

The target as well as the magnetic horn [1] has to be considered as disposal which has to be replaced on the timescale of a year. These highly activated components have to be transported into the hot cell of the Super FRS where they will be disassembled for disposal. Fig. 2 illustrates this process:

The target will be remotely removed from the target station and placed inside a shielded transport container (1). This container will be moved under a slot in the ceiling located about 20 m upstream of the target (2). On top of the slot is a shielding bottle with an internal crane. The target will be pulled inside this bottle (3), the basis of the bottle will be closed and the bottle with the target will be transported to the Super FRS building (4). Since the bottle will be very similar to that one used for the Super FRS target it will be fully compatible with the entrance port of the hot cell. It is assured, that the target is never unshielded and an interception is possible in every stage of this exchange process.

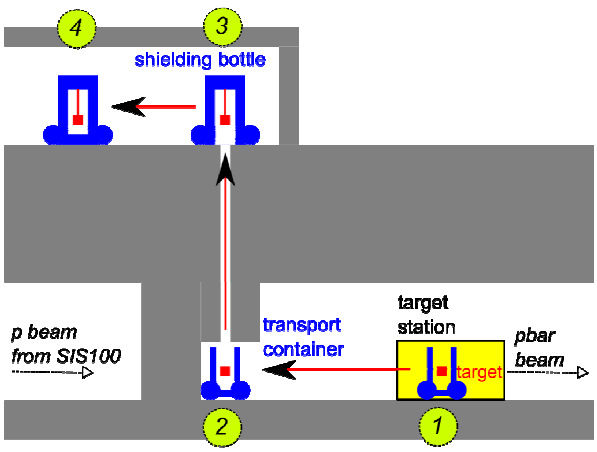

Figure 2: Illustration of the exchange of a target.

References

[1] FAIR Technical Design Report (2008), http://www-win.gsi.de/FAIR-EOI/PDF/TDR_PDF/TDR_p-bar-Targeti.pdf.
[2] A. Fassò, A. Ferrari, J. Ranft, and P.R. Sala, CERN-2005-10 (2005), INFN/TC_05/11, SLAC-R-773.
[3] N.V. Mokhov, Fermilab-FN-628 (1995)

Progress Report on the Collector Ring (CR) for the FAIR Project

A. Dolinskii, C. Dimopoulou, V. Gostishchev, K. Knie, S. Litvinov, F. Nolden, C. Peschke, I. Schurig, M. Steck

GSI, Darmstadt, Germany

In 2009 the CR layout has been refined and extended studies on critical items have been performed. The need to accumulate antiprotons in the HESR skipping the RESR [1] requires a beam extraction on the west side of the ring (fig.1). 4 kicker magnets with a maximum kick angle of 5 mrad are needed to provide injection of the hot beams coming from the separators. 2 of these kickers are also used to extract cooled beams. The injection and extraction septum magnets have to be redesigned. The required space for additional injection and extraction magnets and vacuum components lead to the increased ring circumference of 221 m.

For the larger circumference the lattice of the CR has been recalculated. In order to keep the ion-optical characteristics suitable for efficient stochastic cooling both for antiprotons (pbar) and rare isotopes (RI) the important parameters (such as the transition energy γ_{tr} and the phase advances between stochastic cooling pick-ups and kickers) are unchanged. In Table 1 the present major parameters of the CR are given.

Table 1. Major CR parameters.

Max. magnetic rigidity	13 Tm
Max energy : antiprotons (pbar) rare isotope (RI)	3 GeV 740 MeV/u
Circumference	221.25 m
Betatron tunes Qx/Qy pbar RI	4.26 / 4.84 3.19 / 3.71
Transition energy, γ_{tr}: pbar / RI	3.85 / 2.82
Transverse acceptance: h/v pbar RI	(mm mrad) 240 / 230 200 / 200
Momentum acceptance, pbar /RI	6 / 3 %

In Fig.1 the layout of the CR with the main insertions is shown. This layout is based on the concept that 18 beam position monitors (BPM) have to be integrated in the quadrupole magnets. Due to this aspect the effective aperture of the quadrupole magnets was reduced from 400 mm to 390 mm.

Because of the larger circumference and smaller quadrupole aperture the ring acceptance is reduced by about 5% for the pbar mode operation. For the RI mode operation the ring acceptance is unchanged.

From a beam dynamics perspective the major effects limiting the ring performance are chromatic effects of the large aperture quadrupole magnets [2]. 24 sextupole magnets are used to correct the ring chromaticity and dispersion function over the full momentum spread. Applying the sextupole correction causes a strong filamentation, which leads to a reduction of the transverse ring acceptance for particles with a large momentum deviation.

The tune spread in the CR has been evaluated since there are several sources resulting in a variation of the tune with amplitude. The field interference between magnets, chromatic, kinematic and fringe field effects cause a crossing of "dangerous" resonances and a subsequent dynamic aperture reduction that leads to particle loss. Numerous numerical simulations predict 5-7% of beam loss due to all these effects.

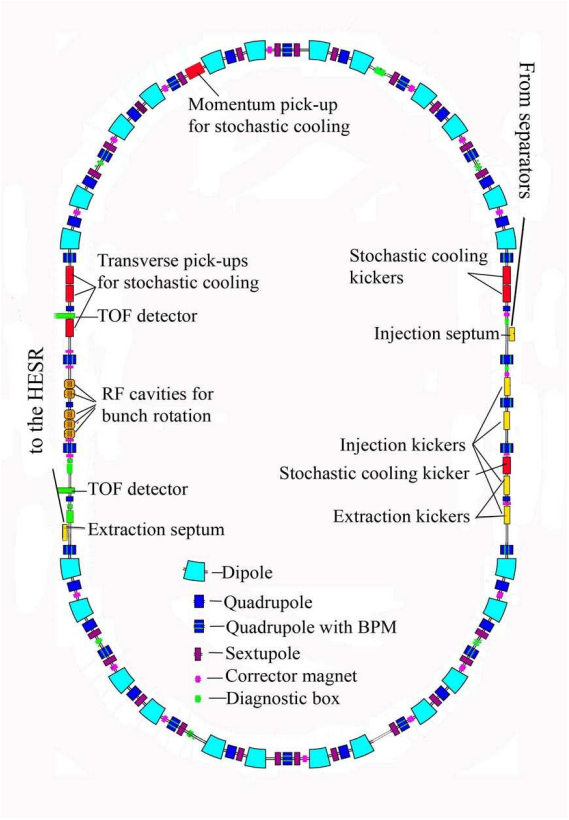

Fig.1. Layout of the CR with main insertions.

Mainly due to the fact that the CR is planned to be used for operation in an isochronous mode ($\gamma_{tr}=\gamma$), where a high mass resolving power is required [3], one has a strong demand on the stability of the power converters. A stability of the power supplies in the order of 5×10^{-6} should be provided for the frequencies from one Hz to some ten kHz. It is also important to avoid a slow drift of the magnetic field.

References

[1] FAIR Baseline Technical Report, 2006.

[2] A. Dolinskii. et.al., Stability boundary of ion beams in the FAIR Storage Rings. Proceedings of PAC 2009 Conference, Vancouver, 2009, TH6PFP078.

[3] A.Dolinskii, S. Litvinov, M.Steck, H.Weick, Nucl. Instr. and Meth. A574 (2007)207

Experimental Demonstration of Beam Accumulation by Barrier Buckets in Combination with Stochastic Cooling

C. Dimopoulou[1], *T. Katayama*[1], *I. Meshkov*[4], *D. Möhl*[3], *F. Nolden*[1], *G. Schreiber*[1], *A. Sidorin*[4], *R. Stassen*[2], *M. Steck*[1], *H. Stockhorst*[2], *and G. Trubnikov*[4]

[1]GSI, Darmstadt, Germany; [2]FZJ, Jülich, Germany; [3]CERN, Geneva, Switzerland; [4]JINR, Dubna, Russia

For the modularized start version of the FAIR project, a scenario was proposed with accumulation of antiprotons in the High Energy Storage Ring (HESR). The accumulation uses pre-cooled antiprotons from the Collector Ring (CR) for longitudinal accumulation by the combination of barrier buckets and stochastic cooling. As a benchmarking of computer simulations and for studies of technical requirements for the components employed in this technique a proof of principle experiment in the ESR was proposed. This benefits from previous investigations in the ESR on accumulation by a combination of barrier buckets and electron cooling [1] and the availability of stochastic cooling as well. Various waveforms for the barrier bucket system are under consideration, fixed barriers, moving barriers and the use of sinusoidal rf at harmonic $h = 1$ with injection of the new beam onto the unstable fixed point.

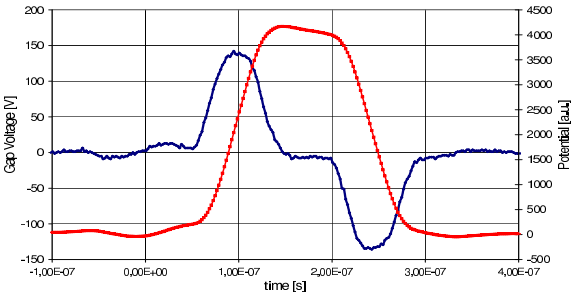

Figure 1: Measured voltage (blue) at the acceleration gap and potential (red) over one revolution period of 500 ns.

As a beam with relatively low electric charge bare argon ions were chosen, the energy of 400 MeV/u is predefined by the operating range of the stochastic cooling system. The ESR is not equipped with a dedicated barrier bucket system which allows operation with arbitrary waveforms. However, as demonstrated before, by adding a 50 Ω resistance in parallel to the acceleration gap the cavity allows operation with single sinusoidal waveforms with a frequency of 5 MHz. The available gap voltage is determined by the power of the rf amplifier driving the gap voltage. With an existing 300 W amplifier a peak voltage of 120 V can be achieved. The voltage measured at the gap is shown in Fig. 1. As the accumulated beam is compressed into a fraction of the ring circumference a precise timing of the injection kicker is needed in order to inject the new beam without kicking out stored particles and even with minimum heating of the stored beam. The fraction of the circumference needed for the stored beam corresponded to a bunch length of about 200 ns, the interval for the rise and fall time of kicker pulse was 100 ns each. With a revolution time of 500 ns a time interval of less than 100 ns was available for the incoming single bunch from SIS.

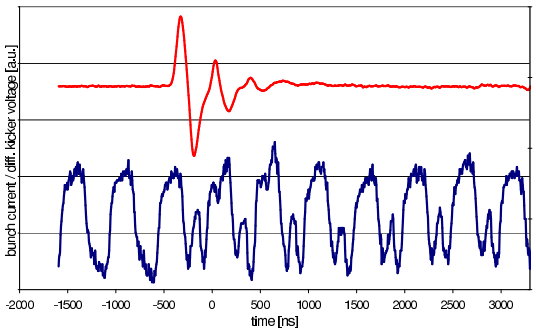

Figure 2: Differentiated current pulse of the injection kicker (red) and bunch signal from a pick-up (blue) over 10 revolutions. After three revolution periods (t=0) a new bunch is injected into the gap of the circulating beam.

The beam signal in the ESR was detected in time domain with a standard ESR position pick-up, which is sensitive to any time modulation in the beam. Figure 2 shows the pick-up signal over 10 revolutions (5000 ns) of the beam in the ESR. After 3 revolutions the incoming bunch occurs in the gap between the circulating bunches formed by the barrier bucket system. The timing between the incoming bunch and the ESR rf system which bunches the accumulated stored particles and the injection kicker is very demanding, but could be controlled with good stability and reproducibility. Thus up to 30 injections could be performed with good efficiency (Fig. 3). Similar performance for all tested rf waveforms could be achieved.

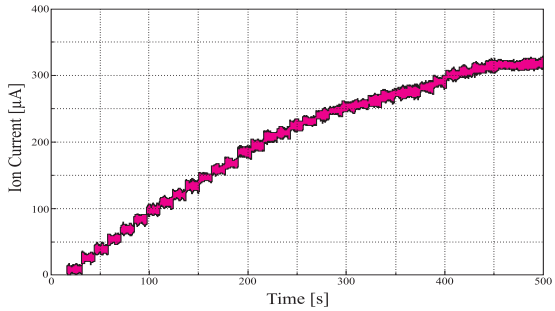

Figure 3: Stored beam current with injections every 10 s.

References

[1] C. Dimopoulou et al., Proceedings of COOL07, Bad Kreuznach, Germany (2007) 21.

IHEP activity for SIS300 development in 2010

A. Ageyev[1], I. Bogdanov[1], S. Kozub[1], V. Pokrovsky[1], P. Shcherbakov[1], V. Sytnik[1], L. Tkachenko[1], S. Zintchenko[1], V. Zubko[1]

[1]Institute for High Energy Physics (IHEP), Protvino, Russia

In 2010 IHEP continued its activity for the development of SIS300 quadrupole and corrector magnets as well as the local cryogenic system of SIS300.

So an analysis of the factors affecting field quality and heat releases of the quadrupole magnet for the SIS 300 was developed. The main parameters of this magnet are: 45-T/m central gradient with a gradient ramp rate of 10 T/m/s in a useful aperture of 105 mm and a coil inner diameter of 125 mm. The geometric length of the magnet is 1 m. The results of the study were presented at the ASC conference in Washington, USA. Particularly the influence of the weak magnetic elements of the design on the field quality in the magnet was examined, as well as the effect of heat releases generated in the resistive parts on the temperature margin of the magnet. Tolerances for the manufacturing accuracy of various geometrical parameters were presented and an examination of the parameters affecting the integral field quality was described. The presented law of the dependence of low integral field multipoles on the thickness of the spacer and its position in the end parts allows one to quickly find an optimized geometry with respect to the integral field quality.

Further, the tooling for the production of a SIS300 quadrupole prototype was manufactured, as well as the magnet's parts. The necessary 6 km of SC wire of 0.825 mm diameter was produced by Bochvar institute. Finally the SIS300 quadruple prototype was assembled (Fig.1).

Also the test facility for cold tests and the device for magnetic measurements of the SIS300 quadruple prototype were modernized.

The Technical Design Report on SIS300 quadruple was completed as well and will be discussed at next SIS300 meeting.

Engineering drawings of the chromaticity sextuple, resonance sextuple, steering magnet and error compensation multiple correctors for the SIS 300 were completed and a proposal for the design of a SIS300 cryomodule (type A) was developed and presented to GSI for discussion.

The Engineering drawings (60% from total volume) of test facility for SIS300 cryomodules were completed.

A report on the local cryogenic system of SIS300 was prepared and presented at the SIS300 meeting 2010. The analysis of the system cooling down, quench mode and warming up was afterwards completed and will be presented at the next SIS300 meeting.

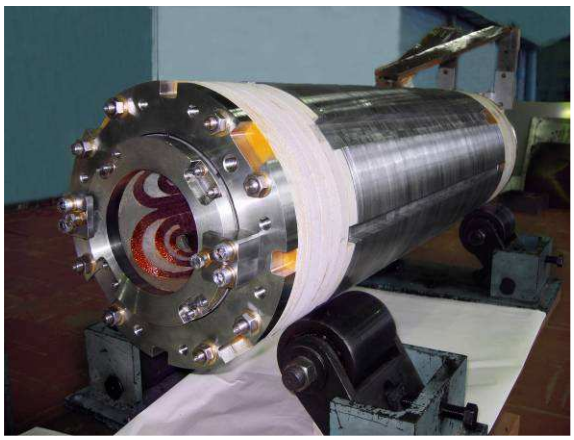

Figure 1: SIS300 quadrupole prototype.

References

[1] L. Tkachenko, S. Kozub, P. Shcherbakov, V. Sytnik, V.Zubko, "Analysis of the Factors Affecting Field Quality and Heat Releases of the Quadrupole Magnet for the SIS 300" presented at ASC 2010, Washington, 2010.

[2] A. Ageyev, I. Bogdanov, S. Kozub, E. Kashtanov, K. Myznikov, A. Orlov, P. Slabodchikov, V. Sytnik, P. Shcherbakov, L. Shirshov, V. Sytchev, V. Pokrovsky, K. Polkovnikov, L. Tkachenko, S. Zinchenko, V. Zubko, "Development and Production of Superconducting and Cryogenic Equipment and Systems for Accelerators by IHEP", RUPAC, 2010, Protvino, pp. 295-299, http://www.jacow.org.

[3] A. Ageyev, S. Zinchenko, V. Zubko, S. Kozub, "Cooling System of the SIS300 accelerator", RUPAC, 2010, Protvino, pp .303-305, http://www.jacow.org.

[4] P. Shcherbakov, I. Bogdanov, S. Kozub, L. Shirshov, P. Slabodchikov, V. Sytnik, L. Tkachenko, V. Zubko, "Materials for Fast Cycling Accelerator Superconducting Magnets", RUPAC, 2010, Protvino, pp .331-333, http://www.jacow.org.

[5] L. Tkachenko, I. Bogdanov, S. Kozub, P. Shcherbakov, P. Slabodchikov, V. Sytnik, V. Zubko, "Development of Fast-Cycling Superconducting Quadrupole and Corrector Magnets for the SIS 300", RUPAC, 2010, Protvino, pp .300-302, http://www.jacow.org.

[6] A. Vlasov, A. Ageev, E. Kashtanov, A. Khartchenko, S. Kozub, S. Zinchenko, "Test Facility for SIS300 Cryomodules", RUPAC, 2010, Protvino, pp .334-336, http://www.jacow.org.

R&D activity in 2010 at INFN for fast cycled magnets with curved shape for FAIR

P.Fabbricatore[1], S.Farinon[1], R.Musenich[1] F. Alessandria[2], G.Bellomo[2], M.Sorbi[2], G.Volpini[2], U.Gambardella[3]

[1]INFN, Genova, Italy; [2]INFN-LASA, Milano, Italy; [3]INFN, Frascati, Italy

A model of the superconducting dipole for FAIR´s SIS300 is under development at INFN. After five years of R&D activities, a magnet 3.9 m long has been constructed at ASG Superconductors.

The magnet will be delivered end of this year to Milano LASA laboratory for an operational test in a vertical cryostat.

Main achievements in 2010 were:

1) The collaring of the coil. During the collaring (Fig.1) it was observed that the pressure to be applied for aligning the holes hosting the keys at the mid-plane was 30% lower than the expected one. This phenomenon has not yet been completely clarified and is under investigation. In order to have the correct azimuthal pre-stress, the collars were removed after re-applying the pressure and taking away the keys. Thicker shims were inserted, before collaring again. This time the collaring was done at the expected pressure.

Figure 1 : The coil inside the press during the collaring operation. The photo captures the moment when the cavities housing the keys on the collars are aligned.

2) Integration into the iron yoke. Fig. 2 shows the collared coil partially assembled into the lower half-yoke. A critical operation is the block assembly. Each block, made of 892 plates, must have the correct curvature for fitting with the neighbouring blocks and the collared coil.

Once the upper yoke was assembled too, the magnet was put inside the same press used for the collaring and a pressure was applied until the two halves of the yoke went into contact at the mid-plane.

3) Integration into the external shell. This operation took a long time. It was decided to post-pone the completion of the magnet to after the test in vertical position at LASA: the end domed flanges were not welded for a definitive solution but only temporarily fixed, for allowing an easy dismount of them in case the axial pre-stress should be modified. Fig.3 shows how the coil ends appear now, before sending the magnet to LASA laboratory.

Figure 2: Lower half yoke hosting the collared coil. Both halves of the yoke are composed of four large blocks in silicon steel and two small blocks in stainless steel at the magnet ends.

Figure 3: End part of the cold mass with temporary welds (to be removed later) of the domed flanges to the cold mass body.

According to the last planning, the cold mass will be tested at LASA within the spring 2011 and then the doomed end caps will be definitively welded. Soon after, the cold mass will be integrated into a horizontal cryostat and be sent to GSI (summer 2011).

References

[1] P.Fabbricatore, F.Alessandria, G.Bellomo, U.Gambardella, S.Farinon, R.Marabotto, R.Musenich, M.Sorbi and G.Volpini, "The construction of the model of the curved fast ramped superconducting dipole for FAIR SIS300 synchrotron", ASC2010 Washington DC, 2010.

Compensation and Tolerances of the Steady and Time-Dependent Field Errors of the SIS300 Superconducting Dipoles

A. Saa-Hernandez[*1,2], *H. Müller*[1], *P. Spiller*[1], *and U. Ratzinger*[2]
[1]GSI, Darmstadt, Germany; [2]IAP, Frankfurt, Germany

The higher order field components, or field errors, of the SIS300 dipoles have been calculated with the code ROXIE [1]. For low currents, the main contribution to the total magnetic field are the persistent currents (pc). The pc flow along the superconducting filaments and decay when the current remains constant. Therefore, the pc are time-dependent. The SIS300 stretcher mode is planned for low-field levels, at 20 and 64 Tm. For high currents, the dominating field error source is the iron saturation, which is steady. For the extraction in the high-energy mode, in this region, at 300 Tm, the pc contribution is negligible.

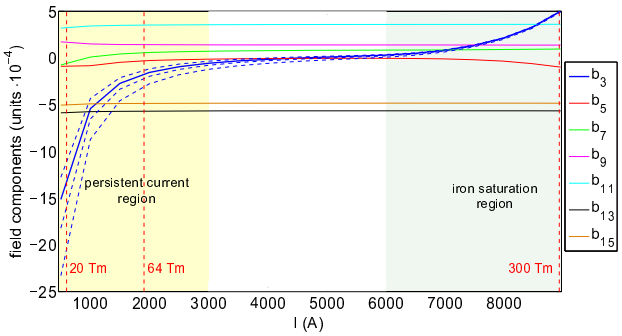

Figure 1: ROXIE calculations for the allowed field errors of the SIS300 dipoles up to b_{15}. The field error b_3 is plotted in blue for different filament diameters (2, 2.5, 3.5 and 4 μm). The absolute b_3 error increases with the thickness of the filaments at low fields. The thick blue line is used as a reference value (2.5 μm) in the text.

The sextupolar component, b_3, contributes to the chromaticity and to the resonance excitation. Its contribution to the chromaticity in the high-energy mode doubles the contribution from the sextupole magnets. Since the Hardt condition is no longer fulfilled, a big broadening of the separatrices and a ten times bigger spread of the entrance angle at the septum is generated, as shown in Fig. 2. The effect of b_3 can be described by the analytical models used in the numerical algorithm derived in [2], which optimize the gradients (k_2) of the different families of sextupoles. Therefore, the b_3 errors can be compensated by means of optimized k_2 settings. The tolerances are derived from the limit where the compensation is no longer possible.

The limits are found for the mean value of the field component in all the magnets (systematic component), and also for its variability from magnet to magnet (random component). Two assumptions are compared: *i)* the systematic and random components are known and can be compensated, which implies all dipoles were measured cold prior to their installation in the tunnel, and *ii)* only the systematic component is known and compensated. In case *i)* the limits can be more relaxed, as shown in table 1.

Table 1: Tolerances for the field components [units · 10^{-4}]

		b_3 systematic		b_3 random	
high-energy mode		15 / 11[1]		9 / 6	
low-energy mode		9 / 5		6 / 4	
systematic	b_5 to b_{15}	a_2	a_3	a_4	a_5 to a_9
both modes	-[2]	$\leq$1	4	2	-[2]

[1] systematic + random compensation / only systematic compensation
[2] upper limit was not found within × 10 their nominal value. The skew errors are taken from measurements on similar dipoles from RHIC [3]

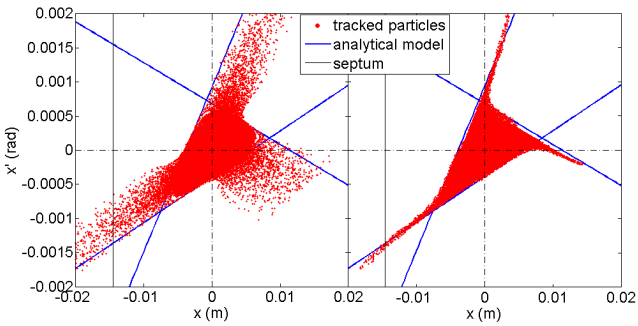

Figure 2: Tracking simulations of the slow extraction before (left plot) and after (right plot) the compensation by means of a new set of optimized gradients for the 2+6 families of chromatic and resonant sextupoles, respectively.

There is no analytical model which provides a full description of the pc decay, as it depends on the magnets history. Therefore, an experimental fitting function expressed in terms of the decay amplitude and the decay rate should be used. To compensate the time-dependent pc decay, new sextupole gradients are calculated using the optimization program. A ramping of the resonant sextupoles along the extraction plateau is proposed as a dynamic compensation for the stretcher mode, see details in [2].

The field errors different from b_3 remain practically constant for all currents. These field errors cannot be compensated by optimizing the sextupole gradients. Therefore, the tolerances, presented in table 1, are proposed such that a high efficiency of the slow extraction is ensured. This is evaluated by means of tracking simulations.

References

[1] S. Russenschuck. *ROXIE*. cdsweb.cern.ch
[2] A. Saa-Hernandez. *PhD Thesis*, to be published.
[3] P. Wanderer. *The RHIC magnet system.* NIM-A 499, 2003.

* a.saahernandez@gsi.de

Synchronization of Distributed Synchrotron RF Components

M. Weber[1], K. Fricke-Neuderth[1], V. Wolff[1], and H. Klingbeil[2]

[1]University of Applied Sciences Fulda, Germany; [2]GSI, Darmstadt, Germany

Introduction

The synchrotrons of the Facility for Antiproton and Ion Research (FAIR) will be equipped with multiple RF cavities to deliver the energy of accelerated ion beams. The process is based on a sine signal, whose frequency is determined by a control room on a microsecond scale. The RF signals are typically generated by Direct Digital Synthesis (DDS) modules. In some applications, two DDS units shall provide the same output even though they are located in different supply rooms and even though a frequency correction by a local control-loop is present. Figure 1 illustrates the schematic structure of the accelerator including the supply rooms and the control room.

One aim of the BMBF-Sub-Project "FAIR-Accelerator: Synchronization of distributed High-Frequency Components" project is to ensure this simultaneous/synchronized operation of the DDS units. In order to reach this target, several synchronization concepts have been investigated.

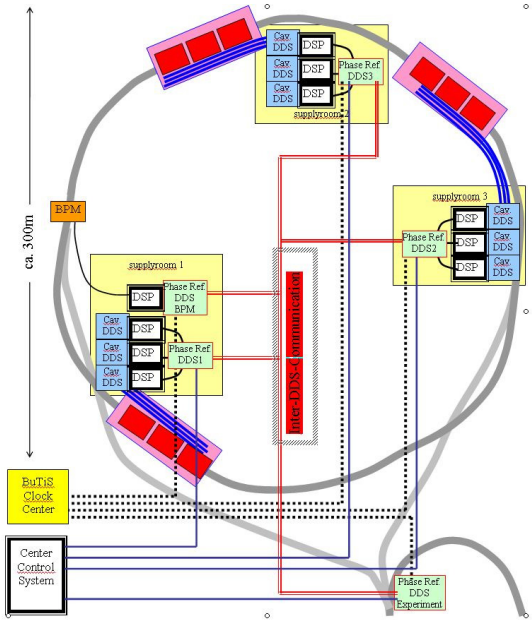

Figure 1: Distributed HF-Components

Approach to synchronization

The DDS units which provide the RF signals for the cavities are almost continuously adjustable. Control of the DDS is based on a Field Programmable Gate Array (FPGA) in order to respond immediately to frequency or phase changes. A system based on FIB2-Boards (FPGA Interface Board) will be developed to compensate signal propagation delays. The FPGA used to control the DDS module must defer its received frequency data until the up-to-date data have been delivered to the DDS module with the largest signal propagation time. This principle relies on known propagation times [1]. This is accomplished with delay-compensated BuTiS-clocks [2], available in all supply rooms. The synchronization clocks are 200 MHz and 100 kHz.

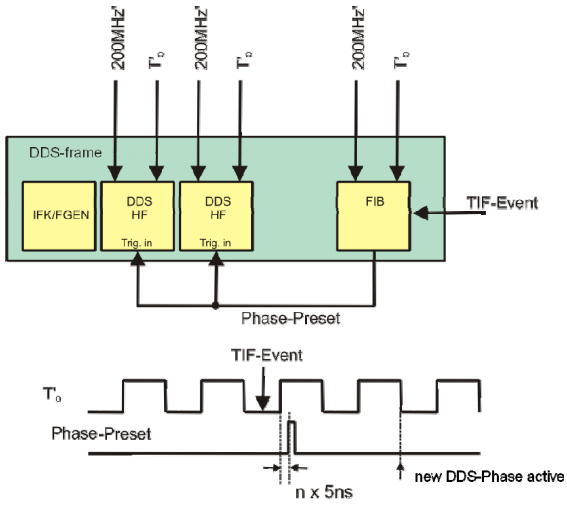

Figure 2: Concept of the reset

An intermediate step in this project is to synchronize two DDS-modules mounted in the same DDS-rack using external trigger access. The figure above illustrates the schematic diagram of the hardware used in the project. Figure 2 shows that a phase reset is delayed two clock cycles. The new DDS-phase becomes valid at the falling edge of the T_0 clock (100 kHz) provided by BuTiS. Since the BuTiS clock is synchronously available in all supply rooms, the new phase will become valid at the same time in all cavity LLRF systems. The corresponding VHDL code has been implemented in the existing FPGA board.

Future Work

This synchronization mechanism will be implemented for other data-telegrams and trigger-telegrams used in the RF components. A board with a larger FPGA (more complex logic blocks) will be available for these features.

References

[1] B. Zipfel, K. Fricke-Neuderth, et al.: "Analysis of a Digital Beam Phase Control System", Workshop LLRF05, CERN, 2005

[2] P. Moritz: "BuTiS – Development of a Bunchphase Timing System", FAIR-ACCELERATORS-20, GSI Annual Report 2006.

High Data Rate Handling with FESA

H. Bräuning and T. Hoffmann
GSI, Darmstadt, Germany

The Front End Software Architecture (FESA) developed at CERN was chosen to serve as the front-end level of the future FAIR control system [1]. FESA provides the tools to design and operate DAQ systems (FESA classes) based on common platforms such as PCI, cPCI and VME. It handles common tasks like multiplexing and publishing of the data to Java based GUI applications. A complete FESA framework environment (V2.10) has now been established at GSI, which already allows developments for the existing accelerators to obtain the expertise with the development techniques and the look-and- feel of the final applications.

One aspect in data acquisition for beam diagnostics is the handling of comparatively high data rates for certain devices. One example is the Large Analog Signal and Scaling Information Environment (LASSIE), which is intended to replace the ABLASS system [1]. It consists of FESA-based data acquisition classes and JAVA GUIs. Recently the readout of a VME scaler array with 192 channels for SIS and connected beam line data was implemented in FESA. While normal operating conditions require sampling rates of all 192 scaler channels in the order of 1 kHz or below, dedicated beam experiments may use sampling rates up to 1 MHz.

One bottleneck for high sampling rates is the transfer of data via the VME backplane. According to the specifications of the used scaler module, the transfer rate via the VME backplane is limited to about 50 MByte/s for MBLT64 block transfer. To compare the rate capabilities of the older PowerPC based CES RIO3 CPUs and the new Intel based Men A20 CPUs, a test system with a single 32 channel scaler and a virtual machine cycle of 2000 ms runtime and 150 ms pause was set-up. Scaler access was done via block transfer (BMA) on the RIO3 and DMA on the Men A20. Figure 1 shows the maximum number of scaler channels which could be read out simultaneously by the FESA class without any connected GUI clients as a function of the latching frequency. For latching frequencies of 200 kHz and above, the Men A20 board consistently can handle more scaler channels than the RIO3. This means a higher data throughput for the Men A20 board with a measured maximum of 34 MBytes/s. A total CPU load of only 10% indicates that this rate is limited by the transfer from the scaler module to the memory and not by data handling in the FESA class. In contrast, a maximum data rate of 22 MBytes/s was measured with the RIO3. This is accompanied by a strong increase in the CPU load, which indicates that the processor power is the limiting factor. However, it must be noted that this superiority of the Men A20 is only valid in the case of DMA usage. For direct access of a single register, the RIO3 has a slight advantage with a measured data rate of 1.4 MBytes/s as compared to 1.2 MBytes/s for the Men A20 board. In addition, setting up the DMA transfer takes some time and is thus suitable only for the transfer of large blocks of data via the VME bus. Moreover, the Men A20 CPU with its 1000 Mbit/s Ethernet interface also allows a higher data transfer rate to the GUI application as compared to the RIO3. Thus the RIO3 CPU will be replaced with the Men A20 CPU in beam diagnostics applications.

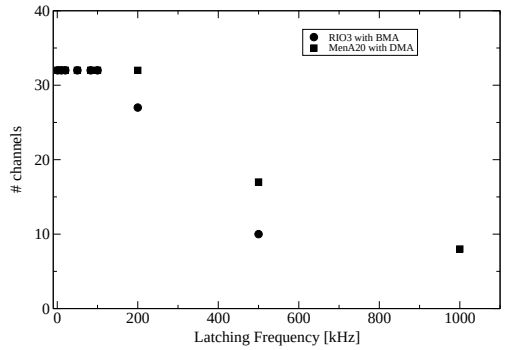

Figure 1: Number of scaler channels which can be readout as a function of the scalers sampling rate.

High data rates also occur in applications using CCD video cameras like for fluorescent screens. Tests have been performed with two Gigabit Ethernet cameras: Prosilica GC650 with 659x493 pixels and IDS uEye Kamera UI524xSE-M with 1280x1024 pixel. For each camera a dedicated FESA class has been written using the SDK supplied by the manufacturer. A Java GUI is used to display the image stream as well as brightness histogram and profiles. The Fesa class as well as the GUI were run on the same computer with an Intel Core2 Duo CPU. The Prosilica camera was connected directly to the accelerator network. Thus a stable frame rate of 20 fps could be achieved before the CPU load reached 100%. Without a live GUI, the CPU load decreases to about 30%. This indicates a significant amount of computing power is used in the live display. The uEye camera was connected directly to a second ethernet adapter of the computer running the FESA class. Due to the higher resolution the uEye camera could be used with frame rates up to 10 fps only.

References

[1] T. Hoffmann and H. Bräuning, “First FESA Implementations for Beam Diagnostics at GSI”, GSI Scientific Report 2009, p. 122

Investigation on Scintillating Screen Materials for FAIR*

B. Walasek-Höhne[1], C. Andre[1], F. Becker[1], W. Ensinger[2], P. Forck[1], E. Gütlich[1,2], K. Gütlich[1], R. Haseitl[1], R. Krishnakumar[1,2], A. Reiter[1]

[1]GSI, Darmstadt, Germany; [2] Technical University Darmstadt, Germany

Scintillating screens are a direct but destructive method to observe transverse ion beam profiles. Depending on ion species, beam current and energy, scintillators can be selected from a large variety of materials and were subject of detailed investigations at UNILAC [1].

In this article we report on a pilot study for FAIR in which scintillating properties of potential materials were systematically investigated at the end of the high-energy beam line HTP.

Experimental Setup

300 MeV/u Uranium ions were extracted from SIS18 with intensities ranging from 10^4 to 10^9 particles per pulse (ppp) and 400 ms pulse length. Sensitive scintillators like CsI:Tl, YAG:Ce, P43 and Ce-doped glass (M382) were tested at lower beam intensities up to 10^7 ppp; ceramics like Al_2O_3, Al_2O_3:Cr, ZrO_2:Y and ZrO_2:Mg as well as Herasil-102 glass up to the maximum available beam intensity. For systematic measurements, a target ladder with nine different scintillating materials (ø80 mm), mounted on a linear drive was specifically designed and installed at HTP (see Fig. 1).

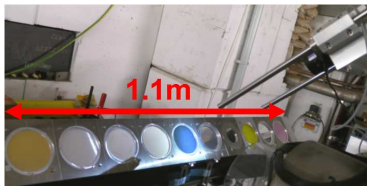

Fig. 1: Movable target ladder with scintillating materials at HTP experimental area in front of the beam dump.

The scintillating screens were monitored with a monochrome CCD camera (AVT Marlin F033B, 8 bit ADC and VGA resolution) and a lens system with remote controlled iris (Pentax, 16 mm focal length) to cope with the large difference in light yield between the materials. The software BeamView [2] was used for data acquisition and on-line analysis. For qualitative investigations, additional images were recorded by a colour CCD camera (AVT Marlin F033C); results are depicted in Fig. 2.

Results

The measured distributions of each material were analysed to obtain the total light yield and transverse beam profiles from projection of the 2-dimensional distribution. To detect image distortions, e.g. due to saturation effects, comparison with reference diagnostics like SEM grids is in progress. As depicted in Fig. 3, the light yield of the tested materials differs by several orders of magnitude and rises almost linearly over a large intensity range. Scintillators like YAG:Ce, CsI:Tl or P43 are much brighter than Herasil-102 glass or ceramic materials, and exceed the dynamic range of the data acquisition system beyond 10^6 ppp. In the present study, ceramics show acceptable signals above 10^5 ppp.

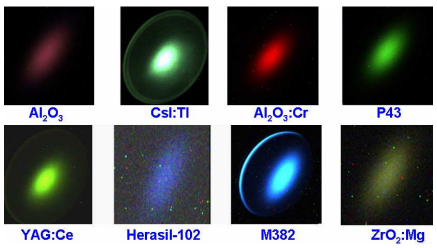

Fig. 2: Scintillating screen images recorded with a colour CCD camera.

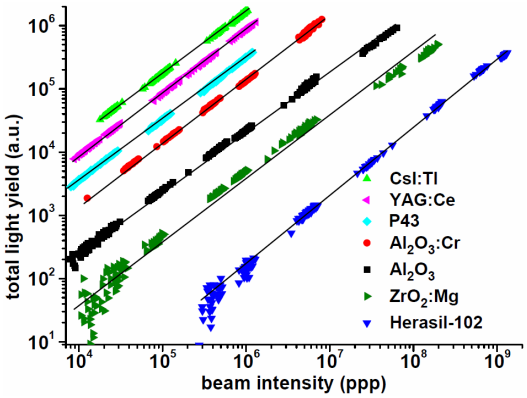

Fig. 3: Light yield as function of ion beam intensity for studied materials. Note: double log plot for overview.

Conclusion

Several scintillating materials were investigated over a wide intensity range for a high-energy Uranium beam (300 MeV/u). Further data evaluation is in progress. Experiments with other ion species are planned at HTP to explore scintillator properties at a wide range of energy deposition (dE/dx). This experimental programme will provide the necessary data required for an appropriate choice of scintillating materials bearing in mind the large variety of ion species and intensities at the FAIR facility.

References

[1] E. Gütlich et al., "Scintillation screen investigations for high current ion beams", 2010, IEEE Transactions Nuclear Science, Vol. 57, No. 3, pp. 1414 (Correction in Vol. 57, No.4 (August 2010)).

[2] R. Haseitl et al., "BeamView – A Data Acquisition System for Optical Beam Instrumentation", PC@PAC'08; http://www.JACoW.org.

* Work supported by BMBF, contract No. 06DA9026.

SEM-Grid Prototype Electronics with Charge-Frequency-Converter (QFW)

M. Witthaus, J. Adamczewski-Musch, H. Flemming, J. Frühauf, S. Löchner, P. Skott and H. Reeg

GSI, Darmstadt, Germany

Overview

GSI Beam Diagnostics department together with Experimental Electronics department has started investigations on a new economical solution for SEM-Grid (Secondary Electron eMission Grid) electronics. The front-end amplifiers and control devices of the existing version are outdated and very expensive. After extensive and promising tests with a 4-channel QFW (Charge-Frequency-Converter) test board [1, 2], it was decided to develop a prototype system with 8 QFW-ASICs (see Fig. 1). The goal of the project was to perform a functional test of ASICs connected to a SEM-Grid under real beam conditions at GSI.

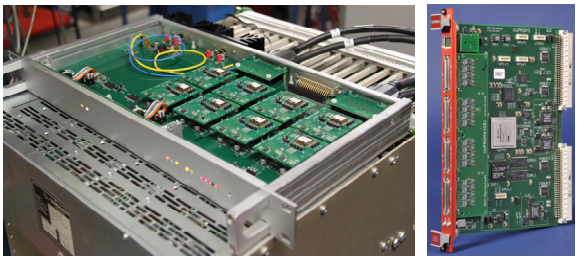

Figure 1: Prototype board with 8 QFW-ASICs (left), standard FPGA-I/O VME board (VUPROM) (right)

Hard- and Software

An important point of the new development was to use existing parts of hard- and software in order to save development time. The new SEM-Grid prototype system consists of:

- 32-ch.-motherboard equipped with 8 QFWs (II)
- VME-Crate
- RIO2-Board (MBS and Ethernet-Connection)
- VULOM-Board (for MBS Trigger operation)
- VUPROM-Board (for QFW Control)
- LEVCON Level-Converter
- Power-supply for QFW motherboard (+7V/3A)
- Go4 (GSI Objected Oriented On-line Off-line system)

The QFW motherboard is controlled by the VUPROM-Board, which sets up the QFW motherboard and operates internally its 32 scalers. The scaler data for different time slices are stored and transferred via the RIO2 board into a PC. The beam profiles are displayed and evaluated with online analysis software Go4. The QFW's parameters are set via a terminal program, and the VULOM board is necessary for the MBS trigger operation.

Measurement Results

The QFW board was tested with a 2x16-wire SEM-Grid assembly at the experimental beamline X2, which already is equipped with three SEM-Grids placed close to each other (< 1m). This experimental setup allowed to perform measurements with the prototype electronics at one SEM-Grid, and to compare the profiles with the two others. As shown in Fig. 2 the beam profiles showed a good signal resolution. Additionally, comparison between old and new electronics using the same SEM-Grid was performed with very good agreement.

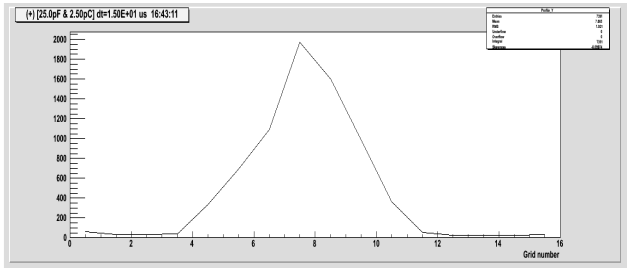

Figure 2: Vertical ion beam profiles obtained with QFW prototype board (grid with 16 wires)

With the support of Go4- and QFW-control software it was possible to display time slices of each beam pulse (see Fig. 3). Observation of the time-dependant changes of the beam profile during a single beam pulse is very helpful for accelerator operations and is not provided by the existing hardware.

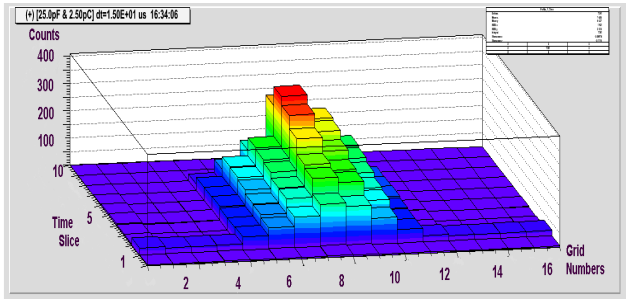

Figure 3: Time dependent and vertical beam profiles. The beam pulse length is around 100 µs, slice length is 15 µs.

Outlook

After the successful beam tests with the new QFW readout board it is planned to add a second 32-channel motherboard to the existing system. Further experiments with different diagnostic components like MWPC (Multi-Wire Proportional Chamber) as well as with different SEM-Grid types are foreseen.

References

[1] H. Flemming and E. Badura, "A high dynamic charge to frequency converter ASIC", GSI Scientific Report, 2004

[2] M. Witthaus et al., "Charge-Frequency-Converter (QFW) Test Board and Results", GSI Scientific Report, 2009

Status of Frankfurt Neutron Source FRANZ

O. Meusel, H. Podlech, A. Schempp, U. Ratzinger, R. Reifarth and K. Volk

Institut für Angewandte Physik, Goethe University, Frankfurt am Main, Germany

One research field of the Frankfurt Neutron Source FRANZ already under construction will be the development of new accelerator concepts for very high ion beam intensities. It is planned to use a proton beam with a current of I_b = 200 mA as a probe for each of the different accelerator components.

Ion Source

To fulfil the requirement on beam luminosity the ion source has to deliver a cold and intense proton beam with a generalized perveance of $K = 3.1 \cdot 10^{-3}$. Therefore, it was decided to use a hot filament driven gas discharge ion source providing very small beam emittances due to the very low plasma temperature. Furthermore, this source type is able to produce high beam intensities. Preliminary experiments using the source prototype exhibit a beam current of I = 245 mA with a proton fraction of 92%.

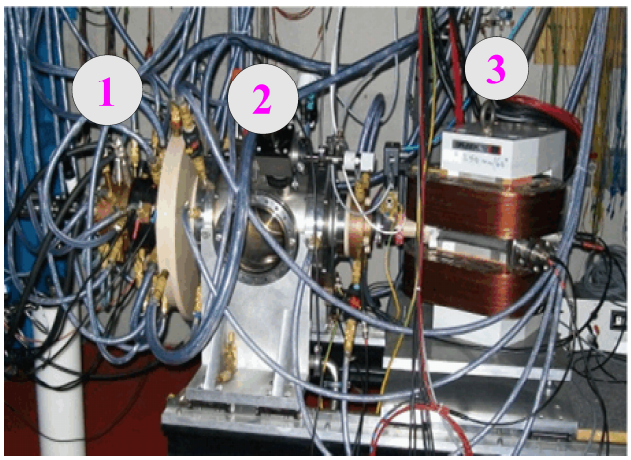

Figure 1: Picture of the ion source test bench: 1) source prototype, 2) Faraday Cup and 3) momentum analyser.

Low Energy Beam Transport

The low energy beam transport section will include an E x B chopper to provide beam pulses of τ = 50 ns with a repetition rate of about 250 kHz. The proton beam will be injected into the accelerator while an electric deflector will compensate the magnetic force of a bending dipole magnet. The high voltage pulse generator for the chopper system has been tested successfully.

Non-destructive beam diagnostics is needed because of a nominal beam power of P_b = 24 kW. High time resolution of the optical diagnostics, which uses a 3D reconstruction algorithm, will provide the possibility to investigate collective phenomena of intense ion beam transport.

Four Solenoids will perform the beam focussing. Accurate field mapping of the solenoids helps to prevent emittance growth by lens aberrations.

Coupled RFQ-IH Cavities

The main accelerator stage of FRANZ consists of an RF coupled RFQ-IH cavity. The four rod RFQ already under construction has been designed to support high power consumption. The main challenge is the thermal load and the design of adequate cooling concepts. The intersection of stems and tuning plates and the cooling capability have been tested extensively in experiments using a test resonator. The design of the IH-cavity has been finished and a detailed investigation of the RF coupling is underway. A model of a coupled RFQ-IH cavity has been constructed to measure the influence of the RF coupling on the field distribution in both accelerator parts.

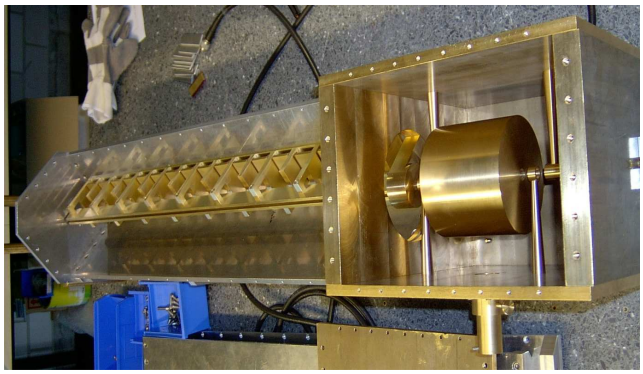

Figure 2: Picture of the accelerator model consisting of the coupled RFQ (right) and the IH cavity (left)

Bunch Compressor

A bunch compressor at the end of the accelerator will provide beam pulses in the 1 ns range with a peek current of about 9 A. The challenge of the compressor is the simulation of the beam dynamics for this multi-track device consisting of duplex gradient dipoles and a multi-aperture rebuncher. The finalisation of the bunch compressor is planned at the end of 2011.

References

[1] U. Ratzinger, et. al. “The Frankfurt Neutron Source FRANZ”, IPAC’10, Kyoto, Japan, May 2010

Beam Dynamics Simulations for the Laser Proton Injector Transport Line*

A. Orzhekhovskaya, W. Barth, I. Hofmann, S. Yaramyshev

GSI, Darmstadt, Germany

The recent development in the field of "laser acceleration of protons and ions" has initiated several investigations of this concept of an innovative and compact accelerator. Unique features of the Laser Ion Source (LIS) are extremely high beam current and very low transverse and longitudinal beam emittances. A general disadvantage of the LIS is a huge spectrum of the proton energies.

A simulation of proton collimation and transport, based on output data from the PHELIX experiment [1], is necessary to study chromatic and geometric aberrations of the first collimator as an interface between the LIS and the adjacent accelerator structure [2].

The multiparticle code DYNAMION [3], dedicated to simulate beam dynamics in linacs, was used as an advanced tool to perform investigations for the laser proton injector beam transport line. Non-linear effects and high order aberrations are included in this code automatically. Space charge effects are also taken into account, while the simulations for the "zero" current case might be treated as the most optimistic case. Diversifications of the input beam parameters leads to additional emittance growth.

The following proton beam parameters were fixed for the investigations:
- energy 10 MeV;
- transverse size ± 0.03 mm;
- transverse divergence up to ± 172 mrad;
- total unnormalized emittance up to 5 mm·mrad;
- phase spread $\Delta\varphi = \pm 0.75°$ (related to 108 MHz);
- energy spread $\Delta W/W$ up to ± 64%;
- current up to 560 mA.

Calculations for different input beam parameters were done for a transport line with quadrupole (Q-line) and solenoidal (S-lines) focusing. A realistic distribution of the solenoidal field [4] was introduced into DYNAMION simulations as a field mapping. The results of simulation for the quadrupole transport line show a much higher emittance growth (up to a factor of five), than for the S-line. The non-paraxial effect and the chromatic aberrations are weaker due to the symmetric solenoid focusing strength, suppressing large transverse deviation of the beam. Therefore we concentrate on the S-lines.

An RF re-buncher is placed at the end of the transport line at a distance of about 240 cm from the LIS. It provides for longitudinal beam focusing and decreases the energy spread of the core particles (energy spread inside ± 4%) to less than ± 0.5%. It is planed to make use of an already existing 108 MHz 3-gap re-buncher. Realistic 3D electric field of the re-buncher is calculated by the DYNAMION code as well, solving the Laplace equation on the base of the real geometry of drift tubes and gaps.

* Work supported by EURATOM (IFK KiT Program) and Helmholtz International Center for FAIR

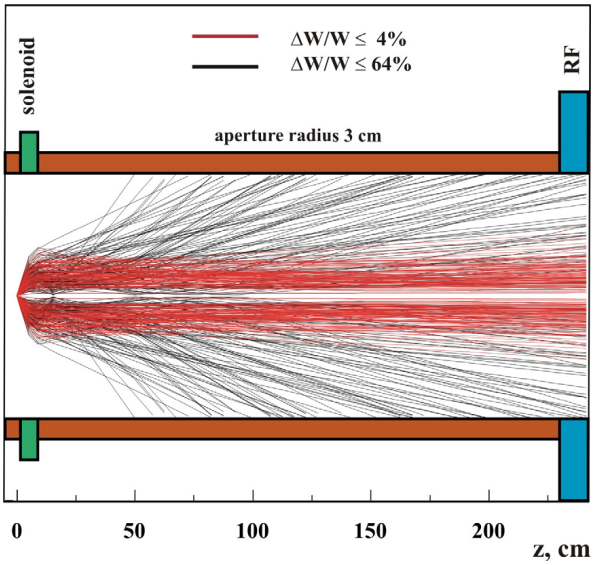

Figure 1: Zero current particle trajectories for different energy spread. Transport line includes focusing solenoid and RF re-buncher.

Only about 20% of the initial particles can be potentially captured in the RF bucket, but the required bunch rotation is successfully implemented only for central part of the energy distribution. Even neglecting space charge effects, only a small amount of about 5% of the initial beam current of 560 mA can be matched to the required beam conditions of the conventional postaccelerator [5].

The very early expansion phase of the proton-electron cloud should be investigated with dedicated codes. Additionally, the influence of the strong magnetic field of the solenoid (up to 5T) on the propagation of the particle distribution has to be taken into account. The obtained results can be used as an input for advanced DYNAMION simulations. Obviously, any complication of the input beam parameters leads to a larger and faster degradation of the beam quality along the transport line.

The LIS provides for an extremely high beam brilliance, while recent studies show serious limitations, mainly due to the huge energy spectra of laser generated protons. Quadrupole and solenoid focusing was considered for different layouts of the transport line. Potentially, a more complicate construction might improve the beam quality, matching the adjacent accelerator structure.

References

[1] F. Nürnberg et al., PAC 09, Vancouver, Canada, 2009.
[2] I. Hofmann et al., HIAT 09, Venice, Italy, 2009.
[3] S. Yaramishev et al., NIM A, Vol 558/1, 2005.
[4] M. Droba, *privat communication.*
[5] L. Groening et al., LINAC 06, Knoxville, USA, 2006.

Simulation study of plasma expansion in the early stage of TNSA

Zsolt Lecz[1], *Oliver Boine-Frankenheim*[2], *and Vladimir Kornilov*[2]
[1]TU, Darmstadt, Germany; [2]GSI, Darmstadt, Germany

For intensities of the PHELIX laser [1] the Target Normal Sheath Acceleration (TNSA) is the most important acceleration mechanism. The ion beams accelerated in this way should be collimated and transported by a solenoid to other accelerator components. In order to optimize the transport and to increase the collimation dedicated simulation studies are needed [1]. The two dimensional phase-space distribution of ions and electrons in the transition regime between the source and the solenoid is still very much unknown. Especially the detailed distribution of the neutralizing electrons. Our task is to develop a model, which describes the phase-space distribution of the generated ions and electrons in two dimensions at μm scale length behind the target. For this we use the VORPAL PIC code [2].

In our 1D simulation we used a 115 fs, 10^{23} W/m^2 laser and a 3 μm thick target, $n_{e0} = 2.43\times10^{28}\,\mathrm{m}^{-3}$. Although the simple plasma expansion is adiabatic, the very beginning of TNSA can be well described with Mora's isothermal model [3]. This feature can be explained by the hot electron supply produced by the laser.

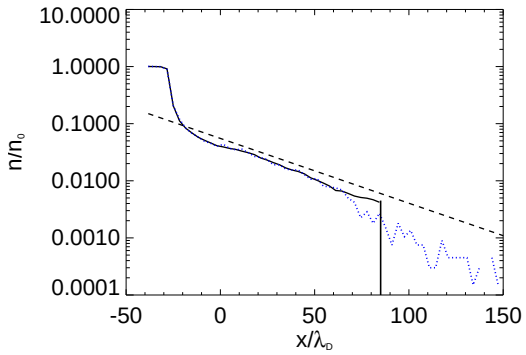

Figure 1: Density profile of ions (full curve) and electrons (dotted curve). The dashed curve is the isothermal solution. λ_D is the initial Debye-length. $\omega_{pi}t = 16$

In Fig. 1 the ion and electron densities are presented and compared with the theoretical prediction [3]: $n_e = n_{eh}\exp(-x/c_st - 1)$, where $c_s = \sqrt{T_{eh}/m_i}$, T_{eh} is the hot electron temperature and n_{eh} is the hot electron density. The rear surface of the target was initially at $x = 0$. As we can see, the density profile from the simulation has a steep drop-down at the beginning and continues with an exponential decrease. This jump in the density is due to the remaining large amount of cold electrons inside of the target. The analytical solution, which assumes a one-temperature electron population, does not have this behavior, but the slope of from the simulation and the isothermal prediction are almost the same. In the simulation the laser-created hot electron density is 15 % of the initial plasma density inside of the target. For the hot electron temperature in the isothermal model we used 400 keV to obtain agreement with the simulation result. The values obtained from the simulation were used for evaluating the expression of maximum ion velocity: $v_m = 2c_s\ln(2\omega_{pi}t/\sqrt{2e})$ [3], where $\omega_{pi} = \sqrt{n_{eh}e^2/\epsilon_0 m_i}$. This is compared with the simulation result in the fig. 2. In the plasma frequency we used the hot electron density. Here the t=0 corresponds to the time when the electrons exit on the rear side of the target. During the pulse length, which corresponds approximately to $\omega_{pi}t = 10$, the maximum velocity increases linearly. This is in agreement with studies using longer pulse lengths and can be explained by the strong electron flow coming out from the target back side. From these results we can

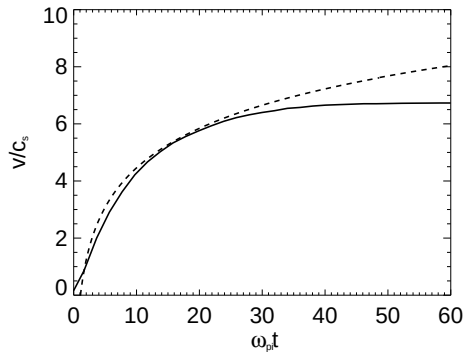

Figure 2: Evolution of the ion front velocity. The dashed curve is the analytical prediction [3].

conclude that the isothermal solution describes quite well the early stage of TNSA expansion, which is driven by the hot electrons. The peak electric field at the ion front and the ion energy distribution are also in good agreement with the theory [3]. In a next step we plan to investigate cooling and beam expansion in the adiabatic regime ($\omega_{pi}t \geq 30$). From 2D simulations we will get more insight into the evolution of transverse beam divergence and the phase-space distribution of neutralizing electrons.

References

[1] F. Nürnberg, Journal of Physics: Conference Series **244**, 022052 (2010)

[2] Web page: http://www.txcorp.com/products/VORPAL

[3] P. Mora, Phys. Rev. Lett., **90**, 185002 (2003)

Space Charge Effect on the Beam Dynamics of P-Bunch Generated by Laser

A. Almomani[1,], M. Droba[1], U. Ratzinger[1] and I. Hofmann[2]*

[1]IAP, Goethe University Frankfurt, Germany; [2]GSI/Helmholtz-Institute Jena, Darmstadt, Germany

Space Charge Effect

The space charge forces action on the beam dynamics of a single proton bunch generated by laser was investigated by the following case. A 10^{10} protons within a bunch length of 500 fs at energies of 10 MeV ± 0.5 MeV, starting at a beam waist with 60 µm radius were assumed. The influence of the great majority of about proton spectrum with different energies in the bunch as well as the electron were neglected in this model.

Absolute transverse emittances of 0.06 π mm·mrad were used. These simulations were done in two steps; the first step was extended up to 1.65 mm along the beam axis in order to study the Coulomb Explosion. The second step was continued up to about 210 mm (bunch centre) along the beam axis as discussed below.

A magnetic solenoid [1] with 18 T field strength was used to catch the protons. The target - front end of the solenoid distance was set to 15 mm [2].

Coulomb Explosion

The simulations for this section were started with a uniform ellipsoidal distribution in space and with ± 1 mrad as an initial angular divergence of the beam in transverse planes (Figure 1 left). This means that the protons are generated in parallel at the target position.

The beam potential was about 500 kV at the beginning. The bunch starts to diverge and it reached about ± 150 mrad after 1.65 mm from the target (Figure 1 right).

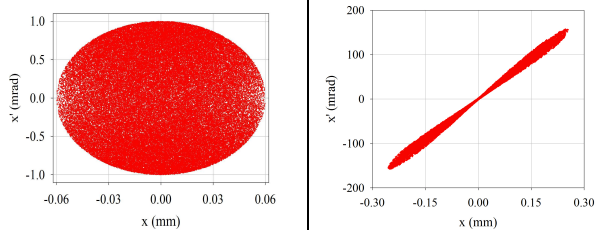

Figure 1: Input and the output distributions in x-x' at the target positions (left) and after the Coulomb's explosion at z = 1.65 mm (right).

Besides this divergence, the energy spread of the bunch was also increased and it reached ±40% at the end (Figure 2), while the beam potential decreased to the 72 kV level.

Transport of p- Bunch through the Solenoid

This part is a continuation for last section, which means that our bunch has an energy spread of about ± 40% and an angular divergence of about ± 150 mrad from the start.

Due to the chromatic aberration [1] particles with different energies are focused at different positions. The energy spread results in a bunch length of about 88.6 mm at a bunch center position of 210 mm from the target.

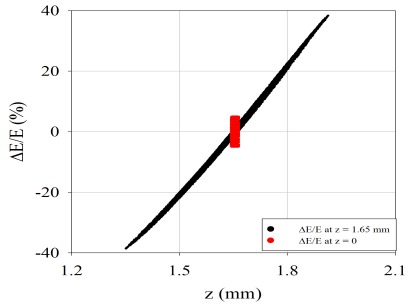

Figure 2: Input and output energy spread distributions in the proton bunch at the target position (red) and after the explosion (black).

Figure 3 shows the x-x' output distribution at the same bunch position. The main influence is given by chromatic aberration, while also geometric aberration together with space charge are contributing.

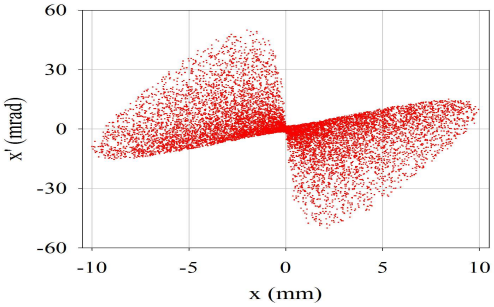

Figure 3: Output distribution in x-x' of proton bunch at the last position which is extended from z = 16.3 mm to z = 25.2 mm.

In conclusion, the simulations show that already the space charge action of one permille of bunch particles around the design particle with 10 MeV ± 0.5 MeV energy range is sufficient to cause a large beam divergence of ± 150 mrad as well as a large additional energy spread of ± 4 MeV along the drift of 210 mm through the magnetic solenoid.

In a next step more detailed simulations, including the full phase space covered by protons as well as electrons should be performed. For realistic starting conditions additional information from measurement are needed.

The simulation results behind the solenoid give valuable input for the interpretation of measurements and can inspire measurement concepts.

References

[1] A. Almomani et. al., FAIR-2010-1 report, p.24 (2010).
[2] A. Almomani et. al., IPAC 10, Kyoto, Japan, THPD035, p.4355 (2010).

* a.almomani@iap.uni-frankfurt.de

Design of a sensitive pickup-structure with variable beta for ion beam

Joel A. Tsemo Kamga, Wolfgang F.O. Müller, and Thomas Weiland
Technische Universität Darmstadt, Institut für Theorie Elektromagnetischer Felder (TEMF), Schlossgartenstrasse 8, 64289 Darmstadt, Germany

Introduction

The main goal of this project is the increasing of the pickup sensitivity for low beta for the analysis of Schottky signals in the frequency range from 3 to 5 GHz. A design for such a problem has been delevoped in [1] for a fixed beam velocity but can also be used for variable beta by inserting a tunable material (ferroelectric) inside the waveguide (see figure 1). Since such tunable materials like for instance BST (Barium Strontium Titanate) are lossy [2], the impact of dielectric losses on the pickup sensitivity will also be investigated in this work.

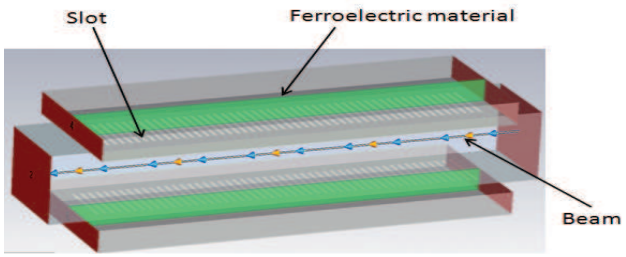

Figure 1: Pickup design for variable beta from [3].

Transfer impedance in frequency domain

The pickup sensitivity is represented by the transfer impedance, which is defined for longitudinal pickups as follows [4]:

$$Z_T = \frac{U}{I_b}, \tag{1}$$

where U and I_b stand for the output voltage and the beam current, respectively. The transfer impedance for different beam velocities is depicted below.

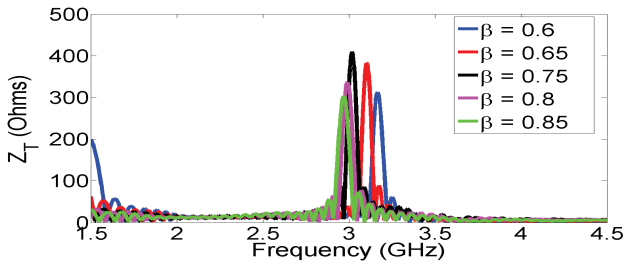

Figure 2: Transfer impedance for different beam velocities. The relative permittivity of the ferroelectric ϵ_r = 50

In figure 2 we can see that for different beam velocities, the system responds at different frequencies. In order to get the response of the system at the same frequency, for instance at 3 GHz, the wave phase velocity in the waveguide must be matched to the beam velocity [1]. This corresponds to a tuning of the relative permittivity of the material in the waveguide. For instance for $\beta = 0.6$, ϵ_r must be equal to 55 and for $\beta = 0.85$, $\epsilon_r = 48$.

Impact of dielectric losses on the sensitivity

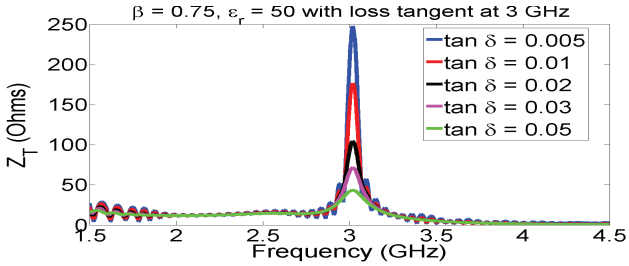

Figure 3: Transfer impedance with different loss tangent at 3 GHz.

In the above figure it is clear to see that the transfer impedance considerably decreases with increasing loss tangent at 3 GHz. Comparing these results with that without loss tangent (look at $\beta = 0.75$ in figure 2) and assuming that the minimum reachable loss tangent be 0.005, the reduction in transfer impedance then corresponds to at least arround 40 percent.

Summary

In this work it has been demonstrated that it is possible to increase the pickup sensitivity and to tune the design to different beam velocities, but the biggest difficulty for the realisation of this pickup design will be the dielectric losses in the material. For this reason the tunable material to use for this design must have a very low loss tangent, for instance Strontium Titanate, whose minimum reachable loss tangent in the frequency range 1...10 GHz is arround 0.002 [5].

References

[1] David McGinnis, “Moment Method Formulation for Beam Excitation of Waveguide Slots”, July 27, 1997
[2] Patrick Scheele, “Steuerbare passive Mikrowellenkomponenten auf Basis hochpermittiver ferroelektrischer Schichten”
[3] CST GmbH, “CST PARTICLE STUDIO”.
[4] C.S. Taylor, “Microwave Kickers and Pickups”.
[5] Eccosorb, “DIELECTRIC MATERIALS CHART”.

Annual neutron doses in the UNILAC experimental hall

C. Pöppe[1], G. Fehrenbacher[1]
[1]GSI, Darmstadt, Germany

Introduction

GSI has the obligation to verify that the accelerator operation is in compliance with the radiation protection ordinance and that the conditions given in the permissions of the authority (HMUELV) are fulfilled. For this purpose, dose measurements must be performed. From these dose measurements the annual dose values are derived for various radiological areas at the UNILAC and the experimental hall. The assumed definition of the different kind of radiological areas (controlled, area, survey area and free accessible areas) must be checked or – if necessary – changed.

Method of measurement

The overall dose values outside the shielding of the accelerators and experimental areas consist in most cases of neutron and photon radiation.
The GSI's Safety and Radiation Protection division provided thermoluminescence detectors (TLD, type 6776) for the dose measurements. The TLD cards consists of two ^{6}LiF (sensitive for n- and γ -radiation) and two ^{7}LiF (sensitive for γ-radiation but not for n-radiation) elements and were mounted in moderator spheres (applicable ~10MeV) made from polyethylene (PE). The TLDs are sensitive to neutrons with energies from the thermal range up to the highest energies. One advantage of this system is that the dose reading is independent on the spill structure of the beam, i.e. there are no dead time effects etc. in contrary to the active systems.

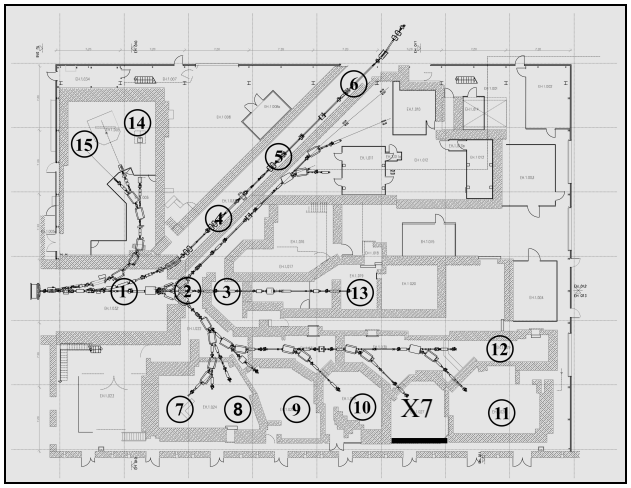

Figure 1: Measurement positions of the neutron doses in the UNILAC experimental hall.

Annual doses in 2009 and 2010

Figure 1 shows the downstream part of the UNILAC, a part of the TK and the experimental areas with the positions of the neutron detectors. The detectors are placed on the roof of the caves.
It can be seen (Tab. 1) that the dose values 2009 and 2010 are in the range of 0.08 mSv/a up to 1.07 mSv/a. The largest dose values in 2009 were measured at X8 and in 2010 at Y7.
The dose values are generally comparable and are within the limits set by the radiation protection ordinance. The exception is Y7 where the annual dose is about the average. An experiment with a Cm-target has been the reason for the increase of the accumulated dose. Additional shielding has been placed on the roof of the cave and the efficiency will be checked in 2011 during the next experiments.
In case of Y7 it is sometimes necessary that the area around the cave must be declared as a temporarily controlled area because the dose rates are higher than 3 µSv/h (threshold dose rate value for the definition of controlled areas).
At the area X7 experiments are carried out with ion beams which have energies below the nominal Coulomb threshold energy. During recent experiment periods it turned out that during the preparatory beam operation for the experiment substantial dose rates can occur (use of illumination targets etc.). Therefore additional shielding was installed in the year 2010.

Table 1: Measured Neutron doses in the UNILAC experimental hall outside the shielding, the positions are shown in Fig. 1

		Neutron - Dose H*(10) [mSv]	
Position	**Area**	**2009**	**2010**
1	end of UNILAC	0.12	0.09
2	end of UNILAC	0.16	0.14
3	end of UNILAC	0.21	0.12
4	TK	0.15	0.13
5	TK	0.15	0.19
6	TK	0.09	0.08
7	X 1	0.12	0.08
8	X 2,3	0.12	0.09
9	X 4	0.22	0.15
10	X 6	0.28	0.13
11	X 8	0.71	0.16
12	X 0	0.38	0.33
13	Y 7	0.41	1.07
14	M 1	0.08	0.09
15	M 3	0.07	0.09

References

[1] G. Fehrenbacher, C. Pöppe, GSI annual report 2009

Annual Doses at SIS 18 and adjacent Experimental Areas

T. Radon, K. Beverung, G. Fehrenbacher, G. Freml, Ch. Pöppe, and J. Sauer

GSI, Darmstadt, Germany

Shielding medium energy beams at GSI

Dealing with medium energy heavy ion beams (range: 100 MeV/u to 1 GeV/u) with intensities up to 1E10 particles per second requires shielding thicknesses up to 5 m for concrete equivalent materials. Due to its perceptible hydrogen mass fraction of roughly 0.5% and its medium large densities of ca. 2.3 g/cm^3, concrete is well suited to cope with neutrons in a wide energy range. Neutrons exhibit the dominant part of the effective dose and thus only the neutron dose will be examined in the present paper.

Measurements in 2010 – Comparison to 2009

Figure 1 shows the SIS and adjacent experimental areas together with the position of the REM counters (BIOREM FHT 750) (larger squares) and passive neutron detectors based on thermoluminescence[1] (smaller squares).

Similar to the last years [2, 3] the annual dose values are largest in the vicinity of the SIS extraction area, the HHD beam dump and the FRS target area. These areas were declared as controlled area as the corresponding dose rate of 3 µSv/h was occasionally slightly transgressed for certain primary beams.

Another zone of high dose levels is found behind Cave A and at the entrance of Cave B. Due to several high intensity experimental runs in Cave A the annual dose reaches values up to 4 mSv, not yet transgressing the monitored area limit but worthwhile to improve the shielding in forward direction. In addition numerous beams which were stopped in the beam dump in HTP and observable beam losses at the entrance of Cave B contribute to this area of higher doses.

Outlook

With the advent of FAIR and hence increasing primary intensities by an order of magnitude the shielding in the area of the SIS extraction and the beam dump HHD has to be improved. Due to a lack of space in height it is impossible to simply put an additional layer of normal concrete.

It is envisaged to replace lower concrete levels with heavy weight concrete (density ca. 4.8 g/cm^3) in order to safe space. The exchange of the lowest level balks next to the beam line consisting of normal concrete however may lead to the problem of enlarged activity because of the considerable amount of high-Z aggregates in the heavy weight concrete.

References

[1] F. Gutermuth, T. Radon, G. Fehrenbacher, and J.G. Festag, Kerntechnik (2003), 68, 4, pp. 172-179.
[2] T. Radon, et al. GSI-Report 2009-1 (2009) p. 137.
[3] T. Radon, et al. GSI-Report 2008-1 (2008) p. 129.

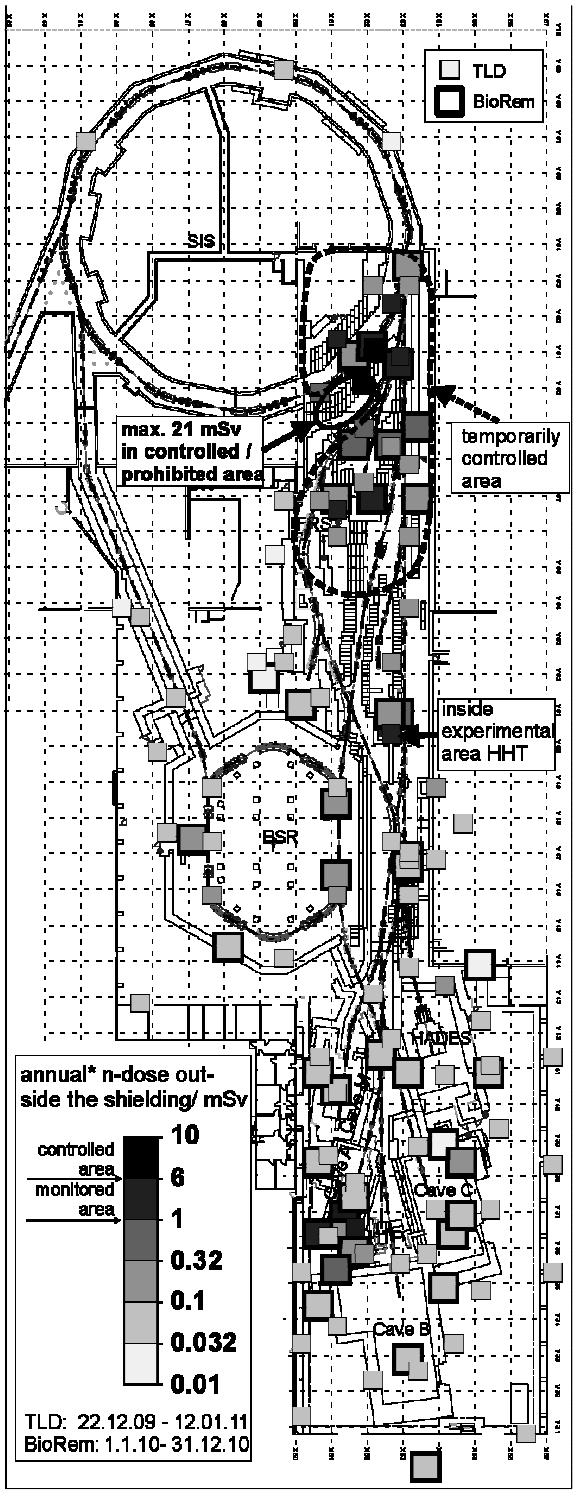

Figure 1: . Dose map of the high energy beam facilities at GSI. The annual dose measured with active (larger squares) and passive (smaller squares) dosimeters is shown. Values below 10 µSv were not taken into account.

Comparison of Shielding Data for 400 MeV/u Carbon Ion Beams

G. Fehrenbacher[1], T. Radon[1]

[1]GSI, Darmstadt, Germany

Shielding data are necessary for the architectural planning of ion accelerator facilities. In the present case the main radiation component is neutron radiation. For the architectural planning in advance it is necessary to give a rough cost quotation for the shielding measures. In an early stage of a project rapid methods for the calculation of shielding thicknesses are required. Line-of-sight (LOS) models are used for this purpose. In this work parameters of line-of-sight models of various authors and groups are used [1, 2, 3] for a comparison of an experiment performed in the framework of the CONRAD measurement campaign carried out at GSI [4].

Line-of-Sight Model

The line-of-sight model considers the angular dependent source term, the overall distance from the interaction point (target) to the reference point outside the shielding and the attenuation in the shielding with a certain thickness. An example for the formulation is given for one or two exponentials respectively:

$$H = \frac{H_1(E_P,\vartheta)}{r^2}\cdot\exp\left[-\frac{d\cdot\rho}{\lambda_{1,\vartheta}}\right] + \frac{H_2(E_P,\vartheta)}{r^2}\cdot\exp\left[-\frac{d\cdot\rho}{\lambda_{2,\vartheta}}\right] \quad (1)$$

where $H_{1,2}$ is the energy and angular dependent source term (Sv·m^2), r the overall distance from the interaction point to the reference point, d the thickness of the shielding (ρ density) and λ the attenuation length (g/cm^2). Parameters of the work of Agosteo (400 MeV/u), Ipe (430 MeV/u) and Fehrenbacher/Radon (400 MeV/u) are summarized in table 1.

Table 1: Parameters of LOS Models cited from 3 different investigations and related to normal concrete.

		GSI [3]		
Angle		**H_1 (Sv·m²)**	**λ (g·cm^{-2})**	
0-10°		2.31E-12	142.2	
10-20°		7.56E-13	138.6	
20-30°		3.10E-13	132.8	
30-40°		1.50E-13	126.5	
40-50°		8.18E-14	119.7	
80-90°		6.04E-15	94.4	
90-95°		3.36E-15	89.6	
		Agosteo [1]		
Angle	**H_1 (Sv·m²)**	**λ_1 (g·cm^2)**	**H_2(Sv·m²)**	**λ_2 (g·cm^2)**
0-10°	-	-	1.93E-12	120.98
10-20°	-	-	4.37E-13	120.21
20-30°	-	-	1.50E-13	122.15
30-40°	-	-	5.75E-14	122.18
40-50°	-	-	2.28E-14	117.03
50-60°	1.03E-14	49.28	7.53E-15	111.74
60-70°	9.98E-15	50.07	3.19E-15	103.86
70-80°	7.62E-15	48.43	1.49E-15	102.23
80-90°	6.11E-15	39.88	9.54E-16	95.87

	Ipe [2]	
Angle	**H_1 (Sv·m²)**	**λ (g·cm^{-2})**
0-10°	3.02E-12	123.81
10-20°	4.81E-13	133.09
20-30°	4.81E-13	133.09
40-50°	4.71E-14	117.64
50-60°	4.71E-14	117.64

Experiment at Cave A

A shielding experiment was carried out at Cave A at GSI for a 400 MeV/u carbon ion beam impinging on a graphite target. The reference points are defined in fig. 1.

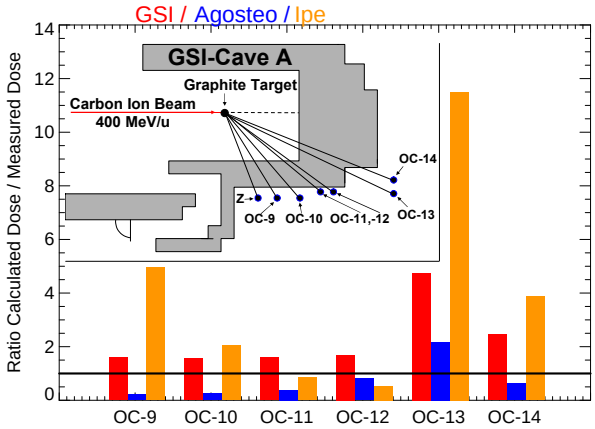

Figure 1: ratio of model dose (GSI-400 MeV/u, Agosteo-400 MeV/u, Ipe-430 MeV/u) values to measured dose values. The inlay illustrates Cave A with definition of reference points.

Results

The evaluation of the three sets of shielding data according to the parameters of table 1 are presented in figure 1. The ratios of calculated dose values (line-of-sight) to the measured ones are indicated for the reference points OC9 to OC14. The measured dose values (H*(10)) are derived from the BSS measurements [4]. Underestimations (factor 0.2) and overestimations (factor 11.5) of the dose can occur depending on the parameters of the models and the positions (OC9 to OC14).

References

[1] S. Agosteo et al., NIMB 217 (2003) 221-236.
[2] N.E. Ipe et al., SATIF 8, (2006).
[3] G. Fehrenbacher, SATIF 10, 2-4 June 2010.
[4] S. Rollet et al., B. Wiegel et al., M. Silari et al., Part 1-3, Rad. Meas., 44 (2009) 649-672.

Shielding design for Tunnel 103 and the area in front of the Super-FRS Target

A. Plotnikov, E. Kozlova, G. Fehrenbacher, and T. Radon

GSI, Darmstadt, Germany

Introduction

After the target and beam catcher area of the Super Fragment Separator has been accomplished in the previous years [1] the upstream and downstream connection of this part had to be designed. Like in all the Monte-Carlo dose rate calculations for FAIR done before, the FLUKA code [2] was employed with heavy ion beams.

Area upstream of the Super-FRS target

This area under investigation connects Tunnel 104 coming from SIS 100 with the target area of the Super FRS. An entrance maze was foreseen to be installed at this area in order to get access to tunnel 104 and to many cable shafts and ducts which guide several tubes for cryogenic as well as power lines to magnets etc. The ducts will be shaped in sinuous matter in order to prevent neutrons passing through without any interaction.

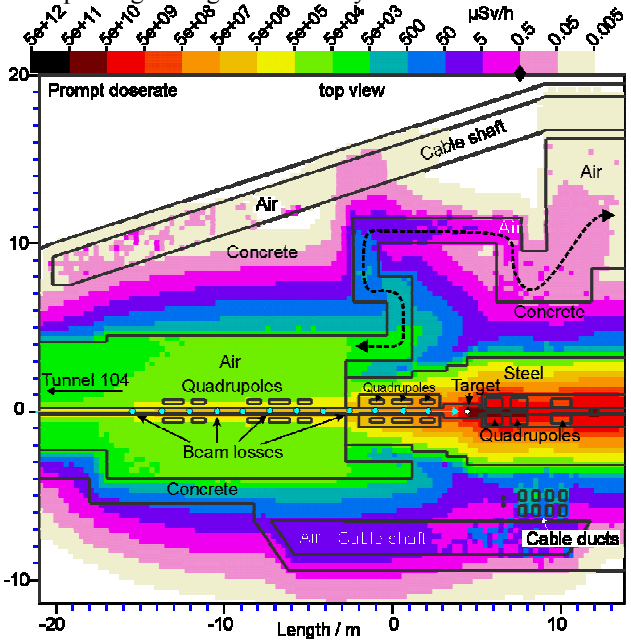

Figure 1: Horizontal dose rate distribution (in µSv/h) in the area upstream of the Super FRS production target. The total beam loss amounts to 1E8 U-238 /s before the target and another 1E11 U-238 /s in the target (10% react. rate).

Tunnel 103

Tunnel 103 contains the main separator of the Super FRS. The major beam losses occur at the two degraders and at two aperture systems. The shielding is mainly achieved here by compacted soil (d=2.5m, ρ=1.8g/cm^3) which is contained in a concrete frame (thickness 0.5m) which seals the compacted soil against the ground so that no soil activation and groundwater contamination can happen. The outer shielding which covers the concrete frame is filled up at least with 5m of soil (ρ=1.5g/cm^3).

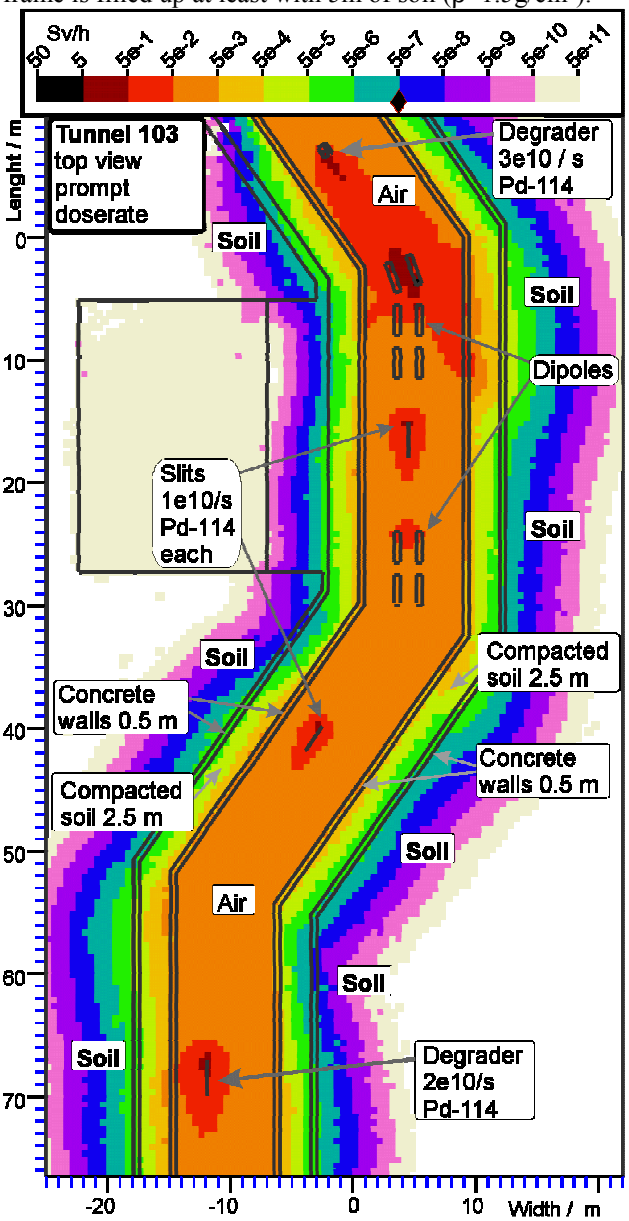

Figure 2: Horizontal dose rate distribution (in Sv/h) of the main separator of the SFRS. Four different beam loss positions are given which sum up to 7E10 particles per second. As a substitute for a large variety of projectile fragments the isotope Palladium 114 with an energy of 1.3 GeV/u was chosen to interact with the beam pipe, magnets etc .

References

[1] E. Kozlova et al. GSI-Report 2008-1 (2008) p. 247.
[2] www.fluka.org.

Assessment of the Radiation Exposure at the Fence of FAIR by Release of Activated Air

A. Knapp[1], G. Fehrenbacher[1], V. Gostishchev[1], K. Knie[1], E. Kozlova[1], A. Plotnikov[1], T. Radon[1], K. Vogt[1]

[1]GSI, Darmstadt, Germany

The release of activated air is expected to contribute substantially to the total radiation exposure during operation of the FAIR facilities. Crucial areas are SIS100/300, Super FRS, and pbar target area for instance. To prevent the activated air in accelerator or experimental areas from diffusing to adjacent areas, a directed flow of the activated air has to be established by pressure gradients: the air ventilation rate will be 1/10 h^{-1}. The radioactive air of several facilities will pass through a tunnel system for a decaying time of two hours before it will be released into the environment by a single 38 m high flue. These two hours decaying time is important, otherwise the activity of the short-lived radio nuclides would be so high that the dose limits defined by the German radiation protection ordinance could not be kept.

The production of radioactive isotopes in air is calculated using the Monte Carlo program FLUKA [1]. For the evaluation of the maximum occurring effective dose according to §47 of the German radiation protection ordinance the air activity of following areas are taken into account: SIS100, S-FRS, NUSTAR cave, pbar target and CBM (note: the air activation calculation of SIS 300 is not considered). Assuming an air ventilation rate of 1/10 h^{-1} table 1 displays the yearly emission of the radio nuclides (shortened list of isotopes) with an activity ≥ 6E+09 Bq. In total more than 200 different radio nuclides will be emitted.

	activity [Bq]		activity [Bq]
C11	5.7E+11	S38	2.6E+10
Ar41	3.2E+11	Sc43	2.6E+10
Cl39	2.1E+11	F18	1.7E+10
Be7	1.4E+11	N13	1.6E+10
Cl38	6.2E+10	H3	8.7E+09
Si31	4.3E+10	Na24	6.0E+09

Table 1: Yearly emission of radio nuclides (shortened list of isotopes).

The effective dose to the public is calculated with the computer program BSAVVL by Brenk Systemsoftware [2]. Additional to the emitted radio nuclides in air the following aspects are taken into account: detailed weather statistics, height of the flue and the course of the premises.

Results

The program BSAVVL calculates the most unfavourable locations for the effective dose resulting from external exposure plus inhalation and from ingestion. It must be checked if the calculated effective doses and the organ doses are below the following yearly limits defined by the German radiation protection ordinance:

- effective dose: 300 microSv
- gonads, uterus and bone marrow: 300 microSv
- bone surface and dermis: 1800 microSv
- colon, lung, stomach, bladder, breast, liver, and remaining organs: 900 microSv.

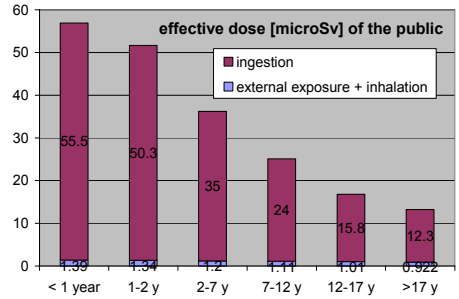

Figure 1: Displayed are the effective doses at the location of the highest exposition outside the premises.

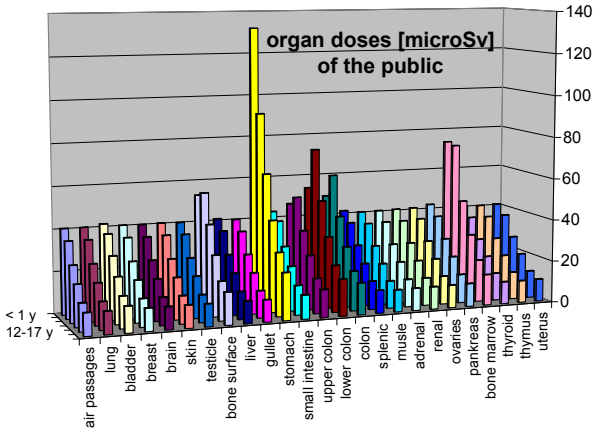

Figure 2: Displayed are the organ doses at the location of the highest exposition outside the premises.

The calculations show that the public group with the highest exposition of 57 microSv are the under 1 year old babies (figure 1), which is 19 % of the legal dose limit of 300 microSv. The group getting the lowest radiation exposition are the adults with 13.3 microSv. Figure 2 shows the organ doses for the public; the baby's stomach gets the highest organ dose, which is 15 % of the legal organ dose for stomach. To conclude, the calculations show that the calculated effective doses are below the legal dose limits. However, it is important to mention that the air activity of the SIS300 could not be taken into account in this dose calculation.

References

[1] information can be found under: www.fluka.org
[2] http://www.brenk.com/software/index.htm

Activation of Aluminium Targets by Uranium Ions*

V. Chetvertkova[1,2,#], L. Latysheva[3], E. Mustafin[1], U. Ratzinger[2], N. Sobolevskiy[3], I. Strasik[1]

[1]GSI, Darmstadt, Germany; [2]IAP, Goethe-University, Frankfurt am Main, Germany; [3]INR RAS, Moscow, Russia

Experiment and Methods

Two types of targets were irradiated. The truncated cylinder covered with organic material (Fig. 1) was used to pre-estimate the stopping range. As ions leave the trace on the organic material, the position of maximum blackening corresponds to the maximum of energy deposition.

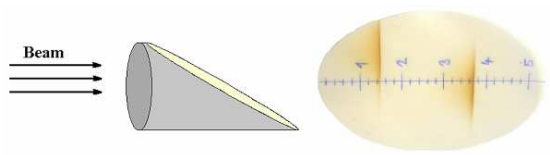

Figure 1: Truncated cylinder, organic foil.

Pre-estimated range values allowed preparing a setup for the second type of the target, the stack-foil target.

Two cylinders assembled from activation foils and spacers were irradiated for depth profiling of nuclides' production. The individual data-points for depth profiling are obtained by measuring the γ-spectra of activation foils after the end of irradiation, using the high-purity germanium (HPGe) detector. The spacers were used to keep the distance between the activation foils.

The irradiations were done at two energies of the primary ions: 500 MeV/u and 950 MeV/u. The total number of ions on the target was $5.07 \cdot 10^{11}$ and $1.02 \cdot 10^{12}$ for 500 MeV/u and 950 MeV/u, respectively.

Simulations and Experimental results

The stopping range of the uranium ions was found by simulating the experiment with FLUKA (2008.3b) [1, 2], ATIMA 1.2 [3] and SHIELD-A [4]. The results of simulations and experiment are shown in Table 1, energy losses in 100 µm stainless steel vacuum window and 1m air gap are taken into account.

Table 1: Stopping ranges of uranium ions.

Measuring technique	500 MeV/u ^{238}U Stopping range±straggling, mm	950 MeV/u ^{238}U Stopping range±straggling, mm
Tr. cylinder	15.45 ± 0.25	37.62 ± 0.25
Depth profile	15.54 ± 0.17	37.68 ± 0.17
ATIMA	16.06 ± 0.01	38.49 ± 0.04
FLUKA	16.50 ± 0.02	41.25 ± 0.03
SHIELD-A	15.52 ± 0.02	38.02 ± 0.02

* Experimental data

*Work was supported by the Helmholtz International Center for FAIR within the framework of the LOEWE program launched by the State of Hesse.

#v.chetvertkova@gsi.de

Depth profiles of the residual activity for both irradiation energies were simulated by FLUKA and SHIELD-A, taking into account exact experimental geometry. Figures 2 and 3 present the depth profiles of ^{22}Na for 500 MeV/u and 950 MeV/u cases, respectively.

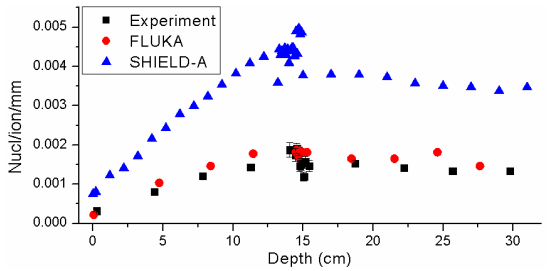

Figure 2: Experimental and simulated depth profile of ^{22}Na for 500 MeV/u incident uranium.

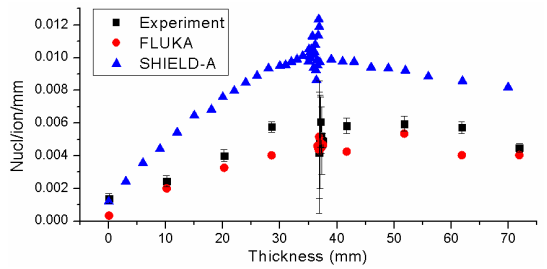

Figure 3: Experimental and simulated depth profile of ^{22}Na for 950 MeV/u incident uranium.

One can observe ~3% discrepancy in simulations of the range by ATIMA. The discrepancy given by SHIELD-A is below 1%. FLUKA gives 5% and 9% larger values for 500 MeV/u and 950 MeV/u respectively. The depth profiles of ^{22}Na calculated by FLUKA are in a very good agreement with the experiment, while SHIELD-A gives overestimation by a factor of 2.

References

[1] G. Battistoni, S. Muraro, P.R. Sala et al., The FLUKA Code: Description and Benchmarking, Proc. of the Hadronic Shower Simulation Workshop 2006, Fermilab 6-8 September 2006, AIP Conference Proceeding 896 (2007) 31.

[2] A. Fasso, A. Ferrari, J. Ranft, P.R. Sala, FLUKA: a multi-particle transport code, CERN-2005-10 (2005), INFN/TC_05/11, SLAC-R-773.

[3] http://www-linux.gsi.de/~weick/atima.

[4] N. Sobolevsky, Modification of the Monte-Carlo particle transport code SHIELD for needs of the FAIR project, GSI internal note, ACC_THEORY-note_internal-2008-001, December 15, 2008.

Annual gamma and neutron doses in the PHELIX Laserhall (PLH)

P. Fensterseifer, S. Götte, T. Radon, G. Fehrenbacher
GSI, Darmstadt, Germany

Introduction

GSI has the obligation to verify that the accelerator operation is in compliance with the radiation protection ordinance and that the conditions given in the permissions of the authority (Hessisches Ministerium für Umwelt, Energie, Landwirtschaft und Verbraucherschutz) are fulfilled. For this purpose, dose measurements must be performed. From these dose measurements the annual dose values are derived for the PHELIX Laserhall (PLH).

At high intensities from 1E18 W/cm^2 up to currently 1E20 W/cm^2 the Petawatt High Energy Laser for Heavy Ion Experiments (PHELIX), which has received the operation permit in 2009, produces ionizing radiation as a secondary process. Doses are small compared to doses measured at the ion beam facilities. Nevertheless they have to be monitored, considering especially that data concerning the production of ionizing radiation with high intensity laser systems are scarce.

Shielding in the target chamber

To shield the radiation produced in high energy or high intensity experiments, iron bricks are put into the chamber, after optical instruments and diagnoses are installed and adjustments are made. The bricks are placed such that direct lines of sight between the target and the chamber hull are avoided.

Initial dose measurement has shown doses of up to 100 mSv inside the target chamber, in proximity to the target. Therefore shielding is necessary.

Method of measurement

The overall dose values outside the shielding of the chamber consist in most cases of photon and potentially neutron radiation. GSI's Safety and Radiation Protection division provided thermoluminescence detectors (TLD, type 7777 and type 6776) for the dose measurements. The 7777 TLD card consists of four ^{7}LiF (sensitive for γ-radiation but not for n-radiation) elements inside GSI fabricated polyethylene (PE) cylinders. The dose quantity measured is H*(10). Five of these cylinders are placed near the walls of the Laserhall. Additionally a type 6776 TLD card, consisting of two ^{7}LiF and two ^{6}LiF (sensitive for n- and γ -radiation) elements, is mounted in a moderator sphere (diameter: 30 cm) made from PE. These TLDs are sensitive to neutrons with energies from the thermal range up to 20 MeV.

Given the extremely short duration of radiation production from the laser pulses, using passive detectors without dead time effects is the only way to produce meaningful dose measurements.

Figure 1 shows an overview of the PHELIX Laserhall and the corresponding positions of the TLD cards. In addition to the five 7777 cards placed on the perimeter of the experimental area, and the 6776 card in the moderator sphere, one TLD card is placed in the PHELIX Control Room (PKR), to make sure the radiation dose is within the limits of a freely accessible area.

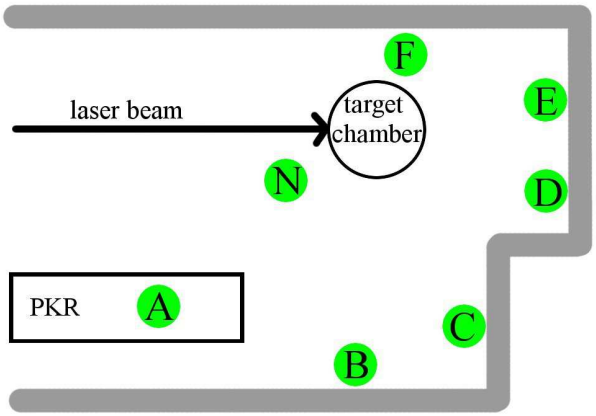

Figure 1: TLD positions in the PLH

Additionally, wipe test are performed after each experimental campaign, to check for contamination.

Table 1: Doses (in µSv) accumulated in 2010

Date	Pos.A	Pos.B	Pos.C	Pos.D	Pos.E	Pos.F	Pos.N
14.01-29.01	30	27	22	24	51	87	3
12.03-26.03	24	12	24	29	29	16	0
14.06-24.06	2	21	23	17	22	30	2
28.06-01.07	12	9	13	7	11	17	10
08.10-12.10	0	0	0	0	0	0	0
12.10-15.10	13	12	11	14	30	15	0
15.10-22.10	10	7	11	11	0	14	0
17.11-18-11	3	5	0	4	6	6	0
Sums(µSv/a):	94	93	104	106	149	185	15

Doses in 2010

Table 1 shows the accumulated doses measured over eight experimental campaigns, including over 450 high energy laser shots. As can be seen, the annual dose approaches 0,2 mSv at the TLD position nearest to the target chamber.

The annual neutron dose falls below detector limits, and seems to be negligible for the present intensities.

Wipe tests have been uniformly negative, no contamination was detected.

Conclusion

The annual dose in the PLH is safely within the limits given by the Radiation Protection Ordinance. Should the amount of experiments producing ionizing radiation increase, additional shielding will have to be provided.

Considerations regarding shielding outside the target chamber have been started, to provide more space within the target chamber to the experimenters while setting up their instruments and diagnostic tools.

Investigation of the dose distribution in the HESR tunnel and surrounding facilities

A. Plotnikov[1], G. Fehrenbacher[1], T. Radon[1], E. Kozlova[1]

[1]GSI, Darmstadt, Germany.

Introduction

The HESR facility will be built in the frame of the FAIR project. For the reason of safety radiation fields have to be considered for the building design. Radiation produced by lost proton and antiproton beams can be dangerous for personnel and equipment. Thus a beam line, where those losses can appear, must be properly shielded by concrete, soil, etc.

A FLUKA [1] simulation was done to estimate the level of effective dose around the accelerator tunnel. A main task of it was to check whether the shielding is effective in the sense of radioprotection.

Conditions of the simulation

The antiproton beam properties were taken as following:

- Reference energy: 8 GeV;
- Consumption and target losses: 1.0e7 pbar/s.

Thus, in case of uniformly distributed losses along the whole ring, the intensity of the losses is proportional to the sector length over the ratio of total length.

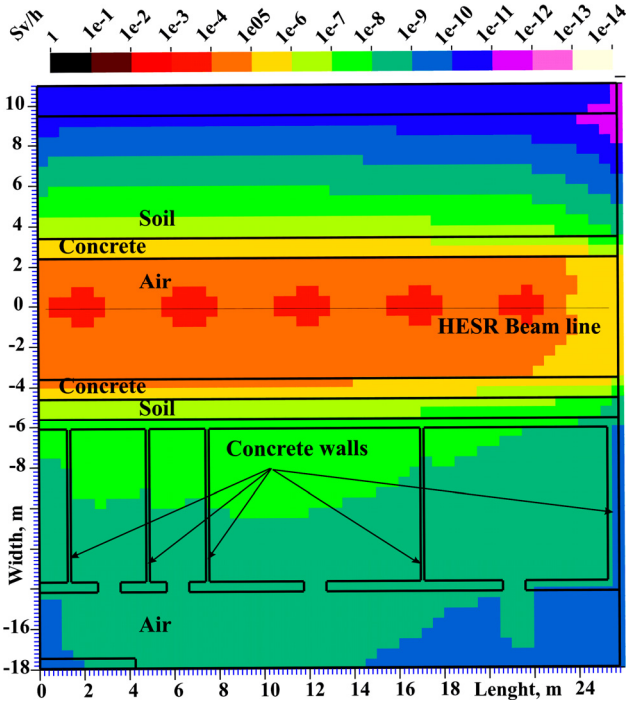

Figure 1: Horizontal cross section of the HESR tunnel with total effective dose distribution from five separate sources with currents 2.0e6 antiproton/sec each.

Results of the simulation

A uniform loss along the sector is represented by five separate sources which are distributed along the beam line. All those sources have the same weight w = 0.2. Thus, the dose rate from each source is calculated by using the following equation:

$$D_{source}[Sv/h] = D_{FLUKA}[pSv/primary] \cdot 10^{12} \cdot 3600[s/h] \cdot 10^{7}[primary/s] \cdot 0.2 \quad (1)$$

The total dose rate is achieved by the sum of dose rates from each source shown as top-view (Fig. 1) and side-view (Fig. 2).

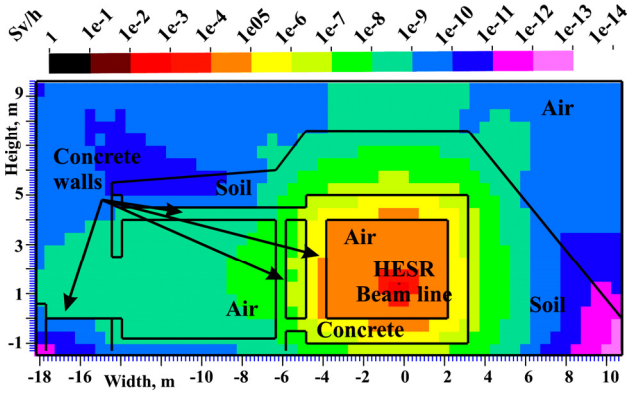

Figure 2: Vertical cross sections of the HESR tunnel with total effective dose distribution on positions 12 m.

Conclusions

Computer simulations with the help of FLUKA showed that the construction of the tunnel and surrounding facilities is acceptable in sense of radiation protection of personnel and equipment. In all regions above the tunnel and inside technical rooms the total effective dose rate is below 0.1 µSv/h (see Figs. 1-2).

In case of accidental losses, when the total amount of particles (10^7 particles per second) is lost in one point of the beam line the effective dose rate is acceptable in the regions of interest. In all regions, like the area above the tunnel, technical rooms and walking areas, the dose rate would amount to 1 µSv/h and less.

References

[1] www.fluka.org.

Frequency-Comb Based Optical Isotope Shift Measurements of ^{12}Be

A. Krieger[1], Ch. Geppert[1,2], R.M. Sánchez[2], M.L. Bissell[3], K. Blaum[4], N. Frömmgen[1], M. Hammen[1], M. Kowalska[5], J. Krämer[1], K. Kreim[4], R. Neugart[1], C. Novotny[1,2], D.T. Yordanov[4], and W. Nörtershäuser[1,2]

[1]Institut für Kernchemie, Universität Mainz, Germany; [2]GSI - Helmholtzzentrum für Schwerionenforschung GmbH, Darmstadt, Germany; [3]Instituut voor Kern-en Stralingsfysica, Katholieke Universiteit ,Leuven; [4]MPI für Kernphysik, Heidelberg, Germany; [5]CERN, ISOLDE Physics Department, Geneva

Introduction: The charge radii of the lightest elements are benchmark tests for nuclear structure models. Moreover, the appearance of the so-called halo nuclei, having an extended nuclear matter distribution due to weakly bound nucleons, makes this region particularly interesting. In 2008 we successfully measured the charge radii of ^{7,9,10}Be and the one neutron halo ^{11}Be by high-resolution laser spectroscopy. We could now extend the measurements to ^{12}Be at ISOLDE at CERN. This isotope has even a smaller lifetime and lower production rate than the other beryllium isotopes. The structure of this nucleus is not sufficiently well understood yet.

Experimental: Measuring the isotope shift of the $2s\ ^2S_{1/2} \rightarrow 2p\ ^2P_{1/2,3/2}$ (D1, D2) transitions of ^{10,12}Be$^+$ delivers information about the nuclear charge radii [1]. Therefore we performed high-resolution collinear laser spectroscopy on a fast beryllium ion beam at the radioactive beam facility ISOLDE. After resonant laser ionization the accelerated ion beam was mass separated and deflected into the collinear laser spectroscopy experiment COLLAPS. There, the ion beam is superimposed with two counter-propagating laser beams at fixed frequencies. Scanning across a resonance is achieved by the so-called Doppler tuning, applying stepwise an additional voltage to the detection region. A detailed description of the laser system and scanning procedure can be found in [2, 3].
The classical optical fluorescence detection system used in the previous studies was now combined with coincident detection of photons and ions to suppress the scattered light of the laser beams. This technique requires that the signal of the photodetector is correlated to the detected ion signal when (after a certain time of flight) an ion was detected, so that only fluorescence photons contribute to the resonance signal. This improved sensitivity and allowed for measurements with very weak ion beam currents. A coincidence detection chamber was built and tested at the TRIGA LASER experiment at the University of Mainz using a weak ion beam of 9.000 ^{40}Ca$^+$ ions/s [4]. The coincidence technique reduced the background by a factor of about 500.

Results: At COLLAPS, spectra in collinear and anticollinear geometry were simultaneously recorded. The absolute transition frequency ν_0 can be extracted according to $\nu_0 = \sqrt{\nu_a \cdot \nu_c}$. Here ν_a and ν_c denote the center of gravity frequency in the collinear and anticollinear spectrum, respectively. The difference $\delta\nu_{\mathrm{IS}}^{A,A'}$ of these extracted absolute frequencies ν_0 for two different isotopes is the isotope shift, which is related to the change in the nuclear charge radii $\delta\langle r^2\rangle^{A,A'}$ according to:

$$\delta\langle r^2\rangle^{A,A'} = \left(\delta\nu_{\mathrm{IS}}^{A,A'} - \delta\nu_{\mathrm{MS}}^{A,A'}\right)/C\ .$$

The mass shift contribution $\delta\nu_{\mathrm{MS}}^{A,A'}$ and the field shift coefficient C must be provided by theory. For the three-electron-system Be$^+$ they can be calculated to a relative accuracy of 10^{-5} [5, 6], which is sufficient to extract the charge radius. At ISOLDE this technique enabled us to determine the $2s\ ^2S_{1/2} \rightarrow 2p\ ^2P_{1/2,3/2}$ transitions in ^{12}Be$^+$ at production rates of less than 10.000 ions / proton pulse. Typcial spectra are shown in Fig. 1. Several systematic effects, *e.g.* ion beam acceleration or deceleration by the resonant laser light, were investigated. The data analysis and determination of the nuclear charge radii are now in progress.

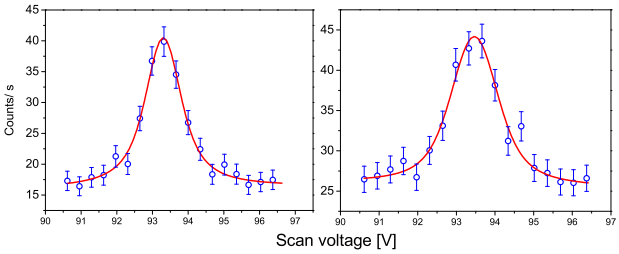

Figure 1: Resonance spectra obtained for ^{12}Be in the D1 line in collinear geometry (left) and anticollinear geometry (right). The signal was accumulated for 2 hours at a production rate of about 10.000 ions / pulse.

Acknowledgment

This work is supported by BMBF Contract 06MZ9178I Helmholtz Association Contract VH-NG-148 and the Carl-Zeiss-Stiftung AZ:21-0563-2.8/197/1.

References

[1] D. Tiedemann, PHD thesis , University of Mainz, (2009)
[2] W. Nörtershäuser et al, PRL 102 (2009) 062503
[3] M. Zákovà et al, J. Phys. G: Nucl. Phys. 37,055107 (2010)
[4] B. Sieber, Diploma thesis, University of Mainz, (2010)
[5] Z.C. Yan et al, PRL 100 (2008) 243002
[6] M. Puchalski, K. Pachucki, Phys. Rev. A 79 (2009) 032510

Direct Determination of the Magnetic Quadrupole Contribution to the Lyman-α_1 Transition in U^{91+}

G. Weber[1,2], H. Bräuning[1], A. Surzhykov[1,3], S. Fritzsche[1], S. Hagmann[1,4], C. Kozhuharov[1], R. Märtin[1,3], N. Petridis[4], R. Reuschl[1], U. Spillmann[1], S. Trotsenko[1,2], D.F.A. Winters[1], and Th. Stöhlker[1,2,3]

[1]GSI, Darmstadt, Germany; [2]Helmholtz Institute Jena, Jena, Germany; [3]University of Heidelberg, Heidelberg, Germany; [4]University of Frankfurt, Frankfurt, Germany

Hydrogen-like ions are the simplest and most fundamental atomic systems whose study along the isoelectronic sequence provides detailed information about the effects of relativity and quantum-electrodynamics on the atomic structure. Since these effects are largest for the 1s ground-state, experimental studies of $L \rightarrow K$ transitions are of paramount importance for such investigations. This is in particular true for the domain of high-Z ions where precision measurements of the Lyman-α_1 (Ly-α_1: $2p_{3/2} \rightarrow 1s_{1/2}$) transition energies are a powerful technique to test the theory of strong field QED [1]. However, due to the lack of efficient polarimeter systems for the hard x-ray regime, previous studies were restricted to measurements of the spectral and angular distribution of the emitted radiation [2].

The experiment was performed at the internal gasjet target of the ESR where bare uranium ions at an energy of 96.6 MeV/u interacted with H_2 molecules. Via the radiative electron capture process, excited U^{91+} ions in the $2p_{3/2}$ state were formed which subsequently decayed to the ground state. The emitted photons were detected by an array of standard solid state x-ray detectors at various observation angles and by two novel-type double-sided segmented x-ray detectors at 35° and 90° with respect to the beam axis. By applying the position sensitive x-ray detectors as Compton polarimeters we performed the first linear polarization measurement of the Ly-α_1 radiation in a high-Z system, namely in U^{91+}. Here, we observed an interference between the electric-dipole (E1) and the magnetic-quadrupole (M2) transition amplitudes leading to a significant depolarization of the Ly-α_1 radiation, see Fig. 1.

Both, studies of the Ly-α_1 angular distribution and its linear polarization, can be utilized in order to derive information about the M2 amplitude relative to the E1 amplitude while relying on a theoretical estimate for the population of the $2p_3/2$ magnetic sub-levels, which is characterized by the alignment parameter $\mathcal{A}_2$ (see [3] and [4] for details). However, in our recent work [5] we show that a combination of both measurements enables a very precise determination of the ratio of the E1 and the M2 transition amplitudes and the corresponding transition rates without any assumptions concerning the population mechanism for the excited $2p_3/2$ state, see Tab. 1. This finding opens a new route to disentangle the population process of the excited ionic state from the subsequent decay. The accuracy of the obtained amplitude ratio will stimulate more detailed quantum-electrodynamical investigations on the transition amplitudes of highly-charged ions beyond Dirac's theory.

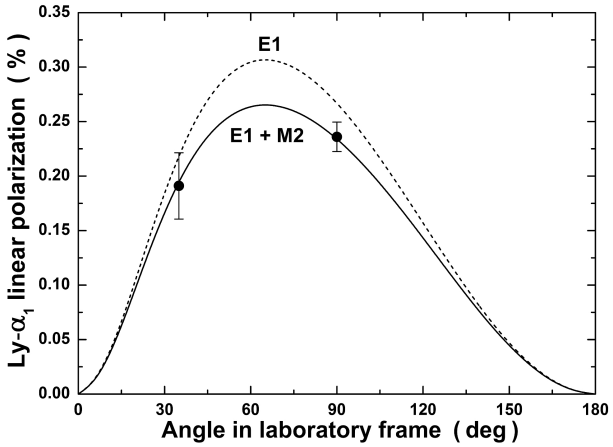

Figure 1: Measured linear polarization of the Ly-α_1 line following the REC into initially bare uranium projectiles with energy 96.6 MeV/u in comparison to theory with (—) and without (- - -) taking into account the E1-M2 interference [5].

Alignment parameter $\mathcal{A}_2$		Amplitude ratio a_{M2}/a_{E1}	
Experiment	Theory	Experiment	Theory
-0.451 ± 0.017	-0.457	0.083 ± 0.014	0.0844

Table 1: Comparison of the measured and the theoretical alignment parameter $\mathcal{A}_2$ for the $2p_{3/2}$ level and the M2/E1 amplitude ratio of the Ly-α_1 decay in H-like uranium. The theoretical values also include the cascade feeding due to capture into high-lying levels [5]. See text for further discussion.

References

[1] A. Gumberidze et al., Phys. Rev. Lett. **94**, 223001 (2005).

[2] Th. Stöhlker et al., Phys. Rev. Lett. **79**, 3270 (1997).

[3] A. Surzhykov et al., Phys. Rev. Lett. **88**, 153001 (2002).

[4] A. Surzhykov et al., Hyperf. Interact. **146-147**, 35 (2003).

[5] G. Weber et al., Phys. Rev. Lett. **105**, 243002 (2010) .

Target effects on the linear polarization of REC radiation from U^{91+} ions *

A. N. Artemyev[1,2], *A. Surzhykov*[1,2], *S. Fritzsche*[2,3], *B. Najjari*[4], *and A. B. Voitkiv*[4]

[1]Physikalisches Institut, Universität Heidelberg, Germany; [2]GSI, Darmstadt, Germany; [3]Department of Physics, University of Oulu, Finland; [4]Max-Planck Institut für Kernphysik, Heidelberg, Germany

In the last decades, the photon emission from highly charged ions has been found a versatile tool for exploring light-matter interactions in strong (Coulomb) fields [1]. Apart from a series of energy and angle resolved experiments, especially for the x-ray emission following the radiative electron capture (REC) into high-Z projectile ions [2], recent emphasis was placed on measuring the linear polarization of this radiation [3], by making use of recent advances in detector technology [4].

However, while most REC calculations for high-Z projectiles are based so far on first-order perturbation theory in the electron-photon interaction, a rigorous analysis of this capture process would require, in general, a time-dependent, two-center Dirac description. Of course, such an extensive description is well beyond of what is presently feasible, but it appears at least necessary for angle-resolved and polarization measurements to take into account the structure of the target atoms. This will be true especially if impact-parameter dependent measurements are to be performed in forthcoming years. Therefore, in order to improve our understanding of the target effects upon the REC (linear) polarization from high-Z ions, we applied the *impulse approximation* as appropriate for fast collisions of heavy projectiles with low- and medium-Z targets [5].

Within the impulse approximation, the collision of the projectile with the target atom is still described in perturbation theory but asymmetrically by introducing an explicit momentum distribution for the target electrons. In this approximation, therefore, the initial state of the captured electron is expressed as

$$\Psi_i(\mathbf{r},t) \;=\; \frac{\mathrm{e}^{-i\varepsilon_a t/\gamma}}{\gamma} \times \int \mathrm{d}^3\mathbf{p}\,\phi_i(\mathbf{p}_\perp;\kappa_z)\,\sqrt{\varepsilon_p}\,\psi_{\mathbf{p}}(\mathbf{r})\,\mathrm{e}^{-i\mathbf{p}\cdot\mathbf{R}(t)} \qquad (1)$$

where $\mathbf{p}$ and $\epsilon_p = \sqrt{c^2p^2+m^2c^4}$ describes the asymptotic momentum and energy of the (originally free) electron but where a convolution is now made over the momenta of the bound target electron. Most further steps in the evaluation of the transition amplitudes and cross sections then follow very similar lines as in (standard) perturbation theory, while the impact parameter dependence here remains explicitly due to the decomposition of the momentum (transfer) into a parallel and perpendicular component.

Using the impulse approximation, the degree of linear polarization of the REC photons in relativistic collisions of high-Z projectiles with low- and medium-Z target atoms has been investigated for a wide range of collision energies and impact parameters. Detailed calculations were carried out especially for bare U^{92+} projectiles in collision with hydrogen, argon, krypton, and xenon targets [6]. For example, Figure 1 displays the linear polarization of the corresponding K-shell REC photons for three different impact parameters b = $1/Z_t$, $2/Z_t$, and $9/Z_t$, and where Z_t is the nuclear charge of the target atoms. As seen from this figure, the effect of the impact parameter becomes most pronounced for a backward emission of the photons ($\theta > 90^o$), for which the degree of linear polarization P_L is significantly reduced as the impact parameter b becomes larger.

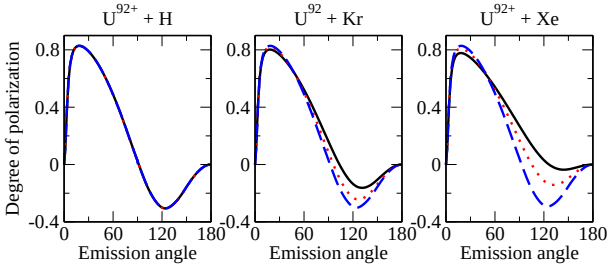

Figure 1: Degree of linear polarization of the K-shell REC photons in collisions of 800 MeV/nucleon bare U^{92+} ions with neutral hydrogen, krypton, and xenon atoms. Calculations are shown for three impact parameters: b = $1/Z_t$ (solid line), $2/Z_t$ (dotted line), and $9/Z_t$ (dashed line). See text for further discussion.

In conclusion, a significant enhancement of the degree of linear polarization is predicted in backward directions and, especially, for small impact parameters and medium-Z target target atoms. This enhancement can be tested at the future Facility for Antiproton and Ion Research (FAIR) in Darmstadt.

References

[1] S. Fritzsche et al., J. Phys. B38, S707 (2005).

[2] J. Eichler and T. Stöhlker, Phys. Rep. 439, 1 (2007).

[3] S. Tashenov et al., Phys. Rev. Lett. 97, 223202 (2006).

[4] U. Spillmann et al., Rev. Sci. Instrum. 79, 083101 (2008).

[5] B. Najjari et al., Phys. Rev. A80, 012701 (2009).

[6] A. N. Artemyev et al., Phys. Rev. A82, 022716 (2010).

* Work supported the Helmholtz Gemeinschaft and GSI (Nachwuchsgruppe VH-NG-421).

Photorecombination of Metastable Beryllium-like Xenon Ions

D. Bernhardt[1], *C. Brandau*[1,2], *C. Kozhuharov*[2], *A. Müller*[1], *S. Schippers*[1], *S. Böhm*[1], *F. Bosch*[2], *J. Jacobi*[1], *S. Kieslich*[1], *H. Knopp*[1], *P. Mokler*[1,2,3], *F. Nolden*[2], *W. Shi*[1], *Z. Stachura*[4], *M. Steck*[2], *and Th. Stöhlker*[2,5]

[1]Universität Gießen; [2]GSI, Darmstadt; [3]MPI-K, Heidelberg; [4]IFJ, Kraków, Poland; [5]Universität Heidelberg

Dielectronic recombination (DR) of beryllium-like Xe^{50+} was investigated by using the ESR electron cooler as a free electron target. Three series of resonances associated with excitations from the $2s^2$ ground state could be measured (Fig. 1), namely $2s^2 \rightarrow 2s2p\,^1P_1$, $2s^2 \rightarrow 2s2p\,^3P_1$ and $2s^2 \rightarrow 2s2p\,^3P_2$. The resonances of the $2s2p\,^3P_2\,n_j$ manifolds are much weaker than the ones of the other series. No signatures of DR resonances with excitation from $2s^2$ to the $^3P_0$ state were observed. In addition to the three ground state DR sequences (Fig. 1) we found resonances associated with *initially metastable* $Xe^{50+}(2s2p\,^3P_0)$ ions (Fig. 2). The metastable state is populated during the stripping process and survived the beam preparation, cooling and storage time in the ESR. In the present case, the Xe isotope $A = 136$ with nuclear spin $I = 0$ was used. In absence of nuclear spin, the $^3P_0$ level in Be-like ions is known to be extremely long-lived because a single photon transition to the $2s^2\,^1S_0$ ground state is forbidden. For $I \neq 0$ the hyperfine interaction quenches the $^3P_0$-state which leads to a substantially accelerated decay [1]. For $I = 0$, as a consequence of strong scaling with the nuclear charge Z, the $E1M1$ double photon transition becomes a relevant but still very slow decay channel for heavy ions [1, 2, 3]. In contrast to He-like ions (see e.g. [2, 4]), in Be-like ions the two-photon decay is scarcely studied. From [3] the transition rate A of a $E1M1$ transition can be estimated:

$$A_{a.u.} = 0.00507\alpha^{12}Z^4\,(\omega_1 + \omega_2)^5$$

Inserting the $Xe^{50+}(1s^2\,^1S_0 \rightarrow 2s2p\,^3P_0)$ excitation energy of $\omega_1+\omega_2$ = 104.482 eV from [5] this yields a lifetime for the $^3P_0$ state of about 30 seconds. With the existing DR setup at the ESR electron cooler, modified with respect to long beam storage times, a DR based technique offers the unique opportunity to study lifetimes and decay modes of $^3P_0$ states in Be-like heavy ions. For this purpose, an approach similar to the one successfully employed at the Heidelberg storage ring TSR to study hyperfine induced transitions [1] of lighter ions is envisaged. At the ESR one decisively benefits from the possibility to perform DR studies with a permanently stochastically cooled ion beam with practically no beam losses during ion beam storage [7].

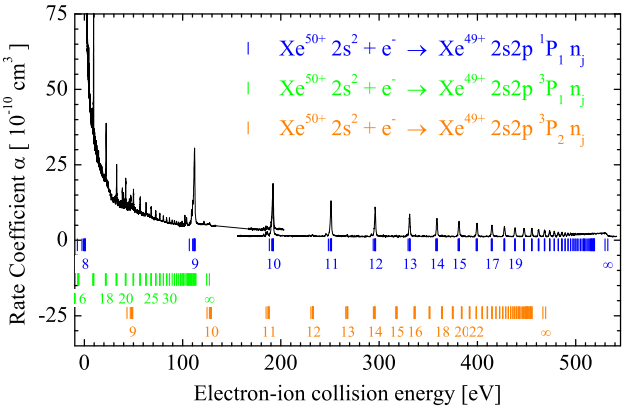

Figure 1: Photorecombination of $^{136}Xe^{50+}$ (overview). The black line denotes the experimental data. Energy levels of three DR series associated with excitation from the ground state are indicated by vertical bars: $2s^2 \rightarrow 2s2p\,^1P_1$ (blue), $2s^2 \rightarrow 2s2p\,^3P_1$ (green) and $2s^2 \rightarrow 2s2p\,^3P_2$ (orange). The DR energy levels were approximated using the excitation energies from [5] and H-like binding energies [6].

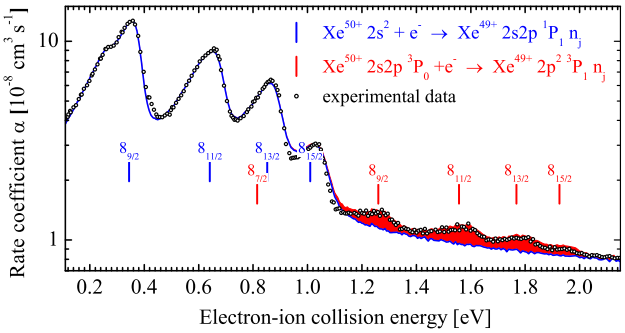

Figure 2: Low energy part of the $^{136}Xe^{50+}$ recombination spectrum: resonances attributed to initially metastable $^3P_0$ states are marked in red. Energy levels for ground state DR ($2s^2 \rightarrow 2s2p\,^1P_1$; blue) and for DR from the metastable state ($2s2p\,^3P_0 \rightarrow 2p^2\,^3P_1$; red) are shown as vertical bars.

D.B., C.B. and A.M. acknowledge support by BMBF under contract number 06 GI 911I.

References

[1] S. Schippers, et al., Phys. Rev. Lett. **98**, 033001 (2007).
[2] P. H. Mokler and R. W. Dunford, Phys. Scr. **89**, C1 (2004).
[3] C. Laughlin, Phys. Lett. A **75**, 199 (1979).
[4] S. Trotsenko, et al., Phys. Rev. Lett. **104**, 033001 (2010).
[5] M. S. Safronova, et al., Phys. Rev. A **53**, 4036 (1996).
[6] C. Brandau, et al., Phys. Rev. Lett. **89**, 053201 (2002).
[7] D. Bernhardt, et al., Phys. Rev. A, in print.

Polarization properties of elastic scattering processes in the hard x–ray regime investigated at the synchrotron facility DORIS III

M. Schwemlein[1,2], *T. Groß*[1,2], *U. Spillmann*[1], *G. Weber*[1,3], *R. Märtin*[1,2], *M. von Zimmermann*[4], *and Th. Stöhlker*[1,2,3]

[1]GSI, Darmstadt; [2]University of Heidelberg; [3]Helmholtz Institute Jena; [4]DESY, Hamburg

The elastic (Rayleigh) scattering of polarized energetic photons by atoms has attracted continuous theoretical and experimental interest [1, 2]. Observations under large scattering angles are of particular importance as they are well resolved from Compton scattering contributions and, in case of high-Z targets, are most sensitive to relativistic effects on the K-shell electrons. In addition, the theoretical description of Compton to Rayleigh differential cross section is of particular challenge. The recent development of efficient and precise Compton polarimeters for the energy region between 70 keV and a few hundred keV [3] together with the availability of intense beams of polarized hard x–rays at synchrotron facilities enables for differential cross section measurements of Rayleigh scattered photons. Furthermore, for best of our knowledge, no experimental data for the degree of linear polarization of elastic (Rayleigh) scattered photons are available, up to now.

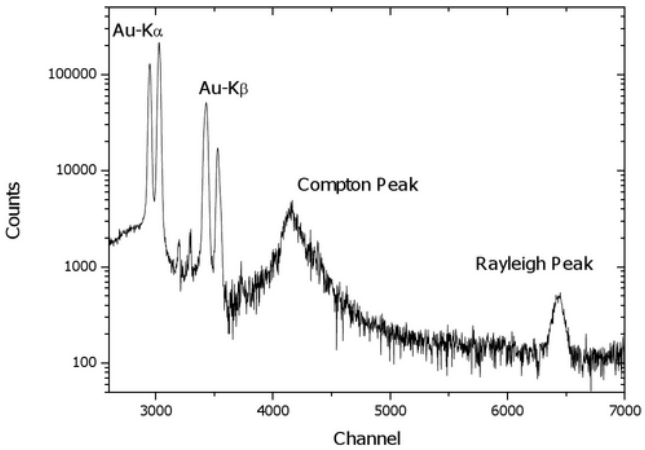

Figure 1: A linearly polarized photon beam with an energy of 147 keV, is backscattered from an Au-target. The spectrum was measured with a standard Germanium detector under a scattering angle of 156 °.

Therefore, we performed a first test experiment at Helmholtz Centre DESY in Hamburg. The synchrotron DORIS III provides us with both, a high intensity as well as a 92 % linearly polarized photon beam. Despite a high detector efficiency, a low count rate was expected because of low cross section under large scattering angles Θ. With three days of test–beamtime, the goal was to explore count rate, background radiation and the property of DORIS III for x–ray spectroscopy and polarimetry at the energy range of 100 keV.

In our experimental setup we investigated backscattered Compton and Rayleigh photons from a primary beam with an energy of 147 keV. A typical spectrum is given by figure 1, which shows the Compton– and Rayleigh–Peak at a scattering angle of $\Theta = 156\,^{\circ}$ as well as the $K_{\alpha_{2,1}}$ and $K_{\beta_{1,2}}$ radiation of a thin Au target. Points of interest are the Compton and Rayleigh cross sections at high energies and large scattering angles Θ. A preliminary analysis yields in Compton to Rayleigh count rate of 22 ± 5 (Au–target) and 230 ± 20 (Ni–target).

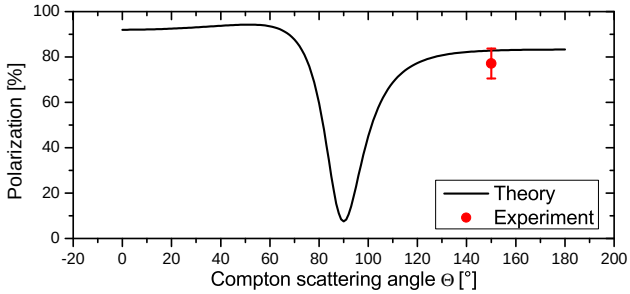

Figure 2: Expected degree of linear polarization of Compton scattered photons.

After the installation at the beamline, we started a proof–of–principle measurement with a 2D Si(Li) Compton–Polarimeter [4] to figure out, if a polarization study with low count rate of scattered photons and a high intensity of background radiation was feasible in general. Figure 2 shows the theoretical polarization of Compton scattered photons, calculated for a 92 % linearly polarized primary beam [5]. Polarization analysis leads us to a $77.1 \pm 6.6\,\%$ linear polarization of the Compton scattering peak, which fits to theory.

In this first pilot experiment, counting statistics of Au–Compton and Au–Rayleigh is low. But based on existing data we are now applying for an extended run. This future experiment, planned for 2011, will make use of an improved target chamber. This intends to reduce background radiation, which enables polarization studies of Rayleigh scattering.

References

[1] Kane *et al.*, Phys. Rep. **140** 75 (1986)

[2] Hopersky *et al.*, JETP **105** 549 (2007)

[3] Spillmann *et al.*, Rev. Sci. Instrum. **79** 083101 (2008)

[4] Weber *et al.*, JINST **5** C07010 (2010)

[5] Lei *et al.*, Space Sci. Rev., **82** 309 (1997)

First *g*-Factor Measurement of Hydrogen-like Silicon*

A. Wagner† [1], *S. Sturm*[1], *W. Quint*[2], *G. Werth*[3], *J. Zatorski*[1], *Z. Harman*[1], *C. H. Keitel*[1], *and K. Blaum*[1]

[1]Max-Planck-Institut für Kernphysik; [2]GSI, Darmstadt, Germany; [3]Institut für Physik, Universität Mainz

High-precision measurements of the gyromagnetic factor (*g*-factor) of the electron bound in highly-charged ions allow for a stringent test of bound-state quantum electrodynamics (BS-QED) calculations [1]. Therefore, it is planned to measure the *g*-factor of lithium- (Si^{11+}) and hydrogen-like (Si^{13+}) silicon in a triple Penning trap setup [2]. We have calculated the theoretical *g*-factor value with a precision of $8{\cdot}10^{-10}$, also including nuclear structural terms. Many technical improvements in the last two years have led to very stable operating conditions of the trap. They allowed to detect spin-flips in a single Si^{13+} ion and to measure for the first time a Larmor-resonance with an accuracy of about 10^{-7}.

Improvements

Basic requirements for the precise determination of the *g*-factor are extremely stable operating conditions of the Penning trap. A temperature stabilization system with a stability of about 10 mK was implemented to stabilize the temperature around the cryostat and the electronics. In order to improve the stability of the ion's axial oscillation frequency new carefully polished and gold-plated trap electrodes were implemented. Problems with the transport between the two traps were solved by five short transport electrodes replacing two long ones. Moreover, a phase-sensitive measurement technique [3] in the analysis trap was implemented, which allows for a faster measurement of the axial frequency.

First spin-flips

A spin-flip is induced by irradiating microwaves into the trap. In the analysis trap a ferromagnetic ring electrode produces a magnetic inhomogeneity which couples the magnetic moment to the axial frequency [1]. Thus, the axial frequency ν_z depends slightly on the spin orientation. A spin-flip results in a frequency jump of about 230 mHz ($@\,\nu_z \approx 410$ kHz) [2]. Accordingly, the axial frequency has to be stable enough to detect this small frequency jump, which could be achieved by the improvements mentioned above. Therefore, the first spin-flips (Fig. 1) of a single $^{28}Si^{13+}$-ion could be induced and detected in the last year.

First Larmor resonance in the analysis trap

Being able to induce and detect spin-flips, the irradiated microwave frequency was scanned and the number of spin-flips per unit time at each frequency was counted [1]. This results in a Larmor-resonance as shown in Fig. 2. The asymmetric Boltzman shape of the resonance is caused by the coupling of the axial mode energy to a thermal bath in the inhomogeneous magnetic field of the analysis trap [4]. From this resonance a preliminary value of the *g*-factor with an uncertainty in the 10^{-7} range could be deduced.

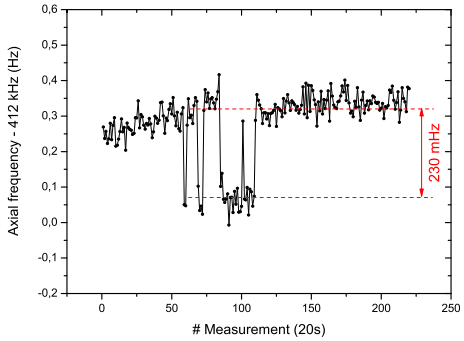

Figure 1: Spin-flips of a $^{28}Si^{13+}$-ion in the analysis trap detected with the phase-sensitive measurement technique.

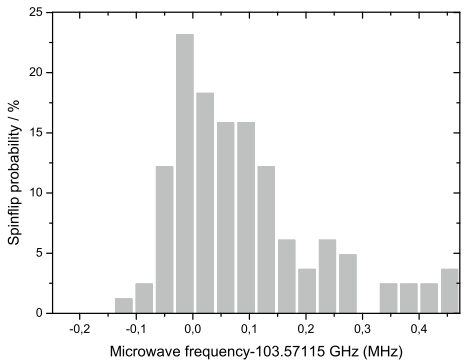

Figure 2: Larmor resonance in the analysis trap.

Outlook

Since we are now able to detect spin-flips in the analysis trap (AT) and the transport between the analysis and the precision trap (PT) is working, the next step is the *g*-factor measurement in the PT. This is presently under way. The spin-flips are induced in the homogeneous magnetic field of the PT while simultaneously the eigenfrequencies of the ion are measured. After this, the ion is transported to the AT to see if a spin-flip occurred or not. A significant improvement of the *g*-factor is expected.

References

[1] G. Werth *et al.*, Int. J. Mass Spectrom. **251**, 152 (2006)

[2] S. Sturm *et al.*, J. Phys. B **43**, 074016 (2010)

[3] S. Stahl *et al.*, J. Phys. B **38**, 297 (2005)

[4] M. Diederich *et al.*, Hyperfine interactions **115**, 185 (1998)

* Work supported by Max Planck Society

† ankewag@uni-mainz.de

QED and Electron-Impact Excitation in Stored Heliumlike Uranium Ions

*D.B. Thorn[1,2], A. Gumberidze[*1,2], S. Trotsenko[3,4], D. Banaś[5], H. Beyer[3,4], W. Chen[3], F. Currel[6], R.D. DuBois[7,1], S. Geyer[3,8], R. Grisenti[†3,8], S. Hagmann[3,8], M. Hegewald[3,8], P. Indelicato[9], C. Kozhuharov[3], R. Märtin[3,10], N. Petridis[3,8], R. Schuch[11], U. Spillmann[3], A. Surzhykov[‡3,10], A. Warczak[12], G. Weber[3,4], W. Wen[3,13], D.F.A. Winters[3,10], N. Winters[3,10], Y. Zhang[3,10], and Th. Stöhlker[3,4,10]*

[1]ExtreMe Matter Institute/GSI, Darmstadt; [2]FIAS, Frankfurt am Main, Germany; [3]GSI, Darmstadt; [4]Helmholtz Institute Jena; [5]Jan Kochanowski University, Kielce, Poland; [6]Queens University Belfast, UK; [7]Missouri University of Science and Technology, Rolla, USA; [8]Frankfurt University; [9]LKB, Paris, France; [10]Heidelberg University; [11]Stockholm University, Sweden; [12]Jagiellonian University, Krakow, Poland; [13]IMP, Lanzhou, China

At GSI we have extended our previous study of the effect of electron-impact excitation in heavy highly charged ions (HCI) undergoing collisions with neutral atoms [1]. Electron-impact excitation (EIE) of bound electrons is one of the most fundamental excitation processes. In particular, it is responsible for the vast majority of x-ray radiation produced in high energy density physics experiments and at laboratory fusion devices. In addition, QED effects are predicted to affect the EIE process through the generalized Breit interaction [2]. Most EIE measurements have thus far only been performed at electron beam ion trap facilities with low- to mid-Z ions [3]. To study EIE in the heaviest HCI possible, intense HCI beams are needed because the impact excitation cross-sections are on the order of one barn. The only excitation studies that have thus far been performed have used multi-proton gases or solids in an effort to have reasonable x-ray yields [4].

In a recent (Oct. 2010) ESR experiment, we looked for EIE effects in relativistic collisions between He-like uranium ions and hydrogen and argon targets. The target gases were produced by a cryogenically cooled liquid micro-jet, achieving densities of $\sim 10^{13}$ cm^{-2}. At energies of 220 and 300 MeV/u, x-ray spectra from uranium ions were recorded to investigate the produced excitation lines ($1s^2 \rightarrow 1s2p_{3/2}$) K$\alpha_1$ and ($1s^2 \rightarrow 1s2p_{1/2}$) K$\alpha_2$. These energies were at, and above the EIE threshold of $\sim$ 200 MeV/u. We used five HP-Ge detectors, mounted at different angles around the interaction region, and a novel 2D-Si(Li) polarimeter.

Electron and proton impact excitation processes both lead to the emission of Kα_1 and Kα_2 radiation. However, since excitation by the nuclear field scales as Z_T^2, whereas EIE scales as Z_T, different targets can be used to disentangle both excitation mechanisms. Changes caused by the target can then be studied via the Kα_1/Kα_2 peak ratio, and as a function of the projectile energy. For instance, excitation for collisions with argon atoms is mainly due to protons. But, at higher energies, *i.e.* above the EIE threshold, for collisions with hydrogen atoms, the proton and electron contribute equally to the excitation.

Preliminary spectra from the experiment are shown in Figure 1, where the Kα_1 and Kα_2 peaks are shown for two targets (hydrogen and argon). For the case of impact with hydrogen gas, the intensity of the Kα_1 peak as compared with the Kα_2 peak is smaller then for the case of argon gas as a target. The most probable reason for this is the suspected large increase from QED effects to the electron-electron scattering component of the excitation process.

To understand these effects and to disentangle the EIE contribution to the excitation, polarization analysis and data taken below and at the electron excitation threshold are currently under evaluation. To fully quantify the electron and proton impact processes, new calculations involving alignment (as described in Ref. [5]) are needed.

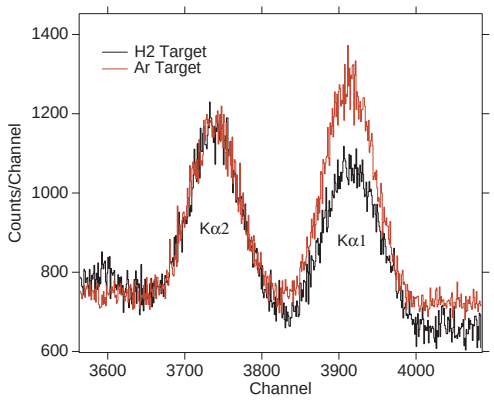

Figure 1: Preliminary data: Kα spectrum of 220 MeV/u U^{92+} ions.

References

[1] D. B. Thorn, A. Gumberidze, S. Trotsenko *et al.*, GSI annual report (2009).

[2] C.J. Fontes, D.H. Sampson and H.L. Zhang, Phys. Rev. A **49**, 053704 (1994).

[3] H. Chen and P. Beiersdorfer, Can. J. Phys. **86**, 55-71 (2008).

[4] T. Ludziejewski, Th. Stöhlker, H. Beyer *et al.*, Nucl. Instr. Meth. Phys. Res. B **154**, 204 (1999)

[5] A. Surzhykov, U.D. Jentschura, Th. Stöhlker *et al.*, Phys. Rev. A **77**, 042722 (2008).

* supported by Helmholtz Alliance EMMI.
† Work supported by the Helmholtz Association (VH-NG-331).
‡ Work supported by the Helmholtz Association (VH-NG-421).

Resonant coherent excitation of Li-like uranium in a Si crystal*

A. Ananyeva[1, 2], T. Azuma[3,4], H. Bräuning[1], A. Bräuning-Demian[1], D. Dauvergne[5], Y. Kanai[3], Y. Nakano[3], T. Shindo[4], S. Suda[4], Y. Yamazaki[3].

[1] GSI - Helmholtzzentrum für Schwerionenforschung GmbH, [2] Tomsk Polytechnic University, [3]RIKEN, [4]Tokyo Metropolitan University,[5] IPNL - Institut de Physique Nucléaire de Lyon

A channelled ion passing between oriented rows of atoms in a crystal lattice with a velocity v experiences a coherent periodic perturbation of frequencies $\nu = k(v/d)$, where $k = 1, 2, 3, \ldots$ and d is the distance between the atoms in a row. When one of these frequencies coincides with $\nu_\gamma = \Delta E_{fi}/h$, where ΔE_{fi} is the energy difference between electronic states i and f of the ion, a resonant coherent excitation of the atomic level might occur.

Predicted by V.V. Okorokov in 1965 [1], the phenomenon was first experimentally clearly observed in light ions at energies of few MeV/u [2]. Later advances in accelerator technology made the extension of these studies towards much heavier projectiles and relativistic energies possible [3, 4, 5]. These investigations, using relativistic highly charged Ar and Fe ions [4, 5] extended the RCE studies to the region where relativistic effects in the resonance properties can be observed. Using beams of highly charged ions delivered by the SIS-ESR facility of the GSI the energy of the $1s^2 2s_{1/2} \rightarrow 1s^2 2p_{3/2}$ transition in Li-like uranium ions was measured using the REC process in a Si crystal.

A cooled, well collimated beam of U^{89+} ions was sent after the slow extraction from the ESR through a 10 µm equivalent Si crystal. The crystal orientation and the fine tuning of the incoming ion energy for the resonant condition were done by using a high precision, 5-axis goniometer. The identification of the resonant excitation of the $2p_{3/2}$ state was made by measuring the photon yield emitted by the deexcitation of the $2p_{3/2}$ state in Li-like uranium (E_γ= 4459 eV) and the survival fraction of the initial projectile charge state. The emitted photons were measured by four silicon drift detectors (SSD) placed around the crystal in vacuum, at ±33 deg, +62 deg and -44 deg and the charge state distribution by a position sensitive detector placed behind the analyzing magnet.

In the case of the resonant coherent excitation of an atomic level in a planar crystal orientation the transition energy, E_{trans}, is given by the relation:

$$E_{trans} = h\gamma v\left(\frac{k\cos\theta}{A} + \frac{l\sin\theta}{B}\right) \qquad (1)$$

where h is the Planck constant, γ the Lorentz factor, v the velocity of the ions, k and l are Miller indices, A and B are constants determined by the crystal structure and θ is the angle of the direction of incident ion with respect to one axis in the plane. For the present measurement performed in the (220) planar orientation of the Si crystal, the coefficients (k, l) = (1, 2) and the resonant condition for the transition is satisfied for an incident ion energy of about 191.1 MeV/u.

Figure 1 shows, independently for each detector, the measured photon yield as function of the rotation angle θ. The photon yield was normalized to the total number of ions passing the crystal and the geometrical detection efficiency of the SDD detectors assuming the isotropic emission. The positions of the maxima of the distributions were identified as occurring at 5.06 deg ≤ θ ≤ 5.08 deg. Using this result and the relation (1) an energy value of 4462.9 eV was obtained for the $1s^2 2s_{1/2} \rightarrow 1s^2 2p_{3/2}$ transition.

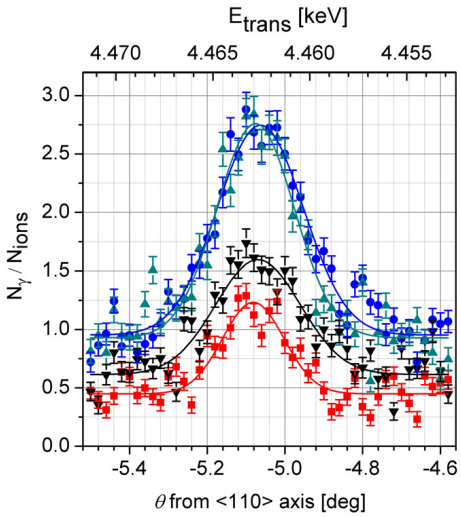

Figure 1: X-ray yield of 191.1 MeV/u U^{89+} ions excited in a 10 µm thick Si crystal in the (220) planar orientation.

A detailed analysis of the data to explain the contributions responsible for the observed position of the resonance maximum and the resonance width (relaxation of the coherence, energy loss in the crystal, beam divergence, momentum distribution of the incoming ion beam, etc.) is in progress. Also, the different photon yields observed at different observation angles suggest a possible polarization of the emitted radiation.

References

[1] V.V. Okorokov, Yad. Fiz. 2 (1965) 1009, [Sov. J. Nucl. Phys. 2, (1966) 719].
[2] S. Datz, *et al.*, Phys. Rev. Lett. 40 (1978) 843-847.
[3] K. Komaki,*et al.*, NIM B 146 (1998) 19−28.
[4] T. Azuma, *et al.*, Phys. Rev. Lett. 83 (1999) 528-531.
[5] Y. Nakai, *et al.*, NIM B 230 (2005) 90−95.

*Work supported by GSI and Grants-in-Aid for Scientific Research (No. 19104010) from JSPS, Japan.

Fragmentation dynamics of $(CH_4)^{3+}$ from collisions with 3.6 MeV/u Xe^{21+}

U. Werner[1], *B. Siegmann*[2], *and R. Mann*[3]
[1]Universität Bielefeld, Germany; [2]TU Dortmund, Germany; [3]GSI Darmstadt, Germany

In continuation of previous work [1], we had a more detailed look at the threefold ionization and fragmentation of methane in collisions with 3.6MeV/u Xe^{21+} ions provided by the UNILAC at GSI. For the complete fragmentation into three fragment ions two processes are observed:

$$(CH_4)^{3+} \longrightarrow H^+ + H^+ + CH_2^+ \qquad (1)$$
$$(CH_4)^{3+} \longrightarrow H^+ + H_2^+ + CH^+ \qquad (2)$$

Detailed information about the fragmentation dynamics is obtained by a position- and time-sensitive multi-particle detector [2] which allows the coincident measurement of the momenta of correlated fragment ions. If all fragments from a particular fragmentation are detected, a kinematically complete study of the molecular break-up process is possible [3, 4] and the kinetic energy release (KER) as well as angular correlations between the momenta can be derived for each individual event.

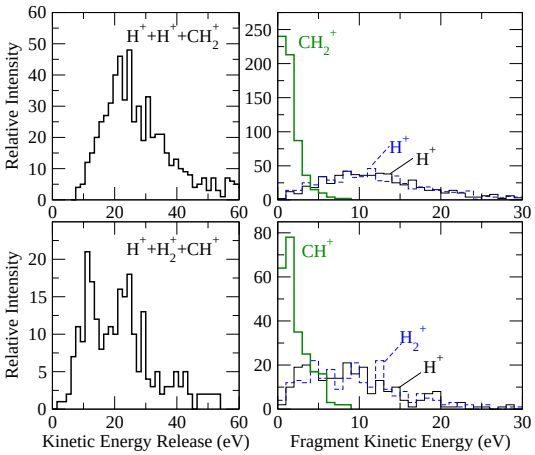

Figure 1: Total kinetic energy release (left) of coincident fragment ions observed in collisions of CH_4 with 3.6MeV/u Xe^{21+}. The right column shows the corresponding kinetic energies of the individual fragment ions.

The kinetic energy released (Fig. 1) in the symmetric coulomb fragmentation channel (1) is unspectacular, i.e. it shows one broad maximum around 23 eV and the kinetic energies of the individual fragments behave as expected for a simultaneous breaking of both CH-bonds: both H^+ have identical energy distributions and the heavy CH_2^+-ion gains only a small energy. Since favorable conditions for a formation of H_2^+ are only met "at the right moment" of some vibration modes of the CH_4 molecule the asymmetric channel (2) is about three times less abundant than the symmetric channel. Despite of the low intensity the total kinetic energy spectra reveal a more rich structure which is not compatible with an unimodal distribution. The reason for this complexity is not yet clear, e.g. contributions from different states of the intermediate CH_4^{3+}-ion or from different fragmentation mechanisms are possible.

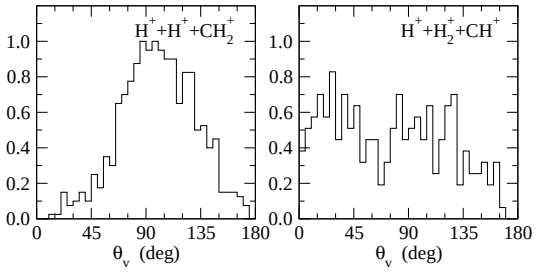

Figure 2: θ_v-distributions of coincident $H^+ + H^+ + CH_2^+$ (left) and $H^+ + H_2^+ + CH^+$ fragment ions (right) from collisions of CH_4 with 3.6 MeV/u Xe^{21+}-ions. The distributions were normalized with repect to their area.

Further information can be derived by an analysis of angular correlations[4]. As an example Figure 2 shows the measured spectra of the angle θ_v in velocity space given by $\angle(\vec{v}_{H^+} - \vec{v}_{CH_2^+}, \vec{v}_{H'^+} - \vec{v}_{CH_2^+})$ and $\angle(\vec{v}_{H^+} - \vec{v}_{CH^+}, \vec{v}_{H_2^+} - \vec{v}_{CH^+})$, respectively. If both bonds break simultaneously this angle will show a single peak reflecting the corresponding bond angle of the parent molecule. If the bonds break in a stepwise fashion, e.g. a H^+ is emitted followed by a delayed fragmentation of the intermediate CH_3^{++} ion, the strong correlation between the emission directions of the light fragments will be lost due to molecular rotation.

For the symmetric fragmentation (1) Figure 2 shows a broad maximum around $\theta_v \approx 100°$. The corresponding tetrahedral H-CH_2-H bond angle is $\approx 109.5°$ which is shifted by the (screened) Coulomb interaction of the emerging ions and broadened due to molecular vibrations. Thus the measured energy and θ_v spectra are consistent with the assumption of a simultaneous fragmentation. In case of the asymmetric channel (2) the θ_v spectrum shows no significant structure. Therefore the velocity vectors of the light fragments are mostly uncorrelated which suggests that a stepwise fragmentation dominates in this channel.

References

[1] B. Siegmann, U. Werner, and R. Mann, Nucl. Instrum. Methods **B 233**, (2005) 182.

[2] J. Becker, K. Beckord, U. Werner and H.O. Lutz, Nucl. Instrum. Methods **A 337**, (1994) 409.

[3] U. Werner, K. Beckord, J. Becker, and H.O. Lutz, Phys. Rev. Letter **74**, (1995) 1962.

[4] B. Siegmann U. Werner, H.O. Lutz, and R. Mann, J. Phy. B **35**, (2002) 3755.

Laser Spectroscopy of the Ground State Hyperfine Splitting in Lithiumlike Bismuth *

R. Sánchez[1,2], M. Lochmann[1,2], C. Geppert[2], C. Novotny[1,3], W. Nörtershäuser[1,2], M. Hammen[2], Th. Kühl[1,2], Th. Stöhlker[1,4], D.F.A. Winters[1,4], V. Hannen[5], R. López Coto[5], J. Mader[5], C. Weinheimer[5], and the E083 collaboration

[1]GSI, Darmstadt; [2]Universität Mainz; [3]Helmholtz-Institut Mainz; [4]Universität Heidelberg; [5]Universität Münster

Laser spectroscopic measurements of the ground state hyperfine splitting (HFS) in hydrogenlike heavy ions have triggered great interest because they can be used to test QED effects in extremely strong electric and magnetic fields. However, the interpretation of the experimental value is difficult because the uncertainty of the contribution of the nuclear magnetization distribution (Bohr-Weisskopf effect) hinders to test the size of the QED contributions. It has been suggested to overcome this limitation by measuring the HFS in both hydrogen- and lithium-like heavy ions of the same species [1]. Thus, tests of the QED effects on the level of a few percent become feasible [2].

Bismuth is the only stable isotope where the ground state hyperfine transitions of both hydrogen- and lithium-like ions are in a range accessible by laser spectroscopy. The HFS-transition wavelength for hydrogenlike bismuth ($^{209}Bi^{82+}$) has already been measured with a relative accuracy of 1.6×10^{-4} by Klaft *et al.* in 1993 [3].

We are currently commissioning an experiment at the ESR to measure the HFS in lithiumlike bismuth at an energy of 400 MeV/u (which is equivalent to 70 % of the speed of light). Due to the relativistic Doppler shift at $\beta = 0.7$, the HFS-transition wavelength is shifted from $\lambda_0 \approx 1555$ nm in the rest frame of the ion to the visible range $\lambda \approx 640$ nm. Laser light at this wavelength can be easily provided by a dye laser. We have acquired a new laser system, consisting of a frequency-doubled pulsed Nd:YAG laser-pumped dye laser, which delivers now up to 120 mJ at 30 Hz at the desired wavelength. This laser light is transported to the ESR and overlapped collinearly with a lithiumlike bismuth ion beam at the electron cooler section where the ions are electron cooled and bunched at the second harmonic of the revolution frequency. One bunch is illuminated with the laser light while the other one is used as a reference to correct for ion-beam-induced background.

Since the transition is rather long-lived ($\approx$ 80 ms), the fluorescence is emitted along the entire length of the ESR. We have developed a new light collection system consisting of a copper mirror that can be moved close to the trajectory of the ion beam allowing the fluorescence photons to be efficiently directed into a photomultiplier [4, 5]. We have tested this device successfully using both a $^{7}Li^{+}$ beam (at 59 MeV/u) [6] and a $^{238}U^{90+}$ beam (at 200 MeV/u) in 2010. Figure 1 shows an example of the signals recorded during these beamtimes. The analysis of the data showed that the ion beam is not disturbed significantly once the copper mirror gets close to the beam path. Thus it becomes feasible to use it for the bismuth beamtime.

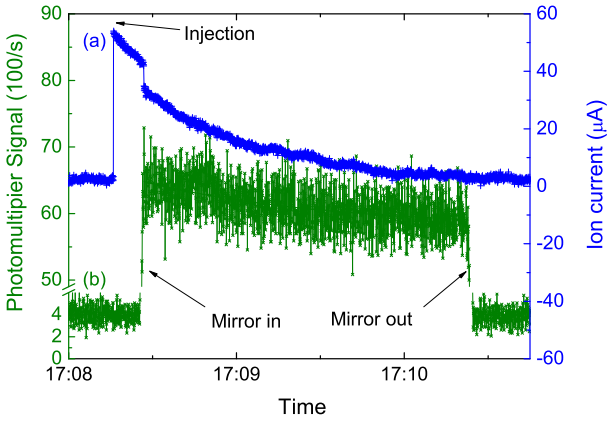

Figure 1: (a) Ion current and (b) photomultiplier signal as a function of time after injection obtained during a test beamtime at the ESR where a $^{7}Li^{+}$ beam was used at an energy of 59 MeV/u. As soon as the mirror moves towards to the ion beam path (Mirror in), there is a sudden decrease in the ion current but this does not change drastically the ion beam lifetime. As expected, the photomultiplier signal increases as soon as the mirror is moved in, and drops when the mirror moves out.

An existing segmented mirror which was used in the past during similar experiments was also refurbished by inserting new high-reflecting aluminium foils.

Further tests are being performed on the laser transport system between the laser laboratory and the laser-ion-beam interaction region located about 50 m away. For this, piezo-controlled mirrors are under test in order to ensure a good pointing stability, and therefore a stable ion-beam laser-beam overlap.

References

[1] V. M. Shabaev *et al.*, Phys. Rev. Lett. 86, (2001) 3959.

[2] D. F. A. Winters *et al.*, Can. J. Phys. 85, (2007) 403.

[3] I. Klaft *et al.*, Phys. Rev. Lett. 73, (1994) 2425.

[4] D. Anielski, Diplomarbeit, Universität Münster, 2010.

[5] M. Lochmann *et al.*, GSI Scientific Report 2009, AP-23.

[6] R. López Coto, Master Thesis, Universität Münster, 2010.

*This work was supported by the Helmholtz Association under contract No. VH-NG-148 and by the BMBF under contract No. 06MZ9179I. The Work in Münster was supported by the BMBF under contract No. 06MS9152I.

A new test of Time Dilation at ESR using fast $^7Li^+$-ions*

B. Botermann[1,2], T. Kühl[1], W. Nörtershäuser[1,2], C. Novotny[1,2], R. Sánchez[1], T. Stöhlker[1], C. Geppert[2], G. Huber[2], S. Karpuk[2], D. Bing[3], D. Schwalm[3], A. Wolf[3], G. Gwinner[4], T. W. Hänsch[5], S. Reinhardt[5], and G. Saathoff[5]

[1]GSI Helmholtzzentrum für Schwerionenforschung, Darmstadt, Germany; [2]Johannes Gutenberg Universität Mainz, Germany; [3]MPI für Kernphysik, Heidelberg, Germany; [4]University of Manitoba, Winnipeg, Canada; [5]MPI für Quantenoptik, Garching, Germany

One of the fundamental principles in modern physics is Local Lorentz Invariance (LLI), which describes space time symmetry in the theories of the electromagnetic, the strong and the weak force as well as the local part of general relativity. Time dilation is one of the well known consequences of LLI and Special Relativity (SR), respectively.

In 2010 we have performed an experiment to probe time dilation by simultaneous measurements of forward and backward Doppler shifts of an electric dipole transition of fast moving ions. In the presented measurements, $^7Li^+$ ions are stored in the experimental storage ring (ESR) with a velocity of 33.8 % of the speed of light. Those ions have a strong dipole transition (2s $\rightarrow$ 2p) which has an excitation wavelength of $\lambda_0 = 548.5$ nm in the ions' rest frame. The transition is simultaneously addressed by two laser beams overlapped parallel (p) and anti parallel (a) with the ion beam. Due to the relativistic time dilation, the frequencies of the exciting lasers are shifted according to the Doppler formula to $\nu_{a,p} = \nu_0 \cdot \gamma \cdot (1 \pm \beta)$, where $\gamma = (1-\beta^2)^{-1/2}$ is the Lorentz factor and $\beta = v/c$ is the velocity of the ions in terms of the speed of light. Multiplication of the Doppler shift formulas shows that SR predicts the relation $\nu_a \cdot \nu_p = \nu_0^2$. Any violation of special-relativistic time dilation would result in a deviation $\varepsilon(\beta)$ of the form

$$\frac{\nu_a \cdot \nu_p}{\nu_0^2} = 1 + \varepsilon(\beta) \qquad (1)$$

When the lasers address different hfs-components of the dipole transition with frequencies ν_1 and ν_2, ν_0^2 in eq. (1) is replaced by $\nu_1 \cdot \nu_2$. Non vanishing values of the parameter $\varepsilon(\beta)$ can be interpreted in the frameworks of test theories [1, 2].

Figure 1 shows two types of spectroscopy signals we have recorded during a recent beam time in October 2010. The Λ-type signal (lower panel) is produced by coupling two levels of the hyperfine structure of the ground state of the metastable $^7Li^+$ ions via one excited level [3] and recording the fluorescence of the ion beam. With our setup we were able to measure the laser frequencies ν_a and ν_p with an absolute accuracy of 1 MHz which corresponds to a relative accuracy of $\Delta\nu/\nu = 2 \cdot 10^{-9}$. Together with the corresponding rest frequencies ν_1 and ν_2 [3], an upper bound for the parameter $\varepsilon(\beta)$ has been determined 25 times more accurate compared to the previous experiment at GSI [4]. The interpretation of this value in the frameworks of test theories [1, 2] shows that we were able to test SR with a four times higher precision than the currently leading experiment [5]. Within the experimental uncertainties no deviations from SR could be found.

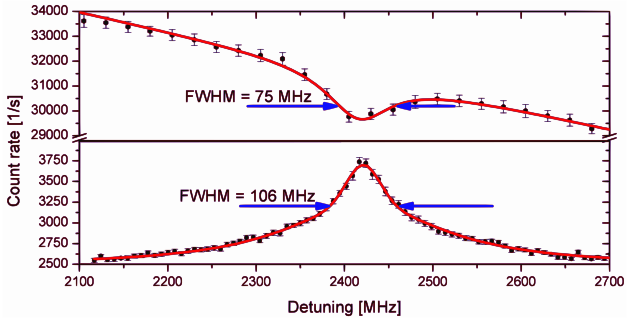

Figure 1: Two types of Doppler-free spectroscopy signals which can be used for determining laser frequencies with high accuracy. **Bottom:** Λ spectrum with good signal to noise ratio but large FWHM was used to calculate an upper bound of hypothetical deviations from SR. **Top:** Saturation spectroscopy signal which may provide higher precision in future experiments.

The upper part of figure 1 shows a signal which has been achieved via saturation spectroscopy where both lasers excite the same hfs transition. In this spectroscopy scheme a two level transition in the lithium ions is investigated and the dip can be observed only if both lasers interact simultaneously with the ions. This allows for signals which are narrower than those achieved with Λ spectroscopy. This method has been applied during this beam time for the first time at GSI and promises an even higher precision for the determination of the transition frequencies in the future.

References

[1] R. Mansouri et al., General Relativity and Gravitation **8**, 515 (1977)

[2] V. Kostelecký et al., Physical Review D **39**, 683 (1989)

[3] C. Novotny, PhD thesis, Johannes Gutenberg-University Mainz, 2008

[4] C. Novotny et al., Physical Review A **80**, 022107 (2009)

[5] S. Reinhardt et al., Nature Physics **3**, 861 - 864 (2007)

*This work was supported by the Helmholtz Association under Contract No. VH-NG-148, by the BMBF under Contract No. 06MZ9179I and by the Helmholtz Institute Mainz (HIM).

X-ray emission from laser-plasma acceleration experiments

S. Trotsenko[1,2], D. B. Thorn[2,3], G. R. Plateau[4,5], C. G. R. Geddes[4], N. H. Matlis[4], E. H. Esarey[4], M. Battaglia[4], C. B. Schroeder[4], S. Shiraishi[4], Th. Stöhlker[1,6], S. Tashenov[2,6], C. Tóth[4], and W. Leemans[4]

[1]Helmholtz Institute Jena, 07743 Jena, Germany; [2]GSI, 64291 Darmstadt, Germany; [3]ExtreMe Matter Institute EMMI/GSI, 64291 Darmstadt, Germany; [4]Lawrence Berkeley National Laboratory, Berkeley, CA 94720, USA; [5]École Polytechnique, 91128 Palaiseau, France; [6]University of Heidelberg, 69120 Heidelberg, Germany;

Laser driven plasma-based accelerators [1,2] have been shown to generate quasi-monoenergetic electron beams with energies up to GeV [3,4]. The studies have shown a big potential of this accelerators to become a cost efficient alternative to the conventional linear accelerators. In such accelerators, a femtosecond laser pulse drives a plasma wave whose space charge field accelerates electrons from the plasma. Even though, for the replacement of conventional linear accelerators with the laser-plasma accelerators requires further development, the latter offer several unique applications. In particular, x-ray emission from oscillations of the electrons (betatron motion) in the intense focusing field of a laser-plasma accelerator show promise for use in femtosecond-scale time-resolved radiography of ultrafast processes. However, the spectral characteristics of this betatron emission have been so far characterised only from filter pack measurements.

In order to achieve higher resolution in spectroscopy of betatron radiation, we used an x-ray charge-coupled device to record the spectrum of betatron radiation, with a full width at half maximum resolution of ≤ 250 eV. Moreover, simultaneous measurements of x-ray and electron spectra has been performed along with x-ray images that allowed for determination of the betatron emission source size. This allows for a determination of differences in the x-ray spectra as a function of the energy spectrum of accelerated electrons.

Details of the experimental setup are shown in Fig. 1. Here, a pulse from Berkeley's LOASIS Ti:sapphire laser was focused above a gas-jet nozzle oriented transversely to the beam line. The peak power was 10 TW [0.45 J in 45 fs FWHM] and was focused onto a 7.5 μm FWHM spot. The plasma density profile had a peak density of $3 \cdot 10^{19}$ cm^{-3}. For a characterization of the electron beam a combination of integrating current transformer (ICT), phosphor screen and an optical CCD was used.

For the x-ray imaging as well as measuring their energy distribution, a 1024x256 pixel back-illuminated CCD camera was used with 26 μm square pixels and a 40 μm deep depletion region. The CCD was placed 220 cm from the laser/gas-jet interaction region and was operating under a high vacuum. A thin window (0.1 μm Al, 14 μm polycarbonate, 18 μm Kapton) was installed between the CCD and the laser interaction chamber, because of the different vacuum requirements for them.

For the measurements of the betatron emission source size, few fiber wires with different thicknesses (and materials) were fabricated in order to form crosshairs that were placed between the laser/gas-jet interaction region and the CCD.

In order to reduce background from high energy photons (resulting from stopping many MeV electron beams in the magnetic spectrometer) the CCD was placed in a lead brick enclosure. In addition, the line of sight of the camera was restricted by a rectangular stainless steel pipe that was fitted to the size of the CCD chip (~25x7 mm^2). Also the part of the aluminium target chamber on the CCD side was covered with plastic in order to reduce on-axis hard x-ray bremsstrahlung. For further details of the experiment we refer to [5].

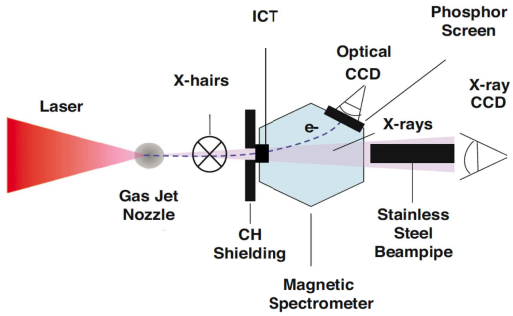

Figure 1: Schematic of the experimental setup.

The studies were extended to the higher energy region, well above the Si *K*-edge of the synchrotron radiation. The second amplifier of the LOASIS laser system (<60 TW) was used. The higher energy region was chosen in order to avoid uncertainties related to the low-energy features of the photon spectrum [5]. In addition, this measurements were supplemented by use of filter packs.

From a preliminary data analysis one can conclude that a high flux (~10^6) of ~5 keV collimated photons (~2.7x0.7 mrad) was achieved. Also correlation of the x-ray flux with the electron beam charge was observed with insensitivity of the first to other accelerator parameters. The data analysis is in progress.

The support by the US Department of Energy, NA-22 and NSF is gratefully acknowledged..

References

[1] T. Tajima and J. M. Dawson, Phys. Rev. Lett. 43, 267 (1979).
[2] E. Esarey *et al.*, IEEE Trans. Plas. Sci. 24, 252-288 (1996).
[3] K. Nakamura *et al.*, Physics of Plasmas 14, 056708 (2007).
[4] J. Osterhoff *et al.*, Phys. Rev. Lett. 101, 085002 (2008).
[5] D. B. Thorn *at al.*, Rev. of Scient. Instr. 81, 10E325 (2010).

Laser cooling of relativistic C^{3+} ions at the ESR

M. Bussmann[1], F. Kroll[1], M. Löser[1], M. Siebold[1], U. Schramm[1], C. Novotny[2], W. Nörtershäuser[2,3], C. Dimopoulou[3], F. Nolden[3], M. Steck[3], C. Kozhuharov[3], Th. Kühl[2,3], Th. Stöhlker[3,4,5], D.F.A. Winters[3,4], S. Tichelmann[6], G. Birkl[6*], T. Beck[6*], B. Rein[6*], Th. Walther[6*], X. Ma[7], W. Wen[1,3,7†]*

[1]Helmholtz-Zentrum Dresden-Rossendorf; [2]Johannes-Gutenberg-Universität Mainz; [3]GSI Helmholtzzentrum für Schwerionenforschung GmbH, Darmstadt; [4]Ruprecht-Karls-Universität Heidelberg; [5]Helmholtz Institut Jena; [6]Technische Universität Darmstadt; [7]Institute of Modern Physics, Lanzhou (China)

Recent experiments [1,2] at the Experimental Storage Ring (ESR) at GSI have shown that relativistic Li-like carbon (C^{3+}) ion beams can be laser-cooled to an unprecedented momentum spread of $\Delta p/p \approx 10^{-7}$. Here, a single-frequency laser was tuned to the Doppler-shifted $1s^22s \rightarrow 1s^22p$ ($^2P_{1/2}$ and $^2P_{3/2}$) transitions. These results encourage the application of laser cooling to beams of other Li- and Na-like ions at even higher energies, as will *e.g.* be available at FAIR [3]. However, before that, two important techniques still need to be demonstrated:

1) Efficient laser cooling of ion beams with a large initial momentum spread. *Additional pre-electron cooling, as was required in the past, should be omitted. In addition, a continuous scan of the bunching frequency was applied to bring the laser frequency in overlap with ions of different velocities inside the bunch.*

2) All-optical measurements of the relevant beam parameters. *The ultra-low momentum spread of a laser-cooled ion beam lies below the sensitivity of the Schottky pick-up system and possible ordering effects in the regime of strong coupling between the ions cannot be resolved.*

The aim of the upcoming beamtime is to prove the successful technical realization of these techniques at the ESR. In the setup (see Fig. 1) we will apply a new data acquisition and control system, new laser systems, add detectors for fluorescence measurements, and make full use of all new and existing diagnostic tools at the ESR [4].

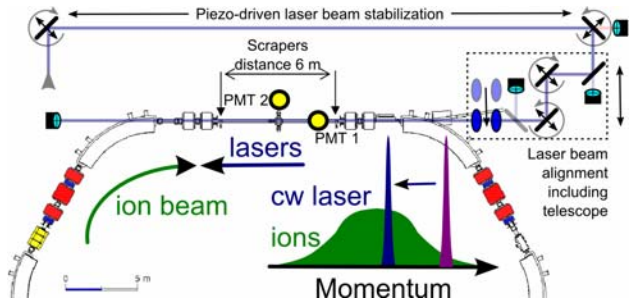

Figure 1: Schematic of the laser cooling experiments at the ESR. The C^{3+} ions have an energy of 122 MeV/u, and will be laser-cooled on the two $1s^22s \rightarrow 1s^22p$ transitions.

Data acquisition and control system

The new data acquisition and control system (CompactRIO by NI) is based on FPGA technology. This system can control the laser systems, control drift tube voltage, read out the ESR diagnostics, and record the fluorescence rate. With these diagnostics we will be able to get full information on the longitudinal and transversal beam phase space at unprecedented resolution.

Laser Systems

The transition wavelengths in C^{3+} are at ~155 nm, but due to the large relativistic Doppler-shift the counter-propagating laser light (see Fig. 1) should have a wavelength of about 257 nm. For these experiments, a diode-based CW laser system (1028 nm) with two frequency doubling stages (514 and 257 nm) will be used. This system is being set up in the group of Prof. Walther (TUD). The difficulty here is to scan a large range (~30 GHz) in a short (~10 ms) time, thus addressing all ions in phase space. This can replace initial electron cooling as well the bunching frequency scan previously used. In addition, the feasibility of using a compact pulsed laser system for laser cooling is investigated at HZDR.

Fluorescence detection

The detection of laser-induced fluorescence will be done by means of UV-sensitive solar-blind photomultiplier tubes outside the beam tube and by CsI-coated photo-channeltrons which are mounted inside the vacuum. This activity is being coordinated by the group of Prof. Birkl (TUD).

ESR diagnostics

In order to study as many of the laser-cooled ion-bunch properties as possible, we will measure the ESR ion current, record the ion's dynamics using the Schottky pick-up systems, and exploit the new beam profile monitoring system.

The preliminary beamtime is scheduled for summer / autumn 2011.

References

[1] U. Schramm, D. Habs, Progr. Part. Nucl. Phys. **53**, 583 (2004).
[2] M. Bussmann, U. Schramm, D. Habs *et al.*, J. Phys. Conf. Series. **88**, 012043 (2007).
[3] H. Backe, Hyp. Int. **171**, 93 (2006).
[4] M. Bussmann *et al.*, COOL09 Proceedings, IMPCAS Lanzhou, Atomic Energy Press, 22 (2009)

* Work supported by BMBF
† Work supported by DAAD

Forward angle electron spectroscopy at the ESR

P.-M. Hillenbrand[1,2], S. Hagmann[3], A. Müller[1], S. Schippers[1], A. Gumberidze[4], C. Kozhuharov[2], R. Reuschl[4], H. Rothard[5], U. Spillmann[2], D. Winters[2,6], and Th. Stöhlker[2,6,7]

[1]Universität Giessen; [2]GSI Darmstadt; [3]Universität Frankfurt; [4]ExtreMe Matter Institute Darmstadt; [5]CIRIL-Ganil, Caen, France; [6]Universität Heidelberg; [7]Helmholtz Institut Jena

In fast heavy ion-atom collisions electron emission from the projectile permits high resolution studies of ionization and transfer. For corresponding experiments an electron spectrometer has been built at the jet target zone of the ESR. Located 90 cm downstream from the Gas target, it is built to detect electrons emitted during ion-atom collisions, having a velocity comparable to the ion beam velocity $v_e \approx v_i$ (i.e. cusp electrons). Electrons within a forward angle of up to 3.6° horizontally and 1.6° vertically with respect to the ion beam axis are collected, which gives a solid angle of $\Delta\Omega \approx 4 \cdot 10^{-4}$. The spectrometer has already shown successful operation in a pioneering coincidence measurement of electrons and photons originating from the high energy end of electron-nucleus bremsstrahlung [1].

The electrons which are to be detected, are bent by a 60° magnet away from the ion beam, focused by a magnetic quadrupole lens, bent again by a 60° magnet, after which they pass momentum defining slits and hit a position sensitive MCP delay line detector. The electron optics (Figure 1) have been calculated using the GSI beam simulation software *MIRKO* [2].

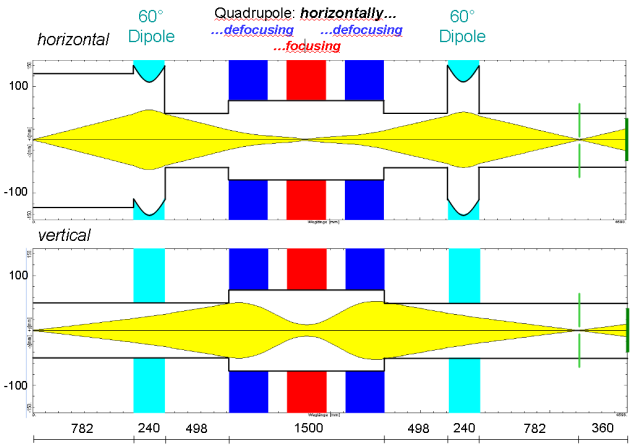

Figure 1: Electron optical simulation with MIRKO for the $x-$ and the $y-$plane (distances in mm)

Compared to the setup used in [1], the spectrometer is currently being improved in several aspects:

1. A new *quadrupole triplet* was installed. It has been specially designed to be iron free and thus free of hysteresis. Using this focusing element the spectrometer will be able to run in a telescopic mode, projecting the emission cone of the electrons from the gas target onto the position sensitive detector.

2. A new *hexapole delay line detector* will be implemented. Compared to the previously used quadratical delay line anode, both using a set of MCPs with ø=80 cm, the 3-layer grid of the hexapole anode improves multi hit capability, thus leading to a higher accessible count rate [3].

3. A redesign into a *+60°/-60°-configuration* by mirroring the 2nd dipole will lead to a better momentum focus on the plane of the slits and offer a significant increase in momentum resolution.

In order to investigate these modifications a commissioning setup has been build (Figure 2). Here the relevant beam line of the ESR is replaced by a test beam line in which a high intensity β^--source is to be located, e.g. ^{207}Bi.

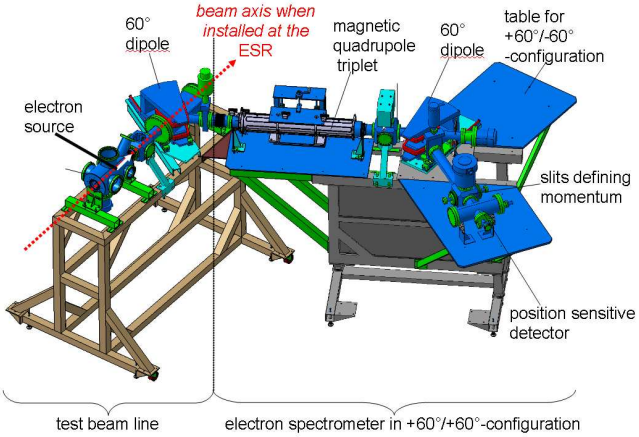

Figure 2: Commissioning setup

After commissioning the spectrometer new experiments with regard to electron-nucleus bremsstrahlung and the radiative electron capture into the continuum (RECC), as well as ionization of the projectile are planned to be conducted. Besides a higher momentum resolution, the telescopic mode is expected to give insight into the angular distributions of the electrons emitted in these processes.

References

[1] M. Nofal *et al.*, Phys. Rev. Lett. **99** 163201 (2007)

[2] MIRKO: www.gsi.de/beschleuniger/groups/BBE/MIRKO/mirko.html

[3] O. Jagutzki *et al.*, IEEE Transact. on Nucl. Science, **49** 2477 (2002)

Effect of the nozzle geometry on the internal target density at the ESR

N. Petridis[*1], *U. Popp*[2], *A. Kalinin*[1], *R. Dörner*[1], *A. Khoukaz*[4], *T. Stöhlker*[2,3], *and R. E. Grisenti*[†1]

[1]IKF, J.W.G.-University Frankfurt; [2]GSI, Darmstadt; [3]Physikalisches Institut, Ruprecht-Karls-University Heidelberg; [4]Institut für Kernphysik, Westfälische Wilhelms-Universität, Münster

The internal target station at the ESR has been modified in 2008 to improve the reachable area density for low-Z targets by using pinhole orifice nozzles to produce beams of liquified gas that form a so called microdroplet target beam [1]. This setup was tested and improved during numerous beamtime campaigns in the last two years.

However, the operation of the pinhole nozzle with heavier gases such as argon, krypton or xenon was ineffective. Target densities of $n_x \approx 10^{13}\ cm^{-2}$ could easily be achieved at the former laval-type target setup without cooling at a nozzle diameter of $d_0 = 50\ \mu m$, whereas no stable target beam could be produced with the tiny pinhole nozzle ($d_0 = 5 - 10\ \mu m$). At room temperature a target beam could not be formed due to the large angular divergency of the emissive gas through the pinhole and at low temperatures a stable target operation could not be achieved due to fluctuations in density over several orders of magnitude.

In order to improve the performance of the new target station for heavy target gases a different type of nozzle was installed. It has a trumped-shaped geometry and a nominal nozzle diameter of about $d_0 = 13\ \mu m$. The group of A. Khoukaz from the University Münster provided the nozzle, which was originally manufactured at CERN, and performed several target tests with hydrogen gas in the past [2]. The technical drawing is shown in Fig. 1. A custom-made adapter was manufactured to implement the new nozzle geometry on the existing closed cycle cryostat setup.

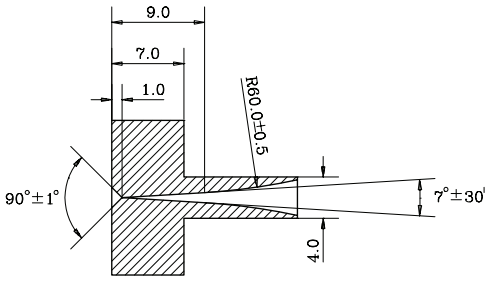

Figure 1: Sketch of the CERN trumpet-shaped nozzle.

We performed a systematical investigation of the target area density with the heavy gases argon, krypton and xenon at room temperature and variable backing pressure. In addition, we applied hydrogen at a nozzle temperature of about $T_0 = 40\ K$ to investigate the performance of the CERN-nozzle with lighter target gases. The results are shown in Fig. 2. The temperature had to be reduced to $T_0 = 200\ K$ for argon to reach an adequate target area density.

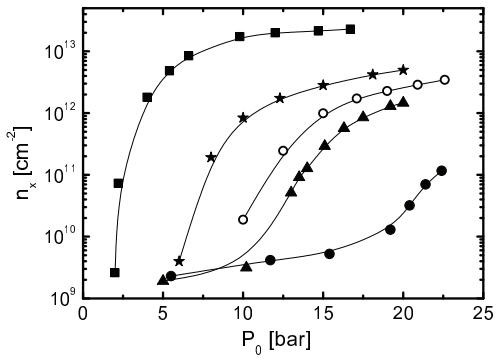

Figure 2: Measured target area density with the trumped-shaped nozzle as a function of the backing pressure P_0. The investigated gases were argon (closed circles), krypton (triangles) and xenon (stars) at room temperature. In order to reach higher target area densities for argon the nozzle temperature was decreased to $T_0 = 200\ K$ (open circles). The performance for the low-Z target gas was tested with H_2 at $T_0 = 40\ K$ (squares).

We reached very stable target area densities for the used heavy target gases in the region between $n_x = 10^{12} - 10^{13}\ cm^{-2}$. The experimental data for argon show that the target area density can be further increased by decreasing T_0 if necessary. The new nozzle seems to be viable even in case of a hydrogen target for which a very stable target area density of $n_x \approx 3 \cdot 10^{13}\ cm^{-2}$ was measured. A fluctuation in target density of $1.85\ \%$ was detected during a ten hour measurement period. The major difference between the CERN nozzle and the pinhole nozzle is that the target beam is produced by condensation of an expanding gas and not by fragmentation of a liquid.

The results suggest that the existing internal target setup is capable to produce internal targets of low-Z as well as high-Z target gases at very high stability. Hence, one system combines the advantages of both cluster and microdroplet target.

References

[1] M. Kühnel, N. Petridis, D.F.A. Winters, U. Popp, R. Dörner, Th. Stöhlker, R.E. Grisenti, Nucl. Instr. and Meth. A 602 (2009) 311-314.

[2] A. Khoukaz, T. Lister, C. Quentmeier, R. Santo, and C. Thomas, Eur. Phys. J. D 5, 275-281 (1999)

* petridis@atom.uni-frankfurt.de

† This research has been funded by the Helmholtz society under grant Nr. VH-NG-331

High Data Rate Initiative: Electronic Readout for a Si(Li) – Compton – Polarimeter

U. Spillmann[1], E. Badura[1], K.H. Blumenhagen[2], H. Bräuning[1], J. Hoffmann[1], K. Koch[1], N. Kurz[1], R. Märtin[1,2], S. Minami[1], W. Ott [1], Th. Stöhlker[1,2,3], G. Weber[3], M. Weber[4]

[1]GSI, Darmstadt, Germany; [2]PI, University of Heidelberg, Germany; [3]HI Jena, Germany; [4]IPE, KIT, Karlsruhe, Germany

Within the High Data Rate Initiative (HDRI) [1] of the Helmholtz research program "Photons, Neutrons, and Ions" KIT and GSI collaborate closely within the working package "Real Time Data Processing" bringing together the expertise of the partners in the development of advanced detector readout systems. As one of the first common projects between KIT and GSI we started the development of a self-triggering 2-dimensional position-, time-, and energy sensitive Si(Li)-strip detector read out with modern custom designed FPGA-based signal digitizer hardware as a demonstrator system. This project is of great importance for future x-ray spectroscopy and polarimetry experiments of the SPARC collaboration [2] at GSI and FAIR.

As detector platform we have chosen an already existing Si(Li)-strip detector [3] that has worked reliable in several beam times at the ESR as well as external places, e.g. TU Darmstadt and DESY, Hamburg, and has produced excellent results [4]. Up to now it was equipped with standard NIM and VME electronic. The outcome of this project using custom designed FPGA-based signal digitizer hardware will serve as a blue print for the next generation of readout electronics of thick planar strip detectors with the collaboration.

The concept is based on the fast digitizing of the preamplifier signals coming from the detector to acquire the small signals directly. The consecutive employment of pulse shape analysis techniques will show the energy and timing information of an event.

For this first demonstrator we profit from recent developments of the Experiment Electronics department of GSI. They provide us with a set of 8 FEBEX2 – ADC boards [5] with 8 input channels each. Sampling the data is performed with a frequency of 65 Ms/s and a resolution of 12 bit at an input range of +/-1V. A 1.6 GBit fiber link connects the digitizer board with the PLEXOR3-PCIe Interface hosted by a commercial PC that manages the event building and data transport by ethernet. In addition a TRIXOR1-PCIe board takes over the trigger handling and the dead time locking. The PC runs a LYNX RT-operating system and as DAQ we employ MBS [6] to take advantage of the GSI data acquisition and storage environment. To adapt the signal output of the preamplifier to the input of the FEBEX2 board the fast linear amplifier SiLiVer was developed. It has a single ended input and gives a differential output. The two consecutive amplifier stages provide a voltage gain of forty. The small form factor of the amplifier boards allows us to mount them inside the preamplifier housing to avoid losses on the signal cables.

In a first step the pulse shape analysis of the event data will be managed by PC hardware. It allows us to optimize the algorithms within a short time. The main goal of this first step is to rebuild the functionality of the NIM and VME hardware and to be able to handle photo effect and Compton events. From this point on we can make use out of the system in atomic physics experiments. In collaboration with the KIT we will refine the algorithms for the digital pulse shape analysis with the aim to manage more complex event histories like two or three Compton events for one incident photon. We plan to meet the demand of increased computing power by dedicated hardware solutions designed by KIT.

Most parts of the hardware for the demonstrator have been produced and tested already. A few parts are still in the assembly phase. First tests of the complete system are planned for March 2011.

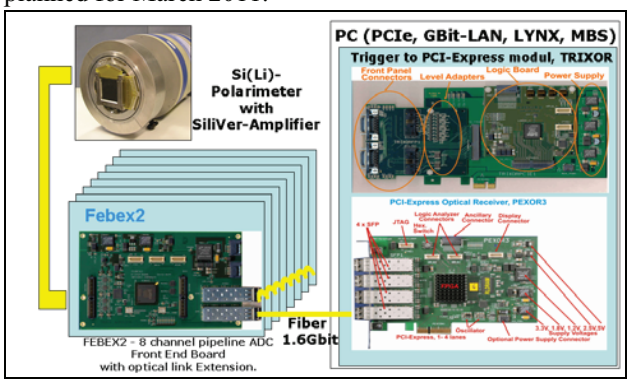

Figure 1: Sketch of the new readout chain of the Si(Li)-Polarimeter Demonstrator

References

[1] http://www.hdri-pni.de

[2] Technical Report of the SPARC collaboration http://www.gsi.de/fair/experiments/sparc/index_e.html

[3] G. Weber et al., "Performance of a position sensitive Si(Li) x-ray detector dedicated to Compton polarimetry of stored and trapped highly-charged ions", JINST 5,C07010 (2010)

[4] Th. Stöhlker et al., "Polarization and angular correlation studies of X-rays emitted in relativistic ion-atom collisions", EPJ-ST 169, 5-14 (2009)

[5] http://www.gsi.de/onTEAM/grafik/1130845854/febex2.pdf

[6] http://www-win.gsi.de/daq/

Development of a crystal spectrometer for studies with helium-like argon

N. Winters[1,2,3], Z. Yin[1,2], H.F. Beyer[1,4], D.F.A. Winters[1,2] and Th. Stöhlker[1,2,4]*

[1]GSI Darmstadt; [2]Universität Heidelberg; [3]EMMI; [4]Helmholtz-Institut Jena

Introduction

We report on the development of a crystal spectrometer for experiments with helium-like argon ions as a target. The spectrometer will be used as a precise diagnostic tool to study a) collisions between relativistic highly charged ions and argon atoms at the ESR; b) the interaction between pulses from the PHELIX laser and large argon clusters; and c) studies of He-like argon as created in the SPARC EBIT. The spectrometer is optimised for accurate x-ray spectroscopy of inner-shell transitions in He-like argon (Ar^{16+}) with an energy of about 3 keV.

Crystal spectrometer

The Bragg crystal spectrometer is arranged in the Johann geometry with a Rowland circle diameter of 1.28 m. A Monte Carlo simulation program (*MacRay*, see e.g. [1]) was used to obtain the optimum geometry. We use a cylindrically bent InSb (220) crystal with outer dimensions of 20x15 mm^2 and a lattice constant of $2d$ =4.58 Å. Bragg's Law for diffraction states that $n\lambda = 2d\sin\theta$, where λ is the wavelength of the impinging radiation according to $E = hc/\lambda = hc/(2d\sin\theta)$. First order diffraction then gives an energy of E = 3.129 keV. The diffraction angle θ=59.9° can then be related to a position X by focussing the diffracted x-rays onto a CCD camera. The size of the CCD is 26.6x6.6 mm^2, and the pixel size is 26x26 μm^2. The quantum efficiency is about 95% for ~3 keV x-rays. The spectrometer's total detection efficiency and resolution depend on the size of the x-ray source and its distance from the crystal.

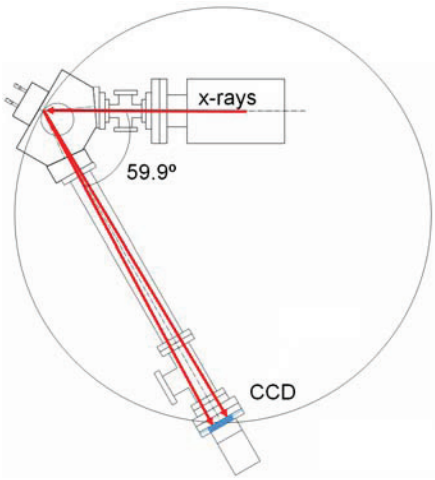

Figure 1: Schematic of the crystal spectrometer. The x-rays are diffracted from a InSb(220) crystal and detected by a CCD camera. The Bragg angle is 59.9°. The spectrometer is optimised for resolving the 1s2p → $1s^2$ ($^3P_1$, $^3P_2$, $^1P_1$) transitions in He-like argon ions at ~3.13 keV.

First results: reference spectra

For the first tests, we used the $L_{\alpha 1,2}$ lines from cadmium (Cd) and terbium (Tb) at around 3.13 keV as a reference. These lines were obtained by irradiating solid state Cd and Tb targets with an x-ray tube.

The background-subtracted CCD data were analysed using a program that features *cluster analysis* (see e.g. [2]). Clusters are caused by charge splitting on the CCD, *i.e.* one photon hits more than one pixel. In the analysis, the 2D position data from the CCD is converted into an energy spectrum, which can be used to determine transition energies and line intensities.

Figure 1 shows a reference spectrum of Cd, as obtained with the crystal spectrometer. One can clearly separate the $L_{\alpha 1}$ from the $L_{\alpha 2}$ line, and the lines have an almost perfect Lorentzian profile, as expected.

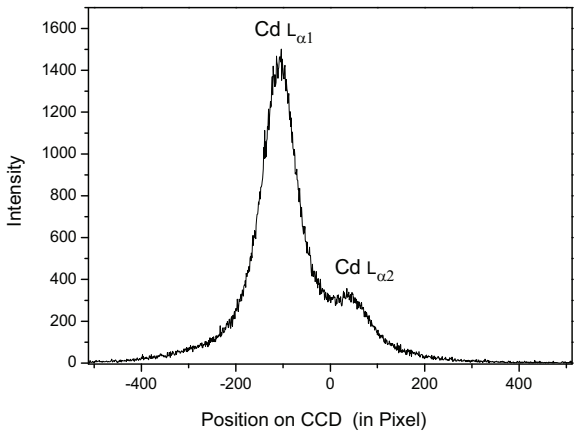

Figure 2: Cd reference spectrum recorded with the CCD camera of the crystal spectrometer.

Planned experiments

The spectrometer is designed to spectrally resolve the 1s2p → $1s^2$ ($^3P_1$, $^3P_2$, $^1P_1$) inner-shell transitions in He-like argon ions, see *e.g.* [3]. In the beginning of 2011, first tests at the SPARC EBIT are foreseen. Later, in spring 2011, experiments in the PHELIX laser bay are planned. At a later stage, the spectrometer can be installed at the internal target at the ESR.

References

[1] H.F. Beyer, Nucl. Instrum. Meth. Phys. Res. A **400**, 137 (1997).

[2] M. Trassinelli *et al.*, GSI Scientific Report 2006, atomic-physics-19, 263 (2006).

[3] R.D. Deslattes, H.F. Beyer and F. Folkmann, J. Phys. B: At. Mol. Phys. **17** L689 (1984).

Measurement of the (anti)proton *g*-factor - Status of the experiment*

C.C. Rodegheri[1,2], *K. Blaum*[2,3], *H. Kracke*[1,4], *A. Mooser*[1,4], *W. Quint*[3,5], *S. Ulmer*[1,2,5], *and J. Walz*[1,4]

[1]Johannes Gutenberg-Universität, Mainz; [2]Max-Planck Institut für Kernphysik, Heidelberg;
[3]Ruprecht-Karls-Universität, Heidelberg; [4]Helmholtz-Institut Mainz, Mainz; [5]GSI, Darmstadt

The measurement and comparison of the magnetic moment (or *g*-factor) of the proton and antiproton provide a stringent experimental test of the CPT-theorem in the baryonic sector [1]. We set up an experiment for the first self-contained and direct high-precision measurement of the *g*-factor of a single isolated proton stored in a Penning trap [2]. In previous experiments the *g*-factor was determined indirectly, being currently known to a relative precision of 10^{-8} [3]. We aim to achieve a relative uncertainty of 10^{-9} or better. The application of the continuous Stern-Gerlach effect [4] to detect quantum jumps between the spin states of the particle offers the possibility of measuring the magnetic moment not only of a single proton but also later of a single antiproton, whose *g*-factor is currently known to a relative precision of only 10^{-3} [5].

The magnetic moment of the proton can be calculated as $g = 2\nu_L/\nu_c$, with ν_L being the Larmor frequency and ν_c the free cyclotron frequency of the stored ion. The proton motional frequencies in a Penning trap ν_+, ν_- and ν_z are measured non-destructively by detecting image-currents induced in the trap electrodes by the oscillatory motion of the particle. Applying the "invariance theorem" $\nu_c^2 = \nu_+^2 + \nu_-^2 + \nu_z^2$ [6] the free cyclotron frequency can be calculated. The Larmor frequency can be determined from the proton spin flip resonance curve, obtained by the application of an external excitation field at the Larmor frequency. The detection of the proton spin state is based on a coupling of its magnetic moment μ to its axial oscillation frequency ν_z in the trap. This coupling is achieved by an inhomogeneous magnetic field component B_2, the "magnetic bottle", and results in an axial frequency shift ($\delta\nu_z \propto B_2\mu_z/m_p\nu_z$) according to the spin orientation. A double Penning trap setup allows the spatially separated measurement of the cyclotron frequency in a homogeneous magnetic field in the so-called precision trap and the detection of the proton spin state for the determination of the Larmor frequency in the so-called analysis trap, in which the magnetic field is strongly inhomogeneous.

Comparing to other experiments, in which the same technique was used to detect the spin state of charged particles, as in [4] for the electron, the determination of the spin state of the proton constitutes a very challenging task since the ratio μ_z/m_p is about 1.2×10^6 times smaller, so that a much stronger B_2 is necessary to provide a detectable frequency shift.

A new trap design was specially developed to provide a sufficiently strong magnetic bottle as well as a geometry capable of providing a compensated and orthogonal trapping potential. The new design consists of a cylindrical Penning trap with 1.8 mm inner diameter and a CoFe ring electrode, geometrically optimized for a maximized B_2 term. With this set up a magnetic bottle of $325\,\mathrm{mT/mm^2}$ could be achieved (see Figure 1 (a)), corresponding to an axial frequency shift of about 200 mHz at 690 kHz.

The cyclotron frequency of a single proton can be already determined to a relative uncertainty of 10^{-8} in the precision trap. The first single proton ever stored in a magnetic bottle of $325\,\mathrm{mT/mm^2}$ was recently detected in the analysis trap as shown in Figure 1 (b).

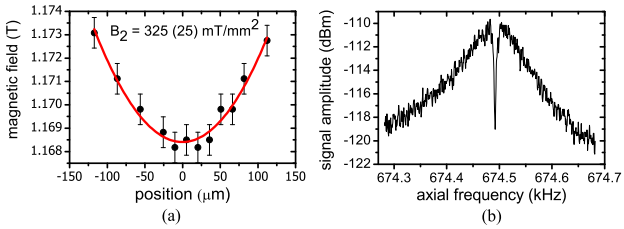

Figure 1: (a) Magnetic field for different positions of the proton in the analysis trap. The B_2 term can be obtained from the fit. (b) Single proton in thermal equilibrium with the axial tank circuit at 4 K in a strong magnetic field inhomogeneity of $325\,\mathrm{mT/mm^2}$.

The determination of the Larmor frequency depends essentially on the detectability of a proton spin flip. To this end an axial frequency resolution below 200 mHz at 690 kHz is required. The stabilization of the axial frequency in the analysis trap is a laborious task since the eigenmotions of the proton are not decoupled in the strong magnetic field inhomogeneity since $\Delta\nu_z = \frac{1}{4\pi^2 m_p \nu_z}\frac{B_2}{B_0}\Delta E_r \Rightarrow 1\,\mathrm{Hz}/\mu\mathrm{eV}$. Preliminary optimization like trap-tuning, particle cooling and filtering led to a stability of 200 mHz. The next step consists in successfully inducing spin flip transitions and detecting the axial frequency shift in the analysis trap.

References

[1] R. Bluhm et al., Phys. Rev. Lett. 79, 1432 (1997).

[2] C. C. Rodegheri et al., Hyperfine Interact. 194, 93 (2009).

[3] P. F. Winkler et al., Phys. Rev. A 5, 83 (1972).

[4] R.S. Van Dyck et al., Phys. Rev. Lett. 59, 26 (1987).

[5] T. Pask et al., Phys. Lett. B 678, 55 (2009).

[6] L. S. Brown et al., Rev. Mod. Phys. 58, 233 (1986).

*Work supported by Deutsche Forschungsgemeinschaft, the Programme Alßan, the European Union Programme of High Level Scholarships for Latin America, scholarship no. (E06D101305BR), the International Max Planck Research School for Quantum Dynamics, the Frankfurt Institute for Advanced Studies and Helmholtz-Institut Mainz.

HITRAP – Heavy, Highly-Charged Ions at Rest

F. Herfurth[1], W. Barth[1], G. Clemente[1], L. A. Dahl[1], P. Gerhard[1], M. Kaiser[1], O. K. Kester[1,2,3], H.-J. Kluge[1], N. Kotovskiy[1], C. Kozhuharov[1], M. Maier[1], J. Pfister[3], W. Quint[1], U. Ratzinger[3], A. Schempp[3], A. Sokolov[1], Th. Stöhlker[1], H. Vormann[1], G. Vorobjev[1] and S. Yaramishev[1]

[1]GSI, Darmstadt, Germany; [2]NSCL, MSU East Lansing, MI, USA, [3]IAP, Frankfurt, Germany.

Introduction

At the GSI accelerator complex, using the universal linear accelerator UNILAC and the synchrotron SIS, highly-charged ions up to U^{92+} are produced by passing a 400 MeV/u beam through a gold foil stripping off all or nearly all electrons. The HITRAP facility is built to decelerate those ions to almost rest and to provide them to the experiments [1]. First, the ions are decelerated in the experimental storage ring ESR from 400 to 4 MeV/u accompanied with stochastic and electron cooling to keep the emittance small. Then, in the HITRAP linear decelerator the deceleration is performed in two additional steps. An interdigital H-type (IH) structure and a radio-frequency quadrupole (RFQ) structure are operated in inverse mode to decelerate first from 4 MeV/u to 0.5 MeV/u and then further to 6 keV/u. For final cooling below one meV the ions are captured in a Penning trap.

Technical Improvements

This year, for the first time, a new mode of operation has been used in order to shorten the cycle time, i.e. the time between consecutive decelerated ion bunches. For this, the heavy-ion synchrotron SIS accelerates only to 30 MeV/u before the bunch is transferred to the ESR. This removes the first deceleration and cooling step in the ESR and reduces the cycle time from about 50 to below 30 seconds.

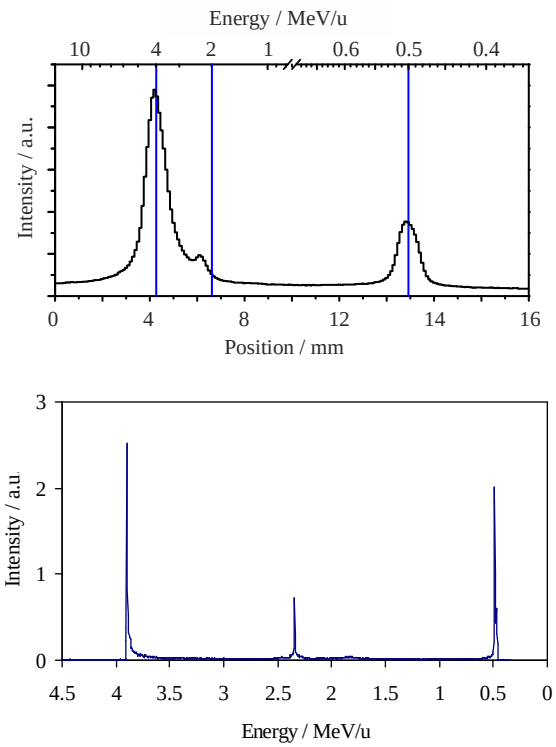

Figure 1. Energy spectrum of ions behind the IH. Upper panel: Measured spectrum vs. position. Lower panel: calculated spectrum using the LORASR code.

To speed up the tuning of the decelerating structures it turned out that it was indispensable to have shot by shot information of the complete spectrum of different energies produced during deceleration. A specially designed one-shot energy analyser [2] based on a permanent dipole magnet and a MCP – phosphor screen detector has been implemented in the beginning of 2010. In figure 1 a typical spectrum for a well tuned IH section is shown. Almost 40% of the detected beam has been decelerated to 0.5 MeV/u, which is close to the theoretically expected maximum of about 55 %.

Additionally, as in the years before, extensive simulations of the beam dynamics have been carried out. For the transversal beam dynamics optimisation we used COSY INFINITY extended by an advanced description of the action of the accelerating gaps, which enables the complete calculation of the beam from the ESR up to the entrance of the RFQ. The result is shown in fig. 2.

A major outcome was that the narrow pumping barrier, introduced to decouple the vacuum of ESR and the linear decelerator, had to be increased for efficient transport and

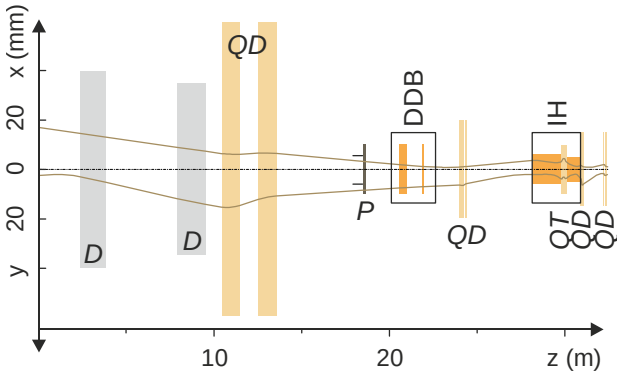

Figure 2. Ion optical system of HITRAP from the ESR to the RFQ. Transversally the beam is controlled by magnetic dipoles *D*, magnetic quadrupole doublets *QD*, and triplets *QT*. The diaphragm *P* separates ESR and HITRAP vacuum and the black lines show the old aperture in scale. The lines are the beam envelopes in horizontal *h* and vertical *v* direction and the vertical size of the optical components is proportional to the available aperture. Note that transversal and longitudinal scales differ.

deceleration. Before the third beam time in 2010, the diameter of the 150 mm long tube was increased from 12 to 20 mm.

Longitudinal Beam Dynamics in IH and RFQ

For the longitudinal ion beam dynamics LORASR [4], has been used for the DDB and the IH structure, and PARMTEQ [5] as well as DYNAMION [6] for the RFQ structure.

Qualitatively, the beam energy output behind the IH was reproduced (see fig. 1) assuming a DC beam from the ESR. The resulting particle distributions were further calculated with PARMTEQ, which was also used during the design of the RFQ, to find a preliminary working point and to get guidelines for the commissioning.

It was predicted and measured that a 500 keV/u beam is transported with almost 100 % efficiency. The longitudinal acceptance for deceleration to the desired 6 keV/u was calculated to be 500 ± 5 keV/u with a phase spread acceptance of ± 10 deg. As during the first commissioning beam time there was no proof of slowed down ions behind the RFQ the code DYNAMION was additionally used to exclude that simplified assumptions yielded a wrong working point estimate. For now, the simulations have been reduced to the idealized regular part of the RFQ cells and to a beam on axis. The resulting upper limit for longitudinal acceptance, as shown in fig. 3, is 515 ±10 keV/u with a phase spread of ±15 deg, different from the PARMTEQ predictions. A further increase of the accepted beam energy is expected when the measured electrode geometry including the radial matching sections is included in the simulation.

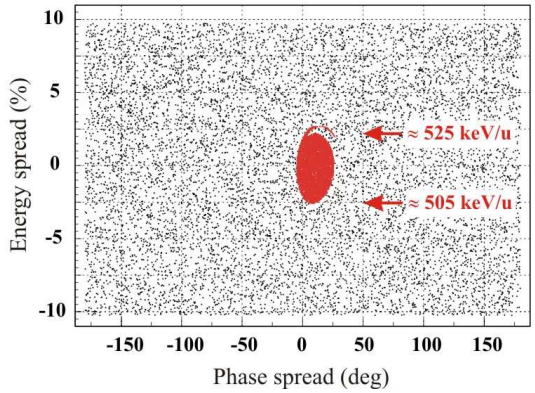

Figure 3: DYNAMION simulation of the longitudinal RFQ acceptance (red) depending on energy and phase of the incoming particles (black).

Those simulation results have been taken into account during the second commissioning beam time in November 2010 and the IH output energy has been changed in a range of about 30 keV/u. Additionally, an improved detection system was used to make sure that the 500 keV/u ions enter and leave the RFQ before activating the RF for deceleration. Still no decelerated ions have been detected.

Post inspection of the RFQ structure has revealed an electrode misalignment that is for now attributed to temperature-stress induced length changes. Those will be investigated by local heating tests in 2011. Furthermore, the IH output energy will be measured more precisely to match it to the narrow acceptance window of the RFQ. Once the electrode geometry of the RFQ has been measured more precise simulations will be done to finally match the IH beam emittance to the RFQ acceptance.

Cooler Penning Trap

The HITRAP cooler penning trap has been tested offline during 2010. For this the cold electron source, built at MPIK Heidelberg [3], has been taken into operation and first electrons have been passed through the bore of the trap magnet. It was then possible to optimize the injection scheme and hence to compare the optimal settings to OPERA simulations. In fig. 4 the calculated field map is shown that is created by the 10 coils used to bring the electron beam onto the trap axis. Diagnosed by two detectors on axis it was possible to establish a well understood set of parameters and guide the required electrons (~$5 \cdot 10^9$/pulse) onto the axis for injection into the trap.

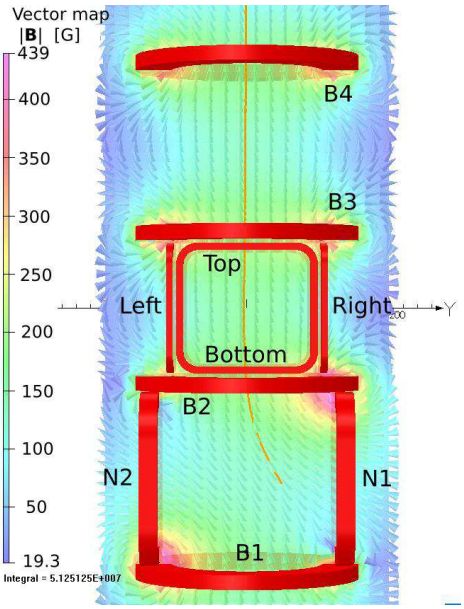

Figure 4. Arrangement of coils for electron injection into the cooler Penning trap as modelled in OPERA. Shown is a vector map of the magnetic field B in Gauss on the symmetry plane of the device. Electrons run upwards and are shown in yellow.

References

[1] H.-J. Kluge et al., Adv. Quant. Chem. **53** (2008) 83.
[2] F. Herfurth et al., Act. Phys. Pol. B **41** (2010) 457.
[3] C. Krantz, PhD University of Heidelberg, http://www.ub.uni-heidelberg.de/archiv/10009.
[4] U. Ratzinger, Habilitationsschrift, Universität Frankfurt am Main (1998)
[5] R.H. Stokes, T.P. Wangler, K.R. Crandall, Part. Acc., IEEE NS-28, 1981, S. 1999
[6] S. Yaramyshev et al, Nuclear Inst. and Methods in Physics Research A, Vol. 558/1 pp 90-94, (2006)

Temperature distribution in the HITRAP cooler Penning trap*

J. Steinmann[1,2], *N. Brantjes*[1], *S. Fedotova*[1], *J. Groß*[2], *F. Herfurth*[1], *N. Kotovskiy*[1], *M. Shaaban*[1], *A. Sokolov*[1], *and G. Vorobyev*[1]

[1]GSI Helmholtzzentrum, Darmstadt, Germany; [2]Hochschule Darmstadt, Darmstadt, Germany

The HITRAP (Highly charged Ions Trap) facility at the GSI was developed for the investigation of slow highly charged ions up to U^{92+}. The facility consists mainly of three parts. After deceleration in the first part of the facility the ions are trapped in a cryogenic Penning trap in the second part. From there, the ions passed into the experimental part of the facility. Since it takes at least four days to cool the ion trap down to liquid helium temperature, it is important to calculate the temperature distribution and verify it with measured temperatures to understand its operation.

We simulated the local temperature of a cryogenic Penning trap by using the finite element software package COMSOL MULTIPHYSICS [1]. In order to determine the local heat transfer rate, care has been taken of heat conduction and heat radiation. Heat transfer due to convection has been neglected, because of the high vacuum of 10^{-13} mbar. Subsequently, the results of our simulation were compared to measured temperatures, which were taken during several cooling cycles at specific points inside the Penning trap.

The geometry that was used for the simulation is based on simplified CAD models and technical drawings. To keep the geometry as simple as possible screws and chamfer were removed, screw holes were filled and inner surfaces from two adjacent components were removed.

To cool down the ion trap a cryocooler from "Sumitomo Heavy Industries, Ltd" is used. This cooler operates with two stages. The first one is in thermal contact with the second stage shield with a cooling power of 35 W at 50 K and the second one is in thermal contact with the magnet with a cooling power of 1.5 W at 4.2 K, which surrounds the tube with the trap placed inside. The numerical simulation model takes care of these two stages by using two appropriate boundary conditions. The surface in contact with the first stage was set to 48 K and the surface in contact with the second stage got a temperature of 3.84 K. These values were taken from measurements. For the surfaces in thermal contact with the outer environment, the model uses 300 K. The ion trap is an open endcap construction, which means radiation can penetrate into the trap from outside. A detailed simulation of the heat radiation exchange between all surfaces inside the ion trap is too complex for the available main storage and computational time. Instead, it was assumed that most of the radiation hits the inner surfaces of the electrodes, resulting in a fourth boundary condition. We assumed that the inner surfaces of the electrodes receive an incoming net heat flux of $q = 60\ \frac{W}{m^2}$.

The ion trap itself is assembled from many smaller components, which are screwed together. Hence, an ideal thermal contact is impossible and therefore, the model uses a reduced thermal conductivity at these junctions. To reach the measured temperature the thermal conductivity had to be reduced by a factor of 1000.

For the temperature measurement seven resistive thermometers have been installed at certain places. To ensure a good comparability of the measured and calculated temperature, the temperature was evaluated along a path which cross most of the measuring probes. In Figure 1 the black line marks the path where the temperature was evaluated. The plotted points are used as a guide for figure 2, which shows the temperature as a function of the path length.

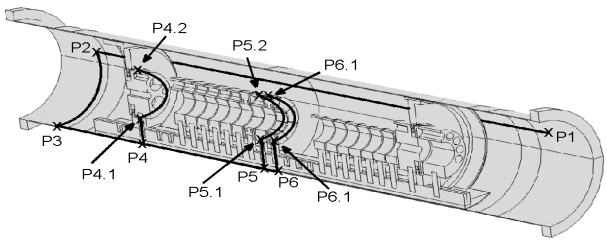

Figure 1: Path of temperature evaluation plotted as a solid line. The Points P_k are used as a guide for figure 2.

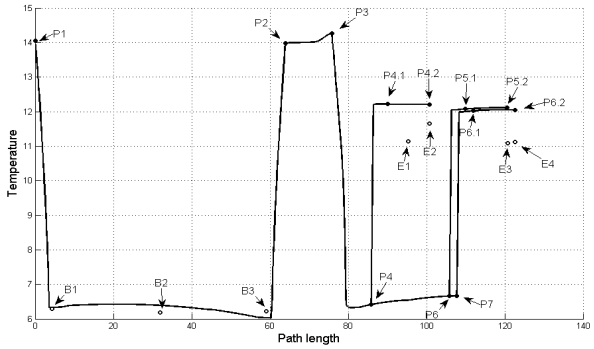

Figure 2: Temperature as a function of the path length. B1-B3 and E1-E4 are the measured temperatures.

Figure 2 shows that the measured temperature fits well into the result of our simulation, although the model use an unrealistic value for the thermal conductivity for some parts. One of the reason for this fact may be, that the model does not take into account the limited cooling power of the crycooler.

References

[1] "COMSOL MULTIPHYSICS", COMSOL Multiphysics GmbH, http://www.comsol.de/.

* Work supported by FE, Project-Number DAGROS1012.

The New Gas Jet Target for Experiments at HITRAP

D. Tiedemann[1*], A. Malarz[6], *W. Quint*[2,3], K. Stiebing[1*], *Th. Stöhlker*[2,3,4], *V. Varentsov*[5†], *A. Warczak*[6‡] *and D.F.A. Winters*[2,3]

[1]Institut für Kernphysik, Goethe University Frankfurt am Main, Germany, [2]GSI, Darmstadt, Germany, [3]University Heidelberg, Germany, [4]Helmholtz Institute Jena, Germany, [5]ITEP, Moscow, Russia, [6]Jagiellonian University, Cracow, Poland

Introduction

A new pulsed supersonic gas jet target for x-ray experiments with very slow (heavy) highly charged ions at HITRAP [1] is being set up at the IKF in Frankfurt. In 2009, this project received funding from the BMBF within the framework "SPARC experiments at Fair". Due to the combination of pulsed ion beams from HITRAP and the pulsed gas jet target, only a moderate pumping system (three 500 l/s turbo molecular pumps and a 2000 l/s roots pump assembly) is required to maintain good UHV conditions (~10^{-10} mbar). This allows for a compact design of the pumping stages (see Fig. 1), combined with good access for x-ray detectors to the target area.

Vacuum Vessel

In order to accomplish both the installation of standard and x-ray detectors, and modern large diameter x-ray polarimeters and/ or calorimeters, the design [1] has been revised thoroughly. Now, either five CF100 ports (at 30, 90, 135, 240 and 300º with respect to the ion beam direction), or three CF100 ports (at 20, 90 and 135º) and one CF200 port (at 90º) can be used for spectroscopy, as illustrated in figure 2. In the latter variant, closest access to the jet, e.g. by calorimetric detectors, is possible.

Alignment and set up

For optimum experimental results (high rates), it is crucial to achieve the best possible overlap between the gas jet and the ion beam. For this purpose, translational and rotational stages for the jet have been designed and are currently under construction. The angular adjustment is realized by a pivot point at the nozzle´s opening, which avoids lateral misalignment. Main target design parameters and gas operation conditions, used for the construction of the setup, were calculated by V. Varentsov. In order to align the gas jet on the skimmer axis, and to determine an optimum nozzle-skimmer distance, the supersonic jet profiles will be measured using a Pitot tube placed at the position of the 1st skimmer.

Figure 1 The 2000 l/s roots pump assembly.

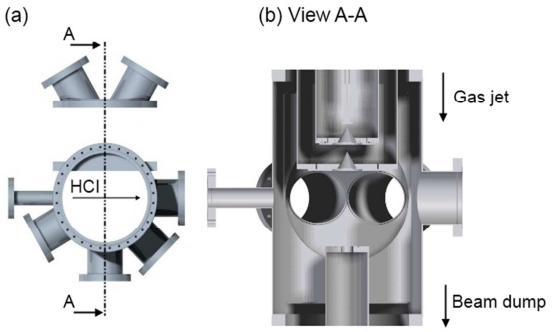

Figure 2 (a) Top view of the target chamber illustrating the accessible ports for spectroscopy. (b) Cut through the collision chamber around the target.

Safety Concerns

Hydrogen will be most frequently used as target gas. Therefore, special safety precautions have to be considered. For this purpose, a fail-safe logic unit has been developed, which is currently under construction. All critical parameters (pressure, hydrogen leak, pumps failure, etc.) are constantly monitored and controlled to guarantee a good safety and precaution scheme.

Experiments

After construction, alignment, and characterization, the setup will be installed at the high-energy beam line of the ECRIS RFQ facility in the IKF. First test experiments will focus on K-REC processes, i.e. radiative electron capture into the projectile's K-shell. Then, the setup will be installed at the HITRAP beam line. At HITRAP, the scientific program will focus on:

- 2p → 2s intrashell transitions in He-like HCI
- Total cross-sections for single-electron capture and hardness ratios
- Intrashell resonant transfer excitation in Li-like HCI
- Multi-electron capture studies

References

[1] K. Stiebing *et al.*, GSI Annual Report 2009, ATOMIC-PHYSICS-26, 376 (2009).

*Work supported by the BMBF (06FY9098I).
†Work supported by INTAS (Ref. Nr. 06-1000012-8956)
‡Target chamber design and construction supported by the Polish MNiSW (contract: PB 1044/B/H03/2010/38)

A versatile polarized electron beam instrument for ESR and HITRAP

M. Lestinsky[1], *S. Hagmann*[1,2], *and T. Stöhlker*[1,3,4]

[1]GSI, Darmstadt; [2]Frankfurt University; [3]Helmholtz-Institute Jena; [4]Heidelberg University

The emission of bremsstrahlung in the scattering of polarized electrons on nuclei is a elementary process and an instructive example of coupling the radiation field to an electron-atom system [1]. Systematic studies of polarization and angular correlations in such experiments permit stringent tests of modern theoretical models. For the realization of experiments on such processes, we propose the realization of a low-energy polarized electron target setup. It provides a pure, monoenergetic electron beam with full control over its spin orientation in e^--ion collisions. A signature of this process are cusp electrons in the continuum of the projectile in coincidence with photon emission [2]. Both can be detected with the existing forward electron spectrometer and the Compton polarimeter. Moreover, realizing the electron target in a modular and portable assembly, it will be available for experiments at ESR and at HITRAP. This gives a unique opportunity for studies of polarization and other effects in electron-ion collision experiments on highly charged ions using inverse kinematics and covering an enormous dynamic range of collision energies.

Since the early works of [3], GaAs semiconductor photocathodes have been realized as efficient sources for polarized electron beams and everal setups were implemented e.g. at JLab, SLAC, MAMI at Mainz University, and the S-Dalinac at TU-Darmstadt. There, highly polarized electron beams are yielded from semiconductor photocathodes in superlattice structures. These grow multiple periods of the photoactive and interleaved straining layers and enhance the quantum efficiency. GaAsP/GaAs- [4] and AlInGaAs/AlGaAs-configurations [5] achieve simultaneously high quantum efficiencies of about 1% and high degrees of polarization $P > 85\%$

Our proposed setup is shown schematically in Figure 1. We aim for electron currents of ≥ 100 μA and maximum polarization. Higher electron currents can be generally provided from the cathode, however, the Coulomb repulsion between the electrons strongly decreases the beam quality at higher intensities since most of the beam optics have to use electrostatic elements. Avoiding magnetic fields for beam optics is particularly important, as the spin orientation of low-energy electrons is highly sensitive to magnetic fields. Thus, solely Einzel lenses, electrostatic steerers and electrostatic quadrupole multiplets are foreseen for beam shaping and imaging.

The spin orientation with respect to the electron momentum can be manipulated using either electrostatic cylindrical benders, which retain the spatial orientation of the spin vector, while the direction of electron momentum is changed, or using Wien filters, where the electron spin precesses in an appropriately tuned magnetic field for its controlled alignment, while the momentum direction is conserved.

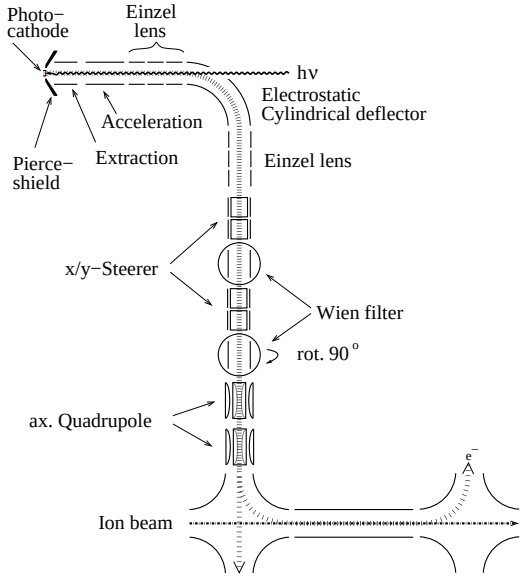

Figure 1: Schematic beam line for the polarized electron target. The electron beam is indicated using a hatched thick line, the ion beam is indicated with a thin dash-dotted line. Both, perpendicular and longitudinal merging options are indicated. The wiggled line shows the laser beam.

We consider two possible electron-ion merging configurations. In a perpendicular configuration a very small, localized interaction volume can be achieved. Longitudinal beam merging allows for smallest relative energies. This option for longitudinal merging can e.g. be accomplished non-magnetically with large-aperture electrostatic quadrupoles.

Presently, the general method for the electrostatic beam transport has been worked out. We performed electron trajectory simulations for all major sections using SimIon, the results are currently being optimized. Options for an efficient electron beam polarimetry are being investigated. The mechanical design has been started.

References

[1] E. Haug & W. Nakel, The Elementary Process of Bremsstrahlung *World Scientific Lecture Notes in Physics*, Vol. 73, 2004.

[2] M Nofal, et al., *Phys. Rev. Lett.*, 99:163201, 2007.

[3] D. T. Pierce, et al., *Rev. Sci. Instrum.*, 51:478, 1980.

[4] T. Maruyama, et al., *Appl. Phys. Lett.*, 85:2640, 2004.

[5] Y. A. Mamaev, et al., *Appl. Phys. Lett.*, 93:081114, 2008.

Development of the SPECTRAP experiment *

Z. Andjelkovic[1], *R. Cazan*[1], *W. Nörtershäuser*[1,2], *M. Vogel*[2], *V. Hannen*[3], *R. Jöhren*[3], *C. Weinheimer*[3], *D. Church*[4], *S. Bharadia*[5], *R. Thompson*[5], *G. Birkl*[6], *and the HITRAP collaboration*[2]

[1]Institut für Kernchemie, Johannes Gutenberg-Universität, Mainz; [2]GSI, Darmstadt; [3]Westfälische Wilhems-Universität, Münster; [4]Texas A&M University; [5]Imperial College London; [6]TU Darmstadt

The first laser spectroscopy experiments on highly charged ions in the 90s suffered from very high Doppler broadening due to large ion temperatures in storage rings and electron beam ion traps. During the last two decades ion traps became standard tools for high precision experiments. They offer a variety of cooling methods to sub-Kelvin regions and can reduce the Doppler broadening by several orders of magnitude. Going in the same direction, SPECTRAP employs a Penning trap for ion storage [1] and a laser system for laser cooling of magnesium [2], which can be used for sympathetic cooling of any other ion species trapped simultaneously.

In 2010 the cryogenic electronic components were completed and went through last tests before they were incorporated in the final design of the trap, shown in Fig. 1. The whole system has been inserted into the bore of the superconducting magnet, evacuated to high vacuum and is now ready for the first ions. Two ion sources were prepared for initial experiments with Mg^+ and Ar^+/Ar^{2+} ions, before connecting the setup to the HITRAP facility and the EBIT for the first experiments with highly charged ions.

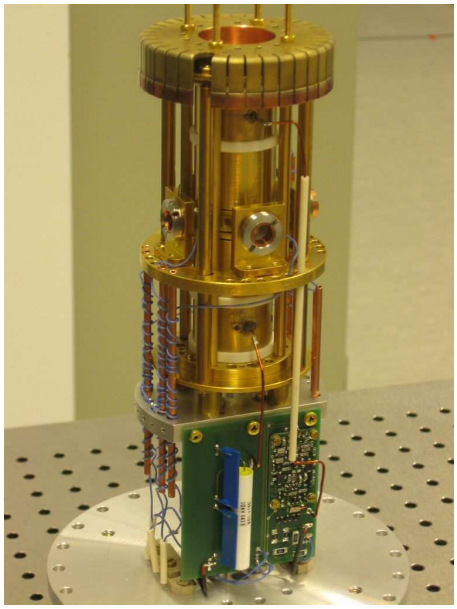

Figure 1: Overview of the SPECTRAP ion trap with the attached electronic components.

Below the SPECTRAP platform a fully functional laser laboratory was installed. It houses now a 1118-nm fibre laser system with two frequency doubling stages shown in Fig. 2 for laser cooling of Mg^+. After the two doubling stages, with approx. 500 mW of input power, up to 5 mW of 279 nm laser radiation was measured, which is guided upwards through the platform supporting the experimental setup into and through the magnet and the trap. Additional free space in the laboratory is designated for other laser experiments associated with HITRAP.

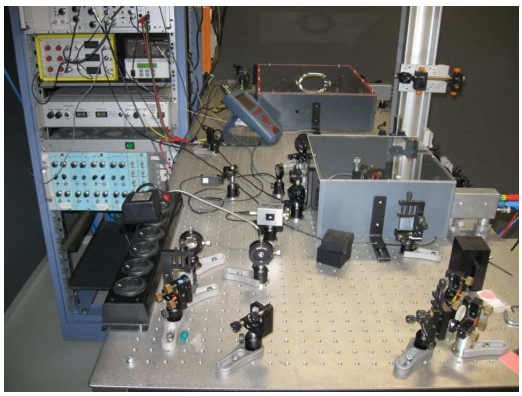

Figure 2: The fibre laser system for laser cooling of Mg ions, stationed in the new laser laboratory directly under the SPECTRAP platform.

The fluorescence detectors, prepared at the University of Münster, also went through final tests and will be incorporated into the system in January 2011. This will be followed by magnet cool-down and the first trapped ions. The results will demonstrate the feasibility of ion trapping and cooling in the SPECTRAP experimental setup, both by means of resistive and laser cooling. This will pave the way for further laser spectroscopy experiments with highly charged ions from the GSI accelerator facility and the EBIT.

References

[1] Z. Andjelkovic, S. Bharadia, B. Sommer, M. Vogel and W. Nörtershäuser, Hyp. Int. 196, 81 (2010)

[2] R. Cazan, C. Geppert, W. Nörtershäuser, R. Sanchez: Hyp. Int. 196, 177 (2010)

*Work supported by HGF under contract VH-NG-148 and BMBF grant 06DA414I.

LN2 cooled APD detector setup for SPECTRAP*

R. Jöhren[†1], *Z. Andjelkovic*[2,3], *D. Bonaventura*[1], *W. Buglak*[1], *V. Hannen*[1], *W. Nörtershäuser*[2,3], *R. Sánchez*[2,3], *and C. Weinheimer*[1] *for the SPECTRAP collaboration*

[1]WWU Münster, Institut für Kernphysik, Wilhelm-Klemm-Str. 9, 48161 Münster; [2]Johannes Gutenberg-Universität Mainz, Institut für Kernchemie, Fritz-Straßmann-Weg 2, 55128 Mainz; [3]GSI Helmholtzzentrum für Schwerionenforschung GmbH, Planckstr. 1, 64291 Darmstadt

The Institut für Kernphysik in Münster develops and characterizes detector systems capable of single-photon counting for the SPECTRAP experiment and related ESR measurements (E083). The wavelengths of interest range from the UV (244 nm) to the near infrared (1550 nm).

An APD detector setup for SPECTRAP

Avalanche Photo Diodes (APDs) of type S0223 manufactured by Radiation Monitoring Devices Inc. (RMD) will be used as detector at SPECTRAP to cover the wavelength region from 400 nm to 1100 nm. Test measurements described in [1] have shown, that these devices can reliably be operated near LN_2 temperature with a gain of about 8000 at 1480 V bias. We performed measurements to determine

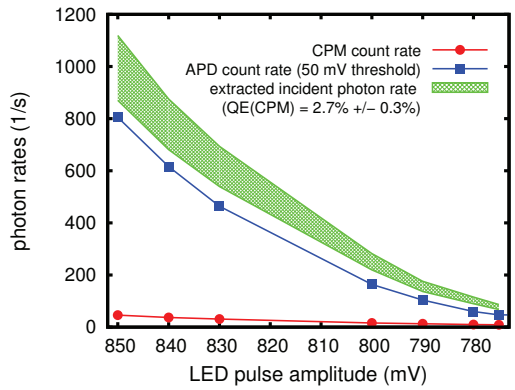

Figure 1: CPM count rates (red dots), resulting incident photon rates (green band) and APD count rates (blue squares) as a function of the LED pulse amplitude.

the single photon sensitivity of the APDs first in the visible regime. A 635 nm LED driven by 20 ns pulses with amplitudes between 775 mV and 850 mV at 100 kHz pulse rate was used as a single photon source. To calibrate the source, photons were counted by a CPM 1993 P channel photomultiplier manufactured by PerkinElmer, which will also be used at the SPECTRAP experiment for detection of fluorescence light down to 240 nm. Using the measured signal and background rates, we calculated the rate of photons incident on the CPM photocathode assuming a CPM quantum efficiency (QE) of $(2.7 \pm 0.3)\%$ at 635 nm. The measurement was repeated with the APD for different threshold settings between 240 mV and 50 mV. Results obtained for a 50 mV threshold are shown in Fig. 1. Comparing the count rate of the APD (blue squares) to the incident photon rate (green band), a photon detection efficiency (PDE) of $(68\pm7)\%$ can be extracted. This value is consistent with the QE quoted in the datasheet. A dark count rate of ca. 2000 cts/s was observed. Raising the threshold to 60 mV results in a dark count rate below 100 cts/s at a remaining PDE of ca. 50%.

First measurements with single photons at 1050 nm, prepared by a continuous light source and a grating spectrograph, delivered promising results with a preliminary PDE in the 10% range.

For use at SPECTRAP a detector chamber (see Fig. 2)

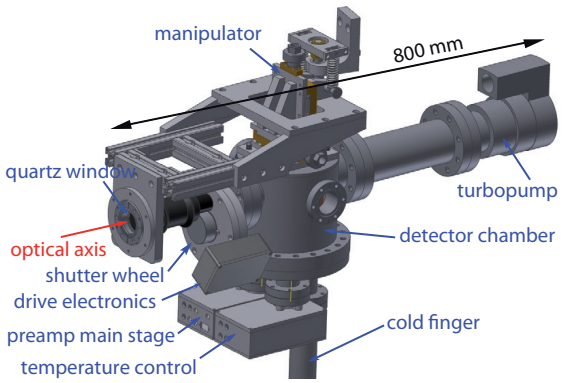

Figure 2: APD detector chamber.

with a special shutter wheel has been developed and is currently being build at the mechanics workshop in Münster.

Movable parabolic mirror system for the ESR

Updates and first results regarding the performance of the movable mirror system for HFS measurements in $^{209}Bi^{80+}$ at the ESR presented in last year's annual report [1, 2] can be found in [3] and in [4].

References

[1] R. Jöhren *et al.*, GSI Scientific Report 2009, AP-29

[2] M. Lochmann *et al.*, GSI Scientific Report 2009, AP-23

[3] R. López Coto, Master Thesis, Universität Münster, 2010.

[4] R. Sánchez *et al.*, this volume.

* Supported by BMBF under contract number 06MS9152I

† rjoehren@uni-muenster.de

Double-resonance spectroscopy of highly charged ions in a Penning trap

M. Vogel[1], *D. von Lindenfels*[1,2], *and W. Quint*[1,2]
[1]GSI, Darmstadt; [2]Ruprecht Karls-Universität Heidelberg

We have elaborated experimental schemes for the precise determination of electronic and nuclear magnetic moments by laser-microwave double-resonance spectroscopy of highly charged ions confined in a Penning trap [1, 2]. Spectroscopic properties of highly charged ions contain valuable information both about atomic and nuclear properties of these systems and open new ways to access fundamental quantities [3, 4]. Experimental approaches to precision spectroscopy especially of forbidden transitions are manifold with novel methods under implementation which also build a bridge between optical and microwave spectroscopy [5, 6, 7]. In doing so, they allow experimental links between transition frequencies and both electronic and nuclear magnetic moments of these ions.

The principle of the laser-microwave double resonance technique is to use fluorescence light from an optical hyperfine transition as a probe both for the laser excitation of the hyperfine transition and for the microwave excitation between corresponding Zeeman sublevels. An example of such a scheme (here: the $^{209}Bi^{82+}$ ion) is depicted in figure 1: after an initial population of a selected Zeeman sublevel (left), the optical transition between different F-levels is used as a probe for a MW-transition between Zeeman sublevels (right). The energy of the microwave

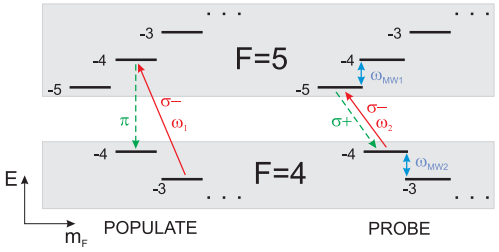

Figure 1: Spectroscopy scheme.

transitions directly yields the total magnetic moment (g_F-factor) of the ion in that F state. From two such magnetic moments belonging to different quantum numbers F, both the bound electron magnetic moment as given by its electronic g-factor g_J and the nuclear g-factor g_I of the ion can be expressed independently in terms of experimentally obtained values [1]. Such a measurement of atomic g_F-factors on the ppb level of accuracy allows a simultaneous and independent determination of the electronic g_J-factor and the nuclear g_I-factor on the ppb and ppm levels of accuracy, respectively. For the first time, precise values for nuclear magnetic moments can be inferred without the use of diamagnetic corrections, which currently limit the obtainably accuracy substantially. At the same time, diamagnetic shielding effects can for the first time be quantified in a spectroscopic measurement. This information may be used to benchmark corresponding theories. It furthermore allows stringent tests of theoretical values for g-factors as calculated in the framework of quantum electrodynamics of bound states in extreme electromagnetic fields.

To this end, a 7 Tesla superconducting magnet with a Penning trap designed for such spectroscopy has been set up in the framework of the HITRAP project. Decelerated highly-charged ions will be captured and confined in the Penning trap for spectroscopic studies nearly at rest. Figure 2 schematically shows the Penning trap design for

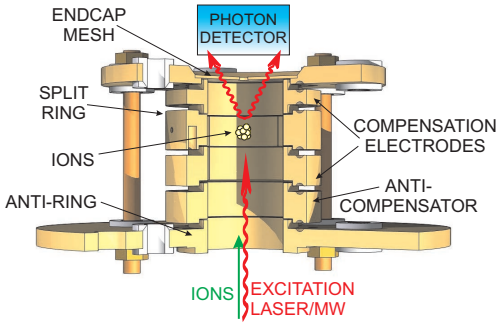

Figure 2: Halfopen Penning trap for spectroscopy of highly charged ions close to rest.

such a measurement. The trap components have been built and will be assembled and installed soon. Components for offline-tests on the fine structure of $^{40}Ar^{13+}$ ions have been designed and partially been built. Cyro-electronics for ion manipulation and detection are currently being built. A test setup for the characterization of such cryo-components has been set up and will be put into operation soon.

References

[1] W. Quint, D. Moskovkhin, V.M. Shabaev and M. Vogel, Phys. Rev. A **78** (2008) 032517.

[2] M. Vogel and W. Quint, J. Phys. B **42** (2009) 154016 and Europhysics News **40** 4 (2009) 15.

[3] M. Vogel and W. Quint, Physics Reports **490** (2010) 1-47.

[4] M. Vogel, Contemporary Physics **50** (2009) 437.

[5] M. Vogel and W. Quint, New J. Phys. **11** (2009) 013024.

[6] M. Vogel and W. Quint, Hyperfine Interactions **196** (2010) 93-105.

[7] M. Vogel, W. Quint and W. Nörtershäuser, Sensors **10** (2010) 2169.

A gas source at 4 Kelvin – injection and charge breeding simulations of Ar gas

M. Vogel[1], *C. Marzini*[2], *D. von Lindenfels*[1,3], *and W. Quint*[1,3]
[1]GSI, Darmstadt; [2]Hochschule Darmstadt; [3]Ruprecht Karls-Universität Heidelberg

We have designed and built a cold source for gases to be injected in cryogenic surroundings. It is based on a hollow metal structure with interior baffles which at cryogenic temperatures like presently 4 Kelvin act as a cryopump and prevent gas from flowing through, as depicted in figure 1. A resistive heating element is used to temporarily warm up the source to a well-defined temperature where adsorption to the inner surfaces is small enough for gas to flow through and in the present case enter an ionization chamber where the gas atoms are charge-bred in an electron beam to form highly charged ions [1].

We have performed simulations of the gas flow through the cold source as a function of temperature using the Molflow+ simulation software [2]. It allows to trace particle trajectories through a user-defined geometry when the gas pressure is in the molecular flow regime where only particle-wall interactions like adsorption and desorption are relevant. These processes depend on both the gas and wall temperatures as well as on the type of gas and wall material and have been taken into account appropriately [3]. Additionally, the subsequent charge breeding process by

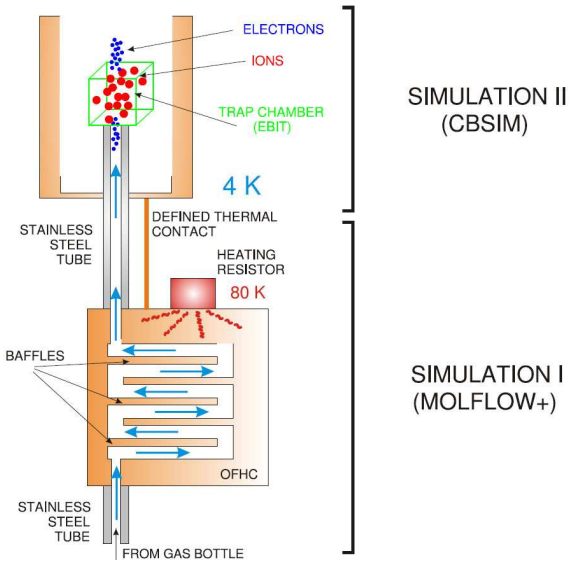

Figure 1: Schematic view of the cold gas source (bottom) and the attached ionization chamber (top) where the gas atoms are ionized by electron impact ionization. The structure shown is a few cm high.

electron impact ionization of the injected gas atoms by an attached mini-EBIS (miniature electron beam ion source) has been simulated by use of the CBSIM simulation software [4], see figure 2. The aim of the present study was to find the proper working parameters for an efficient production process of defined amounts of order 10^5 Ar^{13+} ions, which are going to be used in laser spectroscopy studies in the framework of the HITRAP project. We have found that a structure as depicted in figure 1 needs to be heated to about 200 K before gas output becomes significant enough for our subsequent electron impact ionization. The optimum electron beam energy has been found to be 1855 eV, about 2.7 times the ionization potential for Ar^{13+}.

This type of cold source attached to an EBIS-like ionizer will be installed in a 4-K-cryostat inserted into the warm bore of a superconducting magnet and will deliver highly charged ions for our Penning trap experiment [5].

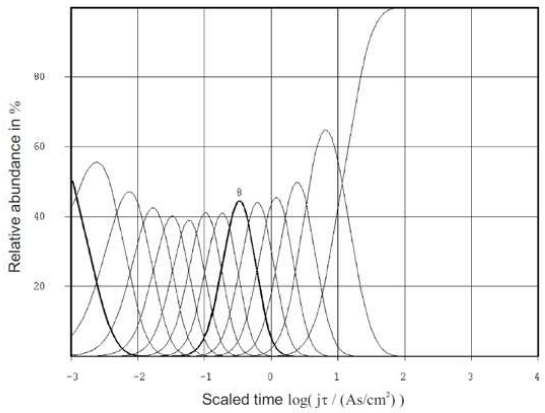

Figure 2: Example of a simulation result for optimal charge breeding of Ar^{13+} under the present experimental conditions.

Tests of the cold source will be undertaken soon using an offline cryocooler. Charge breeding tests will be performed during the upcoming year.

We thank E. Kammer, M. Müller and K. Dermati from the GSI technology lab for their excellent support.

References

[1] D. von Lindenfels, "Development of an Ion Trap Experiment for the Measurement of the Electron Magnetic Moment by Double-Resonance Spectroscopy", Diplomarbeit, Universität Heidelberg (2010).

[2] R. Kersevan and J.L. Pons, "Introduction to molflow+", AVS **27** (2009) 1017-1023.

[3] C. Marzini, "Simulationen zur optimalen Erzeugung von Argon in einer kryogenen Penningfallen-Apparatur", Praktukumsbericht, Hochschule Darmstadt (2010).

[4] O. Kester et al., private communication (2010).

[5] D. von Lindenfels, N. Brantjes, G. Birkl, W. Quint, V. Shabaev and M. Vogel, Can. J. Phys. **89** (2011) 79.

A Penning trap for multiphoton ionization studies in extreme laser fields

M. Vogel[1], *W. Quint*[1,2], *Th. Stöhlker*[1,2,3], *and G. Paulus*[4]

[1]GSI, Darmstadt; [2]Ruprecht Karls-Universität Heidelberg; [3]Helmholtz-Institut Jena; [4]Universität Jena

We are presently developing a Penning-trap based tool for advanced studies of multiphoton ionization of confined particles and other reactions by highly intense laser light. Particularly, ion manipulation techniques allow control over the particles' localization and spatial density. It is thereby possible to optimize the laser-particle interaction which is of special importance when laser foci are small. Non-destructive detection of reaction products in the trap supports advanced studies by maintaining the products for further studies at extended confinement times of up to hours. The interaction of highly intense radiation

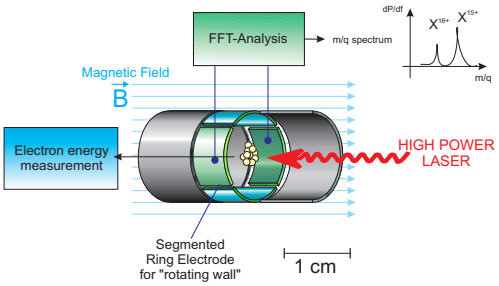

Figure 1: Schematic view of the open-endcap Penning trap with segmented ring electrode for non-destructive mass spectrometry.

with matter and the corresponding non-linear effects have been subject of lively research, both theoretical and experimental, especially in the infrared and visible photon energy regimes. Laser systems capable of producing high intensities also at photon energies in the EUV and (soft) X-ray regime open access to novel effects like non-linear Compton effects or simultaneous elastic and inelastic photon scattering, and allow multiphoton-ionisation experiments in a new domain. Recently, exceptionally strong non-linear photoionization has been observed using high-intesity EUV laser light and been connected with the excitation of collective giant resonances. However, most experiments have so far relied on time-of-flight mass spectrometry or related methods and have been unable to analyse the reaction products with high accuracy, nor were they able to select or prepare products for further studies in a well-defined way.

The present development is a Penning-trap-based experiment for the advanced investigation of multiphoton-ionisation of confined particles by highly intense laser light, e.g. from free-electron lasers, see figures 1 and 2. Focus is on control over the confined particles' localization and optimized overlap with the laser light by Penning trap techniques like the use of trap electrodes as "electrostatic tweezers" and by applying a "rotating wall", respectively. Also, the non-destructive detection of reaction products is a central property.

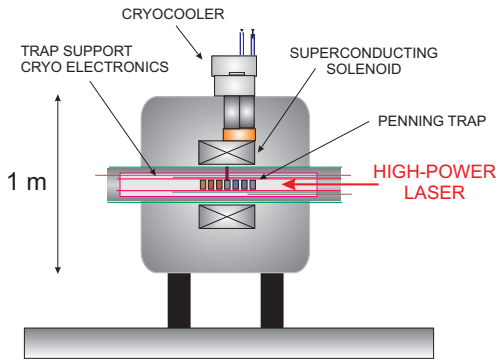

Figure 2: Schematic view of the setup. The Penning trap is located inside a horizontal superconducting magnet and traversed by the laser light. Cryogenic electronics is used for non-destructive spectrometry of confined mass and charge states.

As an application example, the FLASH laser facility at DESY, Germany, is currently capable of producing light down to 4.5 nm (275 eV) in pulses of few fs length with peak powers of around 5 GW with repetition rates of 10 Hz [1]. This laser has previously been used for example to perform soft X-ray laser spectroscopy on highly charged ions, photo-ionization studies [2], photo-dissociation of molecular ions, and in studies of the photoelectric effect at ultra-high intensities. As a user facility, FLASH is capable of providing light under well-controlled conditions to guest experimental setups like the present one. The same is true for the PHELIX laser at GSI, Darmstadt, which can be used for studies with highly charged ions from the HITRAP facility. The potential for further studies with the same setup at even more brilliant light sources is huge, both with regard to the current upgrades to FLASH, the POLARIS laser in Jena, the future XFEL facility [3] with photon energies up to 12.4 keV and other facilites [4].

References

[1] K. Tiedtke et al., New J. Phys. **11** 023029 (2009).

[2] M.C. Simon et al., Phys. Rev. Lett. **105**, 183001 (2010).

[3] XFEL technical design report at http://www.xfel.eu.

[4] W. Ackermann et al., Nature Photonics **1** 336 (2007).

Probing Correlated Ionization Dynamics at relativistic intensities with atomic ion beams

T. Rathje[1,2], A.M. Sayler[1,2], D. Hoff[1,2], S. Trotsenko[1,3], T. Stöhlker[1,3,4] and G.G.Paulus[1,2]

[1]Helmholtz-Institut Jena, D-07743 Jena, Germany;
[2]Institut für Optik und Quantenelektronik, Friedrich-Schiller-Universität Jena, D-07743 Jena, Germany;
[3]GSI Helmholtzzentrum für Schwerionenforschung, D-64291 Darmstadt, Germany;
[4]Physikalisches Institut, Ruprecht-Karls-Universität Heidelberg, D-69120 Heidelberg, Germany

Strong few-cycle lasers enable sequential ionization of more than one electron per optical half-cycle. Understanding these correlated electron ionization events is crucial in developing a model of ionization dynamics in few-cycle laser fields and describing the foundations of laser plasma generation [1]. We have developed an experimental setup capable of characterizing correlated ionization events (see Fig. 1). In our approach, ions from a fast cold ion beam are used as this eliminates several major experimental limitations that have hampered such studies in the past, most notably, ionization of background gas.

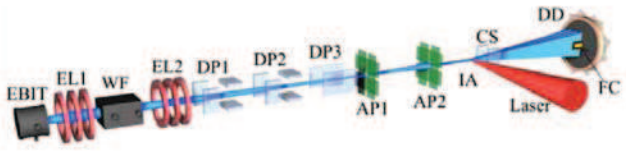

Figure 1: Experimental setup of the ion beam apparatus, which includes an electron beam ion trap (EBIT), two Einzel lenses (EL1, EL2), a Wienfilter (WF), three deflector plates (DF1, DF2, DF3), two adjustable pinholes (AP1, AP2), an interaction region (IA), a charge separator (CS), a faraday cup (FC) and a delay- line detector (DD). The laser beam is focused vertically linear polarized into the ion beam.

The beam is produced by an EBIT (Electron beam ion trap), which enables the investigation of ions in a wide range of charge states and opens the possibility of switching on and off correlations electron ionization by varying the initial charging slate. The sum momentum of the electrons as well as the final charge stale of the ion is determined by measuring the recoil of the parent nuclei on a time- and position-sensitive detector. Moreover, the use of an ion beam means that background ionization is spatially and temporally separated from events of interest and thus easily eliminated. Additionally, the use of laser fields with relativistic intensities eliminates the possibility of rescattering, thereby enabling a clean study of correlated sequential ionization even with linearly polarized light. These studies are expected to open up a new regime of collective ionization in which more than one electron is ionized during an optical half-cycle.

Figure 2: Existing experimental setup at Jena

Actual Status

During the year 2010 the ion beam apparatus was assembled at a laboratory at Jena. Since summer 2010 the ion source is in operation and the first test runs were started in fall. The main experimental target was the optimization of the ion beam density and profile. Spring 2011 the first ionization experiments are planned.

Publication

We have investigated the relative yields and momentum distributions of highly charged atomic ions produced by a short intense (10^{14} – $5{,}0\text{x}10^{18}$ W/cm^2) laser pulse using a Monte-Carlo simulation. We present numerical results as well as semi analytic estimates and scaling relations. A surprising result of our study is that the maximum (centroid) of the longitudinal ion momentum distribution shifts from zero momentum, even for pulses much longer than few-cycles provided the laser intensity is high enough. The magnitude of this shift is proportional to the field and inversely proportional to the pulse duration. This effect should be experimentally detectable for pulses with duration of 25-30 fs at FWHM. In addition, we have demonstrated that even for short pulses barrier-suppression ionization pays a minor role in the production of multiply charged ions due to the temporal variation of the laser field [1].

References

[1] N.I. Shvetsov-Shilovski, A. M. Sayler, T. Rathje, and G. G. Paulus, “Momentum distributions of sequential ionization generated by an intense laser pulse”, 2011 accepted to Phys. Rev. A.

Circular polarimetry of gamma-rays with tracking detectors

S. Tashenov[1,2]

[1]GSI, Darmstadt, Germany; [2]Stockholm University, AlbaNova University Center, Roslagstullsbacken 21, SE-10691 Stockholm, Sweden

Photon helicity - a projection of the photon spin on its momentum direction, also called circular polarization, can provide information about processes in which angular momentum and spin interactions play an important role. In particular it can be used in atomic, nuclear and particle physics to study effects of parity violation for testing the Standard Model of elementary particles [1]. In gamma-ray astronomy it might be able to distinguish stars and galaxies composed of matter and antimatter [2]. First measurements of circular polarization of gamma rays were performed in 1950's by exploiting Compton scattering off polarized electrons [3]. This technique, however, has a substantial limitation associated with the mandatory use of passive magnetized scattering targets. In particular it does not allow for gamma-ray imaging. Modern segmented imaging detectors which exploit the principles of gamma-ray tracking have a number of advantages over their older non-segmented counterparts. Gamma-ray tracking algorithms, which are developed for such detectors, reconstruct the sequence of the photon scatterings for the purposes of imaging, linear polarimetry and background reduction. Recently it was demonstrated that it is also possible to reconstruct the secondary gamma-ray tracks produced by the bremsstrahlung photons emitted by the Compton recoiled electrons [4]. This possibility opens up new perspectives for gamma-ray circular polarimetry.

Spin transfer in Compton scattering of a circularly polarized gamma-ray produces a polarized energetic recoiled electron from an initially unpolarized electron. While slowing down in the solid detector volume such an electron may emit bremsstrahlung. A transversally polarized electron emits photons asymmetrically to the left and to the right of the plane defined by its momentum and spin [5], see Fig.1. Therefore measurement of the left-right asymmetry of the emitted bremsstrahlung photons will yield the circular polarization measurement of the incoming photons.

For Compton scattering of circularly polarized photons off initially unpolarized electrons, the recoiled electrons obtain polarization [6]

$$P_q^{el} = -\frac{P_3^{ph}\sin^2\theta}{mc^2(1+\cos^2\theta)+(E_0-E_1)(1-\cos\theta)}\cdot \cdot\sqrt{\frac{mc^2(E_1mc^2-E_0mc^2+2E_1E_0)}{E_0-E_1+2mc^2}} \quad (1)$$

where P_3^{ph} is the degree of the incoming photon circular polarization in terms of the Stokes parameters and E_0 and E_1 are the incoming and the first scattered photon energies. The transverse polarization transfer reaches its maximum of $\approx 40\%$ when $\approx$1 MeV photons scatter on $\approx 70^\circ$.

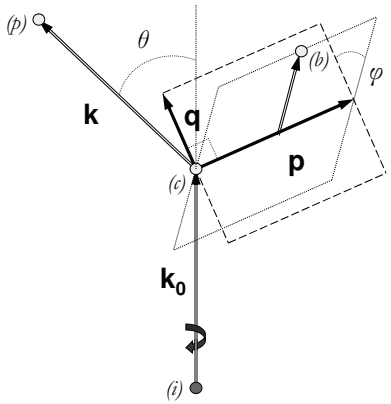

Figure 1: Momentum transfer in Compton scattering. $\mathbf{k_0}$ and $\mathbf{k}$ are the incoming and the scattered photon momenta; θ - Compton scattering angle; $\mathbf{p}$ - recoiled electron momentum; $\mathbf{q}$ - unit vector in the direction of the transversal electron spin component. Vectors $\mathbf{k_0}$, $\mathbf{k}$, $\mathbf{p}$ and $\mathbf{q}$ lie in the reaction plane; *(i)* - incoming photon origin; *(c)*,*(p)* - incoming photon interaction points; *(b)* - bremsstrahlung photoabsorption point; φ angle of the bremsstrahlung photon direction with respect to the reaction plane.

The bremsstrahlung cross section can be written in the following way

$$d\sigma(E,E_b,\psi,P_q^{el},\varphi) = d\sigma_0(E,E_b,\psi)\cdot \cdot\left[1+P_q^{el}\sin\varphi\, C_{20}(E,E_b,\psi)\right] \quad (2)$$

where E - electron kinetic energy, E_b - bremsstrahlung photon energy, ψ - photon emission angle, and C_{20} is the correlation coefficient which is responsible for the left-right asymmetry. In order to obtain the incoming photon circular polarization P_3^{ph}, the energy-angular distribution of the bremsstrahlung events has to be fitted using the Eq. 1 and Eq. 2.

This technique can be naturally integrated into a concept of gamma-ray telescope which would allow for imaging spectropolarimetry. The absence of the magnet can also be useful in atomic and nuclear physics experiments with ion beams. Further work is required to test this technique using the real data from the gamma-ray tracking detectors.

References

[1] E.G. Adelberger, Ann. Rev. Nucl. Part. Sci. 35 (1985) 501.

[2] J.G. Cramer, Phys. Rev. Lett. 39 No.17 (1977) 1104.

[3] H. Schopper, Nucl. Inst. 3 (1958) 158.

[4] S. Tashenov, J. Inst., 5 (2010) P10004.

[5] H.K. Tseng, R.H. Pratt, Phys. Rev. A 7 No.5 (1973) 1502.

[6] F.W. Lipps, H.A. Tolhoek, Physica 20 (1954) 395.

Characterization of the Dresden EBIS-A as a charge breeder

A. Thorn[*1], *R. Mertzig*[1], *E. Ritter*[1], *L. Bischoff*[2], *F. Herfurth*[3], *O. Kester*[3], *W. Pilz*[2], *F. Ullmann*[4], *and G. Zschornack*[1]

[1]Fachrichtung Physik, Technische Universität Dresden, Germany; [2]Helmholtzzentrum Dresden-Rossendorf, Germany; [3]GSI Helmholtzzentrum für Schwerionenforschung, Darmstadt, Germany; [4]Dreebit GmbH, Dresden, Germany

Highly charged ions (HCIs) are important tools in various fields of basic and applied research. However, the species of interest cannot always be directly produced by a primary ion source. Therefore, 'charge breeding' has become an important technique applied, e.g., in nuclear physics experiments with post-accelerated radioactive beams or high-precision ion mass measurements.

The machines commonly used in such experiments are high-power cryogenic electron beam ion sources (EBIS) [1, 2]. In 2009, we presented results showing that charge breeding is also possible with room-temperature electron beam ion traps of the Dresden EBIT type [3, 4] which opens up new possibilities for designing compact, resource efficient, relatively inexpensive charge breeding setups. In this report, we present follow-up measurements using the Dresden EBIS-A as a charge breeder. Like the EBIT, it is based on permanent magnet technology, yet, it has a higher trap capacity and a larger ion output per pulse [5]. We have investigated the electron beam properties as well as its performance in breeding highly charged Au ions.

Figure 1 shows the projection of an X-ray image of the electron beam region of the EBIS for typical operating parameters by which the radial electron distribution can be investigated (for details on the experimental method see [3]). Using the two common theoretical assumptions, box-shaped and gaussian radial distribution, fits result in characteristic radii of $r = 131\mu$m and $r_{80\%} = 137\mu$m, respectively. The best agreement is reached using an average of the two for which an electon current density of $j_e = 125 \pm 30 \mathrm{A/cm}^2$ can be given.

The electron current density can be used to estimate the required ionization time τ_q for a charge state q according to

$$\tau_q \approx \frac{1}{j_e} \sum_{k=1}^{q} \frac{1}{\sigma_k}, \qquad (1)$$

where σ_k are the single ionization cross sections from one charge state to the next. Estimated values are in reasonable agreement with the measurement for charge bred Au ions presented in figure 2.

The charge breeding measurements were performed using an injection setup and scheme similar to the one described in [4]. The Au^{1+} ions were produced by a AuGe liquid metal alloy ion source [6]. Breeding efficiencies into individual charge states were on the order of 10^{-5} due to the limited accuracy of 10 ms for the timing of the injection. Previously reached efficiencies for K^{q+} breeding with the EBIT were in the same order of magnitude, so was the measured ionization factor. Advantages for the EBIS-A compared to the EBIT can be found in its trap capacity which was measured to be one order of magnitude higher than for the EBIT. In the future, more detailed efficiency investigations for both sources as well as emittance measurements will be presented.

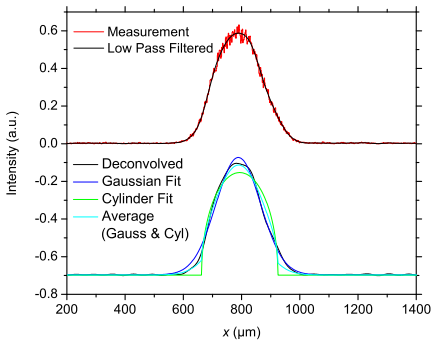

Figure 1: Upper lines: 1D-projection of an X-ray image of the electron beam region (raw data and low-pass filtered). Lower lines: Result of the deconvolution to eliminate slit width influence and several fits to determine the radial electron distribution.

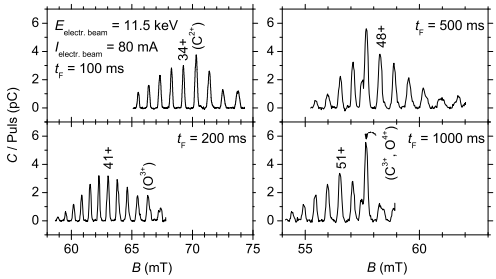

Figure 2: Magnet scans of charge bred Au ion pulses from the EBIS-A for various ionization times t_F.

This work is supported by the GSI R&D cooperation project DD.ZSCH.

References

[1] S. Nagy et al.: Eur. Phys. J. D 39 (2006) 1

[2] F. Wenander et al.: Nucl. Instr. and Meth. B 266 (2008) 4346

[3] A. Thorn et al.: JINST 5 (2010) C09006

[4] A. Sokolov et al.: JINST 5 (2010) C11001

[5] G. Zschornack et al.: Rev. Sci. Instrum. 79 (2008) 02A703

[6] L. Bischoff: Nucl. Instr. and Meth. B 266 (2008) 1846

* a.thorn@hzdr.de

Progress Report on the Ultra-low Energy Storage Ring Project*

O. Gorda[1,2], J. Harasimowicz[4,5], O. Karamyshev[1-3], G. Garamysheva[1-3], A. Papash[1-3], M. Putignano[4,5], M.R.F. Siggel-King[4,5], and C.P. Welsch[4,5,#]

[1]GSI, Darmstadt, Germany; [2]Max Planck Institute for Nuclear Physics, Heidelberg, Germany;
[3]JINR, Dubna, Russia; [4]Cockcroft Institute, Warrington, UK; [5]University of Liverpool, Liverpool, UK

The research of the QUASAR Group focuses on the development of several key components of the ultra-low energy storage ring (USR) at the facility for low-energy antiproton and ion research (FLAIR). This includes the design of the storage ring in view of a future TDR, studies into the ring's beam dynamics, the design of an in-ring gas jet target for use as a two dimensional beam profile monitor, as well as the development of beam diagnostics elements for the full characterization of the stored beam. The understanding of the beam dynamics in electrostatic rings was significantly advanced in 2010 and prototypes of all diagnostics elements have now been built up.

Beam Dynamics Studies

In order to fulfil the requirements from the envisaged experiments on the characteristics of the stored and extracted antiproton beams, a complete re-design of the USR was realized in 2009. The resulting split-achromat lattice had not been proposed for any electrostatic storage ring. It allows for capturing a rather large and un-cooled antiproton beam from the low energy storage ring (LSR) at 300 keV, beam cooling and deceleration to 20 keV, features a special short bunch operation mode and was designed to incorporate slow and fast extraction. Based on this layout, the detailed design of a combined fast and slow extraction system was worked out in 2010 [1]. The slow extraction system relies on the use of a third-integer resonance and knock-out extraction using an rf field, exciting beam oscillations with a frequency that is resonant to a harmonics of the betatron frequency. Different positions of the sextupole elements used for phase space distortion have been analyzed as part of the optimization process. The USR will be the first electrostatic storage ring that features such extraction.

As essentially all accelerator design codes do not readily foresee the use of electrostatic elements, new simulation tools had to be developed to study the USR beam dynamics in detail. This included the development of a three-dimensional model of an entire electrostatic ring in OPERA to investigate its real field distribution and the effect of fringe fields. MAD-X studies showed the dependence of the dynamic aperture from the ion optical elements used in the ring and explained experimental beam losses at the storage ring ELISA. A more than a factor of 5 reduction in dynamic aperture in a configuration relying on spherical electrodes, rather than cylinder electrodes [2] led to significantly reduced beam life times.

With the aim to optimize the performance of the planned in-ring collision experiments, studies into the lateral beam spread on the residual gas and the internal target were carried out as part of the optimization process for in-ring collision studies with a so-called reaction microscope.

To complement the USR studies, a small electrostatic ring has been designed and developed in collaboration with the groups of J. Ullrich, H. Knudsen and Y. Yamazaki. This small fixed-energy electrostatic ring is a prototype of the USR for storing antiprotons at energies between 3-30 keV and uses similar ion optics elements and beam diagnostics.

Beam Diagnostics

The beam instrumentation for the commissioning phase of the USR with proton/H^- beams was developed, as well as specialized diagnostics for the operation with antiproton beams. This was a focus of the Group's work in 2010. For non-destructive beam position determination, up to eight capacitive pick-ups (PUs) will be installed at the USR. The expected weak signals require the use of high input resistance, high gain/low noise amplifiers, together with a narrowband processing system. A prototype pickup has been developed and built up and is presently being prepared for tests in a purpose-built test stand. A scintillator-based monitor will provide information on the transverse beam profile. For similar applications, limited sensitivity and decreased light yield due to surface sputtering had been reported previously. The Group carried out experiments with low energy and low intensity proton beams at INFN-LNS. The possibility for monitoring beams at intensities and energies comparable to those expected at FLAIR was successfully demonstrated [3]. In addition to the above monitors, an ionization beam profile monitor relying on a supersonic gas-jet, shaped into an extended thin curtain, was developed. Detailed investigations into the process of gas jet formation have been realized and indicated ways to control the jet properties [4]. All parts of the jet and experimental chambers have been manufactured and first experimental tests were started.

References

[1] G.A.Karamishev, et al., "Study of Slow and Fast Extraction for the Ultralow Energy Storage Ring USR", Particle Physics and Nuclei Letters, *accepted* (2010)

[2] A.I. Papash, et al., "Simulation of Space Charge Effects in Low-energy Electrostatic Storage Rings", Proc. IPAC, Kyoto, Japan (2010)

[3] J. Harasimowicz, et al., "Scintillating Screens Sensitivity and Resolution Studies for Low Energy, Low Intensity Beam Diagnostics", Rev. Sci.Instr. **81** (9) (2010)

[4] M. Putignano, et al., "Optimization Studies of Planar Supersonic Gas Jets for Beam Profile Monitor Applications", Proc. IPAC, Kyoto, Japan (2010)

* Work supported by GSI/HGF under contract VH-NG-328, EU contract PITN-GA-2008-215080 and STFC.

carsten.welsch@quasar-group.org

The nuclear anapole moment in polarized helium-like highly-charged ions*

A. Bondarevskaya[1], *A. Prozorov*[1], *L. Labzowsky*[1,2], *G. Plunien*[3], *D. Liesen*[4], *and F Bosch*[4]

[1]St.Petersburg State University, St. Petersburg, Russia; [2]Petersburg Nuclear Physica Iinstitute, 188300 Gatchina, St.Petersburg, Russia; [3]Technische Universität Dresden, Germany; [4]GSI Darmstadt, Germany

He-like HCI provide an unique opportunity to observe a net nuclear spin-dependent P-odd effect due to the near-degeneracy of the 2^1S_0 and 2^3P_1 levels for the nuclear charge numbers close to Z = 32. This degeneracy has been discussed for the first time in connection with an attempt to estimate the nuclear spin-dependent PNC effect in the HFQ transitions in He-like HCI within the framework of the electroweak theory [1]. In [1] it was assumed that the observation of circularly polarized x rays could be possible. Later in [2] it was proposed to measure the angular asymmetry of the radiation of a polarized ion beam due to the contribution of the nuclear anapole moment to the HFQ decay of the metastable 2^1S_0 level.

The PNC nuclear spin-dependent interaction of an atomic electron with the nucleus can be written in the form [3]

$$\hat{H}_W^{(2)}(\vec{r}) = \frac{G_F}{\sqrt{2}} \frac{K(\vec{I}\vec{\alpha})}{I(I+1)} \kappa \rho(r)\,, \qquad (1)$$

where $\vec{I}$ is the nuclear spin, $K = (I+1/2)(-1)^{I+1/2-l}$ with l being the orbital angular momentum of a valence nucleon, $\vec{\alpha}$ are the Dirac matrices. The dimensionless constant κ in Eq. (1) consists of three terms [2]:

$$\kappa = \kappa_a + \frac{1/2-K}{K}\kappa_2 + \frac{I+1}{K}\kappa_H\,, \qquad (2)$$

where κ_a denotes the contribution of the nuclear anapole moment [4] and the constant κ_2, which for unpaired protons and neutrons is determined by $\kappa_{2p} = -\kappa_{2n} = -\frac{1}{2}(1-4sin^2\theta_W) \times 1.25 = -0.047$, is due to the weak neutral-current interaction of an electron with the spin of a nucleus [3]. The constant κ_H is due to the coupling of the nuclear spin-independent weak electron-nucleus interaction with the magnetic hyperfine interaction.

For the $2^1S_0 \to 1^1S_0$ HFQ M1 transition in He-like ions the evaluation yields

$$dW_{2^1S_0\to 1^1S_0} = dW^{M1}_{2^1S_0\to 1^1S_0}[1 + a_F P_2(\cos\theta)C + \lambda_F(\vec{\zeta}\vec{\nu})R_2^a]\,, \qquad (3)$$

where a_F defines the "degree of alignment" and can be expressed as $a_F = \sum_{M_F} n_{FM_F} M_F^2 - a_F^0$, where a_F^0 is given by $a_F^0 = \sum_{M_F} \frac{1}{2F+1} M_F^2 = \frac{1}{3}F(F+1)$, θ is an angle between the directions of the ion polarization ζ and the photon emission ν, P_2 is the Legendre polynomial, $\lambda_F = \frac{1}{F}\sum_{M_F} n_{FM_F} M_F$ the degree of polarization and the coefficient $C = C(F,F')$ is given by

$$C = \frac{(-1)^{F+F'+1}\,\Pi_{2\,F}\Pi_1^3 \left\{ \begin{array}{ccc} 1 & F' & F \\ F & 2 & 1 \end{array} \right\}}{\sqrt{(2F-1)F(F+1)(2F+3)}\;\Pi_{1/2}} \qquad (4)$$

and the coefficient R_2^a by

$$R_2^a = \frac{i\langle FIJ\|\hat{H}_{\rm W}^{(2)}\|FI\tilde{J}\rangle}{\Delta E} \frac{R_{E1}(2\tfrac{1}{2}1;1\tfrac{1}{2}0)}{R_{M1}(2\tfrac{1}{2}0;1\tfrac{1}{2}0)} \times \frac{(-1)^{F'+F}\frac{\Pi_{F1/2}\Pi_1^3}{\sqrt{F(F+1)}} \left\{ \begin{array}{ccc} 1 & F' & F \\ F & 1 & 1 \end{array} \right\} \Delta E_S}{e(-1)^{I+J+F}\Pi_{IJ} \left\{ \begin{array}{ccc} J'' & I & F \\ I & J & 1 \end{array} \right\} \langle J\|A_e^1\|J''\rangle_S \langle I\|A_N^1\|I\rangle}\,. \qquad (5)$$

Here I, J are the nuclear and the total electron angular momenta, FM_F is the total angular momentum of an ion and its projection, $\langle J\|A_e^1\|J''\rangle_S$ and $\langle I\|A_N^1\|I\rangle$ are the reduced matrix elements for the nuclear vector $\vec{A}_N = \mu_N g_N \vec{I}$ and electron vector $\vec{A}_e = -e\sum_{i=1}^2(\vec{\alpha}_i \times \vec{r}_i)\frac{1}{r_i^3}$, $R_{E1}(2\frac{1}{2}1;1\frac{1}{2}0)$, $R_{M1}(2\frac{1}{2}0;1\frac{1}{2}0)$ are the reduced matrix elements for the electric and magnetic dipole transitions and the standard notations for the $6j$-symbols are used. Finally, ΔE is the energy between the levels 2^1S_0 and 2^3P_1 mixed by the weak interaction; ΔE_S is the difference between the levels 2^1S_0 and 2^3S_1.

For the particular case of the transition $2^1S_0 \to 1^1S_0$ via the admixture of the 2^3P_1 state by the weak interaction $\hat{H}_W^{(2)}$ the expression in Eq. (5) coincides with the coefficient R_2^a evaluated in [2]. The second term on the right-hand side of Eq. (3) was not mentioned in [2]. In principle, this term provides an opportunity to measure the alignment (or to check the maximum polarization) in a rather simple way: just measure the angular dependence of HFQ transitions for polarized or aligned HCI. In order to determine a_F one has to measure dW^{HFQ} for two different angles: $[dW^{HFQ}(\theta=0) - dW^{HFQ}(\theta=\pi/2)]/dW_0^{HFQ} = -\frac{18}{35}a_F$.

* Work supported by GSI

References

[1] V.G. Gorshkov and L.N. Labzowsky, Zh. Eksp. Teor. Fiz. Pis'ma **19**, 768 (1974) [Sov. Phys. JETP Lett. **19**, 394 (1974)]

[2] A.V. Nefiodov, L.N. Labzowsky, D. Liesen, G. Plunien and G. Soff, Phys. Lett. B **534**, 52 (2002)

[3] I.B. Khriplovich, Parity Nonconservation in Atomic Phenomena, Gordon and Breach, London (1991)

[4] V.V. Flambaum and I.B. Khriplovich, Zh. Eksp. Teor. Fiz. **79**, 1656 (1980) [Engl. Transl. Sov. Phys. JETP **52**, 835 (1980)]

Atomic Parity-Violation in Highly-Charged Ions*

F. Ferro[†1,2], *A. Artemyev*[1,2], *A. Surzhykov*[1,2], *and T. Stöhlker*[1,2,3]

[1]GSI, Darmstadt, Germany; [2]Heidelberg University, Germany; [3]Helmholtz-Institut Jena, Germany

The investigation of parity-violation (PV) in forbidden atomic transitions is an active and fundamental research area, especially for its implications on the physics beyond the Standard Model [1]. Atomic transitions may be employed to study PV effects originating from weak neutral currents, i.e. due to the exchange of a Z^0 boson between a nucleon of the nucleus and a bound electron.

Experiments with He-like heavy ions in interaction with high-intensity polarized lasers have the potentiality to further increase the measurement accuracy reached so far. The facilities of GSI, combining the Experimental Storage Ring (ESR) together with the Petawatt High-Energy Laser for Heavy-Ion Experiments (PHELIX) and taking advantage of the precision spectroscopy techniques available for highly-charged ions, offer suitable conditions for future PV experiments.

The PV Hamiltonian H_{PV}, due to its pseudoscalar structure, may mix atomic levels of opposite parity $|\pm\rangle$. This results in a state of non-definite parity $|+\rangle + i\eta|-\rangle$, with

$$i\eta = \frac{\langle -|H_{PV}|+\rangle}{E_+ - E_-}, \qquad (1)$$

that gives rise to observable forbidden transitions [2].

A precise theoretical knowledge of the energy splitting $\Delta E \equiv E_+ - E_-$, including its isotopic dependence, is the starting point for the design of any forthcoming experiment. In fact, as it straightforwardly follows from Eq. 1, energy degeneracy can amplify the evanescent PV mixing coefficient η. Since, among the first excited levels of He-like ions, $2\,^1S_0 \equiv 1s2s\,^1S_0$ and $2\,^3P_0 \equiv 1s2p\,^3P_0$ are closely-lying in energy in ions with atomic number $54 \leq Z \leq 93$ [3], we performed a calculation of electron correlations for several isotope in this Z-interval.

Our theoretical treatment is based on relativistic many-body perturbation theory to all-orders, as a mean to treat electron-electron correlations. We found [4] that $2\,^1S_0 - 2\,^3P_0$ degeneracy occurs in the stable isotopes $A = 155, 156$ of gadolinium ($Z = 54$), and in the radioactive isotopes $A = 219, 220$ of protoactinium ($Z = 91$), as shown in Fig. 1. He-like ^{238}U, with $\Delta E = 2.793$eV, represents an excellent alternative to the short-lived protoactinium ($\tau = 2.9$ms), thanks to the significant overlap between its atomic wave-functions and the nucleus, which implies a large matrix element $\langle -|H_{PV}|+\rangle$.

Among several proposed experimental set-ups, the PV mixing can be measured by means of a stimulated two-photon $2E1$ transition from state $2\,^1S_0$ to $2\,^3P_0$, induced by a polarized laser-light. In this specific case, the two levels must not be degenerate; Rather, their separation should match twice the energy of the photons employed. Limits for optical spectroscopy are evidenced by dashed lines in Fig. 1.

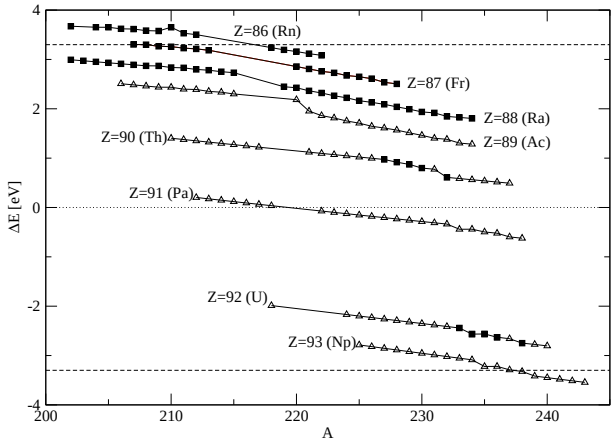

Figure 1: Isotopic shift of $\Delta E = 2\,^1S_0 - 2\,^3P_0$ energy splitting in actinide ($86 \leq Z \leq 93$) He-like ions with mean life $\tau > 1$ms. Filled squares represent nuclides whose nuclear radius has been experimentally measured, while empty triangles represent nuclides with interpolated nuclear radius. Horizontal dashed lines at ± 3.306eV show the limits for $2E1$ optical $2\,^1S_0 \rightarrow 2\,^3P_0$ transitions. This figure is taken from Ref. [4].

We found [4] that the He-like isotopes of radon ($Z = 86$) with $A \leq 212$ and the one isotope of francium ($Z = 87$, $A = 207$) allow using laser light in the optical regime. We should mention that also the transuranic isotope of neptunium ($Z = 93$) with $A \geq 237$ offers these conditions, and is long-lived ($\tau = 2 \cdot 10^6$yr).

The required extremely high laser intensity $I \sim 10^{21}$W/cm^2 makes PV experiments with heavy-ions not yet feasible. Nevertheless high-power laser facilities (e.g. PHELIX) are getting closer to the required conditions.

References

[1] J. S. M. Ginges and V. V. Flambaum, Phys. Rep. **397** 63 (2004).

[2] I. B. Khriplovich, "Parity Nonconservation in Atomic Phenomena", Gordon and Breach Science Publishers, Philadelphia, 1991.

[3] F. Ferro *et al.*, Journal of Instrumentation **5** C08006 (2010).

[4] F. Ferro *et al.*, Phys. Rev. A **81** 052112 (2010).

* Work supported by the Helmholtz association under the project VH-NG-421, and by the ExtreMe Matter Institute EMMI in the framework of the Helmholtz Alliance HA216/EMMI

† f.ferro@gsi.de

Effect of the parity nonconservation with laser-induced $2^3S_1 - 2^1S_0$ transitions*

V. M. Shabaev[1,2], *A. V. Volotka*[1,3], *C. Kozhuharov*[2], *G. Plunien*[3], *and Th. Stöhlker*[2,4,5]

[1]St. Petersburg State University, Russia; [2]GSI, Darmstadt, Germany; [3]Technische Universität Dresden, Germany; [4]Universität Heidelberg, Germany; [5]Helmholtz-Institut Jena, Germany

Investigations of parity nonconservation (PNC) effects with heavy few-electron ions can provide new opportunities for tests of the Standard Model in the low-energy regime. This is mainly due to the fact that, in contrast to neutral atoms, in highly charged ions the electron-correlation effects are suppressed by a factor $1/Z$ and, therefore, can be accounted for by perturbation theory to a high accuracy. Theoretical investigations of the PNC effects with highly charged ions started with Ref. [1], where it was proposed to use the close opposite-parity levels 2^1S_0 and 2^3P_1 in He-like ions for $Z \approx 6$ and $Z \approx 29$. Various scenarios appeared later (see, e.g., Ref. [2]) which exploited the near-degeneracy of the 2^1S_0 and 2^3P_0 states in He-like ions at $Z \approx 64$ and $Z \approx 90$, where the PNC effects are strongly enhanced.

Here we report the recently suggested scenario [3], where it has been proposed to consider the PNC effect on the laser-induced $2^3S_1 - 2^1S_0$ transitions in heavy He-like ions nearby $Z = 64$ (transition energy of about 114 eV) and $Z = 90$ (transition energy of about 240 eV). Because of the large transition energies, until recently experiments with laser-induced $2^3S_1 - 2^1S_0$ transitions in heavy He-like ions were far from being possible. However, the situation has changed in view of the very significant progress in X-ray laser development. Already now, first X-ray lasers, where photon energies of up to 200 eV can be reached, are getting developed at the PHELIX facility at GSI [4] as well as at the Helmholtz-Institute in Jena. As an alternative scenario, the excitation energy can be obtained by counter-propagating the ultraviolet laser beam with the photon energy in the range from 4 to 10 eV and the He-like ion beam with the energy up to 10.7 GeV/u, which will be available at the FAIR facility in Darmstadt [5].

The cross section for the absorption of a photon with nearly resonant energy $\omega \approx E_{2^1S_0} - E_{2^3S_1}$ and a circular polarization $\lambda = \pm 1$ by a heavy heliumlike ion being initially prepared in the 2^3S_1 state can be written as

$$\begin{aligned} \sigma^{(2^3S_1 \to 2^1S_0)} &= \sigma_0^{(2^3S_1 \to 2^1S_0)} + \sigma_{\rm PNC}^{(2^3S_1 \to 2^1S_0)} \\ &= (1 + \lambda\varepsilon)\sigma_0^{(2^3S_1 \to 2^1S_0)}, \end{aligned} \qquad (1)$$

where ε is a parameter which characterizes the relative value of the PNC effect. Utilizing the rigorous formulas for the first-order interelectronic-interaction and QED corrections to the transition amplitudes we have shown that for the $E1$ transition between degenerate levels $(2s, 2p_{1/2})$ these corrections can be accounted for within the zeroth-order approximation in the length gauge, provided the transition energy includes the corresponding corrections. Taking this in account, we derive a simple analytical formula for the PNC correction [3],

$$\varepsilon = -2\xi \frac{3(1+\gamma)\sqrt{1+2\gamma}}{\alpha Z(\sqrt{2(1+\gamma)} - 2\gamma)}, \qquad (2)$$

where $\gamma = \sqrt{1-(\alpha Z)^2}$ and ξ is the PNC mixing parameter.

Table 1: The zeroth-order cross section $\sigma_0^{(2^3S_1 \to 2^1S_0)}$, the PNC correction $\sigma_{\rm PNC}^{(2^3S_1 \to 2^1S_0)}$, and the parameter ε, for the laser-induced $2^3S_1 \to 2^1S_0$ transition in He-like Gd and Th. The cross sections are given in barn.

Ion	$\sigma_0^{(2^3S_1 \to 2^1S_0)}$	$\sigma_{\rm PNC}^{(2^3S_1 \to 2^1S_0)}$	ε
$^{158}Gd^{62+}$	4084.1	± 2.1	-0.00051
$^{232}Th^{88+}$	1217.6	± 0.6	-0.00053

The $2^3S_1 - 2^1S_0$ transition energies are taken from Ref. [6], while for the $2^3P_0 - 2^1S_0$ energies we use conservative estimate $0.074(74)$ eV for Gd and $0.44(40)$ eV for Th. The widths of the levels 2^1S_0 and 2^3S_1 have been calculated within the systematic perturbative QED approach. The results of the calculations for Gd and Th are presented in Table 1. As one can see from the table, in both Gd and Th cases the PNC effect amounts to about 0.05%, which is a rather large value for parity-violation experiments.

The PNC effect is to be measured by counting the intensity difference in the 2E1 decay of the 2^1S_0 state for photon polarizations $\lambda = \pm 1$. The background emission can be separated by switching off the laser light. Changing the photon energy allows one to eliminate the interference with a non-resonant transition via the 2^3P_0 state, which could also be evaluated to a good accuracy if necessary. Moreover, since the 2E1 emission can be measured relative to the intensity of the M1 X-ray line (decay of the 2^3S_1 state), such an experimental scenario appears to be quite realistic.

* Work supported by DFG and GSI

References

[1] V. G. Gorshkov and L. N. Labzowsky, JETP Lett. **19**, 394 (1974); Sov. Phys. JETP **42**, 581 (1975).

[2] L. N. Labzowsky *et al.*, Phys. Rev. A **63**, 054105 (2001).

[3] V. M. Shabaev *et al.*, Phys. Rev. A **81**, 052102 (2010).

[4] V. Bagnoud *et al.*, Appl. Phys. B **100**, 137 (2010).

[5] Th. Stöhlker *et al.*, Nucl. Instr. Meth. Phys. Res. B **261**, 234 (2007).

[6] A. N. Artemyev *et al.*, Phys. Rev. A **71**, 062104 (2005).

Quantum correlations in the two–photon decay of heavy helium–like ions*

F. Fratini[1,2], *A. Surzhykov*[†1,2], *T. Jahrsetz*[1,2], *M. Tichy*[3], *A. Buchleitner*[3], *and S. Fritzsche*[2,4]

[1]University of Heidelberg, Germany; [2]GSI, Darmstadt, Germany; [3]University of Freiburg, Germany; [4]University of Oulu, Finland

Studies on the two-photon transitions in atomic systems have a long tradition, going back to the 1930's. Originally focused on the decay of the light atoms and ions, the interest in these investigations has recently shifted towards the high-Z domain. For instance, a series of experiments were performed recently at the GSI storage ring to explore the two-photon decay of helium-like uranium U^{90+} ions [1]. Until now these experiments were restricted to the total and energy-differential rates. Owing to the recent advances in x–ray detector technologies, however, the photon-photon angular and *polarization* correlations are also likely to be observed in the future. Analysis of these correlations will reveal important information on the relativistic, many–body and parity non–conservation phenomena in heavy atomic systems [2].

Beside atomic structure-related studies, $\gamma - \gamma$ polarization correlations in the two–photon decay may provide a route to probe fundamental aspects of modern quantum theory. For example, two–photon decay of low–Z atomic systems has been employed to test the Bell inequality and, hence, to prove that nature does exhibit quantum-mechanical non-locality [3]. For heavy few–electron species such polarization–resolved studies are likely to be performed in the future at the GSI facility. A proper analysis of (polarization) quantum correlations in high–Z domain requires, however, detailed knowledge of relativistic and of many-electron effects, as well as of those contributions that arise from the higher–order terms in the expansion of the electron-photon interaction.

In this contribution, we have performed theoretical analysis of the quantum correlations between the polarization states of two photons emitted in the decay of helium–like ions. Based on the relativistic, second–order perturbation approach and density matrix theory, detailed calculations have been performed for the degree of *entanglement* (given by the concurrence measure $\mathcal{C}$) for the $1s2s\,^1S_0 \to 1s^2\,^1S_0$ and $1s2p\,^3P_0 \to 1s^2\,^1S_0$ two–photon transitions [4]. For these two transitions in helium–like uranium U^{90+} we display in Fig. 1 the concurrence measure as a function of the opening angle between the photons. The predictions have been obtained for the *energy sharing* parameter $y = E_{\gamma_1}/(E_{\gamma_1} + E_{\gamma_2})$ = 1/4. As seen from the figure, the (degree of) quantum correlations is very sensitive to the decay geometry. In particular, our calculations show that the concurrence of two photons emitted in the $1s2s\,^1S_0 \to 1s^2\,^1S_0$ decay vanishes at the opening angle $\theta = \pi/2$, while it is maximal for the parallel (θ = 0) and back–to–back ($\theta = \pi$) photon emission. This behaviour can be well understood from the conservation of the projection of the total angular momentum of the overall system "ion + two photons". For $\theta = 0$ and π, for example, such a conservation law immediately implies maximally entangled Bell (linear polarization) states $|\Psi_{\theta=0}>= |yy> + |xx>$ and $|\Psi_{\theta=\pi}>= |yy> - |xx>$ and, hence, maximal degree of entanglement, $\mathcal{C} = 1$.

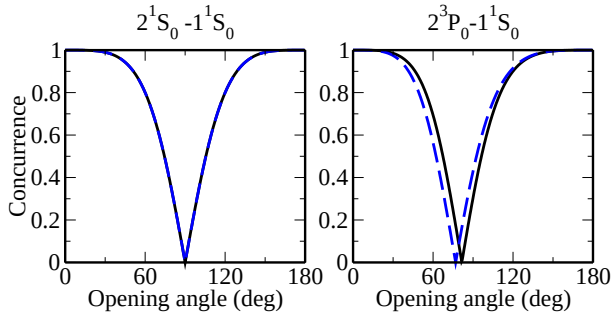

Figure 1: Concurrence of two photons emitted in the $1s2s\,^1S_0 \to 1s^2\,^1S_0$ (left panel) and $1s2p\,^3P_0 \to 1s^2\,^1S_0$ (right panel) decay of helium-like uranium. Results of the rigorous relativistic theory (solid line) are compared to those obtained within the dipole approximation (dashed line). Such a dipole approximation accounts for the leading $2E1$ and $E1M1$ channels for the decay of 2^1S_0 and 2^3P_0 states, correspondingly. Calculations have been carried out for the energy sharing parameter y =1/4.

A qualitatively similar behaviour of the concurrence measure can be observed for the $1s2p\,^3P_0 \to 1s^2\,^1S_0$ two–photon transition. However, in contrast to the decay of $^1S_0$ state, the degree of entanglement is not symmetric anymore with respect to the opening angle $\theta = \pi/2$. Such an asymmetric shift in the concurrence is caused by the interference between two pathways which appear for each multipole component of the $2^3P_0 \to 1\,^1S_0$ decay [2, 4]. For this decay, moreover, polarization correlations appear to be sensitive to non–dipole effects in the electron–photon interaction. As seen from the right panel of Fig. 1, a slight shift of the concurrence measure can be observed if apart from the leading $E1M1$ decay channels, higher multipole contributions are taken into account.

References

[1] S. Trotsenko *et al.*, Phys. Rev. Lett. 104, 033001 (2010).

[2] A. Surzhykov *et al.*, Phys. Rev. A 81, 042510 (2010).

[3] H. Kleinpoppen *et al.*, Phys. Scr. T72, 7 (1997).

[4] F. Fratini *et al.*, Phys. Rev. A, submitted.

*Work supported by the Helmholtz Gemeinschaft under the project VH–NG–421.

† surz@physi.uni-heidelberg.de

A novel approach to the two–center Dirac problem*

A. N. Artemyev[†1,2], *A. Surzhykov*[1,2], *P. Indelicato*[3], *G. Plunien*[4], *and Th. Stöhlker*[1,2,5]

[1]University of Heidelberg, Germany; [2]GSI, Darmstadt, Germany; [3]École Normale Supérieure, Paris, France; [4]TU Dresden, Germany; [5]Helmholtz-Institut Jena, Germany

With the recent experimental advances in accelerator and storage ring techniques, novel opportunities arise to study slow collisions between heavy, highly–charged ions. In these collisions, one can observe the formation of *quasi–molecules*, i.e. short–living systems in which electrons move in the Coulomb field of two nuclei. The quasi–molecules have proven to be a versatile tool for investigating a number of fundamental problems in modern physics. In particular, the analysis of quasi–molecular spectra can provide unique knowledge on relativistic, many–body and quantum electrodynamic (QED) effects in the non–perturbative domain of high nuclear charges and super–critical electromagnetic fields. Moreover, the electron–positron pair production under such extreme conditions might be utilized to better understand the properties and behaviour of the quantum vacuum.

Any theoretical analysis of the structural properties and dynamical behaviour of heavy quasi–molecules may be traced back to the two–center time–dependent Dirac equation. For low collision velocities one can treat this equation *adiabatically* and, hence, reduce it to the solution of the static (two–center) eigenproblem:

$$\left(\hat{H}_{\rm free}(\boldsymbol{r}) + V(\boldsymbol{r},\boldsymbol{R})\right)\Psi_R(\boldsymbol{r}) = \epsilon\Psi_R(\boldsymbol{r})\,, \qquad (1)$$

which is written here for the simplest case of the "one–electron-two–nuclei" system. In this expression, $\hat{H}_{\rm free}$ is the Hamiltonian of a free electron and $V(\boldsymbol{r},\boldsymbol{R})$ describes the Coulomb interaction between an electron and two nuclei with $\boldsymbol{R}$ being the inter–nuclear vector.

In the past, a large number of methods have been proposed to deal with the two–center Dirac eigenproblem. Apart from the the direct numerical integration of Eq. (1), various LCAO (linear combination of atomic orbitals) and monopole approximations as well as methods employing prolate spheroidal coordinates have been implemented to understand better the structure and dynamics of heavy quasi–molecules. Many of these approaches, however, have restricted range of application, allowing to describe well either very small or very large inter–nuclear distances. Moreover, the proper description of the positive– as well as the negative–continuum solutions of the (two–center) Dirac equation remains still a rather difficult task.

In this contribution, we developed a novel theoretical approach for the treatment of the relativistic two–center problem (1) at arbitrary inter–nuclear distance [1]. We argue that such an analysis can be performed most naturally in Cassini coordinates as proposed in Refs. [2, 3]. In such a coordinate system we employ the finite (discrete) basis constructed from the B–spline sets, in order to solve Eq. (1) and to find a *complete* spectrum of the quasi–molecule, including not only bound states but also positive– as well as negative–continuum solutions. By making use of these solutions, further analysis can be performed both, for the quantum electrodynamics (QED) corrections to quasi–molecular energy levels and for the electron dynamics in (slow) ion–ion collisions.

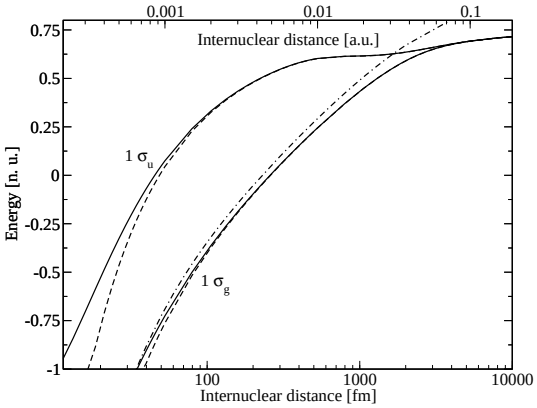

Figure 1: The energy of 1σ states in U_2^{183+} as a function of the internuclear distance. The solid and dashed lines correspond to finite-size and point-like nuclei, respectively. The dash-doted line represents the energy of the $1s$ state in the mono–pole approximation. The left border of the figure indicates the nuclear diameter of uranium.

To illustrate the application of our approach, detailed calculations have been performed for the energies of $1\sigma_g$ and $1\sigma_u$ states of the U^{92+}-U^{91+} quasi–molecule. These energies have been evaluated for a wide range of internuclear distances R by employing the point–like and finite–size nuclear charge distributions. As seen from Fig. 1, the nuclear size corrections are of paramount importance for an accurate description of molecular spectra, especially at small R. These corrections not only reduce (the absolute value of) the ground–state energy by about 10% but also prevent the first excited level $1\sigma_u$ from the "diving" into the Dirac negative continuum [1].

References

[1] A. N. Artemyev *et al.*, J. Phys. B 43, 235207 (2010).

[2] P. Schlüter *et al.*, J. Phys. A 16, 1999 (1983).

[3] K.-H. Wietschorke *et al.*, J. Phys. A 16, 2017 (1983).

*Work supported by the Helmholtz Gemeinschaft under the project VH–NG–421.

† artemyev@physi.uni-heidelberg.de

Relativistic Calculations of the Charge-Transfer Probabilities and Cross Sections for Low-Energy Collisions of H-like Ions with Bare Nuclei *

I. I. Tupitsyn[1], *Y. S. Kozhedub*[1], *V. M. Shabaev*[1], *G. B. Deyneka*[1], *S. Hagmann*[2], *C. Kozhuharov*[2], *G. Plunien*[3], *and Th. Stöhlker*[2,4]

[1]St. Petersburg State University, Russia; [2]GSI, Darmstadt, Germany; [3]TU Dresden, Germany; [4]Universität Heidelberg, Germany

Collisions of highly charged ions provide tests of relativistic and QED effects on dynamic atomic processes [1, 2, 3]. Investigations of such processes can give unique access to QED in supercritical fields. Indeed, ultra-strong electromagnetic fields, occurring in highly-charged heavy ions, can be further increased in experiments with heavy ions passing each other. The field strengths achieved in such experiments can well exceed the critical value for diving of the lowest-energy bound quasi-molecule state into the negative-energy Dirac continuum (see, e.g., Ref. [4] and references therein). A direct evidence for the diving effect could consist in observing the spontaneous positron emission. But the observation of this emission is embarrassed due to relatively small collision period with respect to the positron emission time. One may expect, however, that the diving phenomenon can be examined indirectly via some other effects that take place during the collision. To search for such effects, first of all, one needs clearly understand and properly to describe low-energy heavy-ion collisions.

The desired approach for the calculation of electron-excitation and charge-transfer processes has been developed in Ref. [5], where the time-dependent two-center Dirac equation is solved by the coupled-channel method. The one-electron wave function is represented as a sum of atomic-like Dirac-Sturm orbitals, localized at the ions. The atomic orbitals are obtained by solving numerically the finite-difference one-center Dirac and Dirac-Sturm equations with the potential, which is the sum of the exact reference-nucleus potential and a monopole-approximation potential from the other nucleus. The time-depended Dirac equation is solved using the evolution operator method.

The approach was tested by calculations of the excitation, charge-transfer and ionization cross sections for collision of a hydrogen atom with a proton in a wide range of energies (0.5-100 keV) and impact parameters (0.1-10 au). The results were compared with experimental data and nonrelativistic calculations (relativistic effects are negligible for collisions of light ions). They are in good agreement with the recent most accurate nonrelativistic calculations [6]. To probe the role of relativistic effects, the charge-transfer transition probabilities and cross sections for $Ne^{9+}(1s)$-Ne^{10+}, $Xe^{53+}(1s)$-Xe^{54+} and $U^{91+}(1s)$-U^{92+} low-energy collisions were calculated in both the relativistic and the nonrelativistic cases. The role of the relativistic effects for $U^{91+}(1s)$-U^{92+} collisions (at the projectile energy E = 6.0 MeV/u) can be seen in Fig. 1, where the relativistic and non-relativistic results for charge-transfer probabilities are plotted.

In further investigations we intend to study in more detail the effect of the diving of the ground level of the U_2^{183+} quasimolecule into the negative-energy Dirac spectrum and the influence of this effect on the values of the charge-transfer probability. We also plan to extend our method to collisions involving many-electron ions and neutral atoms. This will allow us to study the 1s-1s charge transfer in low-energy heavy ion-atom collisions. Such experiments, which were successfully performed for low-Z collisions many years ago [7, 8], are presently under preparation for high-Z collisions at GSI.

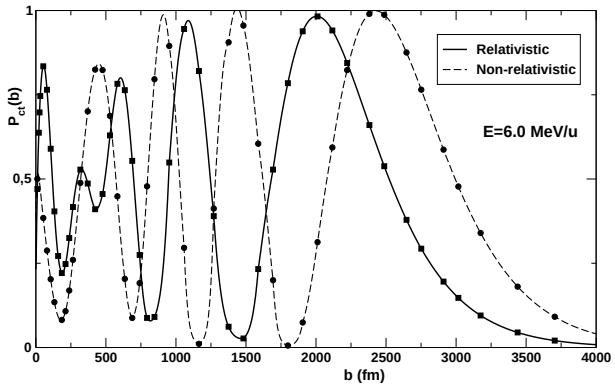

Figure 1: Charge-transfer probability $P_{\rm ct}(b)$ for $U^{91+}(1s)$ – U^{92+} collisions as a function of the impact parameter b. The solid line interpolates the relativistic values (squares) and the dashed line corresponds to the nonrelativistic limit. In both cases, the projectile energy is $E = 6.0$ MeV/u.

References

[1] J. Eichler, W.E. Meyerhof, *Relativistic Atomic Collisions* (Academic Press, San Diego, 1995).

[2] V.M. Shabaev, Phys. Rep. **356**, 119 (2002).

[3] J. Eichler and Th. Stöhlker, Phys. Rep. **439**, 1 (2007).

[4] W. Greiner, B. Müller, J. Rafelski, *Quantum Electrodynamics of Strong Fields* (Springer-Verlag, Berlin, 1985).

[5] I.I. Tupitsyn *et al.*, Phys. Rev. A **82**, 042701 (2010).

[6] T. Winter, Phys. Rev. A **80**, 032701 (2009).

[7] S. Hagmann *et al.*, Phys. Rev. A **36**, 2603 (1987).

[8] R. Schuch *et al.*, Phys. Rev. A **37**, 3313 (1988).

* Work supported by DFG and GSI.

The cross sections for K-shell ionization by charged particle impact*

A.I. Mikhailov[1], *A.V. Nefiodov*[1], *A. Pernice*[2], *and G. Plunien*[2]

[1]PNPI, 188300 Gatchina, St. Petersburg, Russia; [2]TU Dresden, Mommsenstr. 13, D-01062 Dresden, Germany

The single ionization of inner-shell electrons by the impact of charged particles is one of the fundamental processes, which is being persistently investigated during last decades. In recent works [1-3], we have deduced the universal scaling laws for differential and total cross sections of the single K-shell ionization by electron and positron impact within the entire non-relativistic energy domain. In paper [4], we have extended the previous formulas on the case of relativistic projectiles. The study is performed to leading orders of QED perturbation theory with respect to the small parameters $1/Z$ and αZ, where α is the fine-structure constant. Since it is assumed that $\alpha Z \ll 1$ and $Z \gg 1$, the results turn out to be applicable for a wide family of atomic targets (both for multicharged ions and neutral atoms) with moderate values of nuclear charge numbers Z.

Let us consider the inelastic electron scattering on a hydrogen-like ion, which results in the ionization of a K-shell bound electron. The multicharged ion in the ground state is characterized by the Coulomb ionization potential $I = \eta^2/(2m)$, where $\eta = m\alpha Z$ is the average momentum of the bound electron and m is the electron mass ($\hbar = 1$, $c = 1$). An incident electron is characterized by the energy E and the asymptotic momentum p, which are related via $E^2 = p^2 + m^2$. The relativistic domain implies that $E_{\rm kin} \gtrsim m$, where $E_{\rm kin} = E - m$ denotes the kinetic energy.

The final expression for the total K-shell ionization cross section $\sigma_{\rm K}^+$ is given by two-fold integral, which can be easily calculated numerically. In Table 1, we present the results for $\sigma_{\rm K}^+$ in the case of multicharged ions. Although the formulas obtained in work [4] are not expected to be applicable for heavy targets, the agreement of the theoretical predictions with the experimental data appears to be remarkably good.

If the nuclear charge number Z is not too high, then the total cross section is given by the analytical formula [4]

$$\sigma_{\rm K}^+ = \frac{2^7\alpha^2\sigma_0}{Z^2v^2e^4}\frac{13}{27}\left(\ln\varepsilon - v^2 + C\right), \qquad (1)$$

$$C = \frac{511}{192} + \frac{(81e^4 - 3136)\ln 2}{624} \simeq 4.091\,.$$

Here $\varepsilon = (p/\eta)^2$, $v = p/E$, $\sigma_0 = \pi a_0^2 = 87.974$ Mb, where $a_0 = 1/(m\alpha)$ is the Bohr radius, and $e \simeq 2.718$ is the Napier-Euler number. As can be seen, in the relativistic case, the dependence of the cross section on the nuclear charge Z differs from that in the non-relativistic limit. Nevertheless, in the energy range $I \ll E_{\rm kin} \ll m$, Eq. (1) is consistent with the non-relativistic formula obtained in work [1]. A formula similar to Eq. (1) has been also found by Kolbenstvedt. However, our numerical coefficient C differs from that in Ref. [7].

Table 1: For various multicharged ions, the Coulomb ionization potentials $I = m(\alpha Z)^2/2$, the kinetic energies $E_{\rm kin} = E - m$ of incident electrons, and the theoretical and experimental cross sections $\sigma_{\rm K}^+$ are tabulated. For uranium ions, the measurements are performed by Marrs et al. [5]. The other experimental data are adopted from Ref. [6].

	I	$E_{\rm kin}$	$\sigma_{\rm K}^+$ (b)	
Target	(keV)	(keV)	Ref. [4]	Experiment
Mo^{41+}	24.0	64.8	34.4	30.8 ± 2.6
		95.6	35.7	34.7 ± 7.2
Dy^{65+}	59.3	95.1	3.90	4.17 ± 0.58
		153.1	6.19	6.29 ± 0.83
Au^{78+}	84.9	153.1	2.32	2.33 ± 0.33
Bi^{82+}	93.7	191.6	2.23	2.37 ± 0.19
U^{91+}	115	198	1.22	1.55 ± 0.27
U^{90+}	115	198	2.44	2.82 ± 0.35

In work [4], the generalizations have been also made on the case of arbitrary charged projectiles with the mass $M > m$ ionizing the atomic targets, in which the K shell is completely occupied. The agreement with experimental data is found to be quite satisfactory for wide family of atomic targets and different incident charged particles.

References

[1] A.I. Mikhailov, A.V. Nefiodov, and G. Plunien, Phys. Lett. A 372 (2008) 4451.

[2] A.I. Mikhailov, A.V. Nefiodov, and G. Plunien, Phys. Lett. A 372 (2008) 5171.

[3] A.I. Mikhailov, A.V. Nefiodov, and G. Plunien, J. Phys. B 43 (2010) 085201.

[4] A.I. Mikhailov, A.V. Nefiodov, and G. Plunien, JETP 109 (2009) 762.

[5] R.E. Marrs, S.R. Elliott, and D.A. Knapp, Phys. Rev. Lett. 72 (1994) 4082.

[6] R.E. Marrs, S.R. Elliott, and J.H. Scofield, Phys. Rev. A 56 (1997) 1338.

[7] H. Kolbenstvedt, J. Appl. Phys. 46 (1975) 2771.

* Work supported by GSI

Target effects on the linear polarization of electron-nucleus bremsstrahlung*

R. Märtin[1,2], *R. Barday*[3], *J. Enders*[3], *Y. Poltoratska*[3], *U. Spillmann*[1], *G. Weber*[1,4], *and Th. Stöhlker*[1,2,4]

[1]GSI Helmholtzzentrum für Schwerionenforschung GmbH, Darmstadt, Germany; [2]Physikalisches Institut, Universität Heidelberg, Heidelberg, Germany; [3]Institut für Kernphysik, Technische Universität Darmstadt, Darmstadt, Germany; [4]Helmholtz-Institut Jena, Jena, Germany

The polarization properties of electron-nucleus bremsstrahlung occurring both in electron-atom collisions and, in inverse kinematics, in ion-atom collisions have continuously attracted strong theoretical interest [1, 2]. Due to the recent development of efficient Compton polarimeters precise studies of photon linear polarization in the energy region from roughly 70 up to a few hundred keV have become possible [3]. However, for the correct interpretation of bremsstrahlung polarization measurements using solid state targets one has to consider the electron transport properties within the target. As for high-Z materials the mean free path length of electrons with energies below a few hundred keV is in the order of a few nm, target effects can be expected even for the thinnest target foils that can be used practically.

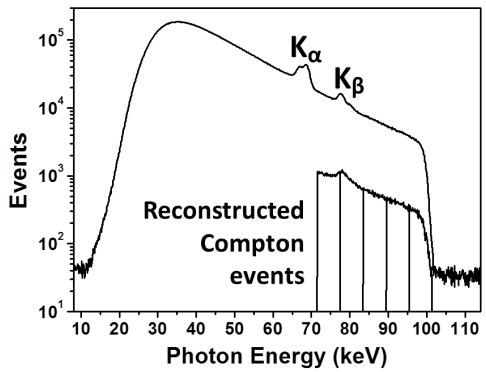

Figure 1: Bremsstrahlung distribution of 100 keV unpolarized electrons impinging on a gold target (90 $\frac{\mu g}{cm^2}$) recorded at 130° observation angle. The bottom curve shows the fraction of the reconstructed Compton events which can be used for the polarization analysis.

We performed a bremsstrahlung measurement at the polarized electron source SPIN at the TU Darmstadt [4, 5] using gold targets of different thicknesses (90 $\frac{\mu g}{cm^2}$ and 178 $\frac{\mu g}{cm^2}$, respectively). The available electron energy of 100 keV is well suited for the use of our novel-type Si(Li) Compton polarimeter, which we applied for x-ray detection. Fig. 1 shows the bremsstrahlung distribution recorded at 130° observation angle. The bottom curve shows the fraction of reconstructed Compton scattering events within the detector crystal from which one can obtain the linear polarization properties.

* Work supported by DFG through SFB 634 and by the state of Hesse through the LOEWE centre HIC for FAIR

Fig. 2 shows the degree of linear polarization of bremsstrahlung measured for the two different gold targets. The polarization has been evaluated for different photon energies reaching from the endpoint of the distribution down to 71.5 keV. As seen, the degree of linear polarization is reduced for the thicker target. This is due to the deflection of electrons inside the target, mainly due to elastic scattering in the field of the nucleus, which leads to a superposition of different observation angles with respect to the electron momentum direction at the detector position.

Currently, we are developing an electron transport Monte-Carlo code to estimate the effects of the finite target thickness on bremsstrahlung polarization. Preliminary results already indicate that the bremsstrahlung polarization is much more sensitive to target effects than the spectral distribution, which has been studied extensively in the past.

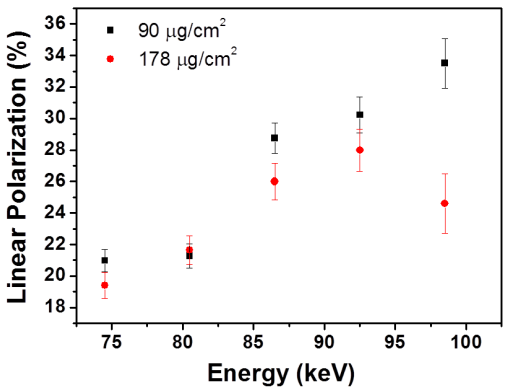

Figure 2: Preliminary: Degree of bremsstrahlung linear polarization for two different target thicknesses as a function of the energy of the emitted photon. Here only the statistical uncertainty is considered for the error bars.

References

[1] D. Jakubaßa-Amundsen, J. Phys. B: At. Mol. Opt. Phys. **40** (2007) 119

[2] V. A. Yerokhin and A. Surzhykov, Phys. Rev. A **82**, 062702 (2010)

[3] G. Weber *et. al*, JINST **5** C07010 (2010)

[4] C. Heßler, Conf. Proc. EPAC08, 1482-1484 (2008)

[5] R. Märtin *et. al*, GSI Scientific Report 2009, ATOMIC-PHYSICS-01

Electron cooling of light and heavy ions in HITRAP*

G. Zwicknagel
Institut für Theoretische Physik, Universität Erlangen, Germany

In previous simulation studies we investigated the electron cooling of highly charged ions in HITRAP based on a scheme where the motion of each ion is numerically calculated taking into account the stopping force due to collisions with magnetized electrons which is taken from microscopic calculations [1, 2, 3]. These simulations provide the time evolution of the energy distribution of the ions, the related cooling times and the surviving probability $\langle P_{\rm RR}\rangle$ of the initially injected ion species with respect to losses by radiative ion-electron recombinations, and of the electron temperature which, despite synchrotron radiation cooling, strongly increases due to the energy lost by the ions.

These studies have been focused on highly charged ions, like bare Uranium, and showed that cooling times of less than a second with radiative recombination losses of $\lesssim 15\%$ are feasible if a sufficient number of trapped electrons is available. But for recent tests of the HITRAP cooler trap mainly light ions with lower charge states will be used and we therefore performed some calculations for these conditions. This will allow a comparison and an extrapolation of the results obtained in these test experiments towards the expected behavior and performance of the trap for highly charged ions.

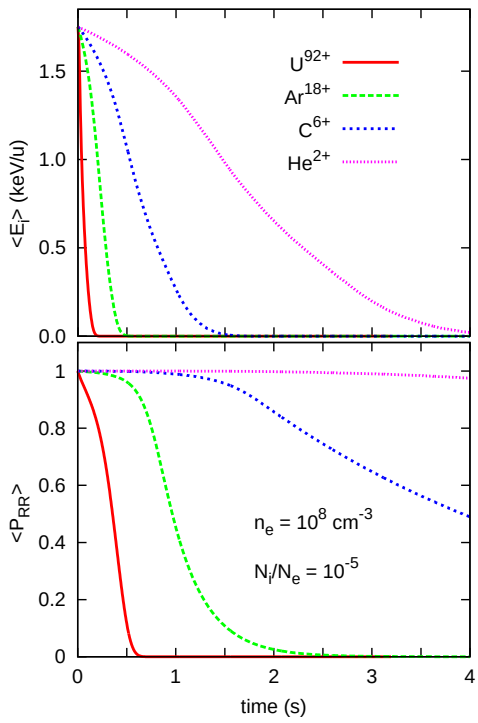

Figure 1: Temporal evolution of the mean energy of the ions $\langle E_i\rangle$ and the surviving probability $\langle P_{\rm RR}\rangle$ for different ion species, $N_e = 10^9$, an electron density $n_e = 10^8$ cm^{-3}, and $N_i = 10^4$ ions in the trap.

Some corresponding examples are shown in Figs.1 and 2, for different ion species and two different numbers of trapped electrons N_e. The magnetic field in the trap is $B = 6$ T and the ambient temperature is 4 K. For light ions like He^{2+} the cooling times are roughly a factor ten larger compared to the highly charged species with $Z \gtrsim 20$ and are in the range of a few seconds for a cloud of $N_e = 10^9$ trapped electrons (Fig.1). For less trapped electrons, $N_e = 10^8$, which leads to a stronger heating of the electrons and a smaller cooling force on the ions, the cooling times even exceed to a few tens of seconds (Fig.2).

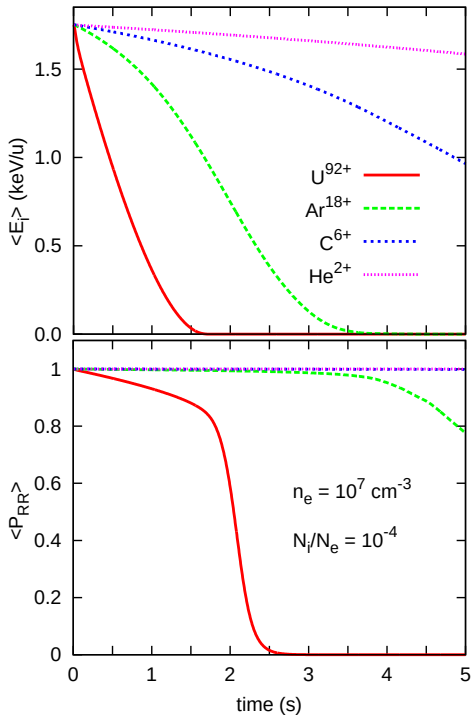

Figure 2: Same as Fig. 1 but now for 10-times less electrons $N_e = 10^8$ and $n_e = 10^7$ cm^{-3}, $N_i = 10^4$.

References

[1] G. Zwicknagel, in *AIP Conference Proceedings*, vol 862, (AIP, New York 2006) pp 281–291

[2] H. Nersisyan, C. Toepffer, G. Zwicknagel, *Interactions Between Charged Particles in a Magnetic Field* (Springer, Berlin Heidelberg New York 2007)

[3] B. Möllers, PhD-thesis, University Erlangen 2007, `www.opus.ub.uni-erlangen.de/opus/volltexte/2007/547/`.

*Work supported by the BMBF (06ER9064)

Giant Crystal Grain Rotation in Au-Bombarded NiO

S. Klaumünzer[1], D. Severin[2], M. Bender[2], A.O. Delgado[3], S. Mickat[2]

[1] Helmholtz-Zentrum Berlin, Germany; [2] GSI, Darmstadt, Germany; [3] University of Sao Paulo, Brazil .

This work was stimulated by the large shape changes of ion-bombarded NiO layers found by Bolse [1]. His observations were somewhat reminiscent of ion-hammering of amorphous materials, an effect of shear stress relaxation in liquid ion tracks [2]. Schattat et al. [3] provided evidence for liquid ion tracks in NiO. On the other hand, first x-ray diffraction measurements revealed that NiO remained crystalline during swift heavy ion bombardment and any shear stress relaxation within the liquid ion tracks should be annihilated during subsequent recrystallization. This contribution aims at a clarification of the ion-induced deformation mechanism. Previous irradiations of NiO single crystals at 90 and 300 K with a 600 MeV Au beam at ISL, Berlin, had suggested that the deformation direction was set by the beam direction and that thermally activated migration was unimportant. Under normal irradiation (angle $\alpha = 0$ between the NiO slab normal and ion beam), the single crystal exhibited a slight mosaicity and a large in-plane compressive stress of ~ –3.5 GPa. For $\alpha \neq 0$, however, the NiO single crystals rapidly fragmented into nanocrystals of ~30 nm diameter and the bombarded layer underwent shear flow.

Inaugurating the newly installed on-line x-ray diffractometer at the M2-branch at the UNILAC, NiO single crystals were bombarded at ~40°C with 940-MeV Au ions. The following results were obtained: i) The shear flow originated from a combined rotation and translation of the nanocrystals. ii) The rotation angle Ω increases with increasing ion fluence Φt. No saturation has been found (see fig. 1). iii) The rotation is reversible (cf. fig. 1).

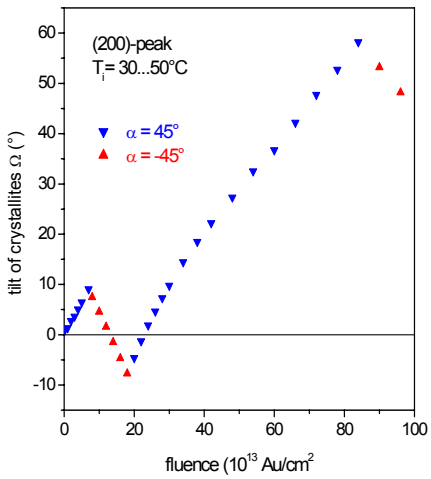

Figure 1: Tilt angle Ω of the nanocrystallites as a function of fluence. Reversing the angle α of beam incidence reverses the rotation. Reversibility is clearly demonstrated around $\Omega = 0°$ and 50°.

iv) The angular speed $\dot{\Omega}$ of the crystallites is rather independent of the starting orientation of the single crystals. v) The evolution of the x-ray line width, σ_χ, which characterizes the uniformity of the rotation, consists of a stochastic and a deterministic part (cf. fig. 2). The stochastic part, $\sigma_\chi^2 \sim \Phi t$, is due to fluctuations in the number of ions impacting on individual crystallites. The deterministic part, $\sigma_\chi^2 \sim (\Phi t)^2$, is due to the variation of the electronic stopping power along the ion trajectory. vi) The integrated x-ray intensity of the rotated nanocrystals decreases slowly with increasing Φt.

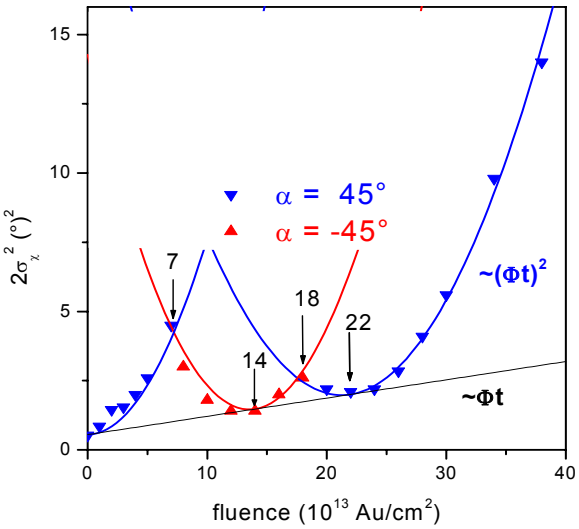

Figure 2: Squared linewidth $2\sigma_\chi^2$ versus fluence Φt. The stochastic part is proportional to Φt while the deterministic part is proportional to $(\Phi t)^2$. Reversing the angle of beam incidence α reverses also the increase of the deterministic part of the linewidth.

The experimental results collected so far are compatible with pressure relaxation of transiently molten ion tracks by the emission of prismatic interstitial loops. These loops are repelled from the track to a distance between 15 and 20 nm. During subsequent recrystallization of the liquid track the missing atoms are compensated by vacancy loops, presumably aligned along the track axis. Entanglement of the loops forms the small-angle boundaries necessary for crystal fragmentation. The microscopic details for the crystallite rotation are not yet clear.

References

[1] W. Bolse, Nucl. Instr. & Meth. B 244 (2006) 8.
[2] H. Trinkaus and A.I. Ryazanov, Phys. Rev. Lett. 74 (1995) 5072.
[3] B. Schattat et al., Appl. Phys. Lett. 87 (2005) 173110.

Stabilization of high-pressure phase in HfO_2*

B. Schuster[1,2], C. Trautmann[1], and F. Fujara[2]

[1]GSI, Darmstadt, Germany; [2]TU-Darmstadt, Darmstadt, Germany.

On the search for materials with novel and/or improved performances, synthetic control of structural diversity plays an important role. Tuning atomic structures of different phases allows optimization of a variety of materials properties. There exist, e.g., solids with crystalline high-pressure or high-temperature phases of specific characteristics such as excellent conductivity or extreme hardness. The best known example is diamond, the high-pressure polymorph of carbon, known as the hardest material on Earth. Among various techniques, one of the traditional approaches to search for new materials involves the application of pressure. However, in many cases the high-pressure phase cannot be stabilized and explored at ambient condition, because the material transforms back to the original phase when the pressure is released. In this report we demonstrate that the combination of two extreme conditions, namely pressure and the irradiation with swift heavy ions, allows the stabilisation of a high-pressure phase to ambient condition.

The experiments are performed by placing a miniaturized specimen in a small chamber between two opposing diamonds. By mechanical force the diamonds squeeze the sample creating pressures of several GPa. A liquid pressure medium ensures hydrostatic conditions up to ~ 10 GPa inside the diamond anvil cell. The pressurized sample is then exposed to relativistic heavy ions, preferably Au, Pb, or U ions, at the SIS at GSI. Because the ions have to pass through the first diamond, these experiments require beam energies of about 200 MeV/u [1].

As material we investigated HfO_2, a well known ceramics with high toughness, hardness, and excellent chemical and radiation resistance. Its complex phase diagram with several different crystalline phases (see Fig. 1) makes it an interesting candidate. Under pressure, the monoclinic phase transforms to the orthorhombic I phase at 4 GPa. The stability field of this first high pressure phase extends up to 14.5 GPa. The transition is fully reversible, thus the ortho-I polymorph is not accessible at room pressure.

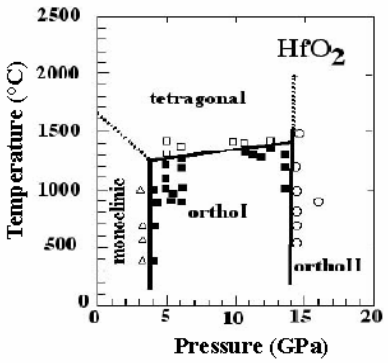

Figure 1: Phase diagram of HfO_2 [2].

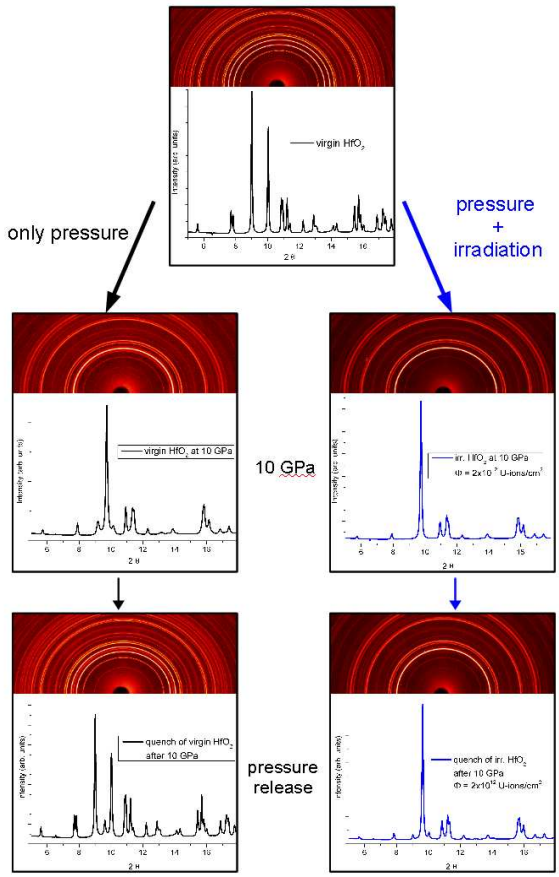

Figure 2: X-ray analysis of pressurized HfO_2 without (left) and with (right) simultaneous irradiation to U ions (2×10^{12} cm^{-2}).

The structure of HfO_2 with and without ion irradiation was monitored at different pressures by synchrotron X-ray diffraction (λ = 0.495 nm) at the new P08 beamline at PETRA III (DESY, Hamburg). The top image of Fig. 2 shows virgin HfO_2 at ambient conditions. The left and the right branch display the pressure behaviour of virgin and irradiated material, respectively. At 10 GPa, ortho I is the predominant structure, with the strongest peak at 9.7°. While the virgin material still shows some residues of the monoclinic structure (reflex at 9.1° and 10.1°), the irradiated sample seems completely transformed. After quickly releasing the pressure, the unirradiated material transforms back to the monoclinic phase while the irradiated material remains in its high pressure phase. This phase stabilization opens the possibility for material science.

References

[1] M. Lang et al; Nature Materials 8 (2009) 793.
[2] O. Ohtaka et al; J. Am. Ceram. Soc. 84 (2001) 1369

* Work supported by the German Science Foundation DFG (Project No. FU 308/12)

Highly porous tracks in fluorapatite*

W.X. Li[1,#], L.M. Wang[1], K. Sun[1], M. Lang[1], C. Trautmann[2], and R.C. Ewing[1]

[1]University of Michigan, Ann Arbor, MI, U.S.A.; [2]GSI, Darmstadt, Germany

In volatile-rich fluorapatite, which represents 70 % of all fission track age-determinations, tracks produced along the trajectories of fission fragments have been considered to be cylinders of radiation-damaged amorphous material, similar to tracks in other minerals, such as zircon [1]. The atomic-scale structure of unetched fission tracks controls temperature-induced "fading" and finally leads to shortening of the etchable length of a track. Here, we demonstrate that tracks in apatite are actually highly porous tubes instead of amorphous cores [2]. The atomic-scale studies of the highly-porous tracks in apatite are essential not only for geophysics community to unravel mechanisms of track annealing but also for the ion-matter community to understand the track formation mechanism.

Two types of tracks were investigated in fluorapatite ($Ca_{10}(PO_4)_6F_2$), from Durango, Mexico: (1) randomly oriented thermal-neutron induced tracks from fission of ^{235}U; (2) parallel tracks produced along the *c*-axis of the material by exposing 50-μm thick single crystals to 2.2-GeV Au ions from the UNILAC accelerator of GSI. For transmission electron microscopy (TEM) observations the samples were crushed and suspended on a carbon film supported Cu grid. *In situ* heating of fission tracks was performed by using a hot-stage TEM specimen holder.

A high resolution TEM (HRTEM) image of highly porous tracks produced with 2.2-GeV Au ions is shown in Fig. 1. During this TEM analysis the electron current density (~ 0.5 A/cm^2) was low to minimize electron-beam induced damage. The central core region of the track has the same bright contrast as the free space outside the sample grain, suggesting that no solid components remain in the track core. The Airy pattern in the fast Fourier transform (FFT) image (inset) from a region centred in a track confirms that the track is highly porous. During the *in situ* heating of fission tracks (Fig. 2), Cu atoms obviously diffuse through the track opening into some of the highly porous fission tracks, forming cylindrical Cu nanorods through capillary action.

The formation of the porous track in apatite is ascribed to the highly ionizing energy deposition of fission fragments inducing radiolytic decomposition of fluorapatite accompanied by the loss of volatile elements [2]. As a result of the significant mass loss and "density jump" between the tracks and the surrounding crystalline matrix, the Fresnel contrast (contrast change at different TEM focus conditions) can be seen for tracks in apatite (see Ref. 2 for details). This is in contrast to amorphous tracks, where the interface to the matrix remains dark when changing the focus, because the track density change is insignificant as compared to that of the porous track [2].

* Work supported by the Office of Basic Energy Sciences of the U.S. DOE (DE-FG02-97ER45656).

#wxli@umich.edu

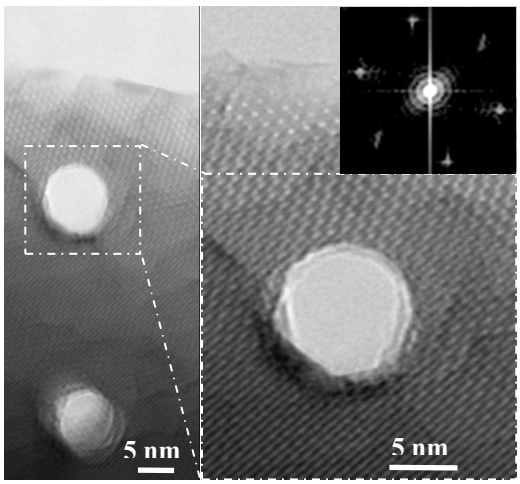

Figure 1: Plan-view HRTEM images of tracks in apatite induced by 2.2-GeV Au ions showing a highly porous core. Airy pattern shown in the FFT image (inset) is caused by the electron diffraction from the highly porous track, acting as an aperture.

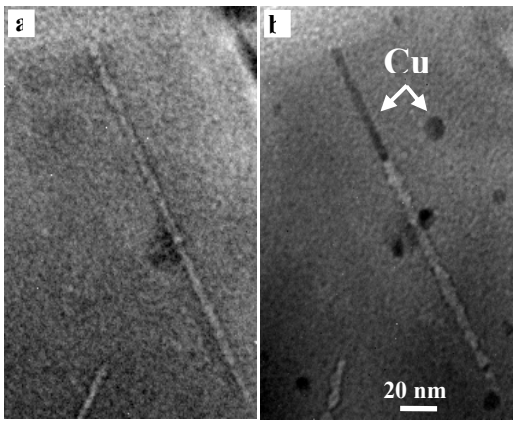

Figure 2: *In situ* heating of fission tracks in apatite. TEM images (a) before heating and (b) after the temperature is stabilized at 700 °C for 1 min. Cu atoms from the supporting copper grid (dark features in (b)) diffuse into a fission track through the open end and form a nanorod inside the track.

References

[1] M. Lang, J. Lian, F.X. Zhang, B.W.H. Hendriks, C. Trautmann, R. Neumann, R.C. Ewing, Earth Planet. Sci. Lett. 274 (2008) 355.

[2] W.X. Li, L.M. Wang, K. Sun, M. Lang, C. Trautmann, R.C. Ewing, Phys. Rev. B 82 (2010) 144109.

Thermal annealing mechanisms of latent tracks: Apatite *versus* zircon*

W.X. Li[1,#], L.M. Wang[1], M. Lang[1], C. Trautmann[2], and R.C. Ewing[1]

[1]University of Michigan, Ann Arbor, MI, U.S.A.; [2]GSI, Darmstadt, Germany

Etched tracks of apatite and zircon are both widely used for the determination of the thermal history of Earth's crust. The present understanding of the annealing process is largely limited to mathematical fits to data for etched track-lengths as a function of temperature and time. Details of the annealing of unetched, latent tracks at the atomic scale have remained elusive, as the original track is destroyed during chemical etching. In the absence of actual observations of the atomic-scale process, tracks in apatite and zircon have been considered to anneal by the same mechanism, essentially epitaxial recrystallization. In this study, direct, atomic-scale observations of thermal annealing of latent tracks at elevated temperatures by transmission electron microscopy (TEM) demonstrate that the annealing behavior of tracks in apatite is entirely different from that of the amorphous tracks in zircon [1]. This is a direct result of differences in the internal structure of the track, consisting of an amorphous domain in zircon but of low atomic density void in apatite [2].

Parallel tracks were produced in natural zircon (Beaune-sur-Arzon, France) by exposing the single crystals to 2.2 GeV Au ions from the UNILAC accelerator of GSI. Randomly oriented tracks in Durango fluorapatite were produced by thermal neutron-induced fission of ^{235}U. *In situ* thermal annealing experiments were performed in a TEM equipped with a hot-stage holder, which enables us to directly observe track thermal annealing behavior during the TEM analysis.

The dynamic process of thermal annealing of tracks in apatite was observed by heating the sample in TEM at 700 ^{o}C (Figs. 1a-d). Between image recording, the electron beam was moved away to reduce the effects of electron-induced annealing. Initially, the track radius either shrinks or grows along the ion trajectory without much periodicity in the intervals. After annealing times in excess of 53 min, the fission track breaks into segments, randomly fragmented along the ion trajectory. The track segmentation and the Brownian motion of track segments can be ascribed to the high mobility of atoms at the surface within the highly porous track structure. This is in clear contrast to the annealing behavior of amorphous tracks in zircon, which gradually shrink and eventually disappear at 830 ^{o}C after 90 min due to defect elimination (Figs. 1e-h). No track segmentation or Brownian motion of track segments in zircon was observed. This is because the surface tension and the diffusivity of atoms on the surface of amorphous tracks are too low for track segmentation into separate droplets.

These TEM observations of *in situ* thermal annealing of tracks provide a bridge between the current empirical models of annealing and a fundamental understanding of the atomic-scale process [1]. Remnants of the latent tracks in apatite can be seen after *in situ* heating at 700 ^{o}C for 130 min, in clear contrast to the complete disappearance of etchable tracks heated at 360 ^{o}C for 1 hr. The thermally-induced discontinuity of porous tracks in apatite prevents solutions from entering into the porous tracks for further etching, thus reducing the etched track length. This accounts for the complete disappearance of etchable tracks in apatite at much lower temperatures, as compared to that of the latent tracks observed by TEM. In contrast, the amorphous tracks in zircon do not segment or move randomly due to the low surface energy and low diffusivity of atoms at the track-matrix boundary. This explains the similarity between the complete disappearance of latent tracks in zircon at 830 ^{o}C after 90 min and that of etchable tracks at 800 ^{o}C after 1 hr.

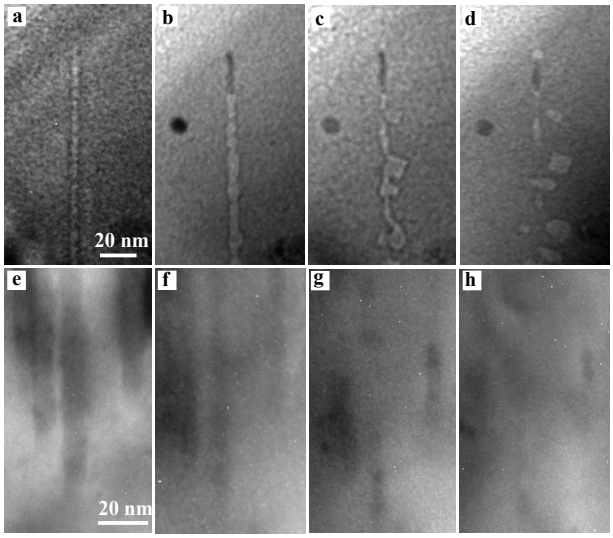

Figure 1: *In situ* isothermal annealing of latent tracks in apatite and zircon observed by TEM. (a-d) At 700 ^{o}C, a porous fission track in apatite gradually segments into shorter lengths; (a) before heating, and (b) after 1, (c) 53 and (d) 130 min. (e-h) At 830 ^{o}C, the amorphous tracks created by 2.2 GeV ions in zircon gradually disappear without track segmentation; (e) before heating, and (f) after 10, (g) 53, and (h) 90 min.

References

[1] W.X. Li, L.M. Wang, M. Lang, C. Trautmann, and R.C. Ewing, Earth Planet. Sci. Lett. (2010) In press, doi:10.1016/j.epsl.2010.12.016.

[2] W.X. Li, L.M. Wang, K. Sun, M. Lang, C. Trautmann, and R.C. Ewing, Phys. Rev. B 82(2010) 144109.

*Work supported by the Office of Basic Energy Sciences of the U.S. DOE (DE-FG02-97ER45656).

#wxli@umich.edu

Ion-Track Annealing Kinetics in Apatite

B. Afra[1], M. Lang[2], M. D. Rodriguez[1], N. Kirby[3], R. C. Ewing[2], C. Trautmann[4], and P. Kluth[1#]

[1]Australian National University, Canberra, Australia; [2]University of Michigan, Ann Arbor, MI, USA; [3]Australian Synchrotron, Clayton, Australia; [4]GSI, Darmstadt, Germany

Fission tracks in minerals, such as apatite and zircon, generated by energetic nuclear fragments that result from spontaneous fission of ^{238}U, are used for determining the age and thermal history of Earth's crust. Taken together with other techniques, the data infer rates of tectonic uplift and landscape evolution [1]. At elevated temperatures, these tracks shrink in size and fragment into sections until they are completely annealed. The current fission-track dating technique utilizes chemical etching, which preferentially attacks the radiation-damaged volume in the undamaged bulk. The etching procedure dissolves the nanometer-sized latent track and thus enlarges the structure such that it can easily be observed by optical microscopy. The number-density and length distribution of an etched-track population correlated with the present uranium content are then used to determine the age and thermal histories of archaeological and geological samples. The etching, however, completely erases the initial damage structure that essential information on the atomic scale of the underlying radiation damage is irrevocably lost. Little is known about the primary damage track, and how its morphology depends on geological parameters such as pressure, temperature, and mineral composition.

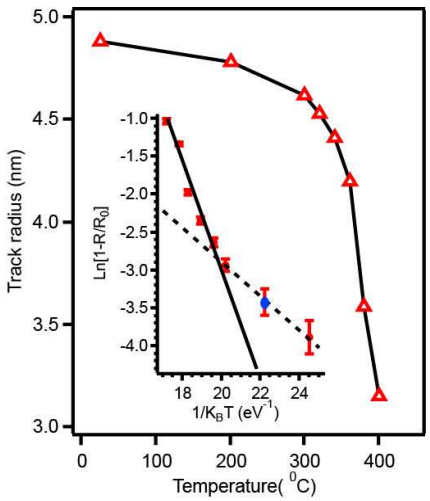

Figure 1: Ion-track radius deduced from SAXS measurements as a function of annealing temperature in apatite irradiated with 2.2 GeV Au ions. The inset shows the Arrhenius plot of the track radii.

Synchrotron based small angle X-ray scattering (SAXS) is a powerful tool for studying ion-track damage. It is sensitive to small density changes at the nanometer scale that often occur in the damaged track regions [2]. Here, we present SAXS measurements of the ion-track morphology and its annealing kinetics in high-energy ion irradiated Durango apatite, measured as an average over millions of tracks at a time [3].

Samples were prepared by irradiating 30-40 µm thick Durango apatite at the UNILAC accelerator using a variety of ion/energy combinations. In all cases the ion tracks extend through the entire thickness of the samples with approximately uniform electronic energy loss. The applied fluences were sufficiently low to yield well-separated aligned tracks. Without further preparation, the samples were investigated using transmission SAXS at the SAXS/WAXS beamline at the Australian Synchrotron. To study the annealing kinetics, we have performed isochronal annealing experiments as a function of temperature on a sample irradiated with 2.2-GeV Au ions. In contrast to track etching, the same sample can be used for a complete annealing series, thus reducing uncertainties associated with processing of multiple samples.

The track morphology is well described by a cylinder with a radius of ~5 nm and constant density, different from that of the matrix material, consistent with the formation of amorphous tracks [3]. Figure 1 shows the evolution of the track radius as a function of annealing temperature. The inset shows the same data as Arrhenius plot with linear fits to deduce the activation energies involved. The annealing is characterised by two stages. In stage I, up to 300ºC, there is a small but measurable reduction of the track radius, while stage II exhibits a more rapid decrease at higher temperatures. The activation energies amount to 0.23±0.05 eV for stage I and 0.72±0.02 eV for stage II. Stage I of the annealing is essentially athermal and consistent with a structural relaxation of the amorphous phase, possibly facilitated by point defect annihilation. A rapid quenching of the liquid phase in the ion track can leave an amorphous phase in a state that relaxes into an energetically more favourable configuration upon annealing below the recrystallization temperature. Stage II of the annealing process, characterized by the higher activation energy and lower rate, is consistent with recrystallization of the amorphous material in the ion track.

These results are central to a fuller development and exploitation of current fission-track methods in both geochronology and thermochronology.

References

[1] R.L. Fleischer, P.B. Price, and R.M. Walker, *Nuclear tracks in solids : principles and applications* (University of California Press, Berkeley, 1975).

[2] P. Kluth *et al.*, Phys. Rev. Lett. 101, 175503 (2008).

[3] B. Afra *et al.*, Phys. Rev. B (2011) accepted.

#patrick.kluth@anu.edu.au

Annealing Studies on Ion Tracks in Metallic Glasses

M.D. Rodríguez[1,#], B. Afra[1], C. Trautmann[2], N. Kirby[3], and P. Kluth[1]

[1]Australian National University, Australia; [2]GSI, Darmstadt, Germany; [3]Australian Synchrotron, Melbourne, Australia.

High energetic ions can lead to the formation of long columnar defects along the ion trajectories, so called "ion tracks". In amorphous metals, overlapping tracks produce macroscopic anisotropic growth phenomena [1]. Characterization and imaging of single ion tracks in these materials is challenging and has been successful only in a few cases using chemical etching [2], scanning probe [3] and transmission electron microscopy [4], and small angle X-ray scattering (SAXS) [5].

SAXS is a non destructive technique, highly sensitive to density changes at the nanometer length scale, and thus can yield important information about the damage morphology of ion tracks without modifying the studied samples. SAXS is also suitable to study ion track damage recovery by annealing experiments. Here, we investigate the ion damage recovery and the influence of the high energy irradiation on the recrystallization process with simultaneous SAXS and wide angle X-ray scattering (WAXS) measurements.

The ion tracks were produced by irradiating amorphous $Fe_{80}B_{20}$ with 11.1 MeV/u Au ions at a fluence of 1×10^{11} ions/cm^2 at the UNILAC accelerator. The track structure was studied using SAXS performed at the Australian Synchrotron. Measurements as a function of angle between the X-ray beam and the track orientation show a high anisotropy of the scattering pattern. This is consistent with aligned structures of high aspect ratio and provides clear evidence for the existence of tracks.

SAXS intensities of the ion tracks extracted from detector images can be well modelled assuming a cylindrically symmetrical density distribution with a constant density that is different from that of the matrix material. This model assumes continuous track damage and approximately constant energy loss throughout the sample. To study the kinetics of track annealing, we performed isochronal annealing experiments applying temperatures between 200°C and 450°C. The annealing of the irradiated samples leads to a gradual decrease of the track radii due to the relaxation of the ion track boundaries. The track radii obtained from the SAXS analysis of the irradiated $Fe_{80}B_{20}$ sample are plotted in figure 1, showing the recovery of the damage as a function of temperature. The annealing of this sample is characterized by an activation energy for the ion track damage recovery of 0.4±0.1 eV. At 360°C, after the onset of recrystallisation, we could not detect a SAXS signal from the ion tracks.

The WAXS spectrum shown in figure 2 indicates that the presence of ion tracks enhances the recrystallization of the sample. Once the recrystallization process is complete, no differences were found in the WAXS spectra of the irradiated and unirradiated samples. A possible explanation for the observed differences during the recrystallization of both samples is the formation of nucleation centers during the ion irradiation process.

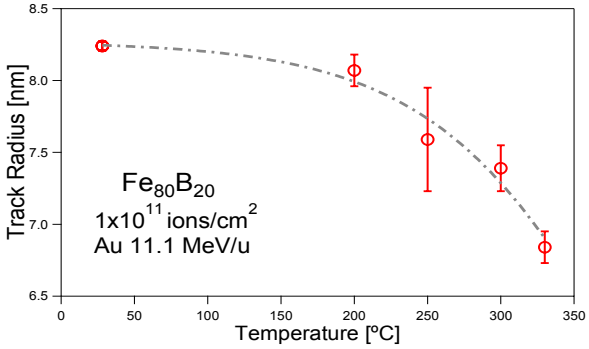

Figure 1: Track radii extracted from fits to the SAXS data versus of annealing temperature. The line is plotted to guide the eye.

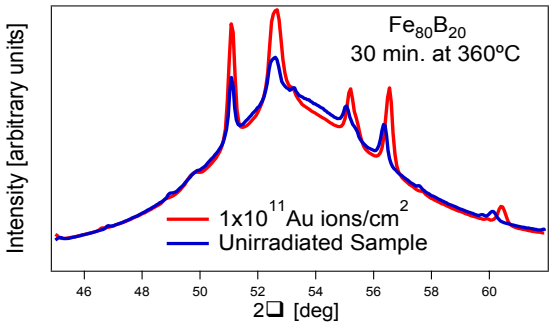

Figure 2: WAXS spectra of irradiated and unirradiated $Fe_{80}B_{20}$ samples after annealing for 30 minutes at 360°C.

Similar experiments are planned using $Fe_{85}B_{15}$, $Fe_{81}B_{13.5}Si_{3.5}C_2$, and $Fe_{40}Ni_{40}B_{20}$ samples, as well as different irradiation conditions in order to systematically characterize the track recovery and the recrystallization of metallic glasses.

References

[1] M.-D. Hou *et al.*, Phys. Rev. B 41 (1990) 1144
[2] C. Trautmann*et al.*, Nucl.Instr. Meth. In Phys. Res. B 107 (1996) 397
[3] A. Audouard*et al.*, Europhys. Lett. 40 (1997) 527
[4] G. Rizza *et al.*, J. Phys: Cond. Matter 16 (2004) 1547
[5] M.D. Rodríguez *et al.*, (in preparation)

#Matias.rodriguez@anu.edu.au

Color centers beyond ion range in LiF crystals irradiated with Ni ions

M. Ditter[1], K. Schwartz[2], F. Fujara[1], B. Schuster[1,2], C. Trautmann[2] and K.-O. Voss[2]

[1]TU Darmstadt, Darmstadt, , Germany; [2]GSI, Darmstadt, Germany.

LiF crystals exposed to swift heavy ions exhibit unexpected coloration phenomena at a depth up to 3 mm beyond the ion range. The induced color centers were investigated by thermo-stimulated luminescence, optical absorption, and nuclear magnetic resonance (NMR) spectroscopy. The crystals were irradiated with various ions from ^{12}C to ^{238}U at the UNILAC accelerator (see [1] and references therein). The experimental conditions exclude the possibility of diffusion of point defects, migration of electronic excitations, or recoil atoms producing color centers beyond the ion range. We assumed that the observed effects are due to some kind of radiation which can transfer energy from the irradiated crystal layer ($z \leq R$) to the non-irradiated part beyond the ion range ($z > R$).

For LiF irradiated with heavier particles such as ^{130}Xe, ^{197}Au, and ^{238}U ions, this radiation was identified as the characteristic X-ray emission from the projectile ions [1]. Also, nuclear reactions between the projectiles and target nuclei can lead to compound nuclei producing long-range effects by the emission of γ rays and light charged particles such as protons and alphas [2].

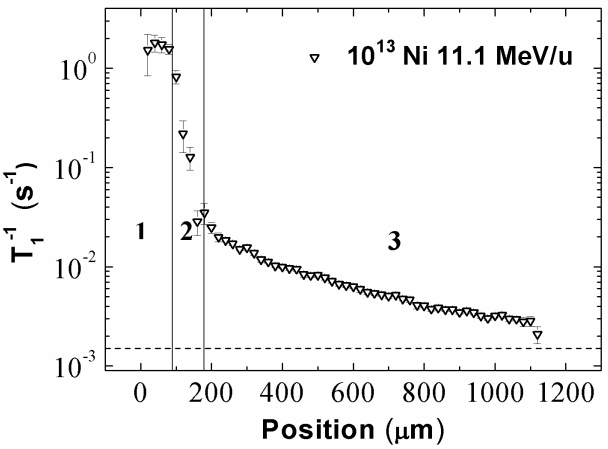

Figure 1: Spin-lattice relaxation rate as a function of depth position in a LiF crystal irradiated with Ni ions.

Recently, additional irradiation experiments were performed using ^{64}Ni ions (8.3 and 11.1 MeV/u). Although the range of 8.3 MeV/u Ni ions in LiF is only R = 87 μm, secondary radiation was measured with a Si detector even behind a 400 μm thick LiF sample. The energy of this radiation was between 3 and 28 MeV. This secondary radiation produces coloration of the crystal far beyond the projected ion range and is probably due to protons and/or α particles [2].

To investigate the color centers produced within and beyond the ion range, a special NMR method was applied which allows the measurement of the profile of the one-dimensional spin-lattice relaxation rate (T_1^{-1}). The spatial resolution is around 10 μm [1]. This method is most suitable for LiF crystals, because T_1^{-1} is decisively influenced by paramagnetic defects, such as F-centers and we can measure the distribution of F centers created by irradiation with heavy ions. The spin-lattice relaxation rate was studied in the irradiated part ($z \leq R$) of the crystal and beyond the ion range. Due to the low concentration of F centers beyond the range, LiF crystals irradiated with a high fluence of 10^{13} ions/ cm² were examined.

The relaxation rate profile of a LiF crystal irradiated with 11.1 MeV/u ^{64}Ni shows three characteristic regions (Fig. 1) in agreement with previous experiments [1]. Region 1 ($z \leq R$) within the ion range is characterized by a high density of F centers, responsible for the observed strongly increased relaxation rates. Region 2 is ascribed to the interface between the irradiated and non-irradiated crystal. The width of this transition is probably due to improper alignment of the sample with respect to the magnetic field. Region 3 ($z > R$) is clearly beyond the ion range. Compared to the non-irradiated crystal (dotted line), the relaxation rate is significantly enhanced. For larger depths, T_1^{-1} slowly decreases.

Compared to heavier ion beams such as ^{130}Xe, ^{197}Au, and ^{238}U, the sample irradiated with 11.1 MeV/u ^{64}Ni ions the beyond-range effect ($z > R$) is more pronounced and the overall T_1^{-1} level is higher. A similar relaxation rate profile was observed in LiF irradiated with 8.3 MeV/u Ni ions, however, due to the lower energy, the effect is less pronounced.

The concentration of F centers beyond the ion track ($z > R$) was measured by optical absorption spectroscopy [1]. The total thickness of the LiF crystal irradiated with 8.3 MeV/u ^{64}Ni ions was 3 mm. In the layer 400 μm beyond the irradiated layer, the concentration of the F centers was 5.7×10^{14} cm^{-2} in agreement with the NMR measurements.

Additional experiments (NMR and EPR) with other light ions and LiF crystals with different trace elements are planned.

References

[1] H. Stork, K.-P. Dinse, M. Ditter et al.,J. Phys.: Condens. Matter **22** (2010) 185402.

[2] J. Czudek et al., Phys. Rev. **43** (1991) 1248.

Energy Dependence of XRD Intensity Change in Au-Irradiated CeO_2

N. Ishikawa[1], K. Takegahara[1], O. Michikami[2], C. Trautmann[3], R. Neumann[3]

[1]JAEA, Tokai, Ibaraki 319-1195, Japan; [2]Iwate Univ., Morioka, Iwate 020-0066, Japan, [3]GSI, Darmstadt, Germany

Introduction

It is already known that nanometer-sized ion tracks are formed in CeO_2 by irradiation with Xe ions of energy in the range of 80-210 MeV [1]. Although the -tracks are not completely amorphized, each of them can be observed as cylindrically disordered regions using transmission electron microscopy [1]. The study of radiation-induced damage in this material is important for elucidating the mechanism of damage creation during burn-up of oxide nuclear fuels. High-density electronic energy deposition of energetic ions is a key process for ion-track formation. In this study, the energy dependence of damage in ion-irradiated CeO_2 is analyzed.

Experimental

Thin films of polycrystalline CeO_2 were prepared on sapphire substrates by dc sputtering. The films had a thickness of about 0.3 μm and were irradiated at room temperature with 1.7-GeV Au ions from the UNILAC accelerator at GSI and with 170- and 340-MeV Au ions from the tandem accelerator at Tokai Research and Development Centre, Japan Atomic Energy Agency (JAEA-Tokai). In order to characterize the ion-induced damage, X-ray diffraction (XRD) profiles were measured before and after the irradiation.

Results and Discussion

Before irradiation, the (200) as well as the (111) and (400) peaks of CeO_2 are observed as strongest XRD peaks. As shown in Fig.1, marked decrease in the intensity and the area of the (200) peak appear after the irradiation with 1.7-GeV Au at fluences of 1×10^{12} ions/cm^2 and higher. This observation clearly indicates pronounced damage in the crystal by the accumulation of ion tracks. Moreover, the peak position slightly shifts to larger angles corresponding to a monotone decrease of the lattice parameter with increasing fluence. New peaks are not observed after the irradiation. The changes of the peak profile observed for 170- and 340-MeV Au irradiations are qualitatively the same as those for 1.7-GeV Au irradiation.

In this report, we focus on the decrease in the (200) peak intensity. Figure 2 shows the energy dependence of the slope of the peak intensity as a function of fluence assuming a linear evolution. In the same figure, the energy dependence of the electronic stopping power, S_e, estimated by the SRIM code [2] is plotted for comparison. In contrast to the energy loss curve, the magnitude of the slope for the irradiation with 340-MeV Au ions is higher than for 1.7-GeV and 170-MeV ions. The results for the change in peak width and lattice parameter exhibit the same trend. To explain this behaviour, it may be necessary to take into account that the damage quantitatively does not only scale with the electronic stopping power but also with the ion velocity which was demonstrated to affect the size of the ion track [3].

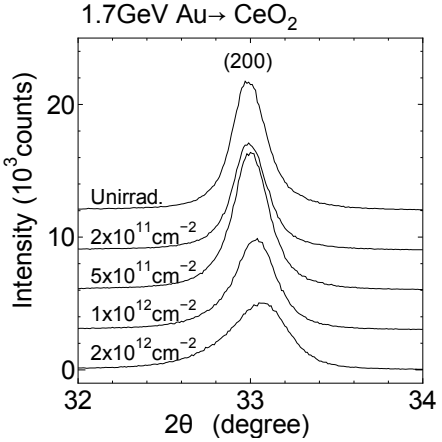

Figure 1: XRD profiles of CeO_2 irradiated with 1.7-GeV Au at different fluences. The curves are shifted in vertical direction in order to facilitate comparison of profiles.

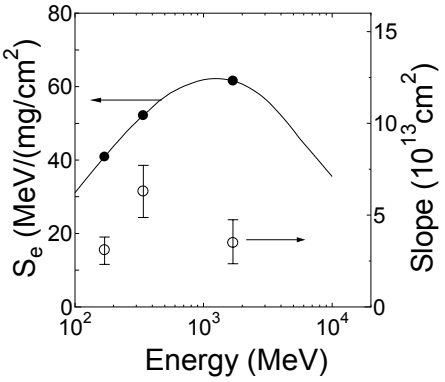

Figure 2: Magnitude of the slope of the decrease in peak intensity plotted against ion energy (open circles) for CeO_2 crystals irradiated with Au ions. The energy dependence of the energy loss S_e (closed circles and solid curve) is also shown for comparison.

References

[1] T. Sonoda et al., Nucl. Instr. Meth. B 250 (2006) 254.
[2] J.F. Ziegler, Nucl. Instr. Meth. B 219-220 (2004) 1027.
[3] A. Meftah et al., Phys. Rev. B 48 (1993) 920.

Study on effects of swift heavy ion irradiation in CeO_2 using XRD method

Y. Tahara[1], A. Iwase [1,#], R. Neumann[2], and C. Trautmann[2]

[1]Osaka Prefecture University, Sakai, Osaka, Japan; [2]GSI, Darmstadt, Germany

Introduction

In our previous study, we have used CeO_2 as a simulation material of a fission fuel, UO_2, because CeO_2 has many properties that are similar to UO_2. We reported the effects of swift heavy ion irradiation (mainly 200 MeV Xe ions) in CeO_2 to simulate radiation effects of high energy fission products in UO_2 [1,2]. To study radiation effects at higher energies and with heavier ions additional irradiation experiments were performed with 1.7 GeV Au ions. Beam-induced structural modifications were analysed by means of X-ray diffraction (XRD).

Experimental procedure

Samples used in this study were pellets of pure cerium dioxide, CeO_2. They were irradiated at room temperature with 8.6 MeV/u (1.7 GeV) Au ions at the UNILAC accelerator, applying fluences of 5×10^{11}, 1×10^{12}, 2×10^{12}, and 5×10^{12} ions/cm^2. To estimate the radiation effects, the irradiated pellets were investigated by conventional Cu-Kα XRD.

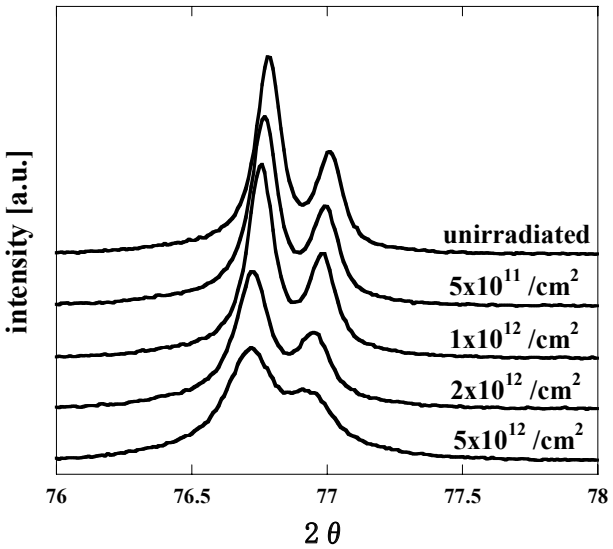

Figure 1: The XRD spectra showing the (331) reflection of unirradiated sample and those irradiated with 8.6 MeV/u Au ions at various ion-fluences.

Results and discussion

After the irradiation no new peaks are observed in the broadly scanned XRD spectra. The lattice structure obviously remains unchanged after the irradiation.

However, when analyzing diffraction peaks at each angle, it can be observed that the peaks shift to lower angles and broaden with increasing ion fluence. Fig. 1 illustrates the (331) diffraction peaks of unirradiated and irradiated samples. Figure 2 shows the corresponding lattice constant and full width at half maximum (FWHM) as a function of the ion fluence. The increasing lattice constant and FWHM is an indication that the irradiation induces an expansion and disordering of the lattice. These results are similar to our previous study on CeO_2 irradiated with 200-MeV Xe ions [2]. Quantitative comparison is in progress.

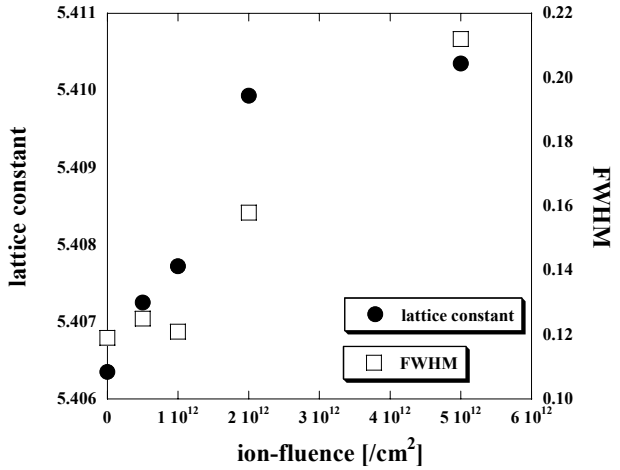

Figure 2: Lattice constant and FWHM of (331) diffraction peaks as a function of fluence of 8.6 MeV/u Au ions.

References

[1] H. Ohno, A. Iwase, D. Matsumura, Y. Nishihata, J. Mizuki, N. Ishikawa, Y. Baba, N. Hirao, T. Sonoda, M. Kinoshita, Nucl. Instr. Meth. B 266 (2008) 3013.

[2] Y. Tahara, B. Zhu, S. Kosugi, N. Ishikawa, Y. Okamoto, F. Hori, T. Matsui, A. Iwase, Nucl. Instr. Meth. B (2011) online available.

iwase@mtr.osakafu-u.ac.jp

Structural modification of swift heavy ion irradiated amorphous Ge layers at low temperatures*

T. Steinbach[1,#], C.C. Jacobi[1] , W. Wesch[1], D. Severin[2], M. Bender[2] and C. Trautmann[2]

[1]FSU Jena, IFK, Jena, Germany; [2] GSI, Darmstadt, Germany

Recent room-temperature irradiation experiments exposing amorphous germanium (a-Ge) to 185-MeV heavy ions (SHI) at the ANU accelerator facility (Canberra, Australia) revealed strong volume expansions [1]. A detailed study of this effect using various irradiation parameters [2] demonstrates that this swelling is caused by the formation and growth of randomly distributed voids leading to a gradual transformation of the a-Ge layer into a porous structure. Moreover, the swelling linearly depends on the ion fluence and on the value of electronic energy deposition. This clearly demonstrates that the structural changes are determined solely by the electronic energy deposited within the amorphous layer. We thus conclude that voids are formed in a-Ge, if a specific threshold value of the energy deposited by electronic processes is exceeded [2].

In this project we investigated the effect of the irradiation temperature as well as the influence of higher electronic energy deposition on the void formation in a-Ge. Prior to the irradiation at GSI, crystalline Ge-wafers were amorphised by ion irradiation with various low energy (0.1 - 6.7-MeV) Ge-ions and fluences at 80 K, resulting in a 3.1 µm thick amorphous layer. The irradiations with SHI were performed at the new M3-branch at the UNILAC. For this purpose, a new target holder was constructed allowing simultaneous irradiations at room (RT) and low temperature (LT), which enables the comparison of both samples under same irradiation conditions. The sample was irradiated at T ~ 290 and 55 K with 940-MeV Au ions (projected range ~ 39 µm). The beam flux was 1×10^9 cm^{-2} s^{-1} and the fluence ranged between 2×10^{11} and 2.3×10^{13} cm^{-2} (accuracy ± 30%). In order to quantify the swelling by direct comparison of irradiated and unirradiated material, one half of the sample was masked.

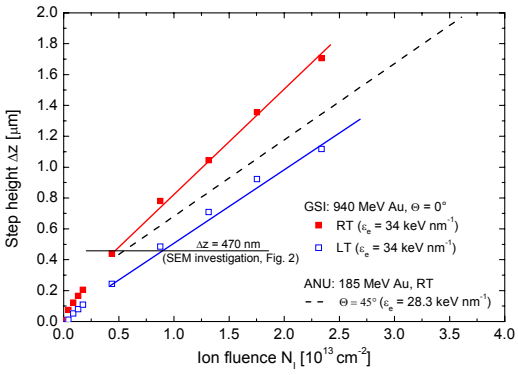

Figure 1: Mean step height Δz at the surface of a-Ge irradiated with 940-MeV Au ions at RT (full symbols) and at 55 K (open symbols) as a function of ion fluence. The dashed line corresponds to swelling induced with 185-MeV Au ions from irradiation experiments at ANU [2].

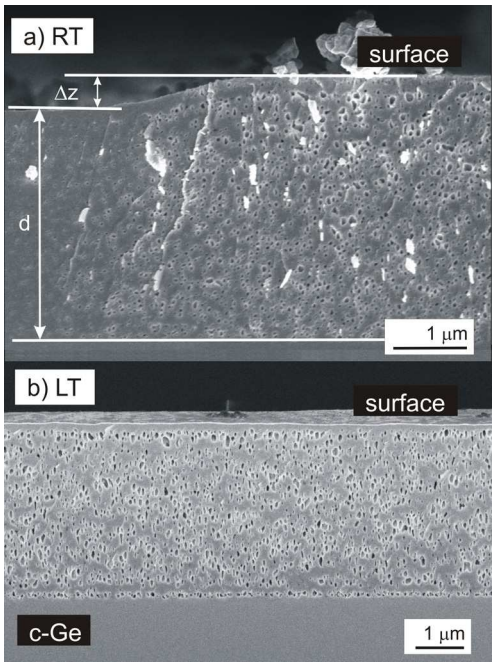

Figure 2: Cross section SEM images showing the formation of voids after the irradiation at room temperature (a) and at 55 K (LT) (b).

In Fig. 1 the step height Δz determined by surface profilometry is depicted as a function of the ion fluence. For both irradiation temperatures, a linear dependence is observed similar to previous results (dashed line, data from Ref [2]). For a given ion fluence, the volume expansion is significant smaller for LT than for RT. Cross section scanning electron microscopy (SEM) investigations revealed the transformation of the initially homogeneous a-Ge layer into a porous structure with irregularly shaped voids (Fig. 2). The samples shown in Fig. 2 had approximately the same step height of Δz ~ 470 nm (see Fig. 1). The formation of voids, which accumulate with increasing ion fluence to form a porous layer, takes place solely in the 3.1 µm thick amorphous surface layer while the underlying substrate remains crystalline and free of voids.

The mechanisms of void formation and the transformation into a sponge like structure are not yet understood and will be subject of further investigations.

References

[1] W. Wesch et al., J. Phys. D: Appl. Phys. 42 (2009) 115402.

[2] T. Steinbach et al., Phys. Rev. B, accepted

* Work supported by BMBF, contract no. 05KK7SJ1.

tobias.steinbach@uni-jena.de

Radiation damage in heavy ion-irradiated carbonate minerals investigated by Raman and infrared spectroscopy*

S. Pabst[1], M. Burchard[1], U.A. Glasmacher[1#], R. Miletich[1], R. Neumann[2], B. Schuster[2], C. Trautmann[2]

[1]Institut für Geowissenschaften, Heidelberg, Germany; [2]GSI, Darmstadt, Germany

The carbonates calcite (hexagonal; $CaCO_3$), aragonite (orthorhombic; $CaCO_3$), and dolomite ($CaMg(CO_3)_2$) belong to the most abundant minerals at the Earth's crust. They are major constituents of limestone and marble and are incorporated in the shell material of many organisms. Natural carbonate minerals can contain U and Th atoms leading to spontaneous fission. The fission fragments have high kinetic energy and produce particle tracks on a geological time scale, which is used to estimate the time that elapsed since the onset of track accumulation.

At present, only little is known about the specific radiation damage in carbonates induced by energetic particles [1,2]. To improve the understanding of damage production in carbonate minerals, natural calcite, aragonite, and dolomite were exposed to relativistic heavy ^{238}U and ^{197}Au ions of 5.6 and/or 11.1 MeV/u kinetic energy and fluences between 10^6 and 10^{12} ions/cm^2 at the UNILAC accelerator. Irradiation of pressurized calcite was performed with a Paris-Edinburgh-cell (PE-cell). The applied pressure was 2.9 GPa at room temperature during irradiation with ^{238}U at a fluence of 10^{12} ions/cm^2 with a primary kinetic energy of 400 MeV/u. The high energy provided by the heavy ion synchrotron (SIS) at GSI, allows the ions to penetrate through the diamond anvil as well as through the complete sample.

The effect of irradiation on the crystal lattice was investigated by means of micro-Raman spectroscopy. Irradiated calcite reveals changes in the Raman spectra above 10^{11} ions/cm^2 (Fig. 1). Structural damage is probably accompanied by the formation of new phases such as CaO due to loss of CO_2. Our investigation further suggests weakening and/or shortening of bonds combined with amorphization caused by intense irradiation with swift heavy ions.

Irradiation of calcite under a pressure of 2.9 GPa modifies the frequency and shape of the Raman signals as a function of fluence and reduces the Raman intensities due to pressure. New bands appear at ~430 and ~494 cm^{-1} and the satellite band at 1066 cm^{-1} disappears (Fig. 2).

No significant changes in the Raman spectra of dolomite and aragonite could be detected. Further investigation is needed to better understand how and to what extent the carbonate mineral structures change by irradiation with swift heavy ions.

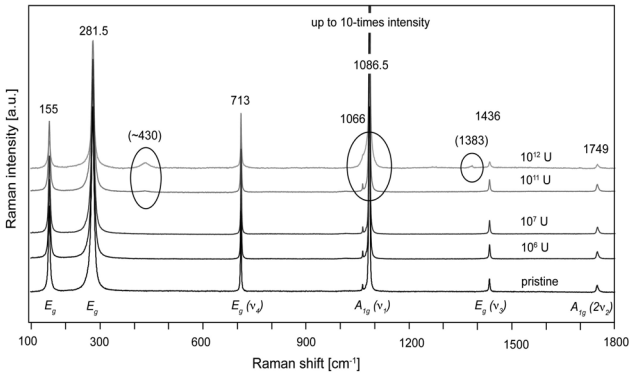

Figure 1: Raman spectra (baseline corrected) of calcite irradiated with U ions at different fluences. Peak positions are given for pristine calcite, values in brackets indicate new bands of irradiated calcite.

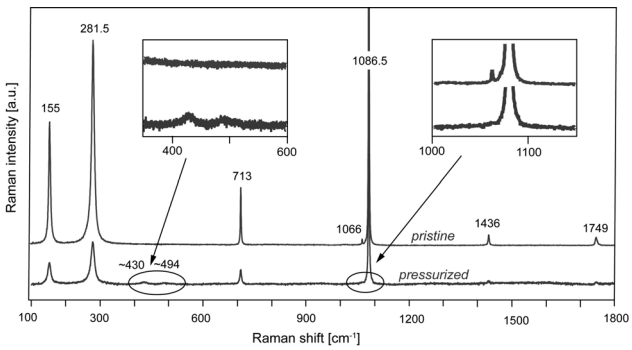

Figure 2: Raman spectra (baseline corrected) for pristine calcite compared to calcite irradiated under a pressure of 2.9 GPa (10^{12} U ions/cm^2, 5.6 MeV/u).

References

[[1] F.M. Ohnesorge et al., Nucl. Instr. Meth 166 (2000) 938.

[2] H. Nagabhushana, S. C. Prashantha, B. M. Nagabhushana, B. N. Lakshminarasappa, F. Singh, Spectrochimica Acta Part A 71 (2008) 1070.

* Work supported by BMBF Verbundprojekt grant No 05KK7VH and 05K10VH1

#ulrich.a.glasmacher@geow.uni-heidelberg.de

Etching of Calcite for Fission-Track Dating*

Sebastian Dedera[1], Michael Burchard[1], Ulrich A. Glasmacher[1#], Sonja Pabst[1], Christina Trautmann[2]

[1]Institute of Earth Sciences, University of Heidelberg, Heidelberg, Germany; [2]GSI, Darmstadt, Germany

The method of fission-track dating is highly established in thermochronology to define the range of temperature rocks have been exposed to in the past. As carbonate rocks are abundant in Earth's crust, our new approach tries to apply the fission-track thermochronology to calcite dominated rock formations. First steps of this project include defining suitable etching agent and specifying etching conditions. Different etching recepies [1-3] have been tested with respect to their effectiveness.

As the uranium content of natural calcite is highly variable, we simulated natural fission fragments of ^{238}U by using accelerated heavy ions. The experiments were performed with annealed natural calcite crystals irradiated with 11.1 MeV/u ^{238}U or ^{197}Au ions at the UNILAC. Fluences between 10^6 and 10^8 ions/cm^2 were applied. During irradiation, the surface of some calcite crystals was covered with a hexagonal mask to create irradiated and non-irradiated sites next to each other (Fig. 1).

Agents tested for etching are formic acid (CH_2O_2), sodium hydroxide (NaOH), hydrochloric acid (HCl), and a 1:1 mixture of ethylenediaminetetraacetic acid (EDTA) and 5% acetic acid, the latter showing best results so far.

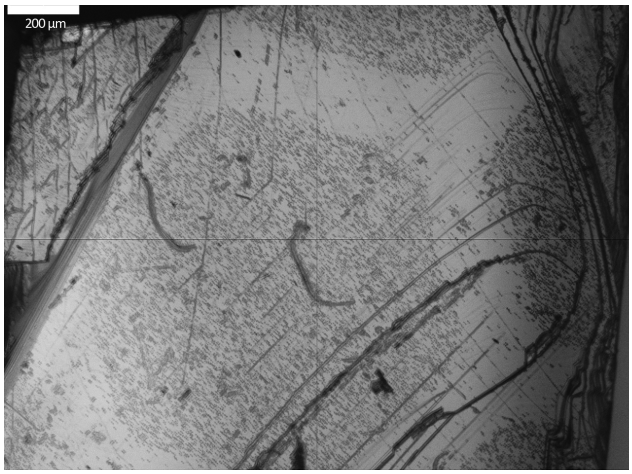

Figure 1: Ion-irradiated surface of Calcite after etching in a mixture of EDTA and 5% acetic acid (30 s). Irradiated areas containing etch pits (grey) and masked areas (light) are visible.

After 15 s etching in the EDTA and acetic-acid mixture, etch pits are visible in reflected light as small black dots on the calcite surface. The best visibility of the etch tracks is given after 20-30 s, then the etch pits are fully developed in shape but do not yet overlap (Figs. 2). The etch pits have a elongated hexagonal shape. After 30 seconds of etching they are approximately 8 µm long and 4 µm wide. For etch times larger than 30 s, the size of etch pits became to large and started to overlap with neighboring pits. The number of etch pits is in good agreement with the applied fluence giving evidence that the etching process has a high efficiency. The fact that each ion track is converted into an etch pit provides optimal conditions for future track dating by means of fission fragments etching in natural calcite. It remains to be demonstrated that also tracks of lighter ions (typical mass of fission fragments between 80 and 130) are etchable with the same high efficiency. Further activities will in addition focus on other carbonate minerals such as dolomite, aragonite, azurite, malachite, and rhodochrosite.

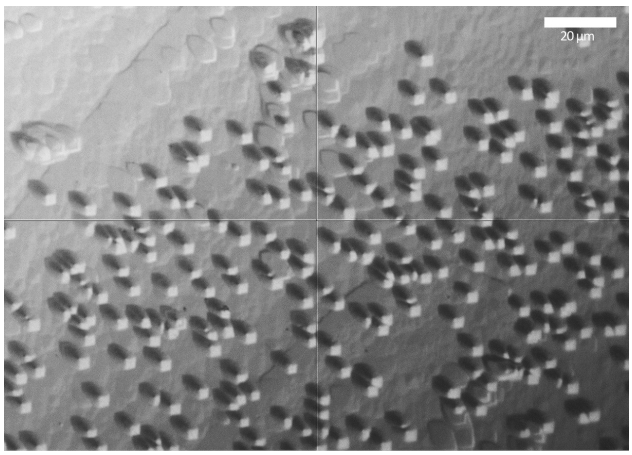

Figure 2: Calcite surface after 30 s in EDTA + 5% Acetic Acid. The border between irradiated and non-irradiated areas is located in the top left corner (scale bar 20 µm).

References

[1] S. Krishnaswami, D. Lal, N. Prabhu, A.S. Tamhane, Olivines, "Revelation of Tracks of Charged Particles", Science 174 (1971) 287.

[2] R.F. Sippel and E.D. Glover, "Fission Damage in Calcite and the Dating of Carbonates", Science 144 (1964) 409.

[3] D. MacDougall, P.B. Price, "Attempt to Date Early South African Hominids by Using Fission Tracks in Calcite", Science 185 (1974) 943.

* Work supported by BMBF Verbundprojekte under No. :05KK7VH and No. 05K10VH1.

#ulrich.a.glasmacher@geow.uni-heidelberg.de

Ion-beam induced luminescence in n-type ZnO

R. Stübner[1], M. Allardt[1], D. Severin[2], M. Bender[2] and J. Weber[1]

[1]Technische Universität Dresden, Germany; [2]GSI, Darmstadt, Germany

In this project, the creation and evolution of radiation-induced defects in semiconductors was studied by ionoluminescence. This technique allows in-situ studies of radiative recombination of electron-hole pairs produced during the irradiation with energetic ions.

Damage formation by high energy ions is complex and includes different processes starting with initial defects, followed by diffusion, annihilation, and clustering of defects until finally stable defects are formed. At present, it is not well understood how the properties of intermediate defects influence the final damage state. Some of these defects have a very short lifetime and cannot be investigated after the irradiation. For example, Si-interstitials in p-type silicon are very mobile even at very low temperatures (4.2 K) [1]. Because they easily interact with impurities, it is very challenging to observe them as isolated defects. By exploiting the luminescent recombination of electron-hole pairs created during the initial damage process, we want to get insight into the electronic properties of transient defects.

Ion-beam induced luminescence measurements were performed using a dedicated system attached to the M3 branch of the UNILAC. The first experiments were performed with several wide-band gap semiconductors such as ZnO and GaP, as it is much easier to optimise the equipment using visible light. In the future, we plan to extend our investigations to the near infrared range to investigate also semiconductors with smaller band-gaps (e.g. Si, GaAs).

The investigated samples were vapour phase grown n-type ZnO single crystals (Helbig). They were mounted on a closed-cycle He-cryostat and irradiated with 4.8 MeV/amu Au ions at different sample temperatures (T= 300 K, 30 K)**.** The samples were irradiated with a flux of approximately 5×10^9 ions $cm^{-2}s^{-1}$. The induced ionoluminescence disappeared after ~ 15 min corresponding to a fluence of ~5×10^{12} ions/cm^2. Ionoluminescence spectra measured within the first 15 min. are presented in Fig. 1 [2]. All spectra show a broad peak near the band edge of ZnO which are probably of excitonic origin.

Additional photoluminescence (PL) investigations after the irradiation revealed pronounced changes in the spectrum, the most obvious being the complete disappearing of the green band between 450 and 600 nm (Fig. 2), which is related to copper impurities. In the samples grown at our Institute, the disappearance of the green band was accompanied by the creation of a new broad band centered at 700 nm (not shown). The responsible defect of this band is not known. Also in all investigated samples, the hydrogen content seems to be reduced in the implanted layer, as the H-related PL-peak is clearly reduced in intensity (not shown).

We found that the ionoluminescence spectra are similar but not equal to the PL spectra of the samples. To find the energy levels of the transient defects we have to identify the origin of the peaks in the excitonic region to separate the transient defects from the stable defects.

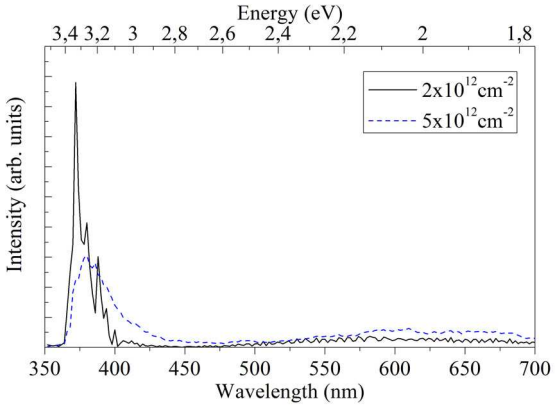

Figure 1: Ionoluminescence spectra of ZnO during irradiation at ~30 K with 4.8 MeV/amu Au ions for two different fluences.

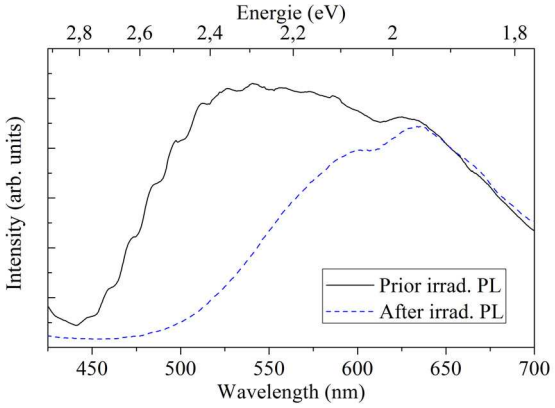

Figure 2: PL spectra of ZnO crystals before and after irradiation with 4.8 MeV/amu Au ions of fluence of approx. 5×10^{12} cm^{-2}.

References

[1] G. Watkins, "Intrinsic defects in silicon", Materials Science in Semiconductor Processing, Volume **3,** 2000, pp 227-235

[2] R. Stübner, "Untersuchung Ionenstrahl-induzierter Lumineszenz im Zinkoxid", diploma thesis, TU Dresden (2010)

Depth Profiling of Damage in Graphite Induced by Swift Heavy Ions*

M. Tomut[1,2,#], W. Ensinger[3], M. Krause[1,3], C. Trautmann[1]

[1]GSI, Darmstadt, Germany; [2]NIMP, Bucharest, Romania, [3] TU Darmstadt, Germany

Information on radiation damage in graphite is mainly available from neutron irradiation in nuclear reactors. Damage induced by neutrons is quantified in dpa (displacements per atom). For swift heavy ions (SHI), dpa values are not relevant, because they produce damage via electronic excitations and ionization, and damage creation strongly depends on the class of material. At the future Super-FRS at FAIR, the graphite production target will be operated in transmission mode. Here, the primary beam loses energy mostly by inelastic collisions, while in the beam catchers also elastic collision cascades will contribute to damage. The present work assesses damage in the nuclear and electronic stopping regimes in graphite by means of Raman spectroscopy.

Samples of polycrystalline isotropic graphite (SGL-R 6650 grade) were irradiated at room temperature with 11.1 MeV/u ^{238}U ions, at the UNILAC. The fluence was 1×10^{13} ions/cm^2, corresponding to complete coverage of the irradiated layer with ion tracks and to overlapping of collision cascades at the end of the ion range. Energy-loss and range (~120 µm) were calculated using the SRIM 2008 code. The depth evolution of the damage was monitored by performing micro-Raman spectroscopy on the cross-section of the sample starting from the surface down to the end of the irradiated layer. The Raman laser spot had a diameter of 2 µm and the step size for the depth profiling of damage was 8 µm.

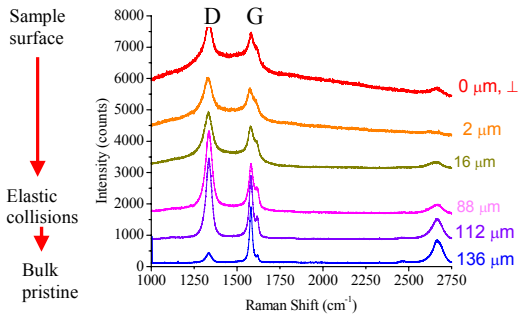

Figure 1: Raman spectra of isotropic graphite irradiated with 1×10^{13} U ions/cm^2 within the depth of the irradiated layer. Ion range is ~120 µm.

The Raman spectra within the irradiated graphite layer show that the graphitic structure evolves toward glassy carbon in the case of electronic stopping regime or towards nanocrystalline carbon in the elastic collisions regime (Fig. 1). The glassy carbon structure on the surface of the irradiated graphite is confirmed by the presence of the characteristic broad peak in the X-ray diffraction pattern of this sample (Fig. 2). We have used two parameters deduced from Raman spectra to characterize the structure of the irradiated samples. One is the intensity of a broad peak at about 1460 cm^{-1},*Iam*, that can be fitted between the defect peak, D, and the graphitic peak, G. The other parameter takes into account the tortuosity of the graphitic layers. It is called the average continuous graphene length including tortuosity, *Leq* [1]. The intensity of the broad peak *Iam* in the Raman spectra scales with the electronic energy loss (Fig. 3). Higher values at the surface of the sample indicate increased sensitivity of the surface to damage. The Leq, scaling with the phonon mean free path increase abruptly at depths larger than 120 µm, indicating no damage beyond the ion range, in good agreement with SRIM calculations.

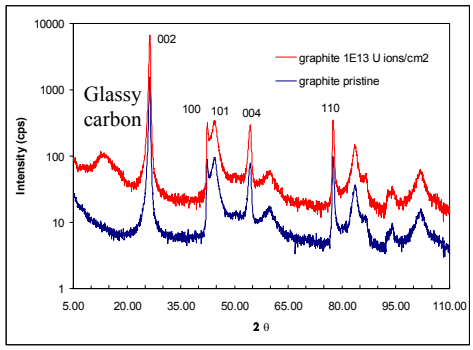

Figure 2: XRD pattern of irradiated and pristine graphite.

Glassy carbon is a non-graphitizing carbon allotrope characterized by closed porosity surrounded by strongly bent graphitic layers. It has a lower density than graphite, and is probably responsible for swelling observed in graphite irradiated with swift heavy ions. Sswelling, also leads to stress development at the interface between irradiated and non-irradiated material.

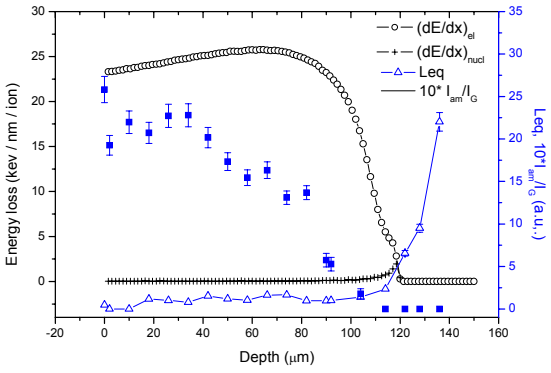

Figure 3: Depth profile of ion–induced damage quantified by the ratio of the intensities (*Iam/IG*) and by *Leq*. Superimposed are the total (circles) and nuclear (crosses) energy loss of 11 MeV/u U ions in polycrystalline graphite.

m.tomut@gsi.de

[1] N. Larouche, B.L. Stansfield, Carbon 48 (2010) 620.

High Temperature Irradiation Experiments at M-branch Relevant for Ion-Induced Damage Annealing in High Power Production Targets

M. Avilov[1], M. Bender[2], W. Mittig[1], F. Pellemoine[1,3], M. Schein[1], D. Severin[2], M. Tomut[2,4,#] and C. Trautmann[2]

[1]MSU, East Lansing, MI, U.S.A; [2]GSI, Darmstadt, Germany; [3]GANIL, Caen, France; [4]NIMP, Bucharest, Romania

The FRIB and Super-FRS high power graphite production targets [1] will undergo bombardment with very intense heavy ion beams with up to 5×10^{13} U ions/s at 200 MeV/u and 1×10^{12} U ions/s at 1 GeV/u, respectively. Graphite behaviour under such extreme conditions is of great importance, since a strong swelling has been observed in a number of experiments [2]. Study of defect annealing in carbon was mostly limited to damages induced by neutrons and temperatures up to 900 °C. In the present work we discuss the annealing behaviour of heavy ions induced radiation damage at irradiation temperature up to 1500 °C.

Thin graphite foils with dimensions $25\times12.5\times0.075$ mm^3 made of MERSEN CL2320 and CL2360 graphite [3] were placed on a fixture inside the vacuum chamber (Fig. 1). The chamber comprises the 6-way cross made of stainless steel, with one port connected to the M3-beamline at GSI-UNILAC.

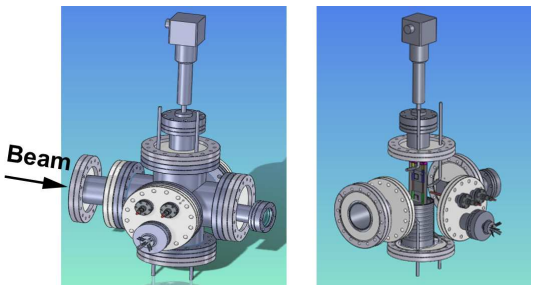

Figure 1: Sketch of the experimental setup.

Other ports are closed with flanges, on which linear feedthrough, current inlets, and beam dump are mounted. Samples are electrically connected to current inlets that make possible Ohmic heating using DC current. A quartz window allows the monitoring of sample temperature with an infrared thermal camera. Sample thicknesses of about 75 µm, smaller than the range the 8.6 MeV/u ^{197}Au ions in graphite have been used to simulate the target irradiation in transmission mode.

During the experimental series, samples being heated by DC current to different temperatures were irradiated. Sample with no external heating irradiated to 10^{14} ions/cm^2 total fluence showed strong pocket-like deformation (with 5-10% size increase) attributed to the beam spot (Fig. 2a). Sample heated to 900°C irradiated to the same fluence (Fig. 2b) revealed moderate deformation and resulting cracks around the beam spot. No notable deformation has been observed on a sample irradiated at 1500°C up to 10^{14} ions/cm^2 (Fig. 2c). Finally, the sample shown in Fig. 2d was exposed in total to 10^{15} ions/cm^2 being heated up to 1500°C. Some deformation is seen. This sample broke during dismounting.

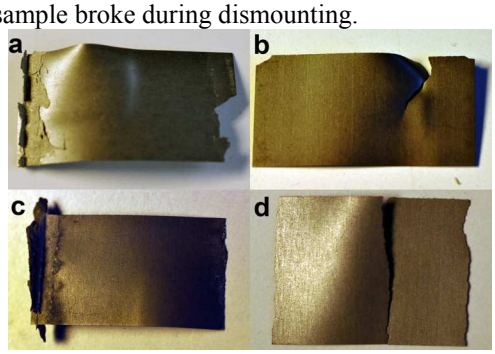

Figure 2: Graphite samples after experiment.

The structure of heavy ion irradiated samples evolves towards glassy carbon, initiating the swelling. As a result, strong stress develops at the interface between irradiated and non-irradiated material leading to sample curvature towards the side facing the beam. The effect is reduced at 900 °C and especially at 1500°C where the vacancies are mobile. The maximum fluence of 10^{15} ions/cm^2 corresponds in some estimation to 55 hours of FRIB operation under U beam of 400 kW power. Sample resistance measured during irradiation increase with the accumulated ion dose. This increase was a factor of 5 weaker for the sample irradiated at 1500°C (Fig. 3) showing pronounced defect annealing at this temperature. A detailed analysis of ion-induced damage by Raman spectrometry and profilometry is in progress.

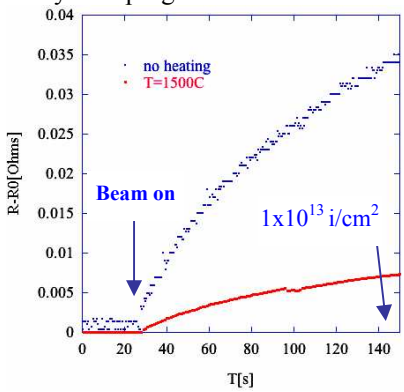

Figure 3: Graphite foil resistance vs. exposure time for irradiation with 8.6 MeV/u Au ions with no external heating and at 1500°C (same ion flux has been used).

[1] G. Bollen, International Symposium on Exotic Nuclei (EXON-2009), 28 Sept.-2 Oct., 2009, Sochi, Russia.
[2] M. Tomut et al., GSI Scientific Report 2007, 69.
[3] www.mersen.com

m.tomut@gsi.de

Positron annihilation lifetime spectroscopy study of vacancy cluster evolution in swift heavy ion irradiated HOPG

M. Krause[1,2,#], W. Egger[3], W. Ensinger[1], C. Hugenschmidt[4], B. Löwe[3], L. Ravelli[3], M. Tomut[2,5] and C. Trautmann[2]

[1]Technische Universität Darmstadt, Germany; [2]GSI, Darmstadt, Germany; [3]Uni Bw München, Neubiberg, Germany; [4]TU München, Germany; [5]NIMP, Bucharest, Romania

Isotropic carbon is the material of choice for the rare-isotope production target and beam catchers of the future Super-FRS. During operation both components are exposed to high-intensity ion beams and may suffer from radiation damage. To better understand damage formation processes in graphite, irradiation experiments were performed at the X0 beamline using 11.1 MeV/u Au-ions and different fluences. As material we selected highly oriented pyrolytic graphite (HOPG), because in contrast to isotropic graphite, it has a well defined structure and as such serves as a model material. The irradiated samples were studied by positron annihilation lifetime spectroscopy (PALS) performed at the pulsed low-energy positron system (PLEPS) at the Munich research reactor FRM II [1].

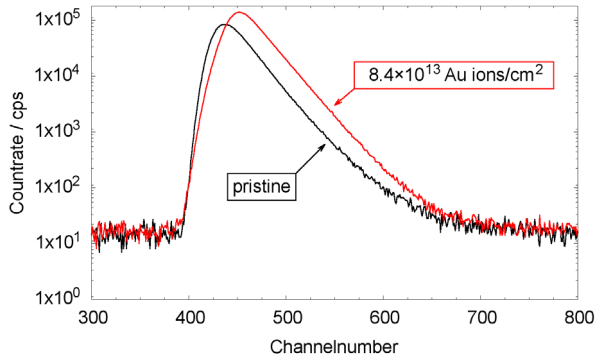

Figure 1: Typical positron lifetime spectrum (16 keV e^+-beam) of pristine and irradiated (8.4×10^{13} Au-ions/cm^2) HOPG.

A typical PALS spectrum is shown in Fig. 1. The deconvolution of the spectra into different lifetimes was performed with POSWIN [2]. The resulting lifetimes including the mean lifetime $\left(\tau_m = \sum I_i \times \tau_i\right)$ for different positron energies are plotted in Fig. 2. The interpretation of the positron lifetimes follows Tang et al. [3]. The mean implantation depth of positrons (upper abscissa of Fig. 2) is estimated according to Ghosh [4] taking into account the HOPG density of $\rho = 2.26$ g/cm^3.

Fits of the spectra of unirradiated HOPG (Fig. 2a) yield two lifetimes $\tau_1 = 221$ ps and $\tau_2 = 408$ ps in the bulk ($E(e^+) \geq 8$ keV). These values are in agreement with the values for high-quality HOPG as reported in [5].

To fit the spectra of irradiated samples a third lifetime is required. However, its intensity is small and at the present stage difficult to quantify. At a fluence of 1×10^{12} Au-ions/cm^2 (Fig. 2b), the lifetime fits yield a reduced bulk value of $\tau_1 \sim 106$ ps and $\tau_2 \sim 280$ ps. The latter is compatible with the lifetime of planar V_n vacancy clusters with n = 2-4 [3].

For fluences greater than 1×10^{13} Au-ions/cm^2 (regime where track overlapping takes place), the bulk lifetime τ_1 is also reduced but its intensity is strongly decreased (Fig. 2c). Most positrons are trapped in defects with a lifetime of $\tau_2 \sim 270$ ps. Similar to the sample irradiated with 1×10^{12} Au-ions/cm^2, these lifetimes can be attributed to twofold to fourfold (chain) vacancy clusters.

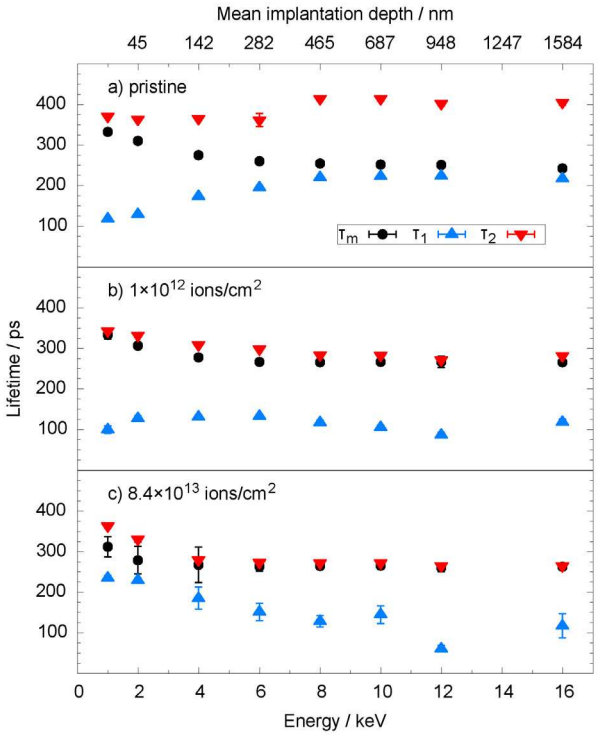

Figure 2: Energy dependent positron annihilation lifetimes before and after the irradiation of HOPG with Au-ions (11.1 MeV/u) a) pristine b) 1×10^{12} ions/cm^2 c) 8.4×10^{13} ions/cm^2.

References

[1] W. Egger et al, Phys Stat. Sol. C 4, 10 (2007) 3969.
[2] D. Bochert, Diploma thesis, Universität der Bundeswehr München, 2004.
[3] Z. Tang et al, Phys. Rev. Lett. 82 (1999) 2532.
[4] V. J. Ghosh, Appl. Surface. Science. 85 (1995) 187.
[5] M. Shimotomai et al, J. Nuc. Mat. 103&104 (1981) 779.

#m.krause@gsi.de

Heavy-Ion Induced Damage in Carbon Composites for LHC Collimators*

M. Tomut[1,2,#], R. Assmann[3], O . Aberle[3], A. Bertarelli[3], A. Dallocchio[3], G. A. Izquierdo[3], N. Mariani[3], J. Stadlmann[1], C. Trautmann[1]

[1]GSI, Darmstadt, Germany; [2]NIMP, Bucharest, Romania,[3]CERN, Genève, Switzerland

The high luminosity performance of the Large Hadron Collider (LHC) at CERN means very high transverse energy density. Very small losses of the stored beam could lead to quenching of super-conducting LHC magnets or even to destroying parts of the accelerators. A complex collimator system has been installed around the LHC ring and the transfer lines in order to absorb the beam halo and protect the machine from damage. The one-meter long collimators absorb the particles in the halo by closing a set of 'jaws' of various materials around the beam. The most robust of them consist of a carbon-carbon composite for the jaws. These materials situated always closest to the particle beam will experience radiation damage, which can affect dimensional stability, electro-magnetic properties, and survival to beam induced thermal shocks.

This report summarizes studies of heavy-ion radiation effects in carbon-carbon composites AC-150 produced in Japan. Radiation hardness tests are performed at GSI within the frame of the EuCARD FP7 project, as part of the ColMat work package addressing materials and collimators for high intensity beams.

The anisotropic structure of the AC-150 can be seen in Fig. 1 for two perpendicular sections. The longitudinal section shows a parallel arrangement of fibres, while the transversal section reveals the woven structure.

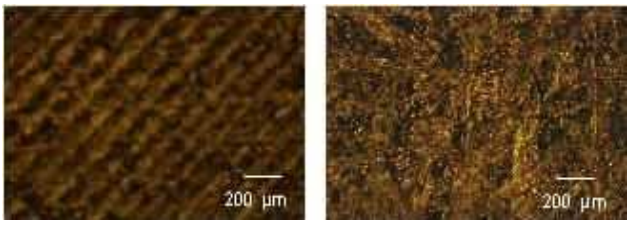

Figure 1: Low magnification micrographs: a) longitudinal and b) transversal section of carbon composite AC-150.

Structural and dimensional stability of heavy ion-irradiated carbon-carbon composites have been investigated using profilometry. Figure 2 shows for the longitudinal section the histograms of the roughness distribution of a AC-150 pristine and irradiated with 8×10^{13} U-ions/cm^2 samples. After irradiation the surface is more even, mainly due to ion-induced fragmentation of carbon fibers. This is indicated by the large decrease of the peaks situated on the positive half of the histogram, sugesting that also the high thermal conductivity of the composites, determined by the fibers, is degraded by irradiation.

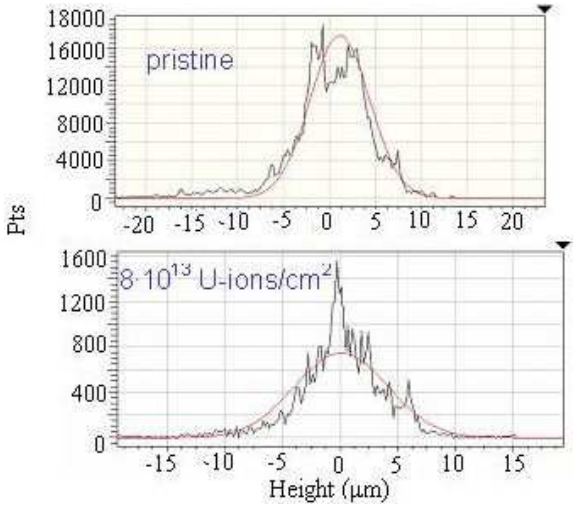

Figure 2: Histograms of roughness distribution for pristine (upper figure) and 11.1 MeV/u ^{238}U ions -irradiated AC-150 (lower figure).

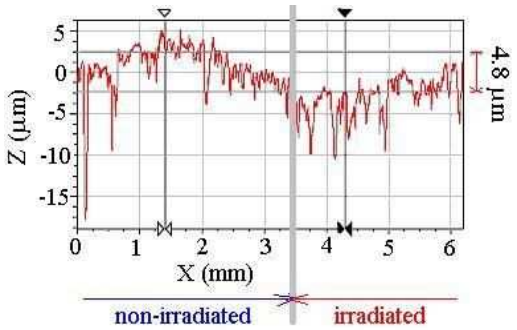

Figure 3 : Profilometer scan showing shrinking of AC-150 irradiated with 11.1 MeV/u, 8×10^{13} ^{238}U ions/cm^2 .

Ion-irradiated carbon-carbon composites shrink, as shown by profilometry scans across the irradiated non-irradiated interface of samples exposed to ion beam with a mask (Fig. 3). It has been previously shown that ion-irradiated isotropic graphite swells [2], indicating that this shrinking behaviour of the composite is controlled by the contraction along the longitudinal axis of the fibres.

Radiation hardness of novel candidate materials such as diamond-metal composites is currently also investigated at GSI within the ColMat project. Depending on the specific modifications and functional properties, the most suitable material will be selected for the construction of collimators to be used for the LHC upgrade.

* Work supported by EU, EuCARD contract No. 53102.
#m.tomut@gsi.de

[1] "LHC Design Report, Vol. I: The LHC Main Ring", CERN Editorial Board, CERN-2004-003, 2004.
[2] M. Tomut et al., GSI Scientific Report 2007, 69.

Heavy-ion induced desorption of cryogenic surfaces

E. Mahner[1], L. Evans[1], M. Bender[2,#], D. Severin[2], H. Kollmus[2], M. Wengenroth[2]

[1]CERN, 1211 Geneva 23, Switzerland; [2]GSI, 64291 Darmstadt, Germany

Introduction

Ion-induced desorption is a severe luminosity limitation of low charge state heavy-ion accelerators. Studying the phenomena for almost 10 years using different target materials and various ion beams and energies, provides a rather clear picture of the physical processes involved in ion-induced desorption at room temperature [1]. Because of limited experimental data [2], the situation is less obvious for gas desorption of cryogenic surfaces. Due to the importance of cryogenic surfaces in future heavy ion accelerators, we investigated the desorption behaviour in combination with the surface coverage of cryogenic surfaces at different temperatures.

For the irradiation experiment we used two disk-shaped targets, bare copper and gold-coated (7µm) copper with a nickel diffusion barrier (2µm). The targets were mounted on a commercial vacuum cold head including radiation shielding and temperature diagnostics. A resistive heater allowed the control of the target temperature by means of a software power control (PID).

The cold head including the target was mounted at the LINAC-3 beamline at CERN [1,2]. Before cooling, the whole setup was UHV-baked to achieve low pressures. This procedure should help to keep the surface gas coverage of the target as low as possible. From single shot measurements the pumping speed of the setup was measured by the decay of the pressure bump from the beam pulse. This information is necessary, since the surface of the target and shielding contribute to the pumping speed. During ion irradiation of the targets, desorption yields were measured by the pressure-rise method with a Bayard-Aplert vacuum gauge and a residual gas analyzer (RGA), both calibrated. The desorption yields η were derived by the ideal gas law as follows:

$$\eta = \frac{\Delta p \cdot S}{\dot{N} \cdot k \cdot T}$$

where Δp is the pressure rise in the setup due to irradiation, S denotes the pumping speed, $\dot{N}$ is the number of projectile ions per second, k is the Boltzmann factor and T is the temperature.

The irradiation experiments were performed with 4.2 MeV/u lead ions at an impact angle of 0° and a flux of 10^9 ions/cm^{2}s. The results of both targets are displayed in figure 1 for three different temperatures. The desorption yields decrease over one order of magnitude from room temperature to cryogenic temperatures. As measured by RGA, the dominating desorbed gas at room temperature was CO, followed by H_2. At cryogenic temperatures (77 and 6.2 K), H_2 is the most prominent species followed by CO. This behaviour can be explained by the vapour pressure of these gas species at the respecting temperatures.

#m.bender@gsi.de

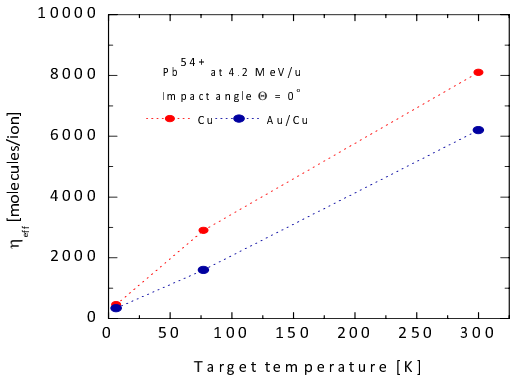

Figure 1: Desorption yields of pure and Au-coated copper targets at temperatures of 300, 77, and 6.2 K.

In the second part of the experiment, the influence of the surface coverage on desorption yields was analysed. By means of a dedicated gas inlet system, the target surface was covered by a well-defined amount of CO and subsequently exposed to the beam. The desorption yield directly scales with the number of adsorbed layers, clearly demonstrating the distinctive role for desorption at cryogenic temperatures. The yield can be much higher than at room temperature and is almost independent of the target composition. These results clearly emphasize the need for excellent vacuum conditions before the cooling cycle starts.

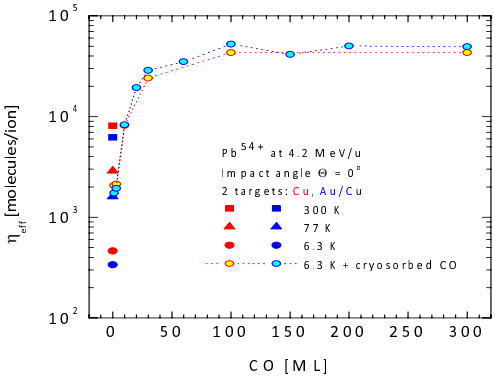

Figure 2: Desorption yields as a function of gas frozen on top of the target.

References

[1] E. Mahner, Phys. Rev. ST Accel. Beams 11, 104801 (2008), and references therein.

[2] E. Mahner et al., AIP Conf. Proc. 773, 219 (2005)

Low-temperature thermal conductivity of polyimide irradiated with Ni ions*

T. Seidl[1,2,#], W. Ensinger[1], E. Floch[2], B. Merk[2], E. Mustafin[2], S. Müller[2], D. Severin[2], C. Trautmann[2], K. O. Voss[2]
[1]Technische Universität Darmstadt, Germany; [2]GSI, Darmstadt, Germany;

Introduction

The planned International Facility for Antiproton and Ion Research (FAIR) will consist of a superconducting double-ring synchrotron offering ion beams of intensity increased by a factor of 100-1000 compared to the existing GSI accelerators. Materials close to the beam tube will be exposed to secondary radiation of neutrons, protons, and heavier particles, possibly limiting reliable function and lifetime of device components. The present study investigates the radiation hardness of insulating components with focus on polyimide used as electrical insulation of the quench heaters of superconducting magnets. In this special application, polyimide has to provide (i) electrical insulation of the heater as well as (ii) heat transmission to the magnet to guarantee thermal exchange to the superconducting coils. In case radiation-induced degradation decreases the thermal conductivity, higher heating powers for a given temperature step would be required. We thus performed measurement of low temperature thermal conductivity of ion-irradiated polyimide.

Experimental

Commercial foils of Apical AV type polyimide were room-temperature irradiated at the UNILAC with Ni ions of 11 MeV/u. The projected ion range is ~150 µm and thus larger than the thickness of the foils (125 µm). The irradiation was performed with two fluences, 1×10^{11} and 5×10^{12} cm^{-2} ions/cm^2 corresponding to a radiation dose of ~0.5 and 25 MGy, respectively.

The apparatus for the thermal conductivity measurement is based on the method of uni-directional heat flow according to [1]. The steady state measurements were performed inside of a cryochamber in the temperature range from 6-100 K at a pressure of 2×10^{-4} Pa. The film was fixed between two copper blocks, one of them being connected to the cooling finger of a Gifford-McMahon refrigerator as thermal sink, while the other block is equipped with a heater. The applied temperature difference between both blocks at a given base-temperature of the cryostat was in the range of 2-3 K and was monitored by means of silicon diode sensors. The thermal properties of the holders are deduced from reference measurements without sample.

Results and Discussion

The thermal conductivity λ across pristine and irradiated Apical films is shown in Fig. 1. In agreement with results reported for Kapton-type polyimide [2-4], λ steadily increases as a function of temperature. A direct comparison with absolute λ values reported in literature is problematic because the measuring techniques applied are rather different, and reported values scatter by a factor of approximately 5. Within this uncertainty, our measurements on a single 125 µm Apical AV polyimide foil are consistent [2-4]. The reproducibility of our set-up was tested by using 3 different unirradiated samples yielding identical results within 10%.

The ion irradiation leads to a decrease of the thermal conductivity in the entire temperature range. The change is more pronounced for the sample exposed to the higher fluence. After exposure to 25 MGy, the initial thermal conductivity is decreased by 50%. The evolution of λ with temperature remains unchanged.

In conclusion, beam-induced changes of the thermal conductivity are observed, but the effect is not as drastic as for the breakdown voltage reported earlier [5]. The results clearly demonstrate that the thermal conductivity of polyimide insulations will decrease with extending operation time. Depending on the expected radiation dose close to the superconducting magnets, possibly higher heat power values have to be considered when designing the quench heaters.

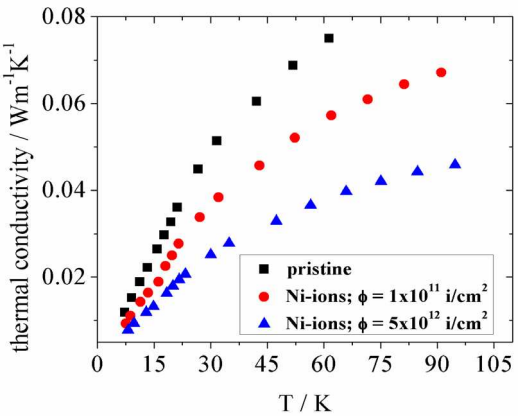

Figure 1: Low-temperature thermal conductivity of pristine polyimide (black squares) and samples irradiated with 11-MeV/u Ni ions of fluence 1×10^{11} cm^{-2} (red circles) and 5×10^{12} cm^{-2} (blue triangle) corresponding to a dose of about 0.5 and 25 MGy, respectively.

References

[1] H. Lee, Rev. Sci. Instrum. 53(6) (1982) 884
[2] B. Baudouy, Cryogenics 43 (2003) 667
[3] J. Lawrence, A. B. Patel, J.G. Brisson, Cryogenics 40 (2000) 203
[4] M. Barucci, E. Gottardi, I. Peroni, G. Ventura, Cryogenics 40 (2000) 145
[5] T. Seidl et al., GSI Scientific Report, Materials-09 (2008), p. 341

* Work supported by BMBF (06DA90251).
#t.seidl@gsi.de

Radiation hardness of low-mass readout cables for the CBM experiment

D. Severin[1], M. Bender[1], and J.M. Heuser[1]

[1]GSI, Darmstadt, Germany

Introduction

For the fixed-target heavy-ion experiment CBM at FAIR, a low-mass silicon tracking detector system is being developed that can track at high rates the hundreds of charged particles that will be created when an intense beam of heavy nuclei interacts with the target [1]. The detector is based on silicon microstrip detector technology. Fast self-triggering front-end electronics will be located at the periphery of the tracking system. The distance between the detectors and the electronics will be bridged with thin long aluminium cables structured into microstrip lines and insulated with polyimide. In the CBM environment, the exposure to ionizing radiation is estimated to about 100-200 kGy in several years of operation. For reliable operation, radiation-induced changes of the bulk and/or surface conductivity of the dielectric material have to be excluded.

Experiments and Results

Several cable prototypes with lengths between 10 and 30 cm, shown on Fig. 1, have been manufactured at SE SRTIIE, Kharkov, Ukraine [2]. A cable consists of two signal layers, a shielding layer, and a mesh spacer. Each signal layer is structured into 64 aluminium lines (14 µm thick, 20 µm wide, at 100 µm pitch, on 10 µm thick FDI-A-24 dielectric).

Figure 1: Different prototypes of microstrip line cables.

For a first radiation hardness test, a 10 cm long multi-layer flat-wire of the CBM detector demonstrator was mounted on an aluminium plate and irradiated with 4.8 MeV/u Au ions at the M3-beamline of the UNILAC. The size of the beam spot was about 1 cm^2. Three single-circuit paths were connected to a charge-frequency converter (IFC). The IFC records charges down to 100 fC and is triggered by the beam pulse. On-line measurements thus allow us to monitor beam-induced currents passing through the device.

In stage A of the experiment, the beam spot was set besides the flat-wire lines to check any indirect radiation effect (section A in Fig. 2). Comparing the ion-beam flux (red) and the signal during the irradiation of the test device clearly shows that no additional electric current appears in the back-plate.

During stage B, the middle part of the flat-wire was irradiated on a length of 1 cm with a flux of 2.5×10^7 ions/cm^2s. The IFC recorded a signal of 22 pC which follows synchronously the beam flux signal. Even small flux variations are visible.

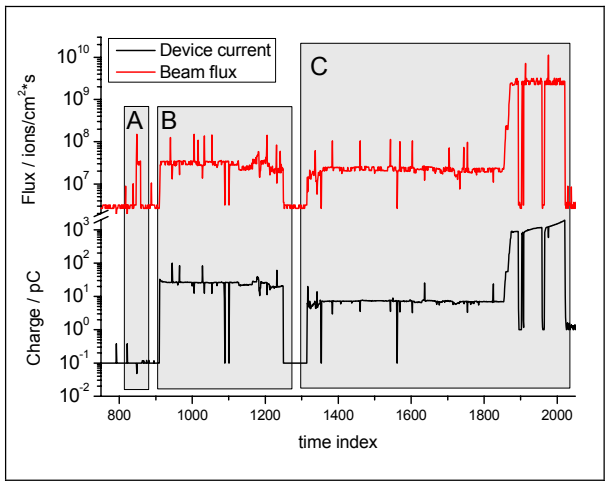

Figure 2: Device signal (black, bottom) and flux of the ion beam (red, top) during different irradiation tests A – C (see text for details).

In stage C, one single wire (instead of three) was measured. At a fixed flux of 2.3×10^7 ions/cm^2s, the current for three contacted wires was 21.9 pC compared to 7.2 pC for a single wire, confirming a linear scaling behaviour.

In the last phase of experiment C, the flux was increased by two orders of magnitude. Under this high flux condition, the current increased significantly indicating either a serious temperature increase or a pronounced change of the electrical properties.

This demonstrator device, which has been exposed in total to 1.56×10^{12} ions/cm^2, will be tested off-line especially with respect to loss of insulation properties due to radiation damage of polyimide [3].

References

[1] J.M. Heuser, PoS: VERTEX 2008 (2008) 017

[2] V.M. Borshchov, J.M. Heuser et al., CBM Progress Report 2009 (2010) 15

[3] D. Severin et al., Nucl. Instr. Meth. B 236 (2005) 456

Degradation of polyethylene oxides during irradiation with uranium ions

V. Lima[1,#], T. Seidl[1], U.H. Hossain[1], O. Baake[1], D. Severin[2], M. Bender[2], C. Trautmann[2], and W. Ensinger[1,]

[1]Technische Universität Darmstadt, Germany; [2]GSI, Darmstadt, Germany

This project focuses on polyepoxides used in glass fiber reinforced polymer (GFRP) compounds, to be applied as insulators or structure-support materials for magnets of the future FAIR facility. As such, polyepoxides have to withstand high radiation levels of X-rays, gammas, neutrons, protons, and heavier particles [1]. Radiation hardness tests are important in order to estimate lifetimes and performance risks of such materials.

Ionizing radiation induces scission of covalent bonds of organic compounds leading to free radicals and unsaturated bonds. In high-radiation dose environment, organic materials undergo property changes even at rather low fluences typically accompanied by outgassing of small volatile degradation products [2,3].

In order to better understand criteria important for radiation resistance, our first experiments were performed with one of the most simple polyepoxides, namely polyethylene oxide (PEO). By varying the molecular weight (MW), the identification of critical structural parameters is expected.

Samples were prepared by mixing ethanol and PEO of different molecular weight (MW: 10^5, 3×10^5, and 10^6 Dalton). The solution was deposited on a flat surface of a glass plate. Once the ethanol was evaporated, PEO films of 10-15 µm thickness were lifted off from the substrate and mounted in the multi-purpose vacuum chamber available at the M3-beamline of the UNILAC. During irradiation with 4.8 MeV/u uranium ions, the PEO films were analysed by in-situ Fourier-transform infrared (FTIR) spectroscopy.

The spectra (Fig. 1) of all pristine PEO samples are characterized by bands due to C-H-stretching in the wavenumber region 3000-2600 cm^{-1}, asymmetric

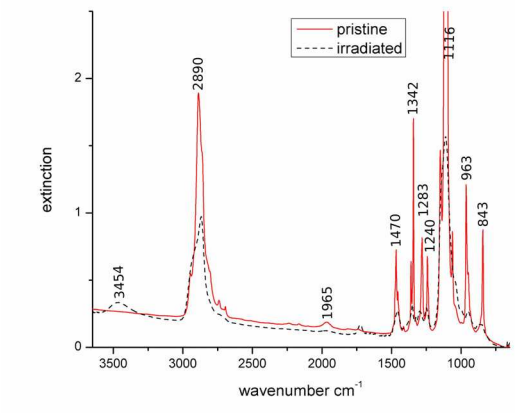

Figure 1: In-situ FTIR spectra of unirradiated and irradiated (3×10^{11} ions/cm^2) PEO films (MW 10^6 Da).

#v.lima@gsi.de

stretching of the PEO main chain (1965 cm^{-1}), CH_2-scissoring (1550-800 cm^{-1}), stretching vibration of the ether (1116 cm^{-1}) as well as CH_2 twisting and wagging (963 and 843 cm^{-1}) [4]. Upon ion irradiation, the intensity of all these bands decreases due to ion-induced destruction of the molecular structure of the polymer. Additionally, a new broad band appears in the regime of OH-vibrations (3600-3300 cm^{-1}) increasing with fluence. The formation of these new OH endgroups is ascribed to the recombination of ion-induced O- and H-radicals (Fig. 2).

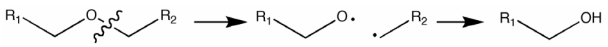

Figure 2: Scheme of radiation-induced scission of PEO.

The peak area A of the OH-band is normalised to the peak area A_0 of the respective pristine foils and plotted as a function of the ion fluence (Fig. 3). Under irradiation, foils of larger MW (10^6 Da) obviously produce a significant larger amount of OH groups than foils of MW 10^5 and 3×10^5 Da.

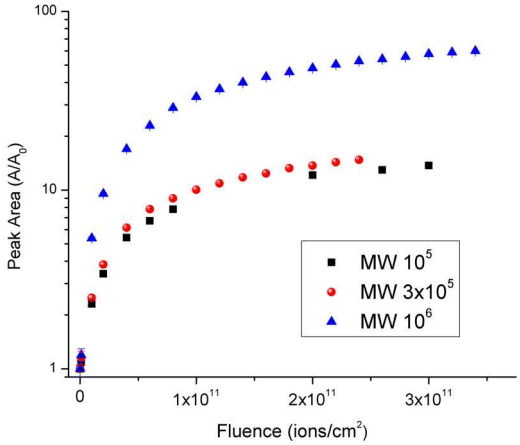

Figure 3: Normalized peak area of OH-group vibration band (3600 - 3300 cm^{-1}) as a function of ion fluence for samples of different molecular weights (given in Da)

References

[1] L. Latycheva et al., Proc. 9th Europ. Particle Accel. Conf. 2004, Lucerne, Switzerland (2004) 1408
[2] D. Severin et al., Nucl. Instr. Meth. B 236 (2005) 456
[3] V. Picq et al., Nucl. Instr. Meth. B 151 (1999) 76
[4] S. Rajendran, R. Kannan; J. Power Sources 96 (2001) 406

In-Situ Investigation of SHI Induced Dewetting of a Fe_2O_3-Film on Si*

S. Amirthapandian[1,2], F. Schuchart[1] and W. Bolse[1#]

[1]Institut für Halbleiteroptik und Funktionelle Grenzflächen, Universität Stuttgart, Stuttgart, Germany

[2] on leave from: Material Physics Division, Indira Gandhi Centre for Atomic Research, Kalpakkam, India

We have investigated swift heavy ion (SHI) induced dewetting [1] of a 50 nm thin Fe_2O_3-film on Si utilizing our new in-situ scanning electron microscope (SEM) [2]. Before the experiment, the sample was pre-irradiated with ^{197}Au-ions of 1 MeV/u to a fluence of 1×10^{14}/cm^2. Because of this treatment, the film already exhibited dewetting holes with diameters of the order of 1 µm. This sample was then irradiated in our in-situ SEM setup with 3.6 MeV/u ^{197}Au-ions to a total fluence of $11.5\times\cdot10^{14}$/cm^2 in steps of 0.5×10^{14}/cm^2. After each irradiation step, SEM images of one and the same surface area were recorded. Figure 1 shows a series of such images taken after irradiation with different fluences. As can nicely be seen, we are able to monitor the growth of individual holes, which is hardly possible in a conventional ex-situ experiment.

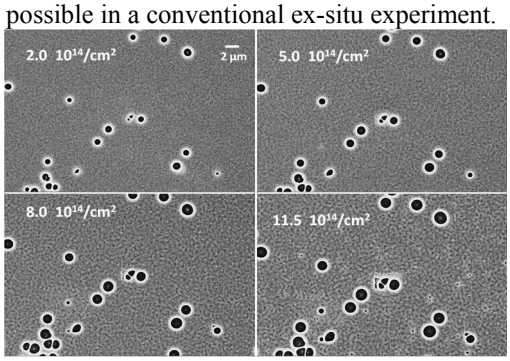

Figure 1: SEM images of the sample after irradiation at the different fluences given in the images .

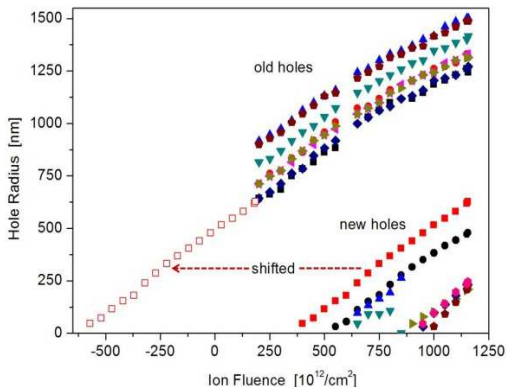

Figure 2: Development of radii of dewetting holes as a function of ion fluence.

Figure 2 shows that the radii of all pre-existing as well as newly formed holes grow at the same, almost linear rate. This is expected for a mechanism, where the capillary-force driven growth is partly hindered by the build-up of a rim around the hole (white rings in SEM images).

* Work supported by BMBF under contract 05KK7VS1.

w.bolse@ihfg.uni-stuttgart.de

A very interesting result is obtained when plotting the hole-number density versus the total deposited energy density. As shown in figure 3, at low fluences the number of holes stays almost constant. This means that the majority of holes being present at this stage were nucleated early during pre-irradiation, most probably at interfacial defects (heterogeneous nucleation).

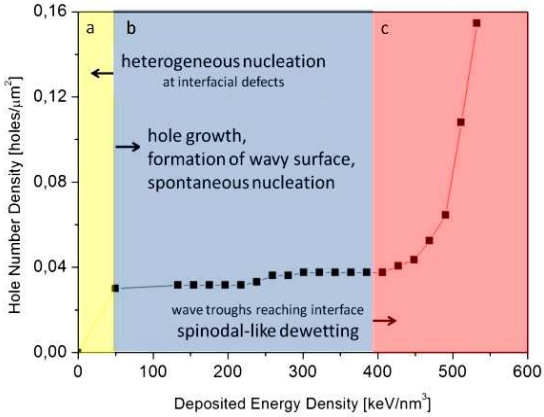

Figure 3: Average hole-number density as a function of deposited energy density (= fluence × energy loss).

At high fluences, however, the number of holes suddenly increases exponentially. This points at a second hole nucleation mechanism. In fact, careful inspection of the SEM images reveals that surface undulations of increasing amplitude are built up during irradiation and finally, at the highest fluences, small new holes form all over the surface in the wave troughs. This is a clear hint at a spinodal-like dewetting mechanism. Such mechanism has also been suggested for dewetting of liquid polymer films [3], but it is still under strong debate. There it is assumed that preferential amplification of capillary waves at a certain wavelength produces dry spots as soon as the wave troughs reach the substrate and thus causes hole nucleation. In the present case, we believe that the in-plane compressive stresses generated by the impinging ions [4] result in an instability of the oxide-film against self-amplifying surface undulations of a certain wavelength [5]. Again, as soon as the wave troughs reach the film/substrate interface, a hole is formed which then, due to capillary forces, grows during further ion irradiation.

References

[1] T. Bolse, et al., Nucl.Instr. Meth. B 244 (2006) 115.
[2] S. Amirthapandian, et al., Rev. Sci. Instr. 81 (2010) 033702.
[3] S. Herminghaus, et al., Science 282 (1998) 916.
[4] H. Trinkaus, et al., Phys. Rev. Lett. 74 (1995) 5072.
[5] D.J. Srolovitz, Acta metal 37 (1989) 621.

Swift Heavy Ion Shaping of Sub-Micron Structures*

R. Ferhati[1], M. Fritzsche[2], S. Amirthapandian[1,3], N. Guilliard[1], T. Weishaar[1], and W.Bolse[1#]
[1] Institut für Halbleiteroptik und Funktionelle Grenzflächen, Universität Stuttgart, Stuttgart, Germany
[2] Institute of Ion Beam Physics and Materials Research, Forschungszentrum Dresden-Rossendorf, Germany
[3] on leave from: Material Physics Division, Indira Gandhi Centre for Atomic Research, Kalpakkam, India

We applied swift heavy ions (SHI) for shaping of already existing submicron- and nano-scale structures by irradiation at small angles and simultaneous azimuthal rotation. The investigated samples consisted of 100-nm thick films of NiO or ZnO deposited on an oxidized Si-wafer by reactive magnetron sputtering. Prestructuring into 3-dimensional sub-µm and nm-sized objects with quadratic or rectangular cross-sections was done by means of focused ion beam technique. The process produced a grid of perpendicular lines cut into the film, reaching from the surface down to the interface and having line distances varying between 5 µm and 250 nm. These samples were then irradiated with SHI in the chamber of our new in-situ scanning electron microscope (SEM) [1] installed at the M1-beamline of the UNILAC. In both cases the samples were tilted by 80° with respect to the ion beam axis and continuously rotated at 1.45 deg/s around the surface normal of the film during irradiation. The irradiation was carried out in small fluence steps and in between these steps SEM images of the pre-structured and irradiated surface were taken. In this way, the development of the shape of individual objects during SHI bombardment could be monitored. The NiO film was exposed to 5.9 MeV/amu U ions of 38.6×10^{13} cm^{-2} total fluence and steps between $2.5\text{-}5\times10^{13}$ ions/cm^2. For ZnO the respective parameters were: 4.8 MeV/amu Au ions, total fluence $495\cdot10^{13}$ ions/cm^2, and steps between 10 and 50×10^{13} ions/cm^2.

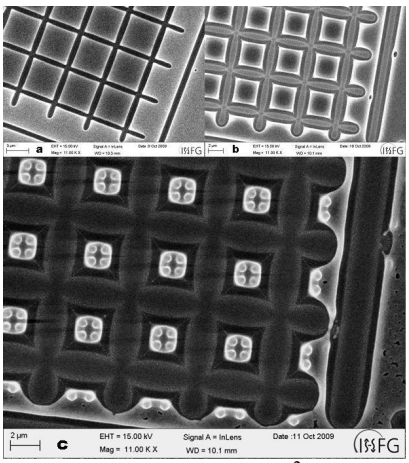

Figure 1: Developement of 5×5 µm² squares on a NiO film at low (a), medium (b) and high (c) fluence.

Figure 1 shows the development of the largest quadratic objects after low (6×10^{13} cm^{-2}), medium (18×10^{13} cm^{-2}) and high fluence (38.6×10^{13} cm^{-2}) irradiation. First one recognizes a lateral shrinking of the objects with increasing ion fluence. Careful inspection of the images also reveals the formation of a basis with truncated pyramid shape, which shows that the deformation rate is smaller next to the substrate than at higher regions (most probably due to adhesion effects). On top of this basis additional 4 round substructures appear.

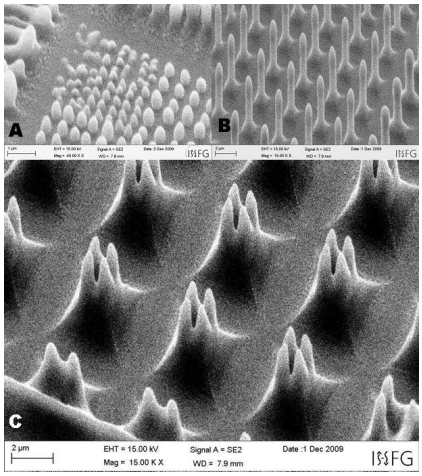

Figure 2: Perspective SEM images of final structures on NiO specimen. Initial object size: (A) 0.25·× 0.25 µm², (B) 2 × 2µm², and (C) 5×5 µm².

Similar results were obtained for initially smaller objects (one round substructure only) as well as for objects with unequal edge lengths (one substructure at each of the small edges). Perspective images of the final state (Fig. 2) show that the round substructures are of pillar-like shape. For the initially smallest objects the final structures do not exhibit a basis and the final shape appears lens-like (smallest) or egg-like (next bigger objects).

The deformation of the initially rectangular objects can be understood when taking into account the ion hammering effect [2,3] (responsible for the lateral shrinking [4]), the influence of surface tension (producing round shapes), and adhesion and dewetting effects (leading to less deformation in the bottom part of the objects). Similar results were obtained with the ZnO film, except that deformation proceeds much slower as compared to NiO.

References

[1] S. Amirthapandian, et al, Rev. Sci. Instr. 81, 033702 (2010)
[2] S. Klaumünzer, et al, Phys. Rev. Lett. 51, 1987 (1983)
[3] H. Trinkaus, J. Nucl. Mater. 223, 196 (1995)
[4] W. Bolse, Nucl. Instr. Meth. B 244, 8 (2006)

* Work supported by BMBF under contract 05KK7VS1.
# w.bolse@ihfg.uni-stuttgart.de

Attempts to realize quantum dots by interrupted conductive ion tracks*

H.-G.. Gehrke[1#], M. Brötzmann[1], J. Krauser[2], C. Trautmann[3], A. Weidinger[4], and H. Hofsäss[1]
[1] II. Physikalisches Institut, Universität Göttingen, Germany; [2]Hochschule Harz, Wernigerode, Germany; [3]GSI Helmholtzzentrum, Darmstadt, Germany; [4] Helmholtz-Zentrum Berlin für Materialien und Energie, Berlin, Germany.

Swift heavy ion irradiation of tetrahedral amorphous carbon (ta-C) leads to electrically conductive tracks along the ion path. This phenomena is attributed to a transformation of the sp^3-rich bond structure of the ta-C to a sp^2-rich bond structure caused by the energy deposition of the ion [1,2]. This work focuses on the fabrication of a dot-like structure consisting of interrupted conductive ion tracks. The size of the dot should be small enough to show Coulomb blocking.

The ta-C films were synthesized by mass selected ion beam deposition (MSIBD) using 100 eV carbon ions. The desired interruption of the ion track is achieved by depositing thin boron nitride layers in between the ta-C films. The BN has a high resistivity and shows no significant change in conductivity by ion-beam irradiation. The BN layers were also deposited in-situ by MSIBD.

The quality of the interfaces was checked by Transmission Electron Microscopy (TEM). Fig. 1 shows the ta-C layer interrupted by two hexagonal boron nitride (h-BN) films. The TEM image also reveals the structural differences of the amorphous ta-C and the turbostratic grown h-BN. Beneath each boron nitride layer a 2-nm thick amorphous mixed layer is visible before the ordered h-BN structure begins. The interfaces are flat and homogeneous. The TEM examinations prove the possibility to produce these multilayer films with nanometer precision.

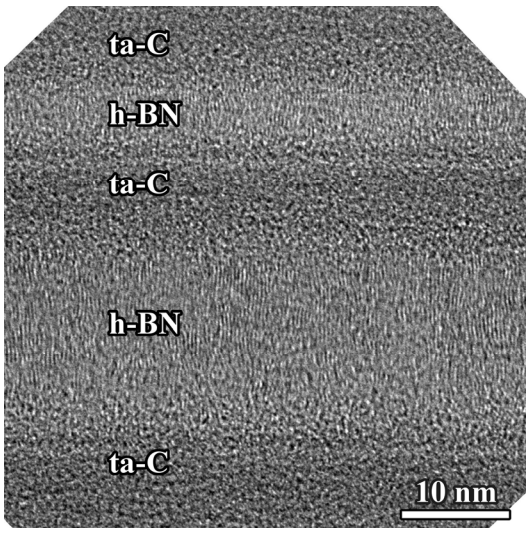

Figure 1: Cross-sectional TEM image of a multilayer sample consisting of ta-C layers interrupted by h-BN. The image was rotated into growth orientation

The multilayer systems were irradiated with gold or uranium ions at the UNILAC. The fluences ranged from 10^9 – 10^{10} ions/cm^2 and the energy was 1 GeV in order to achieve high electronic stopping power. Each projectile produces a conducting track in ta-C but not in the two h-BN layers. The track is thus a self aligned conductive nano-structure being interrupted and insulated by the h-BN layers. The insulating layer can easily be controlled by adjusting the thickness of the BN film.

The electrical conduction of these track structures was analysed by atomic force microscopy (AFM) using conductive tips. Fig. 2 shows the I-U characteristics of a single track in a sample with a central ta-C layer of 8-nm thickness, which is similar to the track diameter.

The effect of the insulating h-BN is clearly visible. Compared to a track in pure ta-C, the conductivity of the BN-interrupted track changes by two orders of magnitude. The h-BN layer shows good stability withstanding fields of 10^5 V/cm and beyond. The continuous track has an ohmic characteristic, whereas the interrupted track is dominated by Frenkel-Poole conduction at low fields. At higher voltages, the characteristics is dominated by the resistance the ion track and the interfaces. The current resolution of the setup is 3 pA.

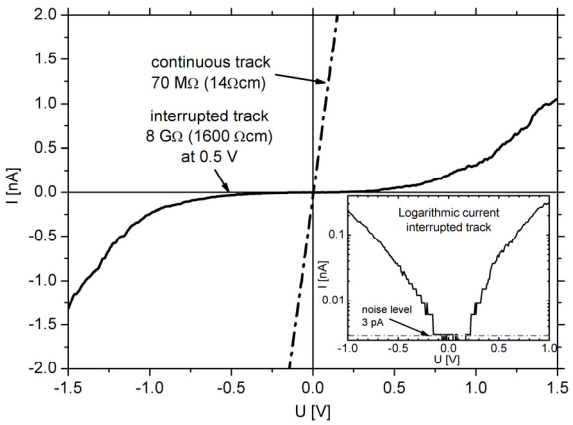

Figure 2: Current voltage characteristics of single ion tracks: (dashed line) continuous track in ta-C, (solid line) track in ta-C interrupted by two 10-nm thick h-BN layers. The inset shows the logarithmic plot of the interrupted track.

In summary, we successfully produced multilayer films of ta-C and h-BN using MSIBD. By irradiation with high-energy heavy ions, interrupted conductive ion tracks were created. In the I-U plots, the insulating effect of the interruptions is clearly visible, but Coulomb blocking has not been observed so far. Attempts to improve the structure and low temperature measurements are in progress.

RReferences

[1] M. Waiblinger, et al. J. Appl. Phys. 69 (1999) 239
[2] J. Krauser, et al. J. Appl. Phys. 94 (2003) 1959

New measurements of *W*-values in argon, nitrogen and air for protons, helium and carbon ions

J. Beck[1], *U. Giesen*[1], *M. Bender*[2], *D. Schardt*[2], *and D. Severin*[2]
[1]Physikalisch-Technische Bundesanstalt (PTB), Braunschweig, Germany; [2]GSI, Darmstadt, Germany

Introduction

In particle therapy for cancer the dosimetry of the charged-particle radiation is mostly performed by measuring the ionization produced in air-filled ionization chambers. The conversion of the reading of an ionization chamber into absorbed dose requires *W*-values, which are defined as the average energy needed to produce an ion pair by a particle in a gas. Because of the increasing importance of ion therapy and the lack of experimental *W*-values for charged particles in air, new measurements of *W*-values are being carried out at PTB and GSI. Existing measurements for protons in air indicate an uncertainty of 4 % [1,2] and the main goal of the present studies is to achieve an accuracy of about 1 %. A new experimental set-up has been developed at PTB for the measurement of *W*-values in argon, nitrogen and air for protons and helium ions at energies from 0.5 to 3.5 MeV/u at PTB and for carbon ions between 3.6 and 7.0 MeV/u at GSI.

Experimental Methods

A schematic overview of the PTB set-up is shown in Figure 1. The ionization chamber is filled with gases, usually at atmospheric pressure. The active volume has a length of 25 cm, which is sufficient to stop protons and helium ions up to about 4 MeV/u and carbon ions up to about 7 MeV/u. The electric field direction in the ionization chamber is orthogonal to the beam direction, which minimizes the corrections due to recombination effects in the gas. A low rate of 100 to 500 incoming ions per second is produced by scattering of the primary beam from the accelerators on a thin gold foil at the center of a scattering chamber. At 45° on either side relative to the beam direction, the scattered ions are detected in the ionization chamber and a monitor detector. The determination of the number of particles entering the active volume of the ionization chamber is measured using two independent methods. First, the fast pulse of electrons inside the ionization chamber is measured behind a Frisch grid at the anode. This signal provides the number and energy spectrum of ions for most gases. However, this method does not work with air because of the electronegativity of oxygen. Secondly, the spectrum and number of particles is simultaneously detected in a silicon particle detector using a similar geometry. This rate of particles in the silicon detector is used for measurements with air, after additional calibrations against the count rate inside the ionization chamber using the anode measurements in argon or using a silicon detector.

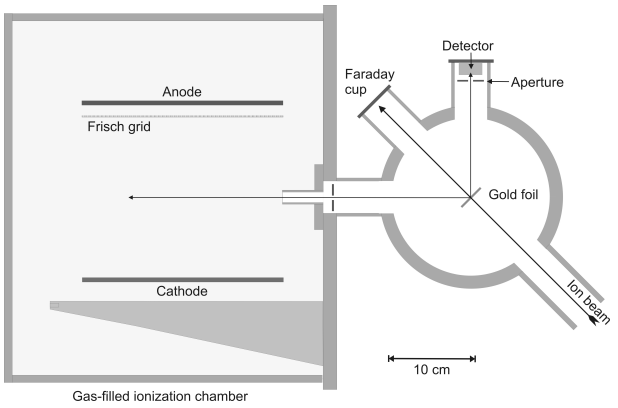

Figure 1: Set-up for *W*-value measurements at PTB and GSI. The ion beam enters the scattering chamber from the lower right, passes a thin Au foil in the centre and is stopped in the Faraday cup. The scattered beam is monitored at +45° by a particle detector and at -45° stopped in the gas volume of the ionization chamber (left).

The number of ion pairs produced in the gas volume is determined from the simultaneous measurement of the ionization current collected at the cathode of the chamber using a calibrated Keithley electrometer.

Measurements

Up to now, measurements with 2 MeV/u protons and helium ions at energies from 0.5 to 3.5 MeV/u were performed at PTB. Furthermore, measurements with carbon ions of 3.6 MeV/u and 5.9 MeV/u were carried out at GSI. Corrections of recombination effects were determined from series of measurements with different voltages at the ionization chamber for each energy. The background from beam-induced γ-radiation was measured without particles in the ionization chamber. Detailed analyses are in progress and further measurements with carbon ions up to 7.0 MeV/u are planned.

References

[1] G.H. Hartmann et al., Determination of water absorbed dose in a carbon ion beam using thimble ionization chambers, Phys. Med. Biol. 44,1193(1999).

[2] B. Grosswendt and W.Y. Baek, W-values and radial dose distributions for protons in TE-gas and air at energies up to 500 MeV, Phys. Med. Biol. 43,325(1998).

A Laser Microbeam Implemented at the Heavy-Ion Microbeam Facility

B. Merk[#], K.-O. Voss, B.E. Fischer, B. Jakob, G. Taucher-Scholz, and M. Durante

GSI, Darmstadt, Germany

Introduction

The heavy-ion microbeam is used for targeted irradiation of living cells (in culture) with ions from the UNILAC linear accelerator of GSI [1]. A custom-made epifluorescence microscope is available for beam targeting as well as for observation of proteins (tagged by fluorescent dyes) in sub-compartments of interest.

In order to gain better insight into DNA damage repair processes, we intend to employ a focused laser beam to locally bleach these fluorescent markers, thus unmarking sub-sets of molecules and analysing their dynamics and kinetics (FRAP, FLIM) [2].

Here, the development of a dedicated laser system for such bleaching experiments at the bio-endstation of the GSI microbeam facility is described.

Experimental Setup

Aside from requirements for bleaching experiments (wavelength, intensity, continuous/pulsed), a laser system has to fulfil the following specific requests related to the existing microbeam setup: (1) thermal and mechanical stability, (2) integration into the existing current microscope illumination under limited space, and (3) interface to the irradiation software. All these points together can only be fulfilled by a custom-made laser system.

The basic idea is to use a diode laser system (iBeam smart, Toptica Photonics AG, Germany) in combination with two galvanometers (Quantumscan 7, Nutfield Technology Inc., USA) to deflect the laser beam over the field of view (FOV) of the microscope (figure 1).

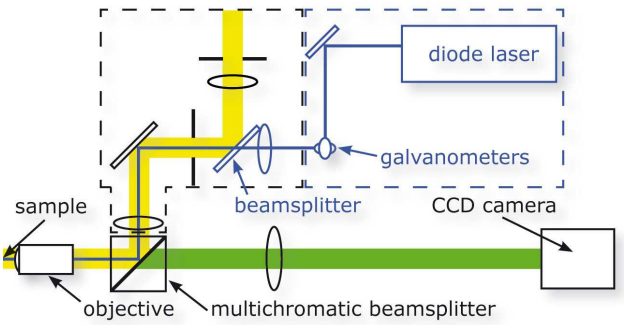

Figure 1: Schematic of the original microscope (black), extended laser system (blue), and excitation light (yellow) of the full FOV. The light (green) emitted from the fluorescent markers is recorded in the CCD camera.

The parallel laser beam (blue) is deflected by a pair of galvanometers and focused onto an aperture passing a beamsplitter, where the laser beam is combined with the epifluorescence illumination (yellow). This aperture acts as a luminous-field diaphragm and is imaged by an objective into the object plane and defining the area of illumination. The fluorescence light is detected by a CCD camera after passing a multichromatic beamsplitter and projective lens.

The simulation of the optical light path in ZEMAX (ZEMAX Development Corporation, USA) yielded the optimum configuration for the smallest focal spot size. On the basis of these simulations, all necessary mounts for lenses, scanners, laser, and beamsplitter were designed in CAD, machined and integrated into the existing setup (figure 2).

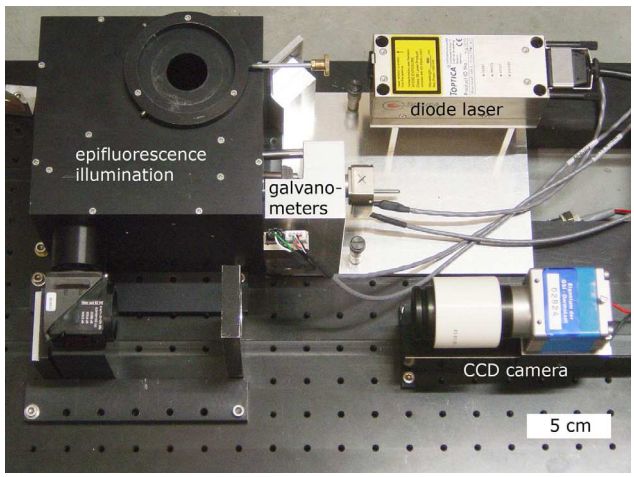

Figure 2: Setup with new laser system

Measurements of the laser spot size gave a maximum FWHM of 2 µm. Calculating the laser spot for an objective with a numerical aperture of 0.55, focal length of 3.3 mm, wavelength of 488 nm, and beam diameter of 2.8 mm (at objective entrance) result in a focal spot of 1.4 µm. This first result fulfilled the requirements necessary for bleaching experiments.

References

[1] M. Heiss et al., Targeted irradiation of mammalian cells using heavy-ion microprobe. Radiation Research 165 (2006) 231

[2] D. Axelrod et al., Mobility measurement by analysis of fluorescence photobleaching recovery kinetics. Biophysical Journal 16 (1976) 1055

[#] B.Merk@gsi.de

Nano-pore channels in a mica sheet with high aspect ratio as a mask

B. Naydenov[1], S. Pezzagna[2], F. Dolde[1], F. Jelezko[1], J. Wrachtrup[1], C. Trautmann[3], J. Meijer[2,#]

[1] 3. Physikalisches Institut, Universität Stuttgart, Germany; [2] RUBION, Ruhr-Universität Bochum, Germany; [3]GSI, Darmstadt, Germany

Negatively charged Nitrogen-Vacancy (NV) centres in diamond are considered to be one of the most promising quantum bits (qubits) for a solid state quantum computer. These defects have a strong optical transition from the triplet ground state to the triplet excited state allowing the detection of single centres [1]. Moreover, the electron and nuclear spin of NV can be measured and manipulated even at room temperature [2,3]. The first experiments were performed on diamonds with intrinsic NVs built in during the growth of the crystal. For future technological application, it is important to produce NVs on demand and under well-controlled conditions. Implantation of nitrogen followed by sample annealing under vacuum conditions provides a suitable approach [4,5], however, precise positioning of the NV requires a mask with nanometre apertures. Quite recently, such masks were realized by a piercing with an AFM tip [6] and by e-beam lithography [7]. Here we report an alternative approach using swift heavy ions as structuring tool.

A mask with nanometer-sized apertures was prepared by irradiating 10-µm thick mica sheets at the UNILAC accelerator using Sm ions of 11.1 MeV/u. For this energy, the ion range is much larger than the sample thickness. The fluence of the test experiment was ~ 10^9 ions/cm^2. For future mask fabrication, the mean distance between tracks can be adjusted to any preset value via control of the applied ion fluence.

After irradiation, the samples were immersed in a diluted hydrofluoric acid solution, where the ion tracks are dissolved and converted into open channels. The etching time determines the resulting diameter of the channels. Figure 1 shows scanning electron microscopy (SEM) images of 200 and 100 nm large channels obtained after respectively etching 60 and 30 min. In mica, the channel cross sections have a rhombic shape due to different bulk etching rates along different crystal directions. The diameter distribution of the channels is very small due to the fact that each channel is produced by an individual ion projectile. The ratio of the etch rate along the track is much larger than of the bulk resulting in cylindrical channel geometry [8]. For example, for 50 nm diameter *D* and 5 micron length *L*, the aspect ration *L/D* is 100, hardly achievable with other methods. Given by the small ion beam divergence, the channels are parallel oriented but stochastically spread across the sample.

A mask as shown in Fig. 1 will provide suitable apertures for implanting high-energy (> 1 MeV) nitrogen ions into diamond. The thickness of the mica sheet is large enough to stop the N ions i.e. to act as a mask. The spatial resolution of the implantation area will only be limited by straggling effects. The high implantation energy is required for two reasons: (i) the NV yield, i.e., the ratio of implanted ions to the NVs measured depends on the ion energy. It yields more than 40 % for implantation energies above 1 MeV [9]. (ii) the electron spin coherence time T_2 of the NVs also depends on the implantation energy. Longer T_2 values were measured in the above energy range [10] and are crucial for the application of NVs both as a qubit as well as magnetic field sensor

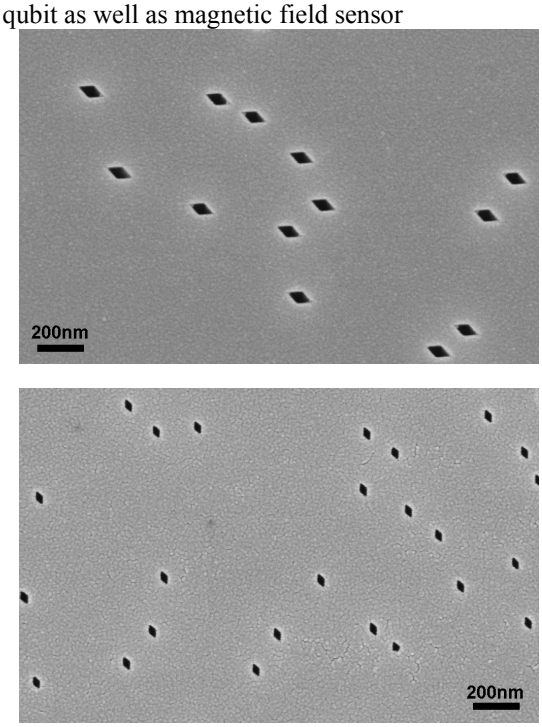

Figure 1: SEM images showing etched ion-tracks created in 10-µm thick mica sheets with 11.1 MeV/u Sm ions. Chemical etching in aqueous HF solution results in diamond-shaped cylindrical channels with a diameter of the long axis of 200 nm after 1 h etching (top) and 100 nm after 30 min etching (bottom).

References

[1] A. Gruber et al., Science 276, 2012 (1997).
[2] F. Jelezko et al., Phys. Rev. Lett. 93, 130501 (2004).
[3] F. Jelezko et al., Phys. Rev. Lett. 92, 076401 (2004).
[4] J. Meijer, et al., Appl. Phys. Lett. 87, 261909 (2005)
[5] J.R. Rabeau et al., Appl. Phys. Lett. 88, 023113 (2006).
[6] S. Pezzagna et al., Small 6, 2117 (2010).
[7] D.M. Toyli et al., Nano Lett. 10, 3168 (2010).
[8] H.A. Khan, Nucl. Instr. Meth. 189, 577 (1981).
[9] S. Pezzagna et al., New J. Phys. 12, 065071 (2010).
[10] P. Neumann et al., Nat. Phys. 6, 249 (2010).

#jan.meijer@rub.de

ATP-Controlled Molecular Transport through Cylindrical Nanochannels Fabricated in Ion Track Etched Polymer Membranes

Q. H. Nguyen[1,2,#], M. Ali[1,2], V. Bayer[2], R. Neumann[2] and W. Ensinger[1]

[1]Technische Universität Darmstadt, Germany; [2]GSI Helmholtzzentrum, Darmstadt, Germany

Nanoscale devices based on solid-state nanochannels have attracted enormous interest owing to the emergence of novel ion transport properties that mimic their biological counterparts. Compared to the fragile and sensitive biological systems, synthetic nanochannels fabricated in solid-state materials have proven a good alternative because of their (a) stability under harsh conditions, (b) easy to tailor surface properties to achieve desired interactions with molecules of interest, and (c) biologically comparable gating mechanisms [1]. To date, molecular transport in synthetic nanochannels mostly focused on selective ionic transport through nanoporous filters based on charge, molecular size as well as bio-/chemical interactions [2,3].

Here, we report the construction of a molecular gate based on nanochannels in which molecular transport can be controlled by the presence of Adenosine-5'-triphosphate (ATP) in the external environment. For this purpose, nanochannels were fabricated in heavy-ion irradiated polyethylene terephthalate (PET) foils of 12 µm thickness by symmetric chemical ion-track etching. The etching process leads to carboxyl ($–COO^-$) groups on the channel surface that are suitable partners for further chemical modifications performed with branched polyethyleneimine (PEI) by carbodiimide coupling chemistry [4].

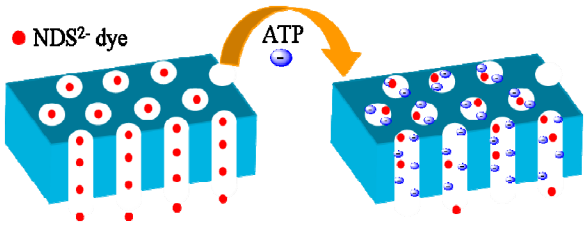

Figure 1: Schematic representation of molecular transport through PEI-modified cylindrical nanochannels.

The gating function of nanochannels was investigated by monitoring the flux of doubly charged 1,5-naphthalenedisulfonate (NDS^{2-}) dye molecules through PEI-modified membranes containing an array of parallel cylindrical nanochannels (10^9 channels/cm^2) of ~ 18 nm in diameter (Figure 1). For this purpose, a PEI-modified membrane was mounted between the two halves of a conductivity cell. The feed half-cell contained NDS^{2-} analyte of known concentration, whereas the permeate half-cell was filled with pure buffer solution. After a preset time, the concentration of analyte in the permeate half-cell was determined by measuring the UV absorbance with a UV/VIS spectrometer. Figure 2 displays the flux of NDS^{2-} across the membrane before and after the addition of ATP along with analyte in the feed solution. It is evident that, in the absence of ATP, the membrane selectively permeates NDS^{2-} molecules across the membrane. The charged channel walls play a significant role in this process. Initially, an electrical double layer was generated inside the charged channel, which contains a higher concentration of NDS^{2-} ions. Therefore, NDS^{2-} ions selectively diffused through the membrane, while co-ions were electrostatically prohibited from entering the nanochannel. However, the flux of NDS^{2-} was drastically decreased in the presence of ATP in the feed solution. A possible explanation for this is that the bulky ATP molecules electrostatically attached to the inner walls, resulting in the reduction of surface charges and also inner channel diameter, which in turn suppresses the selectivity and also the observed NDS^{2-} ion flux.

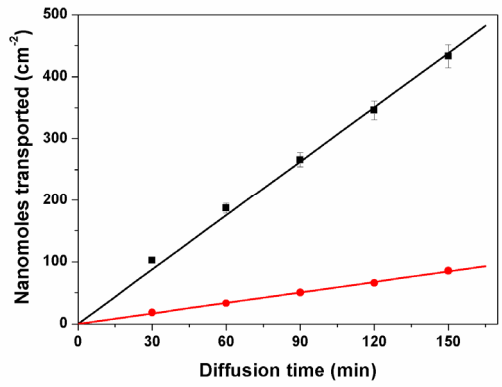

Figure 2: Diffusion of NDS^{2-} analyte through PEI-modified membrane prior to (black square) and after (red circles) the addition of ATP in the analyte solution.

In conclusion, we described the construction of a nanoporous filter which provides ATP-modulated molecular transport through synthetic nanochannels. The function is based on the electrostatic /hydrogen-bonding interactions of ATP molecules which in turn control the ion flux through the nanochannels. We believe that such simple and economically affordable nanofilters would be applicable for sensing, directed molecular transport and separation, and targeted drug delivery at nanoscale level.

References

[1] Z. S. Siwy, Adv. Funct. Mater. 16 (2006) 753
[2] C. R. Martin et al., J. Phys. Chem. B 105 (2001) 1925
[3] Q. H. Nguyen et al., Nanotechnology 21 (2010) 365701
[4] M. Ali et al., ACS Nano 4 (2010) 7267

* Work supported by Beilstein-Institut, project NanoBiC
# q.h.nguyen@gsi.de

Single Conical Ion-Track Nanochannels Modified *via* Horseradish Peroxidase Enzyme–Concanavalin A Protein Bioconjugation*

M. Ali[1,2,#], Q. H. Nguyen[1,2], V. Bayer[2], R. Neumann[2], and W. Ensinger[1]

[1]Technische Universität Darmstadt, Germany; [2]GSI Helmholtzzentrum, Darmstadt, Germany

Synthetic nanochannels have recently attracted enormous interest because their geometry and surface chemistry can be fully controlled. They also feature excellent mechanical robustness and compatibility with various electronic measurement systems. Synthetic nanochannels fabricated in polymer and silicon-based films as well as glass nanopipettes have already been applied for the detection of DNA and protein analytes.[1-3]

Incorporation of bio-recognizable elements and biomolecular conjugation in nanoscale architectures have been achieved by two types of surface modification techniques: (i) covalent attachment to the channel walls, and (ii) electrostatic self-assembly of polyelectrolytes on the inner walls by exploiting the existing charged chemical groups on the channel surface.[2-5]

Moreover, biospecific interactions such as sugar–lectin affinity could also be used for the bioconjugation of biomolecules on a channel surface bearing sugar residues.[6] However, the implementation of sugar–lectin interactions to immobilize biomolecules in nanochannels remains a challenge which is addressed here by using the horseradish peroxidase (HRP) enzyme. It is known that HRP is a mannose-rich glycoprotein and the mannose residues are accessible to binding with lectin protein molecules. Concanavalin A (Con A) is a lectin protein that exists as a tetramer at neutral pH.[6]

Single nanochannels were fabricated in heavy-ion irradiated PET foils of 12 µm thickness by asymmetric chemical track etching using 9 M NaOH solution. This resulted in a conical channel (small aperture 16 nm) with carboxylate (-COO^-) groups on the channel surface.[2-5] The COOH groups were first activated into sulfo-NHS-esters by using an aqueous solution containing *N*-(3-dimethylaminopropyl)-*N'*-ethylcarbodiimide hydrochloride and *N*-hydroxysulfosuccinimide for 30 minutes.[2] Then, the amine-reactive sulfo-NHS-ester molecules were covalently coupled to the amino group present on the HRP enzyme molecule. After HRP-immobilization, the Con A solution was introduced on both sides of the enzyme-modified single-channel membrane. The exposure for 3 hours at room temperature allowed the sugar residues of glycoenzyme to couple through biospecific interaction to the Con A. The functionalized membrane was mounted in a conductivity cell, and current-voltage (*I-V*) curves were measured at neutral pH using 0.1 M KCl as an electrolyte solution.

The ionic current through the as-prepared channel, measured at +1 V, was +1.5 nA (Fig. 1). After HRP immobilization, the current decreased to 0.95 nA. Finally, the Con A complexation with HRP enzyme resulted in a further reduction of current to 0.55 nA (approximately 3 times lower than the original value). At neutral pH, both the HRP enzyme and the Con A molecules are negatively charged. Consequently, the channel displayed current rectification before and after the enzyme and Con A immobilization. The ion current decreases for both voltage polarities, consistent with the dependence of the ionic current on the effective cross-section area of the nanochannel.

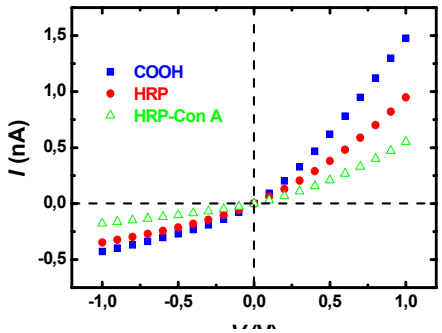

Figure 1: Current–voltage curves of a single conical channel containing COOH, HRP and Con A molecules, respectively.

In conclusion, we have demonstrated the bioconjugation of Con A protein with glycoenzyme HRP by means of sugar–lectin interaction inside single polymer nanochannels. First, the HRP-enzyme was covalently immobilized on the channel surface by carbodiimide coupling chemistry. Second, the bioconjugation of Con A onto the HRP-modified channel surface was achieved through the biospecific mannose-lectin interactions. The experimental data revealed that the immobilization of biomolecules inside the nanochannel produces a significant reduction in the area available for ion transport. The channel blocking effect can be exploited to tune the channel conductance and selectivity. This should allow designing biosensors based on the decrease in electrical conductance of the nanochannel that occurs upon bioconjugation of proteins.

References

[1] Z.S. Siwy and S. Howorka, Chem. Soc. Rev. 39 (2010) 1115
[2] M. Ali et al., ACS Nano 4 (2010) 7267
[3] M. Ali et al., J. Am. Chem. Soc. 130 (2008) 16351
[4] M. Ali et al., Nanotechnology 19 (2008) 085713
[5] M. Ali et al., J. Am. Chem. Soc. 132 (2010) 8338
[6] J. Anzai and Y. Kobayashi, Langmuir 16 (2000) 2851

* Work supported by the Beilstein-Institut, project NanoBiC.

#M.Ali@gsi.de

Synthesis of segmented silver-gold nanostructures and nanogaps

I. Alber[1,#], S. Müller[1], O.Picht[1], M.Rauber[1,2], M.E. Toimil-Molares[1], R. Neumann[1]

[1]GSI, Darmstadt, Germany; [2] Technische Universität Darmstadt, Germany

By interaction of metallic nanowires (NWs) with electromagnetic radiation of appropriate wavelength, resonant surface charge density oscillations, called surface plasmons, can be excited. These oscillations are responsible for a large electromagnetic field enhancement in the NW near-field, turning the wires into promising devices for highly sensitive detection of molecules using surface enhanced infrared spectroscopy[1] and surface enhanced Raman spectroscopy[2,3].

Recently, much work has been devoted to plasmon coupling at nm-size gaps between two metal nanostructures. The resulting high field enhancement in the vicinity of these gaps depends strongly on the gap size.[4,5,6] A current experimental challenge is to develop techniques that enable the reproducible fabrication of large amount of nanogaps with controlled dimensions. [7]

Here we report the synthesis of nanogaps by electrochemical deposition of segmented Au/Ag/Au NWs. A nanogap is realized between two gold segments by etching the silver segment which has the width of the intended gap. The NWs were prepared from a single electrolyte containing both silver and gold ions instead of exchanging the electrolyte for each segment. Using this approach, very narrow gaps down to 8 nm were created in a cost-effective and well controllable manner.

Polycarbonate membranes with randomly distributed cylindrical pores were fabricated by heavy-ion irradiation at the UNILAC (ion energy E =11.1 MeV/u) and subsequent etching of the ion tracks in 6M sodium hydroxide solution at 50°C. Au/Ag/Au wires were electrodeposited in the pores at 60°C, with an electrolyte consisting of $KAu(CN)_2$ and $KAg(CN)_2$, employing a suitable sequence of pulses. We have studied the influence of electrolyte concentration and applied voltage characteristics on composition and length of the different Au and Ag segments.

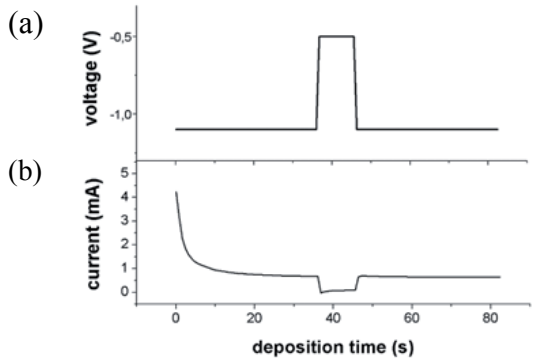

Figure 1: (a) Applied pulse sequence leading to the growth of a segmented Au/Ag/Au NW array and (b) corresponding current-versus-time.

i.alber@gsi.de

Fig.1a shows a representative pulse sequence leading to the deposition of a Au/Ag/Au NW array. At more negative potentials Au-rich segments are deposited (in this case -1.1 V vs sat. Ag/AgCl), whereas at less negative voltages (i.e. -0.5 V vs sat. Ag/AgCl) Ag-rich segments grow. The duration of the different pulses determines the lengths of the segments. The corresponding current recorded during the growth of the array is depicted in Fig.1b. In this case average segment lengths of 1000/22/1000 nm were created. By varying the duration of the second pulse between 10 and 25 s, Ag segments with average lengths between 22 nm and 150 nm have been synthesized. The length distribution of the Ag segments in the sample corresponding to the curves in Fig.1 ranges from 8 to 36 nm.

Fig.2a shows the SEM image of a Au/Ag/Au NW. A zoom-in of the Ag segment region is displayed in the inset. The content of Ag in the NW segments was analyzed by energy-dispersive X-ray spectroscopy and amounted to (37 ± 3) % for the long segments and to (84 ± 3) % for the short middle segment.

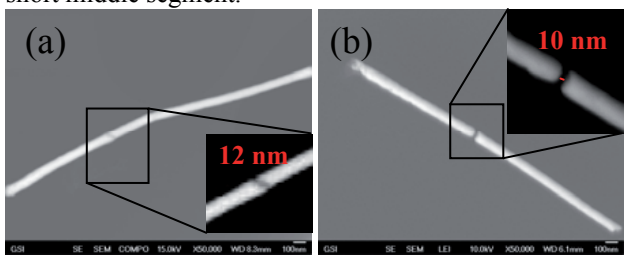

Figure 2: (a) SEM images visualizing the Au/Ag/Au segments of a NW and (b) a Au/Au nanogap, both originating from the array corresponding to the curves in Fig.1. The insets show the silver segment and the gap with higher magnification.

As last step the Ag segment was etched using nitric acid. A scanning electron microscopy image of a resulting 10 nm gap is shown in Fig. 2b.

In conclusion, segmented Au/Ag/Au NWs and nanogaps were synthesized by electrochemical deposition followed by chemical dissolution of the Ag segment. The average gap size is controlled by the deposition time of the Ag segments. Plasmon resonance measurements on the structures are being performed in collaboration with the group of Prof. A. Pucci at the University of Heidelberg.

References

[1] F. Neubrech et al., Phys. Rev. Lett. 101, 157403 (2008).
[2] S. Nie et al., Science 275, 1102 (1997).
[3] K. Kneipp et al., Phys. Rev. Lett. 78, 1667 (1997).
[4] S. Li et al., Nano Lett. 10, 1722 (2010).
[5] L. Qin et al., PNAS 103, 13300 (2006).
[6] H. Xu et al., Phys. Rev. E. 62, 4318 (2000).
[7] T. Li et al., Adv. Materials 21, 1, (2009).

XRD Characterization of $Bi_{1-x}Sb_x$ Nanowire Arrays with Controlled Sb Content*

S. Müller† [1], *C. Schötz*[1], *O. Picht*[1], *M. Rauber*[1,2], *I. Alber*[1], *R. Neumann*[1], *and M. E. Toimil-Molares*[1]

[1]GSI, Department of Materials Research, Darmstadt; [2]TU Darmstadt, Department of Material- and Geo-Sciences

In 1993, Hicks and Dresselhaus published theoretical calculations of the electrical conductivity (σ), the Seebeck coefficient (S), and the thermal conductivity (κ) that predicted an enhanced $ZT = \frac{\sigma S^2}{\kappa} T$ for quantum wires [1], resulting in a new direction of research searching for more efficient thermoelectric (TE) materials. ZT is the TE figure of merit and T the temperature in K. $Bi_{1-x}Sb_x$ nanowires are in particular expected to exhibit enhanced ZT values at 77 K. In addition, due to the unique characteristics of these low-dimensional systems, ZT can be tailored as a function of the Sb concentration x and the nanowire diameter [2].

Arrays of $Bi_{1-x}Sb_x$ nanowires with a diameter of 60 nm were electrodeposited in nanoporous ion-track membranes. The channels in the membranes were produced by irradiating polymer foils at the UNILAC facility followed by chemical track etching. The wires were characterized via X-ray diffraction using a Cu-Kα-source and a HZG4 goniometer. The results presented here demonstrate that it is possible to fabricate $Bi_{1-x}Sb_x$ nanowires alloying Bi with different concentrations of Sb. Fig. 1 shows the (110) reflections recorded for a series of nanowire arrays deposited at room temperature, under different potentials U (between -195 and -245 mV vs. a saturated calomel electrode) and different concentrations of Bi and Sb in the electrolyte, namely (a) $[Sb^{3+}] = 0.03$, (b) 0.02, and (c) 0.01 mol/l (with $[Bi^{3+}] + [Sb^{3+}] = 0.1$ mol/l).

The (110) reflection clearly shifts to larger angles for lower deposition voltages and larger $[Sb^{3+}]$. Bragg's law and the lattice parameters of the unit cell of the $Bi_{1-x}Sb_x$-alloys allowed us to calculate x in the nanowires, since the lattice parameters are strictly monotonically decreasing with increasing x, while the crystalline structure remains unchanged ($R\bar{3}m$) [3]. The values are plotted in Fig. 2 as a function of U and $[Sb^{3+}]$.

The concentration of Sb x in nanowire arrays, an important parameter with respect to their thermoelectric properties, can be determined from X-ray diffractograms. The transport properties of individual nanowires are currently investigated to understand the behaviour of low-dimensional thermoelectric materials [4].

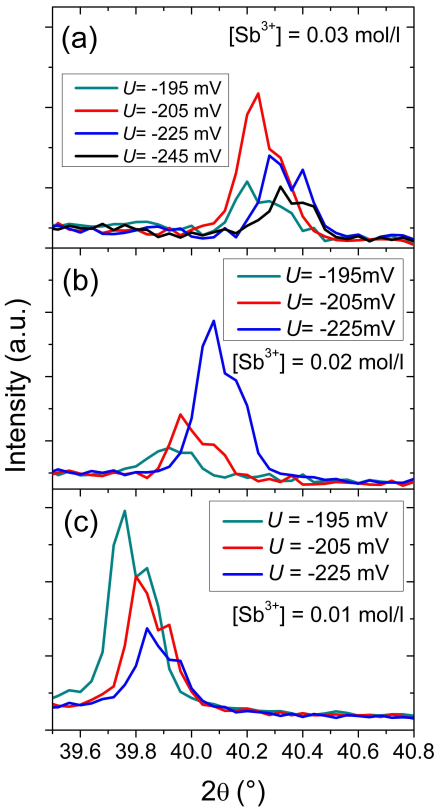

Figure 1: (110) reflections from $\omega - 2\theta$ scans of $Bi_{1-x}Sb_x$ nanowire arrays, deposited at different potentials and Sb concentrations in the electrolyte.

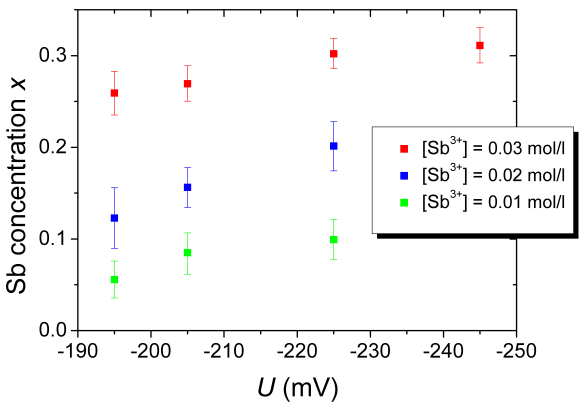

Figure 2: Concentration of Sb x in nanowires versus deposition voltage U plotted for the different Sb concentrations in the electrolyte.

References

[1] L. D. Hicks and M. S. Dresselhaus, PRB **47**, 16631 (1993).

[2] O. Rabin, Y.-M. Lin, M. S. Dresselhaus, APL **79**, 81 (2001).

[3] J. P. Dismukes et al., J. Chem. Eng. Data **13**, 317 (1968).

[4] F. Völklein et al., J. Electron. Mater. **38**, 1109 (2009).

* Research supported by DFG Schwerpunktprogramm 1386

† Electronic mail: Sven.Mueller@gsi.de

Electrochemical fabrication of textured Bi_2Te_3 nanowire arrays

O. Picht[1,#], S. Müller[1], M. Rauber[1,2], I. Alber[1], M.E. Toimil-Molares[1,#] and R. Neumann[1]

[1]GSI, Department of Materials Research [2]TU Darmstadt, Department of Material- and Geo-Sciences

Initiated by the theoretical works of Hicks and Dresselhaus [1], the interest in nanostructured materials as more efficient thermoelectric materials has increased enormously. Recent experimental results on structures ranging from superlattices [2] to Si nanowires [3,4] emphasize the potential of tailoring materials properties by implementing finite- and quantum-size effects to circumvent classical limitations. In particular, Bi_2Te_3 nanowires are expected to exhibit important enhancements of the thermoelectric efficiency in comparison to their bulk counterparts. Our research focuses on two important aspects of nanoscale thermoelectrics: (i) fabricating thermoelectric nanowires with very small well-controlled diameters, serving as low-dimensional model systems, and (ii) demonstrating that the preferential crystalline orientation of the nanowires can be tuned by the synthesis parameters.

Bi_2Te_3 nanowire arrays were electrochemically grown in a thermostated 3-electrode setup with a saturated calomel electrode (SCE) using ion-track etched polycarbonate (PC) membranes with controlled geometrical characteristics prepared at GSI. PC foils with thicknesses of 10 µm (Makrofol KG, Bayer) and 30 µm (Makrofol N, Bayer) were irradiated at the UNILAC with heavy ions (fluence: 10^8 – $5x10^9$ ions/cm^2) and subsequently etched in 6M NaOH at 50°C.

Figure 1 shows STEM-in-SEM images of segments of Bi_2Te_3 wires grown in 10 µm thick PC. Systematic investigations to attain smaller structures led to fabrication of nanowires with average diameter 19 ± 2 nm.

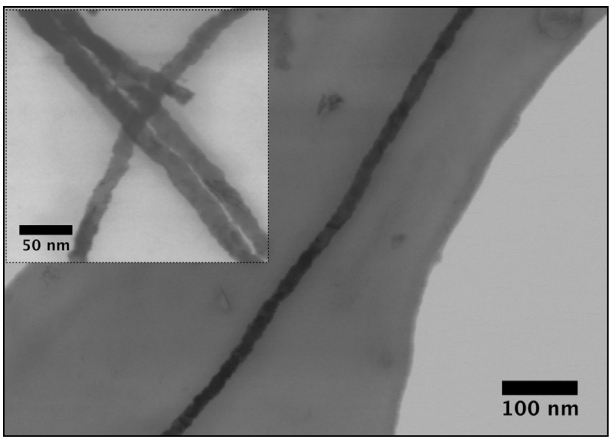

Figure 1: STEM-in-SEM images of segments of Bi_2Te_3 nanowires electrodeposited at 20°C and 0 mV vs. SCE. Their average diameter is 19 ± 2 nm.

Figure 2 presents ω-2θ scans measured on 120-nm diameter wires embedded in the membrane, electrodeposited at room temperature (top) and 4 °C (bottom). Varying the deposition potential from 0 to -100 mV vs. SCE leads to a shift from preferential (110) and (205) reflections to dominant diffraction at the (015) and (205) planes of the crystallites. Nanowires with higher (015) texture are synthesized by lowering the deposition temperature from 20 to 4°C.

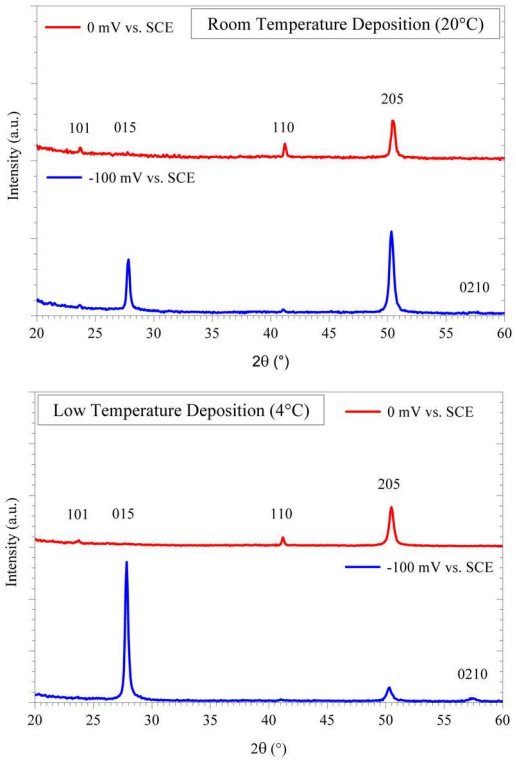

Figure 2: X-ray diffractograms showing the influence of deposition temperature and potential on preferential crystalline orientation of nanowire arrays with average wire diameters of 110 - 120 nm. The arrays were grown in 30-µm thick membranes.

Template-assisted electrochemical growth is a versatile approach to Bi_2Te_3 nanowire fabrication. By controlling this process, we are able to deposit nanowires with minimum diameters below 20 nm, sizes at which nanoscale effects are predicted to yield a signifcant increase of the thermoelectric efficiency. By varying deposition temperature and potential, we can tune the texture of the nanowire arrays, a very important parameter due to the orientation dependent performance of Bi_2Te_3.

References

[1] L.D. Hicks, Phys. Rev. B 47 (1993) 12727.
L.D. Hicks, Phys. Rev. B 47 (1993) 16631.
[2] R. Venkatasubramanian, Nature 413 (2001) 597.
[3] A.I. Hochbaum, Nature 451 (2008) 163.
[4] A.I. Boukai, Nature 451 (2008), 168.

* This research was partially supported by DFG SPP 1386.

Electronic mail : o.picht@gsi.de , m.e.toimil-molares@gsi.de

Cyclic-voltammetry study of bismuth telluride electrodeposition in polycarbonate etched ion -track membranes

N. Stein[1], C. Boulanger[1], C. Frantz[1], O. Picht[2] and M.E. Toimil-Molares[2]

[1]Institut Jean Lamour, CNRS, University Paul Verlaine-Metz, France; [2] GSI, Darmstadt, Germany

Bismuth telluride compounds are well-known to be among the most efficient thermoelectric materials at room temperature. Currently, some efforts are made to synthesize nanowires, since theoretical predictions have shown that their transport properties can be favourably modified compared with bulk materials.

The feasibility of the electrochemical synthesis of bismuth telluride nanowires in porous membranes has been already demonstrated, but literature data report opposite effects of the nanostructures on the Seebeck coefficients, exhibiting both lower and higher values than those of bulk references [1]. This disparity among data can be due to the chemical composition of the nanowires. Indeed, the thermoelectric properties of chalcogenide compounds are directly linked to their stoichiometry.

The aim of this work was to define a specific protocol of electrodeposition, leading to Bi_2Te_3 nanowires with controlled composition and with high filling ratio. Thus we have analyzed the electrochemical deposition of bismuth telluride in etched ion-track polycarbonate membranes, which acts as an array of embedded ultra microelectrodes.

Polycarbonate foils of thickness 30 µm were irradiated with gold ions (E = 11.1 MeV/u) at the UNILAC accelerator. A fluence of 10^8 ions/cm^2 was applied which is low enough to avoid pore overlapping in the resulting templates. After UV sensitizing, the pore diameters were adjusted to 60, 90, and 120 nm by chemical track etching in 6N caustic soda at 50°C.

All electrochemical experiments were carried out at room temperature with a three-electrode setup that consisted of the track-etched template with a 160-nm thick sputtered platinum layer on one side acting as the working electrode, a saturated Ag/AgCl reference electrode, and a platinum disk counter-electrode. All electrolytes contained 10 mM Te^{IV}, 1N HNO_3, 50% v/v dimethyl sulfoxide (DMSO), and different concentrations of Bi^{III}. DMSO as a wetting agent. Further experimental details can be found in reference [2].

In a first set of experiments, bismuth telluride nanowires were grown in acidic media under potentiostatic conditions at U = -100 mV with electrolytes containing Bi^{3+} and $HTeO_2^+$ at equal concentrations. This value of -100 mV was chosen based on previous results for stoichiometric films. The filling ratio of the pores was increased from 51 to 80% by adding DMSO to the electrolyte. The global composition of the samples displayed a large excess of Te (80 at.%) versus Bi (20 at.%), with or without DMSO in the electrolyte [2].

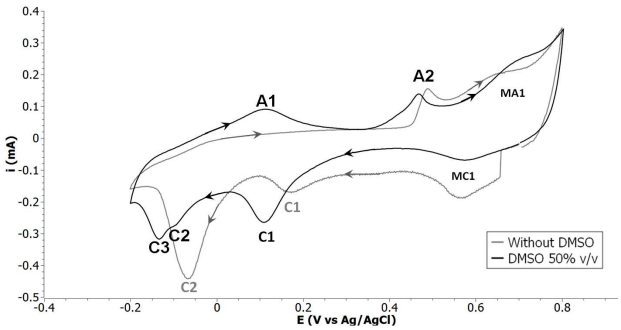

Figure 1: Cyclic voltammograms at 5mV.s^{-1} within 120 nm diameter pores membrane with and without DMSO, $|Bi^{III+}|=|Te^{IV}|=10^{-2}$M

To understand the reason of the Te excess, voltammetric studies were performed using membranes with 120-nm diameter pores. Fig. 1 shows two cyclic voltammograms (CV) recorded using one electrolyte with and another one without DMSO. Both CVs show anodic and cathodic peaks (MC1/MA1) at high potentials. They are observed in both electrolytes (aqueous and DMSO) but only in acidic medium. They are not governed by diffusion process since the peaks are not proportional to $v^{1/2}$ according the Randles-Sevčik relationship. Both peaks could be related to electrochemical activity of the membrane or to the Pt electrode. In the presence of bismuth and telluride salts, we observe two additional cathodic peaks C1 and C2 and two anodic peaks A1 and A2. With DMSO, a shoulder (C2 and C3) in the more cathodic peak is observed whereas A1 becomes larger. The presence of DMSO shifts all cathodic peaks in the cathodic direction. All peaks are similar to those reported on bulk electrodes [3], except for C1, which is due to the growth of pure Te. C2 is attributed to the cathodic growth of Bi_2Te_3. In order to avoid a large excess of Te, the ratio of Bi/Te was increased to 3/2 in the electrolyte, leading to the electrodeposition of stoichiometric Bi_2Te_3 nanowires.

References

[1] C. Boulanger, Journal of Electronic Materials 39 (2010) 1818.

[2] C. Frantz, N. Stein, L. Gravier, S. Granville, and C. Boulanger, Journal of Electronic Materials 39 (2010) 2043.

[3] M. Martin-Gonzalez, A.L. Prieto, R. Gronsky, T. Sands, A.M. Stacy, Journal of the Electrochemical Society 149 (2002) C546.

Measurement of thermoelectric properties of nanowires grown in track-etched polymer membranes*

F. Völklein[1], D. Huzel[1,2,#], H. Reith[1,2], M. C. Schmitt[1,2], R. Sachser[2], M. Huth[2], S. Müller[3], O. Picht[3], M. E. Toimil-Molares[3]

[1]IMtech, Hochschule RheinMain, Rüsselsheim, Germany; [2]Physikalisches Institut Universität Frankfurt, Germany; [3]Materials Research GSI, Darmstadt, Germany

Thermoelectric materials can be characterized using the so-called figure of merit ZT, a dimensionless "efficiency" number which can be calculated using the electrical conductivity σ, the thermal conductivity λ, and the Seebeck coefficient S, along with the absolute temperature T: $ZT = (\sigma * S^2 * T)/\lambda$.

Much effort is being put forward into the search for new nanostructured materials that lead to a higher ZT. By decreasing dimensionality, a reduction of λ due to increased surface phonon scattering is expected without decreasing σ. This project focuses on the thermoelectric properties of 1-dimensional nanowires made of bismuth, bismuth telluride or bismuth antimonide.

The nanowires were prepared by electrochemical deposition in pores produced by chemical etching of ion tracks in polymer membranes [1]. The diameter of the wire is adjusted by the etching process, the wire length is controlled by the deposition time but limited to the template thickness. In this study, nanowires with a length of around 40 µm and diameter of 150-200 nm were used. After dissolving the polymer template, the nanowire-containing solution was drop-casted onto Si wafer.

Subsequent micro-structuring processes including photolithography, lift-off techniques along with deposition and selective-etching methods, created microchip platforms around individual nanowires for the measurement of S, σ, and λ [2-4].

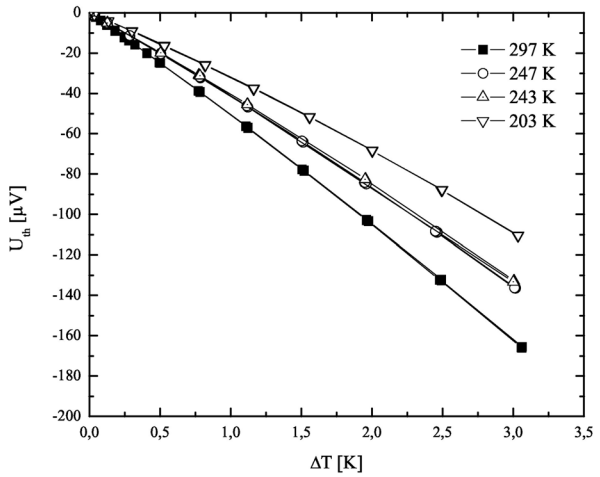

Fig. 1: Thermovoltage of a 175-nm diameter Bi_2Te_3 nanowire at different ambient temperatures.

Using the Seebeck-chip, a temperature difference of a few Kelvin is applied. Over the length of the nanowire across electrodes (15 µm), this yields a temperature gradient as high as 10^6 K/m. The temperature difference is measured using a bismuth reference layer of known Seebeck-coefficient.

Thermovoltage measurements were performed on Bi_2Te_3 and $Bi_{1-x}Sb_x$ nanowires. Figure 1 shows data for an n-type Bi_2Te_3 nanowire as a function of the applied temperature difference at various ambient temperatures. The slope of the graph equals the Seebeck-coefficient and amounts to -55 µV/K for room temperature.

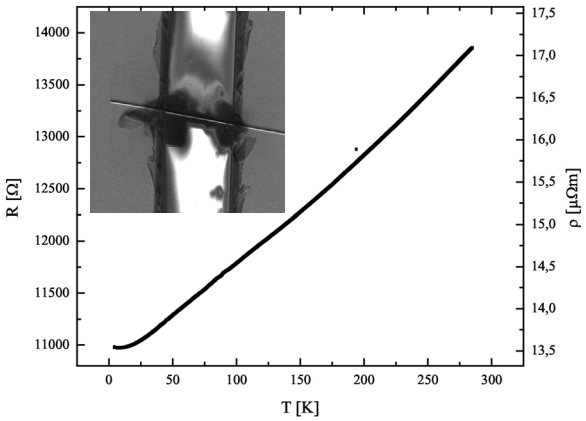

Fig. 2: Resistivity of a 175-nm diameter Bi_2Te_3 nanowire from 4 K to room temperature; inset: SEM image of nanowire between contact pads, gap distance 18 µm.

With the same setup, the electrical conductivity was measured over a wide temperature range for Bi, $Bi_{1-x}Sb_x$ and Bi_2Te_3 nanowires. Fig. 2 displays the resistivity vs temperature curve measured on a single Bi_2Te_3 nanowire. The almost linear evolution indicates a metallic behaviour of this nanowire (in agreement with the temperature dependence of the Seebeck coefficient), possibly due to small excess of Te content.

References

[1] T. Cornelius et al., Nanotechnology 16 (2005) S246
[2] F. Völklein, J. Electr. Mat. 39 (2010) 1950
[3] H. Reith et al., Nanotechnology 20 (2009) 325706
[4] M.C. Schmitt et al., J. Electr. Mat. 38 (2009) 1109

* Work supported by BMBF Nanotherm, DFG SPP 1386
# huzel@imtech-fhw.org

Electrolessly synthesized gold nanotubes as efficient flow-through reactors

F. Münch[#], U. Kunz, C. Neetzel, S. Lauterbach, H.-J. Kleebe, W. Ensinger

Technische Universität Darmstadt, Darmstadt, Germany

Motivation

Electroless metal plating in combination with nanochannel-containing templates is a versatile method for the fabrication of metal nanotubes [1]. In contrast to the electrodeposition of metals, electroless plating relies on the surface-selective chemical reduction of a metal precursor [2]. The simultaneous coverage of the whole template surface with metal nanoparticles favors the formation of tube-like structures. Metal nanotubes have been applied in different fields ranging from catalysis [3] to sensing [4] and separation [5]. In the presented paper [7], we significantly refined the standard synthesis of gold nanotubes [6] in ion track etched polycarbonate. A precise control of the template properties such as track density, template thickness and tube diameter is required for potential applications. Therefore, we fabricated our templates by etching polycarbonate foils irradiated at the UNILAC. Finally, we utilized the obtained nanostructures as efficient microreactors [7].

Results and Discussion

A common problem of the electroless fabriaction of high aspect ratio nanotubes is the diffusion limited supply of reagents to the central regions of the templates [6]. To reduce the reaction speed and thus the reagent depletion, we introduced 4-(N,N-dimethylamino)pyridine (DMAP) as an auxiliary reagent. This electron rich pyridine and its protonated pyridinium ion reversibly bind to gold surfaces [8] and reduce the autocatalytic activity of the plated gold films by steric interaction. By adjusting the DMAP concentration and the pH value, the grain size, shape and the deposition speed can be easily controlled, allowing the synthesis of highly defined gold nanotubes (Fig. 1) [7].

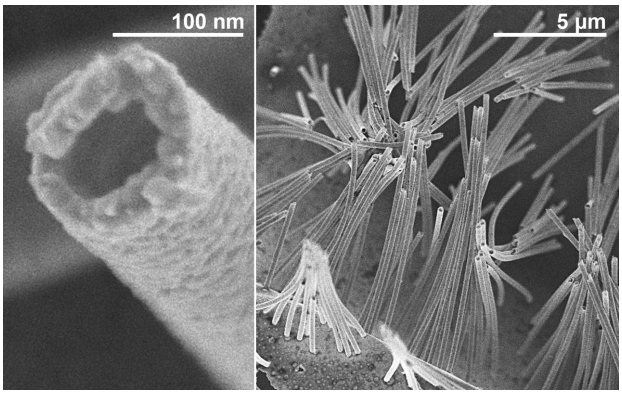

Figure 1: SEM images of a single gold nanotube (left) and a gold nanotube field (right).

[#] muench@ca.tu-darmstadt.de

Template-supported nanotubes consisting of partly agglomerated gold particles of 5 ± 2.1 nm size have been applied as flowthrough reactors in the reduction of 4-nitrophenol by sodium borohydride [7]. The reaction progress was monitored by UV-vis spectroscopy. Fig. 2 shows the decrease of the educt absorbance (4-nitrophenolate, 400 nm) and the rise of the product absorbance (4-aminophenolate, 300 nm) with increasing reaction time. The nanotube membrane proved to be a microfluidic system of excellent catalytic activity: Despite a relatively high flow rate, the reaction showed 99% conversion after a distance of just 0.06 mm, representing a consecutive passage of the reaction solution through two nanotube membranes [7].

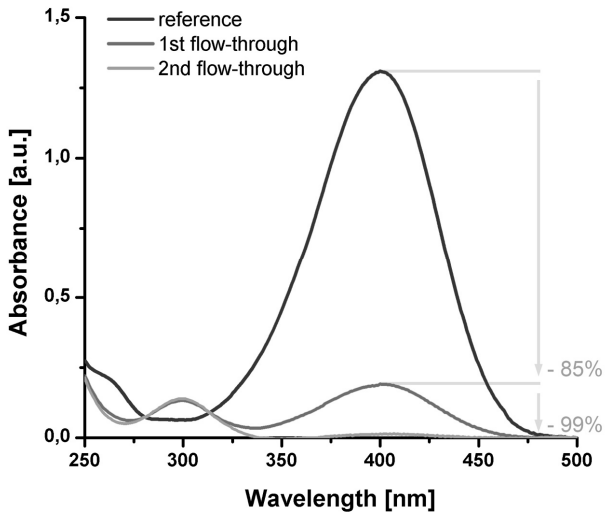

Figure 2: UV-vis spectra before and after the flow through a gold nanotube membrane of 30 µm thickness.

References

[1] C. J. Brumlik, V. P. Menon and C. R. Martin, J. Mater. Res. 9 (1994) 1174.

[2] C. R. K. Rao and D. C. Trivedi, Coord. Chem. Rev. 249 (2005) 613.

[3] M. A. Sanchez-Castillo, C. Couto, W. B. Kim and J. A. Dumesic, Angew. Chem. Int. Ed. 43 (2004) 1140.

[4] S. Yu, U. Welp, L. Z. Hua, A. Rydh, W. K. Kwok and H. H. Wang, Chem. Mater. 17 (2005) 3445.

[5] S. Yu, S. B. Lee and C. R. Martin, Anal. Chem. 75 (2003) 1239.

[6] R. J. Gilliam, S. J. Thorpe and D. W. Kirk, J. Appl. Electrochem. 37 (2997) 233.

[7] F. Muench, U. Kunz, C. Neetzel, S. Lauterbach, H.-J. Kleebe and W. Ensinger, Langmuir 27 (2011) 430.

[8] B. C. Barlow and I. J. Burgess, Langmuir 23 (2007) 1555.

Correlation between field emission current limits and morphology changes of poly- and single-crystalline gold nanowire patches

A. Navitski[1], P. Serbun[1], G. Müller[1,*], I. Alber[2], M.E. Toimil-Molares[2], C. Trautmann[2]
[1]Physics Department, University of Wuppertal; [2]GSI Helmholtzzentrum, Darmstadt, Germany

Well aligned and highly efficient field emission (FE) results have been obtained with regular arrays of gold nanowire (NW) patches [1]. However, strong variations of the maximum current I_{max} among single Au-NW patches have been attributed to contact problems between wires and substrate [2]. Recently we have focused our research in finding a systematic correlation between FE properties and morphology changes of preselected patches caused by FE current processing. Typical SEM images of a polycrystalline Au-NW patch before and after FE scanning microscope measurements are shown in Fig. 1. The patch (as fabricated) is formed by randomly distributed NWs, most of which are solitary and vertically aligned. After processing, about 30-40% of the patch area is modified. The NWs located within the patch area where the local FE measurements were performed suffered dramatic morphological changes, while NWs at several μm distance from the bright area seem not to be affected. Therefore, these unmodified emitters are responsible for the final emission current of this patch (~ 0.7 μA at 90 V/μm).

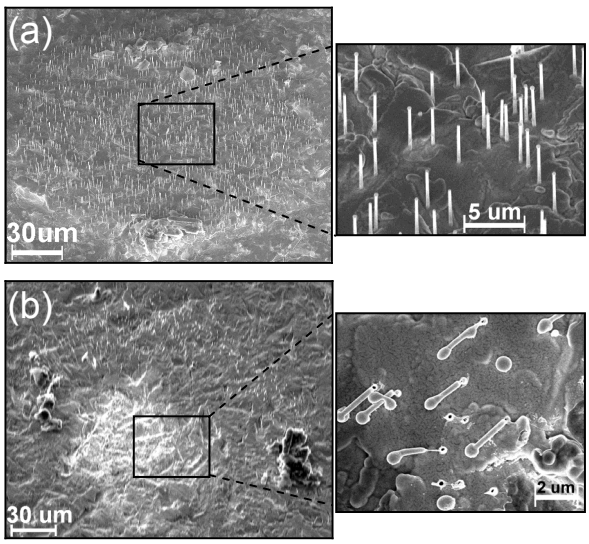

Figure 1: SEM images of the same polycrystalline Au-NW patch before (a) and after (b, rotated 90°) current processing (1 μA at 88 V/μm), where the bright area reflects Au coating due to NW destruction. The insets are zooms into the respective areas [3].

SEM images showing morphology changes undergone by most of the processed NWs and the formation of a sphere at the top of the NW (see inset of Fig.1b) driven by Rayleigh instability [4]. The heating of electron emitting NWs is enhanced by geometrical constrictions and high resistance in the contact region to the substrate [2]. The presence of such contact problems is revealed by ring-like marks on the processed cathodes (inset in Fig.1b). As first approach for improvements, single-crystalline Au-NWs were prepared using a cyanide-based electrolyte. SEM images of such a structured cathode confirm stable solitary and vertically aligned 200 nm diameter NWs (10^7/cm^2) with reduced length (8 vs. 12 μm) compared to the polycrystalline ones. In Fig. 2 typical current-field curves of single- and polycrystalline NWs are compared. Both show similar strong current fluctuations due to their successive processing, but the onset field and I_{max} values are on average slightly higher for the single-crystalline Au-NWs (42 vs. 32 V/μm, 25 vs. 22 μA). Despite their improved crystallinity, some of the processed single-crystalline NWs still exhibit ring-like contacts and severe destructions by partial melting as shown in Fig. 3.

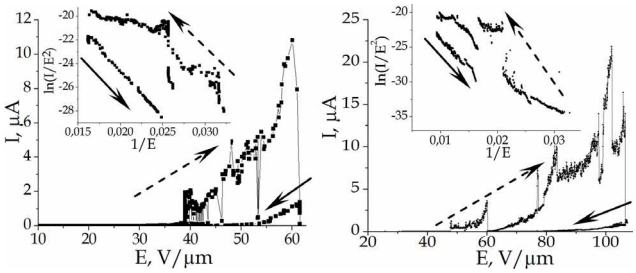

Figure 2: Typical I(E) and Fowler-Nordheim plots (insets) of poly- (left) and single-crystalline (right) patches.

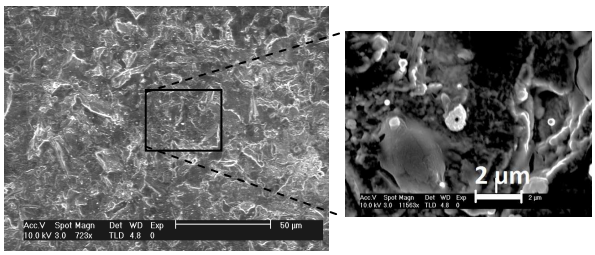

Figure 3: SEM images of single-crystalline Au-NW patch after current processing (destroyed at 19 μA at 67 V/μm).

In conclusion, the FE measurements on single-crystalline Au-NWs exhibit slightly improved performance values. Fabrication of nanocones with much enlarged contact area has been started to get a higher mechanical stability and current carrying capability of our structured cathodes.

References

[1] A. Navitski et al., Eur. Phys. J. Appl. Phys. 48, 30502 (2009).
[2] A. Navitski, et al., Techn. Digest IVNC09, Hamamatsu, IEEE Cat. No. CFP09VAC-PRT, p. 137 (2009).
[3] A. Navitski et al., Techn. Digest IVNC2010, Palo Alto, IEEE Cat. No. CFP10VAC-PRT, p. 163 (2010).
[4] S. Karim, et al. Nanotechnology, 17, 5954 (2006).

* contact: gmueller@uni-wuppertal.de

Improvements and Operation of PHELIX*

V. Bagnoud[1], C. Brabetz[2], U. Eisenbarth[1], J. Fils[1], S. Götte[1], T. Kühl[1,3], S. Kunzer[1], M. Kreutz[1], T. Merz-Mantwill[1], D. Reemts[1], T. Stöhlker[1,4,5], A. Tauschwitz[1], L. Tymura[1], B. Zielbauer[3]

[1]GSI, Darmstadt, Germany; [2]Goethe-Universität Frankfurt, Germany; [3]Johannes Gutenberg-Universität Mainz, Germany; [4]Helmholtzinstitut Jena, Germany; [5]Ruprecht-Karls-Universität Heidelberg, Germany

General overview

PHELIX[1], a high-energy short-pulse laser, is a user facility opened to the international scientific community, and a unique opportunity for combined ion-laser experiments to support the science programs of the Plasma Physics and Atomic Physics departments of GSI. In 2010, a significant improvement has been the conversion of PHELIX to the 527-nm wavelength to further develop the experimental capabilities at the Z6 target area for experiments done in combination with the UNILAC[2]. In particle acceleration studies, we actively supported the LIGHT project[3] by adding a short pulse compressor to the Z6 target area. This compressor enables experiments with high-intensity short laser pulses at Z6, a major milestone towards coupling laser-accelerated particles into conventional accelerator structures. Other experiments done with PHELIX have focused on X-ray generation and X-ray diagnostics.

Improvements of the laser system

In the past, various measurements have been performed in order to characterize the cool-down behavior of the flashlamp-pumped modules of the preamplifier. Like most laser systems of this type, the wavefront aberrations due to temperature gradients in the active medium while pumping is the main limiting factor for the pulse repetition rate. So far, the waiting time between two preamplifier shots at PHELIX was limited to 2 minutes. In the turn of the year, we demonstrated a significant increase of the repetition rate using a constant shot rate scheme in combination with adaptive optics. Detailed measurements showed that, at a constant shot rate, the thermal aberrations do not pile up over all limits but reach an equilibrium state already after typically 5-6 shots. In case of a repetition rate of one shot every 20 s with the 19-mm amplifier heads, the overall transmitted wavefront error stays below 1.5 λ (peak to valley; the error is given in units of the fundamental wavelength λ = 1053 nm). These aberrations can still be easily compensated for using the adaptive optics system developed earlier. We observed stable operation of the laser over bursts of 50-100 shots with residual wavefront aberrations of less than 0.15 λ at output energies of up to 600 mJ. The increased repetition rate is in particular very interesting for performing systematic measurements in the field of X-ray laser development. Future improvements will include an additional compensation of upcoming birefringence effects which currently lead to some reduction of the output energy.

Recently, PHELIX has been configured to amplify simultaneously two independent laser beams. For this, two spatially separated laser beams have been created at an early stage of the laser amplifier, using a well-controlled technique of beam shaping by lithographically-etched masks. The beams are then amplified in parallel using the PHELIX beam line. A single 500-fs long pulse has been used to seed both beams, for a total energy in excess of 100 J. In addition the setup allows for a variable delay of up to 2.5 ns between the pulses and separate focusing within a few millimeters. The focusing is realized with two independent focusing off-axis parabolas that add full flexibility to the experimental setup. An experiment using this new capability has been recently conducted with two pulses whose intensity was higher than 100 TW[4]. This installation opens new possibilities for PHELIX and represents a capability very much unique in Germany that increases the attractiveness of PHELIX for external users.

The conversion to 527-nm wavelength established by a setup in the transmission beamline to Z6 eliminates the danger of back-reflection that can be damageable to the system and also improves the quality of the experimental conditions as predicted by earlier simulations. For details please refer to another article[5] within this report.

During the year, the last radiation safety measures were taken to comply with the operating licence of PHELIX. The PHELIX-specific radiation protection training is additionally now available online, allowing especially external users to efficiently prepare their visit to PHELIX from their home institutions. An overview about radiation protection at PHELIX is given in this report[6].

The effort to offer an additional 100-TW short-pulse experimental capability at the Z6 area was nearly completed within the last 12 months. Together with the Helmholtz Institute Jena, the PHELIX team has constructed a short-pulse compressor and its set of diagnostics in the Z6 area. The commissioning of the beamline is happening at the very beginning of 2011.

Last but not least, the project dealing with the improvement of the temporal contrast of the laser pulse was continued. This project aims at reducing the nanosecond intensity background by replacing the first amplifier of PHELIX by an ultrafast optical parametric amplifier (uOPA). In the last months, the development of a pump laser by the Helmholtz Institute Jena made significant progress. The first part of the laser based on a fiber laser amplifier has been demonstrated and fully tested. Additionally, the main components for the second stage of this pump laser have been delivered and tested. At GSI, the model of the OPA, developed using the Miro software, has been bench marked to frequency doubling experi-

ments done on the millijoule level with the broadband short pulse of PHELIX. There, a conversion efficiency in excess of 60% has been predicted and experimentally measured. Based on this, our model predicts an even higher conversion efficiency for the laser pulses of the pump laser, because its expected parameters are more favourable for this process. This helps build confidence in the performance of the system. The pump laser will be installed at GSI, integrated to the PHELIX Control System and frequency doubled in the spring of 2011. Experiments on parametric amplification should happen a few months thereafter.

Operation of the laser facility

Figure 1 shows the activity of PHELIX in 2010. The time devoted to operation is the same as it was last year with 41% of the working days. If one looks in detail, the time dedicated to experiments, either internal or external, represents 61% of the working days. The time necessary for experiment preparation has been reduced thanks to a better planning and the experience gathered in the previous years. The shut down time has increased slightly because of a long-due service of the clean room facility and implementation of necessary safety measures related to the operation of the laser bay target area. The maintenance of the facility, which includes also the time dedicated to developments and improvements, has risen because of the support to the 2ω and 100 TW projects. This impact on the facility schedule has nevertheless been very moderate and did not reduce the time available for external users.

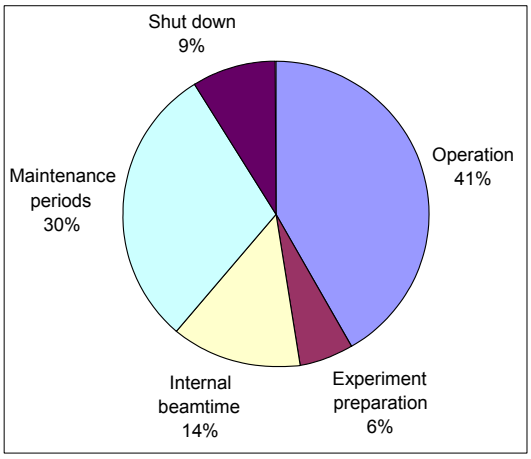

Figure 1: PHELIX usage in 2010

PHELIX delivered laser pulses for nine experiments, distributed among ten beam times and 106 days. During the year, PHELIX was available 9 hours per day for laser stand-alone experiments and 14 hours for combined laser-ion experiments.

Contribution to the scientific program and outreach

In 2010, nine peer-reviewed articles have been published using data collected at PHELIX by internal and external user groups[7,8,9,10,11,12,13,14,15]. These publications report on experiments that have been conducted at PHELIX in the last 18 months.

In May, the PHELIX group held the first Laserlab-NAHEL (Network Activity on High Energy Lasers) meeting at Darmstadt to exchange views on operation of mid-scale laser facilities. The meeting included participants from the four laboratories participating in NAHEL over a two-day event, where ideas and experience on topics including facility operation, laser diagnostics, data acquisition, and large-size optics were shared. In addition, PHELIX has given two beam times to experiments supported by Laserlab in the fields of X-ray laser generation and electron transport.

Outlook for 2011

The plasma physics advisory committee met in November 2010 to review new proposals for the PHELIX facility, which amounted to nearly three times the annual beamtime availability, illustrating the vitality of the field and the high demand for beam time. The approved experiments and those in the queue will be scheduled within the next 18 months. In addition to the operation, the existing projects LIGHT, 2ω and temporal contrast improvement (uOPA) will continue together with new activities in the direction of better data acquisition and target area developments.

[1] V. Bagnoud et al., Appl. Phys. B **100** (1) 137-150 (2010)
[2] A. Frank et al., this report
[3] https://www.gsi.de/documents/DOC-2010-Nov-36-1.pdf
[4] D. C. Hochhaus et al., this report
[5] E. Onkels et al., this report
[6] P. Fensterseifer et al., this report
[7] A. Frank et al., Phys. Rev. E **81** 026401 (2010)
[8] A. Blazevic et al., The Open Plasma Physics Journal **3** 116-121 (2010)
[9] T. Kuehl et al., Hyperfine Interact **196** 233-241 (2010)
[10] D. Zimmer et al., Phys. Rev. A **82** 013803 (2010)
[11] K. Harres et al., Phys. Plasmas **17** 023107 (2010)
[12] G. A. Vergunova et al., Journal of Russian Laser Research **31** (5) 509-518 (2010)
[13] P. Neumayer et al., Physics of Plasma **17** 103103 (2010)
[14] J. Seres et al., Nature Physics **6** 455-461 (2010)
[15] D. C. Hochhaus et al., Appl. Phys. B **100** (4) 711-716 (2010)

Spatial and temporal resolved measurements of the free electron density in laser-generated plasmas

M. Börner[1], *A. Blaževi*ć[2], *J. Fils*[2], *A. Frank*[1], *T. Hessling*[2], *D. Schumacher*[1], *and M. Roth*[1]
[1]Technische Universität Darmstadt, Germany; [2]GSI, Darmstadt, Germany

The interaction of heavy ions with plasma is investigated by the laser-plasma physics group of the TU Darmstadt at the GSI Helmholtzzentrum für Schwerionenforschung. The unique combination of two high energy laser systems and the UNILAC at the experimental area Z6 allows the investigation of the charge transfer and energy loss [1]. In these experiments the density of free electrons is an important plasma parameter. As the experimental conditions like laser energy and intensity change considerably from experiment to experiment a multi-frame diagnostics is necessary. Additionally, the spatial plasma expansion of several millimeters changes on a nanosecond timescale. These conditions require a sophisticated plasma diagnostics with corresponding spatial and temporal resolution.

For this task a multi-frame Nomarski-type interferometer was developed, first experiments were successfully conducted and the results were compared to those of RALEF-2D simulations [3]. The interferometer provides the possibility to take 4 pictures within 6 ns, each separated by 2 ns. The time resolution of each image is given by the interferometry pulse length of 0.5 ns.

A 0.5 μm carbon foil target was irradiated on both sides by the two high energy laser systems PHELIX and nhelix, with intensities of 0.46 TW/cm^2, a focus diameter of 1 mm and a temporal profile of 7.5 ns FWHM.

The experimental setup of the interferometer is shown in Fig. 1. First, the probe laser frequency is tripled to 355 nm in order to raise the critical electron density to $n_c = 8.8{\cdot}10^{21}$ cm^{-3} representing the highest electron density accessible. Then, an optical ring generates a pulse train from the single start pulse. Behind the ring these pulses have the same spatial origin, but a fixed difference in the propagation direction caused by a defined angle of rotation of the thin film polarizer (TFP). The round trip time determines the temporal separation of 2 ns. Afterwards, the pulses are transported into the plane of observation by a Kepler telescope. Because of the same spatial origin the pulses interact with the same plasma volume and therefore provide the same plane of observation. Using a lens and micro mirrors, the pulses are spatially separated into different Nomarski interferometers. In this way four interferometer images of a single laser-plasma interaction can be taken.

By using the Abel transformation, the free electron densities are determined from the fringe shift induced by the variation of the refractive index of the plasma. The resulting spatial resolution is about 50 μm, the resolution for the electron density is about $0.5 \cdot 10^{19}$ cm^{-3}. The field of view and the magnification can be adapted by the lens system in front of the cameras.

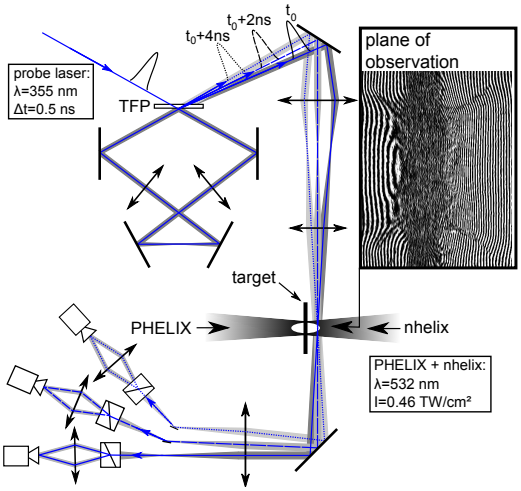

Figure 1: Conceptual set-up of the interferometer.

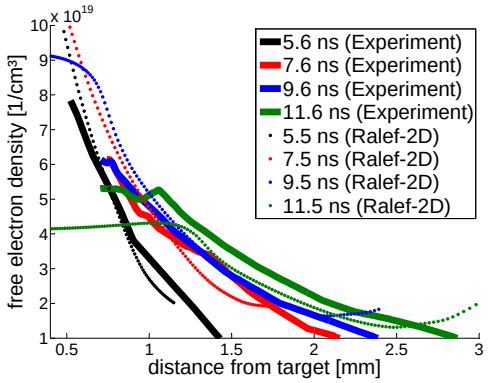

Figure 2: Measured free electron density evolution in comparison to results of RALEF-2D simulations for one laser-plasma interaction

The experimental results were compared to those of simulations and show excellent agreement (see Fig. 2). In the future this multi-frame interferometer will be used as a diagnostics for directly and indirectly heated foils and hohlraum experiments (see [1], [2]).

References

[1] A. Frank et al., this annual report

[2] D. Schumacher et al., this annual report

[3] An. Tauschwitz et al., GSI annual report 2009, p. 409

Space-charge effects on laser-accelerated proton beams captured by a solenoidal magnetic field

F. Nürnberg[1], D.P. Grote[2,3], K. Harres[1], T. Burris[4], S. Busold[1], O. Deppert[1], and M. Roth[1]

[1]Technische Universität, Institut für Kernphysik, 64289 Darmstadt, Germany; [2]Lawrence Berkeley National Laboratory, Berkeley, CA 94720, USA; [3]Lawrence Livermore National Laboratory, Livermore, CA 94550, USA; [4]Forschungszentrum Dresden-Rossendorf, 01328 Dresden, Germany

In context of the LIGHT project (Laser-Ion Generation, Handling and Transport) [1], studies on the capability of a solenoidal magnetic field to collimate and transport laser-accelerated proton beams were carried out. Results of preliminary particle-in-cell simulations [2] and experiments at the PHELIX laser facility [1, 3] demand a detailed analysis of the space-charge influence. Therefore, the WarpRZ simulation code [4] is used.

The drawbacks of laser-accelerated proton beams such as large envelope divergence and broad exponential energy distribution are experimentally corrected by using a solenoidal magnetic field of 7.5 T to collimate and focus protons. The simulation setup exactly fits the experiment. An increase of almost 6% (10^{11} particles) in proton transmission through the solenoid could be observed in comparison to simulations neglecting the co-moving electrons and the Poisson self-field solver (fig. 1).

Due to the solenoidal magnetic field, the electrons are forced down on axis (fig. 2a) and attract protons (fig. 2b). As soon as the electron density decreases, the attracted proton distribution starts to expand, meanwhile the main distribution starts to focus (fig. 2c).

A beam of 8.4×10^9 focussed protons of (6.7±0.1) MeV energy is measured with Δ E/E = 3%. It is focussed onto a 2 mm spot and has a pulse duration of 170 ps. On the other hand, a collimated beam in the energy range (13.5±0.5) MeV containing 3×10^9 protons with a final pulse duration of 300 ps could be transported over a distance of 50 cm.

References

[1] LIGHT project, see GSI report 2010.
[2] F. Nürnberg et al., Journal of Physics: Conference Series 244, 022052 (2010).
[3] K. Harres et al., Phys. Plas. 17, 023107 (2010).
[4] D.P. Grote et al., AIP Conf. Proc. 749, 1 (2005).

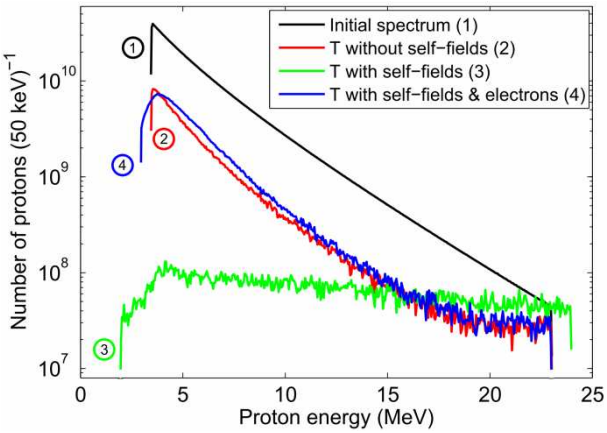

Figure 1: The initial proton spectrum (1) and proton transmissions (T) through the solenoid for three simulation cases: proton beam without self-field solver (2), proton beam with self-field solver (3) and proton beam with self-field solver and co-moving electrons (4). For case (2) and (3) the total transmission decreases to 18.6% and 1.6%, but it increases as soon as the co-moving electrons are included to 24.2% (4).

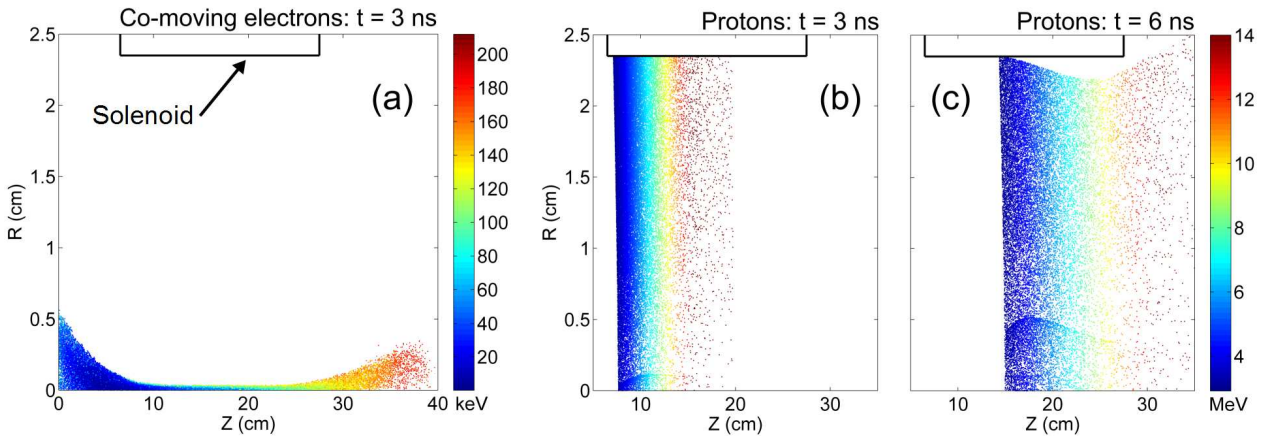

Figure 2: R-Z snapshot of the initial co-moving electron (a) and proton (b,c) expansion.

Annular shaped laser-accelerated proton beams

O. Deppert[1], *K. Harres*[1], *F. Nürnberg*[1], *S. Busold*[1], *V. Bagnoud*[4], *G. Schaumann*[1], *M. Schollmeier*[2], *M. Geissel*[2], *D. Neely*[3], *and M. Roth*[1]

[1]Institut für Kernphysik, TU Darmstadt, Germany; [2]Sandia National Laboratories, USA; [3]Rutherford Appleton Laboratory, UK; [4]GSI Helmholtzzentrum für Schwerionenforschung, Germany

Since their discovery in 1999 [1] the topic of laser-accelerated ions has attracted high attention both in the field of plasma-physics and in the accelerator community.
In a typical laser-accelerated ion scheme a thin metal foil is irradiated by an ultra-intense chirped pulse amplified laser beam which leads to the generation of relativistic electrons. These electrons are accelerated through the cold target material in laser beam direction, escaping at the vacuum boundary and forming a Gaussian-like electron-sheath at the target rear-side. A field-strength on the order of several TV/m leads to an instantaneous field-ionisation of the atoms at the rear surface and an acceleration of these ions perpendicular to the target surface by the Target-Normal-Sheath-Acceleration mechanism (TNSA, [2]).
In the scope of this report we present a technique to alter the transverse proton beam-profile from the ”source” of its creation. With this technique we could already demonstrate the generation of an annular shaped proton beam at the PHELIX laser system with the use of an optimised cone-guided target geometry [5].

Experimental Results

Figure 1 shows the transverse profile of the proton beam measured with radio-chromic films (RCF, [3]) in a stacked configuration shown in the optical density (OD). The laser parameters for this shot were 118 J before compression with a pulse length of about 500 fs (FWHM) at best focus.

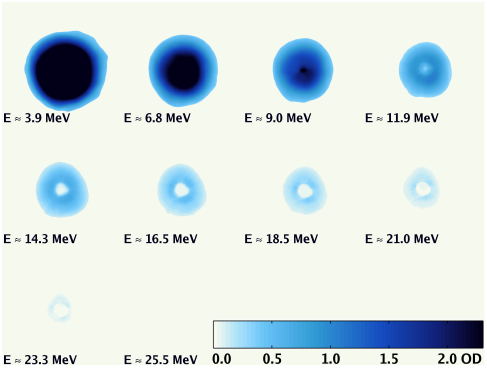

Figure 1: RCF: Transverse proton beam-profile

It can clearly be seen that the proton beam is focused for a proton energy around 9 MeV. For higher energies the beam starts to form a stable ”ring-structure”.

Simulation Results

In order to model the physics behind this beam manipulation several two-dimensional Particle-In-Cell simulations were carried out with the use of the Plasma-Simulation-Code (PSC, [4]).
Figure 2 shows the normalised logarithmic ion density of a miniaturised model of the cone-guided target used in the PHELIX experiments. It can be seen that the propagating proton beam is narrowed due to the interaction with a TNSA sheath field at the inner wall of the cone. This results in a guided and collimated transport of the proton beam through the outlet port.

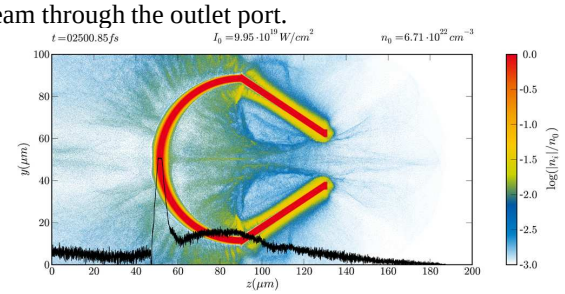

Figure 2: PIC: Normalised logarithmic ion density

Figure 3 shows that the divergence angle of the high energetic protons is more collimated and concentrated around the laser beam-axis compared to simulation results for a flat-foil target [5].

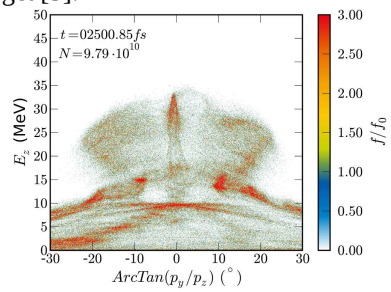

Figure 3: PIC: Proton energy vs. divergence angle

At the moment the PIC simulation is only able to explain the experimental results for the low energetic protons up to 9 MeV. Due to the difference in the geometric scale of almost a factor of eight, the generation of the annular feature for the high energetic protons can not be interpreted by the simulation. The formation of the ”ring-structure” basically depends on the temporal delay between the hot electrons to be laterally pushed through the target towards the cone tip and the propagation time of the protons to reach the outlet port. This thesis needs further investigations and will be verified by continuative PIC simulations.
In acknowledgement of my gratitude O. Deppert thanks HGS-HIRe and HIC for Fair for funding my scholarship. This project is supported by BMBF 06 DA 9044I.

References

[1] S.P. Hatchett *et al.*, Phys. Plasmas **7**, 2076, 2000
[2] S.C. Wilks *et al.*, Phys. Plasmas **8**, 542, 2001
[3] F. Nürnberg *et al.*, Rev. Sci. Instr. **3**, 13, 2009
[4] H. Ruhl *et al.*, *An introduction into the PSC*
[5] O. Deppert, Master-Thesis, TU Darmstadt, 2010

Investigation of co-moving electrons in laser ion acceleration experiments with a magnetic electron spectrometer

S. Busold[1], F. Nürnberg[1], K. Harres[1], and M. Roth[1]

[1]Institut für Kernphysik, Technische Universität Darmstadt, Germany

Collimation and transport of laser-accelerated protons via a pulsed solenoid is intensely investigated at the PHELIX laser at GSI [1] and will be pushed further by the upcoming LIGHT collaboration [2]. The solenoid acts as an energy-selective ion optic to collimate or focus a small energy interval of the laser-accelerated proton beam, which shows an exponential energy spectrum with a sharp energy cut-off. However, plasma models describe the proton expansion as a quasi-neutral plasma cloud accompanied by co-moving electrons. Simulations [3] have shown that these electrons are tightly focused on the solenoid axis and affect the protons via Coulomb force.

As the protons are in the energy range of 1 to 60 MeV, the relevant energy interval of the co-moving electrons is 1 to 30 keV. In this low energy region of the electron spectrum no experimental data are available. Hence, an electron spectrometer has been designed, calibrated and applied in an experimental campaign.

The electron spectrometer

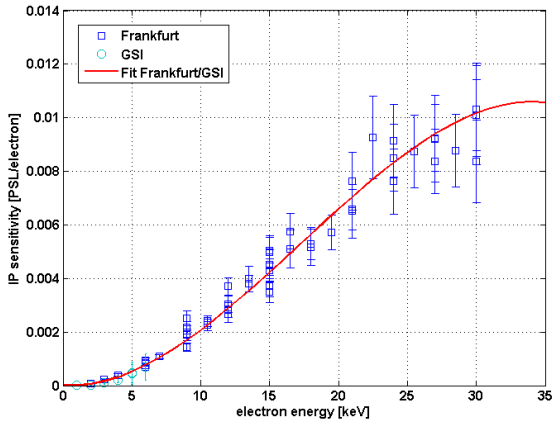

Figure 1: Sensitivity of the IP (type: AGFA MD4.0 without protection layer) to electrons in the relevant energy interval. The measurements on two different systems on the lower energies are in very good agreement.

The spectrometer contains a small electro-magnet providing a magnetic field of a few mT. A part of the quasi-neutral beam enters the spectrometer through a pinhole. While the protons are (almost) not affected by the field and leave the spectrometer through another pinhole, the electrons are deflected and can be measured on the detector. As detector an image plate (IP) is used. IPs are sensitive to all kind of ionizing radiation and give a readout in units of PSL [4].

First, the IP had to be absolutely calibrated to electrons. This calibration was done with two electron gun systems: one system with electron energies up to 6 keV at GSI and another up to 30 keV at the Johann Wolfgang Goethe Universität Frankfurt. Results are shown in Fig. 1.

First Experiments

First experimental data on the electron spectrum were recorded during a campaign at the Callisto laser system at the Lawrence Livermore National Laboratory, California, USA. The electron spectrum did not show the exponential behaviour as expected (like the proton spectrum), but a peaked feature at an energy too high to be co-moving. Fig. 2 shows measured spectra of protons and electrons of one experiment.

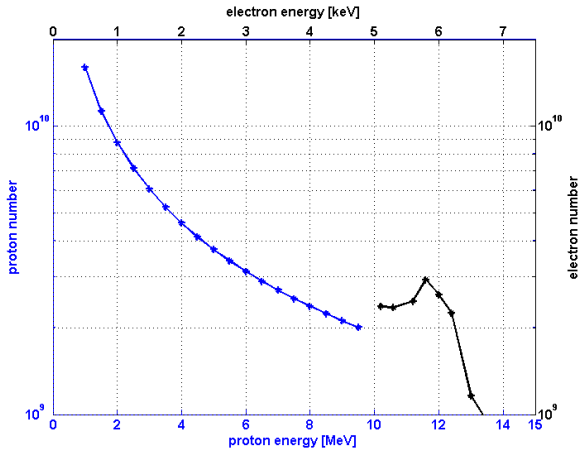

Figure 2: Comparison of proton (blue) and electron (black) spectrum with respect to particle velocities.

In absolute numbers, there are not enough electrons to fully neutralize the proton beam. Furthermore, the velocities (energies) of the electrons are too high to be co-moving with the protons.

The electron spectrometer was placed 260 mm behind the source. At this distance, no neutralized expansion could be observed anymore. A beamtime at PHELIX dedicated to the co-moving electrons will follow in 2011.

References

[1] K. Harres et al., Phys. Plas. 17 (2010) 023107
[2] LIGHT project, see GSI report 2010
[3] F. Nürnberg et al., Journal of Physics: Conference Series 244, 022052 (2010)
[4] I. J. Paterson et al., Meas. Sci. Tech. 19 (2008) 095301

First hohlraum shots with the frequency doubled PHELIX laser beam

D. Schumacher[1], *A. Blazevic*[2], *A. Frank*[1], *T. Hessling*[2], *G. Schaumann*[1], *and M. Roth*[1]
[1]TU Darmstadt, Germany; [2]GSI, Darmstadt, Germany

Introduction

The energy loss of heavy ions in plasma is one of the fields of research of our group. So far, only directly laser heated plasmas have been investigated [1]. To probe more homogeneus, slower expanding and denser plasmas an indirect heating scheme has been developed, where the plasma is heated by soft x-ray radiation. In this scheme the x-ray radiation is generated by a laser driven hohlraum. This hohlraum radiation is used to heat a secondary hohlraum, containing a carbon foil. The carbon foil is then heated to plasma temperature and can be investigated by ions.

Target design

For this purpose a target has been designed (fig. 1) at the target laboratory at the TU Darmstadt. The target consists of two hohlraums, connected by a hole. The upper one is the converter cavity. The laser is coupled in through a 300 micrometer hole in the front of the ball-shaped hohlraum. The primary x-ray radiation from the hot laser spot in the cavity thermalizes and passes through the hole between the hohlraums. Thin carbon foils are attached to the lower, cylinder-shaped target hohlraum. In the base areas are 500 micrometer sized holes, on one hand to let the x-rays pass and heat the foil, on the other hand to let the heavy ions pass, so they only penetrate the carbon and are not influenced by the gold, the target wall consists of.

A third diagnostic hole with a diameter of 150 micrometer in the shell of the cylinder is for the characterisation of the black body like radiation. This allows for a radiation temperature measurement in the hohlraum.

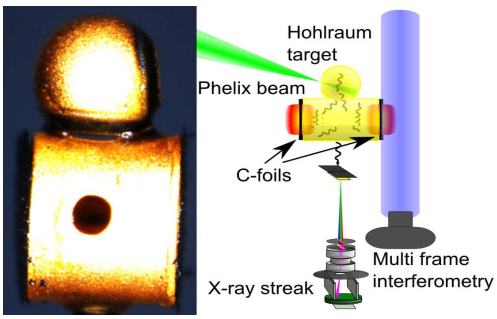

Figure 1: Setup with target and diagnostics

Experiment setup

In first experiments during the commissioning campaign at Z6, using the 527 nm frequency doubled laser option of the PHELIX facility, the temperature of the primary hohlraum was determined (fig. 1). The second harmonic of the laser wavelength was used for the better x-ray conversion of shorter laser wavelength and to avoid strong back reflection of the first harmonic due to stimulated brillouin scattering. As diagnostics a x-ray streak camera and an interferometry were used.

The x-ray streak camera recorded the radiation passing through the diagnostic hole. A free standing x-ray grating with 1000 lines per mm was used to split up the spectrum. This spectrum was then taken over a 100 ns time scale with temporal resolution of about 1 ns. With the streak setup used, the spectrum between 2 and 25 nm with a wave length resolution of 1.5 nm could be recorded.

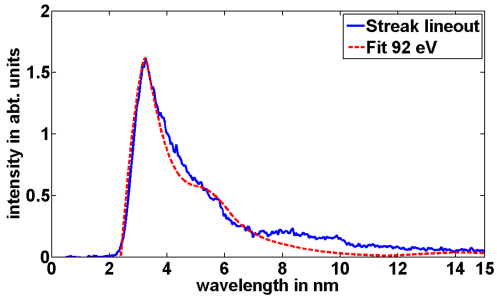

Figure 2: Planckian curve convolved with the transmittance of the streak camera fitted to a lineout of the measurement

Results

For interpretation a lineout from the streak images at the maximum hohlraum temperature was taken (fig. 2) and fitted with a Planckian curve.

This streak image was recorded with an laser energy of 110 J in 1.5 ns. The maximum temperature of the converter hohlraum was determined to be 92 ± 5 eV.

References

[1] A. Frank, “Energy loss of argon in a laser-generated carbon plasma”, Phys. Rev. E 81, February 2010

Experiments on conversion of the PHELIX laser light into soft X-rays using a hohlraum scheme

O.N. Rosmej[1], V. Bagnoud[1], U. Eisenbarth[1], V. Vatulin[2], N. Zhidkov[2], N. Suslov[2], D. Schäfer[3], Th. Nisius[3], T. Rienecker[4], J. Wiechula[4], Y. Zhao[5]

[1]GSI, Darmstadt, Germany; [2]VNIIEF-Sarov, Russia; [3]University of Applied Science, Remagen, Germany; [4]Goethe University Frankfurt, Germany; [5]IMP Lanzhou, China

In experiments on the conversion of the PHELIX laser light into soft X-rays, the *Petawatt High-Energy Laser system for Ion beam eXperiments – "Phelix"* (Nd:glass, λ=1054 nm) was used at the basic frequency. The chirped laser pulse of 1.4 ns duration and energies up to 270 J was focused onto the target by a lens with 4 m focal length. The diameter of the focal spot on the wall of the primer hohlraum measured by means of a pin-hole camera in X-rays with hν >1.5 keV was of ~200-300 μm, resulting in the laser intensities up to $2\cdot10^{14}$ W/cm^2. The laser irradiates the wall of the gold cylinder at the 45° through the open entrance hole (see fig.1). Diagnostic tools were placed around the target inside the spherical chamber with diameter of 110 cm evacuated up to P ≈10^{-4} mbar [1]

The plasma diagnostics experimental setup includes different types of techniques providing spectral, spatial and temporal resolution of X-ray radiation [2]. Two pin-hole cameras were used to image the hohlraum plasma in X-rays. By means of the pin-hole placed on the front target side and covered with a 5 μm thick Ti-filter one could view the radiation occurring in the laser focal spot; the pin-hole placed at the rear target side was equipped with a glance incidence glass mirror and thin 0.9μm CH-filter, allowing the hohlraum plasma imaging at the photon energies of 0.2-0.28 keV. Absolutely calibrated vacuum X-ray diodes (XRD) with carbon cathodes covered by 0.9 μm thick CH-filters were used for time resolved measurements of the X-ray flux transmitted through the 0.1 μm Au-foil in the range of 0.1-1 keV. Two symmetrically placed transmission grating spectrometers (TGS) measured the spectra distribution of the hohlraum radiation from the rear target side.

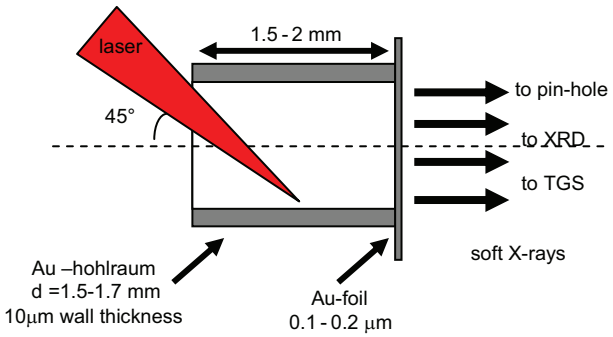

Fig.1. Geometry of the laser-target interaction

In the experiments the spatial and spectral distribution of the hohlraum radiation after transmission through the thin gold foil was measured from the target rear side. Figure 2 shows experimental results at laser energies 240 - 270J: (a) spectral distribution of the hohlraum radiation recorded at photon energies 60-1200 eV onto the calibrated UF4-film; (b) homogeneous pin-hole image of the hohlraum in the selected photon energy range of 200-280 eV; (c) duration of the converter radiation measured by means of XRD of 5-7 ns; (d) fitting of the measured by TGS spectral distribution of hohlraum radiation intensity by a Planckian function with equivalent radiative temperature of 38 eV.

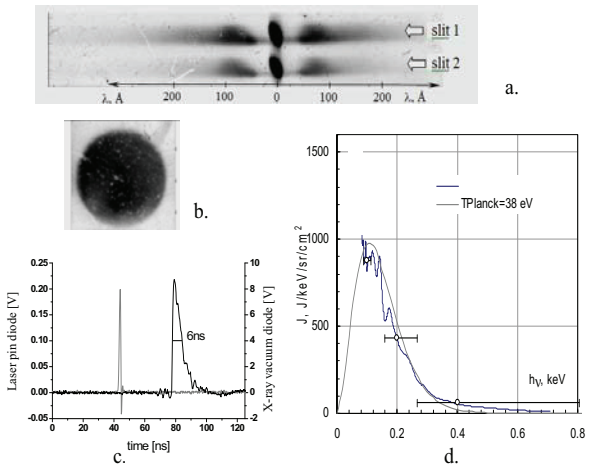

Fig. 2. Experimental results (for explanations see the text)

In conclusion, a large scale (~1.7mm) uniform X-ray source with the spectrum well approximated by the Planckian radiation distribution was obtained. Measured soft X-ray pulse duration in the photon range of 0.1-1 keV was of 5-7 ns and equivalent radiation temperature approaches 30-40 eV. This corresponds to 30-40 J in soft X-rays (60-1200eV) and up to 17 % of the laser energy conversion at the basic laser frequency.

References

[1] O.N. Rosmej *et al.*, *GSI-report 2009, p. 318*

[2] O.N. Rosmej, V. Bagnout, U. Eisenbath *et al.*, *NIMA* (2011) accepted

The work was supported by ISTC#2264-project

Absorption properties of CHO-foam layers volumetrically heated by soft X-rays

N. Orlov[1], O.N. Rosmej[2], D. Schäfer[3], Th. Nisius[3], Th. Wilhein[3]
[1] JIHT, Moscow, Russia; [2]GSI, Darmstadt, Germany; [3]University of Applied Science, Remagen, Germany

Experimental studies of heavy ion beam interaction with ionized matter [1, 2] require the creating of a large dense plasma target, which can keep temperature and density during further interaction with heavy ion beams. Indirect heating of CHO foams of 2-20 mg/cm^3 density by laser pulse can be used for theses purposes. In experiments the Nd:glass PHELIX laser pulse at the basic frequency, duration of 1.4 ns and energy $E_L \approx$ 200-270 J was focused onto the hohlraum wall into the focal spot of 200-300 µm resulting in laser intensities up to $2 \cdot 10^{14}$ W/cm^2 [4, 5]. During the interaction of the laser pulse with a gold converter wall equilibrium X-ray radiation is generated. Soft X-ray radiation with a Planckian frequency distribution with the temperature of 30-40 eV penetrates the foam and heats it volumetrically up to temperature of 15-30 eV at free electron density up to 10^{21} cm^{-3}. An important part of this study is connected with temperature diagnostics of the plasma target using the deformation of the absorption K-edge when solid material is heated to a plasma state [4, 5]. The theoretical model, known as the Ion Model (IM) of plasma [3], can be used to ground the temperature diagnostics method, where experimental measurements of the radiative opacity characteristics in the vicinity of carbon K-edge (4.2 nm) are performed [4, 5]. The model (IM) is based on the solution of the general set of self-consistent field equations that describe the state of the whole ensemble of plasma atoms and ions. The set contains: (a) the Hartree-Fock equations for all atoms and ions with different electronic configurations; (b) the unbound electron densities in phase space for all atoms and ions with different electron configurations; (c) the Gibbs distribution; (d) the electro-neutrality condition. In plasma compared to cold matter, absorption occurs not only into the ground state of the atom, but into the ground and excited states of multi-charged ions. As a result, K-edge positions of ions are considerably changed on the energy scale. Fig. 1 (a) presents the spectral coefficients for X-ray absorption K(E) (cm^2 /g) calculated for (H12 C8 O6) plasma at the density 0.002 (g/cc) and the temperature T = 5 eV (blue line) and T = 20 eV (violet line). The K-edge positions corresponding to carbon ions are denoted here with corresponding notations, which present the electronic configurations 1s(2)2s(2)2p(1) and 1s(2)2s(1)2p(1) (T = 5 eV, red line), and the K-edge position of carbon ion 1s(2) (T = 20 eV, violet line). Fig. 1 (b) shows the spectrum of the Plankian radiation J(E) (J/keV/sr/cm^2) transmitted through the 800µm thick CHO plasma target with temperature T =5 eV (red line), and T = 20 eV (violet line). The green line gives the spectrum of external radiation. One can see that the spectrum of the transmitted radiation J(E) (Fig. 1 (b)) has a specific steps, which coincide with the K-edge positions of carbon ions (Fig. 1 (a)) on the energy scale.

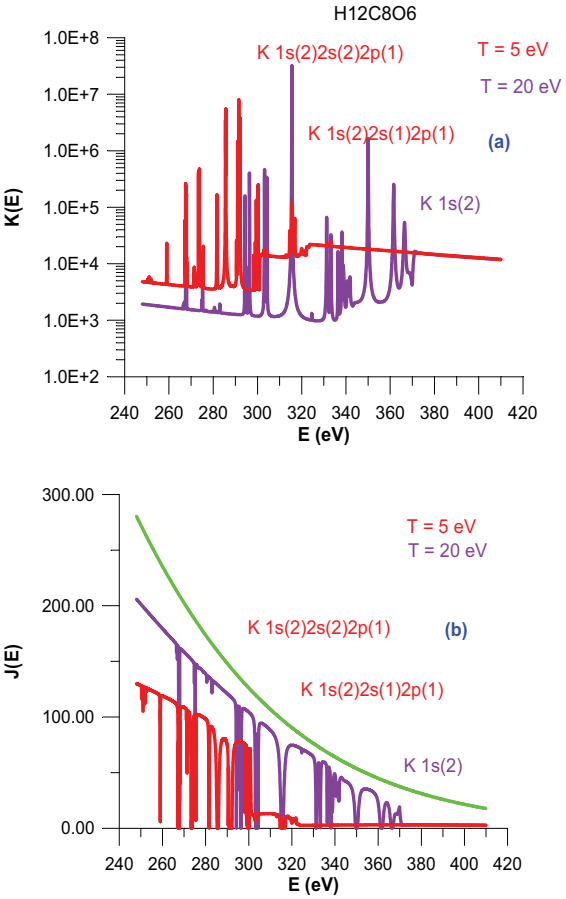

Fig. 1. (a) Spectral coefficients for X-ray absorption K(E) (cm^2 /g); (b) transmitted through the foam plasma hohlraum radiation with radiation temperature of 40 eV

The specific step positions on the energy scale are different for different plasma temperatures. This fact can be used to estimate the temperature of CHO plasma target.

References:

[1] D.H.H. Hoffmann *et al.*, (1990). *Phys. Rev. A,* **42**, 2313-2321
[2] D.H.H. Hoffmann *et al.*, (2005). *Laser Part. Beams* **23**, 47-53.
[3] N.Yu. Orlov, *Laser Part. Beams* **15** (1997), 627–634.
[4] N. Orlov, A. Denisov, O.N. Rosmej *et al.*, accepted to *LPB (2011)*
[5] O.N. Rosmej, V. Bagnout, .U. Eisenbarth *et al.*, accepted to *NIMA (2011)*

Experiments on heating of low density CHO-foams by soft X-rays

O.N. Rosmej[1], V. Bagnoud[1], U. Eisenbarth[1], N. Zhidkov[2], N. Suslov[2], V. Vatulin[2],D. Schäfer[3], Th. Nisius[3], T. Rienecker[4], J. Wiechula[4], Y. Zhao[5], N. Borisenko

[1]GSI, Darmstadt, Germany; [2]VNIIEF-Sarov, Russia; [3]University of Applied Science, Remagen, Germany; [4]Goethe University Frankfurt, Germany; [5]IMP Lanzhou, China; [6] Lebedev Physical Institute, Moscow, Russia

Experiments, which use a combination of the PHELIX laser kJ-option and the heavy ion beam of 4-10 MeV/u energy delivered by the UNILAC- accelerator, are aimed at investigation of the heavy ion energy loss in ionized matter. In these experiments a large scale (~1mm) long living (~5ns) high density plasma target with homogeneously distributed plasma density, temperature and ionization degree is required. The time is defined by the duration of the heavy ion bunch of 3 ns, the spatial size of the plasma target by the diameter of the heavy ion beam of ~ 0.5 mm. Highly homogeneous and slowly expanding plasma can be obtained when a low-density foam layer is volumetrically heated by soft X-rays. The indirectly heated laser target design for combined heavy ion beam - laser experiments was proposed by Vatulin and Vasina [1]. In this scheme the laser interacts with the gold wall of the cylindrical converter (a primer hohlraum) where the laser energy is effectively converted into the soft X-rays with spectral distribution close to the Planckian one. Hohlraum generated X-rays heat volumetrically a low-density foam which serves as a plasma target for probing with heavy ion beams.

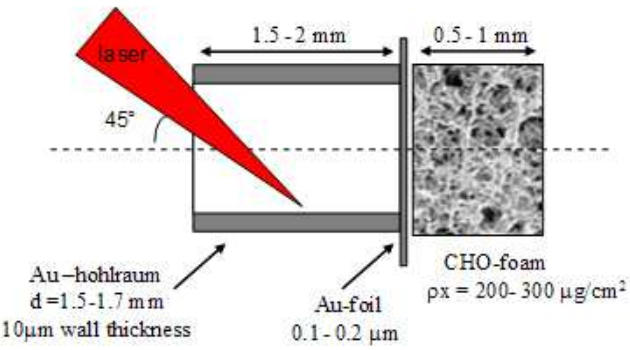

Fig.1 Interaction of the laser with a combined target which consist of a gold cylindrical hohlraum (converter) and a polymer foam layer of 2 mg/cm^3 density and 0.8 -1 mm thickness divided from the hohlraum by a 100 nm thin Au-foil

In this work we report experimental results on heating of low density CHO-foams layers by means of the Planckian radiation generated in gold hohlraums. Plexiglas (PMMA, $C_8H_8O_3$) and triacetate cellulose (TAC, $C_{12}H_{16}O_8$) of different volume and areal densities were used as foam materials. The goals of the experimental program were measurements of the absorption properties of foam layers and plasma parameters of the foam targets heated by the Plankian radiation.

Characterization of the hohlraum spectrum (fig.2) transmitted through the foam placed at the rear-side of the combined target (fig. 1) was made using transmitting grating spectrometers [2].

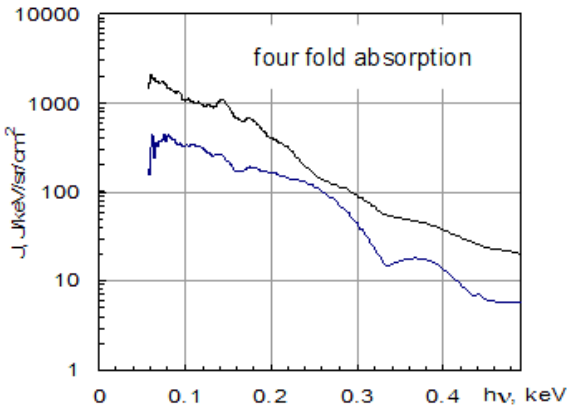

Fig.2 Spectral distribution of the hohlraum radiation (black) and the hohlraum radiation transmitted through CHO-foam-plasma (blue). Measurements show a 4-fold absorption of soft X-rays (60-1200eV) in the 0.8mm thick foam layer.

Due to effective absorption of soft x-rays, foam layer was heated to a plasma state. The spectra of the hohlraum radiation (converter only) and those transmitted through the 2 mg/cm^3 dense and 800 µm thick TAC-plasma recorded by means of TGS are shown in fig. 2. In these experiments the laser energy was of 120-130 J and estimations for the reached equivalent hohlraum radiative temperature give 30 eV. Fig 2c demonstrates the comparison between spectral distribution of the hohlraum radiation intensity versus a photon energy after the calibration procedure between the converter spectrum (black curve) and the spectrum attenuated in the TAC-foam layer (blue curve). We have measured a four-fold absorption of the hohlraum radiation in the foam layer, which for given experimental conditions corresponds to 10 J of X-ray energy. Expected electron temperature of heated plasma is of 15 eV at the initial foam density of 3.10^{20} ions/cm^3.

References

[1] E. Vasina, V. Vatulin. GSI-Report 2000 -2, p.52.

[2] O.N. Rosmej, V. Bagnout *et al.*, *NIMA* (2011) accepted

The work was supported by ISTC#2264-project

Pump-Probe Experiments at High Energy Densities Performed at PHELIX

D. C. Hochhaus[1,2,3], B. Aurand[1,2,3,4], B. Ecker[2,3,4], B. Zielbauer[2], D. Zimmer[2], T. Kuehl[2,4] and P. Neumayer[1,2,3]

[1]ExtreMe Matter Institute EMMI, GSI, Darmstadt, Germany; [2]GSI, Darmstadt, Germany; [3]Frankfurt Institute of Advanced Studies, Frankfurt, Germany; [4]University of Mainz, Mainz, Germany

Introduction

Matter at extremes of density and temperature occurs widely in astrophysical objects such as giant gas planets or highly evolved stars. Accurate modelling of matter at high energy density (HED) is of great importance in understanding the structure and evolution of these objects [1]. Creation of electromagnetic HED plasmas in the laboratory requires very powerful drivers. Intense heavy ion pulses from the GSI and FAIR facility allow generation of matter in the regime of warm dense matter [2]. Bright x-ray sources produced by high-energy and intense laser pulses are ideally suited to penetrate and diagnose such dense plasmas. The unique combination of the GSI accelerator with the short-pulse high-energy laser PHELIX [3] enables advanced pump-probe schemes for characterizing the HED samples.

Recent developments

Within the EMMI fellow group for plasma physics we develop and optimize high-brightness laser driven K_α sources for probing of high-energy density plasmas at GSI [4]. To demonstrate the potential of K_α radiography for measuring the hydrodynamic evolution of high-energy density plasmas we have performed the first pump-probe experiment using the PHELIX laser. In close contact with the PHELIX laser team, a two-beam capability has been implemented in the laser system [5]. A specially shaped serrated aperture splits the laser beam into two identical, squared beams that propagate through the amplification chain with a relative delay adjustable between -0.5 ns and 3 ns. After being compressed in the petawatt compressor, the two beams are individually focussed by off-axis parabolic mirrors. This allows independent focusing and timing of the two laser pulses in the target chamber. Each beam exceeds a peak power of 100 TW. This scheme will allow a wide range of laser-pump/laser-probe experiments.

In our experiment one of the two PHELIX beams was focused to relativistic intensities onto the tip of a thin titanium wire. During the intense-laser plasma interaction at the target surface copious amounts of relativistic electrons are produced, which subsequently propagate along the wire and isochorically heat it on a ps-timescale. We monitor the hot electron production efficiency, energy distribution and propagation along the wire using a suite of diagnostics. These diagnostics comprise an absolutely calibrated single-hit camera, multi-channel hard x-ray detectors, and a newly developed spatially resolving spectrometer resolving the characteristic radiation emitted along the wire.

The second laser beam was focused on a thin copper foil to generate a high brightness Cu K_α source, used for x-ray backlighting the hot dense wire. The source size of K_α radiation has shown to be in the order of the thickness of the target foil [6], which allows taking high-resolution point-projection radiographic images employing thin foils as backlighter target (see Fig. 1). Applying variable delays between the two pump beams, we were able to radiograph the exploding wire.

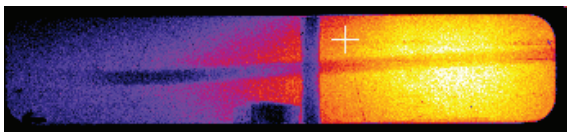

(a)

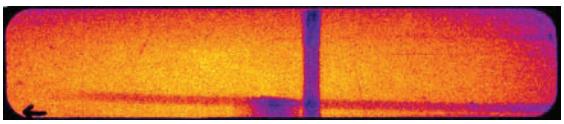

(b)

Figure 1: X-ray radiograph of a 80 µm (a) and 50 µm (b) thick titanium wire

Conclusions

We successfully implemented a pump-probe capability at PHELIX and performed a first experiment to generate and characterize warm dense titanium via K_α radiography and –spectroscopy. The results are currently being evaluated.

K_α x-ray radiography is a powerful technique allowing high-resolution images of the target density distribution. It is well suited for combined ion-beam/laser experiment to follow the hydrodynamic evolution of large samples of HED matter, as produced by intense heavy ion beams at GSI and FAIR. It will also be an interesting complementary tool to the planned proton-radiography project for FAIR

References

[1] T. Guillot et al., Science **286**, 72 (1999)
[2] N. Tahir et al., New Journal of Physics **12**, 073022C (2010)
[3] V. Bagnoud et al., Appl. Phys. B: Lasers and Optics, December 2009
[4] P. Neumayer et al., Physics of Plasmas **17** 103103 (2010)
[5] V. Bagnoud et al., this report
[6] H. Park et al., Physics of Plasmas **15** 072705 (2008)

Designing a Beam Stripper for Fast Ion - Slow Ion Collision (FISIC) Experiments at SPIRAL2 *

N.A. Tahir[1], V. Sultanov[2], I.V. Lomonosov[2], E. Lamour[3], Th. Stöhlker[1], C. Prigent[3], M. Trassinelli[3], J.-P. Rozet[3], and D. Vernhet[3]

[1]GSI, Darmstadt, Germany; [2]IPCP, Chernogolovka, Russia; [3]INSP, CNRS–UPMC, Paris, France

Performing Fast Ion - Slow Ion Collision (FISIC) experiments is a long standing project for atomic collision physicists. Whereas such experiments are currently performed by high energy physicists, ion - ion collisions for atomic physics have so far been performed only in the case of slow ions, in the context of magnetically confined plasmas. Besides the fundamental interest in understanding the mechanisms involved in ion - atom collisions, such studies are also motivated by various aspects of the energy deposition by fast ions in matter, including inertial confinement fusion plasmas, material modifications and biological effects [1]. With the advent of new facilities such as SPIRAL2 at Caen (France) which are able to deliver intense stable ion beams,the INSP team proposes a project named FISIC to explore ion - ion collisions and their dynamics for heavy ions in the unknown regime of intermediate velocities. FISIC will use crossed beams of high intensities for which the charge state of both the incoming projectile ions (Fast Ions from SPIRAL2) and the target ionized medium (Slow Ions from an ECR ion source) will be controllable. The ability to produce a high intensity high energy projectile ion beam of the desired charge state makes the process of stripping one of the key parameters to make the project FISIC a success. This requires that the stripper stays stable and survives the impact of the incident ions with a very high repetition rate over an extended period of time.

First numerical simulations of the interaction of an oxygen beam with a simple Al stripper target (see Fig. 1) are reported. These calculations are the first step towards designing a viable stripper system for the FISIC experiments.

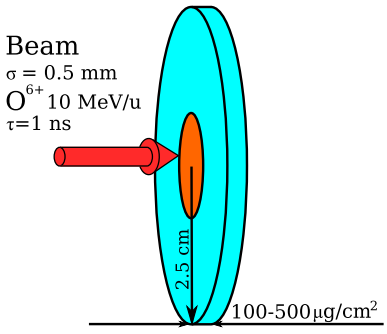

Figure 1: Disc shaped stripper foil.

In the FISIC experiments, different species of projectile particles will be used, although the energy range will be the same [4 - 14 MeV/u] in all the cases. These include, for example, ${}_{18}O^{6+}$ having beam currents between 10 - 50 pμA while another option is ${}_{20}Ne^{7+}$ with beam currents between 10 - 25 pμA. It is also intended to use ${}_{40}Ar^{14+}$ with beam currents between 10 - 15 pμA. The beam comprises of a bunch train with a bunch frequency of 88 MHz and each bunch is about 1 ns long so that the bunch separation is 10.36 ns. The transverse particle intensity distribution in the focal spot is Gaussian with σ = 0.5 mm. The desired stripper thickness is within the range 100 - 500 μg/cm^2.

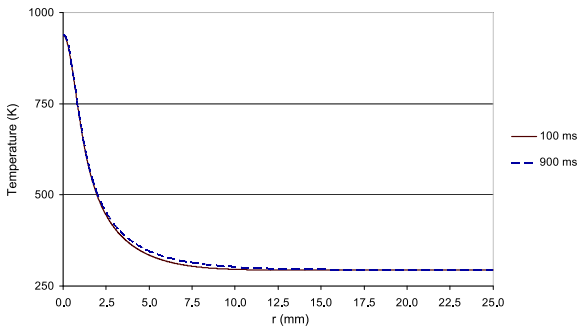

Figure 2: Temperature vs radius at t = 100 ms and 900 ms.

We assume that the stripper is a disc of Al (see Fig. 1) with a diameter = 5 cm and a thickness of 100 μg/cm^2. The beam comprises of 10 MeV/u ${}_{18}O^{6+}$ ions with a current of 10 pμA which means a beam intensity of 8.77x10^{12} particles / s that leads to a bunch intensity of about 10^5 particles. The beam is incident along the target axis.

A 3D computer code that includes ion energy deposition, heat conduction, solid constitutive properties of matter (elastic-plastic effects), a good model for the equation of state and radiation losses from the target surface, has been used to simulate the beam-target interaction.

Fig. 2 presents the temperature vs target radius at t = 100 ms and 900 ms, respectively. It is seen that the temperature at the center of the stripper is about 960 K in both cases. This is because the temperature saturates around this value at t = 100 ms due to the thermal radiation losses from the target surface. As the melting temperature of Al is 930 K, the central part of the target (stripper) is damaged within 100 ms. This problem can be overcome by designing a rotating target instead of a fixed target. This is intended for the future work.

References

[1] A. Diehl, et al., J. Phys. B 34 (2001) 4073.

* This work was financially supported by the BMBF

Opacity Measurements in Ion Beam Heated Warm Dense Matter

A. Tauschwitz[1], B. Ecker[1,5,6], D.C. Hochhaus[1,2,3,4], J. Jacoby[3], J. Otto[3], P. Neumayer [1,2,4], V.G. Novikov[7], F.B. Rosmej[8], An. Tauschwitz[2,3], J. Wiechula[3]

[1]GSI Darmstadt, [2]EMMI, [3]Goethe University Frankfurt, [4]FIAS Frankfurt, [5]Johannes Gutenberg University Mainz, [6]Helmholtz Institute Jena, [7]KIAM Moscow, Russia, [8]University Paris and LULI

Opacity measurements can be used to benchmark theoretical approaches for the description of atomic properties of warm dense matter [1]. Hydrodynamic calculations have shown that heating of thin foils with intense heavy ion beams can create isothermal warm dense matter samples that are suitable for such measurements. Several metals have transparency windows in the VUV region. For several materials the tabulated data for the absorption of cold materials in this wavelength range which are available from CXRO [2] and NIST [3] differ from each other. Models that predict the absorption of heated materials have an even higher uncertainty. Bismuth was chosen as a material to test the applicability of the different theories and tabulated data.

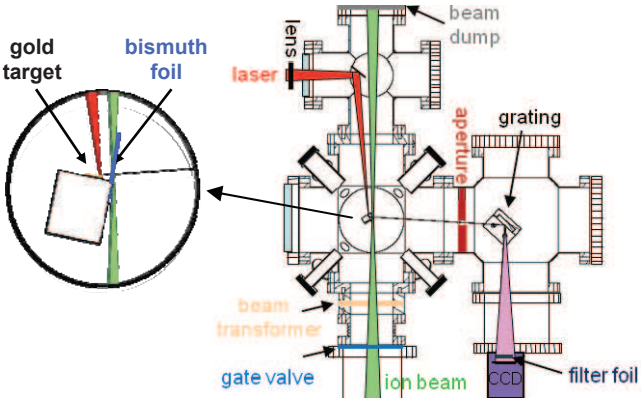

Figure 1: Opacity set-up at the HHT ion beam line.

The experimental set-up is shown in figure 1. A laser produced backlighter source provides broadband radiation in the wavelength region 50-80 nm. The wavelength resolved source spectrum and the transmission spectra are produced by a concave flat -field grating and recorded with a soft X-ray camera. A combination of a 400 nm Al foil and 3 mbar He gas are used as filters to suppress higher spectral orders. The warm dense matter sample is generated by a thin ion beam heated Bi-foil. An elaborate alignment procedure ensures that only backlighter radiation that has crossed the heated target zone is recorded.

Low energy electrons that are generated in the ion beam- target interaction were identified as main source of background noise. Fig. 2 shows that apertures and optimized filters could reduce this noise to a tolerable level.

The measured transmission in cold matter is in the range of the tabulated data given by NIST and CXRO. In the ion beam experiment the achieved Bi temperatures were limited to 3500K mainly due to large transmission losses in the beamline. Since this temperature is well below the

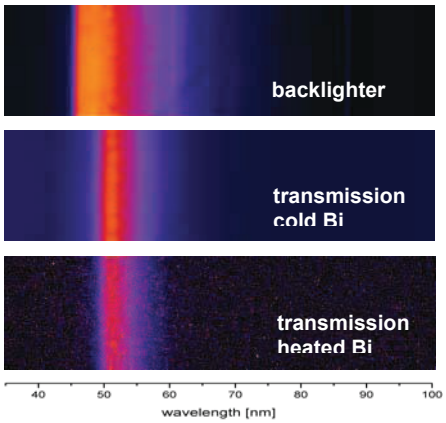

Figure 2: Spectra of filtered backlighter radiation and its transmission through cold and ion beam heated bismuth foils.

envisioned 1eV-range, a correspondence with the theoretical predictions cannot be expected. Moreover fluctuations of the backlighter intensity have led to an uncertainty of about 50% in the transmission. Nevertheless the first experimental data in fig. 2 show that the measurements have sufficient quality to discriminate between different models.

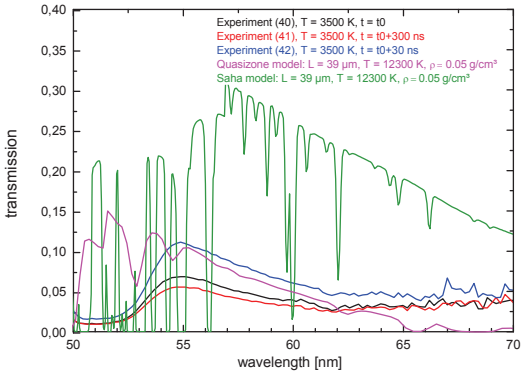

Figure 3: Measured transmission compared to calculated data based on a Saha and the Quasizone Modell [4].

[1] An. Tauschwitz, V.G. Novikov, A. Tauschwitz, F.B. Rosmej, J. Abdallah, E. Onkels, J. Jacoby, J.A. Maruhn, Appl Phys B 95 (2009) 13-16

[2] The Center of X-Ray Optics; http://www.cxro.lbl.gov

[3] National Institute of Standards and Technology; http://www.nist.gov

[4] A.F. Nikiforov, V.G. Novikov, V.B. Uvarov, Quantum-statistical models of hot dense matter: methods for computation of opacity and equation of state, Birkhäuser, 2005

Energy loss of ^{40}Ar in carbon plasma created by two-sided irradiation

A. Frank[1], A. Blazevic[2], M. Börner[1], W. Cayzac[1], T. Hessling[2], A. Pelka[1], D. Schumacher[1], T. Stöhlker[2], and M. Roth[1]

[1]TU Darmstadt, Germany; [2]GSI, Darmstadt, Germany

The stopping power of heavy ions in matter is a field of research that has been addressed for about a century. The understanding of the interaction of charged particles with cold matter has continuously evolved, however for ionized matter it is not yet fully understood. In the past the nhelix laser system alone was used to heat thin carbon foils to the plasma state which were then probed by the Unilac ion beam. While the experimental data after the heating phase were in very good agreement with our theoretical model, for the first 10 ns during the irradiation of the target by the nhelix laser, a significant decrease in the energy loss has been observed which could not be explained at this time [1]. The most promising explanation found for this decrease was that the microscopic intensity fluctuations in the 1 mm laser focus on the target created by a random phase plate lead to huge pressure differences in the plasma and hence to large inhomogeneities in the target's mass distribution simulated with the RALEF-2D code [2]. These simulations show that the inhomogeneities can be significantly reduced by irradiating the target with the second harmonic of the Phelix and the nhelix laser systems at $\lambda_{Phelix/nhelix} = 527/532$ nm from both sides. According to the simulations at $2\,\omega$ due to the increase of the critical density a lot more energy is transfered into radiation of the plasma which heats the whole target a lot faster and hence much more homogenously which is essential for reliable experimental data. The implementation of the frequency doubling of the Phelix laser at the experimental area Z6 lead to the possibility to use both laser systems to irradiate the target from two sides as shown in Fig. 1.

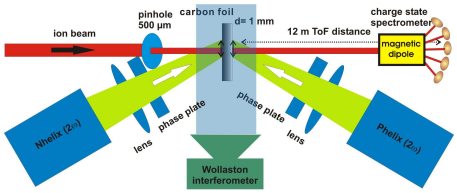

Figure 1: Experimental setup using the Phelix and the nhelix laser for the homogenous plasma creation at 2ω.

Besides the more homogenous heating this setup offers the advantage that the time needed to heat the whole foil via heat conduction is reduced. Furthermore the laser energy of each laser pulse can be reduced so that the temperature of the ablated plasma is lower compared to the energy of one laser pulse from one side needed to fully heat the carbon foil to a highly/fully ionized plasma state. So, the 3-dimensional plasma expansion which leads to a decrease of the target mass penetrated by the ion beam remains tolerable for the ion beam bunch length. The experiment described here was carried out with laser pulses of a length of 7 ns (FWHM), E=30 J which corresponds to an average intensity of $I = 4.6 \times 10^{11} W/cm^2$ on the target. The ion beam used here is ^{40}Ar at 4.0 MeV/u with an incident charge of 16+. The heating laser pulses of nhelix and Phelix were properly synchronized with a Δt of 1 ns. The laser parameters were chosen according to RALEF-2D hydrodynamic simulations [2], so that the whole carbon target is fully ionized at the end of the laser pulse.

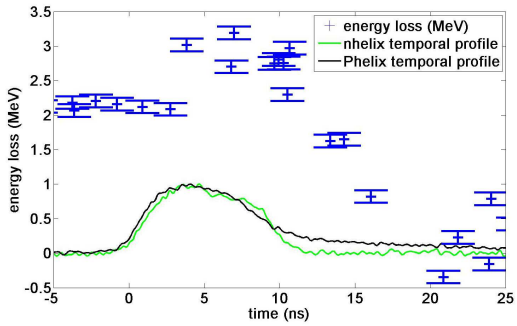

Figure 2: Energy loss of ^{40}Ar at 4.0 MeV/u.

The experimental results obtained from this experimental campaign are presented in Fig. 2. The central CVD diamond detector of the spectrometer described in detail in [3] was used as ToF detector for this experiment. The energy loss data shown in this graph has been obtained through several shots. At the bottom the temporal profiles of both nhelix and Phelix are shown. When the lasers start irradiating the target the energy loss remains constant for the first 3 ns due to the still arising inhomogeneities in the plasma which is in agreement with our theoretical calculations. After they dissolve on much shorter timescale compared to the 1ω case, an increase of about 50% from 2 MeV to 3.2 MeV is measured mainly due to the more efficient energy transfer to free electrons in the highly ionized plasma until the energy loss drops to zero due to the three dimensional expansion of the plasma. Compared to the two-sided irradiation at 1ω [4] an increase of the energy loss over the initial solid state level has been recorded which is in good agreement with our theoretical models.

References

[1] A. Frank et al, Phys. Rev. E 81, 026401 (2010)

[2] An. Tauschwitz et al, this annual report

[3] W. Cayzac et al, GSI annual report 2009, 398

[4] A.Frank et al, GSI annual report 2009, 390

Ion Beam Induced Light Emission from Dense Gas Targets*

A. Fedenev[1], S. El Moussati[2], A. Fertman[3], A.A. Golubev[3], T. Heindl[5], D.H.H. Hoffmann[2], A. Hug[1,2], B. Ionita[2], A. Kantsyrev[3], A. Khudomyasov[3], M. Kulish[4], J. Ling[2], N. Markov[3], V. Mintsev[4], D. Nikolaev[4], N. Shilkin[4], V. Ternovoi[4], V. Turtikov[3], S. Udrea[2], D. Varentsov[1], K. Weyrich[1], J. Wieser[6], D. Yuriev[4], Y. Zhao[7], and A. Ulrich[5]

[1]GSI, Darmstadt, Germany; [2]TUD, Darmstadt, Germany; [3]ITEP, Moscow, Russia; [4]IPCP, Chernogolovka, Russia; [5]TU-München, Garching, Germany; [6]Optimare Analytik GmbH &Co. KG, Wilhelmshaven, Germany; [7]IMP, Lanzhou, China.

Intense, focused heavy ion beams from SIS can deposit a high power and high energy in the target material. The primary excitation and subsequent relaxation- and thermalization processes can be studies when gases are used as the target material. Light emission from the whole beam excited volume can be observed at least at wavelengths where the target material is optically thin. This aspect can be used to study the beam profile by optical methods.

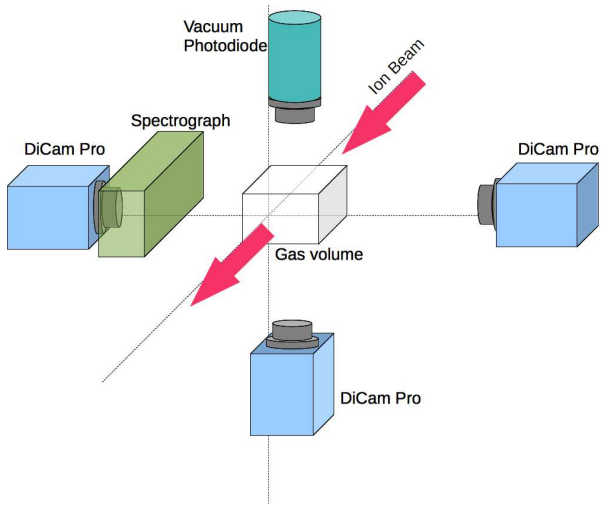

Figure 1: Experimental setup.

A pulsed 300 MeV/u ^{238}U beam from SIS was used to excite argon gas at pressures ranging from about 100 to 1000 mbar. A fast pulsing mode with 100 ns pulse width and pulse trains of 4 bunches within 1µs were used. More than 10^9 ions per pulse were available from the accelerator. Light emission was studied in a wavelength range from 300 to 800 nm. A small grating spectrometer was used to obtain spectral information in one direction on a two-dimensional, gated detector (DiCam Pro, see figure 1) and spatial information could be obtained from the intensity distribution in the other direction. Beam position and wavelength integrated beam profiles could be obtained with the other cameras shown in fig. 1. A fast (sub – ns) vacuum photodiode with MgF_2 window was used for time resolved recording of wavelength integrated light emission including the vacuum ultraviolet (VUV) spectral range. The gas was contained in a stainless steel cell. Gas purification was performed by flushing the gas through the cell and by activating a non evaporable getter in the closed cell, respectively.

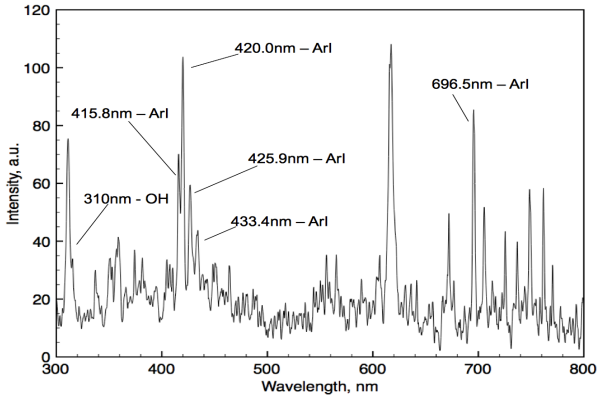

Figure 2: Overview over the time integrated light emission from argon at 500 mbar excited by a 1 µs beam pulse of 3.2×10^9 particles.

Time integrated wavelength spectra as the one shown in fig. 2 allowed most of the emission features to be identified. Atomic and ionic argon lines were found in the spectra besides some remaining impurities as the OH (A-X) transition at 310 nm on the short wavelength side of fig. 2. By recording spectra in coincidence with the 100 ns beam pulse for various target gas pressure values it was possible to obtain a consistent picture of the beam profiles. The results are shown in fig. 3. This work has significantly improved the results described in ref. [1]. A detailed data analysis is in progress.

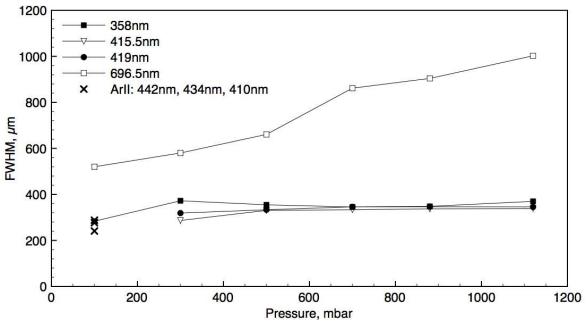

Figure 3: Beam profile widths vs. pressure.

References

[1] D. Varentsov et al., "Transverse Optical Diagnostics for Intense Focused Heavy Ion Beams", Contributions to Plasma Physics **48**, 586-594 (2008)

* Work supported by HRJRG-112

The PHELIX frequency doubling module

S. Borneis[1], E. Onkels[1], V. Bagnoud[1], A. Blazevic[1], C. Brabetz[1], C. Bruske[1], G. Catella[2] R. Eckardt[2] D. Eimerl[3], J. Fils[1], A. Frank[4], T. Hahn[1], T. Heßling[4], G. Klappich[1], F. Knobloch[1], S. Kunzer[1], M. Kreutz[1], L. Latanich[2], P. Marlowe[2], T. Merz-Mantwill[1], D. Reemts[1], D. Schumacher[4], T. Stöhlker[1,5], A. Tauschwitz[1], R. Thiel[1], K. Witte[6], B. Zielbauer[5]

[1]GSI Darmstadt; [2]Gooch and Housego; [3]Eimex; [4]TU Darmstadt; [5]Helmholtzinstitut Jena; [6]LMU München

SHG baseline design

One of the main challenges of the design of the frequency doubling module (SHG) was the goal to optimize the efficiency for 1 ns pulses at a maximum input energy of 450 J required for the heating of hohlraums while maintaining highest possible efficiency for up to 10 ns pulses at a maximum energy of 1 kJ for other laser interaction experiments. This factor of four in intensity requires careful design considerations because frequency conversion is a nonlinear process, scaling with the square of the input intensity to first order. Comprehensive model calculations and numerous engineering considerations such as alignment sensitivity, beam pointing and temperature stability determined that a 310 mm diameter and 25 mm thick type II 70 % deuterated potassium dihydrogen phosphate crystal (DKDP) would fulfill our requirements best. Fig. 1 depicts the model predictions of a 3D full beam calculation for a 25 mm thick DKDP crystal.

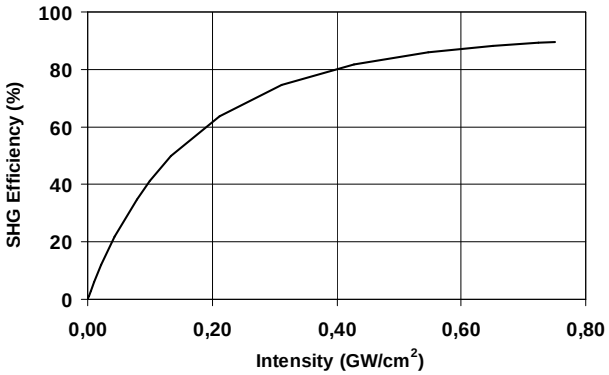

Fig. 1: Efficiency vs. input intensity for a 25 mm thick type II DKDP crystal assuming a spatial beam modulation of 70 % and a phase modulation corresponding to ± 100 micro radians local beam tilt external to the crystal.

Implementation of SHG at Z6

Aside geometrical constraints, important pre-conditions of the SHG system location were driven by the aim to achieve high contrast between converted light at 527 nm and residual laser light at 1054 nm with a minimum of PHELIX system changes. Consequently, our decision was to place the SHG directly behind the exit lens of the vacuum transport telescope of the Z6 beam line, which allows for two dichroic mirrors within the 10° beam line and one additional dichroic mirror within the 90° beam line of Z6, as shown in Fig. 2. The proper orientation of the DKDP crystal is set by a three-axis step motor actuated precision rotatable mount with tip and tilt.

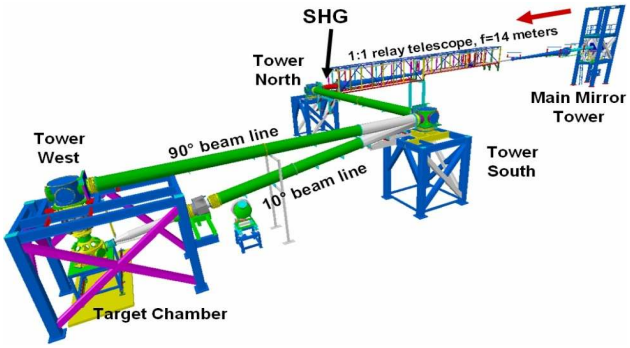

Fig. 2: 10°- and 90°-beam transport to the target chamber at the experimental area Z6.

The crystal assembly is installed in a window sealed chamber with dry N_2 purge gas supply surrounded by a temperature stabilized clean room class 100 tent. Extensive calculations were carried out to determine those locations behind the exit lens of the transport telescope, which prevent catastrophic optical damage of the lens, the SHG and the chamber window. The damage, related to so-called ghost foci, arises from the convergence of beams undergoing multiple residual reflections between the optical surfaces of all three optical components.

First commissioning results

During our first commissioning experiments we have achieved a maximum efficiency of almost 60 % which was far enough energy for a first experiment at Z6. Fig. 3 shows the measured SHG efficiency versus input energy. The commissioning of the SHG will be continued in 2011.

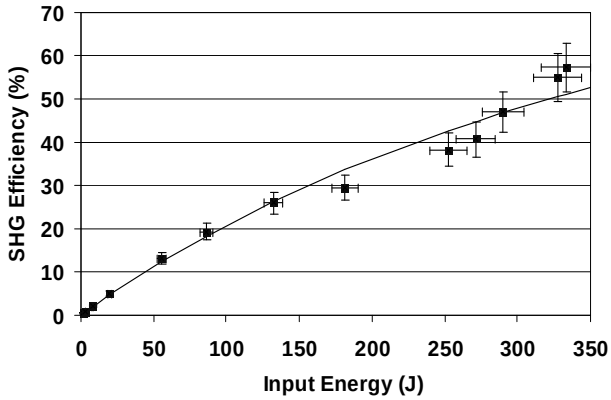

Fig. 3: Measured SHG efficiency vs. input energy

LIGHT Update: A laser-based ion-source at Z6

B. Zielbauer[1], A. Almomani[2], V. Bagnoud[1, 3], A. Blazevic[3], C. Brabetz[2, 3], S. Busold[4], O. Deppert[4], H. Eickhoff[3], U. Eisenbarth[3], O. Kester[2, 3], T. Merz-Mantwill[3], F. Nürnberg[4], M. Roth[4], T. Stöhlker[1, 3, 5]

[1]Helmholtzinstitut Jena, Germany; [2]Goethe-Universität Frankfurt, Germany; [3]GSI, Darmstadt, Germany; [4]Technische Universität Darmstadt, Germany; [5]Ruprecht-Karls-Universität Heidelberg, Germany

Introduction

The LIGHT[*,1] project was officially started in 2010 as a collaborative effort between GSI, the Helmholtz Institute Jena and surrounding universities. The project aims at injecting laser-accelerated ions into conventional accelerator structures and later at manipulating them. The first year of the project has dealt with the necessary infrastructure preparation, namely the installation of the laser-based ion-source at the Z6 experimental area, which led to the successful commissioning of our ion source.

In parallel, the collaboration has worked at strengthening the theoretical studies done on the subject, as was highlighted by the large and lively audience to the LIGHT summer workshop, held at GSI.

Short-pulse infrastructure development at the Z6 experimental area

The largest task for the project has been the development of short-pulse laser capabilities at the Z6 experimental area. For this, the addition of a short-pulse compressor and its diagnostics suite to the existing laser hardware was necessary. This so-called "100-TW" sub-project was conducted as a joint-effort between the PHELIX team, the HI-Jena, the TU-Darmstadt and the plasma physics department of GSI.

For the short pulse compressor, two options have been pursued in order cope with the somehow aggressive schedule of the project. At first, a compressor equipped with already existing gold-coated diffraction gratings has been designed and fabricated. This 12-cm aperture short-pulse compressor allows for compressing 20-joule pulses while maintaining the laser fluence below 300 mJ/cm^2, i.e. twofold below the laser-induced damage threshold of the gratings. The compressor can also easily accommodate for an upgrade to a larger clear aperture with a consequent increase of the maximum energy to 31 Joules.

Together with the compressor, a short pulse diagnostic package has been developed for both the compressor alignment and the on-shot control of the laser parameters. The diagnostics include near field and far field beam measurements, pulse energy and duration, and wavefront measurements. The diagnostic package was designed, and fielded in 2010. Its integration in the general laser control system of PHELIX will be continued in 2011.

The transport of the short pulses in a vacuum beam line between the compressor located in the south tower clean room of the Z6 experimental area and the target area has been another major step. The beamline is 20 m long and includes 5 turning boxes to drive the laser beam into the Z6 target chamber.

In parallel, several steps had to be taken to comply with radiation safety regulations: The concrete-block walls of the Z6 target area were made higher where possible, and an additional 50-mm thick iron wall was built around the target area to protect the visitor gallery.

Commissioning of the ion source

Recently, a two-week experiment has been conducted to demonstrate the generation of laser-accelerated ions at Z6. The laser beam was focused using a 30-cm focal distance parabola to a ~10 µm spot on a 10-µm thin gold foil. Together with the beam-handling equipment, precise target positioning tools have been validated in our setup. During the experiment, 10 MeV protons have been observed for a laser-pulse energy of 5 J and pulse duration equal to 700 fs +/-100 fs. The Figure 1 shows a photographic picture of the target at the time of laser impact together with the particle beam generated at the foil.

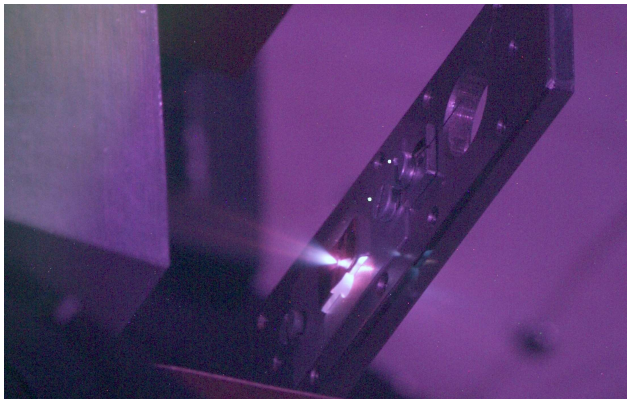

Figure 1: Image of the backside of a target shot by PHELIX. The laser pulse comes from the right and the plasma beam escaping from the back of the target can be seen on the picture.

Outlook for 2011

Based on the successful commissioning of the ion source, we will proceed with the next steps, namely the collimation of the ion beam using a pulsed solenoid and the preparation of the ion beam optics.

[1]https://www.gsi.de/documents/DOC-2010-Nov-36-1.pdf

* The acronym stands for **L**aser **I**on **G**eneration, **H**andling and **T**ransport.

High Brightness Coherent X-ray Sources by High-Order Harmonic Generation and Parametric X-ray Amplification

B. Ecker[1,3,5], B. Aurand[1,4,5], V. Bagnoud[1], D.C. Hochhaus[1,4,6], T. Kuehl[1,4,5], B. Zielbauer[3], D. Zimmer[1,5], J.Seres[2], E.Seres[2], C. Spielmann[2]

[1]GSI, Darmstadt, Germany; [2] Friedrich-Schiller-Universität Jena, [3] Helmholtz Institut Jena, [4]ExtreMe Matter Institute, [5]Johannes Gutenberg-University Mainz, [6]JohannWolfgang von Goethe-University Frankfurt

Progress in HH Generation at GSI

The development of high-order harmonic (HH) generation at GSI aims at creating a seed source for soft X-ray lasers (SXRL) that are based on amplification of spontaneous emission. It has been demonstrated that a seeded SXRL possesses a higher beam quality in terms of spatial homogeneity and spatial coherence [1]. In combination with the narrow spectral bandwidth, seeded SXRL represent attractive diagnostic tools for highly charged heavy-ion spectroscopy experiments [2].

In 2010 the investigations on HH generation at GSI succeeded in shifting the HH radiation in a large spectral range, covering 50% of the spectrum between 17 nm and 35 nm [3]. Furthermore, a new process called x-ray parametric amplification (XPA) was discovered, demonstrating an exponential increase of the XUV pulse energy by three orders of magnitude [4].

HH- / XPA-Setup and Experimental Results

The HH and XPA experiments utilize the front-end of the PHELIX laser system, which delivers up to 10 mJ of pulse energy compressed to 350 fs FWHM pulse duration at a repetition rate of 10 Hz. The beam is focused by either a 40 cm or 60 cm focal length lense to an almost diffraction-limited focal spot of 50 µm FWHM in diameter, resulting in an intensity of up to 1.5e15 W/cm². The gaseous medium used to create the XUV radiation is provided by a Ni tube backed by an electronic valve. The combination with a precision valve controller allows for applying a well-defined pressure in the range between 50 mbar and 1200 mbar. Further parameters to optimize the XUV signal are the IR laser pulse energy and the position of the gas tube relative to the focal spot. The XPA and HH radiation is directed to an in-house developed XUV diagnostics chamber, providing both a XUV footprint camera and a spectrometer. The first is used to measure the spatial profile of the XUV beam, allowing the estimation of the XUV pulse energy, the beam divergence and the spatial energy distribution. The latter consists of a 1200 l/mm flat-field gold grating and a back-illuminated CCD camera, recording the XUV spectrum in the range between 17 nm and 35 nm. To separate the XUV and the IR light two separate Al filters of 200 nm thickness are used.

Figure 1 shows the measured beam profile of the 41st harmonic at 25.7 nm, integrated over fifty XUV pulses. The FWHM beam diameter of 0.6 mm x 0.8 mm corresponds to a divergence of 0.9 mrad x 1.1 mrad, respectively. The ellipticity can be related to a spatial chirp of the IR pump laser, which was caused by a misalignment of the pulse compressor and resulted in an elliptical focal spot.

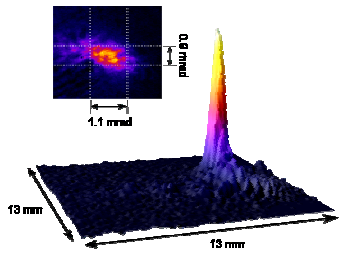

Figure 1: Spatial profile of the XUV beam at 25.7 nm in 2D and 3D integrated over fifty consecutive shots. The FWHM spot size of 0.6 x 0.8 mm² corresponds to a divergence of 0.9 x 1.1 mrad.

Summary and Outlook

The demonstrated the spectral overlap of the HH radiation and several SXRL transitions has been the key prerequisite for carrying out future SXRL seeding experiments at GSI. In addition, the newly discovered XPA process has been studied in experiments performed at GSI and at the JETI laser system in Jena. The data obtained from the latter is currently being evaluated. Further experiments utilizing the PHELIX and JETI lasers are planned for 2011.

References

[1] Ph. Zeitoun et al., “A high-intensity highly coherent soft X-ray femtosecond laser seeded by a high harmonic beam”, Nature 431, 426-429 (2004)

[2] A. Gumberidze et al., Nucl. Instrum. Methods Phys. Res., Sect. B, Beam Interact. Mater. Atoms 267, 248 (2009)

[3] D. C. Hochhaus et al., “Tuning the high-order harmonic lines of a Nd:Glass laser for soft x-ray laser seeding”, Appl. Phys. B 100, 711-716 (2010)

[4] J. Seres et al. , Nature Physics 6, 455-461 (2010)

Development and Test of New Thomson-Parabolas for Laser-Ion-Acceleration

B. Aurand[*1,2,3]; *F. Klos*[1]; *M. Weipert*[1]; *P.D. Eversheim*[4] *and T. Kühl*[1,2,3]

[1]GSI, Darmstadt, Germany; [2]EMMI, Darmstadt Germany; [3]Johannes Gutenberg University Mainz, Germany; [4]Rheinische-Friedrich-Wilhelms University, Bonn, Germany

Thomson parabolas [1] (TP) have become a standard diagnostic tool for laser-ion-acceleration experiments. A particularly compact and versatile version has been designed and was tested and calibrated using a cyclotron.

The design (Fig. 1) is similar to the TPs developed at Rutherford-Appleton-Laboratory [2]. Permanent magnets create a magnetic field of up to 0.7 T. In combination with the variable electric field applied by tilted potential plates, the energy acceptance is in the range between 0.7 and 16 MeV per nucleon (Fig. 2). For diagnostics we use re-usable Image Plates (IPs) mounted on a rotatable drum. In this way, the device is capable of measuring four consecutive shots before the experimental chamber has to be opened to exchange the IPs.

The IP mount can be replaced by a pre-aligned laser diode holder, which in combination with the fully adjustable baseplate allows for a quick alignment inside the target chamber.

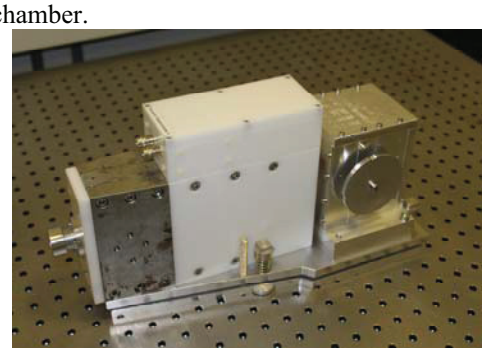

Fig.1: Picture of the fully equipped Thomson spectrometer

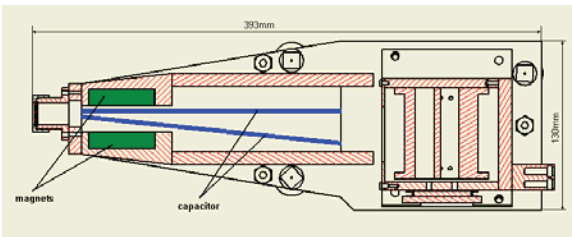

Fig.2: Scheme of the magnets and the capacitor inside the spectrometer

Calibration

After construction and assembly of the TP, the magnetic field distribution was mapped with a Hall probe to determine the distribution of the field strength along the ion trajectories. The data obtained were used to simulate the ion trajectories using the ion-optics computer program SIMION 8.0 [3].

A helium beam from the cyclotron of the Helmholtz Institut für Strahlen- und Kernphysik at Bonn University was used for an absolute calibration of one of the parabolas.

Up to now, for five different energies in the range of 6-14MeV per nucleon – $^4He^{2+}$ -ion trajectories were measured with different high-voltage settings, resulting in a varying E-field deflection. Simulation results and measured values are in good agreement.

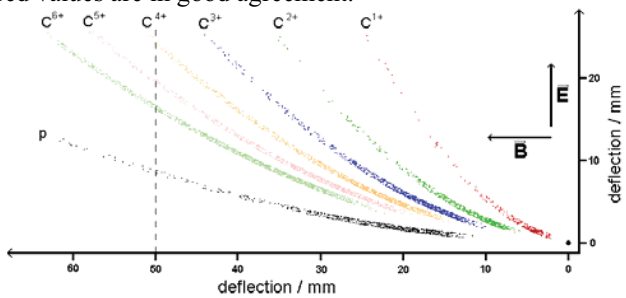

Fig.3: Simulated signal of relevant ion species in the energy range from 0-200MeV. The active detector size is 50x50mm

Outlook

A further improvement will be a new data acquisition by a micro-channel-plate (MCP) based imaging system. By the use of fiber-connectors the design could be small enough to replace the existing image-plate box without changing the dimensions of the parabola.

In addition, using the feature of a gateable MCP with a rise time in the few-ps-range would lead to an effective suppression of background radiation, by the short acceptance time window for accumulating particles.

Acknowlegements

We would like to thank D.Carroll and D. Neely from Rutherford-Appleton-Laboratory for their support concerning the parabola design.

Also we thank the staff of the cyclotron of the "Helmholtz Institut für Strahlen- und Kernphysik" at Bonn University for their support during the calibration experiment.

References

[1] J.J. Thomson; Phil. Mag. 21 225 (1911)
[2] D.C. Carroll et al.; Central Laser Facility Annual Report 2005/2006
[3] D.A. Dahl; Int. J. Mass. Spectrom. 200 (2000)

* B.Aurand@gsi.de

Imaging Interferometer for Ion-Beam Driven HEDP Experiments*

B. Ionita[1], S. El Moussati[1], D.H.H. Hoffmann[1], A. Hug[1,2], J. Ling[1], S. Udrea[1], A. Fedenev[2], D. Varentsov[2], K. Weyrich[2], E. Brambrink[3], A. Fertman[4], A. Golubev[4], A. Kantsyrev[4], A. Khudomyasov[4], V. Turtikov[4], M. Kulish[5], N. Markov[4], V. Mintsev[5], D. Nikolaev[5], A. Pyalling[5], N. Shilkin[5], V. Ternovoi[5], and D. Yuriev[5]

[1]TUD, Darmstadt, Germany; [2]GSI, Darmstadt, Germany; [3]LULI, Paris, France;
[4]ITEP, Moscow, Russia; [5]IPCP, Chernogolovka, Russia

An imaging displacement interferometer in a Twyman-Green configuration has been constructed and commissioned in heavy-ion beam driven high energy density physics (HEDP) experiments at the HHT area of GSI. Spatial and temporal pressure profiles of boiling lead heated by an intense uranium beam have been determined by detecting the motion of a sapphire window due to the impact of expanding target material. The temporal profiles were obtained with a time resolution of about 50 ns.

In these experiments in which the interferometer was successfully used, the following configuration was implemented (Fig.1): a beam with an elliptic focal spot heated the sample near its surface, a sapphire window (1mm thickness) was placed parallel to the sample surface at a distance of 1mm and the interferometer recorded the motion of the rear surface of this window. The target that was used can be seen in Fig.2(a).

The ion beam parameters were as follows: ^{238}U, 350 AMeV, ~$2\cdot10^{9}$ particles/pulse, 900ns pulse duration.

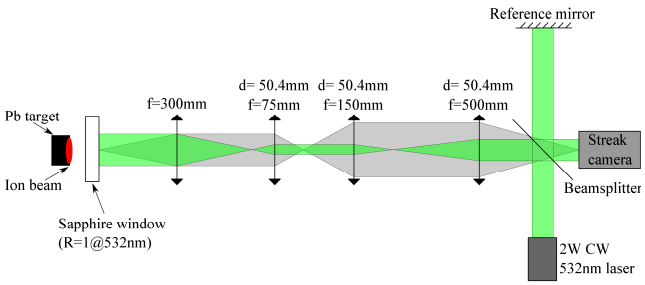

Figure 1: Experimental setup schematics.

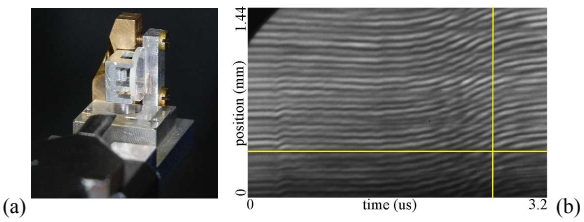

Figure 2: (a) Target; (b) interferogram recorded with the streak camera.

Interferograms (Fig.2(b)) were analyzed with a Fourier-transform based method[1,2] to obtain the displacement profile (Fig.3(a)) from which the velocity profile for the free (rear) surface of the window was obtained (Fig.3(b) and Fig.3(c)). From this profile, the pressure profile on the front surface of the window was computed (Fig.3(d)).

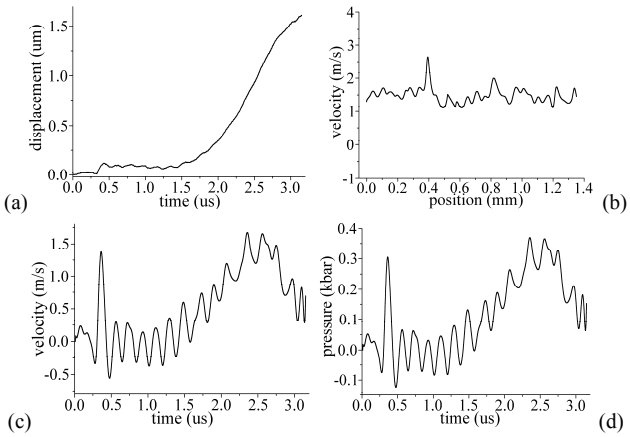

Figure 3: (a) Displacement profile for a fixed point on the free (rear) surface; (b) velocity spatial profile on the free (rear) surface; (c) velocity profile for a fixed point on the free (rear) surface; (d) pressure profile for a fixed point on the front surface.

The period of oscillations on the velocity and pressure profiles (Fig.3(c) and Fig.3(d)) is 188 ns, corresponding to the time required by sound waves in sapphire to travel back and forth between the front and rear window surfaces (180 ns).

The interferometer was proven to be successful in recording the surface velocity profiles for pressures up to several kbar. The analysis method will be extended to all obtained interferograms.

For measurements in the km/s and Mbar region a line-VISAR is currently being developed by our group. This region of the phase diagram will be reached in HEDP experiments with the PHELIX laser and with intense heavy-ion beams at FAIR.

References

[1] M. Takeda, H. Ina, and S. Kobayashi, "Fourier-transform method of fringe-pattern analysis for computer-based topography and interferometry," J. Opt. Soc. Am. 72, 156-160 (1982).

[2] P. M. Celliers, D. K. Bradley, G. W. Collins, D. G. Hicks, T. R. Boehly, and W. J. Armstrong, "Line-imaging velocimeter for shock diagnostics at the OMEGA laser facility," Rev. Sci. Instrum. 75, 4916 (2004).

*Work supported by Helmholtz-Russia Joint Research Group HRJRG-112 and BMBF 06DA9033I.

Development of a non-contact electrical conductivity measurement technique for heavy ion driven warm dense matter*

J. Ling[1], *S. Udrea*[1], *N. Shilkin*[2], *S. El Moussati*[1], *A. Fedenev*[3], *A. Fertman*[4], *D.H.H. Hoffmann*[1], *A. Hug*[1,3], *A. Kantsyrev*[4], *A. Khudomyasov*[4], *M. Kulish*[2], *N. Markov*[4], *V. Mintsev*[2], *D. Nikolaev*[2], *V. Ternovoi*[2], *V. Turtikov*[4], *A. Ulrich*[5], *D. Varentsov*[3], *D. Yuriev*[2], *and Y. Zhao*[6]

[1]TUD, Darmstadt, Germany; [2]IPCP, Chernogolovka, Russia; [3]GSI, Darmstadt, Germany; [4]ITEP, Moscow, Russia; [5]TUM, Garching, Germany; [6]IMP, Lanzhou, China

Characterisation of matter irradiated by intense, focused particle beams is of special interest for many research areas including nuclear (Super–FRS at FAIR) [1] and particle physics (LHC at CERN) [2]. Few years ago the development of an experimental setup for non-contact measurements by eddy currents has been initiated and first proof of principle experiments have been performed with different target geometries [3] and [4]. The conclusion drawn from these experiments is that the best approach is to use planar targets. This geometry allowed for a robust and improved target assembly design which is shown in Fig. 1 and was for the first time employed during experiments with intense heavy ion beams in 2010. The sensor [4] is mounted in a

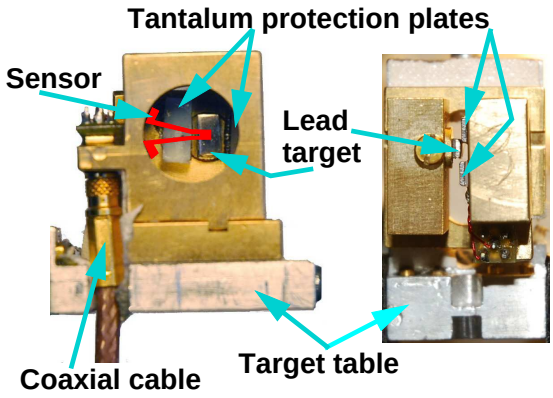

Figure 1: Target assembly used for non-contact electrical conductivity measurements. The sensor has been marked in red for visibility.

brass frame and is protected from direct ion beam irradiation by two tantalum slabs, which also delimit the region within which ion beam heated target material is allowed to expand. At about 0.8 mm the target slab made out of lead is hold by a second frame. The target slab is irradiated and heated by the ion beam and thus expands towards the sensor where it impacts on the surface of the 2.5 μm thick sapphire protecting layer. A hot target material layer thus forms in the proximity of the sensor modifying its impedance and S_{11} scattering parameter. This change is observed in the 850 MHz RF experimental signal of Fig. 2 as a variation of it's amplitude and phase. Thus by processing this signal one can determine the change in the amplitude and phase

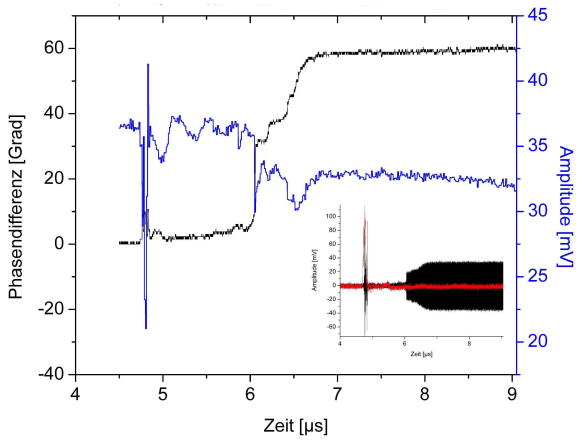

Figure 2: Main diagram: amplitude and phase of the 850 MHz RF signal reflected at the sensor. Small diagram: raw sensor signal – black; ion beam time profile – red.

of the sensor's S_{11} parameter. To finally compute the electrical conductivity of the investigated layer a precise calibration of the sensor is needed. This is still hampered by the fact that the calibration procedure is altering the sensors and the technological process for a reliable series production of the sensors is not yet completely established. Fig. 2 shows also the result of the processing of the raw experimental signal.

The measurement presented in this report was the first to benefit from the new bunch compressor commissioned at SIS-18. Thus the target was heated by a 90 ns FWHM pedestal-less Uranium ion beam with an intensity of about $3{\cdot}10^9$ particles and a specific ion energy of 300 AMeV. This allowed for a good separation between the useful signal and the distorsions produced by the ion beam, see Fig. 2. The analysis of former signals, showed that this was not the case in previous experiments.

References

[1] M. Winkler et al., GSI Report 2009-1 (2009) p. 86

[2] N.A. Tahir et al., J. Appl. Phys. 97 (2005) p. 083532

[3] S. Udrea et al., GSI Report 2009-1 (2009) p. 325

[4] J. Ling et al., GSI Report 2010-1 (2010) p. 403

* Work supported by BMBF and HRJRG

Fast ignition with ponderomotively accelerated ions *

T. Schlegel[1,2], C. Regan[3], and V. Tikhonchuk[3]
[1]GSI, Darmstadt, Germany; [2]Helmholtz-Institute, Jena, Germany; [3]CELIA, Université Bordeaux, France

Contrary to the central spark ignition concept, the fuel of the deuterium-tritium (DT) capsule in a fast ignition (FI) scheme will be compressed at lower implosion velocities to densities of several hundred g/cm^3, what reduces problems with high symmetry and hydrodynamic instabilities [1].

To ignite such a precompressed pellet, additional internal energy must be allocated in a local region of its dense core, the so-called hot spot, at the moment of stagnating implosion. As soon as fusion chain reactions will set in, a burn wave spreads over the whole volume of the target. For this secondary heating, intense beams of fast electrons or ions produced with help of an additional short and intense laser pulse were proposed.

With the advent of ultra-intense laser pulses, a scheme of efficient ponderomotive ion acceleration from overdense plasma regions becomes conceivable, which may provide high particle numbers in the accelerated ion bunch [2]. This regime of hole boring should allow ion acceleration directly inside the fusion pellet without any secondary target (see Fig. 1 (a)), thus enabling fuel ignition and burn in high repetition rate operation [3].

To reduce the needed laser energy and power in a demonstration experiment, a cone-guided DT target could be applied [5], where the laser beam propagates through low-density carbon inside the cone and accelerates carbon ions with high efficiency and small beam divergence, as shown in Fig. 1 (b). The design of the ion beam parameters for such an experiment, based on analytical studies [4], was checked in hybrid numerical simulations. Ion beam propagation and energy deposition in the precompressed DT target were modeled with a two-dimensional kinetic transport code. The successive hydrodynamic evolution of the beam-heated target was calculated with the radiative hydrodynamic code CHIC. For a laser pulse with an intensity $I_{\rm las} \simeq 5 \times 10^{21}$ W/cm^2 and the focal radius $r_{\rm f} \simeq 10\,\mu$m, which propagates through the 200 μm thick overcritical carbon layer of density $\rho_{\rm C} = 0.2$ g/cm^3, the generated beam of 175 MeV carbon ions will deposit 13.5 kJ of energy in the dense core of the pellet. The acceleration efficiency equals 16%. A transverse beam spread of 3° was supposed, which can be evaluated from two-dimensional particle-in-cell simulations. The ion temperature at this stage is shown in Fig. 2 (a). A CHIC simulation starting from these plasma parameter distributions confirmed pellet ignition after about 10 ps. The time delay can be explained by the density and temperature dependence of the DT fusion reaction rate, which describes the efficiency of the α-particle release. The characteristic times for energy equilibration between α-particles and electrons and for the subsequent energy transfer to fuel ions are of the order of 1 ps in the parameter range at hand. The time dependence of the fusion power is depicted in Fig. 2 (b). The integral fusion energy amounts to 20 MJ, the corresponding gain factor is 180. The ignitor laser energy is 100 kJ, its power equals 15 PW and the pulse duration is 7 ps.

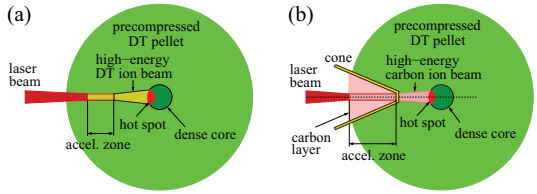

Figure 1: Ponderomotive ion acceleration in the stagnation phase of DT capsule compression. (a) DT acceleration in front of the dense core. (b) Scheme with a low-density carbon layer inside a cone embedded in the DT pellet.

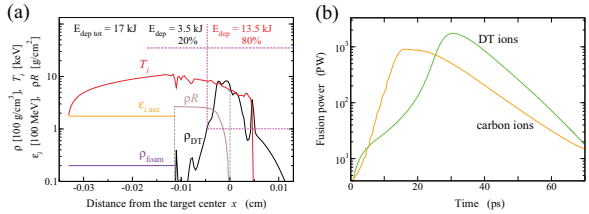

Figure 2: (a) Plasma parameters just after energy deposition of high-energy carbon ions. (b) Fusion power as function of time for both cases discussed in the text.

The pure DT scheme requires higher laser intensity, energy and power because of lower acceleration efficiency, larger ion beam spread and less localized energy deposition. For a large-scale fusion target [6] with an areal mass density $\simeq 2.6$ g/cm^2, a short-pulse laser energy of 180 kJ was needed in simulations to ignite the pellet. The fusion power history is shown in Fig. 2 (b) and yields a gain of 150.

References

[1] M. Tabak et al., Phys. Plasmas 1 (1994) 1626.
[2] N. Naumova et al., Phys. Rev. Lett. 102 (2009) 025002.
[3] V.T. Tikhonchuk et al., Nucl. Fusion 50 (2010) 045003.
[4] T. Schlegel et al., Phys. Plasmas 16 (2009) 083103.
[5] A. Debayle et al., J. Phys.: Conf. Ser. 244 (2010) 022032.
[6] D.S. Clark and M. Tabak, Nucl. Fusion 47 (2007) 1147.

* Work supported by the European support program Marie Curie IRSES project # 230777, by EURATOM in the framework of keep-in-touch activities and by the HiPER European project.

Modeling of hohlraum targets for experiments at the Phelix laser

An. Tauschwitz[1,2], *M.M. Basko*[1,2,3], *V.G. Novikov*[4], *A. Grushin*[4], *and J. Maruhn*[1,2]

[1]EMMI, Darmstadt, Germany; [2]University of Frankfurt, Germany; [3]ITEP, Moscow, Russia; [4]KIAM, Moscow, Russia

The unique combination of a high energy laser and a swift heavy ion beam is available at GSI at the Z6 experimental area. One of the experimental schemes at Z6 is dedicated to measurements of energy loss and charge state distribution of heavy ions in a plasma. Plasma targets, which are indirectly heated by x-ray radiation created in a laser irradiated hohlraum, are expected to be fairly homogeneous in space and time [1]. To heat up the hohlraum, a frequency doubled beam of the Phleix laser ($\lambda = 0.527\,\mu m$) is used. In this report we present 2D radiation hydrodynamic calculations of the radiative hohlraum target used in the experimental campaign in October 2010. The calculations were done with the newly developed 2D radiation-hydrodynamics code RALEF-2D [2]. The equation of state, thermal conduction coefficients and LTE spectral opacities have been generated by the THERMOS code [3].

The Au hohlraum case with a laser-entrance and a diagnostic holes is depicted in Fig. 1. Simulations have been done in the quasi-Lagrangian mode. Initially, the hohlraum was filled with an Au gas at a density of 10^{-5} g/cm^3 to avoid folding up of the plasma-vacuum boundary. The radiation transport was calculated with 5 frequency groups. The problem was simulated in the Cartesian cylindrical (x, y) geometry preserving the dimensions of the spherical hohlraum used at the experiment. The laser power was rescaled according to $W_{cyl} = W_{sph}/2R$, where R is the hohlraum radius. The laser pulse with a power $W_{sph} = 0.1$ TW delivered in a pulse of 1.5 ns full length and 0.2 ns edges was assumed. The radius of the Gaussian focal spot was 0.05 mm.

Figure 2 shows the radiation temperature distribution at $t = 0.5$ ns. Except for the hot spot at the laser deposition zone, the radiation temperature is well homogenized inside the hohlraum. The emitted spectra integrated over the diagnostic slit at $t = 0.5$ and 1 ns are plotted in Fig. 3. The spectrum at 0.5 ns can be approximated by a Planckian curve with a temperature of 87 eV. By $t \simeq 1$ ns the intensity of the emitted radiation drops due to the closure of the diagnostic hole.

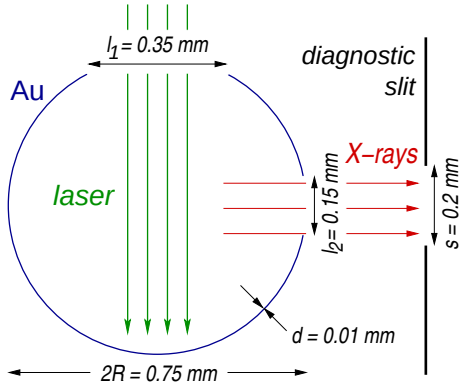

Figure 1: Layout of the hohlraum target.

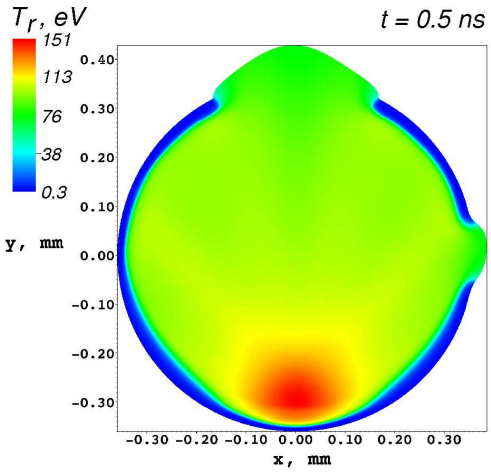

Figure 2: Radiation temperature distribution in the hohlraum at t = 0.5 ns.

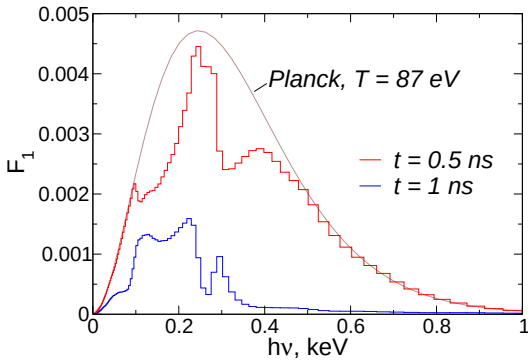

Figure 3: Radiation spectra from the diagnostic hole at t = 0.5 and t = 1 ns.

References

[1] A. Frank, A. Blazevic, P.L. Grande et al., Phys. Rev. E **81**, 026401 (2010)

[2] M.M. Basko, J. Maruhn, and An. Tauschwitz, GSI Report 2010-1 (GSI Scientific Report 2009), p. 410.

[3] A.F. Nikiforov, V.G. Novikov, V.B. Uvarov, *Quantum-statistical models of hot dense matter: methods for computation of opacity and equation of state*, Birkhäuser, 2005.

Optimization of the hohlraum wall composition

E.Yu. Arapova, M.A. Barinov, M.A. Vronskii, G.V. Dolgoleva, V.F. Yermolovich
RFNC-VNIIEF, Sarov, Russia

Experimental investigations of the conversion of Nd-laser energy (λ = 532 nm, intensity 10^{13} W/cm^2) into X-rays by irradiation of gold/copper alloys have shown a dependence on the atomic percentage of gold and copper [1, 2]. The X-ray yield in the photon energy region up to 1 keV reaches the maximum when the alloy contains 43% of gold. For harder X-rays above 1 keV the yield decreases drastically with a higher percentage of gold. Adding 12 % of gold into the copper of the originally investigated alloy results in a decrease by a factor of 2.1 for X-ray's above 1 keV.

The one-dimensional code SND [3] is developed for calculations of two temperature gas dynamics of plasma expansion and includes the radiation transport in a diffusion approximation. The wavelength dependent radiation diffusion in materials was used to determine the conversion of laser radiation into X-rays in AuCu alloys by variation of the gold content. The needed spectral opacities were obtained using the THERMOS code [4], which calculates spectral absorption ratios on the basis of the average atom model in the modified Hartree–Fock -Slater approximation. Fig.1 shows the curves calculated for the X-ray flux (energies up to 1 keV) emitted from a $Au_{0.43}Cu_{0.57}$ - alloy at a laser intensity of 10^{13} W/cm^2.

For a part of the X-ray spectrum the maximum yield of the radiation from the Au/Cu-alloy is higher than that from laser irradiated pure gold- or copper-targets. For example the X-ray´s yield from the $Au_{0.43}Cu_{0.57}$ - alloy at 0.15 keV, 0.3 keV and between 0.7 – 1 keV is higher than the yield from the pure gold or copper, irradiated with the same laser parameters.

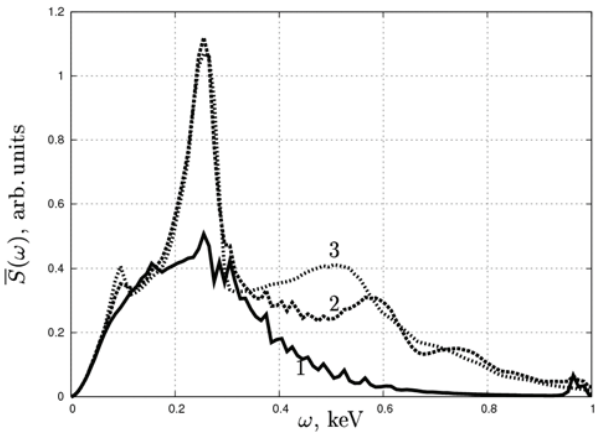

Figure 1: The calculated values of the radiation flux S(ω), ω ϵ (0,1) keV for different target materials: 1 - for Cu, 2 - for $Au_{0.43}Cu_{0.57}$, 3 -Au.

From Fig. 1 we can conclude that at laser intensities of 10^{13} W/cm^2 the X-ray yield in the photon energy range of 0.55 – 1.1 keV considered for $Au_{0.43}Cu_{0..57}$ alloy is 12 % higher than for a pure gold target and by a factor of 1.7 for a copper one.

For the X-ray energies higher than 1 keV a significant decrease in the X-ray yield is observed for alloys containing more gold, see Fig. 2.

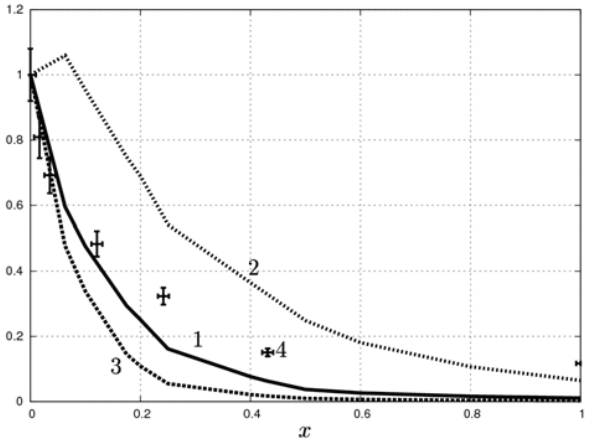

Figure 2: Ratios of the X-ray flux generated by the laser irradiation pure Au in the photon energy range of 1.15-1.6 keV: $S_{[1.15,1.6]keV}(Au_x$

the laser intensities: 1 - $10^{13}\ W/cm^2$, 2 - $5\cdot10^{12}\ W/cm^2$, 3 - $3\cdot10^{13}\ W/$

in the mixture

Numerical simulations of the experimental results on the laser radiation conversion into X-rays demonstrate the non-linear behavior of the output radiation energy (increase) within the spectral range of 0.55 - 1.1 keV and a strong decrease within the range 1.15 – 1.6 keV depending on the atomic percentage of Au in the AuCu-alloy.

The results of these investigations will be used for optimization of the hohlraum design in combined laser – heavy ion beam experiments at GSI.

This work was performed within the framework of the ISTC Project#2264.

References

[1]. J. A. Chakera, V. Arora, S. Sailaja, S. R. Kumbhare, P. A. Naik, P. D. Gupta, N. K. Gupta, B. K. Godval // Applied Physics Letters v. 83, 1, 2003, pp. 27-29

[2]. V. Arora, J. A. Chakera, P. A. Naik, S. R. Kumbhare, P. D. Gupta, N. K. Gupta // Journal of Applied Physics 100, 033306. 2006.

[3]. G.V. Dolgoleva // VANT, Ser.: Methods and Programs for Numerical Simulation of Computational Physics Problems, 1983, Issue. 2, pp. 29- 33

[4]. A.F. Nikiforov, V.G. Novikov, V.B. Uvarov, Quantum-Statistical Models of High-Temperature Plasma, Moscow: "Fizmatlit" Publishers, 2000

Simulations of low density foam heating by means of hohlraum radiation

G.Vergunova[1], S.Guskov[1], V. Rozanov[1], O. N. Rosmej[2]

[1] Lebedev Physical Institute Moscow, Russia; [2] GSI Helmholtzzentrum für Schwerionenforschung, Darmstadt, Germany

Introduction

In combined experiments using the PHELIX laser facility and the heavy ion beam delivered by the linear accelerator UNILAC at the GSI-Darmstadt, the ion beam deceleration in the laser-produced plasma is under study [1]. The plasma is produced via direct heating of solid carbon foils or indirect heating of low-density polymer foams by means of X-rays. The soft X-rays with close to Planckian spectral distribution are generated by the direct irradiation of the gold cylindrical hohlraum with a laser pulse [2, 10]. The authors theoretically investigate the plasma formation in a plane polymer TAC foam layer ($C_{12}H_{16}O_8$) of 2 mg/cm^3 mean density and 800 μm thickness under the action of an external soft X-ray source.

Numerical simulations and results

For numerical simulation of the foam heating process the following experimental results were used as input parameters: the Planckian radiation spectrum with temperature T_{rad} = 20 - 40eV, and time of the soft X-ray pulse of t_{rad} = 5ns [3, 10].

Simulations of the plasma production in a thin foam layer were performed using a one-dimensional numerical code [5]. More details you will find in [6]. Absorption coefficients calculated by the DESNA [7], and THERMOS [8] codes were used.

In the figure 1 the temporal evolution of plasma temperature and density are presented. Calculations of the electron temperature inside the heated foam layer in dependence on time show that during 5 ns about 500 μm of the foam is heated by the external radiation source up to 20 eV. After the end of the external source action, the heat transfer is realized by the electron heat conductivity flow. The plasma temperature drops down to 17-10 eV and is uniformly distributed over 750 μm of the target thickness. Over 10 ns the plasma target keeps the initial foam density. The thickness of the uniformly heated plasma layer is sufficient for the heavy ion beam-plasma interaction experiments, since the ion beam diameter is of 500 μm.

As it was expected, an increase in hohlraum temperature and therefore of the incident on to the foam energy flux leads to an increase of plasma temperature and decrees of the amount of the radiation absorbed in the foam layer. Experimentally it was shown that 75% of he hohlraum radiation in the photon energy range of 60-1200eV was absorbed in a foam layer leading to plasma

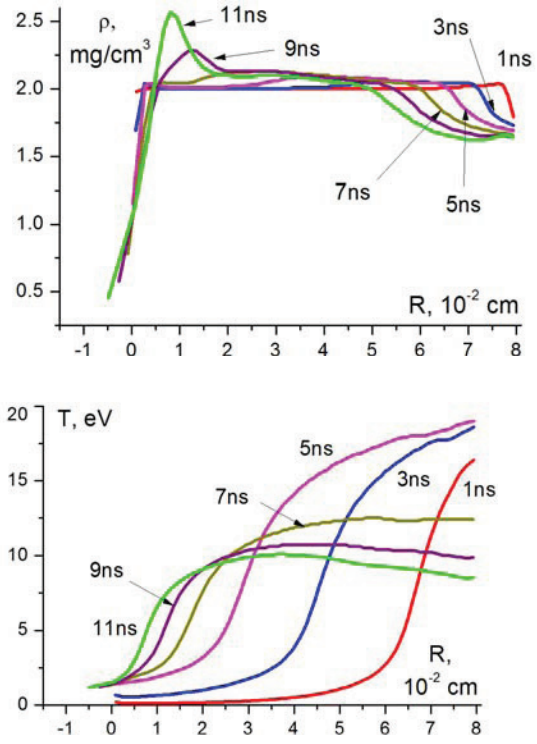

Fig.1. Density and temperature profiles formed in a plane plasma layer heated by Plankian radiation with temperature 40eV at indicated times.

formation [6]. Calculations of the radiation transfer in CHO-plasma carried out using opacity values calculated for a TAC-foam chemical composition for different plasma temperatures [10] show a good agreement with experimental results.

References

[1] Hoffmann D. *et al.*, *Laser Part. Beams,* ***23****, 47 (2005).*

[2] Rosmej *et al.*, *GSI-report 2009, p. 318*

[3] Rosmej *et al.*, *GSI-report 2009, p. 387*

[4] Gus'kov S.Yu. *et al.*, *Laser Part. Beams,* ***17****, 415 (1999).*

[5] Govorun T.K. *et al.*, *Preprint* ***176****, IAM, Moscow (1986).*

[6] Vergunova G.A. *et al.*,JRLR, **31**, N5, 504(2010)

[7] Ivanov, E., *et al.*, *SPIE Proc.* ***4424****, 308 (2001).*

[8] Nikiforov A.F.et al, Birkhauser Verlag, Boston-Basel (2005)

[9] O.N. Rosmej, V. Bagnout, U. Eisenbarth *et al.*, *NIMA* (2011) accepted

[10] N. Orlov, A, Denisov, O.N. Rosmej *et al.*, *Laser Part. Beams* (2011), accepted

This work was supported by the RFBR Grant #10-02-92104-YaF-a.

The ray effect in simulations of radiation transport with the RALEF-2D code

M.M. Basko[*1,2,3], *An. Tauschwitz*[†2,3], *and J. Maruhn*[2,3]

[1]ITEP, Moscow, Russia; [2]EMMI, Darmstadt, Germany; [3]ITP, University of Frankfurt am Main, Germany

The two-dimensional (2D) radiation-hydrodynamics code RALEF-2D, developed recently [1] for simulations of laser irradiated targets, solves the quasi-static equation of radiation transfer

$$\mathbf{\Omega} \cdot \nabla I_\nu = k_\nu \left(B_\nu - I_\nu \right) \qquad (1)$$

by applying the S_n method [2] for discretization of the angular dependence of the spectral intensity $I_\nu = I_\nu(\mathbf{x}, \mathbf{\Omega})$. Despite its many undisputable advantages, the S_n method has one important drawback: because the discrete angular directions of the S_n angular quadrature are fixed in space, it generates significant spurious intensity variations when certain target areas "see" bright emitting spots at relatively small solid angles — the so called "ray effect" [3].

The ray effect, inherent in the RALEF-2D code, is vividly illustrated in Fig. 1 as the angular (azimuthal) variation of the radiation energy density in an empty cylindrical cavity $R_1 < r < R_2 = 4R_1$ above a hot and opaque central radiation source of radius $R_1 = 1$, in which a constant value $B_\nu = B_0$ of the source function was assumed. The exact solution would display a perfectly uniform (along the azimuthal angle ϕ) radiation energy distribution.

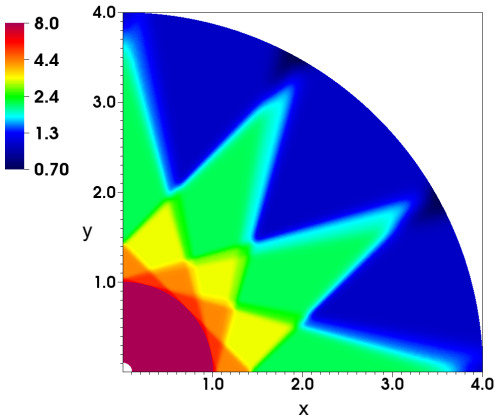

Figure 1: Radiation energy density in an azimuthally uniform cylindrical cavity as calculated with the S_6 method.

A straightforward way to suppress the ray effect is by increasing the order n of the S_n quadrature, based on $n(n+2)$ discrete directions over the 4π of the solid angle. What concrete value of n ensures satisfactory accuracy, depends entirely on the specific problem being solved. Figure 2 shows how the spurious angular variation of the radiation flux at the outer surface $r = R_2$ of a cylindrical cavity with the receiver-to-emitter aspect ratio $R_2/R_1 = 4$ depends on n. The corresponding L_2-norm errors are listed in Table 1.

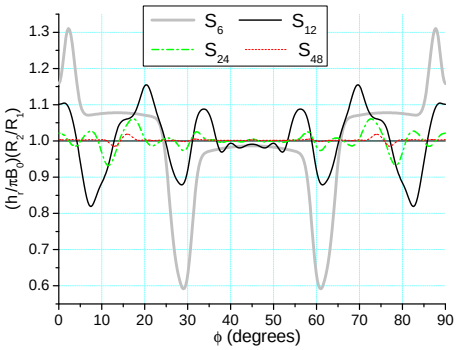

Figure 2: Azimuthal profiles of radiation flux at the outer boundary $r = R_2$ of a cylindrical cavity with an aspect ratio $R_2/R_1 = 4$ as calculated with different orders n of the S_n quadrature.

Table 1: The L_2-norm errors for the radiation flux at the outer boundary $r = R_2$ of a cylindrical cavity for two values of its aspect ratio R_2/R_1 and different orders of the S_n quadrature.

R_2/R_1	S_6	S_{12}	S_{24}	S_{48}	S_{96}
4	0.15	0.085	0.024	0.0052	0.0023
8	0.90	0.20	0.069	0.018	0.005

From Fig. 2 and Table 1 one sees that the amplitude of the ray effect drops rather rapidly with the increasing n (almost like n^{-2}). Nevertheless, our results indicate that, to be able to simulate hohlraum-like cavities with a subpercent accuracy, one would have to resort to S_n quadratures of rather high order ($n \gtrsim 40$ for $R_2/R_1 = 4$, and $n \gtrsim 60$–70 for $R_2/R_1 = 8$) — which poses serious demands on the required computing power.

References

[1] M.M. Basko, An. Tauschwitz, J. Maruhn, "Development of a 2D radiation-hydrodynamics code RALEF for laser plasma simulations", GSI Report 2010-1 (GSI Scientific Report 2009), p. 410.

[2] B. Carlson and K. Lathrop, In "Computing Methods in Reactor Physics" (H. Greenspan, C. Kelber, and D. Okrent, editors), Gordon & Breach, New York (1968).

[3] K.D. Lathrop, "Ray Effects in Discrete Ordinates Equations", Nucl. Sci. Eng., **32** (1968) 357.

* basko@itep.ru

† An.Tauschwitz@gsi.de

Irradiation of thin carbon foils with non-homogeneous laser beams

An. Tauschwitz[1,2], *M.M. Basko*[1,2,3], *V.G. Novikov*[4], *A. Grushin*[4], *and J. Maruhn*[1,2]

[1]EMMI, Darmstadt, Germany; [2]University of Frankfurt, Germany; [3]ITEP, Moscow, Russia; [4]KIAM, Moscow, Russia

Thin C-foils heated with intense laser beams are used at the Z6 experimental area to investigate energy loss and charge state distribution of heavy ions in a plasma [1]. The presented calculations show the advantage of the 2-sided foil heating versus its 1-sided heating when the irradiating laser flux is spatially strongly non-uniform. Irradiation from two opposite sides can be realized by using the Phelix and the nhelix lasers. In the simulations we assumed that the beam parameters of both lasers are identical. The frequency doubled lasers have an intensity of $5 \cdot 10^{11}$ W/cm^2 and are focused on a spot of 1 mm in diameter. The intensity distribution over the focal spot is approximated as $F_{las}(x) = 1 + 0.5\cos(2\pi x/l)$, $l = 50\,\mu$m. The laser pulse is 13 ns long, ramped with a 3 ns rise and fall times. Initially the C-foil has a mass thickness of $\langle\rho x\rangle = 0.1$ mg/cm^2. The simulations were done in the Cartesian (x, y) geometry. The laser beam is incident from the right along the x-axis, the foil is placed at $x = 0$. For the 2-sided heating the y-axis is treated as a reflective boundary and only half of the foil is considered. The simulations were done with the new radiation-hydrodynamics code RALEF-2D [2]. The equation of state, thermal conduction coefficients and LTE spectral opacities have been generated by the THERMOS code [3].

Figure 1 shows the linear density $\langle\rho x\rangle$ as a function of y. The peaks of $\langle\rho x\rangle$ correspond to the minima of the laser intensity. For the 1-sided heating the highest density variation occurs at $t = 3.5$ ns, whereas by $t = 9$ ns the density distribution becomes almost uniform. For the 2-sided heating the corresponding times are 3 ns and 6.5 ns. Although for 1-sided heating the density variations are suppressed at later times, the fully ionized plasma state, required for stopping measurements, is not achieved. Figure 2 compares the 2D distributions of the ionization degree Z at $t = 5$ ns for the 1-sided and 2-sided cases. The laser comes from the right, strong non-uniformities of Z are formed at the rear non-illuminated side. The profiles of Z along $\langle\rho x\rangle$ at $y = 0.125$ mm, $t = 5$ and 6.5 ns in the 2-sided case are shown in Fig. 3. It is seen that the plasma column becomes practically homogeneous and fully ionized by $t = 6.5$ ns, and, therefore, well suited for ion stopping measurements.

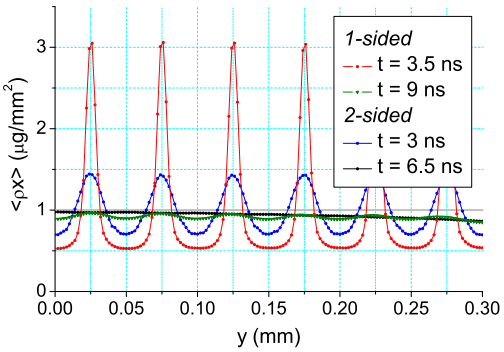

Figure 1: Linear density $\langle\rho x\rangle$ as a function of y for the 1-sided and 2-sided heating at different times.

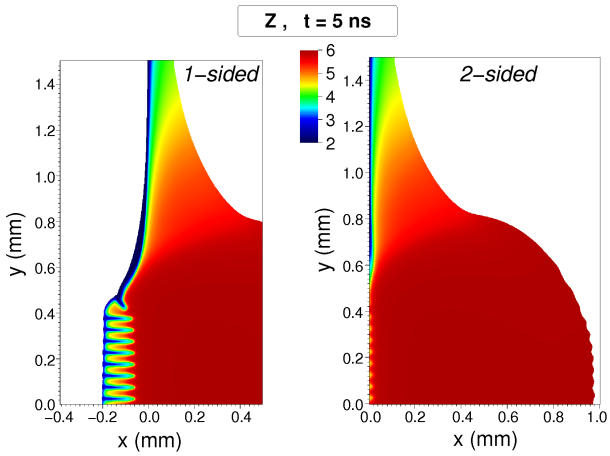

Figure 2: Distribution of the ionization degree Z in the 1-sided and 2-sided irradiated foil at $t = 5$ ns.

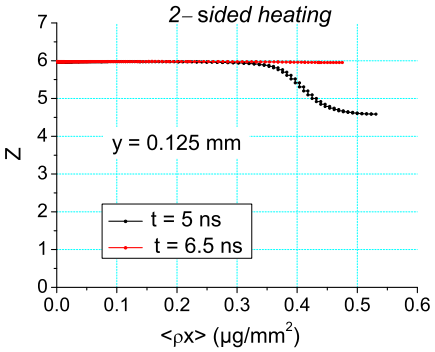

Figure 3: Ionization degree as a function of linear density at $y = 0.125$ cm for $t = 5$ and $t = 6.5$ ns.

References

[1] A. Frank et al., Phys. Rev. E **81**, 026401 (2010)

[2] M.M. Basko, J. Maruhn, and An. Tauschwitz, GSI Report 2010-1 (GSI Scientific Report 2009), p. 410.

[3] A.F. Nikiforov, V.G. Novikov, V.B. Uvarov, *Quantum-statistical models of hot dense matter: methods for computation of opacity and equation of state*, Birkhäuser, 2005.

Dynamic stabilization of Rayleigh-Taylor instability in ablation fronts *

A. R. Piriz#, L. Di Lucchio, and G. Rodriguez Prieto
University of Castilla-La Mancha, Spain

Mitigation of Rayleigh - Taylor instability (RTI) in an ablation front is of great importance in inertial confinement fusion (ICF). Specially for ICF directly driven by ion beams since in this case the resulting cut-off wave number k_c above which the front becomes stable, may be considerably large as a consequence of the relatively small fraction of the beam energy that is transported by thermal conduction [1]. In this framework, dynamic stabilization driven by the vertical vibration of the interface has been suggested as a possible method for the stabilization of an ablation front [2]. However, these studies were performed at a time when RTI instability on ablation fronts was not yet well understood. In addition, a sinusoidal driving of the interface acceleration was considered which leads to a Mathieu equation type. This kind of equations is very difficult to analyse and the stability regions were not found.

Here we use a modulation in the driving acceleration $G(t)$ that consists of a sequence of Dirac deltas: $G(t) = g + b\Gamma(\omega t)$, where ω is the oscillation frequency, $\Gamma(\omega t) = \delta(\omega t - 2m\pi) - \delta[\omega t - 2(m+1)\pi]$, $b = \omega^2 A$, and A is the amplitude. This approach allows us to find complete closed solutions for the problem of the dynamic stabilization of RTI in an ablation front. In particular, we get explicit analytic solutions for the growth rate and for the boundaries of the stability region in terms of the parameters of the modulation and of the steady state ablation front. The evolution equation for the linear perturbation amplitude ξ on the interface was obtained in Ref.[1]: $\ddot{\xi} + \frac{4kv_2}{1+r_D}\dot{\xi} + [\phi_0 \frac{k^2 v_2^2}{r_D} - A_T kG(t)]\xi = 0$, where v_2 is the ablation velocity, $A_T = (1-r_D)/(1+r_D)$ is the Atwood number and $r_D = \rho_1/\rho_2$ is the density jump at both sides of the front. The previous equation is a Hill equation that can be treated analytically by means of the Floquet theory in order to find the dispersion relation. Typical results for the instability growth rate are shown in Fig. 1 for $\kappa_c = k_c v_2^2/g = 0.3, \varpi = \omega v_2/g = 0.6$ and several values of b/g. As b/g increases, the cut-off wave number is reduced from k_c [case a)] to k_m [case b)] but above a minimum value of b/g the system enters in the region of parametric instabilities and two unstable regions exist [case c)]. In general, there are minimum and maximum values of b/g that determine the region of stability for each value of the desired cut-off wave number κ_m. A typical case is shown in Fig. 2. As it can be appreciated, relatively large values of b/g are required for dynamic stabilization. Since in the ablation front the modulation

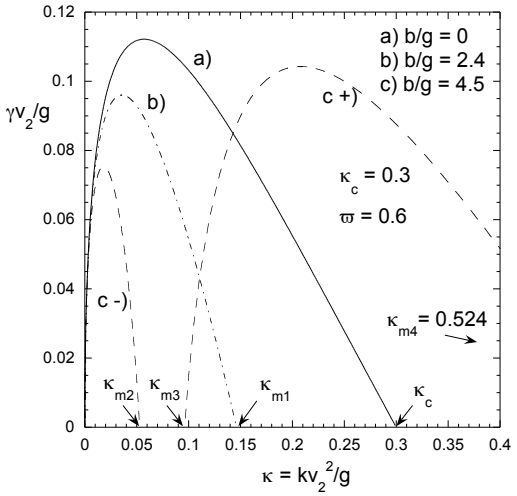

Fig.1: Instability growth rate for three different oscillation amplitudes and $\kappa_c = kv_2^2/g = 0.3, \varpi = \omega v_2/g = 0.6$.

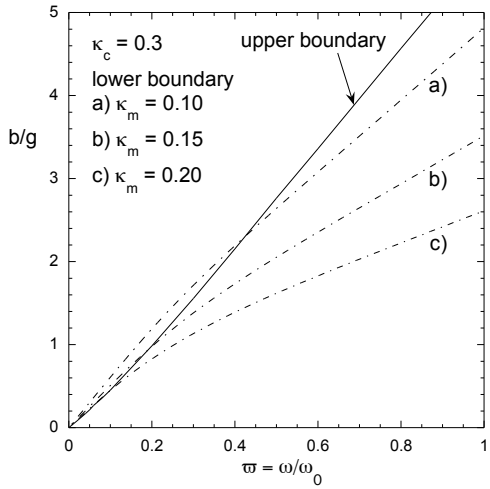

Fig.2: Stability region for three values of κ_m and for $\kappa_c = kv_2^2/g = 0.3, \varpi = \omega v_2/g = 0.6$.

$\Delta p/p$ in the ablation pressure must be less than one, such values of b/g are only possible thanks to the compressibility of the shell layers close to the front. Such an effect determines κ_m in terms of the oscillation frequency [3].

* Work supported by JCCLM and MICINN (Spain)
# roberto.piriz@uclm.es

References

[1] S. A. Piriz, A. R. Piriz, and N. A. Tahir, Phys. Plasmas **16**, 082706 (2009).
[2] J. P. Boris, Comments Plasma Phys. Controlled Fusion **3**, 1 (1977). R. Betti, R. L. McCrory, and C. P. Verdon, Phys. Rev. Lett. **71**, 3131 (1993).
[3] A. R. Piriz, L. Di Lucchio, and G. Rodriguez Prieto, Phys. Plasmas **in press** (2011).

Studies of Richtmyer–Meshkov Instability Growth in Ideal Fluids Using Intense Heavy Ion Beams at FAIR / HEDgeHOB *

N.A. Tahir[1], A. Shutov[2], A.P. Zharkov[2], A.R. Piriz[3], and Th. Stöhlker[1]
[1]GSI, Darmstadt, Germany; [2]IPCP, Chernogolovka, Russia; [3]UCLM, Ciudad Real, Spain

A new technique that employs the Mach reflection scheme, has been used to generate a stationary plane shock wave [1] using an intense uranium beam that is going to be generated at the FAIR facility. Numerical simulations that show that such a shock can be used to study the growth of Richtmyer–Meshkov (RM) instability in an ideal fluid are presented. Further details can be found in [2].

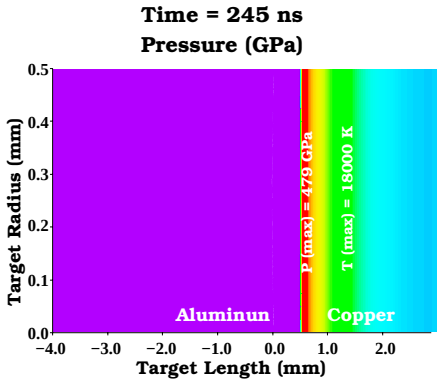

Figure 1: Pressure distribution at t = 245 ns.

Fig. 1 presents the pressure distribution at t = 245 ns. It is seen that the shock (propagating from the right to the left) has arrived close to the Cu–Al boundary, but is still in the Cu region. This corresponds to the case when the maximum intensity of 5×10^{11} uranium ions / bunch with a particle energy of 400 MeV/u is used. The FWHM of the Gaussian intensity distribution in the focal spot is 2 mm. The temperature in the shock heated Cu is about 18000 K

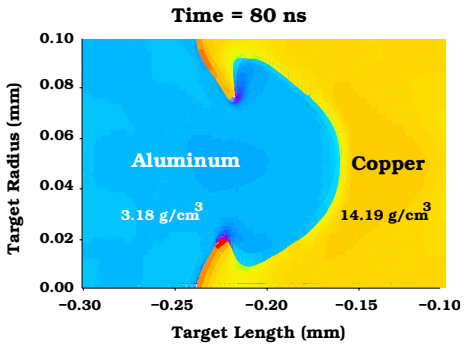

Figure 2: Perturbation amplitude at t = 80 ns after the shock crosses the interface.

which represents an ideal fluid state. Fig. 2 shows the perturbation amplitude at t = 80 ns after the shock crosses the interface (initial amplitude is 25 μm). A typical mushroom growth is seen due to the RM instability. Moreover, the phase of the perturbation is inverted which also is a well known phenomenon. In Fig. 3 we plot the peak–to–valley

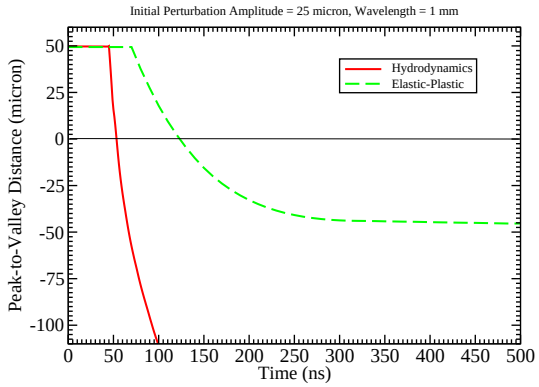

Figure 3: Peak–to–valley distance vs time for case in Fig. 2.

distance of the perturbation vs time. It is seen that in case of an ideal fluid (red curve), the amplitude increases without any limits as no damping mechanism exists. Fig. 4 shows

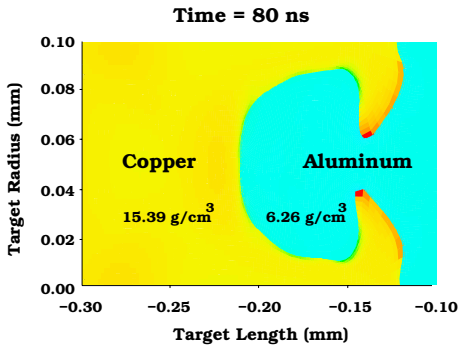

Figure 4: Same as in Fig. 2, but for configuration Al–Cu.

the same variable as Fig. 2, but the shock propagates from Al to Cu. In this case, however, the perturbation phase is not inverted.

References

[1] A. Shutov, A.P. Zharkov and N.A. Tahir, GSI Report, GSI-208-2, p.TH-17 (2008).

[2] N.A. Tahir et al., Phys. Plasmas (2011) Accepted.

* Work supported by the BMBF

Studies of Richtmyer–Meshkov Instability Growth in Solids Using Intense Heavy Ion Beams at FAIR / HEDgeHOB *

N.A. Tahir[1], A. Shutov[2], A.P. Zharkov[2], A.R. Piriz[3], and Th. Stöhlker[1]
[1]GSI, Darmstadt, Germany; [2]IPCP, Chernogolovka, Russia; [3]UCLM, Ciudad Real, Spain

In this contribution we present numerical simulations of the Richtmyer–Meshkov (RM) instability growth in solids, using a plane shock driven by an intense ion beam. The plane shock is generated using the Mach reflection technique [1]. Fig. 1 shows the position of the shock front at t = 500 ns that is propagating from the right to the left. It is seen that the shock is close to the Cu–Al boundary, but is still in the Cu region. The shock pressure is around 55 GPa and is generated by a beam intensity of 5×10^{10} per bunch. The temperature in the shock heated Cu is about 900 K so that the material is in solid state and possesses solid constitutive properties.

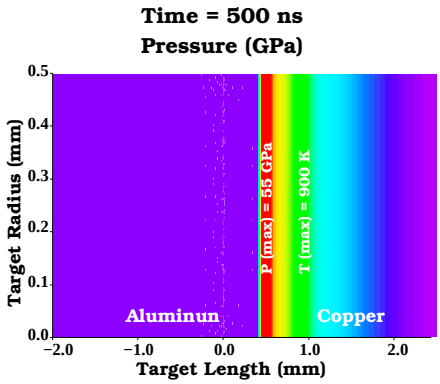

Figure 1: Pressure distribution at t = 500 ns.

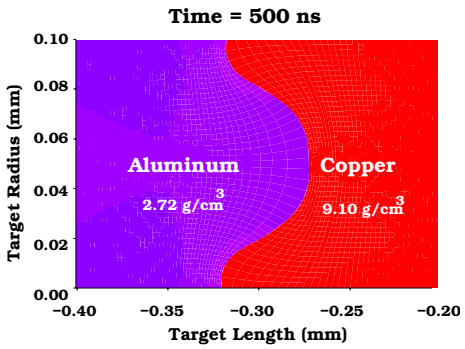

Figure 2: Perturbation amplitude at t = 500 ns after the shock crosses the interface.

Fig. 2 shows the perturbation amplitude at t = 500 ns after the shock moves through the corrugated Cu–Al interface. The initial perturbation amplitude, A, was 25 μm. It is seen that the perturbation phase has been inverted, which is always the case when shock propagates from a high density to a low density medium. However, the amplitude stabilizes due to the solid constitutive properties of the material. This is further demonstrated in Fig. 3 where we plot the peak–to–valley distance vs time for the solid case (green curve). It is seen that after the phase inversion, the peak–to–valley distance stabilizes at t = 25 ns to a value of about 44 μs. Fig. 4 shows the same variables as Fig. 2, but in a configuration where the shock propagates from Al to Cu. It is seen that the perturbation amplitude is stabilized due to the solid constitutive properties, but no phase inversion occurs in this case.

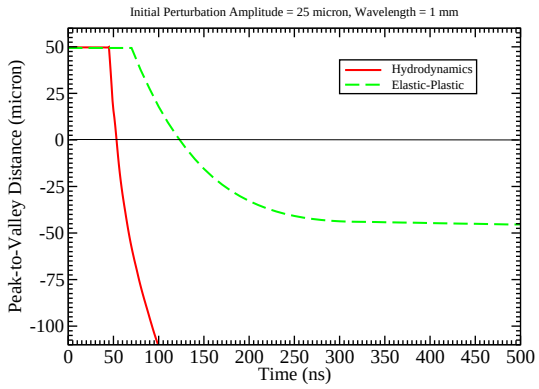

Figure 3: Peak–to–valley distance vs time for case in Fig. 2.

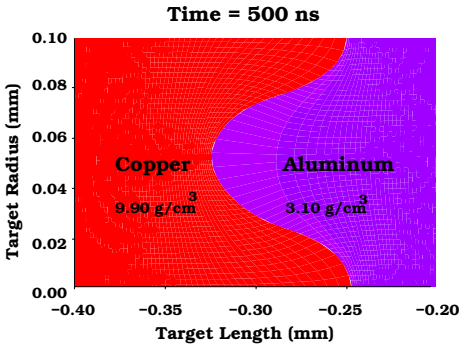

Figure 4: Same as in Fig. 2, but for configuration Al–Cu.

References

[1] N.A. Tahir et al., Phys. Plasmas (2011) Accepted.

* Work supported by the BMBF

Simulations of Interaction of 440 GeV Proton Beam With a Solid Copper Cylindrical Target: The HiRadMat Facility at CERN *

N.A. Tahir[1], J. Blanco Sancho[2], A. Shutov[3], and R. Schmidt[2]
[1]GSI, Darmstadt, Germany; [2]CERN-AB, Geneva, Switzerland; [3]IPCP, Chernogolovka, Russia

In this contribution we present numerical simulation results of interaction of 440 GeV protons generated by the Super Proton Synchrotron (SPS) with a solid Cu cylindrical target that is facially irradiated by the beam. These simulations have been performed by iteratively running the FLUKA code (that calculates energy loss of the protons and the shower in matter) and the 2D hydrodynamic code BIG2 with an iteration step of 1 μs. These simulations have been carried out to design fixed target experiments at a dedicated facility named HiRadMat (High Radiation on Materials) that is being constructed at CERN. The main purpose of these future experiments is to assess the damage caused to the equipment in case of an accidental release of the beam.

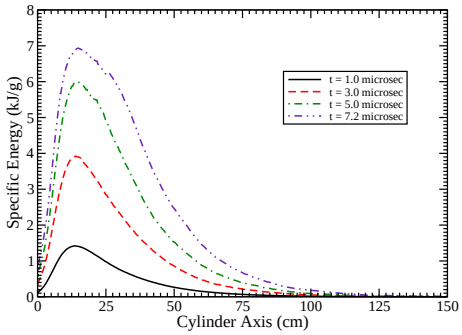

Figure 1: Specific energy deposition vs axis at different times during irradiation.

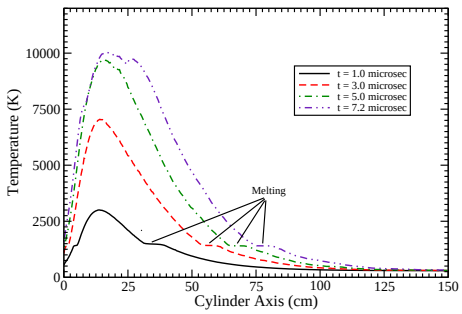

Figure 2: Temperature vs axis at different times.

The SPS beam consists of 288 bunches with each bunch comprising of 1.15 $\times$ 10^{11} protons. The bunch length is 0.5 ns while two neighboring bunches are separated by 25 ns so that the total duration of the bunch train is 7.2 μs. The transverse intensity distribution in the focal spot is Gaussian with σ = 0.5 mm.

* Work supported by EuCARD

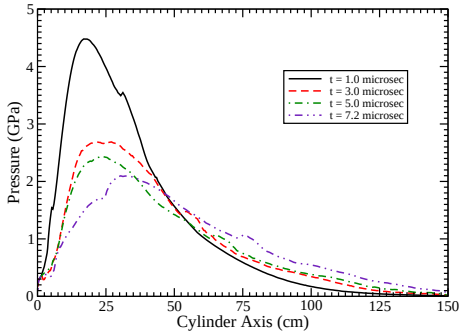

Figure 3: Pressure vs axis at different times.

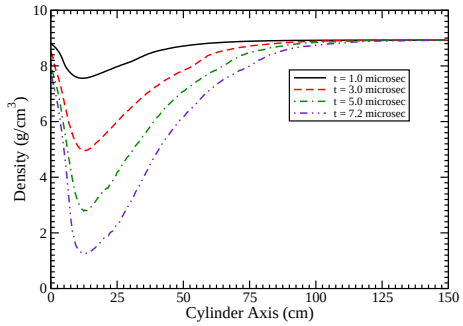

Figure 4: Density vs axis at different times.

In Fig. 1 we present the specific energy deposition profiles along the axial direction (r = 0.0 mm) at different times during the irradiation. It is seen that at t = 1 μs when 40 out of 288 bunches have been delivered, the maximum specific energy deposition is of the order of 1 kJ/g. Subsequent curves show that the specific energy deposition increases with time and at t = 7.2 ns (end of the beam), the maximum specific energy deposition is about 6 kJ/g.

The corresponding temperature profiles are plotted in Fig. 2 which exhibits a behavior similar to that shown in Fig. 1. It is seen that the temperature increases steadily while a maximum temperature of about 9000 K is achieved at the end of the pulse. Flat section of each curve shows melting of the material in that region. The pressure profiles are shown in Fig. 3. It is seen that a maximum pressure of about 3.5 GPa is generated at t = 1 μs which launches an outgoing compression wave which leads to density depletion at the axis, as seen in Fig. 4. This causes deeper penetration of the protons that are delivered in the subsequent bunches. This is a very important effect from the point of view of the machine protection.

Ion Source Development and Operation

P. Spädtke, A. Adonin, B. Gutermuth, F. Heymach, R. Hollinger, R. Lang, J. Mäder, F. Maimone, K. Ochs, J. Roßbach, P. Schäffer, S. Schäffer, M. Stork, K. Tinschert, C. Vierheller, and S. Zulauf
GSI, Darmstadt, Germany

High Charge State Injector HLI

Regular operation of the CAPRICE ECR ion source (ECRIS) at the High Charge State Injector (HLI) was performed for the ion species listed in the table below:

Table 1: Ion beams delivered from the HLI in 2010.

Ion species	Auxiliary gas	Duration (days)	Analyzed intensity (eμA)
$^{4}He^{1+}$	He	2	60
$^{12}C^{2+}$	O_2	7	60
$^{14}N^{2+}$	He	6	250
$^{24}Mg^{5+}$	He	11	60
$^{40}Ar^{8+}$	He	6	130
$^{48}Ca^{10+}$	He	72	85
$^{64}Ni^{9+}$	He	46	45
$^{86}Kr^{12+}$	O_2	8	30

Beams of $^{4}He^{1+}$ and of $^{40}Ar^{8+}$ were exclusively used for some periods of commissioning of the new RFQ structure at the HLI. $^{12}C^{2+}$ was provided for biophysics experiments at the SIS under therapy conditions and for biophysics experiments at the UNILAC. For the first time a $^{14}N^{2+}$ ion beam was delivered for various biophysics experiments at the SIS and at the UNILAC, respectively.

All other ion beams were produced from highly enriched isotopic materials in standard operation and were dedicated to experiments at the UNILAC. Besides $^{86}Kr^{12+}$ all these beams were used for experiments at SHIP and TASCA, respectively, for investigations in the field of Super Heavy Elements (SHE). In total the beam time for SHE amounts to more than 80 % of the beam time for experiments.

As the SHE experimental programme intends to perform experiments using ^{50}Ti ions as projectiles a dedicated development work to establish the ion beam production from the ECRIS has been started at the ECR injector test setup (EIS). A severe problem with the handling of titanium for the production of ion beams is related to the very high chemical reactivity of its vapor with any material at the temperatures which are required for evaporation. The evaporation is achieved by means of the resistively heated standard oven used for metal ion production with the GSI CAPRICE type ECRIS. It provides the transformation of the solid material into the gaseous state for plasma feeding. Due to the known critical properties of titanium the materials used for the assembly of the standard oven are not appropriate for the evaporation of titanium. Therefore systematic studies were established investigating various configurations of ceramic materials and refractory metals for modified assemblies of the oven. Preliminary results have been obtained but the investigations are ongoing in order to achieve the required stable long time operation at sufficient ion beam intensity.

As the heating of plasma electrons in an ECRIS is provided by introducing microwaves into the plasma chamber the properties of the microwave injection are a crucial parameter for the ion source performance. The tuning of the microwave frequency and the combination of waves of two different frequencies heating the plasma can enhance the ECRIS performance concerning the generation of the extracted ion beam in terms of intensity, beam shape and emittance. In order to analyze these effects, several measurements have been carried out with the CAPRICE-Type ECRIS, installed at the ECR Injector Setup (EIS), by sweeping the frequency in the range of 12.5-16.5 GHz and by using two microwave frequencies for different ion source settings. During the experiments the reflection coefficient, the beam currents of different charge states and the total drain current of the extraction were recorded simultaneously. In addition viewing targets at different positions inside the beam line monitored the beam shape evolution.

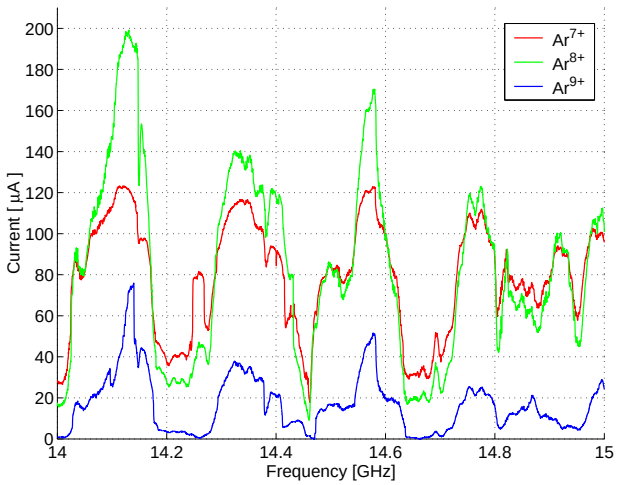

Figure 1: Evolution of the ion currents for 3 different argon charge states with the microwave frequency.

The effect of the frequency tuning is reported in figure 1 which shows the evolution of the Ar^{7+}, Ar^{8+} and Ar^{9+}

beam currents as a function of the microwave frequency. As an example a cutout of 1 GHz width of the whole sweep is shown in the figure. This measurement clearly demonstrates that the frequency and the corresponding electromagnetic field heating the plasma affects the ECRIS performance in terms of an ion current enhancement mainly for the higher charge states. It has to be remarked that during the frequency sweeps all other ion source parameters were kept constant and the measurements were reproducible. By making use of the viewing targets it has been observed that the microwave frequency variation affects also the shape and the emittance of the ion beam [1].

High Current Injector HSI

Table 2: Ion beams delivered from the MUCIS and MEVVA in 2010. For ^{124}Xe, enriched material has been used.

element	duration (days)	Analyzed intensity (emA)
$^{58}Ni^{1+}$	10	3...4
$^{238}U^{4+}$	91	10...20
$^{40}Ar^{1+}$	38	18...22
$^{86}Kr^{2+}$	19	4...6
$^{124}Xe^{2+}$	7	2...4

MEVVA

In 2010 more than 13 weeks of Uranium beam time has been delivered to the accelerator. That is the longest period with the MEVVA ion source we ever have had during one year for Uranium. Stable operation of the ion source VARIS, a specific type of the MEVVA ion source, provided a high intensity uranium beam for the experiments. Compared to earlier beam times the source was operated in a special mode: the plasma electrode was biased to cathode potential. Ions leaving the plasma are preaccelerated with the additional voltage drop within the sheath and will have therefore a lower space charge force in this first region of extraction. With this operation mode the ion source was able to work more than one week without any service interruption. During the Uranium beam time we had improved our service procedure to reduce service time to only two hours to resume regular operation. There was no single ion source failure during the whole beam time. One of the reasons for this was the very successful commissioning of a new, more powerful trigger device (40 kV, 100 A), to ignite the arc current of the source.

MUCIS

A new gas control system for the MUCIS was implemented on the high voltage platform. Operation with a rare isotope (enriched material) of $^{124}Xe^{2+}$ was performed with an extremely low gas flow. In this mode the Xe consumption was as low as 0.1 liters a day at normal pressure. Nevertheless, it was possible to achieve a beam current of up to 12 mA in front of the RFQ, which is its space charge limit.

PIG Ion Source

Using the Penning source we delivered elements covering the full mass range, from singly charged Lithium up to higher charge states of uranium. Depending on the experiment, the duty cycle of the ion source is optimized. The source had to be tuned either for low duty cycle operation for SIS injection or for high duty cycle operation when experiments at UNILAC energies were served.

Table 3: Ion beams delivered from the PIG in 2010.

element	duration (days)	analyzed intensity [eμA]
$^{7}Li^{1+}$	14	100
$^{20}Ne^{1+}$	14	200
$^{40}Ar^{2+}$	32	300
$^{84}Kr^{2+}$	8	500
$^{136}Xe^{6+}$	8	10
$^{152}Sm^{3+}$	47	100
$^{197}Au^{8+}$	30	50...300
$^{238}U^{4+}$	20	400
$^{238}U^{10+}$	20	100

A new dipole chamber for the housing of the ion source has been manufactured, but a longer shut down period is required for installation and commissioning

References

[1] F. Maimone, K. Tinschert, P. Spädtke, J. Mäder, J. Roßbach, R. Lang, L. Celona, Proc. of the 19^{th} International Workshop on ECR Ion Sources, Grenoble, 23-26 August 2010

Development of further heavy elements for MEVVA operation

A. Adonin, R. Hollinger, and P. Spädtke
GSI, Darmstadt, Germany.

The high current ion sources at GSI provide more than 15 elements for acceleration including 8 metallic elements. However, it is of the great interest to enlarge this number especially for heavy elements in the region between ^{181}Ta and ^{238}U in order to increase the experimental capabilities of the GSI facility. It is planned to develop three additional elements for operation with the MEVVA ion source: ^{197}Au, ^{208}Pb and ^{209}Bi. Particular difficulties with these elements are caused by the physical properties. These are soft and fusible elements with low melting point compared to Ta or U. Therefore the ion source operation with high arc discharge current can cause melting of the cathode material. Another important aspect is the metal vapours pressure at the cathode surface that indicates flux of the neutrals to the plasma and it strongly depends on surface temperature.

Since the maximum mass-over-charge ratio of ions injected into the RFQ is 65, the requested charge state for considered elements is 4^+. With low discharge current operation the ion charge state in the spectrum is usually distributed like below: more than 90% of 1^+, less than 10% of 2^+, and a very small fraction of 3^+ (depending on the element, surface quality, confining magnetic field, etc.). In order to shift the ion spectrum to higher charge states, it is necessary to increase the discharge current of vacuum arc in the ion source. But that will cause an increase of the cathode surface temperature and as the result, the flux of the neutrals to the plasma. The increasing neutrals flux dramatically reduces the average charge state of ions in the plasma during the pulse. This process is relatively fast, in 20-30μs after the ignition of the arc the influence of the neutrals on the ion spectrum becomes sufficient, and in 100÷130μs the fraction of 4^+-ions in the plasma is reduced more than 10 times. This time is critical because in the most cases the beam pulses requested for the SIS injection should exceed 150μs in duration.

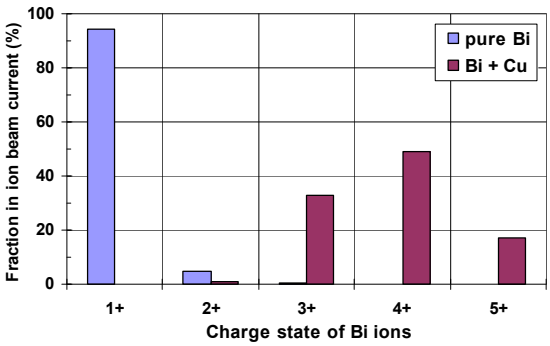

Figure 1: Shift the ion spectrum of Bi to higher charge states by using Bi-Cu cathodes.

The neutral production can be reduced by changing the physical properties of the cathode material, namely by increasing the melting point and reducing vapour pressure on the surface at certain temperature. This can be achieved by using an alloy or a mixture of the desired material with a more refractory metal. As it is well known from the material science, even a small admixture of foreign element can sufficiently change the physical properties of the metal [1]. So this is the matter of finding a proper alloy or a mixture for each of the considered elements (Au, Pb and Bi). Since the admixed material will be also ionized during the arc discharge and the ions will be present in the extracted beam, it is important to choose the element for that the ***M/Q*** ratios are not intersecting with ratios for desired element. Otherwise it would not possible to filter other elements from the desired beam.

The first experimental investigation has been performed with ^{197}Au and ^{209}Bi. Using the cathodes with pure Bi it was not possible to produce 4^+ charge states trying the various operation modes (Fig.1). With discharge current below 400A the plasma density in the ion source was not high enough to produce 4^+, and with discharge current above 400A the neutrals flux became very high and destroyed the high charge states. To check how the situation can be improved a few cathodes containing Bi with small admixture of Cu (between 8% and 15%) were manufactured. Fig.2 shows the structure of the cathode material, so one can see that this was not an alloy but the mixture of two metals. However the situation was dramatically improved. It became possible to increase vacuum arc discharge current up to 900A and shift the maximum of ion spectrum distribution to 4^+ (Fig.1). With Bi-Cu cathodes we obtained the ion beam currents up to 12mA of Bi^{4+} in front of the RFQ with pulse length of 250μs in 1Hz mode. The Cu fraction in the ion spectrum was less than 10%. That is quite good and sufficient for high current SIS operation.

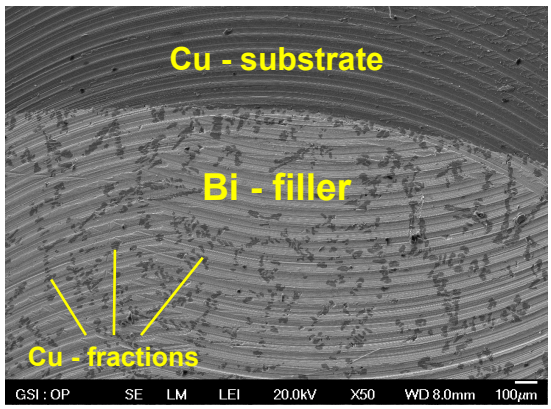

Figure 2: Image of the longitudinal section of Bi-Cu cathode taken with a scanning electron microscope.

The experiments with pure Au cathodes gave better results then with pure Bi. However the effect of increasing neutrals flux did not allow to see 4^+ charge states in the ion spectrum after 150μs after vacuum arc ignition process. Therefore the best results achieved with pure Au cathodes were the ion beam current of 4.5mA of Au^{4+} in front of the RFQ with pulse length of 150μs in 1Hz mode.

As a next step it is planned to test different mixture types of Bi with Cu and find the optimum material composition for the cathodes. Also to test the alloys of Au with small amounts of Zr, Fe or Ta, that looks quite promising from the material properties point of view.

References

[1] Colin J. Smithells: Metals Reference Book, London, Butterworths, 1967.

Characterization of a Non-Intensified Ionization Profile Monitor @ UNILAC

F. Becker[1], *C. Andre*[1], *T. Giacomini*[1], *P. Forck*[1], *B. Walasek-Höhne*[1], *P. Abbon*[2], *J. Egberts*[2], *F. Jeanneau*[2], *J. Marroncle*[2], *J.-P. Mols*[2], *T. Papaevangelou*[2]

[1]GSI, D-64291 Darmstadt, Germany; [2]Centre CEA de Saclay, F- 91191, France

Introduction & Experimental Focus

For the operation of the FAIR accelerators, non-destructive beam diagnostics will be essential. At GSI two almost complementary gas-based methods for profile determination have been realized and investigated during the last decade. For ultra high vacuum conditions in synchrotrons an intensified Ionization Profile Monitor (IPM) was developed [1]. It is installed at GSI SIS-18 and ESR as well as at COSY (FZ-Jülich). For the installation in transport-lines, the Beam Induced Fluorescence BIF-monitor, using an image intensifier has been investigated in detail [2]. Meanwhile there are four BIF-stations in operation at the UNILAC. There is a certain overlap in the field of application, so that non-intensified IPMs with electrical readout might be a robust alternative for transfer-lines. Furthermore they are more radiation tolerant.

Within a collaboration between CEA-Saclay and GSI-BD an IPM prototype, designed for the IFMIF/EVEDA facility [3] was characterized at the UNILAC X2-beamline for various beam and gas conditions [4].

Experimental Results & Outlook

The tested stripline-IPM consists of a 55x61 mm^2 field-box (Fig. 1) with a switchable $\pm$ 5 kV extraction voltage for either gas-ion or electron detection and field inhomogeneities $\leq$ 4 %. 32 striplines on a 40 mm wide active area are attached to transimpendance, integrating or logarithmic amplifiers, multiplexed to an 8-bit 1 GHz ADC.

The IPM worked reliably for 1,7 mA U^{28+} and 1,1 mA Xe^{21+}-beams @ 4,8 MeV/u. As compared to the BIF-monitor, mounted at the same position, the IPM is about one order of magnitude more sensitive. Beam profiles recorded with both detectors agree very well for the investigated rare gases and nitrogen, see Figure 2. The relative differences in the recorded beam width σ are below 5 %. A slight energy drift during the six hours machine run might be the reason for decreasing beam width from N_2 to Xe. More details about this experiment can be found in [4].

Further development of a non-intensified IPM as an alternative profile monitor for transport sections is proposed.

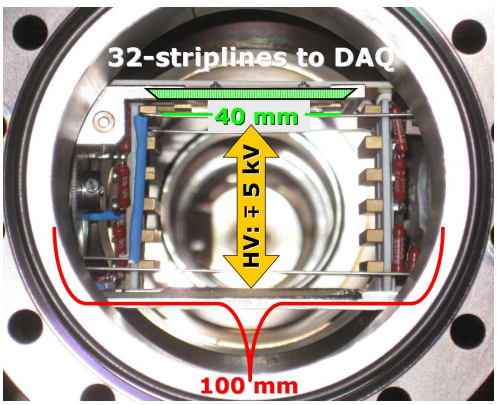

Figure 1: Photograph of the IPM, mounted inside the diagnostic chamber (ø = 100 mm). The E-field produced in the field-box points perpendicularly to the beam direction.

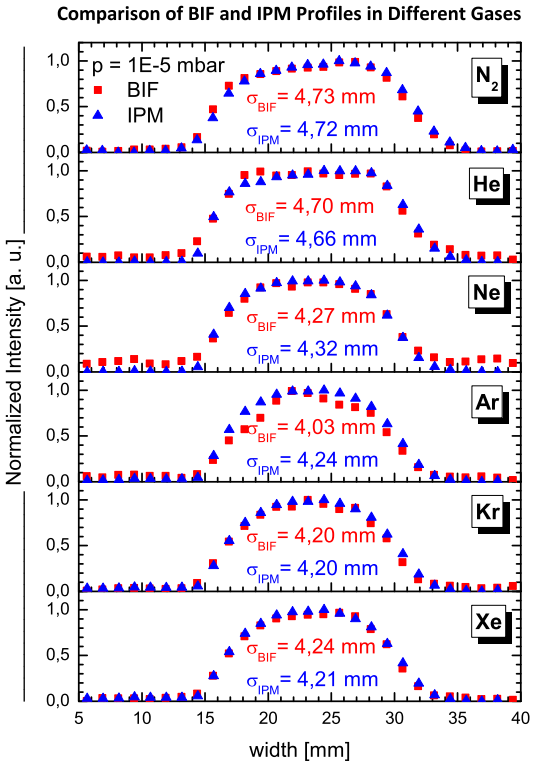

Figure 2: Normalized beam profiles (BIF and IPM) in different gases at $1{\cdot}10^{-5}$ mbar (averaged over 300 Xe^{21+}-pulses of 1,1 mA and 250 μs pulse length). 172 BIF pixels were smoothed with a 20 points 3^{rd}-order Savitzky-Golay filter and interpolated to the 32 IPM-channels (28 displayed here). σ was calculated within 15-35 mm ROI.

References

[1] T. Giacomini et al., "Improving the Reliability of an IPM", DIPAC'05 (POT004), Lyon, 2005, p. 150-152.

[2] F. Becker et al., "BIF-Monitor - Imaging Spectroscopy of Different Gases", DIPAC'09 (TUPB02), Basel, 2009, p. 161.

[3] A. Mosnier et al., "Development of the IFMIF/EVEDA Accelerator", PAC'09 (TU2RAI01), Vancouver, 2009, p. 663.

[4] J. Egberts et al., proceedings of DIPAC'11, Hamburg, 2011.

Characterization of the Nuclear-wide γH2AX Response after Ion Irradiation*

B. Meyer[1], KO. Voss[1], B. Jakob[1], M. Herrlitz[1], G. Becker[1], M. Durante[1,2] and G. Taucher-Scholz[1]

[1]GSI, Darmstadt, Germany; [2]TUD, Darmstadt, Germany.

Introduction

The phosphorylation of H2AX at DNA lesions is one of the most widely analyzed responses to DNA damage. We recently described a novel nuclear-wide formation of phosphorylated H2AX (γH2AX) occurring after ion irradiation and the method we utilize to evaluate γH2AX intensity [1]. As a first step we start to characterize the response with respect to specificity, causation and dose.

Results

The specificity of the response was demonstrated by a lack of signal in $H2AX^{-/-}$ cells after Au ion irradiation. Additionally, extraction of soluble protein before fixation did not change the signal which indicates that H2AX is directly phosphorylated in the entire chromatin and not diffusing through the nucleus from damage sites (data not shown). Subsequently, we checked that hitting the cell nucleus is a requisite for inducing the response as cytoplasmatic targeting with 1 Au ion using the microbeam did not induce the pan-nuclear H2AX phosphorylation (Fig. 1).

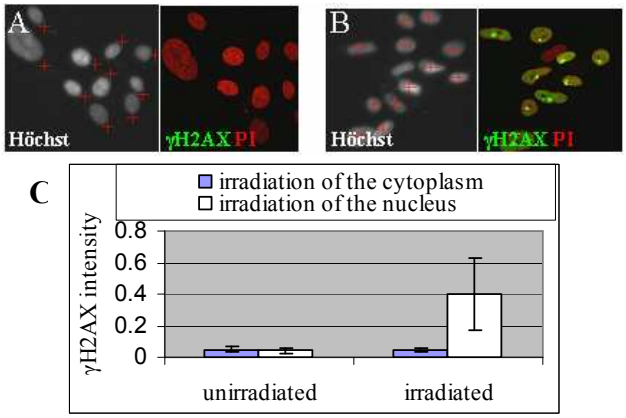

Figure 1: Human fibroblasts were irradiated in the nucleus (A) or cytoplasm (B) with 1 Au ion (12800 keV/µm, 4.8 MeV/u), fixed 1h after irradiation and stained for γH2AX and propidium iodide (PI); γH2AX intensity was analyzed (C).

The response is active in all cell cycle phases with a tendency to lower signals in G2 which was analyzed by using the G2 marker CENPF (data not shown). We utilized Annexin staining to test whether the H2AX phosphorylation is connected to the induction of apoptosis as described by Solier and Pommier [2.] Up to 24h after irradiation human fibroblasts are Annexin negative (Fig. 2) which indicates that initiation of cell death is not the cause for the pan-nuclear response after ion irradiation.

* Work supported by BMBF Grant 02NUK001A

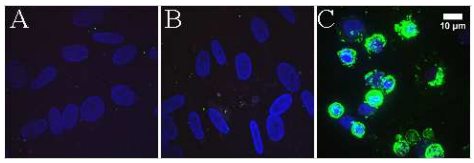

Figure 2: Human fibroblasts were irradiated with Au ions (13050 keV/µm, 4.6 MeV/u, $3 \cdot 10^6 p/cm^2$) and fixed 1 h (A) and 24 h (B) after irradiation. (C) Positive control: human lymphocytes were fixed 24 h after x-ray irradiation (10 Gy); cells were stained with Annexin (green), Hoechst (blue) and PI (red).

We analyzed whether phosphorylated forms of other repair proteins that could bind to γH2AX would also form a pan-nuclear signal. However, only a very faint pan-nuclear signal of pATM (S1981), pDNA-PK (S2056), pRPA (S4/S8) and pNBS1 (S343) was detected (data not shown). To test whether the γH2AX response occurs only at high doses or a threshold dose is needed we irradiated human fibroblasts with different numbers of carbon ions using the heavy ion microprobe. As shown in Fig. 3 there is a linear increase of the pan-nuclear signal at low doses without a threshold dose.

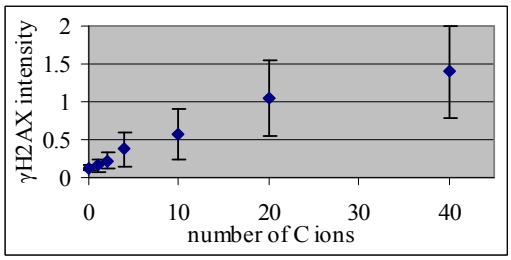

Figure 3: Human fibroblasts were irradiated with different numbers of carbon ions (290 keV/µm, 4.8 MeV/u) and fixed 1h after irradiation; γH2AX intensity was measured.

Conclusion

Here we show that the nuclear-wide H2AX phosphorylation occurs in the chromatin as a response to ion irradiation of the cell nucleus. It is different from the described pan-nuclear γH2AX responses as signs of apoptosis and an intense pan-phosphorylation of other repair proteins is missing in human fibroblasts. The response is found in all cell cycle phases and is directly dependent on dose. The evaluation of its regulation as well as LET and time dependency are the matter of further studies.

References

[1] B. Meyer et al. GSI Scientific Report 2009, 2010, p.465

[2] S. Solier and Y. Pommier Cell Cycle 2009, 8:12, 1853-1859

ChIP-Seq genome wide analysis of γH2AX induced by X-rays or heavy ions*

F. Natale[1,2,#], A. Rapp[3], A. Gogol-Doering[4], W. Chen[4], M. Durante[1,2,3], G. Taucher-Scholz[2] and M. C. Cardoso[3]

[1]FIAS, Frankfurt; [2]GSI, Darmstadt; [3]Technische Universität Darmstadt; [4]MDC, Berlin

Introduction

Heavy ions are extensively used at GSI as a tool to study DNA repair processes and chromatin structure dynamics. Ionizing radiation (IR) produces DNA double strand breaks (DSB) triggering the DNA damage response (DDR). One of the earliest events of DDR consists of the extensive phosphorylation of H2AX histone variant (γH2AX), whose distribution throughout the genome appears to be non-random[1]. γH2AX spreads through megabases from the DNA DSB and its distribution has been reported to be uneven and asymmetric[2]. However, in previous experiments DNA DSB had been induced by enzymes. Whilst this offers some advantages (e.g. position of DNA damage is known), on the other hand this method can be biased by efficiency and limiting factors (e.g. DNA damage induction cannot be quenched). Moreover, IR-induced DSB may be qualitatively different from those introduced enzymatically into the genome. Although it has been proposed that chromatin density as well as cellular metabolism (e.g. transcription[2]) may regulate the γH2AX spreading, there is little evidence of such a mechanism on a genome scale.

Next generation sequencing technologies offer the possibility to address issues on a genome scale. Coupling such high-throughput technology to chromatin immunoprecipitation (ChIP) provides a powerful tool (ChIP-Seq) to map the position of the desired target throughout the genome.

We are using ChIP-Seq to provide a genome scale precise map of IR-induced γH2AX. Our goal is to describe how such histone modification propagates in the context of chromatin density.

Methods

DNA DSBs and, consequently, γH2AX signals are induced in HepG2 cells by irradiating cells with both X-rays and 1 GeV/n nickel ions. After fixation, lysis and chromatin shearing, ChIP is performed to select H2AX / γH2AX-enriched chromatin fractions. Following a multistep biochemical procedure§, the DNA collected from the H2AX / γH2AX-enriched chromatin fractions is converted to "libraries" and sequenced. The sequences are then compared to the human genome sequence (reference). The abundance of a certain sequence is proportional to the abundance of the target being enriched (H2AX / γH2AX) by the ChIP process, thus quantitatively reflecting the position of the target itself into the genome.

Preliminary Results and Perspectives

γH2AX libraries were produced from samples exposed to IR or mock-irradiation and incubated 30 min, when the maximum signal is achieved. H2AX and H3 libraries were produced to normalise the data. γH2AX libraries from irradiated samples yielded a significantly higher number of sequences (Fig.1, left) when compared to unirradiated samples, confirming the increase of γH2AX levels following irradiation. As expected, no significant differences are observed in the sequence number from H2AX and H3 libraries (Fig.1, right).

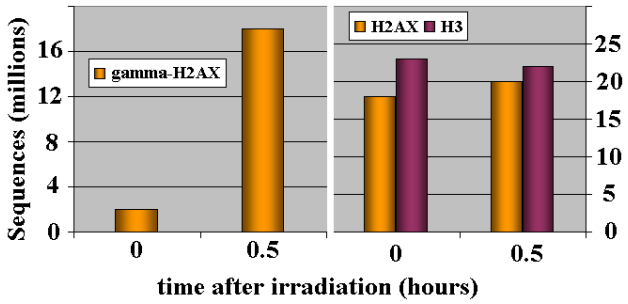

Figure 1: Number of sequences of γH2AX, H2AX and H3 libraries from unirradiated and irradiated samples (only X-rays data are presented).

Ongoing investigation is focused on the characterization of the chromatin domains corresponding to the obtained sequences. Histone modifications and gene density are being addressed, taking advantage of on-line database information. Preliminary analysis suggests that γH2AX signature is excluded from gene-poor, transcriptionally inactive chromatin. Heavy ion irradiation data are currently under analysis

To conclude, by coupling IRs to ChIP-Seq we will be able to provide a detailed genome scale distribution of γH2AX and describe how such histone modification propagates in the context of diverse chromatin features.

References

[1] J. Bewersdorf et al., "H2AX chromatin structures and their response to DNA damage revealed by 4Pi microscopy", PNAS. 2006

[2] J. S. Jacovoni *et al.*, "High-resolution profiling of gamma-H2AX around DNA double strand breaks in the mammalian genome", EMBO J. 2010

* Work supported by Beilstein Stiftung (NanoL project)

§ http://grcf.jhmi.edu/hts/protocols/11257047_ChIP_Sample_Prep.pdf

f.natale@gsi.de

Design and validation of a microscopic Förster Resonance Energy Transfer setup to measure protein interactions*

F. Tobias[1], R. Khan[1], A. L. Leifke[1], M. Durante[1,2], B. Jakob[1], and G. Taucher-Scholz[1]

[1]GSI, Darmstadt, Germany; [2]Technische Universität Darmstadt, Institut für Festkörperphysik, Darmstadt, Germany

Introduction

In the cellular response to ionizing radiation a complex network of molecular pathways is activated leading to endpoints like repair, cell cycle arrest or apoptosis. Protein interactions constitute a fundamental process in these responses, but it is highly challenging to make them experimentally accessible. With the use of GFP and the production of numerous kinds of fluorescent derivates it became possible to measure Förster Resonance Energy Transfer (FRET) between fluorescently labelled proteins in living cells. Here we describe a setup to measure FRET by detecting fluorescence polarization anisotropy. The setup was then validated with live cell measurements of GFP and mCherry constructs.

Results

Design of the setup

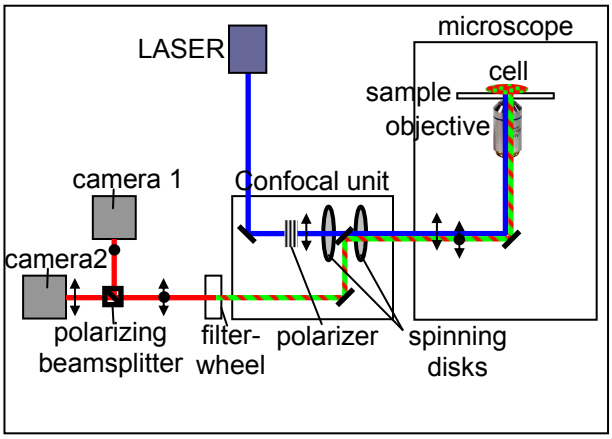

Figure 1: Experimental FRET setup.

The experimental setup is based on a Nikon TiE inverted microscope equipped with 488 nm and 561 nm LASERs, a Yokogawa CSU-X1 confocal spinning disk unit and an image splitter with two Andor EMCCD cameras (Figure 1). A polarizer is placed in the excitation light path right before the first spinning disk within the CSU-X1. Hence the fluorescence is excited with linear polarized light. A polarizing beamsplitter is used in the emission light pass after the CSU-X1 and a filter wheel. The two different polarization components of the emission light are separated and directed to two different cameras. The images of both cameras are used to calculate fluorescence polarization anisotropies. FRET is detectable by a reduction in the fluorescence polarization anisotropy [1]. This technique prevents false positives, as it is less sensitive to excitation and emission crosstalk than other FRET techniques and has all the advantages of a confocal spinning disk microscope for live cell applications.

Live cell measurements

To validate the system for live cell applications cells were either transiently transfected with GFP only, with GFP linked to mCherry by 13 amino acids (GFP-mCherry) or cotransfected with GFP and mCherry †. Only in the case of GFP-mCherry the chromophores get close enough for FRET to occur. As expected, cells transfected with GFP-mCherry showed a clear reduction in the fluorescence polarization anisotropy compared to GFP only and co-transfection of GFP and mCherry (Figure 2). Hence this confocal spinning disk setup is well suited to measure FRET by fluorescence polarization anisotropy.

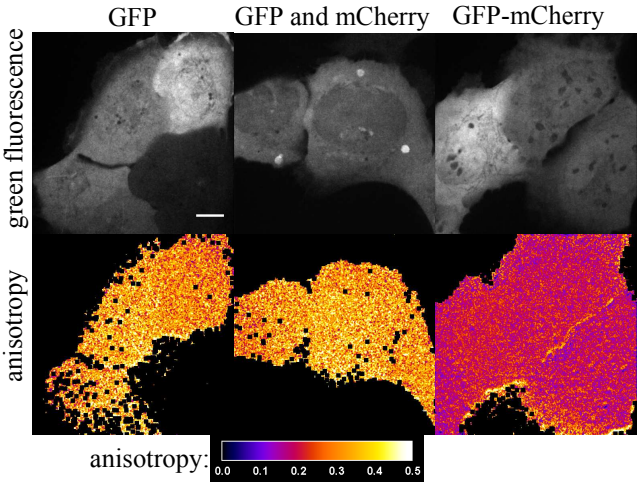

Figure 2: FRET measurements of U2OS cells transfected with GFP only, GFP-mCherry or cotransfected with GFP and mCherry. Scalebar 10 µm.

Conclusion

A microscopic setup was established that enables the measurement of protein interactions and will be used in DNA damage response studies in living cells.

References

[1] Piston, D. W. & Rizzo, M. A. FRET by fluorescence polarization microscopy Methods in Cell Biology, 2008, 85, 415-430

* Work supported by BMBF Grant 02NUK001A

† Plasmids were kindly provided by S. V. Kozlov, Queensland Institute of Medical Research, Australia

DNA Damage after High-LET Exposure

M. Ensminger[1], S. Conrad[1], A. Beucher[1], G. Taucher-Scholz[2] and M. Löbrich[1]
[1]Darmstadt University of Technology, Germany; [2]GSI, Darmstadt, Germany

It has been known for several years that DNA double strand breaks (DSBs) evoked by particle radiation are generally more slowly repaired than breaks induced by photon irradiation. Moreover, the fraction of residual breaks after prolonged repair incubation correlates with the cell killing capacity of high-LET radiation. However, the understanding of the molecular processes is still incomplete.

In this study we focus on the complexity of DSBs induced by heavy ions. Owing to the high ionisation density of high-LET particles, heavy ion irradiation induces DSBs that are generally more complex with additional lesions in very close proximity to the DSB. Recently we have reported that complex breaks require processing before repair, performed by the nuclease Artemis that is operating in a common repair pathway with the kinase ATM. Cells deficient in one of these factors are specifically defective in the repair of DSBs with slow repair kinetics and the level of unrepaired breaks seems to depend upon the complexity of the DSB ends. After α-particle irradiation a higher proportion of DSBs is repaired in an ATM and Artemis dependent manner than after X-irradiation. By contrast ATM and Artemis are dispensable for the repair of "clean" DSBs induced by the topoisomerase II inhibitor etoposide [1, 2].

To determine the amount of complex DSBs after heavy ions, we irradiated stationary wildtype (82-6 hTert) and Artemis deficient cells (CJ hTert) with ^{12}C (LET: 170keV/μm) ions using the UNILAC at the GSI. The repair of the DSBs was observed by PFGE analysis and compared to the repair after similar X-ray doses. The data demonstrate that DSBs induced by ^{12}C ions are more slowly repaired than breaks after X-irradiation. Furthermore, the level of unrepaired DSBs in Artemis defective cells compared to wildtype cells is higher after ^{12}C ions. While Artemis deficient cells exhibit only a very small repair defect after X-rays (≤10%), they show more than 30% unrepaired DSBs after ^{12}C ions (Fig.1A).

To confirm our results with another approach we established a γH2AX immunofluorescence assay for analysing DSB repair after high-LET irradiation. Here, human wildtype (HSF1), Artemis (CJ179) and BRCA2 (HSC62) defective cells were seeded on cover slips and irradiated with ^{12}C ions under a small angle to the beam. γH2AX foci along the ion tracks were analysed in G1 and G2 cells and compared to γH2AX foci numbers after X-irradiation. Similar to the results of the PFGE analysis we observed faster DSB repair kinetics after X-rays compared to ^{12}C ions. Moreover, the high repair defect in Artemis deficient cells was also detected with this approach (Fig.1B) therefore supporting our notion of a high proportion of complex DSBs after high-LET irradiation.

BRCA2 defectiv cells are impaired in homologues recombination (HR). Whereas the DSB repair in these cells is not affected after X-irradiation in G1 phase, they exhibit a small repair defect in G2. This defect is comparable to the one observed in Artemis deficent cells and indeed Artemis dependent DSBs after X-rays are repaired via HR in G2 [2]. Also after ^{12}C ions, BRCA2 defectiv cells show a repair defect in G2 that is similar to Artemis deficient cells (Fig. 1C). This demonstrates that a high amount of complex DSBs after high-LET irradiation is repaired via HR in G2. Interestingly, the level of unrepaired DSBs is sligthly higher in Artemis cells indicating that Artemis also contributes to some extent to repair processes via non-homologues end-joinig in G2 phase.

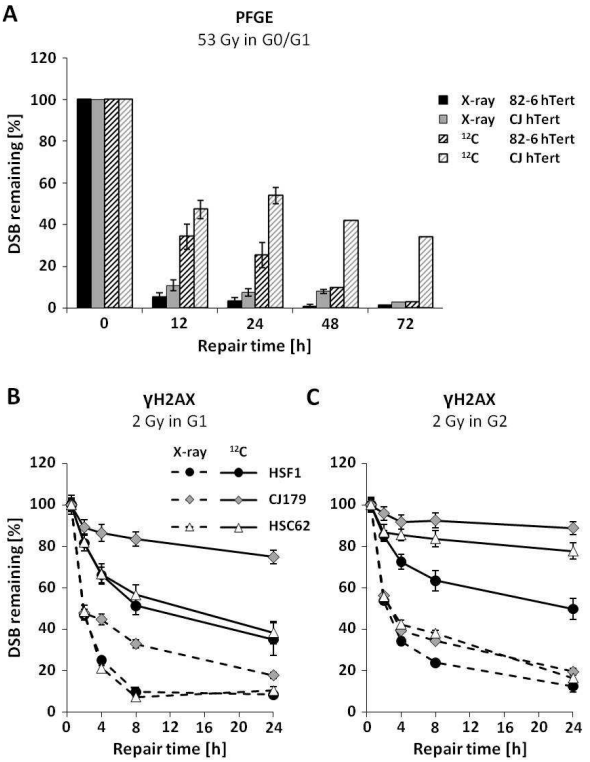

Fig.1: DSB repair in wildtype (82-6 hTert, HSF1), Artemis (CJ hTert, CJ179) and BRCA2 (HSC62) deficient cells after X-rays or ^{12}C ions measured by PFGE in G0/G1 (A) or γH2AX immunofluorescence in G1 (B) and G2.

References

[1] E. Riballo, M. Kühne, N. Rief, A. Doherty, et al., Molecular Cell 16 (2004) 715-724
[2] A. Beucher, J. Birraux, L. Tchouandong, O. Barton et al., EMBO J. 28 (2009) 3413-3427

DNA lesions within the heterochromatin elicit fast damage response and are re-located to euchromatic regions *

M. Beuke[1], Iris Müller[1], B. Jakob[1], J. Splinter[1], K.-O. Voss[1], B. Merk[1], G. Becker[1], M. Durante[1,2], G. Taucher-Scholz[1]

[1]GSI, Darmstadt, Germany; [2]TUD, Darmstadt, Germany

DNA is highly compacted by wrapping around histones and folding into higher order structures building chromatin. This chromatin can be subdivided in two classes: the highly transcriptional active, sparse euchromatin and the densely packed heterochromatin. The heterochromatin is transcriptionally inert but essential for the regulation of the gene expression and the entire architecture of the nucleus [1]. Here, we studied the DNA damage response within the heterochromatin. The distinct delimitation of euchromatin and heterochromatin in embryonic mouse fibroblasts, forming heterochromatic chromocenters, enabled us to clearly distinguish between these two chromatin fractions. For an aimed irradiation of the chromocenters with single ions we made use of the unique submicrometer resolution of the GSI microprobe.

Results and Discussion

Previous work in our group (Splinter MS in preparation) indicated that, against the widely held belief, there is damage induced H2AX phosphorylation in heterochromatin after ion irradiation, accompanied by a local decondensation at the sites of ion hits. Moreover we observed a damage relocation of initially central hit chromocenters toward their periphery within the first 20 minutes after damage induction. In order to confirm this relocation process over a more extended time period, we targeted the chromocenters with single ions and fixed our samples after 2 to 45 minutes post irradiation.

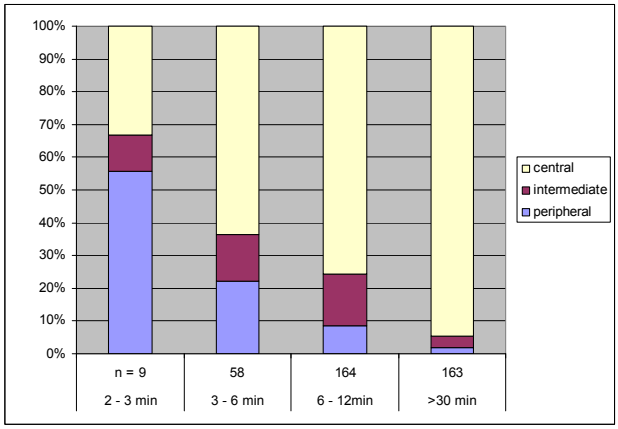

Figure 1: MEF wt cells, chromocenters were irradiated with Ni ions (4.8MeV/u; LET 3800 keV/µm) at the GSI microprobe and fixed after the indicated times post irradiation.

For analysis we divided the γH2AX-tracks in three classes: (i) centrally located tracks, where the damage marker signal peak is totally enclosed by bright DNA staining, (ii) intermediately located tracks which are only in part enclosed depending on the direction of the intensity profile and (iii) peripherally located tracks which generally flank the chromocenter. We monitored these γH2AX-tracks and observe a decrease in the central and intermediate fraction in favour of the peripheral fraction within the first half hour after damage induction (Fig. 1).

This shift of tracks and the decrease of DNA density at the site of traversal (Fig. 2) as a potential driving force lead us to the conclusion that the DNA damage induced within the chromocenter is relocated to its periphery for damage repair.

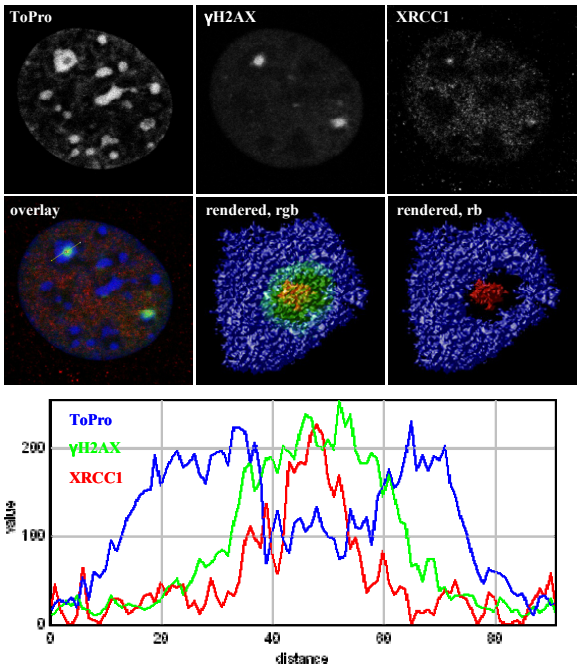

Figure 2: MEF wt cells, irradiated with Au ions, 4.8 MeV/u, 12815 keV/µm, targeted at chromocenters at the GSI microprobe, fixed 12 min post irradiation. The DNA-density in the area of this centrally hit chromocenter decreases considerably.

References

[1] A.A. Goodarzi et al., The influence of heterochromatin on DNA double strand break repair : Getting the strong, silent type to relax, DNA Repair 9 (2010) 1273-1282

*This work was partly supported by BMBF contract [02NUK001A].

Human Glioblastoma slice cultures for the evaluation of heavy ion therapy

F. Merz[1], G. Taucher-Scholz[2], M. Durante[2,3], F. Gaunitz[5], K. Schopow[6], H. Stoecker[2,4] and I. Bechmann[1,4#]

[1]Institute of Anatomy, University of Leipzig, [2] GSI, Darmstadt, Germany, [3] Technical University Darmstadt, [4] Frankfurt Institute for Advanced Studies, [5]Klinik und Poliklinik für Neurochirurgie, Universitätsklinikum Leipzig, [6]Dr.Senckenbergische Stiftung, Frankfurt

Introduction

Glioblastoma is among the most common lethal tumors with an average life expectancy of less than 18 month after diagnosis and little success in the recent decades.

Current research often employs immortalized cell lines or primary cells derived from tumor resections, but it is difficult to directly relate observations to the human disease and to develop accurate or even individualized therapeutic strategies based on such experiments. Using human brain slice cultures obtained from epilepsy surgery, we have shown that non-malignant human, but not mouse cells (Walczak et al., 1999; Nitsch et al. 2000) are susceptible to lysis by the tumor-necrosis-factor-related-apoptosis-inducing ligand (TRAIL). This exemplified the need for the development of human test systems for the evaluation of toxicity and preclinical research, (Dowsing T, Kendall MJ 2007; Kenter MJ, Cohen AF 2006). Here, we established similar slice cultures from human glioblastomas directly upon the surgical elimination and irradiated them with carbon ions at GSI. This approach should help determining effects of heavy ions (HI) on human tumors and help understanding their escape mechanisms.

Experimental Setup

Tissue slice preparation

Brain tumor biopsies were obtained from surgery and slice cultures were prepared using a vibratome at a thickness of 300 µm. Slices were then transferred to membrane culture inserts in 6-well-plates and cultivated on a liquid-air-interface.

Histology

After several time points, slices were fixed in 4% paraformaldehyde and processed for paraffin embedding. Paraffin sections (6 µm) were stained with hematoxilin/eosin for histology.

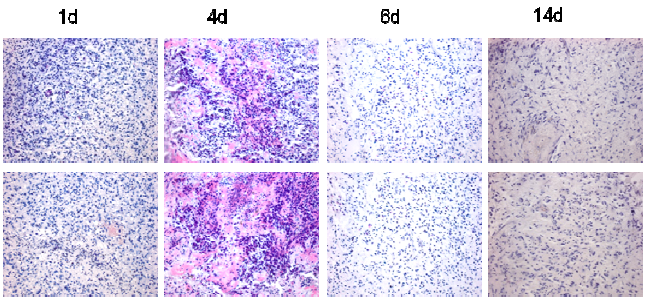

Figure 1: Histology of human GBM slice cultures at various times in vitro. Paraffin sections (6µm), H/E staining.

Immunohistochemistry

Sections were stained with antibodies for proliferation (Ki67), apoptosis (Caspase 3), or DNA damage (γH2AX)

Irradiation

In a pilot experiment, brain tumor slices were irradiated at SIS with a dose of 4 Gy of carbon ions (spread-out bragg peak) and fixed after 1 or 24 h (Mueller et al., 2010, Merz et al., 2010). Cryosections were produced and stained as described above.

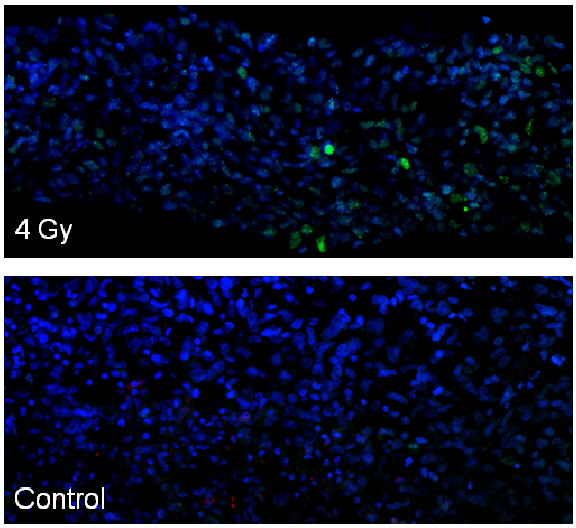

Figure 2: DNA damage in human GBM slice cultures 1h after Carbon irradiation. Cryosections (16µm); green: DNA DSBs (γH2AX), blue: Nuclei

Conclusion

We have established a system allowing us to cultivate human brain tumor tissue and maintaining the typical tumor phenotype over at least two weeks. This enables us to perform examinations such as irradiation or treatment with chemotherapeutics. With this model system, we can ex vivo test HI effects on tumor tissues with the ultimate goal to provide personalized treatment regimes.

References

[1] Walczak *et al*, Nat Med (1999) 5(2):157-63
[2] Nitsch *et al*, Lancet (2000) 356(9232):827-8
[3] Dowsing *et al*, J Clin Pharm Ther (2007) 2(3):203-7
[4] Kenter *et al*, Lancet (2006) 368(9544):1387-91
[5] Merz *et al*, Radiat Environ Biophys (2010) 49(3):457-62
[6] Mueller *et al*, EPJD (2010) 60(1):171-176

#Ingo.Bechmann@medizin.uni-leipzig.de

Live Cell Observations: Velocity of NBS1 Recruitment to DNA Double Strand Breaks Does Not Depend on Ku80 or 53BP1

N. B. Averbeck[1], B. Jakob[1], A. L. Leifke[1], M. Durante[1,2], G. Taucher-Scholz[1]

[1]GSI Helmholtzzentrum für Schwerionenforschung GmbH, Darmstadt, Germany;
[2]TUD, Institut für Festkörperphysik, Darmstadt, Germany

We study the spatiotemporal behaviour of DNA repair factors during and shortly after ion irradiation within living cells. Charged particle irradiation is an outstanding tool to study DNA double strand break (DSB) repair as due to its dose deposition it generates distinct sites of DNA damage [1].

Here we investigated the influence of the DNA repair factors Ku80 and 53BP1, which are involved in DSB end stability [2, 3, 4], on the rate of DSB recruitment of GFP - tagged NBS1. The latter itself represents a member of a DSB end stabilizing complex, the MRN complex [5]. NBS1 is recruited very early to DSBs after DNA damage occurred [6]. In order to study the influence of Ku80 and 53BP1 on NBS1-2GFP recruitment to DSBs we decreased their availability within the cells [human osteosarcoma cells (U2OS) stably expressing NBS1-2GFP] by the siRNA knock down technique (Figure 1).

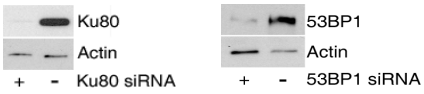

Figure 1: Successful knock down of Ku80 and 53BP1. Western analysis of Ku80, 53BP1 siRNA (+), and mock treated (-) cells. The same amount of protein was loaded per lane; actin served as a loading control.

Live cells were irradiated and monitored (up to 13 min post irradiation) at the beamline microscope. For the Ku80 knock down experiment cells were irradiated with ^{20}Ne ions (UNILAC, 11.4 MeV/u, Fluence: 3 x 10^6 p/cm^2, LET: 462 keV/µm) and with ^{64}Ni ions (SIS, 500 MeV/u, Fluence: 2 x 10^6 p/cm^2, LET: 195 keV/µm) for the 53BP1 knock down experiment. The velocity of the NBS1-2GFP recruitment neither depends on the DSB stabilizing effect of Ku80 nor has 53BP1 any influence (Figure 2). However, it seems to depend on the LET and thus, complexity of the caused damage as with increasing LET NBS1-2GFP appears to be recruited faster (Figure 2).

Taken together, from these results several intriguing questions arise. Namely, how NBS1 can speed up and whether there exist a speed limit for NBS1. And last but not least whether the other components of the MRN complex, MRE11 and RAD50, show a similar behaviour.

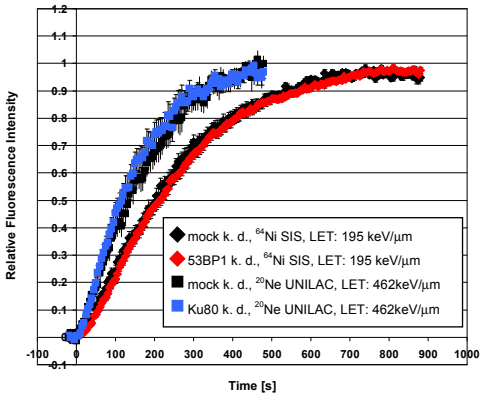

Figure 2: DSB recruitment kinetics of NBS1-2GFP upon ^{20}Ne and ^{64}Ni ion irradiation. The cells were mock treated and Ku80 and 53BP1 siRNA treated, respectively.

References

[1] F. Tobias *et al.*, "Spatiotemporal analysis of DNA repair using charged particle radiation" (2010) Mutation Research, vol. 704, p. 54 - 60

[2] E. Soutoglou *et al.*, "Positional stability of single double-strand breaks in mammalian cells" (2007) Nat. Cell Biol., vol. 9, p. 675 - 682

[3] N. Dimitrova *et al.*, "53BP1 promotes non-homologous end joining of telomeres by increasing chromatin mobility" (2008) Nature, vol. 456, p. 524 - 528

[4] S. Difilippatonio *et al.*, "53BP1 facilitates long-range DNA end-joining during V(D)J recombination" (2008) Nature, vol. 456, p. 529 – 533

[5] R. S. Williams *et al.*, "Mre11 Dimers Coordinate DNA End Bridging and Nuclease Processing in Double-Strand-Break Repair" (2008) Cell, vol. 135, p. 97 - 109

[6] B. Jakob *et al.*, "Live cell microscopy analysis of radiation-induced DNA double-strand break motion" (2009) PNAS, vol. 106, p. 3172 -3177

Acknoledgements

We want to thank Claudia Lukas (University of Kopenhagen, Denmark) for providing the U2OS-NBS1-2-GFP cells. This work is partially funded by BMBF grand 02NUK001A.

RBE of heavy ions for producing chromosome aberrations in human lymphocytes: metaphase versus G_2-PCC analysis*

R. Lee[1], E. Nasonova[1,2], C. Hartel[1], P. Hessel[1], D. Szypkowski[1], M. Durante[1,3] and S. Ritter[1,#]

[1]GSI, Darmstadt, Germany; [2]JINR, Dubna, Russia; [3]TU Darmstadt, Darmstadt, Germany

The analysis of chromosome aberration in peripheral blood lymphocytes is a sensitive and frequently applied method to assess the individual dose following accidental, occupational or medical exposure to ionizing radiation. According to the standard protocol [1], lymphocytes are cultured *in vitro* for 48 h. Then, metaphases are harvested and chromosome aberrations are scored with the expectation that the data are representative of the whole cell population. However, we and others have shown that this protocol is not reliable in the case of high LET exposure [2, 3 and references therein]. Heavy ions induce a severe G_2-arrest and the measurement of aberrations in metaphases at 48 h will result in very low RBE estimates, because heavily damaged cells are drastically delayed in cell cycle and are not included in the analysis.

To overcome this problem, the measurement of aberrations in G_2-cells collected at 48 h by chemically-induced premature chromosome condensation (PCC) has been proposed [4]. However, up to now little is known about the LET-dependence of the G_2-arrest in human lymphocytes and it has not been experimentally demonstrated to what extent the PCC-assay at 48 h post-irradiation accounts for high LET induced cell cycle delay of heavily damaged lymphocytes.

To clarify this point we exposed lymphocytes of a healthy volunteer to heavy ions (C-, Fe-, Xe- and Cr-ions) or X-rays. Aberration yields were measured at several sampling times (48, 60, 72 and 84 h) in both first cycle G_2-PCC and metaphase cells and RBE values for the induction of 1 aberration per cell were derived (for details see [3]). As shown in Fig. 1 (a), RBE estimates derived from metaphase data at 48 h increased with LET, reached a maximum around 155 keV/µm and decreased with a further rise in LET. In addition, for cells exposed to particles with LET>30 keV/µm, higher RBE values were derived at later sampling times due to the mitotic delay of heavily damaged cells. This effect was most pronounced after exposure to 175 keV/µm C-ions.

Accordingly, Fig. 1 (b) shows the RBE values obtained for G_2-PCC cells. As observed for metaphase cells, the RBE peaked at 155 keV/µm. However, in contrast to metaphase analysis the RBE estimates from PCC-samples declined less steeply with increasing LET. Furthermore, the time-dependent changes of the RBE values were smaller for G_2-PCC analysis than for metaphase analysis.

Altogether our data demonstrate that the standard analysis of aberrations in metaphase cells 48 h post-irradiation will considerably underestimate the RBE of high LET radiation. Scoring of aberrations in G_2-PCCs at 48 h accounts for most, but not all, of high LET induced delay of severely damaged cells. However, when particles with LET>150 keV/µm are applied, still a fraction of multiple damaged cells escape detection by G_2-analysis 48 h post-irradiation. Thus, in case of a suspected exposure to particles with a very high LET aberrations should be measured at a second (later) sampling time even if the G_2-PCC assay is applied. For a more detailed discussion see [3].

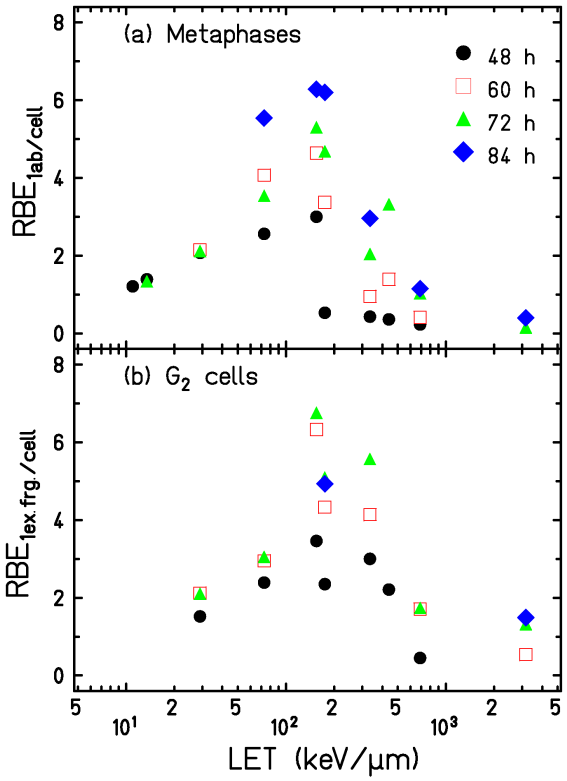

Figure 1: RBE of heavy ions for the induction of aberrations in first cycle cells. RBE was calculated based on the dose that induces one aberration per cell. (a) RBE derived from metaphase data (all types of aberrations detectable by Giemsa staining were included in the analysis). (b) RBE derived from G_2-PCC data (note that only excess fragments can be detected in G_2-PCCs after Giemsa-staining).

References

[1] IAEA, Technical Reports Series 405. Vienna (2001)
[2] S. Ritter and M. Durante, Mut Res 701 (2010) 38.
[3] R. Lee *et al.*, Rad. Env. Biophys., submitted.
[4] M. Durante *et al.*, Int J Radiat Biol 74 (1998) 457.

* Work supported by BMBF, Bonn, under contract 02S8497 and by the ESA-IBER project.

s.ritter@gsi.de

Cytogenetic fingerprint of heavy ion exposure detected with mBAND *in vitro* and in prostate cancer patients treated with IMRT and C-ions

D. Pignalosa[1], R. Lee[1], A. Nikoghosyan[2], S. Sommer[3], M. Durante[1,4] S. Ritter[1]
[1]GSI, Darmstadt; [2]Radiology Clinic, Heidelberg, Germany; [3]INTC, Warsaw, Poland; [4]TUD, Darmstadt, Germany .

Identification of a chromosomal biomarker that allows to determine if an individual has been exposed to high or low LET radiation is a long-standing goal in radiation biology and several chromosome aberration (CA) types have been proposed as fingerprints. Low LET radiation is characterized by a homogenous distribution of the ionization events in the target, while for high LET exposure the energy is released along the particle track resulting in an inhomogeneous ionization pattern. Based on this difference in the energy deposition it has been suggested, for example, that high LET radiation induces a higher rate of intrachromosomal exchanges in comparison to sparsely ionizing radiation. In other words the likelihood to hit several regions belonging to the same chromosome domain is higher when ionization events are densely distributed. *In vitro* studies have partially confirmed this hypothesis, showing that complex intrachanges (CAs arising from 3 or more breaks and where at least two of them occur on the hybridized chromosome) are more common after exposure to heavy ions than after exposure to sparsely ionizing radiation, while the yield of simple intrachanges was not radiation quality dependent [1]. Yet, it is still not clear, if a similar pattern is observable after *in vivo* exposure.

To address this question we measured CAs in peripheral blood lymphocytes (PBLs) from patients treated with photon IMRT (Intensity Modulated Radiation Therapy) alone or in combination with a C-ion boost. CAs were visualized by means of the mBAND technique, which allows the detection of both inter- and intrachromosomal aberrations. Two patient groups were selected for the cytogenetic investigation: prostate cancer patients treated with Photon-IMRT alone (IMRT*, 38x2 Gy, mean target volume 936 cm^3) and patients exposed at GSI to a C-ion boost (6x3 GyE) followed by IMRT (30x2 Gy, mean target volume 119 cm^3). PBLs were obtained at the end of the therapy treatment from 2 patients per group. Chromosome spreads were collected 48h after stimulation *in vitro* following standard procedures. Chromosome preparations were hybridized with the mBAND kit for chromosome 2 and images were captured using an Olympus microscope equipped with UV lamp and appropriate filter sets. Processing and image analysis were performed with the ISIS software (MetaSystems). For comparison, PBLs obtained from a healthy donor were exposed *in vitro* to X-rays (4 Gy) and to C-ions (2 Gy, 11.4 MeV/n). In total more than 2500 spreads were analysed.

The frequency of aberrant cells in patients treated with IMRT alone (0.11±0.01) was significantly higher ($p < 0.01$) than the rate observed in patients treated with the combined approach (0.018±0.003). This outcome can be explained by the different target volumes, i.e. in the IMRT* group the target volume was larger than in the group receiving C-ion boost and IMRT, resulting in a higher number of exposed lymphocytes and subsequently in a higher frequency of aberrations. This result confirms previous data obtained with the mFISH technique [2]. The yield of simple interchanges did not change significantly for any radiation quality, both from *in vivo* and from *in vitro* exposures (Fisher exact test $p > 0.1$). However, after *in vitro* exposure a higher ($p < 0.05$) incidence of complex intrachanges was found after high LET in comparison to low LET radiation in line with previous finding [1]. The frequency of simple intrachanges showed no radiation quality dependence (Fig.1).

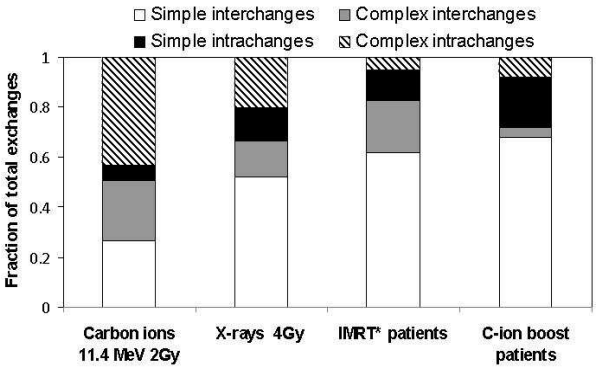

Figure 1: Aberration types detected in lymphocytes after an *In vivo* or *in vitro* exposure by means of the mBAND-staining of chromosome 2. Terminal deletions (1-5% of total aberrations) are excluded from the presentation.

Likewise, for both patient groups no significant differences in the yield of simple intrachanges were detected. In contrast to the in vitro exposures, the fraction of complex intrachanges was similar for both patient groups. An explanation for the discrepancy between the *in vivo* and *in vitro* results could be that the high LET contribution to the whole treatment is too small to induce a difference visible by means of the applied banding-technique. Interestingly, the yield of complex interchanges was higher ($p < 0.05$) for IMRT* patients in comparison to C-ion boost patients. One possible explanation is the larger field size applied for the IMRT* patients. The likelihood that a circulating PBL is damaged during subsequent therapy sessions (thus increasing the complexity of the cytogenetic damage) is higher when the field size is larger. Further investigations on this topic are needed. In conclusion, our results do not support the existence of a characteristic CA class which allows to determine the quality of the absorbed radiation *in vivo*.

References

[1] D. Pignalosa et al. *Rad. Res.* 170, 458-466 (2008).
[2] C. Hartel et al. *Radiot. Oncol.* 95, 73-78 (2010).

The work was funded by the BMBF grant 02S8497.

Clonogenic survival of metastatic prostate cancer cells and normal prostate epithelial cells irradiated with X-rays or carbon/ nitrogen ions and pre-treated with sodium selenite

P. Virsik[1,#], R. Lee[2], A. Gregus[1], P. Hessel[2], and S. Ritter[2]

[1]GSI Darmstadt, [2]Dept. of Environ. Medicine, University of Göttingen, Germany

We continued our experiments with metastatic radioresistant prostate cancer cell lines PC-3 and DU-145 and studied also the normal primary prostate epithelial cell line PrEC. Here we present the clonogenic survival results after irradiation with 200 kV X-rays or carbon ions (PC-3 and DU-145) and nitrogen ions (PrEC), without or with 6h pre-treatment with sodium selenite, applied at concentrations of 7.5 µM (PC-3 and PrEC) and 20 µM (DU-145) in order to increase oxidative stress. 95 % confluent cells were irradiated with SOBP ions at the SIS facility.

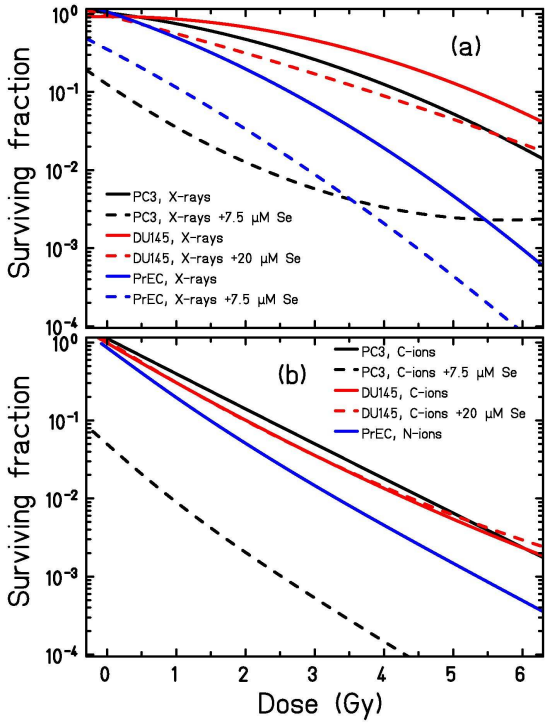

Fig. 1. Clonogenic survival of cells irradiated with 200 kV X-rays (a) and carbon or nitrogen ions (b) without or with sodium selenite pre-treatment for 6 hours. Curves were fit to experimental data.

First, our results show for X-rays, that metastatic prostate cancer cells (PC-3 and DU-145) are, more radioresistant than normal primary epithelial prostate cells (PrEC) as shown in fig. 1a. For ion irradiation, however, the differences are much smaller (see fig. 1b). Experiments with sodium selenite pre-treatment were performed for all three cell lines combined with X-ray exposure, and for two cancer cell lines with ion irradiation. With respect to X-ray irradiation, PC-3 cancer cells and normal PrEC cells were sensitized with 7.5 µM sodium selenite, normal cells being less sensitized up to about 3 Gy. For higher X-ray doses, no further radiosensitization of PC-3 cells could be achieved.

Sodium selenite sensitized mostly the PC-3 cells, with sensitization factor of about 20 at 10 % survival. The other cell lines, DU-145 and the normal PrEC show similar sensitization factors of ca. 1.4 and 2.3 respectively, at 10 % survival. DU-145 cells were, however, much more resistant against sodium selenite pre-treatment since 20 µM sodium selenite pre-treatment was necessary to achieve the sensitization shown in fig.1a.

Combination of sodium selenite pre-treatment and carbon ion irradiation was very effective in PC-3 cells, as can be seen in fig. 1b. The sensitization factor is about 5 at 1 % survival. However, even the pre-treatment of DU-145 cells with much higher concentration of sodium selenite was practically ineffective in this cell line.

The results indicate that DU-145 cells can cope with increased oxidative stress very well, in contrast to PC-3 cells which are very vulnerable with respect to sodium selenite pre-treatment.

We measured two cellular antioxidants, glutathione (GSH) and superoxide dismutase (SOD) in order to learn about the antioxidative status of the studied cell lines and the change induced by selenite only (see table 1).

Cell line and treatment	**GSH (µM per cell)**	**SOD (RLU per cell)**
DU-145 control	$0{,}40 \times 10^{-6}$	$0{,}71 \times 10^{-6}$
DU-145 plus 20 µM sodium selenite	$1{,}23 \times 10^{-6}$ ↑	$0{,}44 \times 10^{-6}$ ↓
PC-3 control	$1{,}02 \times 10^{-6}$	$0{,}33 \times 10^{-6}$
PC-3 plus 7.5 µM sodium selenite	$0{,}41 \times 10^{-6}$ ↓	$0{,}32 \times 10^{-6}$ ↓
PrEC control	$3{,}80 \times 10^{-6}$	$5{,}14 \times 10^{-6}$
PrEC plus 7.5 µM sodium selenite	$3{,}97 \times 10^{-6}$	$7{,}89 \times 10^{-6}$ ↑

Table 1. Glutathione and superoxide dismutase levels in untreated and treated cells. Arrows indicate changes.

Due to selenite treatment, GSH level is depleted in PC-3 cells, constant in normal PrEC cells and strongly increased in DU-145 cells. The individual antioxidative cell profile is thus indicated to be very variable and an important factor modulating new therapeutic possibilities.

Acknowledgement: The authors thank BMBF for financial support of this study by a grant no. 02S8203 and 02S8497.

patricia.virsik@medizin.uni-goettingen.de

Electrophysiological response of cardiomyocytes after low and high LET exposure

F. Steger[1], A. Daus[1], A. Helm[2], S. Ritter[2] and C. Thielemann[1]
[1]biomems lab, University of Applied Sciences Aschaffenburg
[2]Abteilung Biophysik, Gesellschaft für Schwerionenforschung mbH Darmstadt

There is emerging epidemiological evidence of an increased risk of adverse cardiovascular effects at low or moderate doses of ionizing radiation occurring many years after the exposure [1, 2]. However, essentially no information is available on the potential cardiovascular risks associated with the exposure to heavy ions. With the increasing use of heavy ions in cancer therapy, an assessment of their possible cardiovascular late effects is important, in particular when young patients are treated. Likewise, for the planning of manned space missions the risk of developing adverse cardiovascular effects must be seriously considered [3].

To address the question, if high LET radiation affects the cardiac functionality, we performed experiments with cardiac myocytes isolated from chicken embryos. Briefly, fertilized chicken eggs at E8 were taken and the hearts were extracted. Cardiac cells were enzymatically dissociated and seeded onto microelectrode array (MEA) chips [4], where they recreated cell-to-cell connections and restarted beating. After about 1 to 2 days an extended network had been built and spontaneously generated action potentials could be recorded via 60 electrodes on the MEA chip. An example of one recorded action potential is shown in figure 1.

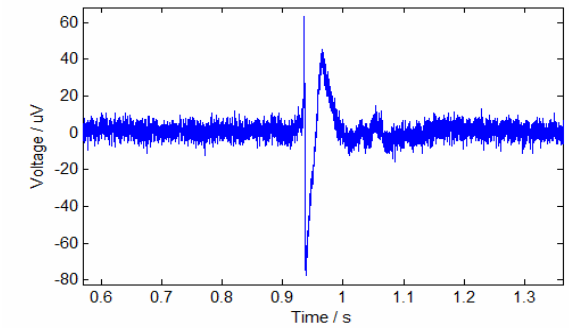

Figure 1: A typical extracellular cardiac action potential, so called spike, monitored by a single microelectrode.

To study the effects of ionizing radiation, 2 -6 samples were exposed to 2 and 15 Gy X-rays (20mA, 250kV) and to 10 Gy N-ions (400 MeV/u, 15 keV/µm), respectively. At different time points after the radiation the electrophysiological properties of the cells were measured. Generally, cardiac cells grown in a monolayer can be recorded for about one week in vitro. During this period the recorded data were analysed in terms of beating rate, signal amplitude, spread direction and spike form changes.

One parameter of special interest was the velocity of action potentials propagating from cell to cell via gap junctions, and possible effects of heavy ion exposure. In Figure 2 a representative examples of signal spreading in a monolayer from the upper left corner of the electrode field to the lower right corner is shown. Recordings were done and data was processed after an exposure to 15 Gy X-rays.

A relatively stable spreading velocity value of about 0.044 s/m could be measured before and after irradiation. This indicates a high survival rate of the cells and intact gap junctions for fast and direct signal propagation after exposure.

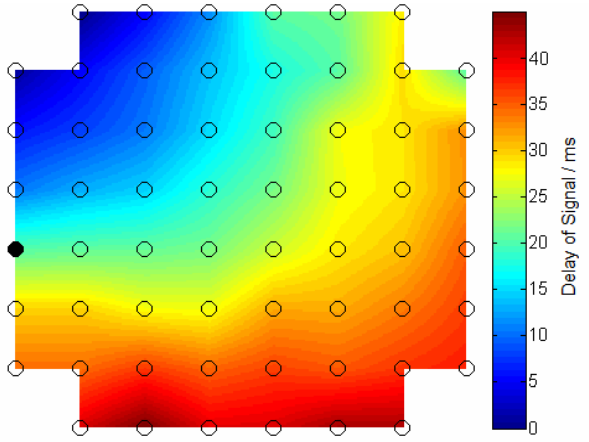

Figure 2: The pseudocolor plot visualizes the time delay of the spike propagating starting in the upper left corner of the MEA chip. The circles indicate the position of the recording sides.

Conclusions

The method for recording electrophysiological data from cardiomyocytes grown on MEAs and exposition to either X-rays or heavy ion has been successfully established. The preliminary experiments revealed no statistically significant radiation induced changes of the electrophysiology. Further experiments will be performed with a higher number of samples. In addition immunohistochemical analyses of gap junction proteins and the measurements of cell proliferation and apoptosis are planned.

References

[1] R. Roychoudhuri et al., BMC Cancer. 2007 Jan 15;7:9.
[2] M. Hooning et al., J Natl Cancer Inst. 2007 Mar 7;99(5):365-75.
[3] M. Durante and F. Cucinotta, Nature Reviews Cancer 8, 465-472 (June 2008).
[4] U. Egert and T. Meyer, Practical Methods in Cardiovascular Research 2005, Part 2, 3, 432-453.

Impact of senescence and irradiation on cellular metabolism in human cells

M. Frenzel[1], M. Soehn[1], M. Durante[2], C. Fournier[2], S. Ritter[2] and N. A. Dencher[1]
[1]Technische Universität Darmstadt; [2]GSI, Darmstadt, Germany

Introduction:
The cellular metabolic status differs between different cell types and depends on the physiology of the organism. Alterations in the cellular energy converting machinery occur during ageing of organisms or senescence of cell cultures [1, 2] and upon irradiation [3].
Recently, we observed in long-term human cell cultures (NHDF) a senescence accompanied decline in the total amount of ATP synthase (complex V of the OxPhos machinery) as well as of individual respiratory chain complexes and supercomplexes. This effect appeared delayed in progeny of irradiated cells (X-rays, 8 Gy) [1]. Less OxPhos supercomplexes may cause a lower respiration rate. Less ATP synthase, due to its role as ATP generating enzyme, may have a direct impact on the overall energy status of the cell. To reveal if the decline in protein abundance of the ATP synthase is proportional to a decline in the ATP level of a cell, normal human dermal fibroblasts (NHDF) were irradiated (X-rays, nitrogen ions) and subcultured afterwards for ~200 days. Changes in cellular ATP level were analysed.

Materials and Methods:
Confluent NHDF, were irradiated with X-rays (8 Gy) and in a parallel experiment with nitrogen ions (2 Gy, SIS, 100 MeV/u, LET 70 keV/µm). The cells were subcultured the first day after irradiation and thereafter in intervals of two to three weeks. The cellular ATP-level was analysed by the luciferin/luciferase ATP assay (BioThema) with reference to ATP standards (Luminometer 1251, BioOrbit).
Analysis of the mitochondrial proteome was performed using digitonin (8 g/g) for gentle solubilisation followed by two-dimensional blue-native/SDS PAGE and fluorescent protein staining for quantitation of protein abundances [4].

Results and Conclusions:
Up to day 30 after irradiation cell doubling is decelerated due to induced damages (data not shown). Thereafter, progeny of irradiated and non-irradiated cells show similar proliferation frequency and enter the phase of reduced cell proliferation after 128 days.
Previous experiments with different cell lines (NHDF, AG1522D and WI38) reveal a decline in the amount of ATP synthase in progeny of irradiated and non-irradiated cells from the time point cell proliferation slowed down. The cellular amount of ATP in progeny of non-irradiated NHDF is around 4 x 10^{-15} mol/cell independent of the age status (Fig. 1). At day 15 after X-ray (Fig. 1) and heavy ion (data not shown) irradiation, the abundance of cellular ATP is significantly increased by a factor of about 2 for both X-rays and heavy ion, respectively, compared to controls, followed by a sharp decrease at day 43. Later on, until day 128 for both irradiation conditions the amount of ATP is at the level of non-irradiated cells. Thereafter, there is a constant decline until day 193. At this time point the cellular ATP level in progeny of X-ray as well as of nitrogen ion irradiated cells is 1/3 of the level in the respective controls.

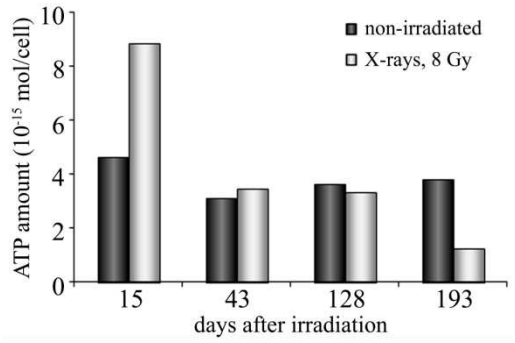

Fig. 1: Changes in the cellular ATP level in progeny of X-ray (8 Gy) irradiated and non-irradiated cells

The senescence-associated decrease in ATP synthase abundances in non-irradiated cells is not accompanied by a simultaneous decline in ATP amount. There are two possible explanations: (1) the specific activity of ATP synthase increases during senescence or/and (2) senescent cells consume less ATP and the observed reduced amount of ATP synthase is sufficient to maintain the cellular energy status of a cell.
In progeny of irradiated cells (X-rays and nitrogen ions), there is a pronounced increase of cellular ATP level at day 15. At the protein level, no radiation-induced increase of the ATP synthase amount was observed, indicating that complex V can adapt to higher ATP energy level required by increased specific activity. But the senescence-associated decline of ATP synthase in irradiated cells was accompanied by a decrease in ATP amount. This may demonstrate a late-effect of X-ray and heavy ion radiation on the ATP synthase that is reflected by a loss of ability to modulate its specific activity.
To further explain these data and their molecular interpretation, enzyme activity tests have to be performed to determine the specific activity of the ATP synthase and its dependence on X-ray or heavy ion exposure.

References:
[1] M. Frenzel *et al.*, in preparation
[2] P. Stöckl *et al.*, Free Radic. Biol. Med, 2007, **43**, 947–958
[3] P.C. Sundgren *et al.*, J. Magn. Reson. Imag., 2009, **29**, 291–297
[4] M. Frenzel *et al.*, Exp. Geront., 2010, **45**, 563–572

The work was supported by BMBF (Bonn), grant 02S84978 and grant 0315584D (*"GerontoMitoSys"*).

Influence of ionizing radiation on cellular adhesion in a human co-culture model of endothelial cells and lymphocytes

Jonas Klinger[1], Till Dettmering[1], Sophie Richter[3], Marco Durante[1,2], Gerhard Kraft[1] , Claudia Fournier[1],
[1]GSI, Darmstadt, Germany; [2]TU Darmstadt, Germany; [3]Hochschule Darmstadt, Germany

Introduction

Chronic inflammatory diseases such as arthritic disorders are efficiently treated by irradiation with low doses of photons or α-particles [1,2]. However, the molecular and cellular background remains widely unknown. Adhesion of peripheral blood mononuclear cells to endothelial cells (EC) is one of the initial steps in the inflammation cascade and is an important step in the recruitment of immune cells to inflamed tissue [3]. It was shown in an *in vitro* co-culture-model under static conditions that the adhesion of peripheral blood lymphocytes (PBL) to EC was reduced after irradiation with low doses of ionizing radiation (0.5 Gy), in contrast to higher doses [4]. In the present study we investigated the changes of cellular adhesion of PBL to EC after exposure to low doses of ionizing radiation, in a comparison between primary- und immortalized EC and for different radiation qualities (photons vs. carbon- and nitrogen-ions). In addition, the expression of adhesion molecules was studied.

Materials and Methods

Irradiations were performed using X-rays (250kV, 16mA), carbon ions (LET 160-170keV/µm) or nitrogen ions (LET 70keV/µm). Adhesion assays were performed using hybrid- (EA.hy.926) or primary- (HUVEC) endothelial cells, in co-culture with peripheral blood lymphocytes (PBL). The EC were cultured under static conditions to form confluent monolayers. After irradiation they were stimulated with TNF-α (1-10ng/ml) and incubated for 24h. Subsequently the labelled lymphocytes were seeded onto the EC monolayer and incubated for 30min. Afterwards the unbound lymphocytes were removed by washing the samples with PBS and analysed using flowcytometer or a fluorescent microscope. For staining of adhesion molecules, cells were labelled with fluorescent antibodies and analysed by flowcytometry.

Results and Conclusion

24h after irradiation of EA.hy.926 cells with a low dose of X-ray (0.5Gy), a decrease of 30% in PBL adhesion compared to unirradiated controls was detected (data not shown). Our results confirm the data previously reported for EA.hy.926 cells by Rödel et. al. [4]. In contrast, after irradiation with particles like carbon ions (LET=160-170keV/µm, data not shown) or nitrogen ions (LET=70keV/µm) and for primary EC of the umbilical vein (HUVEC), no decrease of PBL adhesion was observed [Fig. 1A]. Even in a period of 8 days no significant change in the adhesion of PBL was detectable. Only a slight increase of adhesion after 8 days was observed for an irradiation with 6Gy [Fig. 1B]. To confirm our results on the molecular level, the expression of the adhesion molecules ICAM-1 was investigated. There was an increase of ICAM-1 in TNF-α stimulated HUVEC 24 h, but no decrease after irradiation with 0.5Gy (data not shown). These results are in good accordance with the results for the PBL adhesion: An increase of ICAM-1 expression was only detectable 7d after irradiation with doses ≥2Gy (data not shown).

Our data show for immortalized EC (Ea.hy.926), that in contrast to photon irradiation, exposure to carbon ions had no effect on PBL adhesion. For HUVEC actually no reduction of adhesion could be observed after irradiation neither with X-ray nor with carbon-ions. These findings demonstrate that the cellular response differs after irradiation with photons or charged particles, but the *in-vitro* results for immortalized EC can not be simply assigned to primary cells or the *in-vivo* situation. In this ongoing work we intend to improve our assay system to investigate more parameters concerning the adhesion process, i.e. other primary cells and dynamic flow conditions.

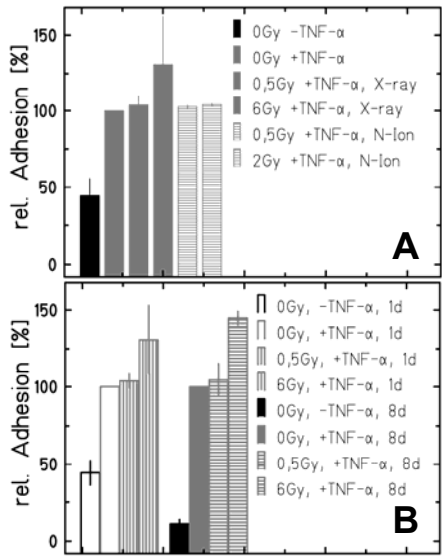

Figure 1: *Adhesion of PBL to TNF-α (1ng/ml) stimulated endothelial cells (HUVEC).* **A** *24h after irradiation with X-ray (250kV, 16mA) or nitrogen ions (LET: 70keV/µm).* **B** *Kinetic of PBL adhesion to HUVEC after irradiation with X-ray (N=1-5, n=2-10) .*

References

[1] Seegenschmiedt et.al., *Strahlenther. Onkol.* 180: 718-730 (2004).
[2] Falkenbach et.al., Rheumatol Int., 25(3): 205-10 (2005)
[3] Middleton et.al., Blood, 100: 3853–60. (2002)
[4] Rödel et. al., Strahlenter Onkol., 180:194-200 (2004)

* Work supported by FOI BadGastein, Austria

Loss of pulmonary function after carbon ion irradiation of the rat lung*

P. van Luijk[1,#], R.P. Coppes[1,2], T. Dettmering[3], C. Fournier[3], M.J. van Goethem[2,4], M. Scholz[3]

[1]dept. Radiation Oncology and [2]Cell biology, University Medical Center Groningen, University of Groningen, Groningen, The Netherlands; [3]GSI Darmstadt, Germany, [4]Kernfysisch Versneller Instituut, University of Groningen, Groningen, The Netherlands

Radiotherapy is a common and effective treatment for many cancers. For most cancers, however, normal tissues are inevitably co-irradiated. This may lead to severe toxicity. For tumours in e.g. the thoracic region, this limits treatment dose and efficacy. Therefore, development of particle therapy aimed at minimizing dose and volume to which the normal tissues are irradiated. Particles such as carbon ions lose most of their energy in the target volume resulting in a superior physical dose distribution compared to classically-used photons. In addition, the biological effect of particle dose differs from that of photon dose. To translate currently-applied photon therapy to equivalent particle therapy, these differences in biological effect need to be corrected for. The uncertainty in models predicting these differences is the main source of uncertainties in the prescribed dose of particle therapy [1].

The testing and development of these models requires e.g. data on the response of normal tissues to carbon ion irradiation. Therefore in the present project an established model of partial rat lung irradiation [2] was used to determine the response of the rat lung to carbon ions. The present report describes a first dose-finding study.

Groups of 3 rats were irradiated on the whole lung or 50% of the lung with plateau or spread-out-Bragg peak carbon ions. As a measure of pulmonary function, respiratory rate was measured bi-weekly up to 28 weeks after irradiation. Early (4 – 12 weeks after irradiation) increases in breathing rate result predominantly from an acute inflammatory response [3]. At later time points (16 – 28 weeks after irradiation) increases are due to chronic inflammation and fibrosis. As a measure of the loss of pulmonary function the mean increase in respiratory rate in these time spans compared to the mean respiratory rate in 0 – 2 weeks is calculated.

Both irradiation of the whole lung and 50% of the lung resulted in loss of pulmonary function in the early time span. Similar to observations after photon irradiation [4], this response was only followed by a fibrotic response after irradiation of 50% of the lung, where higher dose levels have been assessed Observations after irradiation of the whole lung with spread-out Bragg peak ions showed similar patterns in the overlapping dose range (figure 2). The dose range used for irradiation of 50% of the lung did not result in any significant response. Histological analysis of tissue of animals sacrificed at 8 weeks after irradiation is in progress.

Based on these results more detailed dose-volume-response studies will be designed and performed to obtain the data required for the development of risk models for carbon ion irradiation of the lung to facilitate optimized application of carbon ions in thoracic radiotherapy.

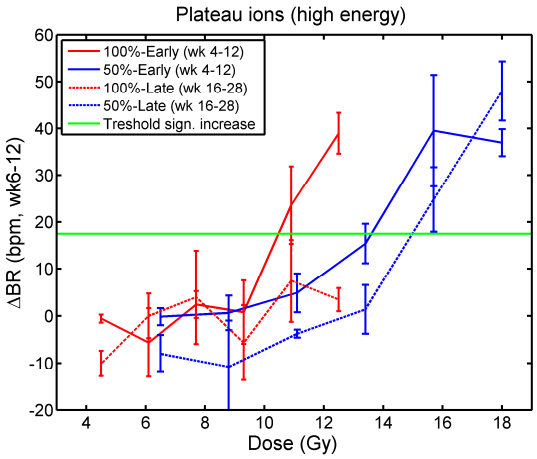

Figure 1: Breathing rate changes(ΔBR) vs. dose after (partial) lung irradiation with plateau carbon ions.

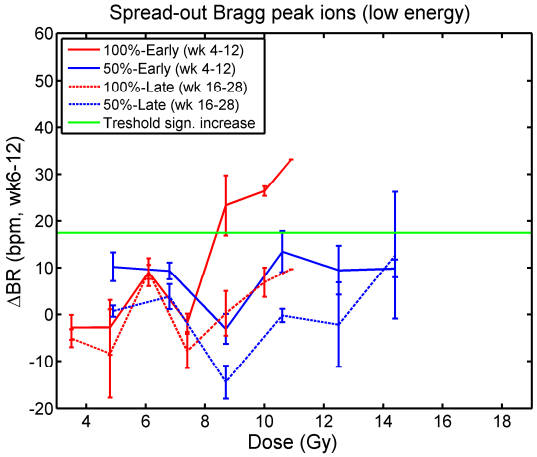

Figure 2: Changes in breathing rate (ΔBR) after (partial) lung irradiation with spread-out Bragg peak carbon ions.

References

[1] M. Durante, J.S. Loeffler. Nat. Rev. Clin. Oncol 7 (2010) 37.

[2] van Luijk P, Novakova-Jiresova A, Faber H, Schippers JM, Kampinga HH, Meertens H, Coppes RP. Cancer Res. 65 (2005) 6509.

[3] Novakova-Jiresova A, van Luijk P, van Goor H, Kampinga HH, Coppes RP. Cancer Res. 65 (2005) 3568.

[4] Novakova-Jiresova A, van Luijk P, van Goor H, Kampinga HH, Coppes RP. Int J Radiat Oncol Biol Phys. 2007 Apr 1;67(5):1510-8.

* Supported by grant CBR-754842 from the University of Groningen

#p.van.luijk@rt.umcg.nl

Repair of radiation induced DNA damage in human hematopoietic stem and progenitor cells and mature lymphocytes

L. Bauer[1], D. Becker[1,2], E. Nasonova[3], A. Czernok[4], M. Durante[1], S. Ritter[1], L. Wiesmüller[4] and C. Fournier[1]

[1]GSI, Darmstadt, Germany; [2]Institute for Transfusion Medicine and Immunohaematology, Frankfurt, Germany; [3]JINR, Dubna, Russia; [4]Department of Obstetrics and Gynaecology, University of Ulm, Germany

Introduction

Hematopoietic stem and progenitor cells (HSPC) are responsible for the constant renewal of all mature blood cells (lymphocytes, PBLs included). In view of the increasing application of heavy ions in radiotherapy [1, 2] and as HSPC may be located in the radiation field during radiotreatment, their radiobiological features and those of their descendents have to be investigated. Since the effect of radiation on cells results mainly from the damage induced in the DNA, the aim of the study was to compare the DNA repair capacity and fidelity of human HSPC and PBLs. Because several types of DNA damage exist, which induce different mechanisms of DNA repair, a test system for HSPC was established, to enable the observation of distinct repair pathways after the induction of targeted DNA double strand breaks (DSBs), with focus on correct versus incorrect repair of those breaks (according to [3]). Additionally, after exposure to photons and densely ionizing nitrogen ions early radiation-induced damage in chromosomes and the rejoining was studied (PCC method).

Materials and Methods

HSPC were enriched for a $CD34^+$ cell population and PBLs were isolated in parallel from the peripheral blood of healthy donors as described elsewhere [4]. Cells were cultured for 48-72h in expansion media supplemented with appropriate cytokines (HSPC) or PHA (PBLs) [4]. A plasmid-based system for the detection of different DNA repair pathways for DNA damage, which had previously been applied to the analysis of PBLs, was successfully used for HSPC, as described elsewhere [3]. For chromosomal analysis, the asynchronous cell populations were exposed to X-rays (16mA, 250kV) or nitrogen ions (130 MeV/u, 47-65 keV/µm) at the SIS facility at GSI. At appropriate time points post-irradiation (0-9h) chromosome breaks were measured in G_1- and G_2-phase cells by the premature chromosome condensation (PCC) technique as described elsewhere [5, 6]. Briefly, calyculin A was added to the culture to induce PCC. PCC spreads were stained with Giemsa and cells identified as damaged when the number of chromosome pieces exceeded 46 (excess fragments per cell, see figure 1 and 2).

Results

First results with the plasmid-based system revealed that in HSPC high-fidelity pathways of DSB repair were used more frequently compared to PBLs (not shown). Upon modification of the protocol, the plasmid-based system was successfully used in a first X-ray experiment demonstrating radiation-induced generation and repair of DSBs. Despite the observed differences between HSPC and PBLs concerning the use of specific repair pathways after induction of DSBs, the repair of chromosomal fragments was quite similar in both cell types with respect to kinetics and the level of unrepaired fragments, even though there were small differences with respect to the initial chromosomal damages (for X-rays, see figure 2). After exposure to nitrogen ions, higher values of unrepaired, residual damage could be found in both cell types (not shown).

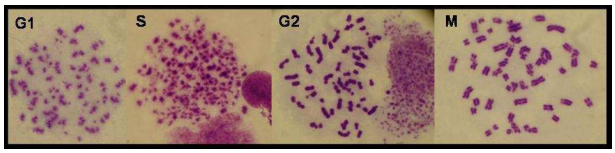

Figure 1: Chromosome condensation in different cell cycle phases, exemplarily shown for HSPC exposed to a dose of 2 Gy nitrogen ions (20 min post-irradiation).

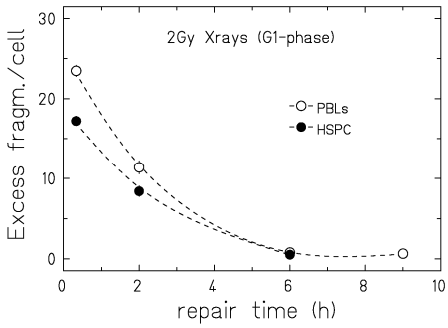

Figure 2: Time course of the aberration yields (number of excess fragments) in G_1-cells (PBLs, HSPC) after irradiation with a dose of 2 Gy for X- rays, determined by the PCC technique (n=1, error bars were calculated assuming Poisson statistics).

Having established pathway-specific DSB repair analysis, we will employ the plasmid-based assay to investigate the effect of densely ionizing radiation on the capacity and quality of DNA repair in irradiated HSPC (supported by BMBF 02S8497 and GSI no. 178).

References

[1] Durante & Löffler (2010), Nat Rev Clin Oncol. 7(1):37-43
[2] Schulz-Ertner and Tsujii (2007), J Clin Oncol.10; 25(8):953-64
[3] Akyüz et al. (2002), Mol Cell Biol. 22(17):6306-17
[4] Becker et al (2009), Int J Radiat Biol, 85(11):1051-1059
[5] Nasonova & Ritter (2004), Cytogenetic Genome Res 104:216-220
[6] Durante et al (1998), Int J Radiat Biol, 74(325:331)

Embryonic Stem Cell Derived Cardiomyocytes: a Model System to Study Cardiac Effects of Heavy Ion Exposure

A. Helm[1], S. Luft[1,2], P. Hessel[1],D. Pignalosa[1], M. Durante[1,2], P. Layer[2], D. Pollet[3] and S. Ritter[1,#]
[1]GSI, Darmstadt, Germany; [2]Technische Universität Darmstadt, Germany, [3]Hochschule Darmstadt, Germany

Pluripotent embryonic stem cells (ESCs) isolated from the inner cell mass of early embryonic blastocysts can be differentiated *in vitro* into all three germ layers, i.e. endoderm, ectoderm and mesoderm and subsequently a wide variety of cell types can be generated including cardiomyocytes [1]. These *in vitro* differentiated heart muscle cells display typical morphological and electrophysiological features seen *in vivo* or in primary cultures. For example, they express cardiac specific genes, have a similar sarcomeric structure and show spontaneous contractility triggered by the expression of membrane-bound ion channels [2]. Due to these very reasons ESC-derived cardiac cells provide a versatile tool to study normal cardiac development and function as well as the cardiac response to drugs, ionizing radiation or other stressors and are being investigated for their potential use in regenerative medicine.

To study cardiac effects of heavy ions, we recently established at GSI the technique of differentiating cardiomyocytes from the mouse ESC line D3. Basically, we applied the protocol accredited by the European Centre for the Validation of Alternative Methods (ECVAM) [3]. Briefly, pluripotent D3 cells are forced to differentiate by *Leukemia inhibitory factor* (LIF) withdrawal from the medium. Furthermore, differentiation requires the aggregation of cells. This was achieved by culturing the cells (750/20 µl) in a hanging drop (see Fig. 1). As a result of gravity, cells aggregate and form the so called embryoid body (EB) which resembles the developing embryo. After 3 days EBs are transferred into a suspension culture and are kept there for 2 days. During this time EBs grow and finally can be seen with the naked eye. Subsequently, a single EB is transferred into each cavity of a gelatine-treated 24-well tissue culture plate. EBs attach to the surface, flatten and grow. While differentiating and extending into the periphery, EBs give rise to several cell types. Cardiomyocytes can be easily detected about 10 days after initiation of the differentiation (5 days after transfer in 24-well plate) due to their visible contractions.

Since a crucial factor for generating a high number of beating EBs is the serum, we measured the efficiency of 3 different sera at day 10 after initiation of the differentiation. Interestingly, the tested sera induced a similar proportion of beating EBs, i.e. serum 1 yielded 76 ± 11% (mean±SD from 5 independent experiments), while 83% and 79% were measured for serum 2 and 3, respectively (one experiment each).

Additionally, we determined the time interval in which the EBs were beating. Exemplarily, in Fig. 2 an assay performed with serum 1 is shown. About 70% of beating EBs were observed between 10 and 15 days after initiation of the differentiation assay. At the subsequent days this number decreased, reaching 10% at day 20 in line with data reported by Boheler et al. [4].

In further studies we intend to investigate, if the differentiation of pluripotent mouse ESC into cardiomyocytes is affected by high or low LET exposure. Another aspect that will be studied is the impact of radiation on electrophysiological parameters of cardiac cells as described [5].

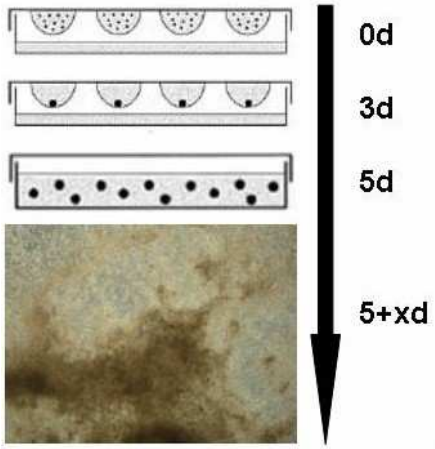

Fig. 1: Scheme of the differentiation assay (modified from [4]). The procedure starts with a hanging drop culture through which embryoid bodies are formed. They are plated and start growth.

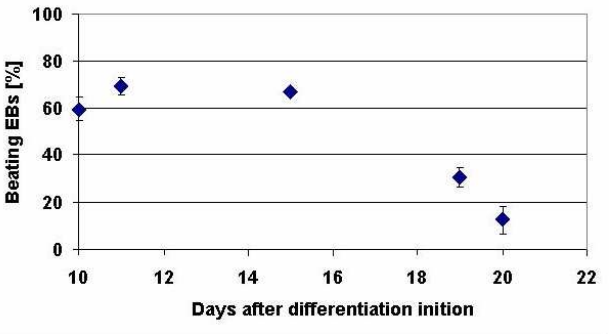

Fig. 2: The percentage of beating EBs after initiation of cell differentiation. EBs start beating about 10 days after initiation of cell differentiation.

References

[1] Keller, Genes Dev, 2005, 19, 1129-1155
[2] Wobus et al., Physiol Rev, 2005, 85, 635-678
[3] ECVAM (2002) Embryonic Stem Cell Test (EST): INVITTOX no. 113. Embryotoxicity/Teratogenicity
[4] Boheler et al., Circ Res, 2002, 91, 189-201
[5] Steeger, Bachelorarbeit, Hochschule Aschaffenburg, 2010

#s.ritter@gsi.de

Investigations on the transforming growth factor beta signalling pathway in human umbilical vein endothelial cells after radiation exposure

T. Dettmering, J. Klinger, A. Groo, S. Ullrich, J. Zink, G. Kraft, M. Durante, C. Fournier

GSI, Darmstadt, Germany

Introduction

More than 60.000 patients are treated annually for chronic inflammatory pain with low dose radiation therapy (LD-RT), i.e. the α-particle emitter radon. Since the mechanisms of the positive effects achieved are largely unknown, we set out to investigate a possible impact of ionizing radiation on the initial steps of inflammation.

Endothelial cells (EC) constitute the inner lining of blood vessels and play an important role during inflammation. Upon stimulation with cytokines such as TNFα, EC present a diverse set of cellular adhesion molecules (*e. g.* E-Selectin) on their surface necessary for the adhesion of leucocytes to the blood vessel wall. This marks the first step of the inflammatory cascade at the site of inflammation [1]. After transmigration of leucocytes into the tissue and clearance of the cells causing inflammation, the inflammatory response has to be downregulated and the healing process can be induced. These steps are mediated by cytokines, i. e. *TGFβ,* which is released by several cell types. In the target cells, an intracellular cascade is activated by phosphorylating and nuclear translocation of transcriptional regulators—the so-called Smad-proteins [2]. Based on previously published results using photon irradiation of established endothelial cells [3], we hypothesize that this downregulation of adhesion and transmigration contributes to the effects of LD-RT.

In our work we used primary human cells (umbilical vein EC, HUVEC) to assess the impact of radiation on three steps potentially involved in the inhibition of inflammation: the expression and release of TGFβ, as well as the activity of the Smad-pathway.

Materials and Methods

HUVEC were purchased from Lonza and cultivated following the supplier's protocol. Cells were irradiated at doses up to 2 Gy (250 kV X-rays). 2 ng/ml human $TGF\beta_1$ was added directly after irradiation. RNA was isolated using a MasterPure kit (Epicentre) and cDNA was synthesized using 500 ng RNA (RevertAid cDNA Synthesis Kit, Fermentas). PCR was performed using a TopTaq Master Mix (Quiagen) with primers for TGFβ and GAPDH as an internal control and detected on a 2% agarose gel after ethidium bromide staining. The nuclear and cytoplasmic extracts from cells were prepared by using the Nuclear Extract Kit (Active Motif®). The cells were resuspended in hypotonic buffer to release the cytoplasmic fraction. After collection of the cytoplasmic fraction, the nuclei were lysed and the nuclear proteins were solubilised in lysis buffer.

Results and Discussion

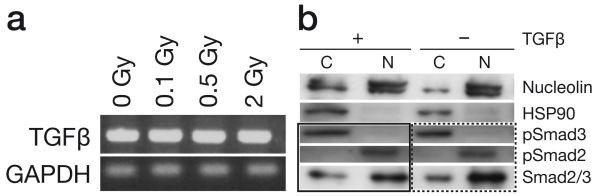

Fig. 1 – a) The TGFβ gene is expressed constitutively in HUVEC, irrespective of radiation dose. b) TGFβ treatment has no impact on phosphorylation status or intracellular location of the Smad proteins; as indicated by the solid and dashed boxes. Separation of nuclear and cytoplasmatic fractions were checked by detection of nucleolin and HSP 90 (C: Cytoplasm; N: Nucleus)

The TGFβ gene is expressed regardless of radiation exposure (Fig 1a, determined by PCR, has to be confirmed using qRT-PCR). However, the release of TGFβ increased with increasing dose, with carbon ions leading to a more pronounced increase compared to X-rays at the same dose [4].

Our experiments revealed so far a clear phosphorylation and translocation of Smad2/3 to the nucleus in human fibroblasts after exposure to TGFβ, X-ray or carbon ions using immunofluorescence (IF) and Western blot technique (not shown). This was not observed in HUVEC as they showed in IF experiments similar nuclear signal intensities, independent of the presence of TGFβ or previous radiation exposure (not shown). Results of Western Blot analysis after nuclear extraction are in agreement with the IF analysis and show no change in location or phosphorylation status of Smad2/3 proteins in the presence of TGFβ (Fig 1b).

These results suggest that the Smad-signalling pathway is constantly, but not fully activated in HUVEC. This could be due to the static culture conditions or the fetal origin of HUVEC. However, in agreement with our results, Gamble *et al.* showed that HUVEC lose their responsiveness to TGFβ shortly after isolation [5]. Whether static culture conditions, the fetal origin or the *in vitro* age of the cells play a role will be further tested.

Literature

[1] Ley, K. Adhesion molecules: function and inhibition. 2007, Basel: Birkhäuser.
[2] Wrana, J. L. Cytokine Growth Factor Rev, 2000. 11(1-2): p. 5-13.
[3] Roedel, F. Int J Radiat Biol, 2002. 78(8): 711-9.
[4] Klinger, J. GSI Scientific Report, 2009.
[5] Gamble, J. R. J Immunol, 1991. 146(4): p. 1149-54.

This work is in part supported by FOI Bad Gastein, Austria.

Localization of DNA Double-Strand Breaks in Mouse Tissues after X-irradiation

A. Raths[1], A. Bock[1], S. Grudzenski[1], D. Deckbar[1], S. Conrad[1] and M. Löbrich[1]
[1]Darmstadt University of Technology, Germany; GSI;

The most deleterious form of IR (ionizing radiation)- induced DNA damages is the DNA double strand break (DSB), and its efficient repair is essential for the maintenance of the genomic integrity. Ataxia telangiectasia mutated (ATM), a protein kinase defective in the hereditary disorder ataxia telangiectasia (AT), is activated after the induction of DSB by IR and phosphorylates several key proteins essential for cell cycle checkpoint control and efficient repair of a subset of DSBs. One target of ATM is the histone H2AX which is phosphorylated in the DSB surrounding chromatin and can be visualized by immunofluorescence microscopy as γH2AX foci. A further sensitive marker for DSBs is the 53BP1 protein, which is recruited to DSB sites within several minutes after IR and also forms discrete nuclear foci colocalizing with γH2AX. This sensitive method allowed the investigation of DSB induction and repair in single cells even after physiologically relevant low doses.

We established this method of γH2AX and 53BP1 foci staining in different mouse tissues after *in vivo* x-ray irradiation in collaboration with the group of C. E. Rübe to quantify the number of DSBs and measure DSB repair (Figure 1). It is known that ATM deficient cells reveal a DSB repair defect *in vitro*, which also is observable in different tissues in AT mice measured by γH2AX and 53BP1 foci analysis [1]. In a publication of Goodarzi et al., it has been demonstrated that DSB repair differs in heterochromatic and euchromatic regions. In ATM-deficient cells the DSBs remaining unrepaired over a long period of time are preferentially located at heterochromatic regions [2]. This finding reveals an involvement of ATM in the repair of heterochromatin associated DSBs.

Utilizing specific markers for heterochromatic regions like antibodies against trimethylated K9 of histone 3, we are able to visualize chromocenters in different mouse tissues which colocalize with densely stained DAPI regions (Figure 2). In combination with the sensitive method of γH2AX and 53BP1 foci staining we are now able to quantify the DSBs in tissue after *in vivo* irradiation and additionally can investigate the localisation of the DSBs in the nuclei with regard to the chromatin structure.

In a first study, we measured the DSB repair in heart, lung and kidney of C57BL/6 wild type mice and quantified the number of initial and remaining 53BP1 foci associated with heterochromatic regions. The distribution of eu- and heterochromatic DSBs directly, as well as 24 h after IR was very similar to what has been found earlier *in vitro* (Figure 3).

In further studies we plan to analyze the localization of DSBs in tissues of ATM deficient mice to validate the involvement of ATM in the repair of heterochromatin-associated DSBs *in vivo*.

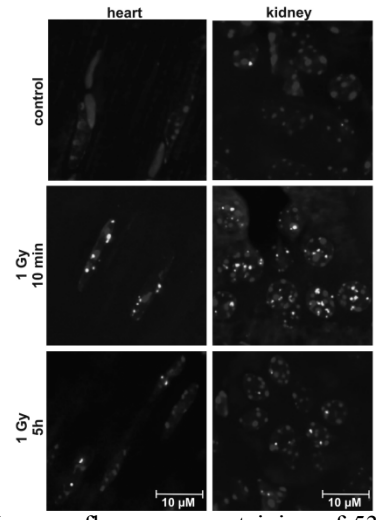

Figure 1: Immunofluorescence staining of 53BP1 (bright foci) in unirradiated (control) nuclei of mouse heart and kidney, and 10 min or 5 hr after *in vivo* irradiation with 1 Gy.

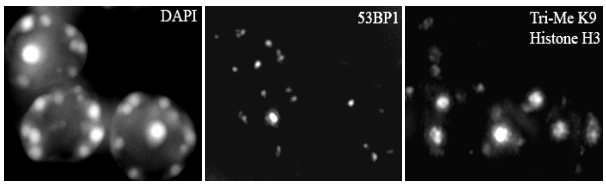

Figure 2: Localization of 53BP1 foci in euchromatic and heterochromatic (trimethylated K9 of histone 3) regions in nuclei (DAPI) of a mouse kidney after *in vivo* irradiation with 1 Gy.

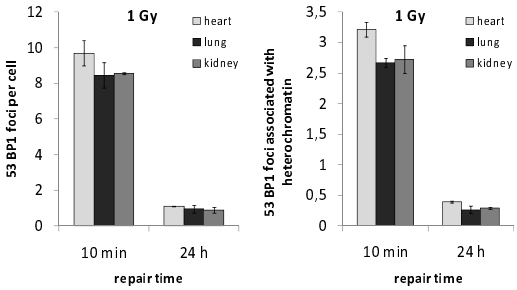

Figure 3: Quantification of 53BP1 foci in cells of mouse heart, lung and kidney 10 min and 24 h after *in vivo* irradiation with 1 Gy and their association with heterochromatic regions.

References

[1] C.E. Rübe, S. Grudzenski, et al., Clin Cancer Res. 2008; 14 (20) 6546-55.
[2] A.A. Goodarzi, A. T. Noon, et al., Mol. Cell 2008; 31, 167-177.

Role of hypoxia and HIF for the effects of heavy ion radiation in the human lung adenocarcinoma cell line (A549)

F. Kamlah[1], A. Arenz[1], V. Bill[1], B. Bischoff[1], R. Engenhart-Cabillic[1], C. Fournier[2], J. Hänze[3], C. Hornickel[1], F. Rose[1], M. Scholz[2], and G. Taucher-Scholz[2]

[1]Dept. of Radiotherapy and Radiooncology, University of Marburg, Germany; [2]GSI, Darmstadt, Germany; [3]Department of Internal Medicine II/V, University of Gießen, Germany

Hypoxia inducible factors (HIF) regulate adaptive cellular processes in response to hypoxia. Also, HIF can be activated by non-hypoxic stimuli such as oncogenes and in particular by reactive oxygen species which are affected by irradiation [1]. Clinical trials demonstrated a direct relationship between tumor hypoxia and poor clinical outcome after photon radiation (X-ray) [2]. First, we compared the effect of different irradiation qualities (heavy ions (^{12}C and ^{14}N) and X-ray irradiations) on the clonogenic survival of human non small lung adenocarcinoma cells (A549). Biological equivalent doses (RBE) of survival were determined after irradiation with ^{14}N (LET 70 keV/µm, energy 130 MeV/u on target), ^{12}C (LET 170 keV/µm, energy 9.8 MeV/u on target) and photons (6 MV-X) (Figure 1). The survival curves after ^{12}C- and ^{14}N irradiations were identical and revealed a 10% survival level at 2 Gy. This value corresponded to an isosurvival dose of approximately 6 Gy of X-ray irradiation.

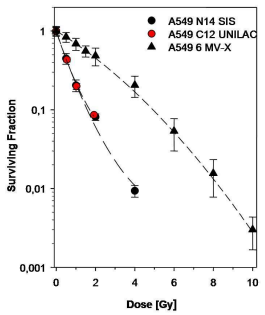

Figure 1. Survival curves of A549 cells after irradiation with nitrogen ions (^{14}N), carbon ions (^{12}C), and 6 MV-X-rays. The curves were fitted by least squares to a linear-quadratic equation.

In the next step, we analyzed the cellular survival of A549 cells after ^{14}N (2 Gy) and photon irradiation (6 Gy) cultured under different oxygenation conditions (Figure 2). We found significant higher survival rates in X-irradiated cells in hypoxia when compared to conditions of normoxia or reoxygenation whereas cell survival after ^{14}N irradiation was not affected by the oxygenation condition (Figure 2).

In parallel, we investigated gene regulation of the HIF-1 dependent target gene GLUT-1-mRNA by real time RT-PCR (Figure 3). The relative expression level of GLUT-1-mRNA is presented by the ΔCt values. ΔCt = Ct PBGD [porphobilinogen deaminase]-mRNA) – Ct (GLUT-1-mRNA). A difference of 1 corresponds approximately to a twofold increase of GLUT-1-mRNA. We observed the typical induction of GLUT-1-mRNA in hypoxia when compared to normoxia and reoxygenation. Interestingly, in hypoxia irradiation by X-ray or ^{14}N led to a further significant increase of GLUT-1-mRNA levels. Further experiments will analyze whether augmentation of HIF-1 targets by X-ray and ^{14}N irradiation in hypoxia are of clinical relevance and can contribute to the development of therapy resistance towards the different irradiation qualities. These ongoing studies will employ cell culture experiments and in an *in vivo* subcutaneous mouse tumor models.

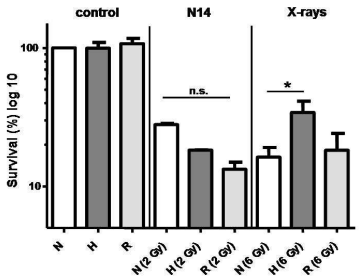

Figure 2. Cellular survival after ^{14}N and X-ray irradiation under normoxia, hypoxia (1% O2) and reoyxgenation, followed by irradiation under normoxia. Data reflect the mean ± s.e.m. (n=3 [X-rays] n=1 [^{14}N]; *P<0.05, Mann-Whitney-test).

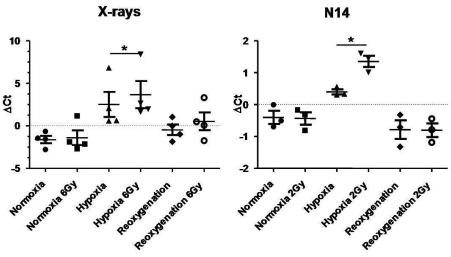

Figure 3. Realtime RT-PCR of GLUT-1-mRNA after ^{14}N (48 h) and X-ray (24 h) irradiation. Data reflect the mean ± s.e.m. (n=3 [X-rays] n=1 [^{14}N]; *P<0.05, paired t-test).

References

[1] Semenza, G. L. (2003) Targeting HIF-1 for cancer therapy. *Nat Rev Cancer* **3**, 721-732

[2] Brizel, D. M., Dodge, R. K., Clough, R. W., and Dewhirst, M. W. (1999) Oxygenation of head and neck cancer: changes during radiotherapy and impact on treatment outcome. *Radiother Oncol* **53**, 113-117.

The influence of the oxygen status of tumor cells on the survival under co-culture conditions: preparatory measurements

S. Lai[1,3,4], M. Durante[1,2], C. Hartel[1], N. Ma[1,3,4], T. Wetzel[1],and W. K. Weyrather[1]

[1]GSI,Darmstadt,Germany;[2]TU,Darmstadt,Germany;[3]Department of Radiation Oncology, Fudan University Shanghai Cancer Center, Shanghai,China;[4]Department of Oncology, Shanghai Medical School, Fudan University, Shanghai,China

Introduction

In order to investigate the influence of hypoxic structures on the cells representing the normal tissue, experiments have been started for the co-culture of normal cells and formerly hypoxic or anoxic tumor cells. For norm-oxic cells growing under co-culture the cell-interaction has been shown for prostate cancer and intestinal cells in [1].This type of experiments are of basic interest because cells from hypoxic parts of the tumor are often the source of later metastasis and especially cells surviving chronic hypoxia or anoxia may represent a subgroup, which is also more resistant to irradiation.

Materials and methods

R3327 AT-1 (RAT-1) prostate cancer cells and the intestinal epithelium cells (IEC-6) from rats were both raised on RPMI-1640 medium supplemented with 10% fetal calf serum (FCS) and 1% Penicillin/Streptomycin, and maintained in a humidified atmosphere of 5% CO_2 at 37°C. For the measurements under different oxygen states, cells were kept under norm-oxic (air), hypoxic (0.5% O_2, 94.5% N2; 5% CO2) or anoxic (95% N2; 5% CO2) conditions. The method of gassing and irradiation using the hypoxia exposure chamber has been described in [2]. To induce chronic hypoxia, cells were kept for 24 hours under hypoxic conditions. Irradiation was performed using 250 kVp x-rays. Cell survival was measured with a colony forming assay.

For the co-culture experiments IEC-6 cells were irradiated with 0 Gy or 1 Gy, simulating the dose in the normal tissue and RAT-1 cells were irradiated with 0, 2 or 6 Gy. After irradiation, both cell lines were reseeded together in the same flasks in septuplet. The plating efficiency (PE) and the survival level of the co-cultures were compared to mono-cultures of un-irradiated and irradiated cells.

Results and discussion

Survival under different states of oxygenation

Fig.1 shows the survival of RAT-1 cells irradiated under chronic hypoxia and acute anoxia. The oxygen enhancement ratio at 10% survival (OER_{10}) was 2.80 under acute anoxia and 1.24 under chronic hypoxia(pO_2 =0.5%). Measurements under chronic anoxia could not be evaluated due to the extremely low PE.

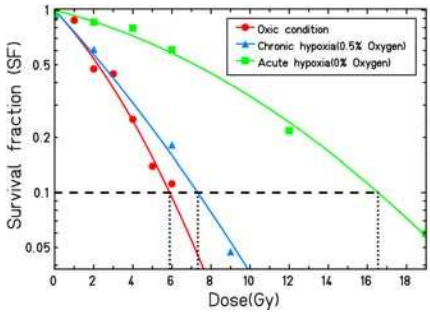

Figure 1: Survival of RAT-1 cells in air, under acute hypoxia or chronic hypoxia.

Co-culture of RAT-1 and IEC-6

Fig.2 shows the survival under co-culture conditions. For IEC-6 cells, the ratio of co-culture- survival divided by mono-culture- survival increases with the dose given to the co-cultured RAT-1 cells. This effect is more expressed for the IEC-6 cells irradiated with 1 Gy. This indicates a stimulating effect on proliferation and repair of the IEC-6 cells coming from the irradiated RAT-1 cells and mediated by the medium. A similar effect on the RAT-1 cells could not be observed, survival ratios co-culture/mono-culture fluctuated about 1.0. The results are in agreement with ref.[1]. Future measurements will show, whether the effect of previously hypoxic or anoxic RAT-1 cells will be similar.

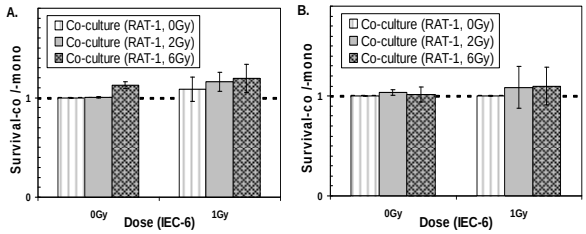

Figure 2: Survivals in co-culture fashion. A,IEC-6 cell line. B,RAT-1 cell line.

References

[1] C. von Neubeck, et al. GSI scientific report. 375 (2008).

[2] W. Tinganelli, et al. GSI scientific report. 482 (2009).

Cellular response of CHO-K1 cells to X-ray irradiation under different states of oxygenation

N. Ma[1,2,3], M. Durante[1,4], S. Lai[1,2,3], W. Tinganelli[1,4] and W. K. Weyrather[1]

[1]GSI, Darmstadt, Germany; [2]Department of Radiation Oncology, Fudan University Shanghai Cancer Center, Shanghai, China;[3]Department of Oncology,Shanghai Medical School,Fudan University,Shanghai,China;[4]TU Darmstadt,Germany

Introduction

Hypoxia is known to contribute to resistance to radiation therapy directly by depriving of oxygen or indirectly by promoting tumour cells malignant progression.[1] To investigate the mechanism of the radiation sensitivity of hypoxic cells to low LET irradiation, experiments of cell survival and cell cycle distribution of CHO-K1 cells under different states of oxygenation were performed.

Material and Methods

CHO-K1 cells, cultivated under standard conditions, were investigated under normoxia (air), hypoxia (0.5% O_2 ,95% N2; 5% CO2) or anoxia (95% N2; 5% CO2). The method of gassing and irradiation using the hypoxia exposure chamber has been described in [2]. To induce chronic hypoxia or anoxia cells were kept for 24 hours under hypoxic or anoxic conditions. For the measurements of reoxygenation the rings were exposed to air again. Irradiation was performed using 250 kVp x-rays. Cell survival was measured with a colony forming assay. Cell cycle analysis was performed with the flow cytometer PAS III (Partec).

Results and Discussion

To investigate the influence of the oxygenation state on proliferation, growth curves have been measured over 24 hours (data not shown). Whereas the growth under hypoxia did not differ significantly from oxic conditions, the proliferation was nearly completely stopped under anoxia.

Measurements of the plating efficiency (PE) after anoxia showed a constant decrease between 2 and 24 hours of anoxia to around 50 % of the initial PE, indicating that only a certain subgroup of the cells recovered.

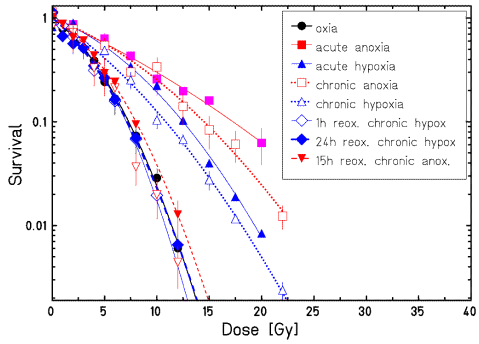

Figure 1: Survival of CHO-K1 cells after X-ray irradiation under different states of oxygenation.

Figure 1 shows the clonogenic survival after x-ray irradiation for the different states of oxygenation and for different times of reoxygenation after chronic hypoxia and anoxia. The resulting OER values are shown in table 1.

Table 1 OER after irradiation with X-ray irradiation under different states of oxygenation

Survival level	Acute anoxia	Acute hypoxia	Chronic anoxia	Chronic hypoxia
50%	1.95	1.73	1.90	1.28
10%	2.35	1.71	1.98	1.48
5%	2.44	1.70	2.00	1.52

From these data, the oxygen effect was dose modifying only for the acute hypoxia. In all other cases it was dependent on the survival level, showing an increasing OER with decreasing survival. The measurement of the reoxygenated curves showed, that there was no permanent influence after hypoxia and also for the formerly anoxic cells the survival rate was similar to that from normoxic cells with a slightly reduced PE.

As the most prominent reason for the difference between acute and chronic anoxia and the dose dependency of the OER the influence on the cell cycle can be expected. To investigate this fact, the cell cycle distribution for cells reoxygenated after chronic anoxia has been measured over 24 hours in comparison to normoxic cells (fig. 2). The results show a G1-block and a smaller block in G2 and a nearly complete depletion of S-cells directly after chronic anoxia. The distribution changes rapidly in the first 12 hours and is comparable to normoxic cells after 15-20 hours.

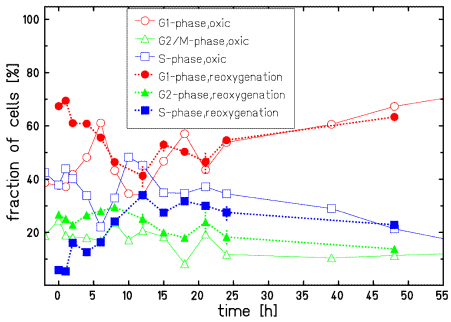

Figure 2: Cell cycle distribution under oxia and reoxygenation after chronic anoxia.

References

[1] Wouters A, et al. Oncologist. 12:690-712(2007).
[2] Tinganelli W,et al. GSI scientific report:482(2009).

Data base of cell survival experiments for testing the Local Effect Model*

T. Friedrich[1], *U. Scholz*[1], *T. Elsässer*[2], *M. Durante*[1,3], *and M. Scholz*[1]

[1]GSI, Darmstadt, Germany; [2]Siemens Healthcare, Erlangen, Germany; [3]Institut für Festkörperphysik, Technische Universität Darmstadt, Darmstadt, Germany

Introduction

One important rationale for tumor therapy with carbon ions is the enhanced relative biological effectiveness (RBE) compared to conventional photon therapy. As the RBE depends on many factors such as the LET distribution in a given depth in tissue, the delivered dose and the radiosensitivity of the cells or tissues under investigation, it can not be investigated experimentally for all relevant parameters. Thus, biophysical models such as the Local Effect Model (LEM) have been set up in order to simulate the RBE. The LEM was developed at GSI, has been refined over the years and has been applied at different ion beam facilities [1]. For validating the LEM, a widespread comparison with experimental data is necessary. For this purpose a data base of in-vitro cell survival experiments with both ions and photon radiation has been set up. A software has been developed which allows to perform LEM simulations on that data base. The data base is designed such that new data can be added easily and it can be used with other RBE models with minor effort.

The data base

To establish the data base, a representative collection of publications was selected, each of which provides photon and ion irradiation survival experiments. Currently the data base comprises 379 survival experiments taken from 16 publications. The experiments were performed at different labs all over the world. They were carried out with different cell lines and different ions from H to Si accelerated to therapy relevant energies. For each experiment the experimental RBEs at specified survival levels were evaluated. Figure 1 shows the biologic variety of cell lines considered in the data base, expressed in the photon dose response coefficients α and β of the linear-quadratic (LQ) model. We suspect that the distribution of the coefficients is generally representative for in-vitro cell lines. Hence besides for testing, the data base also may serve for evaluating typical experimental fluctuations of RBE, which establish a lower precision limit for biophysical models.

First results

The LEM derives the effect of ion radiation to cells based on the effect of photon radiation. The latter one may be parameterized by the LQ model. At high doses above several Gy it is believed that the dose response becomes linear. For applying the LEM this dose range is important, and hence

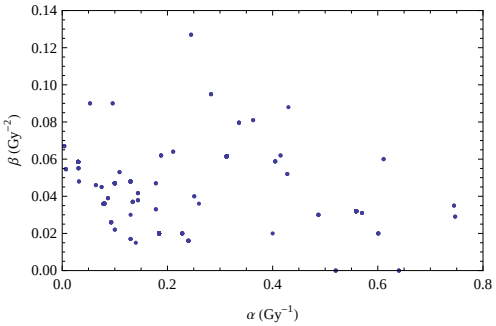

Figure 1: Parameters α vs β for cell lines of the data base.

the photon response is assumed to enter into a purely linear part above a threshold dose D_t. The knowledge of D_t is necessary for using the LEM, but unfortunately only in rare cases it can be obtained from experiments. We thus fitted D_t as a free parameter of the LEM calculation to match the experimental RBEs of each experiment in the data base. The obtained D_t grows linearly with the parameter ratio α/β. This finding is in line with a suggestion by Astrahan et al. [2] and matches our previous experience using more restricted data sets. Figure 2 shows the dependence for carbon ions with a sufficient high linear energy transfer (LET) corresponding to the Bragg Peak region in therapy. For lower LET and different ion species the linear dependence remains, while offset and slope vary. Investigating this relationship in more detail will lead to an empirical method to estimate D_t, widening the applicability of the LEM.

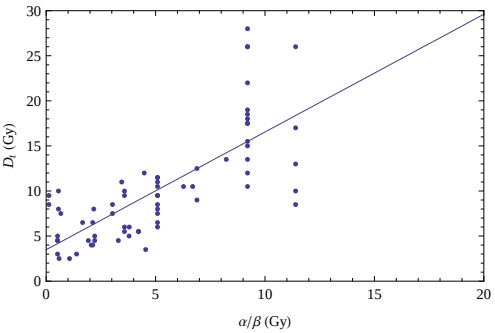

Figure 2: Relationship between threshold dose D_t and α/β for carbon ions with LET $> 70\,\mathrm{keV}/\mu\mathrm{m}$.

References

[1] T. Elsässer et al., Int. J. Radiat. Oncol. Biol. Phys. 78 (2010) 1177.

[2] M. Astrahan, Med. Phys. 35 (2008) 4161.

* Work supported by Siemens Healthcare.

Implementation of the full simulation in the Local Effect Model

U. Scholz[*1], *T. Friedrich*[1], *M. Durante*[1,2], *and M. Scholz*[1]

[1]GSI, Darmstadt, Germany; [2]Institut für Festkörperphysik, Technische Universität Darmstadt, Darmstadt, Germany

The purpose of the Local Effect Model (LEM) is to calculate the dose dependent relative biological effectiveness (RBE) of charged particle radiation with respect to conventional photon radiation [1]. Because of computation time reasons, this is done within a low fluence approximation where the biological damage of a radiation field at arbitrarily high irradiation fluence is deduced from the dose distribution pattern deposited by one single charged particle.

The recent change in the LEM to simulate the actual distribution of discrete DNA damage sites [2] comprises the advantage that discrete DNA double strand break positions have to be considered instead of performing a time consuming numerical summation of a continuous distribution of local doses of different ion tracks to deduce the biological effect of high fluence radiation. This enables us to investigate the reliability of the current approximation at high fluences by simulating the actual damage pattern of an arbitrarily high number of ion traversals and their stochastic distribution by means of a full Monte Carlo simulation in reasonable time.

The Full Simulation Approach

Applying a macroscopic dose D to an ensemble of cells means that the frequency distribution of ion hits follows a Poisson distribution. In our approach, cell nuclei are classified into different "hit classes", each corresponding to a certain number of ion hits of the cell nucleus. The mean cell survival is then deduced by summing up over the Poisson weighted mean survival of every hit class. Using this approach, the linear-quadratic (LQ) parameters α and β, expressing the intra- and intertrack component of radiation action in DNA can be determined by performing a least-square fit on the simulated survival values. Figure 1 shows an example of a simulated survival curve of an arbitrary cell line with known photon dose response, irradiated with carbon ions with a linear energy transfer (LET) of 70 keV/μm.

Empirical Findings

In general it turned out that the β-term in the current LEM approximation is slightly underestimated, which is expressed by the less pronounced bending of the dotted line compared to the full simulation points in Fig. 1.

Repeating the fitting procedure for different LET values for carbon ions as described above, we can compare the LQ parameters α and β resulting from the low fluence approximation and the full simulation approach (Fig. 2).

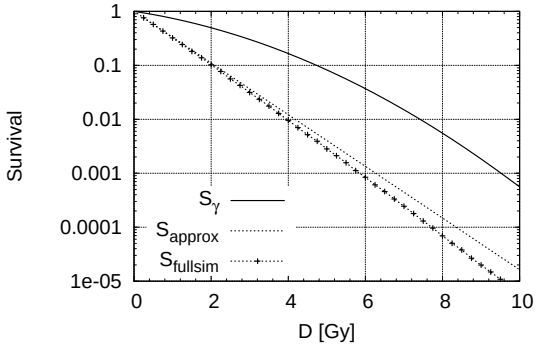

Figure 1: Survival curves of a cell line for photon radiation (solid) with $\alpha_\gamma = 0.25\,\mathrm{Gy}^{-1}$, $\beta_\gamma = 0.05\,\mathrm{Gy}^{-2}$ and threshold dose for the transition to the linear part of the dose response of $D_\mathrm{t} = 9.5\,\mathrm{Gy}$. Also, the simulated curves for carbon irradiation (LET = 70 keV/μm) with the current approximation (dotted line) and the full simulation approach (symbols) are shown.

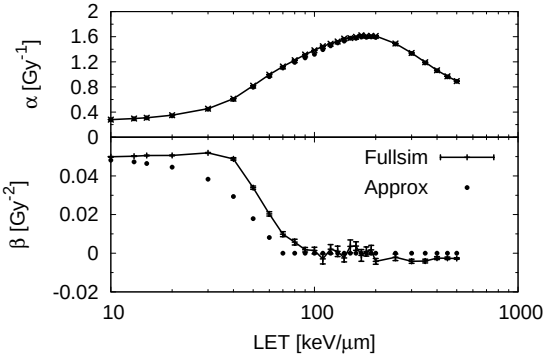

Figure 2: LQ-parameter α and β for the low fluence approximation and the full simulation. Irradiation with carbon ions was simulated for the same cell line as above. The fit was performed in the survival range $S_\mathrm{fit} = 0.01$ to 1.

The resulting LQ-parameters are then used to determine the RBE of the carbon ions compared to conventional γ radiation. In LET regions with an increased β, the RBE of the full simulation is also increased in comparison to the low fluence approximation. The impact e.g. of the choice of α_γ and β_γ on the difference between the full simulation and the approximation is currently analyzed in more detail.

References

[1] M. Scholz et al., Radiat. Environ. Biophys., 36 (1997) 59.

[2] T. Elsässer et al., Int. J. Radiat. Oncol. Biol. Phys., 78 (2010) 1177.

[*] u.scholz@gsi.de

Influence of different states of oxygenation on cell growth after reoxygenation

A. Maier[1,2], *M. Durante*[1,3], *and W. K. Weyrather*[1]
[1]GSI, Darmstadt, Germany; [2]TU Ilmenau, Germany; [3]TU Darmstadt, Germany

Introduction

Hypoxia is a characteristic feature in solid tumors resulting from an inefficient growth of blood vessels in the tissue. These hypoxic cells show an aggressive phenotype resulting in enhanced migration and risk for metastasis[1]. To get a closer look to these features, the construction of a climat chamber for the videomicroscopic observation under defined hypoxic states has been started. In preparation for this previously hypoxic cells have been observed in a conventional climat chamber.

Material and methods

Cell line and culture conditions

CHO-K1 (Chinese hamster ovary) cells cultivated under standard conditions were seeded into petridishes with ∅35mm and 1000 cells per sample in 3ml medium. After seeding the cells were incubated in a humidified atmosphere at 37 °C and 5% CO_2 for 24h.
A special designed exposure chamber has been used to get defined hypoxic (0,5% oxygen, 94.5 % nitrogen, 5% CO_2) or anoxic (95 % nitrogen, 5% CO_2) conditions in the cell culture [2] [3]. After 2 hours of gassing the chambers were closed and kept in the incubator for 24 hours to reach chronic hypoxia or anoxia.

Climat chamber and videomicroscope

To observe the cells over a period of 48h they have to be placed in a climat chamber. For the experimental setup, see Figure 1. The climat chamber is placed on a movable

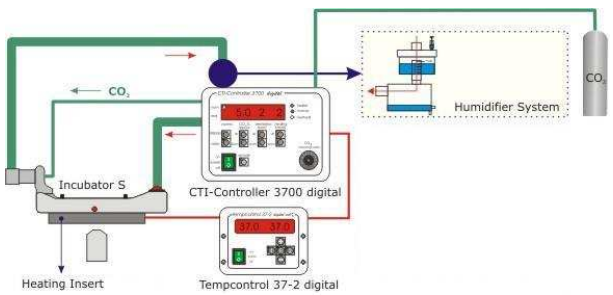

Figure 1: The cells were placed on a heating insert in an incubator directly on the microscope. Warm humidified air with 5% CO_2 is routed over the samples [4].

microscope stage. At the begining of the experiment interesting positions in the samples were manually selected and stored. In an interval of 30 minutes the microscope stage moves to these positions and the microscope takes pictures. So it is possible get a fast motion of the cells over 48 hours.

Results

By counting the number of cells at different time steps it was possible to calculate the doubling time at the various positions. In Figure 2 the comparison between different hypoxic states of oxygenation is displayed. The average doubling time for chronic anoxic cells is bigger than the measurement time. The doubling time for chronic hypoxia is 14,3h and for the oxic cells 15,0h. Chronic

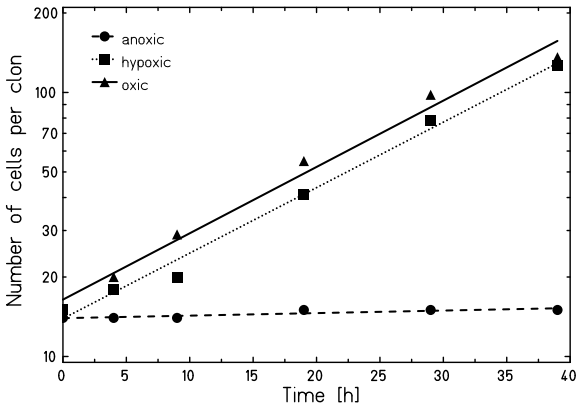

Figure 2: Cell growth after reoxygenation of cells in formerly different chronic states of oxygenation.

hypoxia with 0,5% oxygen seem to be still tolerable for CHO-K1 cells and not influence their clonogenic potential, whereas chronic anoxia seem to interrupt the cell doubling for more than 24 hours after reoxygenation. Also there is no detectable difference in the behavior of the cells like increased movement.

References

[1] K. Ameri et al., Circulating tumour cells demonstrate an altered response to hypoxia and an aggressive phenotype, British Journal of Cancer, 2010, 102, p.561-569.

[2] C. Schicker, C. von Neubeck, U. Kopf, W. Kraft-Weyrather, Patent: Ep 09 002 402.7, Zellkultur-Bestrahlungskammer, 2009.

[3] C. Schicker, C. von Neubeck, U. Kopf, W. Kraft-Weyrather, Patent: De 10 2008 010 918.5, Zellkultur-Bestrahlungskammer, 2008.

[4] `http://www.pecon.biz/images/Applications/CO2Incubation_S2_Leica.png`

Mapping of RBE-weighted doses between HIMAC- and LEM-based treatment planning systems*

O. Steinsträter[1], R. Grün[1], U. Scholz[1], T. Friedrich[1], M. Durante[1], and M. Scholz[1]

[1]GSI, Darmstadt, Germany

Introduction

Starting in 1994 and 1997, extensive clinical studies on carbon-ion radiotherapy have been conducted at the heavy-ion medical accelerator complex (HIMAC) at the National Institute of Radiological Science (NIRS), Chiba, Japan and at the Gesellschaft für Schwerionenforschung (GSI), Darmstadt, Germany. At both centres treatment planning has been based on RBE (relative biological effectiveness) - weighted doses, but influenced by the different beam delivery systems the approaches to estimate RBE-weighted doses have been quite different. To draw maximal benefit from these studies a conversion between both RBE estimation methods is required to allow the comparison of clinical outcomes.

Methods and Materials

The HIMAC irradiation system uses passive beam shaping [1]: Different ridge filters are available to realise fixed SOBP (spread-out bragg peak) shapes from 20 mm to 150 mm. RBE values for treatment planning are derived from invitro experimental data in conjunction with clinical neutron experience. At GSI an active scanning and beam shaping technique is used and RBE values for planning are estimated using the Local Effect Model (LEM) [2,3]. The proposed conversion between RBE-weighted doses, $d^{HIMAC} \rightarrow d^{LEM}$, has been based on a simulation of the physical dose distribution connected with d^{HIMAC} by the LEM based treatment planning system used at GSI. The RBE estimation used at HIMAC is independent of the tumour type, but LEM calculations are based on photon dose response curves of the underlying tissue. Results are therefore presented for the LEM version and the tumour specification used during the clinical trials at GSI as well as for the recently published refined LEM version [3]. For the improved LEM version the description of the tumour tissue has also be updated.

Results

Figure 1 shows the mapping $d^{HIMAC} \rightarrow d^{LEM}$ for the LEM version used during the clinical trials at GSI (upper panel) and for the most recent LEM version (lower panel) in double logarithmic plots for SOBP widths from 20 mm to 120 mm. In all cases, in the lower dose region (d^{HIMAC} below about 5 Gy (RBE)) the LEM predicts higher RBE values, corresponding to conversion factors d^{LEM}/ d^{HIMAC} larger than one. In contrast, for higher doses the conversion factor is typically lower than one. The results for both LEM versions are comparable but significant different from the $d^{HIMAC} = d^{LEM}$ relation. For low dose levels the dependence on the SOBP width is larger for the refined LEM version. This results from a higher gradient in the dependence between biological effect and LET found for the refined LEM version. In contrast, for the LEM version used during the clinical trials experimental studies have shown a systematic tendency to underestimate the ratio of the RBE in the Bragg peak region to the RBE in the entrance channel.

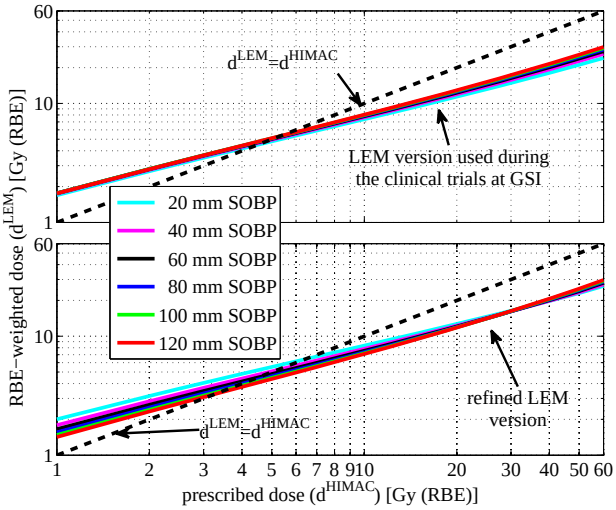

Figure 1: HIMAC and LEM based estimations of RBE weighted doses for different SOBP width and for two LEM versions.

Conclusion

As it could be shown [4] that the biological effect of carbon-ion beams at NIRS and GSI are nearly identical if the physical depth dose distributions are the same, reliable conversion factors can be expected from the method proposed here. They should be helpful in comparing clinical outcomes from studies based on the HIMAC and the LEM based carbon ion treatment planning systems.

References

[1] T. Kanai et al., Int. J. Radiat. Oncol. Biol. Phys. 44 (1999) 201

[2] M. Scholz et al., Radiat. Environ. Biophys. 36 (1997) 59

[3] T. Elsässer et al., Int. J. Radiation Oncology Biol. Phys. 78 (2010) 1177

[4] A. Uzawa et al., Int. J. Radiat. Oncol. Biol. Phys. 73 (2009) 1545

* Work supported by Siemens Healthcare.

RADIOBIOLOGICAL MEASUREMENTS FOR RADIATION THERAPY: EXTENSION TO OTHER IONS*

W. Tinganelli,[1,2] M.Durante, [1,2] and W. K.Weyrather, [1]

[1]GSI, Darmstadt, Germany, [2]TUDarmstadt, Germany.

Introduction

A combined proton and carbon machines is used in Heidelberg (HIT) and will be running in Pavia, Marburg, and Kiel. In addition to proton and carbon it might be possible that several other ions can offer specific advantages which need to be investigated. In this report data from ^{7}Li as lighter ion and ^{14}N as heavier ion are shown. For the heavier ion, especially measurements under different oxygen states are of interest, as high -LET irradiation is supposed to reduce the radio-resistance of hypoxic tissues.

Material and methods

CHO-K1 (Chinese hamster ovary) cells, grown under standard conditions were used for the experiments. For the measurements of the oxygen effect a special designed exposure chamber has been used [1] and irradiated under norm-oxic and anoxic conditions at the SIS with an extended volume of 1 cm. The dose averaged LET values were 100 and 130 keV/µm for carbon ions and 160 keV/µm for nitrogen. For the survival measurements along the Bragg peak with a 116 MeV/u ^{7}Li beam cells were positioned in a stack of polyethylene slides in an acrylic phantom. For the ^{7}Li survival curves the initial energy of from the accelerator of 70 MeV/u was reduced by a 9.8 mm PMMA absorber resulting in an energy of 50.8 MeV/u on target, a LET of 11.3keV/µm and a residual range was 17.2 mm.

Results

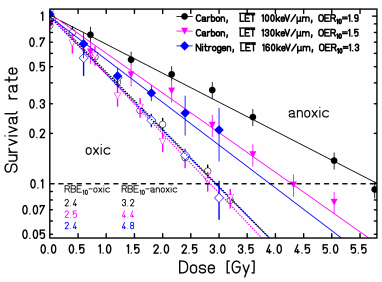

Figure 1: OER and RBE dependence on LET

Fig. 1 shows the measured clonogenic survival after carbon and nitrogen irradiation. Whereas the RBE under oxic conditions at the used LET values is already in a plateau phase, there is still an increase in effectivity with increasing LET under anoxic conditions, resulting in an increased OER with increasing LET. Similar results are reported in Furusawa [2].

The survival curve for 50.8 MeV/u lithium, representing the entrance channel, is shown in figure 2 in comparison to x-ray irradiation. Within the error bars, the resulting RBE can be defined as 1.

The survival rate along the 116 MeV/u ^{7}Li beam is shown in figure 3. The measured results are compared to two different version of the LEM model [3]. The maximal measured RBE in the dose maximum is around 2. As the maximum is very sharp, it needs to measure the irradiation in an extended volume, to see the complete RBE effect under therapeutic conditions.

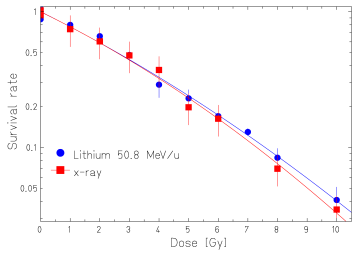

Figure 2: Clonogenic survival after irradiation with lithium 50.8 MeV/µ ions and x-rays

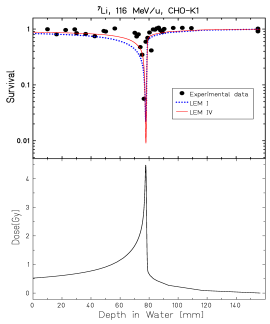

Figure 3 Clonogenic survival along a 116 MeV/u lithium ion beam (upper panel) compared to the corresponding dose (lower panel). The lines show the survival values predicted by two different versions of the LEM model.

References

[1] GSI report 2008-01 page 370 Schicker et al.

[2]Furusawa et al., "Inactivation of aerobic and hypoxic cells from three different cell lines by accelerated (3)He-, (12)C- and (20)Ne-ion beams". Radiat. Res. 2000 Nov;154(5):485-96.

[3]Elsaesser et al. "Quantification of the relative biological effectiveness for ion beam radiotherapy: direct experimental comparison of proton and carbon ion beams and a novel approach for treatment planning" Int. J. Radiation Oncology Biol. Phys. 78(4): 1177-83

* Work supported by EU, PARTNER PROJECT No. 215840.

Verification of the LEM IV for the biological based treatment planning

R. Grün[1,2], *T. Friedrich*[1], *M. Krämer*[1], *M. Durante*[1,3], *and M. Scholz*[1]

[1]GSI, Darmstadt, Germany; [2]Institut für Medizinische Physik und Strahlenschutz, FH-Gießen-Friedberg, Gießen;
[3]Institut für Festkörperphysik, Technische Universität Darmstadt, Darmstadt, Germany

Introduction

The promising clinical results of the ion therapy pilot project at *GSI* have led to an increased interest in carbon therapy with active beam delivery [1]. Carbon ions have an increased biological effectiveness compared to photons. To predict the relative biological effectiveness (RBE) of particles in the irradiated volume the Local Effect Model (LEM I) was developed and used successfully in the pilot project [2]. A better understanding of the biological mechanisms is expected to further improve the treatment planning for carbon ions. Thus the main goal of this work was to benchmark the current version LEM IV [3] against LEM I under treatment-like conditions with idealized geometries as a first step on the way to clinical application.

Methods

Idealised target geometries, e.g. spherical and cubic volumes with different extensions and depth positions were used as target volumes. The impact of the target geometry and position on the dose distribution is analysed. For the simulation of the irradiation process the software package TRiP98 was used [4]. The analysis is based on the dose per fraction applied in the pilot project, i.e. 3 Gy (RBE). This value is a RBE-weighted dose that accounts for the RBE of the carbon ions in the specified tissue. The analysis of changes in the RBE-weighted dose distribution that results from the change of the model version is based on a reference physical dose profile optimized according to LEM I. Exactly the same profile is then reanalysed using the LEM IV. Differences in the RBE-weighted dose therefore solely result from changes in the RBE prediction.

Results

The mean RBE-weighted dose based on the LEM IV shows a clear dependence on the longitudinal extension and decreases with increasing extension in beam direction (Fig. 1). With the application of the LEM IV on the underlying physical dose an increase of the RBE-weighted dose with increasing penetration depth is observed. This increase can be explained by the steeper gradient of the RBE compared to LEM I. A superposition of a second field yields a homogenization of the gradient depending on the field extension. With increasing extension the resulting under dosage in the centre of the target gets broader. In contrast to the target extension the influence of the depth localization is negligible. Only slight differences in the RBE-weighted dose distribution are observed.

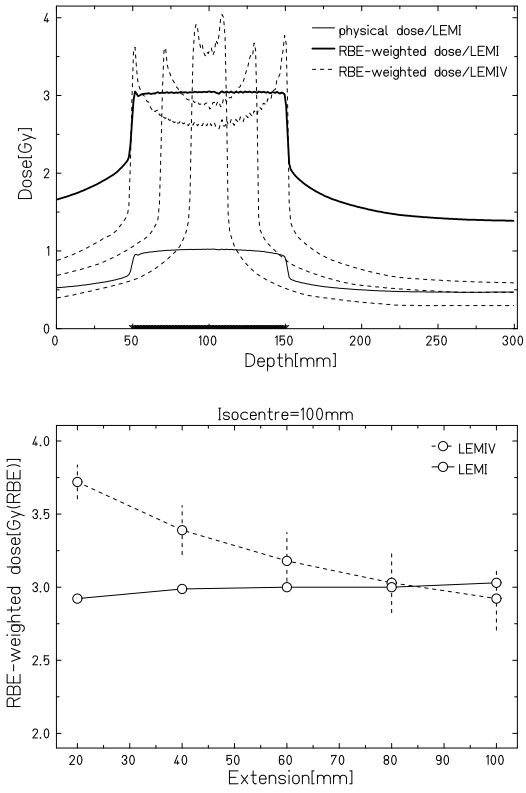

Figure 1: Depth dose profiles for a two-field irradiation of different spherical target volumes with 20, 60 and 100 mm diameter and a isocentre at 100 mm (upper).Mean RBE-weighted dose based on the LEM IV approach vs. the target extension (lower). In addition the optimized RBE-weighted dose based on the original approach (LEM I) is shown.

Conclusion

The results showed that for the typical tumor extension of 50-60 mm regarding the mean tumor volume in the pilot project the RBE-weighted dose predicted by the LEM IV are in good agreement with the LEM I predictions and other studies with protons and heavy ions from the literature and thus can describe the clinical results adequately.

References

[1] D. Schardt,T. Elsässer and D. Schulz-Ertner, Rev. Mod. Phys. 1(2010) 82

[2] M. Scholz et al., Radiat. Environ. Biophys. 36 (1997) 59.

[3] T. Elsässer et al., Int. J. Radiation Oncology Biol. Phys. (2010) 78.

[4] M. Krämer, M. Scholz, Phys. Med. Biol., 11(2000) 45.

A Software for Quantitative Analysis of Irradiated X-Ray Films

P. Steidl[1,2], *M. Durante*[1,2], *and C. Bert*[1]
[1]GSI, Darmstadt, Germany; [2]TUD, Darmstadt, Germany

Irradiation of X-Ray films is a commonly used method for quality asurance in radiation therapy. Films can also be used for dosimetry for heavy-ion irradiation [1]. To ease the analysis of film data and to be compatible with scanners other than the current of GSI, we implemented a film analysis software. Description of the core functionality along with examples is reported.

Visualization: To enable the user to do a visual analysis of film data as comfortable as possible the new software is based on an interactive display realized by VTK [2]. Data is read as `tiff` images (up to 32bit color depth) and in ASCII format. Interactive funtionality includes zoom, movement and color-window adjustment. The actual color window as well as the coordinates and optical density at mouse position is displayed and can be exported. Information of the current view can be stored to file to allow automated use.

Registration: To be able to correlate measured optical densities to calculated nominal data it is necessary to register the film to the ISO-center. Based on positioning information such as the four black piercings in fig. 1 indicating the laser positioning system the software calculates the rotation angle and the center of the coordinate system. Figure 1 shows a registered film with isocenter marks (green lines).

Background Correction: To enable comparability of different films it is necessary to correct films for background. One can specify a certain background value or define an area within which the mean optical density is calculated and used as background value. In addition, a whole film can be subtracted from another one to enable complex background correction or analysis of difference images.

ROI Definition: Parts of the analysis are done for the whole film parts only for specified regions of interest (ROI). ROIs are defined as binary images which have to be of the same size as the film. Therefore, it is possible to use ROIs of any shape. At the moment rectangles, circles and circular rings are implemented.

Analysis: For the whole film and each ROI a histogram of the optical densities is generated. Mean, maximum and minimum optical density as well as the standard deviation of the mean are calculated. In addition, horizontal and vertical profiles are plotted at any requested position (example in figure 2). For plotting functionality `ROOT` libraries were linked [3]. In addition full width at half maximum and the penumbra are calculated for each profile. An automized beam spot detection enables for beam spot size analysis including horizontal and vertical profiles through its center.

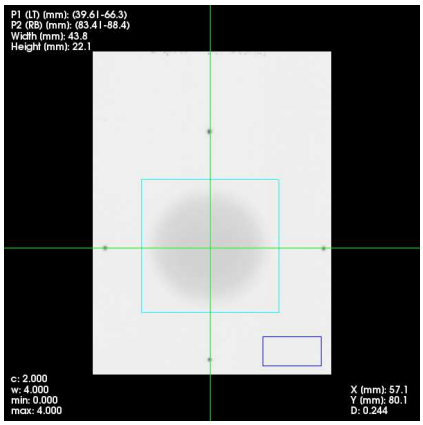

Figure 1: Example of a film response which is already registered to the isocenter based on the four piercings. With the blue region of interests the background is defined.

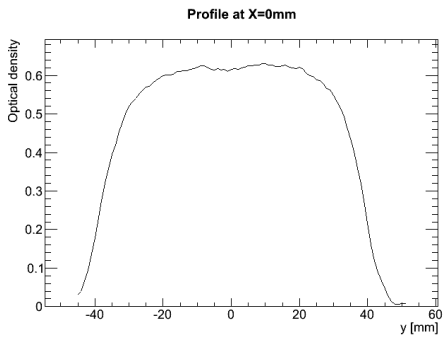

Figure 2: Vertical profile at $x = 0$ of the film data shown in fig. 1.

Automized Processing: Since only the definition of the coordinate system requires manual user input, almost all processing can be automized. Special parameter- and command-files can be combined with bash scripts to manipulate and analyze a large number of films that are already registered to the isocenter in a non-interactive way.

References

[1] B. Spielberger et al., Nucl. Instrum. Methods Phys. Res. 209B (2003) 277.

[2] Kitware, Visualization Toolkit, http://www.vtk.org/

[3] http://root.cern.ch/drupal/

Deformable registration of 4DCT data for ion beam therapy of moving tumors*

N. Saito[1], A. Gemmel[2], M. Durante[1,3], E. Rietzel[2] and C. Bert[1]

[1]GSI, Darmstadt, Germany; [2]Siemens AG, Particle Therapy, Erlangen, Germany, [3]Technical University of Darmstadt, Darmstadt, Germany

Introduction

For radiotherapy with ion beams precise information of the patient's internal anatomy is required. For moving organs such as lung or liver, time-resolved (4D) computed tomography (CT) can be applied to extract anatomical changes due to respiration of a patient. A 4DCT data set consists of several 3-dimensional (3D) CT volumes (typically 10), and each volume corresponds to the anatomical 3D image at a motion phase of the breathing cycle. By comparing two image volumes in a 4DCT set, internal motion including organ deformation can be extracted and used to register one volume to the other. In this report, the quality assessment of the performed deformable registration at GSI is presented.

Materials and Methods

Deformable registration software [1] was used for this study. The software offers various choices of image registration parameters (~ 20 parameter variables). More than 150 parameter combinations have been tested with 4DCT data sets provided by DIRLab [2]. Registration quality was deduced from 300 internal anatomical landmarks in lung for five 4DCT data sets (patient case 1 to 5) [2]. For all cases, the CT image of the maximum inhale phase was registered to the reference image at the maximum exhale phase. The deformation field maps were stored and used to transform the landmarks of the inhale image using a library of the software. Accuracy of the registration was quantified as mean Euclidean distance of all 300 landmark-pairs (transformed landmark position vs. landmark position in reference image).

Results

Figure 1 shows mean distances of the 300 landmark-pairs for the initial displacements without registration (NoRegi) together with the mean distances after registration with default parameter sets (Default) and with the parameters which gives the best results (Best). The initial mean landmark displacement is ranging from 3.9 to 9.8 mm. After the registration with the default parameters of the software, the mean landmark distances show reduction ranging from 2.3 to 6.5 mm. The results lead to the percentages of landmark distance relative to the corresponding initial displacements to be from 56 up to 76 %. The worst case in the percentage, 76 %, is the patient case 5, therefore intensive trials to find optimum parameters had been performed especially for the case 5. Mean distances after registration with the selected parameters resulted in 1.1 to 2.2 mm mean distances. Percentages relative to the initial displacements are ranging from 22 to 29 %. The best percentage of 22 % was obtained for the cases 4 and 5 among them.

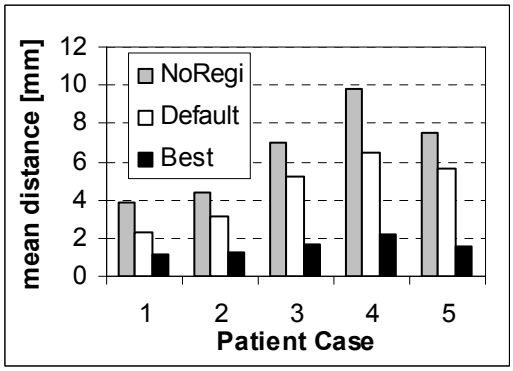

Figure 1: Mean distances in 3D [mm] for the 5 cases with no registration (NoRegi), registration with default parameters (Default) and with parameter giving the best results (Best).

Discussion

The software showed excellent performance with the accuracy of registration better than 2.2 mm for the all tested 5 cases. The parameters chosen for the presented best results are characterized by narrow windowing on CT values to cover the CT value of lungs only. Since lung volumes tend to move separately from the surrounding organs, registration of both lung and surrounding tissues is difficult [4]. It seems that the narrow selection of CT values makes optimization of registration parameters free from the restriction of a smooth connection to the surrounding tissue. For tumours in the lung, the narrow windowing possibly leads to larger uncertainties in the tumour volume since the tumours have CT values outside of the window. Therefore further investigation of registration quality with lung tumours will be conducted.

Conclusion

Deformable registration has been performed and excellent accuracy of less than 2.2 mm was obtained for the 300 landmarks in the tested 5 lung 4DCT data sets..

References

[1] A. Khamene et al, Med. Imag. Comp. Comp. Assist. Interv. 12 828 (2009)
[2] http://www.dir-lab.com
[3] E. Castillo *et al*, Phys. Med. Biol. 55 305 (2010)
[4] E. Rietzel and G. Chen, Med. Phys. 33 4423 (2006)

* Work supported by Siemens AG, Particle Therapy

Estimation of positron emitter distributions from experimental yields

M. Priegnitz[1], *W. Enghardt*[2], *K. Laube*[2], *S. Schöne*[1], *and F. Fiedler*[1]
[1]Helmholtz-Zentrum Dresden-Rossendorf, Germany; [2]OncoRay, TU Dresden, Germany

At GSI Darmstadt targets of different materials have been irradiated with carbon ions in order to verify an approach for the prediction of positron emitter distribution based on experimental yields. Depth dependent thick target yields calculated with this approach are presented and compared to experimental results.

Introduction

Online monitoring of ion beam tumor therapy by means of in-beam PET requires a precise simulation of the expected β^+-activity distribution on the basis of the treatment plan. This predicted distribution is then compared with the measured activity in order to draw conclusions on the correctness of the treatment in particular on the particle range. Up to now, for this Monte Carlo simulation the cross sections of all reactions leading to positron emitting nuclides are necessary. Apart from a few reaction channels these cross sections have not been measured with the accuracy required for in-vivo dosimetry for therapy relevant ions and energies. Thus, an approach has been developed to predict positron emitter distributions on the base of experimental yields rather than on cross sections for these ions, eg. ^{7}Li [1, 2]. To prove the reliability of this method, it has to be compared to the already well established simulation for carbon ions. Therefore, homogeneous targets and targets composed of different materials have been irradiated with carbon ions at GSI. The results of the calculation of positron emitter yields with the yield approach are compared with depth dependent thick target yields obtained from the experiments.

Materials and Methods

By means of the in-beam PET scanner [3] installed at the former therapy site at GSI, Darmstadt, the β^+-activity in targets of different materials has been measured. The targets consisting of graphite (G), polyethylene (PE) and water (W), respectively, have been irradiated with monoenergetic pencil-like beams of ^{12}C with energies relevant for tumor therapy. Measurement of the induced activity has been performed during the irradiation and further 30 min afterwards. From these experiments depth dependent thick target yields for the most abundant positron emitters (^{11}C, ^{15}O, ^{10}C, ^{13}N) in the respective targets have been calculated for intervals with thickness corresponding to 10 *A*MeV energy loss of the primary ions as described in [1] and [2]. To allow for a successful monitoring, the prediction of positron emitters resulting from the reactions of the impinging ions with C, H and O atoms of the tissue gives sufficiently precise results. Thus, the experimental yields from water, graphite and PE serve as a database for the calculation of yields in tissue of any known composition.

$$Y_i(\vec{r}, \text{Target}) = a_1 Y_i(\vec{r}, \text{G}) + a_2 Y_i(\vec{r}, \text{W}) + a_3 Y_i(\vec{r}, \text{PE}),$$

where a_1, a_2, a_3 are coefficients depending on the target material and Y_i are the depth dependent thick target yields in the interval i.

Results

This yield approach has been tested on different materials irradiated with monoenergetic carbon ions. Using the database the positron emitter yield distribution is calculated and compared with experimental yields. Fig. 1 shows the results for a homogeneous polymethyl methacrylate (PMMA) target and an inhomogeneous target consisting of 4 cm graphite and 30 cm water. The energies of the impinging carbon ions were 215 *A*MeV and 266 *A*MeV, respectively. The measured as well as predicted ^{11}C-, ^{15}O- and ^{10}C-yields are presented and found to be in good agreement. Therefore, the developed yield approach is a promising alternative for modeling the β^+-activity induced by ion beam irradiation. A comparison for patient data is in progress.

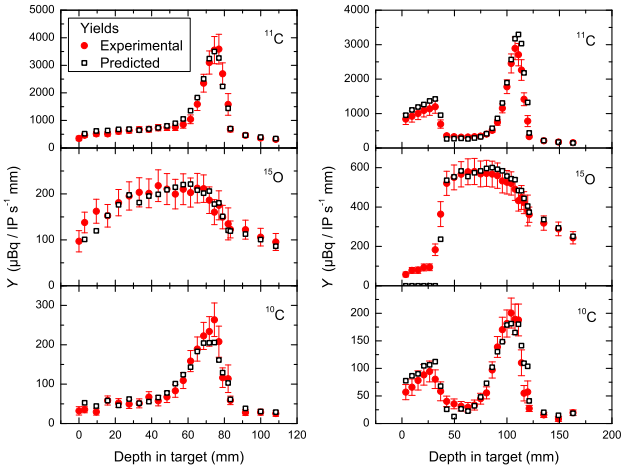

Figure 1: Comparison between experimental and predicted depth dependent thick target yields in a homogeneous target of PMMA (left) and an inhomogeneous target (right) irradiated with monoenergetic carbon ions.

References

[1] M. Priegnitz, D. Möckel, K. Parodi *et al*, Phys. Med. Biol. 53, pp 4443-4453, 2008

[2] M. Priegnitz, F. Fiedler, D. Kunath *et al*, IEEE NSS/MIC Conference Records M08-4, 2008

[3] W. Enghardt, P. Crespo, F. Fiedler *et al*, Nucl. Instr. Meth. A 525, pp 284-288, 2004

Influence of a point source motion in PET images and its compensation

K. Laube[1], *F. Fiedler*[2], *S. Schöne*[2], *C. Bert*[3], *and W. Enghardt*[1]

[1]OncoRay, Dresden, Germany; [2]HZDR, Dresden, Germany; [3]GSI, Darmstadt, Germany

Introduction

Positron emission tomography (PET) allows to assess the relevant parameters of the applied dose distribution in ion beam therapy. It has been clinically implemented but only for the treatment of static targets. The planned application of hadron therapy to intra-fractional moving tumor sites demands an upgrade of the dose monitoring system in terms of regarding the shifted decay locations of the positron emitters due to the patient's motion.

Offline PET measurements of a moving point source have been performed at GSI Darmstadt in order to validate the motion influence in the PET images in the dependence of the motion amplitude. In addition the results of 4D reconstruction with motion compensation are discussed.

Materials and Methods

A β^+-emitting ^{22}Na point source with an activity of 811 kBq was used for offline PET measurements by means of the double head in-beam PET scanner BASTEI at the former medical treatment site [1]. The ^{22}Na source was placed at the iso center and performed a 1D sinusoidal motion. The motion direction (along the y-axis) was parallel to the detector surfaces to recognize a clear motion influence despite the limited solid angle coverage of the PET scanner. A motion period lasted approximately 2.9 s and peak-to-peak amplitudes between 1 mm and 49 mm were chosen (cf. Table 1). Listmode measurements were done for 3 minutes. The sinusoidal elongation was simulateously detected and logged by a laser sensor system. PET images were generated from the data sets containing about $1.5 \cdot 10^6$ events by the well established iterative 3D MLEM (maximum likelyhood expectation maximization) reconstruction algorithm with correction for attenuation, limited solid angle and detector efficiency. The resulting β^+-activity distribution in the detector's midplane was fitted with the 2D Gaussian

$$A(x,y) = a_0 + a_1 \cdot \exp\left\{ -\frac{(x-x_0)^2}{2\,{\sigma_x}^2} - \frac{(y-y_0)^2}{2\,{\sigma_y}^2} \right\} \quad (1)$$

where x_0, y_0 are the center coordinates and σ_x, σ_y are the width of the Gaussian in x- and y-direction, respectively. For non-static measurements the Gaussian is prolonged in y-direction, thus the quotient σ_y/σ_x was used to quantify the motion influence. For the 4D reconstruction the listmode data sets were divided into 9 subsets according to the motion's amplitude or phase, respectively. To overcome the lack of statistics in the single subsets the applied 4D MLEM algorithm make use of all projection data in each iteration step [2, 3] by using rigid-body transformation matrices. The final β^+-activity distribution was fitted with equation (1).

Results

Table 1 shows the calculated quotients σ_y/σ_x of the respective β^+-activity distributions for nine investigated amplitudes. The values for the 3D reconstructions are fast-growing with increasing amplitude. Actually for amplitudes smaller than a single crystal width of the detector (6.75 mm) the Gaussian is signifantly prolonged in motion direction. The motion influence on the image quality is considered as significant when the value of σ_y is about 10% larger than the value of σ_x, i.e. for ratios greater than 1.10. The 4D reconstruction algorithm turned out as suitable for diminishing the motion influence in the final PET images independent of creating the subsets by phase or amplitude sorting. Nevertheless the sorting by amplitude offers better results with significantly suppressed motion influence also for larger amplitudes because in each single subset the residual motion has the same range. However, the sorting by motion phase has the advantage that all subsets contain roughly the same number of coincidences with a constant signal-to-noise ratio.

Table 1: Ratio of the Gaussian's widths obtained from the fit of the β^+-activity distribution in the detector's midplane with equation (1) for the investigated peak-to-peak amplitudes. Values are shown for the 3D reconstruction and the 4D reconstructions of the data sets subdivided by phase and amplitude, respectively.

peak-to-peak amplitude	σ_y/σ_x		
	3D	$4D_{phase}$	$4D_{amplitude}$
1.0 mm	0.995	0.976	0.977
2.5 mm	1.073	0.987	0.995
5.6 mm	1.245	1.031	1.017
7.1 mm	1.443	1.041	1.033
10.1 mm	2.106	1.065	1.054
15.4 mm	3.441	1.138	1.083
21.4 mm	4.960	1.158	1.079
29.7 mm	7.061	1.187	1.091
49.3 mm	11.555	1.466	1.104

Conclusion

Intra-fractional motion influences significantly the quality of PET images, even for sub-centimetre peak-to-peak amplitudes. Consequently, to implement in-beam PET as a quality control system for ion beam therapy of moving tumor sites image reconstruction algorithms have to be applied which compensate the organ motion and thus reproduce an reliable β^+-activity distribution.

References

[1] W. Enghardt *et al.*, Nucl. Instr. Meth. A 525, 2004, pp. 284–8

[2] T. Li *et al.*, Med. Phys. 33, 2006, pp. 1288–98

[3] F. Qiao *et al.*, Phys. Med. Biol. 51, 2006, pp. 3769–83

Implementation of Beam Tracking and Dose Compensation in TRiP4D*

R. Lüchtenborg[1], *D. Richter*[1], *M. Durante*[1], *G. Kraft*[1], *and C. Bert*[1]
[1]GSI, Biophysics, Darmstadt, Germany

Introduction

Scanned particle beams are used since 1997 for treatment of stationary tumors [1]. One current field of research aims at transferring this highly tumor conformal treatment technique to moving tumors. Therefore, techniques to mitigate dose deteriorations caused by interference between beam scanning and tumor motion are needed [2]. Technical feasibility of different motion mitigation techniques has already been shown in phantom measurements [3–5].

Simulations incorporating patient data (e.g. 4D-CT) are important to bring scanned particle therapy of moving tumors closer to clinical practice. Therefore, the GSI treatment planning software TRiP98 is currently extended to be able to cope with moving tumors [8]. In this work the implementation of beam tracking (BT) and real-time dose compensation (RD) has been done. While BT adapts the beam position to the moving tumor position [5], RD is an extension of BT improving dose homogeneity in the presence of non-translational motion components [6, 7].

Material & Methods

The TRiP98 research version TRiP4D [8] is already capable of calculating dose distributions under consideration of tumor motion. In this work it has been further extended by a BT functionality. Raster positions are adapted in all three dimensions according to pre-calculated compensation vectors. As even BT can preserve the homogeneity of the planned dose distribution only in case of purely translational motion the technique has been extended by a RD functionality. Dose changes resulting from beam delivery in the presence of non-translational motion are calculated from pre-calculated base data and used to adapt the particle numbers deposited at individual raster positions [7].

A treatment plan has been optimized to deliver 1 Gy to a box-shaped target area. It has been delivered to a rotational water phantom using BT alone and BT combined with RD (RDBT), respectively. Resulting dose distributions can be assessed in two different ways in TRiP4D:

RECO Dose distributions are reconstructed based on measured delivery data (e.g. target motion, beam position, particle numbers). This method does not rely on the newly implemented BT and RD functionalities as BT and RD adaptations performed by the therapy control system are inherently included in the measured beam delivery data.

SIM Dose distributions can be simulated taking into account the experimental motion trajectory, accelerator intensity and pre-calculated base data for BT and RD. The newly implemented BT and RD functionalities are employed. No measured beam monitoring data is used.

Both methods have been used. The agreement between both is assed by calculating the dose difference at each CT voxel position.

Results

As can be seen in Fig. 1 both ways to assess experimental dose distributions are in very good agreement.

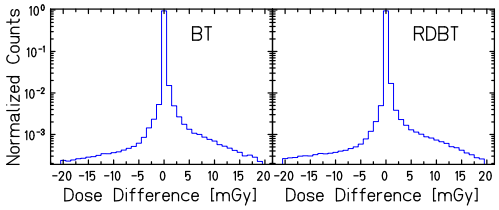

Figure 1: Distribution of voxel dose differences between **SIM** and **RECO** for a BT measurement and a RDBT measurement. For both measurements the dose assessment methods are in good agreement. Note the logarithmic scale.

Conclusion

BT and RD have been successfully implemented to TRiP4D. From the good agreement between reconstructed and simulated dose delivery it is concluded that the newly implemented functionalities reproduce the functionalities of the therapy control system very well. This enables extensive treatment planning studies based on measured data (e.g. 4D-CT, respiratory motion traces, accelerator intensities) incorporating BT and RD. These simulations will facilitate anticipation of treatment delivery results on moving tumors as well as optimization of treatment delivery parameters to guarantee safe dose delivery.

References

[1] M. Durante and J. S. Loeffler *Nat. Rev. Clin. Oncol.* **7** (2010).
[2] M. H. Phillips et al. *Phys. Med. Biol.* **37** (1992).
[3] C. Bert et al., *GSI Scientific Report* (2008).
[4] C. Bert et al., *Int. J. Rad. Onc.* **73** (2009).
[5] C. Bert et al., *Med. Phys.* **34** (2007).
[6] C. Bert and E. Rietzel, *Rad. Onc.* **2** (2007).
[7] R. Lüchtenborg et al., *Proc. WCMP* (2009).
[8] D. Richter et al., *GSI Scientific Report* (2010).

* Work supported by Siemens Healthcare, Imaging & Therapy, Particle Therapy, Erlangen.

Refined method for calculation of compensation parameters*

J. Nguyen[1,2], M. Durante[1,2], and C. Bert[1,#]

[1]GSI, Darmstadt, Germany, [2]TU Darmstadt, Germany

Introduction

Irradiations of intra-fractionally moving organs with a scanned ion beam need to be performed with a dedicated motion mitigation technique to avoid cold-spots in the delivered dose distribution due to interplay [1]. One possible way to achieve this is beam tracking [2]. Beam tracking compensates organ motion by adjusting the position of the pencil beam in real-time during treatment delivery. This approach requires 4D treatment plan optimization, i.e. lateral and a longitudinal compensation parameters for each combination of beam position and motion phase [3].

This report presents a novel approach for compensation parameter optimization that takes the scanpath and the dose distribution of an individual beam position into account. We aim at less performance demands for the energy compensation system (energy change in between beam positions, i.e. within 10 ms).

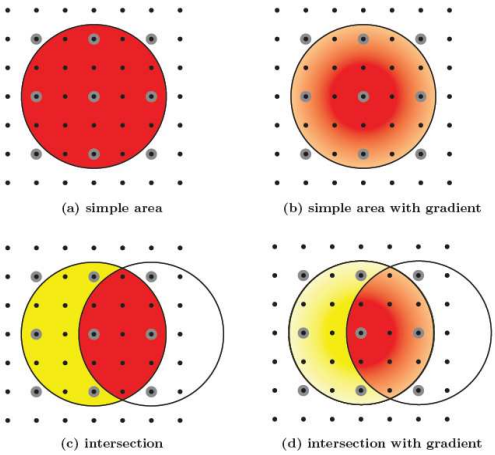

Figure 1: At each beam position (grey spots) a Gaussian dose profile is delivered (red gradient). Four new methods for compensation parameter calculation are presented (a-d). They take the Gaussian dose profile and the transition to the next beam position into account by weighting the compensation parameter calculated for each black spots with the dose at its position (red gradient). The scanpath is incorporated by increasing the weight of neighbouring beam positions (red: high, yellow: low).

Materials and Methods

Beam scanning within an iso-energy slice is performed in a pre-defined order, the scanpath. In addition, there intentionally is a fairly broad overlap of the dose distribution delivered by neighbouring beam positions that is used to minimize the dosimetric influence of small deviations in the beam position (see fig. 1). We incorporated these facts in the calculation of compensation parameters. Instead of calculating the compensation parameter just for the central ray of the pencil beam at each grid position, a larger area (e.g. 2σ) of the Gaussian shaped beam is incorporated. As illustrated in fig. 1, four different calculation methods were investigated.

We tested the method on a 4D treatment plan for a lung tumour patient. Only changes in the magnitude of the longitudinal compensation (dz) when going from one beam position to the next will be reported, i.e. ddz values in units of millimetre water-equivalent.

Results & Conclusion

Fig. 2 shows the change in dz (ddz) for the four methods indicated in fig. 1 in comparison to the original method that incorporated the central ray only. Two different scanpaths were investigated. The cumulated data show that all new methods increase the amount of low ddz values. Comparing the amount of low ddz values among the four new methods shows the following behaviour: intersection with gradient > simple area with gradient > intersection > simple area. The two methods that incorporate the dose gradient of the Gaussian pencil beam have the highest amount of low ddz values.

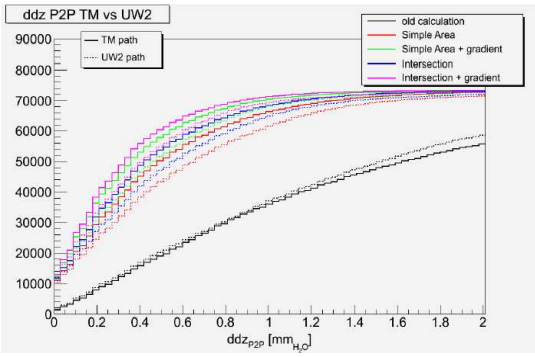

Figure 2: Results for the 4D lung treatment plan of a single patient (cumulated histogram of the changes in dz). Two perpendicular scanpaths (TM and UW2) and the four methods presented in fig. 1 were investigated. The black data indicate the results for the old calculation method.

Alternative methods for calculation of compensation parameters for beam tracking are promising since the number of low ddz can be increased. This lowers the demands of the performance of the energy compensation system for longitudinal beam adaptations.

References

[1] Bert et al., *Phys. Med. Biol.* **53**(9), 2008
[2] Grözinger et al., *Radiat. Oncol.* **3**(34), 2008
[3] Bert and Rietzel, *Radiat. Oncol.* **2**(24), 2007

*in part supported by Siemens AG, Particle Therapy
#c.bert@gsi.de

Simulation of beam record data for 4D dose calculation*

D. Müssig[1], M. Durante[1], and C. Bert[1]

[1]GSI, Biophysics, Darmstadt, Germany.

Introduction

Treatment of moving targets can result in local over and under dosage due to interference effects of the beam application and the motion of the target. First experimental studies [1] as well as theoretical works [2, 3] showed that multiple irradiations with an accordingly reduced dose per irradiation reduce these inhomogeneities due to averaging effects. If the multiple irradiations are performed within one fraction this method is called rescanning.

We build up a simulation environment based on TRiP4D [4] to compare different motion mitigation methods. Input to 4D dose calculations are simulated beam records. In this work, we present a tool which allows simulating the beam progression data of the beam records, i.e. the irradiation time of each beam position (referred to as rasterpoint).

Material & Methods

The tool needs two input parameters. 1) the treatment plan that contains the beam parameters of every single rasterpoint (energy, focus, position, particle number, and the specific rescanning option) and 2) the information of the beam extraction profile (i.e. average shape and intensity per pulse). These data are processed taking into account the specific GSI irradiation characteristics.

The functionality was tested by using a simple rectangular beam extraction profile and a treatment plan of a lung cancer patient (4DCT based, Lujan motion with 3.5 s period).

For this study we compared different strategies. 1) Slice by slice rescanning [2]: Each iso-energy slice (IES) is irradiated multiple times before changing the energy. 2) Breath sampled rescanning [5]: The irradiation time of each IES is controlled such that it takes as long as the motion period. 3) Gating: Irradiation is only allowed in specific motion states.

Results

In the figures the black lines denote the accelerator signal (high/low denotes on/off). The blue line is the normalized motion signal and the red line is the progress of the irradiation in terms of irradiated rasterpoints which is the outcome of the beam record data simulation.

In Figure 1 the beam structure is of regular periodic shape. The beginning of the irradiation is independent of the motion cycle and each IES finishes after different time periods which is consistent with slice by slice rescanning.

In Figure 2 we simulated the beam record for breath-sampled rescanning. The special characteristics of breath sampled rescanning are clearly visible: the irradiation time of each IES matches to the motion period of 3.5 s.

Figure 3 shows the result for a gated treatment. The simulated beam record shows that irradiation is only allowed when the normalized motion amplitude is between 0 and 0.05.

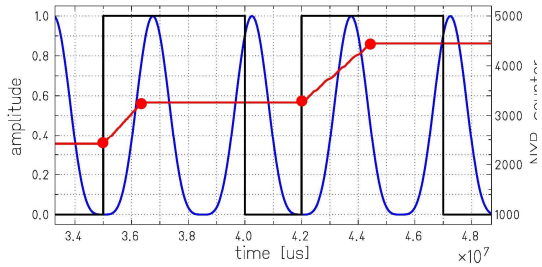

Figure 1: slice by slice 5x rescanning

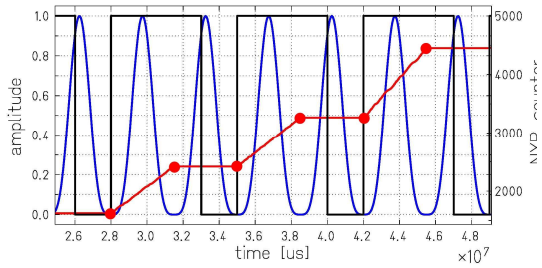

Figure 2: breath sampled 5x rescanning

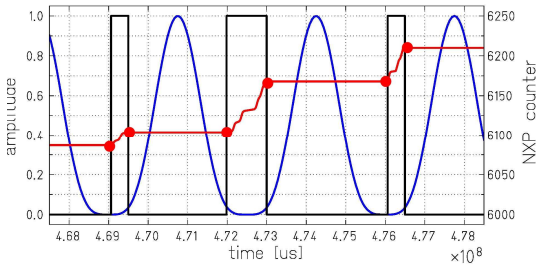

Figure 3: gating

Conclusions

We implemented and tested a tool to generate beam record data of the temporal irradiation sequence for different motion mitigation strategies.

References

[1] Bert et al., GSI Scientific Report 2008, 397
[2] Philips et al., Phys. Med. Biol. 37 (1992), 223-243
[3] Bortfeld et al., Phys. Med. Biol. 47 (2002), 2203-2220
[4] Richter et al. – this report
[5] Seco et al., Phys. Med. Biol. 54 (2009), 283-294

* This work is in part supported by Siemens AG, Particle Therapy and the EU-FP7 project ULICE (Union of Light Centres in Europe)

Robustness of Beam Tracking for Moving Tumors*

J. Eley[1,2], *R. Lüchtenborg*[3], *D. Richter*[3], *M. Durante*[3], *and C. Bert*[3]
[1]The University of Texas Graduate School of Biomedical Sciences, Houston, TX, USA;
[2]The University of Texas M. D. Anderson Cancer Center, Houston, TX, USA; [3]GSI, Darmstadt, Germany

Introduction

Scanned carbon ion radiotherapy beams provide highly conformal dose distributions for stationary tumors and excellent sparing of nearby normal tissues due to the sharp energy-loss maximum (Bragg peak) near the end of the particle range and minimal lateral Coulomb scattering. For moving targets (e.g., respiratory motion) treatment delivery with scanned ion beams becomes considerably more complex, and individual pencil beams may inadvertently overlap a previously-irradiated region (overdose) or entirely miss a desired region in the target (underdose). A beam tracking method developed by Grözinger et al [1] minimizes these effects by adapting the scanned pencil beam position and energy to follow a moving target. The purpose of the current study was to assess the robustness of beam tracking for moving radiotherapy targets to uncertainties and limitations in the therapy tracking system.

Methods and Materials

An algorithm to compute the lateral and range tracking parameters for carbon beams for all respiratory motion states was adapted from the work of Bert and Rietzel [2] and implemented in a currently developed research version of TRiP98 (TRiP4D) [3, 4]. To understand the robustness of the tracking method, the ability to simulate uncertainty by random and systematic offsets to the tracking parameters Δx, Δy, and $\Delta z_{\mathrm{H_2O}}$ was implemented in TRiP4D. A model describing the limited acceleration of the range-tracking wedge system was also added to compute only those range tracking parameters that are technically possible to deliver. Variations in respiratory cycle period, the starting respiratory phase (when radiation delivery begins), and phase delays (loss of correlation) between internal and external motion signals were investigated by generating sinusoidal motion signals with various period and phase.

A hypothetical planning target volume (PTV) was simulated as a 3 cm diameter sphere in a 10 × 10 × 10 cm^3 water phantom. For a reference state, the target center was located off central-axis at x = -1 cm and y = -0.25 cm and at depth $z_{\mathrm{H_2O}}$ = 3.5 cm. 3D pencil-beam locations, energies, and fluences were optimized to deliver uniform dose (1000 mGy) to the PTV for the reference state. The target motion was sinusoidal with peak-to-peak amplitude (A) A_x = 2 cm, A_y = 0.5 cm, and A_z = 1 cm. 4D tissue transformation vectors were generated for 31 samples of the sinusoidal motion (sampled between 0 and 180°). To analyze robustness of tracking, dose was computed for (1) ideal tracking, (2) individually varying period, number of motion states, wedge acceleration, starting phase, external motion phase delay, systematic x, y, and z offsets, and random x, y, and z offsets, and (3) combinations of varying parameters.

Results and Discussion

Results for the spherical PTV tracking dose distributions are shown in Figure 1 for external motion signal phase delays of 0°, 5°, 10°, and 15°. Degradation of the dose distribution is seen with increasing delay as expected. The uniformity of dose seen in the 0° phase delay (ideal tracking) indicates that the tracking parameters were implemented correctly in the 4D treatment planning system for water phantom studies.

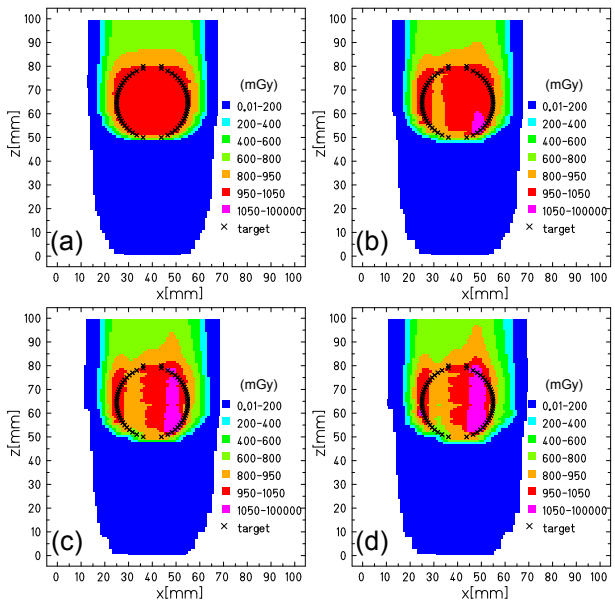

Figure 1: Computed xz dose planes for a spherical PTV (black) with sinusoidal motion (period = 4 s). Prescribed dose was 1000 mGy. Dose for beam tracking shown for (a) 0°, (b) 5°, (c) 10°, and (d) 15° external motion phase delay.

References

[1] S. Grözinger et al, Radiother Oncol, **73** (2004) S77-9.
[2] C. Bert and E. Rietzel, Radiation Oncology, (2007) 2:24.
[3] M. Krämer et al, Phys Med Biol, **45** (2000) 3299-317.
[4] D. Richter et al, GSI Annual Report, 2010.

* Work supported by research grant from the Deutscher Akademischer Austausch Dienst, Bonn, Germany.

Simulation and Visualization of uncertainties in 4D treatment planning*

S.Hild[1], M. Durante[1,2], and C. Bert[1#]

[1]GSI, Darmstadt, Germany, [2]TU Darmstadt, Germany.

Introduction

Along with innovative ideas for treating non static tumours comes the need of a 4D supporting treatment planning software. The GSI code treatment planning for particles (TRiP) [1;2] has recently been extended to 4D capabilities (TRiP4D) [3]. The status of TRiP4D has proceeded to a level which allows the first four dimensional uncertainty simulations. The sum of all uncertainties present at treatment time lead to a change in the estimated dose distribution. A major challenge to uncertainty consideration in general but especially in case of 4D treatment is their visualization.

We are currently working on various concepts of communicating errors by easy and intuitive visualization.

Material and Methods

On the basis of TRiP4D numerous dose calculations are preformed with a different set of errors applied to the input parameters [4;5]. The resulting dose distributions are merged and statistically analyzed (mean/standard deviation/minimum/maximum) with a spatial resolution of the original CT data set. Visualizing the generated data is realized by two different methods, showing either the merged distribution directly or drawing modified versions of the DVH (Dose Volume Histogram) associated with the distribution.

Results / Current status

Distribution

The additional uncertainty information can be added to common dose distributions in different ways. A red/green plot has been found to be one of the best ways. It is simple, easy to read and shows all important information.

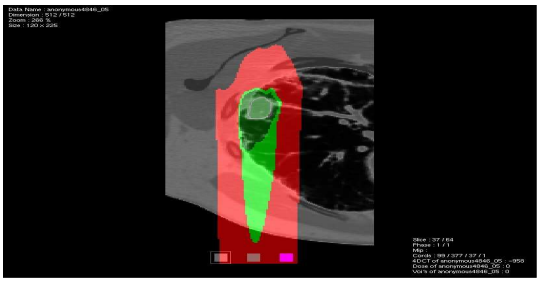

Figure 1: Dose-distribution of a static simulation of a lung cancer treatment showing uncertain areas in red. Threshold for uncertain areas was chosen to be +/- 5% of the prescribed dose. The shaded area around the ROI corresponds to the 95% isodose.

Dose Volume Histograms

The comparison of DVHs appears to be a good method of characterizing an error. The broadening of the DVH-band indicates a considerable influence of the simulated uncertainty to the quality of the treatments dose distribution. Figure 2 shows an example.

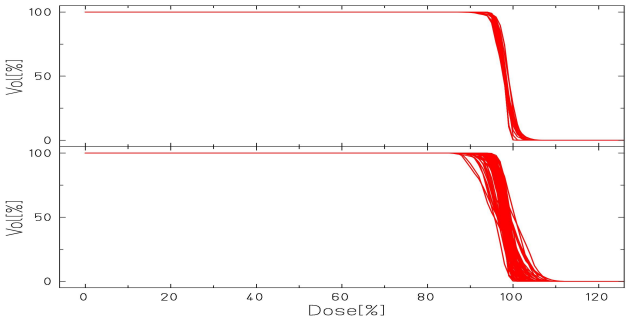

Figure 2: Comparison of Dose Volume Histograms from a simulation using gating assuming no uncertainties (top), with the same simulation assuming a phase shift of ±10° between the internal motion and motion surrogate.

Outlook

Plans for future simulations are combining the distributions for setup (3D) uncertainties with organ motion-related (4D) uncertainties. The result will then be compared to the current simulations. This way we hope to be able to judge the contribution and influence by either source of error to the overall uncertainty.

References

[1] Krämer et al. “Treatment planning for heavy-ion radiotherapy: physical beam model and dose optimization” Phys. Med. Biol. 45 (2000) 3299–3317

[2] Krämer et al. “Treatment planning for heavy-ion radiotherapy: calculation and optimization of biologically effective dose” Phys. Med. Biol. 45 (2000) 3319–3330

[3] Richter et al. – this report

[4] Lomax “Intensity modulated proton therapy and its sensitivity to treatment uncertainties 2: the potential effects of inter-fraction and inter field motions” Phys. Med. Biol. 53 (2008) 1043–1056

[5] Henriquez et al. “A novel method of the evaluation of uncertainty in dose-volume histogram computation” Int. J. Radiation Oncology Biol. Phys., Vol 70, No 4, (2008) 1263-1271

* In part by Siemens AG, Particle Therapy.

#c.bert@gsi.de

Status of 4D Treatment Planning Implementations for TRiP98

D. Richter[1,4], J. Trautmann[1], A. Schwarzkopf[1], M. Krämer[1], R. Lüchtenborg[1], J. G. Eley[2], A. Gemmel[3], M. Durante[1,4], and C. Bert[1]

[1]GSI, Darmstadt, Germany; [2]MD Anderson Cancer Center, Houston, USA; [3]Siemens Healthcare, Particle Therapy, Erlangen, Germany; [4]Technische Universität Darmstadt, Solid State Physics Dep., Germany

Introduction

TRiP98 is a treatment planning program for radiotherapy with scanned ion beams. It was developed at GSI and has been successfully used in clinical routine from 1997-2008 for over 400 patients, predominantly with head and neck tumors [1,2]. The treatment of tumors within moving organs, such as lung tumors, with scanned ion beams involves additional complexity of the beam delivery and the treatment planning process. Therefore, new implementations for 4D treatment planning in TRiP98 were needed and carried out at different stages of development [3-5]. This report gives an overview of recent developments of the 4D treatment planning version of TRiP98 (TRiP4D).

4D Implementations in TRiP4D

4D image registration. In ion radiotherapy treatment planning is based on 3D computed tomography (CT) along with organ delineation done by a physician. For the treatment of moving tumors these data are ideally extended to time resolved data, i. e. a 4D computed tomography [3] and segmentation which reflect anatomical changes during a breathing cycle of the patient. In order to exploit this for treatment planning, 4D image registration has to be employed, delivering transformation maps of anatomical positions between the 4DCT phases, i. e. the assigned 3DCTs.

In the course of treatment planning transformation maps generated by a dedicated software are required. To complement existing specific formats for different image registration programs, a generic format of transformation maps has been newly implemented, representing easy-to-use 3D vector fields. The format and the routines used to apply the transformation maps in TRiP4D enable for the use of a wide range of registration softwares available, while only minimal adjustments to the treatment planning software are required. The transformation functionality of TRiP4D has been validated using patient datasets and commercially available registration software. In addition more efficient memory management and therefore the use of larger patient CT and transformation datasets are possible, which are essential for 4D treatment planning studies.

4D dose calculation. The relative biological effectiveness of heavy ions with respect to photons is a decisive advantage of heavy ion radiotherapy. In order to exploit this potential, biological dose calculation is required for treatment plannning. The capacity of TRiP4D to calculate biological dose for static targets thus had to be transferred to moving targets. First efforts, supported by biological cell experiments, were made by Gemmel et al. [4]. Based on this work biological dose calculation has been implemented into TRiP4D and was verified against the earlier implementation of Gemmel et al. showing negligible deviations. In turn the biological dose calculation algorithm of Gemmel et al. showed good agreement with biological cell experiments [4]. Depending on the complexity of the geometry and the calculation algorithm physical and biological dose calculation can be very time consuming, especially in 4D treatment planning. Hence, parallel computation of physical and biological dose calculation using multicore CPUs has been investigated [6].

4D treatment modalities. In 4D ion radiotherapy different modalities for motion mitigation are studied and discussed, the most important ones being gated irradiation, 3D motion compensation (beam tracking) and rescanning [3]. For beam tracking 3D correction parameters of the beam position are optimized during treatment planning and have to be employed in 4D dose calculation. The existing beam tracking functionality in older implementations has been revised and further improved for the integration into TRiP4D. In beam tracking at GSI beam energy variations for depth corrections are introduced using a system of motor driven interleaved absorber wedges. Detailed modelling of the finite acceleration of the system has been carried out and integrated into TRiP4D, enabling for precise dose reconstruction for beam tracking (see [7] for details).

For moving targets wih non-translational motion components additional compensations of the applied particle numbers further corrections in the applied particle numbers, so called real-time dose compensation, has to be considered. The real-time compensation of dose changes based on pre-calculated base data has been implemented in TRiP4D, providing combined beam tracking and dose compensation functionality for treatment simulations. The reader is referred to [8] for more details.

References

[1] M. Krämer et al., *Phys. Med. Biol.*, **45** (2000) 3299-3317.

[2] O. Jäkel et al., *Phys. Med. Biol.*, **46** (2001) 1101-1116.

[3] C. Bert and E. Rietzel, *Radiat. Oncol.*, **4** (2007) 2-24.

[4] A. Gemmel et al., World Congress on Medical Physics, **1**, (2009) 377-380.

[5] D. Richter et al., *GSI Scientific Report* **2009** 500.

[6] J. Trautmann et al., *GSI Scientific Report* **2010**

[7] J. G. Eley et al., *GSI Scientific Report* **2010**

[8] R. Lüchtenborg et al., *GSI Scientific Report* **2010**

Uncertainty analysis of film dosimetry for ion beam therapy

F. Twumasi-Boateng[1, 2], C. Grupen[2], M. Durante[1,3], and C. Bert[1,#]

[1]GSI, Darmstadt, Germany; [2]University of Siegen, Germany; [3]TU Darmstadt, Germany

Introduction

Radiographic films are well-established 2D dosimeters with excellent spatial resolution. Numerous publications discuss the different aspects of film dosimetry and its response to different radiation fields [1-3].

In this study, we carried out several experiments to assess the uncertainties related to dosimetry with *Kodak X-Omat V* films in scanned ion beam therapy. The measured film response is potentially influenced by the condition of the developing machine, the time delay between irradiation and development, storage temperature of the developed film, and the densitometer. Since quantitative assessments in ion beam therapy are done against the modelled film response that is based on the photon response of the film [1], the study also included ^{60}Co and linear accelerator (linac) based photon beam irradiation. In this report, we present an experiment for dosimetric studies with ^{60}Co based photon beams to investigate changes in the measured optical densities due to cooled storing of the irradiated film and the use of different hand densitometers.

Materials and Methods

Kodak X-Omat V films of the same batch were irradiated with ^{60}Co at the Gammatron of DKFZ Heidelberg. We irradiated different dose levels up to D=5 Gy. For each irradiation, two abutting films were placed below 3 cm of solid water to ensure that they are irradiated with identical conditions. After irradiation, one of the films was kept in a refrigerator at a temperature of ~5° C for more than three weeks before being developed. The other film was developed immediately after irradiation. We developed both films with a developing machine that is in daily clinical use (AFGA CLASSIC E.O.S). The blackening level was determined with two different models of the hand densitometers Pehamed–Densonorm 21E (PTW, Freiburg, Germany).

For analysis, the film blackening data S were measured at multiple positions in the irradiated field and fitted by $S - S_{bg} = S_0\left(1 - \exp(-mD)\right)$ as proposed by Spielberger et al. [1]. To assess if storing and the use of different densitometers have an influence on the outcome, χ^2-analysis was performed by pairwise comparison of measured and fitted data.

Results & Conclusion

Fig. 1 shows measured and fitted data for the two hand densitometers. Fig. 2 shows the corresponding data for different storing conditions. For both experiments tab. 1 lists the fit data. Preliminary data of the analysis indicates, that as expected different hand densitometers yield comparable results. But it also shows that 3 weeks storing of the films prior development has an influence on the outcome. Additional experiments and extended analyses will be performed also incorporating data from irradiations with a scanned carbon beam.

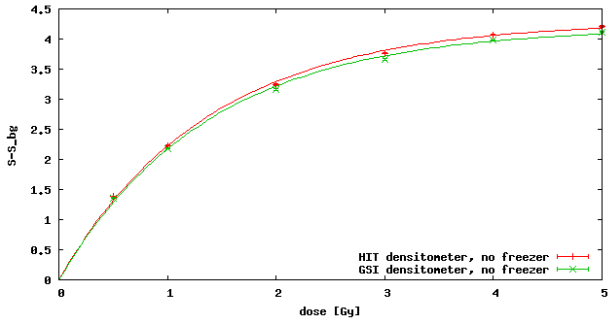

Figure 1: Results for the background corrected saturations curves analyzed by two different hand densitometers from GSI and HIT.

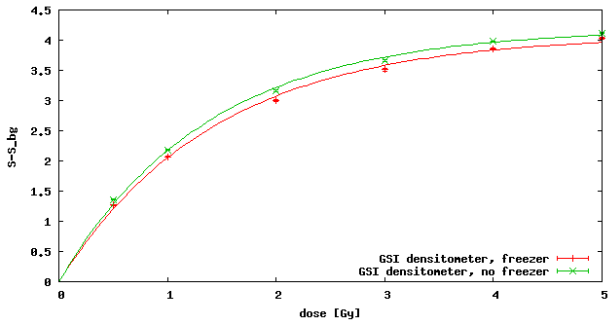

Figure 2: Results for two background corrected saturations curves for different storing conditions: stored at room temperature and at 5° C (freezer).

Table 1: Fitting results for the curves shown in fig.1 and fig. 2.

	m	S_0
GSI densitometer	0.73 ± 0.03	4.19 ± 0.06
HIT densitometer	0.73 ± 0.03	4.29 ± 0.05
GSI dens.+ Freezer	0.70 ± 0.03	4.09 ± 0.07
HIT dens.+ Freezer	0.70 ± 0.03	4.20 ± 0.07

References

[1] B. Spielberger et al., Phys. Med. Biol. **46** (2001) 2889
[2] C. Bert et al., Phys. Med. Biol. **53** (2008) 2253
[3] B. Bathelt, Ph.D thesis, Uni-Kassel, Germany (2000)

#c.bert@gsi.de

TRiP98: Parallelization of Dose Calculation

J. Trautmann[1,2], W. Heenes[2], C. Bert[1], G. Kraft[1], M. Durante[1] and M. Krämer[1]

[1]GSI, Darmstadt, Germany; [2]TU Darmstadt, Germany

Introduction

TRiP98, a treatment planning program, was used in the pilot project of heavy ion radiotherapy with scanned ion beams at GSI [1]. Over 400 patients were treated from 1997 to 2008 [2].

Currently TRiP98 is used for research purposes. One big part of the actual research is to make TRiP98 able to handle 4D data sets [3]. This is needed for the treatment of moving tumors (like lung tumors). Due to this development of TRiP98 and the therefore growing amount of data, the need of being able to calculate data faster is becoming more and more important.

In this approach we focus on the dose calculation of the standard TRiP98 version. In total five different algorithms have to be considered: three for the absorbed dose and two for the biological dose [4].

The aim of the work done here is to show that parallel dose calculation is working. In further steps, this approach could be used as a basis for an implementation in the new 4D developments or even for other parts of TRiP98 such as dose optimization.

Programming environment

Several programming languages and architectures for parallel computing are available. It was decided to use OpenMP for the following reasons.

TRiP98 is written in the C programming language running on IBM Power Systems with AIX as operation system. Modifications should be kept at a minimum to ensure that TRiP98 could further be used as a production code. Design point was not specialized hardware, but existing multicore CPUs (e.g. POWER7).

Taking the actual structure of TRiP98 into account as well, which stores the data in a global structure set, OpenMP seems to be a reasonable solution for this given situation.

OpenMP

OpenMP [5] is an application programming interface supported by many hardware manufactures and compiler developers. It is designed to work on shared memory machines. It normally parallelizes already existing threads or loop cycles. Therefore it uses preprocessor directives (in OpenMP called pragma), which must be included in the C code. In addition a special OpenMP library has to be linked. So the advantage of OpenMP is, that it is not a self-contained programming language and therefore easy to integrate in existing code.

A C compiler, able to handle included OpenMP, and the OpenMP library is available for the given environment.

A very important point is to be aware of data dependencies, such as recursion, which might avoid a parallel execution. Therefore the code must be investigated in detail and if a data dependency is found, this part must be reprogrammed if possible.

Overall OpenMP seemed to fit best for this case.

Results

The implementation has been done for all five different algorithms. For the classic biological dose calculation, which uses random sampling ("Monte Carlo"), special care has to be taken. Therefore it was not possible to get the exact same results in dose distributions like for all the other methods. So a different approach of the random sampling has been implemented to both versions to get bitwise identical results again.

Recalculations of 4 patients from the pilot project with the new parallel approach of TRiP98 and the standard version have been done on our IBM BladeCenter PS701 with its 8 Power7 3.0GHz cores and 4 way simultaneous multithreading (SMT), which leads to 32 threads in total. The time needed for the calculation was measured using an OpenMP function for both versions.

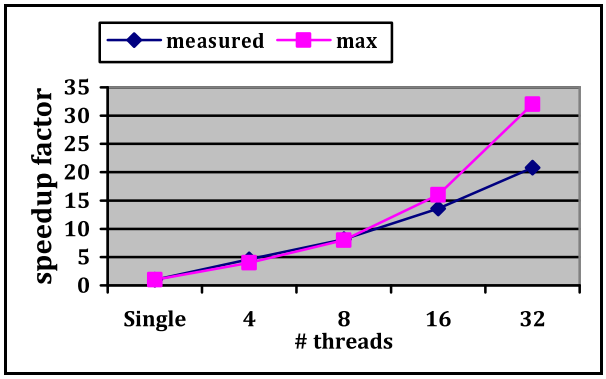

Figure 1: speedup for patient 290, absorbed dose (ms)

References

[1] M. Krämer et al., "Treatment planning for heavy-ion radiotherapy: physical beam model and dose optimization", Phys.Med.Biol., 45 (2000) 3299-3317

[2] O. Jäkel et al., "Treatment planning for heavy ion radiotherapy: clinical implementation and application", Phys.Med.Biol., 46 (2001) 1101-1116

[3] D. Richter et al., "4D Treatment Planning Implementations for TRiP98", GSI Scientific Report 2009, 500

[4] A. Gemmel et al., "Biological dose optimization with multiple ion fields", Phys.Med.Biol. 53 (2008) 6991-7012

[5] http://www.openmp.org

TRAX simulations

M. Krämer[1], *C. Wälzlein* [1,2], *and M. Durante*[1]
[1]GSI, Darmstadt, Germany; [2]FIAS, Frankfurt, Germany

Low-energy secondary electrons play an important role for radiation damage on the microscopic (or even nanoscopic) scale, both as mediators as well as messengers of energy deposition processes. The TRAX Monte Carlo (MC) code has been developed over many years [1] as a tool to describe creation and transport of electrons after ion impact.

Simulations for the Toroid spectrometer

One of the design points of TRAX current developments is the ability to reproduce experimental results obtained by GSI's Toroid low-energy (< 1 keV) electron spectrometer [2]. The main idea is to verify experimentally the model assumptions about electron creation and transport in thin foils bombarded with ions or electrons.

In its latest version TRAX has been extended to formally handle (via external tables) the full periodic system of ionic projectiles as well as a wide range of target materials (atomic, molecular and mixtures). Toroid-specific features such as tilted target foils have been implemented.

As an example Figure 1 compares experimental with calculated angular distributions for various energy intervals. In general the agreement is good in forward direction. Discrepancies in backward direction may originate from inaccurate primary cross sections or from experimental deficiencies. The lowest energy interval spans the region of C-Auger electrons, which are present in the experiment, but not yet in the simulation, hence the large discrepancy.

Inhomogeneous targets

Most MC simulations assume that the target material is homogeneous at least on the macroscopic level. When dealing with low-energy radiation, this is not necessarily true on the microscopic level.

Figure 2 demonstrates the microscopic inhomogeneity of a carbon foil, showing rock-like structures of the order of 5 to 10μ, as well as the possibility of "holes" within the foil, allowing particles to pass without energy loss. It is anticipated that this will have a significant effect on the shape of the experimental spectra.

A simple test case is shown in Figure 3. Experimental data on electron backscattering from carbon foils under various conditions (polished/unpolished) are compared with our calculations.

Good agreement is seen in the case of "polished" surfaces. Reasonable agreement with the "unpolished" results can be achieved under the assumption of 5 by 10μ "rocks", separated by 1μ gaps, roughly in sync with Figure 2.

References

[1] Krämer M., Durante M, Eur. Phys. J. D, 60 (2010) 195.
[2] Lineva N. et al. NIM B 267 (2009) 891
[3] Verma R.L., J. Phys. D 10 (1977) 1167.
[4] Sternglass E., Phys. Rev. 95 (1954) 345.

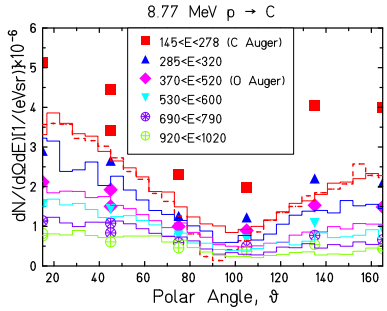

Figure 1: Electron angular distributions from a 3.6μ carbon foil irradiated with protons. Symbols: experimental data taken at the indicated energies [eV], lines: TRAX results. Dashed: target tilt angle=0.

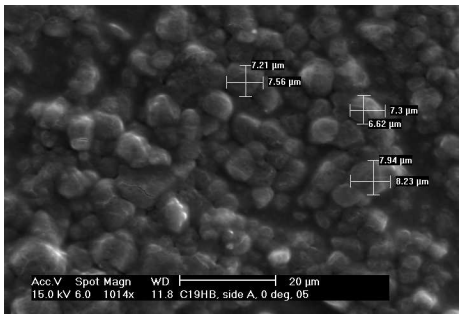

Figure 2: Carbon foil seen through an electron microscope.

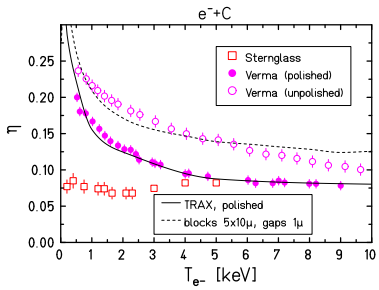

Figure 3: Backscatter coefficients as a function of electron energy. Symbols: experiment [3, 4], curves: TRAX results

Characterization of a pcCVD Diamond for Applications in Biophysics

D. Jarausch[1], D. Schardt[2], and E. Berdermann[2]

[1]TUD, Darmstadt, Germany; [2]GSI Darmstadt, Germany

For biophysics research related to particle therapy trigger detectors are required that can operate at particle rates as high as 10^8 per second in single-particle mode. Potential applications in this field are real time imaging of the dose delivery to the patient by detecting prompt photon or particle radiation produced in nuclear reactions in the patient's body [1] or experimental studies of such nuclear fragmentation reactions using e.g. time-of-flight techniques [2]. In both cases a single-ion detector is required that can operate at typical intensities of particle treatment beams over a long time (radiation hard) and offers very short signal rise-times and narrow signal widths for best timing properties. These requirements are very well met by CVD-diamond detectors [3].

In the frame of a Bachelor Thesis (D.J.) the signal behaviour and the count rate capabilities of a polycrystalline CVD diamond detector (pcCVD) were investigated using high-energy carbon, argon, and nickel beams.

Experimental

The pcCVD diamond crystal (350 µm thick, size 1 cm^2) used for these tests was glued on a ceramic board and mounted in a metallic shielding case. The substrate side was connected by a 50 Ohm microstrip line to a low-noise Diamond Broadband Amplifier (DBA IV/R, P. Moritz / GSI) with a band width of 0.003 – 2.3 GHz. For recording detailed properties and statistics of the detector signals a Digital Sampling Oscilloscope (DSO) LeCroy wavepro 7300 (3 GHz, 20 GS/s) was employed. For timing measurements the DBA output signal was fed into a fast discriminator (CES DISC-8 510 or Canberra CFD 454). Using a ^{241}Am alpha source the charge collection efficiencies were studied over a range of bias voltages from 0 – 1000 V.

With beams of ^{12}C (500 MeV/u), ^{40}Ar (500 and 1000 MeV/u) and ^{64}Ni (500 and 1500 MeV/u) that were available in the biophysics Cave A, signal shapes, rise and decay times, amplitudes and areas were studied in detail. For these measurements the pcCVD detector was mounted on the beam axis either at a position shortly after the vacuum exit window or at about 3m distance in air.

Results

The time resolution for the combination of a pcCVD (start) and a plastic scintillation detector (stop) was measured for Ni and Ar ion beams at high energies. As an example, the resulting time peak for 500 MeV/u Ni ions (155 ps FWHM) is shown in Fig.1. As expected, the time resolution was found to improve with increasing linear energy transfer (LET) of the ions which is due to the increased signal-to-noise (S/N) ratio.

The count rate capability of the pcCVD detector was investigated by comparing the measured count rate over a wide beam-intensity range with a reference value obtained from a gaseous parallel-plate ionization chamber. As can be seen from Fig.2 the pcCVD count rate follows linearly the reference value up to about 3E7 counts/s. The onset of saturation at this point is ascribed mainly to the limitation of the 100 MHz scaler used in these measurements. These results show that pcCVD diamonds offer favourable conditions for the above-mentioned applications.

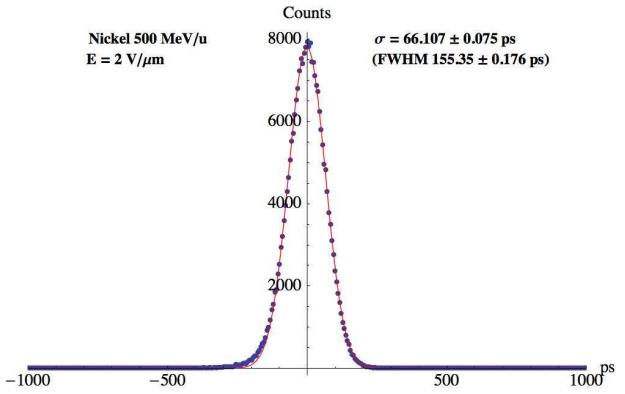

Fig. 1: Time resolution measured for 500 MeV/u Ni-ions. Start-signal: pcCVD, Stop-signal: plastic scintillator

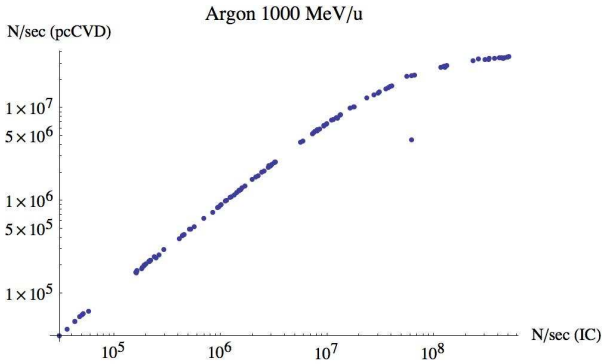

Fig. 2: Average beam intensity (ions per second) measured with a pcCVD-detector for 1 GeV/u Argon ions and plotted versus the reference value (ion chamber)

[1] M. Testa et al., Radiat. Environ. Biophys. 49(3), 337 (2010)

[2] K. Gunzert-Marx et al., New Journal of Physics 10, 075003(2008)

[3] E. Berdermann, K. Blasche , P. Moritz, H. Stelzer, B. Voss, F. Zeytouni, Nuclear Physics B 78, 533-539 (1999)

Energy Spectrum of Fast Neutrons Produced by 130 MeV Protons in Water*

D. Schardt[1], H. Iwase[2], G. Martino[1], R. Kaderka[1], C. La Tessa[1], D. Meer[3], S. Safai[3], L. Sihver[4]

[1]GSI, Darmstadt, Germany; [2]KEK, Tsukuba, Japan; [3]PSI, Villigen, Switzerland; [4]Chalmers Univ., Göteborg, Sweden;

In proton radiation therapy nuclear reactions of high-energy protons hitting beam line components (e.g. collimators or other beam shaping devices) lead to the production of secondary neutrons which may result in significant neutron dose equivalent values (typically of the order of mSv per treatment Gy), depending on the treatment techniques [1]. For scanning devices the neutron dose contribution was found to be very small [2].
Nevertheless, secondary neutrons are also (inevitably) produced in the patient tissue itself and it is interesting to study their characteristics and to compare them with simulations. Neutron spectral fluences were established in earlier work by Yan et al [3] with unfolding techniques from Bonner sphere measurements. It was found that the biggest dose contributions come from fast neutrons in the range of about 0.1 to >100 MeV.

Experimental Methods

The aim of this work was to measure the energy spectrum of secondary fast neutrons directly using time-of-flight techniques at various emission angles relative to the beam axis. A sketch of the experimental setup is shown in Fig.1.

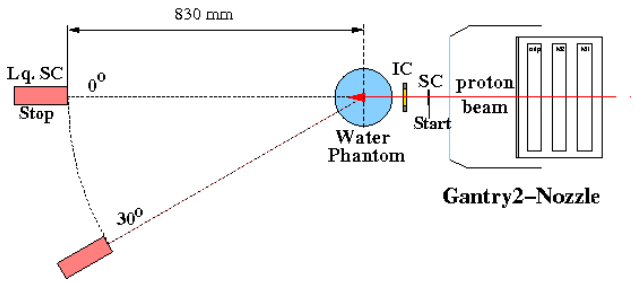

Figure 1: Experimental setup at PSI/PROSCAN.

The measurements were performed at the Gantry2 beam line of the PROSCAN therapy facility at PSI, using pencil-like proton beams at 130 and 200 MeV delivered by the s.c. cyclotron COMET. The beam intensity was reduced to several 10^5 protons/s and monitored by a thin plastic scintillation detector (SC), which also started the time-of-flight measurements, and by a parallel-plate ionization chamber (IC). The proton beam was stopped in a cylindrical water phantom of 15 cm diameter simulating the patient tissue. Secondary fast neutrons emerging from the water phantom were detected with an organic liquid scintillation detector (Lq.SC, 51 mm diameter, 150 mm long). The spectrum shown in Fig.2 was recorded in 2000 s using a relatively short flight path of 83 cm which had to be chosen as a compromise between detection solid angle and energy resolution.

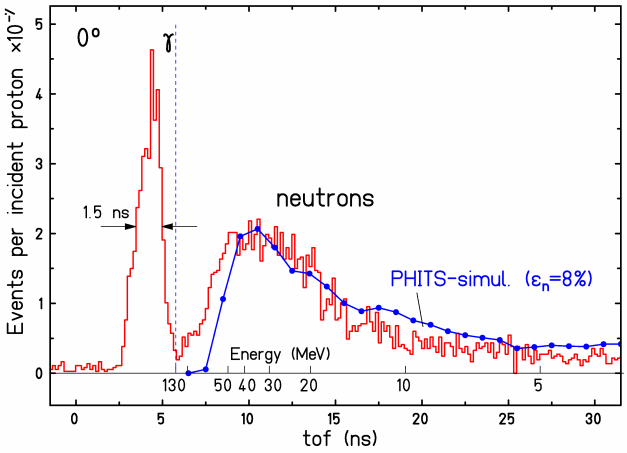

Fig. 2: Time-of-flight spectrum measured with a 130 MeV proton beam at 0° position of the stop detector.

Preliminary Results

The time-of-flight data recorded for 130 MeV protons at 0° are shown in Fig.2. The prompt photon peak appears at about 4.2 ns and was used to calibrate the time axis. Secondary fast neutrons are characterized by a rather broad distribution between 5 and 30 ns (which was the range accessible to the measurement), corresponding to neutron energies between 130 MeV and about 4 MeV.

The experimental spectrum was compared to Monte-Carlo simulations performed with the PHITS code. In view of the limited counting statistics good agreement of the spectral shape was found. Comparison of the neutron yield requires the determination of the neutron detection efficiency of the stop detector, which is still in progress. For the comparison in Fig.2 a constant value of 8% over the measuring range which is a typical value for such detector was assumed, giving best agreement with the neutron yield calculated with PHITS.

References

[1] E. Hall et al., "Intensity-modulated radiation therapy, protons, and the risk of second cancers", Int. J. Radiat Oncol. Biol. Phys. 65,1(2006).

[2] U. Schneider et al., "Secondary neutron dose during proton therapy using spot scanning", Int. J. Radiat Oncol. Biol. Phys. 53,244(2002).

[3] X. Yan et al., "Measurement of neutron dose equivalent to proton therapy patients outside of the proton radiation field", Nucl. Instrum. Meth. A476, 429 (2002)

* Work supported by EU, ALLEGRO-Project, contract No. 231965.

FIRST project: Status of TP-MUSIC IV

C. Schuy[1] *and R. Pleskac*[1]
[1]GSI, Darmstadt, Germany, on behalf of the FIRST collaboration

Motivation

The FIRST (Fragmentation of Ions Relevant for Space and Therapy) project [1], established by an international collaboration (France, Germany, Italy, Spain), aims at studying nuclear fragmentation processes for therapy and space relevant ion beams and measuring double differential cross sections for high energy fragmentation reactions.

Methods

A complex detector array will be used to measure charge, mass, angular distribution and energy of all charged fragments plus high-energy neutrons in forward direction. The experimental setup consists of Aladin detectors [2] (Aladin magnet, TP-MUSIC IV, ToF wall) and LAND (Large Area Neutron Detector) as well as newly designed detectors in the interaction region.

TP-MUSIC IV

TP-MUSIC IV (Time Projection Multiple Sampling Ionization Chamber) is a tracking ionization chamber. It consinsts of two independent drift regions seperated by a cathode plane, each equipped with ionization chambers and proportional counters.

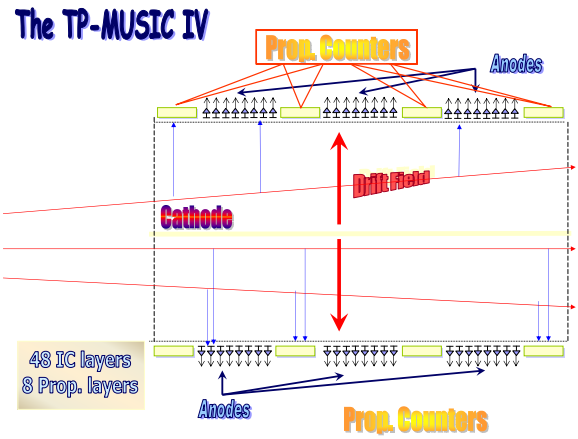

Figure 1: Schematic of TP-MUSIC IV [3].

Status

Vacuum and gas purification: The detector is mounted inside an approximately 10 m^3 vacuum chamber, which contains P10 under measurement conditions. Therefore the maximum reachable vacuum can be used as an estimate for the leakage rate of the chamber and gas quality. After severe changes to the prevacuum system, leak-testing is currently in progress. Standalone tests of the gas purification system were performed sucessfully.

Detector: Cables, connectors and fed-throughs were thoroughly tested and repaired if necessary and the related documentation was completed. Preamplifiers were checked and tested with pulser signals. In October the detector was restarted - chamber filled with 900 mbar P10 - and the inbuilt alpha-sources were succesfully observed with the right side of the detector. Due to the not fully operational gas purification system a test of the left side has not been performed yet.

DAQ: FlashADC modules and a standalone MBS system, based on former Aladin files, were restarted. The system was successfully tested using simple on- and offline analysis programs and pulser signals.

Time schedule

The final assembly of the gas purification system and detector will take place in the beginning of February. When sufficient gas quality is reached over the desired time frame, the left side of the detector will be tested and a full measurement using cosmic radiation will be performed.

References

[1] V. Patera, ”The FIRST experiment on fragmentation of high-energy heavy ions of biomedical interest at GSI”, GSI Biophysics seminar, 2009

[2] M. De Napoli, Phd thesis, 2006

[3] C. Sfienti, “Mass and Isospin Effects in Multifragmentation”, EPS NPDC 18, August 2004

First Sub-Micron Targeting with Single Ions

K.-O. Voss[*1], *B. Merk*[1], *B. Fischer*[1], *B. Jakob*[2], *F. Tobias*[†2], *and G. Taucher-Scholz*[2]

[1]Material Science Department GSI, Darmstadt, Germany; [2]Biophysics Department GSI, Darmstadt, Germany

Introduction

Since 2003, we use the GSI heavy-ion microprobe to irradiate living cells with ions from the UNILAC [1]. Two specific properties of the microbeam method make it stand out among other, more conventional irradiation procedures: First, we precisely control the dose by counting and switching individual particles that are to be delivered to the target, down to the low-dose limit of a single ion per irradiated object. Secondly, the microprobe delivers each ion into a predefined and deliberately chosen location of the target. The deviation of the actual ion impact from the point targeted defines the *absolute targeting accuracy* of a particle microbeam experiment. To allow for selective irradiation of tiny cellular sub-structures of interest, we strive for the best possible targeting accuracy.

Here, we report on the first *in-situ* measurement of the absolute targeting accuracy of the GSI microbeam setup and the first sub-micron targeting accuracy measured at any biological particle microbeam.

What is Targeting and Why is it Difficult?

The GSI microprobe focuses a tiny fraction of the UNILAC beam into a spot of about 600 nm diameter. This beam spot can be shifted horizontally and vertically using a magnetic steerer. To target microscopic objects in a cell culture, we need to locate these objects and we need to know what currents to drive through the steerer coils to deflect the ion beam into their locations. For that purpose, an optical image of either the cell culture or of a scintillator is projected onto a CCD camera by means of a microscope objective. Imaging the scintillator as it is being hit by the beam deflected with a number of different steerer coil currents yields a beam positioning calibration.

Adversely, the rays of light creating the microscope image of the sample are refracted when entering the optically thick cell container or scintillator. Thus, tilted or otherwise minutely misaligned samples or varying optical thicknesses lead to systematically degraded targeting accuracy. For instance, a 50 μm speck of dust sitting below the edge of the scintillator was shown to shift the apparent beam position during beam optics calibration by almost 3 μm [2].

Measurement of Targeting Accuracy

Recently, the biological microbeam toolbox as been expanded to also contain many GMO and tumor cell lines available and in use at the dedicated Biophsics labs and beamlines. While these cell lines will most definitely provide the substrate for interesting radiobiology at the microbeam, here we use a cell line expressing a GFP-tagged DNA damage response protein[1] simply as *in-situ*, fast nuclear-track detector with optical readout (see Fig. 1 left). Trivially and opposing to traditional track detectors, this 'detector' exhibits all the optical effects influencing the targeting accuracy of the system in a biological experiment.

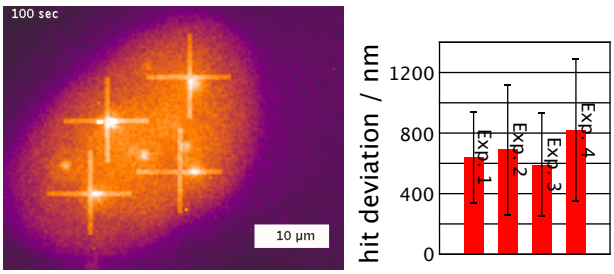

Figure 1: **(left)** Radiation damage in a U2OS cell nucleus visualized by fluorescence of GPF-tagged NBS1 protein (pseudo-color). Image recorded 100 s after ion impact as part of a time sequence. Late timepoint displayed here for sake of focus intensity only, cell slowly moving to right. Target points (CCD pixels) indicated by four crosses. **(right)** Distance between targeted points and center of earliest onset of corresponding radiation foci (20 to 30 seconds after ion impact). 2 σ statistical errors. Four independent measurements. 111 foci evaluated.

Results

Fig. 1 (right) displays the average mismatch of target point and earliest radiation focus for 111 Sm ions shot into many cell nuclei in four independent experiments. The movement of the cells within the 20 to 30 seconds prior to foci formation contributes to the mismatch. The measured value of 670 $\pm$ 400 nm is thus an upper limit for the actual targeting accuracy in this experiment.

References

[1] Fischer, B. E. et al. GSI Scientific Report (2003) pp. 146-147

[2] Fischer, B. E. et al. Nucl Instrum Meth B (2009) vol. 267 (12-13) pp. 2122-2124

* K.-O.Voss@gsi.de

† supported by BMBF grant 02NUK001A

[1]stably transfected U2OS NBS1-GFP cell line kindly provided by C. Lukas, Danish Cancer Society, Copenhagen

Heavy-Ion Computed Tomography applying a stack of ionization chambers*

B. Voss [1], I. Rinaldi [2], S. Brons [3], O. Jäkel [2,3], R. Panse [3] and K. Parodi [3]

[1]GSI, Darmstadt, Germany;
[2]German Cancer Research Centre, Heidelberg, Germany; [3]Heidelberg Ion Therapy Centre, Heidelberg, Germany

In particle therapy there are basically two novel low-dose 2D and 3D in-vivo imaging techniques alternative or complementary to **P**ositron-**E**mission-**T**omography (PET) which probe the density matrix in the target volume (Fig. 1):

A) As a more indirect probe prompt particle emission during irradiation like emerging secondaries [1], in particular gammas or protons, from the therapeutic beams ($E_{treatment}$) may serve to verify the treatment delivery.

B) Measuring the residual energies of a small flux of transmitted primary particles itself which impinge with an initial energy (E_{trace}) higher than the one used for therapy profits from the weak energy dependence of the energy-loss process exploiting the knowledge of the Bethe-Bloch formula. The reconstructed density distribution of the objects volume traversed by the tracing beam particles might be used to evaluate the correct patient positioning and to verify the ions range in-vivo and before treatment.

Here we report on first experimental investigations [2] performed with ^{12}C ions in order to address the feasibility of such particle-based radiographic or tomographic transmission techniques (Heavy-Ion Computed Tomography HICT). Quite similar systems may also be applied to clinically relevant measurements of organ motion in particle therapy as recently proposed [3].

A stack of parallel-plate ionization chambers [4] serving as a range telescope has been assembled and characterized (Fig. 2). It consists of up to 61 parallel-plate ionization chambers interleaved by absorber sections (PMMA) whose thickness can be chosen between 0.5 and 5 mm to adapt to the measurements needs. The set can also be equipped with fixed pre-absorbers adding up to 90 mm water-equivalent range to the material in the phantom. It could as well be combined with a remote-controlled range shifter allowing adding 0.1 to 90 mm thickness of polyethylene in several steps.

The active cross section of each IC has been chosen to be 300 x 300 mm^2 in order to allow for scanned beams of at least 200 x 200 mm^2 field sizes. The readout of the system is performed with commercially available multi-channel electrometers and customized software [5].

Fig. 3 shows an example of a simple 2D back-projected reconstruction of a PMMA phantom (∅=160 mm) containing rods of tissue equivalent material (∅=28 mm). This apparatus has been scanned from angles between 0° to 180° in steps of 5° around the central axis with a ^{12}C pencil-beam of 400 MeV/u initial energy, 3.5 mm Gaussian FWHM width and an intensity of 5 x 10^6 pps. Each field consists of 201 x 27 points on a grid of 1 x 1 mm.

* Work supported by the HGF contract no. VH–VI 303.

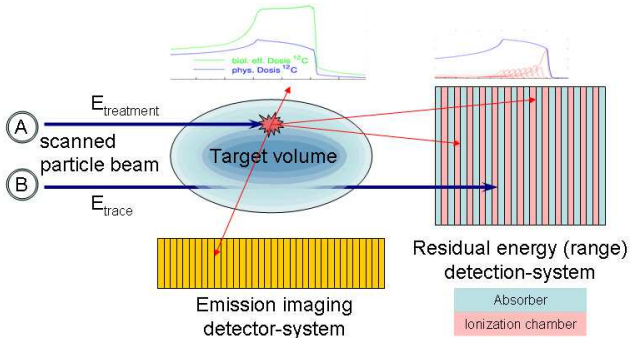

Figure 1: Sketch of the methods principle.

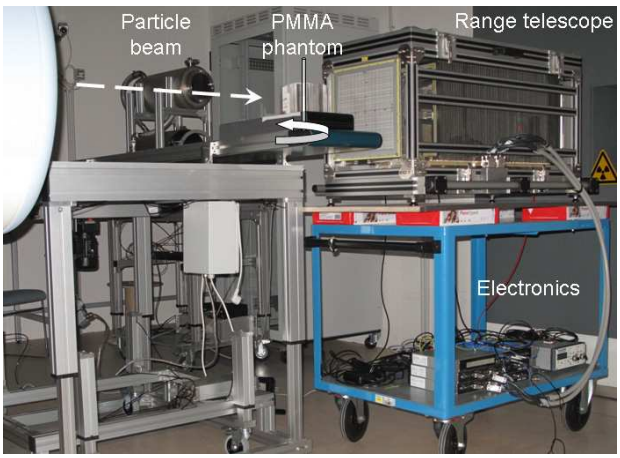

Figure 2: Picture of the experimental setup at HIT.

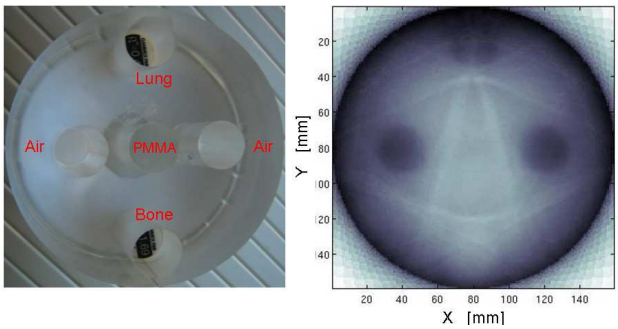

Figure 3: Picture and 2D-HICT reconstruction of a cylindrical PMMA phantom with five tissue-equivalent rods.

References

[1] E. Testa et al, Nucl. Inst. Meth. B 267, 993-996, 2009
[2] I. Rinaldi et al, Imaging 2010, conference contribution, http://www.mi.physics.kth.se/Imaging_2010/
[3] N. Saito et al, GSI BioPAC 2010,Proposal PT-05-006
[4] B. Voss et al, GSI Scientific Report 2005, p379
[5] Pyramid Technical Consultants, Lexington, USA, Models A500, I3200, PS455; http://www.ptcusa.com/

Lateral dose fall-off measurements in photon, proton and heavy-ion therapy

R. Kaderka[1], C. La Tessa[1], U. Ramm[2], J. Licher[2], S. Safai[3], D. Meer[3], C. Vallhagen Dahlgren[4], E. Grusell[4], S. Brons[5], D. Schardt[1], and M. Durante[1]

[1]GSI, Germany; [2]KGU, Germany; [3]PSI, Switzerland; [4]Uppsala University Hospital, Sweden; [5]HIT, Germany

ALLEGRO is an European project investigating health risks following radiotherapy. In this frame our group has performed out-of-field dose measurements to compare different types of radiation therapy, studying the influence of the delivery technique and the beamline structure on the dose profile. The data obtained can be used as validation of Monte Carlo models and for assessing the risk of developing malignancies after radiotherapy.

Methods and materials

Different types of detectors were used in a water phantom for the experiment. The PTW diamond detector offers high spatial resolution and a measuring range over almost six orders of magnitude. It is sensitive to charged particles and photons. The detector read out is the charge produced by the passage of radiation.

Two types of TLDs were used for the experiment: TLD 700, sensitive to photons and charged particles, and TLD 600, sensitive to photons, charged particles and low energy neutrons (up to 200 keV). The latter can therefore be used as an estimate for the neutron production.

A bubble detector is a passive device which is sensitive to neutrons, but not photons. They are ideal for measuring neutrons in environments with a high photon/neutron ratio as in photon therapy. Using different energy thresholds an unfolding yields the neutron spectrum which is important for accurate biological risk assessment.

The water phantom was irradiated with a 5 x 5 cm^2 field and the lateral dose fall-off at the depth of maximum dose was measured. The experiments were performed at several facilities specialized in the respective treatment technique. Photon irradiations were performed at the Klinikum Goethe Universität Frankfurt/Main. Measurements with a scanned proton beam were done at PSI (Paul Scherrer Institute, Switzerland) and HIT (Heidelberg Ion-Beam Therapy Center, Germany). Passively delivered protons were examined at TSL (The Svedberg Laboratory, Sweden). Experiments with a scanned carbon-ion beam were conducted at GSI and HIT.

Results

The figure shows a comparison of different particle species and treatment techniques measured with the diamond detector. The dose is normalized to the value measured in the target. Ions show an advantageous lateral dose fall-off compared to photons.

As expected, the evaluation of TLDs in proton irradiations at TSL and PSI showed that the passive scattering technique results in a higher neutron production compared to the scanning technique.

Using the bubble detectors and the BUNTO unfolding code [1], a peak of 1 MeV was observed in the neutron spectrum produced in photon therapy.

Further experiments investigated the energy dependence of the out-of-field dose in scanned proton and heavy-ion treatments. For all energies measured the edge of the field is sharper for carbon-ions than for protons. An increase of the out-of-field dose far from the edge could be observed for high-energetic carbon-ions due to fragmentation. For protons the energy-dependence of the dose profile is rather small. However, the increase for high energy carbon ions is in a dose region of 10^{-3} or less compared to the target dose, therefore the biological consequences are possibly small.

Outlook

For more accurate evaluation of the biological risk not only the dose, but the particle type and the LET need to be measured; moreover a thorough comparison of the neutron dose and spectrum delivered by scanned and passive systems will shed some light on the difference between the two delivery techniques.

References

[1] C Ongaro, A Zanini and L Tommasino “Unfolding technique with passive detectors in neutron dosimetry”, Proc. Neutron Spectrometry and Dosimetry: Exp. Techniques and MC Calculations 2001, p.117-128

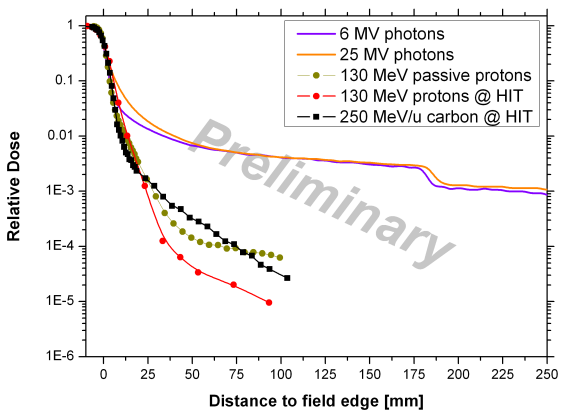

Figure 1: Lateral dose profiles in water for different radiotherapy techniques

Microdosimetric characterization of proton and ^{7}Li beams stopping in water*

G. Martino[1], *M. Durante*[1], *R. Kaderka*[1], *C. La Tessa*[1], *D. Meer*[2], *S. Safai*[2], *and D. Schardt*[1]
[1]GSI, Darmstadt, Germany; [2]PSI, Villigen, Switzerland

The radiation field produced by high-energy beams of proton and ^{7}Li ions was investigated by microdosimetric in-phantom measurements for comparison with ^{12}C data [1]. The objective of this work was to measure out of field doses and radiation qualities to provide basic data for the assessment of secondary cancer risk in heavy ion therapy. The measurements were performed under very similar experimental conditions for protons at the Paul Scherrer Institute (PSI) in Switzerland, and for ^{7}Li ions at GSI. Pencil-like beams of 160 MeV proton and 185 MeV/u ^{7}Li ions were chosen having the same range in water (about 17 cm). The ion beams were stopped in the center of a 30×30×30 cm^3 water phantom and their radiation field was investigated using a Tissue-Equivalent-Proportional-Chamber [2]. The chamber was placed at several different positions in the central plane at various depths along the beam axis and at radial distances of 0, 1, 2, 5 and 10 cm (Fig.1).

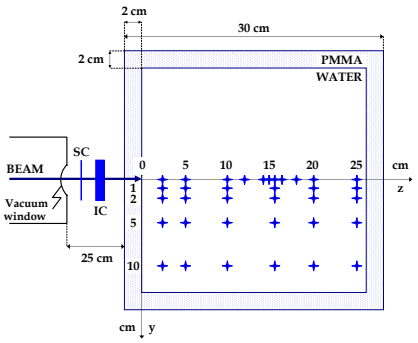

Figure 1: Experimental setup and measurement positions.

Microdosimetry provides single-event energy spectra that relates the absorption of ionizing radiation in matter to the size of biological targets (e.g. cells) where the statistical fluctuations in the amount of energy deposition can be very large. Lineal energy spectra offer a deep understanding of the complex radiation field produced by heavy ions beams in tissue-like materials. The off-axis measurements (Fig.2) show very similar distributions of the lineal energy, all peaking between 1 and 10 keV/μm which is a typical range for secondary hydrogen fragments and neutrons. The relative absorbed dose at each position was obtained by integration of the measured spectra normalized to the number of incident primary beam particles (Fig.3). The depth-dose curves at fixed distance from the beam axis are slowly rising until reaching the depth of the Bragg peak, reflecting the build-up of secondary fragments with increasing penetration depth. The results confirm that the lateral dose profile of heavy ions shows an extremely steep fall-off.

* Work supported by EU (PARTNER), grant agreement No. 215840-2.

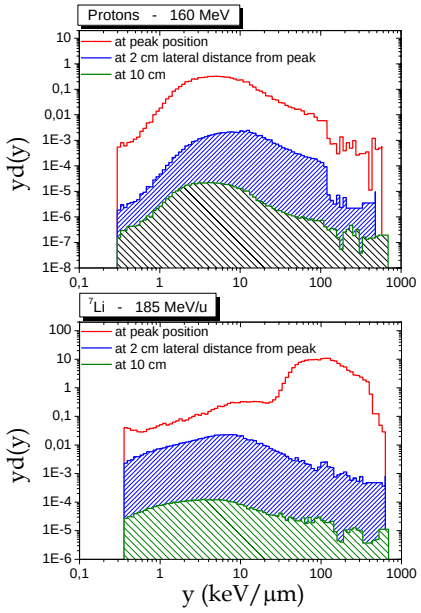

Figure 2: Lineal energy spectra.

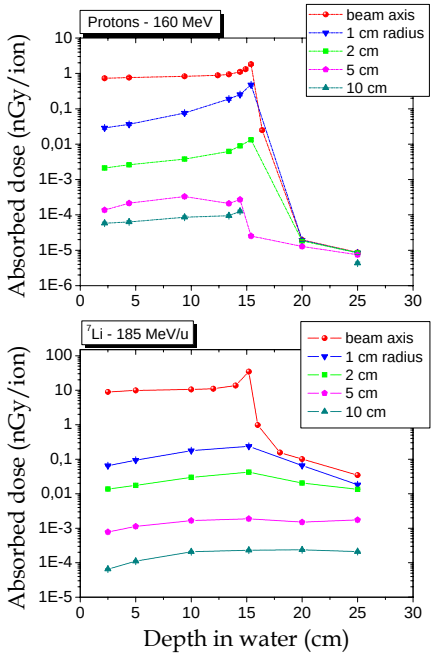

Figure 3: Absorbed dose values.

References

[1] G. Martino et al., Phys. Med. Biol. 55 34413449 (2010).

[2] G. Martino et al., GSI Scientific Report 2008, p.388.

Optimisation of an ion optical range adaptation method for beam tracking of moving tumours with scanned ion beams*

A. Constantinescu[1,2], *N. Saito*[1], *N. Chaudhri*[1,3], *M. Durante*[1,2], *G. Kraft*[1], *and C. Bert*[1]
[1]GSI, Darmstadt, Germany; [2]Technische Universität Darmstadt, Germany; [3]HIT, Heidelberg, Germany

Introduction

A non-mechanical energy variation used for irradiation of moving tumours with scanned ion beams, the ion optical solution, was previously presented [1, 2]. In this method a ramp shaped energy degrader is inserted into the therapy beam line. By using the existing deflection magnets to direct the particles to certain positions on the energy degrader and hence through different thicknesses of the material, a fast adaptation of the beam range can in principle be achieved. After theoretical and experimental feasibility studies [3] a systematic study of the energy degrader parameters (material and shape) and their impact on the beam profile criterias at isocenter was carried out [4]. Some simulations results concerning the effect on the lateral beam profile will be presented here.

Material and Methods

All beam characteristics simulations were carried out with the ion transport code MOCADI [2, 5]. To study the impact of the wedge shape on the inital particle beams, three different wedge slopes were studied with a thickness variation per lateral shift of 0.58, 0.47 and 0.35 $\mathrm{mmH_2O/mm}$ ($\mathrm{mmH_2O}$: thickness in water equivalent lentgh). Furthermore different degrader materials were used (e.g. Beryllium: $\rho_{Be} = 1.848\,\mathrm{g/cm^3}$, Graphite: $\rho_C = 2.23\,\mathrm{g/cm^3}$, Aluminium: $\rho_{Al} = 2.69\,\mathrm{g/cm^3}$). Thereby the water equivalent length of the materials were kept constant. The particles were directed to defined positions on the ramp shaped energy degrader (to its middle thickness: deflection of $0\,\mathrm{mm}$, and deflections of $\pm 15, \pm 25$ and $\pm 30\,\mathrm{mm}$ (-/+: thinner/thicker side of the energy degrader)).

Results

Figure 1 exemplary shows the effect of the energy degrader material and of the wedge slope factor on the lateral beam projections in x direction at isocenter. While the y projection is in all cases Gaussian distributed [4], the x projection shows non-Gaussian contributions in the tail part, increasing with the slope factor. For the particle beam a steeper slope factor causes a bigger difference in the traversed material thickness leading to an increased difference in the energy degradation. Due to a dispersion effect the energy variated particles are deflected differently through the second dipole magnet (in x direction), leading to a broader particle distribution in x direction and hence to an asymetric beam spot. The thefore needed stronger focusing of the particles in the end of the therapy beam line is one of the causes for the non-Gaussian contributions in the x direction. The tail part is reduced for beryllium in comparison to the other studied materials. Matters with low atomic number Z yield a small scattering angle of the energy degraded particles and hence a narrower beam distribution at the isocenter.

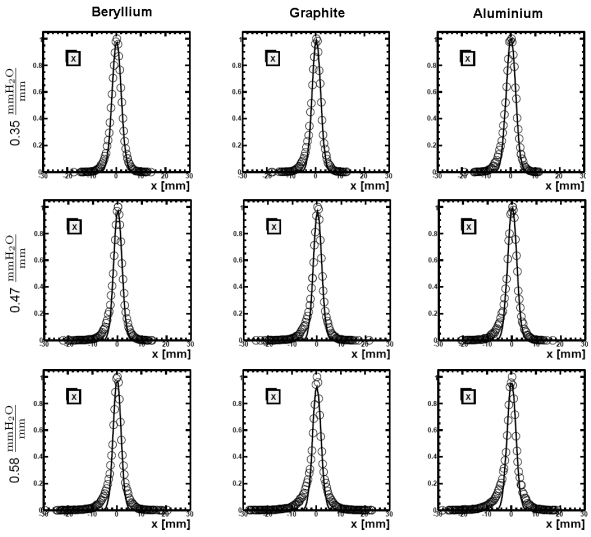

Figure 1: Beam spot projections in lateral x direction (symbols) and corresponding Gaussians fits (solid lines) as a function of the wedge slope factors (rows) and energy degrader material (columns) at a certain deflection position of $+15\,\mathrm{mm}$.

Conclusion

For the impact of the energy degrader shape and material combination on the lateral beam profile a Beryllium degrader with a slope in the range of 0.47 $\mathrm{mmH_2O/mm}$ yields the best result for the studied ion optical solution. Similar results were found in respect to the range shift, transmission and fragmentation yield [4].

References

[1] R.Pleskac et al., GSI Sci. Rep. 2007 (2008) 383
[2] A.Constantinescu et al., GSI Sci. Rep. 2009 (2010) 502
[3] N.Chaudhri et al., PMB 55 3499, 2010
[4] A.Constantinescu, Masterthesis, TU Darmstadt, 2010
[5] http://www-linux.gsi.de/ weick/mocadi

* Work is in part supported by Siemens AG, Particle Therapy

Out-of-field dose studies with an anthropomorphic phantom*

C. La Tessa[1], *T. Berger*[2], *R. Kaderka*[1], *D. Schardt*[1], *C. Körner*[2], *J. Licher*[3], *U. Ramm*[3], *N. Matsufuji*[4], *C. Vallhagen Dahlgren*[5], *E. Grusell*[5], *T. Lomax*[6], *G. Reitz*[2], *and M. Durante*[1]

[1]GSI, Darmstadt, Germany; [2]DLR, Cologne, Germany; [3]KGU, Frankfurt, Germany; [4]HIMAC, Chiba, Japan; [5]Uppsala University Hospital, Uppsala, Sweden; [6]PSI, Villigen, Switzerland

It is well known that short- and long-term side effects following cancer treatment with radiation are strongly related to the dose delivered to normal tissues surrounding the tumour. In fact, primary ions interact along the irradiation path towards the target volume and can both be scattered and undergo nuclear fragmentation. The secondary fragments might have enough range to deposit a non negligible amount of energy even far away from the treatment region. An investigation of the long-term health risks following cancer treatment with radiation has been conducted by the ALLEGRO project. One of the tasks of the project was the experimental investigation of the dose absorbed outside the tumor with a particular effort in the characterization of the secondary neutron field and its contribution to the dose.

The experiment

A characterization of the out-of-field dose profile following irradiation was achieved by exposing an anthropomorphic standard RANDO (C) phantom to a 3-D treatment plan designed for a 5x2x5 cm^3 target volume located in the center of the head. The facility of KGU in Germany (25 MV IMRT photons), TSL in Sweden (passively modulated protons), PSI in Switzerland (scanned protons), HIMAC in Japan (passively modulated carbon ions) and GSI in Germany (scanned carbon ions) were involved in the experiments. TLD 600(^{6}LiF:Mg,Ti) and TLD 700(^{7}LiF:Mg,Ti) were placed along the phantom main axis to measure the inner dose profile delivered by charged particles plus photons(Figure 1) and low-energy neutrons (E$\lesssim$200 keV, data still under evaluation). The physical processes that determine mainly the out-of-field dose profile are the nuclear fragmentation and the lateral scattering affecting both primary and secondary particles. The lateral spreading decreases with increasing mass of the primary beam while the fragments production increases. Furthermore, treatments with passive techniques involve a larger amount of elements along the final part of the beam line (collimator, range modulator, bolus), which contribute to the production of secondary fragments. On the other hand, the presence of a collimator in the proximity of the exit window prevents the passage of particles scattered from the primary beam. Then, delivery with passive technique enhances the production of fragments both along the beam line and at the exit window, which is translated into a higher dose at the entry channel, but the presence of the collimator minimizes the beam spreading, which is translated into a lower dose delivery nearby the tumour. Fragmentation of primary ions inside the phantom increases the dose around the target volume explaining the higher dose delivered by carbon ions compared to protons in that region. Both fragmentation and lateral scattering of primary particles outside the collimator effective area contribute to an increase of the out-of-field dose values inside the phantom for passively shaped beams. The results collected so far indicate strongly that a treatment with photons is characterized by the highest dose values independently of the distance from the PTV. At the present stage, the comparison between passive and active modulations cannot bring to a final conclusion: the scanning technique proved to be optimal if coupled with carbon ions because it minimizes fragmentation along the beam line and does not affect significantly the lateral scattering unlike the case of protons, where the presence of the collimator seems to spare heavily the tissue surrounding the PTV.

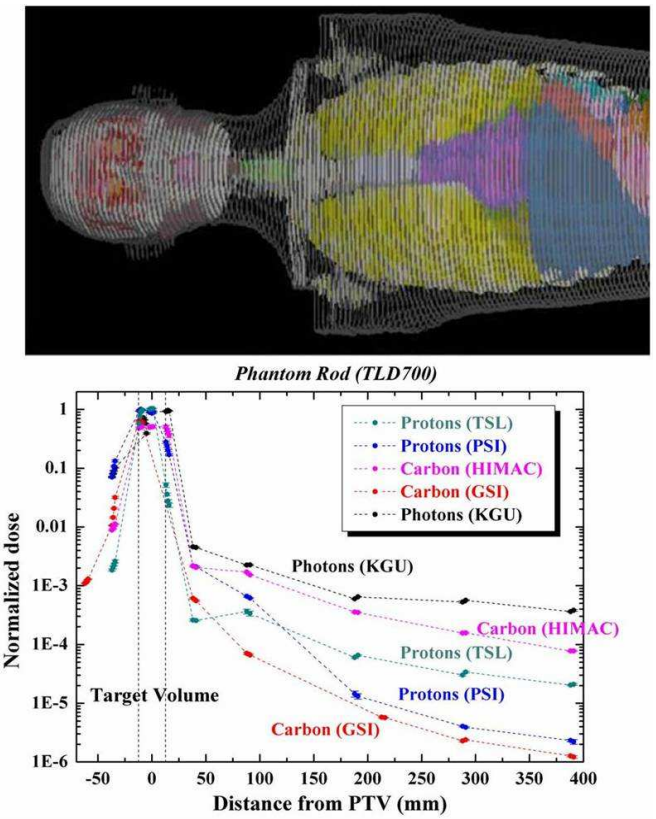

Figure 1: Dose profile delivered by ions and photons along the phantom main axis. The values are normalized to the nominal dose given to the PTV and were measured with TLD 700.

* Work supported by EU, ALLEGRO contract No. 231965.

Towards an oxygen effect implementation of TRiP98*

E. Scifoni[†1], *M. Krämer*[1], *and M. Durante*[1]
[1]GSI, Darmstadt, Germany

The TRiP98 code [1] was successfully used for therapy planning purposes in the pilot project of GSI for patient irradiation with ion beams, and in following times it was extended in several directions [2]. Since it is well known that the radiation resistivity of cells in the absence of oxygen may be drastically increased (oxygen enhancement ratio, OER), one of the key quest for heavy ion therapy which is presently still open is the possibility to include the selective treatment of differently oxygenated areas of a tumor, painting the dose accordingly. The present project aims thus to implement in the TRiP98 code an "OER-driven" optimization accounting for different levels of hypoxic regions. In this way, once obtained oxygen concentration maps of tumors (a feature starting to become available, e.g. through PET tracers [3]), it will be possible to produce the corresponding treatment plans targeted to the specific composition of the tumor to be treated.

This implies an extension of the code on several points: from one side , new tables should be provided for the tissue dose response as a function of LET and oxygen concentration. The volume of interest definition, on the other side, should be extended in order to allow the input of an additional quantity (the local oxygen tension p_{02}) labelling the CT voxels. A new command has been then generated and tested in order to handle OER tables, similarly to the RBE tables, and generate dose cubes weighted for the corresponding factor, voxel by voxel.

A convenient parametric description of both the oxygen pressure and LET dependence has been found to be the following (see Figure 1), by combining different experimental data for ion irradiation in fully anoxic conditions [4] and X-ray data for different oxygen concentrations:

$$OER(L,p) = \frac{B(Am + L^3)/(A + L^3) + p}{B + p} \qquad (1)$$

where L and p are respectively the dose averaged LET and the oxygen pressure, A and B are parameters related to the half effect, and m is a maximum value of OER.

The resulting survival curves obtainable by the code, for such a target with differently oxygenated regions, show the remarkable effect of figure 2. The following steps include the modification of the objective function to be minimized.

As for the experimental validation, preliminary plans were produced in order to test the survival response of mixed cells in anoxic, hypoxic and fully aerobic conditions, through the experimental 1D phantom developed at GSI with hypoxia exposure chamber [6], for the next beamtime scheduled on April.

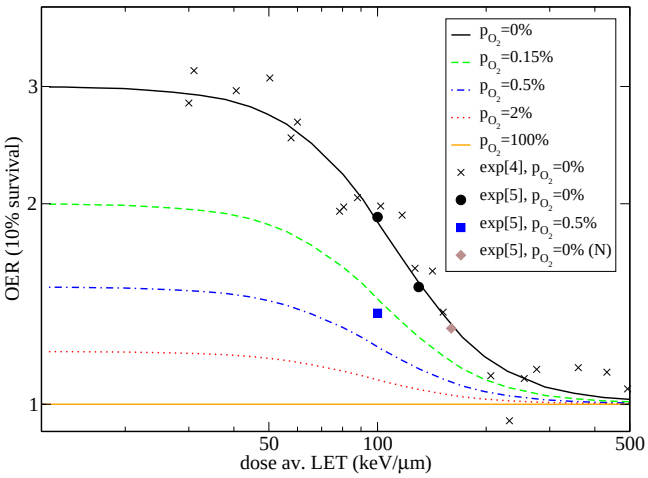

Figure 1: OER dependence on dose averaged LET and oxygen concentration, in the parametric description provided in this work and compared to experimental data [4,5]

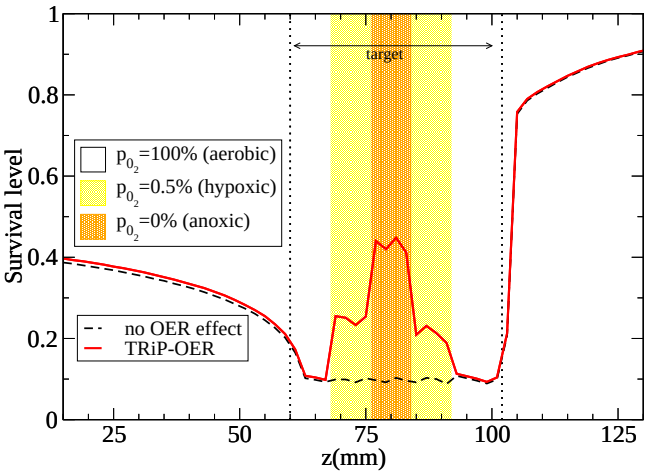

Figure 2: TRiP98 recomputed survival curve (solid line), accounting for differently oxygenated regions, after dose optimization considering the whole aerobic tissue (dashed).

References

[1] M. Kramer et al., Phys. Med. Biol. 45 (2000) 3299.
[2] M. Kramer and M. Durante, Eur. Phys. J. D. 60 (2010) 195.
[3] X. Sun et al., Mol. Imaging Biol. (2010) in print.
[4] Y. Furusawa et al. Rad. Res. 154-5 (2000), 485.
[5] W. Tinganelli et al., this Report.
[6] C. Schicker et al., GSI Rep.2008-01, p.370.

* Work supported by EU, ULICE contract No.228436.
† e.scifoni@gsi.de

Particle Number Optimization Using the BFGS Method in Heavy-Ion Therapy

M. Horcicka, M. Durante, and M. Krämer
GSI Helmholtzzentrum für Schwerionenforschung, Biophysics, Darmstadt, Germany

Introduction

In the GSI therapy pilot project from 1997 until 2008 about 440 cancer patients were successfully treated with carbon ions. Due to the promising healing rates the clinical radiotherapy facility HIT was launched and opened in 2009. Nevertheless, research and improvements of heavy-ion therapy are still in progress at GSI.

For patient treatment planning the software TRiP [1, 2] is used. An essential part of treatment planning is the particle number optimization in order to achieve a target dose distribution as close as possible to the prescribed biological dose distribution by an appropriate sparing of healthy tissue, especially critical structures like the brainstem.

Optimization Task and Methods

The optimization task can be mathematically expressed by the minimization of the following function [3]:

$$X^2(\vec{N}) = \sum_{i \in Target} \frac{(D_{pre} - D^i_{bio}(\vec{N}))^2}{\Delta D^2_{pre}}$$

$$+ \sum_{i \in OAR} \frac{(D_{max} - D^i_{bio}(\vec{N}))^2}{\Delta D^2_{max}} \cdot \Theta(D^i_{bio}(\vec{N}) - D_{max}) \ .$$

$\vec{N}$: vector of particle numbers
D_{pre} : prescribed dose within the target
D_{max} : maximum dose within OAR (Organ-At-Risk)
D^i_{bio} : actual biological dose at voxel i

The nonlinearity of $D^i_{bio}(\vec{N})$ in $\vec{N}$ leads to a nonlinear optimization problem. Hence, the equation $\vec{N}_{opt} := \nabla X^2(\vec{N}) = \vec{0}$ can only be solved with numerical methods. We tested the inverse BFGS method [4]. For the initial matrix we used the unit matrix. As a line search technique we implemented the Armijo rule [6] were we set the starting stepsize with 1.0 and the damping factor with 0.5.

The number of voxels and rasterspots are several tenthousands which leads to long computation times [7].

Results and Discussion

The results of the BFGS method concerning the iterations and the time are presented in Fig. 1 and 2. The data were taken from the patient plan #135. Other patient plans show similar results. We compared them with the results of the Levenberg-Marquardt method (LMM) and the Fletcher-Reeves variant of the conjugate gradients method (CGFR) which we published in [5]. BFGS shows currently no improvements concerning the convergence. In terms of iterations the LMM and CGFR work more efficiently than the BFGS method. With regard to time the BFGS method is similar to the LMM, however, the CGFR is faster.

Various techniques exist to improve the convergence behaviour of the BFGS method. With an angle test one can avoid the echelon form and force a stronger decrease of the objective function. For the Armijo rule approximations of the minimum in a line search can be used for a good starting stepsize. Other matrices besides the unit matrix as an initial matrix can have a benefit on the convergence speed. Currently we are working on these issues.

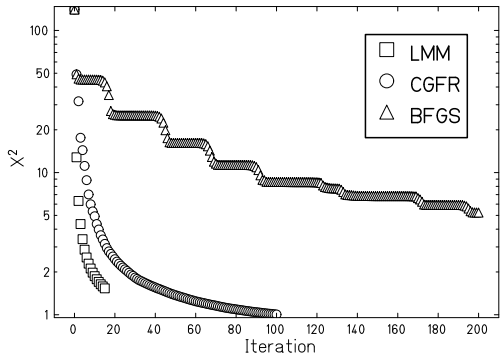

Figure 1: Convergence speed as a function of iterations.

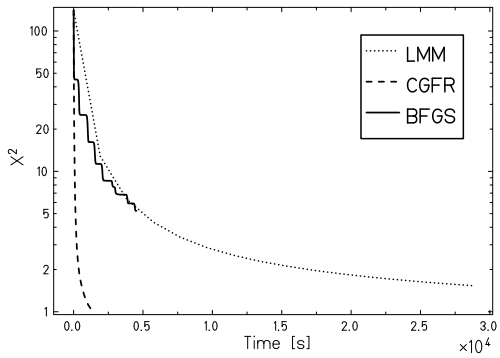

Figure 2: Convergence speed as a function of time.

References

[1] M. Krämer et al, Phys. Med. Biol., 45/11 (2000) 3299.
[2] M. Krämer et al, Phys. Med. Biol., 45/11 (2000) 3319.
[3] M. Horcicka, Dipl.-Thesis, GSI (2008).
[4] B. P. Flannery et al, *Numerical Recipes in C*, 2. Edition, 1992.
[5] M. Horcicka et al, GSI Scientific Report 2009, 488.
[6] W. Alt, *Nichtlineare Optimierung*, Vieweg, 2002.
[7] A. Gemmel et al, Phys. Med. Biol., 53/23 (2008) 6991.

Investigation of Single Event Effects with very High Energy Ions*

S. Metzger[1], E. Daly[2], M.Durante[3], V. Ferlet-Cavrois[2], S.K. Höffgen[1], J. Kuhnhenn[1], C. LaTessa[3], M. Mathes[1], A. Menicucci[2], P. Nieminen[2], R. Pleskac[3], C. Poivey[2], D. Schardt[3]

[1]Fraunhofer INT, Euskirchen, Germany, [2]ESA-ESTEC, Noordwijk, The Netherlands, [3]GSI, Darmstadt, Germany;.

Introduction

Our solar system is bombarded by galactic cosmic rays (GCR). These consist of electrons and nearly all the elements of the periodic table. The energy of the ions can be as high as 10^{20} eV, but they have their maximum fluence around 1 GeV/n [1]. Here on Earth the atmosphere protects us from most of the GCRs but in space they pose a serious hazard for satellite electronics due to their ability to produce a lot of electrical charge inside a very small volume by direct ionization along their path inside the device.

The experimental advantages of very high energy accelerators

Before electronic parts can be sent into space, they have to be qualified on earth. These tests are usually done at heavy ion accelerator facilities with ions of only a few MeV/n energy.

Ions of this low energy have ranges in air of only a few cm and in silicon only about 100 µm. Because of the short range of the ions the tests can only be done inside a vacuum chamber. This poses a challenge to the testing of modern devices, which need to be very close (typically < 10 cm) to the test system because they have to be operated at high data rates.

The range of the ions is also too low to penetrate the package of the device. Even if the package is opened the ions often still not reach the sensitive region. So the substrate of the devices must be thinned down below 100 µm, which can destroy the device.

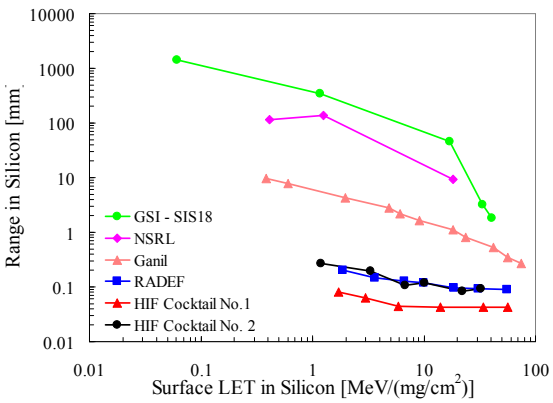

Figure 1: Range vs LET of several ion accelerators.

Figure 1 shows the range of ions versus the LET for accelerators typically used for space irradiation testing (ESA: HIF, RADEF). The SIS 18 is the only heavy ion accelerator covering the energy range of maximum GCR flux for all occurring ion species.

* Work supported by ESA contract no. 4200021985.

Energy Effects

There are indications that particles with the same LET but different energies have different SEU cross section. There have been older studies showing a reduced cross section for high energy ions near the LET threshold [2]. The threshold is the LET below which a particle does not produce enough charge by direct ionization to cause an SEE. A reduction in cross section for higher energy ions would mean that current low energy tests are worst case. But more recent studies found a surprising increase of the cross section below the LET threshold for ions with energies of about 45 MeV/n compared to ions of about 10 MeV/n [3]. This was explained by nuclear reactions. If the produced secondary particles have a higher LET than the projectile, they are able to induce SEUs. If these contribute significantly to the SEU cross section then LET is no longer a valid parameter for SEU tests.

The interesting question is if these increases of the cross section are significant for really high energy ions in the range of several 100 MeV/n. To study this Fraunhofer INT did measurements with the so called ESA SEU Monitor. The results can be seen in Fig. 2. The low energy data is represented by squares and the high energy data by circles. For this chip and energy range the cross section for the high energy ions is about two orders of magnitude lower than for the low energy ions.

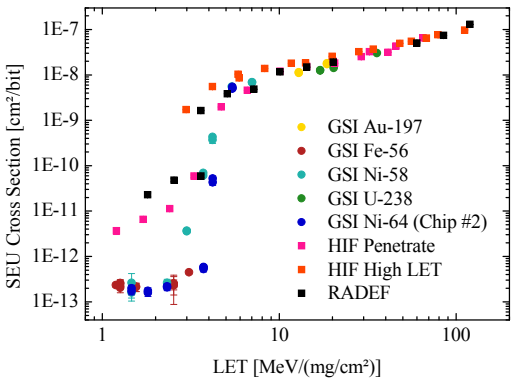

Figure 2: SEU cross sections of the ESA SEU Monitor for low energy (squares) and high energy (circles) ions.

References

[1] G.D. Badhwar, *Radiat. Res.* **148** (1997) 3-10

[2] S. Duzellier et. al., *IEEE Trans. Nucl. Sci* **42** (1995) 1797-1802

[3] P.E. Dodd et. al., *IEEE Trans. Nucl. Sci* **54** (2007) 2303-2311

Program of the new International Open Laboratory at NIRS *

M.Durante[1,#] *and Y. Furusawa*[2]

[1]GSI, Darmstadt, Germany; [2]NIRS, Chiba, Japan

The National Institute for Radiological Sciences (NIRS) is the leading Japanese research institute in radiation research. It is well known worldwide especially for the heavy-ion therapy, which started at the Heavy Ion Medical Accelerator (HIMAC) (Fig. 1) in 1994. Since then, over 5,000 patients have been treated with high-energy C-ions for many different results, and generally with excellent results [1]. For comparison, 440 patients were treated at GSI in the pilot project 1997-2208 [2].

Figure 1: The HIMAC accelerator in Chiba (Japan)

NIRS has a long tradition of collaboration with research groups in Asia, Europe, and USA. To enforce these links, the International Open Laboratory (IOL) program was launched in 2008, where foreign scientists are invited to NIRS to perform experiments together with local groups. The program includes beamtime availability at HIMAC, and a financial support of approximately 10 M¥ in 3 years.

A new IOL has been approved in 2010 which will be led by GSI in collaboration with the Charged particle research centre at NIRS. The new IOL is called "particle Beam Quality Research Unit", and its main activity will be the dependence of human tumour radiosensitivity from the genetic background. In fact, it is known that several genetic mutations confers resistance to cancers, for instance those in apoptotic pathway, controlled by the p53 gene. As roughly 50% of the human cancers carry mutations in the p53 gene, we hypothesize that carbon ions may be able to overcome the genetic sensitivity of this cancers. If correct, these results could greatly expand the number of patients that can potentially benefit from heavy-ion therapy.

To accomplish this task, we plan to exploit the large database of tumors genetically screened developed at NIRS within the RadGenomics Project, led by Dr. Imai [3]. We will also collaborate with Dr. Yamada for the in vivo assay of the tumorigenicity of the cell surviving X-rays or C-ion exposure.

The IOL will also be a unique opportunity to reinforce the links between GSI and NIRS in other topics, such as treatment planning models, where already several collaborative studies have been performed [4], and treatment of moving targets with scanned beams, a field where GSI has a large and consolidated experience [5] and has to be carefully studied also at NIRS in view of the new spot-scanning system recently installed I the new patient irradiation room at NIRS [6].

The activities of the new IOL will start in April 2011.

References

[1] Okada T, Kamada T, Tsuji H, Mizoe JE, Baba M, Kato S, Yamada S, Sugahara S, Yasuda S, Yamamoto N, Imai R, Hasegawa A, Imada H, Kiyohara H, Jingu K, Shinoto M, Tsujii H. Carbon ion radiotherapy: clinical experiences at National Institute of Radiological Science (NIRS). J Radiat Res 2010;51:355-64.

[2] Kraft G. Ion beam therapy in Europe. AIP Conf. Proc. 2009; 1099: 429-34-

[3] Michikawa Y, Suga T, Ishikawa A, Hayashi H, Oka A, Inoko H, Iwakawa M, Imai T. Genome wide screen identifies microsatellite markers associated with acute adverse effects following radiotherapy in cancer patients. BMC Med Genet. 2010;11:123.

[4] Kase Y, Kanai T, Matsufuji N, Furusawa Y, Elsässer T, Scholz M. Biophysical calculation of cell survival probabilities using amorphous track structure models for heavy-ion irradiation. Phys Med Biol. 2008;53:37-59.

[5] Bert C, Gemmel A, Saito N, Chaudhri N, Schardt D, Durante M, Kraft G, Rietzel E. Dosimetric precision of an ion beam tracking system. Radiat Oncol. 2010;5:61.

[6] Furukawa T, Inaniwa T, Sato S, Shirai T, Mori S, Takeshita E, Mizushima K, Himukai T, Noda K. Moving target irradiation with fast rescanning and gating in particle therapy. Med Phys. 2010 ;37:4874-9.

* Work supported by NIRS - IOL

M.Durante@gsi.de; http://www.nirs.go.jp/research/laboratory/eng/index.html

Status of the ESA radiobiology program at GSI *

M.Durante[1,#] and O. Angerer[2]

[1]GSI, Darmstadt, Germany; [2]ESA-ESTEC, Nordwijk, The Netherlands

The IBER project started in January 2009, supporting 13 experiments selected in the AO-08-IBER announcement of opportunity released by ESA in Summer 2008 [1]. A mid-term report was published in the 2009 GSI Annual report [2]. Here we provide the final report, because the program was supposed to run for 2 years. A new ESA announcement of opportunity AO-IBER-10 has been issued this year, and therefore proposals will be selected for a further 2-years program that will start in Fall 2011 or early 2012.

In the framework of the ESA-IBER project, 10 European research groups used heavy ion beams at GSI, in particular C, N, Ar, Fe and Ni. A total of 5 beamtime windows and 11 shifts were dedicated to the program. One further experiment, FIRST; initially selected within IBER, has then applied for beamtime to the G-PAC and is currently also under way [3].

The reports on the status of the different experiments have been reported during the 2nd ESA Investigators Worksop at GSI on 24.11.2010. Several scientific highlights emerged from the scientific reports (see e.g. Fig. 1).

The experiments were generally performed either in cave A (Fig. 2) or in cave M.

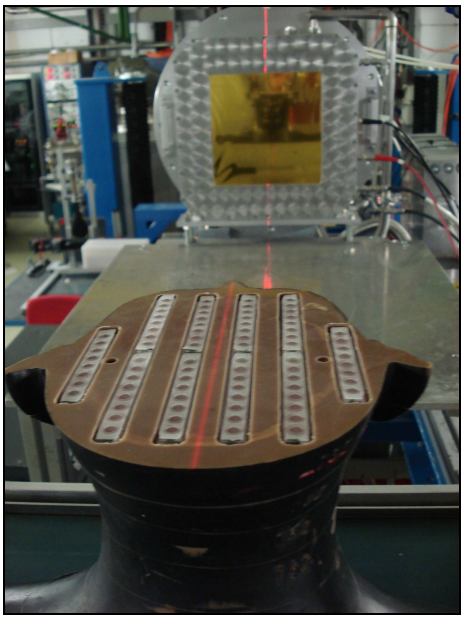

Figure 2: The exposure of the MATROSHKA phantom in Cave A. MATROSHKA head has been filled with tubes containing human embryonic cells. The growth the cells after exposure was then measured by a fluorescent assay. Experiment AO-08-IBER-12, courtesy of Dr. T. Berger (DLR).

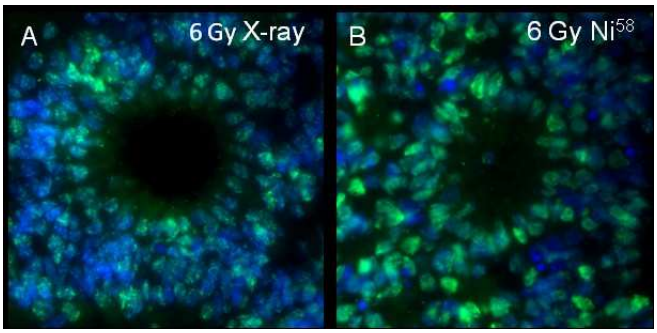

Figure 1: Radiation-induced DNA damage induced in chick-embryo derived retinospheroids after exposure to the same dose of X-rays (A) or 1 GeV/n Ni-ions (B). The γH2AX histone, a marker of DNA double-strand breaks, is immunostained in green. More damage is apparent with heavy ions at the same dose. Experiment AO-08-IBER-16, courtesy of Prof. P. Layer (Techniche Universität Darmstadt).

The FIRST experiment will be instead performed in cave C [4]. Experiments within the IBER project dealt with DNA repair, effects of heavy ions in the retina, bones, membranes and in brain, and mucositis, in addition to physics-oriented experiments including one on low-energy electron measurements. The program has provided outstanding scientific results [5] and will continue in the framework of IBER-10 in close collaboration with the NASA Space Radiation Health Program [6].

References

[1] M. Durante, D. Schardt, S. Metzger and O. Angerer, European space radiation research program at GSI. *GSI Rep.* (2008) 404

[2] M. Durante, D. Schardt, S. Metzger and O. Angerer, Status of the ESA programs at GSI. *GSI Rep.* (2009) 509

[3] R. Pleskac et al., The status of the FIRST project. *GSI Rep.* (2009) 508

[4] R. Pleskac and C. Schuy, Status of the FIRST experiment. *GSI Rep.* (2010) this issue.

[5] M. Durante, G. Reitz and O. Angerer, Space radiation research in Europe: flight experiments and ground-based studies. *Radiat Environ Biophys.* 49 (2010) 295-302.

[6] M. Durante and F.A. Cucinotta, heavy ion carcinogenesis and human space exploration. *Nat. Rev. Cancer* 8 (2008) 465-472.

* Work supported by ESA – IBER contract RFQ-3-12324/08/NL/VJ

#M.Durante@gsi.de; http://www.gsi.de/forschung/bio/iber_e.html

WoS publications to the programme 'Physics of hadrons and nuclei' (incl. the FAIR project) published in 2010

001 Aamodt, K.; Abel, N.; Abeysekara, U.; Abrahantes Quintana, A.; Abramyan, A.; Adamova, D.; Aggarwal, M.; Aglieri Rinella, G.; Agocs, A.; Aguilar Salazar, S.; Ahammed, Z.; Ahmad, A.; Ahmad, N.; Ahn, S.; Akimoto, R.; Akindinov, A.; Aleksandrov, D.; Alessandro, B.; Alfaro Molina, R.; Alici, A.; Almaraz Avia, E.; Alme, J.; Alt, T.; Altini, V.; Altinpinar, S.; Andrei, C.; Andronic, A. ; Anelli, G.; Angelov, V.; Anson, C.; Anticic, T.; Antinori, F.; Antinori, S.; Antipin, K.; Antonczyk, D.; Antonioli, P.; Anzo, A.; Aphecetche, L.; Appelshauser, H.; Arcelli, S.; Arceo, R.; Arend, A.; Armesto, N.; Arnaldi, R.; Aronsson, T.; Arsene, I.; Asryan, A.; Augustinus, A.; Averbeck, R.; Awes, T.; Aysto, J.; Azmi, M.; Bablok, S.; Bach, M.; Badalia, A.; Baek, Y.; Bagnasco, S.; Bailhache, R.; Bala, R.; Baldisseri, A.; Baldit, A.; Ban, J.; Barbera, R.; Barnafoldi, G.; Barnby, L.; Barret, V.; Bartke, J.; Barile, F.; Basile, M.; Basmanov, V.; Bastid, N.; Bathen, B.; Batigne, G.; Batyunya, B.; Baumann, C.; Bearden, I.; Becker, B.; Belikov, I.; Bellwied, R.; Belmont-Moreno, E.; Belogianni, A.; Benhabib, L.; Beole, S.; Berceanu, I.; Bercuci, A.; Berdermann, E. ; Berdnikov, Y.; Betev, L.; Bhasin, A.; Bhati, A.; Bianchi, L.; Bianchi, N.; Bianchin, C.; Bielik, J.; Bielikova, J.; Bilandzic, A.; Bimbot, L.; Biolcati, E.; Blanc, A.; Blanco, F.; Blanco, F.; Blau, D.; Blume, C.; Boccioli, M.; Bock, N.; Bogdanov, A.; Boggild, H.; Bogolyubsky, M.; Bohm, J.; Boldizsar, L.; Bombara, M.; Bombonati, C.; Bondila, M.; Borel, H.; Borisov, A.; Bortolin, C.; Bose, S.; Bosisio, L.; Bossu, F.; Botje, M.; Bottger, S.; Bourdaud, G.; Boyer, B.; Braun, M.; Braun-Munzinger, P.; Bravina, L.; Bregant, M.; Breitner, T.; Bruckner, G.; Brun, R.; Bruna, E.; Bruno, G.; Budnikov, D.; Buesching, H.; Buncic, P.; Busch, O. ; Buthelezi, Z.; Caffarri, D.; Cai, X.; Caines, H.; Camacho, E.; Camerini, P.; Campbell, M.; Canoa Roman, V.; Capitani, G.; Cara Romeo, G.; Carena, F.; Carena, W.; Carminati, F.; Diaz, A. C.; Caselle, M.; Castellanos, J. C.; Castillo Hernandez, J.; Catanescu, V.; Cattaruzza, E.; Cavicchioli, C.; Cerello, P.; Chambert, V.; Chang, B.; Chapeland, S.; Charpy, A.; Charvet, J.; Chattopadhyay, S.; Chattopadhyay, S.; Cherney, M.; Cheshkov, C.; Cheynis, B.; Chiavassa, E.; Barroso, V. C.; Chinellato, D.; Chochula, P.; Choi, K.; Chojnacki, M.; Christakoglou, P.; Christensen, C.; Christiansen, P.; Chujo, T.; Chuman, F.; Cicalo, C.; Cifarelli, L.; Cindolo, F.; Cleymans, J.; Cobanoglu, O.; Coffin, J. P.; Coli, S.; Colla, A.; Conesa Balbastre, G.; del Valle, Z. C.; Conner, E.; Constantin, P.; Contin, G.; Contreras, J.; Morales, Y. C.; Cormier, T.; Cortese, P.; Maldonado, I. C.; Cosentino, M.; Costa, F.; Cotallo, M.; Crescio, E.; Crochet, P.; Cuautle, E.; Cunqueiro, L.; Cussonneau, J.; Dainese, A.; Dalsgaard, H.; Danu, A.; Das, I.; Dash, A.; Dash, S.; Barros, G.; Caro, A.; de Cataldo, G.; de Cuveland, J.; Falco, A.; Gaspari, M.; de Groot, J.; Gruttola, D.; Marco, N.; Pasquale, S.; Remigis, R.; de Rooij, R.; de Vaux, G.; Delagrange, H.; Dellacasa, G.; Deloff, A.; Demanov, V.; Denes, E.; Deppman, A.; D'Erasmo, G.; Derkach, D.; Devaux, A.; Di Bari, D.; Di Giglio, C.; Di Liberto, S.; Di Mauro, A.; Di Nezza, P.; Dialinas, M.; Diaz, L.; Diaz, R.; Dietel, T.; Divi, R.; Djuvsland, O.; Dobretsov, V.; Dobrin, A.; Dobrowolski, T.; Donigus, B.; Dominguez, I.; Don, D.; Dordic, O.; Dubey, A.; Dubuisson, J.; Ducroux, L.; Dupieux, P.; Dutta Majumdar, A.; Dutta Majumdar, M.; Elia, D.; Emschermann, D.; Enokizono, A.; Espagnon, B.; Estienne, M.; Esumi, S.; Evans, D.; Evrard, S.; Eyyubova, G.; Fabjan, C.; Fabris, D.; Faivre, J.; Falchieri, D.; Fantoni, A.; Fasel, M.; Fateev, O.; Fearick, R.; Fedunov, A.; Fehlker, D.; Fekete, V.; Felea, D.; Fenton-Olsen, B.; Feofilov, G.; Fernandez Tellez, A.; Ferreiro, E.; Ferretti, A.; Ferretti, R.; Figueredo, M.; Filchagin, S.; Fini, R.; Fionda, F.; Fiore, E.; Floris, M.; Fodor, Z.; Foertsch, S.; Foka, P.; Fokin, S.; Formenti, F.; Fragiacomo, E.; Fragkiadakis, M.; Frankenfeld, U.; Frolov, A.; Fuchs, U.; Furano, F.; Furget, C.; Fusco Girard, M.; Gaardhoje, J.; Gadrat, S.; Gagliardi, M.; Gago, A.; Gallio, M.; Ganoti, P.; Ganti, M.; Garabatos, C. ; Garcia Trapaga, C.; Gebelein, J.; Gemme, R.; Germain, M.; Gheata, A.; Gheata, M.; Ghidini, B.; Ghosh, P.; Giraudo, G.; Giubellino, P.; Gladysz-Dziadus, E.; Glasow, R.; Glassel, P.; Glenn, A.; Gomez Jimenez, R.; Gonzalez Santos, H.; Gonzalez-Trueba, L.; Gonzalez-Zamora, P.; Gorbunov, S.; Gorbunov, Y.; Gotovac, S.; Gottschlag, H.; Grabski, V.; Grajcarek, R.; Grelli, A.; Grigoras, A.; Grigoras, C.; Grigoriev, V.; Grigoryan, A.; Grigoryan, S.; Grinyov, B.; Grion, N.; Gros, P.; Grosse-Oetringhaus, J.; Grossiord, J. Y.; Grosso, R.; Guber, F.; Guernane, R.; Guerzoni, B.; Gulbrandsen, K.; Gulkanyan, H.; Gunji, T.; Gupta, A.; Gupta, R.; Gustafsson, H. A.; Gutbrod, H.; Haaland, O.; Hadjidakis, C.; Haiduc, M.; Hamagaki, H.; Hamar, G.; Hamblen, J.; Han, B.; Harris, J.; Hartig, M.; Harutyunyan, A.; Hasch, D.; Hasegan, D.; Hatzifotiadou, D.; Hayrapetyan, A.; Heide, M.; Heinz, M.; Helstrup, H.; Herghelegiu, A.; Hernandez, C.; Herrera Corral, G.; Herrmann, N.; Hetland, K.; Hicks, B.; Hiei, A.; Hille, P.; Hippolyte, B.; Horaguchi, T.; Hori, Y.; Hristov, P.; Hrivnacova, I.; Hu, S.; Huang, M.; Huber, S.; Humanic, T.;

Hutter, D.; Hwang, D.; Ichou, R.; Ilkaev, R.; Ilkiv, I.; Inaba, M.; Innocenti, P.; Ippolitov, M.; Irfan, M.; Ivan, C.; Ivanov, A.; Ivanov, M.; Ivanov, V.; Iwasaki, T.; Jachokowski, A.; Jacobs, P.; Janurova, L.; Jangal, S.; Janik, R.; Jena, C.; Jena, S.; Jirden, L.; Jones, G.; Jones, P.; Jovanoviic, P.; Jung, H.; Jung, W.; Jusko, A.; Kaidalov, A.; Kalcher, S.; KaliAak, P.; Kalisky, M.; Kalliokoski, T.; Kalweit, A.; Kamal, A.; Kamermans, R.; Kanaki, K.; Kang, E.; Kang, J.; Kapitan, J.; Kaplin, V.; Kapusta, S.; Karavichev, O.; Karavicheva, T.; Karpechev, E.; Kazantsev, A.; Kebschull, U.; Keidel, R.; Khan, M.; Khan, S.; Khanzadeev, A.; Kharlov, Y.; Kikola, D.; Kileng, B.; Kim, D.; Kim, D.; Kim, D.; Kim, H.; Kim, J.; Kim, J.; Kim, J.; Kim, M.; Kim, M.; Kim, S.; Kim, S.; Kim, Y.; Kirsch, S.; Kisel, I.; Kiselev, S.; Kisiel, A.; Klay, J.; Klein, J.; Klein-Bosing, C.; Kliemant, M.; Klovning, A.; Kluge, A.; Knichel, M.; Kniege, S.; Koch, K.; Kolevatov, R.; Kolojvari, A.; Kondratiev, V.; Kondratyeva, N.; Konevskih, A.; Kornas, E.; Kour, R.; Kowalski, M.; Kox, S.; Kozlov, K.; Kral, J.; Kralik, I.; Kramer, F.; Kraus, I.; Kravakova, A.; Krawutschke, T.; Krivda, M.; Krumbhorn, D.; Krus, M.; Kryshen, E.; Krzewicki, M.; Kucheriaev, Y.; Kuhn, C.; Kuijer, P.; Kumar, L.; Kumar, N.; Kupczak, R.; Kurashvili, P.; Kurepin, A.; Kurepin, A.; Kuryakin, A.; Kushpil, S.; Kushpil, V.; Kutouski, M.; Kvaerno, H.; Kweon, M.; Kwon, Y.; La Rocca, P.; Lackner, F.; de Guevara, P. L.; Lafage, V.; Lal, C.; Lara, C.; Larsen, D.; Laurenti, G.; Lazzeroni, C.; Le Bornec, Y.; Le Bris, N.; Lee, H.; Lee, K.; Lee, S.; LefSvre, F.; Lenhardt, M.; Leistam, L.; Lehnert, J.; Lenti, V.; Len, H.; Monzon, I. L.; Vargas, H. L.; Levai, P.; Li, X.; Li, Y.; Lietava, R.; Lindal, S.; Lindenstruth, V.; Lippmann, C. ; Lisa, M.; Liu, L.; Loginov, V.; Lohn, S.; Lopez, X.; Lpez Noriega, M.; Lpez-Ramirez, R.; Lpez Torres, E.; Lovhoiden, G.; Lozea Feijo Soares, A.; Lu, S.; Lunardon, M.; Luparello, G.; Luquin, L.; Lutz, J. R.; Ma, K.; Ma, R.; Madagodahettige-Don, D.; Maevskaya, A.; Mager, M.; Mahapatra, D.; Maire, A.; Makhlyueva, I.; Mal'Kevich, D.; Malaev, M.; Malagalage, K.; Maldonado Cervantes, I.; Malek, M.; Malkiewicz, T.; Malzacher, P.; Mamonov, A.; Manceau, L.; Mangotra, L.; Manko, V.; Manso, F.; Manzari, V.; Mao, Y.; Mare, J.; Margagliotti, G.; Margotti, A.; Marin, A.; Martashvili, I.; Martinengo, P.; Martinez Hernandez, M.; Martinez Davalos, A.; Martinez Garcia, G.; Maruyama, Y.; Marzari Chiesa, A.; Masciocchi, S.; Masera, M.; Masetti, M.; Masoni, A.; Massacrier, L.; Mastromarco, M.; Mastroserio, A.; Matthews, Z.; Matyja, A.; Mayani, D.; Mazza, G.; Mazzoni, M.; Meddi, F.; Menchaca-Rocha, A.; Mendez Lorenzo, P.; Meoni, M.; Mercado Perez, J.; Mereu, P.; Miake, Y.; Michalon, A.; Miftakhov, N.; Milosevic, J.; Minafra, F.; Mischke, A.; Mitu, C.; Mizoguchi, K.; Mlynarz, J.; Mohanty, B.; Molnar, L.; Mondal, M.; Montao Zetina, L.; Monteno, M.; Montes, E.; Morando, M.; Moretto, S.; Morsch, A.; Moukhanova, T.; Muccifora, V.; Mudnic, E.; Muhuri, S.; Muller, H.; Munhoz, M.; Munoz, J.; Musa, L.; Musso, A.; Nandi, B.; Nania, R.; Nappi, E.; Navach, F.; Navin, S.; Nayak, T.; Nazarenko, S.; Nazarov, G.; Nedosekin, A.; Nendaz, F.; Newby, J.; Nianine, A.; Nicassio, M.; Nielsen, B.; Nikolaev, S.; Nikolic, V.; Nikulin, S.; Nikulin, V.; Nilsen, B.; Nilsson, M.; Noferini, F.; Nomokonov, P.; Nooren, G.; Novitzky, N.; Nyatha, A.; Nygaard, C.; Nyiri, A.; Nystrand, J.; Ochirov, A.; Odyniec, G.; Oeschler, H.; Oinonen, M.; Okada, K.; Okada, Y.; Oldenburg, M.; Oleniacz, J.; Oppedisano, C.; Orsini, F.; Ortiz Velasquez, A.; Ortona, G.; Oskarsson, A.; Osmic, F.; A-sterman, L.; Ostrowski, P.; Otterlund, I.; Otwinowski, J.; Ovrebekk, G.; Oyama, K.; Ozawa, K.; Pachmayer, Y.; Pachr, M.; Padilla, F.; Pagano, P.; Painke, F.; Pajares, C.; Pal, S.; Pal, S.; Palaha, A.; Palmeri, A.; Panse, R.; Papikyan, V.; Pappalardo, G.; Park, W.; Pastirak, B.; Pastore, C.; Paticchio, V.; Pavlinov, A.; Pawlak, T.; Peitzmann, T.; Pepato, A.; Pereira, H.; Peressounko, D.; Perez, C.; Perini, D.; Perrino, D.; Peryt, W.; Peschek, J.; Pesci, A.; Peskov, V.; Pestov, Y.; Peters, A.; Petraek, V.; Petridis, A.; Petris, M.; Petrov, P.; Petrovici, M.; Petta, C.; Peyre, J.; Piano, S.; Piccotti, A.; Pikna, M.; Pillot, P.; Pinazza, O.; Pinsky, L.; Pitz, N.; Piuz, F.; Platt, R.; Posko, M.; Pluta, J.; Pocheptsov, T.; Pochybova, S.; Podesta Lerma, P.; Poggio, F.; Poghosyan, M.; Polak, K.; Polichtchouk, B.; Polozov, P.; Polyakov, V.; Pommeresch, B.; Pop, A.; Posa, F.; Pospiil, V.; Potukuchi, B.; Pouthas, J.; Prasad, S.; Preghenella, R.; Prino, F.; Pruneau, C.; Pshenichnov, I.; Puddu, G.; Pujahari, P.; Pulvirenti, A.; Punin, A.; Punin, V.; Puti, M.; Putschke, J.; Quercigh, E.; Rachevski, A.; Rademakers, A.; Radomski, S.; Raiha, T.; Rak, J.; Rakotozafindrabe, A.; Ramello, L.; Ramirez Reyes, A.; Rammler, M.; Raniwala, R.; Raniwala, S.; Rasanen, S.; Rashevskaya, I.; Rath, S.; Read, K.; Real, J.; Redlich, K.; Renfordt, R.; Reolon, A.; Reshetin, A.; Rettig, F.; Revol, J. P.; Reygers, K.; Ricaud, H.; Riccati, L.; Ricci, R.; Richter, M. ; Riedler, P.; Riegler, W.; Riggi, F.; Rivetti, A.; Rodriguez Cahuantzi, M.; Roed, K.; Rohrich, D.; Roman Lpez, S.; Romita, R.; Ronchetti, F.; Rosinska, P.; Rosnet, P.; Rossegger, S.; Rossi, A.; Roukoutakis, F.; Rousseau, S.; Roy, C.; Roy, P.; Rubio-Montero, A.; Rui, R.; Rusanov, I.; Russo, G.; Ryabinkin, E.; Rybicki, A.; Sadovsky, S.; Safaraik, K.; Sahoo, R.; Saini, J.; Saiz, P.; Sakata, D.; Salgado, C.; Salgueiro Domingues da Silva, R.; Salur, S.; Samanta, T.; Sambyal, S.; Samsonov, V.; Loer, I.; Sandoval, A.; Sano, M.; Sano, S.; Santo, R.; Santoro, R.; Sarkamo, J.; Saturnini, P.; Scapparone, E.; Scarlassara, F.; Scharenberg, R.; Schiaua, C.; Schicker, R.; Schindler, H.; Schmidt, C.; Schmidt, H.; Schossmaier, K.; Schreiner, S.; Schuchmann, S.; Schukraft, J.; Schutz, Y.; Schwarz, K.; Schweda, K.; Scioli, G.; Scomparin, E.; Segato, G.; Semenov, D.; Senyukov, S.; Seo, J.; Serci, S.; Serkin, L.; Serradilla, E.; Sevcenco, A.; Sgura, I.; Shabratova, G.; Shahoyan, R.; Sharkov, G.; Sharma, N.; Sharma, S.; Shigaki, K.; Shimomura, M.; Shtejer, K.; Sibiriak, Y.; Siciliano, M.; Sicking, E.; Siddi, E.; Siemiarczuk, T.; Silenzi, A.; Silvermyr, D.; Simili, E.; Simonetti, G.; Singaraju, R.; Singh, R.; Singhal, V.; Sinha, B.; Sinha, T.; Sitar, B.; Sitta, M.; Skaali, T.; Skjerdal, K.; Smakal, R.; Smirnov, N.; Snellings, R.; Snow, H.; Sogaard, C.; Soloviev, A.; Soltveit, H.; Soltz, R.; Sommer, W.; Son, C.; Son, H.;

Song, M.; Soos, C.; Soramel, F.; Soyk, D.; Spyropoulou-Stassinaki, M.; Srivastava, B.; Stachel, J.; Staley, F.; Stan, E.; Stefanek, G.; Stefanini, G.; Steinbeck, T.; Stenlund, E.; Steyn, G.; Stocco, D.; Stock, R.; Stolpovsky, P.; Strmen, P.; Suaide, A.; Subieta Vasquez, M.; Sugitate, T.; Suire, C.; Sumbera, M.; Susa, T.; Swoboda, D.; Symons, J.; Szanto de Toledo, A.; Szarka, I.; Szostak, A.; Szuba, M.; Tadel, M.; Tagridis, C.; Takahara, A.; Takahashi, J.; Tanabe, R.; Tapia Takaki, D.; Taureg, H.; Tauro, A.; Tavlet, M.; Tejeda Muoz, G.; Telesca, A.; Terrevoli, C.; Thader, J.; Tieulent, R.; Tlusty, D.; Toia, A.; Tolyhy, T.; Torcato de Matos, C.; Torii, H.; Torralba, G.; Toscano, L.; Tosello, F.; Tournaire, A.; Traczyk, T.; Tribedy, P.; Troger, G.; Truesdale, D.; Trzaska, W.; Tsiledakis, G.; Tsilis, E.; Tsuji, T.; Tumkin, A.; Turrisi, R.; Turvey, A.; Tveter, T.; Tydesjo, H.; Tywoniuk, K.; Ulery, J.; Ullaland, K.; Uras, A.; Urban, J.; Urciuoli, G.; Usai, G.; Vacchi, A.; Vala, M.; Valencia Palomo, L.; Vallero, S.; van der Kolk, N.; Vande Vyvre, P.; van Leeuwen, M.; Vannucci, L.; Vargas, A.; Varma, R.; Vasiliev, A.; Vassiliev, I.; Vasileiou, M.; Vechernin, V.; Venaruzzo, M.; Vercellin, E.; Vergara, S.; Vernet, R.; Verweij, M.; Vetlitskiy, I.; Vickovic, L.; Viesti, G.; Vikhlyantsev, O.; Vilakazi, Z.; Villalobos Baillie, O.; Vinogradov, A.; Vinogradov, L.; Vinogradov, Y.; Virgili, T.; Viyogi, Y.; Vodopianov, A.; Voloshin, K.; Voloshin, S.; Volpe, G.; von Haller, B.; Vranic, D.; Vrlakova, J.; Vulpescu, B.; Wagner, B.; Wagner, V.; Wallet, L.; Wan, R.; Wang, D.; Wang, Y.; Watanabe, K.; Wen, Q.; Wessels, J.; Westerhoff, U.; Wiechula, J.; Wikne, J.; Wilk, A.; Wilk, G.; Williams, M.; Willis, N.; Windelband, B.; Xu, C.; Yang, C.; Yang, H.; Yasnopolskiy, S.; Yermia, F.; Yi, J.; Yin, Z.; Yokoyama, H.; Yoo, I. K.; Yuan, X.; Yurevich, V.; Yushmanov, I.; Zabrodin, E.; Zagreev, B.; Zalite, A.; Zampolli, C.; Zanevsky, Y.; Zaporozhets, S.; Zarochentsev, A.; Zavada, P.; Zbroszczyk, H.; Zelnicek, P.; Zenin, A.; Zepeda, A.; Zgura, I.; Zhalov, M.; Zhang, X.; Zhou, D.; Zhou, S.; Zhu, J.; Zichichi, A.; Zinchenko, A.; Zinovjev, G.; Zoccarato, Y.; Zychaek, V.; Zynovyev, M.: **Charged-particle multiplicity measurement in proton-proton collisions at root s7 TeV with ALICE at LHC.** *The European physical journal: C, Particles and fields* **68**(3): 345–354, 2010. DOI:10.1140/epjc/s10052-010-1350-2

002 Aamodt, K.; Abel, N.; Abeysekara, U.; Quintana, A. A.; Abramyan, A.; Adamova, D.; Aggarwal, M. M.; Rinella, G. A.; Agocs, A. G.; Salazar, S. A.; Ahammed, Z.; Ahmad, A.; Ahmad, N.; Ahn, S. U.; Akimoto, R.; Akindinov, A.; Aleksandrov, D.; Alessandro, B.; Molina, R. A.; Alici, A.; Avina, E. A.; Alme, J.; Alt, T.; Altini, V.; Altinpinar, S.; Andrei, C.; Andronic, A. ; Anelli, G.; Angelov, V.; Anson, C.; Anticic, T.; Antinori, F.; Antinori, S.; Antipin, K.; Antonczyk, D.; Antonioli, P.; Anzo, A.; Aphecetche, L.; Appelshauser, H.; Arcelli, S.; Arceo, R.; Arend, A.; Armesto, N.; Arnaldi, R.; Aronsson, T.; Arsene, I. C.; Asryan, A.; Augustinus, A.; Averbeck, R.; Awes, T. C.; Aysto, J.; Azmi, M. D.; Bablok, S.; Bach, M.; Badala, A.; Baek, Y. W.; Bagnasco, S.; Baihache, R.; Bala, R.; Baldisseri, A.; Baldit, A.; Ban, J.; Barbera, R.; Barnafoldi, G. G.; Barnby, L.; Barret, V.; Bartke, J.; Barile, F.; Basile, M.; Basmanov, V.; Bastid, N.; Bathen, B.; Batigne, G.; Batyunya, B.; Baumann, C.; Bearden, I. G.; Becker, B.; Belikov, I.; Bellwied, R.; Belmont-Moreno, E.; Belogianni, A.; Benhabib, L.; Beole, S.; Berceanu, I.; Bercuci, A.; Berdermann, E. ; Berdnikov, Y.; Betev, L.; Bhasin, A.; Bhati, A. K.; Bianchi, L.; Bianchi, N.; Bianchin, C.; Bielcik, J.; Bielcikova, J.; Bilandzic, A.; Bimbot, L.; Biolcati, E.; Blanc, A.; Blanco, F.; Blanco, F.; Blau, D.; Blume, C.; Boccioli, M.; Bock, N.; Bogdanov, A.; Boggild, H.; Bogolyubsky, M.; Bohm, J.; Boldizsar, L.; Bombara, M.; Bombonati, C.; Bondila, M.; Borel, H.; Borisov, A.; Bortolin, C.; Bose, S.; Bosisio, L.; Bossu, F.; Botje, M.; Bottger, S.; Bourdaud, G.; Boyer, B.; Braun, M.; Braun-Munzinger, R.; Bravina, L.; Bregant, M.; Breitner, T.; Bruckner, G.; Brun, R.; Bruna, E.; Bruno, G. E.; Budnikov, D.; Buesching, H.; Buncic, P.; Busch, O. ; Buthelezi, Z.; Caffarri, D.; Cai, X.; Caines, H.; Calvo, E.; Camacho, E.; Camerini, P.; Campbell, M.; Roman, V. C.; Capitani, G. P.; Romeo, G. C.; Carena, F.; Carena, W.; Carminati, F.; Diaz, A. C.; Caselle, M.; Castellanos, J. C.; Hernandez, J. F. C.; Catanescu, V.; Cattaruzza, E.; Cavicchioli, C.; Cerello, P.; Chambert, V.; Chang, B.; Chapeland, S.; Charpy, A.; Charvet, J. L.; Chattopadhyay, S.; Chattopadhyay, S.; Cherney, M.; Cheshkov, C.; Cheynis, B.; Chiavassa, E.; Barroso, V. C.; Chinellato, D. D.; Chochula, P.; Choi, K.; Chojnacki, M.; Christakoglou, P.; Christensen, C. H.; Christiansen, P.; Chujo, T.; Chuman, F.; Cicalo, C.; Cifarelli, L.; Cindolo, F.; Cleymans, J.; Cobanoglu, O.; Coffin, J. P.; Coli, S.; Colla, A.; Balbastre, G. C.; del Valle, Z. C.; Conner, E. S.; Constantin, P.; Contin, G.; Contreras, J. G.; Morales, Y. C.; Cormier, T. M.; Cortese, P.; Maldonado, I. C.; Cosentino, M. R.; Costa, F.; Cotallo, M. E.; Crescio, E.; Crochet, P.; Cuautle, E.; Cunqueiro, L.; Cussonneau, J.; Dainese, A.; Dalsgaard, H. H.; Danu, A.; Das, I.; Dash, A.; Dash, S.; de Barros, G. O. V.; De Caro, A.; de Cataldo, G.; de Cuveland, J.; De Falco, A.; De Gaspari, M.; de Groot, J.; De Gruttola, D.; De Marco, N.; De Pasquale, S.; De Remigis, R.; de Rooij, R.; de Vaux, G.; Delagrange, H.; Delgado, Y.; Dellacasa, G.; Deloff, A.; Demanov, V.; Denes, E.; Deppman, A.; D'Erasmo, G.; Derkach, D.; Devaux, A.; Di Bari, D.; Di Giglio, C.; Di Liberto, S.; Di Mauro, A.; Di Nezza, P.; Dialinas, M.; Diaz, L.; Diaz, R.; Dietel, T.; Divia, R.; Djuvsland, O.; Dobretsov, V.; Dobrin, A.; Dobrowolski, T.; Donigus, B.; Dominguez, I.; Don, D. M. M.; Dordic, O.; Dubey, A. K.; Dubuisson, J.; Ducroux, L.; Dupieux, P.; Majumdar, A. K. D.; Majumdar, M. R. D.; Elia, D.; Emschermann, D.; Enokizono, A.; Espagnon, B.; Estienne, M.; Esumi, S.; Evans, D.; Evrard, S.; Eyyubova, G.; Fabjan, C. W.; Fabris, D.; Faivre, J.; Falchieri, D.; Fantoni, A.; Fasel, M.; Fateev, O.; Fearick, R.; Fedunov, A.; Fehlker, D.; Fekete, V.; Felea, D.; Fenton-Olsen, B.; Feofilov, G.; Tellez, A. F.; Ferreiro, E. G.; Ferretti, A.; Ferretti, R.; Figueredo, M. A. S.; Filchagin, S.; Fini, R.; Fionda, F. M.; Fiore, E. M.; Floris, M.; Fodor, Z.; Foertsch, S.; Foka, P.; Fokin, S.;

Formenti, F.; Fragiacomo, E.; Fragkiadakis, M.; Frankenfeld, U.; Frolov, A.; Fuchs, U.; Furano, F.; Furget, C.; Girard, M. F.; Gaardhoje, J. J.; Gadrat, S.; Gagliardi, M.; Gago, A.; Gallio, M.; Ganoti, P.; Ganti, M. S.; Garabatos, C. ; Trapaga, C. G.; Gebelein, J.; Gemme, R.; Germain, M.; Gheata, A.; Gheata, M.; Ghidini, B.; Ghosh, P.; Giraudo, G.; Giubellino, P.; Gladysz-Dziadus, E.; Glasow, R.; Glassel, R.; Glenn, A.; Jimenez, R. G.; Santos, H. G.; Gonzalez-Trueba, L. H.; Gonzalez-Zamora, P.; Gorbunov, S.; Gorbunov, Y.; Gotovac, S.; Gottschlag, H.; Grabski, V.; Grajcarek, R.; Grelli, A.; Grigoras, A.; Grigoras, C.; Grigoriev, V.; Grigoryan, A.; Grigoryan, S.; Grinyov, B.; Grion, N.; Gros, P.; Grosse-Oetringhaus, J. F.; Grossiord, J. Y.; Grosso, R.; Guber, F.; Guernane, R.; Guerra, C.; Guerzoni, B.; Gulbrandsen, K.; Gulkanyan, H.; Gunji, T.; Gupta, A.; Gupta, R.; Gustafsson, H. A.; Gutbrod, H.; Haaland, O.; Hadjidakis, C.; Haiduc, M.; Hamagaki, H.; Hamar, G.; Hamblen, J.; Han, B. H.; Harris, J. W.; Hartig, M.; Harutyunyan, A.; Hasch, D.; Hasegan, D.; Hatzifotiadou, D.; Hayrapetyan, A.; Heide, M.; Heinz, M.; Helstrup, H.; Herghelegiu, A.; Hernandez, C.; Corral, G. H.; Herrmann, N.; Hetland, K. F.; Hicks, B.; Hiei, A.; Hille, P. T.; Hippolyte, B.; Horaguchi, T.; Hori, Y.; Hristov, P.; Hrivnacova, I.; Hu, S.; Huang, M.; Huber, S.; Humanic, T. J.; Hutter, D.; Hwang, D. S.; Ichou, R.; Ilkaev, R.; Ilkiv, I.; Inaba, M.; Innocenti, P. G.; Ippolitov, M.; Irfan, M.; Ivan, C.; Ivanov, A.; Ivanov, M.; Ivanov, V.; Iwasaki, T.; Jacholkowski, A.; Jacobs, P.; Jancurova, L.; Jangal, S.; Janik, R.; Jena, C.; Jena, S.; Jirden, L.; Jones, G. T.; Jones, P. G.; Jovanovic, P.; Jung, H.; Jung, W.; Jusko, A.; Kaidalov, A. B.; Kalcher, S.; Kalinak, P.; Kalisky, M.; Kalliokoski, T.; Kalweit, A.; Kamal, A.; Kamermans, R.; Kanaki, K.; Kang, E.; Kang, J. H.; Kapitan, J.; Kaplin, V.; Kapusta, S.; Karavichev, O.; Karavicheva, T.; Karpechev, E.; Kazantsev, A.; Kebschull, U.; Keidel, R.; Khan, M. M.; Khan, S. A.; Khanzadeev, A.; Kharlov, Y.; Kikola, D.; Kileng, B.; Kim, D. J.; Kim, D. S.; Kim, D. W.; Kim, H. N.; Kim, J.; Kim, J. H.; Kim, J. S.; Kim, M.; Kim, M.; Kim, S. H.; Kim, S.; Kim, Y.; Kirsch, S.; Kisel, I.; Kiselev, S.; Kisiel, A.; Klay, J. L.; Klein, J. J.; Klein-Bosing, C.; Kliemant, M.; Klovning, A.; Kluge, A.; Knichel, M. L.; Kniege, S.; Koch, K.; Kolevatov, R.; Kolojvari, A.; Kondratiev, V.; Kondratyeva, N.; Konevskih, A.; Kornas, E.; Kour, R.; Kowalski, M.; Kox, S.; Kozlov, K.; Kral, J.; Kralik, I.; Kramer, F.; Kraus, I.; Kravcakova, A.; Krawutschkeb, T.; Krivda, M.; Krumbhorn, D.; Krus, M.; Kryshen, E.; Krzewicki, M.; Kucheriaev, Y.; Kuhn, C.; Kuijer, P. C.; Kumar, L.; Kumar, N.; Kupczak, R.; Kurashvili, P.; Kurepin, A.; Kurepin, A. N.; Kuryakin, A.; Kushpil, S.; Kushpil, V.; Kutouski, M.; Kvaerno, H.; Kweon, M. J.; Kwon, Y.; La Rocca, P.; Lackner, F.; de Guevara, P. L.; Lafage, V.; Lal, C.; Lara, C.; Larsen, D. T.; Laurenti, G.; Lazzeroni, C.; Le Bornec, Y.; Le Bris, N.; Lee, H.; Lee, K. S.; Lee, S. C.; Lefevre, F.; Lenhardt, M.; Leistam, L.; Lehnert, J.; Lenti, V.; Leon, H.; Monzon, I. L.; Vargas, H. L.; Levai, P.; Li, X.; Li, Y.; Lietava, R.; Lindal, S.; Lindenstruth, V.; Lippmann, C. ; Lisa, M. A.; Liu, L.; Loginov, V.; Lohn, S.; Lopez, X.; Noriega, M. L.; Lopez-Ramirez, R.; Torres, E. L.; Lovhoiden, G.; Soares, A. L. F.; Lu, S.; Luettiga, P.; Lunardon, M.; Luparello, G.; Luquin, L.; Lutz, J. R.; Ma, K.; Ma, R.; Madagodahettige-Don, D. M.; Maevskaya, A.; Mager, M.; Mahapatra, D. P.; Maire, A.; Makhlyueva, I.; Mal'Kevich, D.; Malaev, M.; Malagalage, K. J.; Cervantes, I. M.; Malek, M.; Malkiewicz, T.; Malzacher, P.; Mamonov, A.; Manceau, L.; Mangotra, L.; Manko, V.; Manso, F.; Manzari, V.; Mao, Y.; Mares, J.; Margagliotti, G. V.; Margotti, A.; Marin, A.; Martashvili, I.; Martinengo, P.; Hernandez, M. I. M.; Davalos, A. M.; Garcia, G. M.; Maruyama, Y.; Chiesa, A. M.; Masciocchi, S.; Masera, M.; Masetti, M.; Masoni, A.; Massacrier, L.; Mastromarco, M.; Mastroserio, A.; Matthews, Z. L.; Matyja, A.; Mayani, D.; Mazza, G.; Mazzoni, M. A.; Meddi, F.; Menchaca-Rocha, A.; Lorenzo, P. M.; Meoni, M.; Perez, J. M.; Mereu, P.; Miake, Y.; Michalon, A.; Miftakhov, N.; Milano, L.; Milosevic, J.; Minafra, F.; Mischke, A.; Miskowiec, D.; Mitu, C.; Mizoguchi, K.; Mlynarz, J.; Mohanty, B.; Molnar, L.; Mondal, M. M.; Zetina, L. M.; Monteno, M.; Montes, E.; Morando, M.; Moretto, S.; Morsch, A.; Moukhanova, T.; Muccifora, V.; Mudnic, E.; Muhuri, S.; Muller, H.; Munhoz, M. G.; Munoz, J.; Musa, L.; Musso, A.; Nandi, B. K.; Nania, R.; Nappi, E.; Navach, F.; Navin, S.; Nayak, T. K.; Nazarenko, S.; Nazarov, G.; Nedosekin, A.; Nendaz, F.; Newby, J.; Nianine, A.; Nicassio, M.; Nielsen, B. S.; Nikolaev, S.; Nikolic, V.; Nikulin, S.; Nikulin, V.; Nilsen, B. S.; Nilsson, M. S.; Noferini, F.; Nomokonov, P.; Nooren, G.; Novitzky, N.; Nyatha, A.; Nygaard, C.; Nyiri, A.; Nystrand, J.; Ochirov, A.; Odyniec, G.; Oeschler, H.; Oinonen, M.; Okada, K.; Okada, Y.; Oldenburg, M.; Oleniacz, J.; Oppedisano, C.; Orsini, F.; Velasquez, A. O.; Ortona, G.; Oskarsson, A.; Osmic, F.; Osterman, L.; Ostrowski, P.; Otterlund, I.; Otwinowski, J.; Ovrebekk, G.; Oyama, K.; Ozawa, K.; Pachmayer, Y.; Pachr, M.; Padilla, F.; Pagano, P.; Paic, G.; Painke, F.; Pajares, C.; Pal, S.; Pal, S. K.; Palaha, A.; Palmeri, A.; Panse, R.; Papikyan, V.; Pappalardo, G. S.; Park, W. J.; Pastircak, B.; Pastore, C.; Paticchio, V.; Pavlinov, A.; Pawlak, T.; Peitzmann, T.; Pepato, A.; Pereira, H.; Peressounko, D.; Perez, C.; Perini, D.; Perrino, D.; Peryt, W.; Peschek, J.; Pesci, A.; Peskov, V.; Pestov, Y.; Peters, A. J.; Petracek, V.; Petridis, A.; Petris, M.; Petrov, P.; Petrovici, M.; Petta, C.; Peyre, J.; Piano, S.; Piccotti, A.; Pikna, M.; Pillot, P.; Pinazza, O.; Pinsky, L.; Pitz, N.; Piuz, F.; Platt, R.; Ploskon, M.; Pluta, J.; Pocheptsovah, T.; Pochybova, S.; Lerma, P. L. M. P.; Poggio, F.; Poghosyan, M. G.; Polak, K.; Polichtchouk, B.; Polozov, P.; Polyakov, V.; Pommeresch, B.; Pop, A.; Posa, F.; Pospisil, V.; Potukuchi, B.; Pouthas, J.; Prasad, S. K.; Preghenella, R.; Prino, F.; Pruneau, C. A.; Pshenichnov, I.; Puddu, G.; Pujahari, P.; Pulvirenti, A.; Punin, A.; Punin, V.; Putis, M.; Putschke, J.; Quercigh, E.; Rachevski, A.; Rademakers, A.; Radomski, S.; Raiha, T. S.; Rak, J.; Rakotozafindrabe, A.; Ramello, L.; Reyes, A. R.; Rammler, M.; Raniwala, R.; Raniwala, S.; Rasanen, S. S.; Rashevskaya, I.; Rath, S.; Read, K. F.; Real, J. S.; Redlich, K.; Renfordt, R.; Reolon, A. R.; Reshetin, A.; Rettig, F.; Revol, J. P.; Reygers, K.; Ri-

caud, H.; Riccati, L.; Ricci, R. A.; Richter, M. ; Riedler, P.; Riegler, W.; Riggi, F.; Rivetti, A.; Cahuantzi, M. R.; Roed, K.; Rohrich, D.; Lopez, S. R.; Romita, R.; Ronchetti, F.; Rosinsky, P.; Rosnet, P.; Rossegger, S.; Rossi, A.; Roukoutakis, F.; Rousseau, S.; Roy, C.; Roy, P.; Rubio-Montero, A. J.; Rui, R.; Rusanov, I.; Russo, G.; Ryabinkin, E.; Rybicki, A.; Sadovsky, S.; Safarik, K.; Sahoo, R.; Saini, J.; Saiz, P.; Sakata, D.; Salgado, C. A.; da Silva, R. S. D.; Salur, S.; Samanta, T.; Sambyal, S.; Samsonov, V.; Sandor, L.; Sandoval, A.; Sano, M.; Sano, S.; Santo, R.; Santoro, R.; Sarkamo, J.; Saturnini, P.; Scapparone, E.; Scarlassara, F.; Scharenberg, R. P.; Schiaua, C.; Schicker, R.; Schindler, H.; Schmidt, C.; Schmidt, H. R.; Schossmaier, K.; Schreiner, S.; Schuchmann, S.; Schukraft, J.; Schutz, Y.; Schwarz, K.; Schweda, K.; Scioli, G.; Scomparin, E.; Scott, P. A.; Segato, G.; Semenov, D.; Senyukov, S.; Seo, J.; Serci, S.; Serkin, L.; Serradilla, E.; Sevcenco, A.; Sgura, I.; Shabratova, G.; Shahoyan, R.; Sharkov, G.; Sharma, N.; Sharma, S.; Shigaki, K.; Shimomura, M.; Shtejer, K.; Sibiriak, Y.; Siciliano, M.; Sicking, E.; Siddi, E.; Siemiarczuk, T.; Silenzi, A.; Silvermyr, D.; Simili, E.; Simonetti, G.; Singaraju, R.; Singh, R.; Singhal, V.; Sinha, B. C.; Sinha, T.; Sitar, B.; Sitta, M.; Skaali, T. B.; Skjerdal, K.; Smakal, R.; Smirnov, N.; Snellings, R.; Snow, H.; Sogaard, C.; Soloviev, A.; Soltveit, H. K.; Soltz, R.; Sommer, W.; Son, C. W.; Son, H.; Song, M.; Soos, C.; Soramel, F.; Soyk, D.; Spyropoulou-Stassinaki, M.; Srivastava, B. K.; Stachel, J.; Staley, F.; Stan, E.; Stefanek, G.; Stefanini, G.; Steinbeck, T.; Stenlund, E.; Steyn, G.; Stocco, D.; Stock, R.; Stolpovsky, P.; Strmen, P.; Suaide, A. A. P.; Vasquez, M. A. S.; Sugitate, T.; Suire, C.; Sumbera, M.; Susa, T.; Swoboda, D.; Symons, J.; de Toledo, A. S.; Szarka, I.; Szostak, A.; Szuba, M.; Tadel, M.; Tagridis, C.; Takahara, A.; Takahashi, J.; Tanabe, R.; Takaki, J. D. T.; Taureg, H.; Tauro, A.; Tavlet, M.; Munoz, G. T.; Telesca, A.; Terrevoli, C.; Thader, J.; Tieulent, R.; Tlusty, D.; Toia, A.; Tolyhy, T.; de Matos, C. T.; Torii, H.; Torralba, G.; Toscano, L.; Tosello, F.; Tournaire, A.; Traczyk, T.; Tribedy, P.; Troger, G.; Truesdale, D.; Trzaska, W. H.; Tsiledakisar, G.; Tsilis, E.; Tsuji, T.; Tumkin, A.; Turrisi, R.; Turvey, A.; Tveter, T. S.; Tydesjo, H.; Tywoniuk, K.; Ulery, J.; Ullaland, K.; Uras, A.; Urban, J.; Urciuoli, G. M.; Usai, G. L.; Vacchi, A.; Vala, M.; Palomo, L. V.; Vallero, S.; van der Kolk, N.; Vyvre, P. V.; van Leeuwen, M.; Vannucci, L.; Vargas, A.; Varma, R.; Vasiliev, A.; Vassiliev, I.; Vasileiou, M.; Vechernin, V.; Venaruzzo, M.; Vercellin, E.; Vergara, S.; Vernet, R.; Verweij, M.; Vetlitskiy, I.; Vickovic, L.; Viesti, G.; Vikhlyantsev, O.; Vilakazi, Z.; Baillie, O. V.; Vinogradov, A.; Vinogradov, L.; Vinogradov, Y.; Virgili, T.; Viyogi, Y. P.; Vodopianov, A.; Voloshin, K.; Voloshin, S.; Volpe, G.; von Haller, B.; Vranic, D.; Vrlakova, J.; Vulpescu, B.; Wagner, B.; Wagner, V.; Wallet, L.; Wan, R.; Wang, D.; Wang, Y.; Wang, Y.; Watanabe, K.; Wen, Q.; Wessels, J.; Westerhoff, U.; Wiechula, J.; Wikne, J.; Wilk, A.; Wilk, G.; Williams, M. C. S.; Willis, N.; Windelband, B.; Xu, C.; Yang, C.; Yang, H.; Yasnopolskiy, S.; Yermia, F.; Yi, J.; Yin, Z.; Yokoyama, H.; Yoo, I. K.; Yuan, X.; Yurevich, V.; Yushmanov, I.; Zabrodin, E.; Zagreev, B.; Zalite, A.; Zampolli, C.; Zanevsky, Y.; Zaporozhets, S.; Zarochentsev, A.; Zavada, P.; Zbroszczyk, H.; Zelnicek, P.; Zenin, A.; Zepeda, A.; Zgura, I.; Zhalov, M.; Zhang, X.; Zhou, D.; Zhou, S.; Zhu, J.; Zichichi, A.; Zinchenko, A.; Zinovjev, G.; Zoccarato, Y.; Zychacek, V.; Zynovyev, M.; ALICE Collaboration: **Transverse momentum spectra of charged particles in proton-proton collisions at root s900 GeV with ALICE at the LHC.** *Physics letters B* **693**(2): 53–68, 2010. DOI:10.1016/j.physletb.2010.08.026

003 Aamodt, K.; Abel, N.; Abeysekara, U.; Quintana, A. A.; Abramyan, A.; Adamova, D.; Aggarwal, M. M.; Rinella, G. A.; Agocs, A. G.; Salazar, S. A.; Ahammed, Z.; Ahmad, A.; Ahmad, N.; Ahn, S. U.; Akimoto, R.; Akindinov, A.; Aleksandrov, D.; Alessandro, B.; Molina, R. A.; Alici, A.; Avina, E. A.; Alme, J.; Alt, T.; Altini, V.; Altinpinar, S.; Andrei, C.; Andronic, A. ; Anelli, G.; Angelov, V.; Anson, C.; Anticic, T.; Antinori, F.; Antinori, S.; Antipin, K.; Antonczyk, D.; Antonioli, P.; Anzo, A.; Aphecetche, L.; Appelshauser, H.; Arcelli, S.; Arceo, R.; Arend, A.; Armesto, N.; Arnaldi, R.; Aronsson, T.; Arsene, I. C.; Asryan, A.; Augustinus, A.; Averbeck, R.; Awes, T. C.; Aysto, J.; Azmi, M. D.; Bablok, S.; Bach, M.; Badala, A.; Baek, Y. W.; Bagnasco, S.; Bailhache, R.; Bala, R.; Baldisseri, A.; Baldit, A.; Ban, J.; Barbera, R.; Barnafoldi, G. G.; Barnby, L. S.; Barret, V.; Bartke, J.; Barile, F.; Basile, M.; Basmanov, V.; Bastid, N.; Bathen, B.; Batigne, G.; Batyunya, B.; Baumann, C.; Bearden, I. G.; Becker, B.; Belikov, I.; Bellwied, R.; Belmont-Moreno, E.; Belogianni, A.; Benhabib, L.; Beole, S.; Berceanu, I.; Bercuci, A.; Berdermann, E. ; Berdnikov, Y.; Betev, L.; Bhasin, A.; Bhati, A. K.; Bianchi, L.; Bianchi, N.; Bianchin, C.; Bielcik, J.; Bielcikova, J.; Bilandzic, A.; Bimbot, L.; Biolcati, E.; Blanc, A.; Blanco, F.; Blanco, F.; Blau, D.; Blume, C.; Boccioli, M.; Bock, N.; Bogdanov, A.; Boggild, H.; Bogolyubsky, M.; Bohm, J.; Boldizsar, L.; Bombara, M.; Bombonati, C.; Bondila, M.; Borel, H.; Borisov, A.; Bortolin, C.; Bose, S.; Bosisio, L.; Bossu, F.; Botje, M.; Bottger, S.; Bourdaud, G.; Boyer, B.; Braun, M.; Braun-Munzinger, P.; Bravina, L.; Bregant, M.; Breitner, T.; Bruckner, G.; Brun, R.; Bruna, E.; Bruno, G. E.; Budnikov, D.; Buesching, H.; Buncic, P.; Busch, O. ; Buthelezi, Z.; Caffarri, D.; Cai, X.; Caines, H.; Calvo, E.; Camacho, E.; Camerini, P.; Campbell, M.; Roman, V. C.; Capitani, G. P.; Romeo, G. C.; Carena, F.; Carena, W.; Carminati, F.; Diaz, A. C.; Caselle, M.; Castellanos, J. C.; Hernandez, J. F. C.; Catanescu, V.; Cattaruzza, E.; Cavicchioli, C.; Cerello, P.; Chambert, V.; Chang, B.; Chapeland, S.; Charpy, A.; Charvet, J. L.; Chattopadhyay, S.; Chattopadhyay, S.; Cherney, M.; Cheshkov, C.; Cheynis, B.; Chiavassa, E.; Barroso, V. C.; Chinellato, D. D.; Chochula, P.; Choi, K.; Chojnacki, M.; Christakoglou, P.; Christensen, C. H.; Christiansen, P.; Chujo, T.; Chuman, F.; Cicalo, C.; Cifarelli, L.; Cindolo, F.; Cleymans, J.; Cobanoglu, O.; Coffin, J. P.; Coli, S.; Colla, A.; Balbastre, G. C.; del Valle,

Z. C.; Conner, E. S.; Constantin, P.; Contin, G.; Contreras, J. G.; Morales, Y. C.; Cormier, T. M.; Cortese, P.; Maldonado, I. C.; Cosentino, M. R.; Costa, F.; Cotallo, M. E.; Crescio, E.; Crochet, P.; Cuautle, E.; Cunqueiro, L.; Cussonneau, J.; Dainese, A.; Dalsgaard, H. H.; Danu, A.; Das, I.; Dash, A.; Dash, S.; de Barros, G. O. V.; De Caro, A.; de Cataldo, G.; de Cuveland, J.; De Falco, A.; De Gaspari, M.; de Groot, J.; De Gruttola, D.; De Marco, N.; De Pasquale, S.; De Remigis, R.; De Rooij, R.; de Vaux, G.; Delagrange, H.; Delgado, Y.; Dellacasa, G.; Deloff, A.; Demanov, V.; Denes, E.; Deppman, A.; D'Erasmo, G.; Derkach, D.; Devaux, A.; Di Bari, D.; Di Giglio, C.; Di Liberto, S.; Di Mauro, A.; Di Nezza, P.; Dialinas, M.; Diaz, L.; Diaz, R.; Dietel, T.; Divia, R.; Djuvsland, O.; Dobretsov, V.; Dobrin, A.; Dobrowolski, T.; Donigus, B.; Dominguez, I.; Don, D. M. M.; Dordic, O.; Dubey, A. K.; Dubuisson, J.; Ducroux, L.; Dupieux, P.; Majumdar, A. K. D.; Majumdar, M. R. D.; Elia, D.; Emschermann, D.; Enokizono, A.; Espagnon, B.; Estienne, M.; Esumi, S.; Evans, D.; Evrard, S.; Eyyubova, G.; Fabjan, C. W.; Fabris, D.; Faivre, J.; Falchieri, D.; Fantoni, A.; Fasel, M.; Fateev, O.; Fearick, R.; Fedunov, A.; Fehlker, D.; Fekete, V.; Felea, D.; Fenton-Olsen, B.; Feofilov, G.; Tellez, A. F.; Ferreiro, E. G.; Ferretti, A.; Ferretti, R.; Figueredo, M. A. S.; Filchagin, S.; Fini, R.; Fionda, F. M.; Fiore, E. M.; Floris, M.; Fodor, Z.; Foertsch, S.; Foka, P.; Fokin, S.; Formenti, F.; Fragiacomo, E.; Fragkiadakis, M.; Frankenfeld, U.; Frolov, A.; Fuchs, U.; Furano, F.; Furget, C.; Girard, M. F.; Gaardhoje, J. J.; Gadrat, S.; Gagliardi, M.; Gago, A.; Gallio, M.; Ganoti, P.; Ganti, M. S.; Garabatos, C. ; Trapaga, C. G.; Gebelein, J.; Gemme, R.; Germain, M.; Gheata, A.; Gheata, M.; Ghidini, B.; Ghosh, P.; Giraudo, G.; Giubellino, P.; Gladysz-Dziadus, E.; Glasow, R.; Glassel, P.; Glenn, A.; Jimenez, R. G.; Santos, H. G.; Gonzalez-Trueba, L. H.; Gonzalez-Zamora, P.; Gorbunov, S.; Gorbunov, Y.; Gotovac, S.; Gottschlag, H.; Grabski, V.; Grajcarek, R.; Grelli, A.; Grigoras, A.; Grigoras, C.; Grigoriev, V.; Grigoryan, A.; Grigoryan, S.; Grinyov, B.; Grion, N.; Gros, P.; Grosse-Oetringhaus, J. F.; Grossiord, J. Y.; Grosso, R.; Guber, F.; Guernane, R.; Guerra, C.; Guerzoni, B.; Gulbrandsen, K.; Gulkanyan, H.; Gunji, T.; Gupta, A.; Gupta, R.; Gustafsson, H. A.; Gutbrod, H.; Haaland, O.; Hadjidakis, C.; Haiduc, M.; Hamagaki, H.; Hamar, G.; Hamblen, J.; Han, B. H.; Harris, J. W.; Hartig, M.; Harutyunyan, A.; Hasch, D.; Hasegan, D.; Hatzifotiadou, D.; Hayrapetyan, A.; Heide, M.; Heinz, M.; Helstrup, H.; Herghelegiu, A.; Hernandez, C.; Corral, G. H.; Herrmann, N.; Hetland, K. F.; Hicks, B.; Hiei, A.; Hille, P. T.; Hippolyte, B.; Horaguchi, T.; Hori, Y.; Hristov, P.; Hrivnacova, I.; Hu, S.; Huang, M.; Huber, S.; Humanic, T. J.; Hutter, D.; Hwang, D. S.; Ichou, R.; Ilkaev, R.; Ilkiv, I.; Inaba, M.; Innocenti, P. G.; Ippolitov, M.; Irfan, M.; Ivan, C.; Ivanov, A.; Ivanov, M.; Ivanov, V.; Iwasaki, T.; Jacholkowski, A.; Jacobs, P.; Jancurova, L.; Jangal, S.; Janik, R.; Jena, C.; Jena, S.; Jirden, L.; Jones, G. T.; Jones, P. G.; Jovanovic, P.; Jung, H.; Jung, W.; Jusko, A.; Kaidalov, A. B.; Kalcher, S.; Kalinak, P.; Kalisky, M.; Kalliokoski, T.; Kalweit, A.; Kamal, A.; Kamermans, R.; Kanaki, K.; Kang, E.; Kang, J. H.; Kapitan, J.; Kaplin, V.; Kapusta, S.; Karavichev, O.; Karavicheva, T.; Karpechev, E.; Kazantsev, A.; Kebschull, U.; Keidel, R.; Khan, M. M.; Khan, S. A.; Khanzadeev, A.; Kharlov, Y.; Kikola, D.; Kileng, B.; Kim, D. J.; Kim, D. S.; Kim, D. W.; Kim, H. N.; Kim, J.; Kim, J. H.; Kim, J. S.; Kim, M.; Kim, M.; Kim, S. H.; Kim, S.; Kim, Y.; Kirsch, S.; Kisel, I.; Kiselev, S.; Kisiel, A.; Klay, J. L.; Klein, J.; Klein-Bosing, C.; Kliemant, M.; Klovning, A.; Kluge, A.; Knichel, M. L.; Kniege, S.; Koch, K.; Kolevatov, R.; Kolojvari, A.; Kondratiev, V.; Kondratyeva, N.; Konevskih, A.; Kornas, E.; Kour, R.; Kowalski, M.; Kox, S.; Kozlov, K.; Kral, J.; Kralik, I.; Kramer, F.; Kraus, I.; Kravcakova, A.; Krawutschke, T.; Krivda, M.; Krumbhorn, D.; Krus, M.; Kryshen, E.; Krzewicki, M.; Kucheriaev, Y.; Kuhn, C.; Kuijer, P. G.; Kumar, L.; Kumar, N.; Kupczak, R.; Kurashvili, P.; Kurepin, A.; Kurepin, A. N.; Kuryakin, A.; Kushpil, S.; Kushpil, V.; Kutouski, M.; Kvaerno, H.; Kweon, M. J.; Kwon, Y.; La Rocca, P.; Lackner, F.; de Guevara, P. L.; Lafage, V.; Lal, C.; Lara, C.; Larsen, D. T.; Laurenti, G.; Lazzeroni, C.; Le Bornec, Y.; Le Bris, N.; Lee, H.; Lee, K. S.; Lee, S. C.; Lefevre, F.; Lenhardt, M.; Leistam, L.; Lehnert, J.; Lenti, V.; Leon, H.; Monzon, I. L.; Vargas, H. L.; Levai, P.; Li, X.; Li, Y.; Lietava, R.; Lindal, S.; Lindenstruth, V.; Lippmann, C. ; Lisa, M. A.; Liu, L.; Loginov, V.; Lohn, S.; Lopez, X.; Noriega, M. L.; Lopez-Ramirez, R.; Torres, E. L.; Lovhoiden, G.; Soares, A. L. F.; Lu, S.; Lunardon, M.; Luparello, G.; Luquin, L.; Lutz, J. R.; Ma, K.; Ma, R.; Madagodahettige-Don, D. M.; Maevskaya, A.; Mager, M.; Mahapatra, D. P.; Maire, A.; Makhlyueva, I.; Mal'Kevich, D.; Malaev, M.; Malagalage, K. J.; Cervantes, I. M.; Malek, M.; Malinina, L.; Malkiewicz, T.; Malzacher, P.; Mamonov, A.; Manceau, L.; Mangotra, L.; Manko, V.; Manso, F.; Manzari, V.; Mao, Y.; Mares, J.; Margagliotti, G. V.; Margotti, A.; Marin, A.; Martashvili, I.; Martinengo, P.; Hernandez, M. I. M.; Davalos, A. M.; Garcia, G. M.; Maruyama, Y.; Chiesa, A. M.; Masciocchi, S.; Masera, M.; Masetti, M.; Masoni, A.; Massacrier, L.; Mastromarco, M.; Mastroserio, A.; Matthews, Z. L.; Matyja, A.; Mayani, D.; Mazza, G.; Mazzoni, M. A.; Meddi, F.; Menchaca-Rocha, A.; Lorenzo, P. M.; Meoni, M.; Perez, J. M.; Mereu, P.; Miake, Y.; Michalon, A.; Miftakhov, N.; Milano, L.; Milosevic, J.; Minafra, F.; Mischke, A.; Miskowiec, D.; Mitu, C.; Mizoguchi, K.; Mlynarz, J.; Mohanty, B.; Molnar, L.; Mondal, M. M.; Zetina, L. M.; Monteno, M.; Montes, E.; Morando, M.; Moretto, S.; Morsch, A.; Moukhanova, T.; Muccifora, V.; Mudnic, E.; Muhuri, S.; Muller, H.; Munhoz, M. G.; Munoz, J.; Musa, L.; Musso, A.; Nandi, B. K.; Nania, R.; Nappi, E.; Navach, F.; Navin, S.; Nayak, T. K.; Nazarenko, S.; Nazarov, G.; Nedosekin, A.; Nendaz, F.; Newby, J.; Nianine, A.; Nicassio, M.; Nielsen, B. S.; Nikolaev, S.; Nikolic, V.; Nikulin, S.; Nikulin, V.; Nilsen, B. S.; Nilsson, M. S.; Noferini, F.; Nomokonov, P.; Nooren, G.; Novitzky, N.; Nyatha, A.; Nygaard, C.; Nyiri, A.; Nystrand, J.; Ochirov, A.; Odyniec, G.; Oeschler, H.; Oinonen, M.; Okada, K.; Okada, Y.; Oldenburg, M.; Oleniacz, J.; Oppedisano,

C.; Orsini, F.; Velasquez, A. O.; Ortona, G.; Oskarsson, A.; Osmic, F.; Osterman, L.; Ostrowski, P.; Otterlund, I.; Otwinowski, J.; Ovrebekk, G.; Oyama, K.; Ozawa, K.; Pachmayer, Y.; Pachr, M.; Padilla, F.; Pagano, P.; Paic, G.; Painke, F.; Pajares, C.; Pal, S.; Pal, S. K.; Palaha, A.; Palmeri, A.; Panse, R.; Papikyan, V.; Pappalardo, G. S.; Park, W. J.; Pastircak, B.; Pastore, C.; Paticchio, V.; Pavlinov, A.; Pawlak, T.; Peitzmann, T.; Pepato, A.; Pereira, H.; Peressounko, D.; Perez, C.; Perini, D.; Perrino, D.; Peryt, W.; Peschek, J.; Pesci, A.; Peskov, V.; Pestov, Y.; Peters, A. J.; Petracek, V.; Petridis, A.; Petris, M.; Petrov, P.; Petrovici, M.; Petta, C.; Peyre, J.; Piano, S.; Piccotti, A.; Pikna, M.; Pillot, P.; Pinazza, O.; Pinsky, L.; Pitz, N.; Piuz, F.; Platt, R.; Ploskon, M.; Pluta, J.; Pocheptsov, T.; Pochybova, S.; Lerma, P. L. M. P.; Poggio, F.; Poghosyan, M. G.; Polak, K.; Polichtchouk, B.; Polozov, P.; Polyakov, V.; Pommeresch, B.; Pop, A.; Posa, F.; Pospisil, V.; Potukuchi, B.; Pouthas, J.; Prasad, S. K.; Preghenella, R.; Prino, F.; Pruneau, C. A.; Pshenichnov, I.; Puddu, G.; Pujahari, P.; Pulvirenti, A.; Punin, A.; Punin, V.; Putis, M.; Putschke, J.; Quercigh, E.; Rachevski, A.; Rademakers, A.; Radomski, S.; Raiha, T. S.; Rak, J.; Rakotozafindrabe, A.; Ramello, L.; Reyes, A. R.; Rammler, M.; Raniwala, R.; Raniwala, S.; Rasanen, S. S.; Rashevskaya, I.; Rath, S.; Read, K. F.; Real, J. S.; Redlich, K.; Renfordt, R.; Reolon, A. R.; Reshetin, A.; Rettig, F.; Revol, J. P.; Reygers, K.; Ricaud, H.; Riccati, L.; Ricci, R. A.; Richter, M. ; Riedler, P.; Riegler, W.; Riggi, F.; Rivetti, A.; Cahuantzi, M. R.; Roed, K.; Rohrich, D.; Lopez, S. R.; Romita, R.; Ronchetti, F.; Rosinsky, P.; Rosnet, P.; Rossegger, S.; Rossi, A.; Roukoutakis, F.; Rousseau, S.; Roy, C.; Roy, P.; Rubio-Montero, A. J.; Rui, R.; Rusanov, I.; Russo, G.; Ryabinkin, E.; Rybicki, A.; Sadovsky, S.; Safarik, K.; Sahoo, R.; Saini, J.; Saiz, P.; Sakata, D.; Salgado, C. A.; da Silva, R. S. D.; Salur, S.; Samanta, T.; Sambyal, S.; Samsonov, V.; Sandor, L.; Sandoval, A.; Sano, M.; Sano, S.; Santo, R.; Santoro, R.; Sarkamo, J.; Saturnini, P.; Scapparone, E.; Scarlassara, F.; Scharenberg, R. P.; Schiaua, C.; Schicker, R.; Schindler, H.; Schmidt, C.; Schmidt, H. R.; Schossmaier, K.; Schreiner, S.; Schuchmann, S.; Schukraft, J.; Schutz, Y.; Schwarz, K.; Schweda, K.; Scioli, G.; Scomparin, E.; Scott, P. A.; Segato, G.; Semenov, D.; Senyukov, S.; Seo, J.; Serci, S.; Serkin, L.; Serradilla, E.; Sevcenco, A.; Sgura, I.; Shabratova, G.; Shahoyan, R.; Sharkov, G.; Sharma, N.; Sharma, S.; Shigaki, K.; Shimomura, M.; Shtejer, K.; Sibiriak, Y.; Siciliano, M.; Sicking, E.; Siddi, E.; Siemiarczuk, T.; Silenzi, A.; Silvermyr, D.; Simili, E.; Simonetti, G.; Singaraju, R.; Singh, R.; Singhal, V.; Sinha, B. C.; Sinha, T.; Sitar, B.; Sitta, M.; Skaali, T. B.; Skjerdal, K.; Smakal, R.; Smirnov, N.; Snellings, R.; Snow, H.; Sogaard, C.; Soloviev, A.; Soltveit, H. K.; Soltz, R.; Sommer, W.; Son, C. W.; Son, H.; Song, M.; Soos, C.; Soramel, F.; Soyk, D.; Spyropoulou-Stassinaki, M.; Srivastava, B. K.; Stachel, J.; Staley, F.; Stan, E.; Stefanek, G.; Stefanini, G.; Steinbeck, T.; Stenlund, E.; Steyn, G.; Stocco, D.; Stock, R.; Stolpovsky, P.; Strmen, P.; Suaide, A. A. P.; Vasquez, M. A. S.; Sugitate, T.; Suire, C.; Sumbera, M.; Susa, T.; Swoboda, D.; Symons, J.; de Toledo, A. S.; Szarka, I.; Szostak, A.; Szuba, M.; Tadel, M.; Tagridis, C.; Takahara, A.; Takahashi, J.; Tanabe, R.; Takaki, J. D. T.; Taureg, H.; Tauro, A.; Tavlet, M.; Munoz, G. T.; Telesca, A.; Terrevoli, C.; Thader, J.; Tieulent, R.; Tlusty, D.; Toia, A.; Tolyhy, T.; de Matos, C. T.; Torii, H.; Torralba, G.; Toscano, L.; Tosello, F.; Tournaire, A.; Traczyk, T.; Tribedy, P.; Troger, G.; Truesdale, D.; Trzaska, W. H.; Tsiledakis, G.; Tsilis, E.; Tsuji, T.; Tumkin, A.; Turrisi, R.; Turvey, A.; Tveter, T. S.; Tydesjo, H.; Tywoniuk, K.; Ulery, J.; Ullaland, K.; Uras, A.; Urban, J.; Urciuoli, G. M.; Usai, G. L.; Vacchi, A.; Vala, M.; Palomo, L. V.; Vallero, S.; van der Kolk, N.; Vande Vyvre, P.; van Leeuwen, M.; Vannucci, L.; Vargas, A.; Varma, R.; Vasiliev, A.; Vassiliev, I.; Vasileiou, M.; Vechernin, V.; Venaruzzo, M.; Vercellin, E.; Vergara, S.; Vernet, R.; Verweij, M.; Vetlitskiy, I.; Vickovic, L.; Viesti, G.; Vikhlyantsev, O.; Vilakazi, Z.; Baillie, O. V.; Vinogradov, A.; Vinogradov, L.; Vinogradov, Y.; Virgili, T.; Viyogi, Y. P.; Vodopianov, A.; Voloshin, K.; Voloshin, S.; Volpe, G.; von Haller, B.; Vranic, D.; Vrlakova, J.; Vulpescu, B.; Wagner, B.; Wagner, V.; Wallet, L.; Wan, R.; Wang, D.; Wang, Y.; Wang, Y.; Watanabe, K.; Wen, Q.; Wessels, J.; Westerhoff, U.; Wiechula, J.; Wikne, J.; Wilk, A.; Wilk, G.; Williams, M. C. S.; Willis, N.; Windelband, B.; Xu, C.; Yang, C.; Yang, H.; Yasnopolskiy, S.; Yermia, F.; Yi, J.; Yin, Z.; Yokoyama, H.; Yoo, I. K.; Yuan, X.; Yurevich, V.; Yushmanov, I.; Zabrodin, E.; Zagreev, B.; Zalite, A.; Zampolli, C.; Zanevsky, Y.; Zaporozhets, S.; Zarochentsev, A.; Zavada, P.; Zbroszczyk, H.; Zelnicek, P.; Zenin, A.; Zepeda, A.; Zgura, I.; Zhalov, M.; Zhang, X.; Zhou, D.; Zhou, S.; Zhu, J.; Zichichi, A.; Zinchenko, A.; Zinovjev, G.; Zoccarato, Y.; Zychacek, V.; Zynovyev, M.; Alice Collaboration: **Two-pion Bose-Einstein correlations in pp collisions at root s900 GeV.** *Physical Review D, particles, fields, gravitation, and cosmology* **82**(5): 052001, 2010. DOI:10.1103/physrevd.82.052001

004 Aamodt, K.; Abel, N.; Abeysekara, U.; Quintana, A. A.; Abramyan, A.; Adamova, D.; Aggarwal, M. M.; Rinella, G. A.; Agocs, A. G.; Salazar, S. A.; Ahammed, Z.; Ahmad, A.; Ahmad, N.; Ahn, S. U.; Akimoto, R.; Akindinov, A.; Aleksandrov, D.; Alessandro, B.; Molina, R. A.; Alici, A.; Avina, E. A.; Alme, J.; Alt, T.; Altini, V.; Altinpinar, S.; Andrei, C.; Andronic, A. ; Anelli, G.; Angelov, V.; Anson, C.; Anticic, T.; Antinori, F.; Antinori, S.; Antipin, K.; Antonczyk, D.; Antonioli, P.; Anzo, A.; Aphecetche, L.; Appelshauser, S. A.; Arcelli, S.; Arceo, R.; Arend, A.; Armesto, N.; Arnaldi, R.; Aronsson, T.; Arsene, I. C.; Asryan, A.; Augustinus, A.; Averbeck, R.; Awes, T. C.; Aysto, J.; Azmi, M. D.; Andronic, A. ; Bablok, S.; Bach, M.; Badala, A.; Baek, Y. W.; Bagnasco, S.; Bailhache, R.; Bala, R.; Baldisser, A.; Baldit, A.; Ban, J.; Barbera, R.; Barnafoldi, G. G.; Barnby, L. S.; Barret, V.; Bartke, J.; Barile, F.; Basile, M.; Basmanov, V.; Bastid, N.; Bathen, B.; Batigne, G.; Batyunya, B.; Baumann, C.; Bearden, I. G.; Becker, B.; Belikov, I.; Bellwied, R.; Belmont-Moreno, E.; Belogianni, A.; Benhabib,

L.; Beole, S.; Berceanu, I.; Bercuci, A.; Berdermann, E. ; Berdnikov, Y.; Betev, L.; Bhasin, A.; Bhati, A. K.; Bianchi, L.; Bianchi, N.; Bianchin, C.; Bielcik, J.; Bielcikova, J.; Bilandzic, A.; Bimbot, L.; Biolcati, E.; Blanc, A.; Blanco, F.; Blanco, F.; Blau, D.; Blume, C.; Boccioli, M.; Bock, N.; Bogdanov, A.; Boggild, H.; Bogolyubsky, M.; Bohm, J.; Boldizsar, L.; Bombara, M.; Bombonati, C.; Bondila, M.; Borel, H.; Borisov, A.; Bortolin, C.; Bose, S.; Bosisio, L.; Bossu, F.; Botje, M.; Bottger, S.; Bourdaud, G.; Boyer, B.; Braun, M.; Braun-Munzinger, P.; Bravina, L.; Bregant, M.; Breitner, T.; Bruckner, G.; Brun, R.; Bruna, E.; Bruno, G. E.; Budnikov, D.; Buesching, H.; Buncic, P.; Busch, O. ; Buthelezi, Z.; Caffarri, D.; Cai, X.; Caines, H.; Calvo, E.; Camacho, E.; Camerini, P.; Campbell, M.; Roman, V. C.; Capitani, G. P.; Romeo, G. C.; Carena, F.; Carena, W.; Carminati, F.; Diaz, A. C.; Caselle, M.; Castellanos, J. C.; Hernandez, J. F. C.; Catanescu, V.; Cattaruzza, E.; Cavicchioli, C.; Cerello, P.; Chambert, V.; Chang, B.; Chapeland, S.; Charpy, A.; Charvet, J. L.; Chattopadhyay, S.; Chattopadhyay, S.; Cherney, M.; Cheshkov, C.; Cheynis, B.; Chiavassa, E.; Barroso, V. C.; Chinellato, D. D.; Chochula, P.; Choi, K.; Chojnacki, M.; Christakoglou, P.; Christensen, C. H.; Christiansen, P.; Chujo, T.; Chuman, F.; Cicalo, C.; Cifarelli, L.; Cindolo, F.; Cleymans, J.; Cobanoglu, O.; Coffin, J. P.; Coli, S.; Colla, A.; Balbastre, G. C.; del Valle, Z. C.; Conner, E. S.; Constantin, P.; Contin, G.; Contreras, J. G.; Morales, Y. C.; Cormier, T. M.; Cortese, P.; Maldonado, I. C.; Cosentino, M. R.; Costa, F.; Cotallo, M. E.; Crescio, E.; Crochet, P.; Cuautle, E.; Cunqueiro, L.; Cussonneau, J.; Dainese, A.; Dalsgaard, H. H.; Danu, A.; Das, I.; Dash, A.; Dash, S.; de Barros, G. O. V.; de Caro, A.; de Cataldo, G.; de Cuveland, J.; De Falco, A.; De Gaspari, M.; de Groot, J.; De Gruttola, D.; De Marco, N.; De Pasquale, S.; De Remigis, R.; de Rooij, R.; de Vaux, G.; Delagrange, H.; Delgado, Y.; Dellacasa, G.; Deloff, A.; Demanov, V.; Denes, E.; Deppman, A.; D'Erasmo, G.; Derkach, D.; Devaux, A.; Di Bari, D.; Di Giglio, C.; Di Liberto, S.; Di Mauro, A.; Di Nezza, P.; Dialinas, M.; Diaz, L.; Diaz, R.; Dietel, T.; Divia, R.; Djuvsland, O.; Dobretsov, V.; Dobrin, A.; Dobrowolski, T.; Donigus, B.; Dominguez, I.; Don, D. M. M.; Dordic, O.; Dubey, A. K.; Dubuisson, J.; Ducroux, L.; Dupieux, P.; Majumdar, A. K. D.; Majumdar, M. R. D.; Elia, D.; Emschermann, D.; Enokizono, A.; Espagnon, B.; Estienne, M.; Esumi, S.; Evans, D.; Evrard, S.; Eyyubova, G.; Fabjan, C. W.; Fabris, D.; Faivre, J.; Falchieri, D.; Fantoni, A.; Fasel, M.; Fateev, O.; Fearick, R.; Fedunov, A.; Fehlker, D.; Fekete, V.; Felea, D.; Fenton-Olsen, B.; Feofilov, G.; Tellez, A. F.; Ferreiro, E. G.; Ferretti, A.; Ferretti, R.; Figueredo, M. A. S.; Filchagin, S.; Fini, R.; Fionda, F. M.; Fiore, E. M.; Floris, M.; Fodor, Z.; Foertsch, S.; Foka, P.; Fokin, S.; Formenti, F.; Fragiacomo, E.; Fragkiadakis, M.; Frankenfeld, U.; Frolov, A.; Fuchs, U.; Furano, F.; Furget, C.; Girard, M. F.; Gaardhoje, J. J.; Gadrat, S.; Gagliardi, M.; Gago, A.; Gallio, M.; Ganoti, P.; Ganti, M. S.; Garabatos, C. ; Trapaga, C. G.; Gebelein, J.; Gemme, R.; Germain, M.; Gheata, A.; Gheata, M.; Ghidini, B.; Ghosh, P.; Giraudo, G.; Giubellino, P.; Gladysz-Dziadus, E.; Glasow, R.; Glassel, P.; Glenn, A.; Jimenez, R. G.; Santos, H. G.; Gonzalez-Trueba, L. H.; Gonzalez-Zamora, P.; Gorbunov, S.; Gorbunov, Y.; Gotovac, S.; Gottschlag, H.; Grabski, V.; Grajcarek, R.; Grelli, A.; Grigoras, A.; Grigoras, C.; Grigoriev, V.; Grigoryan, A.; Grigoryan, S.; Grinyov, B.; Grion, N.; Gros, P.; Grosse-Oetringhaus, J. F.; Grossiord, J. Y.; Grosso, R.; Guber, F.; Guernane, R.; Guerra, C.; Guerzoni, B.; Gulbrandsen, K.; Gulkanyan, H.; Gunji, T.; Gupta, A.; Gupta, R.; Gustafsson, H. A.; Gutbrod, H.; Haaland, O.; Hadjidakis, C.; Haiduc, M.; Hamagaki, H.; Hamar, G.; Hamblen, J.; Han, B. H.; Harris, J. W.; Hartig, M.; Harutyunyan, A.; Hasch, D.; Hasegan, D.; Hatzifotiadou, D.; Hayrapetyan, A.; Heide, M.; Heinz, M.; Helstrup, H.; Herghelegiu, A.; Hernandez, C.; Corral, G. H.; Herrmann, N.; Hetland, K. F.; Hicks, B.; Hiei, A.; Hille, P. T.; Hippolyte, B.; Horaguchi, T.; Hori, Y.; Hristov, P.; Hrivnacova, I.; Hu, S.; Huang, M.; Huber, S.; Humanic, T. J.; Hutter, D.; Hwang, D. S.; Ichou, R.; Ilkaev, R.; Ilkiv, I.; Inaba, M.; Innocenti, P. G.; Ippolitov, M.; Irfan, M.; Ivan, C.; Ivanov, A.; Ivanov, M.; Ivanov, V.; Iwasaki, T.; Jacholkowski, A.; Jacobs, P.; Jancurova, L.; Jangal, S.; Janik, R.; Jena, C.; Jena, S.; Jirden, L.; Jones, G. T.; Jones, P. G.; Jovanovic, P.; Jung, H.; Jung, W.; Jusko, A.; Kaidalov, A. B.; Kalcher, S.; Kalinak, P.; Kalisky, M.; Kalliokoski, T.; Kalweit, A.; Kamal, A.; Kamermans, R.; Kanaki, K.; Kang, E.; Kang, J. H.; Kapitan, J.; Kaplin, V.; Kapusta, S.; Karavichev, O.; Karavicheva, T.; Karpechev, E.; Kazantsev, A.; Kebschull, U.; Keidel, R.; Khan, M. M.; Khan, S. A.; Khanzadeev, A.; Kharlov, Y.; Kikola, D.; Kileng, B.; Kim, D. J.; Kim, D. S.; Kim, D. W.; Kim, H. N.; Kim, J.; Kim, J. H.; Kim, J. S.; Kim, M.; Kim, M.; Kim, S. H.; Kim, S.; Kim, Y.; Kirsch, S.; Kisel, I.; Kiselev, S.; Kisiel, A.; Klay, J. L.; Klein, J.; Klein-Bosing, C.; Kliemant, M.; Klovning, A.; Kluge, A.; Knichel, M. L.; Kniege, S.; Koch, K.; Kolevatov, R.; Kolojvari, A.; Kondratiev, V.; Kondratyeva, N.; Konevskih, A.; Kornas, E.; Kour, R.; Kowalski, M.; Kox, S.; Kozlov, K.; Kral, J.; Kralik, I.; Kramer, F.; Kraus, I.; Kravcakova, A.; Krawutschke, T.; Krivda, M.; Krumbhorn, D.; Krus, M.; Kryshen, E.; Krzewicki, M.; Kucheriaev, Y.; Kuhn, C.; Kuijer, P. G.; Kumar, L.; Kumar, N.; Kupczak, R.; Kurashvili, P.; Kurepin, A.; Kurepin, A. N.; Kuryakin, A.; Kushpil, S.; Kushpil, V.; Kutouski, M.; Kvaerno, H.; Kweon, M. J.; Kwon, Y.; La Rocca, P.; Lackner, F.; de Guevara, P. L.; Lafage, V.; Lal, C.; Lara, C.; Larsen, D. T.; Laurenti, G.; Lazzeroni, C.; Le Bornec, Y.; Le Bris, N.; Lee, H.; Lee, K. S.; Lee, S. C.; Lefevre, F.; Lenhardt, M.; Leistam, L.; Lehnert, J.; Lenti, V.; Leon, H.; Monzon, I. L.; Vargas, H. L.; Levai, P.; Li, X.; Li, Y.; Lietava, R.; Lindal, S.; Lindenstruth, V.; Lippmann, C. ; Lisa, M. A.; Liu, L.; Loginov, V.; Lohn, S.; Lopez, X.; Noriega, M. L.; Lopez-Ramirez, R.; Torres, E. L.; Lovhoiden, G.; Soares, A. L. F.; Lu, S.; Lunardon, M.; Luparello, G.; Luquin, L.; Lutz, J. R.; Ma, K.; Ma, R.; Madagodahettige-Don, D. M.; Maevskaya, A.; Mager, M.; Mahapatra, D. P.; Maire, A.; Makhlyueva, I.; Mal'Kevich, D.; Malaev, M.; Malagalage, K. J.; Cervantes, I. M.; Malek, M.; Malkiewicz, T.;

Malzacher, P.; Mamonov, A.; Manceau, L.; Mangotra, L.; Manko, V.; Manso, F.; Manzari, V.; Mao, Y.; Mares, J.; Margagliotti, G. V.; Margotti, A.; Marin, A.; Martashvili, I.; Martinengo, P.; Hernandez, M. I. M.; Davalos, A. M.; Garcia, G. M.; Maruyama, Y.; Chiesa, A. M.; Masciocchi, S.; Masera, M.; Masetti, M.; Masoni, A.; Massacrier, L.; Mastromarco, M.; Mastroserio, A.; Matthews, Z. L.; Matyja, A.; Mayani, D.; Mazza, G.; Mazzoni, M. A.; Meddi, F.; Menchaca-Rocha, A.; Lorenzo, P. M.; Meoni, M.; Perez, J. M.; Mereu, P.; Miake, Y.; Michalon, A.; Miftakhov, N.; Milano, L.; Milosevic, J.; Minafra, F.; Mischke, A.; Miskowiec, D.; Mitu, C.; Mizoguchi, K.; Mlynarz, J.; Mohanty, B.; Molnar, L.; Mondal, M. M.; Zetina, L. M.; Monteno, M.; Montes, E.; Morando, M.; Moretto, S.; Morsch, A.; Moukhanova, T.; Muccifora, V.; Mudnic, E.; Muhuri, S.; Mueller, H.; Munhoz, M. G.; Munoz, J.; Musa, L.; Musso, A.; Nandi, B. K.; Nania, R.; Nappi, E.; Navach, F.; Navin, S.; Nayak, T. K.; Nazarenko, S.; Nazarov, G.; Nedosekin, A.; Nendaz, F.; Newby, J.; Nianine, A.; Nicassio, M.; Nielsen, B. S.; Nikolaev, S.; Nikolic, V.; Nikulin, S.; Nikulin, V.; Nilsen, B. S.; Nilsson, M. S.; Noferini, F.; Nomokonov, P.; Nooren, G.; Novitzky, N.; Nyatha, A.; Nygaard, C.; Nyiri, A.; Nystrand, J.; Ochirov, A.; Odyniec, G.; Oeschler, H.; Oinonen, M.; Okada, K.; Okada, Y.; Oldenburg, M.; Oleniacz, J.; Oppedisano, C.; Orsini, F.; Velasquez, A. O.; Ortona, G.; Oskarsson, A.; Osmic, F.; Osterman, L.; Ostrowski, P.; Otterlund, I.; Otwinowski, J.; Ovrebekk, G.; Oyama, K.; Ozawa, K.; Pachmayer, Y.; Pachr, M.; Padilla, F.; Pagano, P.; Paic, G.; Painke, F.; Pajares, C.; Pal, S.; Pal, S. K.; Palaha, A.; Palmeri, A.; Panse, R.; Papikyan, V.; Pappalardo, G. S.; Park, W. J.; Pastircak, B.; Pastore, C.; Paticchio, V.; Pavlinov, A.; Pawlak, T.; Peitzmann, T.; Pepato, A.; Pereira, H.; Peressounko, D.; Perez, C.; Perini, D.; Perrino, D.; Peryt, W.; Peschek, J.; Pesci, A.; Peskov, V.; Pestov, Y.; Peters, A. J.; Petracek, V.; Petridis, A.; Petris, M.; Petrov, P.; Petrovici, M.; Petta, C.; Peyre, J.; Piano, S.; Piccotti, A.; Pikna, M.; Pillot, P.; Pinazza, O.; Pinsky, L.; Pitz, N.; Piuz, F.; Platt, R.; Ploskon, M.; Pluta, J.; Pocheptsov, T.; Pochybova, S.; Lerma, P. L. M. P.; Poggio, F.; Poghosyan, M. G.; Polak, K.; Polichtchouk, B.; Polozov, P.; Polyakov, V.; Pommeresch, B.; Pop, A.; Posa, F.; Pospisil, V.; Potukuchi, B.; Pouthas, J.; Prasad, S. K.; Preghenella, R.; Prino, F.; Pruneau, C. A.; Pshenichnov, I.; Puddu, G.; Pujahari, P.; Pulvirenti, A.; Punin, A.; Punin, V.; Putis, M.; Putschke, J.; Quercigh, E.; Rachevski, A.; Rademakers, A.; Radomski, S.; Raiha, T. S.; Rak, J.; Rakotozafindrabe, A.; Ramello, L.; Reyes, A. R.; Rammler, M.; Raniwala, R.; Raniwala, S.; Rasanen, S. S.; Rashevskaya, I.; Rath, S.; Read, K. F.; Real, J. S.; Redlich, K.; Renfordt, R.; Reolon, A. R.; Reshetin, A.; Rettig, F.; Revol, J. P.; Reygers, K.; Ricaud, H.; Riccati, L.; Ricci, R. A.; Richter, M. ; Riedler, P.; Riegler, W.; Riggi, F.; Rivetti, A.; Cahuantzi, M. R.; Roed, K.; Rohrich, D.; Lopez, S. R.; Romita, R.; Ronchetti, F.; Rosinsky, P.; Rosnet, P.; Rossegger, S.; Rossi, A.; Roukoutakis, F.; Rousseau, S.; Roy, C.; Roy, P.; Rubio-Montero, A. J.; Rui, R.; Rusanov, I.; Russo, G.; Ryabinkin, E.; Rybicki, A.; Sadovsky, S.; Safarik, K.; Sahoo, R.; Saini, J.; Saiz, P.; Sakata, D.; Salgado, C. A.; da Silva, R. S. D.; Salur, S.; Samanta, T.; Sambyal, S.; Samsonov, V.; Sandor, L.; Sandoval, A.; Sano, M.; Sano, S.; Santo, R.; Santoro, R.; Sarkamo, J.; Saturnini, P.; Scapparone, E.; Scarlassara, F.; Scharenberg, R. P.; Schiaua, C.; Schicker, R.; Schindler, H.; Schmidt, C.; Schmidt, H. R.; Schossmaier, K.; Schreiner, S.; Schuchmann, S.; Schukraft, J.; Schutz, Y.; Schwarz, K.; Schweda, K.; Scioli, G.; Scomparin, E.; Scott, P. A.; Segato, G.; Semenov, D.; Senyukov, S.; Seo, J.; Serci, S.; Serkin, L.; Serradilla, E.; Sevcenco, A.; Sgura, I.; Shabratova, G.; Shahoyan, R.; Sharkov, G.; Sharma, N.; Sharma, S.; Shigaki, K.; Shimomura, M.; Shtejer, K.; Sibiriak, Y.; Siciliano, M.; Sicking, E.; Siddi, E.; Siemiarczuk, T.; Silenzi, A.; Silvermyr, D.; Simili, E.; Simonetti, G.; Singaraju, R.; Singh, R.; Singhal, V.; Sinha, B. C.; Sinha, T.; Sitar, B.; Skaali, T. B.; Sitta, M.; Skjerdal, K.; Smakal, R.; Smirnov, N.; Snellings, R.; Snow, H.; Sogaard, C.; Soloviev, A.; Soltveit, H. K.; Soltz, R.; Sommer, W.; Son, C. W.; Son, H.; Song, M.; Soos, C.; Soramel, F.; Soyk, D.; Spyropoulou-Stassinaki, M.; Srivastava, B. K.; Stachel, J.; Staley, F.; Stan, E.; Stefanek, G.; Stefanini, G.; Steinbeck, T.; Stenlund, E.; Steyn, G.; Stocco, D.; Stock, R.; Stolpovsky, P.; Strmen, P.; Suaide, A. A. P.; Vasquez, M. A. S.; Sugitate, T.; Suire, C.; Sumbera, M.; Susa, T.; Swoboda, D.; Symons, J.; de Toledo, A. S.; Szarka, I.; Szostak, A.; Szuba, M.; Tadel, M.; Tagridis, C.; Takahara, A.; Takahashi, J.; Tanabe, R.; Takaki, J. D. T.; Taureg, H.; Tauro, A.; Tavlet, M.; Munoz, G. T.; Telesca, A.; Terrevoli, C.; Thader, J.; Tieulent, R.; Tlusty, D.; Toia, A.; Tolyhy, T.; de Matos, C. T.; Torii, H.; Torralba, G.; Toscano, L.; Tosello, F.; Tournaire, A.; Traczyk, T.; Tribedy, P.; Troger, G.; Truesdale, D.; Trzaska, W. H.; Tsiledakis, G.; Tsilis, E.; Tsuji, T.; Tumkin, A.; Turrisi, R.; Turvey, A.; Tveter, T. S.; Tydesjo, H.; Tywoniuk, K.; Ulery, J.; Ullaland, K.; Uras, A.; Urban, J.; Urciuoli, G. M.; Usai, G. L.; Vacchi, A.; Vala, M.; Palomo, L. V.; Vallero, S.; van der Kolk, N.; Vyvre, P. V.; van Leeuwen, M.; Vannucci, L.; Vargas, A.; Varma, R.; Vasiliev, A.; Vassiliev, I.; Vasileiou, M.; Vechernin, V.; Venaruzzo, M.; Vercellin, E.; Vergara, S.; Vernet, R.; Verweij, M.; Vetlitskiy, I.; Vickovic, L.; Viesti, G.; Vikhlyantsev, O.; Vilakazi, Z.; Baillie, O. V.; Vinogradov, A.; Vinogradov, L.; Vinogradov, Y.; Virgili, T.; Viyogi, Y. P.; Vodopianov, A.; Voloshin, K.; Voloshin, S.; Volpe, G.; von Haller, B.; Vranic, D.; Vrlakova, J.; Vulpescu, B.; Wagner, B.; Wagner, V.; Wallet, L.; Wan, R.; Wang, D.; Wang, Y.; Wang, Y.; Watanabe, K.; Wen, Q.; Wessels, J.; Westerhoff, U.; Wiechula, J.; Wikne, J.; Wilk, A.; Wilk, G.; Williams, M. C. S.; Willis, N.; Windelband, B.; Xu, C.; Yang, C.; Yang, H.; Yasnopolskiy, S.; Yermia, F.; Yi, J.; Yin, Z.; Yokoyama, H.; Yoo, I. K.; Yuan, X.; Yurevich, V.; Yushmanov, I.; Zabrodin, E.; Zagreev, B.; Zalite, A.; Zampolli, C.; Zanevsky, Y.; Zaporozhets, S.; Zarochentsev, A.; Zavada, P.; Zbroszczyk, H.; Zelnicek, P.; Zenin, A.; Zepeda, A.; Zgura, I.; Zhalov, M.; Zhang, X.; Zhou, D.; Zhou, S.; Zhu, J.; Zichichi, A.; Zinchenko, A.; Zinovjev, G.; Zoccarato, Y.; Zychacek, V.; Zynovyev, M.; AL-

ICE Collaboration: **Midrapidity Antiproton-to-Proton Ratio in pp Collisons root s0.9 and 7 TeV Measured by the ALICE Experiment.** *Physical review letters* **105**(7): 072002, 2010. DOI:10.1103/physrevlett.105.072002

005 Aamodt, K.; Abel, N.; Abeysekara, U.; Quintana, A. A.; Abramyan, A.; Adamova, D.; Aggarwal, M. M.; Rinella, G. A.; Agocs, A. G.; Salazar, S. A.; Ahammed, Z.; Ahmad, A.; Ahmad, N.; Ahn, S. U.; Akimoto, R.; Akindinov, A.; Aleksandrov, D.; Alessandro, B.; Molina, R. A.; Alici, A.; Avina, E. A.; Alme, J.; Alt, T.; Altini, V.; Altinpinar, S.; Andrei, C.; Andronic, A. ; Anelli, G.; Angelov, V.; Anson, C.; Anticic, T.; Antinori, F.; Antinori, S.; Antipin, K.; Antonczyk, D.; Antonioli, P.; Anzo, A.; Aphecetche, L.; Appelshuser, H.; Arcelli, S.; Arceo, R.; Arend, A.; Armesto, N.; Arnaldi, R.; Aronsson, T.; Arsene, I.; Asryan, A.; Augustinus, A.; Averbeck, R.; Awes, T.; Aysto, J.; Azmi, M.; Bablok, S.; Bach, M.; Badala, A.; Baek, Y.; Bagnasco, S.; Bailhache, R.; Bala, R.; Baldisseri, A.; Baldit, A.; Ban, J.; Barbera, R.; Barnafoldi, G.; Barnby, L.; Barret, V.; Bartke, J.; Barile, F.; Basile, M.; Basmanov, V.; Bastid, N.; Bathen, B.; Batigne, G.; Batyunya, B.; Baumann, C.; Bearden, I.; Becker, B.; Belikov, I.; Bellwied, R.; Belmont-Moreno, E.; Belogianni, A.; Benhabib, L.; Beole, S.; Berceanu, I.; Bercuci, A.; Berdermann, E. ; Berdnikov, Y.; Betev, L.; Bhasin, A.; Bhati, A.; Bianchi, L.; Bianchi, N.; Bianchin, C.; Bielik, J.; Bielikova, J.; Bilandzic, A.; Bimbot, L.; Biolcati, E.; Blanc, A.; Blanco, F.; Blanco, F.; Blau, D.; Blume, C.; Boccioli, M.; Bock, N.; Bogdanov, A.; Boggild, H.; Bogolyubsky, M.; Bohm, J.; Boldizsar, L.; Bombara, M.; Bombonati, C.; Bondila, M.; Borel, H.; Borshchov, V.; Borisov, A.; Bortolin, C.; Bose, S.; Bosisio, L.; Bossu, F.; Botje, M.; Bottger, S.; Bourdaud, G.; Boyer, B.; Braun, M.; Braun-Munzinger, P.; Bravina, L.; Bregant, M.; Breitner, T.; Bruckner, G.; Brun, R.; Bruna, E.; Bruno, G.; Budnikov, D.; Buesching, H.; Buncic, P.; Busch, O. ; Buthelezi, Z.; Caffarri, D.; Cai, X.; Caines, H.; Camacho, E.; Camerini, P.; Campbell, M.; Canoa Roman, V.; Capitani, G.; Cara Romeo, G.; Carena, F.; Carena, W.; Carminati, F.; Diaz, A. C.; Caselle, M.; Castillo Castellanos, J.; Castillo Hernandez, J.; Catanescu, V.; Cattaruzza, E.; Cavicchioli, C.; Cerello, P.; Chambert, V.; Chang, B.; Chapeland, S.; Charpy, A.; Charvet, J.; Chattopadhyay, S.; Chattopadhyay, S.; Cherney, M.; Cheshkov, C.; Cheynis, B.; Chiavassa, E.; Chibante Barroso, V.; Chinellato, D.; Chochula, P.; Choi, K.; Chojnacki, M.; Christakoglou, P.; Christensen, C.; Christiansen, P.; Chujo, T.; Chuman, F.; Cicalo, C.; Cifarelli, L.; Cindolo, F.; Cleymans, J.; Cobanoglu, O.; Coffin, J. P.; Coli, S.; Colla, A.; Conesa Balbastre, G.; Conesa del Valle, Z.; Conner, E.; Constantin, P.; Contin, G.; Contreras, J.; Corrales Morales, Y.; Cormier, T.; Cortese, P.; Maldonado, I. C.; Cosentino, M.; Costa, F.; Cotallo, M.; Crescio, E.; Crochet, P.; Cuautle, E.; Cunqueiro, L.; Cussonneau, J.; Dainese, A.; Dalsgaard, H.; Danu, A.; Das, I.; Das, S.; Dash, A.; Dash, S.; de Barros, G. O. V.; De Caro, A.; de Cataldo, G.; de Cuveland, J.; De Falco, A.; De Gaspari, M.; de Groot, J.; De Gruttola, D.; De Marco, N.; De Pasquale, S.; De Remigis, R.; de Rooij, R.; de Vaux, G.; Delagrange, H.; Dellacasa, G.; Deloff, A.; Demanov, V.; Denes, E.; Deppman, A.; D'Erasmo, G.; Derkach, D.; Devaux, A.; Di Bari, D.; Di Giglio, C.; Di Liberto, S.; Di Mauro, A.; Di Nezza, P.; Dialinas, M.; Diaz, L.; Diaz, R.; Dietel, T.; Divia, R.; Djuvsland, O.; Dobretsov, V.; Dobrin, A.; Dobrowolski, T.; Donigus, B.; Dominguez, I.; Don, D.; Dordic, O.; Dubey, A.; Dubuisson, J.; Ducroux, L.; Dupieux, P.; Majumdar, A. K. D.; Majumdar, M. R. D.; Elia, D.; Emschermann, D.; Enokizono, A.; Espagnon, B.; Estienne, M.; Esumi, S.; Evans, D.; Evrard, S.; Eyyubova, G.; Fabjan, C.; Fabris, D.; Faivre, J.; Falchieri, D.; Fantoni, A.; Fasel, M.; Fateev, O.; Fearick, R.; Fedunov, A.; Fehlker, D.; Fekete, V.; Felea, D.; Fenton-Olsen, B.; Feofilov, G.; Tellez, A. F.; Ferreiro, E.; Ferretti, A.; Ferretti, R.; Figueredo, M. A. S.; Filchagin, S.; Fini, R.; Fionda, F.; Fiore, E.; Floris, M.; Fodor, Z.; Foertsch, S.; Foka, P.; Fokin, S.; Formenti, F.; Fragiacomo, E.; Fragkiadakis, M.; Frankenfeld, U.; Frolov, A.; Fuchs, U.; Furano, F.; Furget, C.; Girard, M. F.; Gaardhoje, J.; Gadrat, S.; Gagliardi, M.; Gago, A.; Gallio, M.; Ganoti, P.; Ganti, M.; Garabatos, C. ; Garcia Trapaga, C.; Gebelein, J.; Gemme, R.; Germain, M.; Gheata, A.; Gheata, M.; Ghidini, B.; Ghosh, P.; Giraudo, G.; Giubellino, P.; Gladysz-Dziadus, E.; Glasow, R.; Glassel, P.; Glenn, A.; Jimenez, R. G.; Santos, H. G.; Gonzalez-Trueba, L. H.; Gonzalez-Zamora, P.; Gorbunov, S.; Gorbunov, Y.; Gotovac, S.; Gottschlag, H.; Grabski, V.; Grajcarek, R.; Grelli, A.; Grigoras, A.; Grigoras, C.; Grigoriev, V.; Grigoryan, A.; Grigoryan, S.; Grinyov, B.; Grion, N.; Gros, P.; Grosse-Oetringhaus, J.; Grossiord, J. Y.; Grosso, R.; Guber, F.; Guernane, R.; Guerzoni, B.; Gulbrandsen, K.; Gulkanyan, H.; Gunji, T.; Gupta, A.; Gupta, R.; Gustafsson, H. A.; Gutbrod, H.; Haaland, O.; Hadjidakis, C.; Haiduc, M.; Hamagaki, H.; Hamar, G.; Hamblen, J.; Han, B.; Harris, J.; Hartig, M.; Harutyunyan, A.; Hasch, D.; Hasegan, D.; Hatzifotiadou, D.; Hayrapetyan, A.; Heide, M.; Heinz, M.; Helstrup, H.; Herghelegiu, A.; Hernandez, C.; Herrera Corral, G.; Hermann, N.; Hetland, K.; Hicks, B.; Hiei, A.; Hille, P.; Hippolyte, B.; Horaguchi, T.; Hori, Y.; Hristov, P.; Hrivnacova, I.; Hu, S.; Huang, M.; Huber, S.; Humanic, T.; Hutter, D.; Hwang, D.; Ichou, R.; Ilkaev, R.; Ilkiv, I.; Inaba, M.; Innocenti, P.; Ippolitov, M.; Irfan, M.; Ivan, C.; Ivanov, A.; Ivanov, M.; Ivanov, V.; Iwasaki, T.; Jachokowski, A.; Jacobs, P.; Janurova, L.; Jangal, S.; Janik, R.; Jena, C.; Jena, S.; Jirden, L.; Jones, G.; Jones, P.; Jovanovic, P.; Jung, H.; Jung, W.; Jusko, A.; Kaidalov, A.; Kalcher, S.; Kalinak, P.; Kalisky, M.; Kalliokoski, T.; Kalweit, A.; Kamal, A.; Kamermans, R.; Kanaki, K.; Kang, E.; Kang, J.; Kapitan, J.; Kaplin, V.; Kapusta, S.; Karavichev, O.; Karavicheva, T.; Karpechev, E.; Kazantsev, A.; Kebschull, U.; Keidel, R.; Khan, M.; Khan, S.; Khanzadeev, A.; Kharlov, Y.; Kikola, D.; Kileng, B.; Kim, D.; Kim, D.; Kim, D.; Kim, H.; Kim, J.; Kim, J.; Kim, J.; Kim, M.; Kim, M.; Kim, S.; Kim, S.; Kim, Y.; Kirsch, S.; Kisel, I.; Kiselev, S.; Kisiel, A.; Klay, J.; Klein, J.; Klein-Bosing, C.; Kliemant, M.; Klovning, A.; Kluge, A.; Kniege, S.; Koch, K.; Kole-

vatov, R.; Kolojvari, A.; Kondratiev, V.; Kondratyeva, N.; Konevskih, A.; Kornas, E.; Kour, R.; Kowalski, M.; Kox, S.; Kozlov, K.; Kral, J.; Kralik, I.; Kramer, F.; Kraus, I.; Kravakova, A.; Krawutschke, T.; Krivda, M.; Krumbhorn, D.; Krus, M.; Kryshen, E.; Krzewicki, M.; Kucheriaev, Y.; Kuhn, C.; Kuijer, P.; Kumar, L.; Kumar, N.; Kupczak, R.; Kurashvili, P.; Kurepin, A.; Kurepin, A.; Kuryakin, A.; Kushpil, S.; Kushpil, V.; Kutouski, M.; Kvaerno, H.; Kweon, M.; Kwon, Y.; Rocca, P.; Lackner, F.; de Guevara, P. L.; Lafage, V.; Lal, C.; Lara, C.; Larsen, D.; Laurenti, G.; Lazzeroni, C.; Bornec, Y.; Bris, N.; Lee, H.; Lee, K.; Lee, S.; Lefevre, F.; Lenhardt, M.; Leistam, L.; Lehnert, J.; Lenti, V.; Leon, H.; Monzon, I. L.; Vargas, H. L.; Levai, P.; Li, X.; Li, Y.; Lietava, R.; Lindal, S.; Lindenstruth, V.; Lippmann, C. ; Lisa, M.; Listratenko, O.; Liu, L.; Loginov, V.; Lohn, S.; Lopez, X.; Noriega, M. L.; Lopez-Ramirez, R.; Torres, E. L.; Lovhoiden, G.; Soares, A. L. F.; Lu, S.; Lunardon, M.; Luparello, G.; Luquin, L.; Lutz, J. R.; Ma, K.; Ma, R.; Madagodahettige-Don, D.; Maevskaya, A.; Mager, M.; Mahapatra, D.; Maire, A.; Makhlyueva, I.; Mal'Kevich, D.; Malaev, M.; Malagalage, K.; Maldonado Cervantes, I.; Malek, M.; Malkiewicz, T.; Malzacher, P.; Mamonov, A.; Manceau, L.; Mangotra, L.; Manko, V.; Manso, F.; Manzari, V.; Mao, Y.; Mare, J.; Margagliotti, G.; Margotti, A.; Marin, A.; Martashvili, I.; Martinengo, P.; Hernandez, M. I. M.; Davalos, A. M.; Garcia, G. M.; Maruyama, Y.; Chiesa, A. M.; Masciocchi, S.; Masera, M.; Masetti, M.; Masoni, A.; Massacrier, L.; Mastromarco, M.; Mastroserio, A.; Matthews, Z.; Matyja, A.; Mayani, D.; Mazza, G.; Mazzoni, M.; Meddi, F.; Menchaca-Rocha, A.; Lorenzo, P. M.; Meoni, M.; Perez, J. M.; Mereu, P.; Miake, Y.; Michalon, A.; Miftakhov, N.; Milosevic, J.; Minafra, F.; Mischke, A.; Miskowiec, D.; Mitu, C.; Mizoguchi, K.; Mlynarz, J.; Mohanty, B.; Molnar, L.; Mondal, M.; Montao Zetina, L.; Monteno, M.; Montes, E.; Morando, M.; Moretto, S.; Morsch, A.; Moukhanova, T.; Muccifora, V.; Mudnic, E.; Muhuri, S.; Muller, H.; Munhoz, M.; Munoz, J.; Musa, L.; Musso, A.; Nandi, B.; Nania, R.; Nappi, E.; Navach, F.; Navin, S.; Nayak, T.; Nazarenko, S.; Nazarov, G.; Nedosekin, A.; Nendaz, F.; Newby, J.; Nianine, A.; Nicassio, M.; Nielsen, B.; Nikolaev, S.; Nikolic, V.; Nikulin, S.; Nikulin, V.; Nilsen, B.; Nilsson, M.; Noferini, F.; Nomokonov, P.; Nooren, G.; Novitzky, N.; Nyatha, A.; Nygaard, C.; Nyiri, A.; Nystrand, J.; Ochirov, A.; Odyniec, G.; Oeschler, H.; Oinonen, M.; Okada, K.; Okada, Y.; Oldenburg, M.; Oleniacz, J.; Oppedisano, C.; Orsini, F.; Velasquez, A. O.; Ortona, G.; Oskarsson, A.; Osmic, F.; Osterman, L.; Ostrowski, P.; Otterlund, I.; Otwinowski, J.; Ovrebekk, G.; Oyama, K.; Ozawa, K.; Pachmayer, Y.; Pachr, M.; Padilla, F.; Pagano, P.; Paic, G.; Painke, F.; Pajares, C.; Pal, S.; Pal, S.; Palaha, A.; Palmeri, A.; Panse, R.; Papikyan, V.; Pappalardo, G.; Park, W.; Pastirak, B.; Pastore, C.; Paticchio, V.; Pavlinov, A.; Pawlak, T.; Peitzmann, T.; Pepato, A.; Pereira, H.; Peressounko, D.; Perez, C.; Perini, D.; Perrino, D.; Peryt, W.; Peschek, J.; Pesci, A.; Peskov, V.; Pestov, Y.; Peters, A.; Petracek, V.; Petridis, A.; Petris, M.; Petrov, P.; Petrovici, M.; Petta, C.; Peyre, J.; Piano, S.; Piccotti, A.; Pikna, M.; Pillot, P.; Pinazza, O.; Pinsky, L.; Pitz, N.; Piuz, F.; Platt, R.; Ploskon, M.; Pluta, J.; Pocheptsov, T.; Pochybova, S.; Lerma, P. L. M. P.; Poggio, F.; Poghosyan, M.; Polak, K.; Polichtchouk, B.; Polozov, P.; Polyakov, V.; Pommeresch, B.; Pop, A.; Posa, F.; Pospiil, V.; Potukuchi, B.; Pouthas, J.; Prasad, S.; Preghenella, R.; Prino, F.; Pruneau, C.; Pshenichnov, I.; Puddu, G.; Pujahari, P.; Pulvirenti, A.; Punin, A.; Punin, V.; Putis, M.; Putschke, J.; Quercigh, E.; Rachevski, A.; Rademakers, A.; Radomski, S.; Raiha, T.; Rak, J.; Rakotozafindrabe, A.; Ramello, L.; Ramirez Reyes, A.; Rammler, M.; Raniwala, R.; Raniwala, S.; Rasanen, S.; Rashevskaya, I.; Rath, S.; Read, K.; Real, J.; Redlich, K.; Renfordt, R.; Reolon, A.; Reshetin, A.; Rettig, F.; Revol, J. P.; Reygers, K.; Ricaud, H.; Riccati, L.; Ricci, R.; Richter, M. ; Riedler, P.; Riegler, W.; Riggi, F.; Rivetti, A.; Cahuantzi, M. R.; Roed, K.; Rohrich, D.; Lopez, S. R.; Romita, R.; Ronchetti, F.; Rosinsky, P.; Rosnet, P.; Rossegger, S.; Rossi, A.; Roukoutakis, F.; Rousseau, S.; Roy, C.; Roy, P.; Rubio-Montero, A.; Rui, R.; Rusanov, I.; Russo, G.; Ryabinkin, E.; Rybicki, A.; Sadovsky, S.; Safarik, K.; Sahoo, R.; Saini, J.; Saiz, P.; Sakata, D.; Salgado, C.; da Silva, R. S. D.; Salur, S.; Samanta, T.; Sambyal, S.; Samsonov, V.; Sandor, L.; Sandoval, A.; Sano, M.; Sano, S.; Santo, R.; Santoro, R.; Sarkamo, J.; Saturnini, P.; Scapparone, E.; Scarlassara, F.; Scharenberg, R. P.; Schiaua, C.; Schicker, R.; Schindler, H.; Schmidt, C.; Schmidt, H.; Schossmaier, K.; Schreiner, S.; Schuchmann, S.; Schukraft, J.; Schutz, Y.; Schwarz, K.; Schweda, K.; Scioli, G.; Scomparin, E.; Segato, G.; Semenov, D.; Senyukov, S.; Seo, J.; Serci, S.; Serkin, L.; Serradilla, E.; Sevcenco, A.; Sgura, I.; Shabratova, G.; Shahoyan, R.; Sharkov, G.; Sharma, N.; Sharma, S.; Shigaki, K.; Shimomura, M.; Shtejer, K.; Sibiriak, Y.; Siciliano, M.; Sicking, E.; Siddi, E.; Siemiarczuk, T.; Silenzi, A.; Silvermyr, D.; Simili, E.; Simonetti, G.; Singaraju, R.; Singh, R.; Singhal, V.; Sinha, B.; Sinha, T.; Sitar, B.; Sitta, M.; Skaali, T.; Skjerdal, K.; Smakal, R.; Smirnov, N.; Snellings, R.; Snow, H.; Sogaard, C.; Soloviev, A.; Soltveit, H.; Soltz, R.; Sommer, W.; Son, C.; Son, H.; Song, M.; Soos, C.; Soramel, F.; Soyk, D.; Spyropoulou-Stassinaki, M.; Srivastava, B.; Stachel, J.; Staley, F.; Stan, E.; Stefanek, G.; Stefanini, G.; Steinbeck, T.; Stenlund, E.; Steyn, G.; Stocco, D.; Stock, R.; Stolpovsky, P.; Strmen, P.; Suaide, A.; Vasquez, M. A. S.; Sugitate, T.; Suire, C.; Umbera, M.; Susa, T.; Swoboda, D.; Symons, J.; de Toledo, A. S.; Szarka, I.; Szostak, A.; Szuba, M.; Tadel, M.; Tagridis, C.; Takahara, A.; Takahashi, J.; Tanabe, R.; Takaki, D. J. T.; Taureg, H.; Tauro, A.; Tavlet, M.; Munoz, G.; Telesca, A.; Terrevoli, C.; Thader, J.; Tieulent, R.; Tlusty, D.; Toia, A.; Tolyhy, T.; De Matos, C. T.; Torii, H.; Torralba, G.; Toscano, L.; Tosello, F.; Tournaire, A.; Traczyk, T.; Tribedy, P.; Troger, G.; Truesdale, D.; Trzaska, W.; Tsiledakis, G.; Tsilis, E.; Tsuji, T.; Tumkin, A.; Turrisi, R.; Turvey, A.; Tveter, T.; Tydesjo, H.; Tywoniuk, K.; Ulery, J.; Ullaland, K.; Uras, A.; Urban, J.; Urciuoli, G.; Usai, G.; Vacchi, A.; Vala, M.; Palomo, L. V.; Vallero, S.; van der Kolk, N.; Vyvre, P. V.;

van Leeuwen, M.; Vannucci, L.; Vargas, A.; Varma, R.; Vasiliev, A.; Vassiliev, I.; Vasileiou, M.; Vechernin, V.; Venaruzzo, M.; Vercellin, E.; Vergara, S.; Vernet, R.; Verweij, M.; Vetlitskiy, I.; Vickovic, L.; Viesti, G.; Vikhlyantsev, O.; Vilakazi, Z.; Baillie, O. V.; Vinogradov, A.; Vinogradov, L.; Vinogradov, Y.; Virgili, T.; Viyogi, Y.; Vodopianov, A.; Voloshin, K.; Voloshin, S.; Volpe, G.; von Haller, B.; Vranic, D.; Vrlakova, J.; Vulpescu, B.; Wagner, B.; Wagner, V.; Wallet, L.; Wan, R.; Wang, D.; Wang, Y.; Watanabe, K.; Wen, Q.; Wessels, J.; Westerhoff, U.; Wiechula, J.; Wikne, J.; Wilk, A.; Wilk, G.; Williams, M.; Willis, N.; Windelband, B.; Xu, C.; Yang, C.; Yang, H.; Yasnopolskiy, S.; Yermia, F.; Yi, J.; Yin, Z.; Yokoyama, H.; Yoo, I. K.; Yuan, X.; Yurevich, V.; Yushmanov, I.; Zabrodin, E.; Zagreev, B.; Zalite, A.; Zampolli, C.; Zanevsky, Y.; Zaporozhets, S.; Zarochentsev, A.; Zavada, P.; Zbroszczyk, H.; Zelnicek, P.; Zenin, A.; Zepeda, A.; Zgura, I.; Zhalov, M.; Zhang, X.; Zhou, D.; Zhou, S.; Zhu, J.; Zichichi, A.; Zinchenko, A.; Zinovjev, G.; Zoccarato, Y.; Zychacek, V.; Zynovyev, M.; ALICE Collaboration: **Charged-particle multiplicity measurement in proton-proton collisions at root s0.9 and 2.36 TeV with ALICE at LHC.** *The European physical journal: C, Particles and fields* **68**(1): 89–108, 2010. DOI:10.1140/epjc/s10052-010-1339-x

006 Aamodt, K.; Abel, N.; Abeysekara, U.; Quintana, A. A.; Acero, A.; Adamova, D.; Aggarwal, M. M.; Rinella, G. A.; Agocs, A. G.; Salazar, S. A.; Ahammed, Z.; Ahmad, A.; Ahmad, N.; Ahn, S. U.; Akimoto, R.; Akindinov, A.; Aleksandrov, D.; Alessandro, B.; Molina, R. A.; Alici, A.; Avina, E. A.; Alme, J.; Alt, T.; Altini, V.; Altinpinar, S.; Andrei, C.; Andronic, A. ; Anelli, G.; Angelov, V.; Anson, C.; Anticic, T.; Antinori, F.; Antinori, S.; Antipin, K.; Antonczyk, D.; Antonioli, P.; Anzo, A.; Aphecetche, L.; Appelshauser, H.; Arcelli, S.; Arceo, R.; Arend, A.; Armesto, N.; Arnaldi, R.; Aronsson, T.; Arsene, I. C.; Asryan, A.; Augustinus, A.; Averbeck, R.; Awes, T. C.; Aysto, J.; Azmi, M. D.; Bablok, S.; Bach, M.; Badala, A.; Baek, Y. W.; Bagnasco, S.; Bailhache, R.; Bala, R.; Baldisseri, A.; Baldit, A.; Ban, J.; Barbera, R.; Barnafoldi, G. G.; Barnby, L.; Barret, V.; Bartke, J.; Barile, F.; Basile, M.; Basmanov, V.; Bastid, N.; Bathen, B.; Batigne, G.; Batyunya, B.; Baumann, C.; Bearden, I.; Becker, B.; Belikov, I.; Bellwied, R.; Belmont-Moreno, E.; Belogianni, A.; Benhabib, L.; Beole, S.; Berceanu, I.; Bercuci, A.; Berdermann, E. ; Berdnikov, Y.; Betev, L.; Bhasin, A.; Bhati, A. K.; Bianchi, L.; Bianchi, N.; Bianchin, C.; Bielcik, J.; Bielcikova, J.; Bilandzic, A.; Bimbot, L.; Biolcati, E.; Blanc, A.; Blanco, F.; Blanco, F.; Blau, D.; Blume, C.; Boccioli, M.; Bock, N.; Bogdanov, A.; Boggild, H.; Bogolyubsky, M.; Bohm, J.; Boldizsar, L.; Bombara, M.; Bombonati, C.; Bondila, M.; Borel, H.; Borshchov, V.; Bortolin, C.; Bose, S.; Bosisio, L.; Bossu, F.; Botje, M.; Bottger, S.; Bourdaud, G.; Boyer, B.; Braun, M.; Braun-Munzinger, P.; Bravina, L.; Bregant, M.; Breitner, T.; Bruckner, G.; Brun, R.; Bruna, E.; Bruno, G. E.; Budnikov, D.; Buesching, H.; Bugaev, K.; Buncic, P.; Busch, O. ; Buthelezi, Z.; Caffarri, D.; Cai, X.; Caines, H.; Camacho, E.; Camerini, P.; Campbell, M.; Roman, V. C.; Capitani, G. P.; Romeo, G. C.; Carena, F.; Carena, W.; Carminati, F.; Diaz, A. C.; Caselle, M.; Castellanos, J. C.; Hernandez, J. F. C.; Catanescu, V.; Cattaruzza, E.; Cavicchioli, C.; Cerello, P.; Chambert, V.; Chang, B.; Chapeland, S.; Charpy, A.; Charvet, J. L.; Chattopadhyay, S.; Chattopadhyay, S.; Cherney, M.; Cheshkov, C.; Cheynis, B.; Chiavassa, E.; Barroso, V. C.; Chinellato, D. D.; Chochula, P.; Choi, K.; Chojnacki, M.; Christakoglou, P.; Christensen, C. H.; Christiansen, P.; Chujo, T.; Chuman, F.; Cicalo, C.; Cifarelli, L.; Cindolo, F.; Cleymans, J.; Cobanoglu, O.; Coffin, J. P.; Coli, S.; Colla, A.; Balbastre, G. C.; del Valle, Z. C.; Conner, E. S.; Constantin, P.; Contin, G.; Contreras, J. G.; Morales, Y. C.; Cormier, T. M.; Cortese, P.; Maldonado, I. C.; Cosentino, M. R.; Costa, F.; Cotallo, M. E.; Crescio, E.; Crochet, P.; Cuautle, E.; Cunqueiro, L.; Cussonneau, J.; Dainese, A.; Dalsgaard, H. H.; Danu, A.; Das, I.; Das, S.; Dash, A.; Dash, S.; de Barros, G. O. V.; De Caro, A.; de Cataldo, G.; de Cuveland, J.; De Falco, A.; de Gaspari, M.; de Groot, J.; De Gruttola, D.; de Haas, A. P.; De Marco, N.; de Rooij, R.; De Pasquale, S.; de Vaux, G.; Delagrange, H.; Dellacasa, G.; Deloff, A.; Demanov, V.; Denes, E.; Deppman, A.; D'Erasmo, G.; Derkach, D.; Devaux, A.; Di Bari, D.; Di Giglio, C.; Di Liberto, S.; Di Mauro, A.; Di Nezza, P.; Dialinas, M.; Diaz, L.; Diaz, R.; Dietel, T.; Ding, H.; Divia, R.; Djuvsland, O.; Valdiviesso, G. D.; Dobretsov, V.; Dobrin, A.; Dobrowolski, T.; Donigus, B.; Dominguez, I.; Don, D. M. M.; Dordic, O.; Dubey, A. K.; Dubuisson, J.; Ducroux, L.; Dupieux, P.; Majumdar, A. K. D.; Majumdar, M. R. D.; Elia, D.; Emschermann, D.; Enokizono, A.; Espagnon, B.; Estienne, M.; Evans, D.; Evrard, S.; Eyyubova, G.; Fabjan, C. W.; Fabris, D.; Faivre, J.; Falchieri, D.; Fantoni, A.; Fasel, M.; Fearick, R.; Fedunov, A.; Fehlker, D.; Fekete, V.; Felea, D.; Fenton-Olsen, B.; Feofilov, G.; Tellez, A. F.; Ferreiro, E. G.; Ferretti, A.; Ferretti, R.; Figueredo, M. A. S.; Filchagin, S.; Fini, R.; Fionda, F. M.; Fiore, E. M.; Floris, M.; Fodor, Z.; Foertsch, S.; Foka, P.; Fokin, S.; Formenti, F.; Fragiacomo, E.; Fragkiadakis, M.; Frankenfeld, U.; Frolov, A.; Fuchs, U.; Furano, F.; Furget, C.; Girard, M. F.; Gaardhoje, J. J.; Gadrat, S.; Gagliardi, M.; Gago, A.; Gallio, M.; Ganoti, P.; Ganti, M. S.; Garabatos, C. ; Trapaga, C. G.; Gebelein, J.; Gemme, R.; Germain, M.; Gheata, A.; Gheata, M.; Ghidini, B.; Ghosh, P.; Giraudo, G.; Giubellino, P.; Gladysz-Dziadus, E.; Glasow, R.; Glassel, P.; Glenn, A.; Gomez, R.; Santos, H. G.; Gonzalez-Trueba, L. H.; Gonzalez-Zamora, P.; Gorbunov, S.; Gorbunov, Y.; Gotovac, S.; Gottschlag, H.; Grabski, V.; Grajcarek, R.; Grelli, A.; Grigoras, A.; Grigoras, C.; Grigoriev, V.; Grigoryan, A.; Grinyov, B.; Grion, N.; Gros, P.; Grosse-Oetringhaus, J. F.; Grossiord, J. Y.; Grosso, R.; Guarnaccia, C.; Guber, F.; Guernane, R.; Guerzoni, B.; Gulbrandsen, K.; Gulkanyan, H.; Gunji, T.; Gupta, A.; Gupta, R.; Gustafsson, H. A.; Gutbrod, H.; Haaland, O.; Hadjidakis, C.; Haiduc, M.; Hamagaki, H.; Hamar, G.; Hamblen, J.; Han, B. H.; Harris, J. W.; Hartig, M.; Harutyunyan, A.; Hasch, D.; Hasegan, D.; Hatzifotiadou, D.; Hayrapetyan,

A.; Heide, M.; Heinz, M.; Helstrup, H.; Herghelegiu, A.; Hernandez, C.; Corral, G. G.; Herrmann, N.; Hetland, K. F.; Hicks, B.; Hiei, A.; Hille, P.; Hippolyte, B.; Horaguchi, T.; Hori, Y.; Hristov, P.; Hrivnacova, I.; Hu, S.; Huber, S.; Humanic, T. J.; Hutter, D.; Hwang, D. S.; Ichou, R.; Ilkaev, R.; Ilkiv, I.; Innocenti, P. G.; Ippolitov, M.; Irfan, M.; Ivan, C.; Ivanov, A.; Ivanov, M.; Ivanov, V.; Iwasaki, T.; Jachokowski, A.; Jacobs, P. M.; Jancurova, L.; Jangal, S.; Janik, R.; Jayananda, K.; Jena, C.; Jena, S.; Jirden, L.; Jones, G.; Jones, P. G.; Jovanovic, P.; Jung, H.; Jung, W.; Jusko, A.; Kaidalov, A. B.; Kalcher, S.; Kalinak, P.; Kalliokoski, T.; Kalweit, A.; Kamal, A.; Kamermans, R.; Kanaki, K.; Kang, E.; Kang, J. H.; Kapitan, J.; Kaplin, V.; Kapusta, S.; Karavicheva, T.; Karpechev, E.; Kazantsev, A.; Kebschull, U.; Keidel, R.; Khan, M. M.; Khan, S. A.; Khanzadeev, A.; Kharlov, Y.; Kikola, D.; Kileng, B.; Kim, D. J.; Kim, D. S.; Kim, D. W.; Kim, H. N.; Kim, J.; Kim, J. H.; Kim, J. S.; Kim, M.; Kim, M.; Kim, S. H.; Kim, S.; Kim, Y.; Kirsch, S.; Kisel, I.; Kiselev, S.; Kisiel, A.; Klay, J. L.; Klein, J.; Klein-Bosing, C.; Kliemant, M.; Klovning, A.; Kluge, A.; Kniege, S.; Koch, K.; Kolevatov, R.; Kolojvari, A.; Kondratiev, V.; Kondratyeva, N.; Konevskih, A.; Kornas, E.; Kour, R.; Kowalski, M.; Kox, S.; Kozlov, K.; Kral, J.; Kralik, I.; Kramer, F.; Kraus, I.; Kravcakova, A.; Krawutschke, T.; Krivda, M.; Krumbhorn, D.; Krus, M.; Kryshen, E.; Krzewicki, M.; Kucheriaev, Y.; Kuhn, C.; Kuijer, P. G.; Kumar, L.; Kumar, N.; Kupczak, R.; Kurashvili, P.; Kurepin, A.; Kurepin, A. N.; Kuryakin, A.; Kushpil, S.; Kushpil, V.; Kutouski, M.; Kvaerno, H.; Kweon, M. J.; Kwon, Y.; La Rocca, P.; Lackner, F.; de Guevara, P. L.; Lafage, V.; Lal, C.; Lara, C.; Larsen, D. T.; Laurenti, G.; Lazzeroni, C.; Le Bornec, Y.; Le Bris, N.; Lee, H.; Lee, K. S.; Lee, S. C.; Lefevre, F.; Lenhardt, M.; Leistam, L.; Lehnert, J.; Lenti, V.; Leon, H.; Monzon, I. L.; Vargas, H. L.; Levai, P.; Li, Y.; Lietava, R.; Lindal, S.; Lindenstruth, V.; Lippmann, C. ; Lisa, M. A.; Listratenko, O.; Liu, L.; Loginov, V.; Lohn, S.; Lopez, X.; Noriega, M. L.; Lopez-Ramirez, R.; Torres, E. L.; Lovhoiden, G.; Soares, A. L. F.; Lu, S.; Lunardon, M.; Luparello, G.; Luquin, L.; Lutz, J. R.; Luvisetto, M.; Ma, K.; Ma, R.; Madagodahettige-Don, D. M.; Maevskaya, A.; Mager, M.; Mahajan, A.; Mahapatra, D. P.; Maire, A.; Makhlyueva, I.; Mal'Kevich, D.; Malaev, M.; Cervantes, I. M.; Malek, M.; Malkiewicz, T.; Malzacher, P.; Mamonov, A.; Manceau, L.; Mangotra, L.; Manko, V.; Manso, F.; Manzari, V.; Mao, Y.; Mares, J.; Margagliotti, G. V.; Margotti, A.; Marin, A.; Martashvili, I.; Martinengo, P.; Martinez, M. I.; Davalos, A. M.; Garcia, G. M.; Maruyama, Y.; Chiesa, A. M.; Masciocchi, S.; Masera, M.; Masetti, M.; Masoni, A.; Massacrier, L.; Mastromarco, M.; Mastroserio, A.; Matthews, Z. L.; Tavares, B. M.; Matyja, A.; Mayani, D.; Mazza, G.; Mazzoni, M. A.; Meddi, F.; Menchaca-Rocha, A.; Lorenzo, P. M.; Meoni, M.; Perez, J. M.; Mereu, P.; Miake, Y.; Michalon, A.; Miftakhov, N.; Milosevic, J.; Minafra, F.; Mischke, A.; Miskowiec, D.; Mitu, C.; Mizoguchi, K.; Mlynarz, J.; Mohanty, B.; Molnar, L.; Mondal, M. M.; Zetina, L. M.; Monteno, M.; Montes, E.; Morando, M.; Moretto, S.; Morsch, A.; Moukhanova, T.; Muccifora, V.; Mudnic, E.; Muhuri, S.; Muller, H.; Munhoz, M. G.; Munoz, J.; Musa, L.; Musso, A.; Nandi, B. K.; Nania, R.; Nappi, E.; Navach, F.; Navin, S.; Nayak, T. K.; Nazarenko, S.; Nazarov, G.; Nedosekin, A.; Nendaz, F.; Newby, J.; Nianine, A.; Nicassio, M.; Nielsen, B. S.; Nikolaev, S.; Nikolic, V.; Nikulin, S.; Nikulin, V.; Nilsen, B.; Nilsson, M. S.; Noferini, F.; Nomokonov, P.; Nooren, G.; Novitzky, N.; Nyatha, A.; Nygaard, C.; Nyiri, A.; Nystrand, J.; Ochirov, A.; Odyniec, G.; Oeschler, H.; Oinonen, M.; Okada, K.; Okada, Y.; Oldenburg, M.; Oleniacz, J.; Oppedisano, C.; Orsini, F.; Velazquez, A.; Ortona, G.; Oskamp, C.; Oskarsson, A.; Osmic, F.; Osterman, L.; Ostrowski, P.; Otterlund, I.; Otwinowski, J.; Ovrebekk, G.; Oyama, K.; Ozawa, K.; Pachmayer, Y.; Pachr, M.; Padilla, F.; Pagano, P.; Paic, G.; Painke, F.; Pajares, C.; Pal, S.; Pal, S. K.; Palaha, A.; Palmeri, A.; Panse, R.; Pappalardo, G. S.; Park, W. J.; Pastircak, B.; Pastore, C.; Paticchio, V.; Pavlinov, A.; Pawlak, T.; Peitzmann, T.; Pepato, A.; Pereira, H.; Peressounko, D.; Perez, C.; Perini, D.; Perrino, D.; Peryt, W.; Peschek, J.; Pesci, A.; Peskov, V.; Pestov, Y.; Peters, A.; Petracek, V.; Petridis, A.; Petris, M.; Petrov, P.; Petrovici, M.; Petta, C.; Peyre, J.; Piano, S.; Piccotti, A.; Pikna, M.; Pillot, P.; Pinsky, L.; Pitz, N.; Piuz, F.; Platt, R.; Ploskon, M.; Pluta, J.; Pocheptsov, T.; Pochybova, S.; Lerma, P. L. M.; Poggio, F.; Poghosyan, M. G.; Polak, K.; Polichtchouk, B.; Polozov, P.; Polyakov, V.; Pommeresch, B.; Pop, A.; Posa, F.; Pospisil, V.; Potukuchi, B.; Pouthas, J.; Prasad, S. K.; Preghenella, R.; Prino, F.; Pruneau, C. A.; Pshenichnov, I.; Puddu, G.; Pujahari, P.; Pulvirenti, A.; Punin, A.; Punin, V.; Putis, M.; Putschke, J.; Quercigh, E.; Rachevski, A.; Rademakers, A.; Radomski, S.; Raiha, T.; Rak, J.; Rakotozafindrabe, A.; Ramello, L.; Reyes, A. R.; Rammler, M.; Raniwala, R.; Raniwala, S.; Rasanen, S.; Rashevskaya, I.; Rath, S.; Read, K. F.; Real, J.; Redlich, K.; Renfordt, R.; Reolon, A. R.; Reshetin, A.; Rettig, F.; Revol, J. P.; Reygers, K.; Ricaud, H.; Riccati, L.; Ricci, R. A.; Richter, M. ; Riedler, P.; Riegler, W.; Riggi, F.; Rivetti, A.; Cahuantzi, M. R.; Roed, K.; Rohrich, D.; Lopez, S. R.; Romita, R.; Ronchetti, F.; Rosinsky, P.; Rosnet, P.; Rossegger, S.; Rossi, A.; Roukoutakis, F.; Rousseau, S.; Roy, C.; Roy, P.; Rubio-Montero, A. J.; Rui, R.; Rusanov, I.; Russo, G.; Ryabinkin, E.; Rybicki, A.; Sadovsky, S.; Safarik, K.; Sahoo, R.; Saini, J.; Saiz, P.; Sakata, D.; Salgado, C. A.; da Silva, R. S. D.; Salur, S.; Samanta, T.; Sambyal, S.; Samsonov, V.; Sandor, L.; Sandoval, A.; Sano, M.; Sano, S.; Santo, R.; Santoro, R.; Sarkamo, J.; Saturnini, P.; Scapparone, E.; Scarlassara, F.; Scharenberg, R. P.; Schiaua, C.; Schicker, R.; Schindler, H.; Schmidt, C.; Schmidt, H. R.; Schreiner, S.; Schuchmann, S.; Schukraft, J.; Schutz, Y.; Schwarz, K.; Schweda, K.; Scioli, G.; Scomparin, E.; Segato, G.; Semenov, D.; Senyukov, S.; Seo, J.; Serci, S.; Serkin, L.; Serradilla, E.; Sevcenco, A.; Sgura, I.; Shabratova, G.; Shahoyan, R.; Sharkov, G.; Sharma, N.; Sharma, S.; Shigaki, K.; Shimomura, M.; Shtejer, K.; Sibiriak, Y.; Siciliano, M.; Sicking, E.; Siddi, E.; Siemiarczuk, T.; Silenzi, A.; Silvermyr, D.; Simili, E.; Simon-

etti, G.; Singaraju, R.; Singh, R.; Singhal, V.; Sinha, B. C.; Sinha, T.; Sitar, B.; Sitta, M.; Skaali, T. B.; Skjerdal, K.; Smakal, R.; Smirnov, N.; Snellings, R.; Snow, H.; Sogaard, C.; Sokolov, O.; Soloviev, A.; Soltveit, H. K.; Soltz, R.; Sommer, W.; Son, C. W.; Son, H. S.; Song, M.; Soos, C.; Soramel, F.; Soyk, D.; Spyropoulou-Stassinaki, M.; Srivastava, B. K.; Stachel, J.; Staley, F.; Stan, I.; Stefanek, G.; Stefanini, G.; Steinbeck, T.; Stenlund, E.; Steyn, G.; Stocco, D.; Stock, R.; Stolpovsky, P.; Strmen, P.; Suaide, A. A. P.; Vasquez, M. A. S.; Sugitate, T.; Suire, C.; Sumbera, M.; Susa, T.; Swoboda, D.; Symons, T. J. M.; de Toledo, A. S.; Szarka, I.; Szostak, A.; Szuba, M.; Tadel, M.; Tagridis, C.; Takahara, A.; Takahashi, J.; Tanabe, R.; Takaki, J. D. T.; Taureg, H.; Tauro, A.; Tavlet, M.; Munoz, G.; Telesca, A.; Terrevoli, C.; Thader, J.; Tieulent, R.; Tlusty, D.; Toia, A.; Tolyhy, T.; de Matos, C. T.; Torii, H.; Torralba, G.; Toscano, L.; Tosello, F.; Tournaire, A.; Traczyk, T.; Tribedy, P.; Troger, G.; Truesdale, D.; Trzaska, W. H.; Tsiledakis, G.; Tsilis, E.; Tsuji, T.; Tumkin, A.; Turrisi, R.; Turvey, A.; Tveter, T. S.; Tydesjo, H.; Tywoniuk, K.; Ulery, J.; Ullaland, K.; Uras, A.; Urban, J.; Urciuoli, G. M.; Usai, G. L.; Vacchi, A.; Vala, M.; Palomo, L. V.; Vallero, S.; van den Brink, A.; van der Kolk, N.; Vyvre, P. V.; van Leeuwen, M.; Vannucci, L.; Vargas, A.; Varma, R.; Vasiliev, A.; Vassiliev, I.; Vassiliou, M.; Vechernin, V.; Venaruzzo, M.; Vercellin, E.; Vergara, S.; Vernet, R.; Verweij, M.; Vetlitskiy, I.; Vickovic, L.; Viesti, G.; Vikhlyantsev, O.; Vilakazi, Z.; Baillie, O. V.; Vinogradov, A.; Vinogradov, L.; Vinogradov, Y.; Virgili, T.; Viyogi, Y. P.; Vodopianov, A.; Voloshin, K.; Voloshin, S.; Volpe, G.; von Haller, B.; Vranic, D.; Vrlakova, J.; Vulpescu, B.; Wagner, B.; Wagner, V.; Wallet, L.; Wan, R.; Wang, D.; Wang, Y.; Wang, Y.; Watanabe, K.; Wen, Q.; Wessels, J.; Wiechula, J.; Wikne, J.; Wilk, A.; Wilk, G.; Williams, M. C. S.; Willis, N.; Windelband, B.; Xu, C.; Yang, C.; Yang, H.; Yasnopolsky, A.; Yermia, F.; Yi, J.; Yin, Z.; Yokoyama, H.; Yoo, I. K.; Yuan, X.; Yushmanov, I.; Zabrodin, E.; Zagreev, B.; Zalite, A.; Zampolli, C.; Zanevsky, Y.; Zaporozhets, S.; Zarochentsev, A.; Zavada, P.; Zbroszczyk, H.; Zelnicek, P.; Zenin, A.; Zepeda, A.; Zgura, I.; Zhalov, M.; Zhang, X.; Zhou, D.; Zhou, S.; Zhou, S.; Zhu, J.; Zichichi, A.; Zinchenko, A.; Zinovjev, G.; Zinovjev, M.; Zoccarato, Y.; Zychacek, V.; ALICE Collaboration: **First proton-proton collisions at the LHC as observed with the ALICE detector: measurement of the charged-particle pseudorapidity density at root s900 GeV.** *The European physical journal: C, Particles and fields* **65**(1): 111–125, 2010. DOI:10.1140/epjc/s10052-009-1227-4

007 Aamodt, K.; Abel, N.; Abeysekara, U.; Quintana, A. A.; Adamova, D.; Aggarwal, M.; Rinella, G. A.; Agocs, A. G.; Salazar, S. A.; Ahammed, Z.; Ahmad, A.; Ahmad, N.; Ahn, S. U.; Akimoto, R.; Akindinov, A.; Aleksandrov, D.; Alessandro, B.; Molina, R. A.; Alici, A.; Avina, E. A.; Alme, J.; Alt, T.; Altini, V.; Altinpinar, S.; Andrei, C.; Andronic, A. ; Anelli, G.; Angelov, V.; Anson, C.; Anticic, T.; Antinori, F.; Antinori, S.; Antipin, K.; Antonczyk, D.; Antonioli, P.; Anzo, A.; Aphecetche, L.; Appelshauser, H.; Arcelli, S.; Arceo, R.; Arend, A.; Armesto, N.; Arnaldi, R.; Aronsson, T.; Arsene, I. C.; Asryan, A.; Augustinus, A.; Averbeck, R.; Awes, T. C.; Aysto, J.; Azmi, M. D.; Bablok, S.; Bach, M.; Badala, A.; Baek, Y. W.; Bagnasco, S.; Bailhache, R.; Bala, R.; Baldisseri, A.; Baldit, A.; Ban, J.; Barbera, R.; Barnafoldi, G. G.; Barnby, L.; Barret, V.; Bartke, J.; Barile, F.; Basile, M.; Basmanov, V.; Bastid, N.; Bathen, B.; Batigne, G.; Batyunya, B.; Baumann, C.; Bearden, I. G.; Becker, B.; Belikov, I.; Bellwied, R.; Belmont-Moreno, E.; Belogianni, A.; Benhabib, L.; Beole, S.; Berceanu, I.; Bercuci, A.; Berdermann, E. ; Berdnikov, Y.; Betev, L.; Bhasin, A.; Bhati, A. K.; Bianchi, L.; Bianchi, N.; Bianchin, C.; Bielcik, J.; Bielcikova, J.; Bilandzic, A.; Bimbot, L.; Biolcati, E.; Blanc, A.; Blanco, F.; Blanco, F.; Blau, D.; Blume, C.; Boccioli, M.; Bock, N.; Bogdanov, A.; Boggild, H.; Bogolyubsky, M.; Bohm, J.; Boldizsar, L.; Bombara, M.; Bombonati, C.; Bondila, M.; Borel, H.; Borshchov, V.; Borisov, A.; Bortolin, C.; Bose, S.; Bosisio, L.; Bossu, F.; Botje, M.; Bottger, S.; Bourdaud, G.; Boyer, B.; Braun, M.; Braun-Munzinger, P.; Bravina, L.; Bregant, M.; Breitner, T.; Bruckner, G.; Brun, R.; Bruna, E.; Bruno, G. E.; Budnikov, D.; Buesching, H.; Buncic, P.; Busch, O. ; Buthelezi, Z.; Caffarri, D.; Cai, X.; Caines, H.; Camacho, E.; Camerini, P.; Campbell, M.; Roman, V. C.; Capitani, G. P.; Romeo, G. C.; Carena, F.; Carena, W.; Carminati, F.; Diaz, A. C.; Caselle, M.; Castellanos, J. C.; Hernandez, J. F. C.; Catanescu, V.; Cattaruzza, E.; Cavicchioli, C.; Cerello, P.; Chambert, V.; Chang, B.; Chapeland, S.; Charpy, A.; Charvet, J. L.; Chattopadhyay, S.; Chattopadhyay, S.; Cherney, M.; Cheshkov, C.; Cheynis, B.; Chiavassa, E.; Barroso, V. C.; Chinellato, D. D.; Chochula, P.; Choi, K.; Chojnacki, M.; Christakoglou, P.; Christensen, C. H.; Christiansen, P.; Chujo, T.; Chuman, F.; Cicalo, C.; Cifarelli, L.; Cindolo, F.; Cleymans, J.; Cobanoglu, O.; Coffin, J. P.; Coli, S.; Colla, A.; Balbastre, G. C.; del Valle, Z. C.; Conner, E. S.; Constantin, P.; Contin, G.; Contreras, G. J.; Morales, Y. C.; Cormier, T. M.; Cortese, P.; Maldonado, I. C.; Cosentino, M. R.; Costa, F.; Cotallo, M. E.; Crescio, E.; Crochet, P.; Cuautle, E.; Cunqueiro, L.; Cussonneau, J.; Dainese, A.; Dalsgaard, H. H.; Danu, A.; Das, I.; Das, S.; Dash, A.; Dash, S.; de Barros, G. O. V.; De Caro, A.; de Cataldo, G.; de Cuveland, J.; De Falco, A.; De Gaspari, M.; de Groot, J.; De Gruttola, D.; de Haas, A. P.; De Marco, N.; De Pasquale, S.; De Remigis, R.; de Rooij, R.; de Vaux, G.; Delagrange, H.; Dellacasa, G.; Deloff, A.; Demanov, V.; Denes, E.; Deppman, A.; D'Erasmo, G.; Derkach, D.; Devaux, A.; Di Bari, D.; Di Giglio, C.; Di Liberto, S.; Di Mauro, A.; Di Nezza, P.; Dialinas, M.; Diaz, L.; Diaz, R.; Dietel, T.; Ding, H.; Divia, R.; Djuvsland, O.; Dobretsov, V.; Dobrin, A.; Dobrowolski, T.; Donigus, B.; Dominguez, I.; Don, D. M. M.; Dordic, O.; Dubey, A. K.; Dubuisson, J.; Ducroux, L.; Dupieux, P.; Majumdar, A. K. D.; Majumdar, M. R. D.; Elia, D.; Emschermann, D.; Enokizono, A.; Espagnon, B.; Estienne, M.; Evans, D.; Evrard, S.; Eyyubova, G.; Fabjan, C. W.; Fabris, D.; Faivre, J.; Falchieri, D.; Fantoni, A.;

Fasel, M.; Fateev, O.; Fearick, R.; Fedunov, A.; Fehlker, D.; Fekete, V.; Felea, D.; Fenton-Olsen, B.; Feofilov, G.; Tellez, A. F.; Ferreiro, E. G.; Ferretti, A.; Ferretti, R.; Figueredo, M. A. S.; Filchagin, S.; Fini, R.; Fionda, F. M.; Fiore, E. M.; Floris, M.; Fodor, Z.; Foertsch, S.; Foka, P.; Fokin, S.; Formenti, F.; Fragiacomo, E.; Fragkiadakis, M.; Frankenfeld, U.; Frolov, A.; Fuchs, U.; Furano, F.; Furget, C.; Girard, M. F.; Gaardhoje, J. J.; Gadrat, S.; Gagliardi, M.; Gago, A.; Gallio, M.; Gang, S.; Ganoti, P.; Ganti, M. S.; Garabatos, C. ; Trapaga, C. G.; Gebelein, J.; Gemme, R.; Germain, M.; Gheata, A.; Gheata, M.; Ghidini, B.; Ghosh, P.; Giraudo, G.; Giubellino, P.; Gladysz-Dziadus, E.; Glasow, R.; Glassel, P.; Glenn, A.; Gomez, R.; Santos, H. G.; Gonzalez-Trueba, L. H.; Gonzalez-Zamora, P.; Gorbunov, S.; Gorbunov, Y.; Gotovac, S.; Gottschlag, H.; Grabski, V.; Grajcarek, R.; Grelli, A.; Grigoras, A.; Grigoras, C.; Grigoriev, V.; Grigoryan, A.; Grigoryan, S.; Grinyov, B.; Grion, N.; Gros, P.; Grosse-Oetringhaus, J. F.; Grossiord, J. Y.; Grosso, R.; Guarnaccia, C.; Guber, F.; Guernane, R.; Guerzoni, B.; Gulbrandsen, K.; Gulkanyan, H.; Gunji, T.; Gupta, A.; Gupta, R.; Gustafsson, H. A.; Gutbrod, H.; Haaland, O.; Hadjidakis, C.; Haiduc, M.; Hamagaki, H.; Hamar, G.; Hamblen, J.; Han, B. H.; Harris, J. W.; Hartig, M.; Harutyunyan, A.; Hasch, D.; Hasegan, D.; Hatzifotiadou, D.; Hayrapetyan, A.; Heide, M.; Heinz, M.; Helstrup, H.; Herghelegiu, A.; Hernandez, C.; Corral, G. H.; Herrmann, N.; Hetland, K. F.; Hicks, B.; Hiei, A.; Hille, P. T.; Hippolyte, B.; Horaguchi, T.; Hori, Y.; Hristov, P.; Hrivnacova, I.; Hu, S.; Huang, M.; Huber, S.; Humanic, T. J.; Hutter, D.; Hwang, D. S.; Ichou, R.; Ilkaev, R.; Ilkiv, I.; Inaba, M.; Innocenti, P. G.; Ippolitov, M.; Irfan, M.; Ivan, C.; Ivanov, A.; Ivanov, M.; Ivanov, V.; Iwasaki, T.; Jacholkowski, A.; Jacobs, P.; Jancurova, L.; Jangal, S.; Janik, R.; Jena, C.; Jena, S.; Jirden, L.; Jones, G. T.; Jones, P. G.; Jovanovic, P.; Jung, H.; Jung, W.; Jusko, A.; Kaidalov, A. B.; Kalcher, S.; Kalinak, P.; Kalliokoski, T.; Kalweit, A.; Kamal, A.; Kamermans, R.; Kanaki, K.; Kang, E.; Kang, J. H.; Kapitan, J.; Kaplin, V.; Kapusta, S.; Karavichev, O.; Karavicheva, T.; Karpechev, E.; Kazantsev, A.; Kebschull, U.; Keidel, R.; Khan, M. M.; Khan, S. A.; Khanzadeev, A.; Kharlov, Y.; Kikola, D.; Kileng, B.; Kim, D. J.; Kim, D. S.; Kim, D. W.; Kim, H. N.; Kim, J.; Kim, J. H.; Kim, J. S.; Kim, M.; Kim, M.; Kim, S. H.; Kim, S.; Kim, Y.; Kirsch, S.; Kisel, I.; Kiselev, S.; Kisiel, A.; Klay, J. L.; Klein, J.; Klein-Bosing, C.; Kliemant, M.; Klovning, A.; Kluge, A.; Kniege, S.; Koch, K.; Kolevatov, R.; Kolojvari, A.; Kondratiev, V.; Kondratyeva, N.; Konevskih, A.; Kornas, E.; Kour, R.; Kowalski, M.; Kox, S.; Kozlov, K.; Kral, J.; Kralik, I.; Kramer, F.; Kraus, I.; Kravcakova, A.; Krawutschke, T.; Krivda, M.; Krumbhorn, D.; Krus, M.; Kryshen, E.; Krzewicki, M.; Kucheriaev, Y.; Kuhn, C.; Kuijer, P. G.; Kumar, L.; Kumar, N.; Kupczak, R.; Kurashvili, P.; Kurepin, A.; Kurepin, A. N.; Kuryakin, A.; Kushpil, S.; Kushpil, V.; Kutouski, M.; Kvaerno, H.; Kweon, M. J.; Kwon, Y.; La Rocca, P.; Lackner, F.; de Guevara, P. L.; Lafage, V.; Lal, C.; Lara, C.; Larsen, D. T.; Laurenti, G.; Lazzeroni, C.; Le Bornec, Y.; Le Bris, N.; Lee, H.; Lee, K. S.; Lee, S. C.; Lefevre, F.; Lenhardt, M.; Leistam, L.; Lehnert, J.; Lenti, V.; Leon, H.; Monzon, I. L.; Vargas, H. L.; Levai, P.; Li, X.; Li, Y.; Lietava, R.; Lindal, S.; Lindenstruth, V.; Lippmann, C. ; Lisa, M. A.; Listratenko, O.; Liu, L.; Loginov, V.; Lohn, S.; Lopez, X.; Noriega, M. L.; Lopez-Ramirez, R.; Torres, E. L.; Lovhoiden, G.; Soares, A. L. F.; Lu, S.; Lunardon, M.; Luparello, G.; Luquin, L.; Lutz, J. R.; Luvisetto, M.; Ma, K.; Ma, R.; Madagodahettige-Don, D. M.; Maevskaya, A.; Mager, M.; Mahajan, A.; Mahapatra, D. P.; Maire, A.; Makhlyueva, I.; Mal'Kevich, D.; Malaev, M.; Malagalage, K. J.; Cervantes, I. M.; Malek, M.; Malkiewicz, T.; Malzacher, P.; Mamonov, A.; Manceau, L.; Mangotra, L.; Manko, V.; Manso, F.; Manzari, V.; Mao, Y.; Mares, J.; Margagliotti, G. V.; Margotti, A.; Marin, A.; Martashvili, I.; Martinengo, P.; Martinez, M. I.; Davalos, A. M.; Garcia, G. M.; Maruyama, Y.; Chiesa, A. M.; Masciocchi, S.; Masera, M.; Masetti, M.; Masoni, A.; Massacrier, L.; Mastromarco, M.; Mastroserio, A.; Matthews, Z. L.; Matyja, A.; Mayani, D.; Mazza, G.; Mazzoni, M. A.; Meddi, F.; Menchaca-Rocha, A.; Lorenzo, P. M.; Meoni, M.; Perez, J. M.; Mereu, P.; Miake, Y.; Michalon, A.; Miftakhov, N.; Milosevic, J.; Minafra, F.; Mischke, A.; Miskowiec, D.; Mitu, C.; Mizoguchi, K.; Mlynarz, J.; Mohanty, B.; Molnar, L.; Mondal, M. M.; Zetina, L. M.; Monteno, M.; Montes, E.; Morando, M.; Moretto, S.; Morsch, A.; Moukhanova, T.; Muccifora, V.; Mudnic, E.; Muhuri, S.; Muller, H.; Munhoz, M. G.; Munoz, J.; Musa, L.; Musso, A.; Nandi, B. K.; Nania, R.; Nappi, E.; Navach, F.; Navin, S.; Nayak, T. K.; Nazarenko, S.; Nazarov, G.; Nedosekin, A.; Nendaz, F.; Newby, J.; Nianine, A.; Nicassio, M.; Nielsen, B. S.; Nikolaev, S.; Nikolic, V.; Nikulin, S.; Nikulin, V.; Nilsen, B. S.; Nilsson, M. S.; Noferini, F.; Nomokonov, P.; Nooren, G.; Novitzky, N.; Nyatha, A.; Nygaard, C.; Nyiri, A.; Nystrand, J.; Ochirov, A.; Odyniec, G.; Oeschler, H.; Oinonen, M.; Okada, K.; Okada, Y.; Oldenburg, M.; Oleniacz, J.; Oppedisano, C.; Orsini, F.; Velasquez, A. O.; Ortona, G.; Oskamp, C. J.; Oskarsson, A.; Osmic, F.; Osterman, L.; Ostrowski, P.; Otterlund, I.; Otwinowski, J.; Ovrebekk, G.; Oyama, K.; Ozawa, K.; Pachmayer, Y.; Pachr, M.; Padilla, F.; Pagano, P.; Paic, G.; Painke, F.; Pajares, C.; Pal, S.; Pal, S. K.; Palaha, A.; Palmeri, A.; Panse, R.; Pappalardo, G. S.; Park, W. J.; Pastircak, B.; Pastore, C.; Paticchio, V.; Pavlinov, A.; Pawlak, T.; Peitzmann, T.; Pepato, A.; Pereira, H.; Peressounko, D.; Perez, C.; Perini, D.; Perrino, D.; Peryt, W.; Peschek, J.; Pesci, A.; Peskov, V.; Pestov, Y.; Peters, A. J.; Petracek, V.; Petridis, A.; Petris, M.; Petrov, P.; Petrovici, M.; Petta, C.; Peyre, J.; Piano, S.; Piccotti, A.; Pikna, M.; Pillot, P.; Pinsky, L.; Pitz, N.; Piuz, F.; Platt, R.; Ploskon, M.; Pluta, J.; Pocheptsov, T.; Pochybova, S.; Lerma, P. L. M. P.; Poggio, F.; Poghosyan, M. G.; Polak, K.; Polichtchouk, B.; Polozov, P.; Polyakov, V.; Pommeresch, B.; Pop, A.; Posa, F.; Pospisil, V.; Potukuchi, B.; Pouthas, J.; Prasad, S. K.; Preghenella, R.; Prino, F.; Pruneau, C. A.; Pshenichnov, I.; Puddu, G.; Pujahari, P.; Pulvirenti, A.; Punin, A.; Punin, V.; Putis, M.; Putschke, J.; Quercigh, E.; Rachevski,

A.; Rademakers, A.; Radomski, S.; Raiha, T. S.; Rak, J.; Rakotozafindrabe, A.; Ramello, L.; Reyes, A. R.; Rammler, M.; Raniwala, R.; Raniwala, S.; Rasanen, S. S.; Rashevskaya, I.; Rath, S.; Read, K. F.; Real, J.; Redlich, K.; Renfordt, R.; Reolon, A. R.; Reshetin, A.; Rettig, F.; Revol, J. P.; Reygers, K.; Ricaud, H.; Riccati, L.; Ricci, R. A.; Richter, M. ; Riedler, P.; Riegler, W.; Riggi, F.; Rivetti, A.; Cahuantzi, M. R.; Roed, K.; Rohrich, D.; Lopez, S. R.; Romita, R.; Ronchetti, F.; Rosinsky, P.; Rosnet, P.; Rossegger, S.; Rossi, A.; Roukoutakis, F.; Rousseau, S.; Roy, C.; Roy, P.; Rubio-Montero, A. J.; Rui, R.; Rusanov, I.; Russo, G.; Ryabinkin, E.; Rybicki, A.; Sadovsky, S.; Safarik, K.; Sahoo, R.; Saini, J.; Saiz, P.; Sakata, D.; Salgado, C. A.; da Silva, R. S. D.; Salur, S.; Samanta, T.; Sambyal, S.; Samsonov, V.; Sandor, L. S.; Sandoval, A.; Sano, M.; Sano, S.; Santo, R.; Santoro, R.; Sarkamo, J.; Saturnini, P.; Scapparone, E.; Scarlassara, F.; Scharenberg, R. P.; Schiaua, C.; Schicker, R.; Schindler, H.; Schmidt, C.; Schmidt, H. R.; Schossmaier, K.; Schreiner, S.; Schuchmann, S.; Schukraft, J.; Schutz, Y.; Schwarz, K.; Schweda, K.; Scioli, G.; Scomparin, E.; Segato, G.; Semenov, D.; Senyukov, S.; Seo, J.; Serci, S.; Serkin, L.; Serradilla, E.; Sevcenco, A.; Sgura, I.; Shabratova, G.; Shahoyan, R.; Sharkov, G.; Sharma, N.; Sharma, S.; Shigaki, K.; Shimomura, M.; Shtejer, K.; Sibiriak, Y.; Siciliano, M.; Sicking, E.; Siddi, E.; Siemiarczuk, T.; Silenzi, A.; Silvermyr, D.; Simili, E.; Simonetti, G.; Singaraju, R.; Singh, R.; Singhal, V.; Sinha, B. C.; Sinha, T.; Sitar, B.; Sitta, M.; Skaali, T. B.; Skjerdal, K.; Smakal, R.; Smirnov, N.; Snellings, R.; Snow, H.; Sogaard, C.; Sokolov, O.; Soloviev, A.; Soltveit, H. K.; Soltz, R.; Sommer, W.; Son, C. W.; Son, H. S.; Song, M.; Soos, C.; Soramel, F.; Soyk, D.; Spyropoulou-Stassinaki, M.; Srivastava, B. K.; Stachel, J.; Staley, F.; Stan, E.; Stefanek, G.; Stefanini, G.; Steinbeck, T.; Stenlund, E.; Steyn, G.; Stocco, D.; Stock, R.; Stolpovsky, P.; Strmen, P.; Suaide, A. A. P.; Vasquez, M. A. S.; Sugitate, T.; Suire, C.; Sumbera, M. S.; Susa, T.; Swoboda, D.; Symons, J.; de Toledo, A. S.; Szarka, I.; Szostak, A.; Szuba, M.; Tadel, M.; Tagridis, C.; Takahara, A.; Takahashi, J.; Tanabe, R.; Takaki, D. J. T.; Taureg, H.; Tauro, A.; Tavlet, M.; Munoz, G. T.; Telesca, A.; Terrevoli, C.; Thader, J.; Tieulent, R.; Tlusty, D.; Toia, A.; Tolyhy, T.; de Matos, C. T.; Torii, H.; Torralba, G.; Toscano, L.; Tosello, F.; Tournaire, A.; Traczyk, T.; Tribedy, P.; Troger, G.; Truesdale, D.; Trzaska, W. H.; Tsiledakis, G.; Tsilis, E.; Tsuji, T.; Tumkin, A.; Turrisi, R.; Turvey, A.; Tveter, T. S.; Tydesjo, H.; Tywoniuk, K.; Ulery, J.; Ullaland, K.; Uras, A.; Urban, J.; Urciuoli, G. M.; Usai, G. L.; Vacchi, A.; Vala, M.; Palomo, L. V.; Vallero, S.; van den Brink, A.; van der Kolk, N.; Vyvre, P. V.; van Leeuwen, M.; Vannucci, L.; Vargas, A.; Varma, R.; Vasiliev, A.; Vassiliev, I.; Vassiliou, M.; Vechernin, V.; Venaruzzo, M.; Vercellin, E.; Vergara, S.; Vernet, R.; Verweij, M.; Vetlitskiy, I.; Vickovic, L.; Viesti, G.; Vikhlyantsev, O.; Vilakazi, Z.; Baillie, O. V.; Vinogradov, A.; Vinogradov, L.; Vinogradov, Y.; Virgili, T.; Viyogi, Y. P.; Vodopianov, A.; Voloshin, K.; Voloshin, S.; Volpe, G.; von Haller, B.; Vranic, D.; Vrlakova, J.; Vulpescu, B.; Wagner, B.; Wagner, V.; Wallet, L.; Wan, R.; Wang, D.; Wang, Y.; Wang, Y.; Watanabe, K.; Wen, Q.; Wessels, J.; Wiechula, J.; Wikne, J.; Wilk, A.; Wilk, G.; Williams, M. C. S.; Willis, N.; Windelband, B.; Xu, C.; Yang, C.; Yang, H.; Yasnopolsky, A.; Yermia, F.; Yi, J.; Yin, Z.; Yokoyama, H.; Yoo, I. K.; Yuan, X.; Yurevich, V.; Yushmanov, I.; Zabrodin, E.; Zagreev, B.; Zalite, A.; Zampolli, C.; Zanevsky, Y.; Zaporozhets, S.; Zarochentsev, A.; Zavada, P.; Zbroszczyk, H.; Zelnicek, P.; Zenin, A.; Zepeda, A.; Zgura, I.; Zhalov, M.; Zhang, X.; Zhou, D.; Zhou, S.; Zhu, J.; Zichichi, A.; Zinchenko, A.; Zinovjev, G.; Zoccarato, Y.; Zychacek, V.; Zynovyev, M.; ALICE Collaboration: **Alignment of the ALICE Inner Tracking System with cosmic-ray tracks.** *Journal of Instrumentation* **5**: P03003, 2010. DOI:10.1088/1748-0221/5/03/p03003 OPEN ACCESS.

008 Ablikim, M.; Achasov, M. N.; An, L.; An, Q.; An, Z. H.; Bai, J. Z.; Ban, Y.; Berger, N.; Bian, J. M.; Boyko, I.; Briere, R. A.; Bytev, V.; Cai, X.; Cao, G. F.; Cao, X. X.; Chang, J. F.; Chelkov, G.; Chen, G.; Chen, H. S.; Chen, J. C.; Chen, L. P.; Chen, M. L.; Chen, P.; Chen, S. J.; Chen, Y. B.; Chu, Y. P.; Cronin-Hennessy, D.; Dai, H. L.; Dai, J. P.; Dedovich, D.; Deng, Z. Y.; Denysenko, I.; Destefanis, M.; Ding, Y.; Dong, L. Y.; Dong, M. Y.; Du, S. X.; Duan, M. Y.; Fang, J.; Feng, C. Q.; Fu, C. D.; Fu, J. L.; Gao, Y.; Geng, C.; Goetzen, K.; Gong, W. X.; Greco, M.; Grishin, S.; Gu, Y. T.; Guo, A. Q.; Guo, L. B.; Guo, Y. P.; Han, S. Q.; Harris, F. A.; He, K. L.; He, M.; He, Z. Y.; Heng, Y. K.; Hou, Z. L.; Hu, H. M.; Hu, J. F.; Hu, T.; Hu, X. W.; Huang, B.; Huang, G. M.; Huang, J. S.; Huang, X. T.; Huang, Y. P.; Ji, C. S.; Ji, Q.; Ji, X. B.; Ji, X. L.; Jia, L. K.; Jiang, L. L.; Jiang, X. S.; Jiao, J. B.; Jin, D. P.; Jin, S.; Komamiya, S.; Kuehn, W.; Lange, S.; Leung, J. K. C.; Li, C.; Li, C.; Li, D. M.; Li, F.; Li, G.; Li, H. B.; Li, J.; Li, J. C.; Li, L.; Li, L.; Li, Q. J.; Li, W. D.; Li, W. G.; Li, X. L.; Li, X. N.; Li, X. Q.; Li, X. R.; Li, Y. X.; Li, Z. B.; Liang, H.; Liang, T. R.; Liang, Y. T.; Liang, Y. F.; Liao, G. R.; Liao, X. T.; Liu, B. J.; Liu, C. L.; Liu, C. X.; Liu, C. Y.; Liu, F. H.; Liu, F.; Liu, F.; Liu, G. C.; Liu, H.; Liu, H. B.; Liu, H. M.; Liu, H. W.; Liu, J.; Liu, J. P.; Liu, K.; Liu, K. Y.; Liu, Q.; Liu, S. B.; Liu, X. H.; Liu, Y. B.; Liu, Y. F.; Liu, Y. W.; Liu, Y.; Liu, Z. A.; Lu, G. R.; Lu, J. G.; Lu, Q. W.; Lu, X. R.; Lu, Y. P.; Luo, C. L.; Luo, M. X.; Luo, T.; Luo, X. L.; Ma, C. L.; Ma, F. C.; Ma, H. L.; Ma, Q. M.; Ma, X.; Ma, X. Y.; Maggiora, M.; Mao, Y. J.; Mao, Z. P.; Min, J.; Mo, X. H.; Muchnoi, N. Y.; Nefedov, Y.; Ning, F. P.; Olsen, S. L.; Ouyang, Q.; Pelizacus, M.; Peters, K.; Ping, J. L.; Ping, R. G.; Poling, R.; Pun, C. S. J.; Qi, M.; Qian, S.; Qiao, C. F.; Qiu, J. F.; Rong, G.; Ruan, X. D.; Sarantsev, A.; Shao, M.; Shen, C. P.; Shen, X. Y.; Sheng, H. Y.; Sonoda, S.; Spataro, S.; Spruck, B.; Sun, D. H.; Sun, G. X.; Sun, J. F.; Sun, S. S.; Sun, X. D.; Sun, Y. J.; Sun, Y. Z.; Sun, Z. J.; Sun, Z. T.; Tang, C. J.; Tang, X.; Tang, X. F.; Tian, H. L.; Toth, D.; Varner, G. S.; Wan, X.; Wang, B. Q.; Wang, J. K.; Wang, K.; Wang, L. L.; Wang, L. S.; Wang, P.; Wang, P. L.; Wang, Q.; Wang, S. G.; Wang, X.

D.; Wang, X. L.; Wang, Y. D.; Wang, Y. F.; Wang, Y. Q.; Wang, Z.; Wang, Z. G.; Wang, Z. Y.; Wei, D. H.; Wen, S. P.; Wiedner, U.; Wu, L. H.; Wu, N.; Wu, Y. M.; Wu, Z.; Xiao, Z. J.; Xie, Y. G.; Xu, G. F.; Xu, G. M.; Xu, H.; Xu, M.; Xu, M.; Xu, X. P.; Xu, Y.; Xu, Z. Z.; Xue, Z.; Yan, L.; Yan, W. B.; Yan, Y. H.; Yang, H. X.; Yang, M.; Yang, P.; Yang, S. M.; Yang, Y. X.; Ye, M.; Ye, M. H.; Yu, B. X.; Yu, C. X.; Yu, L.; Yuan, C. Z.; Yuan, Y.; Zeng, Y.; Zhang, B. X.; Zhang, B. Y.; Zhang, C. C.; Zhang, D. H.; Zhang, H. H.; Zhang, H. Y.; Zhang, J. W.; Zhang, J. Y.; Zhang, J. Z.; Zhang, L.; Zhang, S. H.; Zhang, X. Y.; Zhang, Y.; Zhang, Y. H.; Zhang, Z. P.; Zhao, C.; Zhao, H. S.; Zhao, J. W.; Zhao, J. W.; Zhao, L.; Zhao, L.; Zhao, M. G.; Zhao, Q.; Zhao, S. J.; Zhao, T. C.; Zhao, X. H.; Zhao, Y. B.; Zhao, Z. G.; Zhemchugov, A.; Zheng, B.; Zheng, J. P.; Zheng, Y. H.; Zheng, Z. P.; Zhong, B.; Zhong, J.; Zhou, L.; Zhou, Z. L.; Zhu, C.; Zhu, K.; Zhu, K. J.; Zhu, Q. M.; Zhu, X. W.; Zhu, Y. S.; Zhu, Z. A.; Zhuang, J.; Zou, B. S.; Zou, J. H.; Zuo, J. X.; Zweber, P.; BESIII Collaboration: **Observation of a p(p)over-bar mass threshold enhancement in psi' → pi(+)pi(-)J/psi(J/psi → gamma p(p)over-bar) decay.** *Chinese Physics* **34**(4): 421–426, 2010.

009 Ablikim, M.; Achasov, M. N.; An, L.; An, Q.; An, Z. H.; Bai, J. Z.; Ban, Y.; Berger, N.; Bian, J. M.; Boyko, I.; Briere, R. A.; Bytev, V.; Cai, X.; Cao, G. F.; Cao, X. X.; Chang, J. F.; Chelkov, G.; Chen, G.; Chen, H. S.; Chen, J. C.; Chen, L. P.; Chen, M. L.; Chen, P.; Chen, S. J.; Chen, Y. B.; Chu, Y. P.; Cronin-Hennessy, D.; Dai, H. L.; Dai, J. P.; Dedovich, D.; Deng, Z. Y.; Denysenko, I.; Destefanis, M.; Ding, Y.; Dong, L. Y.; Dong, M. Y.; Du, S. X.; Duan, M. Y.; Fang, J.; Feng, C. Q.; Fu, C. D.; Fu, J. L.; Gao, Y.; Geng, C.; Goetzen, K.; Gong, W. X.; Greco, M.; Grishin, S.; Gu, Y. T.; Guo, A. Q.; Guo, L. B.; Guo, Y. P.; Han, S. Q.; Harris, F. A.; He, K. L.; He, M.; He, Z. Y.; Heng, Y. K.; Hou, Z. L.; Hu, H. M.; Hu, J. F.; Hu, T.; Hu, X. W.; Huang, B.; Huang, G. M.; Huang, J. S.; Huang, X. T.; Huang, Y. P.; Ji, C. S.; Ji, Q.; Ji, X. B.; Ji, X. L.; Jia, L. K.; Jiang, L. L.; Jiang, X. S.; Jiao, J. B.; Jin, D. P.; Jin, S.; Komamiya, S.; Kuehn, W.; Lange, S.; Leung, J. K. C.; Li, C.; Li, C.; Li, D. M.; Li, F.; Li, G.; Li, H. B.; Li, J.; Li, J. C.; Li, L.; Li, L.; Li, Q. J.; Li, W. D.; Li, W. G.; Li, X. L.; Li, X. N.; Li, X. Q.; Li, X. R.; Li, Y. X.; Li, Z. B.; Liang, H.; Liang, T. R.; Liang, Y. T.; Liang, Y. F.; Liao, G. R.; Liao, X. T.; Liu, B. J.; Liu, C. L.; Liu, C. X.; Liu, C. Y.; Liu, F. H.; Liu, F.; Liu, F.; Liu, G. C.; Liu, H.; Liu, H. B.; Liu, H. M.; Liu, H. W.; Liu, J.; Liu, J. P.; Liu, K.; Liu, K. Y.; Liu, Q.; Liu, S. B.; Liu, X. H.; Liu, Y. B.; Liu, Y. F.; Liu, Y. W.; Liu, Y.; Liu, Z. A.; Lu, G. R.; Lu, J. G.; Lu, Q. W.; Lu, X. R.; Lu, Y. P.; Luo, C. L.; Luo, M. X.; Luo, T.; Luo, X. L.; Ma, C. L.; Ma, F. C.; Ma, H. L.; Ma, Q. M.; Ma, X.; Ma, X. Y.; Maggiora, M.; Mao, Y. J.; Mao, Z. P.; Min, J.; Mo, X. H.; Muchnoi, N. Y.; Nefedov, Y.; Ning, F. P.; Olsen, S. L.; Ouyang, Q.; Pelizaeus, M.; Peters, K.; Ping, J. L.; Ping, R. G.; Poling, R.; Pun, C. S. J.; Qi, M.; Qian, S.; Qiao, C. F.; Qiu, J. F.; Rong, G.; Ruan, X. D.; Sarantsev, A.; Shao, M.; Shen, C. P.; Shen, X. Y.; Sheng, H. Y.; Sonoda, S.; Spataro, S.; Spruck, B.; Sun, D. H.; Sun, G. X.; Sun, J. F.; Sun, S. S.; Sun, X. D.; Sun, Y. J.; Sun, Y. Z.; Sun, Z. J.; Sun, Z. T.; Tang, C. J.; Tang, X.; Tang, X. F.; Tian, H. L.; Toth, D.; Varner, G. S.; Wan, X.; Wang, B. Q.; Wang, J. K.; Wang, K.; Wang, L. L.; Wang, L. S.; Wang, P.; Wang, P. L.; Wang, Q.; Wang, S. G.; Wang, X. D.; Wang, X. L.; Wang, Y. D.; Wang, Y. F.; Wang, Y. Q.; Wang, Z.; Wang, Z. G.; Wang, Z. Y.; Wei, D. H.; Wen, S. P.; Wiedner, U.; Wu, L. H.; Wu, N.; Wu, W.; Wu, Y. M.; Wu, Z.; Xiao, Z. J.; Xie, Y. G.; Xu, G. F.; Xu, G. M.; Xu, H.; Xu, M.; Xu, M.; Xu, X. P.; Xu, Y.; Xu, Z. Z.; Xue, Z.; Yan, L.; Yan, W. B.; Yan, Y. H.; Yang, H. X.; Yang, M.; Yang, P.; Yang, S. M.; Yang, Y. X.; Ye, M.; Ye, M. H.; Yu, B. X.; Yu, C. X.; Yu, L.; Yuan, C. Z.; Yuan, Y.; Zeng, Y.; Zhang, B. X.; Zhang, B. Y.; Zhang, C. C.; Zhang, D. H.; Zhang, H. H.; Zhang, H. Y.; Zhang, J. W.; Zhang, J. Y.; Zhang, J. Z.; Zhang, L.; Zhang, S. H.; Zhang, X. Y.; Zhang, Y.; Zhang, Y. H.; Zhang, Z. P.; Zhao, C.; Zhao, H. S.; Zhao, J. W.; Zhao, J. W.; Zhao, L.; Zhao, L.; Zhao, M. G.; Zhao, Q.; Zhao, S. J.; Zhao, T. C.; Zhao, X. H.; Zhao, Y. B.; Zhao, Z. G.; Zhemchugov, A.; Zheng, B.; Zheng, J. P.; Zheng, Y. H.; Zheng, Z. P.; Zhong, B.; Zhong, J.; Zhou, L.; Zhou, Z. L.; Zhu, C.; Zhu, K.; Zhu, K. J.; Zhu, Q. M.; Zhu, X. W.; Zhu, Y. S.; Zhu, Z. A.; Zhuang, J.; Zou, B. S.; Zou, J. H.; Zuo, J. X.; Zweber, P.; BESIII Collaboration: **Branching fraction measurements of chi(c0) and chi(c2) to pi(0)pi(0) and eta eta.** *Physical Review D, particles, fields, gravitation, and cosmology* **81**(5): 052005, 2010. DOI:10.1103/physrevd.81.052005

010 Ablikim, M.; Achasov, M. N.; An, L.; An, Q.; An, Z. H.; Bai, J. Z.; Ban, Y.; Berger, N.; Bian, J. M.; Boyko, I.; Briere, R. A.; Bytev, V.; Cai, X.; Cao, G. F.; Cao, X. X.; Chang, J. F.; Chelkov, G.; Chen, G.; Chen, H. S.; Chen, J. C.; Chen, L. P.; Chen, M. L.; Chen, P.; Chen, S. J.; Chen, Y. B.; Chu, Y. P.; Cronin-Hennessy, D.; Dai, H. L.; Dai, J. P.; Dedovich, D.; Deng, Z. Y.; Denysenko, I.; Destefanis, M.; Ding, Y.; Dong, L. Y.; Dong, M. Y.; Du, S. X.; Duan, M. Y.; Fang, J.; Feng, C. Q.; Fu, C. D.; Fu, J. L.; Gao, Y.; Geng, C.; Goetzen, K.; Gong, W. X.; Greco, M.; Grishin, S.; Gu, Y. T.; Guo, A. Q.; Guo, L. B.; Guo, Y. P.; Han, S. Q.; Harris, F. A.; He, K. L.; He, M.; He, Z. Y.; Heng, Y. K.; Hou, Z. L.; Hu, H. M.; Hu, J. F.; Hu, T.; Hu, X. W.; Huang, B.; Huang, G. M.; Huang, J. S.; Huang, X. T.; Huang, Y. P.; Ji, C. S.; Ji, Q.; Ji, X. B.; Ji, X. L.; Jia, L. K.; Jiang, L. L.; Jiang, X. S.; Jiao, J. B.; Jin, D. P.; Jin, S.; Komamiya, S.; Kuehn, W.; Lange, S.; Leung, J. K. C.; Li, C.; Li, C.; Li, D. M.; Li, F.; Li, G.; Li, H. B.; Li, J.; Li, J. C.; Li, L.; Li, L.; Li, Q. J.; Li, W. D.; Li, W. G.; Li, X. L.; Li, X. N.; Li, X. Q.; Li, X. R.; Li, Y. X.; Li, Z. B.; Liang, H.; Liang, T. R.; Liang, Y. T.; Liang, Y. F.; Liao, G. R.; Liao, X. T.; Liu, B. J.; Liu, C. L.; Liu, C. X.; Liu, C. Y.; Liu, F. H.; Liu, F.; Liu, F.; Liu, G. C.; Liu, H.; Liu, H. B.; Liu, H. M.; Liu, H. W.; Liu, J.; Liu, J. P.; Liu, K.; Liu, K. Y.; Liu, Q.; Liu, S. B.; Liu, X. H.; Liu, Y. B.; Liu, Y. F.; Liu, Y. W.; Liu, Y.; Liu, Z. A.; Lu, G. R.; Lu, J. G.; Lu, Q. W.; Lu, X. R.; Lu, Y. P.; Luo, C. L.; Luo, M. X.; Luo, T.; Luo, X. L.; Ma,

C. L.; Ma, F. C.; Ma, H. L.; Ma, Q. M.; Ma, X.; Ma, X. Y.; Maggiora, M.; Mao, Y. J.; Mao, Z. P.; Min, J.; Mo, X. H.; Muchnoi, N. Y.; Nefedov, Y.; Ning, F. P.; Olsen, S. L.; Ouyang, Q.; Pelizaeus, M.; Peters, K.; Ping, J. L.; Ping, R. G.; Poling, R.; Pun, C. S. J.; Qi, M.; Qian, S.; Qiao, C. F.; Qiu, J. F.; Rong, G.; Ruan, X. D.; Sarantsev, A.; Shao, M.; Shen, C. P.; Shen, X. Y.; Sheng, H. Y.; Sonoda, S.; Spataro, S.; Spruck, B.; Sun, D. H.; Sun, G. X.; Sun, J. F.; Sun, S. S.; Sun, X. D.; Sun, Y. J.; Sun, Y. Z.; Sun, Z. J.; Sun, Z. T.; Tang, C. J.; Tang, X.; Tang, X. F.; Tian, H. L.; Toth, D.; Varner, G. S.; Wan, X.; Wang, B. Q.; Wang, J. K.; Wang, K.; Wang, L. L.; Wang, L. S.; Wang, P.; Wang, P. L.; Wang, Q.; Wang, S. G.; Wang, X. D.; Wang, X. L.; Wang, Y. D.; Wang, Y. F.; Wang, Y. Q.; Wang, Z.; Wang, Z. G.; Wang, Z. Y.; Wei, D. H.; Wen, S. P.; Wiedner, U.; Wu, L. H.; Wu, N.; Wu, W.; Wu, Y. M.; Wu, Z.; Xiao, Z. J.; Xie, Y. G.; Xu, G. F.; Xu, G. M.; Xu, H.; Xu, M.; Xu, M.; Xu, X. P.; Xu, Y.; Xu, Z. Z.; Xue, Z.; Yan, L.; Yan, W. B.; Yan, Y. H.; Yang, H. X.; Yang, M.; Yang, P.; Yang, S. M.; Yang, Y. X.; Ye, M.; Ye, M. H.; Yu, B. X.; Yu, C. X.; Yu, L.; Yuan, C. Z.; Yuan, Y.; Zeng, Y.; Zhang, B. X.; Zhang, B. Y.; Zhang, C. C.; Zhang, D. H.; Zhang, H. H.; Zhang, H. Y.; Zhang, J. W.; Zhang, J. Y.; Zhang, J. Z.; Zhang, L.; Zhang, S. H.; Zhang, X. Y.; Zhang, Y.; Zhang, Y. H.; Zhang, Z. P.; Zhao, C.; Zhao, H. S.; Zhao, J. W.; Zhao, J. W.; Zhao, L.; Zhao, L.; Zhao, M. G.; Zhao, Q.; Zhao, S. J.; Zhao, T. C.; Zhao, X. H.; Zhao, Y. B.; Zhao, Z. G.; Zhemchugov, A.; Zheng, B.; Zheng, J. P.; Zheng, Y. H.; Zheng, Z. P.; Zhong, B.; Zhong, J.; Zhou, L.; Zhou, Z. L.; Zhu, C.; Zhu, K.; Zhu, K. J.; Zhu, Q. M.; Zhu, X. W.; Zhu, Y. S.; Zhu, Z. A.; Zhuang, J.; Zou, B. S.; Zou, J. H.; Zuo, J. X.; Zweber, P.; BESIII Collaboration: **Measurements of h(c) (P-1(1)) in psi ' Decays.** *Physical review letters* **104**(13): 132002, 2010. DOI:10.1103/physrevlett.104.132002

011 Abraamyan, K. U.; Baznat, M. I.; Friesen, A. V.; Gudima, K. K.; Kozhin, M. A.; Lebedev, S. A.; Nazarenko, M. A.; Nikitin, S. A.; Ososkov, G. A.; Reznikov, S. G.; Sissakian, A. N.; Sorin, A. S.; Toneev, V. D.: **Resonance structure in the gamma gamma invariant mass spectrum in pC- and dC-interactions.** *Physics of Particles and Nuclei* **41**(7): 1097–1100, 2010. DOI:10.1134/s1063779610070257

012 Achenbach, P.; Gayoso, C. A.; Bernauer, J. C.; Bianchin, S.; Bohm, R.; Borodina, O.; Bosnar, D.; Bozkurt, V.; Debenjak, L.; Denig, A.; Distler, M. O.; Esser, A.; Fonvieille, H.; Friscic, I.; Gokuzum, B.; Griessinger, K.; Kim, E.; Maas, F. E.; Makek, M.; Merkel, H.; Minami, S.; Muller, U.; Nakajima, D.; Nungesser, L.; Ozel-Tashenov, B.; Pochodzalla, J.; Potokar, M.; Rappold, C.; Saito, T. R.; Majos, S. S.; Schlimme, B. S.; Sirca, S.; Weinriefer, M.: **First measurements of Lambda and Sigma(0) hyperons in elementary electroproduction at MAMI.** *Nuclear physics A, Nuclear and hadronic physics* **835**(1): 313–316, 2010. DOI:10.1016/j.nuclphysa.2010.01.207

013 Ackermann, D.: **Superheavy elements-Achievements and challenges.** *Nuclear instruments & methods in physics research, Section A, Accelerators, spectrometers, detectors and associated equipment* **613**(3): 371–377, 2010. DOI:10.1016/j.nima.2009.09.079

014 Adamczewski-Musch, J.; Essel, H. G.; Kurz, N.; Linev, S. : **Dataflow Engine in DAQ Backbone DABC.** *IEEE transactions on nuclear science* **57**(2): 614–617, 2010. DOI:10.1109/tns.2010.2042174

015 Adimi, N.; Dominguez-Reyes, R.; Alcorta, M.; Bey, A.; Blank, B.; Borge, M. J. G.; Santos, F. D.; Dossat, C.; Fynbo, H. O. U.; Giovinazzo, J.; Knudsen, H. H.; Madurga, M.; Matea, I.; Perea, A.; Summerer, K.; Tengblad, O.; Thomas, J. C.: **Detailed beta-decay study of Ar-33.** *Physical review C, Nuclear physics* **81**(2): 024311, 2010. DOI:10.1103/physrevc.81.024311

016 Adonin, A.; Hollinger, R. ; Spadtke, P.: **Measurements of transverse ion beam emittance generated by high current ion sources at the GSI test injector facility HOSTI.** *Review of scientific instruments* **81**(2): 02B707, 2010. DOI:10.1063/1.3273066

017 Agakichiev, G.; Balanda, A.; Belver, D.; Belyaev, A. V.; Blanco, A.; Bohmer, M.; Boyard, J. L.; Braun-Munzinger, P.; Cabanelas, P.; Castro, E.; Chernenko, S.; Christ, T.; Destefanis, M.; Diaz, J.; Dohrmann, F.; Dybczak, A.; Fabbietti, L.; Fateev, O. V.; Finocchiaro, P.; Fonte, P.; Friese, J.; Frohlich, I.; Galatyuk, T.; Garzon, J. A.; Gernhauser, R.; Gil, A.; Gilardi, C.; Gobel, K.; Golubeva, M.; Gonzalez-Diaz, D.; Hennino, G. T.; Holzmann, R.; Iori, I.; Ivashkin, A.; Jurkovic, M.; Kampfer, B.; Karavicheva, T.; Kirschner, D.; Koenig, I.; Koenig, W.; Kolb, B. W.; Kotte, R.; Krizek, F.; Krucken, R.; Kuhn, W.; Kugler, A.; Kurepin, A.; Lang, S.; Lange, J. S.; Lapidus, K.; Liu, T.; Lopes, L.; Lorenz, M.; Maier, L.; Mangiarotti, A.; Markert, J.; Metag, V.; Michalska, B.; Michel, J.; Moriniere, E.; Mousa, J.; Muntz, C.; Naumann, L.; Otwinowski, J.; Pachmayer, Y. C.; Palka, M.; Parpottas, Y.; Pechenov, V.; Pechenova, O.; Pietraszko, J.; Przygoda, W.; Ramstein, B.; Reshetin, A.; Rustamov, A.; Sadovsky, A.; Salabura, P.; Schmah, A.; Schwab, E.; Sobolev, Y. G.; Spataro, S.; Spruck, B.; Strobele, H.; Stroth, J. ; Sturm, C.; Sudol, M.; Tarantola, A.; Teilab, K.; Tlusty, P.; Traxler, M.; Trebacz, R.; Tsertos, H.; Wagner, V.; Weber, M.; Wisniowski, M.; Wojcik, T.; Wustenfeld, J.; Yurevich, S.; Zanevsky, V. V.; Zhou, P.: **Origin of the low-mass electron pair excess in light nucleus-nucleus collisions.** *Physics letters B* **690**(2): 118–122, 2010. DOI:10.1016/j.physletb.2010.05.010

018 Agakishiev, G.; Balanda, A.; Bannier, B.; Bassini, R.; Belver, D.; Belyaev, A. V.; Blanco, A.; Bohmer, M.; Boyard, J. L.; Cabanelas, P.; Castro, E.; Chernenko, S.; Christ, T.; Destefanis, M.; Diaz, J.; Dohrmann, F.; Dybczak, A.; Eberl, T.; Epple, E.; Fabbietti, L.; Fateev, O. V.; Finocchiaro, P.; Fonte, P.; Friese, J.; Frohlich, I.; Galatyuk, T.;

Garzon, J. A.; Gernhauser, R.; Gil, A.; Gilardi, C.; Golubeva, M.; Gonzalez-Diaz, D.; Guber, F.; Gumberidze, M.; Heilmann, M.; Heinz, T.; Hennino, T.; Holzmann, R.; Iori, I.; Ivashkin, A.; Jurkovic, M.; Kampfer, B.; Kanaki, K.; Karavicheva, T.; Kirschner, D.; Koenig, I.; Koenig, W.; Kolb, B. W.; Kotte, R.; Krizek, F.; Krucken, R.; Kuhn, W.; Kugler, A.; Kurepin, A.; Lang, S.; Lange, J. S.; Lapidus, K.; Liu, T.; Lopes, L.; Lorenz, M.; Maier, L.; Mangiarotti, A.; Markert, J.; Metag, V.; Michalska, B.; Michel, J.; Mishra, D.; Moriniere, E.; Mousa, J.; Muntz, C.; Naumann, L.; Otwinowski, J.; Pachmayer, Y. C.; Palka, M.; Parpottas, Y.; Pechenov, V.; Pechenova, O.; Cavalcanti, T. P.; Pietraszko, J.; Przygoda, W.; Ramstein, B.; Reshetin, A.; Roy-Stephan, M.; Rustamov, A.; Sadovsky, A.; Sailer, B.; Salabura, P.; Schmah, A.; Schwab, E.; Siebenson, J.; Sobolev, Y. G.; Spataro, S.; Spruck, B.; Strobele, H.; Stroth, J. ; Sturm, C.; Tarantola, A.; Teilab, K.; Tlusty, P.; Traxler, M.; Trebacz, R.; Tsertos, H.; Wagner, V.; Weber, M.; Wendisch, C.; Wisniowski, M.; Wojcik, T.; Wustenfeld, J.; Yurevich, S.; Zanevsky, Y. V.; Zhou, P.; Zumbruch, P.; HADES Collaboration: **In-medium effects on K-0 mesons in relativistic heavy-ion collisions.** *Physical review C, Nuclear physics* **82**(4): 044907, 2010. DOI:10.1103/physrevc.82.044907

019 Agakishiev, G.; Balanda, A.; Bassini, R.; Belver, D.; Belyaev, A. V.; Blanco, A.; Bohmer, M.; Boyard, J. L.; Braun-Munzinger, P.; Cabanelas, P.; Castro, E.; Chernenko, S.; Christ, T.; Destefanis, M.; Diaz, J.; Dohrmann, F.; Dybczak, A.; Eberl, T.; Fabbietti, L.; Fateev, O. V.; Finocchiaro, P.; Fonte, P.; Friese, J.; Frohlich, I.; Galatyuk, T.; Garzon, J. A.; Gernhauser, R.; Gil, A.; Gilardi, C.; Golubeva, M.; Gonzalez-Diaz, D.; Guber, F.; Hennino, T.; Holzmann, R.; Iori, I.; Ivashkin, A.; Jurkovic, M.; Kampfer, B.; Kanaki, K.; Karavicheva, T.; Kirschner, D.; Koenig, I.; Koenig, W.; Kolb, B. W.; Kotte, R.; Krizek, F.; Krucken, R.; Kuhn, W.; Kugler, A.; Kurepin, A.; Lang, S.; Lange, J. S.; Lapidus, K.; Liu, T.; Lopes, L.; Lorenz, M.; Maier, L.; Mangiarotti, A.; Markert, J.; Metag, V.; Michalska, B.; Michel, J.; Mishra, D.; Moriniere, E.; Mousa, J.; Muntz, C.; Naumann, L.; Otwinowski, J.; Pachmayer, Y. C.; Palka, M.; Parpottas, Y.; Pechenov, V.; Pechenova, O.; Pietraszko, J.; Przygoda, W.; Ramstein, B.; Reshetin, A.; Roy-Stephan, M.; Rustamov, A.; Sadovsky, A.; Sailer, B.; Salabura, P.; Schmah, A.; Sobolev, Y. G.; Spataro, S.; Spruck, B.; Strobele, H.; Stroth, J. ; Sturm, C.; Sudol, M.; Tarantola, A.; Teilab, K.; Tlusty, P.; Traxler, M.; Trebacz, R.; Tsertos, H.; Wagner, V.; Weber, M.; Wendisch, C.; Wisniowski, M.; Wojcik, T.; Wuestenfeld, J.; Yurevich, S.; Zanevsky, Y. V.; Zhou, P.; Zumbruch, P.; HADES Collaboration: **Lambda-p femtoscopy in collisions of Ar + KCl at 1.76AGeV.** *Physical review C, Nuclear physics* **82**(2): 021901, 2010. DOI:10.1103/physrevc.82.021901

020 Akkelin, S. V.; Braun-Munzinger, P.; Sinyukov, Y. M.: **Thermal nature of charmonium transverse momentum spectra from Au-Au collisions at the highest energies available at the BNL Relativistic Heavy Ion Collider (RHIC).** *Physical review C, Nuclear physics* **81**(3): 034912, 2010. DOI:10.1103/physrevc.81.034912

021 Alekseev, M. G.; Alexakhin, V. Y.; Alexandrov, Y.; Alexeev, G. D.; Amoroso, A.; Austregesilo, A.; Badeek, B.; Balestra, F.; Barth, J.; Baum, G.; Bedfer, Y.; Bernhard, J.; Bertini, R.; Bettinelli, M.; Birsa, R.; Bisplinghoff, J.; Bordalo, P.; Bradamante, F.; Bravar, A.; Bressan, A.; Brona, G.; Burtin, E.; Bussa, M. P.; Chaberny, D.; Chiosso, M.; Chung, S. U.; Cicuttin, A.; Colantoni, M.; Crespo, M. L.; Dalla Torre, S.; Das, S.; Dasgupta, S. S.; Denisov, O. Y.; Dhara, L.; Diaz, V.; Donskov, S. V.; Doshita, N.; Duic, V.; Dunnweber, W.; Efremov, A.; El Alaoui, A.; Eversheim, P. D.; Eyrich, W.; Faessler, M.; Ferrero, A.; Filin, A.; Finger, M.; Finger, M.; Fischer, H.; Franco, C.; Friedrich, J. M.; Garfagnini, R.; Gautheron, F.; Gavrichtchouk, O. P.; Gazda, R.; Gerassimov, S.; Geyer, R.; Giorgi, M.; Gnesi, I.; Gobbo, B.; Goertz, S.; Grabmuller, S.; Grasso, A.; Grube, B.; Gushterski, R.; Guskov, A.; Haas, F.; von Harrach, D.; Hasegawa, T.; Heinsius, F. H.; Herrmann, F.; Hess, C.; Hinterberger, F.; Horikawa, N.; Hoppner, C.; d'Hose, N.; Ilgner, C.; Ishimoto, S.; Ivanov, O.; Ivanshin, Y.; Iwata, T.; Jahn, R.; Jasinski, P.; Jegou, G.; Joosten, R.; Kabuss, E.; Kang, D.; Ketzer, B.; Khaustov, G. V.; Khokhlov, Y. A.; Kisselev, Y.; Klein, F.; Klimaszewski, K.; Koblitz, S.; Koivuniemi, J. H.; Kolosov, V. N.; Kondo, K.; Konigsmann, K.; Konopka, R.; Konorov, I.; Konstantinov, V. F.; Korzenev, A.; Kotzinian, A. M.; Kouznetsov, O.; Kowalik, K.; Kramer, M.; Kral, A.; Kroumchtein, Z. V.; Kuhn, R.; Kunne, F.; Kurek, K.; Lauser, L.; Le Goff, J. M.; Lednev, A. A.; Lehmann, A.; Levorato, S.; Lichtenstadt, J.; Liska, T.; Maggiora, A.; Maggiora, M.; Magnon, A.; Mallot, G. K.; Mann, A.; Marchand, C.; Martin, A.; Marzec, J.; Massmann, F.; Matsuda, T.; Meyer, W.; Michigami, T.; Mikhailov, Y. V.; Moinester, M. A.; Mutter, A.; Nagaytsev, A.; Nagel, T.; Nassalski, J.; Negrini, T.; Nerling, F.; Neubert, S.; Neyret, D.; Nikolaenko, V. I.; Nunes, A. S.; Olshevsky, A. G.; Ostrick, M.; Padee, A.; Panknin, R.; Panzieri, D.; Parsamyan, B.; Paul, S.; Pawlukiewicz-Kaminska, B.; Perevalova, E.; Pesaro, G.; Peshekhonov, D. V.; Piragino, G.; Platchkov, S.; Pochodzalla, J.; Polak, J.; Polyakov, V. A.; Pontecorvo, G.; Pretz, J.; Quintans, C.; Rajotte, J. F.; Ramos, S.; Rapatsky, V.; Reicherz, G.; Richter, A.; Robinet, F.; Rocco, E.; Rondio, E.; Ryabchikov, D. I.; Samoylenko, V. D.; Sandacz, A.; Santos, H.; Sapozhnikov, M. G.; Sarkar, S.; Savin, I. A.; Sbrizzai, G.; Schiavon, P.; Schill, C.; Schluter, T.; Schmitt, L.; Schopferer, S.; Schroder, W.; Shevchenko, O. Y.; Siebert, H. W.; Silva, L.; Sinha, L.; Sissakian, A. N.; Slunecka, M.; Smirnov, G. I.; Sosio, S.; Sozzi, F.; Srnka, A.; Stolarski, M.; Sulc, M.; Sulej, R.; Takekawa, S.; Tessaro, S.; Tessarotto, F.; Teufel, A.; Tkatchev, L. G.; Uhl, S.; Uman, I.; Virius, M.; Vlassov, N. V.; Vossen, A.; Weitzel, Q.; Windmolders, R.; Wislicki, W.; Wollny, H.; Zaremba, K.; Zavertyaev, M.; Zemlyanichkina, E.; Ziembicki, M.; Zhao, J.; Zhuravlev, N.; Zvyagin, A.; COM-

PASS Collaboration: **Azimuthal asymmetries of charged hadrons produced by high-energy muons scattered off longitudinally polarised deuterons.** *The European physical journal: C, Particles and fields* **70**(1): 39–49, 2010. DOI:10.1140/epjc/s10052-010-1461-9

022 Alekseev, M. G.; Alexakhin, V. Y.; Alexandrov, Y.; Alexeev, G. D.; Amoroso, A.; Austregesilo, A.; Badelek, B.; Balestra, F.; Ball, J.; Barth, J.; Baum, G.; Bedfer, Y.; Bernhard, J.; Bertini, R.; Bettinelli, M.; Birsa, R.; Bisplinghoff, J.; Bordalo, P.; Bradamante, F.; Bravar, A.; Bressan, A.; Brona, G.; Burtin, E.; Bussa, M. P.; Chaberny, D.; Chiosso, M.; Chung, S. U.; Cicuttin, A.; Colantoni, M.; Crespo, M. L.; Dalla Torre, S.; Das, S.; Dasgupta, S. S.; Denisov, O. Y.; Dhara, L.; Diaz, V.; Donskov, S. V.; Doshita, N.; Duic, V.; Dunnweber, W.; Efremov, A.; El Alaoui, A.; Elia, C.; Eversheim, P. D.; Eyrich, W.; Faessler, M.; Ferrero, A.; Filin, A.; Finger, M.; Finger, M.; Fischer, H.; Franco, C.; Friedrich, J. M.; Garfagnini, R.; Gautheron, F.; Gavrichtchouk, O. P.; Gazda, R.; Gerassimov, S.; Geyer, R.; Giorgi, M.; Gnesi, I.; Gobbo, B.; Goertz, S.; Grabmuller, S.; Grasso, A.; Grube, B.; Gushterski, R.; Guskov, A.; Haas, F.; von Harrach, D.; Hasegawa, T.; Heinsius, F. H.; Hermann, R.; Herrman, F.; Hess, C.; Hinterberger, F.; Horikawa, N.; Hoppner, C.; d'Hose, N.; Ilgner, C.; Ishimoto, S.; Ivanov, O.; Ivanshin, Y.; Iwata, T.; Jahn, R.; Jasinski, P.; Jegou, G.; Joosten, R.; Kabuss, E.; Kafer, W.; Kang, D.; Ketzer, B.; Khaustov, G. V.; Khokhlov, Y. A.; Kisselev, Y.; Klein, F.; Klimaszewski, K.; Koblitz, S.; Koivuniemi, J. H.; Kolosov, V. N.; Kondo, K.; Konigsmann, K.; Konopka, R.; Konorov, I.; Konstantinov, V. F.; Korzenev, A.; Kotzinian, A. M.; Kouznetsov, O.; Kowalik, K.; Kramer, M.; Kral, A.; Kroumchtein, Z. V.; Kuhn, R.; Kunne, F.; Kurek, K.; Lauser, L.; Le Goff, J. M.; Lednev, A. A.; Lehmann, A.; Levorato, S.; Lichtenstadt, J.; Liska, T.; Maggiora, A.; Maggiora, M.; Magnon, A.; Mallot, G. K.; Mann, A.; Marchand, C.; Martin, A.; Marzec, J.; Massmann, F.; Matsuda, T.; Meyer, W.; Michigami, T.; Mikhailov, Y. V.; Moinester, M. A.; Mutter, A.; Nagaytsev, A.; Nagel, T.; Nassalski, J.; Negrini, T.; Nerling, F.; Neubert, S.; Neyret, D.; Nikolaenko, V. I.; Nunes, A. S.; Olshevsky, A. G.; Ostrick, M.; Padee, A.; Panknin, R.; Panzieri, D.; Parsamyan, B.; Paul, S.; Pawlukiewicz-Kaminska, B.; Perevalova, E.; Pesaro, G.; Peshekhonov, D. V.; Piragino, G.; Platchkov, S.; Pochodzalla, J.; Polak, J.; Polyakov, V. A.; Pontecorvo, G.; Pretz, J.; Quintans, C.; Rajotte, J. F.; Ramos, S.; Rapatsky, V.; Reicherz, G.; Richter, A.; Robinet, F.; Rocco, E.; Rondio, E.; Ryabchikov, D. I.; Samoylenko, V. D.; Sandacz, A.; Santos, H.; Sapozhnikov, M. G.; Sarkar, S.; Savin, I. A.; Sbrizzai, G.; Schiavon, P.; Schill, C.; Schluter, T.; Schmitt, L.; Schopferer, S.; Schroder, W.; Shevchenko, O. Y.; Siebert, H. W.; Silva, L.; Sinha, L.; Sissakian, A. N.; Slunecka, M.; Smirnov, G. I.; Sosio, S.; Sozzi, F.; Srnka, A.; Stolarsk, M.; Sulc, M.; Sulej, R.; Takekawa, S.; Tessaro, S.; Tessarotto, F.; Teufel, A.; Tkatchev, L. G.; Uhl, S.; Uman, I.; Virius, M.; Vlassov, N. V.; Vossen, A.; Weitzel, Q.; Windmolders, R.; Wislicki, W.; Wollny, H.; Zaremba, K.; Zavertyaev, M.; Zemlyanichkina, E.; Ziembicki, M.; Zhao, J.; Zhuravlev, N.; Zvyagin, A.; COMPASS Collaboration: **Measurement of the Collins and Sivers asymmetries on transversely polarised protons.** *Physics letters B* **692**(4): 240–246, 2010. DOI:10.1016/j.physletb.2010.08.001

023 Alekseev, M. G.; Alexakhin, V. Y.; Alexandrov, Y.; Alexeev, G. D.; Amoroso, A.; Austregesilo, A.; Badelek, B.; Balestra, F.; Ball, J.; Barth, J.; Baum, G.; Bedfer, Y.; Bernhard, J.; Bertini, R.; Bettinelli, M.; Birsa, R.; Bisplinghoff, J.; Bordalo, P.; Bradamante, F.; Bravar, A.; Bressan, A.; Brona, G.; Burtin, E.; Bussa, M. P.; Chaberny, D.; Cotic, D.; Chiosso, M.; Chung, S. U.; Cicuttin, A.; Colantoni, M.; Crespo, M. L.; Dalla Torre, S.; Das, S.; Dasgupta, S. S.; Denisov, O. Y.; Dhara, L.; Diaz, V.; Donskov, S. V.; Doshita, N.; Duic, V.; Dunnweber, W.; Efremov, A.; El Alaoui, A.; Eversheim, P. D.; Eyrich, W.; Faessler, M.; Ferrero, A.; Filin, A.; Finger, M.; Finger, M.; Fischer, H.; Franco, C.; Friedrich, J. M.; Garfagnini, R.; Gautheron, F.; Gavrichtchouk, O. P.; Gazda, R.; Gerassimov, S.; Geyer, R.; Giorgi, M.; Gnesi, I.; Gobbo, B.; Goertz, S.; Grabmuller, S.; Grasso, A.; Grube, B.; Gushterski, R.; Guskov, A.; Haas, F.; von Harrach, D.; Hasegawa, T.; Heinsius, F. H.; Hermann, R.; Herrmann, F.; Hess, C.; Hinterberger, F.; Horikawa, N.; Hoppner, C.; d'Hose, N.; Ilgner, C.; Ishimoto, S.; Ivanov, O.; Ivanshin, Y.; Iwata, T.; Jahn, R.; Jasinski, P.; Jegou, G.; Joosten, R.; Kabuss, E.; Kafer, W.; Kang, D.; Ketzer, B.; Khaustov, G. V.; Khokhlov, Y. A.; Kisselev, Y.; Klein, F.; Klimaszewski, K.; Koblitz, S.; Koivuniemi, J. H.; Kolosovu, V. N.; Kondo, K.; Konigsmann, K.; Konopka, R.; Konorov, I.; Konstantinov, V. F.; Korzenev, A.; Kotzinian, A. M.; Kouznetsov, O.; Kowalik, K.; Kramer, M.; Kral, A.; Kroumchtein, Z. V.; Kuhn, R.; Kunne, F.; Kurek, K.; Lauser, L.; Le Goff, J. M.; Lednev, A. A.; Lehmann, A.; Levorato, S.; Lichtenstadt, J.; Liska, T.; Maggiora, A.; Maggiora, M.; Magnon, A.; Mallot, G. K.; Mann, A.; Marchand, C.; Marroncle, J.; Martin, A.; Marzec, J.; Massmann, F.; Matsuda, T.; Meyer, W.; Michigami, T.; Mikhailov, Y. V.; Moinester, M. A.; Mutter, A.; Nagaytsev, A.; Nagel, T.; Nassalski, J.; Negrini, T.; Nerling, F.; Neubert, S.; Neyret, D.; Nikolaenko, V. I.; Nunes, A. S.; Olshevsky, A. G.; Ostrick, M.; Padee, A.; Panknin, R.; Panzieri, D.; Parsamyan, B.; Paul, S.; Pawlukiewicz-Kaminska, B.; Perevalova, E.; Pesaro, G.; Peshekhonov, D. V.; Piragino, G.; Platchkov, S.; Pochodzalla, J.; Polak, J.; Polyakov, V. A.; Pontecorvo, G.; Pretz, J.; Quintans, C.; Rajotte, J. F.; Ramos, S.; Rapatsky, V.; Reicherz, G.; Richter, A.; Robinet, F.; Rocco, E.; Rondio, E.; Ryabchikov, D. I.; Samoylenko, V. D.; Sandacz, A.; Santos, H.; Sapozhnikov, M. G.; Sarkar, S.; Savin, I. A.; Sbrizzai, G.; Schiavon, P.; Schill, C.; Schluter, T.; Schmitt, L.; Schopferer, S.; Schroder, W.; Shevchenko, O. Y.; Siebert, H. W.; Silva, L.; Sinha, L.; Sissakian, A. N.; Slunecka, M.; Smirnov, G. I.; Sosio, S.; Sozzi, F.; Srnka, A.; Stolarski, M.; Sulc, M.; Sulej, R.; Takekawa, S.; Tessaro, S.; Tessarotto, F.; Teufel, A.;

Tkatchev, L. G.; Uhl, S.; Uman, I.; Virius, M.; Vlassov, N. V.; Vossen, A.; Weitzel, Q.; Windmolders, R.; Wislicki, W.; Wollny, H.; Zaremba, K.; Zavertyaev, M.; Zemlyanichkina, E.; Ziembicki, M.; Zhao, J.; Zhuravlev, N.; Zvyagin, A.; COMPASS Collaboration: **The spin-dependent structure function of the proton g(1)(p) and a test of the Bjorken sum rule.** *Physics letters B* **690**(5): 466–472, 2010. DOI:10.1016/j.physletb.2010.05.069

024 Alekseev, M. G.; Alexakhin, V. Y.; Alexandrov, Y.; Alexeev, G. D.; Amoroso, A.; Austregesilo, A.; Badelek, B.; Balestra, F.; Barth, J.; Baum, G.; Bedfer, Y.; Bernhard, J.; Bertini, R.; Bettinelli, M.; Birsa, R.; Bisplinghoff, J.; Bordalo, P.; Bradamante, F.; Bravar, A.; Bressan, A.; Brona, G.; Burtin, E.; Bussa, M. P.; Chaberny, D.; Chiosso, M.; Chung, S. U.; Cicuttin, A.; Colantoni, M.; Crespo, M. L.; Dalla Torre, S.; Das, S.; Dasgupta, S. S.; Denisov, O. Y.; Dhara, L.; Diaz, V.; Donskov, S. V.; Doshita, N.; Duic, V.; Dunnweber, W.; Efremov, A.; El Alaoui, A.; Eversheim, P. D.; Eyrich, W.; Faessler, M.; Ferrero, A.; Filin, A.; Finger, M.; Finger, M.; Fischer, H.; Franco, C.; Friedrich, J. M.; Garfagnini, R.; Gautheron, F.; Gavrichtchouk, O. P.; Gazda, R.; Gerassimov, S.; Geyer, R.; Giorgi, M.; Gnesi, I.; Gobbo, B.; Goertz, S.; Grabmuller, S.; Grasso, A.; Grube, B.; Gushterski, R.; Guskov, A.; Haas, F.; von Harrach, D.; Hasegawa, T.; Heinsius, F. H.; Herrmann, F.; Hess, C.; Hinterberger, F.; Horikawa, N.; Hoppner, C.; d'Hose, N.; Ilgner, C.; Ishimoto, S.; Ivanov, O.; Ivanshin, Y.; Iwata, T.; Jahn, R.; Jasinski, P.; Jegou, G.; Joosten, R.; Kabuss, E.; Kang, D.; Ketzer, B.; Khaustov, G. V.; Khokhlov, Y. A.; Kisselev, Y.; Klein, F.; Klimaszewski, K.; Koblitz, S.; Koivuniemi, J. H.; Kolosov, V. N.; Kondo, K.; Konigsmann, K.; Konopka, R.; Konorov, I.; Konstantinov, V. F.; Korzenev, A.; Kotzinian, A. M.; Kouznetsov, O.; Kowalik, K.; Kramer, M.; Kral, A.; Kroumchtein, Z. V.; Kuhn, R.; Kunne, F.; Kurek, K.; Lauser, L.; Le Goff, J. M.; Lednev, A. A.; Lehmann, A.; Levorato, S.; Lichtenstadt, J.; Liska, T.; Maggiora, A.; Maggiora, M.; Magnon, A.; Makke, N.; Mallot, G. K.; Mann, A.; Marchand, C.; Martin, A.; Marzec, J.; Massmann, F.; Matsuda, T.; Meyer, W.; Michigami, T.; Mikhailov, Y. V.; Moinester, M. A.; Mutter, A.; Nagaytsev, A.; Nagel, T.; Nassalski, J.; Negrini, T.; Nerling, F.; Neubert, S.; Neyret, D.; Nikolaenko, V. I.; Nunes, A. S.; Olshevsky, A. G.; Ostrick, M.; Padee, A.; Panknin, R.; Panzieri, D.; Parsamyan, B.; Paul, S.; Pawlukiewicz-Kaminska, B.; Perevalova, E.; Pesaro, G.; Peshekhonov, D. V.; Piragino, G.; Platchkov, S.; Pochodzalla, J.; Polak, J.; Polyakov, V. A.; Pontecorvo, G.; Pretz, J.; Quintans, C.; Rajotte, J. F.; Ramos, S.; Rapatsky, V.; Reicherz, G.; Richter, A.; Robinet, F.; Rocco, E.; Rondio, E.; Ryabchikov, D. I.; Samoylenko, V. D.; Sandacz, A.; Santos, H.; Sapozhnikov, M. G.; Sarkar, S.; Savin, I. A.; Sbrizzai, G.; Schiavon, P.; Schill, C.; Schlutter, T.; Schmitt, L.; Schopferer, S.; Schroder, W.; Shevchenko, O. Y.; Siebert, H. W.; Silva, L.; Sinha, L.; Sissakian, A. N.; Slunecka, M.; Smirnov, G. I.; Sosio, S.; Sozzi, F.; Srnka, A.; Stolarski, M.; Sulc, M.; Sulej, R.; Takekawa, S.; Tessaro, S.; Tessarotto, F.; Teufel, A.; Tkatchev, L. G.; Uhl, S.; Uman, I.; Virius, M.; Vlassov, N. V.; Vossen, A.; Weitzel, Q.; Windmolders, R.; Wislicki, W.; Wollny, H.; Zaremba, K.; Zavertyaev, M.; Zemlyanichkina, E.; Ziembicki, M.; Zhao, J.; Zhuravlev, N.; Zvyagin, A.: **Quark helicity distributions from longitudinal spin asymmetries in muon-proton and muon-deuteron scattering.** *Physics letters B* **693**(3): 227–235, 2010. DOI:10.1016/j.physletb.2010.08.034

025 Algora, A.; Jordan, D.; Tain, J. L.; Rubio, B.; Agramunt, J.; Perez-Cerdan, A. B.; Molina, F.; Caballero, L.; Nacher, E.; Krasznahorkay, A.; Hunyadi, M. D.; Gulyas, J.; Vitez, A.; Csatlos, M.; Csige, L.; Aysto, J. A.; Penttila, H.; Moore, I. D.; Eronen, T.; Jokinen, A.; Nieminen, A.; Hakala, J.; Karvonen, P.; Kankainen, A.; Saastamoinen, A.; Rissanen, J.; Kessler, T.; Weber, C.; Ronkainen, J.; Rahaman, S.; Elomaa, V.; Rinta-Antila, S.; Hager, U.; Sonoda, T.; Burkard, K.; Huller, W.; Batist, L.; Gelletly, W.; Nichols, A. L.; Yoshida, T.; Sonzogni, A. A.; Perajarvi, K.: **Reactor Decay Heat in Pu-239: Solving the gamma Discrepancy in the 4-3000-s Cooling Period.** *Physical review letters* **105**(20): 202501, 2010. DOI:10.1103/physrevlett.105.202501

026 Alme, J.; Andres, Y.; Appelshauser, H.; Bablok, S.; Bialas, N.; Bolgen, R.; Bonnes, U.; Bramm, R.; Braun-Munzinger, P.; Campagnolo, R.; Christiansen, P.; Dobrin, A.; Engster, C.; Fehlker, D.; Foka, Y.; Frankenfeld, U.; Gaardhoje, J. J.; Garabatos, C. ; Glassel, P.; Gutierrez, C. G.; Gros, P.; Gustafsson, H. A.; Helstrup, H.; Hoch, M.; Ivanov, M.; Janik, R.; Junique, A.; Kalweit, A.; Keidel, R.; Kniege, S.; Kowalski, M.; Larsen, D. T.; Lesenechal, Y.; Lenoir, P.; Lindegaard, N.; Lippmann, C. ; Mager, M.; Mast, M.; Matyja, A.; Munkejord, M.; Musa, L.; Nielsen, B. S.; Nikolic, V.; Oeschler, H.; Olsen, E. K.; Oskarsson, A.; Osterman, L.; Pikna, M.; Rehman, A.; Renault, G.; Renfordt, R.; Rossegger, S.; Rohrich, D.; Roed, K.; Richter, M. ; Rueshmann, G.; Rybicki, A.; Sann, H.; Schmidt, H. R.; Siska, M.; Sitar, B.; Soegaard, C.; Soltveit, H. K.; Soyk, D.; Stachel, J.; Stelzer, H.; Stenlund, E.; Stock, R.; Strmen, P.; Szarka, I.; Ullaland, K.; Vranic, D.; Veenhof, R.; Westergaard, J.; Wiechula, J.; Windelband, B.: **The ALICE TPC, a large 3-dimensional tracking device with fast readout for ultra-high multiplicity events.** *Nuclear instruments & methods in physics research, Section A, Accelerators, spectrometers, detectors and associated equipment* **622**(1): 316–367, 2010. DOI:10.1016/j.nima.2010.04.042

027 Alt, C.; Anticic, T.; Baatar, B.; Barna, D.; Bartke, J.; Betev, L.; Bialkowska, H.; Blume, C.; Boimska, B.; Botje, M.; Bracinik, J.; Buncic, P.; Cerny, V.; Christakoglou, P.; Chung, P.; Chvala, O.; Cramer, J. G.; Csato, P.; Dinkelaker, P.; Eckardt, V.; Flier, D.; Fodor, Z.; Foka, P.; Friese, V. ; Gal, J.; Gazdzicki, M.; Genchev, V.; Gladysz, E.; Grebieszkow, K.; Hegyi, S.; Hohne, C.; Kadija, K.; Karev, A.; Kniege, S.; Kolesnikov, V. I.; Korus, R.; Kowalski, M.; Kreps, M.; Laszlo, A.; Lacey, R.; van Leeuwen, M.; Levai,

P.; Litov, L.; Lungwitz, B.; Makariev, M.; Malakhov, A. I.; Mateev, M.; Melkumov, G. L.; Mitrovski, M.; Molnar, J.; Mrowczynski, S.; Nicolic, V.; Palla, G.; Panagiotou, A. D.; Panayotov, D.; Petridis, A.; Peryt, W.; Pikna, M.; Pikna, M.; Pluta, J.; Prindle, D.; Puhlhofer, F.; Renfordt, R.; Roland, C.; Roland, G.; Rybczynski, M.; Rybicki, A.; Sandoval, A.; Schmitz, N.; Schuster, T.; Seyboth, P.; Sikler, F.; Sitar, B.; Skrzypczak, E.; Slodkowski, M.; Stefanek, G.; Stock, R.; Strobele, H.; Susa, T.; Szentpetery, I.; Sziklai, J.; Szuba, M.; Szymanski, P.; Trubnikov, V.; Varga, D.; Vassiliou, M.; Veres, G. I.; Vesztergombi, G.; Vranic, D.; Wlodarczyk, Z.; Wojtaszek, A.; Yoo, I. K.; Alexander, J. M.; Danielewicz, P.; Kisiel, A.; Pratt, S.: **Three-dimensional two-pion source image from Pb plus Pb collisions at root S-NN17.3 GeV: New constraints for source breakup dynamics NA49 Collaboration.** *Physics letters B* **685**(1): 41–46, 2010. DOI:10.1016/j.physletb.2010.01.029

028 Alvarez-Pol, H.; Benlliure, J.; Casarejos, E.; Audouin, L.; Cortina-Gil, D.; Enqvist, T.; Fernandez-Dominguez, B.; Junghans, A. R.; Jurado, B.; Napolitani, P.; Pereira, J.; Rejmund, F.; Schmidt, K. H.; Yordanov, O.: **Production of new neutron-rich isotopes of heavy elements in fragmentation reactions of U-238 projectiles at 1A GeV.** *Physical review C, Nuclear physics* **82**(4): 041602, 2010. DOI:10.1103/physrevc.82.041602

029 Andersson, L. L.; Rudolph, D.; Golubev, P.; Herzberg, R. D.; Hoischen, R.; Merchan, E.; Ackermann, D. ; Dullmann, C. E.; Eberhardt, K.; Even, J.; Gerl, J. ; Hessberger, F. P.; Jager, E.; Khuyagbaatar, J.; Kojouharov, I.; Kratz, J. V.; Krier, J.; Kurz, N.; Prokopowicz, W.; Schadel, M.; Schaffner, H.; Schausten, B.; Schimpf, E.; Semchenkov, A.; Turler, A.; Wollersheim, H. J.; Yakushev, A.; Thorle-Pospiech, P.; Hartmann, W.; Hubner, A.; Lommel, B.; Kindler, B. ; Steiner, J.: **TASISpec-A highly efficient multi-coincidence spectrometer for nuclear structure investigations of the heaviest nuclei.** *Nuclear instruments & methods in physics research, Section A, Accelerators, spectrometers, detectors and associated equipment* **622**(1): 164–170, 2010. DOI:10.1016/j.nima.2010.06.243

030 Andreyev, A. N.; Antalic, S. ; Ackermann, D. ; Cocolios, T. E.; Comas, V. F.; Elseviers, J.; Franchoo, S.; Heinz, S.; Heredia, J. A.; Hessberger, F. P.; Hofmann, S. ; Huyse, M.; Khuyagbaatar, J.; Kojouharov, I.; Kindler, B. ; Lommel, B.; Mann, R.; Page, R. D.; Rinta-Antila, S.; Sapple, P. J.; Saro, S.; Van Duppen, P.; Venhart, M.; Watkins, H. V.: **The new isotope Pb-179 and alpha-decay properties of Tl-179(m).** *Journal of physics G, Nuclear and particle physics* **37**(3): 035102, 2010. DOI:10.1088/0954-3899/37/3/035102

031 Andronic, A. ; Blaschke, D.; Braun-Munzinger, P.; Cleymans, J.; Fukushima, K.; McLerran, L. D.; Oeschler, H.; Pisarski, R. D.; Redlich, K.; Sasaki, C.; Satz, H.; Stachel, J.: **Hadron production in ultra-relativistic nuclear collisions: Quarkyonic matter and a triple point in the phase diagram of QCD.** *Nuclear physics A, Nuclear and hadronic physics* **837**(1): 65–86, 2010. DOI:10.1016/j.nuclphysa.2010.02.005

032 Andronic, A. ; Braun-Munzinger, P.; Redlich, K.; Stachel, J.: **Heavy quark(onium) at LHC: the statistical hadronization case.** *Journal of physics G, Nuclear and particle physics* **37**(9): 094014, 2010. DOI:10.1088/0954-3899/37/9/094014

033 Andronic, A. ; Braun-Munzinger, P.; Stachel, J.: **The horn, the hadron mass spectrum and the QCD phase diagram - the statistical model of hadron production in central nucleus-nucleus collisions.** *Nuclear physics A, Nuclear and hadronic physics* **834**(1): 237C–240C, 2010. DOI:10.1016/j.nuclphysa.2009.12.048

034 Antalic, S. ; Hesserger, F. P.; Hofmann, S. ; Ackermann, D. ; Heinz, S.; Kindler, B. ; Kojouharov, I.; Kuusiniemi, P.; Leino, M.; Lommel, B.; Mann, R.; Saro, S.: **Studies of neutron-deficient mendelevium isotopes at SHIP.** *The European physical journal A, Hadrons and nuclei* **43**(1): 35–44, 2010. DOI:10.1140/epja/i2009-10896-0

035 Anticic, T.; Baatar, B.; Barna, D.; Bartke, J.; Betev, L.; Bialkowska, H.; Blume, C.; Boimska, B.; Botje, M.; Bracinik, J.; Buncic, P.; Cerny, V.; Christakoglou, P.; Chung, P.; Chvala, O.; Cramer, J. G.; Dinkelaker, P.; Eckardt, V.; Fodor, Z.; Foka, P.; Friese, V. ; Gazdzicki, M.; Genchev, V.; Grebieszkow, K.; Hohne, C.; Kadija, K.; Karev, A.; Kolesnikov, V. I.; Kowalski, M.; Kreps, M.; Laszlo, A.; Lacey, R.; van Leeuwen, M.; Lungwitz, B.; Makariev, M.; Malakhov, A. I.; Mateev, M.; Melkumov, G. L.; Mitrovski, M.; Mrowczynski, S.; Nicolic, V.; Palla, G.; Panagiotou, A. D.; Petridis, A.; Peryt, W.; Pikna, M.; Pluta, J.; Prindle, D.; Puhlhofer, F.; Renfordt, R.; Roland, C.; Roland, G.; Rybczynski, M.; Rybicki, A.; Sandoval, A.; Schmitz, N.; Schuster, T.; Seyboth, P.; Sikler, F.; Sitar, B.; Skrzypczak, E.; Slodkowski, M.; Stefanek, G.; Stock, R.; Strobele, H.; Susa, T.; Szuba, M.; Varga, D.; Vassiliou, M.; Veres, G. I.; Vesztergombi, G.; Vranic, D.; Wlodarczyk, Z.; Antoniou, N. G.; Diakonos, F. K.; Mavromanolakis, G.; NA49 Collaboration: **Search for the QCD critical point in nuclear collisions at 158A GeV at the CERN Super Proton Synchrotron (SPS).** *Physical review C, Nuclear physics* **81**(6): 064907, 2010. DOI:10.1103/physrevc.81.064907

036 Anticic, T.; Baatar, B.; Bartke, J.; Betev, L.; Bialkowska, H.; Blume, C.; Boimska, B.; Bracinik, J.; Cerny, V.; Chvala, O.; Dolejsi, J.; Eckardt, V.; Fischer, H. G.; Fodor, Z.; Foka, P.; Friese, V. ; Gazdzicki, M.; Hohne, C.; Kadija, K.; Karev, A.; Kolesnikov, V.; Kowalski, M.; Kreps, M.; Makariev, M.; Malakhov, A.; Mateev, M.; Melkumov, G.; Mitrovski, M.; Mrowczynski, S.; Renfordt, R.; Rybczynski, M.; Rybicki, A.; Sandoval, A.;

Schmitz, N.; Seyboth, P.; Stefanek, G.; Stock, R.; Strobele, H.; Susa, T.; Szymanski, P.; Trubnikov, V.; Varga, D.; Vesztergombi, G.; Vranic, D.; Wenig, S.; Wlodarczyk, Z.; Wojtaszek, A.; NA49 Collaboration: **Inclusive production of protons, anti-protons and neutrons in p plus p collisions at 158 GeV/c beam momentum.** *The European physical journal: C, Particles and fields* **65**(1): 9–63, 2010. DOI:10.1140/epjc/s10052-009-1172-2

037 Arcones, A.; Martinez-Pinedo, G.; Roberts, L. F.; Woosley, S. E.: **Electron fraction constraints based on nuclear statistical equilibrium with beta equilibrium.** *Astronomy & astrophysics* **522**: A25, 2010. DOI:10.1051/0004-6361/201014276

038 Arsene, I. C.; Bearden, I. G.; Beavis, D.; Bekele, S.; Besliu, C.; Budick, B.; Boggild, H.; Chasman, C.; Christensen, C. H.; Christiansen, P.; Dalsgaard, H. H.; Debbe, R.; Gaardhoje, J. J.; Hagel, K.; Ito, H.; Jipa, A.; Johnson, E. B.; Jorgensen, C. E.; Karabowicz, R.; Katrynska, N.; Kim, E. J.; Larsen, T. M.; Lee, J. H.; Lovhoiden, G.; Majka, Z.; Marcinek, A.; Murray, M. J.; Natowitz, J.; Nielsen, B. S.; Nygaard, C.; Pal, D.; Qviller, A.; Rami, F.; Ristea, C.; Ristea, O.; Rohrich, D.; Sanders, S. J.; Staszel, P.; Tveter, T. S.; Videbaek, F.; Wada, R.; Yang, H.; Yin, Z.; Zgura, I. S.; Zhukova, V.: **The BRAHMS Collaboration (vol 830, pg 941c, 2009).** *Nuclear physics A, Nuclear and hadronic physics* **847**(1): 118–119, 2010. DOI:10.1016/j.nuclphysa.2010.09.006

039 Arsene, I. C.; Bearden, I. G.; Beavis, D.; Bekele, S.; Besliu, C.; Budick, B.; Boggild, H.; Chasman, C.; Christensen, C. H.; Christiansen, P.; Dalsgaard, H. H.; Debbe, R.; Gaardhoje, J. J.; Hagel, K.; Ito, H.; Jipa, A.; Johnson, E. B.; Jorgensen, C. E.; Karabowicz, R.; Katrynska, N.; Kim, E. J.; Larsen, T. M.; Lee, J. H.; Lovhoiden, G.; Majka, Z.; Murray, M. J.; Natowitz, J.; Nielsen, B. S.; Nygaard, C.; Pal, D.; Qviller, A.; Rami, F.; Ristea, C.; Ristea, O.; Rohrich, D.; Sanders, S. J.; Staszel, P.; Tveter, T. S.; Videbaek, F.; Wada, R.; Yang, H.; Yin, Z.; Zgura, I. S.; BRAHMS Collaboration: **Kaon and pion production in central Au plus Au collisions at,root s(NN)62.4 GeV BRAHMS Collaboration.** *Physics letters B* **687**(1): 36–41, 2010. DOI:10.1016/j.physletb.2010.02.078

040 Atanasova, L.; Balabanski, D. L.; Chamoli, S. K.; Hass, M.; Simpson, G. S.; Bazzacco, D.; Becker, F.; Bednarczyk, P. ; Benzoni, G.; Blasi, N.; Blazhev, A.; Bracco, A.; Brandau, C.; Caceres, L.; Camera, F.; Crespi, F. C. L.; Detistov, P.; Doornenbal, P.; Fahlander, C.; Farnea, E.; Georgiev, G.; Gerl, J. ; Gladnishki, K. A.; Gorska, M.; Grebosz, J.; Hoischen, R.; Ilie, G.; Ionescu-Bujor, M.; Iordachescu, A.; Jungclaus, A.; Bianco, G.; Kmiecik, M.; Kojouharov, I.; Kurz, N.; Lakshmi, S.; Lozeva, R.; Maj, A.; Montanari, D.; Neyens, G.; Pfuetzner, M.; Pietri, S.; Podolyak, Z.; Prokopowicz, W.; Rudolph, D.; Rusev, G.; Saito, T. R.; Saltarelli, A.; Schaffner, H.; Schwengner, R.; Tashenov, S.; Valiente-Dobon, J. J.; Vermeulen, N.; Walker, J.; Werner-Malento, E.; Wieland, O.; Wollersheim, H. J.; Grawe, H.; Hjorth-Jensen, M.: **g-factor measurements at RISING: The cases of Sn-127 and Sn-128.** *Europhysics letters* **91**(4): 42001, 2010. DOI:10.1209/0295-5075/91/42001

041 Azuma, R. E.; Uberseder, E.; Simpson, E. C.; Brune, C. R.; Costantini, H.; de Boer, R. J.; Gorres, J.; Heil, M.; LeBlanc, P. J.; Ugalde, C.; Wiescher, M.: **AZURE: An R-matrix code for nuclear astrophysics.** *Physical review C, Nuclear physics* **81**(4): 045805, 2010. DOI:10.1103/physrevc.81.045805

042 Badalian, A. M.; Bakker, B. L. G.; Danilkin, I. V.: **Hyperfine splittings in bottomonium and the B-q(q n, s, c) mesons.** *Physical Review D, particles, fields, gravitation, and cosmology* **81**(7): 071502, 2010. DOI:10.1103/physrevd.81.071502

043 Bailhache, R.; Andronic, A. ; Braun-Munzinger, P.; ALICE Collaboration: **Z(0) Boson measurement with the ALICE central barrel in pp collisions at 14TeV.** *Indian Journal of Physics* **84**(12): 1695–1700, 2010.

044 Baroni, S.; Macchiavelli, A. O.; Schwenk, A.: **Partial-wave contributions to pairing in nuclei.** *Physical review C, Nuclear physics* **81**(6): 064308, 2010. DOI:10.1103/physrevc.81.064308

045 Bartels, J.; Ewerz, C.; Hentschinski, M.; Mischler, A. M.: **High energy behavior of a six-point R-current correlator in N4 supersymmetric Yang-Mills theory.** *Journal of High Energy Physics* (5): 018, 2010. DOI:10.1007/jhep05(2010)018 OPEN ACCESS.

046 Batist, L.; Gorska, M.; Grawe, H.; Janas, Z.; Kavatsyuk, M.; Karny, M.; Kirchner, R.; La Commara, M.; Mukha, I.; Plochocki, A.; Roeckl, E. : **Systematics of Gamow-Teller beta decay Southeast of Sn-100.** *The European physical journal A, Hadrons and nuclei* **46**(1): 45–53, 2010. DOI:10.1140/epja/i2010-11025-x

047 Bednarczyk, P. ; Grebosz, J.; Kmiecik, M.; Maj, A.; Meczynski, W.; Myalski, S.; Styczen, J.; Domingo-Pardo, C.; Doornenbal, P.; Gerl, J. ; Gorska, M.; Wollersheim, H. J.; Jolie, J.; Reiter, P.; Bracco, A.; Camera, F.: **In-beam gamma-ray angular distribution and lifetime measurements - experience from RISING and perspectives at FAIR.** *Acta physica Polonica B* **41**(2): 505–510, 2010. OPEN ACCESS.

048 Belver, D.; Cabanelas, P.; Castro, E.; Garzon, J. A.; Gil, A.; Gonzalez-Diaz, D.; Koenig, W.; Traxler, M.: **Performance of the Low-Jitter High-Gain/Bandwidth Front-End Electronics of the HADES tRPC Wall.** *IEEE transactions on nuclear science* **57**(5): 2848–2856, 2010. DOI:10.1109/tns.2010.2056928

049 Benlliure, J.; Dragosavac, D.; Perez-Loureiro, D.;

Alvarez-Pol, H.; Blank, B.; Casarejos, E.; Fohr, V.; Gascon, M.; Gawlikowicz, W.; Heinz, A.; Helariutta, K.; Lukic, S.; Montes, F.; Pienkowski, L.; Staniou, M.; Subotic, K.; Summerer, K.; Taieb, J.; Trzcinska, A.; Veselsky, M.: **Investigating the radial distributions of medium-mass nuclei.** *Nuclear physics A, Nuclear and hadronic physics* **834**(1): 467C–469C, 2010. DOI:10.1016/j.nuclphysa.2010.01.066

050 Berdermann, E. ; Pomorski, M.; de Boer, W.; Ciobanu, M.; Dunst, S.; Grah, C.; Kis, M.; Koenig, W.; Lange, W.; Lohmann, W.; Lovrincic, R.; Moritz, P.; Morse, J.; Mueller, S.; Pucci, A.; Schreck, M.; Rahman, S.; Trager, M.: **Diamond detectors for hadron physics research.** *Diamond and related materials* **19**(5): 358–367, 2010. DOI:10.1016/j.diamond.2009.11.019

051 Berezhnoy, A. A.; Bunch, T. E.; Ma, P.; Herzog, G. F.; Knie, K.; Rugel, G.; Faestermann, T.; Korschinek, G.: **Al-26, Be-10, and Mn-53 in martian meteorites.** *Meteoritics and Planetary Science* **45**: A13–A13, 2010.

052 Beutler, F.; Andronic, A. ; Braun-Munzinger, P.; Redlich, K.; Stachel, J.: **The canonical partition function for relativistic hadron gases.** *The European physical journal: C, Particles and fields* **67**(3): 439–444, 2010. DOI:10.1140/epjc/s10052-010-1309-3

053 Blennow, M.; Fernandez-Martinez, E.; Lopez-Pavon, J.; Menendez, J.: **Neutrinoless double beta decay in see-saw models.** *Journal of High Energy Physics* (7): 096, 2010. DOI:10.1007/jhep07(2010)096 OPEN ACCESS.

054 Bodet, C.; Esteve, J.; Oberthaler, M. K.; Gasenzer, T.: **Two-mode Bose gas: Beyond classical squeezing.** *Physical review A, Atomic, molecular, and optical physics* **81**(6): 063605, 2010. DOI:10.1103/physreva.81.063605

055 Bogner, S. K.; Furnstahl, R. J.; Schwenk, A.: **From low-momentum interactions to nuclear structure.** *Progress in particle and nuclear physics* **65**(1): 94–147, 2010. DOI:10.1016/j.ppnp.2010.03.001

056 Boine-Frankenheim, O.: **rf barrier compression with space charge.** *Physical Review Special Topics - Accelerators and Beams* **13**(3): 034202, 2010. DOI:10.1103/physrevstab.13.034202 OPEN ACCESS.

057 Braun, J.; Eichhorn, A.; Gies, H.; Pawlowski, J. M.: **On the nature of the phase transition in SU(N), Sp(2) and E(7) Yang-Mills theory.** *The European physical journal: C, Particles and fields* **70**(3): 689–702, 2010. DOI:10.1140/epjc/s10052-010-1485-1

058 Bruce, A. M.; Lalkovski, S.; Bacelar, A. M. D.; Gorska, M.; Pietri, S.; Podolyak, Z.; Shi, Y.; Walker, P. M.; Xu, F. R.; Bednarczyk, P. ; Caceres, L.; Casarejos, E.; Cullen, I. J.; Doornenbal, P.; Farrelly, G. F.; Garnsworthy, A. B.; Geissel, H.; Gelletly, W.; Gerl, J. ; Grebosz, J.; Hinke, C.; Ilie, G.; Jaworski, G.; Kojouharov, I.; Kurz, N.; Myalski, S.; Palacz, M.; Prokopowicz, W.; Regan, P. H.; Schaffner, H.; Steer, S.; Tashenov, S.; Wollersheim, H. J.: **Shape coexistence and isomeric states in neutron-rich Tc-112 and Tc-113.** *Physical review C, Nuclear physics* **82**(4): 044312, 2010. DOI:10.1103/physrevc.82.044312

059 Celona, L.; Gammino, S.; Ciavola, G.; Maimone, F.; Mascali, D.: **Microwave to plasma coupling in electron cyclotron resonance and microwave ion sources (invited).** *Review of scientific instruments* **81**(2): 02A333, 2010. DOI:10.1063/1.3265366

060 Cheng, M.; Ejiri, S.; Hegde, P.; Karsch, F.; Kaczmarek, O.; Laermann, E.; Mawhinney, R. D.; Miao, C.; Mukherjee, S.; Petreczky, P.; Schmidt, C.; Soeldner, W.: **Equation of state for physical quark masses.** *Physical Review D, particles, fields, gravitation, and cosmology* **81**(5): 054504, 2010. DOI:10.1103/physrevd.81.054504

061 Cheng, Y.; Csernai, L. P.; Magas, V. K.; Schlei, B. R.; Strottman, D.: **Matching stages of heavy-ion collision models.** *Physical review C, Nuclear physics* **81**(6): 064910, 2010. DOI:10.1103/physrevc.81.064910

062 Chen, L.; Plass, W. R.; Geissel, H.; Knobel, R.; Kozhuharov, C.; Litvinov, Y. A.; Patyk, Z.; Scheidenberger, C.; Siegien-Iwaniuk, K.; Sun, B.; Weick, H.; Beckert, K.; Beller, P. ; Bosch, F.; Boutin, D.; Caceres, L.; Carroll, J. J.; Cullen, D. M.; Cullen, I. J.; Franzke, B. ; Gerl, J. ; Gorska, M.; Jones, G. A.; Kishada, A.; Kurcewicz, J.; Litvinov, S. A.; Liu, Z.; Mandal, S.; Montes, F.; Munzenberg, G.; Nolden, F. ; Ohtsubo, T.; Podolyak, Z.; Propri, R.; Rigby, S.; Saito, N.; Saito, T. ; Shindo, M.; Steck, M. ; Ugorowski, P.; Walker, P. M.; Williams, S.; Winkler, M.; Wollersheim, H. J.; Yamaguchi, T.: **Discovery and investigation of heavy neutron-rich isotopes with time-resolved Schottky spectrometry in the element range from thallium to actinium.** *Physics letters B* **691**(5): 234–237, 2010. DOI:10.1016/j.physletb.2010.05.078

063 Chernykh, M.; Feldmeier, H.; Neff, T.; von Neumann-Cosel, P.; Richter, A.: **Pair Decay Width of the Hoyle State and its Role for Stellar Carbon Production.** *Physical review letters* **105**(2): 022501, 2010. DOI:10.1103/physrevlett.105.022501

064 Colonna, N.; Belloni, F.; Berthoumieux, E.; Calviani, M.; Domingo-Pardo, C.; Guerrero, C.; Karadimos, D.; Lederer, C.; Massimi, C.; Paradela, C.; Plag, R.; Praena, J.; Sarmento, R.: **Advanced nuclear energy systems and the need of accurate nuclear data: the n_TOF project at CERN.** *Energy and Environmental Science* **3**(12): 1910–1917, 2010. DOI:10.1039/c0ee00108b

065 Cortina-Gil, D.; Rodriguez-Tajes, C.; Alvarez-Pol, H.; Benjamim, E.; Benlliure, J.; Borge, M. J. G.; Caamano, M.; Casarejos, E.; Chatillon, A.; Eppinger, K.; Faestermann, T.; Gascon, M.; Geissel, H.; Gernhauser, R.; Jonson, B.;

Kanungo, R.; Krucken, R.; Kurtukian, T.; Maierbeck, P.; Nilsson, T.; Nocciforo, C.; Pascual-Izarra, C.; Perea, A.; Perez-Loureiro, D.; Prochazka, A.; Simon, H.; Suemmerer, K.; Tengblad, O.; Weick, H.; Zhukov, M.: **One-neutron knockout of n-rich Ne isotopes at relativistic energies.** *Nuclear physics A, Nuclear and hadronic physics* **834**(1): 485C–487C, 2010. DOI:10.1016/j.nuclphysa.2010.01.072

066 Danilkin, I. V.; Simonov, Y. A.: **Dynamical Origin and the Pole Structure of X(3872).** *Physical review letters* **105**(10): 102002, 2010. DOI:10.1103/physrevlett.105.102002

067 Danu, L. S.; Biswas, D. C.; Saxena, A.; Shrivastava, A.; Chatterjee, A.; Nayak, B. K.; Thomas, R. G.; Choudhury, R. K.; Palit, R.; Mazumdar, I.; Datta, P.; Chattopadhyay, S.; Pal, S.; Bhattacharya, S.; Muralithar, S.; Golda, K. S.; Bhowmik, R. K.; Das, J. J.; Singh, R. P.; Madhavan, N.; Gerl, J. ; Patra, S. K.; Satpathy, L.: **Fine structure dips in the fission fragment mass distribution for the U-238(O-18,f) reaction.** *Physical review C, Nuclear physics* **81**(1): 014311, 2010. DOI:10.1103/physrevc.81.014311

068 Dapo, H.; Schaefer, B. J.; Wambach, J.: **Appearance of hyperons in neutron stars.** *Physical review C, Nuclear physics* **81**(3): 035803, 2010. DOI:10.1103/physrevc.81.035803

069 Daugas, J. M.; Faul, T.; Grawe, H.; Pfutzner, M.; Grzywacz, R.; Lewitowicz, M.; Achouri, N. L.; Angelique, J. C.; Baiborodin, D.; Bentida, R.; Beraud, R.; Borcea, C.; Bingham, C. R.; Catford, W. N.; Emsallem, A.; de France, G.; Grzywacz, K. L.; Lemmon, R. C.; Jimenez, M. J. L.; Santos, F. D.; Regan, P. H.; Rykaczewski, K.; Sauvestre, J. E.; Sawicka, M.; Stanoiu, M.; Sieja, K.; Nowacki, F.: **Low-lying isomeric levels in Cu-75.** *Physical review C, Nuclear physics* **81**(3): 034304, 2010. DOI:10.1103/physrevc.81.034304

070 Dean, D. J.; Langanke, K.; Nam, H.; Nazarewicz, W.: **Pairing Reentrance Phenomenon in Heated Rotating Nuclei in the Shell-Model Monte Carlo Approach.** *Physical review letters* **105**(21): 212504, 2010. DOI:10.1103/physrevlett.105.212504

071 Delahaye, P.; Kester, O.; Barton, C.; Lamy, T.; Marie-Jeanne, M.; Wenander, F.: **Evaluation of charge breeding options for EURISOL.** *The European physical journal A, Hadrons and nuclei* **46**(3): 421–433, 2010. DOI:10.1140/epja/i2010-11042-9

072 Deveaux, M.; Amar-Youcef, S.; Besson, A.; Claus, G.; Colledani, C.; Dorokhov, M.; Dritsa, C.; Dulinski, W.; Frohlich, I.; Goffe, M.; Grandjean, D.; Heini, S.; Himmi, A.; Hu, C.; Jaaskelainen, K.; Muntz, C.; Shabetai, A.; Stroth, J. ; Szelezniak, M.; Valin, I.; Winter, M.: **Radiation tolerance of CMOS monolithic active pixel sensors with self-biased pixels.** *Nuclear instruments & methods in physics research, Section A, Accelerators, spectrometers, detectors and associated equipment* **624**(2): 428–431, 2010. DOI:10.1016/j.nima.2010.04.045

073 Dietz, B.; Friedrich, T.; Harney, H. L.; Miski-Oglu, M.; Richter, A.; Schafer, F.; Weidenmuller, H. A.: **Quantum chaotic scattering in microwave resonators.** *Physical Review E, statistical, nonlinear, and soft matter physics* **81**(3): 036205, 2010. DOI:10.1103/physreve.81.036205

074 Dillmann, I.; Domingo-Pardo, C.; Heil, M.; Kappeler, F.; Walter, S.; Dababneh, S.; Rauscher, T.; Thielemann, F. K.: **Stellar (n,gamma) cross sections of p-process isotopes Part I: Pd-102, Te-120, Ba-130,Ba-132, and Dy-156.** *Physical review C, Nuclear physics* **81**(1): 015801, 2010. DOI:10.1103/physrevc.81.015801

075 Dohrmann, F.; Frohlich, I.; Galatyuk, T.; Holzmann, R.; Kahlitz, P. K.; Kampfer, B.; Moriniere, E.; Pachmayer, Y. C.; Ramstein, B.; Salabura, P.; Stroth, J. ; Trebacz, R.; Van de Wiele, J.; Wustenfeld, J.: **A versatile method for simulating pp → ppe(+)e(-) and dp → pne(+)e(-) p(spec) reactions.** *The European physical journal A, Hadrons and nuclei* **45**(3): 401–411, 2010. DOI:10.1140/epja/i2010-11012-3

076 Doornenbal, P.; Reiter, P.; Grawe, H.; Saito, T. ; Al-Khatib, A.; Banu, A.; Beck, T.; Becker, F.; Bednarczyk, P. ; Benzoni, G.; Bracco, A.; Burger, A.; Caceres, L.; Camera, F.; Chmel, S.; Crespi, F. C. L.; Geissel, H.; Gerl, J. ; Gorska, M.; Grebosz, J.; Hubel, H.; Kavatsyuk, M.; Kavatsyuk, O.; Kmiecik, M.; Kojouharov, I.; Kurz, N.; Lozeva, R.; Maj, A.; Mandal, S.; Meczynski, W.; Million, B.; Podolyak, Z.; Richard, A.; Saito, N.; Schaffner, H.; Seidlitz, M.; Striepling, T.; Walker, J.; Warr, N.; Weick, H.; Wieland, O.; Winkler, M.; Wollersheim, H. J.: **Lifetime effects for high-resolution gamma-ray spectroscopy at relativistic energies and their implications for the RISING spectrometer.** *Nuclear instruments & methods in physics research, Section A, Accelerators, spectrometers, detectors and associated equipment* **613**(2): 218–225, 2010. DOI:10.1016/j.nima.2009.11.017

077 Duguet, T.; Lesinski, T.; Hebeler, K.; Schwenk, A.: **Lowest-order contributions of chiral three-nucleon interactions to pairing properties of nuclear groud states.** *Modern Physics Letters A* **25**(21): 1989–1992, 2010. DOI:10.1142/s0217732310000812

078 Dullmann, C. E.; Schadel, M.; Yakushev, A.; Turler, A.; Eberhardt, K.; Kratz, J. V.; Ackermann, D. ; Andersson, L. L.; Block, M.; Bruchle, W.; Dvorak, J.; Essel, H. G.; Ellison, P. A.; Even, J.; Gates, J. M.; Gorshkov, A.; Graeger, R.; Gregorich, K. E.; Hartmann, W.; Herzberg, R. D.; Hessberger, F. P.; Hild, D.; Hubner, A.; Jager, E.; Khuyagbaatar, J.; Kindler, B. ; Krier, J.; Kurz, N.; Lahiri, S.; Liebe, D.; Lommel, B.; Maiti, M.; Nitsche, H.; Omtvedt, J. P.; Parr, E.; Rudolph, D.; Runke, J.; Schausten, B.; Schimpf, E.; Semchenkov, A.; Steiner, J.; Thorle-Pospiech, P.; Uusitalo,

J.; Wegrzecki, M.; Wiehl, N.: **Production and Decay of Element 114: High Cross Sections and the New Nucleus (277)Hs.** *Physical review letters* **104**(25): 252701, 2010. DOI:10.1103/physrevlett.104.252701

079 Dzhioev, A. A.; Vdovin, A. I.; Ponomarev, V. Y.; Wambach, J.; Langanke, K.; Martinez-Pinedo, G.: **Gamow-Teller strength distributions at finite temperatures and electron capture in stellar environments.** *Physical review C, Nuclear physics* **81**(1): 015804, 2010. DOI:10.1103/physrevc.81.015804

080 Dziuba, F.; Busch, M.; Amberg, M.; Podlech, H.; Zhang, C.; Klein, H.; Barth, W.; Ratzinger, U.: **Development of superconducting crossbar-H-mode cavities for proton and ion accelerators.** *Physical Review Special Topics - Accelerators and Beams* **13**(4): 041302, 2010. DOI:10.1103/physrevstab.13.041302 OPEN ACCESS.

081 Ekstrom, A.; Cederkall, J.; Fahlander, C.; Hjorth-Jensen, M.; Engeland, T.; Blazhev, A.; Butler, P. A.; Davinson, T.; Eberth, J.; Finke, F.; Gorgen, A.; Gorska, M.; Hurst, A. M.; Ivanov, O.; Iwanicki, J.; Koster, U.; Marsh, B. A.; Mierzejewski, J.; Reiter, P.; Siem, S.; Sletten, G.; Stefanescu, I.; Tveten, G. M.; Van de Walle, J.; Voulot, D.; Warr, N.; Weisshaar, D.; Wenander, F.; Zielinska, M.: **Coulomb excitation of the odd-odd isotopes In-106,In-108.** *The European physical journal A, Hadrons and nuclei* **44**(3): 355–361, 2010. DOI:10.1140/epja/i2010-10945-7

082 Ellison, P. A.; Gregorich, K. E.; Berryman, J. S.; Bleuel, D. L.; Clark, R. M.; Dragojevic, I.; Dvorak, J.; Fallon, P.; Fineman-Sotomayor, C.; Gates, J. M.; Gothe, O. R.; Lee, I. Y.; Loveland, W. D.; McLaughlin, J. P.; Paschalis, S.; Petri, M.; Qian, J.; Stavsetra, L.; Wiedeking, M.; Nitsche, H.: **New Superheavy Element Isotopes: Pu-242(Ca-48, 5n)(285)114.** *Physical review letters* **105**(18): 182701, 2010. DOI:10.1103/physrevlett.105.182701

083 Endres, J.; Litvinova, E.; Savran, D.; Butler, P. A.; Harakeh, M. N.; Harissopulos, S.; Herzberg, R. D.; Krucken, R.; Lagoyannis, A.; Pietralla, N.; Ponomarev, V. Y.; Popescu, L.; Ring, P.; Scheck, M.; Sonnabend, K.; Stoica, V. I.; Wortche, H. J.; Zilges, A.: **Isospin Character of the Pygmy Dipole Resonance in Sn-124.** *Physical review letters* **105**(21): 212503, 2010. DOI:10.1103/physrevlett.105.212503

084 Ewerz, C.; von Manteuffel, A.; Nachtmann, O.: **Ioffe times in DIS from a dipole model fit.** *Journal of High Energy Physics* (3): 102, 2010. DOI:10.1007/jhep03(2010)102 OPEN ACCESS.

085 Fehrenbacher, G. ; Radon, T.: **Generation of shielding data for neutron radiation produced by heavy ions.** *Radiation Measurements* **45**(10): 1529–1531, 2010. DOI:10.1016/j.radmeas.2010.05.027

086 Fischer, C. S.; Maas, A.; Muller, J. A.: **Chiral and deconfinement transition from correlation functions: SU(2) vs. SU(3).** *The European physical journal: C, Particles and fields* **68**(1): 165–181, 2010. DOI:10.1140/epjc/s10052-010-1343-1

087 Fischer, T.; Whitehouse, S. C.; Mezzacappa, A.; Thielemann, F. K.; Liebendorfer, M.: **Protoneutron star evolution and the neutrino-driven wind in general relativistic neutrino radiation hydrodynamics simulations.** *Astronomy & astrophysics* **517**: A80, 2010. DOI:10.1051/0004-6361/200913106

088 Fister, L.; Alkofer, R.; Schwenzer, K.: **On the infrared behavior of Landau Gauge Yang-Mills theory with a fundamentally charged scalar field.** *Physics letters B* **688**(2): 237–243, 2010. DOI:10.1016/j.physletb.2010.04.001

089 Fomichev, A. S.; Ter-Akopian, G. M.; Chudoba, V.; Daniel, A. V.; Golovkov, M. S.; Gorshkov, V. A.; Grigorenko, L. V.; Krupko, S. A.; Oganessian, Y. T.; Sidorchuk, S. I.; Slepnev, R. S.; Stepantsov, S. V.; Ershov, S. N.; Lukyanov, V. K.; Danilin, B. V.; Korsheninnikov, A. A.; Goldberg, V. Z.; Pfutzner, M.; Mukha, I. G.; Simon, H.; Tarasov, O. B.; Timofeyuk, N. K.; Zhukov, M. V.; Lawrie, K.; Newman, R. T.: **The suggested new fragment separator ACCULINNA-2.** *Acta physica Polonica B* **41**(2): 475–480, 2010. OPEN ACCESS.

090 Franchetti, G.; Chorniy, O.; Hofmann, I.; Bayer, W.; Becker, F.; Forck, P.; Giacomini, T.; Kirk, M.; Mohite, T.; Omet, C.; Parfenova, A.; Schutt, P.: **Experiment on space charge driven nonlinear resonance crossing in an ion synchrotron.** *Physical Review Special Topics - Accelerators and Beams* **13**(11): 114203, 2010. DOI:10.1103/physrevstab.13.114203 OPEN ACCESS.

091 Friese, V.: **Prospects for strangeness and charm measurements with the CBM experiment.** *Journal of physics G, Nuclear and particle physics* **37**(9): 094025, 2010. DOI:10.1088/0954-3899/37/9/094025

092 Furnstahl, R. J.; Schwenk, A.: **How should one formulate, extract and interpret 'non-observables' for nuclei?.** *Journal of physics G, Nuclear and particle physics* **37**(6): 064005, 2010. DOI:10.1088/0954-3899/37/6/064005

093 Furnstahl, R. J.; Schwenk, A.: **Is chiral symmetry manifested in nuclear structure?.** *Journal of physics G, Nuclear and particle physics* **37**(6): 064004, 2010. DOI:10.1088/0954-3899/37/6/064004

094 Gammino, S.; Celona, L.; Ciavola, G.; Maimone, F.; Mascali, D.: **Review on high current 2.45 GHz electron cyclotron resonance sources (invited).** *Review of scientific instruments* **81**(2): 02B313, 2010. DOI:10.1063/1.3266145

095 Gasenzer, T.; Kessler, S.; Pawlowski, J. M.: **Far-from-equilibrium quantum many-body dynamics.** *The European physical journal: C, Particles and fields* **70**(1): 423–443, 2010. DOI:10.1140/epjc/s10052-010-1430-3

096 Gasparyan, A.; Lutz, M. F. M.: **Photon- and pion-nucleon interactions in a unitary and causal effective field theory based on the chiral Lagrangian.** *Nuclear physics A, Nuclear and hadronic physics* **848**(1): 126–182, 2010. DOI:10.1016/j.nuclphysa.2010.08.006

097 Giacosa, F.; Pagliara, G.: **Decay of light scalar mesons into vector-photon and into pseudoscalar mesons.** *Nuclear physics A, Nuclear and hadronic physics* **833**(1): 138–155, 2010. DOI:10.1016/j.nuclphysa.2009.12.007

098 Golabek, C.; Heinz, S.; Mittig, W.; Rejmund, F.; Villari, A. C. C.; Bhattacharyva, S.; Boilley, D.; De France, G.; Drouart, A.; Gaudefroy, L.; Giot, L.; Maslov, V.; Morjean, M.; Mukherjee, G.; Penionzkevich, Y.; Roussel-Chomaz, P.; Stodel, C.: **Investigation of deep inelastic reactions in U-238+U-238 at Coulomb barrier energies.** *The European physical journal A, Hadrons and nuclei* **43**(3): 251–259, 2010. DOI:10.1140/epja/i2010-10911-5

099 Gotzen, K.; BES-III Collaboration: **Recent results on hadron spectroscopy from BES.** *Chinese Physics* **34**(6): 638–643, 2010.

100 Graeger, R.; Ackermann, D. ; Chelnokov, M.; Chepigin, V.; Duellmann, C. E.; Dvorak, J.; Even, J.; Gorshkov, A.; Hessberger, F. P.; Hild, D.; Hubner, A.; Jager, E.; Khuyagbaatar, J.; Kindler, B. ; Kratz, J. V.; Krier, J.; Kuznetsov, A.; Lommel, B.; Nishio, K.; Nitsche, H.; Omtvedt, J. P.; Petrushkin, O.; Rudolph, D.; Runke, J.; Samadani, F.; Schadel, M.; Schausten, B.; Turler, A.; Yakushev, A.; Zhi, Q.: **Experimental study of the U-238(S-36,3-5n)(269-271)Hs reaction leading to the observation of (270)Hs.** *Physical review C, Nuclear physics* **81**(6): 061601, 2010. DOI:10.1103/physrevc.81.061601

101 Grigorenko, L. V.; Egorova, I. A.; Zhukov, M. V.; Charity, R. J.; Miernik, K.: **Two-proton radioactivity and three-body decay. V. Improved momentum distributions.** *Physical review C, Nuclear physics* **82**(1): 014615, 2010. DOI:10.1103/physrevc.82.014615

102 Gutlich, E.; Forck, P.; Ensinger, W.; Walasek-Hohne, B.: **Scintillation Screen Investigations for High-Current Ion Beams (vol 57, pg 1414, 2010).** *IEEE transactions on nuclear science* **57**(4): 2406–2407, 2010. DOI:10.1109/tns.2010.2060282

103 Gutlich, E.; Forck, P.; Ensinger, W.; Walasek-Hohne, B.: **Scintillation Screen Investigations for High-Current Ion Beams.** *IEEE transactions on nuclear science* **57**(3): 1414–1419, 2010. DOI:10.1109/tns.2009.2035807

104 Hebeler, K.; Lattimer, J. M.; Pethick, C. J.; Schwenk, A.: **Constraints on Neutron Star Radii Based on Chiral Effective Field Theory Interactions.** *Physical review letters* **105**(16): 161102, 2010. DOI:10.1103/physrevlett.105.161102

105 Hebeler, K.; Schwenk, A.: **Chiral three-nucleon forces and neutron matter.** *Physical review C, Nuclear physics* **82**(1): 014314, 2010. DOI:10.1103/physrevc.82.014314

106 Heinz, S.; Comas, V.; Hofmann, S. ; Ackermann, D. ; Heredia, J.; Hessberger, F. P.; Khuyagbaatar, J.; Kindler, B. ; Lommel, B.; Mann, R.: **Investigation of di-nuclear systems as entrance channel to fusion.** *The European physical journal A, Hadrons and nuclei* **43**(2): 181–184, 2010. DOI:10.1140/epja/i2010-10914-2

107 Heinz, S.; Comas, V.; Hofmann, S. ; Ackermann, D. ; Heredia, J.; Hessberger, F. P.; Khuyagbaatar, J.; Kindler, B. ; Lommel, B.; Mann, R.; Golabek, C.; Mittig, W.; Rejmund, F.; Villari, A. C. C.: **Study of heavy di-nuclear systems.** *Nuclear physics A, Nuclear and hadronic physics* **834**(1): 362C–365C, 2010. DOI:10.1016/j.nuclphysa.2010.01.040

108 Henzlova, D. ; Botvina, A. S.; Schmidt, K. H.; Henzl, V.; Napolitani, P.; Ricciardi, M. V.: **Symmetry energy of fragments produced in multifragmentation.** *Journal of physics G, Nuclear and particle physics* **37**(8): 085010, 2010. DOI:10.1088/0954-3899/37/8/085010

109 Heredia, J. A.; Andreyev, A. N.; Antalic, S. ; Hofmann, S. ; Ackermann, D. ; Comas, V. F.; Heinz, S.; Hessberger, F. P.; Kindler, B. ; Khuyagbaatar, J.; Lommel, B.; Mann, R.: **The new isotope Th-208.** *The European physical journal A, Hadrons and nuclei* **46**(3): 337–343, 2010. DOI:10.1140/epja/i2010-11058-1

110 Hessberger, F. P.; Antalic, S. ; Ackermann, D. ; Heinz, S.; Hofmann, S. ; Khuyagbaatar, J.; Kindler, B. ; Kojouharov, I.; Lommel, B.; Mann, R.: **Alpha-decay properties of (261)Bh.** *The European physical journal A, Hadrons and nuclei* **43**(2): 175–180, 2010. DOI:10.1140/epja/i2010-10913-3

111 Hessberger, F. P.; Antalic, S. ; Sulignano, B.; Ackermann, D. ; Heinz, S.; Hofmann, S. ; Kindler, B. ; Khuyagbaatar, J.; Kojouharov, I.; Kuusiniemi, P.; Leino, M.; Lommel, B.; Mann, R.; Nishio, K.; Popeko, A. G.; Saro, S.; Streicher, B.; Uusitalo, J.; Venhart, M.; Yeremin, A. V.: **Decay studies of K isomers in No-254.** *The European physical journal A, Hadrons and nuclei* **43**(1): 55–66, 2010. DOI:10.1140/epja/i2009-10899-9

112 Hofmann, S.: **Experiments on superheavy elements.** *International journal of modern physics E, Nuclear physics* **19**(4): 483–492, 2010. DOI:10.1142/s0218301310014819

113 Hofmann, S.: **Welcome copernicium?.** *Nature Chemistry* **2**(2): 146–146, 2010. DOI:10.1038/nchem.533

114 Hohmann, E.; Fehrenbacher, G. ; Khurana, S.; Radon, T.; Reginatto, M.; Schardt, D.; Schuhmacher, H.; Wiegel, B.: **The simulated workplace field with a high-energy neutron component produced by irradiating a Fe-target with 200 MeV/u C-12-ions.** *Radiation Measurements* **45**(10): 1105–1108, 2010. DOI:10.1016/j.radmeas.2010.06.025

115 Hohmann, E.; Luszik-Bhadra, M.; Schuhmacher, H.; Wiegel, B.; Fehrenbacher, G. : **Bonner shere system with active detector for maesurements inpusled neutron fields.** *Nuclear Technology* **172**(3): 273–277, 2010.

116 Holzmann, R.; Balanda, A.; Belver, D.; Belyaev, A. V.; Blanco, A.; Bohmer, M.; Boyard, J. L.; Braun-Munzinger, P.; Cabanelas, P.; Castro, E.; Chernenko, S.; Diaz, J.; Dybczak, A.; Epple, E.; Fabbietti, L.; Fateev, O. V.; Finocchiaro, P.; Fonte, P.; Friese, J.; Frohlich, I.; Galatyuk, T.; Garzon, J. A.; Gernhauser, R.; Gil, A.; Golubeva, M.; Gonzalez-Diaz, D.; Guber, F.; Hennino, T.; Holzmann, R.; Huck, P.; Ierusalimov, A. P.; Iori, I.; Ivashkin, A.; Jurkovic, M.; Kampfer, B.; Karavicheva, T.; Koenig, I.; Koenig, W.; Kolb, B. W.; Kopp, A.; Kotte, R.; Kozuch, A.; Krasa, A.; Krizek, F.; Krucken, R.; Kuhn, W.; Kugler, A.; Kurepin, A.; Khlitz, P. K.; Lamas-Valverde, J.; Lang, S.; Lange, J. S.; Lapidus, K.; Liu, T.; Lopes, L.; Lorenz, M.; Maier, L.; Mangiarotti, A.; Markert, J.; Metag, V.; Michalska, B.; Michel, J.; Moriniere, E.; Mousa, J.; Muntz, C.; Naumann, L.; Pachmayer, Y. C.; Palka, M.; Parpottas, Y.; Pechenov, V.; Pietraszko, J.; Przygoda, W.; Ramstein, B.; Reshetin, A.; Roskoss, J.; Rustamov, A.; Sadovsky, A.; Salabura, P.; Schmah, A.; Siebenson, J.; Simon, R.; Sobolev, Y. G.; Spruck, B.; Strobele, H.; Stroth, J. ; Sturm, C.; Sudol, M.; Tarantola, A.; Teilab, K.; Tlusty, P.; Traxler, M.; Trebacz, R.; Tsertos, H.; Veretenkin, I.; Wagner, V.; Weber, M.; Wisniowski, M.; Wustenfeld, J.; Yurevich, S.; Zanevsky, Y. V.; HADES Collaboration: **Dilepton Production at SIS Energies Studied with HADES.** *Nuclear physics A, Nuclear and hadronic physics* **834**(1): 298C–302C, 2010. DOI:10.1016/j.nuclphysa.2010.01.003

117 Ilie, G.; Neyens, G.; Simpson, G. S.; Jolie, J.; Blazhev, A.; Grawe, H.; Lozeva, R. L.; Vermeulen, N.; Atanasova, L.; Balabanski, D. L.; Becker, F.; Bednarczyk, P. ; Brandau, C.; Caceres, L.; Chamoli, S. K.; Daugas, J. M.; Doornenbal, P.; Gerl, J. ; Gorska, M.; Grebosz, J.; Hass, M.; Ionescu-Bujor, M.; Jungclaus, A.; Kmiecik, M.; Kojouharov, I.; Kurz, N.; Maj, A.; Mallion, S.; Perru, O.; Pfutzner, M.; Podolyak, Z.; Prokopowicz, W.; De Rydt, M.; Saito, T. R.; Schaffner, H.; Turzo, K.; Walker, J.; Werner-Malento, E.; Wollersheim, H. J.: **g Factor of the 7(-) isomer in Sn-126 and first observation of spin-alignment in relativistic fission.** *Physics letters B* **687**(4): 305–309, 2010. DOI:10.1016/j.physletb.2010.03.033

118 Ivanov, Y. B.: **Baryon stopping in heavy-ion collisions at E-lab2-160 GeV/nucleon.** *Physics letters B* **690**(4): 358–362, 2010. DOI:10.1016/j.physletb.2010.05.051

119 Iwata, Y.; Otsuka, T.; Maruhn, J. A.; Itagaki, N.: **Geometric classification of nucleon transfer at moderate low-energies.** *Nuclear physics A, Nuclear and hadronic physics* **836**(1): 108–118, 2010. DOI:10.1016/j.nuclphysa.2010.01.242

120 Iwata, Y.; Otsuka, T.; Maruhn, J. A.; Itagaki, N.: **Suppression of Charge Equilibration Leading to the Synthesis of Exotic Nuclei.** *Physical review letters* **104**(25): 252501, 2010. DOI:10.1103/physrevlett.104.252501

121 Jachimowicz, P.; Kowal, M.; Rozmej, P.; Skalski, J.; Sobiczewski, A.: **Role of the non-axial octupole deformation in the potential energy of heavy nuclei.** *International journal of modern physics E, Nuclear physics* **19**(4): 768–773, 2010. DOI:10.1142/s0218301310015205

122 Jachimowicz, P.; Kowal, M.; Sobiczewski, A.: **Role of the non-axial shapes in the saddle-point energy of the heaviest nuclei.** *Acta physica Polonica B* **41**(8): 1927–1936, 2010. OPEN ACCESS.

123 Johansson, H. T.; Aksyutina, Y.; Aumann, T. ; Boretzky, K.; Borge, M. J. G.; Chatillon, A.; Chulkov, L. V.; Cortina-Gil, D.; Pramanik, U. D.; Emling, H.; Forssen, C.; Fynbo, H. O. U.; Geissel, H.; Ickert, G.; Jonson, B.; Kulessa, R.; Langer, C.; Lantz, M.; LeBleis, T.; Mahata, K.; Meister, M.; Munzenberg, G.; Nilsson, T.; Nyman, G.; Palit, R.; Paschalis, S.; Prokopowicz, W.; Reifarth, R.; Richter, A.; Riisager, K.; Schrieder, G.; Shulgina, N. B.; Simon, H.; Summerer, K.; Tengblad, O.; Weick, H.; Zhukov, M. V.: **Three-body correlations in the decay of He-10 and Li-13.** *Nuclear physics A, Nuclear and hadronic physics* **847**(1): 66–88, 2010. DOI:10.1016/j.nuclphysa.2010.07.002

124 Johansson, H. T.; Aksyutina, Y.; Aumann, T. ; Boretzky, K.; Borge, M. J. G.; Chatillon, A.; Chulkov, L. V.; Cortina-Gil, D.; Pramanik, U. D.; Emling, H.; Forssen, C.; Fynbo, H. O. U.; Geissel, H.; Ickert, G.; Jonson, B.; Kulessa, R.; Langer, C.; Lantz, M.; LeBleis, T.; Mahata, K.; Meister, M.; Munzenberg, G.; Nilsson, T.; Nyman, G.; Palit, R.; Paschalis, S.; Prokopowicz, W.; Reifarth, R.; Richter, A.; Riisager, K.; Schrieder, G.; Simon, H.; Summerer, K.; Tengblad, O.; Weick, H.; Zhukov, M. V.: **The unbound isotopes He-9,He-10.** *Nuclear physics A, Nuclear and hadronic physics* **842**: 15–32, 2010. DOI:10.1016/j.nuclphysa.2010.04.006

125 Juodagalvis, A.; Langanke, K.; Hix, W. R.; Martinez-Pinedo, G.; Sampaio, J. M.: **Improved estimate of electron capture rates on nuclei during stellar core collapse.** *Nuclear physics A, Nuclear and hadronic physics* **848**(3): 454–478, 2010. DOI:10.1016/j.nuclphysa.2010.09.012

126 Kanada-En'Yo, Y.; Feldmeier, H.; Suhara, T.: **Dineutron correlations in He isotopes.** *Modern Physics Letters A* **25**(21): 1850–1853, 2010. DOI:10.1142/s0217732310000472

127 Kanungo, R.; Nociforo, C.; Prochazka, A.; Utsuno, Y.; Aumann, T. ; Boutin, D.; Cortina-Gil, D.; Davids, B.; Diakaki, M.; Farinon, F.; Geissel, H.; Gernhauser, R.; Gerl, J. ; Janik, R.; Jonson, B.; Kindler, B. ; Knobel, R.; Krucken, R.; Lantz, M.; Lenske, H.; Litvinov, Y. ; Mahata, K.; Maierbeck, P.; Musumarra, A.; Nilsson, T.; Otsuka, T.; Perro, C.; Scheidenberger, C.; Sitar, B.; Strmen, P.; Sun, B.; Szarka, I.; Tanihata, I.; Weick, H.; Winkler, M.: **Structure of Mg-33 sheds new light on the N20 island of inversion.** *Physics letters B* **685**(4): 253–257, 2010. DOI:10.1016/j.physletb.2010.02.008

128 Karpenko, I. A.; Sinyukov, Y. M.: **Energy dependence of pion interferometry scales in ultra-relativistic heavy ion collisions.** *Physics letters B* **688**(1): 50–54, 2010. DOI:10.1016/j.physletb.2010.03.068

129 Khuyagbaatar, J.; Hessberger, F. P.; Hofmann, S. ; Ackermann, D. ; Comas, V. S.; Heinz, S.; Heredia, J. A.; Kindler, B. ; Kojouharov, I.; Lommel, B.; Mann, R.; Nishio, K.; Yakushev, A.: **The new isotope Cm-236 and new data on Cm-233 and Cf-237,Cf- 238,Cf- 240.** *The European physical journal A, Hadrons and nuclei* **46**(1): 59–67, 2010. DOI:10.1140/epja/i2010-11026-9

130 Khvorostukhin, A. S.; Toneev, V. D.; Voskresensky, D. N.: **Viscosity coefficients for hadron and quark-gluon phases.** *Nuclear physics A, Nuclear and hadronic physics* **845**: 106–146, 2010. DOI:10.1016/j.nuclphysa.2010.05.058

131 Kim, M.; Ajimura, S.; Aoki, K.; Banu, A.; Bhang, H.; Fukuda, T.; Hashimoto, O.; Hwang, J. I.; Kameoka, S.; Kang, B. H.; Kim, E.; Kim, J. H.; Maruta, T.; Miura, Y.; Miyake, Y.; Nagae, T.; Nakamura, M.; Nakamura, S. N.; Noumi, H.; Okada, S.; Okayasu, Y.; Outa, H.; Park, H.; Saha, P. K.; Sato, Y.; Sekimoto, M.; Takahashi, T.; Tamura, H.; Tanida, K.; Toyoda, A.; Tshoo, K.; Tsukada, K.; Watanabe, T.; Yim, H. J.: **Coincidence measurement of the weak decay of C-12(Lambda) and the three-body weak decay process (J-PARC 50GeV PS E18).** *Nuclear physics A, Nuclear and hadronic physics* **835**(1): 434–438, 2010. DOI:10.1016/j.nuclphysa.2010.01.237

132 Kindler, B. ; Hartmann, W.; Hubner, A.; Lommel, B.; Steiner, J.: **Development of carbon foils with a thickness of up to 600 mu g/cm(2).** *Nuclear instruments & methods in physics research, Section A, Accelerators, spectrometers, detectors and associated equipment* **613**(3): 425–428, 2010. DOI:10.1016/j.nima.2009.09.092

133 Kizivat, L. T.; Martinez-Pinedo, G.; Langanke, K.; Surman, R.; McLaughlin, G. C.: **gamma-ray bursts black hole accretion disks as a site for the nu p process.** *Physical review C, Nuclear physics* **81**(2): 025802, 2010. DOI:10.1103/physrevc.81.025802

134 Kmiecik, M.; Maj, A.; Gerl, J. ; Neyens, G.; Atanasova, L.; Balabanski, D. L.; Becker, F.; Bednarczyk, P. ; Benzoni, G.; Blasi, N.; Bracco, A.; Brambilla, S.; Caceres, L.; Camera, F.; Ciemala, M.; Crespi, F. C. L.; Chamoli, S. K.; Chmel, S.; Daugas, J. M.; Detistov, P.; Doornenbal, P.; Georgiev, G.; Gladnishki, K.; Gorska, M.; Grawe, H.; Grebosz, J.; Hass, M.; Hoischen, R.; Ilie, G.; Ionescu-Bujor, M.; Jolie, J.; Kojuharov, I.; Krasznahorkay, A.; Kulessa, R.; Lach, M.; Lakshmi, S.; Leoni, S.; Lo Bianco, G.; Lozeva, R.; Maier, K. H.; Mallion, S.; Mazurek, K.; Meczynski, W.; Million, B.; Montanari, D.; Myalski, S.; Petrache, C.; Pfutzner, M.; Pietri, S.; Podolyak, Z.; Prokopowicz, W.; Rudolph, D.; Saito, N.; Saito, T. R.; Saltarelli, A.; Simpson, G. S.; Styczen, J.; Vermeulen, N.; Werner-Malento, E.; Wieland, O.; Wollersheim, H.; Zieblinski, M.: **Spin-alignment and g-factor measurement of the I-pi12(+) isomer in Pb-192 produced in the relativistic-energy fragmentation of a U-238 beam.** *The European physical journal A, Hadrons and nuclei* **45**(2): 153–158, 2010. DOI:10.1140/epja/i2010-11003-4

135 Kolomeitsev, E. E.; Voskresensky, D. N.: **Neutral weak currents in nucleon superfluid Fermi liquids: Larkin-Migdal and Leggett approaches.** *Physical review C, Nuclear physics* **81**(6): 065801, 2010. DOI:10.1103/physrevc.81.065801

136 Kornilov, V.; Boine-Frankenheim, O.: **Head-tail instability and Landau damping in bunches with space charge.** *Physical Review Special Topics - Accelerators and Beams* **13**(11): 114201, 2010. DOI:10.1103/physrevstab.13.114201 OPEN ACCESS.

137 Kosobudzki, G.; Stafiniak, A.: **AC Loss Measurement of Superconducting Magnet.** *Przeglad Elektrotechniczny* **86**(4): 66–68, 2010.

138 Kovalenko, A.; Bychkov, A.; Fischer, E. ; Hess, G. ; Khodzhibagiyan, H.; Konrad, M.; Macavei, J.; Meier, J. P.; Schnizer, P.; Shabunov, A.; Spiller, P.; Stadlmann, J. ; Titova, G.: **The FAIR SIS100 Synchrotron: Engineering Design of Superconducting Magnetic Modules.** *IEEE transactions on applied superconductivity* **20**(3): 180–183, 2010. DOI:10.1109/tasc.2010.2042441

139 Kowal, M.; Jachimowicz, P.; Sobiczewski, A.: **Fission barriers for even-even superheavy nuclei.** *Physical review C, Nuclear physics* **82**(1): 014303, 2010. DOI:10.1103/physrevc.82.014303

140 Kozub, S.; Bogdanov, I.; Pokrovsky, V.; Seletsky, A.; Shcherbakov, P.; Shirshov, L.; Smirnov, V.; Sytnik, V.; Tkachenko, L.; Zubko, V.; Floch, E.; Moritz, G. ; Mueller, H.: **SIS 300 Dipole Model.** *IEEE transactions on applied superconductivity* **20**(3): 200–203, 2010.

DOI:10.1109/tasc.2009.2039342

141 Kraus, I.; Cleymans, J.; Oeschler, H.; Redlich, K.: **Particle production in p-p collisions at root s17 GeV within a statistical model.** *Physical review C, Nuclear physics* **81**(2): 024903, 2010. DOI:10.1103/physrevc.81.024903

142 Kraus, I.; Cleymans, J.; Oeschler, H.; Redlich, K.: **Prospects for strangeness production in p-p collisions at LHC.** *Journal of physics G, Nuclear and particle physics* **37**(9): 094021, 2010. DOI:10.1088/0954-3899/37/9/094021

143 Kumar, R.; Doornenbal, P.; Jhingan, A.; Bhowmik, R. K.; Muralithar, S.; Appannababu, S.; Garg, R.; Gerl, J. ; Gorska, M.; Kaur, J.; Kojouharov, I.; Mandal, S.; Mukherjee, S.; Siwal, D.; Sharma, A.; Singh, P. P.; Singh, R. P.; Wollersheim, H. J.: **Enhanced 0(g.s)(+) → 2(1)(+) E2 transition strength in Sn-112.** *Physical review C, Nuclear physics* **81**(2): 024306, 2010. DOI:10.1103/physrevc.81.024306

144 Kumm, M.; Klingbeil, H.; Zipf, P.: **An FPGA-Based Linear All-Digital Phase-Locked Loop.** *IEEE Transactions on Circuits and Systems, Part I* **57**(9): 2487–2497, 2010. DOI:10.1109/tcsi.2010.2046237

145 Kurcewicz, J.; Bosch, F.; Geissel, H.; Litvinov, Y. A.; Winckler, N.; Beckert, K.; Beller, P. ; Boutin, D.; Brandau, C.; Chen, L.; Dimopoulou, C.; Essel, H. G.; Fabian, B.; Faestermann, T.; Fragner, A.; Franzke, B. ; Haettner, E.; Hausmann, M.; Hess, S.; Kienle, P.; Knobel, R.; Kozhuharov, C.; Litvinov, S. A.; Maier, L.; Mazzocco, M.; Montes, F.; Musumarra, A.; Nociforo, C.; Nolden, F. ; Patyk, Z.; Plass, W. R.; Prochazka, A.; Reda, R.; Reuschl, R.; Scheidenberger, C.; Steck, M. ; Stohlker, T.; Sun, B.; Takahashi, K.; Torilov, S.; Trassinelli, M.; Weick, H.; Winkler, M.: **Studies of two-body beta-decays at the FRS-ESR facility.** *Acta physica Polonica B* **41**(2): 525–536, 2010. OPEN ACCESS.

146 Langanke, K.: **Nuclear input for supernova simulations and nucleosyntheis.** *Nuclear physics A, Nuclear and hadronic physics* **834**(1): 608C–614C, 2010. DOI:10.1016/j.nuclphysa.2010.01.105

147 Langanke, K.; Martinez-Pinedo, G.: **Neutrino-nucleus reaction in supernovae.** *Progress in particle and nuclear physics* **64**(2): 400–403, 2010. DOI:10.1016/j.ppnp.2009.12.058

148 Lee, H. Y.; Greene, J. P.; Jiang, C. L.; Pardo, R. C.; Rehm, K. E.; Schiffer, J. P.; Wuosmaa, A. H.; Goodman, N. J.; Lighthall, J. C.; Marley, S. T.; Otsuki, K.; Patel, N.; Beard, M.; Notani, M.; Tang, X. D.: **Experimental study of the B-11,B-12(n,gamma) reactions and their influence on r-process nucleosynthesis of light elements.** *Physical review C, Nuclear physics* **81**(1): 015802, 2010. DOI:10.1103/physrevc.81.015802

149 Leibrock, H.; Floch, E.; Moritz, G. ; Ma, L. Z.; Wu, W.; Yuan, P.; Weiyue, W.; Wang, Q. L.: **Prototype of the Superferric Dipoles for the Super-FRS of the FAIR-Project.** *IEEE transactions on applied superconductivity* **20**(3): 188–191, 2010. DOI:10.1109/tasc.2010.2040167

150 Leray, S.; Boudard, A.; Cugnon, J.; David, J. C.; Kelic-Heil, A.; Mancusi, D.; Ricciardi, M. V.: **Improved modelling of helium and tritium production for spallation targets.** *Nuclear instruments & methods in physics research, Section B, Beam interactions with materials and atoms* **268**(6): 581–586, 2010. DOI:10.1016/j.nimb.2009.12.003

151 Levai, P.; Skokov, V.: **Nonperturbative enhancement of heavy quark-pair production in a strong SU(2) color field.** *Physical Review D, particles, fields, gravitation, and cosmology* **82**(7): 074014, 2010. DOI:10.1103/physrevd.82.074014

152 Litvinova, E.; Ring, P.; Tselyaev, V.: **Mode Coupling and the Pygmy Dipole Resonance in a Relativistic Two-Phonon Model.** *Physical review letters* **105**(2): 022502, 2010. DOI:10.1103/physrevlett.105.022502

153 Litvinov, Y. A.; Geissel, H.; Knobel, R.; Sun, B.; Xu, H.: **Direct mass measurements of exotic nuclei in storage rings.** *Acta physica Polonica B* **41**(2): 511–523, 2010. OPEN ACCESS.

154 Lopez, X.; Herrmann, N.; Piasecki, K.; Andronic, A. ; Barret, V.; Basrak, Z.; Bastid, N.; Benabderrahmane, M. L.; Buehler, P.; Cargnelli, M.; Caplar, R.; Crochet, P.; Dupieux, P.; Dzelalija, M.; Fabbietti, L.; Fijal-Kirejczyk, I.; Fodor, Z.; Gasik, P.; Gasparic, I.; Grishkin, Y.; Hartmann, O. N.; Hildenbrand, K. D.; Hong, B.; Kang, T. I.; Kecskemeti, J.; Kirejczyk, M.; Kim, Y. J.; Kis, M.; Koczon, P.; Korolija, M.; Kotte, R.; Lebedev, A.; Leifels, Y.; Manko, V.; Marton, J.; Matulewicz, T.; Merschmeyer, M.; Neubert, W.; Pelte, D.; Petrovici, M.; Rami, F.; Reisdorf, W. ; Ryu, M. S.; Schmidt, P.; Schuettauf, A. ; Seres, Z.; Sikora, B.; Sim, K. S.; Simion, V.; Siwek-Wilczynska, K.; Smolyankin, V.; Suzuki, K.; Tyminski, Z.; Wagner, P.; Widmann, E.; Wisniewski, K.; Xiao, Z. G.; Yushmanov, I.; Zhang, X. Y.; Zhilin, A.; Zmeskal, J.; Kienle, P.; Yamazaki, T.; FOPI Collaboration: **Measurement of K(892)(0) and K-0 mesons in Al plus Al collisions at 1.9A GeV.** *Physical review C, Nuclear physics* **81**(6): 061902, 2010. DOI:10.1103/physrevc.81.061902

155 Luecker, J.; Fischer, C. S.; Williams, R.: **Volume behavior of quark condensate, pion mass, and decay constant from Dyson-Schwinger equations.** *Physical Review D, particles, fields, gravitation, and cosmology* **81**(9): 094005, 2010. DOI:10.1103/physrevd.81.094005

156 Lukic, S.; Gevaert, F.; Kelic, A. ; Ricciardi, M. V.;

Schmidt, K. H.; Yordanov, O.: **Systematic comparison of ISOLDE-SC yields with calculated in-target production rates (vol 565, pg 784, 2006).** *Nuclear instruments & methods in physics research, Section A, Accelerators, spectrometers, detectors and associated equipment* **621**(1): 716–716, 2010. DOI:10.1016/j.nima.2010.03.103

157 Luu, T.; Savage, M. J.; Schwenk, A.; Vary, J. P.: **Nucleon-nucleon scattering in a harmonic potential.** *Physical review C, Nuclear physics* **82**(3): 034003, 2010. DOI:10.1103/physrevc.82.034003

158 Maas, A.; Pawlowski, J. M.; Spielmann, D.; Sternbeck, A.; von Smekal, L.: **Strong-coupling study of the Gribov ambiguity in lattice Landau gauge.** *The European physical journal: C, Particles and fields* **68**(1): 183–195, 2010. DOI:10.1140/epjc/s10052-010-1306-6

159 Mader, J.; Rossbach, J.; Maimone, F.; Spadtke, P.; Tinschert, K. ; Lang, R.; Sun, L.; Cao, Y.; Zhao, H.: **Emittance estimation by an ion optical element with variable focusing strength and a viewing target.** *Review of scientific instruments* **81**(2): 02B720, 2010. DOI:10.1063/1.3272891

160 Maeda, K.; Ropke, F. K.; Fink, M.; Hillebrandt, W.; Travaglio, C.; Thielemann, F. K.: **Nucleosynthesis in two-dimensional delayed detonation models of type Ia supernova explosions.** *The astrophysical journal : an internat. review of spectroscopy and astronomical physics: Part 1* **712**(1): 624–638, 2010. DOI:10.1088/0004-637x/712/1/624

161 Mahjour-Shafiei, M.; Kalantar-Nayestanaki, N.; Weick, H.: **Geant4 Simulation of the Forward Magnetic Spectrometer of EXL.** *Chinese Journal of Physics* **48**(5): 560–566, 2010.

162 Marganiec, J.; Dillmann, I.; Pardo, C. D.; Kappeler, F.; Walter, S.: **Stellar (n, gamma) cross sections of p-process isotopes. II. Yb-168, W-180, Os-184, Pt-190, and Hg-196.** *Physical review C, Nuclear physics* **82**(3): 035806, 2010. DOI:10.1103/physrevc.82.035806

163 Martinez-Pinedo, G.; Arcones, A.: **Neutrinos and explosive nucleosynthesis.** *Progress in particle and nuclear physics* **64**(2): 404–406, 2010. DOI:10.1016/j.ppnp.2009.12.059

164 Massimi, C.; Domingo-Pardo, C.; Vannini, G.; Audouin, L.; Guerrero, C.; Abbondanno, U.; Aerts, G.; Alvarez, H.; Alvarez-Velarde, F.; Andriamonje, S.; Andrzejewski, J.; Assimakopoulos, P.; Badurek, G.; Baumann, P.; Becvar, F.; Belloni, F.; Berthoumieux, E.; Calvino, F.; Calviani, M.; Cano-Ott, D.; Capote, R.; Carrapico, C.; Cennini, P.; Chepel, V.; Chiaveri, E.; Colonna, N.; Cortes, G.; Couture, A.; Cox, J.; Dahlfors, M.; David, S.; Dillmann, I.; Dridi, W.; Duran, I.; Eleftheriadis, C.; Ferrant, L.; Ferrari, A.; Ferreira-Marques, R.; Fujii, K.; Furman, W.; Galanopoulos, S.; Goncalves, I. F.; Gonzalez-Romero, E.; Gramegna, F.; Gunsing, F.; Haas, B.; Haight, R.; Heil, M.; Herrera-Martinez, A.; Igashira, M.; Jericha, E.; Kappeler, F.; Kadi, Y.; Karadimos, D.; Karamanis, D.; Kerveno, M.; Koehler, P.; Kossionides, E.; Krticka, M.; Lampoudis, C.; Lederer, C.; Leeb, H.; Lindote, A.; Lopes, I.; Lozano, M.; Lukic, S.; Marganiec, J.; Marrone, S.; Martinez, T.; Mastinu, P.; Mendoza, E.; Mengoni, A.; Milazzo, P. M.; Moreau, C.; Mosconi, M.; Neves, F.; Oberhummer, H.; O'Brien, S.; Pancin, J.; Papadopoulos, C.; Paradela, C.; Pavlik, A.; Pavlopoulos, P.; Perdikakis, G.; Perrot, L.; Pigni, M. T.; Plag, R.; Plompen, A.; Plukis, A.; Poch, A.; Praena, J.; Pretel, C.; Quesada, J.; Rauscher, T.; Reifarth, R.; Rosetti, M.; Rubbia, C.; Rudolf, G.; Rullhusen, P.; Sarchiapone, L.; Sarmento, R.; Savvidis, I.; Stephan, C.; Tagliente, G.; Tain, J. L.; Tassan-Got, L.; Tavora, L.; Terlizzi, R.; Vaz, P.; Ventura, A.; Villamarin, D.; Vlachoudis, V.; Vlastou, R.; Voss, F.; Walter, S.; Wiescher, M.; Wisshak, K.; N TOF Collaboration: **Au-197(n,gamma) cross section in the resonance region.** *Physical review C, Nuclear physics* **81**(4): 044616, 2010. DOI:10.1103/physrevc.81.044616

165 Mayer, S.; Boschung, M.; Fiechtner, A.; Hohmann, E.; Fehrenbacher, G. ; Radon, T.; Pleskac, R.; Wengenroth, M.: **Response studies of fission track detectors within moderators in CAVE A at GSI.** *Radiation Measurements* **45**(10): 1560–1563, 2010. DOI:10.1016/j.radmeas.2010.05.012

166 Mazzocco, M.; Boiano, A.; Boiano, C.; Di Pietro, A.; Farinon, F.; Figuera, P.; Filipescu, D.; Fortunato, L.; Glodariu, T.; Guglielmetti, A.; Inglima, G.; La Commara, M.; Lattuada, M.; Mazzocchi, C.; Molini, P.; Musumarra, A.; Pakou, A.; Parascandolo, C.; Patronis, N.; Pierroutsakou, D.; Romoli, M.; Sandoli, M.; Scuderi, V.; Signorini, C.; Soramel, F.; Stroe, L.; Torresi, D.; Vardaci, E.; Vitturi, A.: **Scattering of F-17 nuclei from a Ni-58 target at energies around the Coulomb barrier.** *Nuclear physics A, Nuclear and hadronic physics* **834**(1): 488C–490C, 2010. DOI:10.1016/j.nuclphysa.2010.01.073

167 Mazzocco, M.; Signorini, C.; Pierroutsakou, D.; Glodariu, T.; Boiano, A.; Boiano, C.; Farinon, F.; Figuera, P.; Filipescu, D.; Fortunato, L.; Guglielmetti, A.; Inglima, G.; La Commara, M.; Lattuada, M.; Lotti, P.; Mazzocchi, C.; Molini, P.; Musumarra, A.; Pakou, A.; Parascandolo, C.; Patronis, N.; Romoli, M.; Sandoli, M.; Scuderi, V.; Soramel, F.; Stroe, L.; Torresi, D.; Vardaci, E.; Vitturi, A.: **Reaction dynamics for the system F-17+Ni-58 at near-barrier energies.** *Physical review C, Nuclear physics* **82**(5): 054604, 2010. DOI:10.1103/physrevc.82.054604

168 McIntosh, A. B.; Hudan, S.; Black, J.; Mercier, D.; Metelko, C. J.; Yanez, R.; de Souza, R. T.; Chbihi, A.; Famiano, M.; Fregeau, M. O.; Gauthier, J.; Moisan, J.; Roy, R.; Bianchin, S.; Schwarz, C.; Trautmann, W. : **Short-lived binary splits of an excited projectile-**

like fragment induced by transient deformation. *Physical review C, Nuclear physics* **81**(3): 034603, 2010. DOI:10.1103/physrevc.81.034603

169 Mengoni, D.; Valiente-Dobon, J. J.; Gadea, A.; Lunardi, S.; Lenzi, S. M.; Broda, R.; Dewald, A.; Pissulla, T.; Angus, L. J.; Aydin, S.; Bazzacco, D.; Benzoni, G.; Bizzeti, P. G.; Bizzeti-Sona, A. M.; Boutachkov, P.; Corradi, L.; Crespi, F.; de Angelis, G.; Farnea, E.; Fioretto, E.; Goergen, A.; Gorska, M.; Gottardo, A.; Grodner, E.; Howard, A. M.; Krolas, W.; Leoni, S.; Mason, P.; Montanari, D.; Montagnoli, G.; Napoli, D. R.; Obertelli, A.; Orlandi, R.; Pawlat, T.; Pollarolo, G.; Recchia, F.; Algora, A.; Rubio, B.; Sahin, E.; Scarlassara, F.; Silvestri, R.; Smith, J. F.; Stefanini, A. M.; Steppenbeck, D.; Szilner, S.; Ur, C. A.; Wady, P. T.; Wrzesinski, J.: **Lifetime measurements of excited states in neutron-rich Ar-44,Ar-46 populated via a multinucleon transfer reaction.** *Physical review C, Nuclear physics* **82**(2): 024308, 2010. DOI:10.1103/physrevc.82.024308

170 Metzger, B. D.; Arcones, A.; Quataert, E.; Martinez-Pinedo, G.: **The effects of r-process heating on fallback accretion in compact object mergers.** *Monthly Notices of the Royal Astronomical Society* **402**(4): 2771–2777, 2010. DOI:10.1111/j.1365-2966.2009.16107.x

171 Metzger, B. D.; Martinez-Pinedo, G.; Darbha, S.; Quataert, E.; Arcones, A.; Kasen, D.; Thomas, R.; Nugent, P.; Panov, I. V.; Zinner, N. T.: **Electromagnetic counterparts of compact object mergers powered by the radioactive decay of r-process nuclei.** *Monthly Notices of the Royal Astronomical Society* **406**(4): 2650–2662, 2010. DOI:10.1111/j.1365-2966.2010.16864.x

172 Mintz, B. W.; Fraga, E. S.; Pagliara, G.; Schaffner-Bielich, J.: **Nucleation of quark matter in protoneutron star matter.** *Physical Review D, particles, fields, gravitation, and cosmology* **81**(12): 123012, 2010. DOI:10.1103/physrevd.81.123012

173 Morita, K.; Lee, S. H.: **Heavy quarkonium correlators at finite temperature: QCD sum rule approach.** *Physical Review D, particles, fields, gravitation, and cosmology* **82**(5): 054008, 2010. DOI:10.1103/physrevd.82.054008

174 Mueller, J. A.; Fischer, C. S.; Nickel, D.: **Quark spectral properties above T (c) from Dyson-Schwinger equations.** *The European physical journal: C, Particles and fields* **70**(4): 1037–1049, 2010. DOI:10.1140/epjc/s10052-010-1499-8

175 Mukha, I.; Summerer, K.; Acosta, L.; Alvarez, M. A. G.; Casarejos, E.; Chatillon, A.; Cortina-Gil, D.; Egorova, I. A.; Espino, J. M.; Fomichev, A.; Garcia-Ramos, J. E.; Geissel, H.; Gomez-Camacho, J.; Grigorenko, L. ; Hofmann, J.; Kiselev, O.; Korsheninnikov, A.; Kurz, N.; Litvinov, Y. A.; Litvinova, E.; Martel, I.; Nociforo, C.; Ott, W.; Pfutzner, M.; Rodriguez-Tajes, C.; Roeckl, E. ; Stanoiu, M.; Timofeyuk, N. K.; Weick, H.; Woods, P. J.: **Spectroscopy of proton-unbound nuclei by tracking their decay products in-flight: One- and two-proton decays of F-15, Ne-16, and Na-19.** *Physical review C, Nuclear physics* **82**(5): 054315, 2010. DOI:10.1103/physrevc.82.054315

176 Nakano, E.; Schaefer, B. J.; Stokic, B.; Friman, B. ; Redlich, K.: **Fluctuations and isentropes near the chiral critical endpoint.** *Physics letters B* **682**(4): 401–407, 2010. DOI:10.1016/j.physletb.2009.11.027

177 Naqvi, F.; Gorska, M.; Caceres, L.; Jungclaus, A.; Pfutzner, M.; Grawe, H.; Nowacki, F.; Sieja, K.; Pietri, S.; Werner-Malento, E.; Regan, P. H.; Rudolf, D.; Podolyak, Z.; Jolie, J.; Andgren, K.; Beck, T.; Bednarczyk, P. ; Benlliure, J.; Benzoni, G.; Bruce, A. M.; Casarejos, E.; Cederwall, B.; Crespi, F. C. L.; Detistov, P.; Dombradi, Z.; Doornenbal, P.; Geissel, H.; Gerl, J. ; Grebosz, J.; Hadinia, B.; Hellstrom, M.; Hoischen, R.; Ilie, G.; Khaplanov, A.; Kojouharov, I.; Kmiecik, M.; Kurz, N.; Lalkovski, S.; Maj, A.; Mandal, S.; Modamio, V.; Montes, F.; Myalski, S.; Prokopowicz, W.; Reiter, P.; Schaffner, H.; Simpson, G.; Sohler, D.; Steer, S. J.; Tashenov, S.; Walker, J.; Wieland, O.; Wollersheim, H. J.: **Isomer spectroscopy of Cd-127.** *Physical review C, Nuclear physics* **82**(3): 034323, 2010. DOI:10.1103/physrevc.82.034323

178 Natowitz, J. B.; Ropke, G.; Typel, S.; Blaschke, D.; Bonasera, A.; Hagel, K.; Klahn, T.; Kowalski, S.; Qin, L.; Shlomo, S.; Wada, R.; Wolter, H. H.: **Symmetry Energy of Dilute Warm Nuclear Matter.** *Physical review letters* **104**(20): 202501, 2010. DOI:10.1103/physrevlett.104.202501

179 Nishio, K.; Hofmann, S. ; Hessberger, F. P.; Ackermann, D. ; Antalic, S. ; Aritomo, Y.; Comas, V. F.; Dullmann, C. E.; Gorshkov, A.; Graeger, R.; Hagino, K.; Heinz, S.; Heredia, J. A.; Hirose, K.; Ikezoe, H.; Khuyagbaatar, J.; Kindler, B. ; Kojouharov, I.; Lommel, B.; Mann, R.; Mitsuoka, S.; Nagame, Y.; Nishinaka, I.; Ohtsuki, T.; Popeko, A. G.; Saro, S.; Schadel, M.; Turler, A.; Watanabe, Y.; Yakushev, A.; Yeremin, A. V.: **Nuclear orientation in the reaction S-34+U-238 and synthesis of the new isotope (268)Hs.** *Physical review C, Nuclear physics* **82**(2): 024611, 2010. DOI:10.1103/physrevc.82.024611

180 Nishio, K.; Ikezoe, H.; Nishinaka, I.; Mitsuoka, S.; Hirose, K.; Ohtsuki, T.; Watanabe, Y.; Aritomo, Y.; Hofmann, S. : **Evidence for quasifission in the sub-barrier reaction of Si-30+U-238.** *Physical review C, Nuclear physics* **82**(4): 044604, 2010. DOI:10.1103/physrevc.82.044604

181 Ohnishi, T.; Kubo, T.; Kusaka, K.; Yoshida, A.; Yoshida, K.; Ohtake, M.; Fukuda, N.; Takeda, H.; Kameda, D.; Tanaka, K.; Inabe, N.; Yanagisawa, Y.; Gono, Y.; Watanabe, H.; Otsu, H.; Baba, H.; Ichihara, T.; Yamaguchi, Y.; Takechi, M.; Nishimura, S.; Ueno, H.; Yoshimi, A.;

Sakurai, H.; Motobayashi, T.; Nakao, T.; Mizoi, Y.; Matsushita, M.; Ieki, K.; Kobayashi, N.; Tanaka, K.; Kawada, Y.; Tanaka, N.; Deguchi, S.; Satou, Y.; Kondo, Y.; Nakamura, T.; Yoshinaga, K.; Ishii, C.; Yoshii, H.; Miyashita, Y.; Uematsu, N.; Shiraki, Y.; Sumikama, T.; Chiba, J.; Ideguchi, E.; Saito, A.; Yamaguchi, T.; Hachiuma, I.; Suzuki, T.; Moriguchi, T.; Ozawa, A.; Ohtsubo, T.; Famiano, M. A.; Geissel, H.; Nettleton, A. S.; Tarasov, O. B.; Bazin, D. P.; Sherrill, B. M.; Manikonda, S. L.; Nolen, J. A.: **Identification of 45 New Neutron-Rich Isotopes Produced by In-Flight Fission of a U-238 Beam at 345 MeV/nucleon.** *Journal of the Physical Society of Japan* **79**(7): 073201, 2010. DOI:10.1143/jpsj.79.073201

182 Pangon, V.; Nagy, S.; Polonyi, J.; Sailer, K.: **Quantum censorship in two dimensions.** *Physics letters B* **694**(1): 89–93, 2010. DOI:10.1016/j.physletb.2010.09.041

183 Paradela, C.; Tassan-Got, L.; Audouin, L.; Berthier, B.; Duran, I.; Ferrant, L.; Isaev, S.; Le Naour, C.; Stephan, C.; Tarrio, D.; Trubert, D.; Abbondanno, U.; Aerts, G.; Alvarez, H.; Alvarez-Velarde, F.; Andriamonje, S.; Andrzejewski, J.; Assimakopoulos, P.; Badurek, G.; Baumann, P.; Becvar, F.; Berthoumieux, E.; Calvino, F.; Calviani, M.; Cano-Ott, D.; Capote, R.; Carrapico, C.; Cennini, P.; Chepel, V.; Chiaveri, E.; Colonna, N.; Cortes, G.; Couture, A.; Cox, J.; Dahlfors, M.; David, S.; Dillmann, I.; Domingo-Pardo, C.; Dridi, W.; Eleftheriadis, C.; Embid-Segura, M.; Ferrari, A.; Ferreira-Marques, R.; Fujii, K.; Furman, W.; Goncalves, I.; Gonzalez-Romero, E.; Gramegna, F.; Guerrero, C.; Gunsing, F.; Haas, B.; Haight, R.; Heil, M.; Herrera-Martinez, A.; Igashira, M.; Jericha, E.; Kadi, Y.; Kappeler, F.; Karadimos, D.; Karamanis, D.; Kerveno, M.; Koehler, P.; Kossionides, E.; Krticka, M.; Lampoudis, C.; Leeb, H.; Lindote, A.; Lopes, I.; Lozano, M.; Lukic, S.; Marganiec, J.; Marrone, S.; Martinez, T.; Massimi, C.; Mastinu, P.; Mengoni, A.; Milazzo, P. M.; Moreau, C.; Mosconi, M.; Neves, F.; Oberhummer, H.; O'Brien, S.; Oshima, M.; Pancin, J.; Papachristodoulou, C.; Papadopoulos, C.; Patronis, N.; Pavlik, A.; Pavlopoulos, P.; Perrot, L.; Pigni, M. T.; Plag, R.; Plompen, A.; Plukis, A.; Poch, A.; Praena, J.; Pretel, C.; Quesada, J.; Rauscher, T.; Reifarth, R.; Rubbia, C.; Rudolf, G.; Rullhusen, P.; Salgado, J.; Santos, C.; Sarchiapone, L.; Savvidis, I.; Tagliente, G.; Tain, J. L.; Tavora, L.; Terlizzi, R.; Vannini, G.; Vaz, P.; Ventura, A.; Villamarin, D.; Vincente, M. C.; Vlachoudis, V.; Vlastou, R.; Voss, F.; Walter, S.; Wiescher, M.; Wisshak, K.; n TOF Collaboration: **Neutron-induced fission cross section of U-234 and Np-237 measured at the CERN Neutron Time-of-Flight (n_TOF) facility.** *Physical review C, Nuclear physics* **82**(3): 034601, 2010. DOI:10.1103/physrevc.82.034601

184 Parascandolo, C.; Pierroutsakou, D.; Martin, B.; Agodi, C.; Alba, R.; Boiano, A.; Coniglione, R.; De Filippo, E.; Del Zoppo, A.; Emanuele, U.; Farinon, F.; Guglielmetti, A.; Inglima, G.; La Commara, M.; Maiolino, C.; Mazzocchi, C.; Mazzocco, M.; Romoli, M.; Sandoli, M.; Santonocito, D.; Signorini, C.; Silvestri, R.; Trifiro, A.; Trimarchi, M.: **Dynamical dipole mode in heavy-ion fusion reactions.** *Nuclear physics A, Nuclear and hadronic physics* **834**(1): 198C–200C, 2010. DOI:10.1016/j.nuclphysa.2009.12.039

185 Paret, S.; Kornilov, V.; Boine-Frankenheim, O.; Weiland, T.: **Transverse Schottky and beam transfer function measurements in space charge affected coasting ion beams.** *Physical Review Special Topics - Accelerators and Beams* **13**(2): 022802, 2010. DOI:10.1103/physrevstab.13.022802 OPEN ACCESS.

186 Pershina, V. ; Borschevsky, A.; Anton, J.; Jacob, T.: **Theoretical predictions of trends in spectroscopic properties of homonuclear dimers and volatility of the 7p elements.** *Journal of Chemical Physics* **132**(19): 194314, 2010. DOI:10.1063/1.3425996

187 Pershina, V. ; Borschevsky, A.; Anton, J.; Jacob, T.: **Theoretical predictions of trends in spectroscopic properties of gold containing dimers of the 6p and 7p elements and their adsorption on gold.** *Journal of Chemical Physics* **133**(10): 104304, 2010. DOI:10.1063/1.3476470

188 Petermann, I.; Langanke, K.; Martinez-Pinedo, G.; von Neumann-Cosel, P.; Nowacki, F.; Richter, A.: **Scales in the fine structure of the magnetic dipole resonance: A wavelet approach to the shell model.** *Physical review C, Nuclear physics* **81**(1): 014308, 2010. DOI:10.1103/physrevc.81.014308

189 Petris, M.; Petrovici, M.; Bartos, D.; Berceanu, I.; Simion, V.; Radu, A.; Andronic, A. ; Garabatos, C. ; Klein-Bosing, M.; Simon, R.; Uhlig, F.; Wessels, J. P.; Wilk, A.: **Rate capability of a high efficienc transition radiation detector.** *Romanian Journal of Physics* **55**(3): 324–332, 2010.

190 Pietraszko, J.; Fabbietti, L.; HADES Collaboration: **Strangeness Production at SIS measured with HADES.** *Nuclear physics A, Nuclear and hadronic physics* **834**(1): 288C–290C, 2010. DOI:10.1016/j.nuclphysa.2009.12.062

191 Pietraszko, J.; Fabbietti, L.; Koenig, W.; Weber, M.: **Diamonds as timing detectors for minimum-ionizing particles: The HADES proton-beam monitor and START signal detectors for time of flight measurements.** *Nuclear instruments & methods in physics research, Section A, Accelerators, spectrometers, detectors and associated equipment* **618**(1): 121–123, 2010. DOI:10.1016/j.nima.2010.02.113

192 Pignatari, M.; Gallino, R.; Heil, M.; Wiescher, M.; Kappeler, F.; Herwig, F.; Bisterzo, S.: **The weak s-process in massive stars and its dependence on the neutron capture cross sections.** *The astrophysical journal : an internat. review of spectroscopy and as-*

tronomical physics: Part 1 **710**(2): 1557–1577, 2010. DOI:10.1088/0004-637x/710/2/1557

193 Potanina, L.; Pantsyrny, V.; Shikov, A.; Salunin, N.; Gubkin, I.; Korpusov, V.; Khodzhibagiyan, H.; Kovalenko, A.; Fischer, E. ; Mueller, H.; Moritz, G. : **Experimental Results on the Development of Superconducting NbTi/Cu-Mn/Cu Wires for Magnet Systems of SIS100 and SIS300 Synchrotrons of FAIR.** *IEEE transactions on applied superconductivity* **20**(3): 1395–1398, 2010. DOI:10.1109/tasc.2010.2043830

194 Rahman, M. S.; Evangelou, E. K.; Androulidakis, I. I.; Dimoulas, A.; Mavrou, G.; Galata, S.: **SILC decay in La2O3 gate dielectrics grown on Ge substrates subjected to constant voltage stress.** *Solid-State Electronics* **54**(9): 979–984, 2010. DOI:10.1016/j.sse.2010.04.023

195 Ramstein, B.; Agakichiev, C.; Agodi, C.; Balanda, A.; Bellia, G.; Belver, D.; Belyaev, A.; Blanco, A.; Bohmer, M.; Boyard, J. L.; Braun-Munzinger, R.; Cabanelas, P.; Castro, E.; Christ, T.; Destefanis, M.; Diaz, J.; Dohrmann, F.; Dybczak, A.; Fabbietti, L.; Fateev, O.; Finocchiaro, P.; Fonte, P.; Friese, J.; Frohlich, I.; Galatyuk, T.; Garzon, J. A.; Gernhauser, R.; Gil, A.; Gilardi, C.; Golubeva, M.; Gonzalez-Diaz, D.; Grosse, E.; Guber, F.; Heilmann, M.; Hennino, T.; Holzmann, R.; Ierusalimov, A.; Iori, I.; Ivashkin, A.; Jurkovic, M.; Kampfer, B.; Kanaki, K.; Karavicheva, T.; Kirschner, D.; Koenig, I.; Koenig, W.; Kolb, B. W.; Kotte, R.; Kozuch, A.; Krasa, A.; Krizek, F.; Krucken, R.; Kuhn, W.; Kugler, A.; Kurepin, A.; Lamas-Valverde, J.; Lang, S.; Lange, J. S.; Lapidus, K.; Lopes, L.; Lorenz, M.; Liu, T.; Maier, L.; Mangiarotti, A.; Marin, J.; Markert, J.; Metag, V.; Michalska, B.; Michel, J.; Mishra, D.; Moriniere, E.; Mousa, J.; Muntz, C.; Naumann, L.; Novotny, R.; Otwinowski, J.; Pachmayer, Y. C.; Palka, M.; Parpottas, Y.; Pechenov, V.; Pechenova, O.; Cavalcanti, T. P.; Pietraszko, J.; Przygoda, W.; Reshetin, A.; Rustamov, A.; Sadovsky, A.; Salabura, P.; Schma, A.; Simon, R.; Sobolev, Y. G.; Spataro, S.; Spruck, B.; Strobele, H.; Stroth, J. ; Sturm, C.; Sudoi, M.; Tarantola, A.; Teilab, K.; Tlusty, P.; Traxler, M.; Trebacz, R.; Tsertos, H.; Veretenkin, I.; Wagner, V.; Weber, M.; Wisniowski, M.; Wustenfeld, J.; Yurevich, S.; Zanevsky, Y. V.; Zhou, P.; Zumbruch, P.: **Study of elementary reactions with the HADES dielectron spectrometer.** *Acta physica Polonica B* **41**(2): 365–377, 2010. OPEN ACCESS.

196 Rappold, C.; Saito, T. R.; Bianchin, S.; Borodina, O.; Kavatsyuk, M.; Maas, F.; Minami, S.; Nakajima, D.; Ozel-Tashenov, B.; Trautmann, W. : **Event reconstruction methods for the HypHI Phase 0 experiment at GSI.** *Nuclear instruments & methods in physics research, Section A, Accelerators, spectrometers, detectors and associated equipment* **622**(1): 231–235, 2010. DOI:10.1016/j.nima.2010.06.365

197 Rebisz-Pomorska, M.; Ciobanu, M.; Kis, M.; Pomorski, M.; Voss, B.: **Diamond detectors for the monitoring of carbon-ion therapy beams.** *Nuclear instruments & methods in physics research, Section A, Accelerators, spectrometers, detectors and associated equipment* **620**(2): 534–539, 2010. DOI:10.1016/j.nima.2010.02.066

198 Reisdorf, W. ; Andronic, A. ; Averbeck, R.; Benabderrahmane, M. L.; Hartmann, O. N.; Herrmann, N.; Hildenbrand, K. D.; Kang, T. I.; Kim, Y. J.; Kis, M.; Koczon, P.; Kress, T.; Leifels, Y.; Merschmeyer, M.; Piasecki, K.; Schuttauf, A.; Stockmeier, M.; Barret, V.; Basrak, Z.; Bastid, N.; Caplar, R.; Crochet, P.; Dupieux, P.; Dzelalija, M.; Fodor, Z.; Gasik, P.; Grishkin, Y.; Hong, B.; Kecskemeti, J.; Kirejczyk, M.; Korolija, M.; Kotte, R.; Lebedev, A.; Lopez, X.; Matulewicz, T.; Neubert, W.; Petrovici, M.; Rami, F.; Ryu, M. S.; Seres, Z.; Sikora, B.; Sim, K. S.; Simion, V.; Siwek-Wilczynska, K.; Smolyankin, V.; Stoicea, G.; Tyminski, Z.; Wisniewski, K.; Wohlfarth, D.; Xiao, Z. G.; Xu, H. S.; Yushmanov, I.; Zhilin, A.: **Systematics of central heavy ion collisions in the 1A GeV regime.** *Nuclear physics A, Nuclear and hadronic physics* **848**(3): 366–427, 2010. DOI:10.1016/j.nuclphysa.2010.09.008

199 Riek, F. ; Knoll, J. : **Self-consistent descriptions of vector mesons in hot matter reexamined.** *Physical review C, Nuclear physics* **82**(2): 025207, 2010. DOI:10.1103/physrevc.82.025207

200 Rodriguez-Tajes, C.; Alvarez-Pol, H.; Aumann, T. ; Benjamim, E.; Benlliure, J.; Borge, M. J. G.; Caamano, M.; Casarejos, E.; Chatillon, A.; Cortina-Gil, D.; Eppinger, K.; Faestermann, T.; Gascon, M.; Geissel, H.; Gernhauser, R.; Jonson, B.; Kanungo, R.; Krucken, R.; Kurtukian, T.; Larsson, K.; Maierbeck, P.; Nilsson, T.; Nociforo, C.; Pascual-Izarra, C.; Perea, A.; Perez-Loureiro, D.; Prochazka, A.; Schwertel, S.; Simon, H.; Summerer, K.; Tengblad, O.; Weick, H.; Winkler, M.; Zhukov, M.: **One-neutron knockout from light neutron-rich nuclei at relativistic energies (vol 82, art no 024305, 2010).** *Physical review C, Nuclear physics* **82**(2): 029910, 2010. DOI:10.1103/physrevc.82.029910

201 Rodriguez-Tajes, C.; Cortina-Gil, D.; Alvarez-Pol, H.; Aumann, T. ; Benjamim, E.; Benlliure, J.; Borge, M. J. G.; Caamano, M.; Casarejos, E.; Chatillon, A.; Eppinger, K.; Faestermann, T.; Gascon, M.; Geissel, H.; Gernhauser, R.; Jonson, B.; Kanungo, R.; Krucken, R.; Kurtukian, T.; Larsson, K.; Maierbeck, P.; Nilsson, T.; Nociforo, C.; Pascual-Izarra, C.; Perea, A.; Perez-Loureiro, D.; Prochazka, A.; Simon, H.; Summerer, K.; Tengblad, O.; Weick, H.; Winkler, M.; Zhukov, M.: **One-neutron knockout from Ne24-28 isotopes.** *Physics letters B* **687**(1): 26–30, 2010. DOI:10.1016/j.physletb.2010.03.006

202 Rodriguez, T. R.; Egido, J. L.: **Triaxial angular momentum projection and configuration mixing calculations with the Gogny force.** *Physi-*

cal review C, Nuclear physics **81**(6): 064323, 2010. DOI:10.1103/physrevc.81.064323

203 Rodriguez, T. R.; Martinez-Pinedo, G.: **Energy Density Functional Study of Nuclear Matrix Elements for Neutrinoless beta beta Decay.** *Physical review letters* **105**(25): 252503, 2010. DOI:10.1103/physrevlett.105.252503

204 Roth, R.; Neff, T.; Feldmeier, H.: **Nuclear structure in the framework of the Unitary Correlation Operator Method.** *Progress in particle and nuclear physics* **65**(1): 50–93, 2010. DOI:10.1016/j.ppnp.2010.02.003

205 Saito, T. R.; Bianchin, S.; Borodina, O.; Bozkurt, V.; Gokuzum, B.; Kavatsyuk, M.; Kim, E.; Minami, S.; Nakajima, D.; Ozel-Tashenov, B.; Rappold, C.; Achenbach, P.; Ajimura, S.; Aumann, T. ; Caesar, C.; Erturk, S.; Fukuda, T.; Guliev, E.; Hayashi, Y.; Hiraiwa, T.; Hoffmann, J.; Ickert, G.; Ketenci, Z. S.; Khaneft, D.; Kim, M.; Kim, S.; Koch, K.; Kurz, N.; Ma, Y.; Maas, F.; Mizoi, S.; Moritsu, M.; Nagae, T.; Okamura, A.; Ott, W.; Pochodzalla, J.; Sakaguchi, A.; Sako, M.; Schmidt, C. J.; Sekimoto, M.; Simon, H.; Sugimura, H.; Takahashi, T.; Tambave, G. J.; Tanida, K.; Tamura, K.; Trager, M.; Trautmann, W. ; Voltz, S.; Yoon, C. J.; Yoshida, K.: **The HypHI Phase 0 experiment.** *Nuclear physics A, Nuclear and hadronic physics* **835**(1): 110–116, 2010. DOI:10.1016/j.nuclphysa.2010.01.182

206 Schaefer, B. J.; Wagner, M.; Wambach, J.: **Thermodynamics of (2+1)-flavor QCD: Confronting models with lattice studies.** *Physical Review D, particles, fields, gravitation, and cosmology* **81**(7): 074013, 2010. DOI:10.1103/physrevd.81.074013

207 Scheck, M.; Grahn, T.; Petts, A.; Butler, P. A.; Dewald, A.; Gaffney, L. P.; Hornillos, M. B. G.; Gorgen, A.; Greenlees, P. T.; Helariutta, K.; Jolie, J.; Jones, P.; Julin, R.; Juutinen, S.; Ketelhut, S.; Kroll, T.; Krucken, R.; Leino, M.; Ljungvall, J.; Maierbeck, P.; Melon, B.; Nyman, M.; Page, R. D.; Pakarinen, J.; Paul, E. S.; Pissulla, T.; Rahkila, P.; Saren, J.; Scholey, C.; Semchenkov, A.; Sorri, J.; Uusitalo, J.; Wadsworth, R.; Zielinska, M.: **Lifetimes of odd-spin yrast states in Hg-182.** *Physical review C, Nuclear physics* **81**(1): 014310, 2010. DOI:10.1103/physrevc.81.014310

208 Scheppach, C.; Berges, J.; Gasenzer, T.: **Matter-wave turbulence: Beyond kinetic scaling.** *Physical review A, Atomic, molecular, and optical physics* **81**(3): 033611, 2010. DOI:10.1103/physreva.81.033611

209 Schmitt, C. ; Schmidt, K. H.; Kelic, A. ; Heinz, A.; Jurado, B.; Nadtochy, P. N.: **Fragmentation of spherical radioactive heavy nuclei as a novel probe of transient effects in fission.** *Physical review C, Nuclear physics* **81**(6): 064602, 2010. DOI:10.1103/physrevc.81.064602

210 Schnizer, P.; Fischer, E. ; Kiesewetter, H.; Klos, F. ; Knapp, T.; Mack, T.; Mierau, A.; Schnizer, B.: **Mole for Measuring SIS100 Magnets Commissioning and First Test Results.** *IEEE transactions on applied superconductivity* **20**(3): 1977–1980, 2010. DOI:10.1109/tasc.2010.2041536

211 Schramm, S.; Steinheimer, J.; Dexheimer, V.; Stocker, H.: **Phase structure of strongly interacting matter and simulations of heavy-ion collisions using a quark-hadron model.** *Journal of physics G, Nuclear and particle physics* **37**(9): 094041, 2010. DOI:10.1088/0954-3899/37/9/094041

212 Schumann, D.; Neuhausen, J.; Dillmann, I.; Pardo, C. D.; Kappeler, F.; Marganiec, J.; Voss, F.; Walter, S.; Heil, M.; Reifarth, R.; Goerres, J.; Uberseder, E.; Wiescher, M.; Pignatari, M.: **Preparation of a Fe-60 target for nuclear astrophysics experiments.** *Nuclear instruments & methods in physics research, Section A, Accelerators, spectrometers, detectors and associated equipment* **613**(3): 347–350, 2010. DOI:10.1016/j.nima.2009.09.072

213 Senger, P.: **Strangeness production in heavy-ion collisions.** *Nuclear physics A, Nuclear and hadronic physics* **835**(1): 102–109, 2010. DOI:10.1016/j.nuclphysa.2010.01.181

214 Shimamoto, D.; Fujisawa, K.; Muramatsu, H.; Hayashi, T.; Kim, Y. A.; Yanagisawa, T.; Endo, M.; Dresselhaus, M. S.: **A simple route to short cup-stacked carbon nanotubes by sonication.** *Carbon* **48**(12): 3643–3647, 2010. DOI:10.1016/j.carbon.2010.05.040

215 Signorini, C.; Pierroutsakou, D.; Martin, B.; Mazzocco, M.; Glodariu, T.; Bonetti, R.; Guglielmetti, A.; La Commara, M.; Romoli, M.; Sandoli, M.; Vardaci, E.; Esbensen, H.; Farinon, F.; Molini, P.; Parascandolo, C.; Soramel, F.; Sidortchuk, S.; Stroe, L.: **Interaction of F-17 with a Pb-208 target below the Coulomb barrier.** *The European physical journal A, Hadrons and nuclei* **44**(1): 63–69, 2010. DOI:10.1140/epja/i2010-10934-x

216 Simon, H.: **Light exotic systems at relativistic velocities.** *Nuclear physics A, Nuclear and hadronic physics* **834**(1): 394C–399C, 2010. DOI:10.1016/j.nuclphysa.2010.01.048

217 Skokov, V.; Friman, B. ; Nakano, E.; Redlich, K.; Schaefer, B. J.: **Vacuum fluctuations and the thermodynamics of chiral models.** *Physical Review D, particles, fields, gravitation, and cosmology* **82**(3): 034029, 2010. DOI:10.1103/physrevd.82.034029

218 Skokov, V.; Stokic, B.; Friman, B. ; Redlich, K.: **Meson fluctuations and thermodynamics of the Polyakov-loop-extended quark-meson model.** *Physical review C, Nuclear physics* **82**(1): 015206, 2010. DOI:10.1103/physrevc.82.015206

219 Skokov, V. V.; Voskresensky, D. N.: **Thermal conductivity in dynamics of first-order phase transitions.** *Nuclear physics A, Nuclear and hadronic physics* **847**(3): 253–267, 2010. DOI:10.1016/j.nuclphysa.2010.07.006

220 Smirnova, N. A.; Bally, B.; Heyde, K.; Nowacki, F.; Sieja, K.: **Shell evolution and nuclear forces.** *Physics letters B* **686**(2): 109–113, 2010. DOI:10.1016/j.physletb.2010.02.051

221 Soyeur, M.; Lutz, M. F. M.: **Dynamics of strong and radiative decays of D-s-mesons in the hadrogenesis conjecture.** *Chinese Physics* **34**(9): 1320–1323, 2010.

222 Spadtke, P.: **Model for the description of ion beam extraction from electron cyclotron resonance ion sources.** *Review of scientific instruments* **81**(2): 02B725, 2010. DOI:10.1063/1.3318157

223 Steier, P.; Dellinger, F.; Forstner, O.; Golser, R.; Knie, K.; Kutschera, W.; Priller, A.; Quinto, F.; Srncik, M.; Terrasi, F.; Vockenhuber, C.; Wallner, A.; Wallner, G.; Wild, E. M.: **Analysis and application of heavy isotopes in the environment.** *Nuclear instruments & methods in physics research, Section B, Beam interactions with materials and atoms* **268**(7): 1045–1049, 2010. DOI:10.1016/j.nimb.2009.10.094

224 Steinheimer, J.; Dexheimer, V.; Bleicher, M.; Petersen, H.; Schramm, S.; Stocker, H.: **Hydrodynamics with a chiral hadronic equation of state including quark degrees of freedom.** *Physical review C, Nuclear physics* **81**(4): 044913, 2010. DOI:10.1103/physrevc.81.044913

225 Steinheimer, J.; Sturm, C.; Schramm, S.; Stocker, H.: **Strange perspectives at FAIR.** *Journal of physics G, Nuclear and particle physics* **37**(9): 094026, 2010. DOI:10.1088/0954-3899/37/9/094026

226 Stokic, B.; Friman, B. ; Redlich, K.: **The functional renormalization group and O(4) scaling.** *The European physical journal: C, Particles and fields* **67**(3): 425–438, 2010. DOI:10.1140/epjc/s10052-010-1310-x

227 Strasik, I.; Mustafin, E.; Pavlovic, M.: **Residual activity induced by heavy ions and beam-loss criteria for heavy-ion accelerators.** *Physical Review Special Topics - Accelerators and Beams* **13**(7): 071004, 2010. DOI:10.1103/physrevstab.13.071004 OPEN ACCESS.

228 Strasik, I.; Mustafin, E.; Seidl, T.; Pavlovic, M.: **Experimental study and simulation of the residual activity induced by high-energy argon ions in copper.** *Nuclear instruments & methods in physics research, Section B, Beam interactions with materials and atoms* **268**(6): 573–580, 2010. DOI:10.1016/j.nimb.2009.12.004

229 Streicher, B.; Hessberger, F. P.; Antalic, S. ; Hofmann, S. ; Ackermann, D. ; Heinz, S.; Kindler, B. ; Khuyagbaatar, J.; Kojouharov, I.; Kuusiniemi, P.; Leino, M.; Lommel, B.; Mann, R.; Saro, S.; Sulignano, B.; Uusitalo, J.; Venhart, M.: **Alpha-gamma decay studies of (261)Sg and (257)Rf.** *The European physical journal A, Hadrons and nuclei* **45**(3): 275–286, 2010. DOI:10.1140/epja/i2010-11005-2

230 Sturm, C.; Sharkov, B.; Stocker, H.: **1, 2, 3 ... FAIR!.** *Nuclear physics A, Nuclear and hadronic physics* **834**(1): 682C–687C, 2010. DOI:10.1016/j.nuclphysa.2010.01.124

231 Sudol, M.; Espi, M. C. M.; Becheva, E.; Boucher, J.; Hennino, T.; Kunne, R.; Marchand, D.; Ong, S.; Ramstein, B.; Van de Wiele, J.; Zerguerras, T.; Maas, F.; Kopf, B.; Pelizaeus, M.; Steinke, M.; Zhong, J.; Tomasi-Gustafsson, E.: **Feasibility studies of the time-like proton electromagnetic form factor measurements with (P)over-barANDA at FAIR.** *The European physical journal A, Hadrons and nuclei* **44**(3): 373–384, 2010. DOI:10.1140/epja/i2010-10960-8

232 Sugita, K.; Fischer, E. ; Khodzhibagiyan, H.; Macavei, J.: **Design Study of Superconducting Corrector Magnets for SIS 100.** *IEEE transactions on applied superconductivity* **20**(3): 164–167, 2010. DOI:10.1109/tasc.2009.2038716

233 Sun, B.; Bosch, F.; Boutin, D.; Brandau, C.; Chen, L.; Dimopoulou, C.; Fabian, B.; Geissel, H.; Knobel, R.; Kozhuharov, C.; Kurcewicz, J.; Litvinov, S. A.; Litvinov, Y. A.; Meng, J.; Munzenberg, G.; Nociforo, C.; Nolden, F. ; Plass, W. R.; Scheidenberger, C.; Steck, M. ; Walker, P. M.; Weick, H.; Winckler, N.; Winkler, M.: **Precise measurement of nuclear isomers in the storage ring at GSI.** *Nuclear physics A, Nuclear and hadronic physics* **834**(1): 476C–478C, 2010. DOI:10.1016/j.nuclphysa.2010.01.069

234 Sun, B.; Knobel, R.; Geissel, H.; Litvinov, Y. A.; Walker, P. M.; Blaum, K.; Bosch, F.; Boutin, D.; Brandau, C.; Chen, L.; Cullen, I. J.; Dolinskii, A. ; Fabian, B.; Hausmann, M.; Kozhuharov, C.; Kurcewicz, J.; Litvinov, S. A.; Liu, Z.; Mazzocco, M.; Meng, J.; Montes, F.; Munzenberg, G.; Musumarra, A.; Nakajima, S.; Nociforo, C.; Nolden, F. ; Ohtsubo, T.; Ozawa, A.; Patyk, Z.; Plass, W. R.; Scheidenberger, C.; Steck, M. ; Suzuki, T.; Weick, H.; Winckler, N.; Winkler, M.; Yamaguchi, T.: **Direct measurement of the 4.6 MeV isomer in stored bare Sb-133 ions.** *Physics letters B* **688**(4): 294–297, 2010. DOI:10.1016/j.physletb.2010.04.020

235 Swisulski, D.; Woloszyk, M.; Woloszyn, M.; Ziolko, M.; Rafinski, L.; Stafiniak, A.: **Testing of the Superconducting Magnets Frequency Characteristics.** *Electronika ir Elektrotechnika* (7): 39–42, 2010.

236 Takechi, M.; Ohtsubo, T.; Kuboki, T.; Fukuda, M.; Nishimura, D.; Suzuki, T.; Yamaguchi, T.; Ozawa, A.; Moriguchi, T.; Sumikama, T.; Geissel, H.; Aoi, N.; Fukuda,

N.; Hachiuma, I.; Inabe, N.; Ishibashi, Y.; Itoh, Y.; Kameda, D.; Kubo, T.; Kusaka, K.; Lantz, M.; Mihara, M.; Miyashita, Y.; Momota, S.; Namihira, K.; Ohishi, H.; Ohkuma, Y.; Ohnishi, T.; Ohtake, M.; Ogawa, K.; Shimbara, Y.; Suda, T.; Suzuki, S.; Takeda, H.; Tanaka, K.; Watanabe, R.; Winkler, M.; Yanagisawa, Y.; Yasuda, Y.; Yoshinaga, K.; Yoshida, A.; Yoshida, K.: **Measurements of interaction cross sections towards neutron-rich Ne isotopes at RIBF.** *Modern Physics Letters A* **25**(21): 1878–1881, 2010. DOI:10.1142/s021773231000054x

237 Takechi, M.; Ohtsubo, T.; Kuboki, T.; Fukuda, M.; Nishimura, D.; Suzuki, T.; Yamaguchi, T.; Ozawa, A.; Moriguchi, T.; Sumikama, T.; Geissel, H.; Aoi, N.; Fukuda, N.; Hachiuma, I.; Inabe, N.; Ishibashi, Y.; Itoh, Y.; Kameda, D.; Kusaka, K.; Lantz, M.; Mihara, M.; Miyashita, Y.; Momota, S.; Namihira, K.; Ohishi, H.; Ohkuma, Y.; Ohnishi, T.; Ohtake, M.; Ogawa, K.; Shimbara, Y.; Suda, T.; Suzuki, S.; Takeda, H.; Tanaka, K.; Watanabe, R.; Winkler, M.; Yanagisawa, Y.; Yasuda, Y.; Yoshinaga, K.; Yoshida, A.; Yoshida, K.; Kubo, T.: **Measurements of nuclear radii for neutron-rich Ne isotopes Ne28-32.** *Nuclear physics A, Nuclear and hadronic physics* **834**(1): 412C–415C, 2010. DOI:10.1016/j.nuclphysa.2010.01.052

238 Tashenov, S.; Gerl, J. : **TANGO-New tracking AlGOrithm for gamma-rays.** *Nuclear instruments & methods in physics research, Section A, Accelerators, spectrometers, detectors and associated equipment* **622**(3): 592–601, 2010. DOI:10.1016/j.nima.2010.07.040

239 Trautmann, W.: **The symmetry energy in nuclear reactions.** *Nuclear physics A, Nuclear and hadronic physics* **834**(1): 548C–551C, 2010. DOI:10.1016/j.nuclphysa.2010.01.087

240 Trautmann, W. ; Bianchin, S.; Botvina, A. S.; Fevre, A.; Leifels, Y.; Sfienti, C.; Buyukcizmeci, N.; Ogul, R.; Mishustin, I. N.; Chartier, M.; Wu, P. Z.; Lemmon, R. C.; Li, Q.; Lukasik, J. ; Pawlowski, P.; Pagano, A.; Russotto, P.; Aladin Collaboration: **The symmetry energy in nuclear reactions.** *International journal of modern physics E, Nuclear physics* **19**(8): 1653–1663, 2010. DOI:10.1142/s0218301310016077

241 Typel, S.; Ropke, G.; Klahn, T.; Blaschke, D.; Wolter, H. H.: **Composition and thermodynamics of nuclear matter with light clusters.** *Physical review C, Nuclear physics* **81**(1): 015803, 2010. DOI:10.1103/physrevc.81.015803

242 Wagner, M.; Walther, A.; Schaefer, B. J.: **On the efficient computation of high-order derivatives for implicitly defined functions.** *Computer Physics Communications* **181**(4): 756–764, 2010. DOI:10.1016/j.cpc.2009.12.008

243 Wang, J. B.; Wang, Y.; Zhu, X. L.; Ding, W.; Li, Y. J.; Cheng, J. P.; Herrmann, N.; Deppner, I.; Zhang, Y. P.; Loizeau, P.; Senger, P. ; Gonzalez-Diaz, D.: **Development of multi-gap resistive plate chambers with low-resistive silicate glass electrodes for operation at high particle fluxes and large transported charges.** *Nuclear instruments & methods in physics research, Section A, Accelerators, spectrometers, detectors and associated equipment* **621**(1): 151–156, 2010. DOI:10.1016/j.nima.2010.04.056

244 Williams, R.; Fischer, C. S.: **Bethe-Salpeter equations: mesons beyond the rainbow-ladder truncation.** *Chinese Physics* **34**(9): 1500–1503, 2010.

245 Xiang, Y.; Kauschke, M.; Schroeder, C. H.; Floch, E.; Leibrock, H.; Moritz, G. : **Conceptual Design of Cryogenic Facilities for Super-FRS of FAIR.** *IEEE transactions on applied superconductivity* **20**(3): 2058–2061, 2010. DOI:10.1109/tasc.2010.2041758

246 Yao, Q. G.; Ma, L. Z.; Zhang, X. Q.; He, Y.; Wu, W.; Moritz, G. ; Leibrock, H.; Han, S. F.; Ni, D. S.; Guo, B. L.; Wu, X.; Zhang, B.; Zhang, S. L.; Yuan, P.; Zhan, W. L.: **Magnetic Field Design of the Dipole for Super-FRS at FAIR.** *IEEE transactions on applied superconductivity* **20**(3): 172–175, 2010. DOI:10.1109/tasc.2009.2038890

247 Yuan, P.; Zhao, H. W.; Leibrock, H.; Ma, L. Z.; Sun, L. T.; Zhang, X. Q.; Zhang, B.; Guo, B. L.; Wu, W.; Yao, Q. G.; Wu, W. Y.; Wang, Q. L.; Wu, X.; Han, S. F.; He, Y.; Zhang, S. L.: **Some Superconducting Magnets at IMP.** *IEEE transactions on applied superconductivity* **20**(3): 214–217, 2010. DOI:10.1109/tasc.2009.2039204

248 Zajac, S.; Rzadkiewicz, J.; Rosmej, O.; Scholz, M. ; Zhao, Y. T.; Gojska, A.; Paduch, M.; Zielinska, E.: **Spatially resolved high-resolution x-ray spectroscopy of high-current plasma-focus discharges.** *Review of scientific instruments* **81**(10): 10E312, 2010. DOI:10.1063/1.3483190

249 Zakova, M.; Andjelkovic, Z.; Bissell, M. L.; Blaum, K.; Drake, G. W. F.; Geppert, C.; Kowalska, M.; Kramer, J.; Krieger, A.; Lochmann, M.; Neff, T.; Neugart, R.; Nortershauser, W.; Sanchez, R.; Schmidt-Kaler, F.; Tiedemann, D.; Yan, Z. C.; Yordanov, D. T.; Zimmermann, C.: **Isotope shift measurements in the 2s(1/2) → 2p(3/2) transition of Be+ and extraction of the nuclear charge radii for Be-7,Be-10,Be-11.** *Journal of physics G, Nuclear and particle physics* **37**(5): 055107, 2010. DOI:10.1088/0954-3899/37/5/055107

WoS publications to the programme 'Large-scale facilities for research with photons, neutrons and ions' published in 2010

001 Ali, M.; Neumann, R. ; Ensinger, W.: **Sequence-Specific Recognition of DNA Oligomer Using Peptide Nucleic Acid (PNA)-Modified Synthetic Ion Channels: PNA/DNA Hybridization in Nanoconfined Environment.** *ACS Nano* **4**(12): 7267–7274, 2010. DOI:10.1021/nn102119q

002 Ali, M.; Nguyen, Q. H.; Neumann, R. ; Ensinger, W.: **ATP-modulated ionic transport through synthetic nanochannels.** *Chemical Communications* **46**(36): 6690–6692, 2010. DOI:10.1039/c0cc01632b OPEN ACCESS.

003 Ali, M.; Schiedt, B.; Neumann, R. ; Ensinger, W.: **Biosensing with Functionalized Single Asymmetric Polymer Nanochannels.** *Macromolecular Bioscience* **10**(1): 28–32, 2010. DOI:10.1002/mabi.200900198

004 Ali, M.; Yameen, B.; Cervera, J.; Ramirez, P.; Neumann, R. ; Ensinger, W.; Knoll, W.; Azzaroni, O.: **Layer-by-Layer Assembly of Polyelectrolytes into Ionic Current Rectifying Solid-State Nanopores: Insights from Theory and Experiment.** *Journal of the American Chemical Society* **132**(24): 8338–8348, 2010. DOI:10.1021/ja101014y

005 Andersson, E.; Fritzsche, S.; Linusson, P.; Hedin, L.; Eland, J. H. D.; Rubensson, J. E.; Karlsson, L.; Feifel, R.: **Multielectron coincidence study of the double Auger decay of 3d-ionized krypton.** *Physical review A, Atomic, molecular, and optical physics* **82**(4): 043418, 2010. DOI:10.1103/physreva.82.043418

006 Artemyev, A. N.; Surzhykov, A.; Fritzsche, S.; Najjari, B.; Voitkiv, A. B.: **Target effects on the linear polarization of photons emitted in radiative electron capture by heavy ions.** *Physical review A, Atomic, molecular, and optical physics* **82**(2): 022716, 2010. DOI:10.1103/physreva.82.022716

007 Artemyev, A. N.; Surzhykov, A.; Indelicato, P.; Plunien, G.; Stohlker, T.: **Finite basis set approach to the two-centre Dirac problem in Cassini coordinates.** *Journal of physics B, Atomic, molecular and optical physics* **43**(23): 235207, 2010. DOI:10.1088/0953-4075/43/23/235207

008 Bagnoud, V.; Aurand, B.; Blazevic, A.; Borneis, S.; Bruske, C.; Ecker, B.; Eisenbarth, U.; Fils, J.; Frank, A.; Gaul, E.; Goette, S. ; Haefner, C.; Hahn, T.; Harres, K.; Heuck, H. M.; Hochhaus, D.; Hoffmann, D. H. H.; Javorkova, D.; Kluge, H. J.; Kuehl, T.; Kunzer, S.; Kreutz, M.; Merz-Mantwill, T.; Neumayer, P. ; Onkels, E.; Reemts, D.; Rosmej, O.; Roth, M.; Stoehlker, T.; Tauschwitz, A.; Zielbauer, B.; Zimmer, D.; Witte, K.: **Commissioning and early experiments of the PHELIX facility.** *Applied physics B, Lasers and optics* **100**(1): 137–150, 2010. DOI:10.1007/s00340-009-3855-7

009 Bender, M.; Kollmus, H.; Bellachioma, M. C.; Assmann, W.: **UHV-ERDA investigation of NEG coatings.** *Nuclear instruments & methods in physics research, Section B, Beam interactions with materials and atoms* **268**(11): 1986–1990, 2010. DOI:10.1016/j.nimb.2010.02.114

010 Bettadj, L.; Inal, M. K.; Surzhykov, A.; Fritzsche, S.: **Effects of the radiative recombination on the intensity and polarization of the Ly-alpha emission of hydrogen-like ions.** *Nuclear instruments & methods in physics research, Section B, Beam interactions with materials and atoms* **268**(23): 3509–3516, 2010. DOI:10.1016/j.nimb.2010.08.013

011 Block, M.; Ackermann, D. ; Blaum, K.; Droese, C.; Dworschak, M.; Eliseev, S.; Fleckenstein, T.; Haettner, E.; Herfurth, F.; Hessberger, F. P.; Hofmann, S. ; Ketelaer, J.; Ketter, J.; Kluge, H. J.; Marx, G.; Mazzocco, M.; Novikov, Y. N.; Plass, W. R.; Popeko, A.; Rahaman, S.; Rodriguez, D.; Scheidenberger, C.; Schweikhard, L.; Thirolf, P. G.; Vorobyev, G. K.; Weber, C.: **Direct mass measurements above uranium bridge the gap to the island of stability.** *Nature* **463**(7282): 785–788, 2010. DOI:10.1038/nature08774

012 Bondarevskaya, A.; Labzowsky, L.; Prozorov, A.; Plunien, G.; Liesen, D.; Bosch, F.: **Linear polarization of x-ray photons in hyperfine-quenched transitions of polarized He-like ions.** *Journal of physics B, Atomic, molecular and optical physics* **43**(24): 245001, 2010. DOI:10.1088/0953-4075/43/24/245001

013 Bosch, F.; Litvinov, Y. A.: **Observation of non-exponential orbital electron-capture decay of stored hydrogen-like ions.** *Progress in particle and nuclear physics* **64**(2): 435–438, 2010. DOI:10.1016/j.ppnp.2009.12.069

014 Breitenfeldt, M.; Borgmann, C.; Audi, G.; Baruah, S.; Beck, D. ; Blaum, K.; Bohm, C.; Cakirli, R. B.; Casten, R. F.; Delahaye, P.; Dworschak, M.; George, S.; Herfurth, F.; Herlert, A.; Kellerbauer, A.; Kowalska, M.; Lunney, D.; Minaya-Ramirez, E.; Naimi, S.; Neidherr, D.; Rosenbusch, M.; Savreux, R.; Schwarz, S.; Schweikhard, L.; Yazidjian, C.: **Approaching the N82 shell closure with mass measurements of Ag and Cd isotopes.** *Physical review C, Nuclear physics* **81**(3): 034313, 2010. DOI:10.1103/physrevc.81.034313

015 Charlwood, F. C.; Billowes, J.; Campbell, P.; Cheal, B.; Eronen, T.; Forest, D. H.; Fritzsche, S.; Honma, M.; Jokinen, A.; Moore, I. D.; Penttila, H.; Powis, R.; Saastamoinen, A.; Tungate, G.; Aysto, J.: **Ground state properties of manganese isotopes across the N28 shell closure.** *Physics letters B* **690**(4): 346–351, 2010. DOI:10.1016/j.physletb.2010.05.060

016 Cheal, B.; Billowes, J.; Bissell, M. L.; Blaum, K.; Charlwood, F. C.; Flanagan, K. T.; Forest, D. H.; Fritzsche, S.; Geppert, C.; Jokinen, A.; Kowalska, M.; Krieger, A.; Kramer, J.; Mane, E.; Moore, I. D.; Neugart, R.; Neyens, G.; Nortershauser, W.; Rajabali, M. M.; Schug, M.; Stroke, H. H.; Vingerhoets, P.; Yordanov, D. T.; Zakova, M.: **Discovery of a long-lived low-lying isomeric state in Ga-80.** *Physical review C, Nuclear physics* **82**(5): 051302, 2010. DOI:10.1103/physrevc.82.051302

017 Cheal, B.; Mane, E.; Billowes, J.; Bissell, M. L.; Blaum, K.; Brown, B. A.; Charlwood, F. C.; Flanagan, K. T.; Forest, D. H.; Geppert, C.; Honma, M.; Jokinen, A.; Kowalska, M.; Krieger, A.; Kraemer, J.; Moore, I. D.; Neugart, R.; Neyens, G.; Nortershauser, W.; Schug, M.; Stroke, H. H.; Vingerhoets, P.; Yordanov, D. T.; Zakova, M.: **Nuclear Spins and Moments of Ga Isotopes Reveal Sudden Structural Changes between N40 and N50.** *Physical review letters* **104**(25): 252502, 2010. DOI:10.1103/physrevlett.104.252502

018 Cornelius, T. W.; Schiedt, B.; Severin, D.; Pepy, G.; Toulemonde, M.; Apel, P. Y.; Boesecke, P.; Trautmann, C.: **Nanopores in track-etched polymer membranes characterized by small-angle x-ray scattering.** *Nanotechnology* **21**(15): 155702, 2010. DOI:10.1088/0957-4484/21/15/155702

019 Costantini, J. M.; Beuneu, F.; Schwartz, K.; Trautmann, C.: **Generation of colour centres in yttria-stabilized zirconia by heavy ion irradiations in the GeV range.** *Journal of physics Condensed matter* **22**(31): 315402, 2010. DOI:10.1088/0953-8984/22/31/315402

020 Dworschak, M.; Block, M.; Ackermann, D. ; Audi, G.; Blaum, K.; Droese, C.; Eliseev, S.; Fleckenstein, T.; Haettner, E.; Herfurth, F.; Hessberger, F. P.; Hofmann, S. ; Ketelaer, J.; Ketter, J.; Kluge, H. J.; Marx, G.; Mazzocco, M.; Novikov, Y. N.; Plass, W. R.; Popeko, A.; Rahaman, S.; Rodriguez, D.; Scheidenberger, C.; Schweikhard, L.; Thirolf, P. G.; Vorobyev, G. K.; Wang, M.; Weber, C.: **Penning trap mass measurements on nobelium isotopes.** *Physical review C, Nuclear physics* **81**(6): 064312, 2010. DOI:10.1103/physrevc.81.064312

021 Eibach, M.; Beyer, T.; Blaum, K.; Block, M.; Eberhardt, K.; Herfurth, F.; Geppert, C.; Ketelaer, J.; Ketter, J.; Kramer, J.; Krieger, A.; Knuth, K.; Nagy, S.; Nortershauser, W.; Smorra, C.: **Transport of fission products with a helium gas-jet at TRIGA-SPEC.** *Nuclear instruments & methods in physics research, Section A, Accelerators, spectrometers, detectors and associated equipment* **613**(2): 226–231, 2010. DOI:10.1016/j.nima.2009.11.034

022 Eliseev, S.; Bohm, C.; Beck, D. ; Blaum, K.; Breitenfeldt, M.; Fedosseev, V. N.; George, S.; Herfurth, F.; Herlert, A.; Kluge, H. J.; Kowalska, M.; Lunney, D.; Naimi, S.; Neidherr, D.; Novikov, Y. N.; Rosenbusch, M.; Schweikhard, L.; Schwarz, S.; Seliverstov, M.; Zuber, K.: **Direct mass measurements of Hg-194 and Au-194: A new route to the neutrino mass determination?.** *Physics letters B* **693**(4): 426–429, 2010. DOI:10.1016/j.physletb.2010.08.071

023 Enculescu, M.; Trautmann, C.: **Luminescence of dye-doped KAP and KDP nanorods.** *Radiation Measurements* **45**(3): 602–604, 2010. DOI:10.1016/j.radmeas.2009.11.015

024 Ensinger, W.; Sudowe, R.; Brandt, R.; Neumann, R. : **Gas separation in nanoporous membranes formed by etching ion irradiated polymer foils.** *Radiation Physics and Chemistry* **79**(3): 204–207, 2010. DOI:10.1016/j.radphyschem.2009.08.045

025 Ferro, F.; Artemyev, A.; Stohlker, T.; Surzhykov, A.: **Isotope shift of the 1s2p P-3(0)-1s2s S-1(0) level splitting in heavy He-like ions: Implications for atomic parity-nonconservation studies.** *Physical review A, Atomic, molecular, and optical physics* **81**(6): 062503, 2010. DOI:10.1103/physreva.81.062503

026 Ferro, F.; Artemyev, A.; Stohlker, T.; Surzhykov, A.: **Isotopic tuning of the 2 P-3(0)-2 S-1(0) and 2 P-3(1)-2 S-1(0) transition energies in He-like ions for future parity-nonconservation experiments.** *Journal of Instrumentation* **5**: C08006, 2010. DOI:10.1088/1748-0221/5/08/c08006 OPEN ACCESS.

027 Fischer, A.; Canali, C.; Warring, U.; Kellerbauer, A.; Fritzsche, S.: **First Optical Hyperfine Structure Measurement in an Atomic Anion.** *Physical review letters* **104**(7): 073004, 2010. DOI:10.1103/physrevlett.104.073004

028 Flanagan, K. T.; Vingerhoets, P.; Bissell, M. L.; Blaum, K.; Brown, B. A.; Cheal, B.; De Rydt, M.; Forest, D. H.; Geppert, C.; Honma, M.; Kowalska, M.; Kramer, J.; Krieger, A.; Mane, E.; Neugart, R.; Neyens, G.; Norter-

shauser, W.; Schug, M.; Stroke, H. H.; Yordanov, D. T.: **Experimental determination of an I-pi2(-) ground state in Cu-72,Cu-74.** *Physical review C, Nuclear physics* **82**(4): 041302, 2010. DOI:10.1103/physrevc.82.041302

029 Frank, A.; Blazevic, A.; Grande, P. L.; Harres, K.; Hessling, T.; Hoffmann, D. H. H.; Knobloch-Maas, R.; Kuznetsov, P. G.; Nurnberg, F.; Pelka, A.; Schaumann, G.; Schiwietz, G.; Schokel, A.; Schollmeier, M.; Schumacher, D.; Schutrumpf, J.; Vatulin, V. V.; Vinokurov, O. A.; Roth, M.: **Energy loss of argon in a laser-generated carbon plasma.** *Physical Review E, statistical, nonlinear, and soft matter physics* **81**(2): 026401, 2010. DOI:10.1103/physreve.81.026401

030 Galow, B. J.; Harman, Z.; Keitel, C. H.: **Intense high-quality medical proton beams via laser fields.** *Optics Express* **18**(25): 25950–25957, 2010. OPEN ACCESS.

031 Gangwar, R. K.; Sharma, L.; Srivastava, R.; Stauffer, A. D.: **Electron-impact excitation of argon: Cross sections of interest in plasma modeling.** *Physical review A, Atomic, molecular, and optical physics* **81**(5): 052707, 2010. DOI:10.1103/physreva.81.052707

032 Gangwar, R. K.; Sharma, L.; Srivastava, R.; Stauffer, A. D.: **Electron-impact excitation of krypton: Cross sections of interest in plasma modeling.** *Physical review A, Atomic, molecular, and optical physics* **82**(3): 032710, 2010. DOI:10.1103/physreva.82.032710

033 Gangwar, R. K.; Tripathi, A. N.; Sharma, L.; Srivastava, R.: **Elastic scattering of electrons from Rb, Cs and Fr atoms.** *Journal of physics B, Atomic, molecular and optical physics* **43**(8): 085205, 2010. DOI:10.1088/0953-4075/43/8/085205

034 Gehrke, H. G.; Nix, A. K.; Hofsass, H.; Krauser, J.; Trautmann, C.; Weidinger, A.: **Self-aligned nanostructures created by swift heavy ion irradiation.** *Journal of Applied Physics* **107**(9): 094305, 2010. DOI:10.1063/1.3354093

035 Geyer, S.; Sokolov, A.; Thorn, A.; Vorobyev, G.; Stohlker, T.; Kester, O.: **Characterization of the SPARC-EBIT at GSI.** *Journal of Instrumentation* **5**: C10003, 2010. DOI:10.1088/1748-0221/5/10/c10003 OPEN ACCESS.

036 Gibbon, P.; Speck, R.; Karmakar, A.; Arnold, L.; Frings, W.; Berberich, B.; Reiter, D.; Masek, M.: **Progress in Mesh-Free Plasma Simulation With Parallel Tree Codes.** *IEEE transactions on plasma science* **38**(9): 2367–2376, 2010. DOI:10.1109/tps.2010.2055165

037 Gonta, D.; Fritzsche, S.: **Multipartite W states for chains of atoms conveyed through an optical cavity.** *Physical review A, Atomic, molecular, and optical physics* **81**(2): 022326, 2010. DOI:10.1103/physreva.81.022326

038 Gryzlova, E. V.; Grum-Grzhimailo, A. N.; Fritzsche, S.; Kabachnik, N. M.: **Angular correlations between two electrons emitted in the sequential two-photon double ionization of atoms.** *Journal of physics B, Atomic, molecular and optical physics* **43**(22): 225602, 2010. DOI:10.1088/0953-4075/43/22/225602

039 Gumberidze, A.; Fritzsche, S.; Bosch, F.; Ionescu, D. C.; Kramer, A.; Kozhuharov, C.; Stachura, Z.; Surzhykov, A.; Warczak, A.; Stohlker, T.: **Shell- and subshell-resolved projectile excitation of hydrogenlike Au78+ ions in relativistic ion-atom collisions.** *Physical review A, Atomic, molecular, and optical physics* **82**(5): 052712, 2010. DOI:10.1103/physreva.82.052712

040 Gumberidze, A.; Trassinelli, M.; Adrouche, N.; Szabo, C. I.; Indelicato, P.; Haranger, F.; Isac, J. M.; Lamour, E.; Le Bigot, E. O.; Merot, J.; Prigent, C.; Rozet, J. P.; Vernhet, D.: **Electronic temperatures, densities, and plasma x-ray emission of a 14.5 GHz electron-cyclotron resonance ion source.** *Review of scientific instruments* **81**(3): 033303, 2010. DOI:10.1063/1.3316805

041 Harres, K.; Alber, I.; Tauschwitz, A.; Bagnoud, V.; Daido, H.; Gunther, M.; Nurnberg, F.; Otten, A.; Schollmeier, M.; Schutrumpf, J.; Tampo, M.; Roth, M.: **Beam collimation and transport of quasineutral laser-accelerated protons by a solenoid field.** *Physics of plasmas* **17**(2): 023107, 2010. DOI:10.1063/1.3299391

042 Havermeier, T.; Jahnke, T.; Kreidi, K.; Wallauer, R.; Voss, S.; Schoffler, M.; Schossler, S.; Foucar, L.; Neumann, N.; Titze, J.; Sann, H.; Kuhnel, M.; Voigtsberger, J.; Malakzadeh, A.; Sisourat, N.; Schollkopf, W.; Schmidt-Bocking, H.; Grisenti, R. E.; Dorner, R.: **Single Photon Double Ionization of the Helium Dimer.** *Physical review letters* **104**(15): 153401, 2010. DOI:10.1103/physrevlett.104.153401

043 Havermeier, T.; Jahnke, T.; Kreidi, K.; Wallauer, R.; Voss, S.; Schoffler, M.; Schossler, S.; Foucar, L.; Neumann, N.; Titze, J.; Sann, H.; Kuhnel, M.; Voigtsberger, J.; Morilla, J. H.; Schollkopf, W.; Schmidt-Bocking, H.; Grisenti, R. E.; Dorner, R.: **Interatomic Coulombic Decay following Photoionization of the Helium Dimer: Observation of Vibrational Structure.** *Physical review letters* **104**(13): 133401, 2010. DOI:10.1103/physrevlett.104.133401

044 Herfurth, F.; Barth, W.; Clemente, G.; Dahl, L.; Gerhard, P.; Kaiser, M.; Kester, O.; Kluge, H. J.; Koszudowski, S.; Kozhuharov, C.; Quint, W. ; Sokolov, A.; Stohlker, T.; Vorobjev, G.; Pfister, J.; Ratzinger, U.; Sauer, A.; Schempp, A.; HITRAP Collaboration: **HITRAP - heavy, highly-charged ions and antiprotons at rest.** *Acta physica Polonica B* **41**(2): 457–462, 2010. OPEN ACCESS.

045 Hochhaus, D. C.; Seres, J.; Aurand, B.; Ecker,

B.; Zielbauer, B.; Zimmer, D.; Spielmann, C.; Kuhl, T.: **Tuning the high-order harmonic lines of a Nd:Glass laser for soft X-ray laser seeding.** *Applied physics B, Lasers and optics* **100**(4): 711–716, 2010. DOI:10.1007/s00340-010-4058-y

046 Hoffmann, D. H. H.; Tahir, N. A.; Udrea, S.; Rosmej, O.; Meister, C. V.; Varentsov, D.; Roth, M.; Schaumann, G.; Frank, A.; Blazevic, A.; Ling, J.; Hug, A.; Menzel, J.; Hessling, T.; Harres, K.; Gunther, M.; El-Moussati, S.; Schumacher, D.; Imran, M.: **High Energy Density Physics with Heavy Ion Beams and related Interaction Phenomena.** *Contributions to Plasma Physics* **50**(1): 7–15, 2010. DOI:10.1002/ctpp.201010004

047 Jentschura, U. D.; Surzhykov, A.; Zinn-Justin, J.: **Multi-instantons and exact results III: Unification of even and odd anharmonic oscillators.** *Annals of Physics* **325**(5): 1135–1172, 2010. DOI:10.1016/j.aop.2010.01.002

048 Ketelaer, J.; Beyer, T.; Blaum, K.; Block, M.; Eberhardt, K.; Eibach, M.; Herfurth, F.; Smorra, C.; Nagy, S.: **Accuracy studies with carbon clusters at the Penning trap mass spectrometer TRIGA-TRAP.** *The European physical journal: D, Atomic, molecular and optical physics* **58**(1): 47–52, 2010. DOI:10.1140/epjd/e2010-00092-9

049 Kluge, H. J.: **High-accuracy mass spectrometry for fundamental studies.** *European Journal of Mass Spectrometry* **16**(3): 269–282, 2010. DOI:10.1255/ejms.1057

050 Kozhedub, Y. S.; Volotka, A. V.; Artemyev, A. N.; Glazov, D. A.; Plunien, G.; Shabaev, V. M.; Tupitsyn, I. I.; Stohlker, T.: **Relativistic recoil, electron-correlation, and QED effects on the 2p(j)-2s transition energies in Li-like ions.** *Physical review A, Atomic, molecular, and optical physics* **81**(4): 042513, 2010. DOI:10.1103/physreva.81.042513

051 Lamperti, A.; Radnoczi, G.; Caricato, A. P.; Trautmann, C.; Ossi, P. M.: **Structural modifications induced by swift heavy ions in thin films of yttria fully stabilized zirconia.** *Nuclear instruments & methods in physics research, Section B, Beam interactions with materials and atoms* **268**(19): 3132–3136, 2010. DOI:10.1016/j.nimb.2010.05.070

052 Lang, M. ; Zhang, F. X.; Zhang, J. M.; Wang, J. W.; Lian, J.; Weber, W. J.; Schuster, B.; Trautmann, C.; Neumann, R. ; Ewing, R. C.: **Review of A(2)B(2)O(7) pyrochlore response to irradiation and pressure.** *Nuclear instruments & methods in physics research, Section B, Beam interactions with materials and atoms* **268**(19): 2951–2959, 2010. DOI:10.1016/j.nimb.2010.05.016

053 Le Pape, S.; Neumayer, P. ; Fortmann, C.; Doppner, T.; Davis, P.; Kritcher, A.; Landen, O.; Glenzer, S.: **X-ray radiography and scattering diagnosis of dense shock-compressed matter.** *Physics of plasmas* **17**(5): 056309, 2010. DOI:10.1063/1.3377785

054 Li, W. X.; Wang, L. M.; Sun, K.; Lang, M. ; Trautmann, C.; Ewing, R. C.: **Porous fission fragment tracks in fluorapatite.** *Physical review: B, Condensed matter and materials physics* **82**(14): 144109, 2010. DOI:10.1103/physrevb.82.144109

055 Logofatu, P. C.; Garoi, F.; Sima, A.; Ionita, B.; Apostol, D.: **Classical holography experiments in digital terms.** *Journal of optoelectronics and advanced materials* **12**(1): 85–93, 2010.

056 Lompe, T.; Ottenstein, T. B.; Serwane, F.; Viering, K.; Wenz, A. N.; Zurn, G.; Jochim, S.: **Atom-Dimer Scattering in a Three-Component Fermi Gas.** *Physical review letters* **105**(10): 103201, 2010. DOI:10.1103/physrevlett.105.103201

057 Lompe, T.; Ottenstein, T. B.; Serwane, F.; Wenz, A. N.; Zurn, G.; Jochim, S.: **Radio-Frequency Association of Efimov Trimers.** *Science* **330**(6006): 940–944, 2010. DOI:10.1126/science.1193148

058 Maiorova, A. V.; Telnov, D. A.; Shabaev, V. M.; Zaytsev, V. A.; Plunien, G.; Stohlker, T.: **The Coulomb glory effect in collisions of antiprotons with heavy nuclei: relativistic theory.** *Journal of physics B, Atomic, molecular and optical physics* **43**(20): 205006, 2010. DOI:10.1088/0953-4075/43/20/205006

059 Malyshev, O. B.; Zajec, B.; Haase, A.; Westerberg, L.; Leandersson, M.; Bender, M.; Kramer, A.; Kollmus, H.; Reich-Sprenger, H.: **Ar beam induced desorption from different materials at TSL.** *Vacuum* **85**(2): 338–343, 2010. DOI:10.1016/j.vacuum.2010.07.007

060 Matei, E.; Ion, L.; Antohe, S.; Neumann, R. ; Enculescu, I.: **Multisegment CdTe nanowire homojunction photodiode.** *Nanotechnology* **21**(10): 105202, 2010. DOI:10.1088/0957-4484/21/10/105202

061 Matei, E.; Preda, N.; Enculescu, M.; Ansermet, J. P.; Molares, M. E. T.; Enculescu, I.: **Sequentical deposition of multisegment nanowires.** *Digest Journal of Nanomaterials & Biostructures* **5**(4): 1067–1076, 2010.

062 Meyer, M.; Cubaynes, D.; Richardson, V.; Costello, J. T.; Radcliffe, P.; Li, W. B.; Dusterer, S.; Fritzsche, S.; Mihelic, A.; Papamihail, K. G.; Lambropoulos, P.: **Two-Photon Excitation and Relaxation of the 3d-4d Resonance in Atomic Kr.** *Physical review letters* **104**(21): 213001, 2010. DOI:10.1103/physrevlett.104.213001

063 Miletich, R.; Gatta, G. D.; Redhammer, G. J.; Burchard, M.; Meyer, H. P.; Weikusat, C.; Rotiroti, N.; Glasmacher, U. A.; Trautmann, C.; Neumann, R. : **Structure alterations in microporous (Mg,Fe)(2)Al4Si5O18 crys-**

tals induced by energetic heavy-ion irradiation. *Journal of Solid State Chemistry* **183**(10): 2372–2381, 2010. DOI:10.1016/j.jssc.2010.07.038

064 Minaev, S.; Alexeev, N.; Golubev, A.; Hoffmann, D.; Kulevoy, T.; Sharkov, B.; Sitnikov, A.; Tahir, N. A.; Varentsov, D.: **Heavy ion hollow beam formation at the energy of 1 AGeV for implosion experiments using an original RF system for fast rotation.** *Nuclear instruments & methods in physics research, Section A, Accelerators, spectrometers, detectors and associated equipment* **620**(2): 99–104, 2010. DOI:10.1016/j.nima.2010.03.097

065 Muller, C.; Voitkiv, A. B.; Lopez-Urrutia, J. R. C.; Harman, Z.: **Strongly Enhanced Recombination via Two-Center Electronic Correlations.** *Physical review letters* **104**(23): 233202, 2010. DOI:10.1103/physrevlett.104.233202

066 Naimi, S.; Audi, G.; Beck, D. ; Blaum, K.; Bohm, C.; Borgmann, C.; Breitenfeldt, M.; George, S.; Herfurth, F.; Herlert, A.; Kowalska, M.; Kreim, S.; Lunney, D.; Neidherr, D.; Rosenbusch, M.; Schwarz, S.; Schweikhard, L.; Zuber, K.: **Critical-Point Boundary for the Nuclear Quantum Phase Transition Near A100 from Mass Measurements of Kr-96,Kr-97.** *Physical review letters* **105**(3): 032502, 2010. DOI:10.1103/physrevlett.105.032502

067 Neumayer, P. ; Aurand, B.; Basko, M.; Ecker, B.; Gibbon, P.; Hochhaus, D. C.; Karmakar, A.; Kazakov, E.; Kuhl, T.; Labaune, C.; Rosmej, O.; Tauschwitz, A.; Zielbauer, B.; Zimmer, D.: **The role of hot electron refluxing in laser-generated K-alpha sources.** *Physics of plasmas* **17**(10): 103103, 2010. DOI:10.1063/1.3486520

068 Neumayer, P. ; Fortmann, C.; Doppner, T.; Davis, P.; Falcone, R. W.; Kritcher, A. L.; Landen, O. L.; Lee, H. J.; Lee, R. W.; Niemann, C.; Le Pape, S.; Glenzer, S. H.: **Plasmons in Strongly Coupled Shock-Compressed Matter.** *Physical review letters* **105**(7): 075003, 2010. DOI:10.1103/physrevlett.105.075003

069 Nguyen, Q. H.; Ali, M.; Bayer, V.; Neumann, R. ; Ensinger, W.: **Charge-selective transport of organic and protein analytes through synthetic nanochannels.** *Nanotechnology* **21**(36): 365701, 2010. DOI:10.1088/0957-4484/21/36/365701

070 Niskanen, J.; Urpelainen, S.; Jankala, K.; Schulz, J.; Heinasmaki, S.; Fritzsche, S.; Kabachnik, N. M.; Aksela, S.; Aksela, H.: **Photoelectron angular distribution and linear magnetic dichroism in the 4p photoemission from Rb atoms.** *Physical review A, Atomic, molecular, and optical physics* **81**(1): 013406, 2010. DOI:10.1103/physreva.81.013406

071 Nuryanthi, N.; Yamaki, T.; Koshikawa, H.; Asano, M.; Enomoto, K.; Sawada, S.; Maekawa, Y.; Voss, K. O.; Trautmann, C.; Neumann, R. : **Poly(vinylidene fluoride)-Based Ion Track Membranes with Different Pore Diameters and Shapes. SEM Observations and Conductometric Analysis.** *Electrochemistry* **78**(2): 146–149, 2010.

072 Pavicevic, M. K.; Bosch, F.; Amthauer, G.; Anicin, I.; Boev, B.; Bruchle, W.; Djurcic, Z.; Faestermann, T.; Henning, W. F.; Jelenkovic, R.; Pejovic, V.: **New data for the geochemical determination of the solar pp-neutrino flux by means of lorandite mineral.** *Nuclear instruments & methods in physics research, Section A, Accelerators, spectrometers, detectors and associated equipment* **621**(1): 278–285, 2010. DOI:10.1016/j.nima.2010.06.090

073 Pawlowski, J. M.; Spielmann, D.; Stamatescu, I. O.: **Lattice Landau gauge with stochastic quantisation.** *Nuclear physics B* **830**(1): 291–314, 2010. DOI:10.1016/j.nuclphysb.2009.12.036

074 Piriz, A. R.; Cela, J. J. L.; Tahir, N. A.: **Comment on Viscous Rayleigh-Taylor Instability Experiments at High Pressure and Strain Rate.** *Physical review letters* **105**(17): 179601, 2010. DOI:10.1103/physrevlett.105.179601

075 Piriz, A. R.; Prieto, G. R.; Diaz, I. M.; Cela, J. J. L.; Tahir, N. A.: **Dynamic stabilization of Rayleigh-Taylor instability in Newtonian fluids.** *Physical Review E, statistical, nonlinear, and soft matter physics* **82**(2): 026317, 2010. DOI:10.1103/physreve.82.026317

076 Potera, P.; Ubizskii, S.; Sugak, D.; Schwartz, K.: **Induced Absorption in Gadolinium Gallium Garnet Irradiated by High Energy U-235 Ions.** *Acta physica Polonica A* **117**(1): 181–183, 2010.

077 Radtke, T.; Fritzsche, S.: **Simulation of n-qubit quantum systems. V. Quantum measurements.** *Computer Physics Communications* **181**(2): 440–453, 2010. DOI:10.1016/j.cpc.2009.10.015

078 Rauber, M.; Brotz, J.; Duan, J. L.; Liu, J.; Muller, S.; Neumann, R. ; Picht, O.; Toimil-Molares, M. E.; Ensinger, W.: **Segmented All-Platinum Nanowires with Controlled Morphology through Manipulation of the Local Electrolyte Distribution in Fluidic Nanochannels during Electrodeposition. 114**(51): 22502–22507, 2010. DOI:10.1021/jp108889c

079 Reed, M. W.; Cullen, I. J.; Walker, P. M.; Litvinov, Y. A.; Blaum, K.; Bosch, F.; Brandau, C.; Carroll, J. J.; Cullen, D. M.; Deo, A. Y.; Detwiller, B.; Dimopoulou, C.; Dracoulis, G. D.; Farinon, F.; Geissel, H.; Haettner, E.; Heil, M.; Kempley, R. S.; Knobel, R.; Kozhuharov, C.; Kurcewicz, J.; Kuzminchuk, N.; Litvinov, S.; Liu, Z.; Mao, R.; Nociforo, C.; Nolden, F. ; Plass, W. R.; Prochazka, A.; Scheidenberger, C.; Steck, M. ; Stohlker, T.; Sun, B.; Swan, T. P. D.; Trees, G.; Weick, H.; Winckler, N.; Winkler, M.; Woods, P. J.; Yamaguchi, T.: **Discovery of Highly Excited Long-Lived Isomers in Neutron-Rich**

Hafnium and Tantalum Isotopes through Direct Mass Measurements. *Physical review letters* **105**(17): 172501, 2010. DOI:10.1103/physrevlett.105.172501

080 Rodriguez, D.; Blaum, K.; Nortershauser, W.; Ahammed, M.; Algora, A.; Audi, G.; Aysto, J.; Beck, D. ; Bender, M.; Billowes, J.; Block, M.; Bohm, C.; Bollen, G.; Brodeur, M.; Brunner, T.; Bushaw, B. A.; Cakirli, R. B.; Campbell, P.; Cano-Ott, D.; Cortes, G.; Lopez-Urrutia, J. R. C.; Das, P.; Dax, A.; De, A.; Delheij, P.; Dickel, T.; Dilling, J.; Eberhardt, K.; Eliseev, S.; Ettenauer, S.; Flanagan, K. T.; Ferrer, R.; Garcia-Ramos, J. E.; Gartzke, E.; Geissel, H.; George, S.; Geppert, C.; Gomez-Hornillos, M. B.; Gusev, Y.; Habs, D.; Heenen, P. H.; Heinz, S.; Herfurth, F.; Herlert, A.; Hobein, M.; Huber, G.; Huyse, M.; Jesch, C.; Jokinen, A.; Kester, O.; Ketelaer, J.; Kolhinen, V.; Koudriavtsev, I.; Kowalska, M.; Kramer, J.; Kreim, S.; Krieger, A.; Kuhl, T.; Lallena, A. M.; Lapierre, A.; Le Blanc, F.; Litvinov, Y. A.; Lunney, D.; Martinez, T.; Marx, G.; Matos, M.; Minaya-Ramirez, E.; Moore, I.; Nagy, S.; Naimi, S.; Neidherr, D.; Nesterenko, D.; Neyens, G.; Novikov, Y. N.; Petrick, M.; Plass, W. R.; Popov, A.; Quint, W. ; Ray, A.; Reinhard, P. G.; Repp, J.; Roux, C.; Rubio, B.; Sanchez, R.; Schabinger, B.; Scheidenberger, C.; Schneider, D.; Schuch, R.; Schwarz, S.; Schweikhard, L.; Seliverstov, M.; Solders, A.; Suhonen, M.; Szerypo, J.; Tain, J. L.; Thirolf, P. G.; Ullrich, J.; Van Duppen, P.; Vasiliev, A.; Vorobjev, G.; Weber, C.; Wendt, K.; Winkler, M.; Yordanov, D.; Ziegler, F.: **MATS and LaSpec: High-precision experiments using ion traps and lasers at FAIR.** *European Physical Journal - Special Topics* **183**: 1–123, 2010. DOI:10.1140/epjst/e2010-01231-2

081 Rodriguez, D.; Sonnenschein, V.; Blaum, K.; Block, M.; Kluge, H. J.; Lallena, A. M.; Raeder, S.; Wendt, K.: **Production of negative osmium ions by laser desorption and ionization.** *Review of scientific instruments* **81**(1): 013301, 2010. DOI:10.1063/1.3276685

082 Rohrbein, D.; Kirchner, T.; Fritzsche, S.: **Role of cascade and Auger effects in the enhanced population of the C3+(1s2s2p P-4) states following single-electron capture in C4+(1s2s S-3)-He collisions.** *Physical review A, Atomic, molecular, and optical physics* **81**(4): 042701, 2010. DOI:10.1103/physreva.81.042701

083 Rzadkiewicz, J.; Gojska, A.; Rosmej, O.; Polasik, M.; Slabkowska, K.: **Interpretation of the Si K alpha x-ray spectra accompanying the stopping of swift Ca ions in low-density SiO2 aerogel.** *Physical review A, Atomic, molecular, and optical physics* **82**(1): 012703, 2010. DOI:10.1103/physreva.82.012703

084 Schouwink, P.; Miletich, R.; Ullrich, A.; Glasmacher, U. A.; Trautmann, C.; Neumann, R. ; Kohn, B. P.: **Ion tracks in apatite at high pressures: the effect of crystallographic track orientation on the elastic properties of fluorapatite under hydrostatic compression.** *Physics and Chemistry of Minerals* **37**(6): 371–387, 2010. DOI:10.1007/s00269-009-0340-0

085 Schuster, B.; Weikusat, C.; Miletich, R.; Trautmann, C.; Neumann, R. ; Fujara, F.: **Influence of radiation damage on ruby as a pressure gauge.** *Physical review: B, Condensed matter and materials physics* **82**(18): 184110, 2010. DOI:10.1103/physrevb.82.184110

086 Schwartz, K.; Volkov, A. E.; Sorokin, M. V.; Neumann, R. ; Trautmann, C.: **Effect of irradiation parameters on defect aggregation during thermal annealing of LiF irradiated with swift ions and electrons.** *Physical review: B, Condensed matter and materials physics* **82**(14): 144116, 2010. DOI:10.1103/physrevb.82.144116

087 Schwellnus, F.; Blaum, K.; Catherall, R.; Crepieux, B.; Fedosseev, V.; Gottwald, T.; Kluge, H. J.; Marsh, B.; Mattolat, C.; Rothe, S.; Stora, T.; Wendt, K.: **The laser ion source trap for highest isobaric selectivity in online exotic isotope production.** *Review of scientific instruments* **81**(2): 02A515, 2010. DOI:10.1063/1.3318259

088 Seres, J.; Seres, E.; Ecker, B.; Hochhaus, D.; Zimmer, D.; Bagnoud, V.; Aurand, B.; Zielbauer, B.; Kuhl, T.; Spielmann, C.: **The super-quadratic growth of high-harmonic signal as a function of pressure reply.** *Nature Physics* **6**(12): 927–928, 2010. DOI:10.1038/nphys1827

089 Seres, J.; Seres, E.; Hochhaus, D.; Ecker, B.; Zimmer, D.; Bagnoud, V.; Kuehl, T.; Spielmann, C.: **Laser-driven amplification of soft X-rays by parametric stimulated emission in neutral gases.** *Nature Physics* **6**(6): 455–461, 2010. DOI:10.1038/nphys1638

090 Severin, D.; Balanzat, E.; Ensinger, W.; Trautmann, C.: **Outgassing and degradation of polyimide induced by swift heavy ion irradiation at cryogenic temperature.** *Journal of Applied Physics* **108**(2): 024901, 2010. DOI:10.1063/1.3457846

091 Shabaev, V. M.; Volotka, A. V.; Kozhuharov, C.; Plunien, G.; Stohlker, T.: **Parity-nonconservation effect with the laser-induced 2(3)S(1)-2(1)S(0) transition in heavy heliumlike ions.** *Physical review A, Atomic, molecular, and optical physics* **81**(5): 052102, 2010. DOI:10.1103/physreva.81.052102

092 Sharma, L.; Surzhykov, A.; Inal, M. K.; Fritzsche, S.: **Polarization transfer in the inner-shell photoionization of sodiumlike ions.** *Physical review A, Atomic, molecular, and optical physics* **81**(2): 023419, 2010. DOI:10.1103/physreva.81.023419

093 Shevelko, V. P.; Stohlker, T.; Tawara, H.; Tolstikhina, I. Y.; Weber, G.: **Electron capture in intermediate-to-fast heavy ion collisions with neutral atoms.** *Nuclear instruments & methods in physics research, Section B, Beam interactions with materials and atoms* **268**(17): 2611–2616,

2010. DOI:10.1016/j.nimb.2010.06.019

094 Simon, M. C.; Lopez-Urrutia, J. R. C.; Beilmann, C.; Schwarz, M.; Harman, Z.; Epp, S. W.; Schmitt, B. L.; Baumann, T. M.; Behar, E.; Bernitt, S.; Follath, R.; Ginzel, R.; Keitel, C. H.; Klawitter, R.; Kubicek, K.; Mackel, V.; Mokler, P. H.; Reichardt, G.; Schwarzkopf, O.; Ullrich, J.: **Resonant and Near-Threshold Photoionization Cross Sections of Fe14+.** *Physical review letters* **105**(18): 183001, 2010. DOI:10.1103/physrevlett.105.183001

095 Simon, M. C.; Schwarz, M.; Epp, S. W.; Beilmann, C.; Schmitt, B. L.; Harman, Z.; Baumann, T. M.; Mokler, P. H.; Bernitt, S.; Ginzel, R.; Higgins, S. G.; Keitel, C. H.; Klawitter, R.; Kubicek, K.; Mackel, V.; Ullrich, J.; Lopez-Urrutia, J. R. C.: **Photoionization of N3+ and Ar8+ in an electron beam ion trap by synchrotron radiation.** *Journal of physics B, Atomic, molecular and optical physics* **43**(6): 065003, 2010. DOI:10.1088/0953-4075/43/6/065003

096 Siomau, M.; Fritzsche, S.: **Entanglement dynamics of three-qubit states in noisy channels.** *The European physical journal: D, Atomic, molecular and optical physics* **60**(2): 397–403, 2010. DOI:10.1140/epjd/e2010-00189-1

097 Siomau, M.; Fritzsche, S.: **Universal quantum Controlled-NOT gate.** *The European physical journal: D, Atomic, molecular and optical physics* **60**(2): 417–421, 2010. DOI:10.1140/epjd/e2010-00226-1

098 Sokolov, A.; Herfurth, F.; Kester, O.; Stoehlker, T.; Thorn, A.; Vorobjev, G.; Zschornack, G.: **SPARC EBIT - a charge breeder for the HITRAP project.** *Journal of Instrumentation* **5**: C11001, 2010. DOI:10.1088/1748-0221/5/11/c11001 OPEN ACCESS.

099 Spohr, R.; Sharma, G.; Forsberg, P.; Karlsson, M.; Hallen, A.; Westerberg, L.: **Stroke Asymmetry of Tilted Superhydrophobic Ion Track Textures.** *Langmuir* **26**(9): 6790–6796, 2010. DOI:10.1021/la904137t

100 Spohr, R.; Zet, C.; Fischer, B. E.; Kiesewetter, H.; Apel, P.; Gunko, I.; Ohgai, T.; Westerberg, L.: **Controlled fabrication of ion track nanowires and channels.** *Nuclear instruments & methods in physics research, Section B, Beam interactions with materials and atoms* **268**(6): 676–686, 2010. DOI:10.1016/j.nimb.2009.12.017

101 Stork, H.; Dinse, K. P.; Ditter, M.; Fujara, F.; Masierak, W.; Neumann, R. ; Schuster, B.; Schwartz, K.; Trautmann, C.: **Spatially resolved nuclear spin relaxation, electron spin relaxation and light absorption in swift heavy ion irradiated LiF crystals.** *Journal of physics Condensed matter* **22**(18): 185402, 2010. DOI:10.1088/0953-8984/22/18/185402

102 Sturm, S.; Blaum, K.; Schabinger, B.; Wagner, A.; Quint, W. ; Werth, G.: **On g-factor experiments with individual ions.** *Journal of physics B, Atomic, molecular and optical physics* **43**(7): 074016, 2010. DOI:10.1088/0953-4075/43/7/074016

103 Surzhykov, A.; Volotka, A.; Fratini, F.; Santos, J. P.; Indelicato, P.; Plunien, G.; Stohlker, T.; Fritzsche, S.: **Angular correlations in the two-photon decay of heliumlike heavy ions.** *Physical review A, Atomic, molecular, and optical physics* **81**(4): 042510, 2010. DOI:10.1103/physreva.81.042510

104 Tahir, N. A.; Stohlker, T.; Shutov, A.; Lomonosov, I. V.; Fortov, V. E.; French, M.; Nettelmann, N.; Redmer, R.; Piriz, A. R.; Deutsch, C.; Zhao, Y.; Zhang, P.; Xu, H.; Xiao, G.; Zhan, W.: **Ultrahigh compression of water using intense heavy ion beams: laboratory planetary physics.** *New Journal of Physics* **12**: 073022, 2010. DOI:10.1088/1367-2630/12/7/073022 OPEN ACCESS.

105 Tashenov, S.: **Identification of bremsstrahlung events in gamma-ray tracking detectors.** *Journal of Instrumentation* **5**: P10004, 2010. DOI:10.1088/1748-0221/5/10/p10004 OPEN ACCESS.

106 Thorn, A.; Ritter, E.; Sokolov, A.; Vorobjev, G.; Bischoff, L.; Herfurth, F.; Kester, O.; Pilz, W.; Thorn, D. B.; Ullmann, F.; Zschornack, G.: **Optimization of the electron beam properties of Dresden EBIT devices for charge breeding.** *Journal of Instrumentation* **5**: C09006, 2010. DOI:10.1088/1748-0221/5/09/c09006 OPEN ACCESS.

107 Thorn, D. B.; Geddes, C. G. R.; Matlis, N. H.; Plateau, G. R.; Esarey, E. H.; Battaglia, M.; Schroeder, C. B.; Shiraishi, S.; Stohlker, T.; Toth, C.; Leemans, W. P.: **Spectroscopy of betatron radiation emitted from laser-produced wakefield accelerated electrons.** *Review of scientific instruments* **81**(10): 10E325, 2010. DOI:10.1063/1.3479118

108 Tikhonchuk, V. T.; Schlegel, T.; Regan, C.; Temporal, M.; Feugeas, J. L.; Nicolai, P.; Ribeyre, X.: **Fast ion ignition with ultra-intense laser pulses.** *Nuclear Fusion* **50**(4): 045003, 2010. DOI:10.1088/0029-5515/50/4/045003

109 Trotsenko, S.; Kumar, A.; Volotka, A. V.; Banas, D.; Beyer, H. F.; Brauning, H.; Fritzsche, S.; Gumberidze, A.; Hagmann, S.; Hess, S.; Jagodzinski, P.; Kozhuharov, C.; Reuschl, R.; Salem, S.; Simon, A.; Spillmann, U.; Trassinelli, M.; Tribedi, L. C.; Weber, G.; Winters, D.; Stohlker, T.: **Spectral Shape of the Two-Photon Decay of the 2 S-1(0) State in He-Like Tin.** *Physical review letters* **104**(3): 033001, 2010. DOI:10.1103/physrevlett.104.033001

110 Tupitsyn, I. I.; Kozhedub, Y. S.; Shabaev, V. M.; Deyneka, G. B.; Hagmann, S.; Kozhuharov, C.; Plunien, G.; Stohlker, T.: **Relativistic calculations of the charge-**

transfer probabilities and cross sections for low-energy collisions of H-like ions with bare nuclei. *Physical review A, Atomic, molecular, and optical physics* **82**(4): 042701, 2010. DOI:10.1103/physreva.82.042701

111 Vergunova, G. A.; Gus'kov, S. Y.; Rozanov, V. B.; Rozmej, O. N.: **FORMATION OF A PLANE LAYER OF PLASMA UNDER IRRADIATION BY A SOFT X-RAY SOURCE.** *Journal of Russian Laser Research* **31**(5): 509–518, 2010.

112 Vogel, M.; Quint, W. : **Trap-assisted precision spectroscopy of forbidden transitions in highly-charged ions.** *Physics Reports* **490**(1): 1–47, 2010. DOI:10.1016/j.physrep.2009.12.007

113 Vogel, M.; Quint, W. ; Nortershauser, W.: **Trapped Ion Oscillation Frequencies as Sensors for Spectroscopy.** *Sensors* **10**(3): 2169–2187, 2010. DOI:10.3390/s100302169 OPEN ACCESS.

114 Volklein, F.; Reith, H.; Schmitt, M. C.; Huth, M.; Rauber, M.; Neumann, R. : **Microchips for the Investigation of Thermal and Electrical Properties of Individual Nanowires.** *Journal of Electronic Materials* **39**(9): 1950–1956, 2010. DOI:10.1007/s11664-009-1046-2

115 Wagner, A.; Sturm, S.; Schabinger, B.; Blaum, K.; Quint, W. : **A battery-based, low-noise voltage source.** *Review of scientific instruments* **81**(6): 064706, 2010. DOI:10.1063/1.3455199

116 Weber, G.; Brauning, H.; Hess, S.; Martin, R.; Spillmann, U.; Stohlker, T.: **Performance of a position sensitive Si(Li) x-ray detector dedicated to Compton polarimetry of stored and trapped highly-charged ions.** *Journal of Instrumentation* **5**: C07010, 2010. DOI:10.1088/1748-0221/5/07/c07010 OPEN ACCESS.

117 Weber, G.; Brauning, H.; Surzhykov, A.; Brandau, C.; Fritzsche, S.; Geyer, S.; Hagmann, S.; Hess, S.; Kozhuharov, C.; Martin, R.; Petridis, N.; Reuschl, R.; Spillmann, U.; Trotsenko, S.; Winters, D. F. A.; Stohlker, T.: **Direct Determination of the Magnetic Quadrupole Contribution to the Lyman-alpha(1) Transition in a Hydrogenlike Ion.** *Physical review letters* **105**(24): 243002, 2010. DOI:10.1103/physrevlett.105.243002

118 Weikusat, C.; Miletich, R.; Glasmacher, U. A.; Trautmann, C.; Neumann, R. : **Heavy-ion irradiation on crystallographically oriented cordierite and the conversion of molecular CO2 to CO: a Raman spectroscopic study.** *Physics and Chemistry of Minerals* **37**(7): 417–424, 2010. DOI:10.1007/s00269-009-0343-x

119 Winckler, N.; Blaum, K.; Bosch, F.; Litvinov, Y. A.: **Two-body beta decay of stored highly-charged ions.** *Nuclear physics A, Nuclear and hadronic physics* **834**(1): 432C–435C, 2010. DOI:10.1016/j.nuclphysa.2010.01.057

120 Yameen, B.; Ali, M.; Alvarez, M.; Neumann, R. ; Ensinger, W.; Knoll, W.; Azzaroni, O.: **A facile route for the preparation of azide-terminated polymers. Clicking polyelectrolyte brushes on planar surfaces and nanochannels.** *Polymer Chemisty* **1**(2): 183–192, 2010. DOI:10.1039/b9py00201d

121 Yameen, B.; Ali, M.; Neumann, R. ; Ensinger, W.; Knoll, W.; Azzaroni, O.: **Proton-regulated rectified ionic transport through solid-state conical nanopores modified with phosphate-bearing polymer brushes.** *Chemical Communications* **46**(11): 1908–1910, 2010. DOI:10.1039/b920870d OPEN ACCESS.

122 Yerokhin, V. A.; Surzhykov, A.: **Off-resonant dielectronic recombination in a collision of an electron with a heavy hydrogenlike ion.** *Physical review A, Atomic, molecular, and optical physics* **81**(6): 062703, 2010. DOI:10.1103/physreva.81.062703

123 Zielbauer, B.; Zimmer, D.; Habib, J.; Guilbaud, O.; Kazamias, S.; Pittman, M.; Ros, D.: **Stable and fully controlled long-time operation of a soft X-ray laser for user application experiments.** *Applied physics B, Lasers and optics* **100**(4): 731–736, 2010. DOI:10.1007/s00340-009-3877-1

124 Zimmer, D.; Ros, D.; Guilbaud, O.; Habib, J.; Kazamias, S.; Zielbauer, B.; Bagnoud, V.; Ecker, B.; Hochhaus, D. C.; Aurand, B.; Neumayer, P. ; Kuehl, T.: **Short-wavelength soft-x-ray laser pumped in double-pulse single-beam non-normal incidence.** *Physical review A, Atomic, molecular, and optical physics* **82**(1): 013803, 2010. DOI:10.1103/physreva.82.013803

125 Zimmer, D.; Zielbauer, B.; Pittman, M.; Guilbaud, O.; Habib, J.; Kazamias, S.; Ros, D.; Bagnoud, V.; Kuehl, T.: **Optimization of a tabletop high-repetition-rate soft x-ray laser pumped in double-pulse single-beam grazing incidence.** *Optics Letters* **35**(4): 450–452, 2010.

WoS Publications to the programme 'Health' in the field 'Cancer research' published in 2010

001 Becherel, O. J.; Jakob, B.; Cherry, A. L.; Gueven, N.; Fusser, M.; Kijas, A. W.; Peng, C.; Katyal, S.; McKinnon, P. J.; Chen, J. J.; Epe, B.; Smerdon, S. J.; Taucher-Scholz, G.; Lavin, M. F.: **CK2 phosphorylation-dependent interaction between aprataxin and MDC1 in the DNA damage response.** *Nucleic Acids Research* **38**(5): 1489–1503, 2010. DOI:10.1093/nar/gkp1149 OPEN ACCESS.

002 Becker, D.; Bauer, L.; Fournier, C. ; Seifried, E.; Tonn, T.: **Resonse of human hematopoietic stem and progenitor cells to energetic carbon ions.** *Vox Sanguinis* **99**: 488–489, 2010.

003 Bert, C.; Gemmel, A.; Saito, N.; Chaudhri, N.; Schardt, D.; Durante, M.; Kraft, G.; Rietzel, E.: **Dosimetric precision of an ion beam tracking system.** *Radiation Oncology* **5**: 61, 2010. DOI:10.1186/1748-717x-5-61 OPEN ACCESS.

004 Bonig, H.; Dauber, K.; Becker, D.; Odendahl, M.; Seifried, E.; Bonig, H.; Tonn, T.: **Performance characteristics of the bd stem cell enumeration kit for various stem cell-rich tissues.** *Cytometry, Part B: Clinical Cytometry* **78B**(6): 447–447, 2010.

005 Chaudhri, N.; Saito, N.; Bert, C.; Franczak, B.; Steidl, P.; Durante, M.; Rietzel, E.; Schardt, D.: **Ion-optical studies for a range adaptation method in ion beam therapy using a static wedge degrader combined with magnetic beam deflection.** *Physics in medicine and biology* **55**(12): 3499–3513, 2010. DOI:10.1088/0031-9155/55/12/015

006 Costes, S. V.; Chiolo, I.; Pluth, J. M.; Barcellos-Hoff, M. H.; Jakob, B.: **Spatiotemporal characterization of ionizing radiation induced DNA damage foci and their relation to chromatin organization.** *Mutation Research - Reviews in Mutation Research* **704**(1): 78–87, 2010. DOI:10.1016/j.mrrev.2009.12.006

007 Deperas-Standylo, J.; Lee, R.; Ayriyan, A.; Nasonova, E.; Ritter, S. ; Gudowska-Nowak, E.: **Time-course of aberrations and their distribution: impact of LET and track structure.** *The European physical journal: D, Atomic, molecular and optical physics* **60**(1): 93–99, 2010. DOI:10.1140/epjd/e2010-00155-y

008 Durante, M.; Bruno, C.: **Impact of rocket propulsion technology on the radiation risk in missions to Mars.** *The European physical journal: D, Atomic, molecular and optical physics* **60**(1): 215–218, 2010. DOI:10.1140/epjd/e2010-00035-6

009 Durante, M.; Loeffler, J. S.: **Charged particles in radiation oncology.** *Nature Reviews Clinical Oncology* **7**(1): 37–43, 2010. DOI:10.1038/nrclinonc.2009.183

010 Durante, M.; Pignalosa, D.; Jansen, J. A.; Walboomers, X. F.; Ritter, S. : **Influence of Nuclear Geometry on the Formation of Genetic Rearrangements in Human Cells.** *Radiation research* **174**(1): 20–26, 2010. DOI:10.1667/rr2063.1

011 Durante, M.; Reitz, G.; Angerer, O.: **Space radiation research in Europe: flight experiments and ground-based studies.** *Radiation and Environmental Biophysics* **49**(3): 295–302, 2010. DOI:10.1007/s00411-010-0300-6

012 Elsasser, T.; Scholz, M. : **Comments on Formalization and Theoretical Analysis of the Local Effect Model by Beuve (Radiat. Res. 172, 394-402, 2009).** *Radiation research* **173**(6): 855–856, 2010. DOI:10.1667/rr2089.1

013 Elsasser, T.; Weyrather, W. K.; Friedrich, T.; Durante, M.; Iancu, G.; Kramer, M.; Kragl, G.; Brons, S.; Winter, M.; Weber, K. J.; Scholz, M. : **Quantification of the relative biological effectiveness for ion beam radiotherapy: direct experimental comparison of proton and carbon ion beas and a novel approach for treatment planning.** *International journal of radiation oncology, biology, physics* **78**(4): 1177–1183, 2010. DOI:10.1016/j.ijrobp.2010.05.014

014 Friedrich, T.; Weyrather, W.; Elsasser, T.; Durante, M.; Scholz, M. : **Accuracy of RBE: experimental and theoretical considerations.** *Radiation and Environmental Biophysics* **49**(3): 345–349, 2010. DOI:10.1007/s00411-010-0298-9

015 Gemmel, A.; Bert, C.; Saito, N.; von Neubeck, C.; Iancu, G.; K-Weyrather, W.; Durante, M.; Rietzel, E.: **Development and performance evaluation of a dynamic phantom for biological dosimetry of moving targets.** *Physics in medicine and biology* **55**(11): 2997–3009, 2010. DOI:10.1088/0031-9155/55/11/001

016 Goetze, K.; Scholz, M. ; Taucher-Scholz, G.;

Mueller-Klieser, W.: **Tumor cell migration is not influenced by p21 in colon carcinoma cell lines after irradiation with X-ray or C-12 heavy ions.** *Radiation and Environmental Biophysics* **49**(3): 427–435, 2010. DOI:10.1007/s00411-010-0297-x

017 Hartel, C.; Nikoghosyan, A.; Durante, M.; Sommer, S.; Nasonova, E.; Fournier, C. ; Lee, R.; Debus, J.; Schulz-Ertner, D.; Ritter, S. : **Chromosomal aberrations in peripheral blood lymphocytes of prostate cancer patients treated with IMRT and carbon ions.** *Radiotherapy and oncology: journal of the European Society for Therapeutic Radiology and Oncology* **95**(1): 73–78, 2010. DOI:10.1016/j.radonc.2009.08.031

018 Kadhim, M. A.; Lee, R.; Moore, S. R.; Macdonald, D. A.; Chapman, K. L.; Patel, G.; Prise, K. M.: **Genomic instability after targeted irradiation of human lymphocytes: Evidence for inter-individual differences under bystander conditions.** *Mutation Research - Fundamental and Molecular Mechnisms of Mutagenesis* **688**(1): 91–94, 2010. DOI:10.1016/j.mrfmmm.2010.03.013

019 Kramer, M.; Durante, M.: **Ion beam transport calculations and treatment plans in particle therapy.** *The European physical journal: D, Atomic, molecular and optical physics* **60**(1): 195–202, 2010. DOI:10.1140/epjd/e2010-00077-8

020 Laube, K.; Bert, C.; Chaudhri, N.; Fiedler, F.; Parodi, K.; Rietzel, E.; Saito, N.; Enghardt, W.: **4D-in-beam PET for periodically moving phantom when irradiated with a comoving 12C-ray.** *Strahlentherapie und Onkologie* **186**: 52–52, 2010.

021 Lee, R.; Sommer, S.; Hartel, C.; Nasonova, E.; Durante, M.; Ritter, S. : **Complex exchanges are responsible for the increased effectiveness of C-ions compared to X-rays at the first post-irradiation mitosis.** *Mutation Research - Genetic Toxicology and Environmental Mutagenesis* **701**(1): 52–59, 2010. DOI:10.1016/j.mrgentox.2010.03.004

022 Le Foulher, F.; Bajard, M.; Chevallier, M.; Dauvergne, D.; Freud, N.; Henriquet, P.; Karkar, S.; Letang, J. M.; Lestand, L.; Plescak, R.; Ray, C.; Schardt, D.; Testa, E.; Testa, M.: **Monte Carlo Simulations of Prompt-Gamma Emission During Carbon Ion Irradiation.** *IEEE transactions on nuclear science* **57**(5): 2768–2772, 2010. DOI:10.1109/tns.2010.2048042

023 Mairani, A.; Brons, S.; Cerutti, F.; Fasso, A.; Ferrari, A.; Kramer, M.; Parodi, K.; Scholz, M. ; Sommerer, F.: **The FLUKA Monte Carlo code coupled with the local effect model for biological calculations in carbon ion therapy.** *Physics in medicine and biology* **55**(15): 4273–4289, 2010. DOI:10.1088/0031-9155/55/15/006

024 Martino, G.; Durante, M.; Schardt, D.: **Microdosimetry measurements characterizing the radiation fields of 300 MeV/u C-12 and 185 MeV/u Li-7 pencil beams stopping in water.** *Physics in medicine and biology* **55**(12): 3441–3449, 2010. DOI:10.1088/0031-9155/55/12/011

025 Merz, F.; Muller, M.; Taucher-Scholz, G.; Rodel, F.; Stocker, H.; Schopow, K.; Laprell, L.; Dehghani, F.; Durante, M.; Bechmann, I.: **Tissue slice cultures from humans or rodents: a new tool to evaluate biological effects of heavy ions.** *Radiation and Environmental Biophysics* **49**(3): 457–462, 2010. DOI:10.1007/s00411-010-0293-1

026 Muller, M.; Durante, M.; Stocker, H.; Merz, F.; Bechmann, I.: **Modeling radiation effects at the tissue level.** *The European physical journal: D, Atomic, molecular and optical physics* **60**(1): 171–176, 2010. DOI:10.1140/epjd/e2010-00030-y

027 Munter, M. W.; Wengenroth, M.; Fehrenbacher, G. ; Schardt, D.; Nikoghosyan, A.; Durante, M.; Debus, J.: **Heavy ion radiotherapy during pregnancy.** *Fertility and Sterility* **94**(6): 2329.e5, 2010. DOI:10.1016/j.fertnstert.2010.04.005

028 Obe, G.; Durante, M.: **DNA Double Strand Breaks and Chromosomal Aberrations.** *Cytogenetic and genome research* **128**(1): 8–16, 2010. DOI:10.1159/000303328

029 Obe, G.; Durante, M.; Ritter, S. ; Reitz, G.: **Special Issue: New Insights into Chromosomal Aberrations - Reports from the 9th International Symposium on Chromosomal Aberrations Introduction.** *Mutation Research - Genetic Toxicology and Environmental Mutagenesis* **701**(1): 1–2, 2010. DOI:10.1016/j.mrgentox.2010.05.015

030 Obe, G.; Johannes, C.; Ritter, S. : **The number and not the molecular structure of DNA double-strand breaks is more important for the formation of chromosomal aberrations: A hypothesis.** *Mutation Research - Genetic Toxicology and Environmental Mutagenesis* **701**(1): 3–11, 2010. DOI:10.1016/j.mrgentox.2010.05.010

031 Parodi, K.; Mairani, A.; Brons, S.; Naumann, J.; Kramer, M.; Sommerer, F.; Haberer, T.: **The influence of lateral beam profile modifications in scanned proton and carbon ion therapy: a Monte Carlo study.** *Physics in medicine and biology* **55**(17): 5169–5187, 2010. DOI:10.1088/0031-9155/55/17/018

032 Pignalosa, D.; Ritter, S. ; Durante, M.: **Inversions in Chromosome 10 of Human Thyroid Cells Induced by Accelerated Heavy Ions.** *Radiation research* **174**(1): 14–19, 2010. DOI:10.1667/rr1963.1

033 Pugliese, M.; Bengin, V.; Casolino, M.; Roca, V.; Zanini, A.; Durante, M.: **Tests of shielding effective-**

ness of Kevlar and Nextel onboard the International Space Station and the Foton-M3 capsule. *Radiation and Environmental Biophysics* **49**(3): 359–363, 2010. DOI:10.1007/s00411-010-0283-3

034 Rietzel, E.; Bert, C.: **Respiratory motion management in particle therapy.** *Medical physics* **37**(2): 449–460, 2010. DOI:10.1118/1.3250856

035 Ritter, S. ; Durante, M.: **Heavy-ion induced chromosomal aberrations: A review.** *Mutation Research - Genetic Toxicology and Environmental Mutagenesis* **701**(1): 38–46, 2010. DOI:10.1016/j.mrgentox.2010.04.007

036 Roelofs, E.; Persoon, L.; Qamhiyeh, S.; Verhaegen, F.; De Ruysscher, D.; Scholz, M. ; Iancu, G.; Engelsman, M.; Rasch, C.; Zijp, L.; De Meerleer, G.; Coghe, M.; Langendijk, J.; Schilstra, C.; Pijls-Johannesma, M.; Lambin, P.: **Design of and technical challenges involved in a framework for multicentric radiotherapy treatment planning studies.** *Radiotherapy and oncology: journal of the European Society for Therapeutic Radiology and Oncology* **97**(3): 567–571, 2010. DOI:10.1016/j.radonc.2010.08.009

037 Schardt, D.; Elsasser, T.; Schulz-Ertner, D.: **Heavy-ion tumor therapy: Physical and radiobiological benefits.** *Reviews of Modern Physics* **82**(1): 383–425, 2010. DOI:10.1103/revmodphys.82.383

038 Splinter, J.; Jakob, B.; Lang, M. ; Yano, K.; Engelhardt, J.; Hell, S. W.; Chen, D. J.; Durante, M.; Taucher-Scholz, G.: **Biological dose estimation of UVA laser microirradiation utilizing charged particle-induced protein foci.** *Mutagenesis* **25**(3): 289–297, 2010. DOI:10.1093/mutage/geq005

039 Testa, M.; Bajard, M.; Chevallier, M.; Dauvergne, D.; Freud, N.; Henriquet, P.; Karkar, S.; Le Foulher, F.; Letang, J. M.; Plescak, R.; Ray, C.; Richard, M. H.; Schardt, D.; Testa, E.: **Real-time monitoring of the Bragg-peak position in ion therapy by means of single photon detection.** *Radiation and Environmental Biophysics* **49**(3): 337–343, 2010. DOI:10.1007/s00411-010-0276-2

040 Tobias, F.; Durante, M.; Taucher-Scholz, G.; Jakob, B.: **Spatiotemporal analysis of DNA repair using charged particle radiation.** *Mutation Research - Reviews in Mutation Research* **704**(1): 54–60, 2010. DOI:10.1016/j.mrrev.2009.11.004

041 Wissmann, F.; Giesen, U.; Klages, T.; Schardt, D.; Martino, G.; Sunil, C.: **Microdosimetric measurements in the secondary radiation field produced in C-12-therapy irradiations.** *Radiation and Environmental Biophysics* **49**(3): 331–336, 2010. DOI:10.1007/s00411-010-0279-z

042 Zaconte, V.; Casolino, M.; De Santis, C.; Di Fino, L.; La Tessa, C.; Larosa, M.; Narici, L.; Picozza, P.: **The radiation environment in the ISS-USLab measured by ALTEA: Spectra and relative nuclear abundances in the polar, equatorial and SAA regions.** *Advances in space research* **46**(6): 797–799, 2010. DOI:10.1016/j.asr.2010.02.032

043 Zahnreich, S.; Melnikova, L.; Winter, M.; Nasonova, E.; Durante, M.; Ritter, S. ; Fournier, C. : **Radiation-induced premature senescence is associated with specific cytogenetic changes.** *Mutation Research - Genetic Toxicology and Environmental Mutagenesis* **701**(1): 60–66, 2010. DOI:10.1016/j.mrgentox.2010.03.010

GSI as Publisher

K.Weyrich (Ed.):
High Energy Density Physics with Intense Ion and Laser Beams: Annual Report 2009

GSI Report 2010-1
K. Große (Ed.): GSI Scientific Report 2009

GSI Diss 2010-18
Petermann, Ilka:
Influence of Fission Processes on Nucleosynthesis on r-Process Network Calculations, Tu Darmstadt.

GSI Diss 2010-17
Becker, Frank: Zerstörungsfreie Profilmessung intensiver Schwerionenstrahlen, TU Darmstadt

GSI Diss 2010-16
Dickel, Timo: Design and commissioning of an Ultra-High-Resolution Time-of-Flight based isobar separator and mass spectrometer, Univ. Gießen

GSI Diss 2010-15
Hinke, Christoph B.: Spectroscopy of the doubly magic nucleus ^{100}Sn and its decay, TU München.

GSI Diss 2010-14
Krämer, Jörg: Construction and commissioning of a collinear laser spectroscopy setup at TRIGA Mainz and laser spectroscopy of magnesium isotopes at ISOLDE (CERN), Univ. Mainz.

GSI Diss 2010-13
Le Bleis, Tudi: Experimental Study of collective electric dipole mode in neutron rich nickel nuclei, Univ. Strasbourg.

GSI Diss 2010-12
Zakova, Monika: Nuclear charge radii of light isotopes based on frequency comp measurements, Univ. Mainz.

GSI Diss 2010-11
Zimmer, Daniel: A new double laser pulse pumping scheme for transient collisionally excited plasma soft X-ray lasers, Univ. Mainz.

GSI Diss 2010-10
Salem, Shadi Mohammad Ibrahim: Projectile X-ray emmission in relativistic Ion-Atom Collision, Univ. Frankfurt/M.

GSI Diss 2010-09
Pfister, Jochen: Entwicklung und Anwendung schneller Strahldiagnose für Ionenstrahlen, Univ. Frankfurt/M.

GSI Diss 2010-08
Weber, Günther: Untersuchung zur Anisotropie und linearen Polarisation radiativer Prozesse in energiereichen Ion-Atom-Stößen, Univ. Heidelberg.

GSI Diss 2010-07
Engert, Tobias: Surface characterisation and surface protection of Germanium detector crystals, Univ. Liverpool.

GSI Diss 2010-06
Paret, Stefan: Transverse Schottky Spectra and beam transfer fuctions of coasting ion beams with space charge, TU Darmstadt.

GSI-Diss 2010-05
Klein, Robert G.: Swift Heavy Ion Irradiated Boron Nitride with and without the application of High Pressure, Univ. Heidelberg.

GSI Diss 2010-04
Heß, Sebastian: Compton-Polarimetrie mit ortsauflösenden Röntgendetektoren, Univ. Frankfurt/M.

GSI Diss 2010-03
Rossi, Dominic M.: Investigation of the Dipole response of Nickel Isotopes in the Presence of a High-Frequency Electromagnetic Field, Univ. Mainz.

GSI Diss 2010-02
Kreim, Susanne Waltraud: Direct Observation of a Single Proton in a Penning Trap, Univ. Mainz.

GSI Diss 2010-01
Wiechula, Jens: Commissioning and Calibration of the ALICE-TPC, Univ. Frankfurt/M.

GSI Dipl 2010-05
Berck, Frederik: Prototyp für ein mobiles Agentensystem in NI LabVIEW, Hochschule Darmstadt.

GSI Dipl 2010-04
Hammen, Michael: Development, construction and test of an efficient fluorescence detection region for collinear laser spectroscopy at TRIGA-Mainz, Univ. Mainz.

GSI Dipl 2010-03
Sieber, Bastian: Aufbau und Test eines Detektorsystems zum Koinzidenznachweis von Ionen und Photonen für die kollineare Laserspektroskopie am TRIGA-Forschungsreaktor, Univ. Mainz.

GSI Dipl 2010-02
Dettmering, Till: Investigations on the radiation-induced accumulation of reactive oxygen species in human fibroblasts, TU Darmstadt.

GSI Dipl 2010-01
Hackler, Thomas: Aufbau einer differentiell gepumpten Strahlführungslinie mittels einer Peltier-Kühlfalle, Fachhochschule Wiesbaden.

GSI BA 2010-04
Krieg, Janina: Fabrication and characterization of Arrays of Conical Metal Nanowires, TU Darmstadt.

GSI BA 2010-03
Gregor, Eleonora Teresia: The double-sided silicon strip detector with excellent position, energy and time resolution / Der doppelseitige Siliziumstreifendetektor mit exzellenter Positions-, Energie- und Zeitauflösung, TU Darmstadt.

GSI BA 2010-02
Flammann, David: Kryomechanische Berechnung und Simulation der SIS 100 Dipolmagnet-Aufhängung, Hochschule Rhein-Main.

GSI BA 2010-01
Klisa, Tristan: Vorentwicklung des Kalt- Warm-Überganges zum Anpumpen an einer kryogenen Kollimatorkammer, Hochschule Rhein-Main.

Doctoral theses 2010 supported by GSI

Compiled by C. Kausch, I. Kraus, K. Kreidi, M. Pantea, and S. Typel

Physics of Hadrons and Nuclei

ALICE

Juan Castillo: Charged particle multiplicity studies in proton-proton collisions at $\sqrt{s} = 10$ TeV with the ALICE detector (Technische Universität Darmstadt, June 2010)

CBM

Dmytro Kresan: Event-by event Fluctuations of the Particle Yield Ratios in Heavy-Ion Collisions at $20 - 158$ A GeV (Johann Wolfgang Goethe-Universität Frankfurt, March 2010)

FOPI

Tae Im Kang: Charged Kaon Flow in Ni+Ni collisions (University of Seoul, South Korea, December 2010)

HADES

Attilio Tarantola: Omega production in p+p reactions at 3.5 GeV with the HADES experiment and new electronics for the readout of the multiwire drift chambers (Johann Wolfgang Goethe-Universität Frankfurt, December 2010)

Nuclear Reactions

Dominic Rossi: High-Frequency Electromagnetic Field (Johannes Gutenberg-Universität Mainz, January 2010)

Nuclear Structure

Tobias Engert: Surface characterization and surface protection of Ge detector crystals (Liverpool University, June 2010)

Timo Dickel: Isobar Separator and Mass Spectrometer (Justus-Liebig-Universität Gießen, July 2010)

Theory

Julian Hofmann: Coupled-channel study of axial-vector mesons with realistic t- and u-channel exchanges (Technische Universität Darmstadt, February 2010)

Alexander Semke: On the quark-mass dependence of baryon ground-state masses (Technische Universität Darmstadt, February 2010)

Ilka Petermann: Influence of Fission Processes on Nucleosynthesis in R-Process Network Calculations (Technische Universität Darmstadt, July 2010)

Accelerator Physics

Stefan Paret: Transverse Schottky Spectra and Beam Transfer Functions of Coasting Ion Beams with Space Charge (Technische Universität Darmstadt, February 2010)

Jochen Pfister: Entwicklung und Anwendung schneller Strahldiagnose für Ionenstrahlen (Johann Wolfgang Goethe-Universität Frankfurt, June 2010)

Beam Diagnostics

Frank Becker: Zerstörungsfreie Profilmessung intensiver Schwerionenstrahlen (Technische Universität Darmstadt, February 2010)

Udo Rauch: Eine hochauflösende Methode zur Messung der transversalen Betatronfrequenz im SIS18 (Johann Wolfgang Goethe-Universität Frankfurt, October 2010)

Research with Photons, Neutrons and Ions

Atomic Physics

Alexey Sokolov: Charge Breeding Investigation in EBIS/T and Collision Study of Ions with Cold Atoms for HITRAP (Ruprecht-Karls-Universität Heidelberg, January 2010)

Sebastian Heß: Compton - Polarimetrie mit ortsauflösenden Röntgendetektoren (Johann Wolfgang Goethe-Universität Frankfurt, January 2010)

Monika Zakova: Nuclear Charge Radii of Light Isotopes Based on Frequency Comb Measurements (Johannes Gutenberg-Universität Mainz, February 2010)

Jörg Krämer: Construction and Commissioning of a Collinear Laser Spectroscopy Setup at TRIGA Mainz and Laser Spectroscopy of Magnesium Isotopes at ISOLDE (CERN) (Johannes Gutenberg-Universität Mainz, July 2010)

Günter Weber: Untersuchung zur Anisotropie und linearen Polarisation radiativer Prozesse in energiereichen Ion-Atom-Stößen (Ruprecht-Karls-Universität Heidelberg, June 2010)

Punita Verma: X-ray Emission from Heavy Atomic Collisions: Couplings of Inner Shells in Superheavy Quasimolecules (Justus-Liebig-Universität Gießen, December 2010)

Materials Research

Robert Klein: Swift Heavy Ion Irradiated Boron Nitride With and Without the Application of High Pressure (Ruprecht-Karls-Universität Heidelberg, June 2010)

Oliver Picht: Growth and Characterization of Bismuth Telluride Nanowires (Ruprecht-Karls-Universität Heidelberg, June 2010)

Plasma Physics/PHELIX

Thomas Heßling: Charakterisierung lasererzeugter Hohlraumstrahlung für die experimentelle Untersuchung der Wechselwirkung von Schwerionen mit Plasmen (Technische Universität Darmstadt, February 2010)

Jurij Menzel: Aufbau und Inbetriebnahme einer Kryoanlage zur Targeterzeugung für Experimente mit Hochenergielasern und Schwerionenstrahlen (Technische Universität Darmstadt, February 2010)

Knut Harres: Strahltransport laserbeschleunigter Ionen (Technische Universität Darmstadt, July 2010)

Alexander Pelka: Röntgenthomsonstreuung als Diagnostik dichter Plasmen (Technische Universität Darmstadt, July 2010)

Daniel Zimmer: A new double laser pulse pumping scheme for transient collisionally excited soft x-ray lasers (Johannes Gutenberg-Universität Mainz, July 2010)

Frank Nürnberg: Laserbeschleunigte Protonenstrahlen als neue Teilchenquelle (Technische Universität Darmstadt, November 2010)

Cancer Research

Biophysics

Diana Pignalosa: Cytogenetic effects induced in human cells after exposure to relativistic heavy ions (Università degli Studi di Napoli "Federico II", Neapel, Italy, January 2010)

Carola Hartel: Qualitative and quantitative investigation of the cytogenetic effects of densely ionizing radiation in vitro and in vivo (Technische Universität Darmstadt, May 2010)

Jörn Splinter: Distribution and dynamics of charged particle-induced DNA double-strand breaks (Technische Universität Darmstadt, May 2010)

Naved Chaudhri: Fast adaptation of ion beam range for moving targets in radiotherapy (Ruprecht-Karls-Universität Heidelberg, July 2010)

Satyendra Kumar Singh: The function of backup pathways of non-homologous end joining in relation to growth state and lesion quality in cells of higher eukaryotes (Universität Duisburg Essen, September 2010)

GSI Projektträger und Drittmittelstelle / KKS

D. Müller / I. Reinhard

Projektträger des Bundesministeriums für Bildung und Forschung (BMBF)

GSI is the managing institution for the BMBF project funding (so called "Verbundforschung") in the field of "Hadron- and Nuclear Physics". These public funds are foreseen to support research groups at universities in Germany to strengthen their ability to participate in experiments and projects performed at scientific institutions like GSI and CERN which are funded to a significant level from federal resources.

BMBF project funding: 128 running projects with a total budget of 12,5 Mio. € in 2010.

GSI F&E contracts ("Forschungs- und Entwicklungsvereinbarungen")

Since 1969 GSI has special research and development contracts with German universities to strengthen the collaboration between these universities and GSI. Mainly resources for personnel are provided to enhance the participation of PhD students and young Post-Docs within GSI projects.

GSI F&E Contracts: 69 running projects with a total budget of 1,8 Mio. € in 2010.

Helmholtz Association "Initiative and Networking Fund (IVF)"

This fund is one of the Helmholtz Association's key instruments in achieving its strategic goals in Research and Innovation. It consists mainly of "Helmholtz Virtual Institutes" (Networks between GSI and University groups), Young Investigator Awards and Graduate Schools.

GSI-HGF-IVF: 8 running projects with a total budget of 1,1 Mio. € in 2010.

EU-Framework Programs 6 and 7

GSI has been involved in **20** projects in the EU Framework Programme 6 and 7 in 2010. The GSI EU and third party funds Office supports scientists at GSI in order to carry out projects successfully in all project phases.

GSI-EU-Framework Programs: **20** projects running in 2010 with a total EC contribution for GSI of about 3 Mio. € in 2010.

GSI is the managing institution for the FAIR EU construction (CNI) contract 'DIRAC -PHASE-1'. It consists of 13 institutions in 9 countries. The administrative management was taken over by the GSI EU Office in 2010.

DIRAC Phase 1: **12** subprojects with a total budget of 101 Mio. € (10 Mio. € EC contribution) over 5,5 years.

GSI R&D contracts with German universities and research centres

Universität Bielefeld

BILAER1012/Learmann:
Numerische Simulation zur Thermodynamik heißer und hadronischer Materie bei nicht-verschwindender Baryondichte

Ruhr-Universität Bochum

BOWIED1012/Wiedner:
Entwicklungen für ein hochauflösendes elektromagnetisches Endcapkalorimeter und Softwareentwicklungen für PANDA

Rheinische Friedrich-Wilhelms-Universität Bonn

BNBRIN1012/Brinkmann:
Auslesechip für die PANDA-Siliziumdetektoren

TU Darmstadt

DAENS1/Ensinger:
Radiation stability of graphite as production target and ion beam dump of the super-FRS

DAGLE2/Glesner:
Systemmodellierung und Vernetzung der digitalen Mehr-Kavitäten-Regelung für das FAIR-Projekt

DAGROS1012/Groß:
Feld- und Trajektorienberechnung für Präzisionsexperimente an HITRAP

DALOEB/Löbrich:
DNA damage after high-LET exposure

DAOESC/Oeschler:
Kalibrationsmethoden und Exp. mit der ALICE-TPC

DAPAYS/Löbrich:
Der Einfl. ionis. Betrahlg. auf die Zytologie, Proliferat. u. Differenz. olfaktorischer Stammzell in vitro

TU Dresden

DDPLUN1012/Plunien:
Quantenelektrodynamische und paritätsverletzende Effekte in hochgeladenen schweren Ionen

DDWEBE1012/Weber:
Ionenstrahl-induzierte Lumineszenz in Halbleitern

DDZSCH/Zschornack:
EBIS/T Injektor für HITRAP u. FLAIR; EBIS/T Ladungsbrüter für MATS

DDZSCH1012/Zschornack:
Charakterisierung u. Weiterentwicklung von Ionenquellen des Dresden EBIS/T-Typs als Testinjektoren u. Ladungsbrüter für HITRAP

DDZUBE1012/Zuber:
Entwicklung von MRPC-Detektoren für NeuLAND (NUSTAR-R3B)

HZDR Rossendorf

DRGROS/Wagner:
Entw. Detektoren und exp. Methoden zur Neutronenenergie-Best. bei R3B

DRKAEM/Kämpfer:
Medium-Modifikation von Charm-Mesonen und Kernmaterie in der Nähe des kritischen Punktes

DRSCHR/Schramm:
Laser cooling of relativistic C3+ ion beams at the ESR (GSI) and in preparation of SIS300/FAIR

Universität Erlangen

EREYRI1012/Eyrich:
PANDA-DIRC

Universitätsklinikum Essen

EILIAK/Iliakis
Spatiotemporal functional interdependences between DNA double strand break repair / checkpoint response

Universität Frankfurt

FRISCH/Rischke:
Der chir. Phasenüberg. in stark wechselwirkender Materie bei hohen Energiedichten

FSCHE1/Schempp:
Optimierung des HITRAP RFQs

FSCHE2/Schempp:
RFQ für hohe Pulsströme für FAIR und RFQ für hohes Tastverhältnis Intensitätserhöhung UNILAC

FSTROT/Stroth:
HADES / CBM / R3B

Universität Freiburg

FRWEID/Weidemüller:
Optically trapped ultracold atoms as a target for low-energetic beams of highly-charged ions and antiprotons

FH Gelsenkirchen

GELOEF1012/Löffler:
Verbesserung der physik. Eigenschaften des HV-Vorwiderstandes in elektrostatischen Septa

Universität Giessen

GIDUER/Düren:
Entwicklung eines DIRC-Cherenkov-Detektors für PANDA

GILENS/Lenske:
Theoretische Untersuchungen zur Erzeugung und Spektroskopie von Hyperkernen (HYPHI)

GIMET2/Scheidenberger:
SFRS: Isobarenseparator und Mulitplexer RFQ (MATS, LASPEC)

GINOVO/Novotny:
Entwicklung und Bau von Komponenten zum Barrel-Kalorimeter von PANDA

Ernst-Moritz-Arndt-Universität Greigswald

GFMARX1012/Marx:
Sensitivitätssteigerung u. Laser-Mikrowellenspektroskopie an SHIPTRAP und zukünftigen GSI-Ionenfallen-Apparaturen

Universität Heidelberg:

HDENSS/Enss:
Entw. von Tieftemp.-Mikrokalorimetern f. d. hochaufl. Photonenspektr. in Präzisionsexp.

HDHERR/Herrmann:
Untersuchung baryonischer Materie mit Hilfe seltsamer Teilchen in den Experimenten FOPI und CBM

HDKEBS/Kebschull:
Modulares Basissystem als Auslese-Frontend- und Detektor-Controll-System für CBM

HDMAEN/Männer:
Front End Elektronik, schnelles Kommunikationsnetzw., Triggerproz. und DEPFET Pixel für CBM@FAIR

HDPUCC/Pucci:
Definierte Metall-Diamantgrenzfläche von einkristallinen Diamantdetektoren

FH Köln

KHARTU1012/Hartung:
Fehlertolerantes Steuersystem für Teilchendetektoren (DCS-CBM)

Universität Köln

KJOLIE/Jolie:
Entwicklungen für HISPEC/DESPEC an FAIR

KJOLIE1012/Jolie:
HISPEC/DESPEC @ FAIR: 1) Plungerapparatur für Lebensdauer-messungen 2) Ultra thin beam tracking detectors sowie PRESPEC-FRS / AGATA

KREITE/Reiter:
Detekt.entw. f. RISING/HISPEC u. f. AGATA bei FAIR u. Exp. m. rel. Strahlen mit dem RISING-FRS-Spekt.

KZILGE1012/Zilges:
Messung astrophysikal. relevanter (p,γ)- und (α,γ)-Reaktionsraten von exotischen Kernen

Universität Kassel

KSZIPF1012/Zipf:
Steuerung von Barrier Bucket Systemen für FAIR

Leuphana Universität Lüneburg

LGGEOR1012/Georgiadis:
CCD-gestützte Röntgennachweissysteme für SPARC

LMU München

LMTHIR1012/Thirolf:
Arbeiten für das Penningfallen-Experiment SHIPTRAP: Aufbau, Test u. Betrieb der kryogenen Puffergas-Stoppzelle

LMHABS1012/Habs:
Ultrahoher Pulskontrast am PHELIX-Kurzpulslaser: Laser-Materie-Wechselwirkung bei Festkörperdichte u. mit Nanotargets

Universität Marburg

MRAN/An:
Genome wide screening to identify candidate genes in cellular respons. induced by heavy ion irradiation

Universität Münster

MSKHOU1012/Khoukaz:
Weiterentwicklung eines Cluster-Jet-Targets hoher Dichte für das PANDA-Exp. an FAIR

MSWESS1012/Wessels:
Integration und Test der TRD-Frontendelektronik für CBM

Universität Mainz

MZJVKR/Kratz:
Entwicklung und Herstellung von Transuran- und sonstigen radioaktiven Targets

Universität Regensburg

RSCHAE1012/Schäfer:
Zeitartige Formfaktoren und verwandte exklusive Prozesse sowie Eigenschaften charmanter Hadronen

TU München

TMFABI1012/Fabbietti:
Development and Construction of a GEM-TPC Detector (FOPI / PANDA)

TMKRUE1012/Krücken:
R3B / EXL / ESR / HADES

TMPAUL1012/Paul:
Entwicklung einer Hochraten-TPC mit GEM-Auslese

TMWEIS1012/Weise:
Komplexe Systeme und Phasen der QCD

Universität Wuppertal

WFODOR1012/Fordor:
Gitter QCD basierte Untersuchungen von nicht-verschwindenden chemischen Potentialen und spektrale Eigenschaften

WKAMPE1012/Kampert:
Monte Carlo Studien zur Optimierung des CBM-RICH und Aufbau einer Prototyp-Kamera mit Spiegelsystem

WMUELL1012/Müller:
Optimierung der Feldemission metallischer Nanodrähte für kalte Elektroquellen

FH Worms

WOKEID1012/Keidel:
Experimentsteuerung (CSS) im FAIR Kontext (CBM)

EU projects at GSI

Compiled by EU-Büro

FAIR Construction 'DIRAC-PHASE 1'/FP6 (515876)
<http://www.gsi.de/fair/EU-Construction/index.html>
Coordinator: GSI, Darmstadt (Germany)
Project coordinator: H. Eickhoff
Contact at GSI: G. Walter

EUROTRANS/FP6 (516520)
<http://www.fzd.de/DB/Cms?pOid=20823>
Coordinator: FZK, Karlsruhe (Germany)
Project coordinator: J. U. Knebel (NUCLEAR)
Project coordinator at GSI: K.-H. Schmidt
Contact at GSI: A. Kelic

FAIR-PP/FP7 (211382)
<http://www.gsi.de/fair/FAIR-Preparatory-Phase/index_e.html>
Coordinator: GSI, Darmstadt (Germany)
Project Coordinator: F. Weißbach
Contact at GSI: F. Weißbach

NuPNET/FP7 (202914)
<http://www.nupnet-eu.org/>
Coordinator: CNRS (France)
Project Coordinator: S. Galès
Project Coordinator at GSI: I. Reinhard
Contact at GSI: I. Reinhard

HiPER/FP7 (211737)
<http://www.hiper-laser.org/>
Coordinator: STFC (UK)
Project Coordinator: M. Dunne
Project Coordinator at GSI: T. Stöhlker
Contact at GSI: T. Stöhlker

SLHC-PP/FP7 (212114)
<http://info-slhc-pp.web.cern.ch/info-SLHC-PP/GB.htm>
Coordinator: CERN, Geneva (Switzerland)
Project coordinator: L.Evans
Project coordinator at GSI: G. Fehrenbacher
Contact at GSI: G. Fehrenbacher

SPIRAL2-PP/FP7 (212692)
<http://www.spiral2pp.eu/>
Coordinator: GANIL, Caen (France)
Project Coordinator: Lewitowicz
Project Coordinator at GSI: J. Gerl
Contact at GSI: J. Gerl

MC-PAD/FP7 (214560)
<http://mc-pad.web.cern.ch/>
Coordinator: CERN, Geneva (Switzerland)
Project Coordinator: C. Joram
Project Coordinator at GSI: C. Schmidt
Contact at GSI: C. Schmidt

MC DITANET/FP7 (215080)
<http://www.kip.uni-heidelberg.de/DITANET/>
Coordinator: KPI Heidelberg (Germany)
Project Coordinator: C. Welsch
Project Coordinator at GSI: P. Forck
Contact at GSI: P. Forck

MC Partner/FP7 (215840)
<http://partner.web.cern.ch/partner/>
Coordinator: CERN, Geneva (Switzerland)
Project Coordinator: M. Dosanjh
Project Coordinator at GSI: W. Kraft-Weyrather
Contact at GSI: W. Kraft-Weyrather

EGEE III/FP7 (222667)
<http://www.eu-egee.org/>
Coordinator: CERN, Geneva (Switzerland)
Project Coordinator: B. Jones
Project Coordinator at GSI: P. Malzacher
Contact at GSI: P. Malzacher

HADRONPHYSICS 2/FP7 (227431)
<http://www.hadronphysics2.eu/>
Coordinator: INFN Frascati (Italy)
Project coordinator: C. Guaraldo (LNF-INFN)
Project coordinator at GSI: F. Weißbach
Contact at GSI: F. Weißbach

EuCARD/FP7 (227579)
<http://www.eu-egee.org/>
Coordinator: CERN, Geneva (Switzerland)
Project Coordinator: J.-P. Koutchouk
Project Coordinator at GSI: J. Stadlmann
Contact at GSI: J. Stadlmann

Laserlab Europe II/FP7 (228334)
<http://www.laserlab-europe.net>
Coordinator: Forschungsverb. Berlin (Germany)
Project coordinator: W. Sandner (Berlin)
Project coordinator at GSI: T. Kühl
Contact at GSI: T. Kühl

ULICE/FP7 (228436)
<http://ulice.web.cern.ch/ULICE>
Coordinator:CNAO (Italy)
Project Coordinator: Roberto Orecchia
Project Coordinator at GSI: W. Kraft-Weyrather
Contact at GSI: W. Kraft-Weyrather

MC ILP-ULTRA/FP7 (230777)
Coordinator: CNRS (France)
Project Coordinator: Tikhonchuk
Project Coordinator at GSI: T. Schlegel
Contact at GSI: T. Schlegel

ALLEGRO/FP7 (231965)
<www.allegroproject.eu/>
Coordinator: Università Pavia (Italy)
Project coordinator: A. Ottolenghi
Project coordinator at GSI: M. Durante
Contact at GSI: M. Durante, C. Kausch

ENVISION/FP7 (241851)
<enlight.web.cern.ch/enlight/cms/index.php?file
=projects/more-information-on-envision>
Coordinator: CERN, Geneva (Switzerland)
Project coordinator: M. Dosanjh
Project coordinator at GSI: C. Bert
Contact at GSI: C. Bert, C. Kausch

ANDES/FP7 (249671)
<fachp1.ciemat.es/andes/>
Coordinator: CIEMAT (Spain)
Project coordinator: E. González Romero
Project coordinator at GSI: A. Kelic-Heil
Contact at GSI: A. Kelic-Heil, V. Ricciardi

ENSAR/FP7 (262010)
<www.ensarfp7.eu/>
Coordinator: GANIL, Caen (France)
Project coordinator: M. Harakeh
Project coordinator at GSI: C. Scheidenberger
Contact at GSI: K. Füssel, M. Pantea

Beamtime Balance of the Year 2010

Exp.	Area	Spokes-person	Affiliation	Short Title	Ion	Main (Parasitic) Shifts Beam
B, E000, S000, U000	UNILAC, SIS	Barth, Dahl,Gerhard, Gütlich, Scheeler, Steck, Spiller	GSI	Commissioning, Beam Adjustment, Machine Experiments	12C, 20Ne, 40Ar,48Ca, 124Xe,197Au, 238U	**309(41)**
E028	UZ7	Egelhof	GSI, Universität Mainz	Detector Tests	48Ca, 238U	**0(11)**
E046	ESR	Stöhlker	GSI, Univ. Heidelberg, HI Jena	Inverse Photoionization	86Kr	**13(0)**
E067	ESR	Novotny	GSI, Univ. Mainz	Test of Special Relativity	7Li	**37(0)**
E071	ESR	Hagmann	GSI, Univ. Frankfurt	Inelasitc Electron Scattering	86Kr	**7(0)**
E075	ESR	Herfurth	GSI	Commissioning HITRAP	84Kr, 86Kr	**49(0)**
E079, E096	ESR	Brandau	LMU München	Dielectronic Recombination	238U	**18(0)**
E082	ESR	Litvinov	MPI-K Heidelberg	Beta-Decay	152Sm	**128(0)**

E084	ESR	Knöbel	GSI	Mass Measurements	238U	**24(0)**
E101	ESR	Thorn	HI Jena	X-ray Polarization	238U	**19(0)**
FRS00	FRS	Geissel	GSI, Univ. Gießen	Detector and Performance Tests	238U	**13(0)**
ESA1	HTA	Duarte, Metzger, Scholz	Fraunhofer Gesellschaft, GSI	Irradiation Experiments	40Ar, 58Ni, 64Ni, 238U	**12(0)**
S272	FRS	Tanihata	RCNP Osaka	Mass Measurements	58Ni	**49(0)**
S306	HTC	Datta Pramanik	Saha Inst. Kolkata	Nuclear Shell Structure	40Ar	**16(0)**
S319	HTC	Saito	GSI, Univ. Mainz	Hypernuclei	20Ne	**29(0)**
S321	HHT	Ulrich	TU München	Ion Pumped Excimer Lasers	238U	**0(15)**
S331	HHT	Mintsev	IPCP Chernogolovka	HEDP/WDM	238U	**0(21)**
S333	HAD	Salabura	Univ. of Kraków	Commissioning HADES	48Ca, 64Ni,197Au, 238U	**4(48)**

S351	HTA	Yamazaki	Univ. of Tokyo	Channelling	238U	**18(0)**
S362	HTB	Ketzer	TU München	Detector Tests	84Kr	**0(12)**
S363	FRS	Bentley	Univ. of York	Commissioning PRESPEC	64Ni, 86Kr	**0(25)**
S367	HHT	Tauschwitz	GSI	Opacity Measurements	238U	**0(7)**
S369	FRS	Jolie	Univ. Köln	PRESPEC	238U	**18(0)**
S372	FRS	Cederkall	Univ. of Lund	PRESPEC	124Xe	**15(0)**
S387	FRS	Marrocchesi	Univ. of Siena	MATRIX	64Ni	**0(11)**
S389	HTC	Wiescher	Univ. of Notre Dame	Coulomb Dissociation	64Ni	**21(0)**
S393	HTC	Aumann	GSI	Neutron-rich Nuclei	40Ar, 48Ca	**51(5)**
S394	HTC, HTD	Lemmon	Univ. of Liverpool	Nuclear Symmetry Energy	152Sm, 197Au	**0(26)**

S397	HHT	Ulrich	TU München	Diagnostics for Heavy Ion Beams	238U	**0(10)**
S401	HTB	Heuser	GSI	Detector Tests	7Li	**(0)13**
SBIO	HTA, HTM	Schardt, Scholz	GSI	Irradiation Experiments	7Li, 12C, 14N, 58Ni, 238U	**17,1(0)**
SESA	HTA	Durante, Schardt	TU Darmstadt, GSI	Irradiation Experiments	40Ar, 58Ni, 64Ni	**7,4(0)**
SMAT	HTA	Schuster	TU Darmstadt, GSI	Irradiation Experiments	197Au, 238U	**58(5)**
STHE	HTA, HTM	Schardt	GSI	Irradiation Experiments	7Li, 14N, 58Ni	**12,5(0)**
U182	UX8	Kratz	Univ. Mainz	Chemistry of SHE	24Mg	**10(0)**
U218	UX7	Boutachkov	GSI	Nuclear Coulomb Excitation	48Ca	**0(20)**
U225	UX8	Heßberger	GSI	Nuclear Structure of SHE	40Ar	**26(0)**
U231	UX8	Türler	PSI	Chemistry of SHE	24Mg	**10(0)**

U238	UY7	Block	GSI	Mass Measurements of SHE	48Ca	**39(9)**
U239	UX8	Düllmann	GSI, Univ. Mainz	Towards Element 117	64Ni	**0(8)**
U241	UX8	Andersson	Uni. of Liverpool	TASISpec	48Ca	**37(0)**
U246	UX7	Leske	TU Darmstadt	Nuclear Structure	86Kr	**16(0)**
U248	UY7	Hofmann	GSI	SHE	48Ca	**94(0)**
U249	HTA	Berdermann	GSI	Detector Tests	40Ar, 86Kr	**0(5)**
U250	UY7	Ackermann	GSI	270Ds	64Ni	**61(0)**
U252	UZ6	Blazevic, Roth	GSI, TU Darmstadt	Energy Loss in Plasma	40Ar, 48Ca	**0(31)**
UBIO	UX0, UX6	Friedrich, Scholz, Voss	GSI	Irradiation Experiments	12C, 14N, 20Ne, 48Ca, 64Ni, 84Kr, 197Au	**37,6(16,1)**
UESA	UX3	Kozhuharov	GSI	Irradiation Experiments	197Au	**6(0)**

UMAT	UX0, M-branch	Schuster, Severin, Trautmann, Voss	TU Darmstadt, GSI	Irradiation Experiments	7Li, 48Ca, 64Ni, 152Sm, 197Au, 238U	**81(151)**

D. Liesen, 23.2.2011

References of experiment proposal numbers to the contributions of this report

U219 PHN-NUSTAR-SHE-06
U219 PHN-NUSTAR-SHE-07
U222 PHN-NUSTAR-FRS-25
U241 PHN-NUSTAR-SHE-08
U248 PHN-NUSTAR-SHE-01
U249 PHN-IS-DL-02,
PHN-IS-DL-03
U250 PHN-NUSTAR-SHE-03
U264 PHN-NUSTAR-SHE-02

S037 PHN-NQM-FOPI-04
S245 PHN-NUSTAR-NR-01,
PHN-NUSTAR-NR-02
S247 PHN-NUSTAR-NR-03
S254 PHN-NUSTAR-NR-15
S272 PHN-NUSTAR-FRS-17
S276 PHN-NUSTAR-NR-17
S295 PHN-NUSTAR-NR-09
S296 PHN-NUSTAR-NR-05
S309 PHN-HSD-HPII-01
S318 PHN-NUSTAR-NR-06,
PHN-NUSTAR-NR-07
S319 PHN-HSD-HPII-02
S322 PHN-NUSTAR-FRS-14,
PHN-NUSTAR-FRS-15,
PHN-NUSTAR-FRS-18,
PHN-NUSTAR-FRS-19
S325 PHN-NQM-FOPI-01,
PHN-NQM-FOPI-02,
PHN-NQM-FOPI-03
S327 PHN-NUSTAR-NR-08
S330 PHN-NUSTAR-FRS-20
S341 PHN-NUSTAR-FRS-16
S362 PHN-HSD-PANDA-09
S363 PHN-NUSTAR-FRS-03
S371 HEALTH-43
S387 PHN-NUSTAR-FRS-12
S389 PHN-NUSTAR-NR-10
S392 PHN-NUSTAR-FRS-13
S393 PHN-NUSTAR-NR-04
S394 PHN-NQM-FOPI-05

E000 PHN-ACC-RD-20,
PHN-ACC-RD-45
E062 PHN-NUSTAR-FRS-26
E073 PHN-NUSTAR-FRS-21
E082 PHN-NUSTAR-FRS-23

BIO-05-003 HEALTH-11,
HEALTH-16
BIO-05-012 HEALTH-14
BIO07 HEALTH-02,
HEALTH-05,
HEALTH-07
BIO20 HEALTH-01,
HEALTH-03
BIO21 HEALTH-08,
HEALTH-10,
HEALTH-15
BIO24 HEALTH-19
PT-05-002 HEALTH-32,
HEALTH-34
PT08 HEALTH-47
PT16 HEALTH-30,
HEALTH-31

Statutory organs and scientific advisory committees of GSI (2010)

Compiled by K.-D. Groß

Supervisory Board/Aufsichtsrat:

Dr. B. Vierkorn-Rudolf [chair],
Bundeministerium für Bildung und Forschung, Bonn/Berlin (Germany),
as representative of the Federal Republic of Germany

Ministerialrätin O. Keppler,
Bundesministerium für Bildung und Forschung, Bonn/Berlin (Germany),
as representative of the Federal Republic of Germany

Ministerialdirigent Dr. R. Bernhardt,
Hessisches Ministerium für Wissenschaft und Kunst, Wiesbaden (Germany),
as representative of the State of Hesse in Germany

Prof. Dr. K.-H. Kampert
Bergische Universität Wuppertal (Germany),
as representative of the Scientific Council of GSI

Scientific Directorate/Wissenschaftliches Direktorium WD:

Prof. Dr. H. Stöcker, C. Neumann (until August 31st, 2010)
Dr. H. Eickhoff, Prof. Dr. K. Langanke, B. Schönfelder

Divisions/Direktionsbereiche:

Accelerator: *H. Eickhoff /O. Kester (since December 1th, 2010)*
Administration: *C. Neumann (until August 31st, 2010)*
Human Resources and Legal Services: *A. Lambert*
Finances / Controlling / admin. Organisations: *J. Heilmann*
FAIR Scientific Director: *B. Sharkov*
FAIR Administration: *S. Richter*
FAIR Research Director: *Z. Majka*
FAIR Technical Director: *D. Krämer*
Research: *K. Langanke*
Scientific and Technical Infrastructure: *B. Schönfelder*

Research Departments/Forschungsabteilungen:

ALICE: *P. Braun-Munzinger*
Atomic Physics: *T. Stöhlker*
Biophysics: *M. Durante*
CBM: *P. Senger*
FOPI: *Y. Leifels*
FRS: *H. Geissel*
HADES: *J. Stroth*
Hadron Physics I: *K. Peters*
Hadron Physics II: *F. Maas*

Materials Research: *R. Neumann (until October 31st, 2010)*
C. Trautmann (provisionally since November 1st, 2010)
Nuclear Reactions and Astrophysics: *T. Aumann*
Nuclear Structure Physics: *C. Scheidenberger*

Plasma Physics and PHELIX: *T. Stöhlker (provisional)*
Superheavy Elements: *F.-P. Hessberger*
Nuclear Chemistry: *M. Schädel / C. E. Düllmann*
Theory - Lattice QCD: *F. Karsch*
Theory - Nuclear Structure and Astrophysics: *H. Feldmeier*
Theory - QCD and Hadron Physics: *J. Wambach*
HP & Scientific Computing and IT: *P. Braun-Munzinger/V. Lindenstruth*

Scientific Council/Wissenschaftlicher Rat WR:

http://www.gsi.de/informationen/users/EAC/wr/

K.-H. Kampert [chair], Bergische Universität Wuppertal (Germany); *D. von Harrach [vice chair]*, Johannes-Gutenberg-Universität Mainz (Germany); *A. Bracco*, University of Milano (Italy); *P. Chomaz*, Irfu/SPP, Gif-sur-Yvette (France); *R. Hayano*, University of Tokyo (Japan); *R. Heuer*, European Organization of Nuclear Research, CERN, Geneva (Switzerland); *B. Jacak*, Stony Brook University, Stony Brook, New York (USA); *S. Myers*, CERN AB, Geneva (Switzerland); *T. Roser*, BNL, Upton (USA); *R. Sauerbrey*, Forschungszentrum Rossendorf, Dresden (Germany); *D. Vernhet*, Université Paris (France); *M. C. Wiescher*, University of Notre Dame, Notre Dame, Indiana (USA).
Secretary: K.-D. Groß

Scientific Committee/Wissenschaftlicher Ausschuss WA:

http://www-w2k.gsi.de/wa/scientific_committee.htm

H. Simon [chair]*; Y. Leifels* [vice chair]*; D. Ackermann; E. Badura; J. Heuser; B. Lommel; M. Lutz; P. Malzacher; M. Reich-Sprenger; C. Schmidt; L. Schmitt; M. Scholz; G. Schreiber; J. Stadlmann; M. Steck; C. Trautmann; H. Weick; U. Weinrich; A. Bräuning-Demian* (guest)*; H. Kreiser* (guest).

Scientific Advisory Committees of GSI

GSI General Program Advisory Committee G-PAC:

http://www.gsi.de/informationen/users/EAC/ea/

P. Giubellino[chair], INFN Turin, Turin (Italy); *B. Blank*, CEN Bordeaux-Gradignan, Gradignan (France); *Y. Blumenfeld*, CERN, Geneva (Switzerland); *W. Catford*, University of Physics, Guilford (UK); *R. Hoekstra*, KVI Groningen, Groningen (The Netherlands); *S. Leupold*, Uppsala University, Uppsala (Sweden); *N. Pietralla*, Technische Universität Darmstadt, Darmstadt (Germany); *H. Schatz*, Michigan State University, East Leasing (USA); *R. Schuch*, Stockholm University, Stockholm (Sweden); *A. Türler*, Paul Scherer Institut, Villigen (Switzerland); *M. Wada*, RIKEN, Saitama (Japan); *M. Weidemüller*, Ruprecht-Karls-Universität Heidelberg, Heidelberg (Germany).

GSI Phelix and Plasmaphysics Program Advisory Committee (PPAC):

http://www.gsi.de/informationen/users/EAC/ppac/

D. Schneider [chair], LLNL-PAT/NIF, Livermore, California (USA); *S. Jacquemot*, LULI, Ecole Polytechnique, Palaiseau (France); *B. G. Logan*, LBL, Berkeley, California (USA); *G. Maynard*, CNRS, Orsay (France); *T. A. Mehlhorn*, Naval Research Laboratory, Washington DC (USA); *O. Willi*, Heinrich Heine Universität Düsseldorf, Düsseldorf (Germany).

GSI Biophysics & Radio-Biology Program Advisory Committee (Bio-PAC):

http://www.gsi.de/informationen/users/EAC/bio-pac/

G. Iliakis [chair], Universitätsklinikum Essen, Essen (Germany); *F. A. Cucinotta*, NASA Johnson Space Center, Houston, Texas (USA); *T. Haberer*, HIT Betriebs GmbH am Universitätsklinikum Heidelberg, Heidelberg (Germany); *A. Kronenberg*, Lawrence Berkeley National Laboratory, Berkeley, California (USA); *R. Okayasu*, International Space Radiation Laboratory, Chiba (Japan); *G. Reitz*, DLR German Aerospace Center, Cologne (Germany); *L. Sabatier*, Institute of Cell. & Mol. Radiation Biology, Fonteney-aux-Roses (France).

GSI Materials Research Program Advisory Committee (Mat-PAC):

http://www.gsi.de/informationen/users/EAC/mat-pac/

P. Apel, JINR, Dubna (Russia); *S. Bouffard*, CEA-CNRS-ENSICAEN, Caen (France); *K. Hjort*, University of Uppsala, Uppsala (Sweden); *W. Wesch*, Friedrich-Schiller-Universität Jena, Jena (Germany).

Program Advisory Committee for FAIR-Related Beam Time Proposals (F-PAC):

J. Stadlmann [chair], GSI; Z. Majka, FAIR; L. Schmitt, GSI; W. Müller, GSI; C. Trautmann, GSI; H. Weick, GSI.

GSI Users' Group Executive Committee (UEC):

http://www.gsi.de/forschung/usersgroup/index.html

Nuclear Structure:
T. Faestermann (Germany); M. Pfutzner (Poland); D. Cortina (Spain); A. Jungclaus (Spain); P. Regan [past chair], (UK)
Nuclear Collision:
P. Salabura (Poland); T. Matulewicz (Poland); Nicole Bastid (France)
Atomic Physics:
D. Dauvergne (France); A. Mueller (Germany)
Plasma Physics:
J. Kratz (Germany); A. Türler (Germany)
Theory:
W. Cassing (Germany)
Biophysics:
M. Löbrich (Germany)
Materials Research:
W. Ensinger [chair], (Germany)
Students:
B. Schuster (Germany)

Scientific Coordination:

Dr. K.-D. Groß

Organigramm

GSI Helmholtzzentrum für Schwerionenforschung GmbH

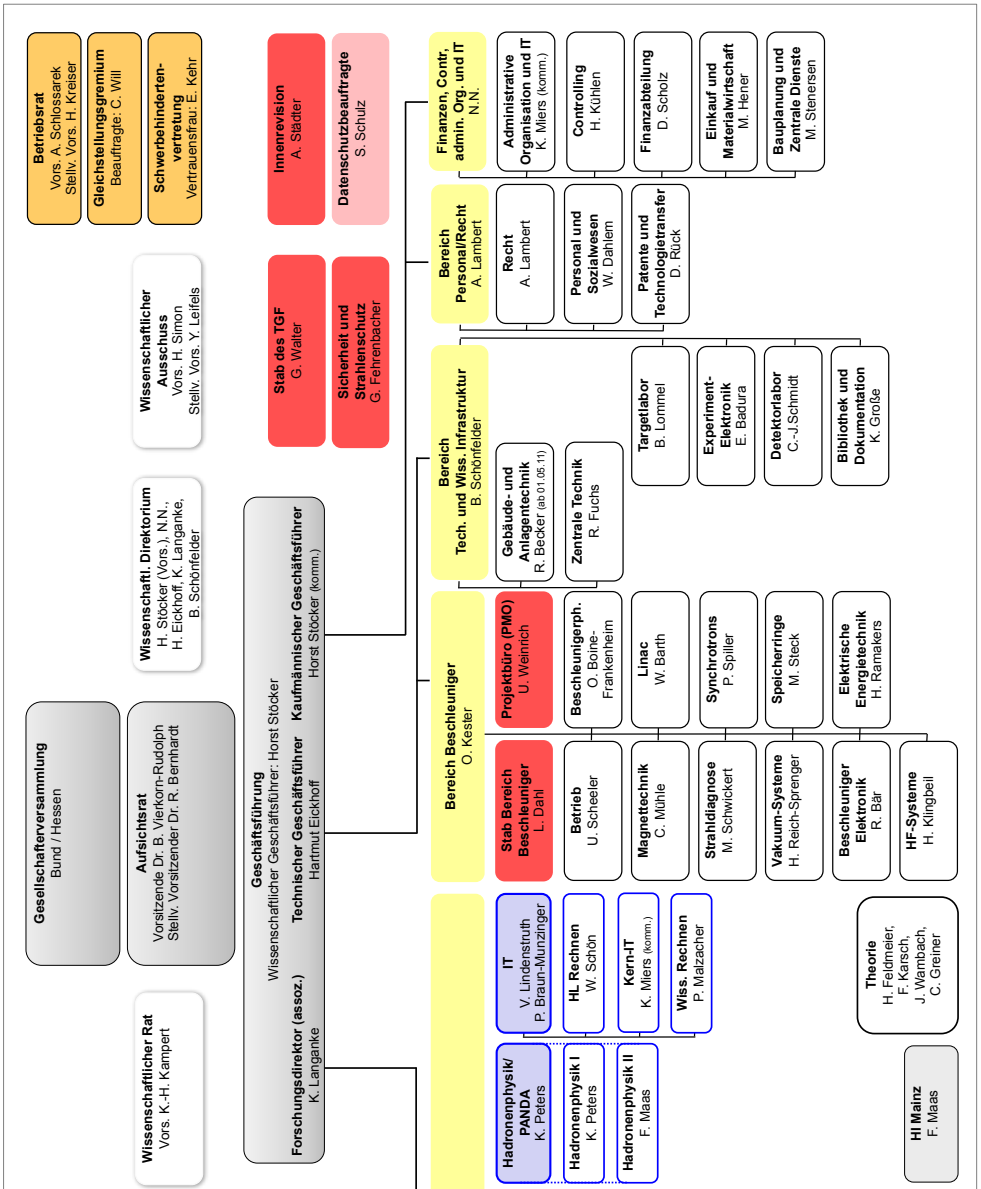

Stand April 2011.
Der Geschäftsbereich FAIR ist mit Gründung der FAIR GmbH am 4. Oktober 2010 weggefallen. Voraussichtlich im Sommer 2011 soll der neue GSI-Gesellschaftsvertrag wirksam werden. Die Länder Rheinland-Pfalz und Thüringen werden weitere Gesellschafter der GSI, die wissenschaftlichen Organe WA und WD werden durch den Wissenschaftlich-Technischen Rat (WTR) ersetzt.

List of Authors